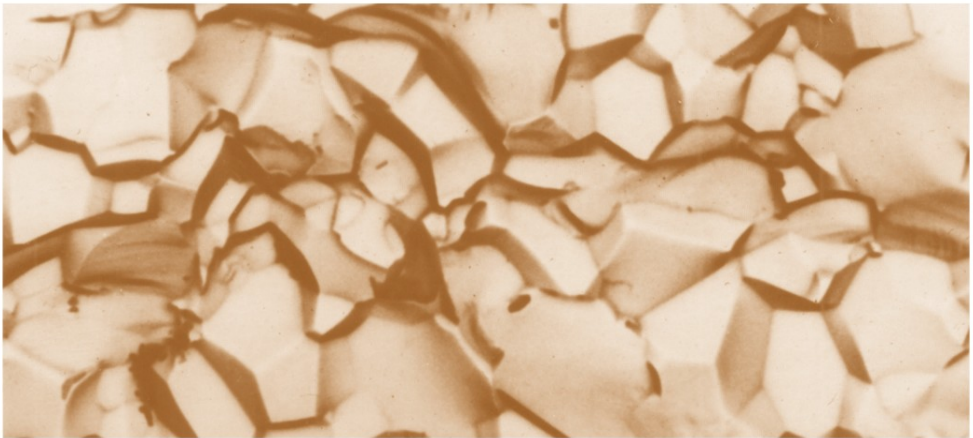


Fracture Mechanics of Ceramics

Active Materials, Nanoscale Materials,
Composites, Glass, and Fundamentals



R. C. Bradt, D. Munz, M. Sakai,
and K. W. White

Fracture Mechanics of Ceramics

Active Materials, Nanoscale Materials,
Composites, Glass and Fundamentals

- Volume 1 Concepts, Flaws, and Fractography
- Volume 2 Microstructure, Materials, and Applications
- Volume 3 Flaws and Testing
- Volume 4 Crack Growth and Microstructure
- Volume 5 Surface Flaws, Statistics, and Microcracking
- Volume 6 Measurements, Transformations, and High-Temperature Fracture
- Volume 7 Composites, Impact, Statistics, and High-Temperature Phenomena
- Volume 8 Microstructure, Methods, Design, and Fatigue
- Volume 9 Composites, R-Curve Behavior, and Fatigue
- Volume 10 Fracture Fundamentals, High-Temperature Deformation, Damage, and Design
- Volume 11 R-Curve Behavior, Toughness Determination, and Thermal Shock
- Volume 12 Fatigue, Composites, and High-Temperature Behavior
- Volume 13 Crack–Microstructure Interaction, R-Curve Behavior, Environmental Effects in Fracture, and Standardization
- Volume 14 Active Materials, Nanoscale Materials, Composites, Glass and Fundamentals

Fracture Mechanics of Ceramics

Active Materials, Nanoscale Materials, Composites, Glass and Fundamentals

Edited by

R. C. Bradt

University of Alabama
Tuscaloosa, Alabama

D. Munz

University of Karlsruhe
Karlsruhe, Germany

M. Sakai

Toyohashi University of Technology
Toyohashi, Japan

and

K. W. White

University of Houston
Houston, Texas



Springer

Proceedings of the 8th International Symposium on Fracture Mechanics of Ceramics, held February 25–28, 2003, at the University of Houston, Houston, Texas

ISSN: 0197-2766

ISBN-10: 0-387-24134-5

Printed on acid-free paper.

ISBN-13: 978-0387-24134-0

© 2005 Springer Science+Business Media, Inc.

All rights reserved. This work may not be translated or copied in whole or in part without the written permission of the publisher (Springer Science+Business Media, Inc., 233 Spring Street, New York, NY 10013, USA), except for brief excerpts in connection with reviews or scholarly analysis. Use in connection with any form of information storage and retrieval, electronic adaptation, computer software, or by similar or dissimilar methodology now known or hereafter developed is forbidden.

The use in this publication of trade names, trademarks, service marks and similar terms, even if they are not identified as such, is not to be taken as an expression of opinion as to whether or not they are subject to proprietary rights.

Printed in the United States of America.

9 8 7 6 5 4 3 2 1 (SPI/EB)

springeronline.com

CONTENTS

| | |
|--|-----|
| Preface | ix |
| 1. Contact Mechanics | |
| Atomic Force Microscopy at Ultrasonic Frequencies Walter Arnold, A. Caron, S. Hirsekom, M. Kopycinska-Müller, U. Rabe, M. Reinstädler | 1 |
| Indentation Size Effect on the Hardness of Zirconia Polycrystals T. Akatsu, S. Numata, M. Yoshida, Y. Shinoda, F. Wakai | 13 |
| Indentation Fracture, Acoustic Emission and Modelling of the Mechanical Properties of Thin Ceramic Coatings S.J. Bull, I. Arce-Garcia, E.G.-Berasetegui and T.F. Page | 21 |
| Nanoindentation, Nanoscratch and Nanoimpact Testing of Silicon-Based Materials with Nanostructured Surfaces Jinjun Lu, T. Xu, Q. Xue, B.D. Beake | 43 |
| Microstructural Control of Indentation Crack Extension under Externally Applied Stress Robert F. Cook | 57 |
| Instrumented Hardness Test on Alumina Ceramics and Single Crystal with Spherical Indenter Shuji Sakaguchi, K. Hirao, Y. Yamauchi, S. Kanzaki | 69 |
| 2. Glass | |
| Controlling the Fragmentation Behavior of Stressed Glass R. Tandon, S.J. Glass | 77 |
| Elasto-Plastic Behavior of Glassy Carbon and Silica Glass by Nanoindentation With Spherical-Tipped Indenter N. Iwashita, M. Swain, J.S. Field | 93 |
| Scratch Test for Evaluation of Surface Damage in Glass S. Yoshida, T. Hayashi, T. Fukuhara, K. Soeda, J. Matsuoka, N. Soga | 101 |
| Shear-Driven Damage and Internal Friction in Indentation Loading of a Glass-Ceramic Anthony Fischer-Cripps | 113 |
| Indentation and Scratching of Glass: Load, Composition, Environment and Temperature Effects Jean-Christophe Sangleboeuf, Tanguy Rouxel | 121 |

| | |
|---|-----|
| Effects of Tin on the Physical Properties and Crack Growth in Soda-Lime-Silica Float Glass Matthew H. Krohn, John R. Hellmann, Carlo G. Pantano, Nathan P. Lower, and Richard K. Brow | 135 |
| Indentation Size Effects for Glasses: Yes, There is a Fracture George D. Quinn | 149 |
| 3. Fracture of Nano-Scale Materials | |
| Slow Crack Propagation in Ceramics at the Nano- and Micro- scale: Effect of the Microstructure J. Chevalier, G. Fantozzi | 173 |
| Toughening and Strengthening Mechanisms in Nanocomposites based on Dislocation Activity Hideo Awaji, S-M Choi | 191 |
| 4. Composites | |
| Creep Behavior and Mechanisms for CMCs with Continuous Ceramic Fibers Jean-Louis Chermant, Gaëlle Farizy, Guillaume Boitier, Séverine Darzens, Jean Vicens, and Jean-Christophe Sangleboeuf | 203 |
| Strain Accumulation and Damage Evolution during Creep of SiC _f /SiC Composites B. Wilshire, H. Burt | 221 |
| Modeling Multilayer Damage in Cross-ply Ceramics Matrix Composites M. Kashtalyan, H.W. Chandler | 233 |
| Quantification of Toughness Increase Due to Metal Particles in Glass Matrix Composites M. Kotoul, A.R. Boccaccini, I. Dlouhy | 245 |
| Fracture Resistance of Hybrid Glass Matrix Composite and its Degradation Due to Thermal Aging and Thermal Shock I. Dlouhy, Z. Chlup, S. Atiq, A.R. Boccaccini | 263 |
| Creep Investigation on SiC _f -SiBC Composites Gaëlle Farizy, Jean-Louis Chermant, Jean Vicens, Jean-Christoph Sanglebœuf | 275 |
| Fracture Toughness of BaTiO ₃ – MgO Composites Sintered by Spark Plasma Sintering S. Rattanachan, Y. Miyashita | 287 |

| | |
|---|-----|
| Contents | vii |
| Fracture Toughness of BaTiO ₃ and BaTiO ₃ -Al ₂ O ₃ Composite Under Applied Electric Field | 297 |
| S. Rattanachan, Y. Miyashita, Y. Mutoh | |
| Room temperature Post-Fracture Tensile (PFT) Study of Two Fiber-Reinforced Ceramic Matrix Composites with a “Strong” Fiber/Matrix Interface | 307 |
| R.A. Longoria, N. Du Souich, K.W. White | |
| An FE Model of Carbon/Carbon Composite Fracture | 317 |
| J. Ohgi, J.H.. Jackson, A.S. Kobayashi, K.W. White | |
| 5. Fracture Fundamentals | |
| Tailoring the Composition of Self-Reinforced Silicon Nitride Ceramics to Enhance Mechanical Behavior | 327 |
| P.F. Becher, G.S. Painter, H.T. line and M.K. Ferber | |
| Nonlinear Fracture of a Polycrystalline Graphite: Size-Effect Law and Irwin’s Similarity | 337 |
| Motosugu Sakai, R. Nonoyama | |
| Fragmentation of Ceramics in Rapid Expansion Mode | 353 |
| S. Maiti, P. Geubelle, K. Rangaswamy | |
| Experimental Approach to Microfracture Process of Ceramics Under Thermal Shock | 365 |
| S. Wakayama, K. Nishino, K. Kubota, T. Wada, S. Kobayashi | |
| Finite Element Analysis of Crack-Path Selection in a Brick and Mortar Structure | 375 |
| R. Sarrafi-Nour, M. Monaharan, and C.A. Johnson | |
| Investigation of Crack Growth Process in Dense Hydroxyapatite using the Double Torsion Method | 387 |
| C. Benaqqa, J. Chevalier, M. Saâdaoui, and G. Fantozzi | |
| Crack Propagation Behavior of Alumina with Different Grain Sizes Under Static and Cyclic Fatigue | 399 |
| H. El Attaoui, M. Saadaoui, J. Chevalier, G. Fantozzi | |
| Effects of Pore/Grain-Size Interaction and Porosity on the Fracture of Electroceramics | 411 |
| C. Lu, R. Danzer, F. Fischer | |
| 6. Fracture of Coatings | |
| Fracture Behaviour of Plasma Sprayed Thermal Barrier Coatings | 421 |
| J. Malzbender, T. Wakui, E. Wessel, R.W. Steinbrech | |

| | |
|---|-----|
| Particle Impact Damage and Point Load-Induced Fracture Behavior in Zirconia Plasma Spray Coating Film Y. Akimune, K. Matsuo, T. Sugiyama, H. Yoshida, S. Sodoeka, S. Shimizu | 437 |
| Mode I, Mode II, and Mixed-Mode Fracture of Plasma-Sprayed Thermal Barrier Coating at Ambient and Elevated Temperatures Sung R. Choi, D. Zhu, R. Miller | 451 |
| 7. Ferroelectric Materials | |
| Modeling of Fracture in Ferroelastic Ceramics C.M. Landis | 471 |
| Strength and Reliability of Lead Zirconate Titanate Ceramics C.S. Watson | 485 |
| 8. Reliability Prediction, Standardization and Design | |
| Standard Reference Material 2100: Fracture Toughness of Ceramics G.D. Quinn, K. Xu, R. Gettings, J.A. Salem, J.J. Swab | 499 |
| Measuring the Real Fracture toughness of Ceramics – ASTM C1421 J.A. Salem, G.D. Quinn, M.G. Jenkins | 531 |
| Predicting the Reliability of Brittle Material Structures Subjected to Transient Proof Test and Service Loading N.N. Nemeth, O.M. Jadaan, T. Palfi, and E.H. Baker | 555 |
| Estimation and Stimulation of Slow Crack Growth Parameters from Constant Stress Rate Data J.A. Salem, A.S. Weaver | 579 |
| On Integrity of Flexible Display P.C.P. Bouten | 597 |
| Fracture of Conductive Cracks in Poled and Depoled PZT-4 Ceramics Tong-Yi Zhang | 609 |
| Increasing Resistance to Low Temperature Ageing Degradation of Y-TZP by Surface Modification A. Feder, P. Morcillo, M.J. Anglada | 625 |
| Index | 635 |

PREFACE

The 8th International Symposium on fracture mechanics of ceramics was held on the campus of the University of Houston, Houston, TX, USA, on February 25-28, 2003. This marks three decades of progress in the science and technology development in ceramics since the first meeting of this group, held at the Pennsylvania State University in 1973, which was published in Volumes 1 and 2 of this series. The meetings continued over approximately four year intervals, held subsequently in Virginia Polytechnic Institute and State University, Japan Fine Ceramics Center, Nagoya, Japan, and Kernforschungszentrum, Karlsruhe, Germany.

With the natural maturing of the fields of structural ceramics, the present symposium has focused on nano-scale materials, composites, thin films and coatings as well as glass. The symposium also addressed new issues on fundamentals of fracture mechanics and contact mechanics, and a session on reliability and standardization.

The International Organizing Committee gratefully acknowledges the support from the Cullen College of Engineering, and the dedicated help from the local organizing committee. This includes Prof. L. Wheeler, Prashant Haldipur, Jennifer Husmo, Sandra Luna, Charlotte Palm and Jonathan Claydon. Additionally, I wish to thank the materials students who participated in the effort: Duo Liu, Mike Chelf, Marcos Flores, Rafael Longo and Yi Fang.

Special thanks are extended to NASA Astronaut Dr. Bonnie Dunbar for her wonderful banquet presentation.

Tuscaloosa, AL USA
Karlsruhe, Germany
Toyohashi, Japan
Houston, TX USA

R.C. Bradt
D. Munz
M. Sakai
K.W. White

ATOMIC FORCE MICROSCOPY AT ULTRASONIC FREQUENCIES

W. Arnold, A. Caron, S. Hirsekorn,
M. Kopycinska-Müller, U. Rabe, and M. Reinstädler*

I. INTRODUCTION

Atomic Force Microscopy (AFM) is a near-field technique to generate high-resolution images of surfaces. A micro-fabricated elastic beam with an integrated sharp sensor tip at its end is scanned over the sample surface. With various dynamic modes, leading to Force Modulation Microscopy [1], Ultrasonic Force Microscopy [2], Atomic Force Acoustic Microscopy (AFAM) [3–5], Microdeformation Microscopy [6], Scanning Local Acceleration Microscopy [7] or Pulsed Force Microscopy [8], images can be obtained in which the contrast depends on the elasticity of the sample surface. However, quantitative determination of Young's modulus of a sample surface with AFM is a challenge, especially when stiff materials such as hard metals or ceramics are encountered. In this presentation the basic idea of AFAM, i.e. the evaluation of the cantilever vibration spectra at ultrasonic frequencies is discussed. The AFAM technique can be used for imaging as well as to discern local elastic data quantitatively. Nanocrystalline magnetic materials [9], multidomain piezoelectric materials and silicon [10], diamond-like carbon layers [11], polymeric materials and clay crystals [12] have been examined previously. The spatial resolution of the AFAM technique is approximately 10 nm.

In an Atomic Force Acoustic Microscopy set-up [3-5] either the sample is insonified or the cantilever suspension is excited at ultrasonic frequencies. The vibration spectra of the cantilever depend on the local sample stiffness and hence

* Fraunhofer-Institute for Nondestructive Testing (IZFP), Bldg. 37, University, D-66123 Saarbrücken, Germany

on the local elasticity of the sample constituents. Acoustic images can be obtained by measuring the cantilever vibration amplitude at a frequency close to a contact resonance or by monitoring the resonance frequency [13,14]. With this technique it is possible to resolve the differences in the local tip-sample stiffness between phases and/or grains having different crystal lattice orientation. In the case of ferroelectric materials the presence of the domains influences the local elastic properties within each individual grain. Depending on the method of sample preparation, for example etching, one can make domain patterns visible on the sample surface using AFM [15]. In this case the contrast is caused by topography. A variety of AFM techniques have been applied to image or modify the domains in ferro- electric single crystals as well as in thin films [16,17]. The AFAM technique allows domain structure imaging in single crystals and in ceramics, even when domains do not appear in the topography image [18]. Coupling the AFAM technique with the so-called piezo-mode [16,18–21] can additionally provide information about domain polarization and the orientation of the grains within the crystal lattice [20].

2. AFAM EXPERIMENTAL TECHNIQUE

An AFM cantilever clamped on one side and free on the other can be described as a micro-beam with a characteristic set of free resonance frequencies. The most common modes excited are either flexural or torsional. Values of the free flexural or torsional oscillations can be measured with e.g. an instrument such as a Dimension 3000 Nanoscope (Digital Instruments, Santa Barbara, Ca USA) or a Solver P47H (NT-MDT, Zelenograd, Russia) which were employed for this study. When the cantilever approaches the sample surface and finally touches it, the forces interacting between the cantilever tip and the surface modify the boundary condition of the vibrating cantilever [4,5]. As a result, the resonance frequencies shift to higher values. These resonance frequencies are called contact resonance frequencies (Fig. 1 and Fig. 2). The values of free and contact resonance frequencies can be calculated as discussed previously [4,5]. From the difference of the contact resonance frequencies relative to the free resonances, one obtains the vertical or lateral contact stiffness [5, 22] which itself depend on both the elastic moduli of the sample and the tip, and their Poisson ratio, respectively [23,24]. As shown in Fig. 1, the tip contacts the sample surface over a certain contact area which is inferred indirectly by using a calibration material of known elasticity. Detailed information about tip-sample interactions and methods of evaluating local tip-sample contact stiffness can be found elsewhere [9,10,25]. Under certain circumstances, the local elastic modulus or the so-called indentation modulus M [24] can be derived from the contact stiffness [9,10,18]. At present the contribution of adhesion forces to the contact stiffness is made small in AFAM measurements by applying a sufficiently high static force on the cantilever so that the Hertzian contact forces are dominant [23]. When evaluating the vertical contact stiffness, the lateral forces to k^* are neglected. The indented volume is about $\pi r_h^2 \times 3r_h \approx 500 \text{ nm}^3$ where r_h is the contact radius, here about 10 nm or less.

The contact resonance frequencies are excited by an ultrasonic transducer, which emits longitudinal waves or shear waves into the sample. Figure 2 displays the normalized contact resonance spectra of the first (Fig. 2a) and second (Fig. 2b) flexural mode measured on fused quartz, silicon, and sapphire. The spring constant

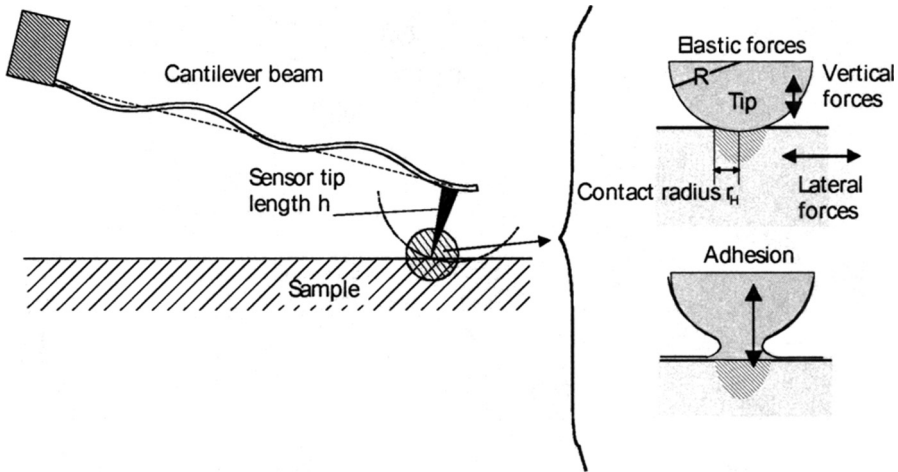


Figure 1. Principle of Atomic Force Acoustic Microscopy. Using the shift of the contact resonance frequencies relative to the free resonances, one can determine the local elastic constants of a material. The adhesion forces contribute to the measured vertical contact stiffness as well. Their influence can be neglected, provided the static forces are adjusted so that they are much larger than the adhesion forces.

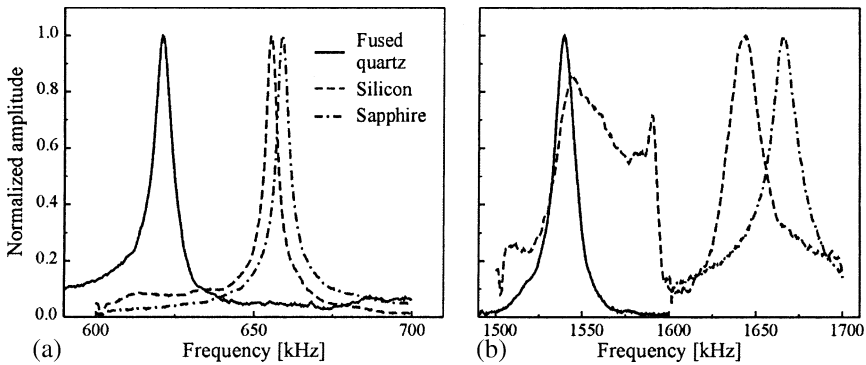


Figure 2. Normalized contact resonance spectra of the first (Fig. 2a) and second (Fig. 2b) flexural mode measured on samples with different elastic properties. The second mode on silicon shows a triple resonance.

of the cantilever was 44 N/m and the free resonance frequencies were 164 kHz and 1023 kHz for the first and second mode, respectively (not shown). The values of the indentation modulus of the reference samples varied from 77 (fused quartz), to 165 GPa (silicon), and to 423 GPa (sapphire). Very often double or triple resonance appear which are caused either by mode-coupling [26] or by multiple contacts between the tip and the surface.

In contact the resonance frequency varies during scanning and hence the amplitude and the phase of the cantilever vibration vary as well if the excitation frequency of the transducer is kept constant. This amplitude and phase contain information about the local tip-sample stiffness, and hence can be used as imaging quantities, see Fig. 3. It shows an AFAM-amplitude image of a lead calcium titanate film annealed at 650° C. The size of the images is $2 \times 2 \mu\text{m}^2$. The cantilever material was coated with a conductive diamond-like layer. The overall spring constant was

44 N/m and the free resonance frequency of the first flexural mode of the cantilever was 188 kHz. The contrast seen in an amplitude image depends on the frequency of the applied ultrasound relative to the contact resonance frequency. At a frequency of 733 kHz the softer grains appear brighter than the stiffer grains (Fig. 3a). Imaging at a higher frequency, 791 kHz, the contrast of the image inverts (Fig. 3b) and the stiffer grains appear now brighter than the more compliant grains. This contrast inversion has been known for a long time and has been noticed by several groups. Figure 4 shows an AFAM image of a nanocrystalline nickel sample based on monitoring the local contact resonance. From this measuring quantity, the local stiffness k^* is determined and then used as an imaging quantity. Values of the k^* ranged from 728 to 992 N/m. The tip used in this experiment was made from silicon, making it susceptible to tip wear [11]. The spring constant of the cantilever employed was 48 N/m and its free resonance frequencies were 166 and 1031 kHz for the first and second mode, respectively. The size of the image is $1.5 \times 1.4 \mu\text{m}^2$. The image clearly shows ensemble of grains in the nanocrystalline structure.

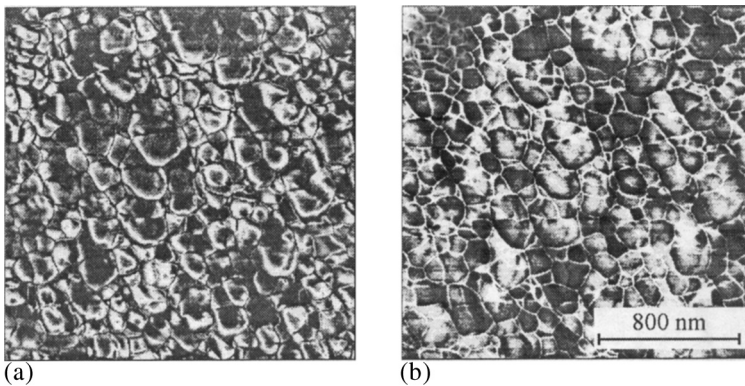


Figure 3. AFAM-amplitude images of a lead calcium titanate thin film annealed at 650°C . The contrast is caused by a shift of the resonance frequency when the contact stiffness changes locally. This in turn causes a change of the signal amplitude when the excitation frequency is kept constant.

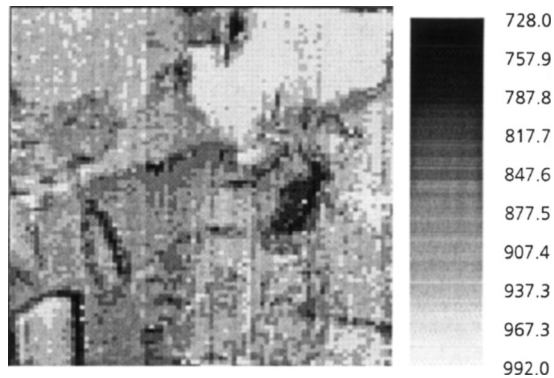


Figure 4. AFAM image of a nanocrystalline nickel sample. The contrast of the image is based on the contact stiffness comprising values between 728 N/m and 992 N/m. These values are determined from the contact resonances. The size of the image is $1.5 \times 1.4 \mu\text{m}^2$.

In the so-called piezo-mode of atomic force microscopy an ac voltage is applied to a conductive AFM cantilever while scanning the surface of a piezoelectric material. The tip of the cantilever senses the local deformation of the surface caused by the electric field between the tip and a counter electrode (Fig. 5b, see also Fig. 10). Usually the ac frequency is far below the free resonance frequency of the AFM cantilever [16,17,19,20]. In BaTiO_3 , an image series based on vertical and torsional cantilever vibration signals of the same surface area allowed the reconstruction of the domain orientation using this mode [20].

The piezo-mode technique can also be performed at frequencies in the range of the first free resonance of the cantilever [27]. In the images shown here, the ac frequency was set equal to a contact resonance frequency [28] which entails resonance amplification increasing the contrast and signal-to-noise ratio in an image. Figures 6a and 6b show images in the AFAM and ultrasonic piezo-mode for comparison. In contrast to AFAM amplitude images, piezo-mode images do not show contrast inversion when the excitation frequency is varied. Furthermore it can be seen that in the piezo-mode image (Fig. 5b) that there are areas with no piezo-activity (area with question mark). Comparing Fig. 5a with Fig. 5b, one can notice that areas of higher tip-sample contact stiffness correspond to areas where there is vertical piezo-activity. This can only happen if the polarization of the domains is dominantly vertical. The dark area in the AFAM image corresponding to low tip-sample contact stiffness can either be caused by an in-plane orientation of the domains or because the film is not piezoelectric at such locations and hence not ferroelectric. Further investigations will follow.

As mentioned above rectangular AFM cantilever beams can also be forced to torsional vibrations. In this case the experimental set-up is such that an ultrasonic transducer emits shear waves into the sample causing in-plane surface vibrations. The shear wave transducer is oriented so that the surface vibrations are polarized perpendicular to the long axis of the cantilever. If low excitation amplitudes (0.1 nm) are applied and if the excitation frequency is set close to a contact resonance frequency, the amplitude and the phase of the cantilever vibration contain now information about the local lateral tip-sample stiffness. Used as imaging quantity, they yield images of shear stiffness. By increasing the lateral excitation amplitude much above

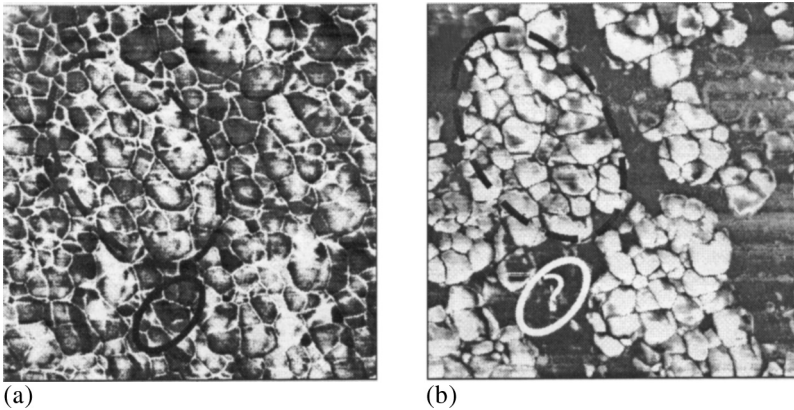


Figure 5. AFAM (a) and ultrasonic piezo-mode (b) images of the lead calcium titanate sample annealed at 650° C. The image in (a) is identical to the one in Fig. 3a.

0.1 nm, there is a change in the shape of the resonance curves. As shown recently [29] stick-slip between tip and sample occurs. This can be identified by taking local lateral spectra at one point of the sample: The maximum of the resonance curve increases linearly with the amplitude of the lateral displacement only at low excitation. At a certain threshold amplitude, the amplitude of the torsional vibrations does not increase any more and the resonance curve flattens out indicating the onset of sliding friction. Additionally, higher harmonics of the excitation signal appear which can be used for imaging. Such an image is shown in Fig. 6. A silicon sample was imaged first in the topography mode (Fig. 6a). At the excitation frequency of $f \approx 238$ kHz, an image was taken in the regime of stick-slip of the cantilever motion (Fig. 6b). Clearly an image could also be taken at $3f$, here 714 kHz (Fig. 6c). It displays information related to the local friction coefficient. This new imaging mode is also at present the object of ongoing research.

3. APPLICATION OF AFM AND AFAM TO CRACK IMAGING

AFM and AFAM can be used to image cracks in ceramics in a similar way as can be done using SEM, Optical Microscopy or Scanning Acoustic Microscopy [30,31]. If one fractures a surface of a brittle material with a Vickers indenter, it is well-known and standard practice to infer from the length of the radial cracks the fracture toughness of the material [32]. There is much experience needed to determine reliably the length of the cracks with any of the microscopies. In this study the crack opening displacement $U(x)$ was measured with an AFM. Measured close to the crack tip away from bridges in the wake of the crack, this would allow one to obtain information on K_{tip} using on the equation [33]

$$U(x) = \sqrt{8x/\pi} K_{tip}/E' \quad (1)$$

Figs. 7a and 7b show AFM images of Si_3N_4 ceramics where fracture was caused in bending specimens of the size $3 \times 4 \times 25$ mm³ by a 10 kg load using a Vickers indenter. The size of the images is 30×30 μ m². One can clearly see the cracks, however, it was difficult to exactly determine the origin of the cracks. Using the routine “section analysis” of the DI 300 AFM instrument, $U(x)$ was measured as a function of x . When evaluating the data, a possible offset for the exact position of

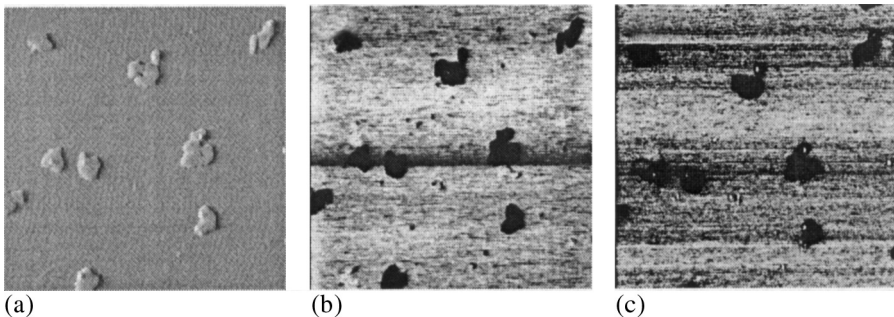


Figure 6. a) Topography of a Si-sample, b) Torsional amplitude $f = f_{excitation}$, c) Torsional amplitude $f = 3 \times f_{excitation}$.

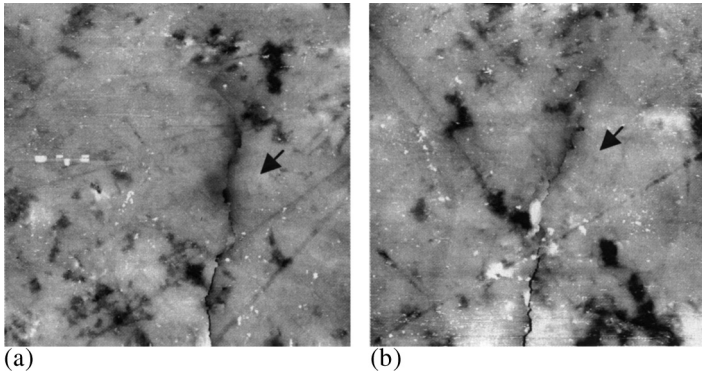


Figure 7. AFM topography images of two Si_3N_4 samples showing radial cracks caused by a Vickers indenter. The COD along the length of the radial cracks (arrows) was measured using standard routines of the DI instrument. A possible offset for the exact location of the tip was allowed in the analysis. The size of the image is $30\text{H}30\ \mu\text{m}^2$ and the topography scale was 120 nm (a) and 130 nm (b).

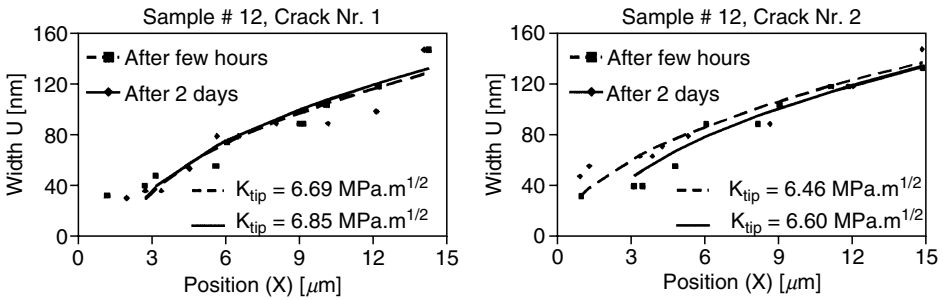


Figure 8. Crack opening displacement (COD) measured with an AFM in the topography mode. The figures display the width of the COD measured a few hours after the indent was made. The measurement was repeated after two days leading to a slight increase in the stress intensity factor. The data shown in Fig. 8a were obtained on the sample shown in Fig. 7a, and Fig. 8b corresponds to Fig. 7b.

the crack tip was taken into account. The reduced modulus E' for Si_3N_4 is 290 GPa. The value for K_{tip} was around $6.7\text{ MPa}\cdot\text{m}^{0.5}$ (Figs. 8) within the range of published data [32]. The high value indicates, however, that wake-effects played a role in the measurements, also the fact that the profile measured was not parabolic, see Figs. 8, as stipulated by Eq. (1)

We also studied in-situ crack propagation in an AFM by inducing cracks electrically, see Fig. 9. Poled PIC 151 PZT samples were loaded electrically with dc voltage of -900 V between the electrodes. Because the upper electrode was smaller than the ground electrode, an inhomogeneous electric field developed which was large enough to induce cracks due to the piezoelectric stresses.

Figure 10a shows a topography image of the environment of an individual crack in a crack field generated this way and Fig. 10b shows the corresponding AFAM image. Continued application of voltage led to additional cracking (Fig. 10c and 10d, arrow). Note that the AFAM images show also the domain structure opening the way to learn in-situ information on the role of the reorientation of domains in crack-shielding etc. which was much discussed during FCM8. Further studies are under way to clarify their role.

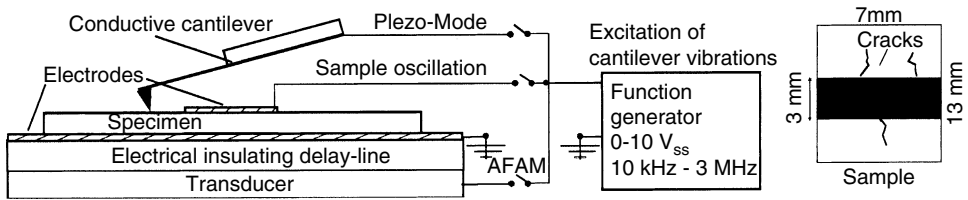


Figure 9. Configuration for the generation of in-situ cracks in an AFM allowing one to observe these cracks using the topography, the AFAM, and the ultrasonic piezo-mode. The insulating delay-line was necessary in order to protect the ultrasonic transducer from the applied dc voltages. The cracks emanate perpendicularly from the top electrode. The figure shows also the use of the electrodes for the ultrasonic piezo-mode.

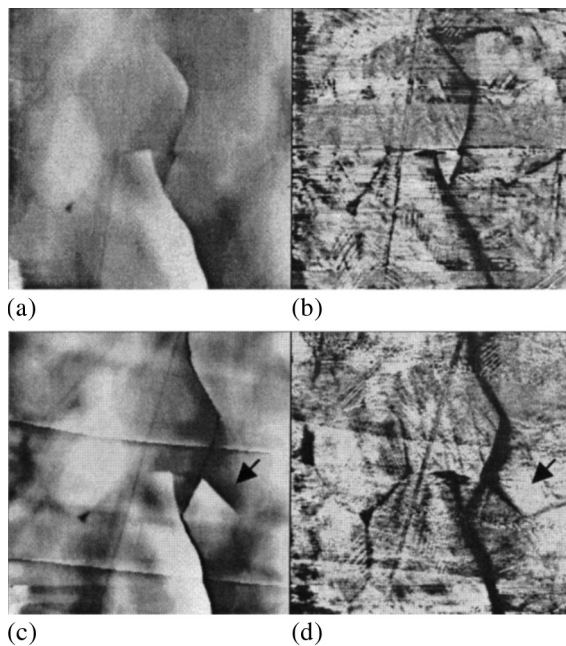


Figure 10. Observation of in-situ crack propagation after applying successive voltages up to -900 V to a PZT sample PIC 151; Fig. 10a: Topography image; Fig. 10b: AFAM image. The domain structure becomes visible. The images were taken with a cantilever having a spring constant of 47 N/m and at a static load of $1,8$ μ N. Continued voltage application leads to additional crack formation and reorientation of the domains (Fig. 10c and d, arrow). Image size of the individual images is $10H10$ μ m². The grey scale in the topography images comprises 70 nm.

Finally we studied crack propagation using the lateral stiffness as contrast in the images. Here the sensor tip vibrates in contact with the sample surface. An excitation frequency close to a torsional contact resonance frequency is selected. The torsional amplitude of the cantilever at this frequency is detected using the lateral channel of the AFM and a lock-in amplifier, and is then displayed as a color-coded image. A change in contact stiffness causes a shift of the contact resonance frequency and hence a change of cantilever vibration amplitude in the same manner as the vertical stiffness images, see above. Here also contrast inversion is observed. Cracks in a nanocrystalline ZrO_2 ceramic were generated by Vickers indents (Fig. 11). Fig. 11a

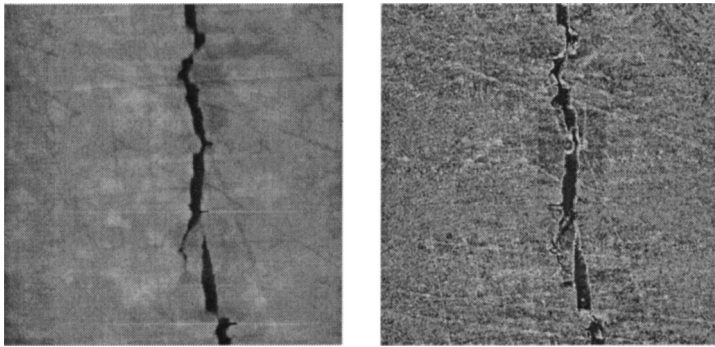


Figure 11. Topography (left) and lateral AFAM image (right) of a ZrO_2 ceramic.

shows topography, Fig. 11b the corresponding torsional resonance images of the identical surface areas. There are darker areas close to the crack flanks showing regions of altered elastic properties. This could be caused for example by the crack system below the surface and is examined further at present.

3. CONCLUSIONS

The AFAM and ultrasonic piezo-mode techniques described here lend itself for studying materials properties in ceramics on a nanoscale. Whereas the various imaging modes become more and more routine, the application of the AFM and ultrasonic AFM technique to study crack propagation are still in the early stage. However, the results presented here show that these techniques may provide much wanted information on the elastic, piezoelectric, and fracture mechanical behavior of ceramics during crack propagation.

4. ACKNOWLEDGEMENT

We gratefully acknowledge the financial support by the German Science Foundation. One of us (M.K-M) was supported by the SFB 277 at the University of the Saarland. Furthermore, it is a pleasure to thank D. Lupascu and J. Rödel for helpful discussions.

REFERENCES

1. P. Maivald, H.T. Butt, S.A. Gould, C.B. Prater, B. Drake, J.A. Gurley, V.B. Elings, and P.K. Hansma, Using Force Modulation to Image Surface Elasticities with the Atomic Force Microscope, *Nanotechnology* **2**, 103–106 (1991).
2. K. Yamanaka, H. Ogiso, and O. V. Kolosov, Ultrasonic force microscopy for nanometer resolution subsurface imaging, *Appl. Phys. Lett.* **64**, 178–180 (1994).
3. U. Rabe and W. Arnold, Acoustic Microscopy by Atomic Force Microscopy, in: *Proc. 21st Int. Symp. Acoustical Imaging*, edited by J. P. Jones, Plenum Press, New York, (1995) 585–592.

4. U. Rabe, K. Janser, and W. Arnold, Acoustic Microscopy with Resolution in the nm-Range, in: *Proc. 24th Int. Symp. Acoustical Imaging*, Eds. P. Tortoli, L. Masotti, Plenum Press, New York (1996) 669–676.
5. U. Rabe, K. Janser, and W. Arnold, Vibrations of Free and Surface-Coupled Atomic-Force Microscope Cantilevers: Theory and Experiment, *Rev. Sci. Instrum.* **67**, 3281–3293 (1996).
6. P. Vairac and B. Cretin, Scanning microdeformation microscopy in reflection mode, *Appl. Phys. Lett.* **68**, 461–463 (1996).
7. N.A. Burnham, G. Gremaud, A.J. Kulik, P.J. Gallo, and F. Oulevy, Scanning local-acceleration microscopy, *J. Vac. Sci. Tech.* **B14**, 794–799 (1996).
8. A. Rosa, E. Weilandt, S. Hild, and O. Marti, The simultaneous measurement of elastic, electrostatic and adhesive properties by scanning force microscopy: pulsed-force mode operation, *Meas. Sci. Technol.* **8**, 1333–1338 (1997).
9. E. Kester, U. Rabe, L. Presmanes, Ph. Tailhades, and W. Arnold, Measurement of Young's Modulus of Nanocrystalline Ferrites with Spinel Structures by Atomic Force Acoustic Microscopy *J. Phys. Chem. Solids* **61**, 1275–1284 (2000).
10. U. Rabe, S. Amelio, M. Kopycinska, S. Hirsekorn, M. Kempf, M. Göken, and W. Arnold, Imaging and Measurement of Local Mechanical Material Properties by Atomic Force Acoustic Microscopy, *Interf. and Surf. Analysis* **33**, 65–70 (2002).
11. S. Amelio, A. V. Goldade, U. Rabe, V. Scherer, B. Bhushan, and W. Arnold, Measurements of Elastic Properties of Ultra Thin Diamond-Like Carbon Coatings using Atomic Force Acoustic Microscopy, *Thin Solid Films* **392**, 75–84 (2001).
12. M. Prasad, M. Kopycinska, U. Rabe, and W. Arnold, Measurement of Young's Modulus of Clay Minerals Using Atomic Force Acoustic Microscopy, *Geophys. Res. Lett.* **29**, 13–16 (2002).
13. U. Rabe, S. Amelio, S. Hirsekorn, and W. Arnold, Imaging of Ferroelectric Domains by Atomic Force Acoustic Microscopy, in: *Proc. 25th Int. Symp. Acoustical Imaging*, edited by M. Halliwell and P.N.T. Wells, Kluwer Academic/Plenum Publishers, 253–260 (2000).
14. K. Yamanaka, Y. Maruyama, T. Tsuji, and K. Nakatomo, Resonance frequency and Q factor mapping by ultrasonic atomic force microscopy, *Appl. Phys. Lett.* **78**, 1939–1941 (2001).
15. A. L. Gruverman, J. Hatano, and H. Tokumoto, Scanning Force Microscopy Studies of Domain Structure in BaTiO₃ Single Crystals, *Jap. J. Appl. Phys.* **36**, 2207–2211 (1997).
16. P. Güthner and K. Dransfeld, Local poling of ferroelectric polymers by scanning force microscopy, *Appl. Phys. Lett.* **61**, 1137–1139 (1992).
17. A. Gruverman, O. Auciello, and H. Tokumoto, Scanning force microscopy: application to nanoscale studies of ferroelectric domains, *Integrated Ferroelectrics* **19**, 49–83 (1998).
18. U. Rabe, M. Kopycinska, S. Hirsekorn, J. Muñoz Saldaña, G.A. Schneider, and W. Arnold, High-resolution characterisation of piezoelectric ceramics by ultrasonic scanning force microscopy techniques, *J. Phys. D: Appl. Phys* **35**, 2621–2536 (2002).
19. K. Franke, J. Besold, W. Haessler, and C. Seegebarth, Modification and detection of domains on ferro-electric PZT films by scanning force microscopy, *Surf. Sci. Lett.* **302**, 283–288 (1994).
20. L. M. Eng, H.-J. Güntherodt, G. A. Schneider, U. Köpke, and J. Munoz Saldana, Nanoscale reconstruction of surface crystallography from three-dimensional polarization distribution in ferroelectric barium-titanate ceramics, *Appl. Phys. Lett.* **74**, 233–235 (1999).
21. S. Hong, J. Woo, H. Shin, J. U. Jeon, Y. E. Pak, E. L. Colla, N. Setter, E. Kim, K. No, Principle of ferroelectric domain imaging using atomic force microscope, *J. Appl. Phys.* **89**, 1377–1386 (2001).
22. V. Scherer, "Ultraschall-Kraft-Mikroskopie mit lateraler Anregung" Naturwissenschaftlich Technische Fakultät III. PhD-Thesis, University of the Saarland, (2002), unpublished.
23. K. L. Johnson, *Contact Mechanics* (Cambridge University Press, Cambridge, 1995).
24. G. M. Pharr, W. C. Oliver, F. Brotzen, On the generality of the relationship among contact stiffness, contact area, and elastic modulus during indentation, *J. Mat. Res.* **7**, 613–617 (1992).
25. K. Yamanaka, T. Tsuji, A. Noguchi, T. Koike, T. Mihara, Nanoscale elasticity measurement with in situ tip shape estimation in atomic force microscopy, *Rev. Sci. Instr.* **71**, 2403–2408 (2000).
26. M. Reinstaedtler, U. Rabe, V. Scherer, J.A. Turner, and W. Arnold, Imaging of flexural and torsional resonance modes of atomic force microscopy cantilevers using optical interferometry, *Surface Science*, (2003) in print
27. M. Labardi, V. Likodimos, and M. Allegrini, Force-microscopy contrast mechanisms in ferroelectric domain imaging, *Phys. Rev.* **B 61**, 14390–14398 (2000).

28. M. Kopycinska, U. Rabe, S. Hirsekorn, W. Arnold, Imaging of the Ferroelectric Domains Pattern in the Ultrasonic Piezo-Mode in: *Proc. 26th Acoustical Imaging*, edited by R. Maev Kluwer Academic Publishers, New York, *Acoustical Imaging*, **26**, 191–198 (2002).
29. M. Reinstädler, U. Rabe, V. Scherer, U. Hartmann, A. Goldade, B. Bhushan, and W. Arnold, On the nanoscale measurement of friction using atomic-force microscope cantilever torsional resonances, *Appl. Phys. Lett.* **82**, 2604–2606 (2003).
30. W. Arnold, G. Weides, and S. Faßbender, Measurement of Elastic Properties Related to the R-Curve-Behavior of Ceramics, in: *Proc. of APCFS & ATEM '01 (Asian Pacific Conference on Fracture and Strength '01 and International Conference on Advanced Technology in Experimental Mechanics '01)*, The Japan Society of Mechanical Engineers, Tokyo, 2001, pp 517–522.
31. T.J. Marrow, G.A.D. Briggs, and S.G. Roberts, In-situ Acoustic Microscopy of Crack Bridging in Alumina, *J. Europ. Ceram. Soc.* **14**, 111–116 (1994).
32. B. Lawn, *Fracture of Brittle Solids*, in Cambridge Solid State Science Series (Cambridge University Press, 1995) pp. 249–306.
33. J. Rödel, J.F. Kelly, and B.R. Lawn, “In-situ Measurements of Bridging Crack Interfaces in the Scanning Electron Microscope”, *J. Am. Soc.* **73**, 3313–3318 (1990).

INDENTATION SIZE EFFECT ON THE HARDNESS OF ZIRCONIA POLYCRYSTALS

Takashi Akatsu, Shingo Numata, Michiyuki Yoshida,
Yutaka Shinoda, and Fumihiro Wakai*

1. INTRODUCTION

The hardness of materials is one of the most important mechanical properties from an engineering point of view. The hardening of metals is realized by the inhibition of dislocation glide, which can be managed through microstructural design. The Hall-Petch hardening $H \propto d^{-1/2}$, where H is the hardness and d is the grain size, is a well-known and useful concept of the design. Conversely, the inverse Hall-Petch relation is recently found out in a metal consisted of very fine grains.^{1,2} Also, it is revealed that the H -value of metals does not depend on only d but indentation size, i.e. the hardness increases with a decrease in indentation size. The indentation size dependence is described through the building-up of geometrically necessary dislocations under a concentrated stress field.^{3,4} In terms of ceramics, correlation between hardness and microstructure has not been cleared, although a lot of research has been done.^{5,6} For example, even the grain size dependence of the hardness has not been generally described. The hardness of ceramic nanopolycrystals, which consists of very fine grains with a diameter less than 1 μ m, has not been examined in detail. Moreover, indentation size effect on the hardness has been scarcely reported. The experimental and theoretical difficulty to estimate the plasticity of a hard elastic-plastic material is one of the reasons for the obscurity in the hardness of ceramics. The development and improvement of the nanoindentation technique helps us to make an accurate evaluation of the plasticity of ceramics.

* Takashi Akatsu, Shingo Numata, Michiyuki Yoshida, Yutaka Shinoda, and Fumihiro Wakai, Materials and Structures Laboratory, Tokyo Institute of Technology, 4259 Nagatsuta, Midori, Yokohama 226-8503, Japan

In this study, the nanoindentation on monoclinic-, tetragonal- and cubic-zirconia polycrystals (referred as MZP, TZP and CZP, respectively) was carried out with a home-made nanoindenter. Relationship between indentation load P and penetration depth h of a diamond stylus was analyzed to derive the true hardness H_T as a function of the plastic depth h_p , which is a measure of plasticity.⁷ The plastic deformation of each zirconia at room temperature was discussed in detail through the examination and the mutual comparison of indentation size dependence of H_T .

2. EXPERIMENTAL

2.1. Samples

The zirconia polycrystals with different crystallographic structure (monoclinic, tetragonal and cubic) were fabricated to be a fine structure. Three kinds of very fine zirconia powders, TZ-0Y, TZ-3Y and TZ-8Y (Tosoh Co.ltd. Japan), were sintered with HIP under 200MPa to make MZP, TZP and CZP, respectively.⁸ The average grain size of as-sintered MZP, TZP and CZP, which was determined through SEM observation and the intercept method, was 60, 60 and 110nm, respectively. In addition, heat treatment of each zirconia was carried out to enlarge their grain size. Nanoindentation on the $\{100\}$ plane of a single crystal of cubic zirconia (YSZ(100), Shinkosha Co.ltd., Japan) was also carried out in comparison. The mirror-finished surface of all samples was carefully prepared by polishing with colloidal silica powders with a diameter less than 60 nm.

2.2. Nanoindentation

Precise h measurement is very important for the accurate evaluation of hardness through the nanoindentation technique. External deformation due to the compliant structure of a conventional nanoindenter must be eliminated from h measured, because h is usually given as the drive of a diamond stylus towards the surface of a sample.⁹ Some calibrations to compensate the extrinsic deformation are conventionally carried out, but they are, in many cases, poor at reproducibility. That is one of the reasons for the inaccurate hardness evaluation with the nanoindentation. In this study, the accurate value of h was directly measured by using a home-made nanoindenter with a unique system as shown in Fig.1. The difference between the drive and deflection of the beam fixed with the stylus (see Fig.1) definitely gives the accurate h without doing any calibrations. The P -value was determined as a function of the deflection and flexibility of the beam. In addition, vertical indentation within an error of $\pm 0.1^\circ$ was confirmed using a laser reflection displacement transducer (see Fig.1) and stages for the tilt and horizontal rotation of a sample. The system shown in Fig.1 was made of super invar alloy with a thermal expansion of $0.7 \times 10^{-6}/^\circ\text{K}$ at room temperature to decrease the error due to the temperature change during indentation. Nanoindentation at room temperature in air was actually carried out by using the nanoindenter with the Berkovich-type diamond stylus at a penetration rate of 50nm/sec.

2.3. Analysis of P - h Curves

It is relatively hard to find ideal quadratic relation between P and h in the very shallow indentation region. That is attributed to the blunt tip of a diamond stylus,

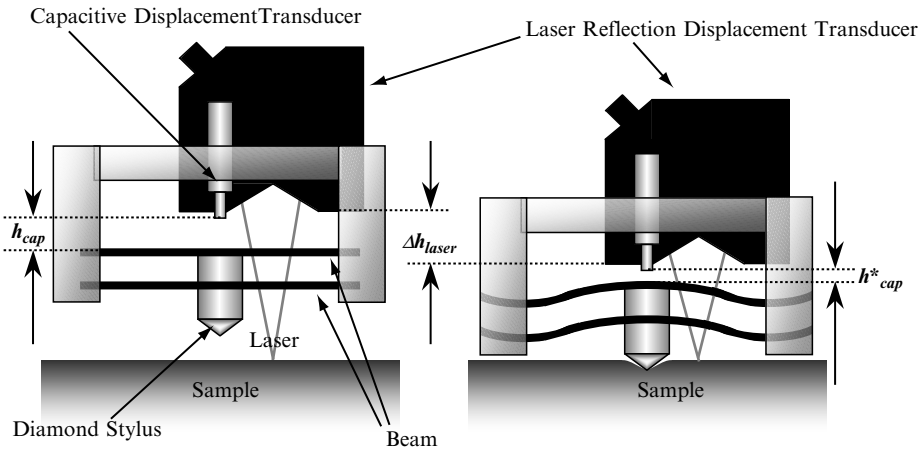


Figure 1. A unique system of a home-made nanoindenter to measure accurate P and h . The difference between the drive Δh_{laser} and deflection $\Delta h_{cap} (= h_{cap} - h_{cap}^*)$ of the beam gives an accurate h . The P -value is given as a function of Δh_{cap} and the flexibility of the beam.

which causes the overestimation of hardness in that region. We made a two-step modification of P - h curves to avoid the overestimation at small h as follows: At first, loading and unloading P - h curves were transferred by the distance Δh between the real and ideal origins, which was determined by the extrapolation of linear relation between $P^{1/2}$ and h at relatively large h into $h = 0$, in the positive direction of h (see Fig. 2). Secondly, P - h data from $h = 0$ to $h > 2\Delta h$ for loading and from h_r to $h_r + 2\Delta h$ for unloading were neglected, respectively, in the following analysis (see Fig. 2). According to the Oliver and Pharr method,¹⁰ the Meyer hardness H_M was derived from the modified P - h curves as follows,

$$H_M = \frac{P_{max}}{gh_c^2} \tag{1}$$

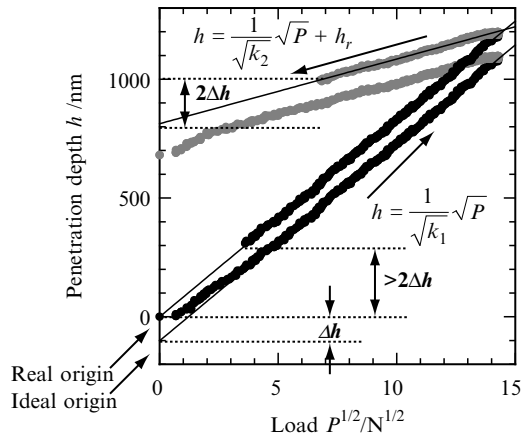


Figure 2. Modification of P - h curves to avoid the overestimation of hardness in the shallow indentation region due to the blunt tip of a diamond stylus.

$$h_c = h_{\max} - \varepsilon \frac{P_{\max}}{S} \quad (2)$$

where P_{\max} the maximum indentation load, h_{\max} the maximum penetration depth of the stylus, g the geometrical factor to be 24.5 for the Berkovich-type stylus, ε the constant to be 0.72 for conical stylus, and S the unloading slope at P_{\max} . An analysis to derive H_T and h_p^9 was also carried out for the modified $p^{1/2}$ - h relationship as follows,

$$H_T = \frac{k_1 / (g / \gamma_p^2)}{\left(1 - \sqrt{k_1 / k_2}\right)^2} \quad (3)$$

$$h_p = \sqrt{\frac{P \gamma_p^2}{g H_T}} \quad (4)$$

where k_1 and k_2 are the linear slopes of $P^{1/2}$ - h relationship on loading and unloading, respectively, and γ_p is the constant to be unity for the perfect plasticity.

2.4. Raman Spectroscopy

Highly concentrated stress field seems to be realized under an indentation. In the case of TZP, stress-induced transformation from tetragonal into monoclinic phase can be predicted to occur under the indentation. Raman spectroscopy by using a focused ultraviolet laser with a diameter of $1\mu\text{m}$ was carried out at the bottom of an indentation to confirm the phase transformation.

3. RESULTS AND DISCUSSION

3.1. Meyer Hardness of Zirconia Polycrystals

The hardness of materials is conventionally evaluated as H_M . The H_M -value is, however, not a measure of the plasticity of ceramics,⁷ because it is definitely affected by the elasticity, e.g. Young's Modulus. Therefore, not only grain size dependence but also indentation size dependence of the H_M -value of MZP, TZP and CZP was obscure as reported in previous studies.^{5,6} In this study, the evaluation of H_T , a measure of plasticity, for each zirconia was carried out, and then revealed the following indentation size dependence.

3.2. True Hardness of CZP

The H_T -value of CZP increased with a decrease in h_p as shown in Fig.3. Also, the grain size dependence of H_T was hardly observed in CZP. Moreover, the H_T -value of a cubic zirconia single crystal as a function of h_p was superimposed just on that of CZP (see Fig.3). According to the theory of the strain gradient plasticity,^{3,4} in which the building-up of geometrically necessary dislocations under an indentation was modeled, the indentation size dependence of hardness is represented as follows,

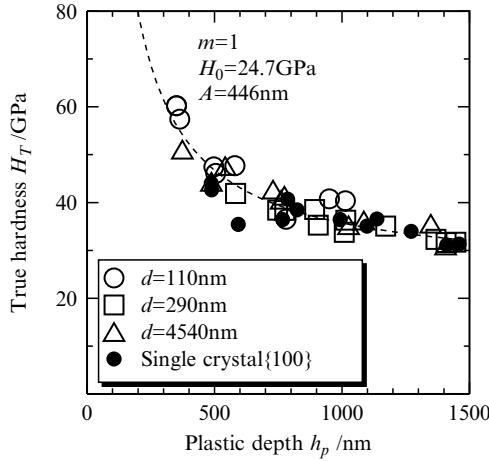


Figure 3. The H_T -value of CZP as a function of h_p . d is the average grain size of CZP. The broken line is drawn by using Eq.(5) with $m = 1$.

$$\left(\frac{H_T}{H_0}\right)^m = 1 + \frac{A}{h_p} \quad (5)$$

where H_0 is the hardness evaluated at $h_p \rightarrow \infty$, A is the constant associated with the material characteristic length such as the Burgers vector of the dislocation, and m is the constant to be 1 or 2. The h_p dependence of H_T shown in Fig.3 was well described by using Eq.(5) with $m = 1$. Good agreement between the experimental and theoretical h_p dependence of H_T regardless of grain size indicates that the plastic deformation of CZP at room temperature is simply due to the accumulation of dislocation glide in each grain. The dislocations seem to be piled-up at grain boundary but are not able to go through the boundary into the neighboring grains such as those in metals because of the lack of the number of active slip system. In other words, the contribution of grain boundary sliding to the plasticity of CZP seems to be negligibly small.

3.3. True Hardness of MZP

The H_T -value of MZP, which was much smaller than that of CZP, scarcely depended on h_p as shown in Fig.4. In addition, the H_T -value of MZP remarkably increased with a decrease in the grain size below 100 nm (see Fig.4). The softness of MZP at room temperature is attributed to the plastic deformation caused by the twinning of the monoclinic crystallographic structure.¹¹ Twinning is quite different from dislocation glide observed in CZP, which is obviously associated with the strain gradient plasticity. That is the reason why h_p dependence of the H_T -value of MZP was hardly observed. In terms of metals, the resistance to plastic deformation due to twinning increases with a decrease in grain size such as the Hall-Petch hardening.¹² Correlation between the twinning and grain size has not been cleared in ceramics. However, the resistance to the twinning of monoclinic zirconia may increase with a decrease in grain size comparably with the size of the twin, which is of the order of 10 nm.¹¹

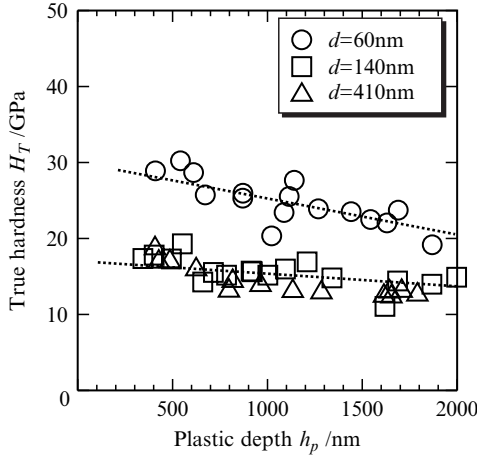


Figure 4. The H_T -value of MZP as a function of h_p . d is the average grain size of MZP.

3.4. True Hardness of TZP

The H_T -value and its h_p dependence of TZP were classified into two categories as a function of grain size. If the grains were larger than 100nm, the H_T -value of TZP was the same as that of MZP and scarcely depended on h_p (see Fig.5). On the contrary, the H_T -value of TZP increased as large as that of CZP and significantly increased with a decrease in h_p if the grain size decreased below 100nm (see Fig.5). As a result of Raman spectroscopy at the bottom of an indentation, the monoclinic phase was observed in the former though only tetragonal phase was detected in the latter. This indicates that the stress-induced transformation from tetragonal to monoclinic phase occurred on loading in the former while it was inhibited in the latter. Therefore, the H_T -value of TZP consisted of grains with a diameter larger than the critical size of the transformation coincided with that of MZP because of the plastic deformation of the transformed monoclinic phase as mentioned above. The decrease of grain size below the critical realizes the stabilization of tetragonal phase.¹³ That is the reason why the H_T -value and its h_p dependence of TZP consisted of grains with a diameter less than 100 nm was the same as those of CZP.

4. CONCLUSION

The H_T -value of zirconia polycrystals increased with a decrease in h_p . This is attributed to the building-up of geometrically necessary dislocations under an indentation. In addition, the grain size dependence of H_T was hardly observed. These results indicate that the plastic deformation of zirconia polycrystals at room temperature is basically due to the accumulation of dislocation glide in each grain. In other words, the contribution of grain boundary sliding to the plasticity was negligibly small even if the grains were of the order of 100nm. The H_T -value of MZP, which was much smaller than that of CZP, scarcely depended on h_p because of the plastic deformation due to twinning. The H_T -value and its h_p dependence of TZP

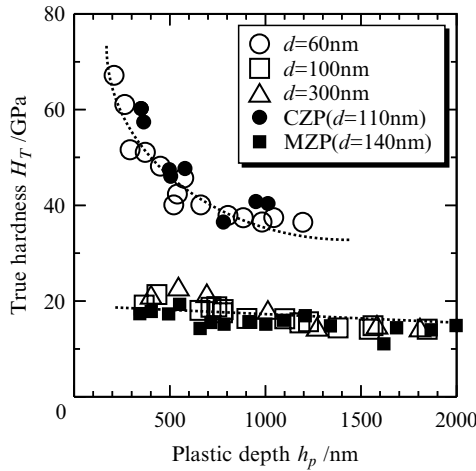


Figure 5. The H_T -value of TZP as a function of h_p . d is the average grain size of zirconia polycrystals.

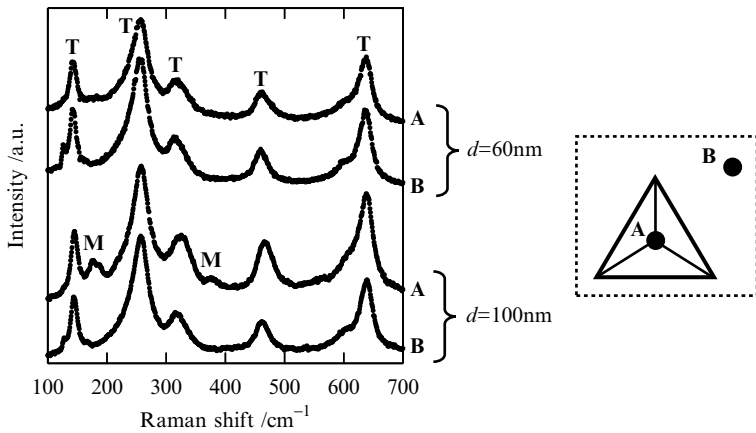


Figure 6. The spectrum of Raman spectroscopy measured at the bottom A of an indentation on TZP. B is the place far from an indentation to obtain the reference spectrum. M and T are assigned to monoclinic and tetragonal phases, respectively. d is the average grain size of TZP.

changed depending on whether the stress-induced phase transformation occurred or not under an indentation, which was determined as a function of grain size.

ACKNOWLEDGEMENT

A part of this research work was supported by the Nippon Sheet Glass Foundation for Materials Science and Engineering and the Grant-in-Aids for Scientific Research (#13750622) of the Ministry of Education, Culture, Sports, Science and Technology, Japan. The authors are grateful to Mr. Y. Teranishi for helping us to carry out Raman spectroscopy.

REFERENCES

1. S.Takeuchi, The Mechanism of the Inverse Hall-Petch Relation of Nanocrystals, *Scripta Mater.* **44**, 1483–1487 (2001).
2. C.A.Schuh, T.G.Nieh, T.Yamasaki, Hall-Petch Breakdown Manifested in abrasive wear resistance of Nanocrystalline nickel, *Scripta Mater.* **46**, 735–740 (2002).
3. W.D.Nix and H.Gao, Indentation Size Effects in Crystalline Materials: A Law for Strain Gradient Plasticity, *J.Mech.Phys.Solids* **46**[3], 411–425 (1998).
4. M.R.Begley and J.W.Hutchinson, The Mechanics of Size-Dependent Indentation, *J.Mech.Phys.Solids* **46**[10], 2049–2068 (1998).
5. R.W.Rice, C.C.Wu, and F.Borchelt, Hardness-Grain-Size Relations in Ceramics, *J.Am.Ceram.Soc.* **77**[10], 2539–2553 (1994).
6. A.Krell, A New Look at the Influences of Load, Grain Size, and Grain Boundaries on the Room Temperature Hardness of Ceramics, *Int'l.J.Ref.Met.Hard Mater.* **16**, 331–335 (1998).
7. M.Sakai, The Meyer Hardness: A Measure for Plasticity?, *J.Mater.Res.* **14**[9], 3630–3639 (1999).
8. M.Yoshida, Y.Shinoda, T.Akatsu, and F.Wakai, Deformation of Monoclinic ZrO₂ Polycrystals and Y₂O₃-Stabilized Tetragonal ZrO₂ Polycrystals Below the Monoclinic-Tetragonal Transition Temperature, *J.Am.Ceram.Soc.* **85**[11], 2834–2836 (2002).
9. M.Sakai, S.Shimizu, and T.Ishikawa, The Indentation Load-Depth Curve of Ceramics, *J.Mater.Res.* **14**[4], 1471–1484 (1999).
10. W.C.Oliver and G.M.Pharr, An Improved Technique for Determining Hardness and Elastic Modulus Using Load and Displacement Sensing Indentation Experiments, *J.Mater.Res.* **7**[6], 1564–1583 (1992).
11. I-W.Chen, Implication of Transformation Plasticity in ZrO₂-Containing Ceramics: II, Elastic-Plastic Indentation, *J.Am.Ceram.Soc.* **69**[3], 189–194 (1986).
12. D.Hull, Effect of Grain Size and Temperature on Slip, Twinning and Fracture in 3% Silicon Iron, *Acta Metall.* **9**[3], 191–204 (1961).
13. F.F.Lange, Transformation Toughening Part 1 Size Effects Associated with the Thermodynamics of Constrained Transformations, *J.Mater.Sci.* **17**, 225–234 (1982).

INDENTATION FRACTURE, ACOUSTIC EMISSION AND MODELLING OF THE MECHANICAL PROPERTIES OF THIN CERAMIC COATINGS

S.J. Bull, I. Arce-Garcia, E.G.-Berasetegui and T.F. Page[†]

ABSTRACT

Fracture is an almost inevitable consequence of highly loaded contacts in ceramic-coated systems. For relatively thick coatings fracture is often similar to that observed in bulk samples of the coating but as the coating thickness is reduced the substrate plays an increasing role in influencing or even controlling fracture behaviour. Both through-thickness and interfacial fracture may be observed depending on the relative toughness of the substrate, coating and interface. Through-thickness fracture is exacerbated by plastic deformation in the substrate and therefore the load support from the substrate is critically important in determining the type and extent of fracture observed. In this paper, nanoindentation testing and post facto atomic force and scanning electron microscopy is used to characterise the types of fracture which occur for hard coatings on softer substrates and multilayer coatings on glass. The effect of fracture on the nanoindentation load-displacement curves and the hardness and Young's Modulus values obtained from them is discussed and a simple model to account for the observed behaviour is introduced. The use of acoustic

[†] School of Chemical Engineering and Advanced Materials, University of Newcastle, Newcastle upon Tyne, NE1 7RU, UK

emission to monitor plasticity and fracture during the indentation cycle is also discussed.

1. INTRODUCTION

The durability and performance of coatings in almost every application depend on their as-deposited mechanical properties such as adhesion, hardness, toughness and elastic modulus. These properties may not be the same as those of the same material in bulk form due to different microstructural and defect states arising from the deposition process. As the coating thickness is reduced it becomes increasingly difficult to measure these properties by conventional methods and low load nanoindentation and scratch testing have been developed to enable measurements to be achieved at scales commensurate with the coating thickness. Continuously recording indentation test methods are well established for the determination of Elastic Modulus and hardness.^{1,2,3} but methods for assessment of fracture toughness and adhesion are much less developed.^{4,5} In part the reason for this is that mechanism of fracture failure around an indentation is complex and depends on the relative properties of coating, substrate and interface and therefore a universal analysis method is unlikely to be produced. However, in some cases it is possible to identify failure modes that are amenable to analysis resulting in reasonable toughness data. Microscopy and analysis of fracture paths is a key part of this approach, particularly as the indentations get smaller.

There are a number of different indentation fracture events which might occur in a coating substrate system (Table 1), the occurrence of which will depend on the relative toughness of coating/substrate and any interfaces present. These failure modes will be altered by plastic deformation in the substrate which can lead to the superposition of bending stresses on to those generated by the indentation.

This paper discusses the type of fracture events which occur for hard coatings on soft and hard substrates and outlines the effect that fracture events have on other mechanical properties measured by indentation (such as hardness and Young's Modulus). It also introduces the use of acoustic emission generation to monitor fracture events in very thin coatings where it is difficult to identify them by conventional microscopy (both scanning electron and atomic force).

2. EXPERIMENTAL

2.1. Sample Preparation

In this study thin ceramic coatings have been deposited onto both brittle and ductile substrates to assess the fracture behaviour of the coating/substrate system. Niobium

Table 1. Fracture events associated with brittle (ceramic) coating/substrate systems.

| Substrate | Coating | Fracture type |
|-----------|---------|---|
| Ductile | Brittle | Through-thickness fracture, brittle fracture in coating parallel to interface, ductile interfacial fracture, microfracture in coating |
| Brittle | Brittle | Bulk chipping, through-thickness fracture, brittle interfacial fracture, microfracture in coating, microfracture in substrate |

nitride coatings were deposited in the same process run on a fully hardened powder metallurgy high speed steel (ASP23) and annealed stainless steel (304) substrates by cathodic arc evaporation using standard commercial deposition parameters.⁶ The substrates were polished to a 3 μm diamond finish prior to coating and a layer of approximately 4 μm was deposited on each. Fullerene-like CN_x was deposited on a range of substrates at thicknesses of 400 nm and 1 μm using unbalanced magnetron sputtering.⁷

A range of oxide and oxynitride coatings was deposited onto float glass using magnetron sputtering to 200 nm thickness. In addition a multilayer stack with a coating architecture similar to current commercial low emissivity solar control coatings was deposited to investigate the effect of internal interfaces in the coating. Details of the coatings deposited are presented in Table 2.

2.2. Nanoindentation Testing

Nanoindentation experiments were performed using two different nanoindentation systems to make indents at peak loads from 100 μN to 500 mN. Hardness and Young's Modulus were extracted from the load-displacement curves using the method of Oliver and Pharr.⁸ All load displacement curves were corrected for thermal drift and the indenter area functions were carefully calibrated following the Oliver and Pharr approach using a fused silica standard sample prior to testing the coated samples.

A Nanoindenter II with a 'blunt' Berkovich tip (tip end radius 250 nm at the time of making the experiments) was used for testing the NbN coated samples and the CN_x coated samples at loads in the complete range. Due to the fact that the

Table 2. Coating/substrate systems investigated in this study.

| Coating | Substrate | Substrate Hardness (GPa) | Thickness (nm) | Deposition Technology | Deposition Temperature ($^{\circ}\text{C}$) |
|-------------------------|--------------------------------|--------------------------|-----------------------|---------------------------------|---|
| NbN | ASP23 steel | 9.5 | 3980 | Arc evaporation | 425 |
| NbN | 304 stainless steel | 1.9 | 2810 | Arc evaporation | 425 |
| CN_x | Silicon | 11.5 | 400, 1000 | Unbalanced magnetron sputtering | 350 |
| CN_x | 1 μm SiC on silicon | 35.0 SiC 11.5 Si | 400, 1000 | Unbalanced magnetron sputtering | 350 |
| CN_x | Sapphire | 32 | 400, 1000 | Unbalanced magnetron sputtering | 350 |
| TiO_xNy | Float Glass | 6.5 | 200 | Magnetron sputtering | 200 |
| SnO_2 | Float glass | 6.5 | 200 | Magnetron sputtering | 200 |
| Zr (O) | Float glass | 6.5 | 200 | Magnetron sputtering | 200 |
| ZnO | Float glass | 6.5 | 200 | Magnetron sputtering | 200 |
| Oxide multi-layer | Float glass | 6.5 | Total thickness 80 nm | Magnetron sputtering | 200 |

indenter is relatively blunt this approach is not suitable for measuring the hardness and Young's Modulus for the CNx coatings as they do not plastically deform before the substrate.⁹ However, the substrate plastic deformation is limited at the higher loads where coating fracture and interfacial detachment occur and this can be useful for interface toughness determination. The constant loading rates used were 500 $\mu\text{N/s}$ for indentations to maximum loads greater than 100 mN and 50 $\mu\text{N/s}$ for lower peak load indentations.

A Hysitron Triboindenter fitted with a sharp Berkovich tip (tip end radius 50 nm) was used to test the CNx and coatings on glass. A fixed loading rate of 100 $\mu\text{N/s}$ was used in all cases to minimise the effects of creep on the measured load-displacement curves. This system can use the tip which is used to make the indent to perform AFM imaging of the impression after the indentation cycle is complete. Given the small size of the impressions made at low loads this is the only practical way to achieve imaging of the impressions as the indent arrays are impossible to find using off-line AFM or SEM even when precision locating stages are used.

Nanoindentations were also performed on the single and multi-layer coated glass with the Hysitron Triboindenter fitted with a 120° conical indenter (blunt tip, radius ~ 500 nm) instrumented for the recording of acoustic emission (AE) during the indentation cycle.¹⁰ Loads from 1 mN to 10 mN were used in this analysis. AE events were sampled at 4MHz; once a threshold signal is exceeded (determined from noise measurements with the indenter in air) the system records the AE signal waveform for subsequent analysis (Figure 1).

The energy in the acoustic event is then calculated from integration of the amplitude of the AE waveform, $A(\tau)$, with respect to time and is given by¹¹:

$$E_A(t) = \int_0^t A(\tau)^2 d\tau \quad (1)$$

To calculate the net energy of the event, the linear background contribution ($\alpha\tau$) is subtracted (Figure 2), assuming that the amplitude of the background contribution is virtually constant during tests and has a mean amplitude α :

$$E_A^{Net}(\tau) = E_A(\tau) - \alpha\tau \quad (2)$$

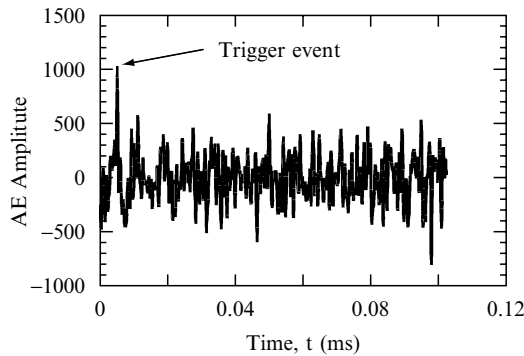


Figure 1. AE amplitude as a function of time after an acoustic emission event which occurred at 4000 μN load in the testing of a 200 nm thick TiOxNy coating on float glass.

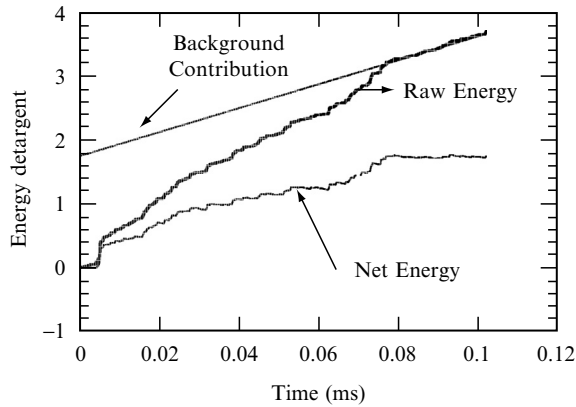


Figure 2. An example of the energy calculation for the event in Figure 1. The net energy is calculated by subtracting background contribution from the raw energy.

The constant α is determined for each acoustic event by fitting the background integrated energy a long time after the event as shown in Figure 2. It is assumed that the background is linear which is reasonable over the AE pulse duration.

To discriminate between different events, not only the shape of the wave can be analysed but also the parameter emission shape factor, defined as:

$$A_{ESF} = \frac{A_{max}}{A_{RMS}} \tag{3}$$

Previous studies have demonstrated that A_{ESF} differentiates between different types of acoustic emission generation process.^{11,12} In addition, the attenuation time of the signal, t_{at} , may be used to differentiate between events.

2.3. Microscopy

Indentations produced at high loads using the Nanoindenter II could be located for post facto imaging and were imaged by scanning electron microscopy (SEM) and atomic force microscopy (AFM). Cracks were easily visible in the SEM and their visibility was enhanced by using backscattered electron imaging. It proved to be almost impossible to see cracks in the AFM images unless they displayed significant residual (opening) displacements. This is probably due to the fact that water from the environment is drawn into the fine cracks by capillary action and the AFM cantilever rides over the open crack on the surface of a water film.

3. RESULTS AND DISCUSSION

3.1. Ceramic Coating on Ductile Substrate: NbN on Steel

No evidence for interfacial detachment was found for any of the NbN coatings investigated in this study but through thickness fracture was observed (Figure 3). The type of fracture observed depends on the hardness of the substrate. For both types of coating fracture initially occurs in the radial direction following the edges of

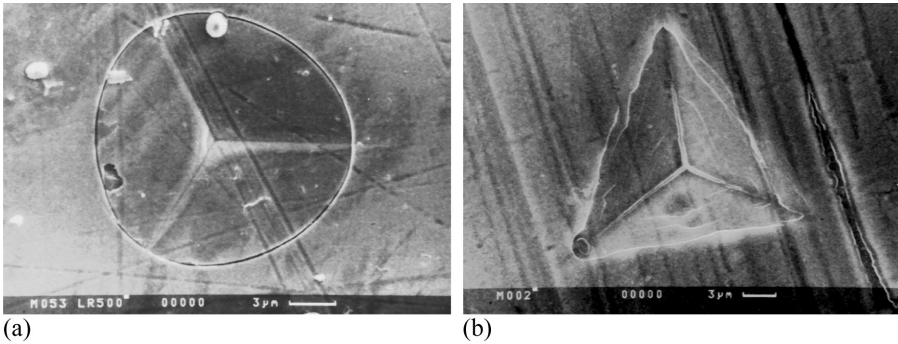


Figure 3. Scanning electron micrographs of 500 mN indents in NbN coated (a) 304 stainless steel and (b) ASP23 high speed steel.

the pyramidal indenter. For the harder ASP23 substrate the only other fracture visible is picture frame cracking within the indent (Figure 3b). However, the coating on the stainless steel substrate shows a circular through-thickness crack at the edge of the contact (Figure 3a) which is some distance from the well defined indent at the centre of the circle. Radial cracks defined by the indenter edges connect this central indent to the edge of the contact but do not extend beyond it.

The difference in behaviour can be understood from the load-displacement curves. Figure 4 shows a comparison between the load-displacement curves for the NbN coatings on the two substrates tested at 500 mN. At low loads the load-displacement curves superpose indicating that it is the coating properties which dominate the measured response and the load is proportional to displacement squared as expected for elastic-plastic indentation of a coating where the substrate provides good load support. However, when the contact-induced shear stresses rise to trigger plastic deformation in the substrate below the coating,¹³ plastic deformation starts in the stainless steel substrate the substrate collapses beneath the coating which consequently has to elastically bend to follow the deforming substrate. There is a change in slope of

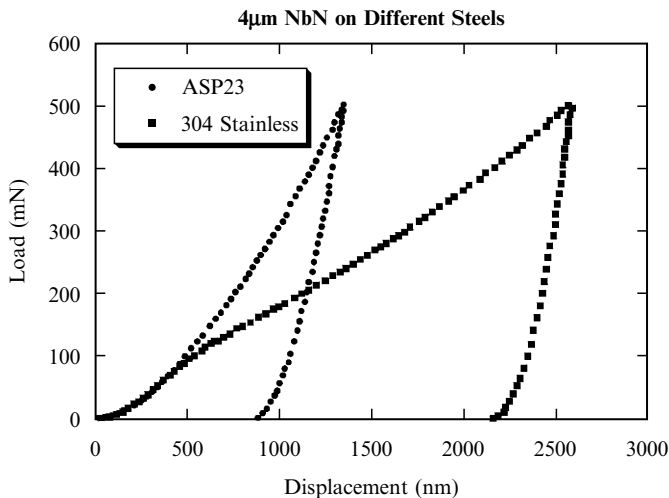


Figure 4. Load-displacement curves for NbN coatings on different steel substrates.

the load-displacement curve at this point. The size of the central indent is the same as the size of an indent with peak load 100 mN (about 400 nm deep) which represents the size of the indent in the coating at the onset of plastic deformation in the stainless steel substrate. The impression caused by plastic deformation of the NbN coating stops growing at this point and further plastic deformation is concentrated in the substrate. The coating remains elastic but is bent into the impression created by substrate deformation. To accommodate this deformation the radial cracks following the indenter edges extend as the plastic zone in the substrate extends. Tensile radial stresses in the coating at the edge of the substrate plastic zone, in combination with these bending stresses lead to the single circular through-thickness crack – under such circumstances the displacement of the indenter increases greatly as the disc of coating is separated from the rest of the coated surface and membrane stresses supporting some of the load drop to zero.

The fact that the load displacement curve shows no discrete discontinuities (“pop-ins” implies that there is a gradual extension of the radial cracks as the load is increased and the through thickness ring crack occurs at close to the peak load. In the absence of a recognisable pop-in event or a clear idea of the normal load at which fracture occurs it is not possible to analyse the fracture toughness of the coating from the available data.

For thinner coatings, through-thickness cracking may be exacerbated by pile-up of substrate material, but pile-up is suppressed by the 4 μm NbN coatings investigated here.

The fracture which occurs for the stainless steel substrate has a measurable effect on the hardness and Young’s Modulus measured for the coating and must be taken into consideration if the performance of the coated system is to be successfully modelled. Recently some success in predicting the hardness of a coating substrate system as a function of contact scale has been achieved using an energy based model in which the contributions to the total work of indentation from coating, substrate and interfaces can be summed and divided by the total deforming volume to determine the system hardness.^{14,15} The total deforming volume is assumed to be the plastic zone associated with the impression and does not take into consideration any plastic deformation associated with cracking which may occur outside this. From the SEM images in Figure 3, where extensive cracking is not observed, this assumption is reasonable. Two interfaces must be considered, thus

$$H = \frac{(V_s H_0(s) + V_f H_o(f) + A_s \gamma_s + A_i \gamma_i)}{V} \quad (4)$$

where V_f and V_s are the deforming volumes of coating and substrate, $H_0(f)$ and $H_0(s)$ are the bulk hardnesses of coating and substrate, A_s is the surface area and A_i is the interfacial area within the plastic deforming region. The total deforming volume is assumed to be hemispherical and the deforming volumes in coating and substrate are given by appropriate slices through the hemisphere. The surface energy terms can be used to account for the fact that the real deforming volume is unlikely to be hemispherical. The radius of the deforming volume is related to the depth of the impression by¹⁶

$$R = k_2 \delta \left(\frac{E}{H} \right)^{1/2} \cot^{1/3} \psi \quad (5)$$

where k_2 is a geometrical constant ($k_2 = 3.64$ for a Berkovich indenter), δ is the plastic indentation depth, E is the Young's Modulus of the material and ψ is the effective indenter angle ($\psi = 70.3^\circ$ for a Berkovich indenter).

To include the effects of fracture in the model is relatively straightforward if we assume that the coating within the cracked region does not contribute to the plastic work of indentation after fracture occurs. Fracture usually occurs when the plastic zone in the substrate is very well-established so we can consider the volume of coating to be a cylindrical disc with the thickness of the coating. The area of the crack produced is small compared to the volume it encloses so we also assume that the surface energy of the crack plays only a minor part in the work of indentation. For a radial cracked system the cracks have radius $k_c\delta$ where k_c is a constant and δ is the plastic indentation depth. These form above a critical depth, δ_c . The area of material bounded by radial cracks increases linearly with indentation size. In this case the correction for the modelled hardness is given by

$$\Delta H = \frac{3(tH_0^F + \gamma_s + \gamma_i)k_c^2\delta^2}{2R^3} \quad (6)$$

$$\Delta E = \frac{3tE_f k_c^2\delta^2}{2R^3}$$

A simple estimate for k_c is that it relates the depth to the radius of an equivalent cone with the same volume as the impression. Thus, for a Berkovich indentation

$$\pi r^2 = 24.5\delta^2 \text{ and therefore } k_c = \sqrt{\frac{24.5}{\pi}} \quad (7)$$

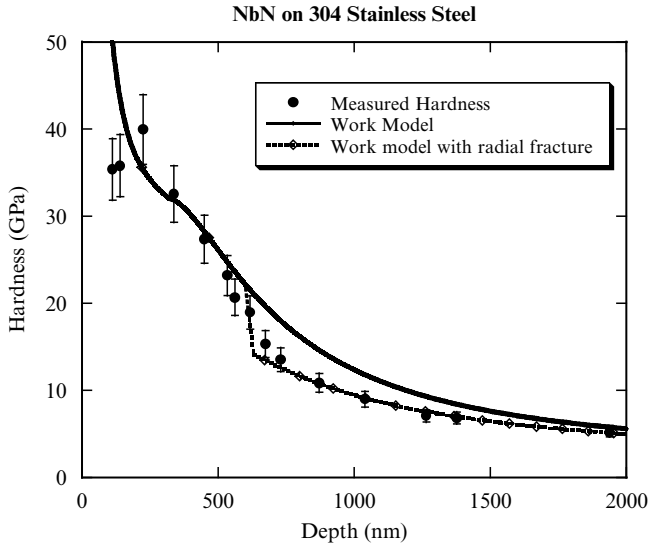


Figure 5. Hardness of NbN on stainless steel as a function of contact depth comparing modelled data with experiment. Correction for fracture is necessary to achieve a good fit. (Modelling parameters; $H_f = 24$ GPa, $E_f = 475$ GPa, $\gamma_f = 15000$ J/m², $H_2 = 1.7$ GPa, $E_s = 210$ GPa, $\gamma_i = 5000$ J/m² and $\alpha = 2.0$).

Corrected hardness predictions are shown in Figure 5 compared to experimental data. The quality of the fit is excellent (correlating coefficient >0.98) and much better than can be achieved by any other hardness modelling approach investigated in this study. An advantage of the model compared to existing hardness models is that it can be used to make predictions of the behaviour of different coating/substrate systems based on only a few scale-corrected physically-meaningful materials constants.¹⁴

3.2. Brittle Coating on Brittle Substrate: CN_x on Silicon, Silicon Carbide and Alumina

For brittle coatings on brittle substrates both through-thickness and interfacial fracture can occur depending on the relative toughness of the coating, substrate and interface. In the case of CN_x coatings the coating and substrate toughness are usually greater than the interface toughness and so detachment of the coating can be produced by high load nanoindentation.

Loading a pyramidal indenter onto the surface of a coated sample creates compressive stress in the coating (see Figure 6). Such stresses can cause the coating to buckle and detach from the substrate around the indenter (see SEM micrograph in Figure 6a). According to Thouless,¹⁷ once buckling starts the mode mixity of the stress at the interfacial crack tip changes in such a way that the interfacial crack is diverted to the surface forming a chip. This is registered in the load-displacement curve, where a long step can be observed in its loading portion as the indenter advances into the sample (see Figure 6b). In this case the buckled material has failed catastrophically and the coating has been ejected from beneath the indenter since the pop-in distance is the thickness of the coating.

If the coating has not undergone catastrophic fracture during loading, on unloading the coating is still under compressive stress and around the indenter it is already detached from the substrate (see Figure 7a). Towards the end of unloading the coating buckles beneath the indenter pushing it up,⁵ which is associated with the linear unloading observed in the $P-\delta$ curve (see Figure 8a). During buckling the outside of the coating is under tensile stress (see Figure 7b) and fracture may initiate where the buckle curvature is highest (Figure 7c). This behaviour is observed for

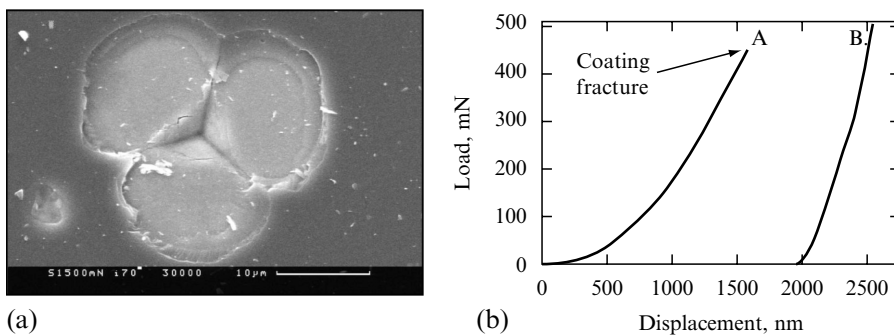


Figure 6. (a) SEM micrograph showing coating detachment during loading of the indenter for a $1\ \mu\text{m}$ thick CN_x coating on 3C SiC (001) substrate. (b) Step (A-B) in the loading curve due to through-thickness cracking of the coating and spalling.

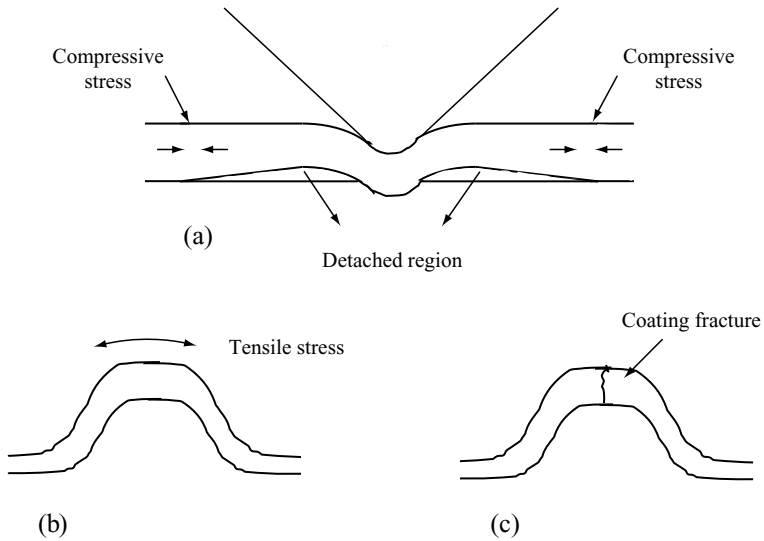


Figure 7. Schematic diagram of the different steps followed by the coating fracture during unloading of the indenter: (a) Coating under compressive stress and detached region (b) Buckling and tensile stress, and (b) fracture of the coating.

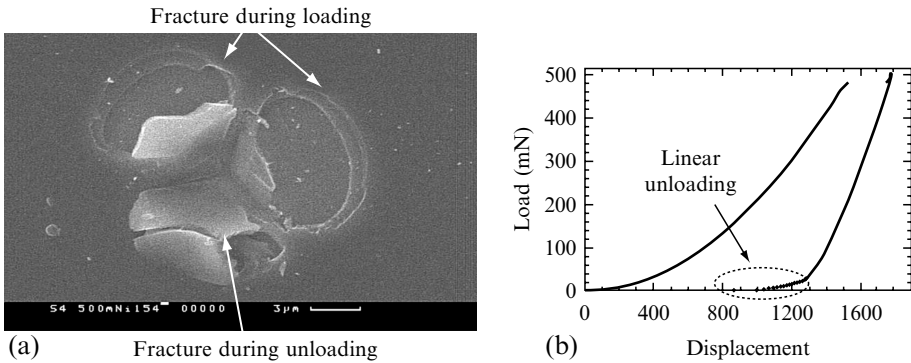


Figure 8. (a) SEM micrograph for a 1 μm thick CN_x coating on Si(001) showing coating fracture during loading and unloading of the indenter at 500 mN applied load. (b) Corresponding P- δ curve showing linear unloading at the bottom of the unloading curve associated with buckling of the coating.

1 μm thick CN_x coatings on Si(001) substrate at 500 mN applied load (Figure 8b). In this case fracture occurs both on loading and unloading.

In order that coating material be ejected from beneath the indenter, radial fracture must occur along the indenter edges such that the coating may be pushed laterally from the contact as the load increases. In such circumstances the size of the pop-in is dictated more by coating thickness and the work of indentation associated with the pop-in event is a complex convolution of the energy needed to slide the coating beneath the indenter and the coating fracture energy. Any fracture toughness measurements based on this failure mode therefore need to be treated with caution.

3.2.1. *Measurements of Fracture Toughness and Interface Toughness*

Since both through thickness and interfacial failure occurs for CN_x coatings on all of the substrates investigated here it is possible to estimate the fracture toughness of coating and interface. However, it must be born in mind that all current analysis methods based on indentation provide only a qualitative assessment and more research is needed to obtain reliable quantitative results.⁴

3.2.1a. *Fracture Toughness of the Coating from Chipping*

The nanoindentation fracture toughness of CN_x films can be estimated by different methods from the literature, the common basis of all of them being the calculation of the energy dissipated in the fracture of the coating. This energy (U_{fr}) is calculated by determining the energy dissipation during chipping from the step observed in the loading part of the load-displacement curve when through-thickness fracture of the coating occurs during indentation.

Three main methods have been used in this study:-

- (a) The method proposed by Li, Diao and Bhushan^{18,19} for which the fracture toughness of the coating is given by,

$$K_{IC} = \left[\left(\frac{E}{(1 - \nu^2)2\pi C_R} \right) \left(\frac{U}{t} \right) \right]^{\frac{1}{2}} \tag{8}$$

where K_{IC} is the critical stress-intensity factor or the fracture toughness of the coating; E is the Young's modulus of the coating,; ν is the Poisson's ratio of the coating; C_R is the crack length,; U is the strain energy difference before and after cracking; and t is the thickness of the coating. In this case the loading curve is extrapolated from the start of the discontinuity to the depth of the end of the discontinuity and U is given by the difference between the extrapolated and measured curves. Toonder et al.⁴ introduced a slight variation to this expression to take into account the number of chipped areas (N; generally 3 when using a Berkovich indenter) and account for the fact that the crack does not propagate perpendicularly to the substrate but at an angle δ . Therefore it is necessary to consider the effective coating thickness ($t = t/\sin \delta$; where δ is the average angle of the chipping edge, see Figure 9) instead of the actual thickness of the coating, t. This leads to the following expression for the fracture toughness of the coating,

$$K_{IC} = \left[\left(\frac{E}{N(1 - \nu^2)2\pi C_R} \right) \left(\frac{U}{t'} \right) \right]^{\frac{1}{2}} \tag{9}$$

- (b) The method of Toonder et al.⁴ based on the calculation of the fracture energy, Γ , from the energy dissipated during chipping, U_{fr}, and the area of the crack formed in the coating by chipping. In this case the total irreversible work, W_{ir}, is determined by measuring the area between the loading and unloading curves and determining the difference before and after chipping by extrapolating the variation of W_{ir} with load for chipped and unchipped samples. The fracture energy is then given by

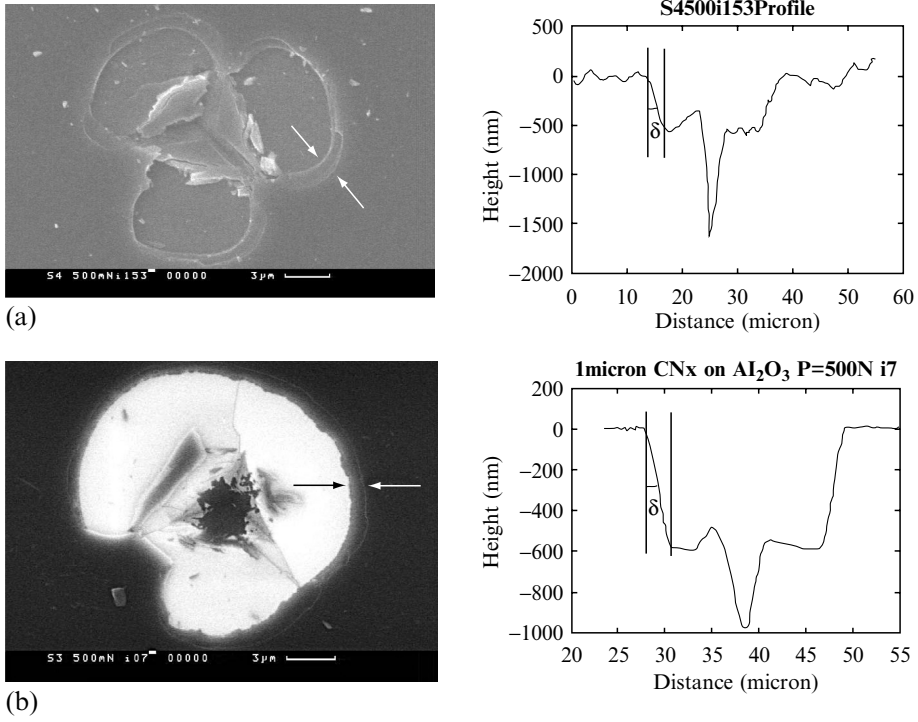


Figure 9. SEM micrographs and corresponding profiles of a 500 mN applied load on 1 μm CN_x coating deposited on (a) Si(001) and (b) Al_2O_3 showing through-thickness fracture and chipping of the coating at an angle, δ .

$$\Gamma = \frac{U_{fr}}{N2\pi t' C_R} \quad (10)$$

The fracture toughness of the coating is then calculated by its general equation,

$$K_{IC} = \sqrt{E\Gamma} = \sqrt{\frac{EU_{fr}}{N2\pi t' C_R}} \quad (11)$$

where E is the elastic modulus of the coating and the other factors have been defined previously.

- (c) Finally, a lower and an upper limit for the fracture toughness of the coating can also be determined by analysis of the load-displacement curve itself at the moment of fracture.⁴ An upper and lower limit for the energy dissipated during chipping of the coating can be calculated by taking into consideration the following assumptions: (i) fully elastic (for the lower limit) or plastic (for the upper limit) behaviour of the material before and after fracture, (ii) P is proportional to δ^2 during loading and unloading²⁰. This would lead to the following limits for U_{fr} ,

$$\frac{2}{3}P_{fr}(\delta_f - \delta_0) \leq U_{fr} \leq P_{fr}(\delta_f - \delta_0) \quad (12)$$

where P_{fr} is the load at which the fracture of the coating is observed and δ_0 and δ_f are the indentation depths before and after the fracture of the coating. The limits for the fracture toughness are calculated by substituting these limits in equations 10 and 11.

Table 3 shows the values for the fracture toughness of CN_x deposited on different substrates for the methods previously presented. There is reasonable agreement between all the methods in the values of the fracture toughness of CN_x except in the case of the original uncorrected expression given by Li et al.^{18, 19} This is due to the fact that for these samples through-thickness of fracture of the coating does not happen perpendicularly to the substrate surface but at a certain angle, as SEM micrographs and optical profilometry show in Figure 9.

3.2.1b. Fracture Toughness of the Interface

Two different expressions have been used to estimate the fracture toughness of the interface between the CN_x coating and different substrates. The first one is that developed by Malzbender and de With²¹ which takes into account the residual stress and the elastic properties of the substrate and is applied to the spalling of coatings during scratch or indentation testing. For this method, the interfacial fracture toughness for a coating possessing residual stress is given by,

$$K_{int}^{\sigma} = \sqrt{\left(0.397 \sin \beta \sqrt{E_{int}} \sqrt{E} \frac{t^{\frac{3}{2}}}{L^2}\right)^2 + \frac{\sigma_{res}^2}{2} t \sqrt{\frac{E_{int}}{E}}} \tag{13}$$

where K_{int}^{σ} is the interfacial fracture toughness; β is the semi angle between two cracks (for a Berkovich indenter $\beta = 60^\circ$); t is the thickness of the coating; L is the crack length (see Figure 10); σ_{res} is the residual stress in the coating; E is the Young’s modulus of the coating;; and E_{int} is the Young’s modulus of the interface, which can be calculated from the following equation assuming equal contributions from coating and substrate,²²

$$\frac{1}{E_{int}} = \frac{1}{2} \left(\frac{1}{E} + \frac{1}{E_s} \right) \tag{14}$$

where, E and E_s are the Young’s modulus of the coating and substrate, respectively.

Table 3. Comparison between the fracture toughness of 1 μm thick CN_x coatings deposited on different substrates based on the energy dissipated during chipping of the coating.

| Substrate | K_{IC} , $\text{MPa}\sqrt{\text{m}}$ | | | |
|-------------------------|--|-------------------|----------------------|--|
| | Bhushan et al.(1997) | Bhushan corrected | Toonder et al.(2002) | Lower and Upper limits Toonder et al. (2002) |
| Si(001) | 6.33 | 3.36 | 2.90 | 5.30 6.50 |
| Al_2O_3 | 5.10 | 2.82 | 2.44 | 2.53 3.10 |
| 3C SiC(001) | 17.70 | 6.37 | 5.51 | 5.50 6.73 |
| 3C SiC(111) | 13.80 | 5.66 | 4.90 | 5.68 6.95 |

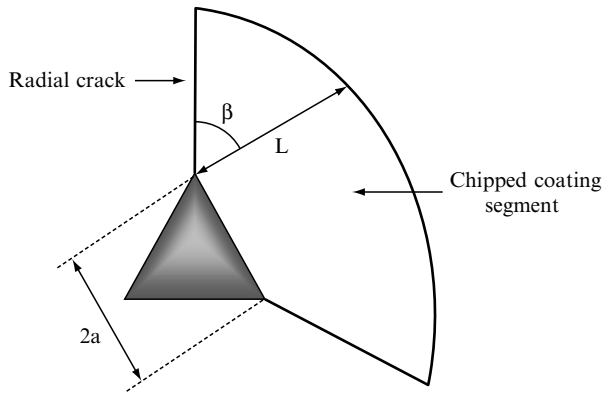


Figure 10. Schematic diagram of the geometry of a chipped segment of coating.

The other expression used is that proposed by Rosenfeld et al.²³ in which the interfacial fracture toughness is related to the size of the delaminated area and the load at which delamination of the coating occurs and is given by,

$$K_{IC} = \frac{0.792H\sqrt{t(1-\nu^2)}}{\left(1 + \nu + \frac{2(1-\nu)HC_R^2}{P_{del}}\right)} \quad (15)$$

where H is the hardness of the coating; t is the coating thickness; ν is the Poisson's ratio of the coating; C_R is the length of the delamination crack; and P_{del} is the load at which delamination occurs.

The results obtained are presented in Table 4. The residual stress in the CN_x coatings deposited on Si(001) has been calculated from the change in radial crack length around Vickers indentations after coating using the following expression introduced by Lawn and Fuller,²⁴

$$1 - \left(\frac{C_0}{C}\right)^{\frac{3}{2}} = \frac{2\sigma t^{\frac{1}{2}}}{K_c} \quad (16)$$

where C_0 and C are the crack length in the substrate and coated sample, respectively; t is the coating thickness; σ is the residual stress in the coating; and K_c is the fracture toughness of the substrate calculated by,²⁵

Table 4. Values of the interfacial fracture toughness for CN_x coatings ($1 \mu\text{m}$ thick) deposited on different samples.

| Substrate | K_{IC} , $\text{MPa}\sqrt{\text{m}}$ | |
|-------------------------|--|-----------------------------|
| | Rosenfeld et al. (1990) | Malzbender & de With (2002) |
| Si(001) | 5.92 | 0.75 |
| Al_2O_3 | 4.67 | 0.68 |
| 3C SiC(001) | 5.51 | 0.40 |
| 3C SiC(111) | 5.58 | 0.41 |

$$K_c = 0.016 \left(\frac{E}{H} \right)^{\frac{1}{2}} PC^{-3/2} \quad (17)$$

where E is the Young's modulus; H is the hardness; P is the applied load; C is the crack length in the uncoated sample. The value for the compressive residual stress in 1 μm thick CN_x coating deposited on Si(001) substrate is $\sim 0.37\text{GPa}$. This value has also been considered for 1 μm thick CN_x coatings deposited on 3C SiC(001) and 3C SiC(111) since the thermal expansion coefficients for 3C SiC are similar to those for Si(001). However, Al_2O_3 substrate presents higher thermal expansion coefficients than Si(001) and therefore the residual stress in CN_x coatings deposited on this substrate is around 0.6GPa.

The values for the fracture toughness of the interface obtained by the two methods differ quite significantly (Table 4) although the trends for the different substrates are the same. One of the reasons for this is that the equation proposed by Rosenfeld et al.²³ does not consider the residual stress in the coating after deposition and the buckling of the coating during indentation, but assumes that the coating has a constant hardness and this is directly proportional to the radial stress. Furthermore, it has been previously seen that for these coated samples the cracks propagate in the substrate/coating interface leading to chipping of the coating, which implies that the fracture toughness of the interface is lower than that of the coating. Thus, comparing Tables 3 and 4 it is expected that the method proposed by Malzbender et al.²¹ provides the most accurate data.

3.3. Brittle Coatings on Brittle Substrates: Oxide Coatings on Glass

In the previous section, clear through-thickness and interfacial fracture events were observed from all of the coating/substrate combinations investigated. However, although interfacial fracture is common in some systems it is by no means universal. The requirement is that buckling of the coating occurs before there is excessive plastic deformation of the substrate leading to through thickness cracking at the edge of the impression prior to delamination during loading. In many cases this cannot be achieved at practical indentation loads and scratch tests are necessary to cause any coating detachment. However, the analysis of failure around a moving indenter is more complicated than for a static indentation and there is no widely accepted analysis method for interfacial toughness in the scratch test.

Oxide coatings on glass do show a range of through-thickness fracture features which can be imaged by scanning electron microscopy if the indentation is large enough (Figure 11). Radial cracking associated with the indenter edges is observed in all cases (Figure 11a) and picture-frame cracking is also observed at higher loads (Figure 11b). However, such cracking is invisible in smaller indents and it is not always clear the conditions of load and indenter geometry necessary to initiate fracture. For this reason there has been an interest in an on-line method for assessing fracture in these small indentations and acoustic emission analysis has been developed with this in mind.

A range of oxide materials which are used in low emissivity and solar control coatings have been deposited on glass to 200 nm thickness and the acoustic emission response monitored during nanoindentation testing. In addition a 200 nm layer on zirconium metal was deposited on the float glass substrate and allowed to oxidise in air

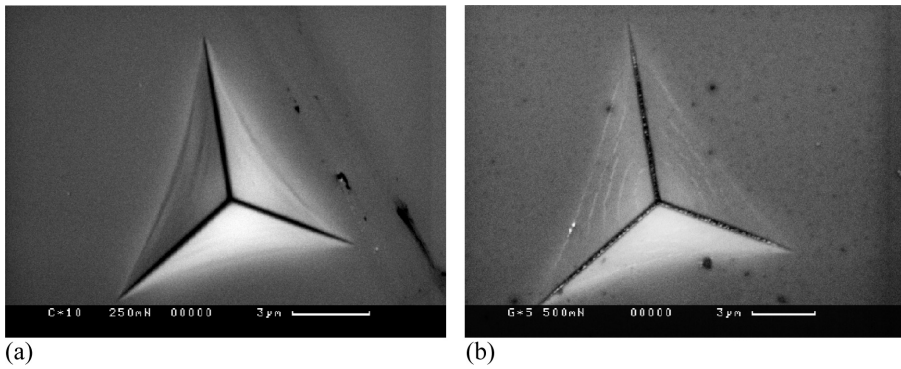


Figure 11. Scanning electron micrographs of high load nanoindentations in multilayer oxide coatings on glass (a) 250 mN indent with radial splitting along the indenter edges and (b) 500 mN indent showing a combination of radial splitting and picture frame cracking.

prior to indentation testing. This is expected to have a higher toughness than the deposited oxides. Figure 12 shows that the first load at which acoustic events are observed above threshold is highest for this coating which would follow if the acoustic events are associated with fracture. Also a multilayer optical stack ending in a 200 nm thick TiO_xN_y layer has been deposited for comparison with the single layer coatings; results are comparable but not identical implying that the substrate is influencing the fracture behaviour of the coating. Indentations in the uncoated substrate showed no acoustic emission events over the complete load range investigated.

AE signals result from the sudden release of elastic energy or from surface interactions such as indenter/surface friction or adhesion. In the case of static indentation testing the release of elastic energy is the dominant mechanism for AE formation; sudden release of elastic energy can arise due to unstable crack growth, high speed phase transformations and plastic instabilities including the initiation of new slip²⁶ or twinning systems, the activation of dislocation sources²⁷ or the sudden acceleration or unpinning of existing dislocations.²⁸ The substrate and coatings investigated here are either amorphous and show poor crystallinity and it is unlikely

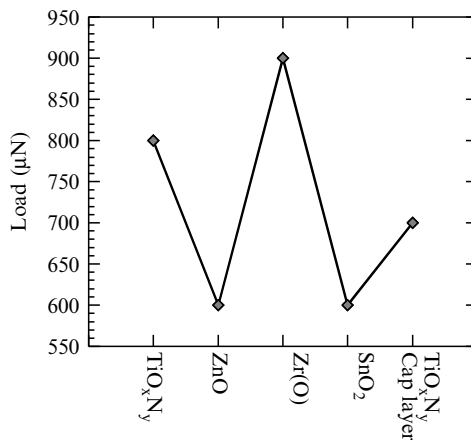


Figure 12. Graph of the load at which the first acoustic emission event is observed for the samples above indicated.

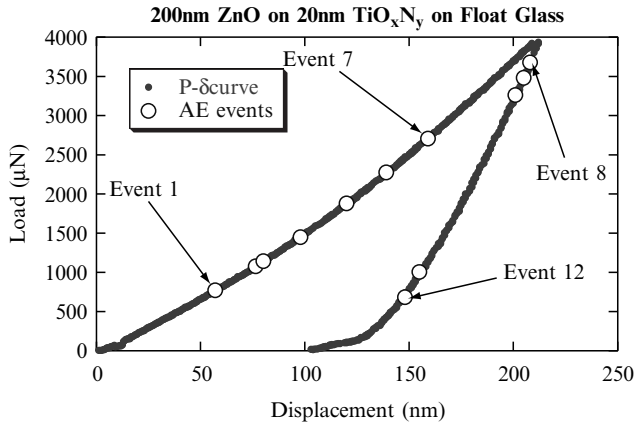


Figure 13. Load-displacement curve for 4000 μN peak load nanoindentation in 200 nm ZnO coated glass where the positions of the acoustic events are indicated.

that dislocation mechanisms will dominate behaviour, particularly as many events occur on unloading as well as on loading (Figure 13). In addition there are no acoustic events observed in the testing of uncoated glass at the same loads and the first events occur well after plastic deformation has initiated and a permanent impression is created. It is most likely that the acoustic emission arises as a result of fracture and the ZnO and SnO₂ layers would therefore appear to have the lowest toughness if it is assumed that the defect distributions within these coatings do not vary greatly. This is a reasonable assumption since they were all deposited in the same coating system using very similar coating conditions.

Detailed characterisation of the acoustic emission waveform of each of the events in terms of A_{EST} and t_{at} reveals that there are two different types of events occurring, a fact which is mirrored for all the coated samples investigated here (Figure 14). The event with the lower A_{ESF} always occurs first in the load-displacement curve and always in groups of three whereas the other event is more random.

The fact that the event with the emission shape factor around two occurs in both the loading and unloading curves is strong evidence that this event is associated with the radial splitting of the coating under the indenter. Radial fracture is expected since the hoop stresses in the material tested with a conical indenter are tensile and this fracture can extend outside the impression on unloading due to the residual stresses created by the plastic deformation which has occurred, akin to the mechanism for the growth of radial cracks in microindentation testing of bulk glasses and ceramics²⁹.

One other interesting observation is that the failures with the lower A_{ESF} tend to occur in threes. This is not expected since the indenter is nominally a 120° cone with no edges. However, a detailed analysis of the indenter geometry reveals that it does not have a circular cross-section but shows three distinct lobes (possibly related to the effects of crystal structure on the ease of polishing) which are visible in the shape of indents made at high load in softer materials. Such lobes will act as stress concentrations like the indenter edges of a Berkovich indenter and will therefore promote fracture. This is added evidence that radial fracture is associated with this failure mode. The higher emission shape factor failure occurs more randomly and at higher loads and is less influenced by the detailed indenter geometry as might be expected for

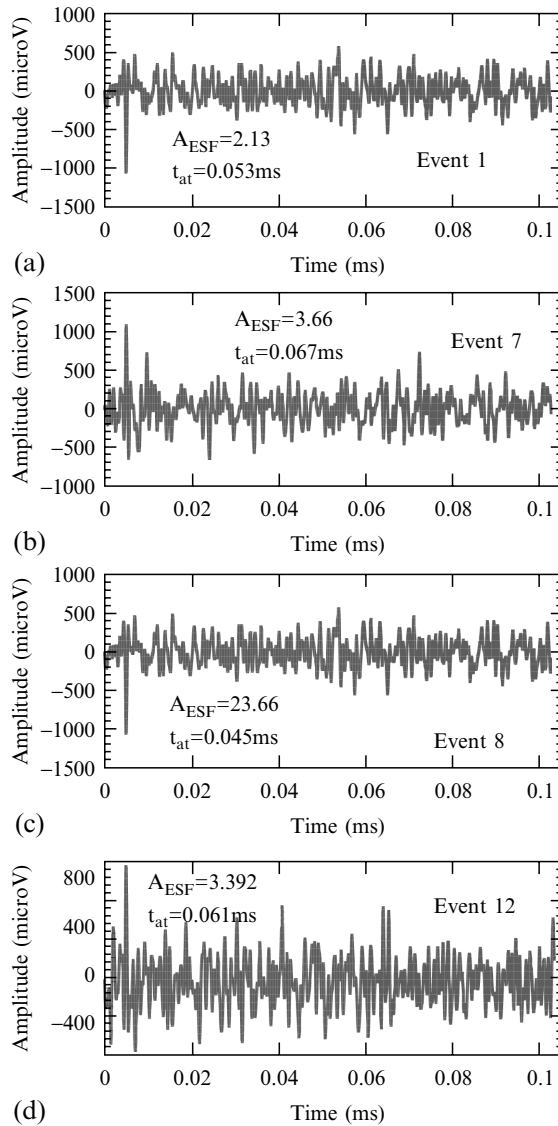


Figure 14. Analysis of the acoustic function for events (a) 1, (b) 7, (c) 8 and (d) 12 in Figure 13. It is clearly observed that event 1 and 8 are the same kind of event since the acoustic wave is similar and the emission shape factor and attenuation time are of the same order of magnitude. The same happens for events 7 and 12, although the similarity is not so pronounced.

picture frame cracking. However, no evidence for fracture was observed in the in situ AFM images obtained with the indenter after making the impressions so assignment of the failure types must be treated with caution.

It is clear from the fact that a number of similar acoustic events are observed in a single load displacement curve that the fracture occurring during indentation is discontinuous and statistically determined depending on the defects in the coating

and substrate. If estimates of the fracture toughness of the coatings are to be achieved using this approach then it is necessary to relate the acoustic events to the extra work of fracture included in the irreversible work of indentation in a similar manner to that outlined previously for CNx coatings. However, Figure 14 clearly shows that there are no obvious pop-in events in the load displacement curve and any changes are too subtle to discern in the raw data. To identify if such events exist the curve must be processed to reveal these changes.

One approach to achieving this is to plot load against displacement squared³⁰ (Figure 15). For an ideal material this ratio should be constant if elastic-plastic deformation occurs but may vary gradually from one value to another as plastic deformation extends from the coating material to the substrate. Any localised excursions from this behaviour represent a change in deformation mechanism as might be caused by fracture. The data from Figure 14 analysed in this manner in Figure 15 show a large number of excursions occur in the loading curve for 200 nm ZnO on glass. However, only seven acoustic events occur during loading and the correlation with the excursions is poor. In general, the number of acoustic emission events increases as the number of excursions increases. It is probable that there are many more fracture events occurring during the indentation cycle than give rise to measurable acoustic emission. The chances of relating a given acoustic event to the detailed changes in the load-displacement curve are therefore very small. In addition, since the length of the radial crack and how it grows are not known (though are probably related to indent size) determining crack area and toughness by this method is not possible.

4. CONCLUSIONS

Fracture is critical in determining the performance of ceramic coatings in a range of applications. Both through-thickness and interfacial fracture can occur but the former is far more likely to be produced in indentation tests. Both through-thickness

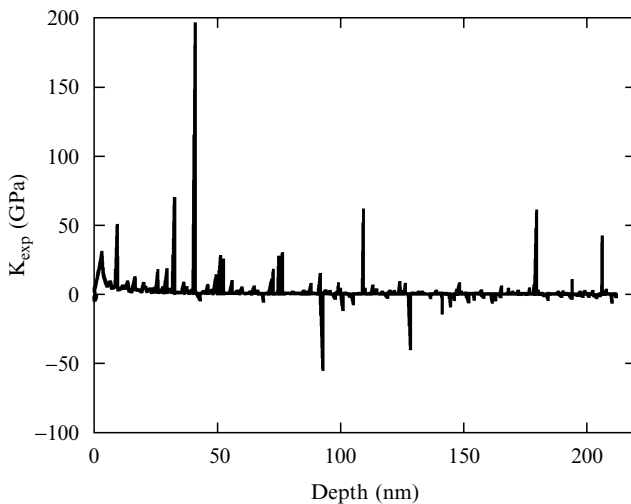


Figure 15. Variation of $K_{exp}(=P/\delta^2)$ with displacement during loading for the loading curve in Figure 13.

radial fracture (associated with the indenter edges) and picture frame cracking are observed for most coating/substrate systems. The radial fracture occurs at the lowest loads and is the first fracture event to be observed in indentation tests. Radial crack growth is discontinuous and occurs both on loading and unloading of the indenter. Acoustic emission may be used to monitor fracture events in coated systems though not all such events produce a measurable acoustic signal. Emission shape factors can be used to differentiate between different types of events which are related to different fracture modes.

Calculation of the fracture toughness of the coating and the interfacial toughness can be undertaken in some cases where the deformation mechanisms can be identified and the type of failure produced is amenable to analysis. However, the analysis methods cannot be regarded as universal as the failure modes vary with materials and are often more complex than the models allow for. As the thickness of the coating is reduced the calculation of toughness is also made more difficult by the need to obtain accurate measurements of crack area and differences in the work of indentation which are beyond the resolution of current instrumentation.

ACKNOWLEDGEMENTS

The authors would like to thank Ion Bond, Linkoping University and Pilkington Technology Centre for the provision of samples and Martin McGurk for the provision of some data.

REFERENCES

1. A.C. Fisher-Cripps, *Vacuum*, **58** (2000) 569.
2. B. Bhushan, in *Handbook of Micro-Nanotribology*, Ed. B. Bhushan, CRC Press, Boca Raton, 1995, pp321–396.
3. S.V. Hainsworth, H. Chandler and T.F. Page, *J. Mater. Res.*, **11** (1996) 1987.
4. J. den Toonder, J. Malzbender, G. de With and R. Balkenende, *J. Mater. Res.*, **17** (2002) 224.
5. S.V. Hainsworth, M.R. McGurk and T.F. Page, *Surf. Coat. Technol.*, **102** (1998) 97.
6. MrR. McGurk, PhD Thesis, University of Newcastle, (1997).
7. N. Hellgren M.P. Johansson, E. Broitman, P. Sandstrom, L. Hultman and J.-E. Sundgren, *Phys. Rev.*, **B59** (1999) 5162.
8. W.C. Oliver and G.M. Pharr, *J. Mater. Res.*, **7** (1992) 1564.
9. S.V. Hainsworth, S.J. Bull and T.F. Page, *Mat. Res. Soc. Symp. Proc.* **522** (1998) 433.
10. A. Daugela, H. Kutomi and T.J. Wyrobek, *Z. Metall.*, **92** (2001) 1052.
11. N.I. Tymiak, A. Daugela, T.J. Wyrobek and O.L. Warren, *Mat. Res. Soc. Symp. Proc. Fall Meeting* (2002), in press.
12. J. Crepin, T. Bretheau, D. Caldemaison and F. Ferrer, *Acta Materialia*, **48**, (2000) 505.
13. S.J. Bull and A.M. Korsunsky, *Tribology Int.*, **31** (1999) 547.
14. S.J. Bull, *J. Vac. Sci. Technol.*, **A19**, (2001) 1404.
15. S.J. Bull, *Thin Solid Films*, **398–399**, (2001) 291.
16. B.R. Lawn, A.G. Evans and D.B. Marshall, *J. Am. Ceram. Soc.*, **63**, 574 (1980).
17. M.D. Thouless, *Eng. Fract. Mech.*, **61** (1998) 75.
18. X.Li, D. Diao and B. Bhushan, *Acta Mater.*, **44** (1997) 4453.
19. X.Li, D. Diao and B. Bhushan, *Thin Solid Films*, **315** (1998) 214.
20. J. Malzbender, G. de With and J.M.J. den Toonder, *J. Mater. Res.*, **15** (2000) 1209.
21. J. Malzbender and G. de With, *Surf. Coat. Technol.*, **154** (2002) 21.
22. J.W. Hutchinson and Z. Suo, *Adv. Appl. Mech.*, **29** (1992) 63.

23. L.G. Rosenfeld , J.E. Ritter, T.J. Lardner and M.R. Lin, *J. Appl. Phys.*, **67** (1990) 3291.
24. B.R. Lawn and E.R. Fuller, *J. Mater. Sci.*, **19** (1984) 4061.
25. G.R. Anstis, P. Chantikul, B.R. Lawn and D.B. Marshall, *J. Am. Ceram. Soc.*, **64** (1981) 533.
26. D. Rouby, P. Fleischman and C. Duvergier, *Phil. Mag.* **A47** (1983) 671.
27. V.D. Natsik and K.A. Chishko, *Sov. Phys. Solid State*, **20** (1978) 1117.
28. J. Weiss and J.R. Grasso, *J. Phys. Chem.*, **101** (1997) 6113.
29. B.R. Lawn and R. Wilshaw, *J. Mater. Sci.*, **10** (1975) 1049.
30. M.McGurk and T.F. Page, *J. Mater. Res.*, **14** (1999) 2283.

NANOINDENTATION, NANOSCRATCH AND NANOIMPACT TESTING OF SILICON-BASED MATERIALS WITH NANOSTRUCTURED SURFACES

Jinjun Lu, Tao Xu, Qunji Xue, and Ben D. Beake*

1. INTRODUCTION

In recent years, nanomaterials receive extensive attention due to their unique properties. Nano-structured Si-based materials are considered as one of the key material issues in microelectromechanical systems (MEMS).¹ Many techniques have been employed to fabricate Si-based materials with nano-structured surface.²⁻³ Nanograin polysilicon ultra-thin film can be deposited on p-type silicon wafers by chemical vapor deposition (CVD).² Ion-beam sputtering (IBS) at low energy (typically 1.2 keV) has been used to fabricate nanodots on silicon wafers, which could meet the key requirement for the development of future optoelectronic and electronic devices.³ For the tribological consideration however, the bonding between nanograin polysilicon ultra-thin film by CVD and its substrate might not strong enough. Therefore, techniques like IBS should be studied to eliminate the interface between the film and the substrate. Micromachine fabrication using ion implantation has the

* Jinjun Lu, Tao Xu, Qunji Xue, State Key Laboratory of Solid Lubrication, Lanzhou Institute of Chemical Physics, Chinese Academy of Sciences, Lanzhou, P. R. China 730000. Ben D. Beake, Micro Materials Ltd. Unit 3, The Byre, Wrexham Technology Park, Wrexham, LL13 7YP, UK

advantage of good controllability of material properties.⁴ Compared with IBS, ion implantation involves two procedures, implantation and sputtering. The most important thing is that implanting reactive species can modify the composition of the implanted layer, which is beneficial for the mechanical and tribological performance. Therefore, ion implantation is chosen as the means of fabrication.

The aims of our research are: 1) to explore the possibility of fabricating nanostructured surfaces on single crystal Si and SiO₂ by ion implantation and 2) to study the nanomechanical and nanotribological behaviors of the ion beam modified layers by nanoindentation, nanoscratch and nanoimpact testing. We found that nanostructured surfaces can be obtained by N ion implantation at doses of 5×10^{16} and 1×10^{17} ions/cm², respectively.⁵ In the present paper, the nanomechanical and nanotribological behaviors of N ion implanted single crystal SiO₂ and Si were studied using nanoindentation, nanoscratch and nanoimpact testing.

2. EXPERIMENTAL DETAILS

N ion implanted single crystal Si and SiO₂ wafer with doses of 5×10^{15} , 1×10^{16} , 5×10^{16} , 1×10^{17} and 5×10^{17} ions/cm² respectively was prepared using an ion implanter at 100 keV. Transmission electron microscopy (TEM) was used to study the microstructure of N ion implanted single crystal SiO₂ wafer.

The NanoTest system (Micro Materials, Wrexham, UK) was used for nanoindentation and nanoscratch testing of ion implanted single crystal silicon and nitrogen ion implanted single crystal SiO₂. For the nanoscratch testing a conical diamond with 25 μm end radius was used throughout. The scratch experiments involved three sequential scans over the same 100 μm track all at 1 μm/s scan speed. In the first topography scan the applied load was kept at 0.2 mN (no wear occurs at this load). In the second (scratch) scan, the applied load was kept at 0.2 mN between 0–20 μm and then was ramped at a constant rate of 1.77 mN/s so that the maximum load reached at 100 μm was 142.5 mN. In the final scan the resultant topography was observed by using a low applied load of 0.2 mN.

For the nanoindentation a Berkovich (3-sided pyramidal) indenter was used throughout. Repeat indentations to 200 mN were performed with loading and unloading rates set equal at 4.04 mN/s and an 0.05 mN initial load was applied. There was a small (5s) dwell time at maximum load to allow for creep before unloading, since continuing plastic deformation during unloading can distort the shape of the unloading curve and lead to inaccurate values of hardness and modulus.

The aim of the nanoimpact testing was to investigate the impact wear-resistance of the ion-implanted Si and SiO₂ samples using the Impact Module of the Micro Materials NanoTest system. The pendulum impulse technique was used. A solenoid connected to a timed relay was used to produce the probe impacts on the surface, as shown schematically Figure 1 (note: magnetic rather than mechanical means was used to actuate the solenoid in this work). The probe was accelerated from 13 microns from the surface for each impact.

The samples were mounted on a standard NanoTest sample stub using superglue. They were cleaned with an “Air Duster” and thermally equilibrated in the NanoTest environmental cabinet before the nano-impact testing. Two different types of impact tests were set up (Table 1).

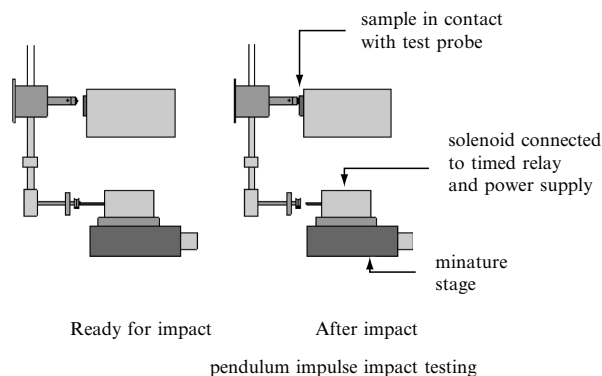


Figure 1. Illustration of nanoimpact testing.

Table 1. Description of two different types of impact tests.

| Mode | Test probe | Impulse load | Test duration |
|--|--|----------------|---------------|
| Preliminary testing with 25 μm radius spherical probe | spherical diamond (nominal radius 25 μm radius) | 5.0 and 8.0 mN | 600 s |
| Inducing fracture with sharp cube corner indenter | cube corner (90 degree) diamond indenter | 2.0 mN | 150 s |

Impulse control cycle: repeat application of the impact load – off for 2 s and then on for 2 s

This cycle corresponds to 1 impact every four seconds, with the probe spending 2 seconds on the sample surface between successive impacts. Note that in all tests the sample was *not* moved during impacting – so that the probe always impacts in the same location on the surface.

3. RESULTS AND DISCUSSION

3.1. Nanoscratch Testing on N Ion Implanted Si and SiO₂

3.1.1. N ion Implanted Single Crystal SiO₂

The critical load for the transition between plastic deformation and fracture failure has been estimated from the inflexion point in the on-load scratch trace (scan 2). This correlates well to the onset of cracking as seen in the final topography scan.

Samples 3 and 4 (5×10^{16} and 1×10^{17} ions/cm²) shows much improved performance over the unimplanted SiO₂. Of the two, sample 3 has the higher critical load (L_c 57.2 mN) for fracture failure. It is clear that ion-implantation does not affect the sample roughness until an ion dose of 1×10^{17} ions/cm² is reached. It is possible therefore that the slight decrease in critical load on sample 4 compared to sample 3 is due to the adverse influence of increasing roughness on the resistance to nanoscratching wear.

In addition, the nanoscratch experiments also clearly reveal the applied load necessary for the transition between elastic and plastic behavior during scratching. On unimplanted SiO₂ there is a long period of elastic behavior (intuitively we expect a single crystal to behave more elastically in compression than the damaged material) before the deformation becomes plastic in nature. This is then followed by a short period of plasticity before fracture (brittle) failure. The behavior on implanted

Table 2. Variation in L_c for plastic deformation to fracture failure transition from inflexion in displacement vs. depth curve, surface roughness, and on-load depth reached in scratch test at maximum load (142.5 mN)

| Implanting doses, N/cm ² | Average L_c (mN) | Roughness(Ra) nm | Mean final depth/nm* |
|-------------------------------------|--------------------|------------------|----------------------|
| Sample 0, 0 | 42.7 | 3.09 | 1085 ± 50 |
| Sample 1, 5×10^{15} | 39.7 | 3.50 | 867 ± 4 |
| Sample 2, 1×10^{16} | 45.8 | 3.47 | 830 ± 5 |
| Sample 3, 5×10^{16} | 57.2 | 3.49 | 833 ± 8 |
| Sample 4, 1×10^{17} | 51.5 | 6.58; 8.40; 8.02 | 877 ± 8 |
| Sample 5, 5×10^{17} | - | 74.4; 67.7; 59.3 | 2150 ± 200 |

Mean values shown 4–6 determinations. “–” inflexion point not clear on this rough sample.

R_a values are over central region (33.3–66.6 μm) of a levelled 100 μm region of surface *before scratch testing*.
*“±” represents the standard error in the mean, after leveling on the initial 0–20 μm (unworn) region of the track.

samples is different – the critical load for the elastic-plastic transition is much lower, and this is followed by a longer period of plastic behavior before brittle failure occurs at higher applied load [as the polycrystallites can move more freely under shear]. Typically the elastic-plastic transition was at 27 mN on the implanted SiO_2 and 6–12 mN on the implanted samples. The final on-load scratch depth is a composite response of the sum of elastic + plastic + fracture deformation which occurs during the scratch test, (\approx a measure of the resistance to scratching wear). It decreases with increasing ion dosage. The high value on the unimplanted sample is due in part to the increased elastic deformation on this material. The closeness of the values on the ion-implanted samples 1–4 shows that at these doses the implantation produces a material whose mechanical properties do not cross the surface (i.e. suggestive of a well-controlled implantation process).

3.1.2 N Ion Implanted Single Crystal Si

In contrast to what is observed on SiO_2 , table 3 below shows that N ion implantation actually decreases the critical load required for the onset of fracture failure in silicon. The on-load scratch traces also show an inflexion at the elastic-plastic transition at much lower load that correlates with final topography data as well. On sample 5 this is at 10 mN. There is also catastrophic failure at a higher applied load than the L_c values in Table 3.

The critical load for catastrophic failure occurs at a higher applied load than the L_c values for the onset of fracture failure tabulated above. It also decreases markedly with increasing N ion dosage, except on sample 2, which appears more resistant to catastrophic failure (Table 3).

Although the on-load depth is lower on sample 4 this does not necessarily represent improved tribological performance in this case. Examination of the curves show that during the on-load scratch the probe is pushed out of the material by cracking (e.g. by uplift at the edge of the scratch track which helps to support the scratch load) which leads to a lower final depth. This material is pushed up over the scratch track as observed in the final topography as shown in the figure 2b.

Micro-scale scratching of bulk Si by Bhushan and co-workers (1995) showed similar behavior to our scratch results on the unimplanted Si wafer.⁶ Using a much smaller probe (conical diamond with 1 μm end radius) they observed (from friction

Table 3. Variation in L_c for plastic deformation-fracture failure transition from inflexion in displacement vs. depth curve and on-load depth reached in scratch test at maximum load (142.5 mN).

| Implanting doses, N/cm ² | Mean L_c /mN | Mean final depth/nm* |
|-------------------------------------|----------------|----------------------|
| Sample 0, 0 | 82.1 ± 4.4 | 490 ± 8 |
| Sample 1, 5×10^{15} | 70.7 ± 5.6 | 467 ± 5 |
| Sample 2, 1×10^{16} | 71.5 ± 6.3 | 561 ± 7 |
| Sample 3, 5×10^{16} | 45.7 ± 0.4 | 524 ± 5 |
| Sample 4, 1×10^{17} | 40.9 ± 4.6 | 390 ± 6 |
| Sample 5, 5×10^{17} | – | 572 ± 26 |

Mean values from 4–6 determinations. * inflexion point not clear on this rough sample.

“±” represents the standard error in the mean, after levelling on the initial 0-20 μm (unworn) region of the track.

and SEM data but with no accurate depth information) the elastic-plastic transition occurred at 4mN and ploughing at higher load until the onset of fracture at 16 mN and catastrophic failure at 18 mN. In view of the differences in contact pressure due to the different tips used these results are in reasonable agreement with those of this study. Post-scratch SEM shows that that much material is moved into/on-top of the scratch track (particulate debris of sub-micron size). This is consistent with the large increases in probe position in the final topography observed in our experiment.

It is clear from Table 3 that N ion implantation does not result in roughening of the Si surface at any of the doses used. To generate sufficient damage to get roughening it is necessary to use argon ions of larger cross-sectional area.

3.2. Pop-in and Pop-out Phase Changes of N Ion Implanted Si

Silicon is well-known as having unusual indentation behavior due to phase changes which occur on loading and unloading. The pop-ins have been associated with transition from semiconducting diamond cubic structure into metallic B-tin structure (i.e. a semiconductor-to-metal) at critical pressure. Unloading causes a volume-expanding reverse phase transformation from B-tin into an amorphous structure.⁷⁻⁸ Since these phase changes occur at critical pressures it is not possible to compare

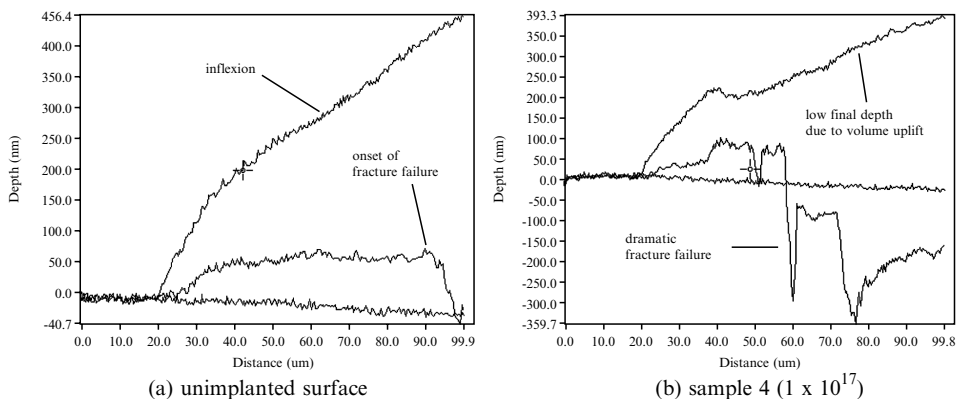


Figure 2. Typical behavior of N ion implanted Si.

Table 4. Pop-in and pop-out phase changes on ion implanted Si

| Implanting doses, N/cm ² | Pop-in load/mN | Pop-out/mN |
|-------------------------------------|---------------------|--|
| Sample 0, 0 | 170, 176 | 115.4, 123.8 |
| Sample 1, 5×10^{15} | 178.3, <i>178.3</i> | 122.5, 126.3, <i>110.5</i> , <i>111.1</i> , <i>111.5</i> |
| Sample 2, 1×10^{16} | # | 86.6, 82.4, 60.5 |
| Sample 3, 5×10^{16} | 152.2 | 53.7 |
| Sample 4, 1×10^{17} | 148.6 | 62.6, 57.9, 65.8 |
| Sample 5, 5×10^{17} | # | 43.3, 52.2 |

*critical load values in repeat tests are shown in italics. Note that the load given is that for the start of the pop-in or out transition. # not clear transition during loading.

exact values with other studies since our indenter geometry will be different (it is likely to be blunter so that a greater applied load is necessary before the critical pressure for phase transformation is reached).

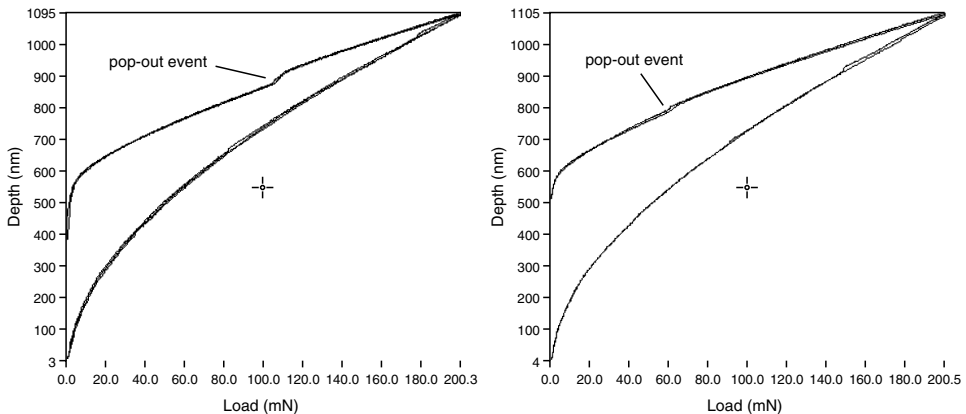
The critical pressures on the Si sample implanted with the lowest dose are very similar to those of the unimplanted Si (Figure 3). At greater pressures the pop-in phase transformation occurs at lower load (i.e. is made energetically favourable) but the unloading transformation occurs at lower load (made energetically unfavourable).

It has been shown previously that CN_x films retard the unloading phase transformation, i.e. that the coating keeps the Si in the dense metallic form.⁹ It has also been shown that amorphous Si does not undergo the same phase transformations on loading and unloading.¹⁰ It appears that the ion implanted samples act as if they were partially amorphised.

The indentation curves also showed that Sample 5 shows a very soft near-surface region – revealed by shapes of loading curves – i.e. plastic flow at low indentation pressures, as has been seen on amorphous Si.

3.3. Comparison Between Si and SiO₂

Various parameters such as the on-load depth and critical load for fracture can be used to compare between the materials. Nanoindentation shows that unimplanted Si is harder and less elastic (higher modulus) than SiO₂. The lower critical loads

**Figure 3.** Pop-outs on sample 1 (5×10^{15}) and sample 4 (1×10^{17}).

observed on SiO₂ and greater maximum on-load scratch depth (by a factor of 2–3) correlate with its lower hardness.

The H/E ratio is a key parameter determining the type of behaviour observed in nanoindentation and nanoscratching wear. Si has a lower H/E ratio than SiO₂ which explains why the transition from elastic to plastic behaviour occurs at higher contact pressure on this material.

It is interesting to speculate why ion implantation does not lead to a similar obvious improvement in the nanotribological performance of Si as it does on SiO₂. Being harder (and having a more closed crystal structure?) the Si may not be damaged sufficiently by N ions at these doses to reach the fully-nanocrystalline state. Supporting evidence is (1) pop-ins and pop-outs are still observed during nanoindentation (even if the critical pressures are changed) – amorphous Si does not do this (2) even the highest N dose does not lead to any roughening of the surface.

Bhushan (2001) has shown that C⁺ ion implantation results in a hardening of the surface layer which results in improved microscratching wear performance. With N ion implantation do the competing mechanisms of 1) softening due to destruction of the matrix 2) hardening due to the formation of Si₃N₄ (or similar) phases, act against each other resulting in no improvement in tribological properties?

3.4. Nanoimpact Testing of N Ion Implanted Single Crystal Si and SiO₂

3.4.1. Preliminary Testing with 25 μm Radius Spherical Probe

It is not possible to use nanoindentation methods to obtain information about the impact fracture and erosive wear performance. High hardness can confer improved wear resistance but it is often associated with brittleness and poor toughness and erosive wear resistance.

3.4.1a N Ion Implanted Single Crystal Si

The preliminary impact test results are shown in Figure 4a. The plots show the evolution of impact-induced damage with time (i.e. plastic deformation, fatigue wear and fracture) throughout the test. The height of the surface is recorded with sub-nm precision when the probe is on the surface.

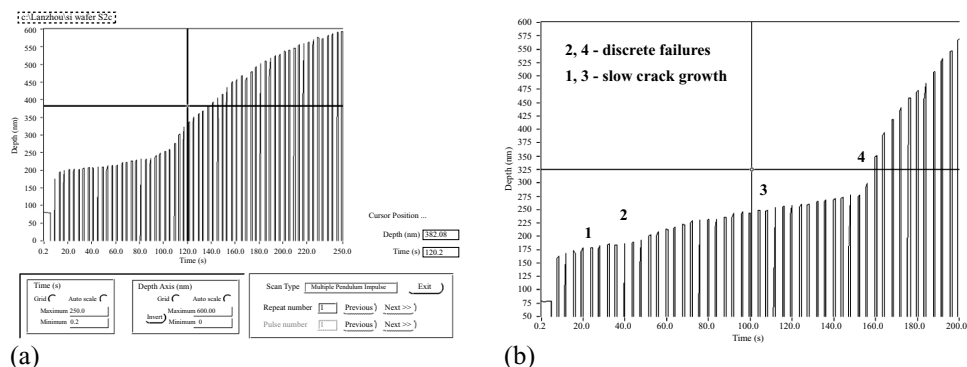


Figure 4. Typical behavior of N ion implanted Si.

The results show typical impact behavior for a brittle material. There are long periods of damage accumulation (“plateau periods”) where small cracks grow sub-surface and the surface position changes relatively little with time. These are separated by more rapid events where material is removed as the cracks propagate and coalesce leading to these failures.

The instrument software allows for “zooming-in” on features of interest such as these failure events. Figure 4b shows zoom to the beginning of the tests. The plot below is very interesting as it shows volume uplift (or surface bulging) just before fractures.

This “volume uplift” is due to the formation of micro- and nano-cracks sub-surface in the material. Because the damaged material is constrained from breaking away from the surface by the (less damaged) material above it, the cracks cause the material to swell up forcing the probe “out of the surface”. This has also been seen on DLC coatings and other brittle materials.

The behavior in extended impact tests (i.e. at longer impact times) shows a similar trend to production of sub-surface damage and surface bulging before surface failure etc.

As well as these very clear multiple fractures another common type of behavior is illustrated below.

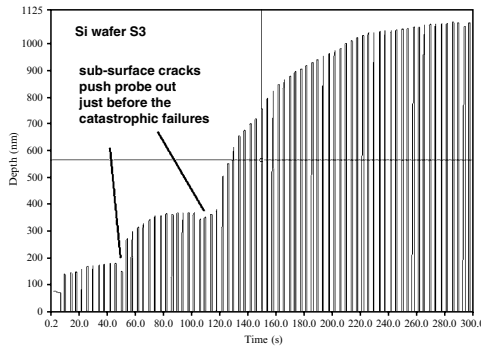


Figure 5. Volume uplift due to the formation of micro- and nano-cracks sub-surface in the material.

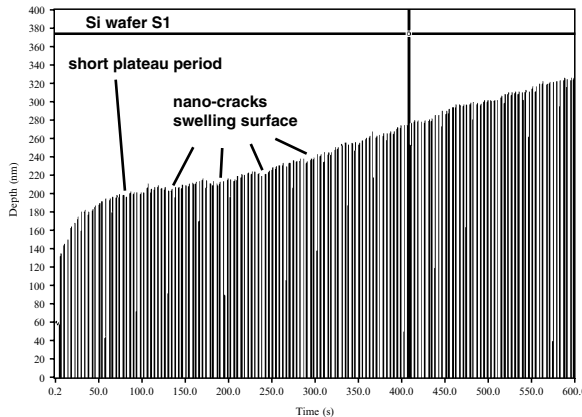


Figure 6. Multiple fractures.

There is a very short plateau period followed by 1 or more small cracking events (the surface bulges before the cracks coalesce, and the process repeats). The first inflexion between the flat plateau and faster wear/cracking occurs after ~30–50 s, (at greater times for higher doses). The depth at this transition is (180 nm ± 20) for all the samples.

3.4.1b N Ion Implanted Single Crystal SiO₂

More common under these conditions than sharp fracture is the type of behaviors shown below.

The probe penetrates ~70 nm into the surface under the static of load of 8 mN. The first impact results in further 80 nm depth penetration (plastic deformation). There is then a plateau period where the probe position levels off (i.e. some plastic deformation occurs but surface not being worn away during this period, erosive wear rate is very low). During this period the plastic deformation results in the initiation and development of cracks underneath the contact surface. At ~54 s (shown by the cursor in the plot) the depth begins to increase again (ie rate of wear increases sharply). The time-at-inflexion is likely to be related to the fracture resistance, since longer times presumably reflect increased barrier to coalescence/propagation of sub-surface nano-/micro-cracks. These times vary on the SiO₂ samples as shown below.

Results at 5 mN (squares) and 8 mN (triangles) show a trend to increasing time-to-inflexion with the ion dose, reaching a maximum at dose 1×10^{16} ions/cm². The inflexions are small.

From the results with the blunt spherical probe we can see that impact testing is a statistical process, since it involves inducing plastic deformation, crack initiation and coalescence/fracture [i.e. fatigue]. Several tests are necessary to get a complete picture of the range of behaviour observed, as is common in fatigue tests.

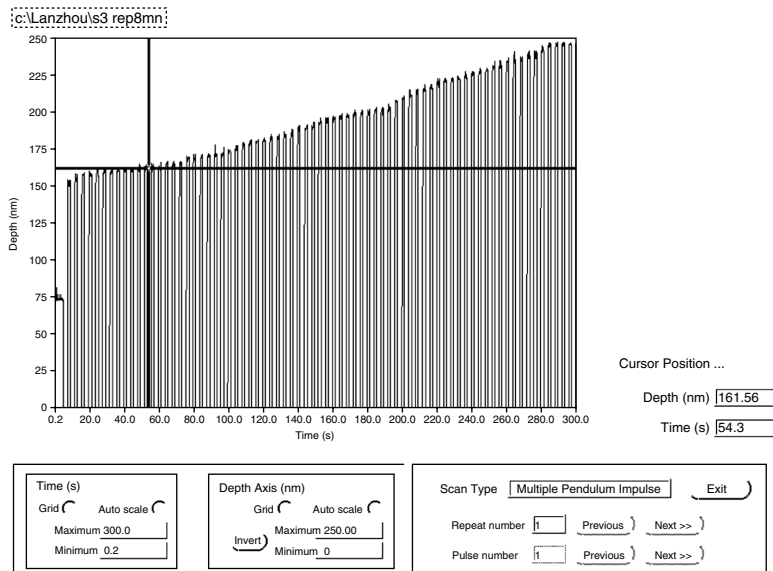


Figure 7. Sharp fracture in N ion implanted single crystal SiO₂.

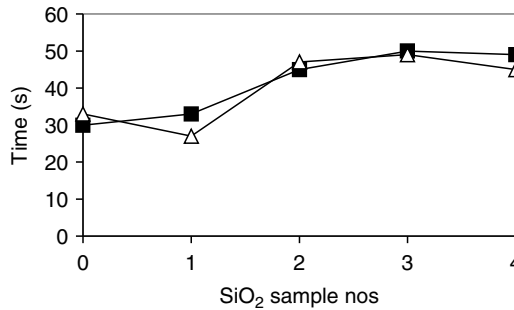


Figure 8. Variation in time-to-first failure (s) with sample.

Clearly the wear rate is not constant through the test and detailed examination of the results allows individual failure events (shown by the changes in slope and abrupt changes in depth) to be investigated.

There was evidence that the time at which the increase in wear rate occurs correlated with ion dose for both the Si and SiO₂ implanted samples (generally greater dose = longer time-to-failure).

3.4.2 Inducing Fracture with Sharp Cube Corner Indenter

A cube corner indenter was used to test these observations and to more easily induce fractures. The cube corner indenter is sharper (higher contact pressure) and the 90 degree angle means that the instantaneous contact strain under the probe on impact is much greater than for the spherical probe.

3.4.2a N Ion Implanted Single Crystal Si

Failures are generally less sharp than on SiO₂. The fracture resistance of the samples can be compared by: (1) wear rate at end of test, (2) depth at end of test, (3) presence or absence of clear surface failure/fracture events, and (4) the time at which first failure/fracture occurs. The type of behavior observed falls into distinct groups (Table 5).

The fracture toughness of sample 4, (i.e. resistance to propagation of the cracks which would cause failure and removal of material) is high. This is seen in the final impact depth data.

These impact depths have been compared with the final on-load scratch depth data in the graph below (impact = circles, scratch = filled squares).

Table 5. Classified group on ion implanted Si.

| Group | Pop-in load/mN |
|-------------------|---|
| Sample 0, 0 | Low wear rate, with little clear fracture |
| Sample 1, 2 and 5 | All are very susceptible to surface damage, cracking/fracture (especially at short times) and also show a high wear rate at 150 s. Short periods of surface bulging/swelling are often followed by cracking, and fast wear rate |
| Sample 3 | generally lower wear rate, with some failures at relatively short times |
| Sample 4 | shows occasional small failures in some tests but mostly they are absent. The wear rate soon drops to near zero and the predominant process is sub-surface cracking causing the slight bulging/swelling of the surface |

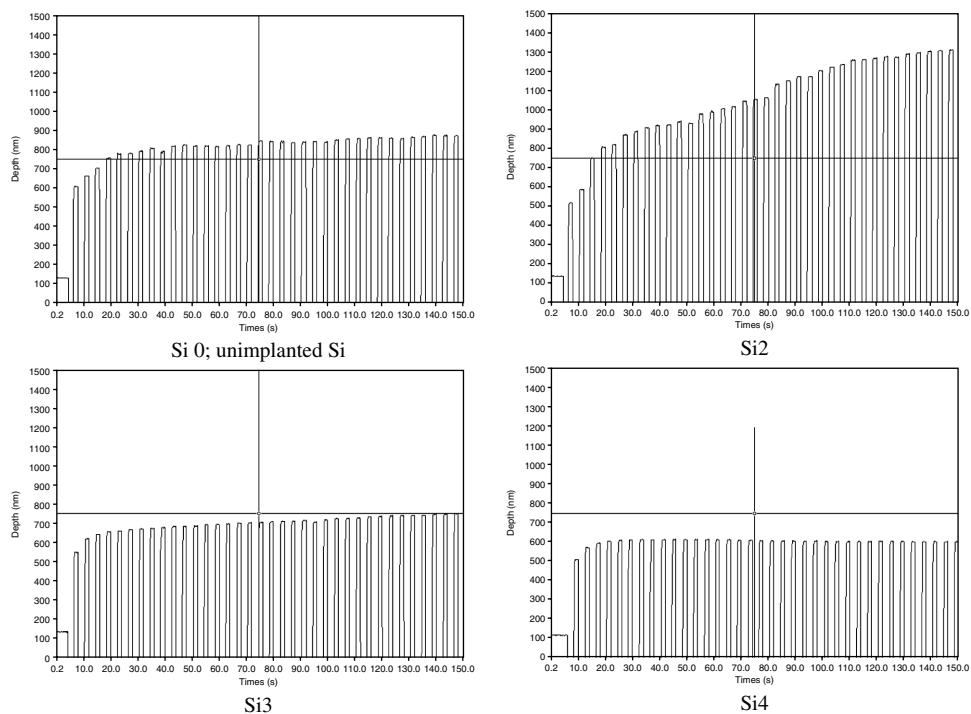


Figure 9. Typical impact behavior of N ion implanted Si.

The correlation between the impact and scratch data is striking. A much higher ion dose is necessary for tribological improvement on the Si than on the SiO₂.

3.4.2b N Ion Implanted Single Crystal SiO₂

Failure events on the SiO₂ samples were clearer (greater change in depth) than on the Si samples. Final depths were also larger which mimics the difference observed in the scratch test data reported previously.

There was some variation in the time at which the first failure occurs and its size. Although there was some variability (e.g. the samples did not always fracture within

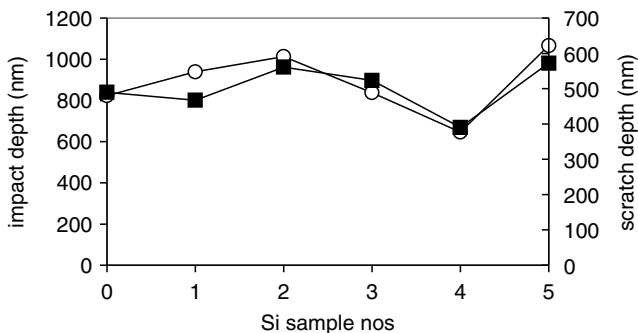


Figure 10. Correlation between impact and scratch data for Si samples.

Table 6. Impact depth of ion implanted Si.

| Implanting doses, N/cm ² | Impact depth after 150 s (nm) |
|-------------------------------------|-------------------------------|
| Sample 0, 0 | 823 ± 30 |
| Sample 1, 5 × 10 ¹⁵ | 939 ± 48 |
| Sample 2, 1 × 10 ¹⁶ | 1013 ± 72 |
| Sample 3, 5 × 10 ¹⁶ | 838 ± 62 |
| Sample 4, 1 × 10 ¹⁷ | 646 ± 42 |
| Sample 5, 5 × 10 ¹⁷ | 1067 ± 27 |

Standard errors in the mean are from 10 measurements at different regions of the sample surface.

150 s), 5–10 repeats for each sample were carried out so that clear trends in behavior could be deduced.

Illustrative results on each of the samples are shown in the following graphs. S3 and s4 generally show much longer time-to-failure. The failure is more extreme on s4 and hence this sample shows the largest depth at 150 s.

We have previously impact tested a variety of hard coatings [DLC, TiN, alumina etc]. The abrupt failures on S4 look quite similar to adhesion failures – i.e. a weak interface/interphase (between the ion implanted and unimplanted regions) eventually gives way catastrophically. It may be that the final depth alone cannot be used as a direct measure of fracture toughness for these SiO₂ samples.

4. CONCLUSIONS

The tribological properties of N ion implanted single crystal Si and single crystal SiO₂ surfaces have been evaluated by nanoscratch and nano-impact testing. Nanoscratch data show the critical loads associated with (1) the elastic-to-plastic transition and (2) the plastic deformation-to-fracture failure transition. The scratch results show that at moderate ion doses the implantation process improves the nanotribological properties of single crystal SiO₂, with similar ion dose of 1 × 10¹⁶ – 1 × 10¹⁷ N cm⁻² also conferring improved resistance to impact/fatigue wear. For the Si samples, the correlation between the impact data and the on-load scratch data was striking. An ion dose of 5 × 10¹⁷ N cm⁻² was necessary for improved resistance to impact/fatigue wear. Impact wear appears to involve 3 processes (1) plastic deformation (2) formation of sub-surface cracks and (3) coalescence of these cracks and failure (by material removal from contact surface).

Table 7. Description of failure.

| |
|--|
| S0 – generally short time to failure |
| S1 – short time-to-first-failure, multiple failures |
| S2 – short time-to-first-failure |
| S3 – longer time to failure, which is often only minor |
| S4 – quite long time to dramatic failure |

S5 were not tested since previous tests under less strong conditions showed very poor performance on this sample – the near-surface layer is too weak that the impact probe punches straight through. Time-to-failure data show an increasing trend S3>S4>S2~S1~S0

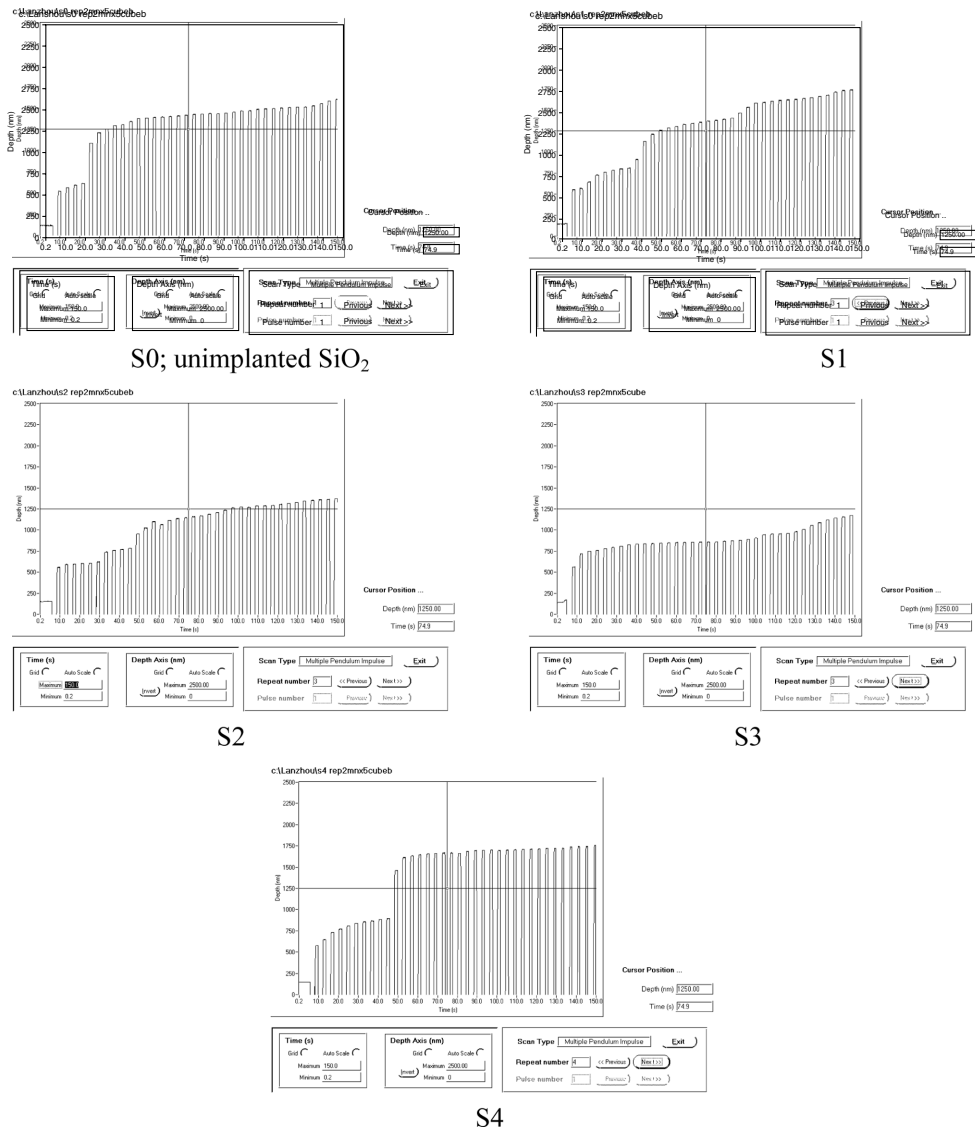


Figure 11. Typical impact behavior of N ion implanted SiO₂.

Table 8. Impact depth of ion implanted Si.

| Implanting doses, N/cm ² | Impact depth after 150 s (nm) |
|-------------------------------------|-------------------------------|
| Sample 0, 0 | 1282 ± 124 |
| Sample 1, 5 × 10 ¹⁵ | 1315 ± 203 |
| Sample 2, 1 × 10 ¹⁶ | 1259 ± 138 |
| Sample 3, 5 × 10 ¹⁶ | 1138 ± 95 |
| Sample 4, 1 × 10 ¹⁷ | 1590 ± 165 |

Standard errors in the mean are from 10 measurements at different regions of the sample

ACKNOWLEDGEMENT

The project is supported by Chinese Natural Science Foundation (No.50172052 and No. 50023001).

REFERENCES

1. S. M. Spearing. Materials issues in microelectromechanical systems (MEMS), *Acta Mater.* 48, 179–196(2000).
2. S. Ecoffey, D. Bouvet, A. M. Ionescu, and P. Fazan. Low-pressure chemical vapour deposition of nanograin polysilicon ultra-thin films, *Nanotechnology* 13, 290–293(2002).
3. R. Gago, L. Vazquezl, R. Cuerno, M Varela, C Ballesteros, and J M Albella. Nanopatterning of silicon surfaces by low-energy ion-beam sputtering: dependence on the angle of ion incidence, *Nanotechnology* 13, 304–308(2002).
4. S. Nakano, H. Ogiso, A. Yabe. Advanced micromachine fabrication using ion-implanted layers, *Nucl. Instr. and Meth. in Physics Research B* 155, 79–84(1999).
5. T Xu, J. J. Lu, J. Tian, and Q. J. Xue. The effect of nitrogen ion implantation on wear behavior of single-crystal SiO₂, *J. of Phys. D: Appl. Phys.* 33, 426–429(2000).
6. Bhushan B., Gupta B.K., and Azarian M. H., 1995, *Wear* 181: 743–758.
7. B. Roos, H. Richter, and J. Wollweber, *Solid State Phenomena* 47–48, 509–516(1996).
8. T. F. Page, W. C. Oliver and C. J. McHargue, *J. Mat. Res.* 7, 450(1992).
9. S. Bull, Applications of nanoindentation to industrial problems. Nanomechanical testing, VITO, Belgium 5th Dec 2001
10. J. S. Williams, et al. Ultra-microindentation of silicon and compound semiconductors with spherical indenters, *MRS* 1999.
11. Bhushan B. Tribology on the macroscale to nanoscale of microelectromechanical system materials: a review, *Proc Instn Mech Engrs* 215, 1–18(2001).
12. B.D. Beake, S.R. Goodes and J.F. Smith, Micro-Impact testing: A new technique for investigating thin film toughness, adhesion, erosive wear resistance and dynamic hardness, *Surface Engineering* 17, 187–193(2001).
13. B.D. Beake, M.J. Ibanez Garcia and J.F. Smith, Micro-impact testing: a new technique for investigating fracture toughness, *Thin Solid Films* 398–399, 438–443(2001).
14. B.D. Beake, S.R. Goodes, J.F. Smith, A. Zhang and J. E. Micro-impact testing: A novel nano-/micro-tribological tool for assessing the performance of wear resistant coatings under impact/fatigue conditions, *Science in China (Series A)* 44 Supp. 418–422 (Proc. 3rd Int. Symp. Tribology, Beijing, Sept 2001)

MICROSTRUCTURAL CONTROL OF INDENTATION CRACK EXTENSION UNDER EXTERNALLY APPLIED STRESS

Robert F. Cook¹

1. INTRODUCTION

In many ceramic and glass materials indentation half-penny cracks extend stably under applied stress to over twice their original length before instability—consistent with an ideal indentation response. Observations of such extension can be made with custom-designed bending fixtures, allowing crack extension in indented specimens to be observed with an optical microscope during controlled loading. The resulting applied stress vs crack length traces exhibit a concave-down shape, with decreasing derivative prior to instability at which the specimen breaks and the derivative vanishes. Many materials, however, do not exhibit this behavior—a consequence of the influences of reactive environments, lateral cracking, microstructural toughening, surface stresses, phase-transformation trapping and preferred crystallographic cleavage planes. These influences lead to substantially suppressed or enhanced stable crack extension, asymmetric extension and stick-slip extension. After a brief development of the indentation fracture model, *in-situ* observations of indentation crack extension in a set of cordierite glass-ceramic composites and a polycrystalline alumina are presented and examined in terms of variability of microstructural interactions giving rise to toughening.

¹ Robert F. Cook, Materials Science and Engineering, University of Minnesota, Minneapolis, MN, 55455.

2. INDENTATION FRACTURE MECHANICS

A fracture system comprising a crack in a brittle material generated by a (sharp) elastic-plastic contact event and subsequently subjected to an applied stress is characterized by the fundamental equilibrium equation^{1,2}

$$K_a + K_r = T_{\text{base}} + T_\mu \quad (1)$$

where K_a is the stress-intensity factor associated with the applied stress field, K_r is the stress-intensity factor associated with the residual contact field, T_{base} is the toughness of the material in the environment of interest and T_μ is a toughness amendment associated with interactions between the crack and the microstructure of the material or the component. By definition, T_{base} is crack-length invariant and is related to the equilibrium (fracture) surface energy of the material, γ , by $T_{\text{base}} = (2\gamma E)^{1/2}$, where E is the material Young's modulus; γ depends on environment and takes a maximum value of γ_0 in an inert, non-reactive, environment, with an analogous maximum base-toughness value of T_0 . The remaining terms in Eq. (1) may all depend on the length of the crack, c , and usually the applied stress-intensity factor is destabilizing, $dK_a/dc > 0$, the residual stress-intensity factor is stabilizing, $dK_r/dc < 0$, and the microstructural interaction leads to toughening, $T_\mu > 0$ and $dT_\mu/dc \geq 0$. Such microstructural toughening can be associated with the material, as in the cases of grain related crack face frictional interlocking in polycrystalline alumina³ or metastable phase transformation crack tip shielding in zirconia alloys.⁴ Or, toughening effects can be imbedded in the component, as in the case of tempering-induced compressive stress profiles generated in ion-exchanged glass parts.⁵ The equilibrium relation of Eq. (1) has been expressed in the component frame of reference, in which the microstructural interactions are associated with the toughness. Equilibrium can also be expressed in the crack-tip frame of reference by setting $T_\mu = -K_\mu$ and collecting all terms but T_{base} on the left side of the equation, or in the applied loading frame of reference by collecting all terms but K_a on the right side of the equation, thereby treating $-K_r$ as a toughening element.

The variables in an indentation crack extension experiment are shown in Fig 1. The indentation flaw consists of residual square contact impression (for a Vickers diamond pyramid indenter) in the component surface with cracks perpendicular to the surface emanating from the impression corners. The crack length, c , is characterized by the surface trace, measured from the impression center. The applied stress, σ_a , is imposed perpendicular to one set of cracks (for a uniaxial loading experiment) The size of the contact impression, and the initial length of the cracks prior to

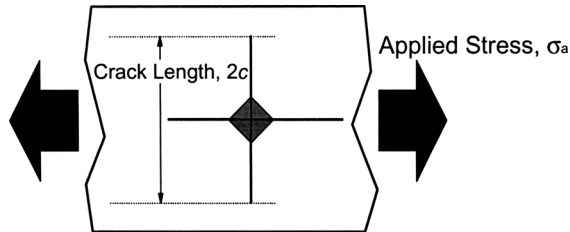


Figure 1. Schematic plan view diagram illustrating the measured parameters during an indentation crack extension experiment: the crack surface-trace length, c ; and the applied stress, σ_a .

application of any stress, is determined by the indentation load P used to generate the flaw. The hardness, H , of the material is related to the load and the area of the contact impression, A , by $H = P/A$.

The driving forces for fracture during an extension experiment, in the context of Eq. (1), are illustrated in Fig. 2. The residual stress-intensity factor, K_r , is modeled as a point-source loading at the center of a circular crack, giving rise to a $1/c^{3/2}$ crack length dependence. The loading arises from the reaction of the surrounding elastic matrix to the strain mismatch imposed by the residual plastic contact impression. The amplitude of the residual term is proportional to the indentation load, modified by an elastic-plastic expanding cavity term, $\chi = \xi(E/H)^{1/2,6}$

$$K_r = \chi P/c^{3/2} \quad (2)$$

The real geometry (finite extent of deformation zone, semi-elliptical crack on a free surface and the presence of other crack systems) of the modeled crack system is accounted for by the material-invariant dimensionless term ξ . The applied stress-intensity factor, K_a , is modeled by a stress acting uniformly over the crack with a $c^{1/2}$ dependence and a dimensionless term ψ accounting for crack-shape and free-surface effects:

$$K_a = \psi \sigma_a c^{1/2} \quad (3)$$

Ideal crack extension behavior is obtained by combining the stress-intensity factors of Eqs. 2 and 3 into the equilibrium equation condition of Eq. 1 under the constraint of an invariant toughness, $T = T_{\text{base}} + T_{\mu}$, and inverting to obtain

$$\sigma_a(c) = (T - \chi P/c^{3/2})/\psi c^{1/2} \quad (4)$$

Equation 4 can be solved for two equilibrium conditions: an initial stable equilibrium configuration at zero stress,

$$c_{\text{init}} = (\chi P/T)^{2/3}, \sigma_a = 0 \quad (5)$$

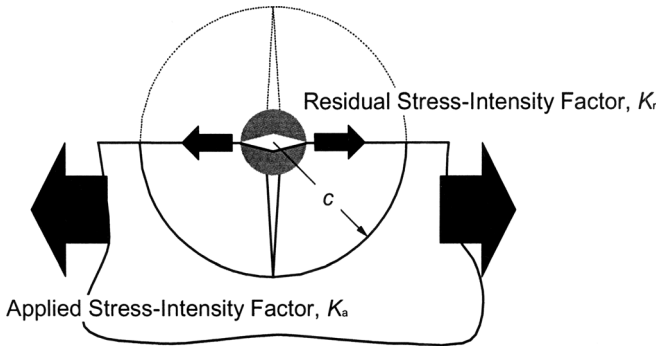


Figure 2. Schematic cross-section illustrating the crack driving forces acting during indentation crack extension: the localized loading of the residual stress-intensity factor, K_r , and the uniform loading of the applied stress-intensity factor, K_a . The semi-elliptical surface crack is modeled as a circular crack in an infinite body.

Table 1. Indentation Crack Extension Behavior of Ceramic Materials.

| Material | Suppressed Crack Extension | Enhanced Crack Extension | Erratic Crack Advance | Asymmetric Crack Advance |
|--|----------------------------------|--------------------------------|-----------------------------|--------------------------------|
| Cordierite Glass Ceramic | | | | |
| Polycrystalline Al ₂ O ₃ (small grain size) ⁷ | | | | |
| Si ₃ N ₄ ⁸ | (wrong shape) | | | |
| Soda-Lime Glass ¹ | X | | | |
| Tempered Glasses ⁹ | X | | | |
| Tetragonal Zirconia Polycrystal ¹⁰ | X | | | X |
| Polycrystalline Al ₂ O ₃ (large grain size) | (wrong shape) | X | X | X |
| Whiser-Reinforced Glass-Ceramic | | X | X | X |
| Al ₂ O ₃ /Al ₂ TiO ₅ ² | | X | X | X |

and a final stable-unstable transition at the maximum sustainable stress,^{1,2}

$$c_m = (4\chi P/T)^{2/3}, \sigma_m = 4T/3\psi c_m^{1/2} \quad (6)$$

Provided the crack propagation is carried out under near equilibrium conditions, the crack system follows the $\sigma_a(c)$ trajectory given by Eq. 4 from the stable configuration of Eq. 5, $(c_{\text{init}}, 0)$, to the onset of instability characterized by Eq. 6, (c_m, σ_m) . Provided, also, that the amplitude terms, χ and ψ , are invariant during propagation, the extension ratio, $c_m/c_{\text{init}} = 4^{2/3} \sim 2.52$. Under these conditions, an alternative formulation of Eq. 4.

$$P/c^{3/2} = (T/\chi)[1 - (\psi/T)\sigma_a c^{1/2}] \quad (7)$$

allows the geometry terms to be evaluated easily from crack extension data, as a plot of $P/c^{3/2}$ vs $\sigma_a c^{1/2}$ follows a straight-line trajectory of constant stress-intensity factor (= toughness) with slope -1 and intercepts T/χ and T/ψ .

In many materials, indentation crack extension behavior does not follow the trajectory of Eqs. 4 or 7, and does not exhibit an extension ratio of 2.52. Table 1 summarizes the crack extension behavior of a number of ceramics. Three classes of behavior are evident: (i) those materials that exhibit the ideal extension ratio and trajectory; (ii) those that exhibit a suppressed extension ratio, < 2.52 , often associated with a non-ideal trajectory; and (iii) those that exhibit an enhanced extension ratio, > 2.52 , usually associated with erratic or asymmetric crack advance. It is the latter group that is the focus here, as their crack extension characteristics are a reflection of the effects of microstructure on toughness. That is, T in Eqs. 4-7 is not invariant. Measurement of the $\sigma_a(c)$ trajectory can then be used to discern the $T_\mu(c)$ variation for a material and its point-to-point variability within a microstructure.

3. EXPERIMENTAL DETAILS

3.1. Materials

Two materials are considered here to illustrate the effects of microstructure on crack extension. The first is a cordierite ($2\text{MgO} \cdot 2\text{Al}_2\text{O}_3 \cdot 5\text{SiO}_2$) based glass-ceramic contain-

ing silicon nitride whiskers. The whiskers were approximately $1 \times 15 \mu\text{m}$ and were mixed in with the base glass-ceramic powder prior to tape-casting at 0, 5, 10 and 15 vol%. The whiskers significantly retarded densification during sintering, such that the modulus and hardness of the composite materials were reduced; E and H were 120 and 8.3 GPa and 104 GPa and 3.1 GPa for the base material and 15 vol% composite respectively. The second material is a large-grained polycrystalline alumina containing 0.1 mol% MgO.² The mixed powder was dry-pressed and then sintered in H_2 at 1800 C for 12 hours to reach $> 99.5\%$ relative density. The mode grain size was $15 \mu\text{m}$.

3.2. Testing Method

Test specimens were cut into bar form, approximately $45 \text{ mm} \times 6 \text{ mm} \times 3 \text{ mm}$. Single Vickers indentations, with one set of cracks aligned perpendicular to the bar axis, were placed in the center of the largest face of the bar. In the case of the cordierite composites, a single 100 N indentation load was used. For the alumina, loads in the range 10–100 N were used. The bars were then placed in a custom-built testing apparatus, illustrated in Fig. 3. The apparatus generated a tensile stress in four-point bending on the indentation surface of the bar. The stress was maintained by displacement control through a stepping motor and the load monitored by a resistance load cell. The entire apparatus was mounted on an inverted optical microscope so that the indentation crack lengths could be monitored during loading. All indentation and testing was performed in air. During the crack extension on loading, the load was incremented and the cracks allowed to come to rest (velocity less than $3 \times 10^{-10} \text{ ms}^{-1}$) before measuring the crack length and then re-incrementing the load. The crack extension responses were thus characteristic of equilibrium fracture in the air environment.

4. RESULTS

Figure 4 shows applied stress-crack length trajectories for the base cordierite glass-ceramic material. Measurements on two opposing cracks on two specimens were made; the trajectories are symmetric and relatively smooth for each specimen and the entire set of data are well described by the (penny-crack based) ideal extension behavior of Eq. 4, shown as the best fit solid line and associated instability crack length and stress values. In this case it appears that the assumptions of extension under conditions of quasi-equilibrium propagation and invariant material toughness and crack geometry are fulfilled. Figure 5 replots the data of Fig. 4 according to the scheme of Eq. 7, emphasizing the shift from residual stress-intensity dominance at the beginning of the test to applied stress-intensity dominance at failure. A straight line fit in these coordinates allows the combined toughness/geometry parameter combinations to be obtained from intercepts as indicated on the Figure. These parameters may be used to evaluate the toughness characteristics of similar materials, referenced to this base material. Combining the full equilibrium expression of Eq. 1 with the crack extension expression of Eq. 7 gives

$$T/T_{\text{base}} = (\psi/\psi_{\text{base}})(\psi_{\text{base}}/T_{\text{base}})\sigma_a c^{1/2} + (\chi/\chi_{\text{base}})(\chi_{\text{base}}/T_{\text{base}})P/c^{3/2} \quad (8)$$

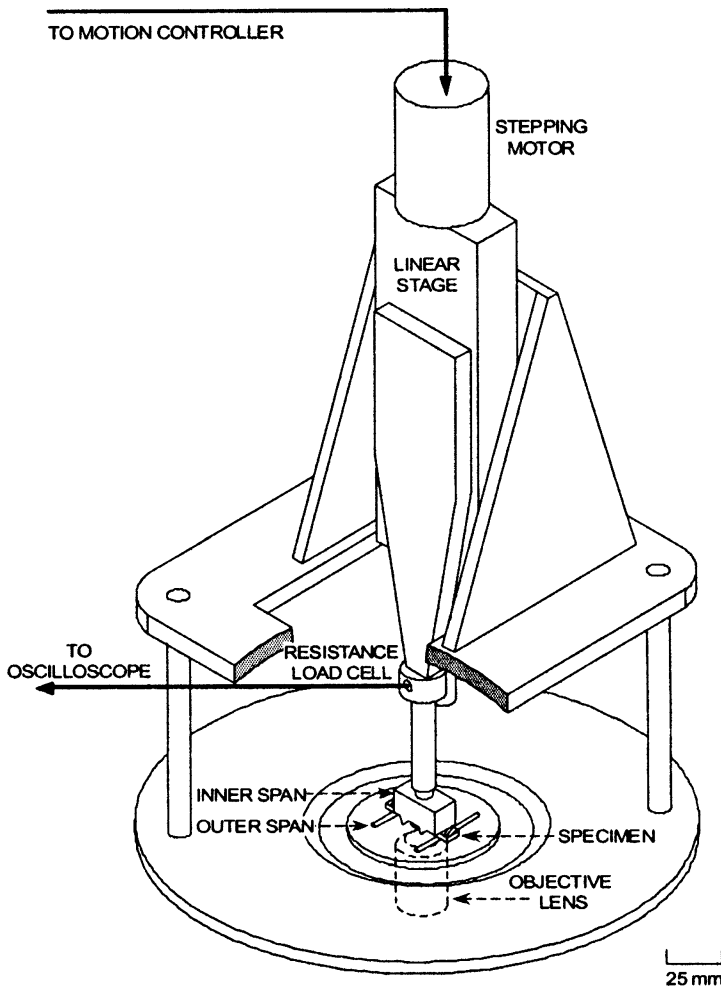


Figure 3. Diagram of the apparatus used to measure indentation crack extension under applied stress.

which indicates that once a base material has been calibrated, the toughness variations with crack length of related materials can be determined from crack extension measurements, once the applied and residual stress geometry transformations are known.

Figure 6 shows the relative toughness behavior of the set of cordierite whisker composites as a function of crack length, determined using crack extension data such as those shown in Fig. 4 and transformed as given by Eq. 8. The applied geometry term was taken as invariant with whisker volume fraction, $\psi/\psi_{\text{base}} = 1$, and the residual geometry term scaled with the elastic-plastic response, $\chi/\chi_{\text{base}} = (E/H)^{1/2}/(E_{\text{base}}/H_{\text{base}})^{1/2}$. As anticipated by Figs. 4 and 5, the base material response is invariant with crack length. The responses of the whisker composites are also relatively invariant, but clearly increase in their near steady-state toughness values with whisker volume fraction. In addition the 15 vol% material exhibits a clear enhancement of crack extension (to almost a factor of five) over that of the base material. The implication

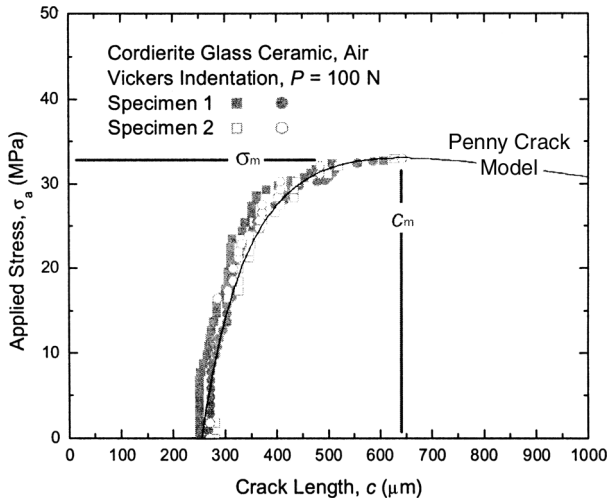


Figure 4. Plot of the equilibrium indentation applied stress-crack length, $\sigma_a - c$, extension behavior for cordierite glass-ceramic in air. The data are well described by an ideal indentation response based on the penny crack model of Fig. 2.

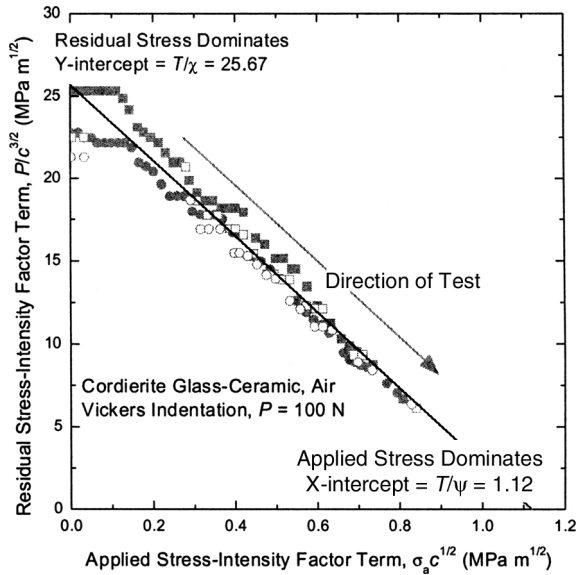


Figure 5. Plot of the equilibrium indentation crack extension behavior for cordierite glass-ceramic in air using parameters related to the residual and applied stress-intensity factors. A straight line best fit to the data allows the crack geometry terms to be evaluated from the intercepts.

of these data is that although the addition of the whiskers to the cordierite glass ceramic increased the porosity and thus degraded the modulus and hardness (and presumably the base toughness), the actions of the whiskers during crack propagation more than compensated to lead to overall tougher materials. The crack length scale associated with the attainment of steady-state toughness characteristics appears from Fig. 6 to be approximately 200–300 μm .

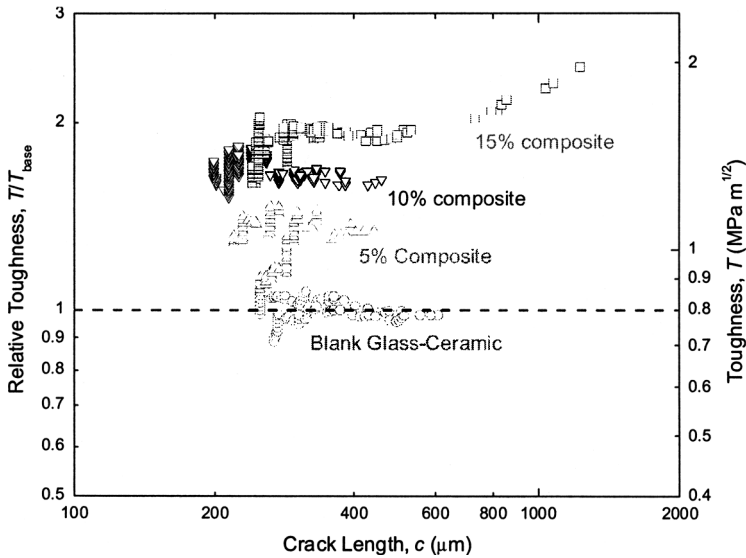


Figure 6. Plot of relative toughness as a function of crack length for cordierite glass-ceramic containing silicon nitride whiskers at the volume fractions indicated. Adding whiskers enhances the toughness over the base material by over a factor of two, approximately $1 \text{ MP m}^{1/2}$ for this material in air.

Figure 7 shows the applied stress-crack length trajectories for the alumina material; measurements on two opposing cracks on a single specimen were made. The trajectories exhibit behavior very different from that of the base glass-ceramic of Fig. 4, as indicated in Table 1. For a given indentation, the crack traces are not of the same length and the cracks do not extend similarly, leading to extremely asymmetric crack extension. On increasing stress, the cracks exhibited erratic “stick-slip” exten-

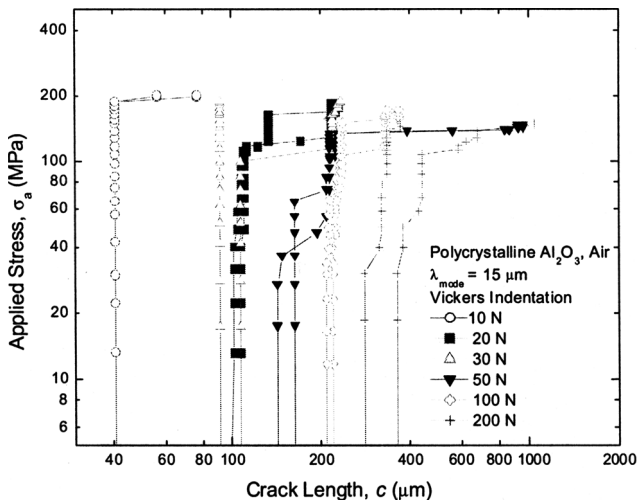


Figure 7. Plot of the equilibrium indentation applied stress-crack length, $\sigma_a - c$, extension behavior for a large grained polycrystalline alumina in air. The data are not well described by an ideal indentation response, exhibiting asymmetry, erratic and variable extension, and very small strength degradation over the flaw size range, indicating a significant interaction between the cracks and the microstructure.

sion, sequences of fixed length for a large stress increase followed by an abrupt increase in length for a small stress increment. This behavior was more prevalent for small indentation flaws. Taken as a group, the indentations exhibited variable crack extension ratios, from zero to approximately eight. And finally, the material exhibited extreme flaw tolerance; over the range of a factor of 20 in indentation load, the strength degraded by a factor of about 0.3, compared with a factor of 2.7 predicted by Eq. 6.

Figure 8 shows the relative toughness behavior of the alumina as a function of crack length, determined using the crack extension data of Fig. 7 and transformed by Eq. 8. The applied and residual geometry terms were taken from the experiments of Braun et al.⁷ on an alumina of similar density and composition. This alumina had much smaller grain size and exhibited an invariant toughness response, taken here as representative of the base toughness of the large grain alumina, such that the values of $T_{\text{base}}/\psi = 3.68$, and $T_{\text{base}}/\chi = 36.0$ determined for the small-grained material were deemed applicable for the large-grained material. As both materials were close to fully dense, the applied and residual geometry terms were assumed to be unaltered by grain size, $\psi/\psi_{\text{base}} = 1$ and $\chi/\chi_{\text{base}} = 1$. As perhaps anticipated by Fig. 7, the toughness response passes through range of values on crack extension and the stick-slip crack extension is evident as increase-decrease sequences in toughness with crack length. Overall, the toughness behavior of the alumina can be characterized as lying within a wedge or triangle pointing to longer crack lengths, bounded by an invariant upper value and with lower values significantly less than that of the base material.

The data of Fig. 8 are very different from those of Fig. 6 and suggest a much more variable interaction between an extending crack and the microstructure over the range of crack extensions examined. The cordierite composite data suggest an

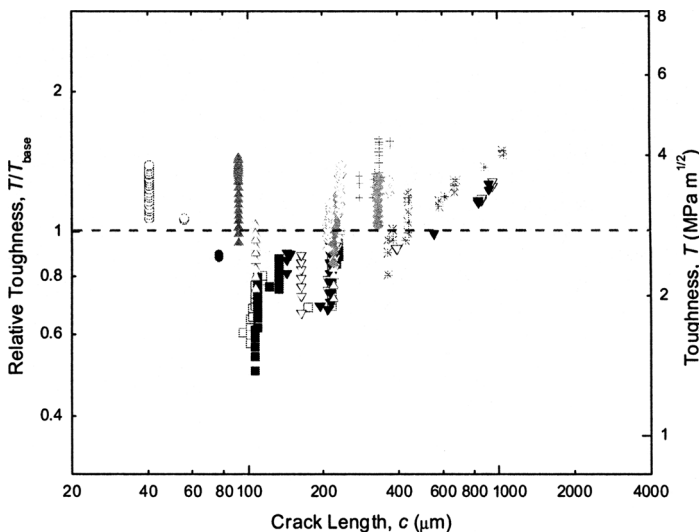


Figure 8. Plot of relative toughness as a function of crack length for a large-grain size polycrystalline alumina. There is considerable variability in the toughness response, although it appears that the toughness is increased by about a factor of 1.5 over fine grained material, approximately $1.35 \text{ MPa m}^{1/2}$ for this material in air.

almost saturated toughening response with little variability, indicative of the influence of many microstructural interactions (whisker-related frictional interlocks) accumulated over the crack face. The alumina data on the other hand suggest a still-accumulating toughening response, with great variability, indicative of the point-to-point stochastic nature of relatively few microstructural interactions (grain-related frictional interlocks) over the crack face. An interpretation of the data is that the toughness of the least tough interface in the alumina is about $1.5 \text{ MPa m}^{1/2}$, reflecting grain boundary fracture. Most of the indentation cracks start out this way and are arrested by grains in the crack path. As the applied stress is increased, the net stress-intensity factor (and thus apparent toughness) increase at the arrested crack length until the instability condition, about $4 \text{ MPa m}^{1/2}$, reflecting fracture of the grains or obstacles, is exceeded and the crack extends until arrested again. The sequence then repeats, but as the crack has extended there are now some toughening interactions over the crack plane and the starting point is thus at a greater toughness value than the previous sequence; the ending point is at about the same toughness value, reflecting the maximum toughness achievable in the microstructure. On continued sequential extension in this way, the value of the toughness at the starting (arrest, stick) part of the sequence approaches the value of the ending (extension instability, slip) part and the variability in the toughness with extension decreases and settles on the upper-bound level associated with homogeneous, steady-state microstructural interactions over the crack plane. Long cracks associated with large indentation loads approach this behavior, as seen in Figs. 7 and 8.

5. CONCLUSIONS

Crack extension from indentation flaws under the influence of an applied stress exhibits a great sensitivity to microstructural effects. This sensitivity is not observed in indentation-strength tests or long crack toughness tests, as the crack extension during failure or creation of the long crack, respectively, accumulate large numbers of microstructural interactions that act to average or saturate the perceived toughness value. Direct observation of indentation crack extension can thus be used to ascertain the probable toughening mechanisms in a microstructure, the length scales associated with toughening and the point-to-point variability in these effects, as well as providing an easy method of evaluating material toughness with great specimen economy.

The results presented here on cordierite composites and polycrystalline alumina typify the enhanced extension ratios (>2.52 predicted for an ideal indentation response) and are reasonably interpreted within the established framework of the cumulative toughening actions of obstacle (whisker or grain)- related crack face frictional interlocking. Such toughening relies on the natural inhomogeneity of the microstructure; an implication here is that significant variability of defect responses to applied stress is inherent in such materials. However, explanations remain to be found for the non-ideal extension trajectories and suppressed extensions exhibited by many of the materials in Table 1 that have no such inhomogeneities (glass, Si_3N_4 , TZP). Such non-idealities point to the need for examination of the crack driving force K terms in Eq. 1 associated with the contact mechanics, rather than the T terms associated with the toughening mechanics.

REFERENCES

1. D.B. Marshall, B.R. Lawn and P. Chantikul, Residual stress effects in sharp contact cracking. II. Strength degradation., *J. Mat. Sci.*, **14**, 2225–35 (1979).
2. R.F. Cook, E.G. Liniger, R.W. Steinbrech, and F. Deuerler, Sigmoidal Indentation-Strength Characteristics of Polycrystalline Alumina, *J. Amer. Cer. Soc.* **77** 303–314 (1994).
3. P. L. Swanson, C. J. Fairbanks, B. R. Lawn, Y.-W. Mai and B. J. Hockey, Crack-interface grain bridging as a fracture resistance mechanism in ceramics. I. Experimental study on alumina, *J. Amer. Cer. Soc.*, **70** 279–89 (1987).
4. R.M. McMeeking and A. G. Evans, Mechanics of transformation-toughening in brittle materials, *J. Amer. Cer. Soc.*, **65**, 242–6 (1982).
5. R. Tandon, D.J. Green and R.F. Cook, Strength Variability in Brittle Materials with Stabilizing and Destabilizing Resistance Fields, *Acta metall.* **41** 399–408 (1993).
6. B.R. Lawn, A.G. Evans, and D.B. Marshall, Elastic/Plastic Indentation Damage in Ceramics: The Median/Radial Crack System *J. Amer. Cer. Soc.*, **63** 574–581 (1980).
7. L. M. Braun, S. J. Bennison and B.R. Lawn, Objective evaluation of short-crack toughness curves using indentation flaws: case study on alumina-based ceramics, *J. Amer. Cer. Soc.*, **75**, 3049–57 (1992).
8. D. B. Marshall, Controlled flaws in ceramics: a comparison of Knoop and Vickers indentation, *J. Amer. Cer. Soc.*, **66**, 127–31 (1983).
9. R. Tandon and R.F. Cook, Indentation Crack Initiation and Propagation in Tempered Glass, *J. Amer. Cer. Soc.*, **76** 885–889 (1993).
10. L. M. Braun and R.F. Cook, in *Science and Technology of Zirconia V*, edited by M.J. Bannister and R.H.J. Hannink (Technomic Press, 1993), pp. 386–400.

INSTRUMENTED HARDNESS TEST ON ALUMINA CERAMICS AND SINGLE CRYSTAL WITH SPHERICAL INDENTER

Shuji Sakaguchi, Kiyoshi Hirao, Yukihiro Yamauchi
and Shuzo Kanzaki*

1. INTRODUCTION

Ceramic materials are expected to be applied to the structural parts, especially to tribological application, as they have high hardness and high elastic constants. For this application, it is important to know the properties of mechanical behavior on the surface of ceramics. Instrumented indentation is one of the tests that can explain the mechanical properties on the surface, as it expresses the relation between the penetration depth of the indenter and the applied force.^{1,2} For metallic materials, the standard test method in instrumented indentation is already published.³ We have tried the instrumented indentation tests on ceramic materials. Figure 1 is a typical example of the loading-unloading curve by this test on alumina ceramics.

If the test force is small enough, the indenter contacts the surface elastically, and no indent shall be made and no energy is consumed for making indent. It means if we increase the test force, the consumed energy ratio for making indent can increase. With this assumption, we tried the measurement of instrumented hardness with conical

* Shuji Sakaguchi, Ceramic Research Institute, National Institute of Advanced Industrial Science and Technology, Nagoya, Japan 463-8560. Kiyoshi Hirao, Yukihiro Yamauchi and Shuzo Kanzaki, Synergy Materials Research Center, National Institute of Advanced Industrial Science and Technology, Nagoya, Japan 463-8687.

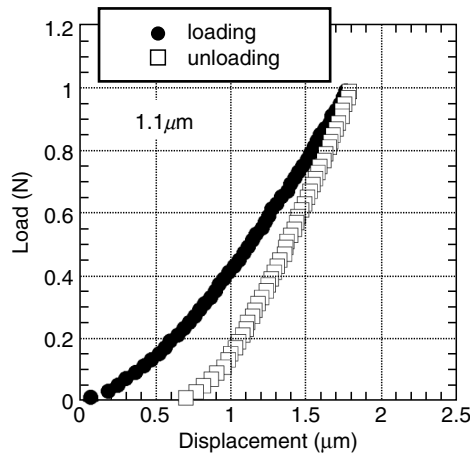


Figure 1. Typical result of instrumented indentation on alumina ceramics, measured with Vickers indenter.

indenters (Berkovic, Knoop and Vickers), and we obtained the relation between the applied test force and the energy consumption ratio for making indents. Figure 2 shows some results of the test force dependence of the consumed energy ratio. In some results obtained with Knoop indenter, the results follow this expectation, but the test force dependence of the energy consumption ratio was not clearly observed. The scattering of the data is relatively large, as the applied test force was small. We could not obtain the grain size dependence of the energy consumption clearly. It was considered that the tip of the indenter was too keen to obtain the elastic contact on these materials. Spherical indenters shall be used for this discussion.

In this study, we tried to use spherical diamond indenters with different tip radius on the instrumented indentation tests. We tried to find the test force dependence of the surface fracture with these indenters, and the grain size dependence of the instrumented indentation results on ceramic materials.

2. EXPERIMENTS

2.1. Testing conditions

Recording hardness test machine supplied by CSIRO, Australia (Type: UMIS-2000) was used for this study. Seven kinds of spherical indenters with different tip radius (1, 2, 5, 10, 20, 50 and 100 μm) were used. Maximum test force was chosen as 20, 50, 100, 200 and 500 mN. Five tests were carried out in the same test condition, and some scattered data that might be caused by some large fracture on the surface were neglected. The data were averaged and the consumed energy was calculated from the loading-unloading curve.

2.2. Specimens

The specimen was alumina sintered body with purity of 99.9%.^{4,5} The average grain size of as-received sample was 1.1 μm . It was annealed in air in three conditions for

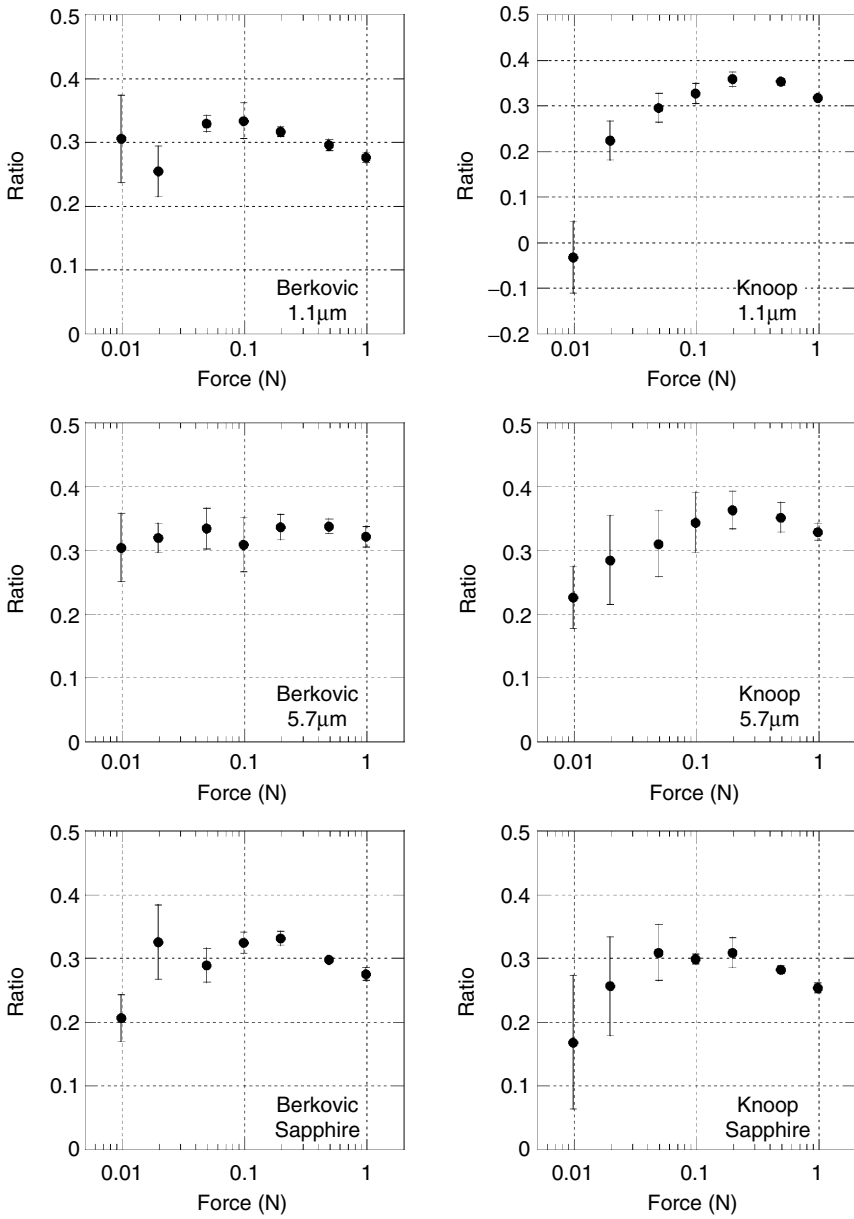


Figure 2. Examples of the relation between the test force and the energy consumption ratio on instrumented indentation with Berkovic or Knoop indenter.

the grain growth. The specimens with average grain sizes of 1.8, 4.4 and 5.7 μm were prepared. The mechanical properties of these specimens are shown in Table 1. The Vickers hardness was not changed with the grain growth. For the comparison, the c-plane of the alumina single crystal (sapphire) was also tested. The Vickers hardness of the sapphire was 19.0 GPa with the standard deviation of 0.5 GPa. It was a little harder than the sintered alumina.

Table 1. Four point bending strength, fracture toughness measured by single edge pre-cracked beam (SEPB) method, and Vickers hardness of the tested alumina specimens. Standard deviations are in brackets.

| Grain size (μm) | Strength (MPa) | K_{IC} ($\text{MPa m}^{1/2}$) | HV (GPa) |
|------------------------------|----------------|-----------------------------------|------------|
| 1.1 | 652 (39) | 3.00 (0.31) | 18.3 (0.4) |
| 1.8 | 555 (40) | 3.20 (0.14) | 18.7 (0.6) |
| 4.4 | 415 (23) | 3.95 (0.24) | 17.3 (0.5) |
| 5.7 | 369 (21) | 4.21 (0.05) | 17.6 (0.6) |

3. RESULTS

Figure 3 shows the results of the energy consumption ratio of every specimen on the indenter of every tip radius. On the indenters of 20 μm and 50 μm , the contacts were almost elastically and no energy consumption was found. However, in the test with 20 μm indenter the scattering of the data became larger. On the indenters of 5 and 10 μm , energy consumption ratio increased continuously with increasing the

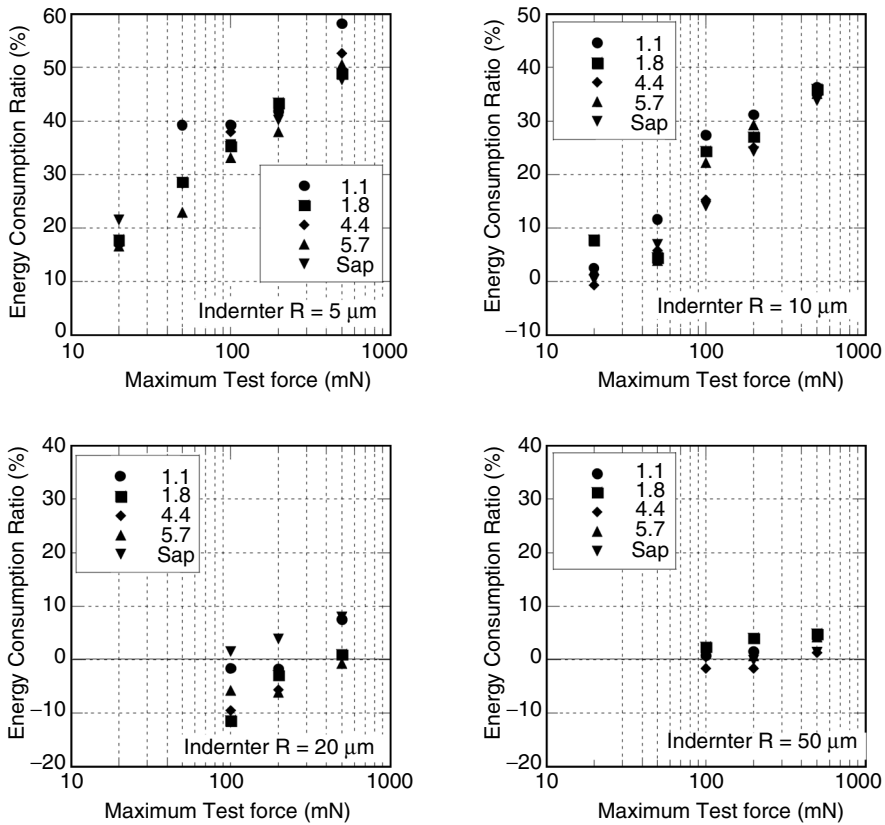


Figure 3. Energy consumption ratio of each test condition with spherical indenters of 5, 10, 20 and 50 μm in radius ('Sap' is sapphire c-plane).

maximum test force. The grain size dependence of the energy consumption was not observed.

If the energy consumption increased abruptly at a certain test force, we can estimate a limit of the surface damage. However, the energy consumption increased gradually with increasing the test force. That means the surface damage is not made at a certain stress but accumulated with increasing the stress.

We could not see the grain size dependence of the energy consumption. The surface damage with compressive stress can be independent of the grain size, as it can be expected from the results of the Vickers hardness.

4. DISCUSSION

For discussing all the data, the results were plotted as the relation between the average contact stress of the indenter calculated with the equations for the elastic contact, and the energy consumption ratio. Table 2 shows the average stress in the contact circle from the equation of the elastic contact on every test condition. The maximum stress, which appears at the center of the contact circle, is 1.5 times larger than the average stress. Figure 4 shows the plot of all the data. The plots can be divided into three regions. (1) Calculated stress is below 12 GPa. No energy consumption was found. (2) Calculated stress is between 12 GPa and 18 GPa. The energy consumption was still around zero, but the scattering of the data becomes larger. (3) Calculated stress is over 18 GPa. The energy consumption increased simply with increasing the applied stress.

These three stress regions correspond to the following conditions; (1) The compressive stress is below the hardness value on all the contact area. (2) The average compressive stress is smaller than the hardness value, but the maximum stress is larger than the hardness. The contact area may partly damaged. (3) The average stress is larger than the hardness. The indent size shall be larger than the calculated elastic contact size.

With these explanations, we can assume the reason why the scattering of the energy consumption became larger in the intermediate stress region. It is schematically shown in Figure 5. In this intermediate stress condition, the average stress is smaller than the hardness. Then the indent with the size of the contact circle cannot be made. However, the stress at the center of the contact circle is larger than the hardness. The surface area at the center shall be damaged, or micro-fractured, by this contact. It is not an elastic contact, but it cannot make a clear indent. That can be a reason why the energy consumption was not clearly increased but only the scattering of the data was increased.

Table 2. Calculated compressive stress (GPa) on elastic contact in every condition.

| Indenter Radius (μm) | Test Force (mN) | | | | |
|-----------------------------------|-----------------|-------|------|------|------|
| | 20 | 50 | 100 | 200 | 500 |
| 5 | 16.1 | 21.9 | 27.6 | 34.8 | 47.2 |
| 10 | 10.2 | 13.8 | 17.4 | 21.9 | 29.7 |
| 20 | (6.4) | (8.7) | 11.0 | 13.8 | 18.7 |
| 50 | (3.5) | (4.7) | 5.9 | 7.5 | 10.2 |

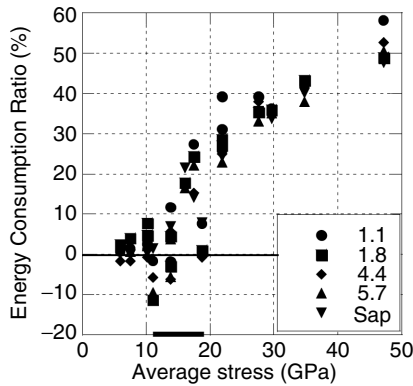


Figure 4. All the data are plotted with the relation between the calculated contact stress and the energy consumption. The results can be divided into three regions; (1) 0-12 GPa, (2) 12-18 GPa, (3) over 18 GPa.

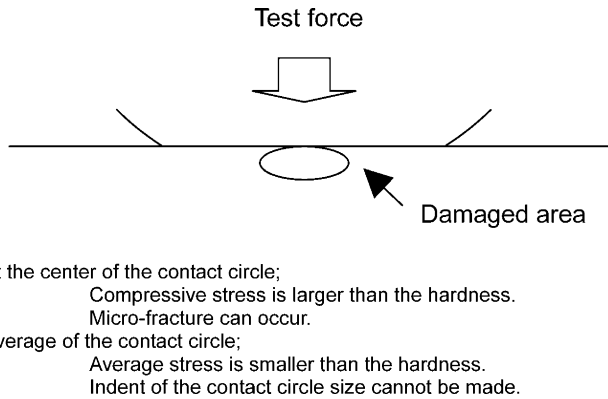


Figure 5. Indentation damage under intermediate test force. The area around the center of the contact circle is damaged. It is not an elastic contact, and it can make a scattering of the energy consumption.

5. CONCLUSION

Instrumented indentation tests were carried out on alumina ceramics with different average grain size, using spherical indenters.

- (1) We could not find the average grain size dependence of the energy consumption for making indents on alumina specimens.
- (2) The stress value for making surface damage is related to the Vickers hardness value. It can be divided into three levels; 1. contacting elastically, 2. contact area is partly damaged, 3. contact area is fully damaged and indent is made.
- (3) The consumption energy ratio for making indents increased continuously with increasing the maximum test force, if the applied stress is more than the Vickers hardness value.

6. ACKNOWLEDGMENTS

This work has been supported by NEDO, as part of the Synergy Ceramics Project promoted by METI, Japan. The authors are members of the Joint Research Consortium of Synergy Ceramics.

REFERENCES

1. M. Sakai and S. Shimizu, Elastic, plastic, and viscoelastic contact problems in axisymmetric indentation, *Ceramic Transactions* (The American Ceramic Society), vol. 133, 105–114, (2002).
2. W. C. Oliver and G. M. Pharr, An improved technique for determining hardness and elastic modulus using load and displacement sensing indentation experiments, *J. Mater. Res.*, 7, 1564–1583, (1992).
3. ISO 14577-1, Metallic materials – Instrumented indentation test for hardness and materials parameters – Part. 1: Test method, (2002).
4. S. Sakaguchi, The relation between the damage tolerance and the R-curve behavior of alumina ceramics, *Fracture Mechanics of Ceramics* (Kluwer Academic / Plenum Press), vol. 13, 229–234, (2002).
5. S. Sakaguchi, R-curve measurement of alumina using straight notched or indented bending bars, *Fracture Mechanics of Ceramics* (Plenum Press), vol. 11, 39–51, (1996).

CONTROLLING THE FRAGMENTATION BEHAVIOR OF STRESSED GLASS

Rajan Tandon and S. Jill Glass[‡]

1. INTRODUCTION

Inducing compressive surface stress profiles in brittle materials is a well-known approach for strengthening. The compressive stress inhibits crack initiation and propagation. The effect has been observed for tempered and ion-exchanged glasses,¹⁻⁴ and for oxide ceramics.^{5,6} While it is generally accepted that the magnitude of the stress and its depth determine the strength response, it has recently been demonstrated that the shape of the compressive stress profile can radically alter the strength distribution.⁷ For tempered glasses, the role of the internal tensile stress in causing fragmentation is well known,⁸ although it is not possible to predict the extent of fragmentation.⁹

Relatively less attention has been paid to the role of the internal compensating tensile stress on the fracture process for ion-exchanged glasses. Zijlstra and Burggraaf¹⁰ described an approach to reduce the sharpness of fragments of ion-exchanged glass. They found a powdering effect at the edges of the fragments when the maximum in the compressive stress profile was shifted approximately 40 μm below the surface, and the difference between the stress maximum and the surface stress was > 147 MPa. This powdering effect rendered the fragments harmless. Bakioglu et al.¹¹ theoretically considered the problem of a partially closed crack that penetrates through the surface compression region. They presented fracture mechanics solutions to analyze the spontaneous propagation of this crack in the internal tensile field aided

[‡] Rajan Tandon, S. Jill Glass, Ceramic Materials Department, Sandia National Laboratories, Albuquerque, NM 87185, USA

by environmental effects. Donald and Hill¹² reported the preparation and properties of lithium magnesium aluminosilicate glasses. The lithium in this glass structure is exchanged by sodium ions in solution, leading to compressive surface stresses. Unusual properties, with the surface being in tension due to extreme stress relaxation, were reported. They also observed fragmentation of this glass after biaxial flexure testing, with the higher strength samples possessing smaller fragments. Bouyne and Gaume¹³ are developing a stress-intensity factor approach to predict fragmentation, and have concluded that the elastic energy stored in the tensile stress region is the parameter controlling the fracture.

The motivation of the present study is to identify the processing conditions, viz., exchange time, temperature, and glass size that produce a desired combination of strength, fragmentation behavior, and reliability. Reliability here encompasses the repeatability and predictability of the fragmentation process in addition to the mechanical strength aspects. In this work, we attempt to relate the strength, indentation, and central tension stress measurements of an ion-exchanged glass to its fragmentation behavior. An energy analysis is proposed to relate the fragment size to measurable parameters. The fracture surfaces of strengthened glasses are examined in order to better understand the fragmentation process.

2. EXPERIMENTAL PROCEDURE

2.1. Materials and Exchange Treatment

The material chosen for this study was an aluminosilicate glass (Corning Code 0317). The approximate composition of the glass (in wt%) was: 61.96% SiO₂, 16.5% Al₂O₃, 11.88% Na₂O, 3.34% MgO, 3.41% K₂O, 1.75% Li₂O, 0.67% TiO₂, 0.41% CaO and rest Fe₂O₃. Glass disks of nominal diameter of 2.54 cm, and three different thickness values (1 mm, 1.8 mm, and 2.2 mm) were used for this study. The process of ion-exchange was used to incorporate the residual stress profiles in the glass. For Code 0317 glass composition, this process consists of exposing the glass to a molten solution of potassium nitrate. Due to a chemical potential difference, the Na⁺ ions in the glass are released into the molten salt, and the K⁺ ions occupy their place in the structure. The bath temperature was controlled to $\pm 2^\circ\text{C}$, and two different temperatures of exchange, 450°C and 500°C were employed. Since both these temperatures are below the glass transition temperature (strain point = 576°C), the K⁺ is not accommodated in the structure of the glass, and the exchanged layer tends to have a larger volume than the bulk. This leads to the development of a surface compressive stress in the glass, and to a compensating tensile stress in the interior. The ion-exchange was conducted for time intervals of 3, 6, 12, 24, 48 and 96 hours. The depth of exchange in some samples was measured using a microprobe, and using the known value of the activation energy for diffusion,¹³ the depths for various treatments were estimated. The depth of the K⁺ ions into the glass is an important parameter as the extent of the compressive stress profile is generally between 0.9-0.99 times the exchange depth. Figure 1a provides a schematic of the ion-exchange process, and Fig. 1b depicts the stress profiles expected in the process. Fig. 1b also includes a stress profile that may be expected when the high surface stress undergoes relaxation due to visco-elastic structural rearrangement.

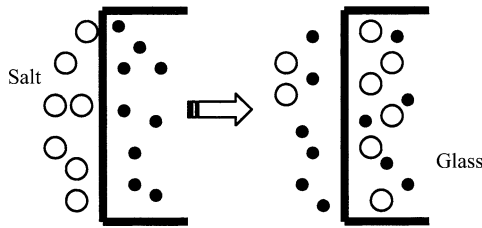


Figure 1a. Schematic of the ion-exchange process is shown. The large K^+ ions from the salt exchange with the Na^+ ions in glass.

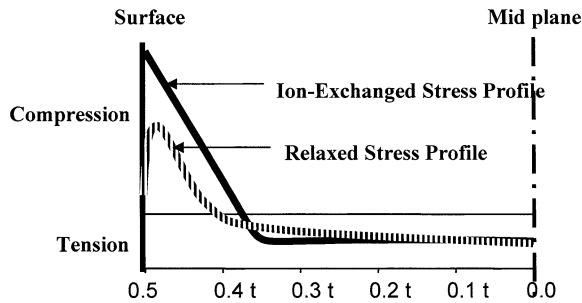


Figure 1b. Schematics of the normal and relaxed stress profiles are shown. In the relaxed profile, the maximum in the surface compression has moved away from the surface of the sample.

2.2. Central Tension Measurement

The measurement of compressive stress profiles in ion-exchange glasses is very tedious, and was not attempted for this study. However, the values of the compensating tensile stress in the bulk were obtained by using a set-up described in Ref. 14. A white light source was viewed through a crossed polarizer and analyzer set to obtain extinction. The samples were then introduced such that the light beam passed along the disk diameter. The birefringence introduced due to the internal tension led to the extinction condition being disturbed, and a particular fringe color was seen in the eyepiece. A Soliel-Babinet compensator and additional quarter wave-plates were then introduced in the light path to re-obtain extinction. Knowing the amount of retardation induced by the compensator-wave-plate combination to attain extinction and the stress optic coefficient of the glass, the central tension values in the samples were calculated.

2.3. Bi-Axial Strength Tests, Indentation Tests, and Fragmentation Observations

The strength values of the disks exchanged under various test conditions were measured using a ring-on-ring biaxial fixture made in accordance with ASTM C1499. For each test condition, one or two samples were fractured, and strength determined. In order to establish a baseline, the strength of five un-exchanged glass disks was measured. To probe the changes in the surface stress as a function of exchange time, Vickers indentation experiments were conducted. A Vickers indenter was loaded onto the surface in air at 40N and 50N peak applied loads, held for fifteen seconds, and then removed. The indentation site was examined within an hour after load removal. Fragmentation experiments on the test samples were conducted by progressively increasing the Vickers

indenter load till spontaneous fragmentation (or simple fracture) of the glass occurred. There were instances when the median crack pop-in and propagation led to the sample separating into two pieces. In most cases, however, fragmentation with multiple crack branching was observed. No records of the load to cause fragmentation for particular exchange conditions were kept. The fragmented pieces were held together by tape. The fragmented pieces, and fracture surface of the fragments were examined using an optical microscope. For comparison, the fracture surface of a tempered glass piece that fragmented spontaneously was also observed. The magnitude of the stress in this piece of glass prior to fracture is unknown.

3. RESULTS AND ANALYSIS

3.1. Central Tension Measurements

Under crossed polarized light, it was observed that the color in the central region of the sample was fairly uniform, and extinction was obtained uniformly across the sample cross-section. These observations indicate that the tensile stress was uniform in the test samples. Samples that exhibited asymmetry in the tensile stress distribution were removed from the set, and were not tested further. The values of central tension measured for various exchange conditions and glass thickness values are shown in Fig 2. Each point in the figure is an average value of three-four measurements made on the same sample, and for two-three different samples. The scatter in the measured stress values was <5%, and the lines drawn through the data are aids to the eye. The open and solid symbols represent exchange temperature of 450°C and 500°C respectively. For all conditions of exchange, the measured central tension increases with increasing exchange time. For identical exchange conditions, the central tension (σ_c)

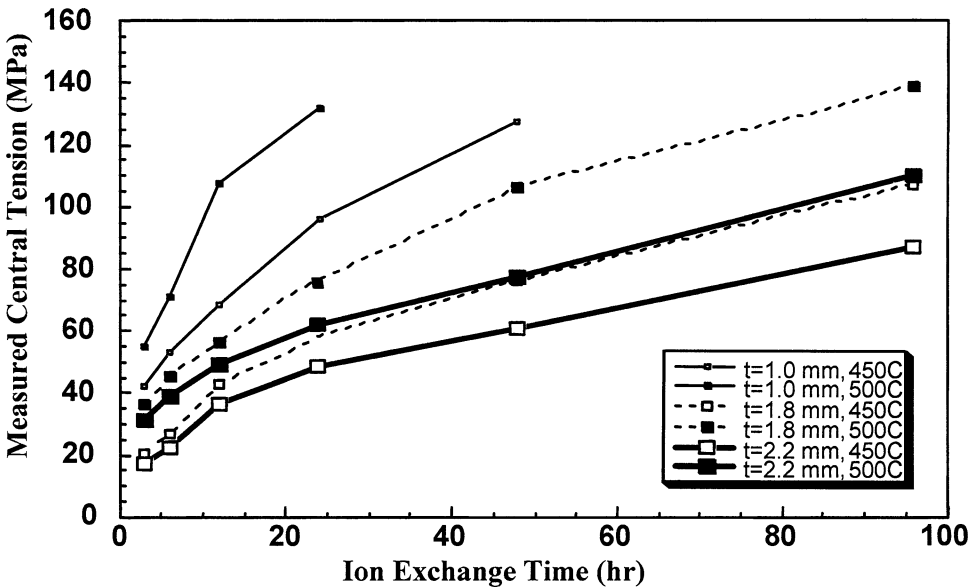


Figure 2. Central tension values for various exchange times, temperatures, and glass thickness values are shown.

values have the following distribution: $\sigma_{t, 1\text{mm}} > \sigma_{t, 1.8\text{mm}} > \sigma_{t, 2.2\text{mm}}$, i.e., the thinner the sample, the higher the value of central tension. For the same thickness, the exchange process at higher temperature yields the higher tension value.

3.2. Biaxial Flexure Strength Measurements

The results of the ring-on-ring biaxial flexure tests, as a function of increasing ion-exchange time, are shown in Figure 3. The open and closed symbols represent the exchange condition at 450°C and 500°C respectively, and the lines are aids to the eye. Due to the large number of conditions that had to be studied, only one-two samples per data point could be strength tested, and no statistical variation was calculated. It can be observed that for equivalent time and thickness, the strength of any sample exchanged at 450°C is higher than the sample exchanged at 500°C. Incidentally, the strength values for all the samples exchanged at 450°C exceed those exchanged at 500°C. At any given temperature of exchange, the strength (σ_f) follows the following distribution: $\sigma_{f, 1\text{mm}} > \sigma_{f, 1.8\text{mm}} > \sigma_{f, 2.2\text{mm}}$, i.e., the thinner the sample, the higher its strength. The strength values decrease with increasing time of exchange for both exchange conditions, and for all sample thickness values. The unexchanged samples have an average strength of 121 MPa.

3.3. Indentation Experiments

The results of observation of the Vickers indentation sites for a 40N peak load for various times of ion-exchange are shown in Fig. 4. The indentation impression size

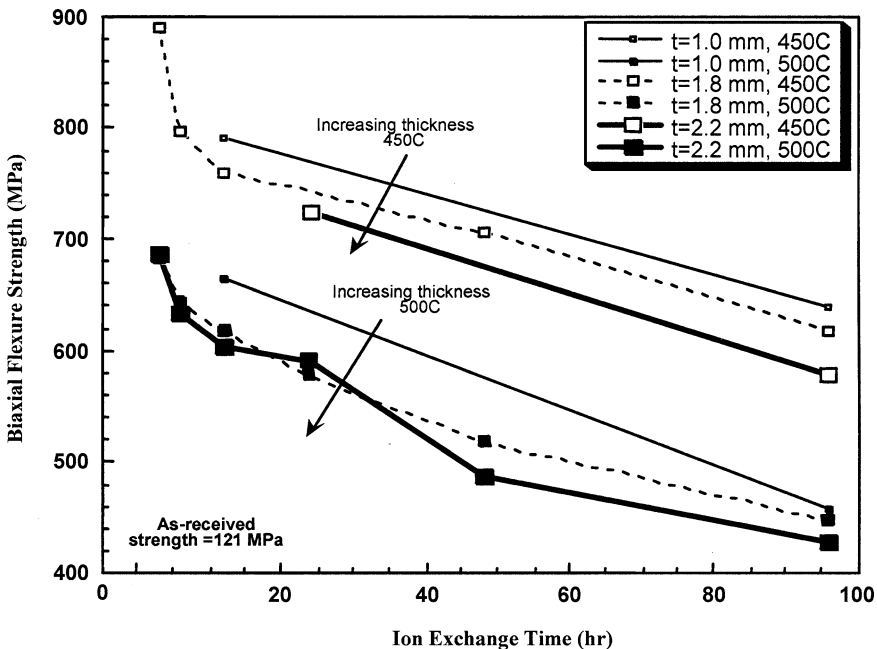


Figure 3. The bi-axial strength results as a function of ion-exchange times for various conditions are shown.

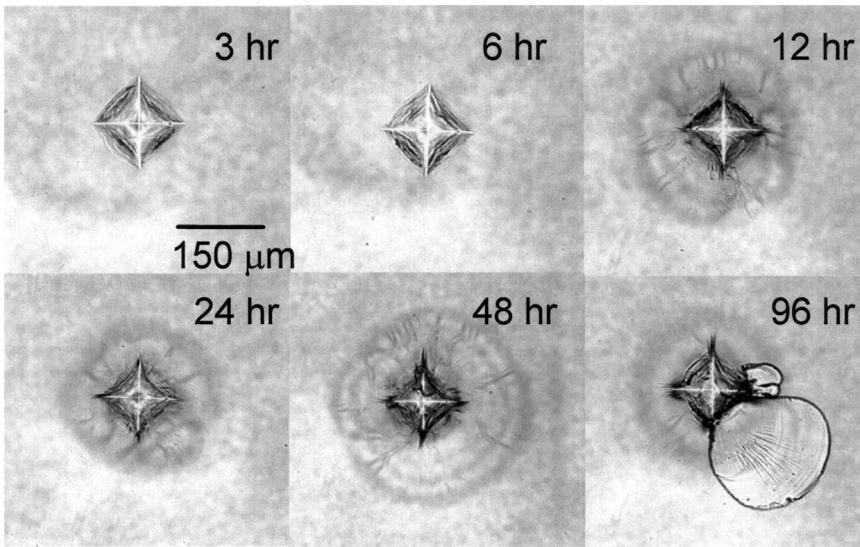


Figure 4. Observation of indentation sites (40N) for various times of exchange for a sample exchanged at 500°C.

(edge to edge) for this load is approximately 150 μm , and all the pictures are at the same magnification. Previous work on the base glass¹⁶ has shown that for peak loads exceeding 20 N, significant radial and lateral cracking may be expected at the indentation site. However, for the 3 and 6 hr. exchange samples, no cracking is detected. Traces of radial cracks emanating from the corners of the indenter can be seen for the 48 and 96 hr. exchange samples. Sub-surface lateral cracks around the indentation site are observed for the 12–96 hr. exchange samples. One quadrant of the lateral crack has grown to intersect the surface, and caused a surface spall for the 96 hr. sample. The results of indentation testing for 50N load are not shown here; however, it was observed that all the indentation sites developed large surface spalls within an hour of load removal.

3.4. Fragmentation and Fracture Surface Observations

The central tension values for the 1.8 mm glass thickness as a function of the ion-exchange time for both exchange temperatures are plotted in Figure 5a. As pointed out in Section 3.1, for a given thickness, central tension values increase with increasing time and temperature. These samples are then subjected to increasing indentation loads, till failure occurs. The fragmentation observations are presented in Figure 5b. For the 3 hr. exchange time, neither of the samples shows fragmentation, and one pair of the indentation cracks extends through and across the sample. For 6 hr. exchange, the 500°C samples exhibit branching from the indentation cracks. The tension in the 450°C sample, however, is sufficient to only cause both pairs of indentation cracks to propagate through the sample. Increasing the exchange time further to 12 hr. leads to the onset of branching for the 500°C sample closer to the origin of fracture, and it appears that further crack bifurcations occur at progressively shorter distances. The 450°C sample exchanged for 12 hr. exhibits crack branching only once from indentation crack pairs. Increasing the exchange times

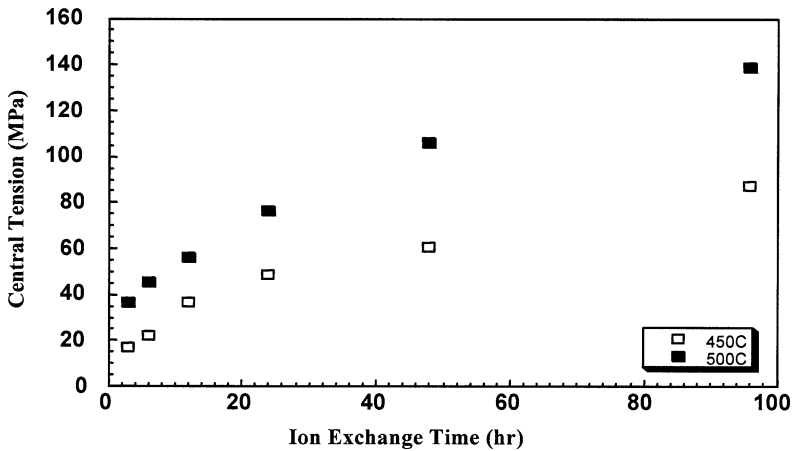


Figure 5a. Central tension values as a function of exchange time for a 1.8 mm thick glass are shown.

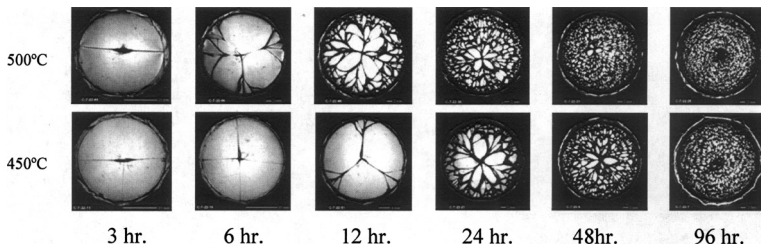


Figure 5b. Observations of fragmentation behavior corresponding to the sample set in Fig. 5a.

further, and thereby increasing the central tension accentuates the branching process, i.e., crack branching starts to occur closer to the origin, and the fragment size distribution is smaller. For the 96 hr. exchange samples, the fragment size is almost uniform, and is < 1 mm for both exchange temperatures. It was also noted that the edges of many of the samples are powdered (fragment size < 0.1 mm) even when the fragments adjacent to them were > 2 mm in size.

Figure 6a is a comparison of the central tension values as a function of ion-exchange time for a 1.8 mm thick sample exchanged at 450°C , with that of a 2.2 mm thick sample exchanged at 500°C . It is observed that for short exchange times, the tension values are lower in the thinner glass, but approach that of the thicker glass with increasing time. The fragmentation observations are presented in Figure 6b. For the 3 hr. exchange samples, the tension value in neither sample is adequate to cause branching. For the thicker sample, branching occurs for a 6 hr. exchange, whereas the cracks in thinner samples start branching for the 12 hr. exchange condition. With increasing tension in both samples, the degree of fragmentation increases. Longer exchange times at the (different) exchange temperatures lead to conditions where the central tension values are nearly equal. This is observed for the 48 hr. and 96 hr. samples. The fragmentation behavior of these samples becomes very similar, more so for the 96 hr. exchange samples.

The fracture surface observations for the tempered glass far from the origin of failure are shown in Fig. 7. The thickness of the sample, t , is 6 mm, and the photographs capture nearly the entire thickness. The dotted line on the picture

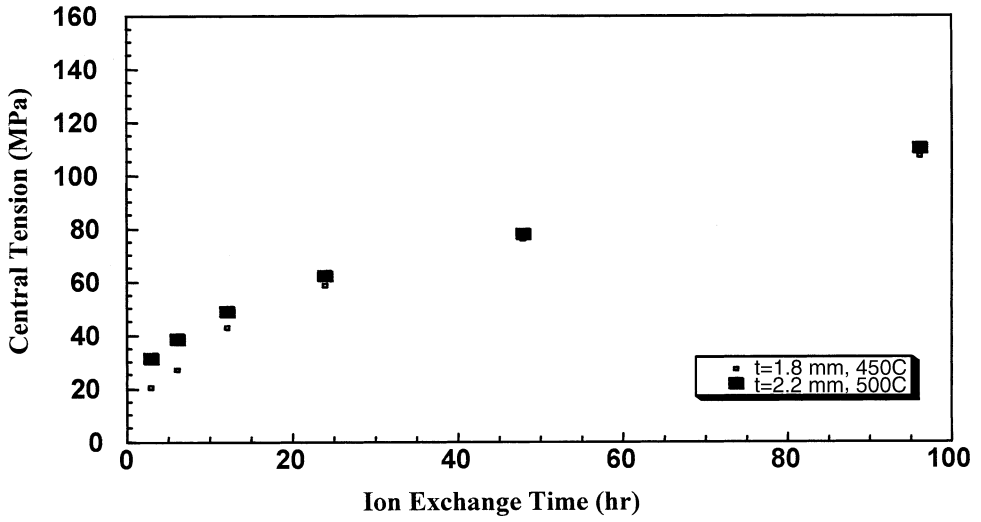


Figure 6a. Central tension values as a function of exchange time for a 1.8 mm, 450°C exchange sample compared with 2.2 mm, 500°C exchanged sample.

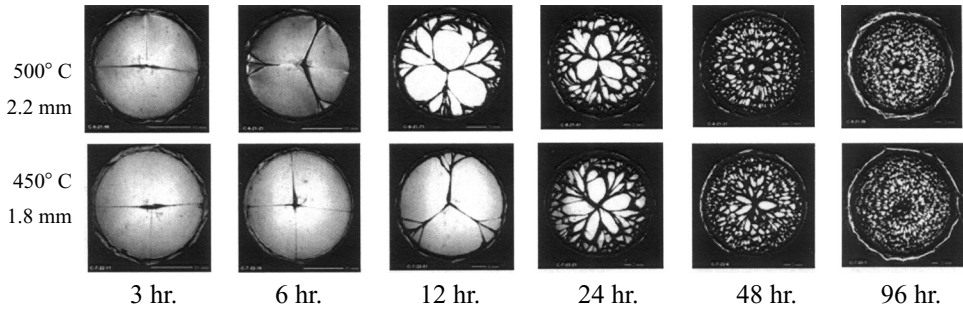


Figure 6b. Observations of fragmentation behavior corresponding to the sample set in Fig. 6a.

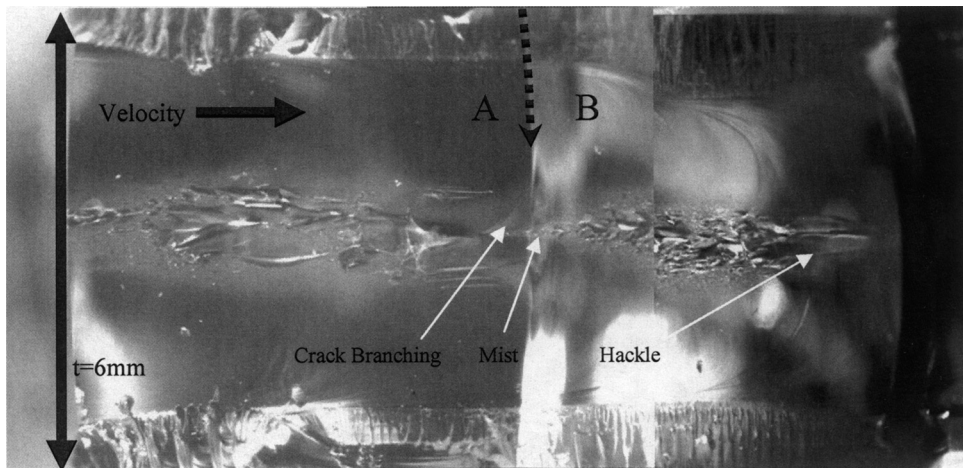


Figure 7. Fracture surface views of two fragments, A and B, for tempered glass.

shows the boundary between the two fragments, A and B. There is a region near each of the surfaces where the fracture process appears to be different than in the core of the sample. This region occupies $\sim 13\%$ of the sample thickness on each side. For normal tempering conditions, tempered glass has $\sim 46\%$ (23% on each side) of the thickness under compression. Wallner lines are visible on the fragment on the right, and the crack propagation direction (marked by the arrow) is deduced from these lines. In the center of the sample, a region where the crack front underwent the mirror-mist-hackle transformations, as it accelerates under increasing stress intensity, are clearly visible. For tempered glass, the central region is the location of maximum tension. The fragments pictured were still adherent to each other across the second fracture plane that is marked by the dotted line.

The fracture surfaces for ion-exchanged glass (500°C , 6hr., central tension = 45 MPa) near (Figure 8a), and far (Figure 8b) from the fracture origin are shown. The entire thickness, $t = 1.8\text{ mm}$, is pictured in Figure 8a. At the bottom right, the plastic deformation and the lateral and median vents from the indentation crack that started the fragmentation process can be seen. Wallner lines at locations where the crack front interacted with the lateral vents can be seen. A second, fainter, series of Wallner lines which are semi-elliptical can be seen just further from the major lines. The direction of the crack velocity is marked. At a distance of about 1.8 mm from the median vent plane, the beginning of mist formation is observed. The mist area then extends and spreads across the thickness of the sample. Figure 8b shows a continuation of this fracture path. Here the mist region gradually changes into hackle. The crack branched macroscopically at the left edge of this photograph. There appears to be a very strong interaction of the crack front with the zone of compression as evidenced by the sharp curvature of the Wallner lines at the top and bottom.

3.5. Analysis

A first estimate of the size of the fragments of ion-exchanged glass may be obtained by equating the stored tensile strain energy in the body to surface energy of the new area created. Warren⁹ has presented a similar analysis for thermally tempered glass. We begin by making several assumptions: (a) that only the tensile strain energy is used in the fragment process, (b) that all the tensile strain energy is used up in the

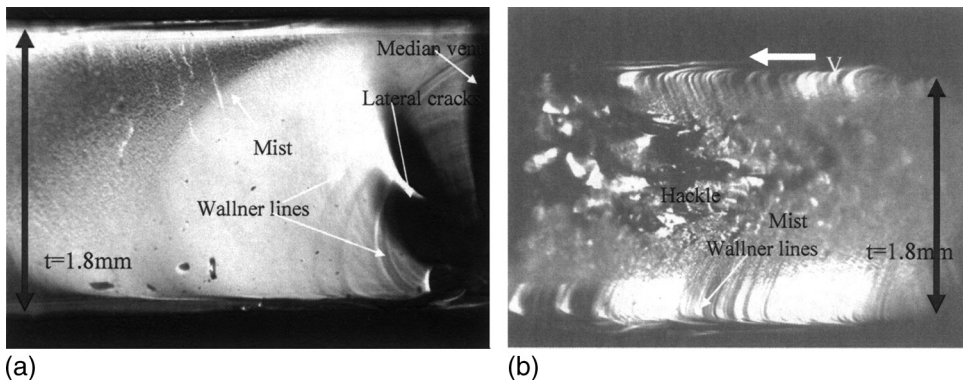


Figure 8 a, and b. Fracture surface views, near the origin (a), and far from the origin (b) for ion-exchanged glass.

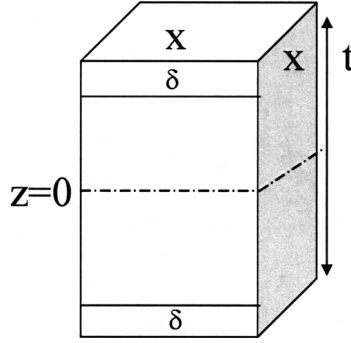


Figure 9. Schematic of an idealized remnant shape used in the energy analysis.

process to create new surface area (i.e., effectively ignoring kinetic and sonic effects, and implicitly assuming that the remnant is stress-free), and (c) that all remnants are identical in size and shape. An idealized remnant is depicted in Figure 9. An assumption with other geometrical cross sections (a hexagon for instance) does not change the material dependences derived. Let σ_t be the central tension, and let δ be the depth of the compressive profile. Hence the energy in a unit volume, dV , of the fragment is ΔU_E , which is given by

$$\Delta U_E = \frac{1}{2} \sum \sigma_{ij} \varepsilon_{ij} \Delta V \quad (1)$$

Now since the state of tension is equi-biaxial, with other components assumed to be zero, we obtain

$$\sigma_{xx} = \sigma_{yy} = \frac{E}{(1-\nu)} \varepsilon_{xx} = \frac{E}{(1-\nu)} \varepsilon_{yy} = \sigma_t \quad (2)$$

where E , ν are the elastic modulus and Poisson's ratio. Substituting in Eq. 1, we obtain

$$\Delta U_E = \frac{(1-\nu)}{E} \sigma_t^2 dx dy dz \quad (3)$$

Integrating to obtain the total tensile strain energy in the fragment, we obtain

$$U_E = \int_{dV} \Delta U_E = \int_{-\left(\frac{t}{2}-\delta\right)}^{\left(\frac{t}{2}-\delta\right)} \int_0^x \int_0^x \frac{(1-\nu)}{E} \sigma_t^2 dx dy dz \quad (4)$$

Equating U_E to the total energy of the new surfaces created, U_S , we obtain

$$U_E = \frac{(1-\nu)}{E} x^2 \sigma_t^2 (t - 2\delta) = U_S = 4xt\gamma \quad (5)$$

where γ is the surface energy.

Simplifying, we obtain

$$x = 2 \frac{2E\gamma}{(1-\nu)} \frac{1}{\sigma_t^2} \frac{t}{(t-2\delta)} = 2(1+\nu) \left(\frac{K_{1c}}{\sigma_t} \right)^2 \frac{t}{(t-2\delta)} \quad (6)$$

where K_{1c} is the fracture toughness of the material. The resulting expression predicts that the size of the fragment scales as tension⁻², and depends (weakly) on the thickness of the sample.

4. DISCUSSION

4.1. Tensile Stress and Bi-axial Strength Measurements

The migration of the K^+ ions into the glass structure is diffusion-controlled, and the depth of penetration is dependent on both time and temperature. The regions with excess K^+ ions have a higher volume at equilibrium (a longer in-plane length) when the process occurs below the glass transition temperature as in this case. The chemical composition, and hence the equilibrium length of the core layers is unaltered. Therefore, the actual state of the body is a length in between the two described above. This sets up a state of residual compression in the K^+ rich layers, and in response, an equi-biaxial state of compensating central tension to ensure force equilibrium across the section. We find that the measured internal tension increases with increase in exchange time for all conditions (Fig. 2). This implies that as more K^+ ions diffuse into the sample, the net compressive force increases, leading to an increase in the compensating tension. It is also observed that for identical conditions of exchange viz., same temperature and time, the tension in the thinner samples is highest. Similar conditions of exchange must lead to identical flux of K^+ ions, and similar compressive stress profiles. Therefore, the thinner samples, which have the least cross-sectional area, must develop a correspondingly higher tensile stress.

Interestingly, the bi-axial tests show a continuous drop in strength with increasing exchange time. We expect a higher ion flux and deeper penetration with increasing time, and therefore, a rise in the net compressive force. Since the compressive stress acts to close the surface cracks, we expect an increase in strength rather than a decrease. These results can be understood if we invoke the phenomena of stress relaxation¹⁷. The highly stressed surface of the glass undergoes a structural relaxation and the values of the near surfaces stress will fall, in some cases to near zero values. Since the flaws causing failure are at or near the surface, this stress relaxation leads to a loss in strength. We observe that the strength for samples treated at 500°C are significantly lower than those treated at 450°C. Since the relaxation phenomena is activated by temperature and stress, higher relaxation rates at higher temperature may be expected. However, it may be noted that even the lowest strengths recorded (~420 MPa) are three times the as-received values. Estimates of the minimum surface compression values for these samples may be made by assuming that the strength is equal to the as-received strength plus the value of the surface compressive stress. For the 450°C, 3 hr. exchange, 1.8 mm thick sample, this leads to a value of -780 MPa (-ve sign implies a compressive stress). We also observe that for each condition, the thinner samples have the highest strength. This may be due to the steeper drop-off of the applied flexure loading across the potentially failure causing flaw in the thinner samples. A steeper drop-off would lead to a lower value of

net stress intensity factor acting on the crack for any given applied stress, and consequently to higher required stress for failure.

Another interesting feature is that although the strength falls, and the peak values of the compression relax for higher exchange times, the internal tension increases monotonically. This implies that the rate of penetration of K^+ ions is such that despite the relaxation, the summation of the compressive stress, across the cross-section increases, i.e., the compressive force increased.

4.2. Indentation Response

Indentation on the base glass at a 40 N load leads to severe radial and lateral cracks.¹⁶ The complete absence of any median, radial or lateral cracks at the indentation site for the 3 and 6 hr. exchanged samples (Fig. 4) is indicative of the strong effect of the residual compression on crack initiation. Unpublished work by the authors has shown that the driving force for lateral cracks is unaffected by the residual compressive stress. Therefore the absence of lateral cracks for 3 and 6 hr. exchange is surprising. However, lateral and small traces of radial cracks appear for higher exchange times. This indicates that the surface stress relaxes with increasing exchange time, and supports the hypothesis advanced for understanding the biaxial strength observations in Sec. 4.1. Observations of the 50 N indentation sites reveal extremely severe lateral cracking and spalling, and will not be described here.

4.3. Fragmentation and Fracture Surface Observations

Fragmented samples, 1.8 mm thick, 500°C exchange for 6, 12 and 24 hr., held together by tape are shown in Fig. 10. The tension values for these samples are 45 MPa, 55 MPa, and 75 MPa respectively. Observation of these samples and the fracture surfaces lends insight into the fragmentation process. A crack (or pair of cracks if the initiation is using an indenter) may penetrate the compressive zone, and is then acted upon by the tensile stress. If the stress intensity factor exceeds the material toughness, the crack propagates as an internal crack entirely in the zone of tension. When the crack becomes sufficiently long, the net stress intensity factor exceeds the branching constant, K_b , and macroscopic branching may occur. For the 6 hr. sample, two pairs of cracks have branched, and the number of crack branches

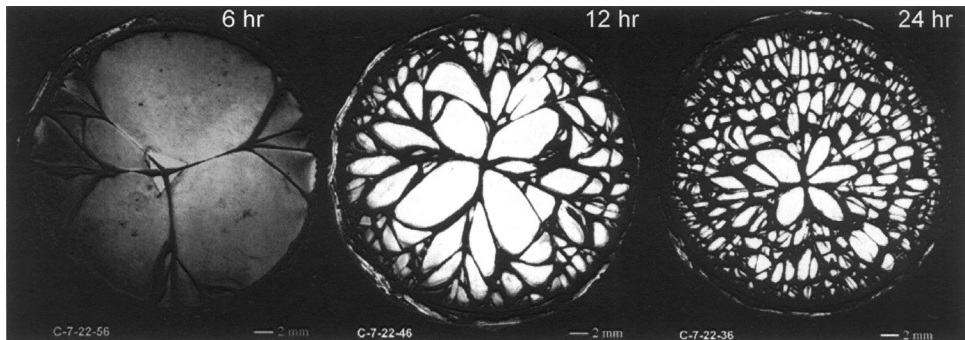


Figure 10. Comparison of crack paths in fragmented samples reveals details of the process.

range from 2-4. Since the 12 hr. sample has a higher value of tension, the value of K_b is reached for shorter crack lengths, and branching occurs closer to the origin. This process is further accentuated for the 24 hr. sample due to its highest tension value in this set. It also appears that the second, third, and subsequent branching events occur progressively closer, i.e., the branching length decreases with each successive branch. The observed decrease in the fragment size as one translates from the origin to the periphery of the sample could be due to this reduction in branching length. However, it is possible that what appears to be a decrease in branching length is simply an artifact of multiple crack propagation and intersection. Studies of larger samples with low values of tension will be used to clarify this behavior.

The data presented in Fig. 5 and Fig. 6 underscore the importance of the central tension value in order to define fragmentation. In Fig. 5, we observe that for samples of identical thickness, higher tension values lead to higher fragmentation. In Fig. 6, the differences in the central tension values are manifest in the fragmentation behavior. For longer exchange times, the tension values become similar, and the fragmentation behavior appears indistinguishable.

For Corning 0317 glass, the depth of K^+ ion diffusion for 24 hr. exchange at 500°C is 180 μm .¹⁴ Using this value, and assuming that the diffusion distance (δ) can be well approximated by $\delta \sim 2(Dt)^{1/2}$ (where D is the diffusion coefficient, t is exchange time), the value of D at 500°C was calculated. The value of the activation energy for diffusion is known to be 113 kJ/mole,¹⁴ and the exponential relationship was used to calculate the diffusion coefficient at 450°C. Using the value of D , the δ for each condition was obtained. These values, with the known value of tension, and the properties of the glass ($K_{Ic} = 0.7 \text{ MPa}\cdot\text{m}^{1/2}$, $\nu = 0.25$) were used in Eq. 6 to estimate the fragment size. The results for the 1.8 mm thick glass series are shown in Table 1.

On comparing the predictions to the actual values of fragmentation, we find that the calculation grossly underestimates the size of the fragments, especially for large fragments. This is due to the assumption that all the energy in the tensile zone is converted into surface energy, which overestimates the available energy. The assumption may be accurate for very small fragments. This is because as the surfaces of a fragment are stress free, the stress state may be expected in the volume as well (somewhat analogous to the case of a thin material being in plane stress condition). Indeed, the predicted values for the 48 and 96 hr. exchanged samples are very close to the actual values (0.45 mm and 0.33 mm compared with 0.27 mm and 0.14 mm predicted). However, for large fragments, complete energy release is extremely unlikely, and observations of fragments in the polarized light reveal birefringence indicative of residual stress.

Table 1. Predicted fragment size (\times) using the energy balance approach.

| Exchange time (hr.) | σ_r at 500°C (MPa) | $\delta_{500}(\mu\text{m})$ | $\times(\text{mm})$ | σ_r at 450°C (MPa) | $\delta_{450}(\mu\text{m})$ | $\times(\text{mm})$ |
|---------------------|---------------------------|-----------------------------|---------------------|---------------------------|-----------------------------|---------------------|
| 3 | 37 | 64 | 1.25 | 16 | 35 | 6.50 |
| 6 | 45 | 90 | 0.87 | 23 | 49 | 3.19 |
| 12 | 55 | 128 | 0.61 | 37 | 69 | 1.26 |
| 24 | 75 | 180 | 0.35 | 47 | 98 | 0.81 |
| 48 | 107 | 255 | 0.19 | 60 | 139 | 0.52 |
| 96 | 140 | 360 | 0.14 | 87 | 196 | 0.27 |

It was also noticed that the edges of many samples were powdered, even when the adjacent fragments were rather large. This may be attributed to the stress wave reflection from the edges interacting with the approaching crack front to magnify the crack loading. It is also possible that ion-exchange from the edges leads to a localized stress state with much higher tension than in the center, leading to powdering.

Observation of the fracture surface of the tempered glass (Fig. 7) indicates that about 26% of the cross-section (13% each on the top and bottom) suffers a shear fracture. Since the zone of compression occupies $\sim 46\%$ of cross-section (23% at the top and bottom), the cracks propagate not only in the tensile zone, but also in the area with low compression. The shear fracture in the near surface region is due to the interaction of the crack front with the compressive stress, and the introduction of mixed mode loading. The main crack front undergoes the mirror-mist-hackle transition near the center of the sample, which in tempered glass is the region of highest tension. The crack branches in-plane to create the boundary between fragments A and B, and one portion of the front continues to generate further misthackle features.

On the fracture surfaces of the exchanged glass (500°C, 6hr., central tension = 45 MPa) in Fig. 8 a, and b, the mirror-mist-hackle transitions are not localized to the center portion. The mist starts from the far edge (away from the indentation), and broadens to encompass almost the entire cross-section. This behavior is due to the uniformity of the central tension. It is also observed that near-surface regions, nearly 300 μm on the near side, and 200 μm on the far side, are free of mist or hackle features (this region is significantly larger than $\delta \sim 90 \mu\text{m}$ for this sample). The Wallner lines clearly visible in this region are strongly curved, indicating that there is a strong interaction between the crack front and the compressive zone. These observations indicate that the compressive stress may be acting to pin the crack, and its effectiveness may extend beyond its physical location in the sample.

5. CONCLUSIONS

For the glass system and the ion-exchange condition studied, the following conclusions may be drawn from the data presented in this study:

1. Increasing the ion-exchange time leads to a decrease in the surface compressive stress, but to an increase in the net compressive force via an increase in the exchanged depth.
2. Compressive stress distributions raise the strength over the base glass by as much as a factor of seven, but near surface stress relaxation processes lead to some lowering of this enhanced value (to nearly three times of the base glass).
3. Compressive stresses are found to subdue median and radial cracking at indentation sites, but the strain energy associated with the indentation leads to enhanced lateral cracking.
4. The compensating tensile stress is found to increase monotonically with time of exchange, and is higher for thinner samples under equivalent conditions of exchange. The tensile stress appears to be very uniform through out the cross-section.
5. Fragmentation in ion-exchanged glass is observed to be a multiple crack branching process yielding progressively smaller fragments further from fracture origin
6. In general, an increase in the tensile stress leads to higher fragmentation density, and a more uniform fragment size.

7. An energy based analysis of the fragmentation process significantly underestimates the observed fragment size.
8. Design of reliable, frangible glasses appears to be constrained by the following factor: For increased fragmentation, a high value of tension is required. Higher exchange times needed to obtain this value leads to strength loss due to surface stress relaxation. This effect may be mitigated by using thinner sections. However, it must be ensured that the load bearing capacity of the system is adequate.

6. ACKNOWLEDGMENTS

Sandia is a multi-program laboratory operated by Sandia Corp., a Lockheed Martin Co., for the United States Department of Energy, under Contract No. DE-AC04-94AL85000.

REFERENCES

1. H. P. Kirchner, *Strengthening of Ceramics, Treatments, Tests, and Design Applications*. Marcel-Dekker, New York, (1979)
2. R. Gardon, *Thermal Tempering of Glass, Glass: Science and Technology V*. Academic Press, New York. (1980)
3. S. Kistler, Stresses in Glass Produced by Nonuniform Exchange of Monovalent Ions, *J. Am. Ceram. Soc.*, 45 [2] 59–68 (1962)
4. M. E. Nordberg, E. L. Mochel, H. M. Garfinkel, and J. S. Olcott, Strengthening by Ion Exchange, *J. Am. Ceram. Soc.*, 47 [5] 215–219 (1964)
5. D. J. Green, A Technique for Introducing Surface Compression into Zirconia Ceramics, *J. Am. Ceram. Soc.*, 66 [9] C178–C179 (1983)
6. A. V. Virkar, J. L. Huang, and R. A. Cutler, Strengthening of Oxide Ceramics by Transformation-Induced Stresses, *J. Am. Ceram. Soc.*, 70 [3] 164–170 (1987)
7. D. J. Green, R. Tandon, and V. M. Sglavo, Crack Arrest and Multiple Cracking in Glass through the Use of Designed Residual Stress Profiles, *Science*, 283, 1295–1297 (1999)
8. J. M. Barsom, Fracture of Tempered Glass, *J. Am. Ceram. Soc.*, 51 [2] 75–78 (1968)
9. P. D. Warren, *Fractography of Glasses and Ceramics IV*, 389–400, The American Ceramic Society, Ohio (2001)
10. A. L. Zijlstra and A. J. Burggraaf, Strength and Fracture behavior of Chemically Strengthened Glass in Connection with the Stress Profile, Part II, *J. Non-Cryst. Solids*, 1, 163–185 (1969)
11. M. Bakioglu, F. Erdogan, and D. P. H. Hasselman, Fracture Mechanical Analysis of Self-fatigue in Surface Compression Strengthened Glasses, *J. Mat. Sci.*, 11, 1826–1834 (1976)
12. I. W. Donald and M. J. C. Hill, Preparation and Mechanical Behavior of some Chemically Strengthened Lithium Magnesium Alumino-Silicate Glasses, *J. Mat. Sci.*, 11, 1826–1834 (1976)
13. E. Bouyne and O. Gaume, Fragmentation of Thin Chemically Tempered Glass Plates, *Proc. Int. Congr. Glass Volume 2, Extended Abstracts, Scotland*, (2001)
14. S. J. Glass, E. K. Beauchamp, C. S. Newton, R. G. Stone, W. N. Sullivan, R. T. Reese, S. D. Nicolaysen, and R. J. Kipp, Controlled Fracture of Ion-Exchanged Glass Rupture Disk, Sandia National Laboratories Report, SAND2000-0828 (2000)
15. H. W. McKenzie and R. J. Hand, *Basic Optical Stress Measurements*, Society of Glass Technology, Sheffield, U.K., 1999
16. R. Tandon, D. J. Green, and R. F. Cook, Surface Stress Effects on Indentation Fracture Sequences, *J. Am. Ceram. Soc.*, 73 [9] 2619–27 (1990).
17. A. Y. Sane and A. R. Cooper, Stress Buildup and Relaxation During Ion Exchange Strengthening of Glass, *J. Am. Ceram. Soc.*, 70 [2] 86–89 (1987)

ELASTO-PLASTIC BEHAVIOR OF GLASSY CARBON AND SILICA GLASS BY NANO-INDENTATION WITH SPHERICAL TIPPED INDENTER

Norio Iwashita, Michael V. Swain
and John S. Field*

1. INTRODUCTION

Glassy carbons (GCs), obtained by pyrolysis and heat treatment of thermosetting resins above 1000°C, are hard and brittle materials that fail suddenly when loaded in tension or compression.¹⁻³ In commercially available GCs, the mean grain diameter, evaluated from micrographs under a field-emission electron gun type scanning electron microscopy, and the crystallite sizes, calculated from X-ray powder diffraction profiles, both slightly increased with the elevation of heat treatment temperature (HTT) from 1000°C to 3000°C.⁴

The Young's modulus and the flexural strength values of the GC heat-treated at 3000°C were smaller than those of the GCs heat-treated at 1000 and 2000°C⁵. However, the fracture toughness, K_{Ic} , of GCs slightly increased with the elevation of HTT.^{5,6}

* Norio IWASHITA, National Institute of Advanced Industrial Science and Technology (*AIST*), 16-1 Onogawa, Tsukuba, Ibaraki 305-8569 JAPAN. Michael V. SWAIN and John S. FIELD, Biomaterials Science Research Unit, The University of Sydney, Suite G11, National Innovation Centre, Australian Technology Park, Eveleigh NSW 1430 AUSTRALIA

GCs have excellent attributes including: isotropy, chemical stability, high hardness, wear resistance, gas impermeability, and are non-contaminating.^{1-3,7,8} In recent years, they have been used as essential materials for components of silicon wafer processing equipment used in the manufacture of semiconductor devices and other applications including fuel cell components, electrochemical electrodes etc.⁹ For such applications, the micro-metrological processing precision and micro-mechanics of GC surfaces are very important.

Sakai and co-workers have investigated the GCs produced by different densification processes using a Vickers indenter.¹⁰ The indentation hysteresis behavior was found on curves of indentation load versus indentation depth for all indentation loads from 10 to 500 N. For GCs, it was also observed that ring/cone cracks were induced by Vickers indentation instead of the median/radial crack systems more usually observed in brittle materials under a sharp indenter. A superior feature of GCs compared to ordinary brittle ceramics is their resistance to strength degradation by contact with hard particles as demonstrated by anomalous ring/cone crack formation.

Field and Swain have studied elasto-plastic response on a number of brittle materials, including silicate glass, silicon single crystal and single crystalline sapphire, by the indentation with small micron sized spherical tipped indenters.^{11,12} The analysis of indentation stress-strain curve was performed from the indentation on these materials.

Field and Swain found that the indentation force-displacement behavior for GC exhibited almost complete recovery with a significant hysteresis between loading and unloading when indented with 3 and 10 μm radius spherical tipped indenters.¹²⁻¹⁵ And also we have studied on elasto-plastic deformation of silica glass and glassy carbons with different type of indenters^{16,17}

In the present work, indentation of GCs heat-treated at different temperatures was carried out using a spherical tipped indenter. For comparison, fused silica glass was also used. Quantitative evaluation of "elasticity" and "plasticity" of elasto-plastic deformation by the spherical tipped indentation on GC and silica was also attempted. The dependence of hysteresis and elasto-plastic deformation of GCs on their crystal structure are discussed from stress-strain curve.

2. EXPERIMENTAL

Glassy carbons (GCs) heat-treated at 1000, 2000 and 3000°C (hereafter, sample codes: GC1000, GC2000 and GC3000) were used in a series of work. For comparison, fused silica glass was used. The surface which was cut after carbonization of a block of precursor thermosetting resin was used for the measurement of small radius spherical tipped indentation. Previous work has shown that the surface of glass-like carbons directly derived from the surface of thermosetting resin blocks exhibit different crystal structure and micro-texture from their bulk.¹⁸ The surface of these samples was polished using diamond slurry.

The following X-ray parameters were measured on the pulverized samples mixed with high-purity silicon powder as an inner standard.¹⁹ Average interlayer spacing (d_{002}) and lattice constant along the a-axis (a_0) were determined from Bragg angles of 002 and 110 diffraction lines by referring to the diffraction positions of the inner

standard silicon, respectively. The crystallite sizes along the c -axis and the a -axis were calculated from the half-maximum width of 002 and 110 diffraction peaks, denoted as $L_c(002)$ and $L_a(110)$, respectively. The correction for the peak broadening due to equipment was made by referring to silicon.¹⁹

Load cycle indentation was performed using a commercial ultra micro-indentation system (UMIS-2000) with a spheroconical diamond indenter with 3 μm radius. The radius of the indenter was calibrated using silica glass, of which the elastic modulus and Poisson's ratio were known. The initial contact force was 0.1 mN, and load controlled tests are performed. Each test was repeated ten times at different positions on the polished surface of the specimen.

3. RESULTS & DISCUSSION

Bulk density and X-ray structural parameters of the used GCs are summarized in Table 1. For comparison, the data of isotropic graphite block is shown in the same table. It was characteristic that the bulk densities of the GCs decrease with the elevation of heat treatment temperature (HTT). Commonly, GCs are non-graphitizable carbon, so that the values of average interlayer spacing d_{002} of the present GC samples are larger than 0.34 nm, even in the sample GC3000 heat-treated at 3000°C. The stacking of carbon hexagonal network layers is turbostratic. As compared with a commercially isotropic graphite block, the crystallite sizes, L_a and L_c , are very small. As the result that the crystallite structure of GCs is not almost grown by heat treatment, it is difficult to evaluate the dependence of mechanical properties of GC on heat treatment temperature by traditional tests, for instance, bending test. In Figure 1, the force-penetration curves for the indentation on fused silica glass with 100 mN terminal force is shown. For the force-displacement response of a spherical indenter on "elastic" surface, Hertz derived the basic relationship between penetration, h_t , and applied force, P , namely²⁰

$$h_t = \left(\frac{3P}{4E^*} \right)^{2/3} \cdot \left(\frac{1}{R} \right)^{1/3}, \quad (1)$$

where R is the radius of spherical indenter and E^* the composite modulus of the indenter and specimen, which is defined by

Table 1. Bulk density and X-ray structural parameters of the used GC samples and isotropic graphite.

| | | GC1000 | GC2000 | GC3000 | isotropic graphite |
|----------------------------|----------------------|--------|--------|--------|--------------------|
| Bulk density | [g/cm ³] | 1.52 | 1.48 | 1.44 | 1.81 |
| X-ray structural parameter | | | | | |
| d_{002} | [nm] | 0.3515 | 0.3482 | 0.3480 | 0.3362 |
| a_o | [nm] | 0.2412 | 0.2426 | 0.2436 | 0.2461 |
| $L_c(002)$ | [nm] | 1.7 | 2.6 | 3.5 | 55.4 |
| $L_a(110)$ | [nm] | 2.2 | 2.7 | 3.5 | 44.6 |

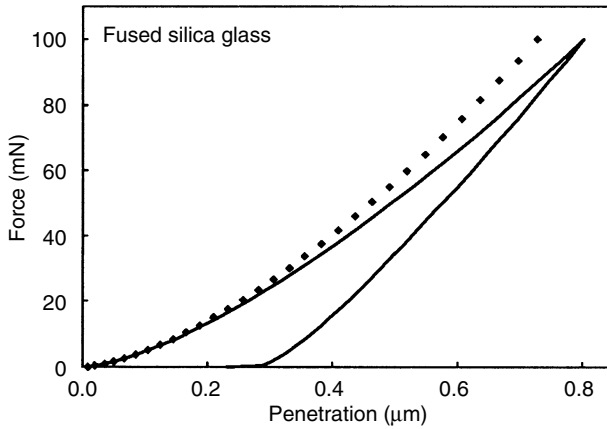


Figure 1. Load-penetration curve of fused silica glass with 3 μm radius spherical tipped indenter.

$$\frac{1}{E^*} = \frac{1 - \nu_s^2}{E_s} + \frac{1 - \nu_i^2}{E_i}, \quad (2)$$

where ν is Poisson's ratio and the subscripts s and i mean specimen and indenter, respectively. From Eq. (1), perfectly elastic curve can be drawn, showing as the dotted line in the same figure. For the indentation with spherical indenter, thus, it is characteristic that elastic deformation is observed at the initial of indentation, and then elasto-plastic behavior is seen beyond a yield point.

Schematically illustrations of deformation on surface with spherical indenter are shown in Figure 2. The geometrical factor for "elastic" surface deformation is equal to 2 for spherical indenter.²⁰ Thus, the contact circle penetration h_p is described as following:

$$h_p = \frac{h_t}{2}. \quad (3)$$

Providing that $h_t \ll R$, the radius of the contact circle is calculated using¹¹:

$$a = \sqrt{R \cdot h_p}. \quad (4)$$

Thus, equation (1) can be rewritten as¹¹:

$$\frac{P}{\pi a^2} = \left(\frac{4}{3\pi} \right) E^* \cdot \frac{a}{R}. \quad (5)$$

The effective strain associated with a spherical tipped indenter may be written as the ratio of radius of contact circle to the radius of indenter, a/R .²¹

As illustrated in Figure 2(b), "elasto-plastic" deformation occurs upon exceeding a critical load for yielding. Thus, h_t is larger than elastic component h_e calculated using Eq. (1). The contact circle penetration h_p is estimate from:¹¹

$$h_p = h_t - \frac{h_e}{2}. \quad (6)$$

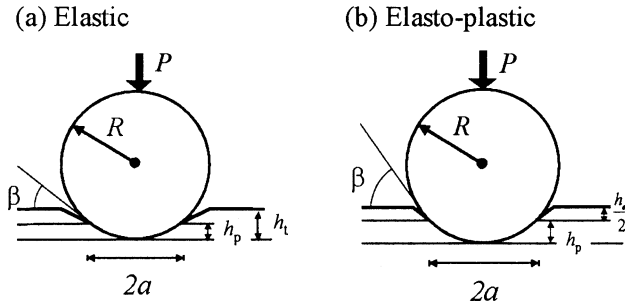


Figure 2. Schematically illustrations of deformation on surface with spherical indenter.

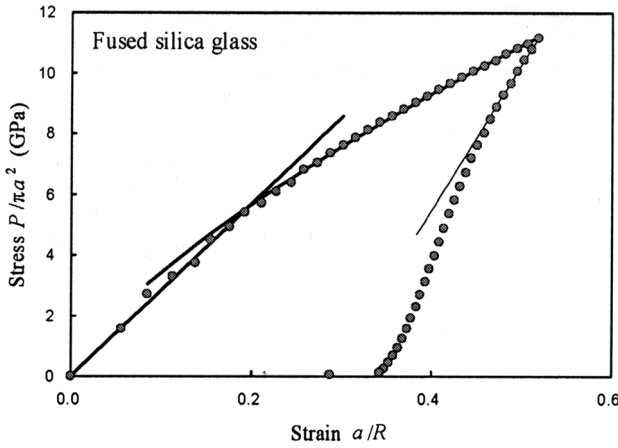


Figure 3. Plot of stress $P/\pi a^2$ – strain a/R of fused silica glass with $3 \mu\text{m}$ radius spherical tipped indenter.

The plot of $P/\pi a^2$ versus a/R analyzed from the force-penetration curve of Figure 1 is shown in Figure 3. A value of elastic modulus E^* is estimated from a linear fitting for the first several points within the linear region on the plots of $P/\pi a^2$ versus a/R . A non-linear relation is observed beyond the yielding point after the initial elastic deformation on the plots of $P/\pi a^2$ versus a/R . Since the secondary mechanism is increasingly more curved at the higher terminal force, it maybe described by a simple power law relationship, as following:¹¹

$$\frac{P}{\pi a^2} = k \cdot \left(\frac{a}{R}\right)^n \tag{7}$$

The power law constants, n and k , were estimated from log-log plots of the non-linear portion of the stress-strain curves.

Force-penetration curves of the indentation on GCs with 100 mN terminal force are shown in Figure 4(a). In the case of inorganic glasses, the spherical tipped indentation unloading is “elastic” deformation, as shown in Figure 1. A residual penetration remains after fully unloading. For glass-like carbons, however, it is characteristic that complete recovery of elasto-plastic deformation is observed on unloading, that is, hysteresis loop. The measured penetration h_t is smaller than h_e for

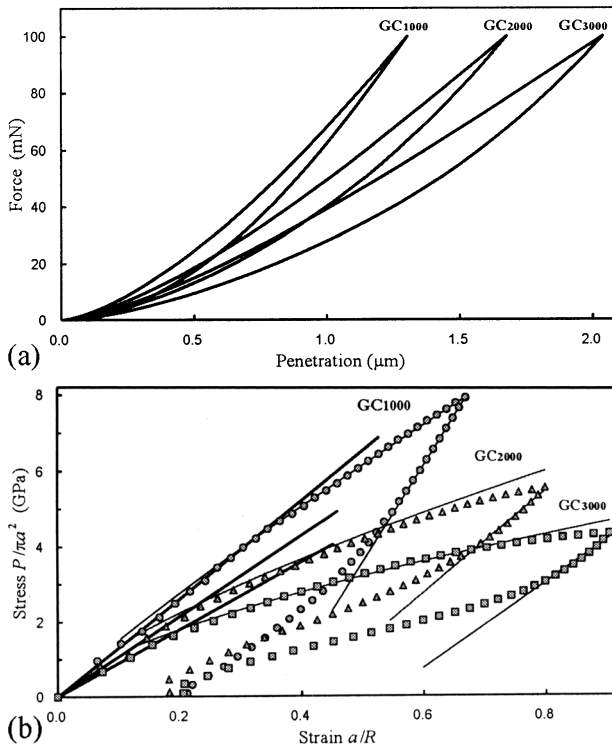


Figure 4. (a) Force-penetration and (b) stress-strain curves of the indentation on GCs with 100 mN terminal force.

the recovery of elasto-plastic deformation. This hysteresis behavior was discussed in the previous papers.^{13,14}

For the elevation of heat-treatment temperature of GCs, it is seen that the penetration by the indentation is deeper and the hysteresis loop is larger. The area of the hysteresis loop on the force-displacement curve corresponds to energy loss during the deformation of the substrate by the indentation.

The loading and unloading elastic moduli, yield stress, yield strain and constants associated with power law fitting of the indentation stress-strain curves on the different GCs are summarized in Table 2. These values decrease with the elevation of HTT of GCs.

In the present results, it was found that elasto-plastic deformation of the GCs by indentation is very sensitive to their crystal structure and micro-texture. The elastic modulus of the GCs reduced with the elevation of HTT (Table 2). The reduction of the elastic modulus is predicted to result from not only the corresponding decrease in bulk density of GC with the elevation of HTT, but also a decrease in shear modulus (rigidity) of the carbon hexagonal network layers with development of the graphitic structure.

The yield stress showed a similar trend to the elastic modulus of significantly decreasing with development of graphitic structure of GCs. The constants of power law fitting, n and k , for the stress-strain curves by the indentation on the different GCs decreased with the elevation of HTT (Table 3). From the reduction of these

Table 2. Elastic modulus, yield stress, yield strain, constants of power law fitting and indentation elasticity index obtained from stress-strain curves with 3 μm radius spherical tipped indenter on GCs and silica glass.

| | | GC1000 | GC2000 | GC3000 | Silica |
|-------------------|-------|--------------|--------------|--------------|--------------|
| E^* (loading) | [GPa] | 30.7 | 24.3 | 21.3 | 67.1 |
| E^* (unloading) | [GPa] | 32.0 | 24.0 | 20.4 | 72.8 |
| Yield Stress | [GPa] | 3.9 | 2.7 | 1.8 | 5.5 |
| Yield Strain | [-] | 0.30 | 0.26 | 0.21 | 0.19 |
| n | [-] | 0.87 | 0.71 | 0.63 | 0.72 |
| k | [GPa] | 11.2 | 7.0 | 5.0 | 18.0 |
| k/E^* | [-] | 0.357 | 0.289 | 0.239 | 0.257 |
| k/Y | [-] | 2.87 | 2.60 | 2.75 | 3.27 |

parameters, the elasto-plastic deformation is more easily generated with developing the graphitic structure and decreasing bulk density of GCs.

The value of k , which is the stress at strain $a/R = 1$, corresponds to hardness for spherical tipped indenter, although the extrapolation of the power law fitting to such strains will invariably introduce errors into the present estimation of the hardness.

Sakai has proposed that the ratio of hardness to elastic modulus E^* , that is, the “elasticity index” as a material parameter.^{22–24} The elasticity index k/E^* for each the GC samples is also listed in Table 2. It is found that the GCs heat-treated at the higher temperature showed the lower elasticity index k/E^* . Thus, elasticity of GC decreases with the elevating HTT of GC.

It is assumed that the value of the ratio of hardness to yield stress, k/Y , is a measure of plasticity. For GCs, the value of k/Y is nearly equal to 3, being independent of HTT. In comparison with fused silica glass, since GC shows slightly smaller value of k/Y , the fused silica glass has a relatively high plasticity. On the other hand, the elasticity index k/E^* of the fused silica glass is smaller than those of GC1000 and GC2000 and larger than that of GC3000

4. CONCLUSION

As shown in the present work, elastic and elasto-plastic deformations derived by spherical tipped indentation on glassy carbons depended strongly on their crystal structure. The elastic modulus and the yield stress of glassy carbons decreased with the elevation of HTT of glassy carbons.

The power law fitting constant k for the elasto-plastic deformation of the loading stress-strain curves by the indentation and the indentation elasticity index k/E^* decreased with development of the graphitic structure of glassy carbon.

In the present work, a variation of “elasticity” and “plasticity” of glassy carbons with the development of the graphitic structure could be readily compared by the parameter, indentation elasticity index k/E^* .

REFERENCES

1. Kobayashi, K., Sugawara, S., Toyoda, S. and Honda, H., *Carbon*, **6**, 359–363 (1968).
2. Fitzer, E., Schaefer, W. and Yamada, S., *Carbon*, **7**, 643–648 (1969).
3. Noda, T., Inagaki, M. and Yamada, Y., *J. Non-Cryst. Solids*, **1**, 285–302 (1969).
4. Yoshida, A., Kaburagi, Y. and Hishiyama, Y., *Carbon*, **29**(8), 1107–1111 (1991).
5. Minnear, W.P., Hollenbeck, T. M., Bradt, R. C. and Walker, Jr. O. L., *J. Non-Cryst. Solids*, **21**, 107–115 (1976).
6. Zhao, J. X., Bradt, R. C. and Walker, Jr. P. L., *Carbon*, **24**(1), 15–18 (1985).
7. Mehrota, B. N., Bragg, R. H. and Rao, A. S., *J. Mater. Sci.*, **18**, 2671–2671 (1983).
8. Bose, S. and Bragg, R. H., *Carbon*, **19**(4): 289–295 (1981).
9. Suzuki, Y., *Tanso*, No. 190, 293–299 (1999). (Japanese)
10. Sakai, M., Hanyu, H. and Inagaki, M., *J. Am. Ceram. Soc.*, **78**(4): 1006–1012 (1995).
11. Field, J. S. and Swain, M. V., *J. Mater. Res.*, **8**, 297–306 (1993).
12. Swain, MV, *Key Eng. Mater.*, **166**, 41–46 (1999).
13. Field, J. S. and Swain, M. V., *Carbon*, **34**(11), 1357–1366 (1996).
14. Iwashita, N., Swain, MV, Field, JS, Ohta, N and Bitoh, S, *Carbon*, **39**(10), 1525–1532 (2001).
15. Iwashita, N, Field, JS and Swain, MV, *Philosophical Magazine Part A*, **82**(10), 1873–1881 (2002).
16. Iwashita, N and Swain, MV, *Molecular Crystals and Liquid Crystals*, **386**, 39–44 (2002).
17. Iwashita, N and Swain, MV, *Philosophical Magazine Part A*, **82**(10), 2199–2205 (2002).
18. Park, S. M, Yasuda, E, Akatsu, T, Tanabe Y, Kakihana, M and Ozawa, K, *Carbon*, **33**(10), 1377–1381 (1995).
19. Inagaki M, *Tanso*, No.36, 9–13 (1963). (Japanese)
20. Johnson, KL, “*Indentation Contact Mechanics*” Cambridge: Cambridge University Press, **1985**.
21. Tabor, D, “*Hardness of Metals*” Oxford: Clarendon Press, **1951**.
22. Sakai, M, *Acta Metall. Mater.*, **41**(6), 1751–1758 (1993).
23. Sakai, M, Shimizu, S and Ishikawa, T, *J. Mater. Res.*, **14**(2), 1471–1484 (1999).
24. Sakai, M, *J. Mater. Res.*, **14**(9), 3630–3639 (1999).

SCRATCH TEST FOR EVALUATION OF SURFACE DAMAGE IN GLASS

Satoshi Yoshida,* Takashi Hayashi,* Tetsuro Fukuhara,*
Kazuki Soeda,* Jun Matsuoka,* and Naohiro Soga**

1. INTRODUCTION

Scratch behavior in glass is very important to understand the interaction between the abrasive particles and the glass product during grinding. In addition, the chipping problem in glass often appears during the glass manufacturing process. A thin sheet glass, such as an LCD(Liquid Crystal Display) or PDP(Plasma Display Panel) glass, is susceptible to scratches, abrasions, rubbing, and chipping, which are mechanical failures caused by a dynamical contact between the glass and a foreign body. In order to suppress these contact problems and to develop a glass with high wearability, it is essential to understand the mechanical response to a scratch as the cumulative actions of a hard material. It is considered that a scratch test is one of the fundamental testing methods to evaluate these mechanical properties. However, only a few papers have been published on scratch behaviors in glass.¹⁻³ Especially, the origin of scratch groove formation has little been understood. The formation of scratch groove is probably related to microscopic fracture, plastic deformation, and material removal. The scratch test surely gives us some important information on the damageability of glasses with various compositions under various conditions.

It is well known that fracture properties in glass are affected by environment. Stress corrosion cracking is believed to be the result from a stress-enhanced chemical reaction between a chemical environment, usually water, and the Si-O-Si bonds.⁴

* Department of Materials Science, The University of Shiga Prefecture, Hikone, Shiga 522-8533, Japan

** National Institute of Advanced Industrial Science and Technology, Chiyoda-Ku, Tokyo 100-8921, Japan

In addition, Westwood and Huntington⁵ reported that both drilling rate and pendulum hardness depended on the number of carbon atoms in n-alcohols and n-alkanes, because these processes included fracture behaviors. Therefore, scratch behaviors of glass also depend on these environments.

In this study, surface damage in glass is evaluated by using a scratch testing equipment. The purpose of this study is twofold; (1) to evaluate the differences between scratch hardness and conventional hardness, and (2) to evaluate the compositional variation of the crack initiation load determined through a dynamic-loading scratch test. It is considered that the crack initiation shows a fracture criterion at the transition point from apparent plastic deformation to macroscopic fracture. The crack initiation load will give some useful information on brittleness of glass.

2. EXPERIMENTAL PROCEDURES

A scratch hardness tester was assembled from two load cells, two moving stages, and a Knoop indenter. A schematic of this measuring system is shown in Fig. 1. In this study, a Knoop indenter was used as a scratching element. Normal load on the specimen was detected with a load cell, which was contact with the indenter and driven by a stepping motor capable of pulling and pushing at a constant speed. Normal load was controlled by changing the position of the indenter. Horizontal load was measured by another load cell connected with another moving stage. The stage was moved in the direction of the long diagonal of Knoop indenter. In this study, the constant speed of the stage, 0.05 mm/s or 0.07 mm/s, was adopted for the scratch test. It has been reported that scratch hardness depends on the scratching speed, especially at the speed of >0.1 mm/s,¹ so the scratch speed was fixed at the above value. Scratch hardness is defined as the load per unit load-bearing area (Fig. 2)⁶ and calculated from the normal load and the groove width using the following equation,

$$H_S = F_N/A = 0.5622 (F_N/w^2), \quad (1)$$

where F_N is the normal load, A the vertical projection of contact area, and w the groove width. The constant in the right side can be determined from the geometry of indenter. In the case of Knoop indenter, the angle between the opposite edges is 172.5° and the other angle between the other two is 130° . By using the groove width, w , the load-bearing area, A , becomes $1.779 w^2$.

On the other hand, Jacobsson *et al.*⁶ also defined the plowing stress, H_P , which is the mean pressure opposing the sliding of the element due to the plowing process only.

$$H_P = F_P/A_P = 1.124 (F_P/w^2), \quad (2)$$

where F_P is the horizontal load and A_P the area of resultant groove cross-section. In this study, however, because of a large scatter of F_P data and its less dependence of composition, only H_S will be employed for discussions on the compositional variation of scratch hardness.

For the determination of scratch hardness of soda-lime glass(Matsunami 0050), a normal load and a scratch speed were fixed at 0.98 N and 0.05 mm/s, respectively. Water and some n-alcohols(1-pentanol, 1-hexanol, 1-heptanol, 1-octanol, 1-nonanol, 1-decanol, and 1-undecanol) were employed as environment. These liquids except for

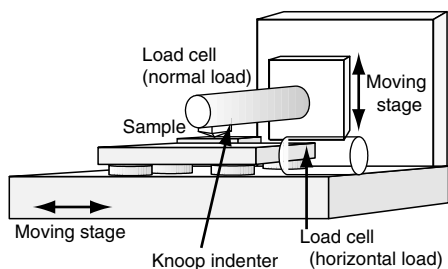


Figure 1. Schematic of a scratch tester.

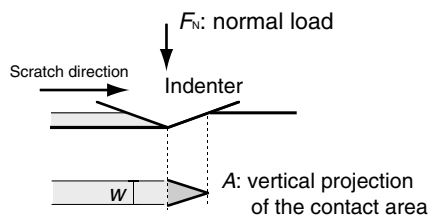


Figure 2. Schematic of a scratch groove.

water were dehydrated with a molecular sieve for at least one week. All the liquids were dropped on the sample surface just before the scratch test. Scratch hardness in each environment was determined from at least 10 runs. For a comparison, Knoop hardness was also measured at the indentation load of 0.49, 0.98, 2.0, and 2.9N in the same liquids.

In the case of the measurements of crack initiation load for silica(Asahi AQ) glass, Pyrex-type glass(Tempax) and soda-lime glass, a normal load was changing at a rate of 0.03N/s. A scratch speed was fixed at 0.07mm/s. The crack initiation was evaluated in water and n-heptane, which was also dehydrated. The width of scratch groove and the existence of crack at the edge of groove were observed by using an optical microscope after the scratch test. In some cases, the crack geometry was observed by using a scanning electron microscope(SEM; Hitachi S-3200N). The crack initiation load was determined from the position of an initial crack at the edge of groove, the scratch speed, and the rate at which the normal load increased. At least 30 specimens were used for the determination of crack initiation load.

3. RESULTS

3.1. Scratch Hardness

Figure 3 shows scratch hardness of soda-lime glass in water and in n-alcohols. Scratch hardness increases with an increase in the number of carbon atoms in each alcohol molecule, but shows a maximum at 1-decanol. Scratch hardness obtained in 1-decanol is 28% larger than that in 1-pentanol. Scratch hardness obtained in water is comparable with that in 1-pentanol.

As a comparison, Knoop hardness in each environment was measured. The result is shown in Fig. 4. A load dependence of Knoop hardness can be observed for all the environments. This load dependence of hardness was also reported by Hirao and Tomozawa,⁷ and will be discussed later. Knoop hardness at a given indentation load increases by 8% with an increase in the length of alcohol chain. In addition, it is found that Knoop hardness(4.3~5.0GPa) is over two times smaller than scratch hardness (10~15GPa).

3.2. Crack Initiation Load

The crack initiation test was performed for silica, Tempax, and soda-lime glasses in water and in dehydrated heptane by using the scratch tester. Figure 5 shows an

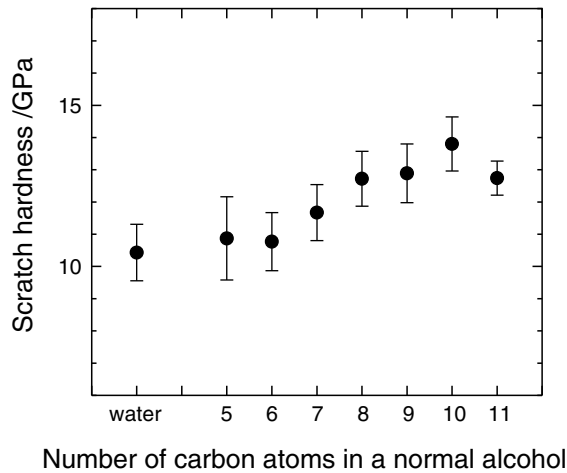


Figure 3. Scratch hardness of soda-lime glass in water and n-alcohols. Error bars indicate ± 1 standard deviations.

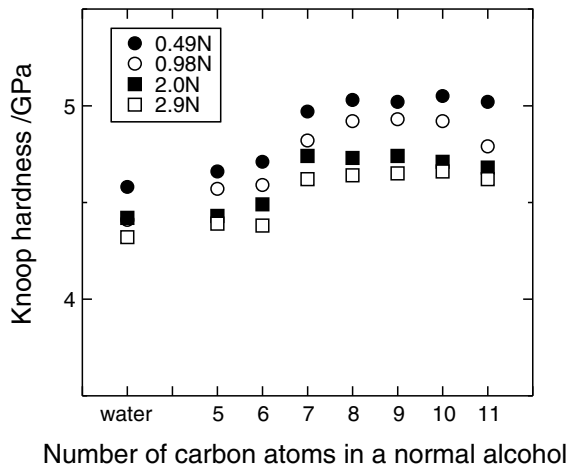


Figure 4. Knoop hardness of soda-lime glass in water and n-alcohols. The indentation loads are 0.49, 0.98, 2.0, and 2.9 N.

example of a relationship between a scratch position and a normal load for soda-lime glass in heptane. Four points labeled A, B, C, and D correspond to the scratch areas noted by the same letters in Fig. 6. The crack initiation can be observed in Fig. 6(B). As for silica glass, a position-load curve obtained in heptane and photos of a scratch groove are shown in Fig. 7 and Fig. 8, respectively. The crack initiation load for silica glass is much smaller than that for soda-lime glass. The lower crack initiation load for silica glass is also observed in water. The crack initiation loads for each glass can be fitted well by a Weibull function. Weibull plots for the data obtained in heptane are shown in Fig. 9. The averaged values of crack initiation loads and Weibull moduli for all the glasses in heptane and in water are listed in Table 1. It is considered that Weibull modulus describes the width of distribution in crack initiation load, and that it is much affected by surface condition. In order to discuss the compositional variation of

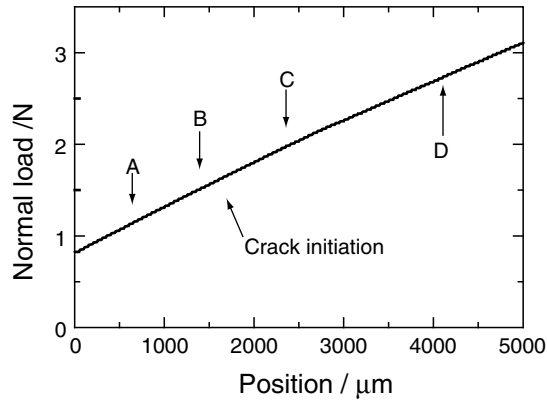


Figure 5. Relationship between normal load and position for soda-lime glass in heptane.

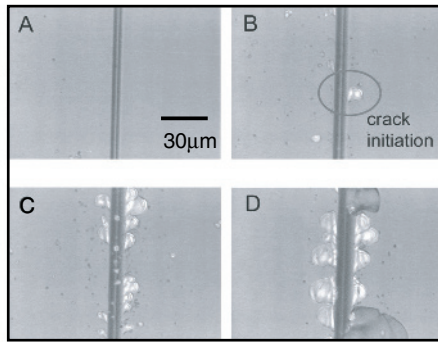


Figure 6. Photos of a scratch groove after the crack initiation test for soda-lime glass in heptane. Scratch direction is from bottom to top in these photos.

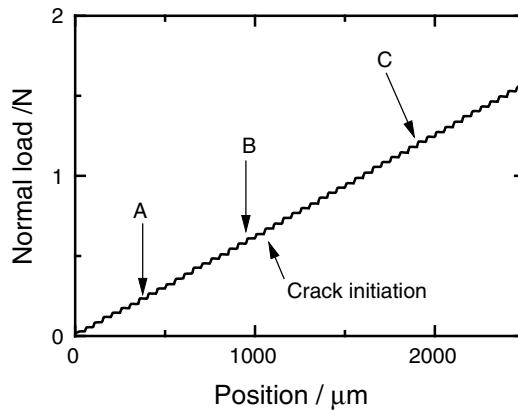


Figure 7. Relationship between normal load and position for silica glass in heptane.

Weibull modulus, some information on the relationship between the detailed finishing grade of glass surface and Weibull modulus will be needed. It is noteworthy that Tempax has the highest crack initiation load in water, but not in heptane.

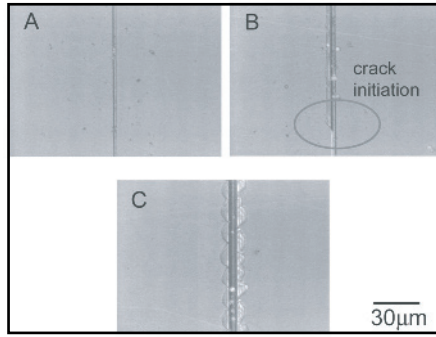


Figure 8. Photos of a scratch groove after the crack initiation test for silica glass in heptane. Scratch direction is from bottom to top in these photos.

4. DISCUSSION

4.1. Scratch Hardness

The load-dependence of Knoop hardness in Fig. 4 is probably caused by a change in surface energy of the glass in each environment. It has been reported that this load dependence of hardness is attributed to the contribution of surface energy to the indentation deformation.⁷ Following the works by Bernhardt⁸ and Fröhlich *et al.*,⁹ Hirao and Tomozawa⁷ separated the indentation deformation into two energy contributions, which were the surface energy contribution and the volume energy contribution. They suggested that Knoop indentation load, L , can be expressed by the following equation,

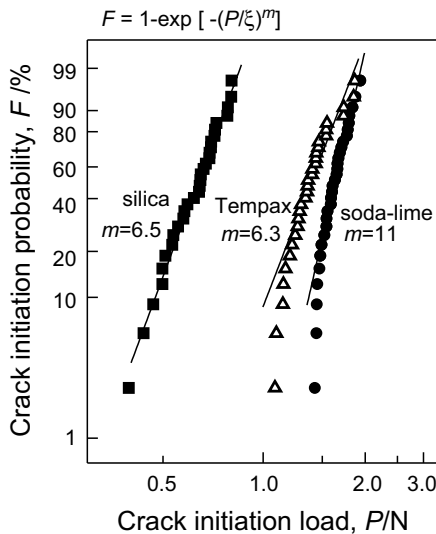


Figure 9. Weibull plots of the crack initiation loads obtained in heptane.

Table 1. Averaged crack initiation loads and Weibull moduli for the glasses.

| Glass | | Crack initiation load /N | Weibull modulus, m^a |
|-----------|------------|--------------------------|------------------------|
| Silica | in heptane | 0.63 | 6.5 |
| | in water | 0.35 | 3.8 |
| Tempax | in heptane | 1.39 | 6.3 |
| | in water | 0.99 | 7.0 |
| Soda-lime | in heptane | 1.63 | 11 |
| | in water | 0.56 | 5.6 |

^a $F = 1 - \exp[-(P/\xi)^m]$

$$L = a_1 l + a_2 l^2, \quad (3)$$

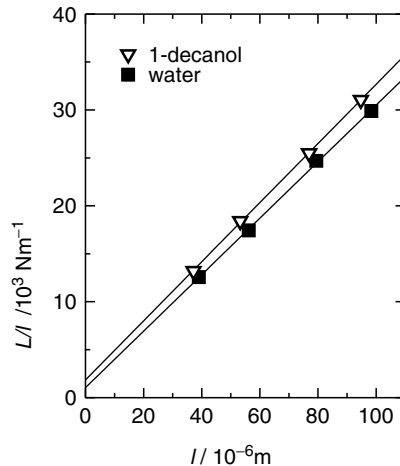
where a_1 and a_2 are fitting parameters, and l is Knoop diagonal length. Because $\int Ldl$ may be related to the total energy of indentation deformation, $a_1(l^2/2)$ is related to the energy to create new surface, and $a_2(l^3/3)$ to the energy for volume deformation. Hence, a_2 corresponds to the load-independent hardness, and a_1 the parameter related to the surface energy. On the other hand, from the values of L and l , Knoop hardness, HK , is defined as the following equation,¹⁰

$$HK = 14.23L/l^2. \quad (4)$$

From Eqs. (3) and (4), if the surface energy term can be negligible, Knoop hardness is independent of the indentation load. Figure 10 shows some examples of the relationship between L/l and l . From Eq. (3), the following expression can be obtained, and a_1 corresponds to the y-intercept, and a_2 to the slope of the line in Fig. 10.

$$L/l = a_1 + a_2 l \quad (5)$$

Figure 11 shows the fitting parameters, a_1 and a_2 , in all the environments. A more distinct increase in a_1 can be observed in this figure as compared with that in a_2 .

**Figure 10.** Relationship between L/l and l for soda-lime glass in water and in 1-decanol.

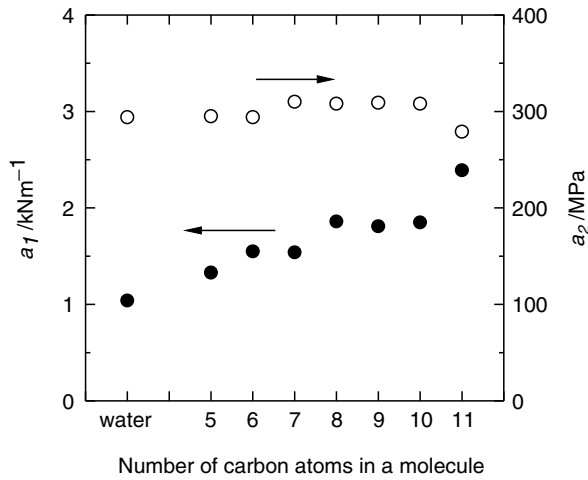


Figure 11. Fitting parameters, a_1 and a_2 in Eq. (5) obtained in water and in n-alcohols.

It implies that the variation in chain-length of n-alcohol affects the surface state between glass and liquid rather than hardness as a bulk property. The surface energy is probably related to the polarity in n-alcohols because the surface charge of soda-lime glass is in general negative. The larger the polarity in n-alcohol is, the less the surface energy of glass in the liquid. Reported dielectric constants of n-alcohols employed are listed in Table 2.

On the other hand, fracture toughness, K_{Ic} , is defined as the following equation,

$$K_{Ic} = (2\Gamma E)^{1/2}, \quad (6)$$

for the plane-stress condition. In this equation, Γ is the fracture surface energy, and E is Young's modulus. Although the surface energy is not coincident with the fracture surface energy, the former covers a large part of the latter for ideal brittle materials. Therefore, the surface energy must affect the fracture-related properties, such as scratch hardness. It can be said that the scratch hardness is closely linked to the surface-creating process, such as micro-cracking, chipping and so on. These energy release processes surely reduce the energy for groove formation. This is the reason

Table 2. Dielectric constants of water and n-alcohols.

| Solvent | Dielectric constant |
|-------------|--------------------------|
| Water | 78.54(25°C) ^a |
| 1-pentanol | 15.13(25°C) ^b |
| 1-hexanol | 13.03(20°C) ^b |
| 1-heptanol | 11.75(20°C) ^b |
| 1-octanol | 10.30(20°C) ^b |
| 1-nonanol | - |
| 1-decanol | 8.1(20°C) ^a |
| 1-undecanol | - |

^a Ref. [11]

^b Ref. [12]

why scratch hardness is much larger than Knoop hardness. The larger variation of scratch hardness originates from a larger contribution of the surface-creating process.

In Fig. 4, a longest-chain alcohol(1-undecanol) causes a decrease in scratch hardness. Although the origin has been unclear, Westwood and Huntington⁵ proposed one reasonable explanation that the hardness of glass can be markedly influenced by the ζ -potential, which is likely to be similar to the surface charge of glass. When ζ is negative, which is true in water and in the lower n-alcohols,¹³ this situation must bring positive charge carriers, e.g. Na^+ ions, into the near-surface region for charge-counter balancing. This locally increased Na^+ ions reduce hardness in this region. When ζ is positive, on the other hand, the migration of OH^- ions is responsible for softening of glass. Glass should be the hardest at its zero point of surface charge. There is no evidence that the sign of ζ -potential is reversed by changing the chain-length of n-alcohol. However, this surface compositional change would be one possible origin of decrease in scratch hardness.

4.2. Crack Initiation Load

The cracks observed around the groove were mainly surface chips or radial(chevron) cracks. There was no median crack beneath the groove. Figure 12 shows the cross section of the scratch groove in soda-lime glass. For the other glasses, no median crack can be also observed in the cross sections.

Water environment promotes crack initiation in silica, Tempax, and soda-lime glasses (Table 1). This is because the crack initiation process is assisted by the adsorption of water molecule. In the conceptual framework of this idea,¹⁴ a water molecule is adsorbed at the strained bonds formed by a scratch process. After that, the attacked Si-O-Si bond and the water molecule break one Si-O bond to leave new two Si-OH bonds. West and Hench¹⁵ reported that the energy barrier of hydrolysis of strained 3-fold rings is 97% smaller than that of fracture by water-free dilation. This water-assisted bond-breakage process is the origin of lower crack initiation load obtained in water.

The crack initiation load of silica glass is much lower than those of Tempax and soda-lime glasses (Table 1). This lower crack initiation load cannot be explained in terms of conventional mechanical properties, e.g. Young's modulus and fracture toughness. Table 3 shows some mechanical properties of silica, Tempax, and soda-lime glasses. Here, Young's modulus and Vickers hardness are the catalogue values,

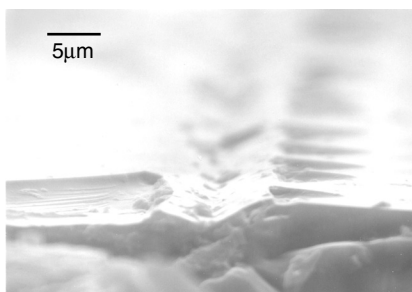


Figure 12. SEM micrograph of a scratch groove of soda-lime glass in air. Normal load = 2.94N.

Table 3. Some mechanical properties of the glasses.

| Glass | Crack initiation load (in heptane)/N | Brittleness / μm^{-1} | Young's modulus ^a / GPa | Vickers hardness ^a / GPa | Fracture toughness ^b / $\text{MPam}^{1/2}$ |
|-----------|--------------------------------------|----------------------------------|------------------------------------|-------------------------------------|---|
| Silica | 0.63 | 10.0 | 74.2 | 7.9 | 0.79 |
| Tempax | 1.39 | 8.5 | 63.0 | 5.5 | 0.65 ^c |
| Soda-lime | 1.63 | 7.1 | 71.5 | 5.4 | 0.76 |

^a Catalogue value.

^b Ref. [16]

^c Ref. [17]

and fracture toughness the reported values. The lower crack initiation load is related not to the weaker bond-strength(Young's modulus), but to the resistance to deformation(hardness). One part of the work done by an external force is used to deform plastically. The rest part may be converted into a residual stress around the groove or into a crack. This means that the decreased ability to deform leads to easy crack initiation. Even if the averaged bond-strength of silica glass is comparable with that of soda-lime glass, less deformability in silica glass causes the crack initiation load to be lowered.

It is considered that the crack initiation load is a measure of brittleness (HV / K_{Ic}) of glass. In Table 3, brittleness of each glass is calculated from HV and K_{Ic} . The higher brittleness of glass causes the lower crack initiation load. This relationship was also reported by Le Hou  rou *et al.*³ It has been still unclear that Tempax shows the maximum crack initiation load in water, but it is suggested that B_2O_3 as a network former plays an important role for deformation. Further experimental investigations will be needed.

Sehgal and Ito¹⁸ have shown that the brittleness of glass can be determined from the Vickers indentation load, the Vickers diagonal length, and the median/radial crack length. However, their technique cannot be applied to the complicated crack patterns by indentation, such as a cone crack in silica glass. It is concluded that the crack initiation test by using a scratch tester is the simple and useful technique for evaluating brittleness of various glasses.

5. CONCLUSIONS

The effect of environment on scratch hardness has been investigated for soda-lime glass. Scratch hardness was much influenced by the chain-length of n-alcohol. The variation of scratch hardness with the chain-length of n-alcohol was more conspicuous than that of Knoop hardness. This result comes from the variation of surface energy of glass in the liquids. From the measurement of load-dependent Knoop hardness in various n-alcohols, it was found that the chain-length in n-alcohol affected the parameter related to the surface energy rather than to the intrinsic hardness. Because the surface energy is directly related to the fracture behavior, scratch hardness including fracture process surely depends on environment.

The crack initiation at the groove-edge can be clearly observed for silica, Tempax, and soda-lime glasses by using a scratch testing machine. The crack

initiation load obtained in water was much lower than that in heptane because of the water-assisted bond-rupture. The crack initiation load for silica glass was lower than those for Tempax and soda-lime glasses. This is attributed to less deformability in silica glass. It is elucidated that the crack initiation load through the dynamic scratch test is a measure of brittleness of glass.

REFERENCES

1. K. Li, Y. Shapiro, and J.C.M. Li, Scratch test of soda-lime glass, *Acta Mater.* **46**(15), 5569–5578(1998).
2. S. Yoshida, H. Tanaka, T. Hayashi, J. Matsuoka, and N. Soga, Scratch resistance of sodium borosilicate glass, *J. Ceram. Soc. Japan* **109**(6), 511–515(2001).
3. V. Le Houérou, J.-C. Sangleboeuf, S. Dériano, T. Rouxel, and G. Duisit, Surface damage of soda-lime glasses: indentation scratch behavior, *J. Non-Cryst. Solids* **316**, 54–63(2003).
4. S.M. Wiederhorn, S.W. Freiman, E.R. Fuller Jr., and C.J. Simmons, Effect of water and other dielectrics on crack growth, *J. Mat. Sci.* **17**, 3460–3478(1982).
5. A.R.C. Westwood and R.D. Huntington, Adsorption-sensitive flow and fracture behavior of soda-lime glass, *Proc. Intl. Conf. Mechanical Behavior of Materials IV*, Society of Materials Science, Kyoto, Japan, 383–393(1972).
6. S. Jacobsson, M. Olsson, P. Hedenqvist, and O. Vingsbo, Scratch testing, *ASM Handbook* **18**, 430–437(1992).
7. K. Hirao and M. Tomozawa, Microhardness of SiO₂ glass in various environments, *J. Am. Ceram. Soc.* **70**(7), 497–502(1987).
8. E.O. Bernhardt, On microhardness of solids at the limit of Kick's similarity law(in German), *Z. Metallkd.* **33**(3), 135–144(1941).
9. F. Frohlich, P. Grau, and W. Grellmann, Performance and analysis of recording microhardness tests, *Phys. Status Solidi* **42**, 79–89(1977).
10. Japanese Industrial Standards, Z 2251(1998).
11. *Kagaku Binran, Kiso-Hen II* (in Japanese), p.1166, Ed. by the Chemical Society of Japan (Maruzen, Tokyo, 1975).
12. D.R. Lide, *Handbook of organic Solvents*, p.254, 265, 370, 380 (CRC Press, Boca Raton, Florida, 1995).
13. M. DeSmet and J. Delfosse, *Colloid Science*, p.230, Ed. by H.R. Kruyt (Elsevier, New York, 1952).
14. T.A. Michalske and S.W. Freiman, A molecular interpretation of stress corrosion in silica, *Nature* **295**, 511–512(1982).
15. J.K. West and L.L. Hench, Silica fracture Part II A ring opening model via hydrolysis, *J. Mat. Sci.* **29**, 5808–5816(1994).
16. S.M. Wiederhorn, Fracture surface energy of glass, *J. Am. Ceram. Soc.* **52**(2), 99–105(1969).
17. J. Sehgal and S. Ito, Brittleness of glass, *J. Non-Cryst. Solids* **253**, 126–132(1999).
18. J. Sehgal, Y. Nakao, H. Takahashi, and S. Ito, Brittleness of glasses by indentation, *J. Mat. Sci. Lett.* **14**, 167–169(1995).

SHEAR DRIVEN DAMAGE AND INTERNAL FRICTION IN INDENTATION LOADING OF A GLASS-CERAMIC

Anthony C. Fischer-Cripps *

1. INTRODUCTION

Indentation damage is a particularly important limitation in the use of brittle materials in structural applications. Some nominally brittle materials have been shown to exhibit plastic type yield in indentation testing.¹⁻¹⁰ These materials are characterized by a relatively coarse grain structure and weak grain boundaries. A particularly convenient material for study is a mica-containing glass-ceramic. As shown in Fig. 1, the microstructure consists of circular mica platelets in a glassy matrix. The size of the platelets can be modified by simple heat treatment during processing. The average platelet diameter and the aspect ratio increase with increasing crystallization temperature. During indentation with a spherical indenter, a sub-surface region of accumulated damage is observed to form in preference to the characteristic Hertzian cone crack normally associated with this type of loading. An indentation stress-strain response shows a shape similar to that obtained on ductile materials.

Previous work indicates that^{11,12} the indentation response of mica glass-ceramic materials is a function of the macroscopic uniaxial compressive yield stress, Y and a strain-hardening characteristic. A range of behavior, from quasi-ductile to nominally brittle, could be attained by simply varying the size and shape of the grains through

* Anthony C. Fischer-Cripps, CSIRO Division of Telecommunications and Industrial Physics, Bradfield Rd, West Lindfield, NSW 2070 Australia.

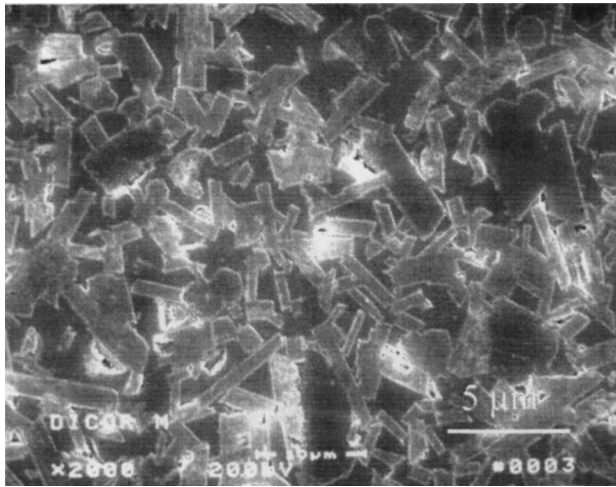


Figure 1. Electron micrograph of microstructure of mica glass-ceramic. Specimen was polished to 1 μm finish and etched in HF for 10 s. Most of the platelets are viewed edge on. The occasional plan view of a platelet can be seen.

heat treatment. Details of the microstructural properties for the glass-ceramic materials studied here are given in Table 1.

The dependence of the yield stress was subsequently found to be consistent with a Mode II fracture mechanism within the microstructure that depended upon the absolute value of the grain size (i.e. platelet diameter). The apparent strain hardening arises from an elastic constraint on the deformation of grains imposed by the glassy matrix and depends on the platelet aspect ratio.¹³ Further study showed that the magnitude of the yield stress was consistent with a mechanism of friction on a microstructural scale quite different to that of the familiar Amonton's law.¹⁴ The present work brings the previously reported work together into a cohesive account of the nature of internal friction on the microstructural scale and its relevance to the macroscopic behaviour of these types of materials. An understanding of these issues assists in the design, at a microstructural level, of these nominally brittle materials to suit the requirements of a particular application.

Table 1. Microstructural parameters for mica glass-ceramic materials. For all materials, the volume fraction is $V_f \approx 70\%$, the elastic modulus $E \approx 70$ GPa and Poisson's ratio $\nu \approx 0.26$. Platelet dimensions measured from sectioned and etched samples. Yield stress was determined according to a procedure given in reference 12.

| Micro-structure | 4 hr heat treatment temp. (°C) | Maximum platelet diameter (μm) | Platelet thickness (μm) | Yield stress Y (MPa) |
|-----------------|--------------------------------|--------------------------------|-------------------------|----------------------|
| Fine | 1000 | 1.2 | 0.40 | 2160 |
| Medium | 1060 | 3.7 | 0.80 | 1230 |
| Coarse | 1120 | 10 | 1.2 | 750 |

2. MACROSCOPIC BEHAVIOUR

For the glass-ceramic materials considered here, the plastic zone resulting from indentation with a spherical indenter is contained within an area bounded by the circle of contact and can be best described in terms of an elastic constraint.¹¹ Fig. 2 shows the results from a bonded-interface specimen for a glass-ceramic specimen loaded with a spherical indenter. The top part of Fig. 2 shows the residual impression in the surface and the bottom part is a section view showing the sub-surface accumulated damage. A quantitative measure of plasticity is given by an indentation stress-strain response as shown in Fig. 3 where it can be seen that the amount of deviation of the expected linearly elastic behaviour depends upon the microstructure of the material, the greater the grain size, the more pronounced the deviation from linear elasticity. The size and shape of the damage zone and the shape of the indentation stress-strain response is similar to that observed in ductile materials under this type of loading.

Elastic-plastic behavior in these nominally brittle ceramics occurs as a result of the relatively large hydrostatic component of stress in the indentation stress field and is routinely observed by researchers in the rock-mechanics field. Sub-surface damage occurs as a result of shear faulting along planes of weakness within the material beneath the indenter. In the present case, cleavage planes within the mica appear to be sources of weakness that lead to shear-driven damage. Finite element work¹² has demonstrated that there is a close connection between the macroscopic yield stress of these materials and the absolute platelet size. A mismatch in elastic properties within the microstructure leads to stress singularities resulting in yield stress which has an inverse square root dependence on the grain size in the manner of a Mode II crack. Evidently, the macroscopic response of the material depends on shear-driven failure events on a microstructural scale, which in turn, are intimately connected with the nature of friction at this scale of contact.

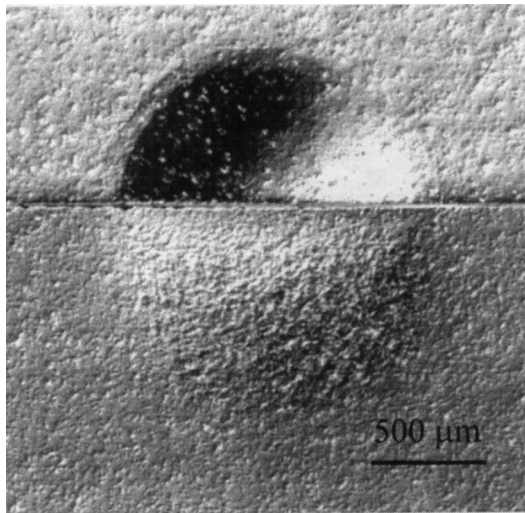


Figure 2. Optical micrograph of indented bonded-interface mica-containing glass-ceramic specimen showing half-surface (top) and section (bottom) views. Indentations performed with WC sphere of radius $R = 3.18 \text{ mm}$ at indenter load $P = 2000 \text{ N}$.

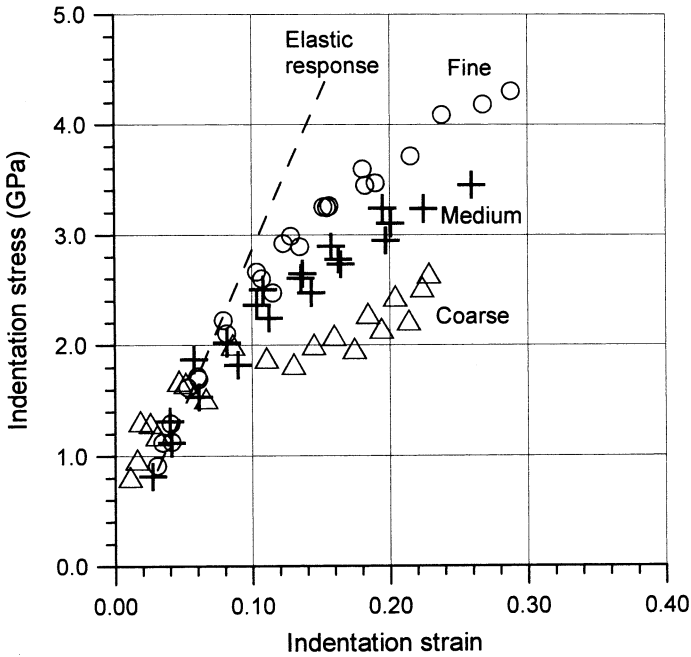


Figure 3. Indentation stress-strain relationships for glass-ceramic. Dashed line shows the expected Hertzian elastic response. Experimental results are shown for the coarse ($10\ \mu\text{m}$ grain size), medium ($5\ \mu\text{m}$) and fine ($2\ \mu\text{m}$) microstructures. The larger the grains, the more deviation from the elastic response.

3. INTERNAL FRICTION AND YIELD

Amontón's law has been shown to be a result of the random roughness of real surfaces and arises as a result of the increasing area of contact between asperities on both surfaces as they are brought into contact as the normal force is increased. It is usually expressed in terms of the friction coefficient μ such that:

$$F = \mu N \quad (1)$$

where N is the applied normal load and F is the sideways force required to initiate tangential sliding between the two bodies. Contact thus only takes place at asperities on each surface and friction forces arise from elastic deformation, shearing, welding, ploughing, or plastic deformation of the asperities as they move past one another. If we divide the terms in Eq. 1 by the real area of contact A , we find that the frictional shear stress τ is in direct proportion to the normal stress σ_N :

$$\tau = \frac{F}{A} = \frac{\mu N}{A} = \mu \sigma_N \quad (2)$$

Jaeger and Cook¹⁵ show that slip along a plane of weakness within a material under compressive loading with confined pressure may occur when the Coulomb criterion is satisfied:

$$|\tau| = S_o + \mu \sigma_N \quad (3)$$

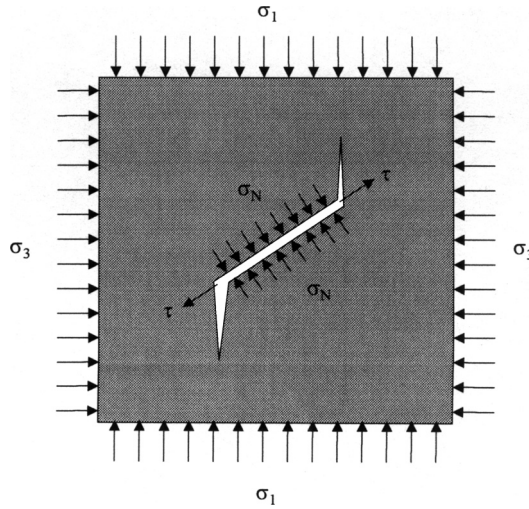


Figure 4. Schematic of a sliding shear fault under hydrostatic stress.

In Eq. 3, τ is the applied shear stress, S_o is the inherent shear strength of the material, and σ_N is the normal stress on the plane under consideration as shown in Fig. 4. Eq. 3 is equivalent to Eq. 2 at $S_o = 0$.

In terms of the principal stresses σ_1 and σ_3 , where σ_3 is the confining pressure and σ_1 is the applied normal stress, the Coulomb criterion becomes:

$$\sigma_1 \left[(\mu^2 + 1)^{1/2} - \mu \right] - \sigma_3 \left[(\mu^2 + 1)^{1/2} + \mu \right] = 2S_o \quad (4)$$

The macroscopic Tresca failure criterion ($\tau = Y/2$) is thus a special case of the Coulomb criterion with $\mu = 0$ and $S_o = Y/2$ where the angle at which sliding occurs is 45° .

Finite element analysis shows that¹² for the glass-ceramic materials considered here, differences in the microstructure can be accommodated by a change in the macroscopic yield stress Y for each material in conjunction with the Tresca criterions implying that the internal friction coefficient μ plays a negligible role in these materials. Further support for this contention is that the strong, but short range Van der Waals forces at the grain boundary maintain the boundary intact under shear loading and that failure occurs within the atomically smooth cleavage planes of the mica platelets.^{16,17} As shown in Fig. 5, atomic force microscope examination of the damaged regions clearly shows fissures within the platelets.

It is thus claimed that any resistance to internal sliding depends upon the inherent shear strength of the mica platelets. This in turn depends upon the grain size, which then impacts on the macroscopic yield strength of the material.

4. DISCUSSION

The task now is to substantiate the conclusions made above given the following conclusions of previously reported work:

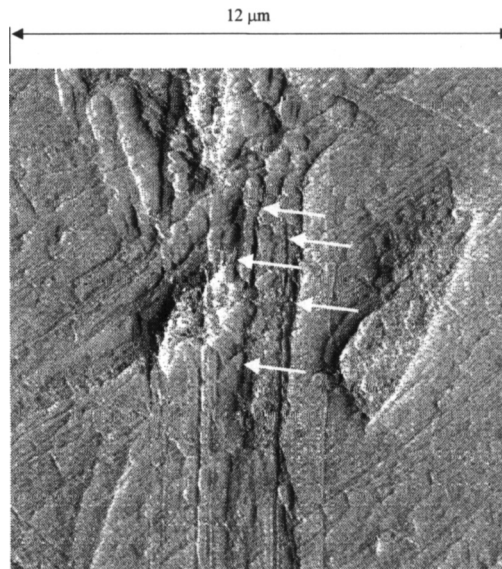


Figure 5. Atomic force microscope image of a cross-section of a mica platelet in the shear driven damage zone. Arrows show fissures in the platelet that are not visible in undamaged material.

1. Experiments on a macroscopic scale demonstrate the presence of internal yield within the microstructure, the degree of which depends upon the physical characteristics of the microstructure.
2. Finite element modelling on a macroscopic scale using the Tresca criterion matches the observed size and shape of the plastic zone and also the shape of the indentation stress-strain curves indicating that the physical characteristics of the microstructure determine its yield strength. The use of the Tresca criterion implies a zero coefficient of friction on the microstructural scale. The range of macroscopic yield stresses for the materials studied here is 750 MPa to 2000 MPa.
3. Finite element modelling on a microstructural scale indicates that internal yield has the appearance of a Mode II crack phenomenon (the shear strength of the microstructure depends on the inverse of the square root of the platelet diameter and is independent of the magnitude of the normal stress on the grain). There is a correlation between the macroscopic yield stress Y used in (2) above with the inverse square root of the grain size.
4. Atomic force microscope observations show that shear faulting occurs within the atomically smooth planes of the mica platelets and that friction is likely to occur under conditions in which the real and apparent area of contact coincide.

Can the observed behaviour on the macroscopic and microstructural scales be reconciled with what we know about frictional sliding under these conditions? To answer this question, we turn to other reported work with mica in which the real and apparent areas of contact coincide. Johnson¹⁸ reports that experiments with an atomic friction microscope (AFM), on mica in which the contact dimension is 2 to 10 nm, indicate a frictional shear stress of 1 GPa. Other measurements performed with a surface force apparatus (SFA), in which the contact dimension is in the order

of 20-80 μm , indicate a frictional shear stress to be approximately constant at 20 MPa. The discrepancy is explained by the mechanism of plastic deformation at the interface. According to Johnson, the physical mechanism of sliding friction is due to the nucleation and propagation of dislocation-like defects through the interface under the influence of the applied shear force. For small contacts ($< 20 \text{ nm}$), dislocation-like defects cannot be nucleated and atoms move relative to one another with a shear strength equal to the theoretical strength of the material. For large contacts, the rate of nucleation of dislocation-like continuities at the edge of the contact becomes equal to the rate at which they disappear at the centre and the frictional stress reaches a steady-state value. In the intermediate range, the shear stress required to nucleate dislocation-like defects at the leading edge of the contact depends upon the square root of the dimension of the contact.

The relevance to the present work is that the scale of “contacts” in the mica platelets studied here is in the order of 1 to 10 μm . This is the intermediate zone referred to by Johnson in which the frictional stress depends upon the inverse square root of the grain size in the manner of a Mode II crack. It has been previously shown that estimations of yield stress for a range of platelet sizes based on an inverse square root law yielded predictions of macroscopic behavior that agreed well with experimentally observed behavior and that the macroscopic yield stress was determined to be in the order of 1 GPa. A yield stress in the order of 1 GPa gives a value of S_0 in the order of 500 MPa, precisely within the intermediate zone described above. The nature of the observed Mode II behaviour on the microstructural scale is thus explained.

What is the nature of these defects that show such a scale effect? Johnson describes them as “dislocation-like” and shows that work involving conventional dislocation mechanics is consistent with observations of the size effects for frictional shear stress given above. The answer lies in molecular dynamics simulations of which are limited by the number of atoms that can be accommodated and as such, usually fall into the small contact regime. Simulations on a larger scale would evidently elucidate the actual mechanism of deformation on the molecular scale. However, from a material science perspective, the scale effects of frictional traction under controlled conditions matches well with those existing at a macroscopic level and thus offers a useful base from which macroscopic material properties may be designed from microstructural variables in some detail. For example, for the materials studied here, if the platelets were made very large ($> 50 \mu\text{m}$), one would expect the size dependence on yield to diminish and that, all other things being equal, the shape of the indentation stress-strain curves would perhaps begin to be independent on the grain size.

6. SUMMARY

The present work examines the role of internal friction in mica-containing glass-ceramic materials subjected to indentation loading. It is proposed that shear-driven damage beneath the specimen surface occurs via internal sliding along cleavage planes within the mica platelets near the mica-glass boundaries. The sliding surfaces in this case are considered to be atomically smooth such that the real and apparent areas of contact coincide. The frictional shear stress is thus independent of the

normal forces arising from thermal mismatch stresses and only depends on the work of adhesion of the interface and the scale of the contacts. The scale of contacts for these materials lies within an intermediate zone in which the frictional shear stress arises from the stress required to nucleate dislocation-like discontinuities within the material. This leads to a size effect similar to that experienced by a crack in Mode II loading and is in accordance with previous work in which a connection between such a size effect and the macroscopic response of the material was identified.

REFERENCES

1. B. R. Lawn, N. P. Padture, H. Cai, and F. Guiberteau, Making ceramics 'ductile', *Science*, 263, 1114–16 (1994).
2. F. Guiberteau, N. P. Padture, H. Cai, and B. R. Lawn, Indentation fatigue. A simple cyclic Hertzian test for measuring damage accumulation in polycrystalline ceramics, *Phil. Mag.* 68(5), 1003–16 (1993).
3. N. P. Padture, B. R. Lawn, Fatigue in ceramics with interconnecting weak interfaces: a study using cyclic Hertzian contacts, *Acta Metall.* 43, 1609–17 (1995).
4. N. P. Padture, In-situ toughened silicon carbide, *J. Am. Ceram. Soc.* 77(2), 519–23 (1994).
5. N. P. Padture and B. R. Lawn, Toughness properties of a silicon carbide with an in-situ-induced heterogeneous grain structure, *J. Am. Ceram. Soc.* 77(10), 2518–22 (1994).
6. H. H. K. Xu, L. Wei, N. P. Padture, B. R. Lawn and R. L. Yeckley, Effect of microstructural coarsening on Hertzian contact damage in silicon nitride, *J. Mat. Sci.* 30, 869–78 (1995).
7. F. Guiberteau, N. P. Padture, and B. R. Lawn, Effect of grain size on Hertzian contact damage in alumina, *J. Am. Ceram. Soc.* 77(7), 1825–31 (1994).
8. H. Cai, M. A. Stevens-Kalceff, B. R. Lawn, Deformation and fracture of mica-containing glass-ceramics in Hertzian contacts, *J. Mater. Res.* 9(3), 762–70 (1994).
9. H. Cai, M. A. Stevens Kalceff, B. M. Hooks, B. R. Lawn, and K. Chyung, Cyclic fatigue of a mica-containing glass-ceramic at Hertzian contacts, *J. Mater. Res.* 9(10), 2654–61 (1994).
10. D. G. Grossman, Machinable glass-ceramics based on tetrasilicic mica, *J. Am. Ceram. Soc.* 55, 446–49 (1972).
11. A. C. Fischer-Cripps, Elastic-plastic behaviour in materials loaded with a spherical indenter, *J. Mat. Sci.* 32, 727–36 (1997).
12. A. C. Fischer-Cripps, A partition-problem approach to microstructural modelling of a glass-ceramic, *J. Am. Ceram. Soc.* 82(7), 1835–43 (1999).
13. A. C. Fischer-Cripps and B. R. Lawn, Indentation stress-strain curves for "quasi-ductile" ceramics, *Acta Mater.* 44(2), 519–527 (1996).
14. A. C. Fischer-Cripps, Role of internal friction in indentation damage in a mica-containing glass-ceramic, *J. Am. Ceram. Soc.* 84(11), 2603–2606 (2001).
15. J. C. Jaeger and N. G. W. Cook, *Fundamentals of Rock Mechanics*, (Chapman and Hall, 1971).
16. Private communication, D. T. Smith, National Institute of Standards & Technology, 1995.
17. R. G. Horn and D. T. Smith, Contact Electrification and Adhesion Between Dissimilar Materials, *Science*, 256, 362–64 (1992).
18. K. L. Johnson, The contribution of micro/nano-tribology to the interpretation of dry friction, *Proc. Instn. Mech. Engrs*, 214 Part C, 11–22 (2000).

INDENTATION AND SCRATCHING OF GLASS: LOAD, COMPOSITION AND TEMPERATURE EFFECTS

Jean-Christophe Sanglebœuf and Tanguy Rouxel*

1. INTRODUCTION

The response of glass to mechanical contact has been the subject of numerous publications. However, most of the investigations were dedicated to standard window glasses, although there is a need for the characterization of functional glasses such as chalcogenide glasses and of newly developed structural glasses, including oxynitride and oxycarbide glasses. Besides, most investigators focused on the phenomenology and on the mechanics of contact damage and the incidences of the glass composition, the environment and the temperatures were little studied and thus remain poorly understood.

In this paper, we intend to show the importance of the glass composition through several examples. Silicon oxycarbide and magnesium-containing soda-lime-silica glasses provide interesting illustrations of the effect of the network polymerization degree and of the compactness on the indentation behavior. A series of soda-lime-silica glasses with different silica contents was studied to get insight into the role of moisture and a pronounced indentation-creep phenomenon was noticed in chalcogenide glasses from the Ge-Se system.

* Jean-Christophe Sanglebœuf, Tanguy Rouxel, Laboratoire de Recherche en Mécanique Appliquée de l'Université de Rennes 1, LARMAUR UPRES JE 2310, Université de Rennes 1, campus de Beaulieu, 35042 Rennes cedex, France.

2. EXPERIMENTAL TECHNIQUES

The glass density (d) was measured on powdered samples by the pycnometry method with an accuracy of $\pm 0.005 \text{ g cm}^{-3}$. Young's modulus (E) and Poisson's ratio (ν) were measured by the pulse-echo technique on 4 mm thick rectangular specimen. Vickers indentations (load of 9.8 N applied during 15 s), were performed to estimate both Meyer's hardness (H) and the "indentation" fracture toughness¹ (K_c) by means of the following equations:

$$H = P/2a^2 \quad (1)$$

and

$$K_c = 0.016(E/H)^{1/2}P/c^{3/2} \quad (2)$$

where P is the load, a is half the mean size of the two diagonals, E is Young's modulus, H is Meyer's hardness, and c is half the mean length of the two radial cracks (tip to tip).

An apparatus allowing for a variable loading cycle during a single experiment was designed, and placed into a glove box in order to achieve a good moisture control ($\pm 2\%$) in the range 0% (< 50 ppm) – 100%, so as to study the effect of the environment² (Figure 1).

The horizontal displacement of the indenter (to produce a groove) is obtained by a bearing slide, while a piezoelectric actuator controls the vertical movement. Both the penetration and the tangential forces are continuously monitored. The main characteristics of the apparatus are a maximal normal load of less than 50 N with an accuracy of 0.05 N, a vertical displacement limited to 100 μm , and a bearing slider allowing for a displacement accuracy better than 1 μm and a maximum speed of

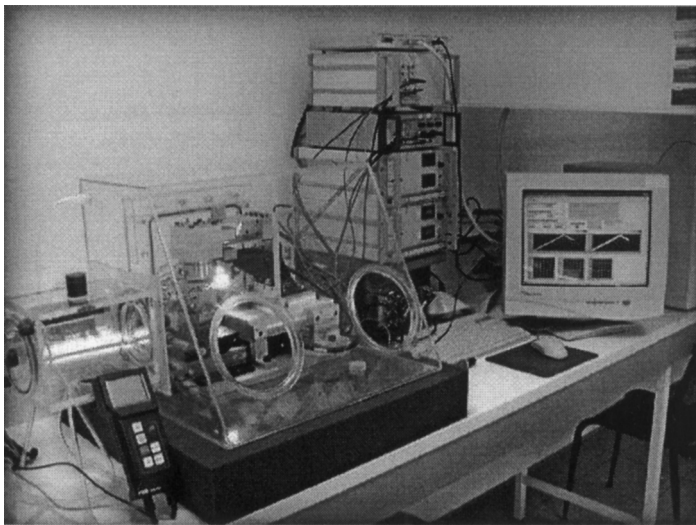


Figure 1. Experimental set-up designed for variable loading scratch experiments in a moisture & temperature controlled atmosphere (gloves are removed on the picture).

5 mm/s. The speed and acceleration of the bearing slider is computer controlled, and displacements and environmental parameters are continuously monitored. The scratch resistance (tangential load) was followed through constant normal load and low rate loading-unloading experiments. Such experiments allow first to study a wide load range within a single experiment and second, to reveal any possible dynamical effect, by studying the symmetry of the scratch pattern. A Vickers penetrator (inverse pyramidal, 136° face to face angle) was used with a leading edge orientation. The samples and the indenters are cleaned with ethanol before each test. Four different grooves were made on each glass and a good reproducibility was observed.

An optical microscope allowing for interferometrical observations and an atomic force microscope (AFM, Digital Instrument, Nanoscope IIIA) operated both in tapping and in contact modes, were used to observe and to analyze the topology of the damaged surfaces. The optical observations were systematically made 1 hr after the mechanical testing, so that the possible incidence of fatigue-corrosion phenomena is about the same for all the specimens.

The specific glass transition temperature (T_g) of each glass was determined by Differential Scanning Calorimetry (DSC) at a heating rate of $10^\circ\text{C min}^{-1}$ and each batch was then annealed at the corresponding T_g temperature for 30 min and cooled again to room temperature at 1°C min^{-1} . Note that the onset of the first endothermal peak was used and an error of $\pm 2^\circ\text{C}$ was estimated. The thermal expansion coefficients (α) of the glasses were determined from the $50\text{--}300^\circ\text{C}$ portions of the dilatometric curves obtained during heating at 5°C min^{-1} .

3. MATERIALS

Silicon-oxycarbide glasses are of great interest because of their remarkable mechanical properties and refractoriness, which clearly correlate to the increase of the average coordination number in the glass network.³⁻⁸ Interest in oxycarbide glasses is hence obvious, as far as carbon atoms form C-Si covalent bonds, as it is mainly the case for the presently studied glasses in which most carbon atoms get into $\text{C}(\text{Si})_4$ four-fold coordinated. The glass preparation has already been previously reported in detail.^{5,6,9} In its mainlines, a ($\text{D}^{\text{H}}, \text{T}^{\text{H}}$) gel is first synthesized from hydrolysis condensation reactions of a mixture of methyldiethoxysilane, $\text{HMeSi}(\text{OEt})_2$, and, triethoxysilane, $\text{HSi}(\text{OEt})_3$, where D^{H} and T^{H} stand for HSiO_2 and HSiO_3 units respectively. The gel is then pyrolysed at 1000°C under inert atmosphere, to obtain black glass rods, 1 to 2 mm thick, and over 30 mm long, consisting in i) an oxycarbide phase with $\text{SiC}_x\text{O}_{2(1-x)}$ stoichiometric composition, where carbon atoms form $\text{C}(\text{Si})_4$ tetrahedra; and ii) free carbon microdomains (which give the black color to the glass). The $\text{D}^{\text{H}}\text{T}^{\text{H}}0.5$ and $\text{D}^{\text{H}}\text{T}^{\text{H}}1$ grades were studied in this work. In addition, a standard soda-lime-silica glass (float glass) and a vitreous silica (hydroxyl content = 30 ppm) were characterized for sake of comparison. The glassy phase theoretical compositions of the $\text{D}^{\text{H}}\text{T}^{\text{H}}0.5$ and $\text{D}^{\text{H}}\text{T}^{\text{H}}1$ grades, are $\text{SiC}_{0.33}\text{O}_{1.33}$ and $\text{SiC}_{0.375}\text{O}_{1.25}$ respectively. Free carbon contents of 0.5 and 4 vol. % were estimated for the $\text{D}^{\text{H}}\text{T}^{\text{H}}0.5$ and $\text{D}^{\text{H}}\text{T}^{\text{H}}1$ grades respectively.

Oxide glasses with compositions based on the soda-lime-silica system were synthesized by mixing in oxide (SiO_2 , Al_2O_3) and carbonate (NaHCO_3 , K_2CO_3 , $\text{Mg}(\text{OH})_2$ (MgCO_3)₄, CaCO_3) powders.¹⁰ The powder mixtures was melted in a 200 cm^3 Pt/

Rh10% crucible at about 1600°C for 3.5 hrs, including a 1 hr long mixing treatment by means of device with two platinum helices called a guinand. The melt was further poured out in a pre-heated (500°C) graphite mould and annealed for 30 min at this temperature, and further cooled to room temperature at 2°C min⁻¹. A serie of glasses with more than 70 mol% SiO₂ (starting powder) was synthesized (Table 1). This “SLS” series consists of glasses with Na₂O/CaO = 1.52, and with rising SiO₂ contents from 71 to 80 mol%.

Ge-Se glasses were synthesized by introducing the appropriate quantities of germanium (Ge) and selenium (Se) in silica ampoules sealed under vacuum, by further heating this mixture at high temperature, typically between 750 and 950°C, and by subsequent quenching (see ref. 11 for details). The physical and mechanical properties of the studied glasses are reported in Table 2.

4. RESULTS AND DISCUSSION

4.1. Normal versus Anomalous Behavior

Concerning the indentation fracture patterns, two different behaviors may be distinguished: the so-called normal glasses tend to develop the radial-median crack

Table 1. Composition (mol %) and thermal properties of the oxide glasses.

| Series | SiO ₂ | Na ₂ O | K ₂ O | MgO | CaO | Al ₂ O ₃ | T _g (°C) | α ($\times 10^{-6} \text{C}^{-1}$) |
|--------|------------------|-------------------|------------------|-----|------|--------------------------------|-----------------------|---|
| SLS1 | 71 | 17.5 | 0 | 0 | 11.5 | 0 | 558 | 10.9 |
| SLS2 | 74 | 15.7 | 0 | 0 | 10.3 | 0 | 559 | 10.1 |
| SLS3 | 77 | 13.9 | 0 | 0 | 9.1 | 0 | 560 | 9.1 |
| SLS4 | 80 | 12.1 | 0 | 0 | 7.9 | 0 | 561 | 7.7 |
| Error | / | / | / | / | / | / | $\pm 2^\circ\text{C}$ | ± 0.1 |

Table 2. Density, elastic moduli, indentation hardness and toughness of Ge-Se glasses. n.d.: non determined. ¹)Partially devitrified. [€]Planilux, Saint-Gobain Co.

| Series | d | E (GPa) | μ (GPa) | ν | H (GPa) | K _c (MPa.√m) | T _g (°C) |
|-----------------------------------|------------|---------------------|---------------------|------------|------------------------|--|---------------------|
| SiO ₂ | 2.2 | 73 | 31.8 | 0.148 | 7.2 | 0.73 | 1190 |
| D ^H T ^H 0.5 | 2.23 | 104 | n.d. | n.d. | 8.63 | 0.7 | ≈ 1350 |
| D ^H T ^H 1 | 2.2 | 110 | n.d. | n.d. | 10.6 | 0.57 | >1350 |
| SLS1 | 2.53 | 70.2 | 29.2 | 0.202 | 5.35 | 0.71 | 558 |
| SLS2 | 2.50 | 69.3 | 29.2 | 0.188 | 5.11 | 0.70 | 559 |
| SLS3 | 2.47 | 68.6 | 29.0 | 0.181 | 5.15 | 0.76 | 560 |
| SLS4 | 2.43 | 68.1 | 29.1 | 0.172 | 5.19 | 0.82 | 561 |
| Float glass [€] | 2.55 | 72.0 | 30.0 | 0.21 | 5.30 | 0.72 | 562 |
| Se ¹⁾ | 4.28 | 10.25 | 3.74 | 0.322 | 0.39 | 0.16 | 41 |
| Ge ₅ Se ₉₅ | 4.31 | 11.05 | 4.18 | 0.316 | 0.57 | 0.09 | 68 |
| Ge ₁₀ Se ₉₀ | 4.34 | 12.08 | 4.59 | 0.307 | 0.77 | 0.12 | 92 |
| Ge ₁₅ Se ₈₅ | 4.36 | 13.8 | 5.33 | 0.295 | 1.05 | 0.22 | 110 |
| Ge ₂₀ Se ₈₀ | 4.37 | 14.73 | 5.72 | 0.286 | 1.38 | 0.28 | 162 |
| Ge ₂₅ Se ₇₅ | 4.36 | 16.05 | 6.25 | 0.281 | 1.72 | 0.22 | 228 |
| Ge ₃₀ Se ₇₀ | 4.32 | 17.9 | 6.82 | 0.264 | 2.02 | 0.20 | 300 |
| Ge ₄₀ Se ₆₀ | 4.36 | 22.38 | 8.80 | 0.273 | 2.35 | 0.16 | 340 |
| Error | ± 0.05 | $\pm 1 \text{ GPa}$ | $\pm 1 \text{ GPa}$ | ± 0.01 | $\pm 0.01 \text{ GPa}$ | $\pm 0.01 \text{ MPa. } \sqrt{\text{m}}$ | ± 2 |

system from the corners of the indents, whereas cone-cracks are observed in the anomalous glasses.^{12,13} Pure fused silica is a model example of the anomalous behavior (Figure 2). In this case, the permanent deformation beneath the indenter can be mainly attributed to a pressure-driven densification process, and this process originates in the flexibility of the Si-O-Si bond angle. The anomalous indentation behavior of gel-derived SiOC glasses was already evidenced in a previous work.⁸ The different indentation-fracture patterns observed in the studied glasses are summarized in Table 3, for three different loads.¹⁴

Whereas well developed radial-medial cracks form in the soda-lime-silica glass, none are observed in pure silica. Instead, cone cracks appear, which intersect the surface to produce ring cracks, some of which having diameters larger than the indentation diagonal (Figure 2). The glass starts to be shivered for loads higher than 4.9 N. In the D^HT^H0.5 grade, the same anomalous behavior is observed, but with the cone-cracks intersecting the surface at the indentation corners. For loads equal or higher than 9.81 N, several secondary cone cracks appear, but no radial-medial crack. The behavior of the D^HT^H1 grade is quite similar to the one of the D^HT^H0.5 grade, but differs by the occurrence of radial-medial cracks as soon as the load exceeds 4.9 N. At higher loads, chipping comes into play and the specimens tend to be shivered. Therefore, it seems that the higher the carbon content is and the more normal the SiOC glass behaves. It is suggested that covalently-bonded carbon atoms reduce the mobility of the residual vitreous silica network (the matrix) at the molecular scale. It follows that deformation becomes less and less displacive (densification) and proceeds more and more by shear.

Noteworthy, an examination of the fine details of the deformation-cracking pattern by AFM reveals the presence of an array of microcracks almost concentric with respect to the load axis, which is well resolved near the indentation corners (Fig. 2). Of particular interest is the fact that these cracks follow the small turbostratic

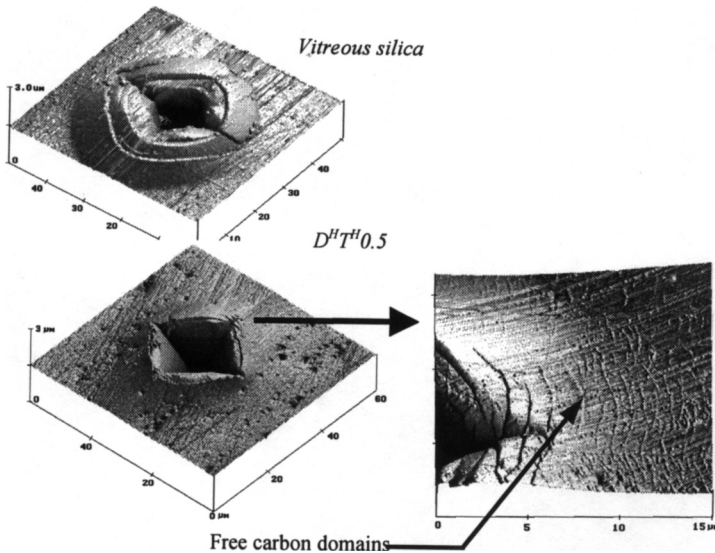








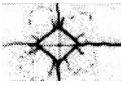





Figure 2. AFM image (contact mode) of Vickers indentations performed on pure vitreous silica and on a D^HT^H0.5 specimen with a 2.94 N indentation load.

Table 3. Vickers indentation patterns obtained for various indentation loads.

| Indentation load (N) | Float glass | Vitreous silica | D ^H T ^H 0.5 | D ^H T ^H 1 |
|----------------------|---|---|---|---|
| 2.94 |  |  |  |  |
| 4.91 |  |  |  |  |
| 9.81 |  |  |  |  |

graphite segments. The ultimate stage of this process is the coalescence of the cracks to form Hertzian-type cone-cracks, the main of which intersecting the indent corners. These observations show that the free carbon plays a major role on the indentation deformation/fracture behavior. The orientation of the graphite domains is likely to be responsible for the indentation anisotropy, and these domains provide easy fracture initiation sites and low energy fracture paths (likely through cleavage along basal planes) and cause the surface ring cracks to initiate just outside of the contact zone, i.e. almost along the indentation edges. Thus, in addition to the densification process, flow beneath the indenter presumably proceeds by the collapsing of the material by successive shear of hemispherical shells or strata. The largest surface ring crack corresponds to the last stratum sheared.

4.2. Elastic Recovery and Time-Dependent Hardness

Chalcogenide glasses from the Ge-Se system exhibit relatively low glass transition temperatures (from 41 (Se) to 340°C (Ge₄₀Se₆₀))^{11,15} and low activation enthalpy for flow (from 285 to 592 kJ/mol).¹⁶ As a consequence, they experience a time – or rate – dependent hardness at room temperature, especially for chalcogen-rich compositions¹⁷ (Fig. 3). Therefore, on one hand, these glasses offer a unique opportunity to study viscoelasticity at room-temperature, as was already mentioned earlier,¹⁸ but on the other hand, structural parts such as lens or fibres for applications in night visibility optical devices or in thermometry, are likely to suffer from creep deform-

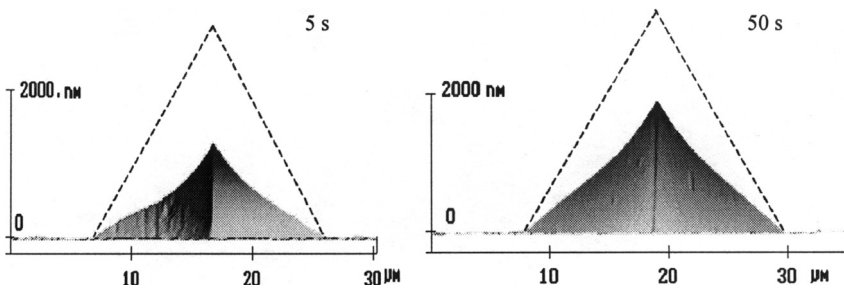


Figure 3. AFM image (contact mode) of Vickers indentations performed on glassy selenium under 0.1 N for 5 (left) and 50 s (right).

ation in service. The higher the germanium content and the larger the elastic contribution.

In terms of the vertical displacement of the tip of the indenter, one can write:

$$u = u_{el} + u_{fl} \quad (3)$$

where u is the total displacement, and u_{el} and u_{fl} are the elastic and flow (or creep) components respectively. The creep displacement was directly measured from the AFM profiles (Fig. 3) and the corresponding elastic contribution was estimated by extrapolating lines from the indentation corners, at an angle of 74° (half of the edge to edge angle) from the vertical. On the basis of a linear viscous behaviour, using fluid-mechanics, the following expression is obtained for the apparent viscosity coefficient:

$$\eta = \frac{\pi \tan \alpha}{4} t H(t) \quad (4)$$

where α is half the face to face angle (for a Vickers indenter $\alpha \approx 68^\circ$), Eq. (4) gives:

$$\eta = 1.943 t H(t) \quad (5)$$

H is far from being simply proportional to $1/t$, as it would be expected. Indeed a pronounced shear-thinning trend is observed, with a more than one order of magnitude decrease of η with rising hardness.¹⁷ The higher the germanium content is and the higher the viscosity becomes. Indeed, as most glasses studied so far at relatively high stresses – or strain-rates – chalcogenide glasses seem to exhibit a pronounced shear-thinning behaviour below T_g and for sufficiently high applied stresses (or strain-rates). It was observed that the behaviour becomes more and more shear-thinning as the germanium content is raised.). An excellent description of the time-dependence of the hardness was obtained on the basis of a non-Newtonian indentation flow mechanism, using the standard Norton-Arrhenius law for creep ($d\varepsilon/dt = A\sigma^n$). The following expression was then derived for the time-dependent hardness:

$$H(t) = \left[\frac{2}{\pi A(1 + \nu) \tan \alpha} \right]^{1/n} t^{-1/n} \exp\left(+ \frac{\Delta G_a}{nRT} \right) \quad (6)$$

It is noteworthy that the time dependence in this expression is similar to the phenomenological expressions proposed by Han et al.¹⁹ in a study of indentation creep in soda-silica glasses, and more recently by Grau et al.²⁰ Interestingly n increases with the germanium content from 11 to 62, whereas Poisson's ratio decreases (with the exception of the $\text{Ge}_{40}\text{Se}_{60}$ grade). It means that for a given normal strain, the volume change is larger and larger as the Ge content increases. It is suggested that this volume change favours the alignment of the structural units toward the stress axis, inasmuch it occurs at low temperature with respect to the T_g , i.e. in a temperature range where the elastic contribution is still important. These trends of η and ν can hence be regarded as correlated to the glass transition temperature: the higher the T_g of the glass is and the more pronounced the non-Newtonian flow behavior becomes.

4.3. Load Dependence

Ge-Se glasses behave normally with respect to indentation, i.e. radial-median cracks tend to form under Vickers indentation. For a given Ge-Se glass composition, the indentation cracking behavior depends much on the applied load. There are typically three major microcracking regimes:²¹ 1) below a critical indentation load, hereafter noted P^* , no crack is observed; 2) above P^* , two cracks show up, symmetrical with respect to the indentation, which indeed correspond to the intersect of a half-penny shape crack with the surface (as the load increases, the number of cracks connected to the indentation corners increases to three and four); and 3) above a critical load, P_c , chipping occurs. Mostly, P_c coincides with the load necessary for the four crack pattern to form. Note that a detailed analysis of the indentation corners reveals the nucleation of several small cracks, less than 10 μm in length, for indentation loads at – or just below – P^* . The load ranges for P^* and P_c are plotted as a function of the Ge content in Fig. 4.

The sensitivity of the glass to crack formation or to chipping increases significantly with the germanium content. Lawn et al.²² and Hagan²³ suggested that the critical load for crack initiation from a pre-existing subsurface flaw be proportional to K_c^4/H^3 . According to our experimental data, the proportionality factor would be about $500 \cdot 10^3$, whereas coefficient of $22 \cdot 10^3$ and 885 were proposed by Lawn and Hagan respectively, from data obtained either on oxide glasses and on ceramic materials. Furthermore, the former dependence of P^* on K_c and H would predict a linear increase of P^* with the germanium content up to 20% germanium whereas the opposite trend is observed.

In a scratching experiment, the scratch pattern also strongly depends on the level of the normal load, and for low loads the different kinds of micro-cracks which form during, or with the scratch process;² they are namely: i) the median cracks, ii) the radial cracks and iii) the lateral cracks. This last kind of cracks induces chipping when crack propagation toward the specimen surface occurs. The radial cracks are significantly inclined toward the sliding direction, and propagate in a curved shape usually ending perpendicular to the scratch direction when there is no combination with another damage phenomenon (i.e. lateral cracks).

Indeed three different regimes appear during a typical scratch experiment at a constant loading rate: i) the first regime is associated with a permanent groove with

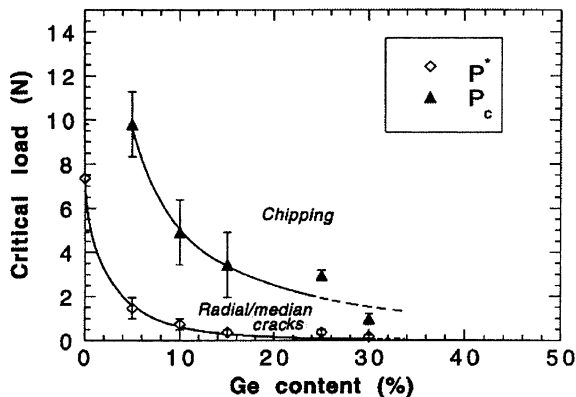


Figure 4. Load ranges for the various microcracking regimes as a function of the germanium content.

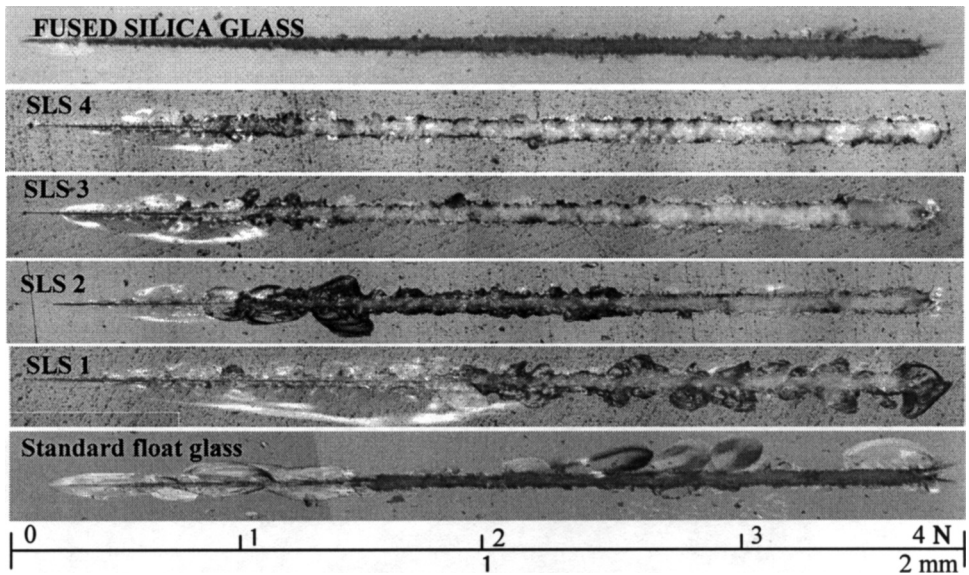


Figure 5. Scratch behavior of SLS glasses (monotonic loading).

eventually the formation of sub-surface lateral cracks, and corresponds to a micro-ductile regime, ii) the second one, so-called micro-cracking regime, is characterized by an important damage (lateral cracks intersecting the surface and radial cracks) and iii) the third one is a micro-abrasive regime and gives birth to many debris. SLS glasses generally fall in a narrow range of compositions along the boundary between devitrite ($\text{Na}_2\text{O} - 3\text{CaO} - 6\text{SiO}_2$) and tridymite (SiO_2) in the $\text{Na}_2\text{O} - \text{CaO} - \text{SiO}_2$ phase diagram. Shifting away from this narrow range affect various important characteristics including the scratchability. A micro-abrasive regime appears in the low-load domain for the SLS3 and SLS4, with high silica contents, whereas lateral chipping occurs for the SLS1 and SLS2 compositions. Glasses from the devitrite phase field are sensitive to chipping and glasses with silica-like networks appear to be much resistant to both crack propagation and chipping during scratch experiments. At the atomic or molecular scale, the resistance of the high silica content glasses to chipping or micro-cracking is due to the opened structure of the glass network, allowing both for the network flexibility and for the flowdensification process.² On the other hand, glasses with high modifying cation content (typically $> 25\%$), such as SLS1 and 2, contain more non-bridging oxygens which provide easy paths for fracture and slip. Note that a similar conclusion can be drawn from the indentation-scratching behavior of silicon-oxycarbide glasses,¹⁴ where the covalently bonded carbon in 4-fold coordination are found to induce a more normal behavior.

4.4. Role of Humidity

Figure 6 shows the scratches conducted on the standard float glass at different humidity levels. Monotonic loading/unloading cycles were conducted in order to screen all the possible damage events in a single scratch experiment.²

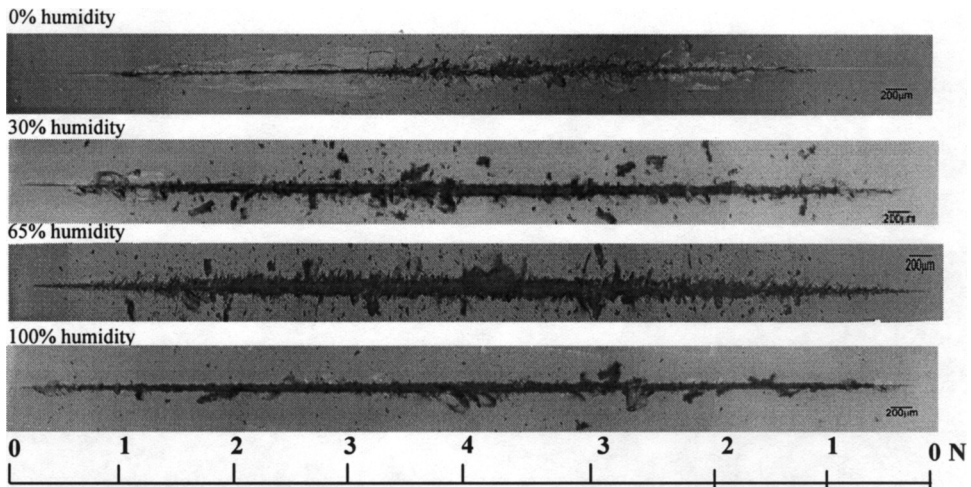


Figure 6. Pictures of scratches conducted under different hygrometric levels with a Vickers penetrator following a slope load-unload process.

As expected from the background studies on the effect of humidity on the fracture behavior of soda-lime-silica glasses,^{24,25} the scratch patterns significantly depend on the hygrometric level: the more important the hygrometric level is, the earlier (with regards to the normal load) the different damage processes appear. Another observation concerns the scratch obtained with 0% of humidity. The damage is characterized by a large lateral crack remaining under the surface of the sample. A similar but shorter crack occurs during the unload process. This phenomenon fades rapidly as the humidity level is raised.

The peculiar morphology of the scratch made at 0% of humidity is interesting. We can notice that there is almost a total lack of radial cracks while lateral cracks, which never reach the surface, extend over a large distance. This observation put in light the mechanism of the chipping process occurring during scratching: a chip is the combination of two radial cracks and a lateral one which then intersects the specimen surface. Two consecutive radial cracks located on the same side of the scratch track may intersect each other as a result of a deviation process resulting from the attractive forces between two close cracks. The coupling with a lateral crack leads to a chip and thus to matter removal. When only one radial crack frames the lateral one, this latter crack stay under the surface.

Subsurface lateral cracks, which propagate after the experiment, were found to be insensitive to the hygrometric rate and to remain under the surface of the material.

4.5. Role of Temperature

Indentation behaviour in temperature has been investigated in three different glasses (a Zr-Cu-Al-Ni bulk metallic glass, a Ge-As-Se chalcogenide glass and the standard float glass (Table 2)) and was revealed to be complex.²⁶ In fact, when temperature increases, glass response becomes time-dependent (as discussed in § 4.2), and in the vicinity of T_g increased permanent deformation is left by the indenter. However, all

glasses showed so-called ‘strong’ character with a relatively low decrease of hardness around T_g ²⁶ (Fig. 7).

Using high indenting loads, brittle behaviour could be generated in standard sodalime-silica glass and chalcogenide glass. The behaviour was revealed to differ strongly from one glass to the other. While standard float glass showed enhanced apparent toughness at elevated temperatures almost no change in apparent toughness was revealed in GeAsSe glass. However, comparison between chevron-notched bars loading and indented samples showed that toughness determination is changed dramatically around transition temperature when the loading rate is changed²⁷ (Fig. 8).

5. CONCLUSION

The indentation and scratching behavior of glasses from different glass forming systems was investigated and was found to depend much on the glass composition. Results were discussed in the light of the glass network structures, with a special

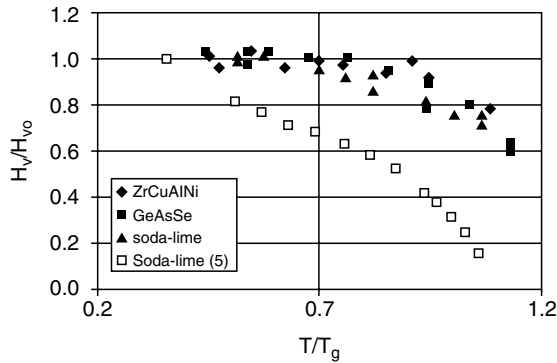


Figure 7. Reduced hardness as a function of the reduced temperature – Vickers indentation under 0.98 N for the GeAsSe glass and under 4.91 N for the other glasses, with a loading duration of 30 s²⁶.

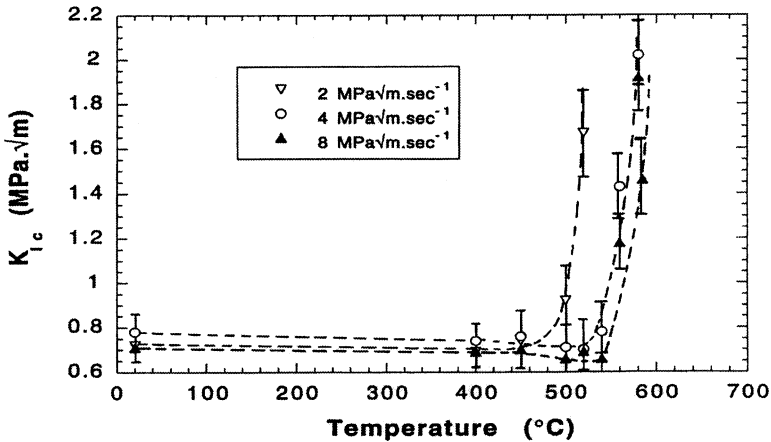


Figure 8. Temperature dependence of the apparent fracture toughness of a standard window glass.²⁷

focus on the normal versus anomalous behaviors, on the critical load for micro-cracking, on the indentation creep phenomenon and on the role of humidity. High silica contents promote flow-densification process beneath the indenter. On the contrary, carbon increases the polymerisation degree and the stiffness of the glass network and lead toward a more normal behavior. Chalcogenide glasses, which can be regarded as low T_g glasses with structures comparable to those of polymeric glasses, exhibit indentation-creep at room temperature, although they are very brittle and sensitive to indentation damage. The scratch resistance can be interpreted in the light of the indentation features. For instance, the role of moisture, which is well documented in indentation studies, is even exemplified during scratching.

REFERENCES

1. G.R. Anstis, P. Chantikul, B.R. Lawn and D.B. Marshall, "A critical evaluation of indentation techniques for measuring fracture toughness: I, direct crack measurements", *J. Am. Ceram. Soc.*, 64 [9] 533–538 (1981).
2. V. Le Houérou, J-C. Sangleboeuf, S. Dériano, T. Rouxel, G. Duisit, Surface damage of soda-lime-silica glasses: indentation and scratch behavior, *J. Non-cryst. Sol.*, 316 54–63 (2003).
3. J. Homeny, G.G. Nelson and S.H. Risbud, "Oxycarbide glasses in the Mg-Al-Si-O-C system", *J. Am. Ceram. Soc.*, 71 [5] 386–390 (1988).
4. H. Zhang and C.G. Pantano, "Synthesis and characterization of silicon oxycarbide glasses", *J. Am. Ceram. Soc.*, 73 [4] 958–963 (1990).
5. F. Babonneau, G.D. Soraru, G. D'Andrea, S. Dire and L. Bois, "Silicon oxycarbide glasses from sol-gel precursors", *Mat. Res. Soc Symp. Proc.*, 271 789–94 (1992).
6. G.D. Soraru, "Silicon oxycarbide glasses from gels", *J. Sol-Gel Science and Tech.*, 2 843–48 (1994).
7. G.M. Renlund, S. Prochazka and R.H. Doremus, "Silicon oxycarbide glasses: Part II. Structure and properties", *J. Mater. Res.*, 6 [12] 2723–34 (1991).
8. G.D. Soraru, E. Dallapiccola and G. D'Andrea, "Mechanical characterization of sol-gel-derived silicon oxycarbide glasses", *J. Am. Ceram. Soc.*, 79 [8] 2074–80 (1996).
9. G.D. Soraru, G. D'Andrea, R. Camprostrini and F. Babonneau and G. Mariotto, "Structural characterization and high temperature behaviour of silicon oxycarbide glasses prepared from Sol-Gel precursors containing Si-H bonds", *J. Am. Ceram. Soc.*, 78 379–387 (1995).
10. S. Dériano, Conception chimique de verres silicatés à hautes performances mécaniques, doctorate thesis, University of Rennes, December 2002.
11. I. Melscoët, "Synthèse, caractérisation et optimisation de verres optiques pour des applications infrarouges dans la fenêtre 8–12 μm ", doctorate thesis, University of Rennes, December 2000.
12. A. Arora, D.B. Marshall, B.R. Lawn and M.V. Swain, "Indentation deformation/fracture of normal and anomalous glasses", *J. Non-cryst. Sol.*, 31 415–428 (1979).
13. C.R. Kurkjian, G.W. Kammlott, M.M. Chaudhri, "Indentation behavior of soda-lime silica glass, fused silica, and single-crystal quartz at liquid nitrogen temperature", *J. Am. Ceram. Soc.*, 78 3 737–744 (1995).
14. T. Rouxel, J-C. Sangleboeuf, J-P. Guin, V. Keryvin, Surface damage resistance of gel-derived oxycarbide glasses: hardness, toughness, and scratchability, *J. Am. Ceram. Soc.*, 84 [10] 2220–24 (2001).
15. V.F. Kokorina, *Glasses for Infrared Optics*, Clarendon Press (1996).
16. See for example: U. Senapati and A. K. Varshneya, "Viscosity of chalcogenide glass-forming liquids: an anomaly in the "strong" and "fragile" classification", *J. Non-cryst. Sol.* 197 (1996) 210–218.
17. J-P. Guin, T. Rouxel, V. Keryvin, J-C. Sangleboeuf, I. Serre, J. Lucas, Indentation creep of Ge-Se chalcogenide glasses below T_g: elastic recovery and non-Newtonian flow, *J. Non-cryst. Sol.*, 298, 260–269 (2002).
18. D. Lewis III, W.C. LaCourse and D.B. Hardy, "Strength of selenium glass in the transformation range", *J. Am. Ceram. Soc.* 60 (3–4) (1977) 107–110.

19. W.T. Han and M. Tomozawa, "Indentation creep of $\text{Na}_2\text{O}-3\text{SiO}_2$ glasses with various water contents", *J. Am. Ceram. Soc.* 73 (12) (1990) 3626–32.
20. P. Grau, G. Berg, H. Meinhard and S. Mosch, "Strain-rate dependence of the hardness of glass and Meyer's law", *J. Am. Ceram. Soc.* 81 (6) (1998) 1557–64.
21. J-P. Guin, T. Rouxel, J-C. Sangleboeuf, Hardness, toughness, and scratchability of germanium-selenium chalcogenide glasses, *J. Am. Ceram. Soc.* 85 [6] 1545–52 (2002).
22. B.R. Lawn and D.B. Marshall, "Hardness, toughness and brittleness: an indentation analysis", *J. Am. Ceram. Soc.*, 62, 7–8, 347–350 (1979).
23. J.T. Hagan, "Micromechanics of crack nucleation during indentations", *J. Mat. Sci.*, 14, 2975–2980 (1979).
24. V. H. Bulsara, "Scratch formation in brittle solids and its application to polishing", PhD Thesis, Perdue University, USA (1997).
25. S.M. Wiederhorn, in *Fracture Mechanics vol 2* Plenum Press New York, (1974) 613.
26. E. Le Bourhis, T. Rouxel, Indentation response of glass with temperature, *J. Non-cryst. Sol.*, 316, 153–159 (2003).
27. T. Rouxel, J-C. Sangleboeuf, The brittle to ductile transition in a soda-lime-silica glass, *J. Non-cryst. Sol.*, 271, 224–235 (2000)

EFFECTS OF TIN ON THE PHYSICAL PROPERTIES AND CRACK GROWTH IN SODA-LIME-SILICA FLOAT GLASS

Matthew H. Krohn,¹ John R. Hellmann,¹ Carlo G. Pantano,¹ Nathan P. Lower,² and Richard K. Brow²

ABSTRACT

The effect of tin on the properties of soda-lime-silica glass was examined in glasses doped with 0.2–3.0 mol % SnO₂. Trends in the properties are consistent with an increase in the network connectivity with increasing tin concentration. The difference in the thermo-elastic properties of the tin doped glasses suggests the creation of residual stresses in the near surface region of float glass, resulting from the tin concentration gradient during cooling. Two-point fiber bend tests were conducted to determine the effect of tin on the stress corrosion susceptibility of tin doped soda-lime-silica glasses. The results showed the stress corrosion exponent for the tin-doped glasses to be a weak positive function of tin concentration.

1. INTRODUCTION

The float process is the predominant method for manufacturing soda-lime-silica (SLS) flat glass for architectural, structural, and automotive applications. Flat

¹ Matthew H. Krohn, John R. Hellmann, Carlo G. Pantano, Department of Materials Science and Engineering, Materials Research Institute, The Pennsylvania State University, University Park, PA 16802, USA

² Nathan P. Lower, Richard K. Brow, Department of Ceramic Engineering, University of Missouri at Rolla, Rolla, MO 64509, USA

glass production accounts for more than 25% of the annual domestic production of glass (20 million tons annually.¹) Therefore, the float process has significant market share, and improvements in the strength and reliability of float glass components will translate into significant cost savings.

Developed over 30 years ago by Pilkington, Ltd., the process involves floating a molten ribbon of glass from the glass tank across a molten tin bath, thereby allowing the production of flat glass panels with uniform thickness across the ribbon, and perfectly flat surfaces without secondary processing steps.² This process revolutionized the flat glass industry, but brought a new suite of technical issues to resolve in order to ensure the glass possesses the requisite elastic and mechanical properties for high reliability in structural applications.

Glass produced using the float process contains a significant amount of tin diffused into the surface in contact with molten tin bath (tin side). The surface of the glass exposed to the atmosphere (air side) contains a negligible amount of tin compared to the tin side. The diffusion profile of the tin into the glass is related to numerous variables such as: glass composition, glass redox, ion exchange between the glass and constituents in the tin bath, oxygen and metallic contamination of the tin bath, float bath atmosphere, temperature and time on the float bath.³ The chemistry of the tin side of float glass has been the focus of many studies.⁴⁻¹⁵ It is generally accepted that the tin penetration on the tin side ranges from 10–40 μm , and that tin is present in both the stannous (Sn^{+2}) and stannic (Sn^{+4}) forms. The stannous form is more prevalent near the surface, while in the sub-surface tail of the diffusion profile the stannic form predominates. Furthermore, the diffusion profiles obtained in most studies exhibit a characteristic “bump” in the subsurface region, approximately halfway through the tin penetration depth.^{4,5} This has been attributed to the accumulation of the slower diffusing stannic form in the sub-surface where the local oxidation potential is increasing.

The local structure of the stannous and stannic species in the glass structure remains a subject of significant debate.^{13,14} It is generally accepted that the Sn^{2+} is accommodated as an intermediate or network modifying cation,¹⁷ but the coordin-

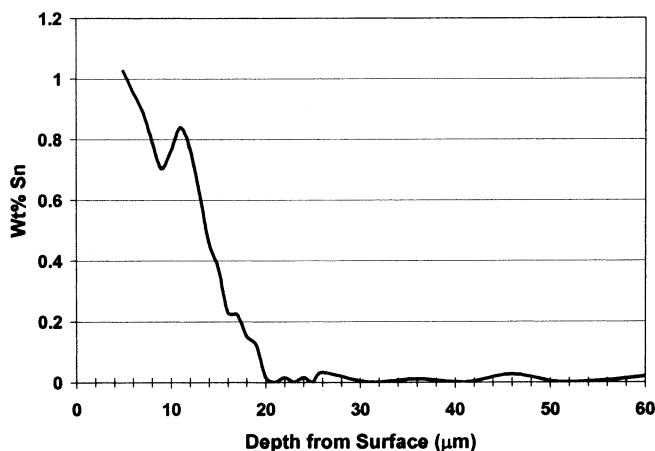


Figure 1. Example of a tin diffusion profile for the float glass surface in contact with the molten tin bath (from reference¹⁶).

ation of Sn^{4+} is less well understood. Although Sn^{4+} exhibits very low solubility in pure silica, recent NMR studies suggest that small concentrations of Sn^{4+} can be accommodated, at least partially, as a network forming cation (i.e. substitute for Si^{4+} .¹⁸) This is consistent with the lower diffusion coefficient of Sn^{4+} . Other studies, using Mössbauer spectroscopy, suggest that Sn^{4+} is accommodated in a significantly more covalently bonded, rigid arrangement than the Sn^{4+} .¹³ This leads to speculation that scission of network bonds may occur differently in tin doped SLS glass, leading to differences in slow crack growth behavior.

The effect of tin concentration and oxidation state on the physical properties of SnO-SiO_2 glasses has been well-studied.¹⁹ However, the role of tin on the physical properties, strength, and slow crack growth behavior of soda-lime-silica float glass has seen only limited study.²⁰⁻²² and interpretations remain inconsistent. Early studies demonstrated that the tin side of SLS float glass exhibits lower strength than the air side (see Figure 2) due largely to differences in the size of flaws introduced by rollers and handling in the post-forming processes.^{21,22} However, other studies reported that the tin side exhibits an enhanced resistance to contact induced damage relative to the air side,¹⁹ suggesting that a difference exists in flaw initiation and slow crack growth characteristics between the two sides of float glass.

Stress corrosion in silicate glasses occurs due to the ability of chemical species in the surrounding environment, most notably water vapor, to cleave strained Si-O bonds by chemical reaction.²³ Changes in the elastic properties if the Si-O bond, chemical reactivity of the adjacent bonds, and in the local structure due to the incorporation of network modifying cations may all play a role in governing the stress corrosion behavior of glass.²⁴⁻²⁷ Therefore, it is possible that the presence of tin could alter the susceptibility of SLS glass to flaw initiation and growth.

Tummala and Foster²² reported a higher resistance to environmentally enhanced slow crack growth for the tin side of the float glass. However, upon close examination of their data, it is questionable as to whether there is a statistically

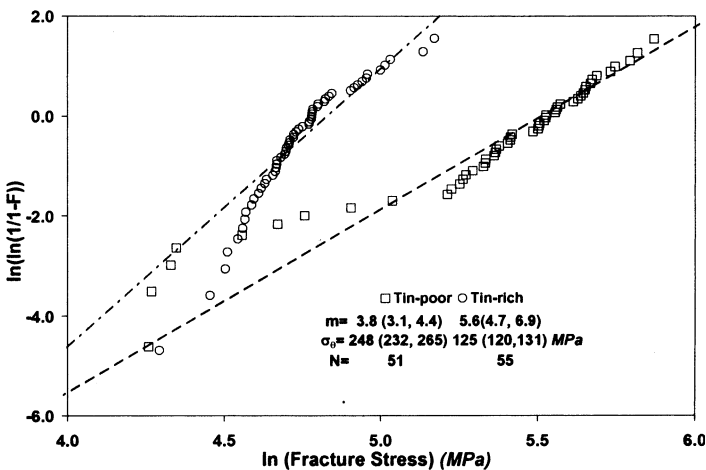


Figure 2. Two-parameter Weibull plots for float glass specimens tested using a ring-on-ring biaxial flexure test at a stressing rate of 2 MPa/sec. The un-biased Weibull modulus (m), characteristic strength (σ_0), and number of specimens tested (N) are displayed on the graph. The values in the parenthesis represent a 90% confidence interval for N specimens (from reference¹⁶).

significant difference in the stress corrosion exponent (n) derived from their dynamic fatigue tests for the air versus tin side of the float glass specimens. Later work by Akcakaya, et al.²¹ reports that the air side is more resistant to stress corrosion, in conflict with Tummala, et al.,²² and further confuses the issue regarding the effect of tin on the stress corrosion resistance of float glass.

We assert that how tin is accommodated in the glass structure will govern the thermal and elastic properties of the glass. These, in turn, govern the magnitude and distribution of residual stress gradients in the tin penetration zone, and the relative susceptibility of Si-O bonds to scission via reaction with water vapor in the environment (stress corrosion). These are the issues governing the crack initiation and growth behavior of the glass, and may be used to rationalize the observed differences in strength and stress corrosion resistance of the tin-versus air-side of float glass.

Therefore, the focus of this investigation was to examine the role of composition on the thermal, elastic, and mechanical properties that contribute to the mechanical reliability and robustness of SLS float glass.

2. EXPERIMENTAL PROCEDURE

Biaxial flexure and dynamic fatigue experiments were performed using commercial soda-lime-silica float glass plates (Solex[™], PPG Industries, Inc., Pittsburgh, PA.) Subsequent experiments focused on tin doped glasses synthesized in the laboratory, based on the composition of Solex[™] glass. The composition of the glass system studied is 72 mol% SiO₂, x mol% SnO₂, (13- x) mol% Na₂O, 9 mol% CaO, and 6 mol% trace element (x ranges from 0 to 3). Sodium stannate (IV) (Na₂SnO₃ · 3H₂O) was used to dope the glasses with SnO₂. The glasses were melted in high silica crucibles for 4 hours at a maximum temperature of 1490 °C. After fining in the furnace, they were poured into large glass slabs, annealed, and machined into flexure test specimens or used to draw fiber for tensile tests.

2.1. Thermal-Elastic Properties

The thermal expansion of the synthesized glasses were measured using a single push rod dilatometer (Orton 1600D, The Edward Orton Jr. Ceramic Foundation, Westerville, OH.) The samples were cut to a length of 25 mm × 4-6 mm. The specimens were heated at a rate of 5 °C/min through the dilatometric softening point. The coefficient of thermal expansion (CTE), glass transition temperature (T_g), and dilatometric softening point (T_d) were determined for the tin doped glasses from the percent linear change versus temperature plots.

The elastic moduli were determined for the tin doped glasses using sonic resonance techniques. The moduli were determined from rectangular specimens following ASTM standard C1198. The moduli were also determined at the University of Missouri-Rolla using an ultrasonic technique on long slender rods (fiber tapers²⁸). The measurements were taken using a Panatherm 5010 (Panametrics, Waltham, MA.)

The viscosities of the tin doped glasses were measured using a beam bending viscometer (Theta 3-9-12V-ST, Theta Industries, inc, Port Washington, NY.) ASTM standard C598 was followed for obtaining the viscosity versus temperature curves.

2.2. Strength Testing

Biaxial flexure testing, using a ring-on-ring methodology reported elsewhere,⁹ was employed for evaluating the strength and stress corrosion exponent for the commercial float glass coupons. Four point flexure (quarter point loading,) and fiber tensile and two point bent test methods were employed for the tin doped glasses synthesized in the laboratory. Dynamic fatigue plots (ln strength versus ln stressing rate) were generated to determine the stress corrosion exponent for both the commercial and synthesized glasses. The stress corrosion exponents calculated from the plots were corrected for the residual stresses resulting from contact induced flaws.^{29,30}

2.3. Direct Observation of Crack Growth Experiments

Median radial cracks, which resulted from Vicker's indents, were grown in a controlled manner on both the air and tin surfaces of commercial float glass components. The cracks were arrested periodically by unloading the specimen to follow the trajectory of the cracks. The fracture surfaces were observed in an optical microscope to determine if there was any evidence of differences in crack growth in the near surface region of the two surfaces of the float glass.

3. RESULTS AND DISCUSSION

3.1. Thermo-Elastic Properties

The results from the thermal expansion measurements can be found in Table 1. The thermal expansion of the tin doped glasses decrease with increasing tin concentration (Figure 3).

The thermal expansion of a glass is not only related to the symmetry of the bonding, as in crystalline materials, but also the free volume of the glass, which can allow for bond bending and rotation.³¹ The tin in the synthesized glasses is substituted for Na₂O, and since the glasses are processed in air it is likely that the majority of the tin is present as SnO₂. The substitution of SnO₂ for Na₂O would result in a more strongly bonded structure. In addition, tin in either the stannous or stannic forms has a higher field strength than sodium. The smaller ionic radius of tin, which may allow for a higher degree of bond bending and rotation compared to sodium, may also play a role in the thermal expansion. These effects of substituting tin for

Table 1. Coefficient of thermal expansion (CTE), glass transition temperature (T_g), and dilatometric softening point (T_d) for tin doped glasses.

| SnO ₂ (mol%) | CTE ^a (ppm/°C) | T _g (°C) | T _d (°C) |
|-------------------------|---------------------------|---------------------|---------------------|
| 0 | 9.1±0.2 | 542±3 | 609±7 |
| 0.2 | 9.2±0.1 | 554±3 | 611±2 |
| 1 | 8.5±0.3 | 560±8 | 634±1 |
| 2 | 8.4±0.2 | 591±4 | 654±1 |
| 3 | 7.7±0.1 | 512±3 | 681±3 |

^b Temperature range of 25 to 550°C

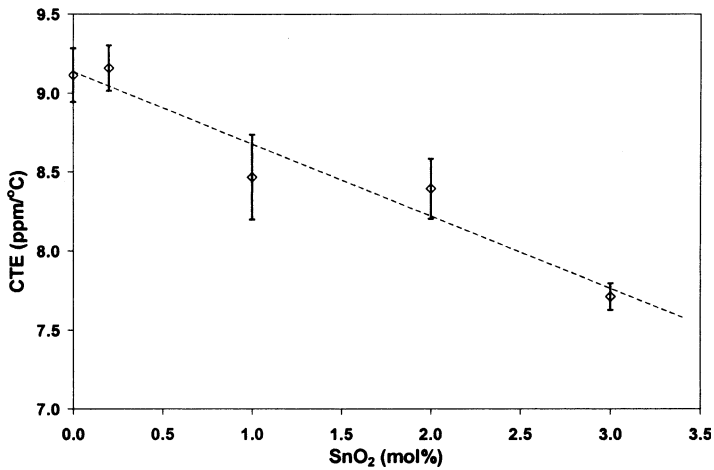


Figure 3. Coefficient of thermal expansion as a function of mol% SnO₂.

sodium would be consistent with the decrease in thermal expansion seen with increase in tin concentration. The viscosity results (Figure 4) also corroborate an increase in the network connectivity.³¹

The results for the elastic modulus measurements using the two techniques are shown in Table 2. The addition of tin to the glass network results in an increase in the elastic modulus (Figure 6) which is consistent with a more strongly bound glass network, as discussed above.³¹

These results demonstrate that substitution of SnO₂ for Na₂O increases the overall bond strength of the network, resulting in a decrease in thermal expansion and an increase in elastic modulus, glass transition temperature, dilatometric softening temperature, and viscosity. Since the tin concentration varies with depth into the surface of the glass (see Figure 1), a gradient in thermo-elastic stress will be established upon cooling the glass, thereby altering the crack trajectory and velocity relative to the tin-poor surface.

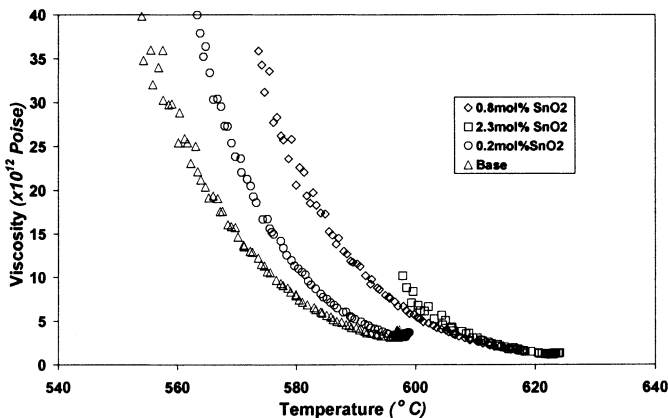


Figure 4. Viscosity versus temperature curves for glasses containing different mol% of SnO₂.

Table 2. Elastic modulus (E), Shear Modulus (G), and Poisson’s ratio (ν) for tin doped glasses.

| SnO ₂ (mol%) | <i>Penn State</i> | | | <i>Rolla</i> |
|-------------------------|------------------------|----------|-------|-----------------------------|
| | <i>Sonic Resonance</i> | | | <i>Ultrasonic Technique</i> |
| | E (GPa) | G (GPa) | ν | E (GPa) |
| 0 | 74.4±1.9 | 31.2±0.6 | 0.17 | 68.6 |
| 0.2 | 71.3±1.5 | 30±0.2 | 0.17 | 70.1±0.5 |
| 1 | – | – | – | 71.5±0.8 |
| 2 | 76.3±1.5 | 32.6±0.2 | 0.16 | 73.7±1.0 |
| 3 | – | – | – | 74.8 |

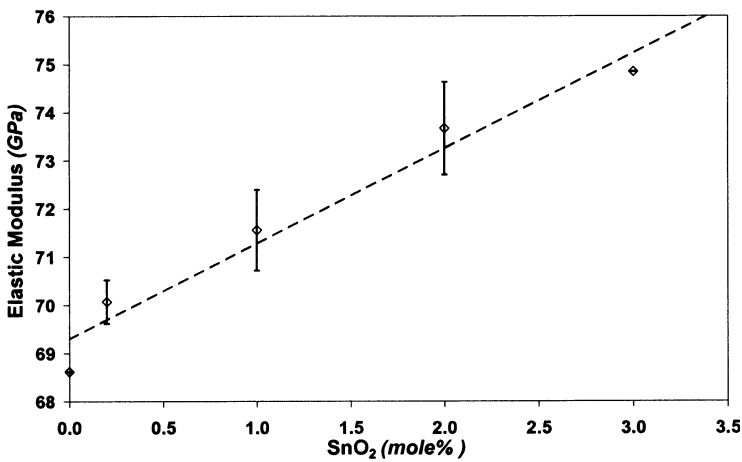


Figure 5. Elastic modulus as a function of mol% SnO₂.

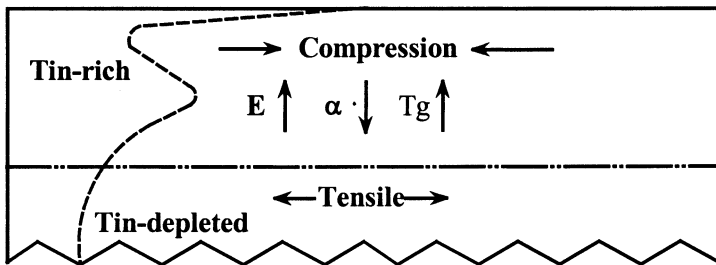


Figure 6. Schematic of the surface of float glass depicting the changes in the thermo-elastic properties resulting in a compressive residual stress state. A schematic of a tin diffusion profile is also shown in the figure.

The presence of a stress fields in the near surface region may be expected to have an affect on the flaw initiation and growth on the tin-rich surface compared to the tin-poor surface. The stress field may result in a difference between the crack velocity in the near surface region and/or the contact damage behavior of the glass surfaces.

Micrographs from the crack growth experiments are shown in Figure 7. There is evidence of crack retardation on the tin-rich surface relative to the bulk of the glass. This may result from the residual stresses that arise due to differences in the

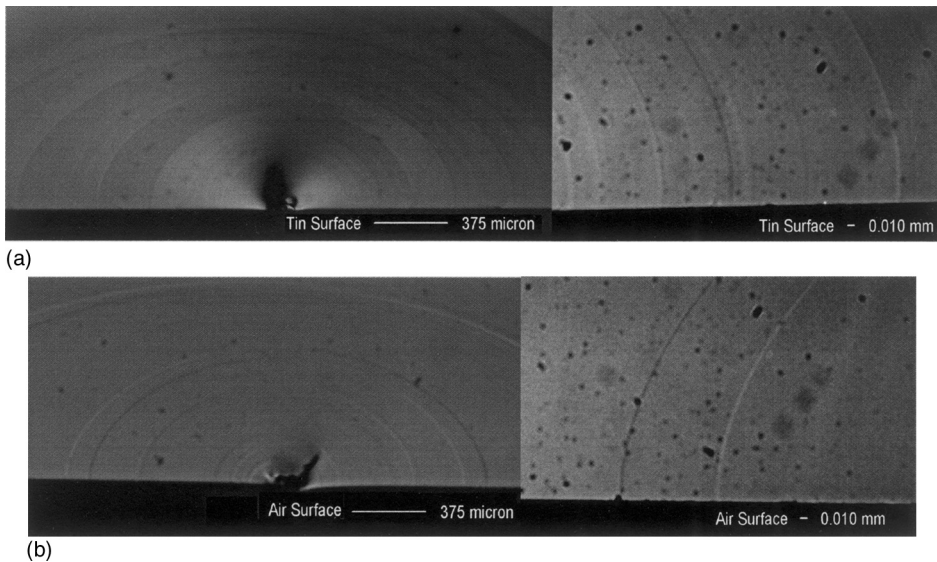


Figure 7. Micrographs of median radial cracks grown on the (a) tin and (b) air surfaces of float glass. There is some evidence of negative curvature on the tin surfaces suggesting crack retardation in the near surface region.

thermo-elastic properties in the tin diffusion region. More quantitative crack growth measurements in combination with finite element models to confirm the stress profile in the near surface region are underway.

3.2. Dynamic Fatigue

Dynamic fatigue tests performed on float glass samples in the as-received conditions (Figure 8a) revealed no statistically significant difference in the stress corrosion exponent (n) between the tin-rich and tin-poor surfaces. However, the variability in the measured strengths is large, due to the wide range of flaw sizes contributing to failure. Therefore, further tests were performed on samples in which a more uniform flaw size was introduced via indentation. Although a significant improvement in strength uniformity was obtained, no difference in the stress corrosion exponent was observed (Figure 8b.) However, the depth of the median radial crack resulting from the indent is large compared to the tin diffusion depth. Hence, the size of the starting flaw may mask differences in the crack growth behavior between the two surfaces. Therefore, subsequent tests were performed on glasses uniformly doped with tin, in a configuration that would ensure highly uniform flaw sizes contributing to failure.

3.2.1. Fiber Strength Tests

A two-point bend test methodology, recently developed by Matthewson, et al.³² and proposed by Kurkjian et al.³³ for evaluating the intrinsic strength of glass fibers, was employed. The experiments were performed using fiber drawing and testing equipment at the University of Missouri-Rolla. The fibers were drawn by an up-draw process onto

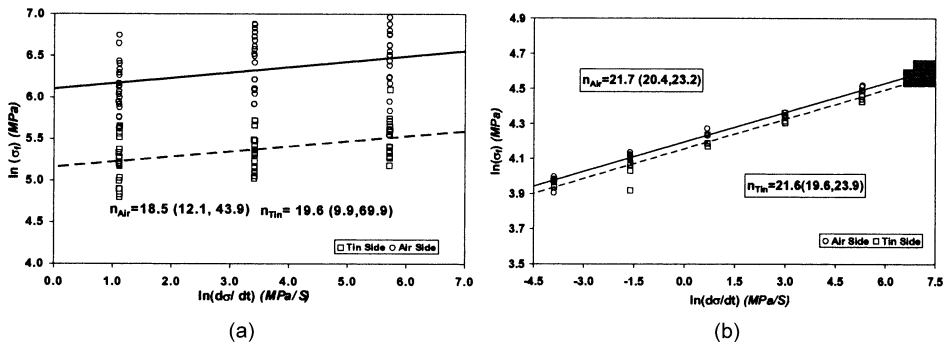


Figure 8. Dynamic fatigue plots for commercial float glass tested in the (a) as-received and (b) indented conditions. Stress corrosion exponents (n), which have been corrected for residual stress are displayed on the graphs. The values in the parenthesis represent a 95% confidence interval.

a drum that allowed for the collection of pristine fibers, followed immediately by strength testing, which allowed little risk of flaw initiation by handling.

The test involves bending a fiber between two faceplates and recording the plate separation when fracture occurs. Using the faceplate separation and fiber diameter the strain at fracture can be calculated.³⁴ The fracture strain can be converted to stress using the elastic modulus of the fiber being tested. Relative to conventional fiber testing, there are many advantages to this test method which contribute to measurement of highly uniform strength distributions, including: no gripping problems, reduced introduction of handling induced flaws, small region of the fiber under uniform tensile stress, relative easy test step-up, fibers can be easily be tested in different environments, only small lengths of fibers are necessary, and only small volume of fiber is lost during the fracture.³²

However, there are some drawbacks to using the 2-pt fiber test. Most notably, there may be some issues with using the linear elastic solution for high strength fibers because of the high strains applied to the fibers. At high strains, higher order effects on the elastic modulus may need to be considered.³² For dynamic fatigue experiments there are some issues with stressing rate since it varies with faceplate separation. However, The effect of loading mode on the dynamic fatigue of fibers in two-point bending has been investigated by Rondinella and Matthewson.³⁵ Calculation of the instantaneous stressing rate at failure was used in this work.

The fibers were tested at different faceplate velocities. An example of the family of Weibull plots collected for the un-doped glass composition is shown in Figure 9. The strength distributions all exhibit high Weibull moduli, which is expected based on the very small surface area stressed uniformly in tension. A comparison of the characteristic strengths of the tin doped fibers shows no dependence on tin concentration at any of the faceplate velocities (Figure 10).

An example of a dynamic fatigue plot generated from the data can be seen in Figure 11. The stress corrosion exponents for each glass were calculated from the dynamic fatigue plots. The results indicate that the stress corrosion exponents increase with increasing tin concentration (Figure 12). A summary of all the stress corrosion exponent data can be found in Table 3.

Also included in Figure 11 are the results from dynamic fatigue experiments performed on glass fibers that had been aged at 50°C in 80% relative humidity for 48

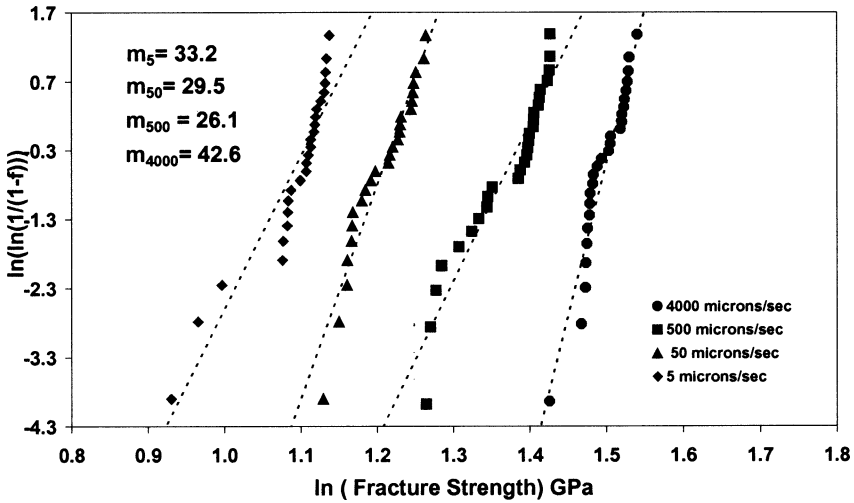


Figure 9. Two-parameter Weibull plots for base glass fibers tested using the 2-pt bend fiber test at different faceplate velocities. Weibull modulus (m) for each data set is displayed on the graph.

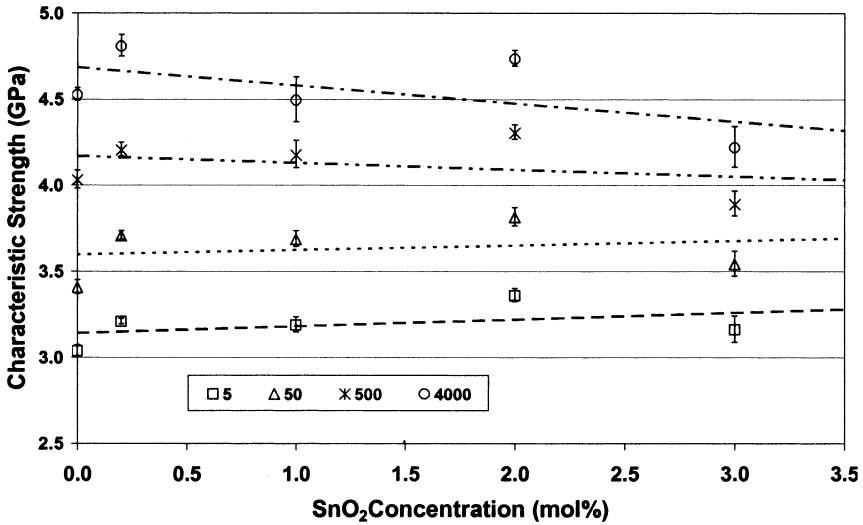


Figure 10. The characteristic strengths of the tin doped glasses measured at different faceplate velocities ($\mu\text{m}/\text{sec}$) as a function of mol% SnO_2 .

hours; in this case, the stress corrosion exponent is *not* a function of tin concentration. This may be related to the formation of a hydrated surface that possesses different elastic properties and chemical reactivity compared to the pristine surfaces. This will be the subject of future research.

4. CONCLUSIONS

The results from the tests performed on the tin doped glasses have given some insight to the role tin plays in governing the structural, chemical, and physical properties of

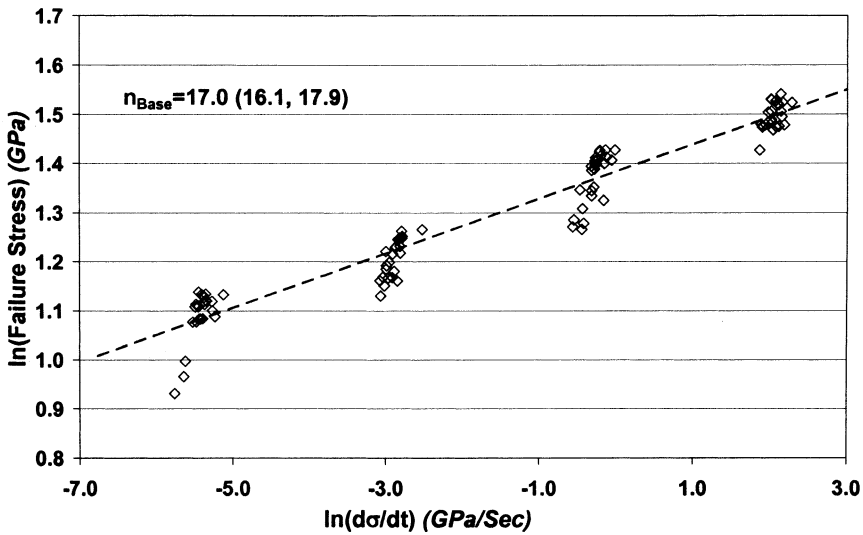


Figure 11. Example of dynamic fatigue plot generated from 2-pt bend data for the base glass composition. The failure strains and faceplate velocities have been converted into failure stress and stress rate, respectively. The stress corrosion exponent along with the 95% confidence interval is displayed on the graph.

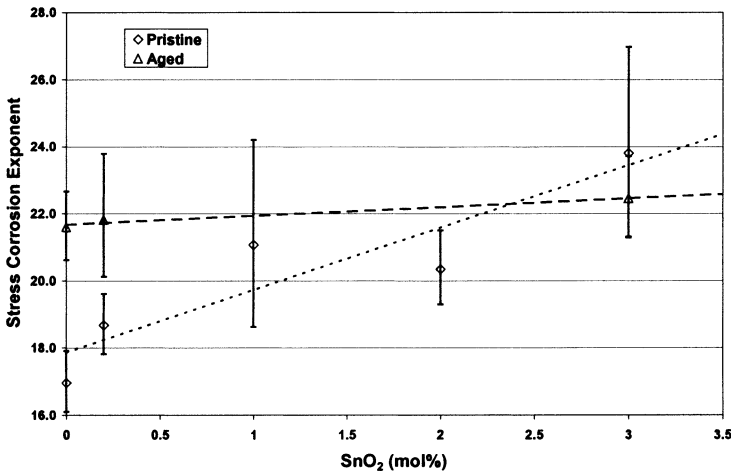


Figure 12. Plots of stress corrosion exponents as a function of mol% SnO₂ plotted for the tests performed on pristine and aged fibers.

soda-lime-silica float glasses. Measurements of the thermo-elastic properties of the tin doped glasses revealed that the substitution of SnO₂ for Na₂O resulted in a change in the thermo-elastic properties of the glass. The change in these properties suggests that the substitution of SnO₂ for Na₂O results in a more strongly bonded glass network.

Dynamic fatigue tests, using conventional flexure geometries on plates and beams yielded strength distributions of insufficient precision to permit an unambiguous determination of the role of tin on stress corrosion exponent. A novel two-point

Table 3. Stress corrosion exponents for tin doped glasses determined using 4-pt bending ($n_{4\text{-pt}}$), fiber tension (n_{fiber}), and 2-pt bending ($n_{2\text{-pt}}$) tests and for commercial glasses tested using ring-on-ring biaxial flexure.

| SnO ₂ (mol%) | $n_{4\text{-pt}}$ (Polished) | $n_{4\text{-pt}}$ (Flame Polished) | n_{fiber} | $n_{2\text{-pt}}$ (Pristine) | $n_{2\text{-pt}}$ (Aged) |
|----------------------------|---------------------------------|---------------------------------------|--------------------|---------------------------------|-----------------------------|
| 0 | 20.8 (14.7,34.0) | 20.5 (14.7, 32.5) | 25 | 17.0 (16.1, 17.9) | 21.6 (20.6, 22.7) |
| 0.2 | 19.8 (13.0,37.6) | 19.0 (13.3, 31.3) | 24 | 18.7 (17.8, 19.6) | 21.8 (20.1, 23.8) |
| 1 | – | – | – | 21.1 (18.6, 24.2) | – |
| 2 | 18.1 (14.7, 23.1) | 19.0 (16.2, 22.9) | 54 | 20.3 (19.3, 21.5) | – |
| 3 | – | – | – | 23.8 (21.3, 27.0) | 22.4 (21.3, 23.7) |

| Commercial | As-received | Indented |
|------------|-------------------|-------------------|
| Air Side | 18.5 (12.1, 43.9) | 21.6 (19.6, 23.9) |
| Tin Side | 19.6 (9.9, 69.9) | 21.7 (20.4, 23.9) |

bend test was employed to limit the strength variability; results indicate that tin has a weak positive affect on the stress corrosion resistance of SLS glass.

Additionally, tin is more strongly bound in the glass structure with a higher field strength compared to sodium, thereby increasing elastic modulus, glass transition temperature, softening point and viscosity, while concurrently decreasing thermal expansion. The dependence of these thermo-elastic properties on tin concentration, coupled with a tin concentration gradient, could lead to a complex compressive residual stress distribution near the tin-rich surface. Crack growth experiments corroborate crack retardation near the tin-rich surface; the role of the compressive stress on flaw initiation and growth is currently being evaluated.

5. ACKNOWLEDGEMENTS

The authors would like to acknowledge Drs. David Green, David Shelleman, and Jonathan Salem for their help and guidance with the test methodologies and testing of the commercial glasses. This work is funded by the NSF Industry-University Center for Glass Research, Site for Glass Surfaces and Interfaces Research at the Pennsylvania State University

REFERENCES

1. *Glass: Industry Technology Road Map*. 2002, Glass Manufacturing Industry Council: Westerville, OH. p. 1–50.
2. L.A.B. Pilkington, The Float-Glass Process, *Proceedings of the Royal Society of London Series A-Mathematical and Physical Sciences*, 1969. **314**: p. 1–25.
3. A. Mishra, G.A. Pecoraro, T.E. Paulson, and C.G. Pantano, Glass-Tin Interactions During the Float Glass Forming Process, *Ceramic Trans.*, 1998. **82**: p. 205–217.
4. M. Verità, F. Geotti-Bianchini, S. Hreglich, C.G. Pantano, and V.J. Bojan, EPMA, RBS and SIMS Analyses of Tin Profiles in Commercial Float Glass, *Bol. Soc. Esp. Ceram. Vidrio*, 1992. **31c**(6): p. 415–420.

5. J.S. Sieger, Chemical Characteristics of Float Glass Surfaces, *J. Non-Crys. Sol.*, 1975. **19**: p. 213–220.
6. C.G. Pantano and V.J. Bojan. Tin Profiles in the Bottom Surface of Float Glass: Manufacturing and Heat Treatment Effects. in *Fundamentals of glass science and technology 1993: proceedings of the Second Conference of the European Society of Glass Science and Technology, Venice, Italy, 21–24 June 1993*. 1993. Murano, Venice, Italy: Stazione sperimentale del vetro.
7. R.A. Chappell and C.T. Stoddart, An Auger Electron Spectroscopy Study of Float Glass Surfaces, *Physics and Chemistry of Glasses*, 1974. **15**(5): p. 130–136.
8. L. Colombin, A. Jelli, J. Riga, J.J. Pireaux, and J. Verbist, Penetration Depth of Tin in Float Glass, *J. Non-Crys. Sol.*, 1977. **24**: p. 253–258.
9. P. Lehuédé and P. Chartier. Comparison of the Atmosphere and of the Tin Sides of Float Glass using SIMS. in *Proceedings of XVIII International Congress on Glass*. 1998. San Francisco, California, USA: American Ceramic Society, Westerville, Ohio.
10. T.E. Paulson, K.E. Spear, and C.G. Pantano. Thermodynamic Analysis of the Tin Penetration Profile in High-Iron Float Glass. in *Proceedings of XVIII International Congress on Glass*. 1998. San Francisco, California, USA: American Ceramic Society, Westerville, Ohio.
11. K.F.E. Williams and M.F. Thomas, The Effect of Tin on Some Physical Properties of the Bottom Surface of Float Glass and the Origin of Bloom, *Glass Tech.*, 1999. **40**(4): p. 103–107.
12. H. Franz, Surface Chemistry of Commercial Float Glass, *Ceram. Eng. Sci. Proc.*, 1995. **16**(2): p. 251–258.
13. K.F.E. Williams, C.E. Johnson, J. Greengrass, B.P. Tilley, D. Gelder, and J.A. Johnson, Tin Oxidation state, depth profiles of Sn^{2+} and Sn^{4+} and oxygen diffusivity on float glass by Mössbauer Spectroscopy, *J. Non-Crys. Sol.*, 1997. **211**: p. 164–172.
14. K.F.E. Williams, C.E. Johnson, O. Nikolov, M.F. Thomas, J.A. Johnson, and J. Greengrass, Characterization of Tin at the Surface of Float Glass, *J. Non-Crys. Sol.*, 1998. **242**: p. 183–188.
15. P.D. Townsend, N. Can, P.J. Chandler, B.W. Farmery, R. Lopez-Herederro, A. Peto, L. Salvin, D. Underdown, and B. Yang, Comparison of Tin Depth Profile analyses in Float Glass, *J. Non-Crys. Sol.*, 1998. **223**: p. 73–85.
16. M.H. Krohn, J.R. Hellmann, C.G. Pantano, D.L. Shelleman, and G.E. Sakoske, Biaxial Flexure Strength and Dynamic Fatigue of Soda-Lime-Silica Float Glass, *J. Am. Ceram. Soc.*, 2002. **85**(7): p. 1777–1782.
17. K.F.E. Williams, C.E. Johnson, J.A. Johnson, D. Holland, and M.M. Karim, Mössbauer spectra of tin in binary Si-Sn oxide glasses, *J. Phys.-Condens. Matter*, 1995. **7**: p. 9485–9497.
18. D. Holland. Combined Techniques for the Study of Glass Structure. in *British ceramic proceedings: Advances in the Characterization of Ceramics, no. 57*. 1996. University of Manchester: Institute of Materials.
19. M.M. Karim and D. Holland, Physical Properties of Glasses in the System SnO-SiO_2 , *Phys. Chem. Glass.*, 1995. **36**(5): p. 206–210.
20. V.R. Howes, “Tin Side” and the “Air Side” of Commercially Produced Thermally Toughened and Un-toughened Float Glass, *J. Am. Ceram. Soc.*, 1978. **57**(11): p. 1049–1060.
21. R. Akcakaya, S. Gulati, and J.R. Varner. Fatigue Behavior of Surface Flaws on Air vs. Tin Side of Soda-Lime-Silica Float Glass. in *Challenges and Break-Through Technologies*. 2000. Amsterdam.
22. R.R. Tummala and B.J. Foster, Strength and Dynamic Fatigue of Float Glass Surfaces, *J. Am. Ceram. Soc.*, 1975. **58**(3–4): p. 156–157.
23. T.A. Michalske and S.W. Freiman, A Molecular Mechanism for Stress Corrosion in Vitreous Silica, *J. Am. Ceram. Soc.*, 1983. **66**(4): p. 284–288.
24. B.C. Bunker, Molecular Mechanisms for Corrosion of Silica and Silicate Glasses, *J. Non-Crys. Sol.*, 1994. **179**: p. 300–308.
25. B.C. Bunker and T.A. Michalske, *Effects of Surface Corrosion on Glass Fracture*, in *Fracture Mechanics of Ceramics vol.8. Microstructure, Methods, Design and Fatigue*, R.C. Bradt, D.P.H. Hasselman, and F.F. Lange, Editors. 1986, Plenum: New York. p. 391–411.
26. S.W. Freiman, G.S. White, and R. Fuller, Jr., Environmentally Enhanced Crack Growth in Soda-Lime Glass, *J. Am. Ceram. Soc.*, 1985. **68**(3): p. 108–112.
27. T.A. Michalske, B.C. Bunker, and K.D. Keefer, Mechanical Properties and Adhesion of Hydrated Glass Surface Layers, *J. Non-Crys. Sol.*, 1990. **120**: p. 126–137.
28. L.C. Lynnworth, Ultrasonic Measurement of Elastic Moduli in Slender Specimens Using Extensional and Torsional Wave Pulses, *Journal of Testing and Evaluation*, 1973. **1**(2): p. 119–125.

29. B.R. Lawn, D.B. Marshall, G.R. Anstis, and T.P. Dabbs, Fatigue Analysis of Brittle Materials Using Indentation Flaws: Part 1 General Theory, *J. Mater. Sci.*, 1981. **16**(10): p. 2846–2854.
30. E.R. Fuller, B.R. Lawn, and R.F. Cook, Fatigue Analysis of Brittle Materials Using Indentation Flaws: Part 1 General Theory, *J. Am. Ceram. Soc.*, 1983. **66**(5): p. 314–321.
31. J.E. Shelby, *Introduction to Glass Science and Technology*. 1997, Cambridge: The Royal Society of Chemistry.
32. M.J. Matthewson, C.R. Kurkjian, and S.T. Gulati, Strength Measurements of Optical Fibers by Bending, *J. Am. Ceram. Soc.*, 1986. **69**(1): p. 815–821.
33. C.R. Kurkjian, P.K. Gupta, R.K. Brow, and N. Lower, The Intrinsic Strength and Fatigue of Oxide Glasses, *J. Non-Crys. Sol.*, In Press.
34. P.W. France, M.J. Paradine, M.H. Reeve, and G.R. Newns, Liquid Nitrogen Strengths of Coated Optical Fibers, *J. Mater. Sci.*, 1980. **15**: p. 825–830.
35. V.V. Rondinella and J.M. Matthewson, Effect of Loading Mode and Coating on Dynamic Fatigue of Optical Fiber in Two-Point Bending, *J. Am. Ceram. Soc.*, 1993. **78**(1): p. 139–144.

INDENTATION SIZE EFFECT FOR GLASSES: YES, THERE IS A FRACTURE CONTRIBUTION

George D. Quinn^a

ABSTRACT

The influence of cracking upon apparent Knoop hardness was investigated for five glasses. The Knoop hardnesses decreased with increasing load in accordance with the classic indentation size effect (ISE). Cracking commenced at moderate loads and, in three of the five glasses studied, altered the indentation sizes and the ISE trends. Cracked indentations were as much as 10 μm longer than uncracked indentations made under identical conditions. Cracking around the indentation enabled the indenter to penetrate deeper into the material and larger indentations were produced.

1. INTRODUCTION

Does cracking influence hardness? This question was raised by M. Swain and M. Wittling at the 1995 Fracture Mechanics of Ceramics conference in Karlsruhe, Germany with their paper titled: "Indentation Size Effects for Brittle Materials: Is There A Simple Fracture Mechanics Explanation?"¹ They contended that median cracks beneath an indentation could enable an indenter to sink deeper into the material and thereby produce larger indentations than if there were no cracking. They suggested that Knoop indentations should be particularly susceptible, but they furnished no Knoop data to support their hypothesis.

This paper will show that cracking does affect Knoop hardness. Figure 1 shows side-by-side Knoop indentations that were made by the identical procedure in an

^a George D. Quinn, Ceramics Division, Stop 852, National Institute for Standards and Technology, Gaithersburg, MD 20899, geoq@nist.gov.

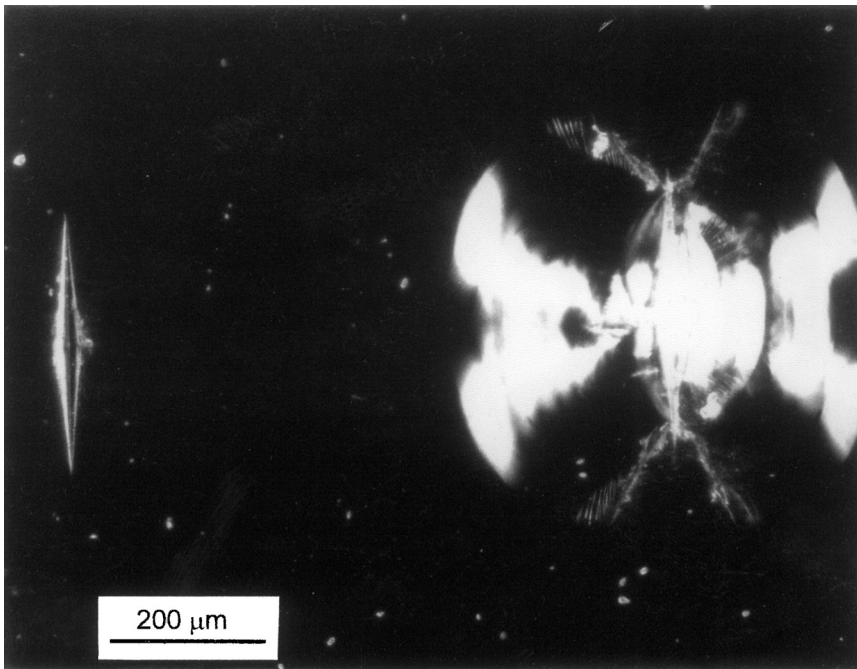


Figure 1. Dark field views of 49 N indentations made in the 1723 aluminosilicate glass. The cracked indentations were $9.0\ \mu\text{m}$ longer on average at this load. Despite the intensive cracking on the sides of the indentation on the right, the tips were undisturbed and the overall diagonal length could easily be read.

aluminosilicate glass. The cracked indentation has a longer diagonal length. This paper reports results of a study to evaluate effect of cracking upon conventionally measured Knoop hardness and the indentation size effect trend.

Hardness tests characterize a brittle material's resistance to deformation, densification, displacement, and fracture. Whether cracking affects hardness or not depends upon the indentation load. Cracking usually is not a factor at low loads. At moderate loads, incidental cracking has little effect upon apparent hardness. At large loads cracking can become so extensive that the indentation is so shattered or spalled that diagonal lengths cannot be read at all. This is more of a problem for Vickers indentations than for Knoop indentations. This paper concerns the effects of cracking in and around Knoop indentations at loads commonly used by conventional microindentation hardness testing machines (1 N to 50 N). A discussion of whether cracked indentations are valid is deferred to the discussion section. We begin first with a brief review of the Knoop indentation size effect.

The indentation size effect (ISE) is a trend wherein hardness decreases with increasing indentation size or indentation load as shown schematically in Figure 2.^{1,2,3,4,5,6,7,8,9,10,11,12,13} A plateau Knoop hardness is reached at loads from 5 N to 20 N in glasses. The ISE exists for both conventional Knoop and Vickers hardness, but usually with different trends due to different amounts of deformation, densification, displacement, displacement rate, and fracture induced by the two indenters. The ISE has been variously attributed to test procedure artifacts, frictional forces, environmental effects, or various material responses including elastic recovery, densifica-

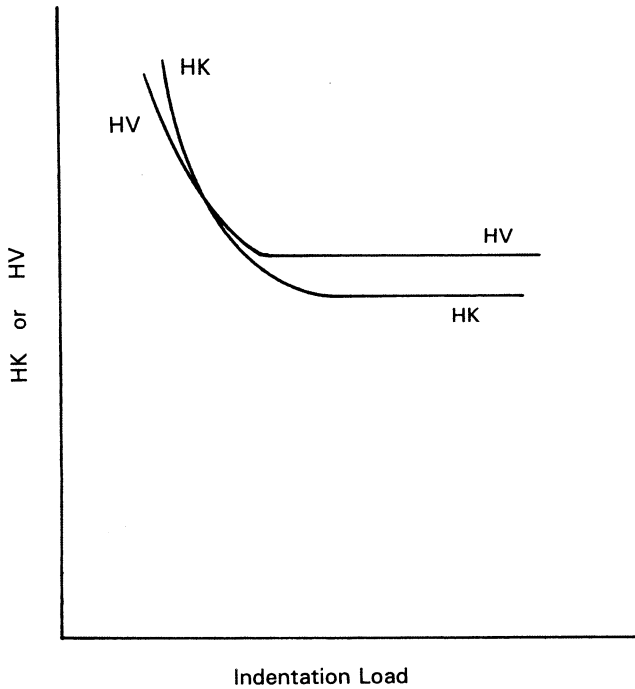


Figure 2. The indentation size effect (ISE) trend whereby hardness decreases with increasing load. Knoop (HK) and Vickers (HV) hardness trends are similar but HK and HV values cannot be interchanged. In very brittle materials, the HV curve may reach a plateau hardness at a distinct transition point.

tion, plastic flow, viscous flow, strain rate effects, or cracking. The author believes that they all play a role. Although there have been many studies of the effects of hardness upon fracture (e.g., References 14,15,16), much less has been written on the effects of cracking on hardness. Cracking may manifest itself as median, radial, or lateral cracks. There may also be generalized crushing or micro fissuring beneath the indentations. Micro fissuring and shear band fracture under an indentation are important deformation components.^{16,17,18}

Frederick Knoop and his colleagues developed the elongated pyramidal indenter as an alternative to the square base pyramidal Vickers indenter, in part to overcome the cracking in brittle materials with the latter.^{19,20} They carefully selected their diamond geometry and a definition of hardness (load normalized by the unrecovered projected area) so that hardness of a variety of metals exhibited a negligible ISE. Nonetheless, they observed a small ISE for flint glass between 1 N and 9.8 N.²⁰ Their 9.8 N flint glass indentations showed no signs of cracking, but as we will show, this is just below the load where cracking affects hardness. Subsequent to their early work, it became apparent that many glasses and crystalline ceramics do have an ISE.

Ideally, one should measure the entire hardness-load curve, but in practice users often chose one reference or standard load for comparisons between materials. Is there an optimum load for a standard test method? Indentations should be as large as possible to reduce measurement uncertainties, yet not so large as to induce excessive cracking that interferes with the measurement or destroys the indentation altogether.

The current world standard for glass hardness (e.g. ASTM C 730,²¹ DIN 52333,²² and ISO 9385²³) specify a 0.98 N indentation load. This load is rather small and evidently was chosen to avoid any cracking at all. It is in a steep load dependent portion of the ISE curve where hardness changes rapidly with load and machine or measurement errors can have a pronounced effect upon the measured hardness. The 0.98 N indentation is far from universal and many researchers have used a variety of indentation loads up to 9.8 N. In their review of the hardness of vitreous silica, Li and Bradt⁴ pointed out the widely divergent results and indentation loads that have been reported over the years.

During a recent study²⁴ of the fracture toughness of an optical glass using Knoop indentations for fracture toughness experiments, it was noticed that cracked 19.6 N indentations were as much as 11 μm longer than uncracked indentations created under identical conditions. The present study was conducted to further investigate the effects of cracking upon apparent Knoop hardnesses and the ISE over a broad indentation load range.

2. MATERIALS

Table 1 lists the five commercial glasses^b that were utilized as well as the manufacturers' values of density, ρ ; elastic modulus, E ; and HK.1 hardness at .98 N.^c Fracture toughness, K_{Ic} , was from Reference 25. Test coupons approximately 50 mm \times 50 mm in size were cut from 5 mm to 10 mm thick plates, slabs, or disks.

The fused silica was an optical grade, pure silica made by flame hydrolysis. A polariscope examination through the polished test coupon faces and 6.3 mm thickness showed no residual strains.

A polariscope examination of the 6.3 mm thick borosilicate test coupon revealed some slight strains. These were eliminated by reannealing at 575°C for 1 hour followed by slow 2°C cool down per minute to 10°C below the strain point and then slow cooling to room temperature. This glass has a composition of 81 w% SiO₂, 13 w% B₂O₃, 4 w% Na₂O, and 2 w% Al₂O₃.

The aluminosilicate glass was cut from a 9.5 mm polished plate and the polariscope examination revealed no residual strains. This glass is a heat shock resisting glass with the ability to withstand higher temperatures than the borosilicates.²⁶ The glass has 57 w% SiO₂, 16 w% Al₂O₃, 10 w% CaO, 7 w% MgO, 6 w% BaO, and 4 w% B₂O₃.

The borosilicate crown glass test piece was a 76 mm diameter \times 5.6 mm thick polished disk cut from a larger block. This optical grade glass was specifically annealed by the manufacturer to eliminate residual strains. Its composition was 69 w% SiO₂, 11 w% B₂O₃, 10 w% Na₂O, 7 w% K₂O, 2 w% BaO, 1 w% CeO, and 0.2 w% CaO. This glass has much greater network modifier content than the borosilicate glass, yet has a similar annealing point.

^b Certain commercial materials or equipment are identified in this paper to specify adequately the experimental procedure. Such identification does not imply endorsement by the National Institute of Standards and Technology nor does it imply that these materials or equipment are necessarily the best for the purpose.

^c HK.1 is the customary designation for Knoop hardness at 0.1 kgf, or 0.98 N indentation load.

Table 1. Properties of the glasses studied. The manufacturer's data for HK.1 for the first three glasses are very different from our results, probably since the former were adjusted for optical resolution limits in accordance with ASTM C 730.

| Glass | ρ (Mg/m ³) * | Annealing Point, °C * | E (GPa) * | HK.1 (GPa)* Manuf. | HK.1 (GPa)** This study | K _{1C} (MPa√m) *** |
|--------------------------------|-------------------------------------|-----------------------------|-----------------|--------------------------|-------------------------------|-----------------------------------|
| Fused silica Corning 7940 | 2.20 | 1084 | 72.5 | 4.79 | 5.88 ± .13 | .741 |
| Borosilicate Corning 7740 | 2.23 | 560 | 62.7 | 4.10 | 4.94 ± .08 | .760 |
| Aluminosilicate Corning 1723 | 2.64 | 710 | 86.2 | 5.04 | 5.94 ± .09 | .846 |
| Borosilicate Crown Schott BK-7 | 2.51 | 559 | 82. | 5.98 | 5.90 ± .10 | .862 |
| Soda lime silicate | ≈2.5 | ≈514 | ≈70 | – | 5.20 ± .11 | ≈.75 |

* Manufacturer's data. HK.1 data for the first three glasses probably has a $7\lambda/(2NA)$ correction.

** Average (GPa), ± standard deviation (GPa) for 12 indentations. No correction for optical resolution limits.

*** With the exception of the soda lime silicate, the fracture toughness data are from double cantilever beam experiments in vacuum by Wiederhorn and Roberts, Reference 25.

The soda lime coupon was cut from a 6 mm thick plate. Typical soda lime glass properties are shown in Table 1. Residual strains were eliminated by annealing at 520°C for 1 hour followed by a slow 2°C cool down to 10°C below the strain point and then a slow cool to room temperature. An examination with a black light failed to detect tin on either surface.

3. EXPERIMENTAL PROCEDURES

3.1. Hardness Testing Machines

Special care was used in this study to obtain accurate and precise readings, otherwise experimental errors or data scatter could mask or obscure the cracking effect. Thibault and Nyquist's masterful 1947 paper¹³ addressed many of the experimental problems in making Knoop hardness measurements in brittle materials. Anyone who has ever made and measured Knoop indentations will certainly appreciate their comments:

As might be expected with Knoop indentations which, even under conditions of maximum resolution, seem to fade gradually away instead of ending at any definite place, differences in the visual acuity of different individuals may greatly affect the determined length of impression and hence the Knoop number. So elusive are the ends of the indentations, particularly in transparent, low index substances, we sometimes wonder to what extent imagination enters into the determination. Of this we are certain: The measurement of Knoop indentations, made in hard substances under low loads, is the most exasperating type of microscopy which we have ever experienced. Harassed by the indistinctiveness of the indentation terminations which actually seem to vacillate while being examined, and the realization that the utmost precision must be obtained, we have never been able to spend more than a very few hours a day measuring Knoop impressions.

Having prepared the world's first standard reference material for Knoop Hardness of Ceramics, SRM 2831,^d the author fully appreciates the metrological and practical problems posed by the Knoop hardness method.²⁷ A broad range of

^d Standard Reference Material 2830, Knoop Hardness of Ceramics, National Institute of Standards and Technology, Gaithersburg, MD 20899.

indentation loads was used in the present study order to explore the full ISE curve. Two indentation hardness machines were used. Initially there were problems ensuring that both machines produced comparable results, but eventually we determined that both machines were working properly and produced consistent indentations and readings. Indentations made by both machines concurred within $0.5\ \mu\text{m}$ to $1.0\ \mu\text{m}$. Some early difficulties that we had in comparing indentations made by the two machines were traced to the use of a low power objective microscope lens for measuring very large indentations as will be discussed below. Standard reference materials, certified length standards, and load cells were used frequently to verify the procedures. A full description of the experimental procedure is described elsewhere.²⁸

A tabletop machine^e was used for indentation loads from 0.98N to 19.6 N. A larger floor mount machine was used for loads from 19.6 N to 98 N.^f All indentation diagonal lengths were measured with the optical system on the tabletop machine. All hardnesses were computed from:

$$\text{HK} = 14.229\text{P}/\text{d}^2 \quad (1)$$

where P is the indentation load and d is the long diagonal length.

The microindentation table, which was used to measure all indentations made by both machines, had a 50X objective lens with a 0.5 numerical aperture. A green filter was used in conjunction with a 10X digital filar eyepiece for a total magnification of 500X to measure most of the diagonal lengths. An optical stage micrometer with $10\ \mu\text{m}$ and $100\ \mu\text{m}$ divisions that had been calibrated by NIST to an accuracy better than 0.05% was used to establish the correct scalar factors for the 50X lens and the digital readout device. The repeatability of making a single diagonal length reading was $0.4\ \mu\text{m}$ - $0.5\ \mu\text{m}$ (standard deviation) or better. This was determined by repeatedly reading single 9.8 N indentations that had been made in a soda lime silicate specimen and a steel reference block. There was no need to correct for the optical resolution limitations of the 50X objective lens. Load was applied carefully to the indenter via a dashpot and care was taken to not touch the machine or the table it was mounted on during an indentation cycle. The initial diamond clearance and contact time were set in accordance with the manufacturer's instructions, and hence the indenter velocity was of the order of $0.042\ \text{mm/s}$ – $0.091\ \text{mm/sec}$ depending upon the applied load. Dwell time was set for 15 seconds, also in accordance with the manufacturer's instructions.

Larger indentations were made with the floor mounted hardness-testing machine that had a 98 N capacity. This dead weight loading machine applied force via a dashpot controlled lever beam and was set in compliance with ASTM E 384 Microhardness of Materials²⁹ and ASTM C 1326.³⁰ The initial diamond clearance and contact time were set in accordance with the manufacturer's instructions, and produced an average indenter velocity of $0.025\ \text{mm/s}$. Dwell time was 15 s – 20 s after which the machine automatically extracted the indenter. Indentations made with this floor mounted larger capacity machine were measured within 10 minutes with the tabletop machine in order to eliminate machine optics as a source of variability. There was one important difference in procedure, however, that initially caused us

^e Miniload II, Wetzlar, Germany.

^f Tukon 300 floor model, Wilson Division of Instron, Canton, MA.

some difficulties. Indentations made at 29.6 and 49 N were so large ($> 300 \mu\text{m}$) that they could not be measured with the tabletop machine's 50X objective lens since they extended beyond the field of view. Consequently, the large indentations were measured with the tabletop machine's lower power 10X, 0.18 numerical aperture lens. This lens and the digital filar scalar factors were also carefully checked with the NIST calibrated optical stage micrometer. Unfortunately, it was more difficult to detect the full length of the large indentations with the 10X low power objective lens due to optical resolution limitations.

3.2. Measuring Knoop Diagonal Lengths: Problems Due to Resolution Limits

Problems in assessing the exact tip location have long bedeviled those who have read Knoop indentation diagonal lengths, especially in glasses. Optical microscope resolution limitations are a problem for Knoop indentations due to their slender tapered tips.^{13,31,32,33} Thibault and Nyquist¹³ devoted seven full pages to this topic in their 1947 paper. Gahm³³ presented compelling evidence that diagonal length readings are strongly dependent upon the lens numerical aperture and errors of up to $4 \mu\text{m}$ are possible with low power lenses. The resolution error in underestimating the true Knoop diagonal length has been estimated as $7\lambda/2(\text{NA})$ where λ is the wavelength of light and NA is the objective lens numerical aperture. The error is independent of indentation size, so the percentage error is greater for smaller indentations. So, for example, the 50X objective lens used on the Leitz Miniload machine in the present study had a 0.50 NA and green filtered light ($\lambda = 0.55 \mu\text{m}$). The calculated correction was $3.9 \mu\text{m}$. This is a huge correction for small ($\approx 50 \mu\text{m}$) indentations made at 0.98 N in glasses, but is proportionately less important for larger indentations. Tarasov and Thibault³² suggested that the entire ISE may be due to this correction factor, since if a constant correction length is applied to diagonal lengths for a range of indentation loads, it will produce a trend similar to the ISE.

A $7\lambda/2(\text{NA})$ correction is incorporated in the ASTM Knoop standard C 730 for glass, but is *not used* in the master microindentation hardness of materials standard E 384, nor in the advanced ceramic standards C 1326 and ISO 14705, nor in the glass standards DIN 52333 or ISO 9385. This variability between the standards has created considerable confusion in hardness testing and probably accounts for a lot of inconsistent results in the literature.

We investigated this matter further as described in detail in reference 28. With good microscopy technique and proper illumination and diaphragm control, measurement errors due to optical resolution limitations with 40X or 50X objective lenses may be only $0.4 \mu\text{m}$ to $1.5 \mu\text{m}$ depending upon the observer and material. The full $7\lambda/2(\text{NA})$ correction factor is excessive. In contrast, a correction factor for resolution limitations in our work was essential for readings made with the low power 10X objective lens. All glass diagonal length readings made with this lens had to be corrected by $+5 \mu\text{m}^{\text{g}}$ as discussed in detail in Reference 28.

^g The length differentials are much less with opaque ceramics. The same experiment was performed on the black silicon nitride SRM 2830 reference hardness block. Three observers repeatedly measured the same indentation with 10X, 20X and 40X objectives lenses. They obtained differentials of only $0.3 \mu\text{m}$ to $1.5 \mu\text{m}$ when switching from the 10X to 40X objectives.

3.3. Evaluation of Cracking and Changes of the Indentations with Time

Cracking assessments were made with the optical microscope while measuring the indentation size on the indented surface.^h Lateral cracks were easily detected, as well as generalized cracking around and underneath the indentation. Ideally, the indentations should have been monitored through the glass specimen during the indentation process, as demonstrated by Cook and Pharr³⁴ or Wilantewicz and Varner,³⁵ but this was beyond the scope of the present short study. The indentations were observed in the same manner most researchers would with their conventional hardness testing machines.

We noticed that cracks grew with time around some of the indentations. Lateral crack shards popped off some large indentations. Nevertheless, the general assessment of whether an indentation was cracked or not did not change over the course of a few weeks. Specific comments about the nature and extent of the cracking are given in the results section. Some indentation diagonal lengths shrank with time. A decrease of the indentation length of as much as several microns over the course of a few days was not uncommon, so it was important to measure the indentation lengths within a few minutes after they were made.

3.4. Modeling the ISE Trend

Various functions have been proposed to model the indentation size effect data. The Meyer law is:

$$P = cd^n \quad (2)$$

where c is a constant and n is the Meyer or logarithmic index. For ceramics and glasses, $n < 2$, and hardness decreases with increasing load. An alternative expression (which often fits glass or ceramic hardness data better) that is attributed to Bernhardt³⁸ that is commonly used is:^{4,7,8,36,37,38,39}

$$P = a_1d + a_2d^2 \quad (3)$$

where a_1 and a_2 are constants. The first term accounts for the ISE trend at low loads, whereas the second term accounts for the constant hardness plateau at larger indentation loads. Combining equations 1 and 3:

$$HK = 14.229(a_1/d) + 14.229a_2 = a'_1/d + a'_2 \quad (4)$$

where 14.229 is the indenter constant for the Knoop indenter and correlates the long diagonal length, d , to the projected surface area. If hardness is load independent ($a'_1 = 0$), then:

$$HK = a'_2 \quad (5)$$

^h The choice of the objective lens sometimes altered the cracking assessment. Lower power lenses with greater depths of field revealed more cracking damage. For the sake of consistency, the assessments in this study were made with the lens that was used for the diagonal length measurements.

The parameter a'_2 is considered by some to be the “true hardness” or the hardness due to volumetric deformation processes in the absence of surface effects.^{2,7,8,12}

4. RESULTS

4.1. Hardness Versus Indentation Load and Cracking Propensities

All five glasses exhibited the classic ISE of decreasing hardness with increasing load. Cracking did not affect the ability to measure the Knoop indentation diagonal lengths in any of these glasses since the cracking damage was along the sides or underneath the indentation and there was very little or no damage or displacement at the tips. Faint, very tight median cracks sometimes emanated from the indentation tips, but since these often extended at a slight angle to the indentation axis, it was not difficult to distinguish them from the indentation itself. This is in sharp contrast to Vickers indentations, wherein tip cracking or spalling renders length measurements difficult or impossible.

Figures 3 and 4 show the outcomes for the aluminosilicate and borosilicate crown glasses wherein cracking had a distinct effect upon the apparent hardness. Cracked indentations were longer than uncracked indentations by as much as 10 μm . The scatter in diagonal lengths of uncracked indentations was quite small in either case, whereas cracked indentations had much greater variability.ⁱ Although a 10 μm length differential is quite pronounced and easy to measure, the percentage difference in length was small. The difference in hardness is magnified, however, since hardness depends on the square of the diagonal length. The difference in hardness between uncracked and cracked indentation was $\approx 5\%$.

Cracking occurred in some aluminosilicate glass specimens at loads as small as 9.8 N, just as the ISE trend approached the plateau. Figure 1 shows a dark field view of indentations. Dark field illumination sometimes revealed that the “uncracked” indentation had some localized damage and possible short lateral cracks. The fully cracked indentations were 9.0 μm longer on average for 49 N. Cracking gradually increased for larger loads. Figure 3 shows two data sets at 19.6 N that were made by the two different hardness machines. The average diagonal size and hardness are in good agreement. A clear distinction between cracked and uncracked lengths was observed with both machines. The differences in average diagonal lengths were only 2.3 μm to 4.2 μm at 19.6 N, but these differences are both statistically significant.^j Even at the largest loads, there were some indentations that had negligible cracking, however, and a dichotomy in hardness trends occurred as shown in Figure 3b. Indentations were sharp and had straight side edges and bottom edges at loads to 29.4 N. The indentation edges became more ragged at 49 N as extensive crushing commenced. Nevertheless, only faint median cracks could be detected from the tips even at these high loads.

Cracking also affected the hardness of the BK-7 borosilicate crown glass as shown in Figure 4. No median, radial, or lateral cracks were detected at 4.9 N.

ⁱ A few cracked indents had lengths similar to uncracked indentations, but usually the cracked indentations were appreciably longer.

^j The two-tailed student's *t* statistic for small sample sizes was 8.96 for HK and 8.96 for d for data from the floor mounted machine, and 5.70 and 5.81, respectively, for data from the tabletop machine. These are greater than the critical *t* ratio for 10 degrees of freedom at the .001 probability level ($t=4.59$).

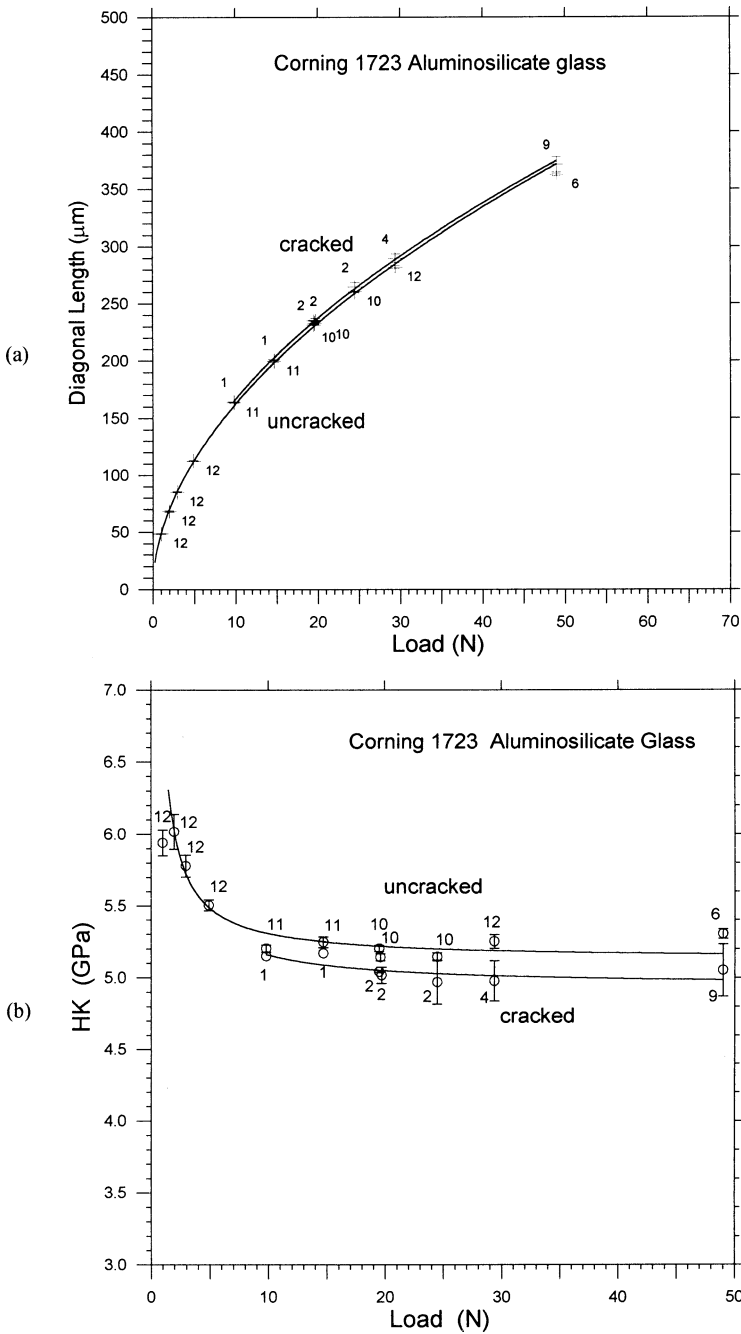


Figure 3. Diagonal length (a) and Knoop hardness (b) for the aluminosilicate glass. Cracked indentations were as much as 10 μm longer than uncracked indentations.

Indentations were sharp and had straight edges at loads up to 49 N. Lateral and other cracks commenced at 9.8 N at the point where the ISE curve approached the plateau and there was an immediate effect upon the diagonal lengths. Upon cracking,

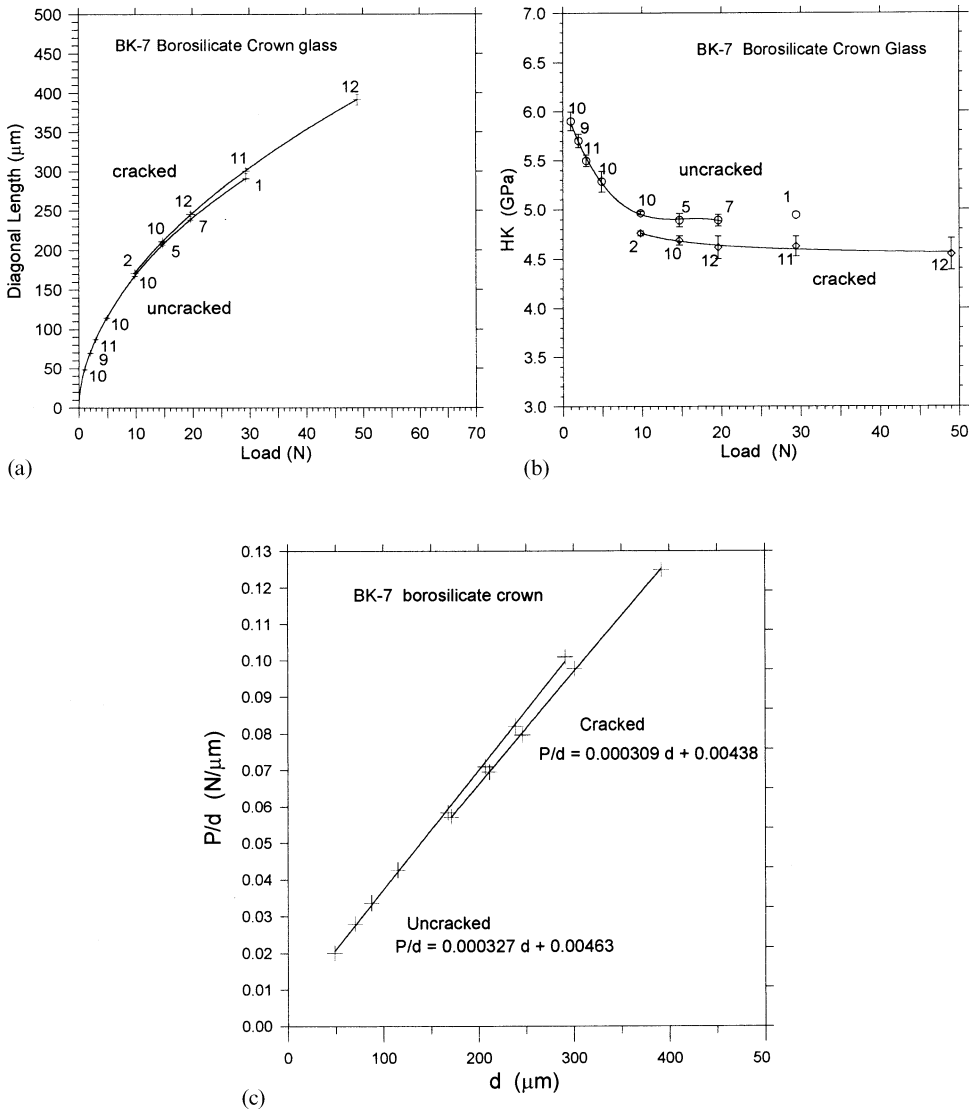
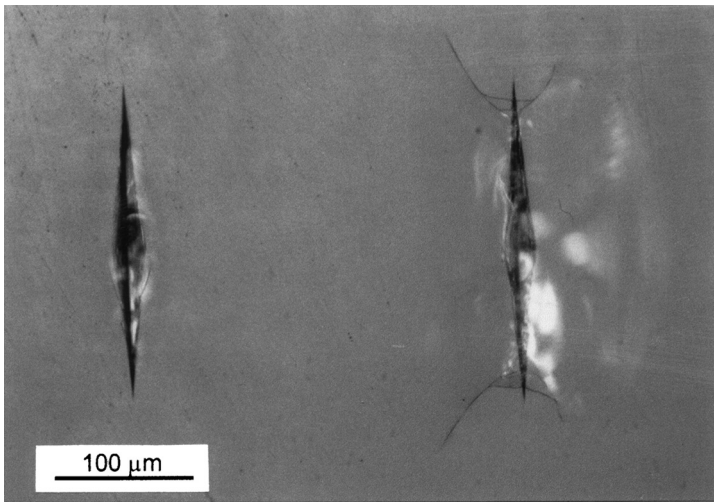


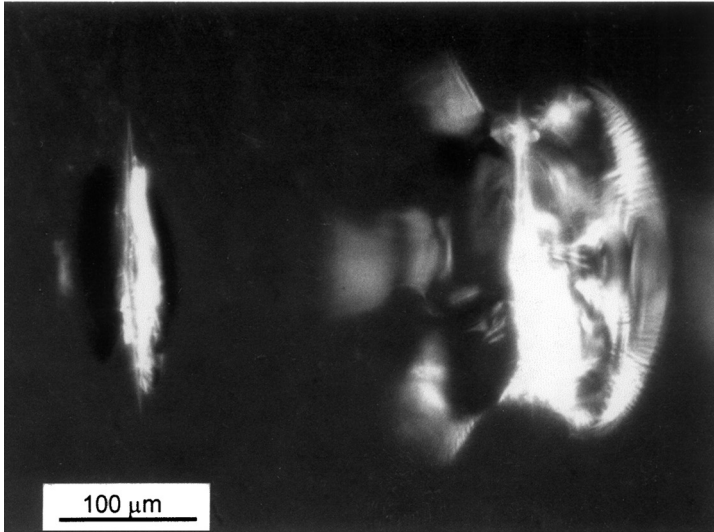
Figure 4. Borosilicate crown BK-7 data. (a) shows diagonal length. (b) shows hardness, and (c) shows P/d versus d .

the data bifurcated into two sets, both with small scatter. At 19.6 N, the cracked indentations were $7.0 \mu\text{m}$ longer than the uncracked indentations. The hardness of the uncracked indentations was 0.27 GPa (5.9 %) greater. Both of these differences are statistically significant.^k The cracked indentations had extended lateral and localized cracking, whereas the uncracked indentations had only a slight disturbance on the side of the impression. At loads of 29 N and above, nearly all indentations were cracked. Figure 5 illustrates adjacent cracked and uncracked indentations made

^k The two-tailed student's t statistic for small sample sizes was 5.93 for HK and 5.59 for d . Both of these are greater than the critical t ratio for 17 degrees of freedom at the .001 probability level ($t=3.97$).



(a)



(b)

Figure 5. Uncracked and cracked Knoop indentations in the BK-7 borosilicate crown glass at 19.6 N. Indentations should be spaced further apart for most testing purposes in order to avoid interference. (a) is a bright field and (b) dark field optical microscope illumination. The dark field photo reveals that some localized cracking occurs under the left indentations, but the extent of cracking is dramatically different. The cracked indentation is $7\ \mu\text{m}$ longer.

at 19.6 N. The $7\ \mu\text{m}$ length difference is not obvious from the photos, but is readily detected with the hardness machine microscope. Figure 4c shows a P/d versus d graph, which in accordance with equation 3 should have a slope of a_2 and an intercept of a_1 . The cracked and uncracked data sets have different lines, but if the data were combined into one set, there is no obvious inflection point since the transition of uncracked to cracked indentations occurs gradually over a range of loads.

Figure 6 shows that in contrast to the above results, cracking had negligible effect on hardness for the soda lime and borosilicate glasses. Lateral cracks developed in a few soda lime silicate indentations at 14.7 N and grew progressively more

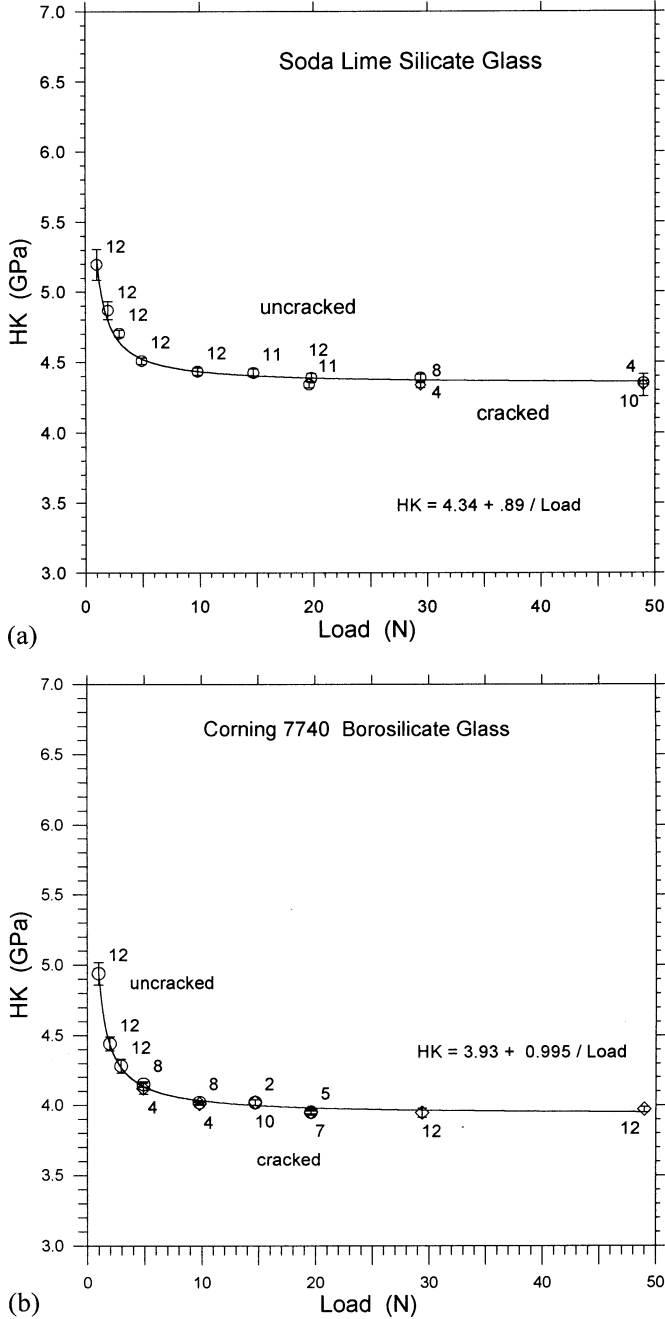


Figure 6. Soda lime silicate (a) and borosilicate 7740 (b) hardness data. Cracking had no effect upon hardness for either material.

prominent at larger loads. Significant lateral cracking and crushing occurred at 29.4 N and larger loads. All of the indentations had straight, sharp, and clear edges and bottoms. Shear bands could be discerned through the sides of the indentation. Despite all this damage, no median or radial cracks were detected on the indentation surface at loads to 49 N.

Cracking also had no effect upon apparent hardness for the borosilicate 7740 glass (Figure 6b). Very localized cracking was observed as close parallel circular arcs on the sides of the borosilicate glass indentations at loads of 4.9 N and above (Figure 7). These may be cone cracks, or possibly shear band cracks due to the large material displacement and uplift along the middle sides of the Knoop indentation. No median cracks were detected. Lateral cracks only formed at the largest loads (49 N) by which time the hardness-load curve had reached a plateau. One curious aspect of these indentations was a significant curvature and pinching in along the sides as shown in Figure 7. Significant elastic spring back probably caused the stiletto appearance.

The fused silica hardness was sensitive to cracking (Figure 8), but this glass was different than the other glasses. Extensive ring-like cone cracks formed on the indentation sides at 9.8 N and above. At larger loads numerous multiple concentric ring cracks appeared. The ring crack damage was much more severe than that detected in the 7740 borosilicate glass. No cracking was detected at the indentation tips. The difference in the average diagonal lengths between cracked and uncracked indentations was small: 1.1 μm and 1.9 μm at 4.9 N and 9.8 N indentation loads, respectively. A greater than normal number of indentations were made at these two loads to confirm this difference. Fragments around the indentation sides spalled off

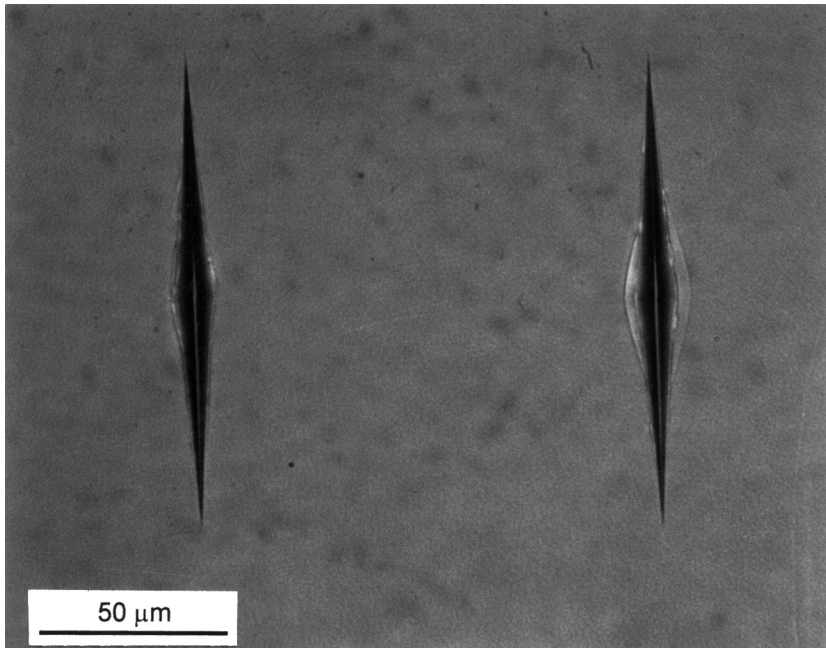


Figure 7. Indentations in the 7740 borosilicate glass. Minor cone or ring cracks form along the sides of the 4.9 N indentations, which have a noticeable pinching in of the sides.

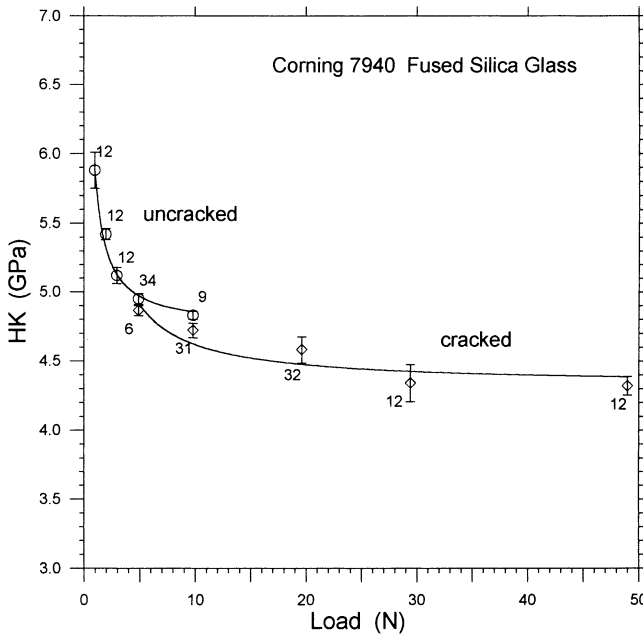


Figure 8. Hardness of fused silica. Cracking did affect hardness in this glass.

at loads of 14.7 N and greater. Major portions of the indentation were lost in some indentations at 19.6 N yet the tips were still intact on the surface. Three separate data sets were generated by the two hardness machines at 19.6 N for a total of 32 measurements. The results concurred. Some of these indentations still had intact indentation bottoms (the cross was still intact), but others had shattered or crushed bottoms. At 29.4 N, the indentation cores were shattered and extensive crushing around the indentation bottom had occurred. In a few indentations, a remnant of the indentation bottom edge was still visible, but skewed relative to the initial orientation of the indentation, attesting to massive displacement and uplift of the indentation bottom. Large scallop cracks popped off the indentation sides. Despite all this damage, the indentation tips were undisturbed and easy to read. No median cracks were detected even for the 49 N load. Cracked indentations were curved or pinched in the middle and did not have the well-defined pyramid shape, evidently a consequence of major elastic spring back of the indentation sides. Furthermore, unlike all the other glasses in this study, equation 4 did not fit the data quite so well and the data did not reach a distinct plateau by 15 N to 20 N.

4.2. Hardness at the Standard Load of 0.98 N

Table 1 has our HK values for 0.98 N (the customary load in the world hardness standards) as well as the manufacturers’ own data. The BK-7 borosilicate crown hardness at 0.98 N concurs since neither the manufacturer nor we applied a correction factor for optical resolution limits. In contrast, our hardnesses do not agree with the manufacturer’s listings for the first three glasses, possibly since the manufacturer

applied correction factors for the optical resolution limits in accordance with ASTM C 730.

4.3. Indentation Size Effect Parameters

The ISE curve parameters for equation 4 are given in Table 2. The plateau hardness at large loads is a'_2 . Single entries are shown for the two glasses for which cracking had no effect on hardness. Two entries are shown for the three glasses that were sensitive to cracking. The uncracked borosilicate crown data did not fit equation 4 very well, so no a'_1 parameter is listed and only an approximate estimate of a'_2 is shown.

The hardness of the fused silica at 1.96 N (5.42 GPa \pm 0.04 GPa) almost exactly matches the 5.41 GPa reported by Hirao and Tomozawa¹¹ for a 20 second dwell time in air. Li and Bradt⁴ analyzed Hirao and Tomozawa's results that were obtained in a variety of environments and concluded that the best estimate for the load independent hardness, a'_2 , for fused silica was 5.30 GPa. Individual data sets for tests in different environments produced estimates from 4.88 to 5.30 GPa with uncertainties (one standard deviation) of \approx 10%. Our new estimate of a'_2 for uncracked indentations (4.74 GPa) is a little below this range. This is because our estimate is based on data from a much broader range of larger indentation loads than utilized in the former studies that had a maximum of only 2 N.

5. DISCUSSION

These findings confirm that cracking affects the hardness response of some but not all glasses. Figure 9 shows the general behavior. Cracking begins to affect HK at about the load where the ISE curve reaches a plateau. Swain and Wittling¹ suggested that median crack opening could account for larger penetrations. Our work suggests that lateral material displacement and lateral cracking can also facilitate greater indentation penetration. The cracking effect on HK can be easily detected with careful but routine testing, but is small and probably has been ignored or lost in data scatter in earlier studies. Many of the earlier studies utilized microhardness

Table 2. Effect of cracking, ISE curve parameters, and brittleness.

| Glass | Did cracking affect HK? | Primary Crack Type | Data set | a'_1 (GPa · N) | a'_2 (GPa) | Brittleness, B ($\times 10^{-8} \text{ m}^{-1}$) |
|-------------------------|-------------------------|--------------------|-----------|------------------|---------------|--|
| Fused silica 7940 | Yes | Ring / Cone | uncracked | 1.16 | 4.74 | 6.28 |
| | | | cracked | 2.90 | 4.32 | – |
| Borosilicate 7740 | No | Cone / Other | – | 1.00 | 3.93 | 4.27 |
| Aluminosilicate 1723 | Yes | Lateral | uncracked | 1.77 | 5.13 | 6.12 |
| | | | cracked | 2.16 | 4.94 | – |
| Borosilicate Crown BK-7 | Yes | Lateral | uncracked | – | \approx 4.9 | 5.43 |
| Soda lime silicate | No | Lateral | cracked | 2.45 | 4.51 | – |
| | | | – | 0.89 | 4.34 | 5.40 |

– Not determined, or not applicable.

machines with load limits of only 9.8 N or 19.6 N and thus missed the onset of cracking. Many didn't reach the hardness plateau which usually occurs at 10 N or greater. Some investigators arbitrarily disregarded cracked indentations.

Several factors could explain why cracking affected the hardness of some glasses and not others. The soda lime and borosilicate glasses were the two softest glasses in the study and were not affected by cracking. They also had the lowest elastic moduli. Evidently the harder and more rigid the glass is, the more likely that cracking affects Knoop hardness.

The timing of the crack formation may also determine whether the cracking affects hardness. Cracks that form during load application probably increase the local compliance of the material and enable the indenter to sink in deeper. Cracks which form during load *removal* probably do not affect the Knoop indentation tip positions and hence the indentation diagonal length. Cook and Pharr³³ observed Vickers indentation cracking sequences in various glasses and ceramics. Their study and ours have four glasses in common. If the same cracking sequences they detected for Vickers indentations are the same as for Knoop indentations, then the timing of the crack formation would account for our results in only two of the four cases, however. Cracking during loading in the fused silica could account for our longer indentations. Cracking during unloading could account for why the soda lime glass cracking did not affect the diagonal lengths and hardness. The Vickers cracking sequences do not match the observed effect on Knoop hardnesses for the other two glasses in common with our study (aluminosilicate and borosilicate). Perhaps the difference in indenter geometries causes different fracture sequences and effects upon apparent hardness.

Arora et al.⁴⁰ characterized glasses into so-called "normal" and "anomalous" categories based upon the behavior during Vickers indentation. "Anomalous" glasses are silica rich and densify during Vickers indentation. Once they do crack, they form ring cracks and steep, deeply penetrating cone cracks. "Normal" glasses

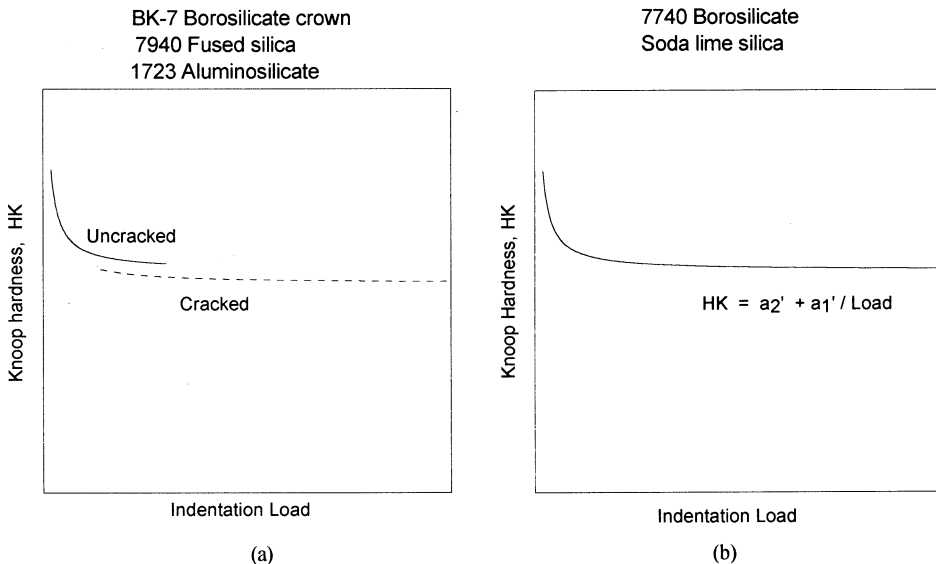


Figure 9. Cracking may (a) affect the Knoop ISE trend, or as shown in (b), may not affect the ISE.

have greater network modifier content and tend to form shear deformation bands and shear micro fissures. Of the two “anomalous” glasses in our study (fused silica and borosilicate), only the former glass exhibited Knoop hardness sensitivity to cracking. Of the three “normal” glasses in this study, two were sensitive to cracking (borosilicate crown, aluminosilicate) and one (soda lime silicate) was not. Thus the normal and anomalous Vickers categorization scheme does not correlate with the present Knoop results

An energy model may account for the different behaviors. Equation 3 may be expressed with units of energy by multiplying both sides by d :

$$Pd = a_1d^2 + a_2d^3 \quad (8)$$

The term Pd is proportional to the external work done by the indenter, $\int Pd\ell$, where ℓ , the indenter penetration depth, is proportional to d . A number of investigators have attempted to correlate surface energy or fracture processes to the a_1d^2 term.^{1,2,4,5,6,8,11,36,37} The a_2d^3 term, on the other hand, is considered to be the “work of permanent deformation”^{5,12,37} or the “volume energy of deformation.”^{2,4,5} In their work on the Knoop hardness of fused silica, Hirao and Tomozawa¹¹ showed a very strong ISE and argued that the Knoop a_1 term was related to the propensity of the glass to crack. Cracking propensity was estimated from a few *Vickers* experiments at loads only up to 1.2 N, however, and Knoop indentation cracking was not actually evaluated. Table 2 shows that the three glasses in which cracking altered Knoop hardness did indeed have larger a_1 values.

A handful of other studies have detected an effect of cracking on the ISE. Fröhlich et al.³⁹ noted distinct cracking events effects during recording Vickers hardness experiments in germanium single crystals, but their work was limited to a maximum load of 2 N. The load versus displacement traces showed discrete load drop offs when cracks popped in and they also associated the a_1 term to cracking and the surface energy of the indentation. Most instrumented (depth sensing) hardness experiments do not discern the onset of cracking during loading. Gahm³³ obtained a subtle shift in a peak $P^{1/2}$ versus final d curves for two glasses once cracking commenced, but these were at very light loads of 0.5 N. At much greater loads up to 40 N, Zeng and Rowcliffe⁴¹ observed a significant increase in the elastic compliance of Vickers indentations during unloading once significant cracking had occurred. They even proposed a damage parameter based upon the extent of the compliance change. Yoo et al.⁴² reported a fascinating example of how cracking contributes to the ISE in MgO single crystals. At low loads, deformation was controlled by dislocation slip and pileups. At larger loads, cracks acted as dislocation sinks that relieved the pileups around the indentation. This led to enhanced plasticity and lower hardness.

A study of Vickers hardness of polycrystalline ceramics revealed that cracking may cause critical transition points in the Vickers ISE trends.⁸ The transition point was associated with extensive cracking in and around the indentation and a shift in the energy balance during indentation. Different ratios of the indentation work are expended on volumetric deformation and surface fracture processes above and below the transition point. The transition point was very distinct for brittle materials such as silicon carbide. The Vickers hardness transition point was related to a new index of ceramic brittleness defined as:⁸

$$B = \frac{H E}{K_{Ic}^2} \propto \frac{H}{2\gamma_f} \quad (9)$$

where H is hardness at the plateau, E is the elastic modulus, K_{Ic} is the fracture toughness and γ_f is the fracture surface energy. Hardness has units of energy per unit volume and may be considered to be the work to deform a unit volume, whereas γ_f is the work to create unit surface area. B is a ratio of volume deformation energy to the surface fracture energy. Table 2 lists values of B for the five glasses using the uncracked Knoop plateau hardness value a_2' for H in equation 9. With the exception of the borosilicate crown glass, the more brittle the glass (higher B), the more likely cracking alters the hardness.

Is a cracked indentation a valid indentation? Most researchers believe that cracked indentations do not yield the correct hardness values. Most standard test methods call for the rejection of cracked indentations. ASTM C 1326 and ISO 14705 for ceramics⁴³ allow limited cracking and furnish guidance on interpretation.¹ ISO 9385 for glass cautions against excessive fracture. On the other hand, to the extent that hardness is deemed a “measure of resistance of penetration by a prescribed indenter under prescribed conditions,” then cracked indentations are legitimate and simply manifest a different material response to indenter penetration. Indeed, sectional views of indentations shown by Hagan and Swain^{17,18} clearly show that micro fissuring and cracked shear bands underneath indentations are important components of deformation even at low loads. One remarkable aspect of the present study is that despite the dramatic cracking at large loads, in no case did it interfere with the ability to see and measure the Knoop tip-to-tip distances since the tips extend well beyond the damage zones. Median and radial cracks from the tips were only detected in a few specimens at the largest loads and were usually easily distinguished from the indentation.

Fifty-five years ago Thibault and Nyquist¹³ called attention to the effect of cracking on hardness in their masterful paper on the metrology of Knoop hardness measurements. They listed six categories of cracking from no cracking (class I) to pronounced cracking such that large portions of the specimen were chipped away (class 6). They relied on direct examination of the indented surface as was done in the present study. Cracking had no measurable effect on the Knoop hardness of silicon carbide or topaz for up to class 3 severity: large amount of subsurface cracking, but none on the surface; or minor subsurface cracking and slight surface cracking. Cracking altered results for topaz once it reached class 4 severity: a large amount of subsurface cracking accompanied by slight to moderate surface cracking. Cracked indentations were longer than uncracked indentations and the apparent hardness was consequently lower. They concluded that Knoop hardnesses based on class 1-3 indentations were not affected by fracturing, class 4 and 5 indentations should be avoided, and class 6 indentations should not be used at all.

Notwithstanding claims to the contrary, the evidence is compelling that the ISE is real and not due to a single phenomenon. Other studies have presented strong evidence that experimental errors (e.g., optical resolution limitations), frictional

¹ Limited cracking was acceptable provided that it did not alter the indentation size compared to uncracked indentations, did not remove portions of the indentation, nor obscure or broaden the indentation tips to the extent that tip location could not be reliably assessed.

forces, environmental effects, or various material responses including elastic recovery, densification, plastic flow, and viscous flow contribute to the ISE. This paper has demonstrated that cracking also can alter the hardness versus load trends. If the cracking is ignored and combined data analyzed, the increased scatter will shift the plateau hardness value by up to 5 %.

The standard test methods for Knoop indentation hardness of glass have specifications that warrant some comment. The correction factor for diagonal length, $7\lambda/2NA$, for optical resolution limitations that is included in ASTM C 730 may need review. This correction factor adds 3 μm or more to the length of an indentation irrespective of its size and can drastically change the hardness number. Uncertainty over whether to add the correction factor or not has caused confusion in reported glass hardness values. For example, the manufacturer of the borosilicate crown glass used in this study formerly published *dual hardness tables* for their glasses.⁴⁴ Hardness values for the borosilicate crown glass were 5.88 GPa without the 3 μm correction and 5.29 GPa with the correction, a difference of 11%! Our limited investigations²⁸ suggest that a $7\lambda/2NA$ correction is not needed with 40X or 50X objective lenses, but a correction is needed for lower power lenses especially for glasses.

The formal glass hardness standard test methods all recommend 0.98 N (100 gf) as the standard test force. Although this is a small load it produces moderate-sized ($\approx 50 \mu\text{m}$) indentations since glasses are not especially hard. Nevertheless, it is merely one point on the very steep portion of the ISE curve. Hardness at a single load may have appeal for routine purposes, but clearly much more useful information is overlooked. Perhaps the glass hardness standards should recommend measurements over a broader load range. ISO 9385 takes a step in this direction by recommending multiple indentation loads.

One last matter deserves a few comments. Cracking appears to affect Vickers and Knoop indentations in different ways as illustrated in Figure 10. Extensive cracking underneath Vickers indentations seem to cause the ISE to have a transition point to a constant hardness plateau as described by Quinn and Quinn.⁸ The effect is most pronounced for very brittle ceramics. On the other hand, the present study shows that cracking around Knoop indentations causes the ISE trend to shift to lower hardness values, but only in some materials. A possible explanation for the differences may be made with reference to the schematics in Figure 10.

At low Knoop indentation loads, cracking damage may be confined to a small zone underneath the indentation. Once significant cracking occurs, material is displaced from underneath the indentation. The indenter sinks deeper into the material, but then becomes supported on its ends like a bridge. The indentation develops a longer diagonal length ($2\Delta d$) than if the cracking had not occurred.

Alternatively, for Vickers indentations, at low loads cracking may also be limited to microcracking underneath the indentation. With increasing load, the extent and volume of the cracking increases. Above a critical load, the micro fissuring damage underneath the indentation may become saturated and reach up to the surface along the sides of the indentation. Material displacement and shear may cause significant uplift on the surface. At this point the balance of indentation energy expended on volumetric and surface deformation damage processes may change. Van der Swagg and Hagan⁴⁵ showed pictures of just such a progression of damage underneath conical indentations as indentation load increased in fused silica and

soda lime glass. Figure 11 shows just how pronounced the uplift may be around indentations.

Hagan’s method of cleaving through an indentation is an effective way to study damage beneath.^{17,18,45,46} Future work could apply his approach to help correlate cracking damage to shifts in the ISE trends for Knoop and Vickers hardness.

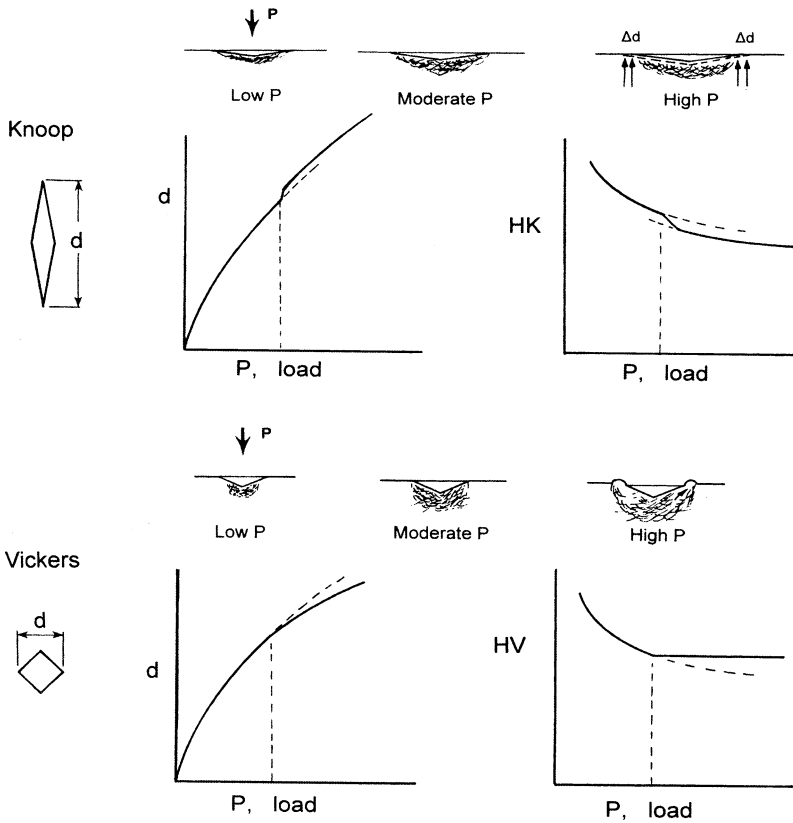


Figure 10. The effect of cracking on the ISE trends for Knoop (top row) and Vickers (bottom row) hardness.

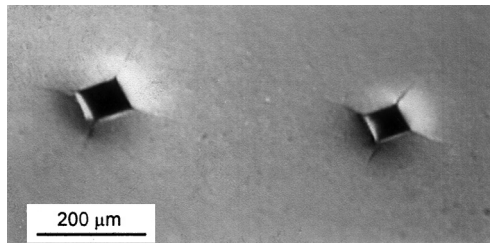


Figure 11. Illustration of the massive uplift on the sides of 98 N and 74 N Vickers indentations in silicon nitride. The specimen is strongly tilted and was photographed by a stereo microscope. The magnification bar is only approximate.

6. CONCLUSIONS

Cracking around the indentation affects the Knoop hardness and ISE in some glasses. Cracked indentations are larger than uncracked indentations by as much as 10 μm , which reduces the Knoop hardness by 5%. Harder, more rigid glasses are more apt to be affected by cracking, but the timing of the crack formation or the brittleness of the glasses may also be contributing factors. Cracking is not the sole cause of the ISE, but does contribute to the trend and affects the plateau hardness.

Measurements of Knoop hardness over a broad load range are preferable to a measurement at a single load. Care must be taken to account for optical resolution limitations and diagonal length underestimates when using low power optical microscope objective lenses.

REFERENCES

1. M. Swain and M. Wittling, Indentation Size Effects for Brittle Materials: Is There A Simple Fracture Mechanics Explanation, in *Fracture Mechanics of Ceramics, Vol 11*, eds. R. C. Bradt, D. P. H. Hasselman, D. Munz, M. Sakai, and V. Y. Shevchenko, (Plenum Press, NY, 1996), pp. 379–388.
2. H. Li and R. C. Bradt, The Microhardness Indentation Size-Load Effect (ISE) in Hard Ceramic Materials, *J. Hard Mat.*, **3** (3–4) 403–419 (1992).
3. H. Li and R. C. Bradt, The Effect of Indentation-Induced Cracking on the Apparent Microhardness, *J. Mat. Sci.*, **31** 1065–1070 (1996).
4. H. Li and R. C. Bradt, The Indentation Load/Size Effect and the Measurement of the Hardness of Vitreous Silica, *J. Non-Cryst. Sol.*, **146** 197–212 (1992).
5. T. Sakai, A. Ghosh, and R. C. Bradt, The Indentation Fracture Resistance of Self Reinforced Mullites, in *Fracture Mechanics of Ceramics, Vol. 10*, ed. R. C. Bradt et al., (Plenum Press, NY, 1992), pp. 119–132.
6. H. Li and R. C. Bradt, The Microhardness Indentation Load/Size Effect in Rutile and Cassiterite Single Crystals, *J. Mater. Sci.*, **28** 917–926 (1993).
7. H. Li, A. Ghosh, Y. H. Han, and R. C. Bradt, The Frictional Component of the Indentation Size Effect in Low Hardness Testing, *J. Mater. Res.*, **8** (5) 1028–1032 (1993).
8. J. B. Quinn and G. D. Quinn, Indentation Brittleness of Ceramics: A Fresh Approach, *J. Mater. Sci.*, **32** 4331–4346 (1997).
9. A. L. Yurkov and R. C. Bradt, Load Dependence of Hardness of SIALON Based Ceramics, in *Fracture Mechanics of Ceramics, Vol 11*, Eds. R. Bradt et al., (Plenum Press, NY, 1996), pp. 369–378.
10. P. M. Sargent, Use of the Indentation Size Effect on Microhardness for Materials Characterization, in *Microindentation Techniques in Materials Science and Engineering*, ASTM STP 889, eds. P. J. Blau and B. R. Lawn, (ASTM, West Conshohocken, PA, 1986), pp. 160–174.
11. K. Hirao and M. Tomozawa, Microhardness of SiO₂ Glass in Various Environments, *J. Amer. Ceram. Soc.*, **70** (7) 497–502 (1987).
12. G. H. Frischat, Load-Independent Microhardness of Glasses, in *Strength of Inorganic Glasses*, ed. C. R. Kurkjian, (Plenum Press, NY, 1986), pp. 135–145.
13. N. Thibault and H. Nyquist, The Measured Knoop Hardness of Hard Substances and Factors Affecting Its Determination, *Trans. A.S.M.*, **38** 271–330 (1947).
14. B. R. Lawn and D. B. Marshall, Hardness, Toughness, and Brittleness, An Indentation Analysis, *J. Am. Ceram. Soc.*, **62** (7–8) 347–350 (1979).
15. D. B. Marshall and B. R. Lawn, Indentation of Brittle Materials, in *Microindentation Techniques in Materials Science and Engineering*, ASTM STP 889, eds. P. J. Blau and B. R. Lawn, (ASTM, West Conshohocken, PA, 1986), pp. 26–46.
16. B. R. Lawn, A. G. Evans, and D. B. Marshall, Elastic/Plastic Indentation Damage in Ceramics: Median/Radial Crack System, *J. Am. Ceram. Soc.*, **63** (9–10) 574–581 (1980).
17. J. T. Hagan, Deformation and Cracking Modes Around Plastic Indentations in Glasses, *Verres Refract.*, **35** (2) 306–314 (1981).

18. J. T. Hagan and M. V. Swain, The Origin of Median and Lateral Cracks Around Plastic Indents in Brittle Materials, *J. Phys. D: Appl. Phys.*, **11** 2091–2102 (1978).
19. F. Knoop, C. Peters, and W. Emerson, A Sensitive Pyramidal-Diamond Tool for Indentation Measurements, *J. Res. Nat. Bur. Stds.*, **23** 39–61, July 1939.
20. C. G. Peters and F. Knoop, Resistance of Glass to Indentation, *Glass Ind.*, **20**, 174–176, May 1939.
21. ASTM C 730–98, Standard Test Method for Knoop Indentation Hardness of Glass, *ASTM Annual Book of Standards*, Vol 15.02, ASTM, West Conshohoken, PA, 1999.
22. DIN 52333, Knoop Hardness Testing, Glass and Glass Ceramic, German Institute for Standards, Berlin, 1987.
23. ISO 9385, Glass and Glass-Ceramics, Knoop Hardness, International Organization for Standards, Geneva, 1990.
24. G. D. Quinn and J. A. Salem, Effect of Lateral Cracks Upon Fracture Toughness Determined by the Surface Crack in Flexure Method, *J. Am. Ceram. Soc.*, **85** (4) 873–80 (2002).
25. S. M. Wiederhorn and D. E. Roberts, Fracture Mechanics Study of Skylab Windows, NBS Report 10 892, National Bureau of Standards, Washington, 1972.
26. D. C. Boyd and D. A. Thompson, Glass, in *Encyclopedia of Chemical Technology*, Vol. 11, 3rd ed., (Wiley, NY, 1980), pp. 807–880.
27. R. Gettings, G. Quinn, W. Ruff, and L. Ives, New Hardness Standard Reference Materials (SRM's) for Advanced Ceramics, *Ceram. Eng. and Sci. Proc.*, **15** (5) 717–826 (1994).
28. G. D. Quinn, P. Green, and K. Xu, Cracking and the Indentation Size Effect for Knoop Hardness of Glasses, accepted by *J. Amer. Ceram. Soc.*, Nov 2002.
29. ASTM Standard E 384–89 (1997), Standard Test Method for Microindentation Hardness of Materials, *ASTM Annual Book of Standards*, Vol. 3.01, ASTM, West Conshohoken, PA, 2001.
30. ASTM Standard C 1326–89 (1996), Standard Test Method for Knoop Indentation Hardness of Advanced Ceramics, *ASTM Annual Book of Standards*, Vol. 15.01, ASTM, West Conshohoken, PA, 2001.
31. B. W. Mott, *Micro-Indentation Hardness Testing*, (Butterworth, London, 1955).
32. L. Tarasov and N. Thibault, “Determination of Knoop Hardness Numbers Independent of Load,” *Trans. A.S.M.*, **38** 331–353 (1947).
33. J. Gahm, Neuere Erkenntnisse zur Mikro-Härte, *VDI Berichte*, Nr. 160, 25–41 (1972).
34. R. F. Cook and G. M. Pharr, Direct Observation and Analysis of Indentation Cracking in Glasses and Ceramics, *J. Am. Ceram. Soc.*, **73** (4) 787–817 (1990).
35. T. Wilantewicz and J. R. Varner, The Effect of Contact Parameters on the Crack Initiation Behavior of Glasses, in *Fractography of Glasses and Ceramics, IV*, Eds. J. R. Varner and G. D. Quinn, Ceramic Transactions Vol. 122, (American Ceramic Society, Westerville, OH, 2001), pp. 403–416.
36. H. Bückle, *Mikrohärteprüfung*, (Berliner Union Verlag, Stuttgart, 1965).
37. R. Mitsche, Über die Eindringhärte Metallischer Fest und Lockerkörper, *Osterr. Chem. Z.*, **49** 186 (1948).
38. E. O. Bernhardt, On Microhardness of Solids at the Limit of Kick's Similarity Law, *Z. Metallkunde*, **33** 135–144 (1941).
39. F. Fröhlich, P. Grau, and W. Grellmann, Performance and Analysis of Recording Microhardness Tests, *Phys. Stat. Sol. (a)*, **42** 79–89 (1977).
40. A. Arora, D. B. Marshall, B. R. Lawn, Indentation Deformation/Fracture of Normal and Anomalous Glasses, *J. Noncryst. Sol.*, **31** 415–428 (1979).
41. K. Zeng and D. Rowcliffe, Analysis of Penetration Curves Produced by Sharp Indentation on Ceramic Materials, *Phil. Mag. A*, **74** (5) 1107–1116 (1996).
42. K. C. Yoo, R. G. Rosemeier, W. L. Elban, and R. W. Armstrong, X-ray Topography Evidence for Energy Dissipation at Indentation Cracks in MgO crystals, *J. Mat. Sci. Ltr.*, 560–562 (1984).
43. ISO 14705 (2000) Fine Ceramics (Advanced Ceramics, Advanced Technical Ceramics) – Test Method for Hardness of Monolithic Ceramics at Room Temperature, International Organization for Standards, Geneva, 2000.
44. *Optical Glass*, Schott Glass Technologies, Duryea, PA, Catalog 3111/1e USA III, 1984.
45. S. Van der Zwagg and J. T. Hagan, Deformation Processes in Silica and Different Soda-Lime Glasses under Conical Indentations, in *Strength of Inorganic Glass*, ed. C. Kurkjian, (Plenum Press, NY, 1986) pp. 147–151.
46. J. T. Hagan, Shear Deformation Under Pyramidal Indentations in Soda Lime Glass, *J. Mat. Sci.*, **15** 1417–1424 (1980).

SLOW CRACK PROPAGATION IN CERAMICS AT THE NANO- AND MICRO-SCALE: EFFECT OF THE MICROSTRUCTURE

J. Chevalier¹ and G. Fantozzi¹

A review of Slow Crack Growth (SCG) results obtained for different oxide and non-oxide ceramics at ambient temperature, under different environments, is presented. They are analyzed on the basis of their crack velocity (V) versus stress intensity factor (K_I) diagrams. The aim of this paper is to consider mechanisms acting at the crack tip (i.e. at the nano-scale) and microstructural mechanisms occurring in the crack wake or at the crack front (i.e. at the micro-scale) to rationalize the approach of SCG.

Fine grained, alumina, zirconia, silicon nitride and silicon carbide ceramics are first compared as model materials with low amount of toughening. Results are all consistent with a stress corrosion mechanism acting at the crack tip. They show that the higher the ionic to covalent ratio, the higher the susceptibility to stress corrosion by water. Some materials doped with amounts of silica rich phases are analyzed. They exhibit different behavior depending on the location of a glassy phase at grain boundaries or triple points. An interesting aspect on a practical point of view is the presence of a threshold stress intensity factor below which no propagation occurs.

The effect of microstructure on V - K_I laws can be investigated by modifying the grain size of non transformable ceramics (e.g. alumina) and the grain size or the amount of stabilizing agent in the case of transformable ceramics (e.g. zirconia or zirconia toughened alumina). The effect of bridging or transformation toughening on V - K_I curves is discussed. If the reinforcement at the microscopic scale is correctly

¹ G.E.M.P.P.M. (U.M.R. C.N.R.S. 55 10) I.N.S.A. de Lyon, 69621 Villeurbanne Cedex France

taken into account, intrinsic V - $K_{I\text{tip}}$ curves, only dependent of the chemical bounds broken at the crack tip, are obtained.

INTRODUCTION

Delayed fracture of brittle materials was first reported by Grenet [1] in glass. Later, Orowan [2] reported such a sub-critical crack growth by observing a strength reduction of a glass in air compared to that measured under vacuum which he attributed to a reduction of fracture energy. Following this work, different systematic studies have been conducted on glass, alumina single crystals and mica [3–6]. As a general trend, they have shown that a unique relation could be established, for a given environment, between the velocity (V) and the stress intensity factor (K_I) with three different stages attributed to distinct mechanisms. In the first stage (Region I, for low velocities), crack propagation is limited by the thermally activated reaction kinetic between the ceramic and corrosive molecules. These molecules were clearly identified in the case of silica as H_2O [7]. Region II, at intermediate velocities, depends on environment, but is much less sensitive to K_I . This region is often attributed to gaseous diffusion along the crack interface. Region III, for high velocities represents the fracture of ceramic bonds without the need of environmental species. Although mentioned by Wiederhorn [8] in glass, the occurrence of a threshold has not always been clearly identified. Recently, Wan et al. [9,10] considered this point and the presence of a threshold was definitely shown in mica. These authors and Maugis [11] considered that the threshold corresponds to an equilibrium with a null crack velocity. In this respect, crack healing should occur below the threshold, which was partly shown in the case of mica [10]. The threshold, in this sense should correspond to the Griffith criterion for crack propagation. However, the presence of a threshold is still in debates in the ceramic society.

To the authors knowledge there is no such detailed study for polycrystalline ceramics, partly because of the scattering caused by the microstructure, which leads to a more distributed fracture. However, a similar general trend with 3 propagation stages has been observed in alumina, mullite, silicon nitride, zirconia etc. [12]. Thus, slow crack growth in polycrystalline ceramics is also attributed to stress corrosion, despite a lack of experimental evidence. The presence of a threshold is even less clarified. In polycrystalline ceramics, R-curve, which traduces an increase of crack resistance with crack extension, can also play a significant role on the sub-critical crack propagation and complicates the slow crack growth analysis [13–15]. The influence of an R-curve behavior has been investigated by different authors. This leads to a progressive shift of the crack propagation to lower velocities as crack resistance increases. Depending on the crack length measurement with respect to the rising part of the R-curve, either a complete shift or a higher slope can be obtained [13,14]. Fett et al. [15] showed that a crack velocity decrease could be observed at the beginning of the propagation of small cracks in alumina. Different microstructural mechanisms can play a role on crack velocities, the most important in ceramics being crack bridging and transformation toughening.

This is the aim of this paper to consider mechanisms acting at the crack tip (i.e. at the nano-scale) and microstructural mechanisms occurring in the crack wake or at the crack front (i.e. at the micro-scale) to rationalize the approach of Slow Crack

Growth (SCG). The knowledge of the respective influence of nano- and micro-scale mechanisms during SCG allows to define strategies for better SCG resistant materials.

1. SCG AT THE NANO-SCALE LEVEL : STRESS CORROSION AT THE CRACK TIP

2.1. Stress Corrosion Equations

Stress corrosion by water at the crack tip is the likely mechanism responsible for crack propagation in ceramics. In this respect, it is interesting to develop briefly the model proposed by Lawn [16] for single crystals or glasses. This model is based on a thermally activated reaction of water and ceramic to form complex. For low crack velocity (stage I), V is given by :

$$V_I = 2 \cdot \nu_0 \cdot a_0 \cdot \exp\left(-\frac{E_{oI}}{kT}\right) \cdot \sinh\left[\frac{\alpha_I \cdot (G^* - 2\gamma)}{kT}\right] \quad (1)$$

where ν_0 is the fundamental reaction frequency ($\nu_0 = kT/h$, with h Planck constant and k Boltzman constant), E_{oI} the activation energy of the reaction, G^* the mechanical energy due to the stresses at the crack tip, a_0 is a characteristic bond separation, α_I is an activation area and γ_e is the fracture surface energy in the presence of water molecules. It is to note that G^* can be easily related to the stress intensity factor at the crack tip, $K_{I\text{tip}}$, by : $G^* = K_{I\text{tip}}^2/E$, where E is the Young's modulus.

In gaseous environment, crack velocity can be limited by a transport of corrosive molecules to the crack tip and is given by:

$$V_{II} = \frac{64 \cdot G^*}{3 \cdot \pi \cdot E \cdot a_0 \cdot \ln\left(\frac{1}{a_0}\right)} \cdot \frac{a_0^3 \cdot p_E}{\sqrt{(2 \cdot \pi \cdot m \cdot kT)}} \quad (2)$$

where E is the Young modulus for zirconia ceramic (220 GPa), p_E the water pressure, m the mass of water molecules and l is the crack opening displacement. Gaseous diffusion and reaction occur in series so the overall crack velocity is given by:

$$\frac{1}{V} = \frac{1}{V_I} + \frac{1}{V_{II}} \quad (3)$$

For higher crack velocities, fracture occurs under vacuum conditions and the crack speed is given by :

$$V_{III} = 2 \cdot \nu_0 \cdot a_0 \cdot \exp\left(-\frac{E_{oIII}}{kT}\right) \cdot \sinh\left[\frac{\alpha_{III} \cdot (G^* - 2\gamma_s)}{kT}\right] \quad (4)$$

with E_{oIII} the activation energy for the fracture of zirconia bonds, α_{III} an activation area and γ_s is the fracture surface energy in the absence of water molecules (under vacuum).

Equations (1) and (4) are consistent with the basic Griffith theory or its generalization with the Dupré work of adhesion. A crack propagates when:

$$G^* = R = 2\gamma_s \quad \text{under vacuum} \tag{5a}$$

$$G^* = R_e = 2\gamma_e \quad \text{in a given environment} \tag{5b}$$

with $\gamma_e < \gamma_s$. Thus the equilibrium of a given crack may be changed either by variation of the loading or by the environmental conditions.

The initial Griffith criteria corresponds therefore to this point of equilibrium. When we move above or below this equilibrium point, the crack velocity increases (backward or forward). This is the theoretical meaning of a threshold in polycrystalline ceramics, below which no propagation occurs (ideally below which a crack heals).

Figure (1) represents examples of V-K_I curves in a polycrystalline zirconia ceramic, which exhibit the typical pattern of SCG due to stress corrosion at the crack tip, including the presence of thresholds under vacuum, water and air conditions. The threshold, K_{I0}, often observed on macro-cracks was questioned because of the differences observed between the behavior of micro- and macro-cracks in polycrystalline ceramics [15]. The results obtained in figure (2) for the same polycrystalline zirconia show that the threshold obtained for macro- (i.e. by Double Torsion) and micro- cracks (indentations) are in agreement. It is of course possible that reinforcement mechanisms, discussed below, can change significantly the value of the threshold if they lead to a R-Curve behavior.

2.2. Influence of the Ionic/Covalent Ratio on Stress Corrosion

With the aim of clarifying the processes involved in stages I and II an idealised representation of a proposed reaction between water and a strained ceramic bond at the crack tip has been proposed [7,16]. Reaction steps involve: (1) adsorption of water to ceramic bond, (2) reaction involving simultaneous proton and electron transfer, and (3) formation of surface hydroxyls. The susceptibility of a given ceramic to the mechanism of stress assisted corrosion by water, hence to SCG, lies in its ability to react with water and to dissociate. Glass was studied in the past as a model ionic material with a high susceptibility to SCG, because stressed Si-O-Si bounds

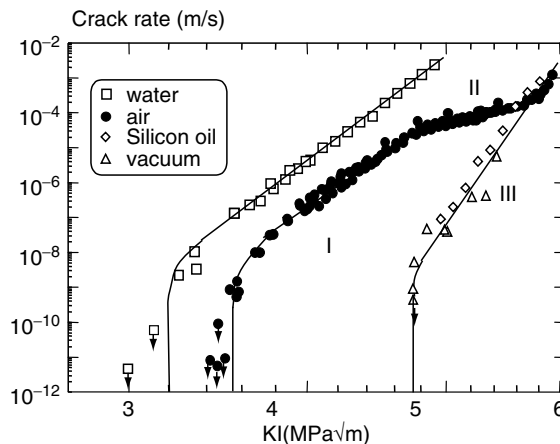


Figure 1. V-K_I diagram of a polycrystalline zirconia ceramic (from [17]).

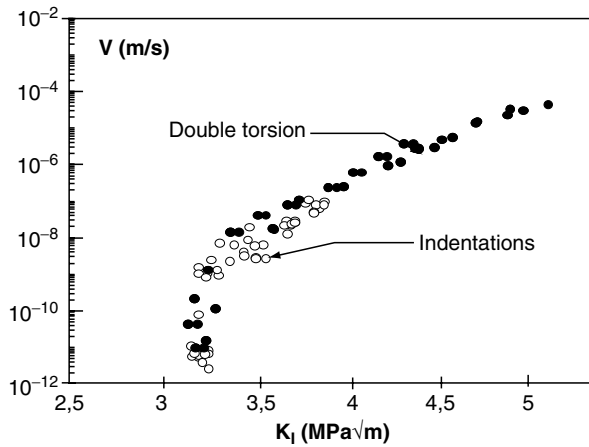


Figure 2. Threshold stress intensity factor determined by two different methods on polycrystalline zirconia (from ref. [17]).

Table 1. Ionic fraction and susceptibility to SCG for different ceramics: in general, the higher the ionic fraction, the higher the intrinsic susceptibility to SCG.

| | ZrO ₂ | SiO ₂ | Si ₃ N ₄ | SiC |
|---|------------------|------------------|--------------------------------|------|
| Ionic fraction | 0,6 | 0,51 | 0,30 | 0,11 |
| K _{I0air} /K _{I0vacuum} | ~ 0,6 | ~ 0,6 | ~ 0,9 | ~ 1 |

could be easily broken by the combined effect of stresses and adsorption of water. This is also the case of zirconia, very prone to SCG [17]. Figure (3) represents schematically the susceptibility of different ceramics to SCG in a V-K_I/K_{I0vacuum} diagram. Very fine microstructures were chosen to avoid any R-Curve effect which would perturb the analysis. Table (1) represents the ionic fraction for different ceramics compared to the ratio of threshold obtained in air to that obtained under

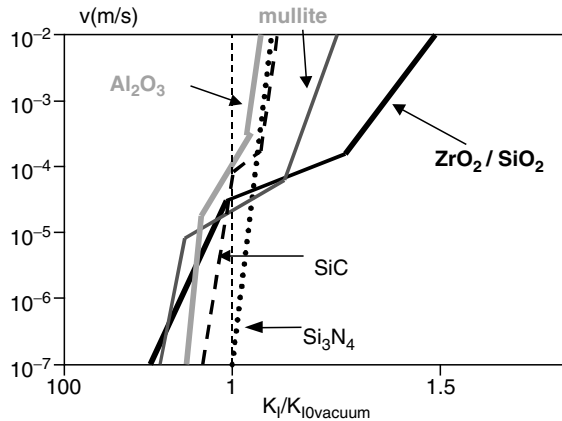


Figure 3. Susceptibility to SCG of different fine grained ceramics. SiO₂ shown for comparison.

vacuum conditions. From these results, it can be argued that the intrinsic susceptibility of a given ceramic to SCG is related to its atomic structure.

2.3. Effect of a Glassy Phase on SCG in Ceramics

The presence of a glassy phase can have a profound effect on the properties of polycrystalline ceramics. Such glassy phases in ceramics sometimes result from silica rich impurities but they can also be added during processing route in order to obtain special physical or mechanical properties. For instance, the addition of glassy phases in yttria doped zirconia ceramics is a way to increase their superplastic behavior [18,19] or their resistance to ageing [20,21]. The common feeling is that the presence of glassy phases in ceramics leads to a decrease of their crack resistance, because silica is brittle by nature and sensitive to SCG. In other words, it would mean that glassy phase leads to a shift of the $V-K_I$ diagram towards low K_I values.

In a recent study, it was shown that silica addition in zirconia materials did not lead necessary to glassy phase at grain boundaries [21,22]. Special processing conditions are required to obtain glassy phase at triple points or grain boundaries. An addition of small amounts of silica and alumina leads more easily to glassy phase at grain boundaries. Figure (4) represents conventional and High Resolution Transmission Electron Microscopy images of three model polycrystalline zirconia materials processed without any silica addition, with 0.5 wt. % silica (the same pattern would be obtained with 2.5 wt.% addition) and 0.5 wt. % silica + alumina addition. The structure at triple points and grain boundaries is different at a nano-scale level.

Undoped zirconia do not show any evidence of vitreous phase neither at grain boundaries nor at triples junctions, confirming the high purity of the starting powder and the absence of any contamination during the process. Silica doped zirconia shows an interesting microstructure with always clean grain boundaries (among more than 30 edge-on grain boundaries studied), but with the presence of a silica rich amorphous phase at triple joints (details can be found in [21,22]). This is in contrast with a generally accepted idea of a continuous vitreous phase in silica doped ceramics. Grains are rounder in comparison to the undoped material, due to the presence of vitreous phase at triple joints. Silica + alumina doped zirconia exhibits another type of microstructure with the presence of a silica and alumina rich phase both at triple joints and, at least partially, at grain boundaries. This means that the surface energies between the amorphous phase and the crystalline grains can be modified by the composition of the silica film.

Is there a detrimental effect of silica addition to zirconia on SCG? The answer is not necessarily. Figure (5) shows that the presence of a glassy phase located at triple points does not induce any important change in SCG. A slight acceleration of the crack rates in stage I is observed for the material doped with 2.5 wt. % silica, since intergranular cracks have to propagate through these glassy pockets. Nevertheless, K_{I0} and K_{IC} are identical in all batches. K_{I0} is related to the surface energy of grain boundaries in the presence of water. Since there is no glassy phase at grain boundaries even with an addition of silica, the surface energy can be considered as constant in average whatever the silica content. The same argument can be used for K_{IC} , which is related to the fracture energy under vacuum conditions.

A grain boundary glassy phase has a small effect, particularly on the threshold stress intensity factor K_{I0} and on stage I (fig.6). In this case, it can be argued that the

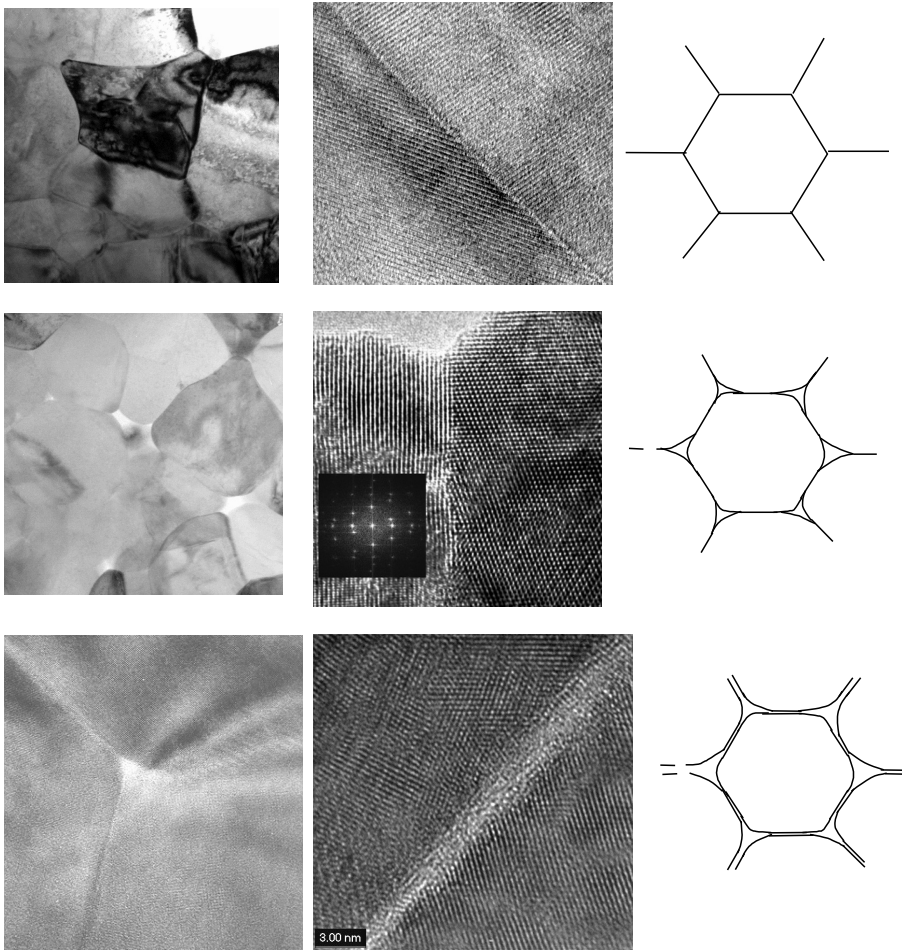


Figure 4. Microstructures of polycrystalline zirconia ceramics : (a) undoped, (b) doped with 0.5 wt.% silica and (c) doped with 0.5 wt.% silica + alumina.

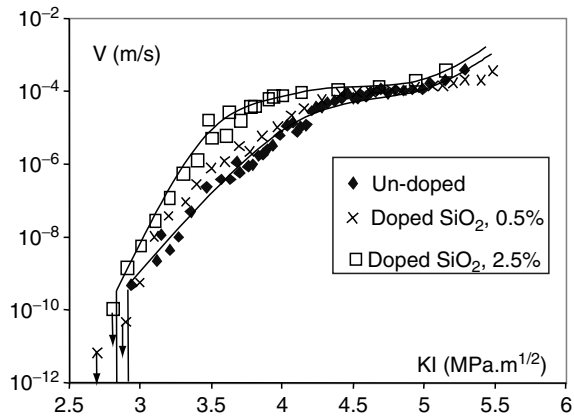


Figure 5. Effect of silica addition on V-K_I curves of zirconia

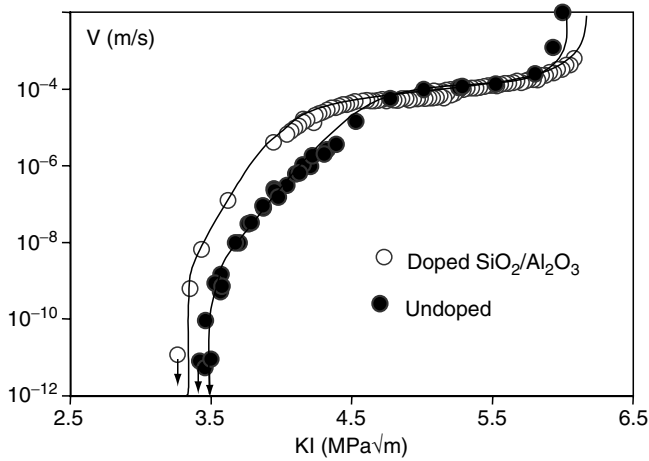


Figure 6. Effect of silica+alumina addition on V- K_I curves of zirconia

behavior of ceramic corresponds to that of the silica rich phase, since crack propagation is still intergranular. However, since the sensitivity of silica to stress corrosion is similar to that of zirconia, the effect is far from detrimental. The conclusions could be different if a glassy phase was present in a ceramic intrinsically less sensitive to stress corrosion.

2. SCG at the Micro-Scale Level : Effect of the Microstructure

The preceding section has shown that SCG was intrinsically related to the bounds that are subjected to the combined effect of stresses and water. However, the microstructure plays a major role on the V- K_I curves obtained experimentally. For polycrystalline zirconia for example, the thresholds obtained in air and vacuum give a crack resistance of 30 J/m^2 and of 50 J/m^2 respectively (they can be calculated from figure (1)). In contrast to the case of glass and single crystals \diamond , these values are far above the surface energy that can be measured by the heat of vaporisation in ceramics (on the order of 1 J/m^2). This means that the crack resistance R (or R_e) is not only related to the surface energy but also to additional energy dissipation. The two main mechanisms contributing to energy dissipation in polycrystalline ceramics are phase transformation toughening and crack bridging. The equations (5) must be transformed as :

$$R = 2\gamma_s + R_\phi \quad \text{under vacuum} \quad (6(a))$$

$$R_e = 2\gamma_e + R_\phi \quad \text{in a given environment} \quad (6(b))$$

where R_ϕ is the contribution of microstructural related reinforcement to the crack resistance. This contribution in the case of Y-TZP is about ten times that of the

\diamond Even in the case of single crystal or glass there is a slight discrepancy between the surface energy measured by vaporisation and the crack resistance, owing to the dissipation unavoidably associated to mechanical fracture.

surface energy. The same order of magnitude is observed for most polycrystalline ceramics. This means that only a portion of the applied stress intensity factor is used to propagate the crack, the other portion being dissipated by reinforcement mechanisms. In terms of stress intensity factors, the stress intensity factor at the crack tip, which rules crack growth, is lower to the applied one, because of reinforcement. This leads to the well known equation:

$$K_{I_{tip}} = K_I - \Delta K_r \quad (7)$$

where K_I and $K_{I_{tip}}$ represent the applied stress intensity factor (by the external loads) and the stress intensity factor at the crack tip respectively and ΔK_r the reinforcement due to the microstructure.

The following sections aim at showing the effect of the microstructure on ΔK_R and consequently on V- K_I curves.

3.1. Effect of the Grain Size on the Slow Crack Growth in Alumina

Slow crack growth in polycrystalline alumina ceramics was first reported by Freiman et al. [23]. The propagation rates are strongly influenced by the grain size, the large grain materials offering more resistance to crack growth.

It is well known that crack propagation properties are related to bridging effect and this effect is more pronounced in coarse-grained materials [24–27]. Coarse-grain alumina shows an R-curve behavior which is characterized by an increase in crack resistance with crack extension, due to crack surface interaction in the crack wake [28–29]. This R-curve behavior is due to the stresses required to overcome the traction of interlocking grains and pullout of unbroken ligaments in the wake of the crack.

The influence of an R-curve behavior on slow crack growth in ceramics corresponds to a shift toward higher stress intensity factor values with crack extension [13,14]. Fett and Munz [15] have shown that a crack velocity decrease could even be observed at the beginning of the crack propagation of small macrocracks in alumina. Crack propagation tests were conducted by Ebrahimi et al. [30] on polycrystalline alumina with average grain sizes d between 2 and 13 μm and equiaxed grain morphology. The tests were performed on a high-purity alumina (> 99,9 wt % purity) doped with 500 ppm MgO (Baikowski, SM8). High density and uniform equiaxed structures were available after sintering because the addition of MgO. The slow crack growth behavior was studied by using the double torsion method which allows to obtain the V- K_I curves. In order to accurately consider the influence of crack resistance curves on slow crack growth, R-curves were also measured with the double torsion technique on pre-cracked specimens.

The results of crack propagation in air for different grain sizes obtained by the relaxation method under constant displacement are shown in Fig.7. The cracking rate da/dt is very sensitive to the stress intensity factor K below 2×10^{-5} m/s for the three alumina ceramics (region I). For da/dt faster than these values, K dependence becomes moderated (region II). However, the slope of region I increases with the grain size and region II of crack propagation is much more limited for higher grain size. Above 10^{-4} m/s, a clear increase of crack rate is observed for fine-grained alumina (region III). It is less visible in the case of coarse-grained alumina.

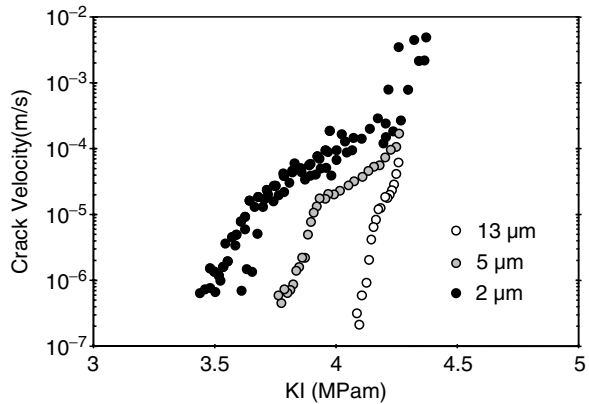


Figure 7. V-KI curves of three alumina with different grain sizes, obtained by the Double Torsion method (from [30]).

The K_{IO} , defined as the minimum stress intensity factor that leads to measurable crack propagation during relaxation, is much higher ($\sim 25\%$) in coarse-grained alumina ($d = 13 \mu\text{m}$) than in fine-grained alumina ($d = 2 \mu\text{m}$). Thus, the slow crack growth resistance becomes higher for the higher grain size. This result can be attributed to crack-bridging R-curve effects which increase with crack extension for coarse-grained alumina.

The R-curves for the alumina, measured with the double torsion technique on pre-cracked specimens, as a function of crack length increment are illustrated in Fig. 8 which depicts the ΔK_r (increase of toughness after pre-cracking) versus Δa (crack extension after pre-cracking) plot. The crack resistance increases with crack growth and this behavior becomes more remarkable when the grain size increases. The results show that increasing the grain size increases both the “steady-state” toughness and the toughening rate (initial slope of the R-curve). This increasing toughness is commonly attributed to “wake” effects which shield the crack tip from the externally applied stress.

Crack shielding in non-transforming ceramics occurs mainly by bridging, branching and deviation and by friction of the crack interfaces. The typical pattern

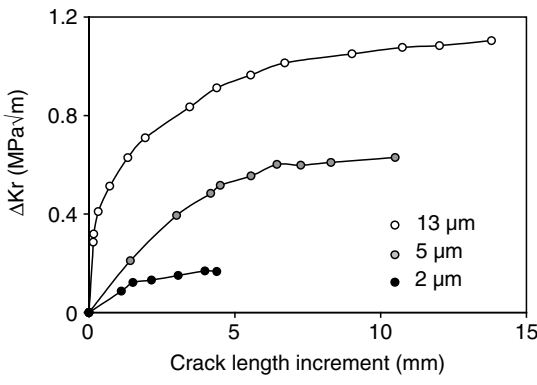


Figure 8. R-Curve behavior of the three alumina ceramics (from [30]).

of an intergranular crack propagation was observed, even for the largest grain size (13 μm). Increases in toughness up to 1 MPa√m are observed between the crack initiation toughness and the final plateau toughness of coarse-grained alumina (d = 13 μm).

The dependence of toughness upon crack extension may be written as:

$$K_{I\text{ appl.}}(a) = K_{I\text{ tip}} + \Delta K_r(a) \tag{7b}$$

where $K_{I\text{ appl}}$ is the total stress intensity factor calculated from the external load by the DT method, $K_{I\text{ tip}}$ the stress intensity factor acting at the crack tip, ΔK_r the toughness contribution from the wake (R-curve) and a the crack length.

According to this explanation and by consideration of the results in Figs.7 and 8, the stress intensity factor acting at the crack tip at various crack lengths can be calculated. Fig.9 shows the $V - K_{I\text{ tip}}$ for the three aluminas. The $K_{I\text{ tip}}$ in the three aluminas is similar and independent of grain size. This definitively shows that the crack growth mechanism, stress corrosion, is the same at the crack tip for the three ceramics. In particular, a steep dependence of V with $K_{I\text{ tip}}$ is observed for each material (region I), followed by a saturation in crack velocity on a so-called region II of slow cracking. The statement that the $V - K_{I\text{ tip}}$ is independent of the grain size underlines the fact that atomic bonds broken during crack growth are intrinsically the same.

Other results were obtained with a higher purity alumina (> 99.99 wt %, AKP 50 Sumitomo), without addition of MgO (Fig.10) [31]. The mean grain size ranges for AKP aluminas were 6–53 μm for the same range of sintering temperatures, because of the absence of MgO . The grain size distribution in AKP aluminas was broader, with the appearance of elongated grains for highest grain sizes (10% and 50% of abnormal grains for the mean grain sizes 35 and 53 μm respectively).

For grain sizes ranging from 6 to 35 μm, the conclusions were the same than before : the larger the grain size, the larger the crack resistance. However, for the largest grain size (53 μm), a marked shift of the $V - K_I$ curve towards low stress intensity factor was observed (Fig.10). In this case, transgranular rupture is prevalent as pointed out by Fig.11 which shows the crack propagation paths in AKP aluminas. For the fine-grained AKP alumina (6 and 9 μm) the crack propagation is mostly

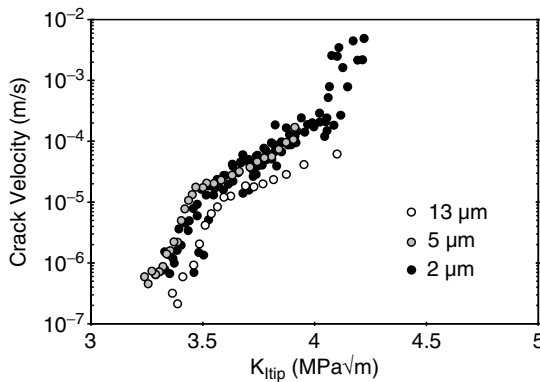


Figure 9. Intrinsic $V - K_{I\text{ tip}}$ curves for the three alumina ceramics.

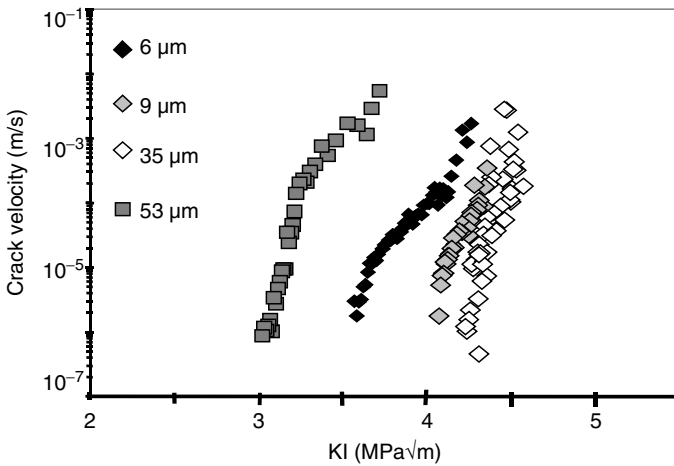


Figure 10. V- K_I curves of four alumina with different grain sizes, up to 53 μm .

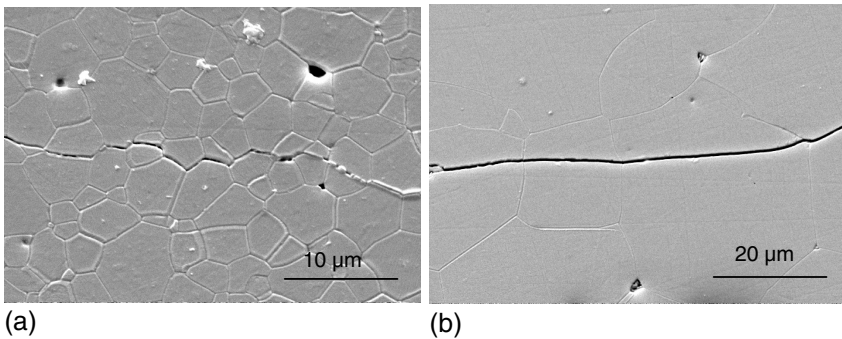


Figure 11. Mode of fracture for an AKP alumina, for 6 μm grain size (a) and 53 μm grain size (b).

intergranular whereas in the alumina with a 53 μm mean grain size, the crack path is mostly transgranular. Thus the shift of the V – K_I curve in the coarse-grained alumina is due to the appearance of transgranular fracture, which leads to a decrease of the R-curve effect.

The experimental results clearly show that the stress corrosion is the key mechanism for crack propagation in alumina ceramics and that a unique crack velocity-crack tip stress intensity factor law can be obtained by taking into account the crack resistance curve in coarse-grain ceramics.

3.2. Effect of Transformation Toughening on V – K_I Curves.

The case of alumina is relatively simple since at least as first approximation, the reinforcement depends only on the crack length. Other cases are more complex, and the reinforcement can also depend on the applied stress. This is the case of the mechanisms acting at the crack front, such as microcracking and phase transformation toughening. A good example of the last case is the reinforcement in zirconia based ceramics. It is based on the tetragonal to monoclinic transformation of particles at the crack tip due to the local high stresses. The associated volume

expansion leads to stress shielding. It can be shown that transformation zone size is related to the stresses applied to the ceramic (the higher the stresses, the larger the transformation zone). It can be demonstrated that shielding stress intensity factor in toughened ceramics is given by [32]:

$$K_r = C_{sh} \cdot K_I \tag{8}$$

$$\text{with } C_{sh} = \frac{0.214 \cdot E \cdot V_f \cdot e^T \cdot (1 + \nu)}{(1 - \nu) \cdot \sigma_m^c} \cdot \left(\frac{\sqrt{3}}{12\pi} \right) \tag{9}$$

where E is the Young modulus, V_f the volume fraction of transformed particles, e^T is the volume dilatation associated to the transformation, ν the Poisson ratio, σ_{mc} is the local stress for phase transformation and K_I the applied stress intensity factor. Eqn (8), which suggests that the shielding stress intensity factor is proportional to the applied one, has been verified experimentally by Chevalier et al.[17]. Reporting Eqn (8) in Eqn (7), the stress intensity factor at the crack tip, $K_{I_{tip}}$, can be expressed as:

$$K_{I_{tip}} = (1 - C_{sh})K_I \tag{5}$$

with C_{sh} increasing with the material transformability. If we assume that the intrinsic mechanism of SCG in a given ceramic is given by:

$$V = A_0 \cdot K_{I_{tip}}^n \tag{6}$$

Then, the analysis means that the experimentally determined V- K_I law in the presence of transformable zirconia particles is:

$$V = A_o \cdot (1 - C_{sh})^n \cdot K_I^n = A \cdot K_I^n \tag{7}$$

These results mean that the effect of transformation toughening on SCG is to shift the V- K_I law towards high stress intensity factors, preserving the n exponent of the SCG power law. This can be applied to zirconia ceramics as well as zirconia based composites. C_{sh} can be modified by changing the stability of the tetragonal phase. In zirconia, it can be easily modified by changing the grain size. Figure (12) shows V- K_I laws of yttria stabilized zirconia ceramics with different grain size, in a log-log plot. The results are compared to a zirconia single crystal. The higher the grain size, the higher the transformation toughening, thus the larger the crack resistance. At the same time, the curves run parallel, as a signature of the ‘intrinsic’ zirconia n exponent.

In this paper, we have analyzed to major mechanisms acting separately. In a certain number of ceramics, the two mechanisms can act at the same time. It is for example the case of Ceria stabilized zirconia ceramics, where the reinforcement is function of both the crack length and the applied stress intensity factor. In this particular case, the analysis of the results is more difficult.

3.3. An Application : Slow Crack Growth in a Zirconia-Toughened Alumina Nanocomposite.

Zirconia-toughened alumina (ZTA) ceramics with high transformation toughening ability can be obtained if a high portion of tetragonal phase with the possibility to transform under applied stress is retained at room temperature. This requires that the

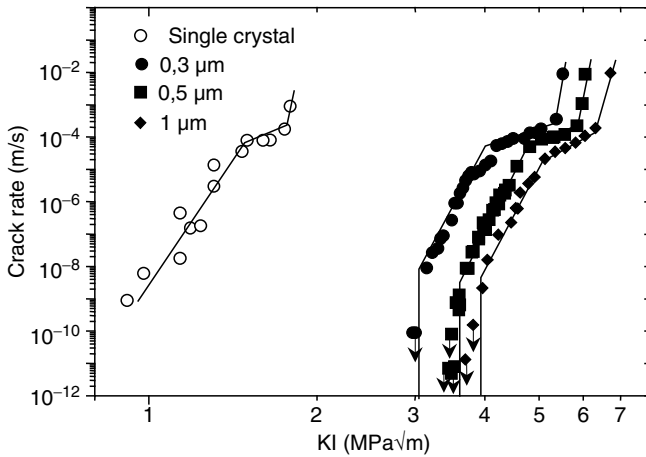


Figure 12. Effect of Grain size on V-K₁ laws in yttria stabilized zirconia, comparison with a single cristal.

zirconia particles must have a size distribution ranging between the critical size for spontaneous transformation on cooling to room temperature after sintering, D_c , and the critical size for stress – induced transformation, D'_c [33,34]. D_c size is in the range of 0.5–0.8 μm for unstabilized zirconia in an alumina ceramic matrix and D'_c is in the order of 0.1 μm .

Colloidal processing may allow to obtain a narrow size distribution of zirconia particles homogeneously dispersed in the alumina matrix [35].

Indeed, as shown by Fig.13, the composites obtained by the colloidal processing route show nano-sized ZrO_2 particles ($D_{50} = 0.4 \pm 0.1 \mu\text{m}$) homogeneously distributed at Al_2O_3 grain boundaries ($D_{50} = 1.2 \pm 0.4 \mu\text{m}$) without agglomerates and a minimum number of microstructure flaws. The composites obtained by conventional powder-mixing processing route show large ZrO_2 particles less homogeneously distributed in the alumina matrix.

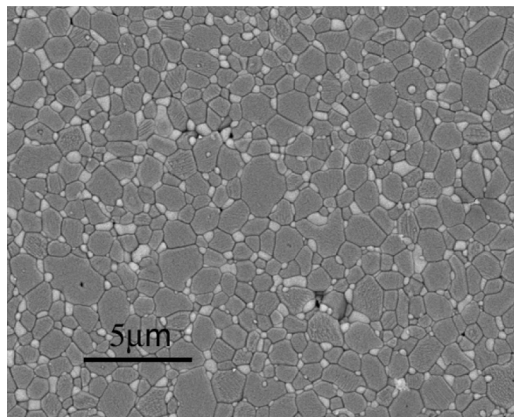


Figure 13. Scanning Electron Microscopy image (Back-scattered electrons mode) of a zirconia toughened alumina nano-composite, showing the narrow distribution of well dispersed zirconia particles in an alumina matrix [39].

The alumina zirconia composites processed by the colloidal route present a narrow distribution that is roughly between D_c and D'_c . This leads to a more efficient transformation toughening in the ceramics processed by the colloidal route and to a shift of the crack velocity versus stress intensity factor curve towards higher K_{Ic} values for the composites obtained by the colloidal route compared to the composites obtained by a powder-mixing technique [35].

The measured $V - K_{Ic}$ diagrams of alumina and the composites prepared with the colloidal route and different volume fraction of unstabilized zirconia are plotted in Fig. 14: Al_2O_3 , A7.5Z, A10Z and A15Z correspond to nanocomposites with 0, 7.5, 10 and 15 vol % ZrO_2 respectively and A7.5Z-2Y is a composite with 7.5 vol % ZrO_2 , stabilized by 2 mol % Y_2O_3 . Subcritical crack growth laws were measured using the double torsion technique and the relaxation method.

The curves exhibit a trend to shift towards higher K_{Ic} values up to a maximum before dropping with increasing volume fraction above 10%. These results are in agreement with previously reported values on the toughness of ZTA composites [36]. The increasing crack resistance of the composites can be explained by the stress induced martensitic transformation of the tetragonal zirconia particles ($t-ZrO_2$) to the monoclinic form ($m-ZrO_2$). As shown by Claussen [36], the amount of stress in the matrix increases with the content of zirconia and, beyond a maximum, the matrix is not able to retain the tetragonal zirconia as a metastable phase. Thus, the K_{Ic} value decreases and the overall $V-K_{Ic}$ curve is shifted towards lower K_{Ic} values for high zirconia content (A15Z).

For the composite processed with 2 mol % of Y_2O_3 (A7.5Z-2Y), the $V-K_{Ic}$ curve is slightly shifted to lower K_{Ic} values compared with the ZTA A7.5Z without yttria. This lower crack resistance corresponds to a lower effective transformation toughening, as really observed, yttria stabilizing the $t-ZrO_2$.

Fig. 14 shows that the ZTA processed by colloidal route always exhibit higher crack resistance than pure alumina, even for A15Z and A7.5Z-2Y where little or non transformation occurs. Transformation toughening is thus not the only mechanism acting to reinforce alumina in ZTA and crack deflection and microcracking also

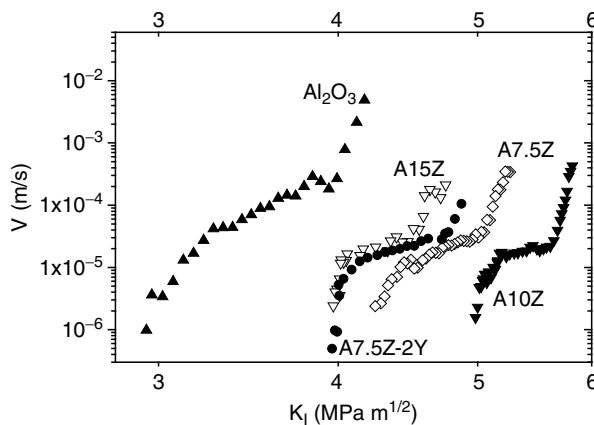


Figure 14. SCG behavior of zirconia toughened alumina nano-composites, with different compositions (from 35).

occur. Finally, the influence of residual stresses in these nano-composites can be significant. In any case, the material exhibiting the highest amount of phase transformation during crack extension (A10Z) presents the highest resistance. The load relaxation method does not allow measurement at very low velocity ($\leq 10^{-7}$ m/s) but present the advantage of being fast and a full curve can be recorded in a single experiment. Measurement of crack velocity under constant load presents the advantage of allowing the measurement of very low velocities. Such measurements were made on alumina, ZTA processed by colloidal route (A15Z) 3Y-TZP (3mol % yttria stabilized zirconia) [37]. The whole crack velocity diagrams are compared in fig.15. The overall curves obtained in air exhibit three distinct stages that can be fitted by a power law:

$$V = AK_I^n$$

The values of parameter n for the first stage I are reported in table 2. Thresholds below which no crack propagation occurs (K_{I0}) were observed at values indicated in table 2. Fig 13 shows that the 3Y-TZP exhibits a higher toughness than alumina but the thresholds of both materials are lower than of the ZTA nanocomposite, meaning that the necessary stress to initiate crack growth is lower in alumina and 3Y-TZP. Additionally, the ZTA nanocomposite has a toughness close to that of zirconia but a higher threshold, a consequence of the steeper slope of its V- K_I diagram.

Slow crack growth in oxyde ceramics is attributed to stress assisted corrosion at the crack tip. This is indeed the combined effect of high stresses at the crack tip and the presence of water, temperature that induce crack propagation in a subcritical manner. Alumina has lower susceptibility to water and thus to stress assisted corrosion. Therefore, the V- K_I curve of alumina presents a higher slope than the curve corresponding to zirconia (see Table 2). From an atomistic point of view, this means that the fracture energy of zirconia is lower in the presence of water, because the zirconia bonds are prone to chemisorption of the polar water molecules. The addition of a small amount of zirconia has two main advantages. First ZTA exhibit crack propagation primarily through the alumina matrix and have a low susceptibility to

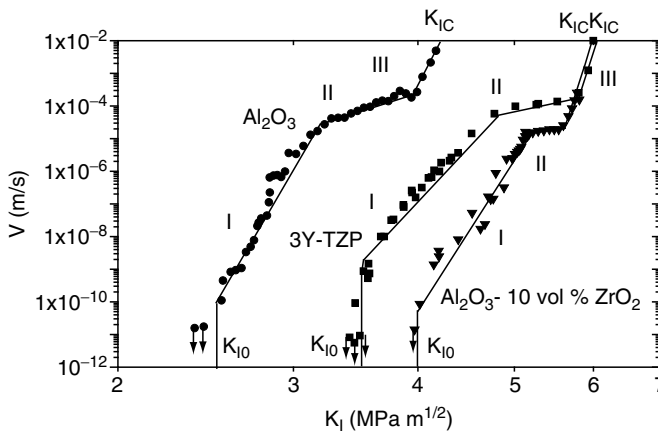


Figure 15. SCG in ZTA composites, compared to alumina and zirconia monoliths (for details, see ref. [35,39]).

Table 2. Threshold (K_{I0}) and Toughness (K_{Ic}) of Al_2O_3 , A10Z and 3Y-TZP ceramics.

| Material | Thresholds (K_{I0}) MPa.m ^{1/2} | Toughness (K_{Ic}) MPa.m ^{1/2} | n 1st stage |
|-----------|--|---|-------------|
| Al_2O_3 | 2.5 ± 0.2 | 4.2 ± 0.2 | 56.8 |
| A10Z | 4.0 ± 0.2 | 5.9 ± 0.2 | 53.5 |
| 3Y-TZP | 3.5 ± 0.2 | 6.1 ± 0.2 | 31.5 |

stress assisted corrosion from water. Second, these composites are reinforced by the presence of transformable zirconia particles, shifting the V- K_I diagram towards higher K_I values while preserving the slope of the curve (table 2).

In any case, the thresholds K_{I0} represents the key parameter as far as durability is concerned [38] (as for orthopedic implants, which must survive in vivo for more than 10 years).

The K_{I0} of the best ZTA composite (A10Z) is twice that of pure alumina. This means that this nanocomposite is expected to work at loads two times greater than monolithic alumina without any delayed fracture. So, these ZTA composites may offer to improve the lifetime of ceramic and to improve the safety range of use of point prostheses or orthopedic implants [39].

4. CONCLUSION

SCG in polycrystalline ceramics can be analyzed at two major scales. At a nano-scale level, the susceptibility of a given ceramic is ruled by the intrinsic response of the atomic bounds to stress assisted corrosion. Ceramics with a high ionic fraction are particularly sensitive to stress corrosion. This is the case of zirconia, silica and hydroxyapatite for example. Non oxide ceramics appear to be almost insensitive to this phenomenon at ambient temperature.

At a microscopic level, the SCG behavior of a given ceramic is dependent on the amount of reinforcement. Thus, for a same type of ceramic, i.e. for the same V- $K_{I\text{tip}}$ intrinsic response, V- K_I curves can be influenced by the microstructure. Two major toughening mechanisms have been discussed: crack bridging and phase transformation toughening. Other mechanisms are postulated to occur: micro-cracking and residual stresses for example. They might also influence V- K_I curves.

REFERENCES

1. L. Grenet, *Bull. Soc. Encour. Ind. Nat.*, 4, 838–48 (1889).
2. E. Orowan, *Nature*, 154, 341–49 (1944).
3. R.J. Charles, W.B. Hilling, pp.511–27 in symposium sur la résistance mécanique du verre et les moyens de l'améliorer, Union Scientifique Continentales du Verre, 24, Charleroi, Belgium, 1962.
4. S.M. Wiederhorn, *J. Am. Ceram. Soc.*, 50, 407–14 (1967).
5. A.I. Bailey, S.M. Kay, *Proc. Roy. Soc. Lond.*, Public. N°A301, 47 (1967).
6. S.M. Wiederhorn, in NBS special publication, *mechanical and thermal properties of ceramics*, Vol. 303, 217–41 (1969).
7. T.A. Michalske, S.E. Freiman, *J. Am. Ceram. Soc.*, 66 [4] 284–88 (1983).
8. S.M. Wiederhorn, P.R. Townsed, *J. Am. Ceram. Soc.*, 53, 486–89 (1970).

9. K.T. Wan, S. Lathabais, B.R. Lawn, *J. Europ. Ceram. Soc.*, 6 [4] 259–68 (1990).
10. K.T. Wan, N. Aimard, S. Lathabais, *J. Mater. Research*, 5 [1] 172–82 (1990).
11. D. Maugis, *J. Mater. Sci.*, 20, 3041–73 (1985).
12. F. Sudreau, PhD. Thesis, INSA de Lyon, France, 272 pages (1992).
13. F. Mignard, C. Olagnon, G. Fantozzi, pp. 565–76 in *Fracture Mechanics of Ceramics*, Vol. 11. 1996.
14. A. Osaka, N. Hirotsaki, M. Yoshimura, *J. Am. Ceram. Soc.*, 73 [7] 2095–96 (1990).
15. T. Fett, D. Munz, *J. Am. Ceram. Soc.*, 75 [4] 958–63 (1992).
16. B.R. Lawn, *Fracture of brittle solids*, Second edition, Cambridge University Press, 378 pages, 1993.
17. Chevalier, J., Olagnon, C., Fantozzi, G, *J. Am. Ceram. Soc.*, 82, 11, p.3129–3138 (1999).
18. K. Kajihara, Y. Yishizawa, T. Sakuma, *Acta metall. mater.* vol. 43 p. 1235–2 (1995).
19. K. Hiraga, H.Y. Yasuda, Y. Sakka, *Mater. Sci. Eng. A* vol. 234–236 p. 1026–9 (1997).
20. M.L. McCartney, *J. Am. Ceram. Soc.* Vol. 70 p. 54–58 (1987).
21. L. Gremillard, T. Epicier, J. Chevalier et al., *Acta Mater.* vol. 48 p. 4647-52 (2000).
22. L. Gremillard, J. Chevalier, T. Epicier, G. Fantozzi, *J. Am. Ceram. Soc.* vol. 85 n°2 p.401–07 (2002).
23. S. W. Freiman, K.R. McKinney and H.L. Smith, in *Fracture Mechanics of Ceramics*, Vol.2, pp.659–676, 1973.
24. R. Knehans and R.W. Steinbrech, in *Science of Ceramics*, edited by P.Vincenzini (Research Institute for Ceramics Technology, Faenza, Italy, 1984), Vol, pp.613–619.
25. P. Chantikul, S. Bennison and B.R. Lawn, *J. Am. Ceram. Soc.* 73, 2419 (1990).
26. G. Vekinis, M.F. Ashby and P.W.R. Beaumont, *Acta Metall. Mater.* 38, 1151 (1990).
27. G. Fantozzi, J. Chevalier and M. Saadaoui, in *Fracture Mechanics of Ceramics*, Vol.13, pp.213–228, 2002.
28. P. Swanson, C. Fairbanks, B.R. Lawn, Y. Mai and B. Hockey, *J. Am. Ceram. Soc.* 70, 279 (1987).
29. G. Pezzotti, O. Sbaizero, V. Sergo, N. Muraki, K. Maruyama and T. Nishida, *J. Am. Ceram. Soc.* 81, 187 (1998).
30. M.E. Ebrahimi, J; Chevalier and G. Fantozzi, *J. Mater. Res.* 15, 142 (2000).
31. M.E. Ebrahimi, PhD. Thesis, INSA de Lyon, France, 220 pages (2000).
32. R.M. McMeeking, A.G. Evans, *J. Am. Ceram. Soc.*, 65 [6] 242–46 (1982).
33. N. Claussen and M. Ruhle, in *Advances in Ceramics*, Vol.3, Science and Technology of Zirconia I, 1981, pp. 137–163.
34. R.C. Garvie, in *Advances in Ceramics*, Vol.24A, Science and Technology of Zirconia III, 1998, pp. 55–69.
35. A.H.De Aza, J. Chevalier, G. Fantozzi, M. Schell and R. Torrecillas, *J. Am. Ceram. Soc.* 86, 115 (2003).
36. N. Claussen, *J. Am. Ceram. Soc.* 59, 49 (1976).
37. J. Chevalier, C. Olagnon and G. Fantozzi, *Composites, Part A*, 30,525 (1999).
38. G. Willmann, *Adv. Eng. Mater.* 2, 114 (2000).
39. J. Chevalier, A.H. De Aza, G. Fantozzi, M. Schell and R. Torrecillas, *Adv. Mater.* 12, 1619 (2000).

TOUGHENING AND STRENGTHENING MECHANISMS IN NANOCOMPOSITES BASED ON DISLOCATION ACTIVITY

Hideo Awaji and Seong-Min Choi*

1. INTRODUCTION

Ceramics have low fracture toughness because dislocations are difficult to move in ceramics especially at room temperature. It is, therefore, hypothesized that a frontal process zone (FPZ) ahead of a crack tip is composed of many nano-cracks rather than dislocations as in metals.^{1,2} To overcome the inherent brittleness of ceramics, a new microstructural design concept must be developed. The design concept of “nanocomposites” is a new, and significantly improved strengths are achieved with moderate enhancement in fracture toughness.³ The typical microstructure of nanocomposites consists of second-phase nano-size particles dispersed within the matrix grains. Thermal expansion mismatch between the matrix and second-phase particles improves several mechanical properties of nanocomposites.

Remarkable characteristics of nanocomposites observed by many researchers are summarized:^{4,5} Drastic change of fracture mode is observed from intergranular fracture of monolithic ceramics to transgranular fracture of nanocomposites, especially in alumina-based nanocomposites.³⁻¹³ Several mechanical properties were also improved, such as fracture strength,^{3,4,7,8,9,14} fracture toughness,^{3,4,7,9,12} thermal shock resistance,³ creep resistance,^{3,4,15} hardness,^{3,9,12,14} and wear resistance.⁴

* Nagoya Institute of Technology, Gokiso-cho, Showa-ku, Nagoya, Japan 466-8555 awaji@mse.nitech.ac.jp, & Fax.: 052-735-5276

Moderate enhancement of fracture toughness with improved fracture strength is typical in nanocomposites, in spite of the well-known trade-off relation between the fracture strength and fracture toughness of monolithic ceramics.

In this paper, strengthening and toughening mechanisms in alumina/silicon nitride nanocomposites are discussed, emphasizing on dislocation activities in an alumina matrix. The strengthening mechanism is expressed as: Dislocations will be generated around dispersed nano-particles at elevated temperatures caused by thermally induced residual stresses, release intrinsically existed residual stresses in sintered alumina grains, and then improve the strength of alumina. The toughening mechanism is expressed as: Dislocations in alumina grains become sessile dislocations at room temperature, act as nano-crack nuclei under highly stressed area such as a main crack tip, expand the frontal process zone at the crack tip, and enhance the fracture toughness.

2. RESIDUAL STRESS

Microstructural characteristics of intra-type nanocomposites are such that dispersed nano-size particles are embedded within matrix grains. Many researchers have observed this microstructure in nanocomposites,^{3,7,8,9,14,17} and this microstructure generates thermally induced residual stresses after sintering due to thermal expansion mismatch between the dispersed particles and matrix¹⁸ and generate dislocations.

We analyze residual stresses around dispersed particles using a simplified model consisting of a spherical particle within a concentric matrix sphere with axial symmetry shown in Fig. 1 to clarify dislocation activities in nanocomposites. Existence of a surrounding interlayer (glassy-phase) on the second-phase particle is also considered for analyzing the effects of the interlayer on the stress distributions.

General solutions of thermal residual stresses and displacement in a homogeneous hollow sphere under a constant temperature difference are derived as:^{19,20}

In the second-phase sphere,

$$\sigma_{rp} = \sigma_{\theta p} = -\frac{2}{3} \frac{\alpha_p E_p \theta_0}{1 - \nu_p} + \frac{E_p}{1 - 2\nu_p} c_1, \quad (1)$$

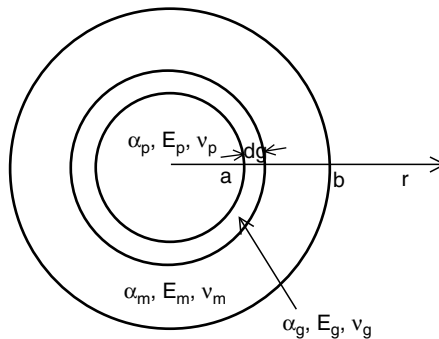


Figure 1. A spherical particle with a glassy phase within a concentric sphere of a matrix grain.

$$u_p = \frac{1}{3} \frac{1 + \nu_p}{1 - \nu_p} \alpha_p \theta_0 r + c_1 r, \quad (2)$$

in the interlayer,

$$\sigma_{rg} = -\frac{2}{3} \frac{\alpha_g E_g}{1 - \nu_g} \theta_0 \left(1 - \frac{a^3}{r^3}\right) + \frac{E_g}{1 - 2\nu_g} c_2 - \frac{2E_g}{1 + \nu_g} \frac{c_3}{r^3}, \quad (3)$$

$$\sigma_{\theta g} = \frac{1}{3} \frac{\alpha_g E_g}{1 - \nu_g} \theta_0 \left(1 - \frac{a^3}{r^3}\right) + \frac{E_g}{1 - 2\nu_g} c_2 + \frac{E_g}{1 + \nu_g} \frac{c_3}{r^3} - \frac{E_g}{1 - \nu_g} \alpha_g \theta_0, \quad (4)$$

$$u_g = \frac{1}{3} \frac{1 + \nu E_g}{1 - \nu_g} \alpha_g \theta_0 \left(r - \frac{a^3}{r^3}\right) + c_2 r - \frac{c_3}{r^2}, \quad (5)$$

and in the matrix hollow sphere,

$$\sigma_{rm} = -\frac{2}{3} \frac{\alpha_m E_m}{1 - \nu_m} \theta_0 \left\{1 - \frac{(a + dg)^3}{r^3}\right\} + \frac{E_m}{1 - 2\nu_m} c_4 - \frac{2E_m}{1 + \nu_m} \frac{c_5}{r^3}, \quad (6)$$

$$\sigma_{\theta m} = \frac{1}{3} \frac{\alpha_m E_m}{1 - \nu_m} \theta_0 \left\{1 - \frac{(a + dg)^3}{r^3}\right\} + \frac{E_m}{1 - 2\nu_m} c_4 + \frac{E_m}{1 + \nu_m} \frac{c_5}{r^3} - \frac{E_m}{1 - \nu_m} \alpha_m \theta_0, \quad (7)$$

$$u_m = \frac{1}{3} \frac{1 + \nu E_m}{1 - \nu_m} \alpha_m \theta_0 \left\{r - \frac{(a + dg)^3}{r^2}\right\} + c_4 r - \frac{c_5}{r^2}, \quad (8)$$

where σ_r and σ_θ are stresses, u displacement in radial direction, r coordinates, $c_1 \sim c_5$ unknown constants, α thermal expansion coefficient, E Young's modulus, ν Poisson ratio, θ_0 temperature difference, a radius of the second phase sphere, b outer radius of the matrix sphere, dg thickness of the interlayer, and the properties with suffix "p", "g", and "m" denote the properties of the second-phase particle, interlayer, and matrix, respectively.

Equations (1) to (8) are normalized by taking the following nondimensional variables

$$\xi = \frac{r}{a}, \sigma_r^* = \frac{\sigma_r}{\alpha_m E_m \theta_0}, \sigma_\theta^* = \frac{\sigma_\theta}{\alpha_m E_m \theta_0}, \tau_{\max}^* = \frac{\tau_{\max}}{\alpha_m E_m \theta_0}, u^* = \frac{u}{\alpha_m a \theta_0}, \quad (9)$$

where τ_{\max} represents the maximum shear stress. The unknown constants in Eqs. (1) to (8) can be determined by boundary conditions.

The analyzed residual stress distributions in the matrix and second-phase particle with no interlayer are shown in Fig. 2, where the ratio of the thermal expansion coefficients of dispersed particle and matrix (α_p/α_m) is 1/2, the ratio of Young's moduli (E_p/E_m) is 1/1, the ratio of the inner and outer radii (a/b) is 1/2, and the Poisson ratios of both the matrix and particle are approximated to be 0.2. In the figure, the thin solid and thin dotted lines indicate the following simple solutions to an infinite body with a spherical second-phase particle with no interlayer analyzed by Weyl²¹ and Selsing.²²

$$\sigma_{rm} = -2\sigma_{\theta m} = -P \frac{a^3}{r^3}, \quad P = \frac{(\alpha_p - \alpha_m)\theta_0}{\frac{1 + \nu_m}{2E_m} + \frac{1 - 2\nu_p}{E_p}}. \quad (10)$$

Figure 2 indicates that the residual stresses have the highest values at the particle/matrix boundary and reduce quickly as distance from the boundary increases. Therefore, this highly stressed area is limited in the vicinity of the particle in the case of the nano-sized particles, and if these stresses are high enough to generate dislocations in the matrix, only dislocations will be generated and locate in the vicinity of the boundary.

Figure 3 shows the residual stress distributions of σ_{θ}^* and τ_{\max}^* in the matrix for the case where a/b is 1/5, 1/2, and 1/1.25. The matrix is assumed to be Al_2O_3 and the second-phase SiC. The material properties of polycrystalline Al_2O_3 and SiC are shown in Table 1. Figure 3 suggests that the matrix with smaller a/b value has higher stress on the particle/matrix boundary, but the distributions of the maximum shear stress are almost independent of a/b .

Figure 4 shows the stress distributions in the particle, interlayer, and matrix for the $\text{Al}_2\text{O}_3/\text{SiC}$ system for supposed values of α_g/α_m , under the assumption of

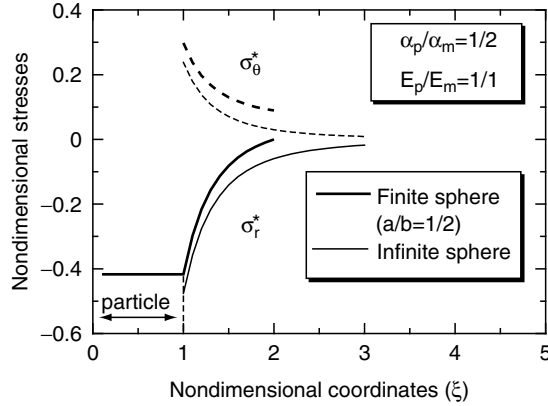


Figure 2. Comparison of stresses around a dispersed particle without an interlayer in matrices of finite and infinite spheres.

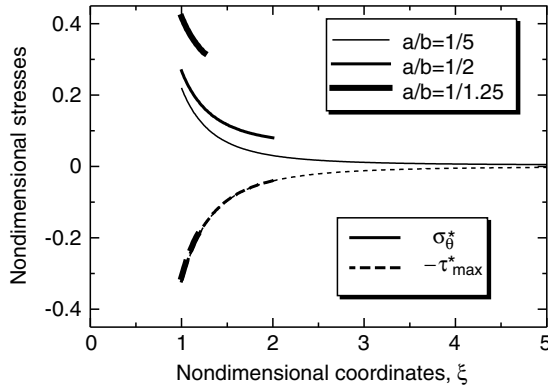
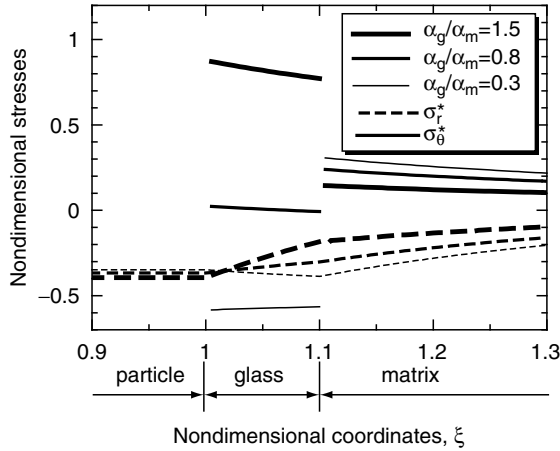


Figure 3. Stress distributions around a second-phase particle embedded within a matrix grain, calculated for the $\text{Al}_2\text{O}_3/\text{SiC}$ system.

Table 1. Residual stresses along the particle/matrix boundary in $\text{Al}_2\text{O}_3/\text{SiC}$ nanocomposites under the assumption of $\Delta T = 1,325^\circ\text{C}$ and $a/b = 1/5$.

| $\alpha_m/\alpha_p \times 10^{-6}(\text{K}^{-1})$ | E_m/E_p (GPa) | ν_m/ν_p | Stresses on the boundary | |
|---|--------------------|---------------|--------------------------|-----------------------|
| | | | σ_θ (GPa) | σ_{\max} (GPa) |
| 8.8/4.7 | 380/490 | 0.21/0.19 | 0.98 | 1.44 |

**Figure 4.** Stresses in a particle, interlayer, and a matrix for the $\text{Al}_2\text{O}_3/\text{SiC}$ system, where $dg/a = 0.1$, $a/b = 1/2$, and $E_g = E_m$.

$dg/a = 0.1$, $a/b = 1/2$, and $E_g = E_m$. It is noted that the existence of interlayer on the spherical particle has significant effects on the stress distributions in the matrix.

Residual stresses calculated on the particle/matrix boundary with no interlayer for the $\text{Al}_2\text{O}_3/\text{SiC}$ system are shown in Table 1, where $\theta_0 = 1325^\circ\text{C}$ and $a/b = 1/5$ are assumed. There is large maximum shear stress on the particle/matrix boundary, which is expected to generate dislocations around the dispersed particles within alumina grains.

3. DISLOCATION ACTIVITY

The temperature dependency of the critical resolved shear stresses (CRSS) for a single $\alpha - \text{Al}_2\text{O}_3$ crystal was estimated by Lagerlöf et al. experimentally.²³ They showed that the relation between temperatures and CRSS of both basal slip and prism plane slip in a single $\alpha - \text{Al}_2\text{O}_3$ crystal could be described by a simple logarithmic law over a wide range of temperature;

$$\ln \tau_c = \ln \tau_0 - B \cdot T, \quad (11)$$

where τ_c represents the CRSS, T temperature [K], and $\tau_0 = 109$ GPa or 9 GPa and $B = 0.0052$ or 0.0026 for basal slip or prism plane slip, respectively. Equation (11) indicates that at room temperature ($T = 300$ K), τ_c is calculated to be 22.9 or 4.1 GPa for basal slip or prism plane slip, respectively, which is higher than the

maximum residual shear stress on the grain boundary listed in Table 1, and also higher than the theoretical strength of a single $\alpha - \text{Al}_2\text{O}_3$ crystal.

Figure 5 shows the temperature dependencies of the CRSS for basal slip and prism plane slip in a single $\alpha - \text{Al}_2\text{O}_3$ crystal and the residual shear stress on the $\text{Al}_2\text{O}_3/\text{SiC}$ boundary in nanocomposites, where τ_{cb} and τ_{cp} represent the CRSS for basal slip and prism plane slip, respectively, and τ_{res} is the maximum residual shear stress on the grain boundary of $\text{Al}_2\text{O}_3/\text{SiC}$ system calculated under the assumption that the residual stress is linearly related to temperature. It is noted that dislocation movement in Al_2O_3 grains is possible at temperature ranging from 700°C to 1200°C , suggesting that this temperature range is quite important in generating dislocations in the Al_2O_3 matrix during the cooling process after sintering or annealing. Therefore, control over the cooling rate and pressure during the cooling process is required for generating dislocations. Further appropriate annealing will lead to the development of dislocation networks as a result of dislocation rearrangement. It is worthy of note that dislocations in a single $\alpha - \text{Al}_2\text{O}_3$ crystal can move at elevated temperatures due to residual stresses, whereas these dislocations cannot move at room temperature and become sessile dislocations.

The mismatches in thermal expansion coefficients and Young's moduli between the matrix and dispersed particles yield highly localized residual stresses around the particles. The stress distribution reduces quickly as distance from the boundary increases because of the nano-sized particles, which can generate small defects such as dislocations in close vicinity of the particles at elevated temperatures during the cooling process, as shown in Fig. 6(A). Large-scale cracks or other large defects will be difficult to create in nanocomposite systems due to the residual stresses. Conversely, if cracks instead of dislocations are created, the FPZ toughening mechanism mentioned later will not operate effectively. Only dislocations can disperse in matrix grains at elevated temperatures and operate as nano-crack nuclei at room temperature. Several researchers have observed embryonic dislocations in the matrix grains,^{8,9,14,16,17} and only Niihara observed highly developed dislocation networks in the annealed $\text{Al}_2\text{O}_3/\text{SiC}$ nanocomposites.³ This fact suggests that appropriate annealing after sintering is important to disperse dislocations and make dislocation

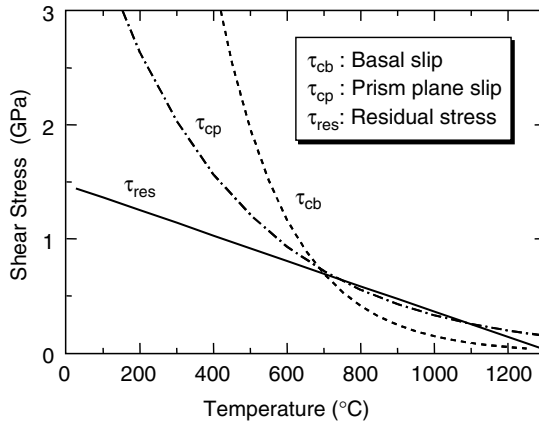


Figure 5. Temperature dependencies of the critical resolved shear stresses in $\alpha - \text{Al}_2\text{O}_3$ and the residual shear stress on the boundary of $\text{Al}_2\text{O}_3/\text{SiC}$ in nanocomposites.

networks around the particles, shown in Fig. 6(B), which will enhance fracture toughness of the nanocomposites.

4. TOUGHENING MECHANISM

Polycrystalline ceramics usually exhibit rising R-curve behavior. A schematic diagram explaining a cracked surface in the polycrystalline ceramics is shown in Fig. 7. This figure indicates that there are two kinds of fracture energy to prevent crack propagation in ceramics; one is the fracture energy for formation of the FPZ at the crack tip, and the other is the mechanical energy consumed at the bridging in the wake. Therefore, the Griffith-Irwin formula can be expressed for mode I crack extension²⁴ as

$$\frac{K_{IC}^2}{E'} = 2\gamma_i + 2\gamma_R \tag{12}$$

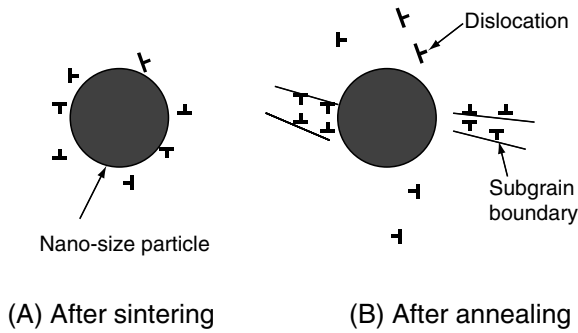


Figure 6. Dislocation creation by sintering, and dislocation dispersion by annealing.

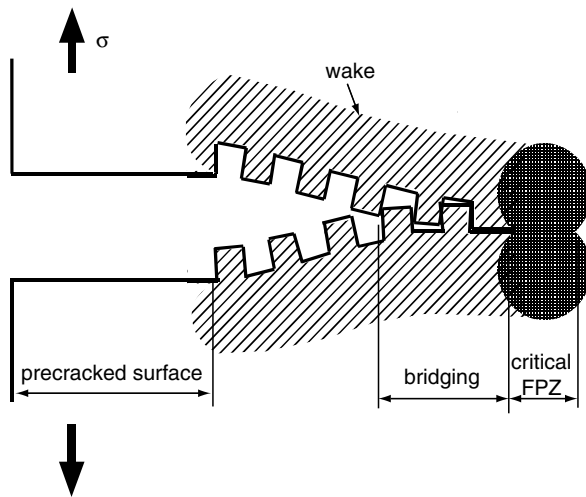


Figure 7. Schematic drawing of a frontal process zone and bridging in a wake for polycrystalline ceramics with R-curve behavior.

where the left side of Eq. (12) indicates the critical energy release rate, the right side is the fracture energy rate, K_{IC} the fracture toughness of the material with rising R -curve behavior, γ_i mode I fracture energy per unit area of the cracked surface to create the critical FPZ size, γ_R fracture energy per unit area to be consumed at the bridging, and $E' = E$ for plane stress, $E' = E/(1 - \nu^2)$ for plane strain. Equation (12) is derived on the premise that the FPZ is small enough to satisfy the condition of small scale yielding.

Referring to Eq. (12), we recognize that toughening of brittle materials can be achieved by increasing the fracture energy of the materials; the intrinsic fracture energy for formation of the FPZ and the extrinsic fracture energy consuming in the bridging. Much effort has been directed toward increasing the intrinsic energy consumed in the FPZ in such ways as phase-transformation toughening and nanocomposites which will be mentioned later, and increasing the extrinsic energy consumed at the bridging by means of whisker, fiber, and platelet reinforcement in the matrix. The former is the FPZ toughening mechanism and the later is the crack-face bridging mechanism. The toughening mechanism of nanocomposites belongs to the FPZ toughening mechanism, where dislocation activities in matrix grains expand the FPZ size and increase the intrinsic fracture energy.²⁴

Figure 8 shows a schematic illustration of the FPZ at a main crack tip in the annealed Al_2O_3/SiC nanocomposites. In a matrix grain, sub-grain boundaries with dislocations or dislocation networks are generated around the dispersed SiC nanoparticles by means of annealing procedure. Therefore, when a main crack tip reaches this area, the sessile dislocations in the ceramic matrix at room temperature will operate as nano-crack nuclei in the highly stressed area. Then the FPZ are expanded owing to nano-crack formation and consequently enhance the fracture toughness of the material.²⁵

4. STRENGTHENING MECHANISM

Nano-size dispersed particles drastically change the fracture mode from intergranular fracture to transgranular fracture, and also improve the fracture strength of ceramics markedly, especially after annealing, mentioned previously. To explain these phenomena, we consider a strengthening mechanism in nanocomposites

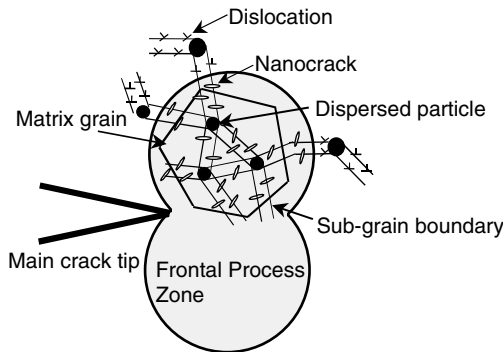


Figure 8. Schematic description of the toughening mechanism in nanocomposites.

based on dislocation activities. A schematic explanation of the mechanism is shown in Fig. 9. A sintered monolithic polycrystalline alumina has tensile residual stresses in grains and at grain boundaries intrinsically because of anisotropic thermal expansion and elastic modulus along the crystal axes, shown in Fig. 9(A). Therefore, it is conceivable in sintered polycrystalline alumina that synergetic effects of both residual stresses and processing defects, such as cavities, create the largest crack along the grain boundary in the material, and the crack can be equivalent to the grain size of the material. The fracture toughness of grain boundaries is usually lower than that within the grains. Hence, polycrystalline alumina exhibit mainly intergranular fracture mode, as schematically shown in Fig. 9(A). The longest crack generated along the boundaries will be the Weibull's weakest crack that dominates the strength of the specimen. Thus, the weakest crack length will become comparable with the grain size. It is widely accepted that the strength of the polycrystalline materials shows dependence on the grain size, which is known as Petch's relation.²⁶ However, the nano-cracks created by dislocations in the matrix are expected to be small compared with the grain size, as shown in Fig. 9(B), and the dislocations reduce the residual stresses at the grain boundaries. Therefore, the weakest crack length dominating the strength is considered to be equal to the grain size in monolithic ceramics, and to the size of the largest cavity in the nanocomposites. This is a source of highly improved strength of nanocomposites.

On the contrary, dislocations generated around the dispersed particles in the nanocomposites relieve the tensile residual stresses in the matrix, and consequently reduce the defect size at the grain boundaries, shown in Fig. 9(B). Also, the dislocations are difficult to move in ceramics at room temperature, serve as origins of stress concentrations, and create small nano-cracks around the main crack tip. The nano-cracks slightly reduce the transgranular strength of the alumina matrix. Then the reduction of both the defect size along the grain boundaries and the transgranular strength in the matrix are attributable to a change in the fracture mode from

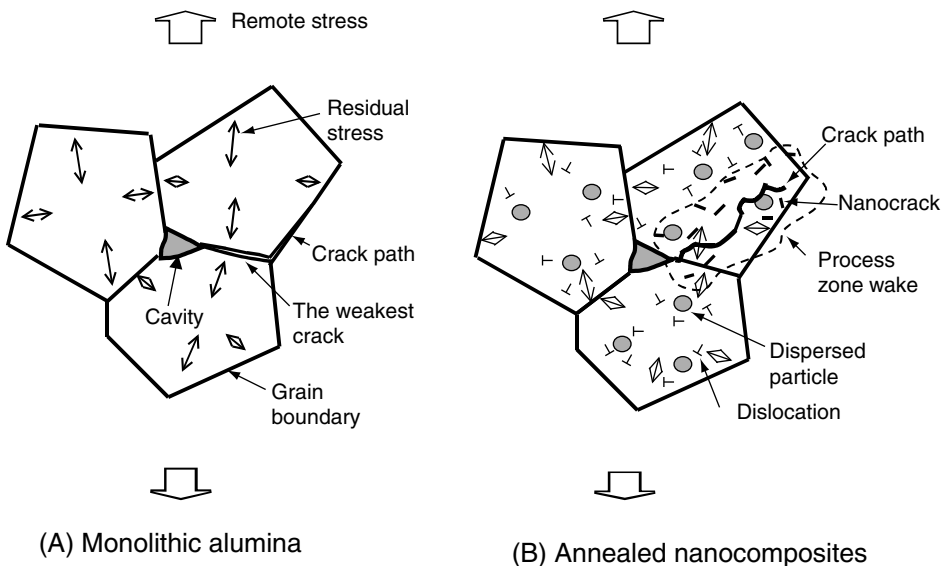


Figure 9. Schematic description of the strengthening mechanism in nanocomposites.

intergranular fracture in monolithic alumina shown in Fig. 9(A) to transgranular fracture in nanocomposites, shown in Fig. 10(B). Also, the fracture surface of the transgranular mode of nanocomposites is not a simple planar cleavage plane. Many steps are observed on the surface,^{6,10,12,13} which can be evidence of nano-cracking around the second-phase particles in the FPZ.

Relieving tensile residual stresses in the matrix grains due to dislocations results in improvement of several mechanical properties of nanocomposites, such as thermal shock resistance, wear resistance, creep resistance, and hardness.

5. CONCLUSIONS

The toughening and strengthening mechanisms in alumina-based nanocomposites were discussed, emphasizing dislocation activities in alumina. The residual stresses around a spherical second-phase nano-particle within a concentric sphere of matrix grain were analyzed to clarify the effects of residual stresses on the dislocation activities. The results revealed that the residual stresses were large enough to generate dislocations at elevated temperatures, and these dislocations become sessile dislocations at room temperature. The generated dislocations relieve tensile residual stresses intrinsically existing in alumina grains, reduce the defect size at the grain boundary, and consequently improve the strength of alumina markedly. Conversely, the sessile dislocations at room temperature serve as origins of stress concentrations, operate as nano-crack nuclei at a main crack tip, expand the frontal process zone at a crack tip, and enhance the fracture toughness of alumina.

REFERENCES

1. R. G. Hoagland and J. D. Embury, A Treatment of Inelastic Deformation Around a Crack Tip due to Microcracking, *J. Am. Ceram. Soc.*, **63**, 404–410 (1980).
2. A. G. Evans and K. T. Faber, Toughening of Ceramics by Circumferential Microcracking, *J. Am. Ceram. Soc.*, **64**, 394–398 (1981).
3. K. Niihara, New Design Concept of Structural Ceramics -Ceramic Nanocomposites-, *The Centennial Memorial Issue of Ceram. Soc. Japan*, **99**, 974–981 (1991).
4. R. W. Davidge, R. J. Brook, F. Cambier, M. Poorteman, A. Leriche, D. O'Sullivan, S. Hampshire, and T. Kennedy, Fabrication, Properties, and Modelling of Engineering Ceramics Reinforced with Nanoparticles of Silicon Carbide, *British Ceramic Trans.*, **96**, 121–127 (1997).
5. M. Sternitzke, Review: Structural Ceramic Nanocomposites, *J. Euro. Ceram. Soc.*, **17**, 1061–1082, (1997).
6. A. Nakahira and K. Niihara, Sintering Behaviors and Consolidation Process for Al₂O₃/SiC Nanocomposites, *J. Ceram. Soc. Jpn*, **100**, 448–453 (1992).
7. J. Zhao, L. C. Stearns, M. P. Harmer, H. M. Chan, G. A. Miller, and R. F. Cook, Mechanical Behavior of Alumina-Silicon Carbide "Nanocomposites", *J. Am. Ceram. Soc.*, **76**, 503–510 (1993).
8. C. E. Borsa, S. Jiao, R. I. Todd, and R. J. Brook, Processing and Properties of Al₂O₃/SiC Nanocomposites, *J. Microscopy*, **177**, 305–312 (1995).
9. L. Carroll, M. Sternitzke, and B. Derby, Silicon Carbide Particle Size Effects in Alumina-Based Nanocomposites, *Acta mater.*, **44**, 4543–4552 (1996).
10. H. Tan and W. Yang, Toughening Mechanisms of Nano-Composite Ceramics, *Mechanics of Materials*, **30**, 111–123 (1998).

11. J. Pérez-Rigueiro, J. Y. Pastor, J. Llorca, M. Elices, P. Miranzo, and J. S. Moya, Revisiting the Mechanical Behavior of Alumina/Silicon Carbide Nanocomposites, *Acta Mater.*, **46**, 5399–5411 (1998).
12. L. Gao, H. Z. Wang, J. S. Hong, H. Miyamoto, K. Miyamoto, Y. Nishikawa, and S. D. De la Torre, Mechanical Properties and Microstructures of Nano-SiC- Al_2O_3 Composites Densified by Spark Plasma Sintering, *J. Euro. Ceram. Soc.*, **19**, 609–613 (1999).
13. H. Z. Wang, L. Gao, and J. K. Guo, The Effect of Nanoscale SiC Particles on the Microstructure of Al_2O_3 Ceramics, *Ceramics Int.*, **26**, 391–396 (2000).
14. M. Sternitzke, B. Derby, and R. J. Brook, Alumina/Silicon Carbide Nanocomposites by Hybrid Polymer/Powder Processing: Microstructures and Mechanical Properties, *J. Am. Ceram. Soc.*, **81**, 41–48 (1998).
15. A. M. Thompson, H. M. Chan, and M. P. Harmer, Tensile Creep of Alumina-Silicon Carbide “Nanocomposites,” *J. Am. Ceram. Soc.*, **80**, 2221–2228 (1997).
16. S. Jiao, C. E. Borsa, and C. N. Walker, The Microstructures of Alumina Ceramics Containing Nanoparticles of Silicon Carbide or Titanium Nitride, *Silicate Industriels*, **7–8**, 211–214 (1995).
17. I. Levin, W. D. Kaplan, D. G. Brandon, and T. Wieder, Residual Stresses in Alumina-SiC Nanocomposites, *Acta metal. Mater.*, **42**, 1147–1154 (1994).
18. T. Sekino and K. Niihara, Fabrication and Mechanical Properties of Fine-Tungsten-Dispersed Alumina-Based Composites, *J. Mater. Sci.*, **32**, 3943–49 (1997).
19. H. Awaji, S.-M. Choi, and E. Yagi, Mechanisms of Toughening and Strengthening in Ceramic-Based Nanocomposites, *Mech. Mat.*, **34**, 411–422 (2002).
20. S. P. Timoshenko and J. N. Goodier, *Theory of Elasticity*, (McGraw-Hill, New York 1970). V. D. Weyl, Influence of Internal Strains on Texture and Mechanical Strength of Porcelains, (in German), *Ber. Deut. Keram. Ges.*, **36**, 319–324 (1959).
21. D. Weyl, Über den Einfluss innerer Spannungen auf das Gefüge und die Mechanische Festigkeit des Porzellans, *Ber. Deut. Keram. Ges.*, **36**, 319–324 (1959).
22. J. Selsing, Internal Stresses in Ceramics, *J. Am. Ceram. Soc.*, **44**, 419 (1961).
23. K. P. D. Lagelöf, A. H. Heuer, J. Castaing, J. P. Rivière, and T. E. Mitchell, Slip and twinning in sapphire ($\alpha - \text{Al}_2\text{O}_3$), *J. Am. Ceram. Soc.*, **77**, 385–97 (1994).
24. H. Awaji, S.-M. Choi, T. Ebisudani, and D. D. Jayaseelan, Toughening Mechanisms of Structural Ceramics, *J. Ceram. Soc. Jpn.*, **108**, 611–613 (2000), (in Japanese).
25. H. Awaji, S.-M. Choi, and D. D. Jayaseelan, Indirect Estimation of Critical Frontal Process-Zone Size Using a Single-Edge V-Notched-Beam Technique, *J. Ceram. Soc. Jpn.*, **109**, 591–595 (2001).
26. N. J. Petch, The Cleavage Strength of Polycrystals, *Iron & Steel Inst.*, **174**, 25–28 (1953).

CREEP BEHAVIOR AND MECHANISM FOR CMCs WITH CONTINUOUS CERAMIC FIBERS

Jean-Louis Chermant, Gaëlle Farizy, Guillaume Boitier, Séverine Darzens, Jean Vicens, and Jean-Christophe Sangleboeuf*

This paper is dedicated to Drs Roger W. Davidge (Great-Britain, † Aug. 1997), Junn Nakayama (Japan, † Dec. 1991) and Reiner Pabst (Germany, † July 1986).

ABSTRACT

This paper gives an overview on the creep behavior and mechanism of some CMCs, with a SiC ceramic matrix, such as C_f-SiC, SiC_f-SiC and SiC_f-SiBC. Tensile creep tests were conducted under argon and air in order to have the influence of the environmental conditions on the macroscopical mechanical response. Nevertheless, multi-scale and multi-technique approaches were required to identify and quantify mechanism(s) which is (are) involved in the creep behavior. The initiation and propagation of damages which are occurring under high stress and temperature conditions were investigated at mesoscopic, microscopic and nanoscopic scales using SEM, TEM and HREM, in order to identify the mechanism(s) involved at each scale. Automatic image analysis was used in order to quantify the evolution of

* Jean-Louis Chermant, 42 rue Jean Hébert, 14000 Caen, France. Gaëlle Farizy, LERMAT, URA CNRS 1317, ISMRA, 6 Bd Maréchal Juin, 14050 Caen Cedex, France. Guillaume Boitier, DCI, ISMRA, 6 Bd Maréchal Juin, 14050 Caen Cedex, France. Séverine Darzens, LERMAT, URA CNRS 1317, ISMRA, 6 Bd Maréchal Juin, 14050 Caen Cedex, France. Jean Vicens, LERMAT, URA CNRS 1317, ISMRA, 6 Bd Maréchal Juin, 14050 Caen Cedex, France. Jean-Christophe Sangleboeuf, LARMAUR, UPRES-JE 2310, Bât. 10B, Université de Rennes 1, Campus de Beaulieu, 35042 Rennes Cedex, France.

some damage morphological parameters. The macroscopical creep behavior has been investigated through a damage mechanics approach which seems to be the most promising route. A good correlation was found between the kinetics of the damage mechanisms and the creep behavior. For such ceramic matrix composites, the governing mechanism is a damage-creep one, with an additional delay effect due to formation of a glass when tests are performed under air.

Key words: Ceramic matrix composites, tensile creep, multiscale investigation, electron microscopy, automatic image analysis, oxidation, damage-creep.

1. INTRODUCTION

Parts for high temperature applications must involve stress and temperature resistant materials, in a domain where classical superalloys are no more efficient. Therefore ceramic matrix composites (CMCs) with continuous ceramic fibers appear as an interesting class of materials for such applications. One can quote for example exhaust vanes, exit cones, nozzle petals, turbine nozzles and wheels, combustor liners, flame holders, hot gas valves, thrust combustion chambers, transition liners, . . . , for aerospace and military turbine engines, or specific parts for nuclear, ballistic applications, or parts for chemical and semi-conductor industry (1–8). Another important domain of applications concerns the brakes for aircrafts, race cars and motorcycles, high speed trains, and now trucks and top (first) class cars (9–11).

Such complex materials regarding their components and architecture require a material science approach in order to understand their mechanical behavior and then to design and manufacture parts in such composites, to characterize their microstructure and then to formulate their constitutive law. If some links are well established between the evolution of microstructures and damages, and mechanical properties, then we can have interaction between the process of such materials and the design of structural parts (12,13).

In this paper we shall show that such a goal is reached only using different experimental tools and if observations and analysis are performed at several scales, from the macroscopic to the nanoscopic one. To illustrate that purpose we shall base this paper on the tensile creep behavior of some CMCs – C_f -SiC, SiC_f -SiC and SiC_f -SiBC – composites, for which SEP, now Snecma Propulsion Solide (S^t Médard en Jalles, France) plays a major role.

2. MATERIALS AND TECHNIQUES

Three composites have been investigated. They were fabricated by Snecma Propulsion Solide (S^t Médard en Jalles, France):

- a 2.5D C_f -SiC composite, constituted of 2.5D preforms of high strength ex-PAN carbon fibers infiltrated by SiC via the chemical vapor infiltration (CVI) process (14),
- a 2D SiC_f -SiC composite, constituted of a 2D preform of NLM 202 SiC_f fibers infiltrated by SiC via CVI process (14),
- a SiC_f -SiBC composite, constituted of a plane multi-layer reinforcement (named 2.5D GUIPEX[®], to prevent the natural delamination sensitivity of 2D mater-

ials) in NLM 202 SiC_{f202} , or Hi-Nicalon, $\text{SiC}_{f\text{HiNi}}$, fibers; these preforms were infiltrated by several CVI cycles of different compositions based on the Si-B-C system (15, 16); it gives a multi-layer and self-sealing matrix composed of Si-C (named X), B-C (named Y) and Si-B-C (named Z). Detail of the process is subject to commercial confidentiality.

All the fibers have previously received a pyrolytic carbon coating and the SiC_f -SiBC specimens a complex seal-coat to protect the material from oxidation.

Figure 1 presents a SiC_f -SiBC material, with longitudinal and transverse yarns (respectively LY and TY), macroporosity between the yarns and microporosity inside the yarns (respectively MP and μP). In the case of C_f -SiC composites some initial cracks appear due to the difference in the thermal expansion coefficients between the C_f fibers and the SiC matrix. **Figure 2** presents at high magnification the nanostructure of the fiber/matrix pyrocarbon interphase existing between matrix and fibers in the case of SiC_f -SiBC and C_f -SiC composites.

Dog-bone tensile specimens ($200 \times 24 \times 5 \text{ mm}^3$ and $74 \times 16 \times 5 \text{ mm}^3$ in the gauge) were tensile creep tested with a Schenck Hydropuls PSB 100 servo-hydraulic machine (Darmstadt, Germany) equipped with a airtight fence and an inductor furnace (AET and Célès, respectively Meylan and Lautenback, France). For tests performed under argon a graphite susceptor was used, while in air it was in MoSi_2 . Strain was measured with two opposite resistive extensometers (Schenck), inside the furnace, with a gauge length of 15 mm. Temperature was measured both with two W-Re 5/26% or Pt/Rh 0/10% thermocouples for tests performed respectively in argon or in air, and an optical pyrometer IRCON Mirage (Nikes, USA). Tests were performed in a partial pressure of argon ($\sim 500 \text{ mbar}$) and also in air for SiC_f -SiBC composites, between 1373K and 1673K and for stresses up to 400 MPa.

In our laboratory we pay a lot of attention to have very accurate creep devices. Particular care has been taken especially regarding the load frame alignment, the thermal gradient and its stability, the temperature and strain measurements and the pressure variation inside the furnace (17–19). For example when tests are performed in air, the temperature cartography in the furnace gave a variation of temperature

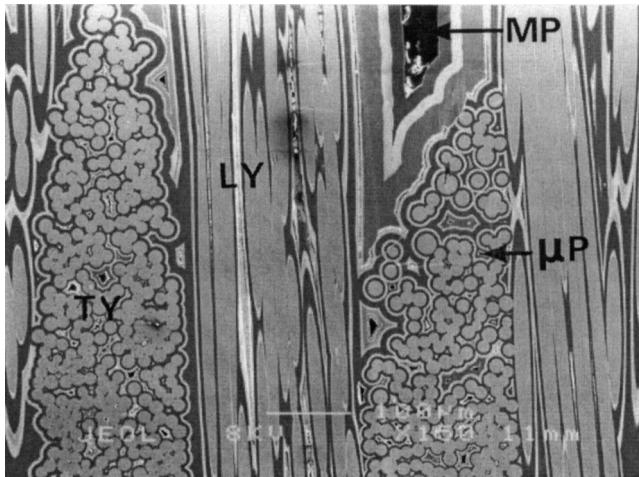


Figure 1. SEM micrograph of a SiC_{f202} -SiBC composite reinforced with NLM 202 SiC_f fibers, with LY, TY, MP and μP , respectively longitudinal yarn, transverse yarn, macroporosity and microporosity.

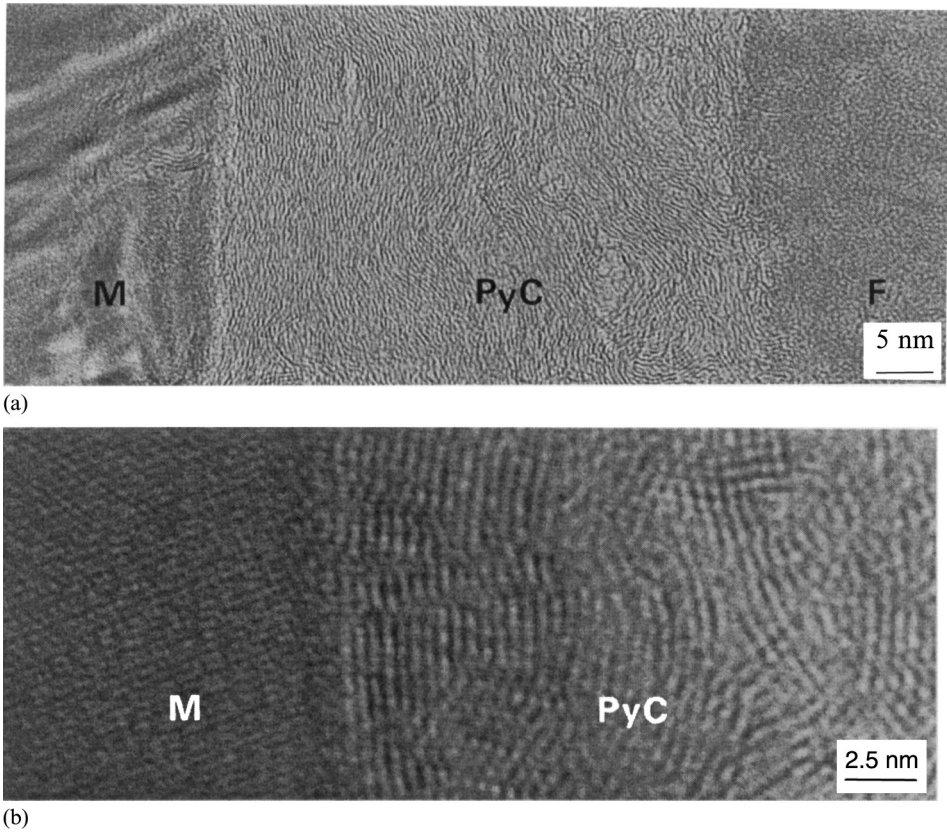


Figure 2. HREM micrographs of the fiber/matrix interphase, between matrix and fiber for $\text{SiC}_{\text{THINi}}\text{-SiBC}$ composites (a) and close to the matrix for $\text{C}_f\text{-SiC}$ composites (b).

less than 7 degrees at 1673K on 22 mm in length, and the bending component for the tensile tests was less than 1 %. If comparison of creep behavior of such high temperature materials have to be made, it absolutely requires that creep tests must be performed in conditions as accurate as possible.

SEM observations were performed with a Jeol 6400 (Jeol, Tokyo, Japan), and TEM and HREM with a Jeol 2010 and a Topcon EM 002B (Tokyo, Japan), both equipped with EDS analysis.

Some tensile tests were performed also in-situ in the SEM at room temperature, using a Deben Microtest machine (Suffolk, UK).

Aphelion[®] software (ADCIS, Caen, France) was used to perform automatic image analysis on optical and SEM images, using more specifically mathematical morphology (20, 21).

3. MACROSCOPICAL APPROACH: TENSILE BEHAVIOR AND MECHANICAL PARAMETERS

From creep tests one obtains several types of information: the change in the strain as a function of time (creep curves), $\epsilon\text{-t}$, or stress, $\epsilon\text{-}\sigma$, of the creep rate as a function of

strain, $\dot{\epsilon}$ - ϵ , time, $\dot{\epsilon}$ - t , stress, $\dot{\epsilon}$ - σ , or temperature, $\dot{\epsilon}$ - $1/T$. **Figure 3** presents some creep curves for these materials tested under air or argon. One notes a primary stage generally very short, followed by a stationary or pseudo-stationary stage where the rupture takes place. To be sure of the stationary stage, the creep strain is plotted as a function of time or strain: the existence of a plateau is a way to confirm the existence of a secondary stage.

If loading-unloading loops are performed during creep tests, one can follow the change in elastic moduli, which are very good indicators of damage. Kachanov (22) and Rabotnov (23) have demonstrated that the damage parameter, D , is given by:

$$D = 1 - \frac{E}{E_0}$$

with: E_0 , the elastic modulus of the as-received material,

E , the elastic modulus of the damaged material at time t .

In these works, we have measured the secant modulus of the hysteresis loops.

Figure 4 presents the evolution of the damage parameter, D , as a function of the inelastic deformation, ϵ_{in} , or time, t . One notes a very important increase of the damage during the loading and probably the first hours of creep, and then a certain stabilization or a slow increase (24). That evolution will be explained later (see part 8).

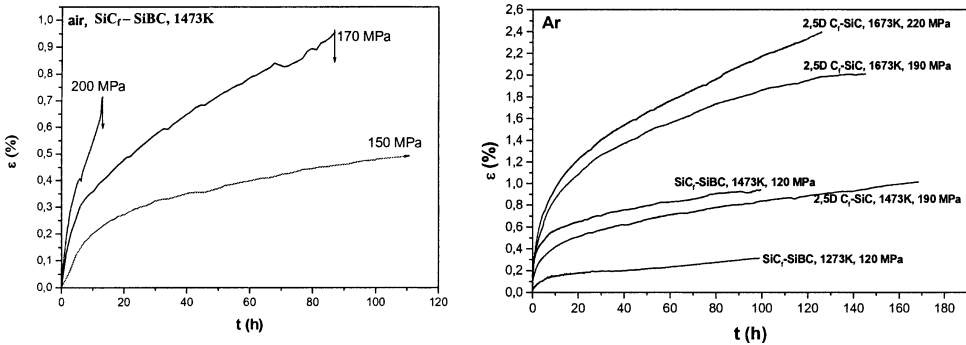


Figure 3. Creep curves, strain as a function of time, ϵ - t , for several CMCs tensile creep tested in air or in argon at several stresses.

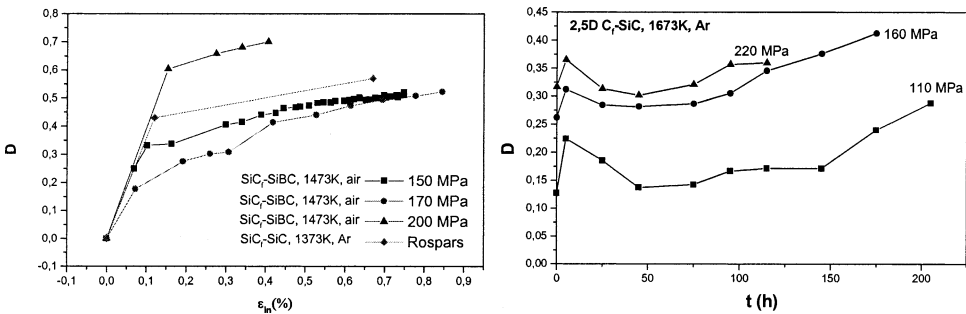


Figure 4. Damage parameter as a function of inelastic strain or time, D - ϵ_{in} or t , for different CMCs creep tested in tension in air or in argon. One has also plotted the result of Rospars et al. (1998) on an old 2D SiC_7-SiC batch, tensile creep tested in argon.

From these macroscopical results, it is impossible to have an idea of the possible creep mechanism: diffusion-creep or dislocation-creep. In the temperature experimental domain investigated – up to 1673 K for C_f -SiC and up to 1523 K for the SiC_f -SiC and SiC_f -SiBC composites – there is no diffusion phenomena as the temperatures are too low (25–28), and the dislocations are not activated in SiC below ~ 1873 K, (29). So it becomes essential to observe and analyze these materials at different scales.

4. MESOSCOPIC AND MICROSCOPIC APPROACH: MICROSCOPIES AND MECHANISM INDICATOR

Observations of specimens after creep reveal the presence of damages, i.e. mainly matrix microcracking, fiber/matrix debonding, yarn/yarn debonding, fiber and/or yarn bridging, fiber and/or yarn pull-out, and matrix layer debonding for CMCs with multilayered matrix. **Figure 5** presents an overview of such damages for specimens creep tested in argon. The matrix microcracks are most often developed first in the transverse yarns, then in the longitudinal ones, allowing to the SiC_f fiber(s) and/or yarn(s) to bridge the microcracks. In the case of creep tests performed in air, up to 1500 K the matrix and inter-layer microcracks are fulfilled by a glass, protecting the fibers and the pyrocarbon layers. At higher temperatures, there is always few glass as most part of it

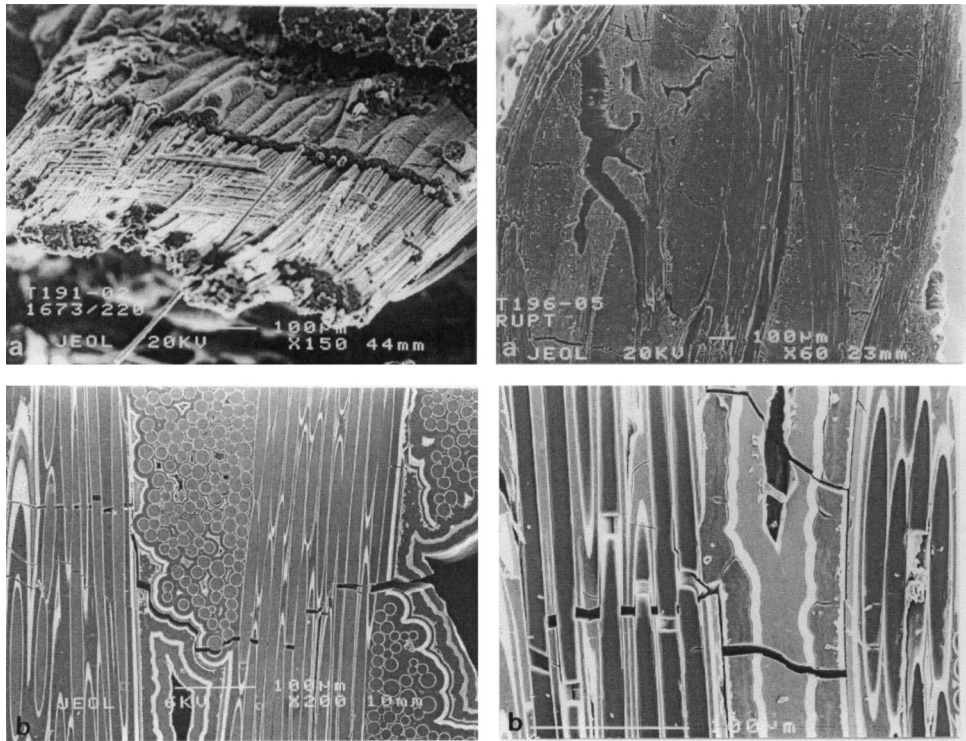


Figure 5. SEM micrographs of damage features for two CMCs tensile creep tested in Ar: a) C_f -SiC, at 1673K, under 220 MPa; b) SiC_{f202} -SiBC, at 1473K, under 120 MPa.

has been volatilized during the test and some fiber degradations are observed (**Figure 6**). If one observes the fracture surface, it is lined by a glass (Figure 6).

Then we can conclude that the creep mechanism indicator will be a damage one, and that no diffusion-creep nor dislocation-creep will operate in our experimental conditions.

TEM observations evidence inter-layer matrix microcracks. Moreover, dislocations are very rarely observed. They also reveal most often a turbostratic texture of the pyrolytic carbon close to the fibers and some mode I \rightarrow mode II microcrack deviations (**Figure 7**). At higher magnification one observes some lenticular pores

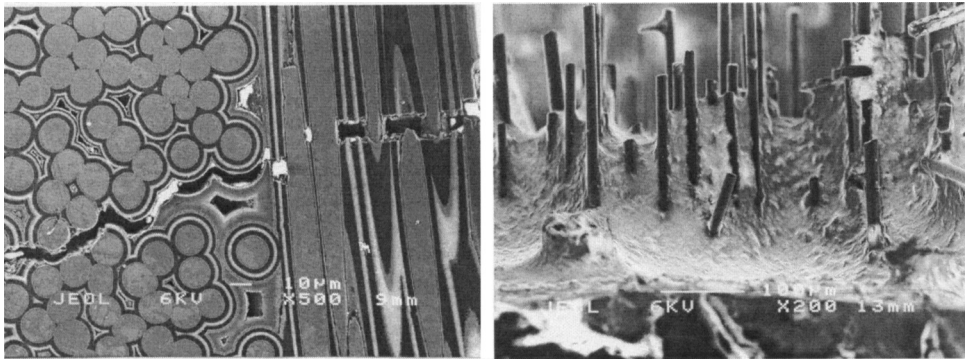


Figure 6. SEM micrographs of damage features for $\text{SiC}_{\text{FHI}}\text{Ni-SiC}$ creep tested in air, at 1473K under 170 MPa, after 87 h of creep.

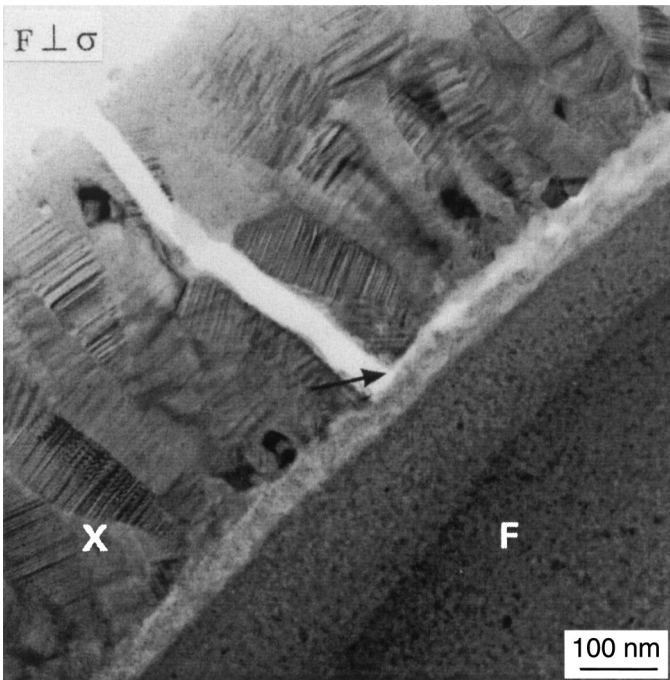


Figure 7. TEM micrograph of a mode I-mode II deviation in $\text{SiC}_{\text{FHI}}\text{Ni-SiBC}$ creep tested in argon from 1473K to 1673K under 120 MPa.

which are the nuclei for the microcrack development and propagation (**Figure 8**), (30,31) In the case of SiBC matrices, during creep tests one notes the crystallization of some matrix layers (Y and Z): in the first one that layer is made of fully crystallized B_4C , while for the second one finds nanocrystals of SiC and B_4C (30,32,33), (**Figure 9**).

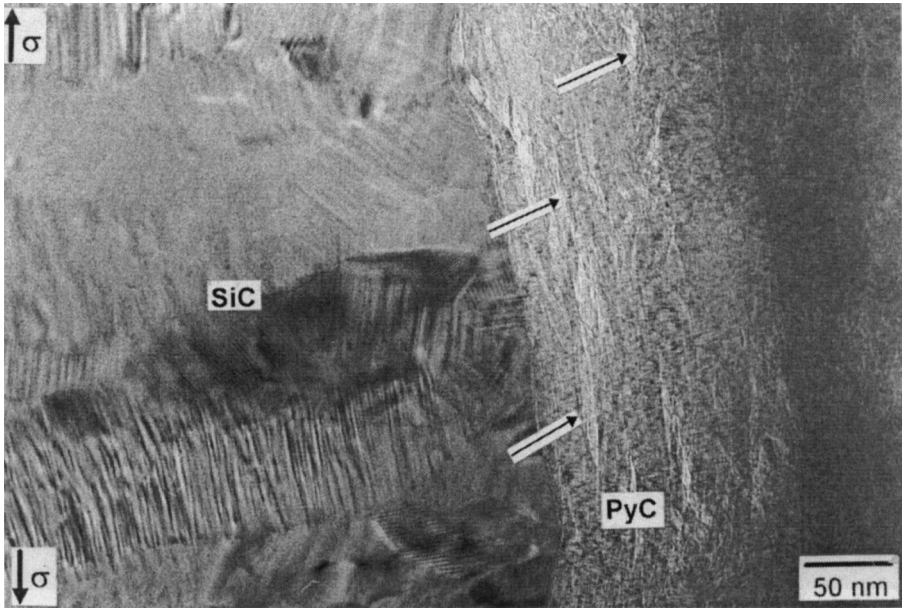


Figure 8. HREM micrograph showing the lenticular pores appearing in the pyrocarbon in C_T -SiC creep tested in Ar at 1473K under 220 MPa.

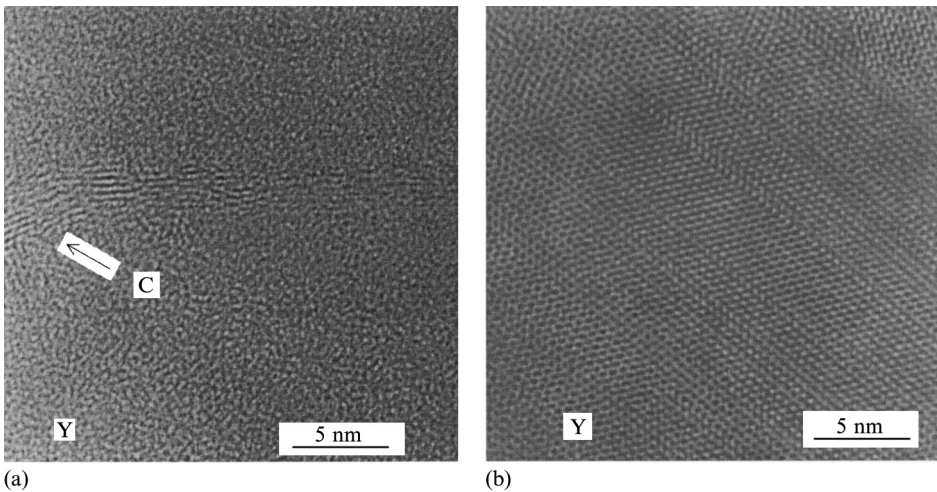


Figure 9. HREM micrograph showing the crystallization of the Y matrix layers: a) as-received SiC_{TiNi} -SiBC ; b) SiC_{TiNi} -SiBC creep tested in air at 1523K under 170 MPa, after 7 h of creep.

5. DAMAGE QUANTIFICATION: IMAGE ANALYSIS AND DAMAGE MORPHOLOGICAL PARAMETERS

The technique of automatic image analysis (AIA) and more specifically mathematical morphology (20,21) have been used to quantify these damages through morphological parameters (34,35). By specific image transformations (i.e. binary threshold, skeletization, pruning and then reconstruction) one can extract only the matrix microcracks in the yarns as a function of time and temperature. For example for C_r-SiC composites after 220 h of creep at 1273 K and 1673 K under 200 MPa, an important increase of the surface area of the cracks in the transverse yarns is observed: from 1.4 % to respectively 6.0 and 6.4 % after creep. That confirms the existence of a swelling of the transverse yarns as they are partly dislocated (31).

If interrupted creep tests are performed, one can follow the progress degree of damage and the matrix microcracking during creep. It is then possible to measure the greatest square (in that case for mathematical morphology, it is called a structuring element (20,21)) included in the matrix microcracks. So, one has shown, for example, that for different SiC_r-SiBC batches there is an opening of the transverse matrix microcracks during creep, e_m , (33,35). This parameter is in fact directly proportional to the inelastic strain of the composite, ϵ_{in} (i.e. the creep deformation as ϵ_{in} corresponds to the total measured strain minus the elastic strain), (24,33,34), (**Figure 10**). We will see later that it is a very important result. Moreover during these interrupted creep tests in Ar, we have observed that all the matrix microcracks occur during the loading (and perhaps the first hours of creep), (30,33).

All these results indicate that there is first a matrix microcracking (of course accompanied by fiber/matrix debonding) until saturation, and then their opening

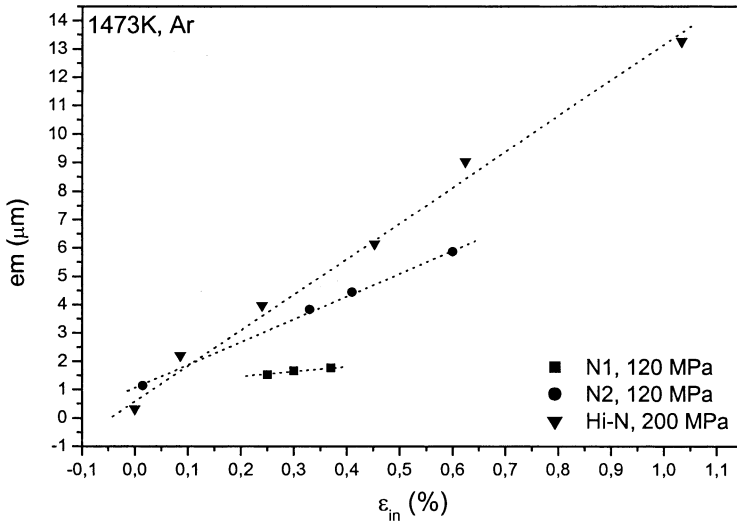


Figure 10. Change in the matrix microcrack opening, e_m , as a function of the inelastic strain, ϵ_{in} , for different SiC_r-SiBC batches, reinforced with Nicalon NLM 202 (N1 and N2) and Hi-Nicalon (Hi-N) fibers, creep tested in argon.

with or without fiber and/or yarn bridging, and not a matrix microcracking due solely to the misfit between the thermal expansion coefficient of the fibers and the matrices. That has been confirmed by SEM observations during interrupted creep tests (**Figure 11**).

6. NANOSCOPIC APPROACH: HREM AND CREEP MICROMECHANISM(S)

Observations and analysis of the materials by HREM after creep permit to accede to the elementary creep micromechanism(s) involved.

In the case of C_f -SiC composites, a nanotexturation effect of the C_f fibers is observed as a function of the temperature: the higher the test temperature is, the stronger the effect is. This nanotexturation is evidenced via the increase of i) the diameter of the basic structural units of carbon planes (BSU), and ii) the longitudinal diameter of the oriented volume of carbon planes parallel to the fiber axis, named local molecular orientations (LMO), (36). Nevertheless these nanostructural modifications contribute very slightly to the macroscopical creep strain. That is what we have called the carbon fiber nanocrep (36), as it corresponds to the very first stage of the creep mechanism for carbon fibers.

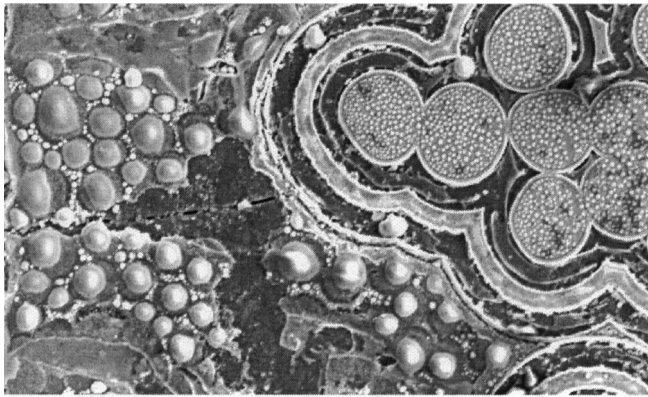
Regarding the SiC_f fibers a more or less important increase of the SiC nanocrystals is observed: for NLM 202 SiC_f fibers, it increases from 2.5 to 3.5 nm after 100 h of creep at 1473 K under 120 MPa, and for Hi-Nicalon SiC_f fibers from 5 to 8 nm after 175 h of creep under successively 150 MPa and 200 MPa (33, 35).

By high resolution electron microscopy, matrix microcracks bridged by carbon ribbons have been observed and confirmed by X-ray diffraction, both for C_f -SiC and SiC_f -SiBC (30,31,33,37). It clearly shows that some microstructural modifications and deformations occur at the nanoscopic scale for C_f -SiC as well as SiC_f -SiBC composites during creep (**Figure 12**).

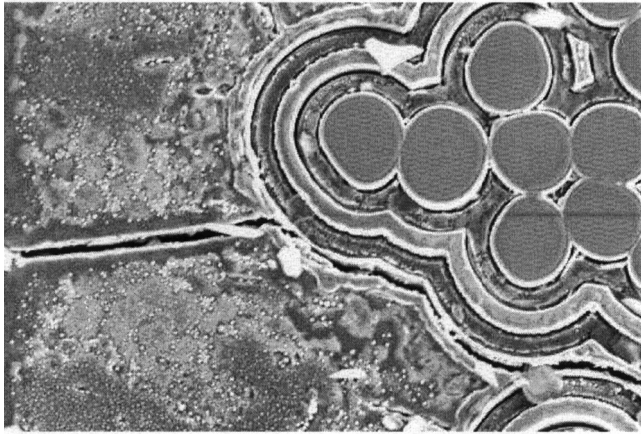
7. MACROSCOPIC MODEL: DAMAGE MECHANICS

Up today the aim of macromechanical models is to try to describe the stress redistribution which operates, in our case, during a creep solicitation and to know how the material can support the strain accumulation. It is evident that these models must take into account the mechanical behavior of the fibers, the matrices, and also the fiber/matrix interfaces and interphases, source of debonding and wear. Due to the complexity of the microstructure and the mechanical behavior, the “interfaces” in a composite imply not to consider them as a simple mathematical discontinuity! Moreover, if one knows the ex-situ characteristics of the fibers and the matrices alone (which is not always the case, as for SiBC matrices), generally we do not know their in-situ behavior in the composite.

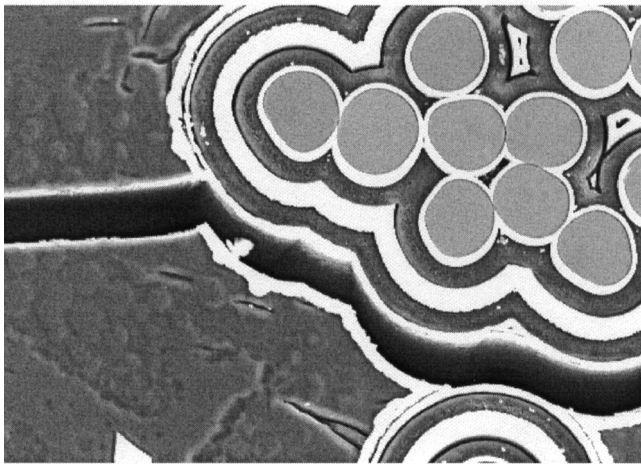
In the case of uni-directional composites, simple models taking account of the load transfer by shear (“shear lag” models) are in agreement with experimental plots. But for 2D materials or with a more complex architecture, it will never be the case. The most significative results are presently given by the damage mechanics of



11 a)



11 b)



11 c)

Figure 11. Evolution of a same area of a matrix microcrack development in a $\text{SiC}_{\text{f}/\text{HfN}_{\text{f}}}$ -SiBC composite, creep tested in Ar at 1473K under 200 MPa, after: a) the loading: $t = 0 \text{ h}$, $\varepsilon_{\text{in}} = 0$; b) $t = 1 \text{ h}$, $\varepsilon_{\text{in}} = 0.09$; c) rupture: $t = 180 \text{ h}$, $\varepsilon_{\text{in}} = 1.03$.

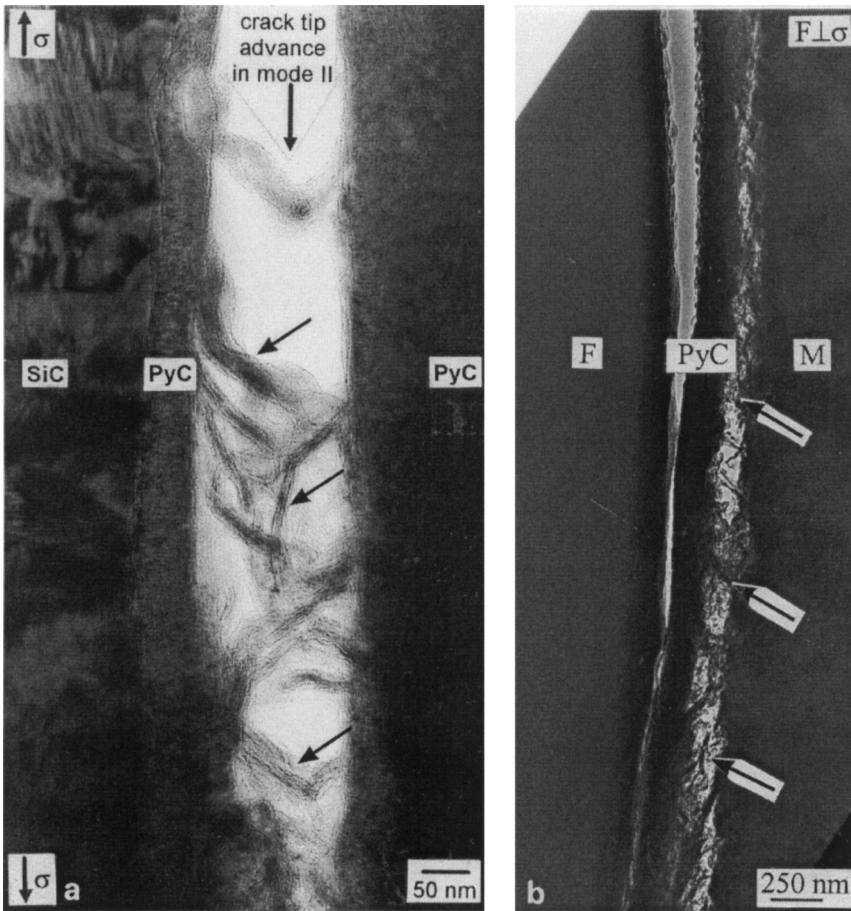


Figure 12. Carbon ribbons, observed by TEM or HREM, which bridge a matrix microcrack in C_f -SiC tensile creep tested in Ar at 1673K under 220 MPa (a), and SiC_{1202} -SiBC tensile creep tested in argon at 1523K under 120 MPa (b).

Kachanov (22) and Rabotnov (23), extended to anisotropic materials by Ladevèze (38, 39) and Chaboche (40). So, Rospars et al. (24) have reasonably simulated creep curves, and Ladevèze et al. (41) tensile tests at room temperature, both for 2D SiC_{1202} -SiC. Now it should be important to introduce in the Kachanov formalism some damage morphological parameters, as those quantitatively obtained by image analysis. From our point of view, they are very good material indicators of damage as a function of time or inelastic deformation (see Figure 10). Whatever the composite type is, this evolution appears similar and instructive.

Another promising model approach will consist to use homogenization based on scale changes. Due to the complexity of the problems linked to the numerous parameters to take into account – material, geometrical, morphological, physico-chemical, ... – it will be surely necessary to turn towards hybrid approaches.

8. CREEP MECHANISM: EVOLUTION OF THE DAMAGES AND CHANGE IN MORPHOLOGICAL DAMAGE PARAMETERS

If we link the change in the damage parameter, D , to the in-situ microscopical observations and to the damage quantification, one must recognize that we are in presence of a two-steps mechanism:

- (1) a large increase of D during the loading (and probably the very first hours of creep), which corresponds to the matrix microcrack development and to the fiber/matrix and longitudinal yarns/transverse yarns debonding; in-situ tests performed at room temperature into a SEM by Delan  e and Faucheux (42), Fauvarque (43) and Farizy (33), have shown that there is a straightening of the longitudinal yarns parallel to the tensile axis (which confirms the results of Shuler et al. (44), that longitudinal yarns take their initial position after unloading), (**Figure 13**),
- (2) a slow evolution of D which then appears and corresponds to the opening of the matrix microcrack by a thermally activated process of slow crack growth type (33, 45, 46); the slight decrease of D observed in the second domain for C_f -SiC is due to the debris (45, 47); then it is the bridged SiC_f fiber or yarn creep which controls the mechanism if temperature and/or stress are enough high (48–52).

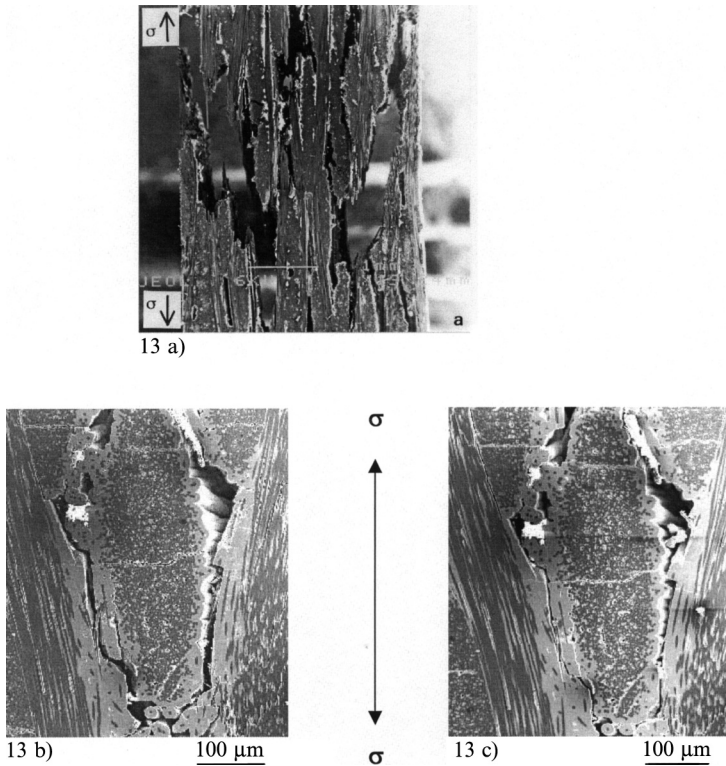


Figure 13. SEM micrographs of in-situ tensile test at room temperature: a) zone of rupture of a mini-specimen in SiC_{fHfNi} -SiBC; b) development of an inter-yarn crack under a load of 1500 N for C_f -SiC; c) same area of the C_f -SiC specimen but at rupture (1500 N).

Figure 14 presents a schematic illustration of such creep mechanism.

Under air, if tests are performed at temperature below 1500 K, matrix microcracks are nearly empty of glass: a similar mechanism is observed than under argon. But at higher temperature, the volatilization of that glass occurs and there is SiC_f fiber degradation by a corrosion/oxidation process. Therefore that glass provides an oxidation delay.

Such creep mechanism is in good agreement with the evolutions of the damage parameter, D , as a function of time, t , or inelastic strain, ϵ_{in} .

9. CONCLUSION

SiC_f -SiBC materials have a good creep resistance ($10^{-8} \cdot \text{s}^{-1} - 10^{-9} \cdot \text{s}^{-1}$) in a domain where classical materials and superalloys are no more efficient. Moreover they exhibit a good creep behavior under air. The matrix layers with boron play a very important role as they allow the formation of a glass which exhibits, up to about 1500 K, a delay effect on fracture due to the crack healing: the matrix is like a smart material. Parts in such composites are presently tested by Snecma Propulsion Solide (**Figure 15**).

In this paper related to the creep of different ceramic matrix composites, one has shown that the macroscopic approach gives access only to the evolution of some mechanical parameters, without any information on a possible mechanism. To reach such information one must observe and analyze the crept specimens at different scales and use different techniques, such as SEM, TEM, HREM, AIA, Other works begin presently to be published on such approaches (multi-scale or multi-level), as by Kwon (53), but an important effort appears to be necessary.

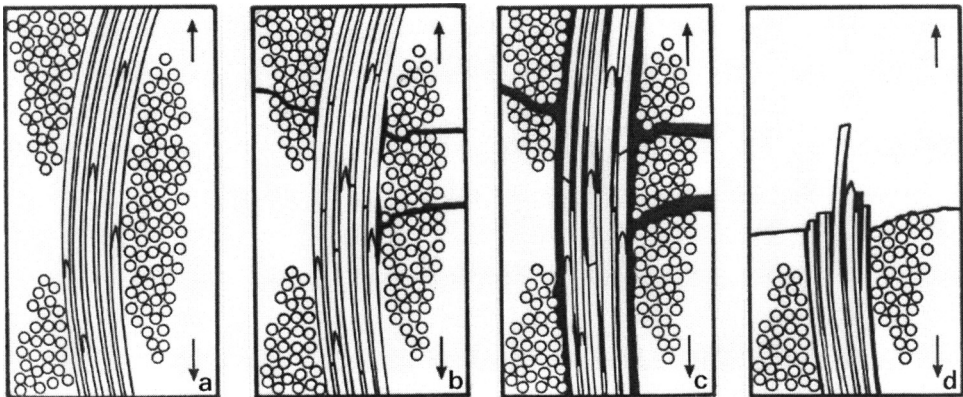


Figure 14. Schematic illustration of the tensile creep mechanism of CMCs: a) as-received material (these sequences are based on true micrographs of the observed damages); b) saturation of the matrix microcracking with fiber/matrix debonding; c) opening of the transverse matrix microcracks with transverse/longitudinal debonding of SiC yarns and fracture of some fibers; d) rupture.

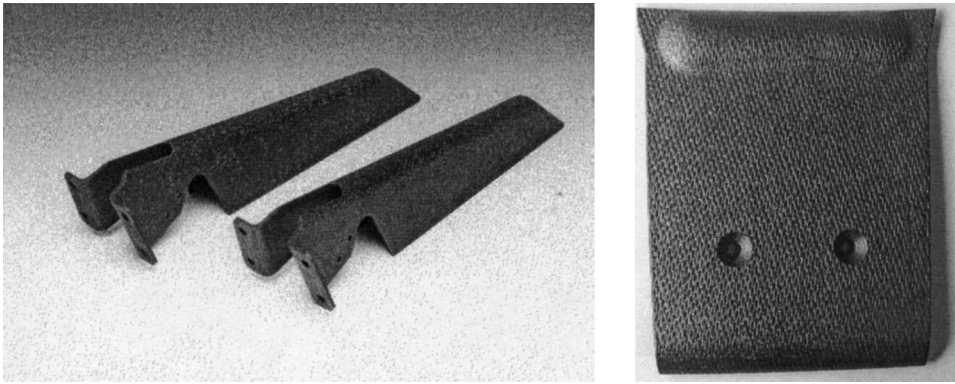


Figure 15. Parts in $\text{SiC}_f\text{-SiBC}$ fabricated by Snecma Propulsion Solide (St Médard en Jalles, France): CMC flame holders and nozzle petal.

ACKNOWLEDGMENTS

These presented works are the achievement of many years of research on CMCs and the consequence of several thesis defended at the LERMAT. We want to warmly thanks Mrs Liliane Chermant for the morphological investigations by automatic image analysis and Mr Henri Cubero for his helpful assistance to perform creep tests in the “best” conditions. All these works were supported by CNRS, Snecma Propulsion Solide (S^t Médard en Jalles, France), and specially Mr M. Bourgeon, E. Pestourie and J.M. Rougès, and Région de Basse-Normandie, in the frame of different “Groupements Scientifiques, GS”, “Contrats Programmes de Recherches, CPR”, and student grants.

REFERENCES

1. W.R. Fohey, J.M. Battison and T.A. Nielsen, Ceramic composite turbine engine component evaluation, *Ceram. Eng. Sci. Proc.*, **16**, 459–466 (1995)
2. P. Spriet, and G. Habarou, Applications of CMCs to turbojet engines: overview of the SEP experience, in: *Ceramic and Metal Matrix Composites, CMMC 96*, San Sebastian, Spain, Sept. 9–12, 1996, Proceedings edited by M. Fuentes, J.M. Martinez-Esnaola, and A.M. Daniel, *Key Eng. Mat.*, **127–131**, 1267–1276 (1997).
3. J.W. Brockmeyer, Ceramic matrix composite applications in advanced liquid fuel rocket engine turbomachinery, *J. Eng. Gas Turbines & Power, Trans. ASME*, **115**, 58–63 (1999).
4. M. Imuta, and J. Gotoh, Development of high temperature materials including CMCs for space application, in: *High Temperature Ceramic Matrix Composites, HT-CMC 3*, Osaka, Japan, Sep. 6–9, 1998, Proceedings edited by K. Niihara, K. Nakano, T. Sekino, and E. Yasuda, *CSJ Series, Ceram. Soc. Jap.*, **3**, 439–444 (1999).
5. K. Nishio, K.I. Igashira, K. Take, and T. Suemitsu, Development of a combustor liner composed of ceramic matrix composite, CMC, *J. Eng. Gas Turbines & Power, Trans. ASME*, **121**, 12–17 (1999).
6. U. Trabandt, H.G. Wulz, and T. Schmid, CMC for hot structures and control surfaces of future launchers, in: *High Temperature Ceramic Matrix Composites, HT-CMC 3*, Osaka, Japan, Sep. 6–9, 1998. Proceedings edited by Niihara K., Nakano K., Sekino T., Yasuda E., *CSJ Series. Ceram. Soc. Jap.*, **3**, 445–450, (1999).

7. R.H. Jones, and C.H. Henager, High-temperature properties of SiC/SiC for fusion applications, *J. Nucl. Mater.* **212–215**, 830–834 (1994).
8. E. Medvedovski, High-alumina armor ceramic tile for ballistic protection, *Amer. Ceram. Soc. Bull.*, **80**, 25 (2001).
9. V. Bensimhon, Les matériaux composites dans le groupe SNECMA, *AMACINFOS*, **11**, 1–2 (1999).
10. R. Renz, and W. Krenkel, C/C-SiC composites for high performance emergency brake systems, in: *Composites: from Fundamentals to Exploitation*, ECCM 9, June 4–7, 2000, Brighton, UK, ECCM 9 CD ROM C 2000, IOM Communications Ltd.
11. R. Gadow, and M. Speicher, Manufacturing and CMC-component development for brake disks in automatic applications, *Ceram. Eng. Sci. Proc.*, **20**, 551–558 (1999).
12. J.L. Chermant, Intérêt des études multi-échelles et multi-techniques en science des matériaux: cas des composites à matrices céramiques, in: *Matériaux 2002: De la Conception à la Mise en Oeuvre*, Tours, France, 21–25 Oct. 2002, CD ROM edited by the University of Technology of Belfort-Montbéliard, France, 2002.
13. J.L. Chermant, G. Boitier, S. Darzens, G. Farizy, J. Vicens, and J.C. Sangleboeuf, The creep mechanism of ceramic matrix composites at low temperature and stress, by a material science approach, *J. Eur. Ceram. Soc.*, **22**, 2443–2460 (2002).
14. F. Christin, R. Naslain, and C. Bernard, A thermodynamic and experimental approach of silicon carbide CVD. Application to the CVD-infiltration of porous carbon-carbon composites, in: *Proceedings of the 7th Int^l Conference on CVD*, edited by T.O. Sedwick, and H. Lydtin (The Electrochemical Society, Princeton, 1979) pp 499–514.
15. S. Goujard, L. Vandenbulcke, J. Rey, J.L. Charvet, and H. Tawil, Matériaux composites réfractaires protégés contre la corrosion et procédé pour son élaboration, 1990, SEP Patent, FR 9013323 (26 Oct. 1990), EP 486 347 (20 May 1992), CA 2 054 257 (27 April 1992), JO 4 263 076 (18 Sept. 1992), US 5 217 755 (8 June 1993).
16. S. Goujard, and L. Vandenbulcke, Deposition of Si-B-C materials from the vapor phase for applications in ceramic matrix composites, *Ceram. Trans.*, **46**, 925–935 (1994).
17. G. Boitier, H. Maupas, H. Cubero, and J.L. Chermant, Sur les essais de traction à longs termes à haute température, *Rev. Comp. Mat. Avancés*, **7**, 143–172 (1997).
18. M.G. Jenkins, S.M. Wiederhorn, and R.K. Shiffer, *Creep Testing of Advanced Ceramics* (Marcel Dekker, New-York, 1998), pp 171–222.
19. G. Boitier, H. Cubero, and J.L. Chermant, Some recommendations for long term high temperature tests, in: *High Temperature Ceramic Matrix Composites, HT-CMC 3*, Osaka, Japan, Sept. 6–9, 1998, *CSJ Series, Publications of the Ceramic Society of Japon*, **Vol. 3**, 309–312 (1999).
20. J. Serra, *Image Analysis and Mathematical Morphology* (Academic Press, New-York, 1982).
21. M. Coster, and J.L. Chermant, *Précis d'analyse d'images* (Les Editions du CNRS, 1985, Paris; 2nd edition, Les Presses du CNRS, Paris, 1989).
22. L. Kachanov, Rupture time under creep conditions, *Izv. Akad. Nauk. SSR*, **8**, 26–31 (1958).
23. M. Rabotnov, *Creep Problem in Structural Members* (North-Holland, Amsterdam, 1969).
24. C. Rospars, J.L. Chermant, and P. Ladevèze, On a first creep model for a 2D SiC_f-SiC composite, *Mat. Sci. Eng.*, **A 250**, 264–269 (1998).
25. G. Sines, Z. Yang, and B.D. Vickers, Creep of carbon yarn and a carbon – carbon composite at high temperatures and high stresses, *Carbon*, **27**, 403–415 (1989).
26. K. Kogure, G. Sines, and J.G. Lavin, Structural studies of postcreep, Pan-based, carbon filaments, *Carbon*, **32**, 715–726 (1994).
27. J.D. Hong, and R.F. Davis, Self diffusion of carbon-14 in high-purity and N-doped α -SiC single crystals, *J. Amer. Ceram. Soc.*, **63 (9–10)**, 546–552 (1980).
28. J.D. Hong, R.F. Davis, and D.E. Newbury, Self-diffusion of silicon-30 in α -SiC single crystals, *J. Mater. Sci.*, **16**, 2485–2494 (1981).
29. C.H. Carter, R.F. Davis, and J. Bentley, Kinetics and mechanisms of high-temperature creep in silicon carbide: II. Chemically vapor deposited, *J. Amer. Ceram. Soc.*, **67**, 732–740 (1984).
30. S. Darzens, Fluage en traction sous argon et microstructure de composites SiC_f-SiBC – Tensile creep under argon and microstructure of SiC_f-SiBC composites, *Thèse de Doctorat of the University of Caen*, 2000.
31. G. Boitier, J. Vicens, and J.L. Chermant, Understanding the creep behavior of a 2.5D C_f-SiC composite. III: From mesoscale to nanoscale microstructural and morphological investigations towards creep mechanism. *Mat. Sci. Eng.*, **A313**, 56–63 (2001).

32. S. Darzens, G. Farizy, J.L. Chermant, and J. Vicens, Quelques résultats de fluage sur les composites SiC_f-SiBC – First results on creep of SiC_f-SiBC composites, in: “12^{èmes} Journées Nationales sur les Composites JNC 12”, Cachan, France, 15–17 Nov. 2001. Proceedings edited by O. Allix, C. Cluzel, and J. Lamon, AMAC, Paris, 2000, pp 931–940.
33. G. Farizy, Mécanisme de fluage sous air de composites SiC_f-SiBC, à matrice autocicatrisante – Creep mechanism under air of SiC_f-SiBC with a self-healing matrix, *Thèse de Doctorat of the University of Caen*, 2002.
34. J.L. Chermant, G. Boitier, S. Darzens, M. Coster, and L. Chermant, Damage morphological parameters, in: 8th European Congress for Stereology and Image Analysis, 8 ECSIA, Bordeaux, France, Sept. 4–7, 2001. *Image Anal. Stereol.*, **20** [3], 207–211 (2001).
35. S. Darzens, J.L. Chermant, J. Vicens, and J.C. Sangleboeuf, Understanding the creep behavior of SiC_f-SiBC composites, *Script. Mater.*, **45**, 433–439 (2002).
36. G. Boitier, J. Vicens, and J.L. Chermant, Carbon fiber “nanocreep” in creep-tested C_f-SiC composites, *Scripta Mater.*, **38** [6], 937–943 (1998).
37. G. Boitier, J.L. Chermant, and J. Vicens, Bridging at the nanometric scale in 2.5D C_f-SiC composites, *Appl. Comp. Mat.*, **6**, 279–287 (1999).
38. P. Ladevèze, *Sur une théorie de l’endommagement anisotrope*, Internal Report, ENS Cachan, France, March 1983, n°34.
39. P. Ladevèze, On an anisotropic damage theory, in: *Failure Criteria of Structured Media*, (edited by J.P. Boehler, Balkema, Rotterdam, 1993), pp 355–363.
40. J.L. Chaboche, and J.F. Maire, New progress in micromechanics-based CDM models and their application to CMCs, *Comp. Sci. Tech.*, **61**, 2239–2246 (2001).
41. P. Ladevèze, A. Gasser, and O. Allix, Damage mechanisms modeling for ceramic composites, *J. Eng. Mat. Tech.*, **116**, 331–336 (1994).
42. A. Delanœ, and V. Fauchoux, Etude de l’endommagement de CMC par des expériences de traction in-situ – Damage investigation of CMC by in-situ tests, *Project of 3rd year at ENSI-ISMRA, Caen, France*, 2001.
43. J.P. Fauvarque, “Etude de l’endommagement de CMC SiC_f-SiBC par des expériences de traction in-situ – Damage investigation of SiC_f-SiBC composites by in-situ tests”, *Project of 3rd year at ENSI-ISMRA, Caen, France*, 2002.
44. S.F. Shuler, J.W. Holmes, X. Wu, and D. Roach, Influence of loading frequency on the room-temperature of a carbon-fiber/SiC-matrix composite, *J. Amer. Ceram. Soc.*, **76**, 2327–2336 (1993).
45. J.L. Chermant, and G. Boitier, The importance of damage and slow crack growth in the creep behavior of ceramic matrix composites, *Adv. Comp. Mater.*, **8**, 77–85 (1999).
46. S. Darzens, J.L. Chermant, J. Vicens, and J.C. Sangleboeuf, Damage creep mechanisms of SiC_f-SiBC composites, in: 26th Annual Int^l Conference on Advanced Ceramics & Composites, Cocoa Beach, FL, USA, Jan. 13–18, 2002, *Ceram. Eng. Sci. Proc.*, **23** (3), 395–402 (2002).
47. P. Reynaud, A. Dalmaz, D. Rouby, and G. Fantozzi, Mechanical stiffening of ceramic matrix composites induced by cyclic fatigue, *Key Eng. Mat.*, **132–136**, pp 1906–1909 (1997).
48. R. Bodet, X. Bourrat, J. Lamon, and R. Naslain, Tensile creep behaviour of a silicon carbide-based fibre with a low oxygen content, *J. Mater. Sci.*, **30**, 661–677 (1995).
49. G. Chollon, R. Pailler, and R. Naslain, Structure, composition and mechanical behavior at high temperature of the oxygen-free Hi-Nicalon fiber, in: *High-Temperature Ceramic-Matrix Composite I: Design, Durability and Performance, HT-CMC 2*, Aug. 20–24, 1995, Santa-Barbara, Ca, USA, *Ceram. Trans.*, **57**, 299–304 (1995).
50. R.E. Tressler, and J.A. DiCarlo, Creep and rupture of advanced ceramic fiber reinforcements, in: *High-Temperature Ceramic-Matrix Composite I: Design, Durability and Performance, HT-CMC 2*, Aug. 20–24, 1995, Santa-Barbara, Ca, USA, *Ceram. Trans.*, **57**, 141–155 (1995).
51. N. Hochet, M.H. Berger, and A.R. Bunsell, Microstructural evolution of the latest generation of a small-diameter SiC-based fibers tested at high temperatures, *J. Microscopy*, **185** [2], 243–258 (1997).
52. M. Narisawa, K. Sano, Y. Katase, and K. Okamura, Temperature-atmosphere dependence of creep behavior of advanced SiC-based fibers, in: *Proceedings of the 7th Int^l Conference on Creep and Fatigue at Elevated Temperatures*, CREEP 7, Japan Society of Mechanical Engineers, Tsukuba, Japan, June 3–8, 2001, pp 281–285.
53. Y.W. Kwon, Multi-level approach for failure in woven fabric composites, *Adv. Eng. Mater.*, **3** [9], 713–717 (2001).

STRAIN ACCUMULATION AND DAMAGE EVOLUTION DURING CREEP OF SiC_f/SiC COMPOSITES

Brian Wilshire and Howard Burt*

1. INTRODUCTION

For many high-performance applications, worldwide research efforts continue to be focussed on ceramic-fibre-reinforced ceramic-matrix composites (CFCMCs), with numerous studies featuring SiC-fibre-reinforced SiC-matrix materials (termed SiC_f/SiC type products). In particular, because these CFCMCs are being considered for components which must operate for long periods without failure under load in hostile high-temperature environments, special attention has then been directed to characterization of their creep and creep fracture behaviour. In turn, many of these studies have been concerned with clarification of the damage processes which cause creep failure, aiming to acquire the understanding needed for future product development and component design.

Creep strain/time curves have been determined for a range of SiC_f/SiC type composites,¹⁻⁶ for various types of SiC fibre⁷⁻⁹ and for other CFCMCs.^{5, 6, 10} However, the factors controlling the creep properties of different composites have usually been discussed by reference to only a few standard parameters, such as the minimum creep rate ($\dot{\epsilon}_m$), and the creep rupture life (t_f). For this reason, the present project seeks to demonstrate that evidence derived from analyses of creep curve shape is relevant to interpretation of the detailed manner in which specific material variables influence strain accumulation and damage evolution during tensile creep of CFCMCs.

* Brian Wilshire and Howard Burt, Materials Research Centre, School of Engineering, University of Wales Swansea, Singleton Park, Swansea SA2 8PP, UK

To illustrate the dependence of composite performance on the properties of the fibres and matrices, creep data comparisons and creep curve shape analyses have been undertaken for three SiC-matrix products reinforced with either silicon carbide or alumina fibres. These materials were selected to assess the effects of variations

- (a) in matrix composition for composites having nominally identical fibre configurations and fibre/matrix interfaces and
- (b) in fibre type for composites produced with essentially the same matrices, fibre/matrix interfaces and fibre architectures.

2. EXPERIMENTAL PROCEDURES

The materials studied, termed standard SiC_f/SiC,⁶ enhanced SiC_f/SiC,³ and Al₂O_{3f}/SiC composites,^{10, 11} were all reinforced with ~40vol% of ~15μm diameter fibres incorporated as bundles of ~500 fibres interwoven to obtain 2D layers of fabric. The plain woven layers or plies were then aligned and stacked to produce multilayer preforms having balanced 0/90° architectures. Carbon interfaces (~0.5μm thick) were deposited onto the fibres by decomposition of a hydrocarbon gas, before the preforms were densified by chemical vapour infiltration to give SiC matrices with porosities of ≥ 15%. The matrices contained large pores (referred to as macropores) between the plies or at yarn intersections within the plies, with small pores in the matrix regions within the fibre bundles (Fig. 1). Yet, while the three composites have many common features, two major differences are relevant to the present analyses.

- (a) The standard SiC_f/SiC and enhanced SiC_f/SiC products were fabricated with Nicalon[™] NLM202 fibres (Nippon Carbon Co.). Hence, both composites had nominally identical fibre types, volume fractions and architectures, as well as similar carbon interfaces. However, the SiC matrix of the enhanced SiC_f/SiC

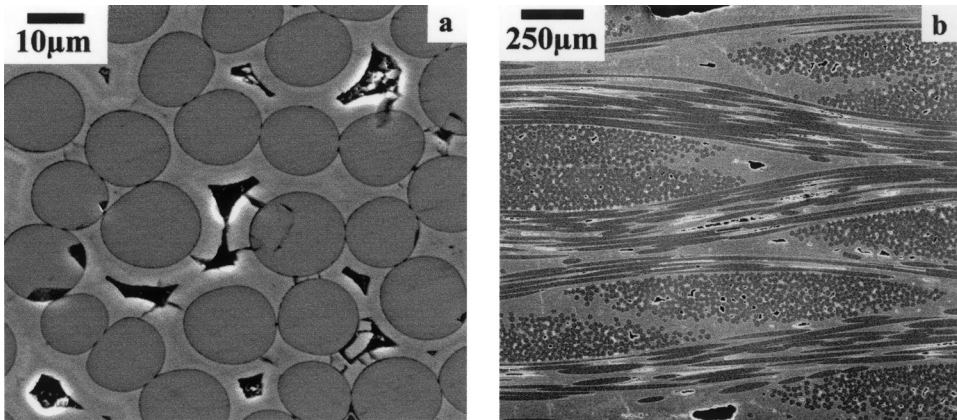


Figure 1. Scanning electron micrograph showing (a) the porous matrix within fibre bundles and (b) the fibre bundle configuration of the standard SiC_f/SiC composite before creep testing.

samples contained boron-based additives which form a sealant glass to limit oxygen penetration into the material during creep exposure at high-temperatures.

- (b) The standard SiC_f/SiC testpieces were reinforced with Nicalon[™] NLM202 fibres, whereas the $\text{Al}_2\text{O}_{3f}/\text{SiC}$ material was made with alumina fibres containing $\sim 85\%$ γ -alumina and $\sim 15\%$ amorphous silica (Sumitomo Chemicals). Even so, both composites were produced with virtually identical matrices and fibre/matrix interfaces, as well as with the same fibre volume fractions and fibre architectures.

Tensile creep tests were carried out using specimens with gauge lengths machined such that the stress axis was parallel (0°) to one of the $0/90^\circ$ fibre directions. With the two SiC_f/SiC samples, the tests were conducted in air at 1573K.^{3,6} However, with the $\text{Al}_2\text{O}_{3f}/\text{SiC}$ product, the alumina fibres transform to mullite above 1400K, so tests were completed at a maximum temperature of 1373K in air and vacuum.^{10,11}

3. EXPERIMENTAL OBSERVATIONS

For clarity, the observed creep behaviour patterns are first analysed for the standard SiC_f/SiC and enhanced SiC_f/SiC products, offering a foundation for subsequent comparisons of data sets recorded for the SiC_f/SiC type materials and the $\text{Al}_2\text{O}_{3f}/\text{SiC}$ composite.

3.1. Data Comparisons for Standard SiC_f/SiC and Enhanced SiC_f/SiC Composites

For a variety of SiC_f/SiC type composites, it has been stated that the SiC matrices are more creep resistant than the Nicalon[™] fibres.²⁻⁴ This conclusion was reached on the grounds that the creep rates reported for silicon carbide produced by chemical vapour deposition appeared to be lower than the rates predicted by extrapolation of results obtained for Nicalon[™] fibres. However, it is a simple matter to demonstrate that the fibres rather than the matrices control the creep strength of both the standard SiC_f/SiC and enhanced SiC_f/SiC composites.

The dominant rôle of the fibres becomes evident from plots of the variations of the minimum creep rate ($\dot{\epsilon}_m$) with stress (σ) for the standard SiC_f/SiC ,⁶ enhanced SiC_f/SiC ,³ and Nicalon[™] NLM202 fibres⁷ at 1573K (Fig. 2a). Clearly, stresses about five times higher must be applied to the Nicalon[™] NLM202 fibres to obtain creep rates comparable with those reported for the Nicalon[™]-fibre-reinforced composites. Both SiC_f/SiC type materials contained 40vol% fibres, so the longitudinal fibres parallel to the tensile stress axes occupied one fifth of testpiece cross-sectional areas. Hence, the creep strength of the composites must be determined by the creep resistance of their longitudinal fibres, with the brittle matrices contributing little to the overall creep strengths. However, with the fibres controlling the creep strengths, it then becomes necessary to explain why the standard SiC_f/SiC material is less creep resistant than the enhanced SiC_f/SiC product (Fig. 2a), when both composites were produced with identical fibre types, volume fractions and architectures.

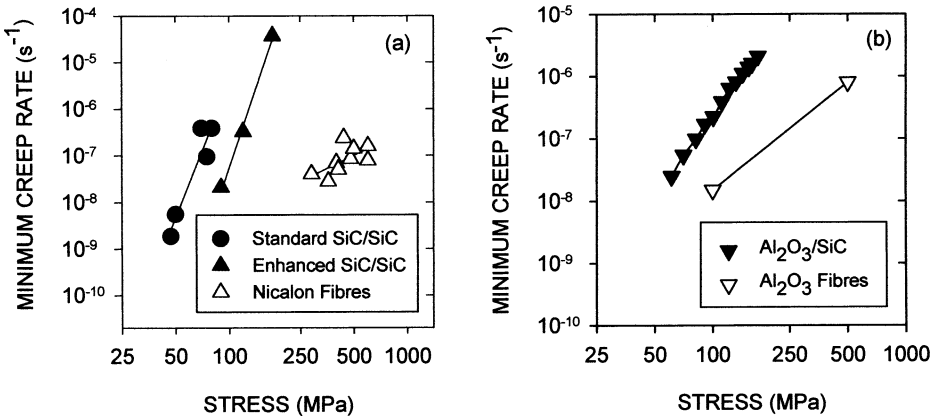


Figure 2. Stress/minimum creep rate relationships for (a) SiC_f/SiC type composites and Nicalon[®] NL202 fibres at 1573K and (b) the Al₂O₃_f/SiC material and alumina fibres at 1373K.

The relative creep strengths of the standard SiC_f/SiC and enhanced SiC_f/SiC samples (Fig. 2a) can be rationalized in a straight-forward manner⁶ by reference to the creep curve shapes recorded for these materials. Over the stress ranges covered at 1573K, both composites displayed continuously decaying ‘primary’ curves, during which the creep rate ($\dot{\epsilon}$) decreased gradually with time (t), reaching a minimum rate ($\dot{\epsilon}_m$) when fracture occurred, ie little or no period of accelerating tertiary creep was apparent before failure. Under uniaxial tension, the creep rupture life (t_f) can be defined conveniently as the time taken for the accumulated creep strain (ϵ) to become equal the limiting creep ductility (ϵ_f). Continuously decaying creep curves therefore terminate at $t = t_f$ and $\dot{\epsilon} = \dot{\epsilon}_m$ when $\epsilon = \epsilon_f$ (Fig. 3).

Except for the small amounts of boron-based additives in the enhanced matrix, the standard SiC_f/SiC and enhanced SiC_f/SiC samples are very similar, with the fibre types, volume fractions and architecture being virtually identical. Because the longitudinal fibres control the rates of creep strain accumulation, the initial portions of the creep strain/time curves are therefore indistinguishable. However, the point of

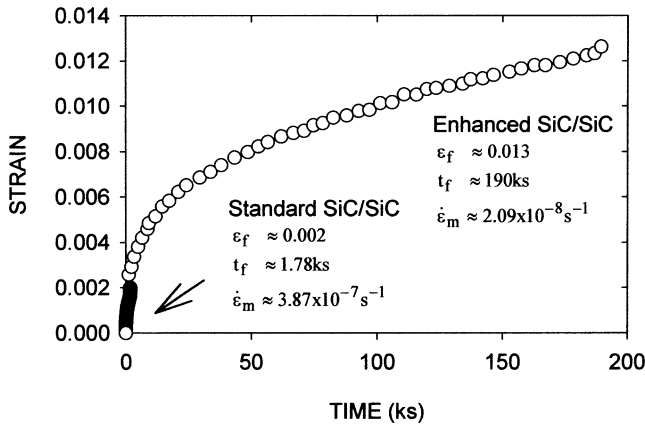


Figure 3. Creep strain/time curves for the standard SiC_f/SiC and enhanced SiC_f/SiC composites tested in air at 1573K under a stress of 90 MPa.

curve termination differs markedly for the two materials under the same test conditions, as evident from the results shown in Fig. 3.

With the standard SiC_f/SiC material, the total creep strains to failure were low over the entire stress range covered at 1573K (with $\epsilon_f \cong 0.002$). Consequently, the decaying creep curves terminate early, giving high $\dot{\epsilon}_m$ and low t_f values (Fig. 3). In contrast, with the enhanced SiC_f/SiC specimens, creep must continue for much longer times when failure occurs at higher creep ductilities. As a result, the minimum creep rates determined for the enhanced SiC_f/SiC samples are over an order of magnitude slower (Fig. 2a) and the times to fracture are almost two orders of magnitude longer than the values observed for the standard SiC_f/SiC product under equivalent test conditions (Fig. 3). Even so, the damage processes governing creep fracture must then be identified in order to account for the differences in the creep ductilities recorded for the standard SiC_f/SiC and enhanced SiC_f/SiC composites.

3.2. Creep Fracture of Standard SiC_f/SiC and Enhanced SiC_f/SiC Composites

For both SiC_f/SiC type composites, the results presented in Fig. 4 demonstrate that the rupture life is almost inversely proportional to the minimum creep rate, such that

$$\dot{\epsilon}_m \cdot t_f = \text{constant} \quad (1)$$

showing that the rate of creep damage development and the time to eventual failure are determined by the rate of creep strain accumulation ie fracture is strain controlled. Thus, with the fibres governing the measured creep rates, creep of the longitudinal fibres must also determine the fracture times (t_f).

With the standard SiC_f/SiC product, creep of the longitudinal fibres was accompanied by crack formation in the brittle matrix. Microcracks originated at pores within the transverse and longitudinal fibre bundles (Fig. 5a), with some longer cracks (Fig. 5b) forming parallel to the stress axis (presumably because of the complex stress states introduced by straightening of the interwoven fibre bundles during tensile creep). However, these types of crack rapidly became arrested, with the

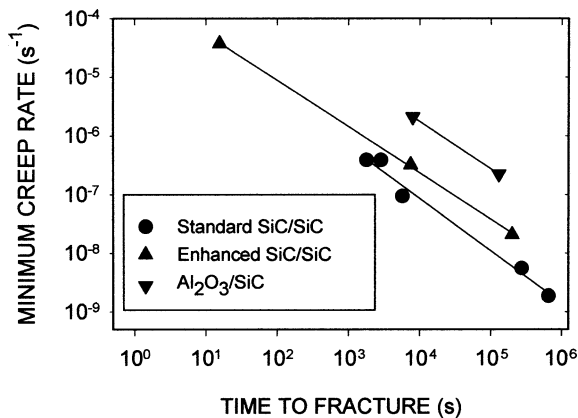


Figure 4. The dependences of the creep lives on the minimum creep rates recorded for standard SiC_f/SiC and enhanced SiC_f/SiC in air at 1573K and the $\text{Al}_2\text{O}_3/\text{SiC}$ composite under vacuum at 1373K.

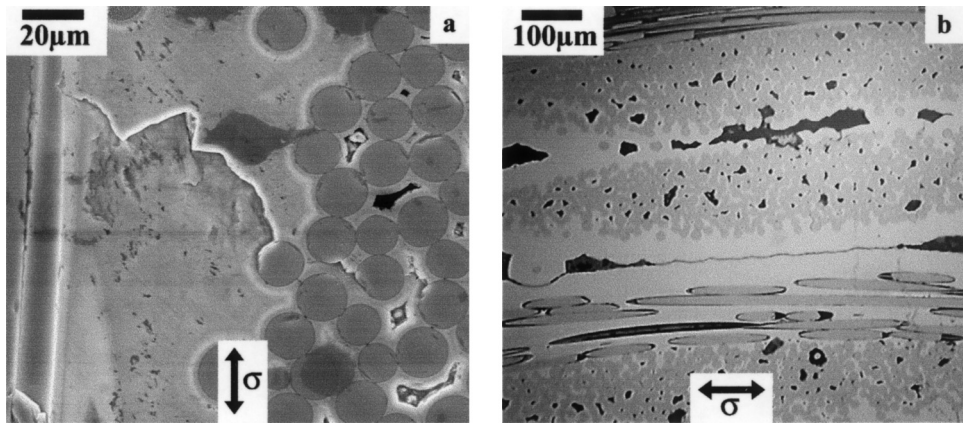


Figure 5. Micrographs showing matrix cracks developing (a) normal and (b) parallel to the tensile stress axis (σ) during creep of standard SiC_f/SiC samples.

fractured testpieces showing a very low crack incidence. Instead, fracture was a consequence of the development of a dominant crack nucleated at inter-bundle macropores at the specimen surface (Fig. 6a). As this dominant crack grew normal to the tensile stress, on penetrating into the longitudinal fibre bundles, the crack faces became bridged by unbroken fibres. The creep strength of the longitudinal fibres therefore governs both the overall creep rates and the crack growth rates, accounting for the dependence of the rupture life on the rates of creep strain accumulation (Fig. 4). Unfortunately, as the surface-nucleated dominant crack grew, direct oxygen penetration along the opening crack oxidized the vulnerable carbon interfaces, promoting failure of the bridging fibres. These events produced fracture surfaces with near-planar crack growth zones, characterized by oxidation-assisted in-plane failure of the longitudinal fibres, together with regions where sudden failure occurred by fibre pull out (Fig. 6b).

The zone characterized by fibre pull out was confined to only one region of the fracture surface, with this zone surrounded by the region of near-planar crack

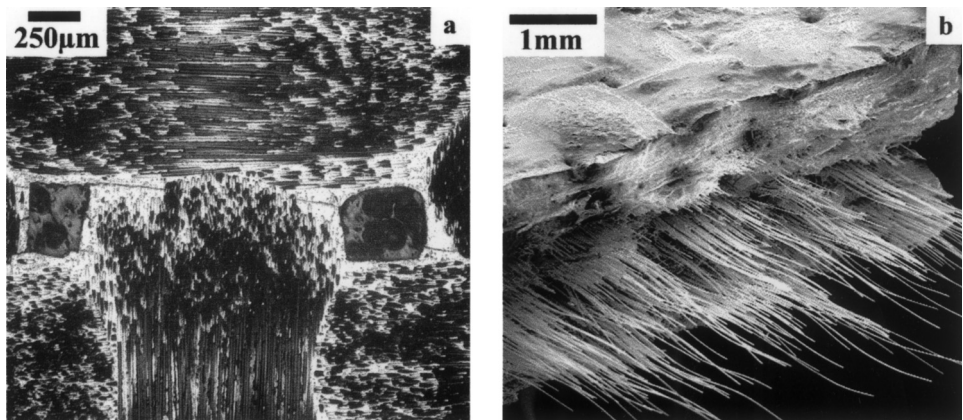


Figure 6. Scanning electron micrographs showing (a) crack nucleation and link-up from macropores and (b) fracture surface of standard SiC_f/SiC samples tested in air at 1573K.

development with negligible pull out (Fig. 6b). Moreover, with the standard SiC_f/SiC composite, the fractional area (A) of the final testpiece cross-section occupied by the near-planar crack increased from around 0.25 to about 0.75 as the applied stress decreased from 80 to 47 MPa at 1573K. Thus, ultimate failure occurred when $\sigma\sqrt{A}$ reached a critical value (~ 40 MPa), ie when the dominant crack grew to the size required to cause sudden fracture by fibre pull out.

With the standard SiC_f/SiC composite, direct ingress of oxygen along the dominant crack promotes rapid failure of the crack-bridging fibres. High crack growth rates then lead to low ductility failure, resulting in poor creep and creep fracture resistance (Fig. 3). Yet, while surface-nucleated macrocracks also form from inter-bundle macropores in the enhanced SiC_f/SiC samples, the boron-based matrix additions react with oxygen to form a sealant glass restricting oxygen penetration.³ Although the initial rates of creep strain accumulation are the same for the standard and enhanced SiC_f/SiC testpieces (Fig. 3), limiting oxygen penetration reduces the crack growth rates. Hence, fracture of the enhanced SiC_f/SiC composite is postponed to higher creep strains (Fig. 3), giving creep rates which are lower (Fig. 2a) and creep lives which are longer (Fig. 4) than the values recorded for the standard SiC_f/SiC product.

3.3. Data Comparisons for SiC_f/SiC and Al₂O_{3f}/SiC Composites

The alumina fibres reinforcing the Al₂O_{3f}/SiC composite are markedly less creep resistant than Nicalon[™] NLM202 fibres.⁸ Even so, as shown in Fig. 2b, a near five fold difference in creep strength is evident for the Al₂O_{3f}/SiC samples and the alumina fibres, with the longitudinal fibres occupying one fifth of the testpiece cross-sectional areas. Although it has been claimed that the SiC matrix is more creep resistant than the alumina fibres,^{10, 11} the results in Fig. 2b confirm that the longitudinal fibres control the creep properties of the Al₂O_{3f}/SiC composite. Furthermore, the dependence of the creep life on the minimum creep rate (Fig. 4) indicates that the longitudinal fibres also govern the rates of crack development and the times to rupture of the Al₂O_{3f}/SiC product.

As with the SiC_f/SiC type materials, the rates of creep strain accumulation and crack growth are therefore determined by the longitudinal alumina fibres in the Al₂O_{3f}/SiC samples. However, unlike the various forms of SiC fibre, alumina fibres might not be expected to be prone to oxidation-assisted fibre failure. Yet, as matrix cracking proceeds, it appears that oxygen penetration into the Al₂O_{3f}/SiC testpieces can destroy the carbon interfaces, accelerating fibre failure and reducing creep ductility. This view is supported by the fact^{10, 11} that, at 100 MPa, the creep ductility of the Al₂O_{3f}/SiC material decreased from ~ 0.10 to ~ 0.01 , with a corresponding decrease in creep rupture life from 2×10^5 s to 5×10^2 s, when the test atmosphere was changed from vacuum to air (Fig. 7).

These observations suggest that the processes of creep strain accumulation and damage development are broadly similar for the SiC_f/SiC and Al₂O_{3f}/SiC composites, even though very different creep curve shapes are displayed (Figs. 3 and 7). Thus, decaying curves are recorded for the standard and enhanced SiC_f/SiC products (Fig. 3), with decaying curves having no discernible tertiary stages also found for Nicalon[™] NLM202 and other types of SiC fibres,⁷⁻⁹ as well as for sintered silicon carbide.¹² In contrast, with the Al₂O_{3f}/SiC testpieces tested in air or vacuum, decaying

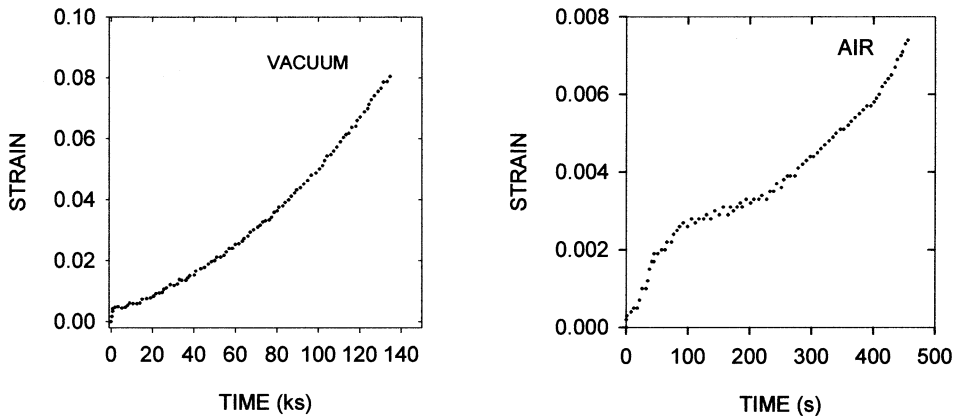


Figure 7. Creep strain/time curves recorded for the $\text{Al}_2\text{O}_3\text{f}/\text{SiC}$ composite tested in (a) vacuum and (b) air under a stress of 100 MPa at 1373K.^{10,11}

primary stages of relatively short duration were followed immediately by extended tertiary stages (Fig. 7). Creep curves exhibiting definite tertiary stages have also been reported for various alumina fibres⁹ and even for monolithic alumina.¹³ On this basis, it appears that the reinforcing fibres determine not only the rates of creep strain accumulation and damage evolution but also the creep curves shapes displayed by CFCMCs.⁶

4. DISCUSSION

With the SiC_f/SiC type composites now considered, the creep strain rates are governed by the creep resistance of the longitudinal fibres. However, the creep strengths and diameters of individual fibres vary, causing the scatter in the data shown in Fig. 1a for Nicalon[™] NLM202 fibres.⁷ Because the weakest fibre regions within the longitudinal bundles deform most easily, the creep rate decays continuously as the load is transferred to the stronger fibres. Although matrix cracks nucleate and grow as the longitudinal fibres extend, microstructural studies have shown that the crack incidence is very low. Because the brittle matrices are weak, crack development therefore has little effect on the decaying creep rate (Fig. 3).

4.1. Creep Curve Shape Analysis for SiC_f/SiC Type Composites

The shapes of continuously decaying creep curves (Fig. 3) can be analysed most easily by describing the accumulation of creep strain (ε) with time (t) as

$$\varepsilon = at^x \quad (2)$$

where a and x are constants, with $x \cong 0.5$ for the standard SiC_f/SiC material at 1573K.⁶ With this form of curve, fracture occurs when $t = t_f$, $\underline{\varepsilon} = \underline{\varepsilon}_m$ and $\varepsilon = \varepsilon_f$. Hence, differentiation of Eq. (2) gives (putting $t = t_f$)

$$\dot{\varepsilon}_m.t_f = X\varepsilon_f \quad (3)$$

with $x = X$. Eq. (3) then reduces to Eq. (1) when the creep ductility (ε_f) does not vary significantly with changing test conditions, as is the case with the standard SiC_f/SiC composite for which $\dot{\varepsilon}_m.t_f \cong 0.001$ and $\varepsilon_f \cong 0.002$, so $x = X = 0.5$ over the full stress range studied at 1573K.⁶ In contrast, with the $\text{Al}_2\text{O}_{3f}/\text{SiC}$ ^{10, 11} and seemingly with the enhanced SiC_f/SiC ,³ as well as with other CFCMCs such as SiC-fibre-reinforced Al_2O_3 -matrix samples,⁶ Eq. (3) rather than Eq. (1) applies when ε_f increases with increasing test duration.⁶ Hence, t_f increases by more than the decrease in $\dot{\varepsilon}_m$, so that $\dot{\varepsilon}_m.t_f$ increases when higher creep ductilities are recorded (Eq. 3).

4.2 Creep Damage Tolerance of SiC_f/SiC Type Composites

While the matrices contribute little to the overall creep strengths of the SiC_f/SiC type products, the composition and properties of the matrices affect the creep property values recorded for the composites by governing the rates of oxygen ingress. In turn, with fibres and fibre/matrix interfaces prone to oxidation, the rates of oxidation-assisted failure of the crack-bridging fibres influences the creep ductility and therefore the measured $\dot{\varepsilon}_m$ and t_f values (Fig. 3). For this reason, ‘self healing’ approaches such as the use of enhanced SiC matrices reduce crack growth rates, improving creep lives by postponing failure to higher creep strains. However, with both the standard SiC_f/SiC and enhanced SiC_f/SiC materials, fracture eventually occurs when a dominant macro-crack grows to a size sufficient to cause sudden failure by fibre pull out (Fig. 6b). Particularly during long-term creep exposure under low stress conditions, large cracks must then develop before failure takes place. Hence, the present SiC_f/SiC materials can be considered as crack tolerant, but this criterion may not be sufficient for selection of these products for safety-critical aerospace applications.

Because the Nicalon[™] NLM202 and other SiC fibres display continuously decaying creep curves,⁷⁻⁹ similar curve shapes are exhibited by SiC-fibre-reinforced composites (Fig. 3). In the absence of distinct tertiary stages, the primary creep strain (ε_p) equals the total creep strain to failure (ε_f), so the tertiary strain ($\varepsilon_f - \varepsilon_p$) is zero. Consequently, near-zero values are also obtained for the creep damage tolerance parameter (λ), given by^{14, 15}

$$\lambda = (\varepsilon_f - \varepsilon_p) / \dot{\varepsilon}_m.t_f \quad (4)$$

The creep damage tolerance value is important in practical situations when materials must withstand local strain concentrations, say, in regions where a change in component cross-section leads to stress concentrations. Values of λ in the range 5 to 10 are then thought to ensure that the strain concentrations encountered during service will not lead to premature failure.¹⁴ Hence, with the standard and enhanced SiC_f/SiC samples, λ values near to zero may represent a severe design constraint.

4.3 Creep Damage Tolerance of the $\text{Al}_2\text{O}_{3f}/\text{SiC}$ Composite

With the $\text{Al}_2\text{O}_{3f}/\text{SiC}$ composite, creep of the longitudinal alumina fibres is also accompanied by crack formation in the brittle SiC matrix. Moreover, for tests carried out under vacuum, matrix cracking continues throughout the decaying primary and accelerating tertiary stages, although fibre failure begins only when the alumina fibres reach their limiting creep ductility under the test conditions imposed. Fracture

of the $\text{Al}_2\text{O}_3/\text{SiC}$ samples therefore takes place by progressive fibre failure and eventual fibre pull out, but only after extended tertiary stages have been recorded (Fig. 7a).

By exhibiting clearly-defined tertiary stages, λ values of 5 or more are found for the $\text{Al}_2\text{O}_3/\text{SiC}$ material, even when low ductility failure occurs during tests conducted in air (Fig. 7b). Consequently, $\text{Al}_2\text{O}_3/\text{SiC}$ type composites are both crack tolerant and creep damage tolerant. Hence, the requirement exists for high-strength high-stability fibres of weavable diameter ($\sim 15\mu\text{m}$) displaying creep curves with extended tertiary stages, allowing development of high-performance CFCMCs possessing the crack tolerance and creep damage tolerance needed for safety-critical aerospace applications.

5. CONCLUSIONS

For three SiC-matrix composites reinforced with interwoven bundles of silicon carbide or alumina fibres, the longitudinal fibres are shown to control the rates of creep strain accumulation and crack development, with oxygen ingress through the matrices affecting the strains and times to fracture. The fibres also govern the shapes of the creep curves displayed by the composites which, in turn, determine whether the creep damage tolerance levels required for safety-critical engineering applications can be attained.

REFERENCES

1. A. G. Evans and C. Weber, Creep damage in SiC/SiC composites, *Mat. Sci. Eng.* A208, 1–6 (1996).
2. S. Zhu, M. Mizano, Y. Kagawa, J. Cao, Y. Nagano and H. Kaya, Creep and fatigue behaviour of SiC fibre reinforced SiC composite at high temperatures, *Mater. Sci. Eng.* A225, 69–77 (1997).
3. S. Zhu, M. Mizano, Y. Nagano, J. Cao, Y. Kagawa and H. Kaya, Creep and fatigue behaviour in an enhanced SiC/SiC composite at high temperature, *J. Am. Ceram. Soc.* 81, 2269–2277 (1998).
4. S. Zhu, M. Mizano, Y. Kagawa, J. Cao, Y. Nagano and H. Kaya, Creep and fatigue behaviour in Hi-Nacolon[®]-fibre-reinforced silicon carbide composites at high temperatures, *J. Am. Ceram. Soc.* 82, 117–128 (1999).
5. G. Fantozzi, J. Chevalier, C. Olagnon and J. L. Chermant, Creep of Ceramic Matrix Composites, in *Comprehensive Composite Materials*, edited by A. Kelly and C. Zureben, (Elsevier, London 2000) 115–162.
6. B. Wilshire, Creep property comparisons for ceramic-fibre-reinforced ceramic-matrix composites, *J. Eur. Ceram. Soc.* 22, 1329–1337 (2002).
7. G. Simon and A. R. Bunsell, Creep behaviour and structural characterization at high temperatures of Nicalon SiC fibres, *J. Mater. Sci.* 19, 3658–3670 (1984).
8. A. R. Bunsell and M–H. Berger, Fine diameter ceramic fibres, *J. Eur. Ceram. Soc.* 20, 2249–2260 (2000).
9. J. A. DiCarlo, H. M. Yun and J. B. Hurst, Fracture mechanisms for SiC fibres and SiC/SiC composites under stress-rupture conditions at high temperatures, in *Proc. Tenth Inter. Conf. on Fracture*, edited by K. Ravi-Chandra, B. L. Karihaloo, T. Kishi, R.O. Ritchie and A. T. Yokabori Jr. (Elsevier, London 2001) Publication No. ICF 100586 (C.D.Rom).
10. F. Lamouroux, M. Steen and J. L. Valles, Damage of a 2D $\text{Al}_2\text{O}_3/\text{SiC}$ composite during uniaxial creep, *Comp. Sci. Tech.* 56, 825–830 (1996).
11. J. N. Adami, Comportement en fluage uniaxial sous vide d'un composite 2D $\text{Al}_2\text{O}_3/\text{SiC}$, Thèse, Ecole Polytechnique de Zürich, 1992.

12. B. Wilshire and H. Jiang, Deformation and failure processes during tensile creep of sintered silicon carbide, *Br. Ceram. Trans.* 93, 213–218 (1994).
13. C. K. L. Davies and S. L. Sinha Ray, High temperature creep deformation of polycrystalline alumina in tension, in *Special Ceramics Vol. 5*, edited by P. Popper (Br. Ceram. Res. Assoc., Stoke-on-Trent, 1972) 193–207.
14. I. N. Goodall, R. D. H. Cockcroft and E. J. Chubb, An approximate description of the creep rupture of structures, *Int. J. Mech. Sci.* 17, 351–359 (1975).
15. M. F. Ashby and B. F. Dyson, Creep damage mechanisms and mechanics, in *Advances in Fracture Research*, edited by S.R. Valluri et al (Pergamon Press, Oxford, 1984), 3–30.

MODELLING MULTILAYER DAMAGE IN CROSS-PLY CERAMIC MATRIX COMPOSITES

M Kashtalyan and HW Chandler*

1. INTRODUCTION

Compared with monolithic ceramics, continuous fibre reinforced ceramic matrix composites (CMCs) have higher fracture toughness, better fatigue resistance and damage tolerance, retaining their load carrying capacity in the presence of damage. Over the years, a large number of experimental and theoretical studies have been conducted on damage evolution and failure mechanisms of CMCs, see review by Birman and Byrd (2000). Much of this work has been concerned with unidirectional materials. However, if CMCs are to be applied under multi-axial stress conditions, multidirectional laminated or woven composites containing fibre reinforcement at more than one orientation need to be employed.

Matrix cracking has long been recognised as a first damage mode observed in unidirectional CMCs under mechanical, thermomechanical or thermal loading. A number of studies of cross-ply CMC laminates under both quasi-static and cyclic uniaxial tensile loading have shown that matrix cracks accumulate both in the 90° and 0° plies. Matrix cracking in the 90° plies leads to formation of macrocracks, or tunnelling cracks, while in the 0° plies matrix cracks are bridged by the fibres and are accompanied by fibre-matrix debonding. Macrocracks, or tunnelling cracks, are perpendicular to the direction of loading and run parallel to the fibres in the 90° layer. The onset of matrix cracking in cross-ply CMCs occurs at lower strain levels than in unidirectional materials, with 90° ply cracks initiating before the 0° ply

* School of Engineering and Physical Sciences, University of Aberdeen, AB24 3UE, UK

cracks, although the latter may reach a higher saturation density (Pryce and Smith, 1994; Erdman and Weitsman, 1998).

Matrix cracking results in reduction in the laminate stiffness and strength. Stiffness reduction in CMCs is greater than that observed in polymer matrix composites due to lower ratio between fibre and matrix moduli. It also affects coefficients thermal expansion and vibration frequencies. A number of models have been suggested to estimate the effect of transverse macrocracks in the 90° plies and matrix cracks bridged by fibres in the 0° plies on the mechanical properties of cross-ply CMC laminates (Pryce and Smith, 1994; Daniel and Anastassopoulos, 1995; Lu and Hutchinson, 1995; Erdman and Weitsman, 1998; Birman and Byrd, 2001; Yasmin and Bowen, 2002; Birman and Weitsman, 2003).

When a cross-ply laminate is subjected to biaxial loading, matrix cracking may lead to formation of macrocracks both in the 90° and 0° plies. The microscopic damage evolution in cross-ply CMCs under biaxial loading has not been well characterised yet. In this paper, stiffness-damage behaviour of cross-ply $[0_m/90_n]_s$ CMC laminates with macrocracks both in the 90° and 0° plies is predicted theoretically using the Equivalent Constraint Model (ECM) of the damaged lamina (Fan and Zhang, 1993; Kashtalyan and Soutis, 1999). To capture simultaneous accumulation of damage both in the 90° and the 0° plies, two ECM laminates are analysed simultaneously, as a coupled problem, instead of the original one. In each ECM laminate, one ply group or layer contains damage explicitly, while the other is replaced with equivalent homogeneous layer(s) with reduced stiffness properties. Following analysis of stresses in the explicitly damaged layer(s) of ECM laminates, closed form expressions for the reduced stiffness properties of the damaged laminate are derived representing them as functions of crack densities in the 90° and 0° plies. Numerical results for SiC/CAS cross-ply laminates of different lay-ups are presented and discussed.

2. EQUIVALENT CONSTRAINT MODEL

The Equivalent Constraint Model (ECM) was introduced by Fan and Zhang (1993) with the aim to analyse the in-situ constraint effects on damage evolution in a particular lamina within a multidirectional laminate. In this model, all the laminae below and above the chosen lamina are replaced with homogeneous layers having the equivalent constraining effect. It is assumed that the in-plane stiffness properties of the equivalent constraint layers can be calculated from the classical lamination theory, provided stresses and strains in them are known.

Figure 1 shows a $[0_m/90_n]_s$ cross-ply laminate damaged by transverse and longitudinal tunnelling cracks (macrocracks). The cracks in each ply are assumed to be spaced uniformly and span the full thickness and width of the ply. Spacings between longitudinal macrocracks are denoted $2s_1$, and between transverse macrocracks $2s_2$. The laminate is subjected to biaxial tension ($\bar{\sigma}_{11}$ and $\bar{\sigma}_{22}$) and shear loading ($\bar{\sigma}_{12}$).

Application of the ECM to the laminate with transverse and longitudinal macrocracks described above means that instead of considering the damaged configuration shown in Fig. 1, the following two ECM laminates will be analysed. In the ECM1 laminate, the 0° lamina (layer 1) contains damage explicitly, while the 90°

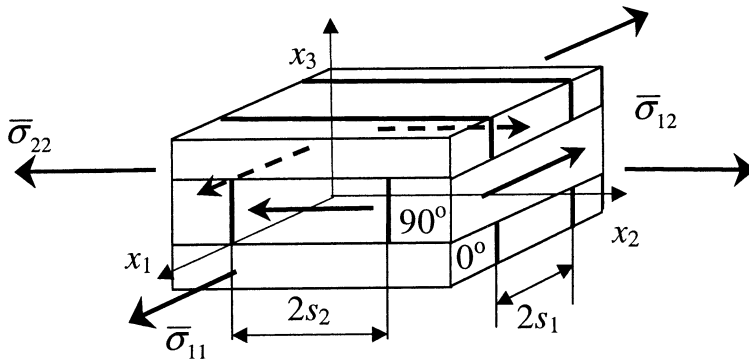


Figure 1. Cross-ply laminate under general in-plane loading damaged by transverse macrocracks in the 90° layer and longitudinal macrocracks in the 0° layer.

lamina (layer 2), damaged by transverse cracks, is replaced with a homogeneous layer with reduced stiffness properties. In the ECM2 laminate, the 90° lamina (layer 2) is damaged explicitly, while the damaged 0° laminae are replaced with homogeneous layers with reduced stiffness properties. Representative segments of the ECM2 and ECM1 laminates, containing a single crack (pair of) crack(s) are shown in Fig. 2.

The purpose of the analysis of an ECM laminate is to determine the reduced stiffness properties of the explicitly damaged layer. Since the reduced stiffness properties of the equivalent constraint layer(s) used in the analysis of an ECM laminate, are assumed to be determined from the analysis of the other ECM laminate, problems for ECM1 and ECM2 laminates are coupled. The advantage of the ECM-based approach is that it avoids cumbersome consideration of a repeated laminate element defined by the intersecting pairs of macrocracks used by other researchers (Hashin, 1987; Tsai and Daniel, 1992; Henaff-Gardin et al, 1996a,b).

3. STRESS ANALYSIS

The ECM1 and ECM2 laminates are referred to the same co-ordinate system $x_1x_2x_3$ (Fig. 2) and assumed to be under generalised plane strain in the planes Ox_1x_3 and Ox_2x_3 , respectively. Due to symmetry, only a quarter of each segment needs to be considered.

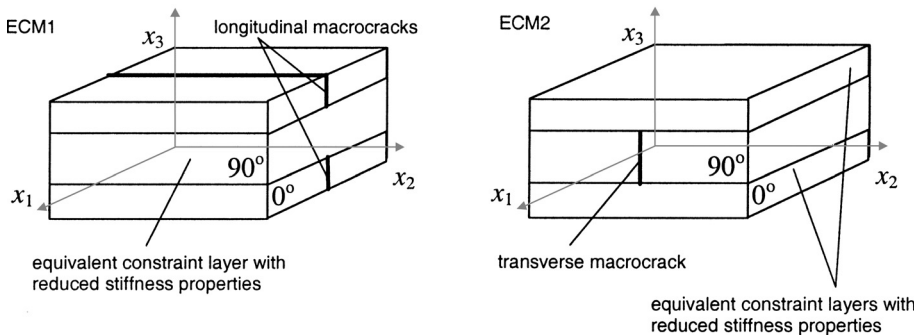


Figure 2. Equivalent Constraint Model of a cross-ply laminate with multilayer damage.

The in-plane stresses in the explicitly damaged μ^{th} layer of the ECM μ laminate ($\mu = 1$ or 2) can be determined from the equilibrium equations

$$\frac{d}{dx_\mu} \tilde{\sigma}_{j\mu}^{(\mu,k)} + (-1)^k \frac{\tau_j^{(\mu)}}{h_k} = 0, \quad j, \mu, k = 1, 2 \tag{1}$$

Here $\tilde{\sigma}_{ij}^{(\mu,k)}$ are the in-plane microstresses (i.e. stresses averaged across the layer thicknesses and the width of the laminate) in the k^{th} layer of the ECM μ laminate and $\tau_j^{(\mu)}$ are the interface shear stresses at the (0/90) interface of the ECM μ laminate. The in-plane microstresses are related to the total stresses $\bar{\sigma}_{ij}$ applied to the laminate by the equations of global equilibrium

$$\chi \tilde{\sigma}_{ij}^{(\mu,1)} + \tilde{\sigma}_{ij}^{(\mu,2)} = (1 + \chi) \bar{\sigma}_{ij} \quad \chi = h_1/h_2, \quad i, j = 1, 2 \tag{2}$$

The constitutive equations for both layers in terms of microstresses and microstrains are

$$\{\tilde{\sigma}^{(\mu,\mu)}\} = [\hat{Q}^{(\mu)}] \{\tilde{\varepsilon}^{(\mu,\mu)}\}, \tag{3a}$$

$$\{\tilde{\sigma}^{(\mu,\kappa)}\} = [Q^{(\kappa)}] \{\tilde{\varepsilon}^{(\mu,\kappa)}\} \tag{3b}$$

Here $[\hat{Q}^{(\mu)}]$ is the in-plane stiffness matrix of μ^{th} layer of the ECM μ laminate, and $[Q^{(\kappa)}]$ is the modified in-plane stiffness matrix of the equivalent constraint layer (κ^{th} layer). Crack surfaces are assumed to be stress-free, so that

$$\tilde{\sigma}_{j\mu}^{(\mu,\mu)}|_{x_\mu=0} = 0, \quad j, \mu = 1, 2 \tag{4}$$

The interface shear stresses $\tau_j^{(\mu)}$ can be expressed in terms of the in-plane displacements $u_j^{(\mu,k)}$, $j = 1, 2$ as

$$\tau_j^{(\mu)} = K_j^{(\mu)} (\tilde{u}_j^{(\mu,1)} - \tilde{u}_j^{(\mu,2)}) \tag{5}$$

where K_j are the shear lag parameters. If out-of-plane shear stresses $\sigma_{j3}^{(\mu,1)}$, $j = 1, 2$, vary linearly with x_3 and in the 0° lamina this variation is restricted to the region of about one ply thickness t , the shear lag parameters will be

$$K_j^{(\mu)} = K_j = \frac{3\hat{G}_{j3}^{(1)}\hat{G}_{j3}^{(2)}}{h_2\hat{G}_{j3}^{(1)} + (1 + (1 - \eta)/2)\eta h_1\hat{G}_{j3}^{(2)}}, \quad \eta = t/h_1, \quad j = 1, 2 \tag{6}$$

Here, $\hat{G}_{j3}^{(k)}$, $k = 1, 2$ are the out-of-plane shear moduli of the k^{th} layer; they are unaffected by the presence of matrix cracks. Equations (1) – (6) provide full set of equations and boundary conditions, required to determine the in-plane microstresses $\tilde{\sigma}_{j\mu}^{(\mu,\mu)}$ $j, \mu = 1, 2$ in the representative segment of the ECM μ laminate. The above-mentioned set is reduced to two single ordinary differential equations

$$\frac{d^2 \tilde{\sigma}_{\mu\mu}^{(\mu,\mu)}}{dx_\mu^2} - L_1^{(\mu)} \tilde{\sigma}_{\mu\mu}^{(\mu,\mu)} + \Omega_{11}^{(\mu)} \bar{\sigma}_{11} + \Omega_{22}^{(\mu)} \bar{\sigma}_{22} = 0 \tag{7a}$$

$$\frac{d^2 \tilde{\sigma}_{12}^{(\mu,\mu)}}{dx_\mu^2} - L_2^{(\mu)} \tilde{\sigma}_{12}^{(\mu,\mu)} + \Omega_{12}^{(\mu)} \bar{\sigma}_{12} = 0 \tag{7b}$$

where $L_1^{(\mu)}$, $L_1^{(\mu)}$, $\Omega_{11}^{(\mu)}$, $\Omega_{22}^{(\mu)}$, $\Omega_{12}^{(\mu)}$ are the laminate constants depending on the layer compliances $\tilde{S}_{ij}^{(\mu)}$, $S_{ij}^{(\kappa)}$, $\kappa \neq \mu$, shear lag parameters K_j and the layer thickness ratio $\chi = h_1/h_2$. In detail, they are presented elsewhere (Kashtalyan and Soutis, 2000). Given the boundary conditions at the macrocrack surfaces, Eq. (4), solutions to Eqs. (7) are

$$\tilde{\sigma}_{\mu\mu}^{(\mu,\mu)} = \frac{1}{L_1^{(\mu)}} \left(1 - \frac{\cosh[\sqrt{L_1^{(\mu)}}(x_\mu - s_\mu)]}{\cosh[\sqrt{L_1^{(\mu)}}s_\mu]} \right) (\Omega_{11}^{(\mu)}\bar{\sigma}_{11} + \Omega_{22}^{(\mu)}\bar{\sigma}_{22}) \quad (8a)$$

$$\tilde{\sigma}_{12}^{(\mu,\mu)} = \frac{1}{L_2^{(\mu)}} \left(1 - \frac{\cosh[\sqrt{L_2^{(\mu)}}(x_\mu - s_\mu)]}{\cosh[\sqrt{L_2^{(\mu)}}s_\mu]} \right) \Omega_{12}^{(\mu)}\bar{\sigma}_{12} \quad (8b)$$

Stress analysis presented here does not take into account residual thermal stresses, generated during fabrication due to mismatch in thermal properties of the CMC constituents. In multidirectional laminates, residual thermal stresses at the lamina level can be estimated using the classical lamination theory (Daniel and Ishai, 1994). For example, residual stresses in the 0° and 90° plies of a cross-ply $[0/90]_s$ SiC/CAS laminate were found to be of magnitude 5 MPa for an assumed temperature difference $\Delta T = -1000^\circ\text{C}$. At that, stresses in the fibre direction are tensile and those in the direction transverse to the fibres are compressive in each ply. The properties of unidirectional SiC/CAS material used in the calculations were as follows (Daniel and Ishai, 1994): longitudinal modulus $E_L = 121$ GPa, transverse modulus $E_T = 112$ GPa, inplane shear modulus $G_{LT} = 44$ GPa, major Poisson's ratio $\nu_{LT} = 0.2$, minor Poisson's ratio $\nu_{TL} = 0.18$, longitudinal thermal expansion coefficient $\alpha_L = 4.05 \cdot 10^{-6}/^\circ\text{C}$, transverse thermal expansion coefficient $\alpha_T = 4.15 \cdot 10^{-6}/^\circ\text{C}$. Shear modulus in the plane perpendicular to the fibres (plane of isotropy) was estimated as $G_{TT} = 45$ GPa, and single ply thickness was taken $t = 0.2$ mm.

4. STIFFNESS ANALYSIS

The reduced stiffness properties of the damaged μ^{th} layer can be determined by applying the classical lamination theory to the ECM_μ laminate after replacing the explicitly damaged layer with an equivalent homogeneous one. Constitutive equations of the homogeneous layer, equivalent to the explicitly damaged one, have the form

$$\{\bar{\sigma}^{(\mu,\mu)}\} = [Q^{(\mu)}]\{\bar{\epsilon}^{(\mu,\mu)}\} \quad (9)$$

The lamina macrostresses $\{\bar{\sigma}^{(\mu,\mu)}\}$ in the equivalent homogeneous layer can be obtained by averaging the in-plane microstresses, Eqs. (8), across the length of the representative segments as

$$\bar{\sigma}_{\mu\mu}^{(\mu,\mu)} = \frac{1}{L_1^{(\mu)}} [1 - \tanh(\sqrt{L_1^{(\mu)}}s_\mu)] (\Omega_{11}^{(\mu)}\bar{\sigma}_{11} + \Omega_{22}^{(\mu)}\bar{\sigma}_{22}) \quad (10a)$$

$$\bar{\sigma}_{12}^{(\mu,\mu)} = \frac{1}{L_2^{(\mu)}} [1 - \tanh(\sqrt{L_2^{(\mu)}}s_\mu)] \Omega_{12}^{(\mu)}\bar{\sigma}_{12} \quad (10b)$$

The lamina macrostrains $\{\bar{\epsilon}^{(\mu,\mu)}\}$ are assumed to be equal to those in the equivalent constraint layer, i.e. $\{\bar{\epsilon}^{(\mu,\mu)}\} = \{\bar{\epsilon}^{(\mu,\kappa)}\}$, as well as to the applied laminate strain, and are calculated from the constitutive equation for the equivalent constraint layer, Eq. (3b). The modified in-plane stiffness matrix $[Q^{(\mu)}]$ of the homogeneous layer equivalent to the μ^{th} layer of the ECM μ laminate is related to the in-plane stiffness matrix $[\hat{Q}^{(\mu)}]$ of the undamaged layer as $[Q^{(\mu)}] = [\hat{Q}^{(\mu)}] - [R^{(\mu)}]$, where

$$[R^{(1)}] = \begin{bmatrix} \hat{Q}_{11}^{(\mu)} \Lambda_{22}^{(\mu)} & \hat{Q}_{12}^{(\mu)} \Lambda_{22}^{(\mu)} & 0 \\ \hat{Q}_{12}^{(\mu)} \Lambda_{22}^{(\mu)} & \frac{(\hat{Q}_{12}^{(1)})^2}{\hat{Q}_{11}^{(1)}} \Lambda_{22}^{(\mu)} & 0 \\ 0 & 0 & \hat{Q}_{66}^{(\mu)} \Lambda_{66}^{(\mu)} \end{bmatrix}, \tag{11a}$$

$$[R^{(2)}] = \begin{bmatrix} \frac{(\hat{Q}_{12}^{(2)})^2}{\hat{Q}_{22}^{(2)}} \Lambda_{22}^{(\mu)} & \hat{Q}_{12}^{(\mu)} \Lambda_{22}^{(\mu)} & 0 \\ \hat{Q}_{12}^{(\mu)} \Lambda_{22}^{(\mu)} & \hat{Q}_{22}^{(\mu)} \Lambda_{22}^{(\mu)} & 0 \\ 0 & 0 & \hat{Q}_{66}^{(\mu)} \Lambda_{66}^{(\mu)} \end{bmatrix} \tag{11b}$$

Here $\Lambda_{22}^{(\mu)}, \Lambda_{66}^{(\mu)}$ are the In-situ Damage Effective Functions for the μ^{th} layer of the ECM μ laminate

$$\begin{aligned} \Lambda_{22}^{(\mu)} &= 1 - \frac{\bar{\sigma}_{\mu\mu}^{(\mu,\mu)}}{\hat{Q}_{1\mu}^{(\mu,\mu)} \bar{\epsilon}_1^{(\mu,\mu)} + \hat{Q}_{2\mu}^{(\mu,\mu)} \bar{\epsilon}_2^{(\mu,\mu)}} \\ &= 1 - \left[1 - \frac{D_{\mu}^{mc}}{\lambda_1^{(\mu)}} \tanh \frac{\lambda_1^{(\mu)}}{D_{\mu}^{mc}} \right] \left[1 + \alpha_1^{(\mu)} \frac{D_{\mu}^{mc}}{\lambda_1^{(\mu)}} \tanh \frac{\lambda_1^{(\mu)}}{D_{\mu}^{mc}} \right]^{-1}, \mu = 1,2 \end{aligned} \tag{12a}$$

$$\begin{aligned} \Lambda_{66}^{(\mu)} &= 1 - \frac{\bar{\sigma}_{12}^{(\mu,\mu)}}{\hat{Q}_{66}^{(\mu,\mu)} \bar{\epsilon}_6^{(\mu,\mu)}} \\ &= 1 - \left[1 - \frac{D_{\mu}^{mc}}{\lambda_2^{(\mu)}} \tanh \frac{\lambda_2^{(\mu)}}{D_{\mu}^{mc}} \right] \left[1 + \alpha_2^{(\mu)} \frac{D_{\mu}^{mc}}{\lambda_2^{(\mu)}} \tanh \frac{\lambda_2^{(\mu)}}{D_{\mu}^{mc}} \right]^{-1}, \mu = 1,2 \end{aligned} \tag{12b}$$

Here D_1^{mc}, D_2^{mc} are damage parameters associated with longitudinal and transverse macrocracks, respectively. The constants $\lambda_i^{(\mu)}, \alpha_i^{(\mu)}, i = 1,2$ depend solely on the layer compliances $\hat{S}_{ij}^{(\mu)}, S_{ij}^{(\kappa)}, \kappa \neq \mu$, shear lag parameters K_j and the layer thickness ratio χ . Through the modified compliances $S_{ij}^{(\kappa)}, \kappa \neq \mu$ of the equivalent constraint layer (κ^{th} layer) of the ECM μ laminate, the functions $\Lambda_{22}^{(\mu)}, \Lambda_{66}^{(\mu)}$ for the μ^{th} layer of the ECM μ laminate implicitly depend on the damage parameter $D_{\kappa}^{mc} = h_{\kappa}/s_{\kappa}$ for the κ^{th} layer. The In-situ Damage Effective Functions for both layers $\Lambda_{qq}^{(k)}, q = 2,6 k = 1,2$ form a system of 4 simultaneous nonlinear algebraic equations, which is solved computationally by a direct iterative procedure. Consequently, all four functions and therefore the reduced stiffness properties of the layers are determined as functions of D_1^{mc}, D_2^{mc} . Once reduced stiffness properties of all layers are known, the extensional stiffness matrix of the damaged laminate can be obtained as

$$[\bar{A}] = \sum_k [Q^{(k)}] h_k \tag{13}$$

If the interaction between the transverse and longitudinal cracks is neglected, it is possible to derived a closed-form expression for reduction in the shear modulus caused by transverse and longitudinal macrocracks

$$\frac{G_{xy}}{\hat{G}_{xy}} = \left[1 - \frac{D_1^{mc}}{\lambda_2^{(1,1)}} \frac{D_2^{mc}}{\lambda_2^{(2,2)}} \tanh \frac{\lambda_2^{(1,1)}}{D_1^{mc}} \tanh \frac{\lambda_2^{(2,2)}}{D_2^{mc}} \right] \times \left[1 + \chi \frac{D_1^{mc}}{\lambda_2^{(1,1)}} \tanh \frac{\lambda_2^{(1,1)}}{D_1^{mc}} + \frac{1}{\chi} \frac{D_2^{mc}}{\lambda_2^{(2,2)}} \tanh \frac{\lambda_2^{(2,2)}}{D_2^{mc}} + \frac{D_1^{mc}}{\lambda_2^{(1,1)}} \frac{D_2^{mc}}{\lambda_2^{(2,2)}} \tanh \frac{\lambda_2^{(1,1)}}{D_1^{mc}} \tanh \frac{\lambda_2^{(2,2)}}{D_2^{mc}} \right]^{-1} \tag{14}$$

Here G_{xy} and \hat{G}_{xy} are the shear moduli of the damaged and intact laminate, respectively. This expression, Eq. (14), is similar to the semi-empirical expression suggested by Tsai and Daniel (1992) on the basis of the ‘superposition’ of solutions for a single set of cracks

$$\frac{G_{xy}}{\hat{G}_{xy}} = \left[1 + \chi \frac{D_1^{mc}}{\lambda_2^{(1,1)}} \tanh \frac{\lambda_1^{(1,1)}}{D_1^{mc}} + \frac{1}{\chi} \frac{D_2^{mc}}{\lambda_2^{(2,2)}} \tanh \frac{\lambda_2^{(2,2)}}{D_2^{mc}} \right]^{-1} \tag{15}$$

However, Eq. (14) contains some additional terms in comparison to Eq. (15). If longitudinal cracks are absent, Eqs. (14) and (15) are reduced to the same expression.

5. RESULTS AND DISCUSSION

The ECM has been already successfully applied to predict reduced stiffness properties (axial and shear moduli and the Poisson’s ratio) in polymer matrix composites with transverse and longitudinal macrocracks (Kashtalyan and Soutis, 1999, 2000). Tables 1 and 2 show reduction of the longitudinal modulus in glass/epoxy cross-ply $[0/90]_s$ and $[0/90_3]_s$ laminates damaged by transverse cracks only and transverse and longitudinal cracks, respectively. Predictions based on the ECM (Kashtalyan and Soutis, 2000) are compared to those of Hashin (1987), who applied variational method to stress analysis and considered a repeated laminate element defined by intersecting pairs of transverse and longitudinal cracks. The results are presented in

Table 1. Normalised longitudinal modulus for glass/epoxy $[0/90]_s$ and $[0/90_3]_s$ laminates with transverse macrocracks only.

| $D_2^{mc} (D_1^{mc} = 0)$ | $[0/90]_s$ | | $[0/90_3]_s$ | |
|---------------------------|---------------|-------|---------------|-------|
| | Hashin (1987) | ECM | Hashin (1987) | ECM |
| 0.02 | 0.990 | 0.992 | 0.980 | 0.985 |
| 0.05 | 0.976 | 0.981 | 0.951 | 0.963 |
| 0.1 | 0.953 | 0.963 | 0.907 | 0.929 |
| 0.2 | 0.910 | 0.928 | 0.830 | 0.867 |
| 0.33 | 0.859 | 0.889 | 0.745 | 0.799 |
| 0.5 | 0.813 | 0.851 | 0.661 | 0.727 |
| 1.0 | 0.775 | 0.801 | 0.548 | 0.613 |
| 2.0 | 0.770 | 0.795 | 0.524 | 0.553 |

Table 2. Normalised longitudinal modulus of glass/epoxy $[0/90]_s$ and $[0/90_3]_s$ laminates with transverse and longitudinal macrocracks.

| $D_1^{mc} = D_2^{mc}$ | $[0/90]_s$ | | $[0/90_3]_s$ | |
|-----------------------|---------------|-------|---------------|-------|
| | Hashin (1987) | ECM | Hashin (1987) | ECM |
| 0.02 | 0.990 | 0.992 | 0.980 | 0.985 |
| 0.05 | 0.975 | 0.980 | 0.951 | 0.962 |
| 0.1 | 0.951 | 0.961 | 0.906 | 0.927 |
| 0.2 | 0.907 | 0.925 | 0.829 | 0.863 |
| 0.33 | 0.853 | 0.882 | 0.743 | 0.792 |
| 0.5 | 0.804 | 0.841 | 0.658 | 0.718 |
| 1.0 | 0.762 | 0.787 | 0.542 | 0.602 |
| 2.0 | 0.757 | 0.765 | 0.516 | 0.541 |

terms of the longitudinal modulus of the damaged laminate, normalised by its value for the intact laminate. Damage parameters D_1^{mc} , D_2^{mc} vary from 0.02 to 2.0. This corresponds to the variation in longitudinal crack density $C_1 = (2s_1)^{-1}$ from 0.5 to 5.0 cracks per millimetre in 0° layers of both laminates. Corresponding variation in the density of transverse cracks $C_2 = (2s_2)^{-1}$ is from 0.5 to 5.0 cracks/mm for a $[0/90]_s$ laminate and from 0.16 to 1.6 cracks/mm for a $[0/90_3]_s$ laminate. Predictions of both models are found to be in good agreement.

Table 3 shows comparison of predictions for the shear modulus reduction in graphite/epoxy $[0_3/90_3]_s$ laminate with transverse and longitudinal macrocracks. The results are presented in terms of the shear modulus of the damaged laminate, normalised by its value for the intact laminate. In most of cases, predictions based on Eq. (15) are within 10% of those obtained from Eq. (14). However, in some cases the difference can be as big as 20%.

Figure 3 shows stiffness reduction in a $[0/90]_s$ SiC/CAS laminate with transverse cracks in the 90° layer without any damage in the 0° plies. The properties of a unidirectional material used in the calculations are again taken from (Daniel and Ishai, 1994). In Fig. 3, stiffness properties of the damaged laminate are normalised by their values for the intact laminate and plotted as a function of transverse crack density C_2 , which varies from 0 (no damage) to 50 cracks/cm. The maximum crack

Table 3. Normalised shear modulus of carbon/epoxy $[0_3/90_3]_s$ laminates with transverse and longitudinal macrocracks.

| D_1^{mc} | D_2^{mc} | Tsai and Daniel (1992), Eq. (15) | ECM model, Eq. (14) |
|------------|------------|-------------------------------------|------------------------|
| 0.39 | 0. | 0.788 | 0.805 |
| | 0.2 | 0.711 | 0.706 |
| | 0.4 | 0.647 | 0.624 |
| | 0.6 | 0.596 | 0.557 |
| | 0.8 | 0.557 | 0.503 |
| 0.66 | 0. | 0.692 | 0.713 |
| | 0.2 | 0.631 | 0.613 |
| | 0.4 | 0.581 | 0.532 |
| | 0.6 | 0.540 | 0.465 |
| | 0.8 | 0.508 | 0.410 |

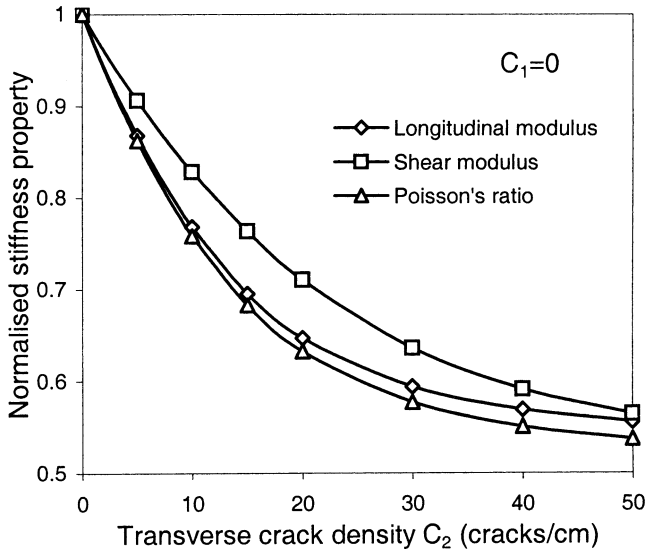


Figure 3. Normalised stiffness properties of a $[0/90]_s$ SiC/CAS cross-ply damaged by transverse macrocracks as function of transverse cracks density C_2 (no longitudinal cracks).

density corresponds to crack spacing of $2s_2 = 0.2$ mm, or one ply thickness. Minimal crack spacing observed in CMC cross-ply laminates under uniaxial loading is comparable to the layer thickness (Daniel and Anastassopoulos, 1995).

It may be seen from Fig. 3 that, as transverse crack density increases, all stiffness properties of the laminate are significantly reduced. Longitudinal and transverse moduli of the undamaged laminate, calculated from the classical lamination theory, are 166.5 GPa, shear modulus 44 GPa, Poisson's ratio 0.19. When transverse cracking in the 90° layer reaches saturation, the laminate longitudinal and shear moduli are predicted to lose more than 45% of their value. Inclusion of tensile residual stresses into the analysis would lead to even more significant reduction in the longitudinal modulus and Poisson's ratio, but reduction in shear modulus would remain the same. Predictions for a $[0/90_2]_s$ SiC/CAS laminate are shown in Fig. 4.

Stiffness reduction in a $[0/90]_s$ SiC/CAS laminate with macrocracks both in 90° and 0° layers is shown in Fig. 5. Crack densities of transverse and longitudinal cracks are assumed to be equal $C_1 = C_2$. Laminate stiffness properties are normalised by their values for the intact laminate and plotted as a function of the transverse crack density C_2 . As one would expect, the longitudinal modulus is not affected by the presence of longitudinal macrocracks. However, the shear modulus and Poisson's ratio undergo further reduction as the density of longitudinal cracks increases. The most significant reduction due to longitudinal cracks is observed for the shear modulus. At $C_2 = 20$ cracks/cm its values for the laminate with ($C_1 = C_2$) and without ($C_1 = 0$) longitudinal cracks are 27.8 GPa and 17.1 GPa, respectively, while the shear modulus of the undamaged laminate was 44 GPa.

Predictions of stiffness reduction due to transverse and longitudinal macrocracks in a $[0/90_2]_s$ SiC/CAS laminate are shown in Fig. 6. Laminate stiffness properties are normalised by their value for the intact laminate and plotted as a function of the longitudinal crack density C_1 . Transverse crack density is $C_2 = 10$ cracks/cm. As longitudinal cracks initiate, and their density increases, the transverse

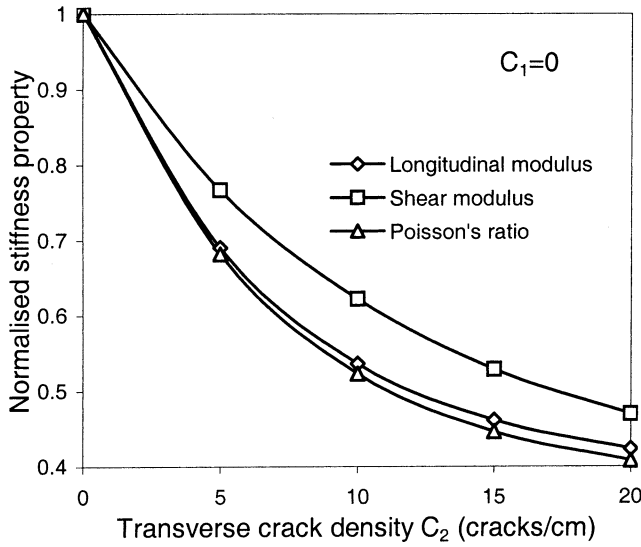


Figure 4. Normalised stiffness properties of a $[0/90]_s$ SiC/CAS cross-ply damaged by transverse macrocracks as function of transverse cracks density C_2 (no longitudinal cracks).

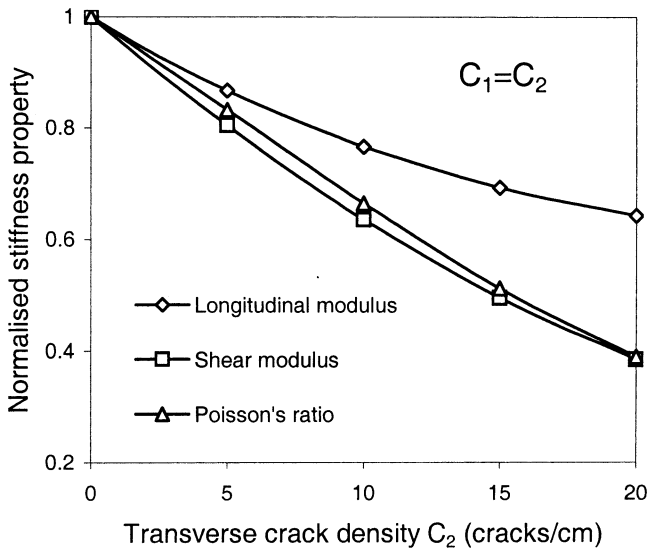


Figure 5. Normalised stiffness properties of a $[0/90]_s$ SiC/CAS cross-ply damaged by transverse and longitudinal macrocracks as function of transverse crack density C_2 . Longitudinal crack density $C_1 = C_2$.

and shear modulus and Poisson's ratio undergo further reduction, but the longitudinal modulus remains unchanged.

6. CONCLUSIONS

In this paper, the Equivalent Constraint Model (ECM) of the damaged lamina was applied to predict theoretically stiffness-damage behaviour of cross-ply $[0_m/90_n]_s$

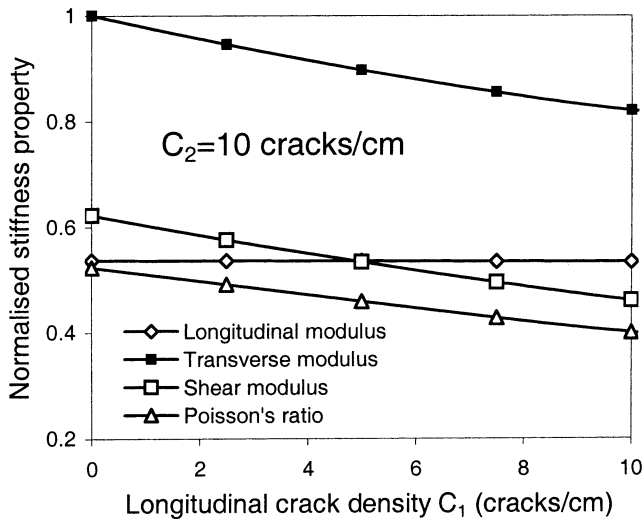


Figure 6. Normalised stiffness properties of a $[0/90]_2$ SiC/CAS cross-ply damaged by transverse and longitudinal macrocracks as function of longitudinal crack density C_1 . Transverse crack density $C_2 = 10$ cracks/cm.

CMC laminates with macrocracks both in the 90° and 0° plies. To capture simultaneous accumulation of damage both in the 90° and the 0° plies, two ECM laminates were analysed simultaneously, as a coupled problem, instead of the original one. Following analysis of stresses in the explicitly damaged layer(s) of ECM laminates, closed form expressions for the reduced stiffness properties of the damaged laminate were derived representing them as functions of crack densities in the 90° and 0° plies. Residual thermal stresses were neglected in the stress analysis, but their value was estimated from the classical lamination theory.

Numerical results for SiC/CAS cross-ply laminates of different lay-ups have shown that transverse and longitudinal cracks cause significant reduction of all laminate stiffness properties. Reduction in the longitudinal modulus occurs mainly due to transverse macrocracks, while the shear modulus appears to be the most affected by the presence of longitudinal macrocracks.

REFERENCES

- Birman, V., and Byrd, L. W., 2000, Review of fracture and fatigue in ceramic matrix composites, *Applied Mechanics Reviews* **53**:147.
- Birman, V., and Byrd, L. W., 2001, Matrix cracking in transverse layers of cross-ply beams subjected to bending and its effect on vibration frequencies, *Composites Part B: Engineering* **32**:47.
- Birman, V., and Byrd, L. W., 2003, Effect of matrix cracking in cross-ply ceramic matrix composite beams on their mechanical properties and natural frequencies, *International Journal of Non-Linear Mechanics* **38**:201.
- Daniel, I. M., and Ishai, O., 1994, *Engineering Mechanics of Composite Materials*, Oxford University Press, New York.
- Daniel, I. M., and Anastassopoulos, G., 1995, Failure mechanisms and damage evolution in crossply ceramic-matrix composites, *International Journal of Solids and Structures* **32**:341.
- Erdman, D. L., and Weitsman, Y., 1998, The multi-fracture response of cross-ply ceramic composites, *International Journal of Solids and Structures* **35**:5051.

- Fan, J., and Zhang, J., 1993, In-situ damage evolution and micro/macro transition for laminated composites", *Composites Science and Technology* **47**:107.
- Hashin, Z., 1987, Analysis of orthogonally cracked laminates under tension, *Transactions ASME Journal of Applied Mechanics* **54**:872.
- Henaff-Gardin, C., Lafarie-Frenot, M.C., and Gamby, D., 1996a, Doubly period matrix cracking in composite laminates Part 1: General in-plane loading, *Composite Structures* **36**:113.
- Henaff-Gardin, C., Lafarie-Frenot, M.C., and Gamby, D., 1996b, Doubly period matrix cracking in composite laminates Part 2: Thermal biaxial loading, *Composite Structures* **36**:131.
- Kashtalyan, M., and Soutis, C., 1999, Application of the Equivalent Constraint Model to investigate stiffness properties of transversally cracked and split FRP laminates, *Advanced Composites Letters* **8**:205.
- Kashtalyan, M., and Soutis, C., 2000, Stiffness degradation in cross-ply laminates damaged by transverse cracking and splitting, *Composites Part A: Applied Science and Manufacturing* **31**:335.
- Lu, T. J., and Hutchinson, J. W., 1995, Thermal conductivity and expansion of cross-ply composite with matrix cracks, *Journal of the Mechanics and Physics of Solids* **43**:1175.
- Pryce, A. W., and Smith, P. A., 1994, Matrix cracking in crossply ceramic matrix composites under static and fatigue loading, *Acta Metallica et Materialia* **42**:861.
- Tsai, C. L., and Daniel, I. M., 1992, Behavior of cracked cross-ply composite laminate under shear loading, *International Journal of Solids and Structures* **29**:3251–3267.
- Yasmin, A., and Bowen, P., 2002, Fracture behaviour of cross-ply Nicalon/CAS-II glass-ceramic matrix composite laminate at room and elevated temperatures, *Composites Part A: Applied Science and Manufacturing* **33**:1209.

QUANTIFICATION OF TOUGHNESS INCREASE DUE TO METAL PARTICLES IN GLASS MATRIX COMPOSITES

M. Kotoul, A. R. Boccaccini and I. Dlouhy¹

1. INTRODUCTION

A number of examples exist that indicate the potential for increasing the toughness of brittle matrix by dispersing a ductile phase. The basics of the mechanism of fracture toughness enhancement were amply analyzed in the literature. Several models were developed which commonly predict the increase of toughness ΔG_c as

$$\Delta G_c = f \int_0^{\Delta_c} \sigma_p(\Delta) d\Delta, \quad (1)$$

where $\sigma_p(\Delta)$ is the T/S law traction, with the integral representing the plastic stretching work to rupture of the particle and f is the volume fraction (area fraction on fracture plane) of the particles. It was found that toughening improves with increasing bridging length. However, it was also proved that increasing bonding imposes lateral constraints on the particles thus prohibiting the full utilization of the particles inherent ductility (see also Kotoul and Urbis, 2001). As a result, the critical crack opening displacement is significantly reduced due to the influence of the stress triaxiality factor. Plastic strains develop only in a thin layer as it can also be seen from FEM simulation of the deformation of the particle constrained by elastic

¹ M. Kotoul, Dept. of Mechanics of Solids, Brno University of Technology, 616 69 Brno, Czech Republic (corresponding author kotoul@umt.fme.vutbr.cz), A. R. Boccaccini, Department of Materials, Imperial College London, London SW72BP, UK, I. Dlouhy, Institute of Physics of Materials ASCR, 61662 Brno, Czech Republic

matrix. The bridging zone length is significantly reduced and the assumption, that bridging zone contains a large number of particles, ceases to hold. In such a case the action of the system of discretely distributed particles cannot be replaced by the action of smeared forces over the bridging zone length, the critical value Δ_c becomes very uncertain and the model in Eq. (1) fails. Particularly in the limit, when the crack is bridged just by one row of particles distributed along the crack front - so called crack trapping, the details of an interaction of the crack front with the particles become of growing importance for an assessment of the toughness increment. The change of the toughening mechanism from crack bridging (extrinsic toughening) to crack trapping (intrinsic toughening) closely relates to the extent of debonding which depends both on internal factors like debonding toughness, particle size and/or volume fraction, and temperature. The paper is focused on a calculation procedure that is capable of discerning subtle changes in fracture toughness behavior of very brittle material reinforced by ductile metallic particle. Rice's perturbation analysis is used to the configuration of the front of a planar crack that is trapped against forward advance by a periodical array of closely spaced bridges. The solution is lifted by analogy from known solutions of a periodic array of through microcracks along the z-axis collinear with the undisturbed crack front and an assessment of the toughness increase is provided.

2. EXPERIMENTAL FACTS

Dlouhy et al. (1997) observed that experimental values of the fracture toughness of borosilicate glass reinforced by vanadium or molybdenum particles, their shape can roughly be treated as spherical one, have fallen far behind to the theoretical expectations of the enhancement of fracture toughness according to the crack bridging view. Specifically, the experimentally found toughening ratio (composite toughness/matrix toughness) was about 1.4 for the volume fraction $f = 0.1$ of vanadium particles while the theoretical prediction based on the crack bridging model according to Eq. (1) is more than one order higher. When the observed particle cleavage in about 85 vol% of the metal inclusions was taken into account, the theoretical prediction of the toughening ratio somewhat decreases but still amounts about 5 times higher value. It should be noted that the observed particle cleavage indicates a decrease in particle plasticity induced due to two causes: (i) constraints imposed by the rigid matrix and (ii) embrittlement due to the high-temperature fabrication process. Uncleaved particles delivered some toughening due to crack bridging, but extensive stretching was not detected and, as a consequence, the bridging zone length was significantly reduced, see Fig. 1.

Choe et al. (2001) reported in their study on Mo-12Si-8.5B alloy that crack trapping by Mo-particles appears to provide the main source of (intrinsic) toughening at lower temperatures. As the vast majority of the α -Mo particles intersected by the crack did not remain intact in the crack wake, there was insignificant crack bridging and hence little crack-growth toughening. The failure of the Mo phase was quite brittle, whereas at 1300°C, the Mo particles debonded from the Mo₃Si/Mo₅SiB₂ matrix with significant amounts of plastic stretching. Such increased ductility of the Mo particles did result in some degree of wake bridging in the Mo-12Si-8.5B alloy at elevated temperatures.

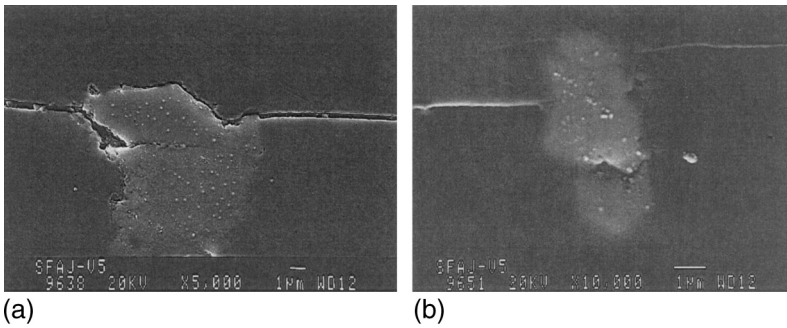


Figure 1. a) Crack in inclusion and partial debonding; b) crack in small particle.

3. ENERGY CONDITION FOR DEBONDING

Before describing a trapped crack front by a row of particles distributed along the crack front, some place will be devoted to the analysis of debonding along the particle/matrix interface. The aim is to estimate the length h of debonded interface of a particle in the vicinity of crack tip under assumption that $h \ll R$ (average radius of particles), i.e. e. for a relatively strong interface. Due to mechanical constraint the plastic strain then develops only in a thin layer of thickness $\sim 2h$ as it can also be seen from FEM simulation of the deformation of the particle constrained by elastic matrix, see Fig. 2. The length h will be estimated from energy considerations. Enclose the debonded layer of particle by a surface Ξ which forms the surface of a cylinder of the height $2h$ and the radius R . As the thickness of the layer $2h$ increases, the part of the surface Ξ migrates in the y -direction accompanied by axisymmetric debonding of particle/matrix interface. The aim is to calculate the potential energy loss associated with the growth of thickness of the debonded layer. To do so, we apply the general result derived by Eshelby (1970) concerning the global change of the Gibbs potential of prestressed body due to the possible migration of the interface Ξ between the bulk and a part of material which undergoes any kind of transformation. Eshelby has shown that a virtual change of the Gibbs potential $\delta\Pi$ associated with a virtual displacement $\delta\xi_i$ at each point of Ξ can be conveniently expressed in terms of the energy momentum tensor of the elasticity P_{ij}

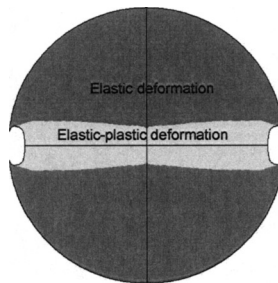


Figure 2. FEM simulation of the elastic-plastic particle constrained by elastic matrix illustrating a layer undergoing a nonzero axial plastic strain increment $\Delta\epsilon_{yy}$.

$$\delta\Pi = - \int_{\Xi} \delta\xi_j [P_{ij}] n_i d\Xi \tag{2}$$

where $n_i d\Xi$ is an oriented surface element and $[P_{ij}]$ is the jump across the interface Ξ of the Eshelby tensor component, P_{ij}

$$P_{ij} = g\delta_{ij} - \sigma_{ki}u_{k,j}. \tag{3}$$

In Eq. (3) g stands for the Helmholtz free energy density in the case of isothermal change, δ_{ij} is the Kronecker symbol, σ_{kj} is the Cauchy stress tensor components, u_k denotes the displacement vector components and $u_{kj} = \partial u_k / \partial x_j$ is the deformation gradient. In the context of the problem investigated, Π reduces to the potential energy and g to the strain energy density. In the cylindric coordinate system (ρ, φ, y) originated in the particle centre Eq. (2) reduces to the following form

$$\delta\Pi = - \left\{ \int_{\Xi_1} \delta\xi_\rho [g - \sigma_{\rho\rho}u_{\rho,y} - \sigma_{y\rho}u_{y,y}] n_\rho d\Xi + \int_{\Xi_2} \delta\xi_y [g - \sigma_{\rho y}u_{\rho,y} - \sigma_{yy}u_{y,y}] n_y d\Xi \right\} \tag{4}$$

where Ξ_1 stands for the area of the cylinder (where debonding takes place) and Ξ_2 stands for the foots of the cylinder, see Fig. 3. The virtual displacement $\delta\xi_y \equiv \delta h$ describes a virtual change of the layer thickness while the virtual displacement $\delta\xi_\rho = \frac{\partial u_\rho^M(y;h)}{\partial h} \delta h$, where $u_\rho^M(y;h)$ is the radial displacement of the debonded matrix face. The jump across the interface Ξ of the Eshelby tensor component, P_{ij} is defined as

$$[P_{ij}] = P_{ij}^M - P_{ij}^P \tag{5}$$

where the superscript ‘ M ’ refers to limiting values of P_{ij} as the interface Ξ is approached along n_i from the matrix whereas the superscript ‘ P ’ refers to limiting values of P_{ij} as the interface Ξ is approached along n_i from the particle. Note that n_i is oriented from the bulk to the particle. The boundary Ξ_1 is traction-free. Thus

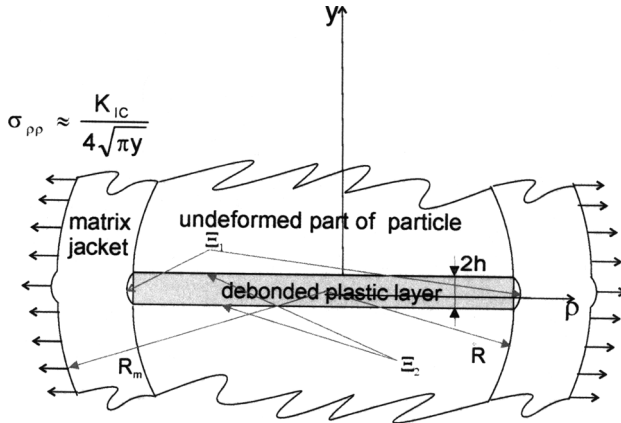


Figure 3. Scheme of debonding model.

Eq. (4) rewrites

$$-\frac{\delta\Pi}{\delta h} = \left\{ \int_{\Xi_1} g^M \frac{\partial u^M(y;h)}{\partial h} d\Xi + + \int_{\Xi_2} (\sigma_{\rho y}^M u_{\rho,y}^M - \sigma_{\rho y}^P u_{\rho,y}^P + \sigma_{yy}^M u_{y,y}^M - \sigma_{yy}^P u_{y,y}^P) d\Xi \right\}, \quad (6)$$

where the strain energy density was already assumed to be continuous across Ξ_2 due to the continuity of tractions and displacements across Ξ_2 . The first term represents the rate of the change in the strain energy $\frac{\partial}{\partial h} \int_V g^M dV$ of the material volume V enclosed by the surface $S \cup \Xi_1 \cup \Xi_2$ due to the motion of the boundary Ξ_1 . In the case of an elastostatic boundary-value problem associated with the material contained within the surface $S \cup \Xi$ for which external loading is imposed only by traction \vec{T} on S , the rate of the change in the elastic strain energy can be inferred from the Clapeyron theorem of elasticity

$$\frac{\partial}{\partial h} \int_{V(h)} g^M dV = \frac{\partial}{\partial h} \frac{1}{2} \int_S T_i u_i dS = \frac{1}{2} \int_S T_i \frac{\partial u_i}{\partial h} dS. \quad (7)$$

It allows to estimate the first term in Eq.(6). Similarly as in Budiansky et al. work (1985) we suppose that stresses in the vicinity of the crack tip debond the particle/matrix interface just ahead of advancing crack for a distance h on each side of the plane of the crack. Due to this symmetry with respect to the plane $y = 0$ it is sufficient to investigate only the upper part of the cylinder. Assume that axisymmetric debonding is produced by an axisymmetric distribution of load applied to the matrix cylinder that jackets the particle. The magnitude of this loading is conservatively taken as the stress

$$\sigma_{\rho\rho}(y) = \frac{K_{IC}}{4\sqrt{\pi|y|}}, \quad (8)$$

which is just the asymptotic distribution of horizontal tension just above the crack-tip and K_{IC} is the critical stress intensity factor of the matrix. The stress distribution from Eq. (8) is applied at the mean radius R_m of the matrix jacket

$$R_m = \frac{1}{2}(l + R), \quad (9)$$

where l is half of the interparticle distance. The cylindrical surface of the radius R_m just corresponds to the surface S in Eq. (7). The deformation of the matrix will be analyzed on the basis of thick-cylinder theory, in which only transverse shear stresses and circumferential tension resist radial displacement. In terms of the matrix cylinder thickness

$$t = l - R \quad (10)$$

and the mean radius R_m the differential equation governing the radial displacement $u_\rho^M(y)$ at $\rho = R_m$ is

$$-\frac{E_m t}{2(1 + \nu_m)} \frac{d^2 u_\rho^M}{dy^2} + \frac{E_m t}{R_m^2(1 - \nu_m^2)} u_\rho^M = \frac{K_{IC}}{4\sqrt{\pi|y|}}, \quad (11)$$

where E_m and ν_m is the Young modulus and Poisson's ratio of matrix respectively. The solution of (11) with the boundary conditions $u_\rho^M(\pm h) = 0$ can be written in the form

$$u_\rho^M(y;h) = \frac{1}{4\sqrt{\pi}} \frac{K_{IC}(1 - \nu_m^2)}{E_m} \frac{R_m^{3/2}}{t} \left(\frac{2}{1 - \nu_m}\right)^{1/4} \tilde{u}\left(\frac{y}{h}H;H\right), \tag{12}$$

where

$$H = \frac{h}{R_m} \left(\frac{2}{1 - \nu_m}\right)^{1/2} \tag{13}$$

and

$$\tilde{u}\left(\frac{y}{h}H;H\right) = - \int_0^{\frac{y}{h}H} \frac{\sinh(\frac{y}{h}H - \eta)}{\sqrt{\eta}} d\eta + \frac{\cosh \frac{y}{h}H}{\cosh H} \int_0^H \frac{\sinh(H - \eta)}{\sqrt{\eta}} d\eta. \tag{14}$$

The solution (12) allows to reduce Eq.(7) to the form

$$\begin{aligned} \frac{\partial}{\partial h} \int_{V(h)} g^M dV &= \frac{1}{2} \int_S \sigma_{\rho\rho}(y) \frac{\partial u_\rho^M}{\partial h} dS = 2\pi R_m \int_0^h \frac{K_{IC}}{4\sqrt{\pi y}} \frac{\partial u_\rho^M}{\partial h} dy = \\ &= \frac{G_{IC}}{8} \frac{R_m^2}{t} \left(\frac{2}{1 - \nu_m}\right)^{1/2} \int_0^H \frac{1}{\sqrt{s}} \frac{\partial \tilde{u}}{\partial H} ds, \end{aligned} \tag{15}$$

where $G_{IC} = K_{IC}^2(1 - \nu_m^2)/E_m$ is the critical matrix crack extension energy release rate. Because $R/2l = (3f/4\pi)^{1/3}$ and

$$\frac{\partial \tilde{u}}{\partial H} = \frac{\cosh \frac{y}{h}H}{\cosh^2 H} \int_0^H \frac{\cosh \eta}{\sqrt{\eta}} d\eta, \tag{16}$$

the change in the elastic strain energy finally becomes

$$\frac{1}{2} \frac{\partial}{\partial h} \int_{V(h)} g^M dV = \frac{G_{IC}}{128\pi} \frac{\left[\frac{1}{2}\left(\frac{4\pi}{3f}\right)^{1/3} + 1\right]^2}{\left[\frac{1}{2}\left(\frac{4\pi}{3f}\right)^{1/3} - 1\right]} \left(\frac{2}{1 - \nu_m}\right)^{1/2} Q(H)2\pi R, \tag{17}$$

where

$$Q(H) = \left\{ \frac{\int_0^H \frac{\cosh \eta}{\sqrt{\eta}} d\eta}{\cosh H} \right\}^2. \tag{18}$$

and the symmetry with respect to the plane $y = 0$ was included. The terms $\sigma_{\rho y}^M u_{\rho, y}^M$ and $\sigma_{yy}^M u_{y, y}^M$ in the second integral in Eq.(6) can be derived from the asymptotic

distribution of vertical tension, shear and displacement just above the crack-tip. Including the above-mentioned symmetry we obtain after some algebra

$$\frac{1}{2} \int_{\Xi_2} (\sigma_{\rho y}^M u_{\rho, y}^M + \sigma_{yy}^M u_{y, y}^M) d\Xi = \frac{G_{IC}(3 - 4\nu_m)}{4\pi(1 - \nu_m)^{3/2}} \frac{1}{\left[\frac{1}{2}\left(\frac{4\pi}{3f}\right)^{1/3} + 1\right]} \frac{\sqrt{2}}{H} 2\pi R. \quad (19)$$

Remaining terms in the second integral in Eq. (6) refer to the particle. Also the energy absorbed in the process of plastic deformation within the plastic layer is a matter of interest. For $h \ll R$ it seems reasonable to approximate the stress-strain fields in the debonded plastic layer by Prandtl's solution for thin circular plastic layer connected with rigid blocks. Prandtl's solution, outlined in Appendix A, gives $u_{\rho, y}^P(h) = u_{y, y}^P(h) = 0$, from where it follows that the terms in the second integral in Eq. (6), referring to the particle, are zero. By inspection of Eqs. (6), (17) and (19) there is observed the loss in the potential energy of the loaded matrix jacket $\frac{\delta II}{\delta h} < 0$ due to debonding. The energy supply is partly dissipated by plastic work in the debonded layer and partly is absorbed in the mechanism of particle/matrix interface debonding. The virtual plastic work δW_p exerted in the half of the layer is

$$\begin{aligned} \delta W_p &= 2\pi \int_0^R \int_0^{h+\delta h} (\sigma_{\rho\rho}^P \delta\varepsilon_{\rho\rho}^P + \sigma_{\varphi\varphi}^P \delta\varepsilon_{\varphi\varphi}^P + \sigma_{yy}^P \delta\varepsilon_{yy}^P + 2\sigma_{\rho y}^P \delta\varepsilon_{\rho y}^P) \rho d\rho dy \cong \\ &\cong 2\pi \int_0^R \int_0^h (\sigma_{\rho\rho}^P \delta\varepsilon_{\rho\rho}^P + \sigma_{\varphi\varphi}^P \delta\varepsilon_{\varphi\varphi}^P + \sigma_{yy}^P \delta\varepsilon_{yy}^P + 2\sigma_{\rho y}^P \delta\varepsilon_{\rho y}^P) \rho d\rho dy, \end{aligned} \quad (20)$$

where $\delta\varepsilon_{ij} = \frac{\partial\varepsilon_{ij}}{\partial h} \delta h$ and a linear approximation with respect to the virtual displacement δh was adopted. At this point is useful to introduce a dimensionless composite parameter k .

$$k = \frac{K_{IC}}{2\sigma_y} \sqrt{\frac{\pi}{2R}} \quad (21)$$

which combines the fracture toughness of the matrix K_{IC} with the yield strength σ_y and the radius of particles R . The parameter k allows to handle further analysis in dimensionless form. Using the results in Appendix A, Eq. (13) and the definition of the parameter k , one can write Eq. (20) as follows

$$\begin{aligned} \frac{\delta W_p}{\delta h} &= \frac{\pi\sigma_y}{\sqrt{3}h} \int_0^R \int_0^h \left[(h^2 - y^2) \frac{\partial u_y'}{\partial h} - y\rho^2 \frac{\partial u_y''}{\partial h} \right] \rho d\rho dy = 2\pi R \frac{1}{k} \frac{G_{IC}}{8\sqrt{6}} \frac{(3 - 4\nu_m)}{1 - \nu_m} \\ &\times \left\{ \frac{14}{15} \left(\frac{1 - \nu_m}{8} \right)^{1/4} \left[\frac{1}{2} \left(\frac{4\pi}{3f} \right)^{1/3} + 1 \right]^{1/2} H^{1/2} + \frac{\frac{1}{3} \left(\frac{8}{1 - \nu_m} \right)^{3/4}}{\left[\frac{1}{2} \left(\frac{4\pi}{3f} \right)^{1/3} + 1 \right]^{3/2} H^{3/2}} \right\}. \end{aligned} \quad (22)$$

Denote by G_d the critical energy release rate for debonding of the particle/matrix interface; then the energy release rate relation

$$2\pi R G_d + \frac{\delta W_p}{\delta h} = -\frac{\delta \Pi}{\delta h} \tag{23}$$

provides the condition governing the debonding length h . The results are presented by the pair of parametric equations

$$\begin{aligned} \frac{h}{R} &= \left[\frac{1}{2} \left(\frac{4\pi}{3f} \right)^{1/3} + 1 \right] \left(\frac{1 - \nu_m}{8} \right)^{1/2} H, \\ \frac{G_d}{G_{IC}} &= \frac{1}{128\pi} \frac{\left[\frac{1}{2} \left(\frac{4\pi}{3f} \right)^{1/3} + 1 \right]^2}{\left[\frac{1}{2} \left(\frac{4\pi}{3f} \right)^{1/3} - 1 \right]} \left(\frac{2}{1 - \nu_m} \right)^{1/2} Q(H) + \\ &+ \frac{\sqrt{2}(3 - 4\nu_m)}{4\pi(1 - \nu_m)^{3/2}} \frac{1}{\left[\frac{1}{2} \left(\frac{4\pi}{3f} \right)^{1/3} + 1 \right]} \frac{1}{H} - \frac{1}{k} \frac{1}{8\sqrt{6}} \frac{(3 - 4\nu_m)}{1 - \nu_m} R(H), \end{aligned} \tag{24}$$

which relate $\frac{h}{R}$ to $\frac{G_d}{G_{IC}}$, where

$$\begin{aligned} R(H) &= \frac{14}{15} \left(\frac{1 - \nu_m}{8} \right)^{1/4} \left[\frac{1}{2} \left(\frac{4\pi}{3f} \right)^{1/3} + 1 \right]^{1/2} H^{1/2} + \\ &+ \frac{1}{3} \left(\frac{8}{1 - \nu_m} \right)^{3/4} \frac{1}{\left[\frac{1}{2} \left(\frac{4\pi}{3f} \right)^{1/3} + 1 \right]^{3/2}} H^{3/2}. \end{aligned}$$

see Fig. 4. Note that equations (24) imply that $\frac{h}{R}$ is not a single-valued function of $\frac{G_d}{G_{IC}}$. The upper part of each curve represents stable debonded lengths, but for debonding to occur at all an energy barrier associated with the region between the horizontal axis and each lower branch must be overcome.

The results in Fig. 4 indicate that there exist threshold values $\left(\frac{G_d}{G_{IC}}\right)^*$ of the ratio of debonding to fracture toughness such that for $\frac{G_d}{G_{IC}} > \left(\frac{G_d}{G_{IC}}\right)^*$ debonding can not occur. The threshold value $\left(\frac{G_d}{G_{IC}}\right)^*$ depends on the composite parameter k and on the

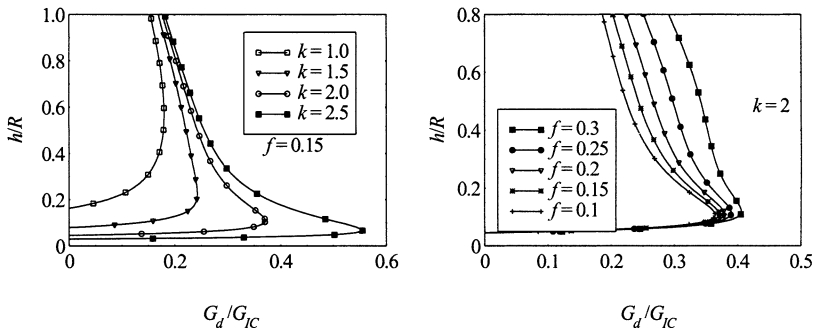


Figure 4. Debond length vs. debond-toughness/matrix-toughness ratio a) for several values of the composite parameter k and the particle volume fraction $f = 0.15$, b) for several values of the particle volume fraction f and the composite parameter $k = 2$.

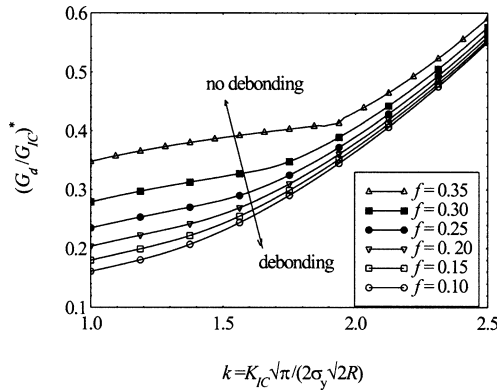


Figure 5. Threshold value $\left(\frac{G_d}{G_{IC}}\right)^*$ as function of the composite parameter k for several values of the particle volume fraction f .

particle volume fraction f . Fig. 5 summarizes threshold values $\left(\frac{G_d}{G_{IC}}\right)^*$ as a function of the composite parameter k for several values of f that would prevent debonding. Note that for a constant value of the matrix fracture toughness the composite parameter k increases with decreasing particle yield stress and/or particle size. As a consequence, threshold values $\left(\frac{G_d}{G_{IC}}\right)^*$ increases with a decrease of the particle yield stress and/or particle size. The results can be envisaged also in another way - specifically, assume that the ratio $\left(\frac{G_d}{G_{IC}}\right)^*$ is virtually constant while the particle yield stress decreases with increasing temperature. Apparently, a composite system can then pass from no debonding region to debonding region.

This is a matter of interest to calculate the threshold debond lengths $\left(\frac{h}{R}\right)^*$ corresponding to the threshold values $\left(\frac{G_d}{G_{IC}}\right)^*$ along the curves $\left(\frac{G_d}{G_{IC}}\right)^*$ vs. k shown in Fig. 5. The results of these calculations are plotted in Fig. 6. It is interesting to note that for a composite system with the particle volume fraction $f \geq 0.30$ the threshold debond length $\left(\frac{h}{R}\right)^*$ dramatically changes due to a small change of k within the range about of $1.75 \div 1.85$.

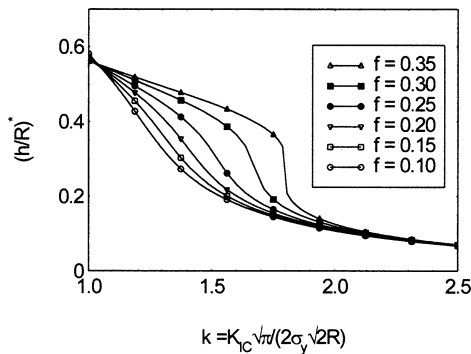


Figure 6. Threshold debond lengths $\left(\frac{h}{R}\right)^*$ corresponding to the threshold values $\left(\frac{G_d}{G_{IC}}\right)^*$.

4. TRAPPED CRACK FRONT MODEL

Assume that the front of a planar crack is trapped against forward advance by a periodical array of closely spaced bridges. As a result, the location of that front differs from a straight line. Following the paper by Rice (1985) consider a half plane crack in the $y = 0$ plane, growing in the direction x and having a straight front along $x = a_0$, see Fig. 7a. Denote the stress intensity factor along the straight crack front parallel to the z -axis by $K_I^0(z; a_0)$ which is given by

$$K_I^0(z; a_0) = K_I^N(a_0) - K_{IR}(z) \tag{25}$$

where $K_I^N(a_0)$ is the remote stress intensity factor, $K_{IR}(z)$ is the restraining stress intensity factor for periodical array of closely spaced bridges and can be readily found, see Appendix B. If the crack front is not straight but lies along the arc $x = a(z)$ in the plane $y = 0$, then Rice (1985) has shown that, provided $a(z) - a_0$ is small such that in an average sense the crack front is still straight and the variation of $K_I^0(z; a_0)$ with a_0 , i.e. $\partial K_I^0 / \partial a_0$ is much smaller than K_I^0 itself, the stress intensity factor $K_I(z; a(z))$ along the moderately curved crack front is

$$\frac{K_I(z; a(z)) - K_I^0(z; a_0)}{K_I^0(z; a_0)} = \frac{1}{2\pi} \int_{-\infty}^{\infty} \frac{\frac{da(z')}{dz'}}{\frac{z' - z}{z' - z}} dz' \tag{26}$$

to the first-order deviation of $a(z)$ from a_0 , i.e. to the first order in $da(z) / dz$. Next consider the situation depicted in Fig 7c. The crack front interacts with physical ligaments of some given distribution. Then $a(z)$ is known along the bridged parts of the crack front L_{brid} but $K_I(z)$ is unknown there. Conversely, $K_I(z) = K_{IC}$ is known along the penetration zones L_{pen} (i.e. the matrix part) but the depth of penetration $a(z)$ is unknown there. These two conditions together reduce (26) to the singular integral equation

$$\frac{K_I^0(z; a_0) - K_{IC}}{K_I^0(z; a_0)} - \frac{1}{2\pi} \int_{L_{brid}} \frac{\frac{da(z')}{dz'}}{z - z'} dz' = \frac{1}{2\pi} \int_{L_{pen}} \frac{\frac{da(z')}{dz'}}{z - z'} dz' \tag{27}$$

for all z included in L_{pen} . Once (27) is solved for $a(z)$ along L_{pen} , $K_I(z)$ along L_{brid} can be found from (26). The solution of (27) can be obtained by analogy from known solutions in two-dimensional crack problems and is shown in Appendix C. The average value of $K_I(z; a(z))$, denoted by $\langle K_I(z) \rangle$ over the bridged crack front ($l - R < |z| < l + R$) is

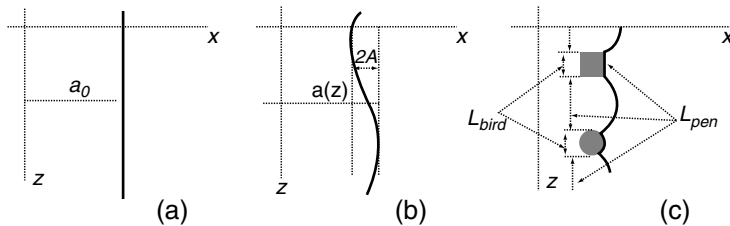


Figure 7. Scheme of the trapped crack front by a periodical array of closely spaced bridges.

$$\langle K_I(z) \rangle = \frac{l[K_I^N - \langle K_{IR}(z \in L_{pen}) \rangle] - (l - R)K_{IC}}{R}. \quad (28)$$

The limiting value of K_I^0 denoted as before $(K_I^N)_{eff}$ corresponds to the instant at which the local stress intensity factor along the bridged crack front $\langle K_I(z) \rangle - \langle K_{IR}(z \in L_{brid}) \rangle$ just attains the value K_{IC} . Eq. (28) then provides

$$\left(\frac{K_I^N}{K_{IC}} \right)_{eff} = 1 + \frac{R}{l} \frac{\langle K_{IR}(z \in L_{brid}) \rangle + \langle K_{IR}(z \in L_{pen}) \rangle}{K_{IC}}. \quad (29)$$

As appropriate approximations for $\langle K_{IR}(z \in L_{brid}) \rangle$ and $\langle K_{IR}(z \in L_{pen}) \rangle$ respectively we choose the value of the restraining stress intensity factor computed at the centre of ligaments given by Eq. (B5) and the value of the restraining stress intensity factor computed in between the ligaments given by Eq. (B7) respectively. When the ratio R/l is transformed to the particle volume fraction f and the parameter k defined through Eq. (21) is introduced, one can put Eq. (29) into the form

$$\left(\frac{K_I^N}{K_{IC}} \right)_{eff} = 1 + \frac{R}{h} \sqrt{\frac{2}{3}} \frac{1}{3k} \times \left[\frac{8}{3}f + \frac{1}{\pi} \left(\frac{3f}{4\pi} \right)^{1/3} (\pi + 4 \arctan(3) - 2 \arctan(2) - \ln(5)) \right], \quad (30)$$

5. DISCUSSION

Consider a specific normalized value of the critical energy release rate for debonding $\frac{G_d}{G_{IC}}$. Then, as Fig. 5 shows, the transition from debonding to no-debonding regime takes place for a set of combination of values of the parameter k and the particle volume fraction f . Each of these combinations relates to a particular value of the debond length $\frac{h}{R}$, see Fig. 6. Choosing f as the independent variable, the toughening ratio $\left(\frac{K_I^N}{K_{IC}} \right)_{eff}$ in Eq. (30) can be plotted vs. f for various values of $\frac{G_d}{G_{IC}}$, see Fig. 8. It is seen that the contribution from the crack trapping diminishes with increasing f when the bridging mechanism progressively takes over. It would appear that the transition in dominant mechanisms depends on $\frac{G_d}{G_{IC}}$; while for $\frac{G_d}{G_{IC}} = 0.18$ it occurs at $f \approx 0.15$, for $\frac{G_d}{G_{IC}} = 0.65$ it occurs at $f \approx 0.38$.

Now compare the experimental toughening data reported by Dlouhy et al. (1997) with theoretical predictions of the model proposed. Note that borosilicate

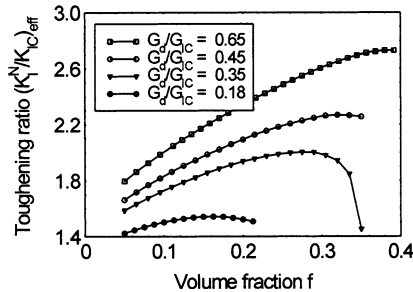


Figure 8. Toughening ratio at the threshold from debonding to no debonding regime.

glass matrix possesses a typical fracture toughness value of only $K_{IC} = 0.7 \text{ MPa}\sqrt{m}$. The average size of the vanadium inclusions was $2R \approx 6 \mu\text{m}$ and their yield strength $\sigma_y \approx 450 \text{ MPa}$. When these values are used in the definition of the composite parameter k in Eq. (21), the value of $k \approx 0.6$ is obtained. The results shown in Fig. 5 indicate that a debonding toughness that is a quite small fraction of the matrix fracture toughness suffices to suppress debonding for such a low value of k and the volume fraction $f = 0.1$. However, if debonding does take place then the results shown in Fig. 6 indicate that a significant extent of debonding can be expected in this case. Apparently, statistical changes in both k and the debonding toughness from particle to particle result in a random occurrence of (i) complete debonding, (ii) partial debonding and (iii) no debonding. This may explain the observed fracture features in the glass composites investigated by Dlouhy et al. (1997): -interfacial debonding (corresponds to the case (i)), -limited crack bridging (corresponds to the case (ii)) and -particle cleavage (corresponds to the case (iii)). It seems that the investigated composite systems were in the regime of transition from extrinsic toughening to intrinsic toughening. Fig. 5 indicates that for $k = 1$ and $f = 0.1$ the threshold value of the ratio of debonding to fracture toughness $\left(\frac{G_d}{G_{IC}}\right)^*$ is about of 0.17. The lowest curve in Fig. 8 shows the plot of the toughening ratio $\left(\frac{K^N}{K_{IC}}\right)_{eff}$ against f for a very close value of $\frac{G_d}{G_{IC}} = 0.18$. It is seen that the calculated toughening ratio for $f = 0.1$ is in a surprisingly good agreement with the experimental value 1.4. The agreement is even better if the fraction of particles effectively interacting with the crack (i.e. taking into account only uncleaved particles) is reduced down to $0.02 \div 0.03$.

6. CONCLUDING REMARKS

The model proposed is capable to explain experimental observations concerning the transition from intrinsic toughening controlled by second phase crack trapping to extrinsic toughening controlled by second phase crack bridging even when the ratio $\frac{G_d}{G_{IC}}$ is virtually constant. The transition relates to the particle yield stress which decreases with increasing temperature. It was also found that the threshold value of the ratio of debonding to fracture toughness $\left(\frac{G_d}{G_{IC}}\right)^*$, such that for $\frac{G_d}{G_{IC}} > \left(\frac{G_d}{G_{IC}}\right)^*$ debonding cannot occur, increases with the particle volume fraction f . Thus, for a fixed value of the dimensionless composite parameter $k = K_{IC}\sqrt{\pi}/(2\sigma_y\sqrt{2R})$ and a fixed value of $\frac{G_d}{G_{IC}}$ particles more readily debond at a higher particle volume fraction f , see Fig. 5. This may explain why the contribution from the crack trapping diminishes with increasing f when the bridging mechanism progressively takes over, see Fig. 8. The diminishing contribution from the crack trapping is mathematically incorporated in Eq. (30) via the dependence of the threshold debond lengths $\left(\frac{h}{R}\right)^*$ on f , see Fig. 6.

ACKNOWLEDGMENTS:

The support through the grant GAČR 101/02/0683 is gratefully acknowledged.

REFERENCES

- Budiansky, B., Hutchinson, J.W., Evans, A.G., 1985, Matrix cracking in fiber-reinforced ceramics, *J. Mech. Phys. Solids* **34**:167.
- Dlouhy, I., Reinisch, M., Boccaccini, A.R. and Knott, J.F., 1997, Fracture characteristics of borosilicate glasses reinforced by metallic particles, *Fatigue Fract. Engng. Mater. Struct.* **20**:1235.
- Choe, H., Chen, D., Schneibel, J.H. et al., 2001, Ambient to high temperature fracture toughness and fatigue-crack propagation behavior in a Mo-12Si-8.5B intermetallic, *Intermetallics* **9**:319.
- Eshelby, J.D., 1970, The energy momentum tensor in continuum mechanics. In: *Inelastic Behavior of Solids*, M.F. Kaninen et al., ed., McGraw-Hill, New York, pp.26–33.
- Kotoul M. and Urbis, R. 2001, On the crack stability in metal particulate reinforced brittle matrix composites, In: *Proc. of ICF10*, A.T. Yokobori, R.O. Ritchie, K. Ravi-Chandar and B.L. Karihaloo, eds., Elsevier, Oxford, CD.
- Rice, J.R., 1988, Cracks fronts trapped by arrays of obstacles: solution based on linear perturbation theory, In: *Analytical, Numerical and Experimental Aspects of Three-Dimensional Fracture Process*, A. Rosakis, K. Ravi-Chandar and Y. Rajapakse, eds., 91, ASME, p. 175.
- Tada, H., 1985, *Handbook for Stress Analysis of Cracks*, 2nd ed., Del. Research Corp., 1985.
- Venkateswara Rao K.T., Soboyejo, W.O., Ritchie, R.O., 1992, Ductile-phase toughening and fatigue-crack growth in Nb-reinforced molybdenum disilicide intermetallic composites, *Metallurgical Transactions A* **23A**:2249.

APPENDIX A

Assume a thin ideally plastic layer connected with two rigid blocks. Cross sections of the layer at $y = 0$, $y = \pm h$ stay planar. Since the layer is thin, it is reasonable to accept the hypothesis of planar cross sections, i.e. $u_y^P = u_y^P(y)$. The equation of incompressibility

$$\frac{\partial u_\rho^P}{\partial \rho} + \frac{u_\rho^P}{\rho} + \frac{\partial u_y^P}{\partial y} = 0 \quad (\text{A1})$$

provides the solution for u_ρ^P which matches the condition $u_\rho^P|_{\rho=0} = 0$

$$u_\rho^P = -\frac{1}{2}u_y^P(y)\rho \quad (\text{A2})$$

Resorting to the deformation theory of plasticity we have

$$\frac{\frac{\partial u_\rho^P}{\partial \rho} - \frac{u_\rho^P}{\rho}}{\sigma_{\rho\rho}^P - \sigma_{\varphi\varphi}^P} = \frac{\frac{u_\rho^P}{\rho} - \frac{\partial u_y^P}{\partial y}}{\sigma_{\varphi\varphi}^P - \sigma_{yy}^P} = \frac{\frac{\partial u_y^P}{\partial y} - \frac{\partial u_\rho^P}{\partial \rho}}{\sigma_{yy}^P - \sigma_{\rho\rho}^P} = \frac{1}{2} \frac{\frac{\partial u_\rho^P}{\partial y} + \frac{\partial u_y^P}{\partial \rho}}{\sigma_{\rho y}^P} \quad (\text{A3})$$

and using (A2) we obtain

$$\frac{0}{\sigma_{\rho\rho}^P - \sigma_{\varphi\varphi}^P} = \frac{-\frac{3}{2}u_y^P}{\sigma_{\varphi\varphi}^P - \sigma_{yy}^P} = \frac{\frac{3}{2}u_y^P}{\sigma_{yy}^P - \sigma_{\rho\rho}^P} = -\frac{1}{4} \frac{u_y^P \rho}{\sigma_{\rho y}^P}. \quad (\text{A4})$$

From (A4) it follows $\sigma_{\rho\rho}^P = \sigma_{\varphi\varphi}^P$ everywhere in the layer. Equilibrium equations now reduce to the form

$$\begin{aligned} \frac{\partial \sigma_{\rho\rho}^P}{\partial \rho} + \frac{\partial \sigma_{\rho y}^P}{\partial y} &= 0 \\ \frac{\partial \sigma_{\rho y}^P}{\partial \rho} + \frac{\sigma_{\rho y}^P}{\rho} + \frac{\sigma_{yy}^P}{\partial y} &= 0 \end{aligned} \tag{A5}$$

and von Mises condition

$$(\sigma_{yy}^P - \sigma_{\rho\rho}^P)^2 + 3(\sigma_{\rho y}^P)^2 = \sigma_y^2. \tag{A6}$$

Boundary conditions at $\rho = R$ will be fulfilled in Saint-Venant' sense

$$\int_{-h}^h \sigma_{\rho y}^P dy = 0, \int_0^h \sigma_{\rho\rho}^P dy = 0. \tag{A7}$$

(A7)₁ requires $\sigma_{\rho y}^P$ to be an odd function of y and in view of relation $h \ll R$ the solution for $\sigma_{\rho y}^P$ is sought in the form

$$\sigma_{\rho y}^P = S(\rho) \frac{\sigma_y}{\sqrt{3}} \frac{y}{h}, \tag{A8}$$

where $S(\rho)$ is an unknown function. Now analyze (A4) at $y = h$. From (A6) one gets for $y = h$ in the case of tension

$$\sigma_{yy}^P - \sigma_{\rho\rho}^P = \sigma_y \sqrt{1 - S^2(\rho)}. \tag{A9}$$

Substitute (A9) into (A4) and obtain

$$\frac{\sqrt{3}u_y^{P'}}{\sqrt{1 - S^2(\rho)}} = -\frac{u_y^{P''} \rho}{2S(\rho)}. \tag{A10}$$

Introduce an arbitrary parameter C

$$\frac{1}{2\sqrt{3}} \left(\frac{u_y^{P''}}{u_y^{P'}} \right)_{y=h} = C \tag{A11}$$

and find the distribution of shear stress along $y = h$ as

$$S = \frac{C_\rho}{\sqrt{1 + C^2 \rho^2}}. \tag{A12}$$

The equilibrium equation (A5)₁ then gives the solution for $\sigma_{\rho\rho}^P$ as

$$\sigma_{\rho\rho}^P = \frac{\sigma_y}{\sqrt{3}h} \int_\rho^R S d\rho + \beta (\beta = const), \tag{A13}$$

where β can be found from the boundary condition (A7)₂. At the outset of plastic deformation $C = 0$ which leads to $S = 0$. For small values of C the function $S(\rho)$ is approximately linear and so is the contact shear stress $\sigma_{\rho y}^P(\rho, h)$. As C increases, $S(\rho)$ deflects from the linear distribution and, in the limit $C \rightarrow \infty$, which corresponds to the fully plastic conditions, $S = 1$. The contact shear stress $\sigma_{\rho y}^P$ approaches the shear yield stress $\sigma_y/\sqrt{3}$ and Eqs. (A7)₂, (A9) and (A13) provide

$$\sigma_{\rho\rho}^P = \frac{\sigma_y}{\sqrt{3}h}(R - \rho) = \sigma_{yy}^P(h). \quad (\text{A14})$$

The average normal stress σ^P acting over the cross section of the layer is

$$\sigma^P = \frac{1}{\pi R^2} \int_0^{2\pi} \int_0^R \sigma_{yy}^P \rho d\rho d\varphi = \frac{\sigma_y}{3\sqrt{3}} \frac{R}{h}. \quad (\text{A15})$$

APPENDIX B

Assume a periodical array of bridging particles along the crack front and replace each particle by square shaped ligament with side length of $2R$. Assume a constant cohesive stress σ^P acting over the bridging particles and use the solution (Tada, 1985) for the stress intensity factor K for point forces of magnitude P applied to both faces of the crack at a horizontal distance z and a vertically downwards distance λ from the crack front

$$K = \frac{P\sqrt{2}\sqrt{\lambda}}{\pi\sqrt{\pi}(\lambda^2 + z^2)}. \quad (\text{B1})$$

Then we obtain for the total restraining stress K_{IR} at the centres of the bridged zones of crack front ($z = \pm(\frac{1}{2} + R + 2nl)$, $n = 0, 1, \dots$)

$$\begin{aligned} K_{IR} \left[z = \pm \left(\frac{l}{2} + R + 2nl \right) \right] &= \frac{4\sqrt{2}\sigma^P R}{\pi\sqrt{\pi}} \sum_{n=1}^{\infty} \int_0^{2R} \frac{\sqrt{\lambda} d\lambda}{\lambda^2 + (2nl)^2} + \frac{\sqrt{2}\sigma^P}{\pi\sqrt{\pi}} \int_{-R}^R \\ &\times \left(\int_0^{2R} \frac{\sqrt{\lambda} d\lambda}{\lambda^2 + z^2} \right) dz, \end{aligned} \quad (\text{B2})$$

where the first term describes the restraining effect of other ligaments while the second term describes the restraining effect of the very ligament being contiguous with the place of evaluation, i. e. along $-R < z < R$. Changing the order of integration and summation in the first term allows (B2) to be expressed as

$$\begin{aligned} K_{IR} \left[z = \pm \left(\frac{l}{2} + R + 2nl \right) \right] &= \frac{2\sigma^P R}{\pi\sqrt{l}} \int_0^{\chi} \left[\frac{\coth\chi'}{\sqrt{\chi'}} - \left(\frac{1}{\chi'} \right)^{3/2} \right] d\chi' + \frac{2\sigma^P\sqrt{R}}{\pi\sqrt{\pi}} [\pi \\ &+ 4 \arctan(3) - 2 \arctan(2) - \ln(5)], \end{aligned} \quad (\text{B3})$$

where $\chi = \frac{\pi R}{l} \leq 1$. The integral in (B3) must be treated in the sense of principal value. Thus, to the order $O(\chi^{7/2})$ finally obtain

$$K_{IR} \left[z = \pm \left(\frac{l}{2} + R + 2nl \right) \right] = \sigma^P \sqrt{\pi} \left(\frac{2R}{3l} \right)^2 \sqrt{R} + \frac{2\sigma^P \sqrt{R}}{\pi \sqrt{\pi}} [\pi + 4 \arctan(3) - 2 \arctan(2) - \ln(5)] \quad (\text{B4})$$

A cohesive stress σ^P can be estimated from the Prandtl's solution for thin circular plastic layer connected with rigid blocks as it is shown in Appendix A, see Eq. (A15)

In a similar fashion one can evaluate the restraining stress intensity factor in between the ligaments, i.e. at $z = \pm 2nl$, $n = 0, 1..$ obtaining

$$\begin{aligned} K_{IR}[z = \pm 2nl] &= \frac{4\sqrt{2}\sigma^P R}{\pi \sqrt{\pi}} \sum_{n=1}^{\infty} \int_0^{2R} \frac{\sqrt{\lambda} d\lambda}{\lambda^2 + [(2n-1)l]^2} \\ &= \frac{2\sigma^P R}{\pi \sqrt{l}} \int_0^{\chi} \frac{\tanh \chi'}{\sqrt{\chi'}} d\chi', \end{aligned} \quad (\text{B5})$$

which to the order $O(\chi^{5/2})$ gives

$$K_{IR}[z = \pm 2nl] = 3\sigma^P \sqrt{\pi} \left(\frac{2R}{3l} \right)^2 \sqrt{R}. \quad (\text{B6})$$

APPENDIX C

Consider a two-dimensional medium in (y, z) plane containing an array of cracks. The medium is loaded remotely in mode I such that the stress $\sigma_{yy} = \sigma^{appl}$ corresponds to K_I^N and the opening gap between $y = 0^+$ and $y = 0^-$ is $2u_y(z) = \delta(z)$. Then $\sigma_{yy}(z)$ along z -axis is obtained as

$$\sigma_{yy}(z) = \sigma^{appl} + \frac{E}{1-\nu^2} \frac{1}{4\pi} \int_{-\infty}^{\infty} \frac{d\delta(z')}{z' - z} dz'. \quad (\text{C1})$$

Eq. (C1) may be rearranged to coincide exactly with (26) if one makes the identifications

$$\begin{aligned} 2[\sigma_{yy}(z) - \sigma^{appl}] \frac{1-\nu^2}{E} &\rightarrow \frac{K_I(z) - K_I^0}{K_I^0} \\ \delta(z) &\rightarrow a(z) \end{aligned} \quad (\text{C2})$$

In this analogy, along L_{brid} the opening displacement is $\delta(z) = a(z)$, whereas along L_{pen} the crack faces sustain the stress $\sigma_{yy}(z) = \sigma^{appl} + \frac{E}{1-\nu^2} \frac{K_{IC} - K_I^0}{2K_I^0}$. The bridges with centre-to-centre spacing $2l$ have a gap $2(l - R)$ between them, where the crack front can propagate. This configuration is reminiscent of a periodic array of through cracks consisting of cracks of length $2(l - R)$ separated by unbroken ligaments of

length $2R$. Its response to a mode I stress field can be determined analytically (see, e.g. Tada et al. 1985), with the y -axis displacement between $y = 0^+$ and $y = 0^-$ given by

$$\delta(z) = \frac{8l(1 - \nu^2)\sigma^{appl}}{E} \ln \frac{\cos \frac{\pi z}{2l} + \sqrt{\cos^2 \frac{\pi z}{2l} - \cos^2 \frac{\pi(l-R)}{2l}}}{\cos \frac{\pi(l-R)}{2l}}. \quad (C3)$$

So with identifications made in (C2) and realizing that $\sigma_{yy}(z) = 0$ along L_{pen} receive for $-(l - R) < z < (l - R)$

$$a(z) = \delta(z) = \frac{4l}{\pi} \left(1 - \frac{K_{IC}}{K_I^0} \right) \ln \frac{\cos \frac{\pi z}{2l} + \sqrt{\cos^2 \frac{\pi z}{2l} - \cos^2 \frac{\pi(l-R)}{2l}}}{\cos \frac{\pi(l-R)}{2l}}. \quad (C4)$$

substituting (C4) into (27) one obtains along the bridged crack front $L_{brid}(l - R < |z| < l + R)$ the following stress intensity factor

$$K_I(z, a(z)) = K_{IC} + (K_I^0 - K_{IC}) \frac{|\sin \frac{\pi z}{2l}|}{\sqrt{\cos^2 \frac{\pi(l-R)}{2l} - \cos^2 \frac{\pi z}{2l}}}, \quad (C5)$$

which is singular at the borders of the bridged zone. The average value $\langle K_I(z) \rangle$ is then given by Eq. (28) in the main body of text.

FRACTURE RESISTANCE OF HYBRID GLASS MATRIX COMPOSITE AND ITS DEGRADATION DUE TO THERMAL AGEING AND THERMAL SHOCK

Ivo Dlouhý, Zdeněk Chlup, Shabbar Atiq,
Aldo R. Boccaccini^{*}

1. INTRODUCTION

In brittle matrix composites reinforced by continuous ceramic fibres, the favourable fracture behaviour is provided by the presence of weak fibre/matrix interfaces, which lead to the fibre pullout effect [1]. The thermal stability and high temperature mechanical properties of silicate matrix composites reinforced by carbon and SiC based fibres in oxidising environments have been investigated quite extensively in the past by conducting thermal aging and thermal cycling experiments over a wide range of temperatures [2–5]. A common result of investigations conducted at temperatures in the range 500–700°C is that there is a decrease of tensile and flexural strength of the composites. It has been shown that this is the consequence of oxidation of the fibres, in case of carbon fibre reinforced composites, or of degradation of the fibre/

^{*} Ivo Dlouhý (corresponding author: idlouhy@ipm.cz), Zdeněk Chlup, Institute of Physics of Materials, Academy of Sciences of the Czech Republic, 61662 Brno, Czech Republic. Shabbar Atiq, Aldo R. Boccaccini, Department of Materials, Imperial College London, London SW7 2BP, UK.

matrix interphase, which is in fact a carbon-rich nanometric interfacial layer, in SiC fibre reinforced composites [2–5].

Hybrid composites are created incorporating simultaneously fibres, particles and/or whiskers as reinforcing elements. The few hybrid glass and glass-ceramic matrix composites described in the literature include: barium magnesium aluminosilicate glass-ceramic matrix composites containing both SiC-Nicalon[®] fibres and SiC whiskers [6,7], cordierite glass-ceramic matrix composites containing SiC monofilament and SiC whiskers [8], borosilicate glass containing SiC-Nicalon[®] fibres, carbon fibres and various ceramic particle fillers (i. e. alumina, zirconia or carbon) [9] and aluminosilicate glass containing SiC-Nicalon[®] fibres and SiC particles [10]. Recently, fused silica matrix composites containing Si₃N₄ particles and chopped carbon fibres have been developed [11]. In hybrid glass matrix composites, the fibres (e. g. chopped or continuous carbon or SiC fibres) are used to impart fracture resistance and toughness by exploiting well-known fracture mechanisms such as fibre pullout and crack deflection. The particulate phase is used to improve other engineering properties relevant for the intended application of the materials, such as thermal shock resistance, wear resistance or impact strength.

Since very little research has been conducted in the area of hybrid glass matrix composites so far, there is need for further investigations, in particular regarding the fracture behaviour of the material after thermal ageing and thermal cycling in oxidising environments. Clearly, an in-depth understanding of the materials degradation and microstructural damage occurring upon long-term exposure at high temperatures is a prerequisite to consider new application areas for these composites.

In the present investigation, the chevron notch specimen technique was used to detect the degradation of the flaw resistance and fracture toughness of hybrid glass matrix composites after thermal ageing in air and thermal shock. The focus of the study was to apply the three-point bending chevron-notch test technique to evaluate fracture toughness (K_{Ic}) of the composites in as-received condition and after thermal exposition. Despite its several advantages [12,13], the chevron notched specimen method has not received wide applicability for K_{Ic} determination in fibre reinforced brittle matrix composites. Indeed the authors are not aware of previous work focused on the application of the chevron notch technique to determine K_{Ic} in hybrid composites, the single edge notch beam specimen method has been mainly used [7,11]. Thus another objective of this article is to examine the applicability of the chevron-notch technique to monitor possible changes in the fracture toughness due to microstructural damage in this class of composite materials.

2. EXPERIMENTAL

The material investigated was a hybrid glass matrix composite supplied by Schott Glas (Mainz, Germany). The composite contained short carbon fibres (24 wt%) as well as ZrO₂ particles (30 wt%) dispersed in a borosilicate glass (DURAN[®], Schott Glas) matrix. The density of the composites was 2.62 g/cm³. The composites were prepared by a proprietary method. Details of the fabrication procedure are given in the literature [9]. The samples were received in the form of plates of thickness of about 4 mm.

Rectangular test bars of nominal dimensions 4 mm × 3 mm × 50 mm were cut from the plates. Thermal ageing for 24 h was carried out in air using an electric

furnace at temperatures of 500, 600 and 700°C. These temperatures were chosen in agreement with those used in separate studies on thermal ageing of unidirectional SiC fibre reinforced composites having the same borosilicate matrix [14]. Another set of specimens was exposed to repeated thermal shocks produced by quenching samples from 500°C into a water bath kept at room temperature. After each quench, the samples were heated again for 15 minutes. Specimens were further characterised after 5,10,20 and 24 cycles. The temperatures chosen for this investigation cover the medium and upper temperature ranges at which the composites are likely to find applications [15]. After thermal treatment, the mass and dimensions of the samples were measured, and the outer surfaces inspected carefully for the appearance of any macroscopic damage, such as change of dimensions, shape, colour, delamination and fibre debonding/protrusion effects.

The microstructure of the as received samples was observed by scanning electron microscopy (SEM) using both secondary electron and backscattered electrons image modes. Selected aged samples were also polished for SEM observations.

Thermally aged samples and samples in the as-received condition were characterised using the chevron-notched specimen technique for fracture toughness determination. Chevron notches with angles of 90° were cut carefully at distances of about 15–20 mm in each test bar using a thin (0.15 mm) diamond wheel. Because the span of the three-point bend test was 16 mm, several notches were introduced in each bar (of 50 mm length), i.e. several fracture toughness tests were carried out using each bar. This approach (one test bar with several notches, keeping the same loading geometry) enables to conduct more tests than in case of different short samples and so a more efficient usage of the available material is possible. Each bar with notches was then placed in the three-point bend fixture and loaded up to fracture initiation. After each test the bar was moved to place another chevron notch into position in the three point bending rig. A constant crosshead speed of 0.01 mm/min was employed for loading. The tests were carried out at room temperature in normal atmosphere. Graphs of load vs. time were recorded and the maximum force was determined from each trace. The fracture toughness value, K_{IC} , was calculated from the maximum load (F_{max}) and the corresponding minimum value of geometrical compliance function (Y_{min}^*) according to the equation [16]:

$$K_{IC} = \frac{F_{max} Y_{min}^*}{BW^{1/2}}$$

where B and W are the thickness and height of the specimens, respectively. The calculation of the geometric function Y_{min}^* for chevron-notched bend bars was based on the use of Bluhm's slice model [17]. The calculation procedure used for the purposes of this investigation has been described in detail elsewhere [16]. The chevron-notch depth a_0 , needed for determining Y_{min}^* , was measured after testing from optical micrographs of fractured specimens.

Additionally, the acoustic emission technique was used during the test. Traces of cumulative number of acoustic emission (AE) events were obtained in the same time scale as the load vs. time plots. This technique allows for an accurate detection of the onset of microcracking at the chevron notch tip, which occurs when a sharp increase in the number of AE events is observed. Valid measurements for computing K_{IC} were those in which this increase of AE events coincided with the end of the linear

part of the force vs. time trace. For all specimens tested, the events producing the AE response increased continuously, practically from the beginning of the test. Some more substantial increase of AE events occurred at two stages during loading: (i) during microcracking development at the crack tip, and (ii) when the maximum force was reached and an unstable jump occurred.

Fracture surfaces of selected broken samples both in as-received condition and after thermal ageing were observed by optical stereomicroscopy and SEM.

A more comprehensive description of other methods applied to characterise the hybrid composites has been presented elsewhere [18].

3. RESULTS

3.1. As-received Material

A SEM micrograph showing the microstructure of an as-received sample is shown in **Figure 1a**. **Figure 1b** shows the same area in backscattered electrons revealing (due to different phase contrast) the distribution of ZrO_2 particles (white phase) in the glass matrix.

The as received material exhibits K_{Ic} values in the range 2.6–6.4 $MPam^{1/2}$, as determined by the chevron notched specimen test [18]. These values are higher than K_{Ic} values quoted for unreinforced borosilicate glass (0.77 $MPam^{1/2}$ [13]) and for Al_2O_3 platelet (30 vol%) reinforced borosilicate glass composites (1.92 $MPam^{1/2}$ [19]). The values are similar to data reported in the literature for hybrid glass matrix composites reinforced by unidirectional SiC fibres and SiC whiskers [7] and for silica matrix composites containing Si_3N_4 particles and C fibres [11], but they are much lower than K_{Ic} data of unidirectional SiC fibre reinforced composites containing 40 vol% fibres (19–26 $MPam^{1/2}$ [13]).

The scatter of data in the present composites was however found to be extremely high [18]. This is connected with different orientations of chopped fibre bundles below the chevron notch tip, as discussed in a previous report [18].

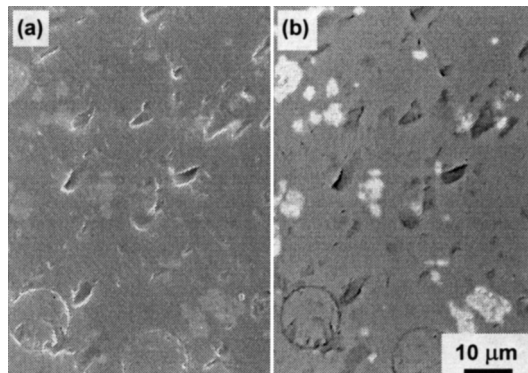


Figure 1. SEM micrographs of a polished section of an as-received sample showing (a) fibres, ZrO_2 particles and absence of porosity; and (b) the same region of the sample in back scattered electrons (BSE) mode, identifying the (bright) ZrO_2 particles.

The fracture surface of an as-received sample is shown in **Figure 2**. The fracture surface exhibits the characteristic fiber pull-out typical of “quasi-ductile” glass matrix composite materials [13,15]. However, inspection of the fracture surfaces reveals that the average pull-out lengths are not uniform across the composite section but depend on the relative orientation of the fibre bundles and the fracture propagation plane. Areas exhibiting fewer fibres are observed when these were oriented parallel to the fracture surface. This behaviour explains qualitatively the lower K_{Ic} values determined in this material in comparison to unidirectional fibre reinforced composites, as mentioned above, where all fibres contribute equally to toughening by the pull-out mechanism [13,15].

3.2. Thermally Aged Material

The fracture toughness values determined by the chevron notched specimen technique are strongly dependent on the ageing condition, as shown in **Figure 3**. In the figure, also data of the as received material are shown.

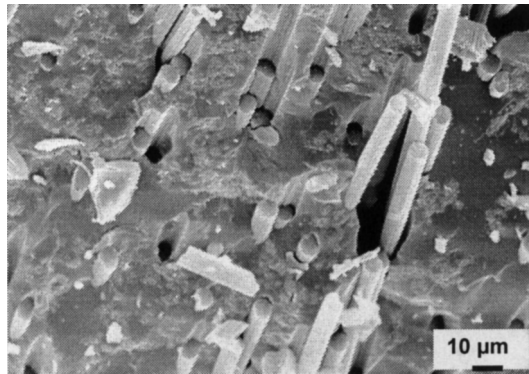


Figure 2. Typical fracture surface morphology of a broken test specimens (material in as received condition), showing fibre pull-out.

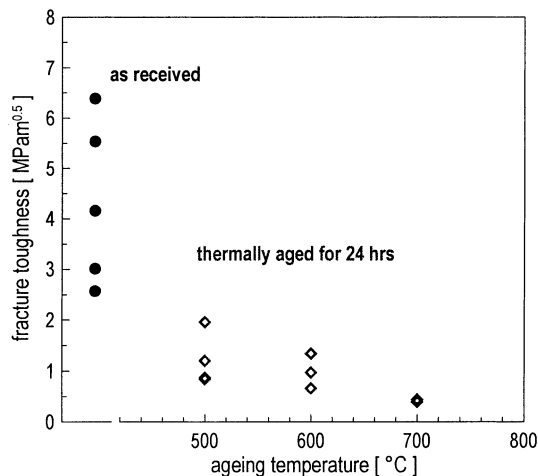


Figure 3. The effect of ageing conditions on fracture toughness of the hybrid composite.

The poorest mechanical response of the samples aged for 24 h at 700 °C is evident from comparison of data in **Figure 3**. It should be noted that microstructural damage accompanying the thermal ageing has produced localised macroscopic shape and volume changes in the samples, with the extent of this damage depending on fiber bundle orientation. This was most evident for the above-mentioned condition of ageing (24 hrs at 700°C), as described elsewhere [18], and it is most probably related to softening of the glass matrix, as discussed below. The measured fracture toughness value for this composite was $K_{Ic} = 0.4 \text{ MPam}^{1/2}$.

The microstructures of thermally aged samples (areas of composite sections orientated perpendicularly to the fibres) are shown in **Figure 4 and 5** for the ageing conditions 500°C/24 h and 700°C/24 h, respectively. It is evident that at 500°C the carbon fibres remain in the composite, however the starting of fibre oxidation leads to the loss of contact between fibre and matrix (**Figure 4**). The image also shows that there is no development of porosity and the overall microstructural damage is limited. Microstructural damage is severe in the composite aged for 24 h at 700°C (**Figure 5**). Comparing to as-received specimens (**Fig. 1**), high porosity in the aged samples is evident, which can be explained by the carbon fibres decomposition due to

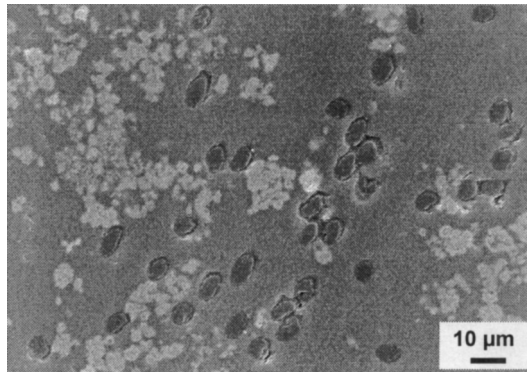


Figure 4. SEM micrograph of a polished section of a sample showing the microstructure after ageing for 24 h at 500°C.

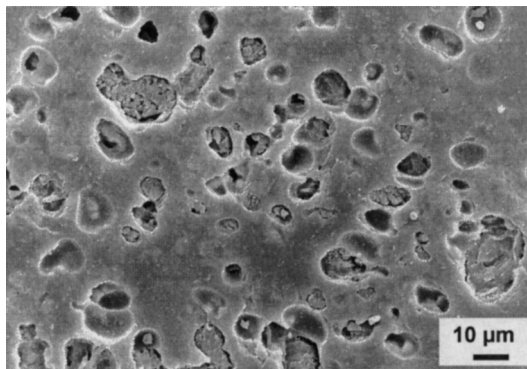


Figure 5. SEM micrograph of a polished section of a sample showing microstructural degradation after ageing for 24 h at 700°C.

oxidation effects. Moreover, softening of the glass matrix at elevated temperature may have contributed to the formation of cavities.

The fracture resistance of the hybrid composite substantially decreased due to the above-described microstructural changes. The progressive change of fracture behaviour with ageing condition can be appreciated from the load deflection traces, shown in **Figure 6**, and analysing fracture features, as discussed elsewhere [18]. The traces for the as received composite and for the material after thermal ageing (**Fig. 6**) show a significant decrease in the maximum value of the fracture load (F_{\max}) for similar chevron notch and specimen geometry. In addition to these quantitative characteristics, directly related to a decrease in fracture toughness values, a change in the slope of the linear part of the traces can also be seen in **Figure 6**.

The decrease in slope with increasing exposure temperature corresponds to a decrease of specimen compliance that can be explained by poorer fibre/matrix interfacial bond and, for the most severe thermal ageing, by matrix damage due to softening and porosity formation as a result of carbon fibre oxidation. A decrease in Young's modulus is a direct consequence of this type of microstructural damage, as also discussed in the literature for other glass composites [14].

For all aged samples, brittle fracture behaviour was observed based on fractographic analysis of the broken specimens, as carried out in the previous investigation [18], whilst the evidence of fibre pull-out mechanism was less frequent with increasing ageing temperature. Moreover X-ray diffraction (XRD) analyses carried out on thermally aged samples showed the formation of a cristobalite phase [18]. This was the sole new crystallisation peak detected and thus XRD confirmed that under the aged conditions investigated there has been no formation of other crystalline phases due to reactions of the ZrO_2 particles and the glass.

3.3. Material exposed to repeated thermal shock

The fracture toughness values determined by the chevron notched specimen technique are strongly dependent on the condition of thermal shock, in particular for the first ten thermal shock cycles, as shown in **Figure 7**. In this figure, the fracture

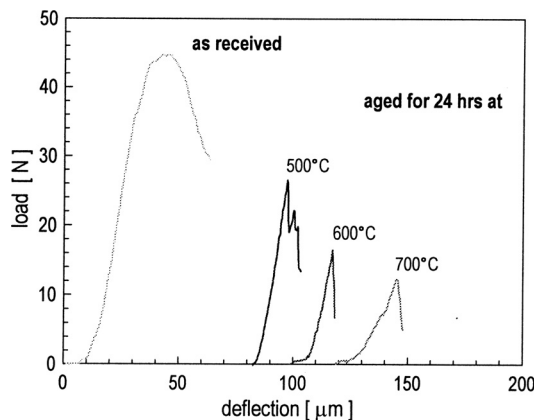


Figure 6. Typical load-displacement plots obtained in chevron-notch tests for samples in as-received condition and after thermal ageing.

toughness values are represented by two kinds of points. Filled triangles represent the values obtained in those specimens where fibers are randomly oriented in relation to the chevron notch plane. The empty triangles are for the fracture toughness values representing data from specimens with fibre bundles parallel to the chevron notch plane. It is clearly evident how the fracture resistance and thus fracture toughness strongly depends on the fibre bundle orientation as mentioned above and also discussed in detail in our previous work [18].

It was noted that the highest number of thermal shock cycles that was applied in this experiment (24 cycles) led to specimen failure without any further mechanical loading: the specimen broke upon quenching into water. Fracture plane analysis showed that the crack had developed along the interface between two fibre bundles.

Figure 8 shows a SEM micrograph of the fracture surface of a sample thermally shocked for 20 cycles. Very limited pull-out is detected in this sample, which is similar to observations on samples thermally aged at 500°C for 24 hours, as discussed above and reported in detail elsewhere [18].

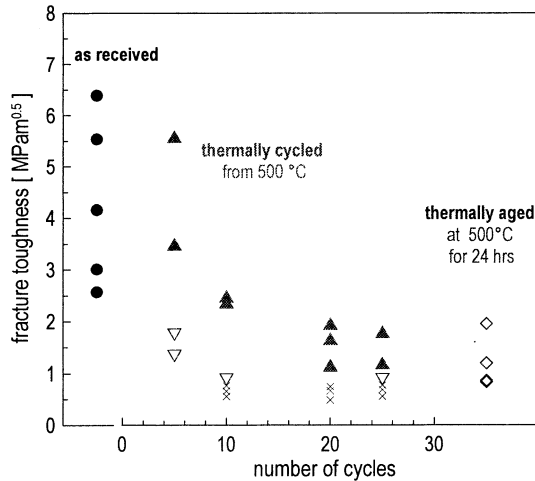


Figure 7. The effect of thermal shock cycling on fracture toughness of the hybrid composite.



Figure 8. SEM micrograph showing a typical fracture surface of a composite after 20 thermal shock cycles

In **Figure 7**, also data of the as received material (filled circles) and material aged at 500°C for 24 hrs (empty rhombi) are shown for comparison. It is seen that the most significant part of composite damage occurred during the first 10 thermal shock cycles. However, the total exposition time at 500 °C during this treatment was comparably shorter than in case of thermal ageing analysed in previous chapter. The more extensive and rapid damage during thermal shock cycling is thus ascribed to the quenching effect, in particular to the effect of cumulative thermal stresses produced during repeated thermal shocks.

The investigation of load-deflection traces provides also very valuable information for the assessment of damage development in thermally shocked samples. The representative curves are shown in **Figure 9**. Similarly as in case of specimens after thermal ageing, the load-deflection curves and fracture toughness values are strongly affected by the orientation of fibre bundles with respect to the chevron notch plane. In case of parallel orientation, the remarkable drop of fracture resistance is associated with the significant change of the load-deflection trace as it can be seen, as example, comparing the curves for specimens after 10 thermal shock cycles in **Figure 9**: specimen 2_3 displayed parallel orientation of fibers and fracture plane, while specimen 2_1 displayed random orientation of fibres.

After the first five thermal shock cycles the fracture behaviour is very similar to that of as received composites (compare the corresponding curves in **Figures 7 and 10**).

For higher number of thermal shock cycles two typical features arise on the load deflection traces. The first one is a marked pop-in behaviour at loads of about 10 N (marked by circles in **Figure 10**). The second phenomenon observed is increasing specimen deflection at fracture (maximum) load, as evident when comparing the curves for 10 and 24 cycles in **Figure 10**. This can be caused by the change of crack tip behaviour affected by damage development at the matrix/fibre interfaces.

4. DISCUSSION

As discussed in the previous investigation [18], the fracture toughness values of the hybrid composites investigated are in the range 2.6–6.4 MPam^{1/2} and they exhibit an

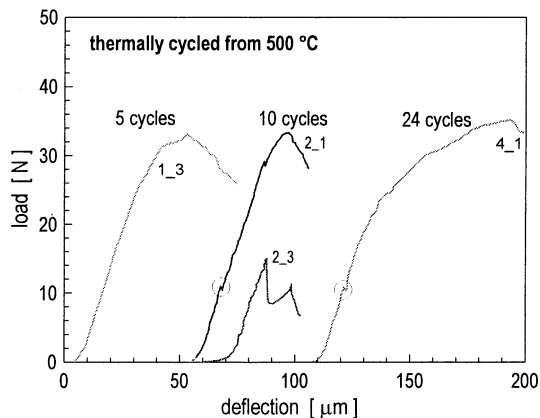


Figure 9. Typical load-displacement plots obtained in chevron-notch tests for samples in as-received condition and after thermal ageing.

extremely large scatter. This was associated with different orientations of short fibre bundles in relation to the chevron notch plane as discussed in detail on the basis of microstructural and fracture surface observations [18]. In general, the as-received material exhibit relatively high K_{Ic} values, in comparison with other hybrid glass matrix composites [7,11,19], which suggests that an effective part of the toughening effect may be provided by the zirconia particles added. The addition of tetragonal zirconia particles to glass matrices should contribute to toughening by the tetragonal-to-monoclinic transformation mechanism, as investigated in the past in a variety of glass and glass-ceramic matrices [20–23]. However in the present composite a monoclinic zirconia particulate phase was added, thus ruling out transformation toughening. In fact the presence of a particulate zirconia phase dispersed in a brittle matrix may further contribute to toughening and strengthening by other mechanisms, mainly by crack deflection and by residual thermal stresses [22,23]. In the present composites, a favourable residual thermal stress field (hoop compressive stresses in the matrix) should develop upon cooling from the fabrication temperature as a result of the thermal expansion mismatch between the zirconia particles ($10.3 \cdot 10^{-6} \text{ 1/}^\circ\text{C}$ [24]) and the borosilicate glass matrix ($3.25 \cdot 10^{-6} \text{ 1/}^\circ\text{C}$ [13]). However, the relative contribution to toughening due to the fibre pull-out mechanism and to zirconia particle related mechanisms cannot be quantitatively determined from the results obtained in this study. In general, however, fibre pull-out is thought to be the dominant and more effective toughening mechanism in these hybrid composites [18].

For the most severe thermal ageing conditions (700°C , 24 h, **Figure 3**), the K_{Ic} values dropped to $0.4 \text{ MPam}^{1/2}$. This value is even lower than K_{Ic} of monolithic borosilicate glass ($0.77 \text{ MPa m}^{1/2}$ [19]), which can be explained by the very high porosity developed in the aged sample as consequence of carbon fibre oxidation, as discussed elsewhere [18]. Thus, for the conditions of thermal ageing investigated here, degradation of carbon fibres due to oxidation occurred, this being more severe with increasing temperature, and therefore the apparent fracture toughness and flaw tolerant resistance of the composites decreased. For the highest temperature tested (700°C), enhanced porosity formation in the matrix was detected, which is thought to be the result of softening of the glass. Indeed the aging temperature (700°C) was well above the transformation temperature of the borosilicate glass matrix used ($T_g = 525^\circ\text{C}$ for borosilicate DURAN[®] glass [15]). Fractographic observations support well this discussion as reported previously [18]. It seems that oxidation of the carbon fibres starts at 500°C , leading to degradation of the fibre – matrix interface. As shown in **Figure 4** for a polished sample, the interface boundary between the glass matrix and fibres appears to be degraded comparing to the initial state (**Figure 1**). The combination of matrix and matrix-fibre interface degradation and the damage to the boundary region between neighbouring fibre bundles, as detected by scanning electron microscopy observations (**Figures 4 and 5**), supplied a more favourable condition for fracture initiation and this resulted in a decrease of both K_{Ic} values and the data scatter in thermally aged materials.

A similar detrimental effect on K_{Ic} values was measured in samples after repeated thermal shocks from 500°C . K_{Ic} dropped to $1.3 \text{ MPam}^{1/2}$ for the maximum number of thermal shocks applied (24 cycles), as shown in **Figure 7**. The figure also indicates that the fracture toughness values of thermally shocked samples lie between those of as received samples and those of specimens thermally aged at 500°C for 24

hours. This is related to the shorter exposure time at high temperature in the thermally shocked samples in comparison to the aged samples.

The actual contribution of the thermal shocks to composite degradation is hard to quantify and the samples have undergone degradation also during the holding time at temperature. There is an important effect that has been detected however when comparing the load-deflection traces of specimens thermally aged (**Fig. 6**, see the curve for 500°C) and specimens after thermal shock cycling (**Fig. 9**, curves for 10 and 24 cycles). Occurrence of pop-in effect at loads of about 10 N appeared to be typical for specimens after thermal shock treatment. An attempt has been made to estimate the stress intensity factor (fracture toughness value) corresponding to this level of load for particular specimens. This is possible assuming that the dependence of the geometrical function on crack length is known for the particular chevron notch depth. The values obtained are represented by crosses in **Fig. 8**; they correspond well to the fracture toughness of the borosilicate glass matrix used in the composite (0.7 MPam^{1/2} [13]). One possible explanation is that whereas high temperature exposition (aging) leads to carbon fiber and fiber matrix interface degradation, the thermal shock loading causes additional damage to the matrix. This can be due to residual thermal stresses developed in the matrix after increasing number of thermal shocks, which causes premature matrix microcracking at the chevron notch tip in the early stages of specimen loading. This indicates that cumulative degradation of the composite due to increasing number of thermal shocks is more detrimental, in terms of fracture toughness, compared to simple thermal exposition (aging) at the same temperature.

5. CONCLUSIONS

The fracture behaviour of hybrid glass matrix composite samples before and after thermal ageing and/or thermal shock cycling in air has been analysed and evaluated for the first time. The fracture toughness values measured were in the range 2.6–6.4 MPam^{1/2} for the as received material and they were significantly reduced by thermal ageing and thermal shock treatments. The K_{Ic} values dropped to 0.4 MPam^{1/2} for ageing at 700°C for 24 h due to fibre oxidation and porosity formation in the matrix as a result of softening of the glass. The K_{Ic} values decreased to 1.3 MPam^{1/2} for the maximum number of thermal shock cycles from 500°C (24 cycles). The damage in the samples due to thermal shock is based on fibre oxidation and porosity formation, as in case of thermal ageing, and, in addition, due to superposed residual thermal stresses in the matrix produced by repeated thermal shocks. The present results are useful to define parameters and conditions for the high temperature application of the composites.

ACKNOWLEDGEMENTS

This research was funded from grant of NATO (Nr. PST.CLG.977558). The experimental part of the research was financially supported by grant Nr. A2041003 of the Grant Agency of the Academy of Sciences, Czech Republic. The authors gratefully acknowledge Prof. W. Beier and Mr. R. Liebold of Schott Glas, Mainz, Germany, for supplying the samples.

REFERENCES

1. A.G. Evans, F.W. Zok FW. Review. The Physics and Mechanics of Fibre-Reinforced Brittle Matrix Composites. *J. Mat. Sci.*, 29, 3857–3896 (1994).
2. S. Sutherland, K.P. Plucknett, and M.H. Lewis, High Temperature Mechanical and Thermal Stability of Silicate Matrix Composites. *Comp. Eng.*, 5, 1367–1378 (1995).
3. W. Sinkler, M. Monthieux, V. Bianchi, P. Goursat, E. Menessier, Carbon Fibre-Reinforced (YMAS) Glass-Ceramic Matrix Comp. II. Struct. Changes in the Matrix with Tem. *J. Europ. Ceram. Soc.*, 19, 305–316 (1999).
4. Y.M. Sung, S. Park, Thermal and Mechanical Properties of Graphite Fibre-Reinforced Off-Stoichiometric $\text{BaO} \cdot \text{Al}_2\text{O}_3 \cdot 2\text{SiO}_2$ Glass-Ceramic Matrix Composites. *J. Mat. Sci. Lett.*, 19, 315–317 (2000).
5. K.M. Prewo, J.A. Batt, The Oxidative Stability of Carbon Fibre Reinforced Glass-Matrix Composites. *J. Mat. Sci.*, 23, 523–527 (1988).
6. N. Chawla, K.K. Chawla, M. Koopman, B. Patel, C. Coffin, J.I. Eldridge, Thermal-Shock Behaviour of a Nicalon-Fiber-Reinforced Hybrid Glass-Ceramic Composite. *Comp. Sci. Technol.*, 61, 1923–1930 (2001).
7. Lewinshon LA. Hybrid Whisker-Fiber-Reinforced Glass- Matrix Composites with Improved Transverse Toughness. *J. Mat. Sci. Lett.*, 12, 1478–1480 (1993).
8. S.B. Haug, L.R. Dharani, D.R. Carroll, Fabrication of Hybrid Ceramic Matrix Composites. *Appl. Comp. Mater.*, 1, 177–181 (1994).
9. R. Reinicke, K. Friedrich, W. Beier, R. Liebold, Tribological Properties of SiC and C-Fibre Reinforced Glass Matrix Composites. *Wear*; 225–229, 1315–1321 (1999).
10. K.P. Gadkaree, Particulate-Fibre-Reinforced Glass Matrix Hybrid Composites, *J. Mat. Sci.*, 27, 3827–3834 (1992).
11. D.C. Jia, Y. Zhou, T.C. Lei, Ambient and Elevated Temperature Mechanical Properties of Hot-pressed Fused Silica Matrix Composites, *J. Europ. Ceram. Soc.*, 23, 801–808 (2003).
12. J.S. Ha, K. K. Chawla, Mechanical Behaviour of Mullite Composites Reinforced with Mullite Fibres. *Materials Science and Engineering; A203*, 171–176 (1995).
13. I. Dlouhy, A.R. Boccaccini, Reliability of the Chevron Notch Technique for Fracture Toughness Determination in Glass Composites Reinforced by Continuous Fibres. *Scripta Mat.*, 44 (3), 531–537 (2001).
14. A.R. Boccaccini, A.J. Strutt, K.S. Vecchio, D. Mendoza, K.K. Chawla, C.B. Ponton, and D.H. Pearce, Behavior of Nicalon-Fiber Reinforced Glass Matrix Composites Under Thermal Cycling Conditions. *Composites A*, 29, (11), 1343–1352 (1998).
15. A.R. Boccaccini, D.H. Pearce, J. Janczak, W. Beier, and C.B. Ponton. Investigation of the Cyclic Thermal Shock Behaviour of Fibre Reinforced Glass Matrix Composites Using a Non-Destructive Forced Resonance Technique. *Mat. Sci. Technol.*, 13, 852–859 (1997).
16. I. Dlouhy, M. Holzmann, J. Man, and L. Válka, The Use of Chevron Notched Specimen for Fracture Toughness Determination. *Metallic Materials*, 32, 3–13 (1994).
17. J.I. Bluhm, Slice Synthesis of a Three Dimensional “Work of Fracture Specimen”. *Engng. Fract. Mech.*; 7: 593–604 (1975).
18. I. Dlouhy, Z. Chlup, S. Atiq, A.R. Boccaccini, Fracture Behaviour of Hybrid Glass Matrix Composites: Thermal Ageing Effects, *Composites Part A*, submitted (2003).
19. A.R. Boccaccini, V. Winkler, Fracture Surface Roughness and Toughness of Al_2O_3 -Platelet Reinforced Glass Matrix Composites. *Composites A*, 33, 125–13 (12002).
20. Z.B. Yu, D.P. Thompson, A.R. Bhatti, Synergistic Role of Carbon Fibres and ZrO_2 Particles in Strengthening and Toughening Li- α -sialon Composites. *J. Europ. Ceram. Soc.*, 22, 225–235 (2002).
21. J.K. Guo, Z. Mao, C. Bao, T. Wang, D.S. Yan, Carbon Fibre Reinforced Silicon Nitride Composite. *J. Mat. Sci.*; 17, 3611–3316 (1982).
22. M. Nogami, and M. Tomozawa, ZrO_2 - Transformation Toughened Glass-Ceramics Prepared by the Sol-gel Process from Metal Alkoxides. *J. Am. Ceram. Soc.*, 69, 99–102 (1986).
23. R.D. Sarno, and M. Tomozawa, Toughening Mechanisms for a Zirconia-Lithium Aluminosilicate Glass-Ceramic. *J. Mat. Sci.*; 30, 4380–4388 (1995).
24. D.J. Green, An Introduction to the Mechanical Properties of Ceramics. Cambridge University Press, Cambridge, UK, 1998.

CREEP INVESTIGATION OF SiC_f-SiBC COMPOSITES

Gaëlle Farizy, Jean-Louis Chermant, Jean Vicens,
and Jean-Christophe Sangleboeuf*

ABSTRACT

The concept of ceramic matrix composites was proposed in the eighties to be used in the aeronautical and space domains. Classical SiC_f-SiC have changed into complex materials, such as SiC_f-SiBC investigated in this work: that composite is reinforced with SiC Hi-Nicalon fibers and has a multi-layer and self-sealing matrix. This matrix has been fabricated by means of several chemical vapor infiltrations with different compositions. Prior to the matrix infiltration, a pyrocarbon interphase has been deposited on the fibrous preform. The self-sealing property of this composite is due to the presence of boron in certain matrix layers, which will react with the atmosphere and particularly oxygen, to create a sealant glass, which protects pyrocarbon and SiC fibers.

Tensile creep behavior of this material was investigated in the 1373–1573 K temperature range, under stresses varying from 130 to 200 MPa, under oxidizing atmosphere. Unloading-reloading loops have permitted to follow the evolution of the damage parameter defined by Kachanov and Rabotnov. Microscopical analysis by means of scanning and transmission electron microscopies have shown microstructural modifications and damage creation in the crept materials. Creep results obtained under air have been compared to similar results under argon: it has been possible to determine the influence of oxygen (which corresponds to real environment for their use), and the efficiency of the sealant glass.

* Gaëlle Farizy, LERMAT, URA CNRS 1317, ISMRA, 6 Bd Maréchal Juin, 14050 Caen Cedex, France, now at LCTS, UMR 5801, Domaine Universitaire, 3 allée de la Boétie, 33600 Pessac, France. Jean-Louis Chermant, 42 rue Jean Hébert, 14000 Caen, France. Jean Vicens, LERMAT URA CNRS 1317, 6 Bd Maréchal Juin, 14050 Caen Cedex, France. Jean-Christophe Sangleboeuf, LARMAUR, UPRES-JE 2310, Bât 10B, Université de Rennes 1, Campus de Beaulieu, 35042 Rennes Cedex, France.

This work has then permitted to determine the creep mechanism(s) involved in this composite and to precise the influence of oxidizing atmosphere on the mechanical behavior.

1. INTRODUCTION

SiC_f-SiC composites development has conducted to a complex material, named SiC_f-SiBC in this work, fabricated by Snecma Propulsion Solide (Saint Médard en Jalles, France) and useable in the aeronautic and space domains.¹⁻⁸ Then, it is very important to determine the thermomechanical behavior of this material. This work was supported by a CPR (Contrat Programme de Recherche) “Modélisation du comportement et de la longévité de composites à matrice céramique – Modeling of the behavior and lifetime of ceramic matrix composites” in which different laboratories are acting to furnish datae and results and to model the mechanical behavior of this material. The aim of this work is to study the creep behavior of the composite, i.e. to determine the creep mechanism(s) under air.⁹

2. MATERIALS AND TECHNIQUES

The material of this work is a composite reinforced by SiC Hi-Nicalon fibers, with a self-sealing matrix. This matrix has been fabricated by Snecma Propulsion Solide by means of several infiltrations with different compositions, based on the Si-B-C ternary system. This matrix has been created to allow the use of the material under oxidative atmosphere, using its smart aspect.¹⁰ In contact with oxygen present in the microcracks, specific matrix layers will react and form a sealant glass which will prevent oxygen to go further in the material and the degradation of fibers and interfaces. Before infiltrations,¹¹ the fibrous architecture has been coated by a thin layer of pyrolytic carbon.

Figure 1 shows the composite at different scales. One can notice on these micrographs the presence of longitudinal and transversal yarns, important macroporosity between the yarns and microporosity inside the yarns, and the multi-layered matrix. The mean diameter of Hi-Nicalon fibers and the volumic fraction of porosity, calculated by automatic image analysis, are respectively about 15,3 μm and 20 %.

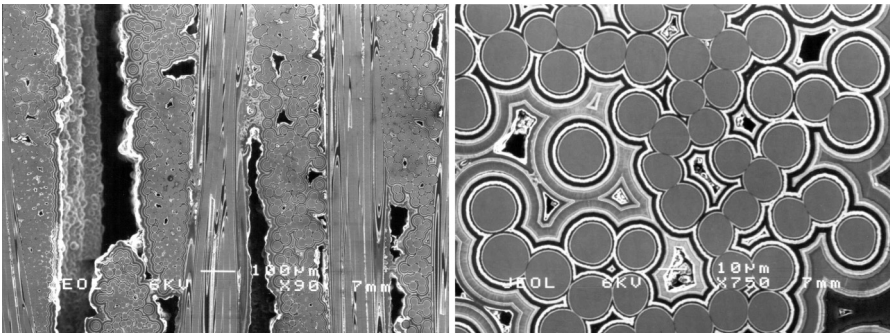


Figure 1. SEM micrographs of the SiC_f-SiBC composite at different scales.

Creep tests were performed in tension with a servohydraulic machine, equipped with an airtight fence and RF furnace. The creep deformation was measured by two resistive extensometers placed face to face on the specimen. Temperature inside the furnace is controlled by two thermocouples (Pt/Rh 0/10 %) and a bichromatic pyrometer. A lot of cares was taken to obtain reproducible and accurate values of the temperature and deformation.^{12,13}

Regularly during creep tests, unloading-reloading loops were performed in order to follow the evolution of one of the elastic moduli. Then, it has been possible to calculate the damage parameter, D , defined by Kachanov¹⁴ and Rabotnov¹⁵ by the following equation :

$$D = 1 - \frac{E_t}{E_0}$$

with : E_t , the modulus at a given time t ,

E_0 , the initial modulus of the composite.

Tests have been performed in the 1373–1573 K temperature range, under stresses varying from 130 to 200 MPa, most often under air.

3. MACROSCOPICAL CREEP RESULTS

Figure 2 presents the creep curves, deformation as a function of time, ϵ - t , for tests performed under different stresses at different temperatures. Two stages can be observed on these curves. The primary stage is characterized by an important increase of the deformation during the first hours of creep. The second one is stationary (constant creep rate) or pseudo-stationary (light decrease of the creep rate until the rupture of the specimen). The tertiary stage has never been observed in our experimental conditions, which is generally the case for CMCs based on

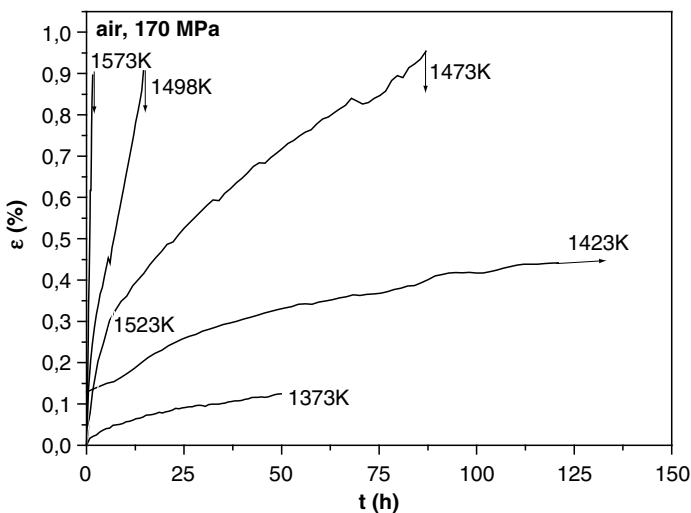


Figure 2. Creep curves, deformation as a function of time, ϵ - t , for tests performed under 170 MPa at different temperatures under air.

SiC_f-SiC. Figure 3 presents the creep rate, $\dot{\epsilon}$, in the second stage as a function of the temperature, under different stresses. One can observe a temperature transition around 1500 K. Below this temperature, the creep rate is really low ($\approx 10^{-8} \text{ s}^{-1}$) and it does not depend on the applied stress. Above this temperature, there is an important increase of the creep rate which then depends on the applied stress. As a consequence, the life time duration is also reduced above this temperature.

The evolution of the damage parameter is shown in Figure 4. Two different stages can be discerned : the first one characterized by an important increase at the beginning of the creep test and the second one by a light and constant increase until the rupture of the composite. A strong increase of this damage parameter has never been observed just before the rupture of the specimen, as it can be observed during fatigue tests on that material.¹⁶ This behavior with two stages has already been observed for other CMCs tested in the same experimental conditions but under a partial pressure of argon.^{9,17-20}

From these macroscopical results, it is not possible to determine the mechanism(s) involved during creep. A multiscale and multitechnique approach is necessary to correlate the different results and to access the creep mechanism.

4. DISCUSSION

4.1. Microscopical Observations

Nanoscopical observations by HRTEM have revealed different microstructural modifications in the creep tested specimens. The most important ones are the growth of SiC- β nanocrystals in Hi-Nicalon fibers and crystallization of certain matrix layers: layers based on B-C becomes fully cristallized and in those based on

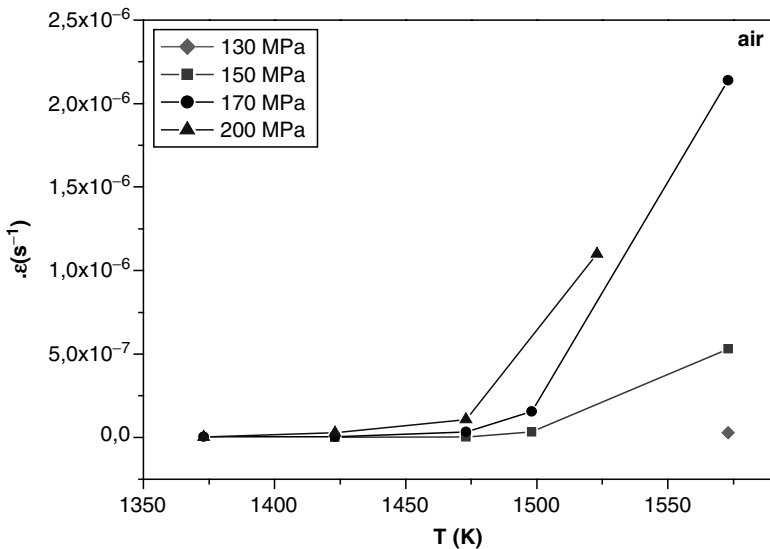


Figure 3. Creep rate as a function of the temperature, $\dot{\epsilon}$ -T, for tests performed under different stresses under air.

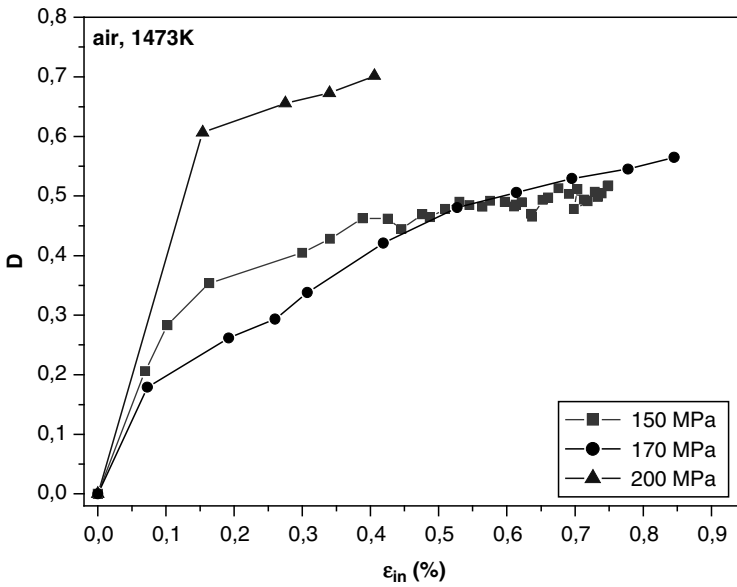


Figure 4. Damage parameter as a function of the inelastic deformation, D - ϵ_{in} , for tests performed under air at 1473 K under different stresses.

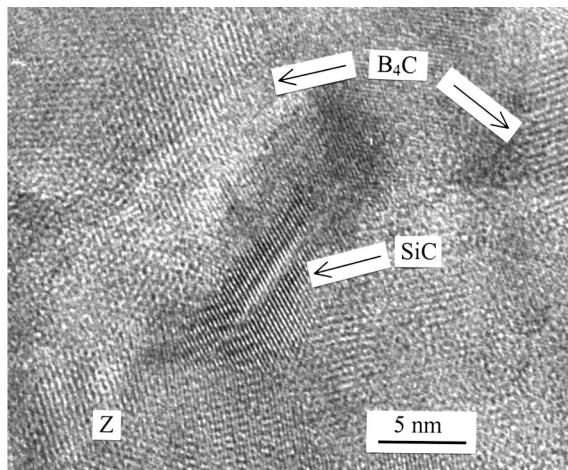


Figure 5. HRTEM micrograph of Z layer of a composite tested à 1573 K under 170 MPa after 2 h.

Si-B-C, crystals of B_4C and SiC are largely observed (Figure 5). An amorphous silica layer (Figure 6) has also been observed at the fiber/matrix interface (after 2 hours of creep test at 1573 K under 170 MPa). EDS analysis have confirmed the composition of this layer. All these microstructural modifications have also been confirmed by Raman spectroscopy analysis. The presence of this thin amorphous silica layer is certainly due to the penetration of oxygen in the specimens or to a reaction at the fiber/matrix interphase.

SEM observations have been performed on the as-received material and after creep tests. Different classical damage features of ceramic matrix composites have

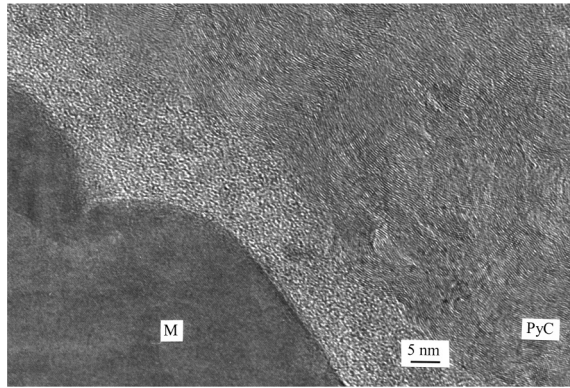


Figure 6. HRTEM micrograph showing the presence of a thin silica layer at PyC/matrix interphase in a composite tested at 1573 K under 170 MPa after 2 h.

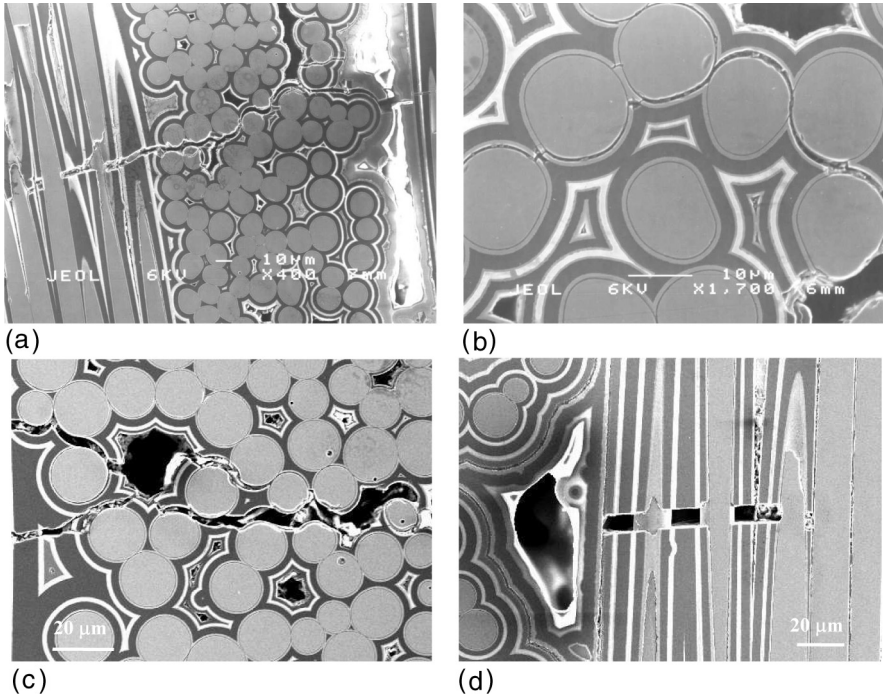


Figure 7. Damage features in creep tested composites under air: a) 1423 K/170 MPa/320 h; b) 1473 K/170 MPa/87 h; c and d) 1573 K/150 MPa/5 h.

been observed, such as matrix microcracking, fiber and yarn ruptures, longitudinal fiber bridging ... (Figure 7).

When tests are performed under argon, one observes the same type of features but without a glassy phase (Figure 8). It clearly shows the matrix interlayer debondings and the propagation of a matrix microcrack in the matrix layer between a transverse and a longitudinal yarn, without any new crack in the longitudinal fibers.

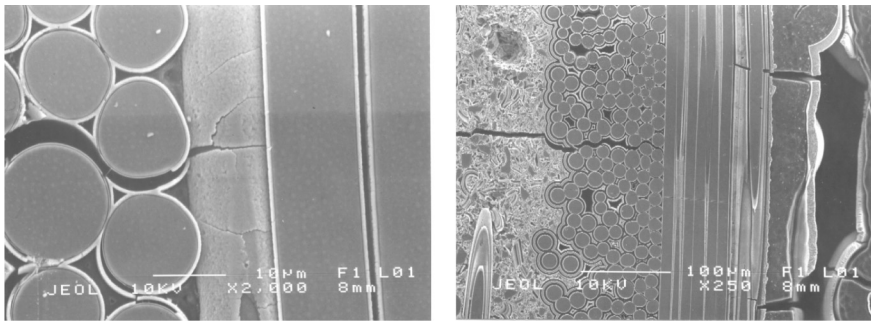


Figure 8. SEM micrographs of composites tested at 1473 K under 200 MPa under argon, after 43 h of creep.

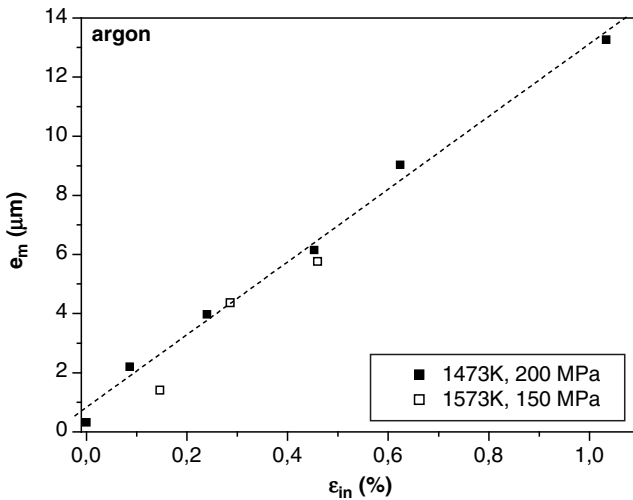


Figure 9. Mean microcracks opening as a function of the inelastic deformation, e_m - ϵ_{in} , for composites tested under argon in different conditions.

As damage plays an important role in the mechanical behavior, it seemed important to determine pertinent parameters characteristic from this damage. The first parameter investigated has been the distance between the microcracks in the transverse yarns. It appears to be constant ($\approx 500 \mu\text{m}$) whatever the temperature and the stress are. We can conclude that microcracking saturation in the composite occurs for a stress level lower than 150 MPa. The second parameter has been the opening of the microcracks during creep tests. Thanks to interrupted creep tests performed under argon, it has been possible to quantify the microcracks opening by means of automatic image analysis.^{21,22} For that purpose, we have used a square structuring element and measured automatically the greatest square included in the cracks. More than one hundred cracks have been analyzed. Figure 9 presents the plot of the microcracks opening, e_m , as a function of the inelastic deformation of the composite, ϵ_{in} . This plot evidences the linear relationship between these two values. These parameters (distance between the microcracks and microcracks opening) have not yet been connected each other but they furnish precious information concerning

the creep mechanism, and must now be used to be included in a creep model from damage-mechanics.

4.2. Influence of oxidation

Most of the creep tests have been performed under air, in order to analyze the influence of oxidation and the effect of the sealant glass. SEM observations on the crept specimen have shown the presence of the sealant glass in the porosity, microcracks and decohesions. They are either partially or completely filled with a glass (Figures 10 a and b). An important quantity of glass is also present on the fracture surface, which are completely embedded (Figures 10 c and d). Some degradations on fibers seem to be due to the contact between Hi-Nicalon fibers and the sealant glass (Figure 10a).

In order to characterize the influence of oxidation on the mechanical behavior, some creep tests have been performed in the same conditions of stress and temperature but under argon. Figure 11 shows creep curves from tests performed in the same conditions under a different atmosphere. For given stress and temperature, the creep rate under air is higher than under argon. As a consequence, the life time duration is lower under air than under argon. One can also notice on these graphs that some curves are really similar (for example 1473 K/170 MPa/air and 1473 K/150 MPa/argon). The behavior under air seems to be penalized from a stress of about 20 MPa. This can be due to a ratio of longitudinal fibers unable to support the charge anymore.

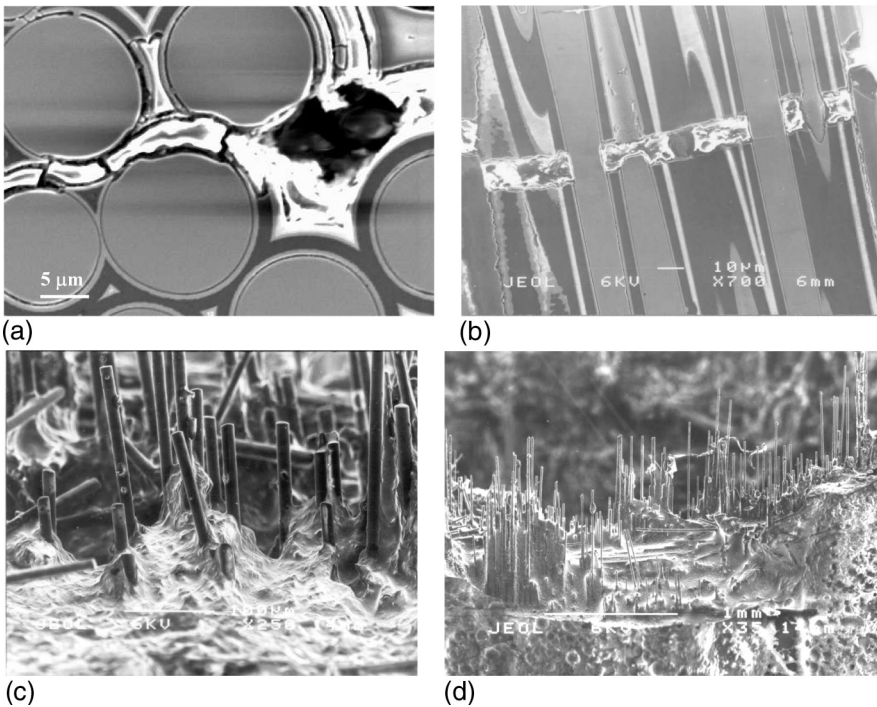


Figure 10. SEM micrographs showing the presence of the sealant glass in the creep tested composites under air; a) 1573 K/170 MPa/2 h; b and c and d) 1473 K/170 MPa/87 h.

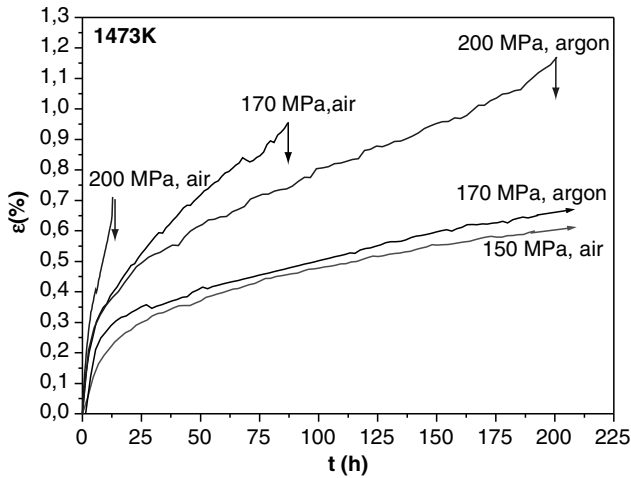


Figure 11. Creep curves, deformation as a function of time, ε - t , for tests performed under different stresses at 1473 K under air or under argon.

4.3. Rupture mechanism

All the previous arguments have permitted to propose a mechanism which will lead to the rupture of that kind of composite. The pure creep mechanism has been identified as a damage-creep one.^{23,24} That means that there is first creation of a microcracking network in the composite during loading and the really first hours of creep test, until the saturation: this corresponds to the first stage on the evolution of the damage parameter, *i.e.* the important increase of the damage at the beginning of creep test. After this creation of the microcrack array, one can only observe the opening of these microcracks until the rupture of the composite corresponding to the constant increase of the damage parameter: there is no new creation of matrix microcrack in the material. If the conditions are required then longitudinal fibers bridging the microcracks can creep.^{25,26}

The influence of oxidation must be added to the pure creep mechanism. In fact, one of these effect will be dominant and cause the rupture of the specimen. The sealant glass will increase the life time duration but its efficiency at high temperature and/or high stress can be improved: degradation or volatilization of the glass during creep tests will permit oxygen to go further in the specimen and cause the rupture of the composite, even if the creep deformation is low (if the fibers have not reached their deformation to rupture).

5. CONCLUSION

These investigations on SiC_f-SiBC composites have permitted to characterize the creep behavior of these composite under air. A multitechnique and multiscale approach has been necessary to determine the mechanism(s) involved during creep, leading to the rupture of the specimen. The knowledge about the creep behavior of this kind of composite has been improved and this work has evidenced the possible use of such SiC_f-SiBC composite under an oxidative environment (for example, the

lifetime duration is more than 400 h for creep tests performed at 1473 K under 150 MPa, under air).

ACKNOWLEDGMENTS

This work has been supported by Snecma Propulsion Solide (Saint Médard en Jalles, France) and by CNRS and Région de Basse-Normandie (GF). It was performed in the frame of the research program contract CPR (Contrat Programme de Recherche) “Modélisation du comportement et de la longévité de composites à matrice céramique – Modeling of the behavior and lifetime of ceramic matrix composites”, with LMT of ENS Cachan, GEMPPM of INSA Lyon, LCTS of Pessac, LERMAT of Caen, ONERA of Châtillon sous Bagneux, and Snecma Propulsion Solide. We wish to warmly thank Mrs M. Bourgeon, E. Pestourie and J.M. Rougès for fruitful discussions and for providing the specimens, Mr H. Cubero for his helpful assistance to perform the creep tests and Mrs L. Chermant for the investigations by automatic image analysis.

REFERENCES

1. C.P. Beesley, The application of CMCs in high integrity gas turbine engines, in: *Ceramic and Metal Matrix Composites, CMMC 96*, San Sebastian, Spain, Sept. 9–12, 1996, Proceedings ed. by Fuentes M., Martinez-Esnaola J.M., and Daniel A.M., *Key Eng. Mat.*, **127–131**, pp 165–174 (1997).
2. H. Ohnabe, S. Masaki, M. Onozuka, K. Miyahara, and T. Sasa, Potential application of ceramic matrix composites to aero-engine components, *Composites Part A*, **30A**, 489–496 (1999).
3. R. Renz, and W. Krenkel, C/C-SiC composites for high performance emergency brake systems, in: *Composites: from Fundamentals to Exploitation*, ECCM 9, June 4–7, 2000, Brighton, UK, (ECCM 9 CD ROM C 2000, IOM Communications Ltd).
4. J.M. Staehler, and L.P. Zawada, Performance of four ceramic-matrix composite divergent flap inserts following ground testing on an F110 turbofan engine, *J. Amer. Ceram. Soc.*, **83**, 1727–1738 (2000).
5. J. Demmel, H. Lallinger, and G. Kopp, Applications of CMC-racks for high temperature processes, in: *High Temperature Ceramic Matrix Composites, HTCMC4*, Munchen, Germany, Oct 1–3, 2001, edited by W. Krenkel, R. Naslain, H. Schneider, (Wiley-VCH verlag GmbH, Weinheim, Germany), pp. 832–838.
6. F. Lamouroux, E. Bouillon, J.P. Cavalier, P. Spriet and G. Habarou, An improved long life duration CMC for jet aircraft engine applications, in: *High Temperature Ceramic Matrix Composites, HTCMC4*, Munchen, Germany, Oct 1–3, 2001, edited by W. Krenkel, R. Naslain, H. Schneider, (Wiley-VCH Verlag GmbH, Weinheim, Germany), pp. 783–788.
7. K. Nishi, J. Gotoh, and S. Aratama, Development of a 3D SiC/SiC component model for HOPE-X (H-2 Orbiting Plane Experimental), in: *High Temperature Ceramic Matrix Composites, HTCMC4*, Munchen, Germany, Oct 1–3, 2001, edited by W. Krenkel, R. Naslain, and H. Schneider, (Wiley-VCH Verlag GmbH, Weinheim, Germany), 754–759.
8. F. Christin, Design, fabrication, and application of thermostructural composites (TSC) like C/C, C/SiC, and SiC/SiC composites, *Adv. Eng. Mater.*, **4[12]**, 903–912 (2002).
9. G. Farizy, Mécanisme de fluage sous air de composites SiC_f-SiBC à matrice auto-cicatrisante – Creep mechanism under air of SiC_f-SiBC composites with a self-sealing matrix, *Thèse de Doctorat of the University of Caen*, (2002).
10. S. Goujard, L. Vandenbulcke, J. Rey, J.L. Charvet and H. Tawil, 1990. Matériaux composites réfractaires protégés contre la corrosion et procédé pour son élaboration, SEP Patent, FR 9013323 (26 Oct 1990), EP 486 347 (20 May 1992), CA 2 054 257 (27 April 1992), JO 4 263 076 (18 Sept 1992), US 5 217 755 (8 June 1993).

11. F. Christin, R. Naslain, and C. Bernard, A thermodynamic and experimental approach of silicon carbide CVD. Application to the CVD-infiltration of porous carbon-carbon composites, in: *7th International Conference on CVI*, Proceedings ed. by T.O. Sedwick, and H. Lydtin, (The Electrochemical Society, Princeton, 1979), pp. 499–514.
12. G. Boitier, H. Maupas, H. Cubero, and J.L. Chermant, Sur les essais de traction à longs termes à haute température, *Rev. Comp. Mat. Avancés*, **7**, 143–172 (1997).
13. G. Boitier, H. Cubero, J.L. Chermant, Some recommendations for long term high temperature tests, in: *High Temperature Ceramic Matrix Composites, HT-CMC 3*, Osaka, Japan, Sept. 6–9, 1998, (CSJ Series, Publications of the Ceramic Society of Japon), **Vol. 3**, 309–312 (1999).
14. L. Kachanov, Rupture time under creep conditions, *Izv. Akad. Nauk. SSR*, **8**, 26–31 (1958).
15. M. Rabotnov, *Creep Problem in Structural Members*, North-Holland, Amsterdam (1969).
16. O. Penas, Etude de composites SiC/SiBC à matrice multiséquencée en fatigue cyclique à hautes températures sous air – Investigation of cyclic fatigue at high temperatures of SiC/SiBC composites with self-sealing matrix, *Thèse de Doctorat of INSA of Lyon*, (2002).
17. C. Rospars, J.L. Chermant, and P. Ladevèze, On a first creep model for a 2D SiC_f-SiC composite, *Mat. Sci. Eng.*, **A 250**, 264–269 (1998).
18. G. Boitier, J.L. Chermant, and J. Vicens, Understanding the creep behavior of a 2.5D C_f-SiC composite. II: Experimental specifications and macroscopical mechanical creep response, *Mat. Sci. Eng.*, **A289**, 265–275 (2000).
19. S. Darzens, J.L. Chermant, and J.C. Sangleboeuf, A comparison of the creep behavior of SiC_f-SiBC composites, with Hi-Nicalon and NLM 202 SiC_f fibers, *J. Amer. Ceram. Soc.*, **86**, ... (2003).
20. G. Farizy, J.L. Chermant, J. Vicens, and J.C. Sangleboeuf, Fluage de composites SiC_f-SiBC sous air et sous argon: points communs et influence de l'oxydation, in: *13^{èmes} Journées Nationales sur les Composites*, JNC 13, Strasbourg, France, 12–14 March 2003. Proceedings ed. by Rémond Y., ... , (2003).
21. J. Serra, *Image Analysis and Mathematical Morphology*, (Academic Press, New-York, 1982).
22. M. Coster, and J.L. Chermant, *Précis d'analyse d'images*, (Les Editions du CNRS, Paris, 1985; 2nd edition, Les Presses du CNRS, Paris, 1989).
23. J.L. Chermant, Creep behavior of ceramic matrix composites, *Sil. Ind.*, **60**, 261–273 (1995).
24. J.L. Chermant, G. Boitier, S. Darzens, G. Farizy, J. Vicens, and J.C. Sangleboeuf, The creep mechanism of ceramic matrix composites at low temperature and stress, by a material science approach, in: *Structural Ceramics and Ceramic Composites for High-Temperature Application*", Sevilla, Spain, Oct. 7–12, 2001, *J. Eur. Ceram. Soc.*, **22**, 2443–2460 (2002).
25. R. Bodet, X. Bourrat, J. Lamon, and R. Naslain, Tensile creep behaviour of a silicon carbide-based fibre with a low oxygen content, *J. Mater. Sci.*, **30**, 661–677 (1995).
26. M. Narisawa, K. Sano, Y. Katase, and K. Okamura, Temperature-atmosphere dependence of creep behavior of advanced SiC-based fibers, in: *Proceedings of the 7th Int^l Conference on Creep and Fatigue at Elevated Temperatures, CREEP 7*, Japan Society of Mechanical Engineers, Tsukuba, Japan, June 3–8, pp 281–285 (2001).

FRACTURE TOUGHNESS OF BaTiO₃-MgO COMPOSITES SINTERED BY SPARK PLASMA SINTERING

Sirirat Rattanachan, Yukio Miyashita
and Yoshiharu Mutoh*

ABSTRACT

BaTiO₃-MgO composites with various compositions were fabricated by using a Spark Plasma Sintering (SPS) method. BaTiO₃-MgO composites with very high density were successfully sintered by SPS method. From the experimental results of as-sintered composites, Vickers hardness decreased and fracture toughness increased with increasing BaTiO₃ content. The higher fracture toughness of BaTiO₃-MgO composite with 10 vol% BaTiO₃ content was achieved compared to monolithic MgO. In order to investigate the effect of piezoelectric BaTiO₃ particles dispersed in MgO matrix, fracture toughness of the polarized composites was also evaluated. After polarization, fracture toughness of the BaTiO₃-MgO composites was improved and higher than that of monolithic MgO, while polarization induced distinct anisotropy in fracture toughness between parallel and perpendicular directions to the poling direction.

1. INTRODUCTION

In the field of engineering ceramics, ceramic composites have been increasingly studied for overcoming brittle nature of monolithic ceramics. Ceramic composites

* The author address: Department of Mechanical Engineering, Nagaoka University of Technology, 1603-1 Kamitomioka, Nagaoka-shi 940-2188 Japan, e-mail: mutoh@mech.nagaokaut.ac.jp

with perovskite-type-ferroelectrics have been developed for introducing ferroelectricity into structural ceramics. Ferroelectric ceramic has the sensing ability of crack propagation using electromotive force¹. Fracture toughness of ferroelectric ceramics is influenced by electric field.

Polarization of ferroelectric materials induces anisotropy of fracture toughness. It is known that this phenomena is caused by domain switching. Yang and Zhu² have proposed a model of stress-assisted 90° polarization switching to explain the toughening behavior. Many experimental and theoretical studies (Mehta and Virkar 1990³, Lynch et al 1995⁴, etc) showed that the intensified stress and electric fields at a crack tip in ferroelectrics can trigger domain switching. If ferroelectric particles are introduced into the structural ceramics, the particles in the composites will also exhibit domain switching and then improve the fracture resistance. This behavior also suggests that the composite will have some intelligent functions such as fracture sensing ability⁵.

The microstructure, grain size and density as well as flaws play an important role to the mechanical properties of ceramics. Spark plasma sintering (SPS) is one of the solid consolidation processes similar to hot pressing, where powders are pressed uniaxially in a graphite die and simultaneously the direct current pulse voltage is applied. Rapid sintering in SPS realizes short soaking time at high sintering temperature and then high density with fine grains⁶⁻⁸.

In the present study, piezoelectric/ferroelectric composites, BaTiO₃-MgO, were fabricated by using an SPS method at 1300°C in vacuum atmosphere with an applied pressure of 38 MPa. Microstructure, phases and fracture toughness of the composites were also studied.

2. EXPERIMENTAL PROCEDURE

2.1. Composite Preparation

Commercial Barium Titanate, BT-05 (Sakai chemical industrial Co. Ltd.) and high purity magnesium oxide (MgO) powders were used as the starting materials. BaTiO₃ and MgO powders with various contents (1,3,5 and 10 vol% BaTiO₃) were mixed by a ball milling machine in ethanol for 24 h. The milled slurry was dried by an rotary evaporator, and then was milled again and sieved through a 150 μm mesh screen. The mixed powders were put into a cylindrical graphite die with a diameter of 25 mm, which was on the vibration table for homogeneous packing of the powders, and then sintered with graphite punches on both sides by using a spark plasma sintering machine at 1300°C under an applied load of 38 MPa in vacuum. The temperature was increased up to a certain sintering temperature at a rate of 100°C/min. After holding about 5 min at the sintering temperature, the d.c. power of the SPS machine was shut off to let the sample rapidly cool down to 600°C in 30 min. During sintering, the linear change in shrinkage was recorded by monitoring the sample length along the pressing direction. Rectangular bar specimens were cut with a diamond saw from the sintered samples. The specimen surfaces were then ground and polished with a 600# SiC abrasive paper and finer diamond paste to yield a mirror-like surface suitable for the subsequent indentation test. The final dimensions of the specimen were 4 mm × 3 mm × 20 mm. The MgO monolithic ceramics was also fabricated by the same sintering procedure.

2.2. Characterization

The bulk density was determined by Archimedes' method in water. To determine the phases of sintered composites, the X-ray diffraction (XRD) analysis was conducted using Shimadzu XRD 6100 with nickel-filtered Cu K_α radiation. The average grain size and pore size of the samples were determined from scanning electron micrographs of the polished and etched samples.

2.3. Polarization

In order to remove carbon contamination on sintered samples, BaTiO₃-MgO composites were annealed at 1000°C before polarization. The 3 × 35 mm surfaces of specimens were polished by using an 800 mesh SiC paper and then applied silver paste as electrode and dried in air oven at 120°C for 10 min. The poling was conducted under an electric field of 1.25 kV/mm at 80°C for 10 min.

2.4. Fracture Toughness Test

The indentation fracture (IF) method for evaluating fracture toughness was adopted. The Vickers indentation test was conducted at room temperature using a load of 49 N for a constant duration of 15 s. The indentation surface was parallel to the poling direction for poled specimens. After unloading, the crack lengths were measured. c_{\perp} and $c_{//}$ were denoted to the crack lengths in the perpendicular and parallel to the poling direction, respectively. Fracture toughness was evaluated using the equation proposed by Tanaka⁹. At least 20 measurements of the crack length were taken for each data, and the average and standard deviation were calculated.

3. RESULTS AND DISCUSSION

3.1. Relative Density and Phases of Sintered Composites

The relative density of BaTiO₃-MgO composites sintered at 1200°C decreased with increasing BaTiO₃ content, as shown in Fig. 1. At 1300°C, the relative density of

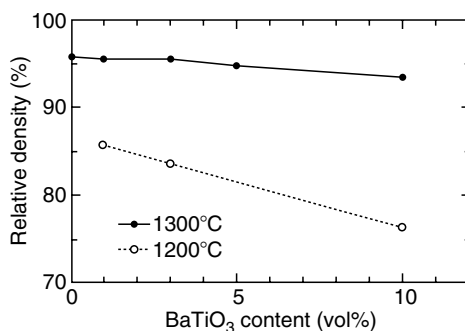


Figure 1. Relative density of the BaTiO₃-MgO composites sintered at 1200°C and 1300°C as a function of BaTiO₃ content.

composites was significantly improved and the reduction with increasing BaTiO₃ content was not significant.

X-ray diffraction patterns of as-sintered BaTiO₃-MgO composites sintered at 1300°C are shown in Fig. 2. All the peaks were assigned to MgO or tetragonal BaTiO₃, and no reaction phase between MgO and BaTiO₃ was detected. This contrasts with the case of BaTiO₃-Al₂O₃ composites, in which the third reaction phases are obviously observed¹⁰. Thus, MgO was found to be compatible with BaTiO₃ for avoiding the reaction phase. Nagai et. al.¹¹ reported that BaTiO_{2.977} phase was found for as-hot-pressed sample of MgO with 10 vol% BaTiO₃ composites. They suggested that the appearance of the reduced BaTiO₃ phase was due to the reaction atmosphere during hot pressing. In this study, due to lower sintering temperature and shorter time of the SPS sintering compared to the hot-pressing, no BaTiO_{2.977} phase was found. However, from the high angle X-ray diffraction analysis of BaTiO₃ dispersions for BaTiO₃-MgO composites in the range of 2θ between 90.5 and 93 degree that Nagai et. al.¹² also found, the peaks showed the tetragonal distortion of BaTiO₃ dispersoids. To confirm the tetragonal phase of BaTiO₃ dispersoids, Raman spectra of the nanocomposites were measured. They concluded that the BaTiO₃ dispersoids were tetragonal and ferroelectric phase. Another their work¹³ by using Raman Spectroscopy exhibited the existence of orthorhombic phase at room temperature for 0.5 and higher mol% MgO-doped BaTiO₃ (99.86 vol% BaTiO₃) ceramics. In the present study, however, less than 10 vol% BaTiO₃ content was dispersed in MgO matrix so that it was expected that there would be tetragonal BaTiO₃ and no orthorhombic phase in the present sintered composites.

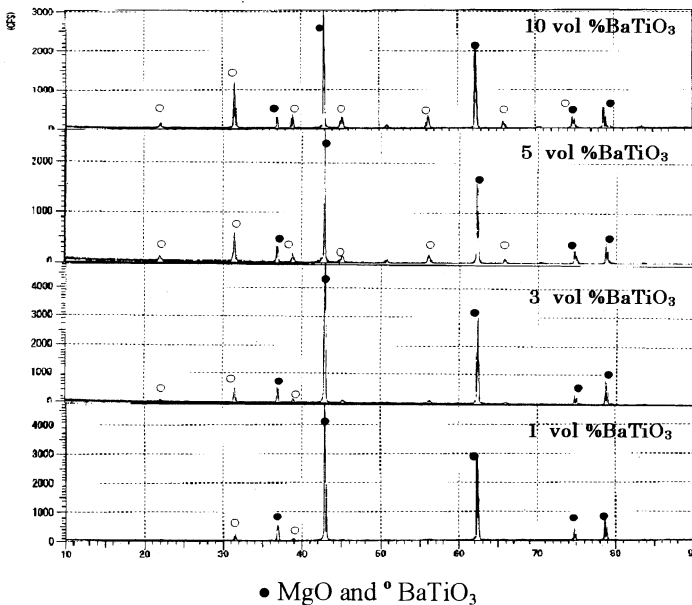


Figure 2. X-ray diffraction patterns of various BaTiO₃-MgO composites sintered by SPS at 1300°C.

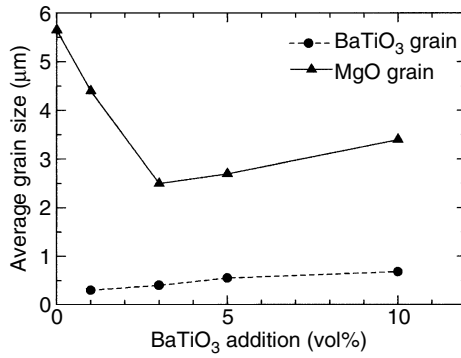


Figure 3. Average sizes of BaTiO₃ particles and MgO grains of the composites sintered at 1300°C.

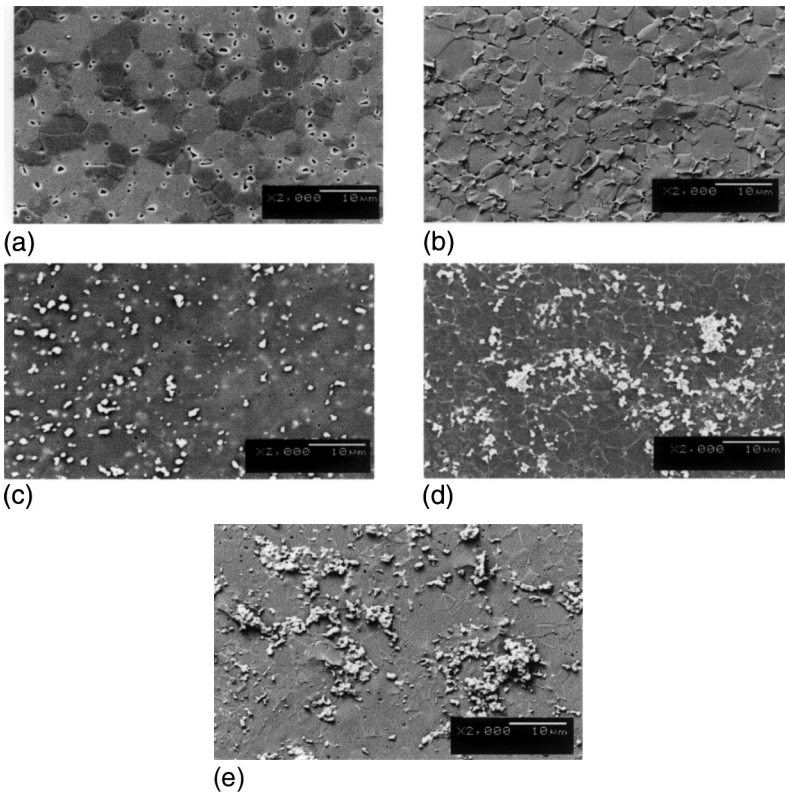


Figure 4. SEM photographs for the thermal etched surfaces of BaTiO₃-MgO composites sintered by SPS at 1300°C: (a) pure MgO, (b) 1, (c) 3, (d) 5 and (e) 10 vol% BaTiO₃-MgO.

3.2. Microstructure

Typical SEM images of the BaTiO₃-MgO composites are shown in Fig. 3. The white BaTiO₃ particles homogeneously dispersed within the MgO matrix grains and at grain boundaries. The average grain size of MgO matrix varied from 5.65 μm for the monolithic MgO to less than 5 μm for the 10 vol% BaTiO₃ added MgO, as shown

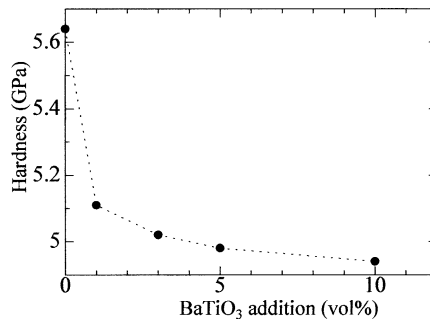


Figure 5. Hardness of the sintered composites as a function of BaTiO₃ addition.

in fig. 3. The presence of BaTiO₃ in MgO matrix seems to prevent grain boundary migration and grain growth. However, amount of intergranular pores was increased with increasing BaTiO₃ addition.

With further increase in BaTiO₃ content, some of BaTiO₃ particles, which were initially located at MgO grain boundaries, were agglomerated into larger particles (fig. 4).

3.3. Hardness and Fracture Toughness of Sintered Composites

From figure 5, hardness of the BaTiO₃-MgO composites decreased with increasing BaTiO₃ content.

Fracture toughnesses of the MgO-based composites with BaTiO₃ contents up to 3 vol% were low, compared with MgO monolithic. This may result from the decrease in MgO grain size, which will be discussed in the next section based on the observations of crack path. With increasing BaTiO₃ content higher than 5 vol%, higher fracture toughness of BaTiO₃-MgO composites was achieved.

After polarization, fracture toughness of BaTiO₃-MgO composites was improved, compared with that of the same samples before polarization. In addition, fracture toughness parallel to the poling direction was higher than that perpendicular to the poling direction for all of the composites (fig. 6). These results indicate that piezoelectric effect of BaTiO₃ plays a role in enhancement of toughness.

3.4. Toughening Mechanism

To investigate toughening mechanisms in the BaTiO₃ secondary phase dispersed MgO ceramic composite, indented crack paths were examined in detail. For monolithic MgO ceramics, most of crack paths were along grain boundaries of MgO grains and some of them cut across the grains, that is, intergranular manner of crack propagation was dominant with some extent of transgranular manner, as shown in Fig.7(a). The SEM micrographs of crack propagation paths for 1 and 3 vol% BaTiO₃-MgO composites are shown in Fig.7(b) and (c), respectively. It can be seen that cracks propagate dominantly in intergranular manner and also cut through BaTiO₃ particles. Rice¹³ reviewed the overall fracture mode of ceramics. He proposed that fracture mode was mainly intergranular for finer grain ceramics and then transferred to transgranular with increasing grain size for a broad range of stress

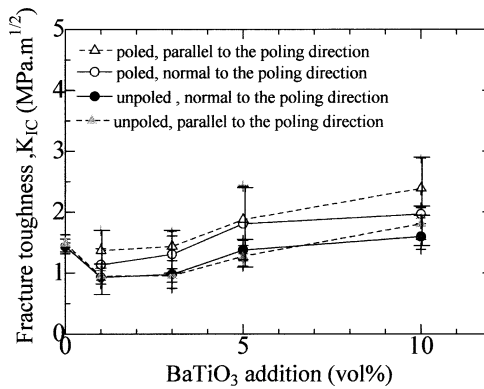


Figure 6. Fracture toughness of the sintered composites before and after polarization.

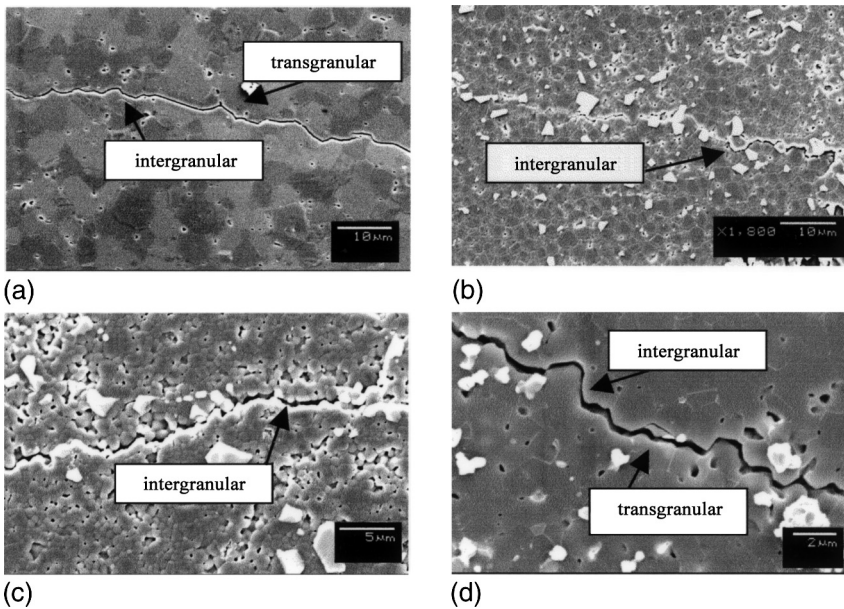


Figure 7. SEM micrographs of crack paths of (a) MgO monolithic and (b), (c) and (d) 1, 3 and 10 vol% BaTiO₃-MgO composites sintered at 1300°C, respectively.

conditions. He noted that transgranular fracture of the matrix was dominant for many particulate and whisker composites and also frequently of the dispersed phase¹³. Further, transgranular fracture preferentially occurred in the larger grains, as in monolithic ceramics, and the degree of transgranular fracture in the composite matrix was typically higher than in the monolithic one with the same grain size¹³. This was clearly shown by the work of Baek and Kim¹⁴, where the monolithic alumina with grain size of around 6 μm predominantly showed intergranular fracture, but with 20% SiC whiskers the alumina matrix with the same grain size showed dominant transgranular fracture. Therefore, the low fracture toughness of 1 and 3 vol% BaTiO₃-MgO composites resulted mainly from the finer grain size and the lower hardness of the these composites. With further increase in BaTiO₃ content,

transgranular crack path at or near BaTiO₃ particle were increasingly observed, as shown in Fig. 7(d). This change of crack path might contribute to higher fracture toughness. This toughening mechanism was also found in LiTaO₃-Al₂O₃¹⁵ and LaNbO₄-Al₂O₃ composites¹⁶.

The existence of domain structures inside grains of LiTaO₃ and LaNbO₄ ceramics confirmed the possibility of domain switching toughening mechanism¹⁵⁻¹⁶. Domain structure like ripples was distinctly detected near the crack tip. Domain switching was suggested as a new toughening mechanism in the ceramic composites. In this work, fracture toughness of all the composites increased after polarization. This indicated that domain switching improves fracture toughness of BaTiO₃-MgO composites. The larger the BaTiO₃ content was, the greater the fracture toughness was, as expected. This toughening mechanism was decompensated by the decrease in hardness and intergranular fracture mode for the composites with 1 and 3 vol% BaTiO₃.

Experimental and theoretical analyses^{2,15-21} indicated that domain switching plays an important role in improvement of toughness of ferroelectrics. The intensified stress in the vicinity of a crack-like flaw in the composite leads to BaTiO₃ domain. The switched domains induce incompatible strain under the constraint of unswitched matrix material, and consequently alter the stress distribution near the flaw. Thus, the apparent toughness of BaTiO₃-MgO composites is improved due to domain switching.

4. CONCLUSION

MgO based composites with addition of BaTiO₃ up to 10 vol% were fabricated by a spark plasma sintering method (SPS) with an applied load of 38 MPa. Nearly full densification and high fracture toughness of BaTiO₃-MgO composites were achieved by SPS method at 1300°C. A high fracture toughness of around $1.81 \pm 0.26 \text{ MPa}\cdot\text{m}^{1/2}$ could be obtained by the addition of 10 vol% BaTiO₃ before polarization. Moreover, after polarization, fracture toughness of BaTiO₃-MgO composites remarkably increased, since a domain switching toughening mechanism was induced in the present composites. Domain switching of piezoelectric BaTiO₃ particles may improve fracture toughness of the BaTiO₃-MgO composites.

ACKNOWLEDGEMENT

The authors wish to thank the Macoh Co. for conducting spark plasma sintering, and Prof. Uematsu's laboratory, chemical engineering, Nagaoka University of Technology for preparing the mixed powders.

REFERENCES

1. T., Noma, S., Wada, M., Satake, T., Otsuka and T., Suzuki, Indentation Fracture of Poled Barium Titanate Ceramics, in *Proceedings of the Annual Meeting of the Ceramic Society of Japan (Yokohama, Japan, April 1996)*. The Ceramic Society of Japan, Tokyo, Japan, pp.551(1996)

2. W., Yang and T., Zhu, Switch-toughening of ferroelectrics subjected to electric fields. *J. Mech. Phys. Solids*, 46 [2], 291–311 (1998)
3. K., Mehta and A. V., Virkar, Fracture mechanism in ferroelectric – ferroelastic lead zirconate titanate (Zr:Ti = 0.54:0.46) ceramics, *J. Am. Ceram. Soc.*, 73, 567–574 (1990)
4. C. S., Lynch, W., Yang, L., Collier, Z., Suo and R.M., McMeeking, Electric field induced cracking in ferroelectric ceramics, *Ferroelectrics*, 166, 11–30 (1995)
5. T., Takagi, A Concept and Perspective of Intelligent Materials, *Bull. Ceram. Soc. Jpn.*, 28 [6], 539–544 (1993)
6. M.P., Hammer and R.J., Brook, Fast firing-microstructural benefits, *J. Br. Ceram. Soc.*, 80, 147–149 (1981)
7. M., Tokita, Trends in advanced SPS spark plasma sintering system and technology. *J. Soc. Powder Technol., Jpn.*, 30 [11], 790–804 (1993)
8. L., Gao, Z., Shen, H., Miyamoto and M., Nygren, Superfast densification of oxide/oxide ceramic composites. *J. Am. Ceram. Soc.*, 82[4], 1061–1063 (1999)
9. K., Tanaka, Elastic/Plastic Indentation Hardness and Indentation Fracture Toughness: the Inclusion Core Model, *J. Mater. Sci.*, 22, pp.1501 (1987)
10. S., Rattanachan, Y., Miyashita and Y., Mutoh, Microstructure and fracture toughness of a spark plasma sintered Al₂O₃-based composite with BaTiO₃ particulates, *Journal of the European Ceramic Society*, 23[8], 1269–1276 (2003)
11. T., Nagai, H.J., Hwang, M., Yasuoka, M. Sando and K., Niihara, Preparation of a Barium Titanate-Dispersed-Magnesia Nanocomposite, *J. Am. Ceram. Soc.*, 81[2], 425–428 (1998)
12. T., Nagai, H.J., Hwang, M., Sando and K., Niihara, Preparation of Ceramic Nanocomposite with Perovskite Dispersoid, *Mat. Res. Soc. Symp. Proc.*, 457, 375–380 (1997)
13. T., Nagai, K., Iijima, H.J., Hwang, M., Sando, T., Sekino and K., Niihara, Effect of MgO Doping on the Phase Transformations of BaTiO₃, *J. Am. Ceram. Soc.*, 83[1], 107–112 (2000)
14. R.W., Rice, Ceramic fracture mode—Intergranular vs. Transgranular Fracture. Ceramic Transactions, 64: Fractography of glasses and Ceramics III (JR Varner, VD Frechette, and GD Quinn, eds). Am. Cer. Soc., Westerville, OH, 1996, p.1–53.
15. Y.K., Baek and C.H., Kim, The Effect of Whisker Length on the Mechanical Properties of Alumina-SiC Whisker Composites, *J. Mat. Sci.*, 24, 1589–1593(1989)
16. Z., Zhang, L., Zhou, Y., Hu and L., Jiang, Preparation and characterization of Al₂O₃-LaNbO₄ composites, *Scripta Materialia*, 47, 637–641 (2002)
17. Y.G., Liu, Y., Zhou, D.C., Jia, Q.C., Meng and Y.H., Chen, Domain switching toughening in a LiTaO₃ dispersed Al₂O₃ ceramic composite, *Scripta Materialia*, 47, 63–68 (2002)
18. G.G., Pisarenko, V.M., Chushko and S.P., Kovalev, Anisotropy of Fracture Toughness of Piezoelectric Ceramics, *J. Am. Ceram. Soc.*, 68[5], 295–265 (1985)
19. S.B., Park and C.T., Sun, Effect of electric field on fracture of piezoelectric ceramics, *Inter. J. Fract.*, 70, 203–216 (1995)
20. A., Kishimoto and S., Seo, Strength control of a ceramic composite by electric field, *Smart Materials*, 4234, 321–327 (2001)
21. W., Lu, D.N., Fang and K.C., Hwang, Micromechanics of ferroelectric domain switching behavior Part I: Coupled electromechanical field of domain inclusions, *Theor. App. Fract. Mechan.*, 37, 29–38 (2001)

FRACTURE TOUGHNESS OF BaTiO₃ AND BaTiO₃-Al₂O₃ COMPOSITE UNDER ELECTRIC FIELD

Sirirat Rattanachan, Yukio Miyashita
and Yoshiharu Mutoh*

ABSTRACT

In order to investigate the effect of electric polarization on fracture toughness of monolithic BaTiO₃ and 5 mol% BaTiO₃-Al₂O₃ composite (5B95A), indentation fracture tests were conducted on unpoled and poled samples under various applied electric fields. From the results, it is found that applied electric fields can increase or decrease fracture toughness in both monolithic BaTiO₃ and 5B95A composite depending on direction of electric field. For unpoled and poled samples under the positive (in the same direction to the poling direction), fracture toughness parallel to the poling direction increased, while that perpendicular to the poling direction decreased. Under the negative (in the opposite direction to the poling direction), fracture toughnesses both parallel and perpendicular to the poling direction for poled monolithic BaTiO₃ and 5B95A composite were decreased with increasing applied electric field. This behavior of 5B95A composite was consistent with that of monolithic BaTiO₃. It was concluded that polarization switching of piezoelectric BaTiO₃ particles phase under electric fields has a significant influence on fracture toughness of the present composite.

* The author address: Department of Mechanical Engineering, Nagaoka University of Technology, 1603-1 Kamitomioka, Nagaoka-shi 940-2188 Japan, e-mail: mutoh@mech.nagaokaut.ac.jp

1. INTRODUCTION

Many approaches to improve the fracture toughness of ceramics have been developed. As a novel approach for toughening of ceramics, composites with piezoelectric secondary phase were proposed, where energy dissipation due to piezoelectric effect and domain switching were suggested as the main toughening mechanisms¹. Various composites such as BaTiO₃/Al₂O₃², BaTiO₃/3Y-TZP³, Nd₂Ti₂O₇/Al₂O₃⁴, Sr₂Nb₂O₇/3Y-TZP⁵ and BaTiO₃/ZrO₂⁶ have been studied. High fracture toughness has been recently achieved for a BaTiO₃ toughened Al₂O₃ system⁷, where the fracture toughness of 5.5 MPa.m^{1/2} attained for an Al₂O₃ matrix composite with 5 mol% BaTiO₃ sintered by a spark plasma sintering, while that of a monolithic Al₂O₃ was about 4 MPa.m^{1/2}.

In the previous work, Al₂O₃ based composites with 3 and 5 mol% BaTiO₃ secondary phases were fabricated by the pressureless sintering method⁸. The Indentation Fracture (IF) method was employed to evaluate fracture toughness before and after polarization. Toughening mechanisms of BaTiO₃/Al₂O₃ composites were discussed. It was verified that an polarization induced distinct anisotropy in fracture toughness of BaTiO₃/Al₂O₃ composites between parallel and perpendicular directions to the poling direction. Crack deflection around BaTiO₃ particles was often observed in the poling direction. Anisotropy in residual stress was also observed after polarization. It was suggested that the polarization induced the domain reorientation along the poling direction and consequently resulted in the anisotropy in residual stress⁸.

Several researches are available on anisotropic behavior of fracture toughness and toughening mechanisms of monolithic piezoelectric materials. Pak and Tobin⁹ performed the IF tests on the isotropic and anisotropic planes of poled PZT samples. They observed that the presence of the electric field in the direction of poling assisted crack growth and retarded it in reversed field. Lynch¹⁰ studied crack growth in a ferroelectric and a relaxor composition of PLZT ceramic using Vickers indentation under electric field. He found that the effect of residual stress was much larger than other mechanisms that interact with crack propagation. Fu and Zhang¹¹ conducted IF tests and compact-tension fracture toughness tests to study the effect of applied electric field on fracture toughness of poled commercial PZT ceramics. Their results were inconsistent with the experimental results by Pak and Sun¹² and also Pak and Tobin⁹. Kishimoto and Seo¹³ reported a change in strength of barium titanate/zirconia composite by polarization treatment. The results exhibited that bending strength of BaTiO₃-8YSZ composite increased by longitudinal poling and decreased by transverse poling compared to the untreated sample. Both strengthened and weakened specimens tended to return almost to the original strength by heating over T_c of barium titanate.

The research works on toughening mechanisms and fracture toughness of ceramic composites with piezoelectric phases have been limited, while those for monolithic piezoelectric/ferroelectric materials have been available, as mentioned above. Therefore, details of toughening behavior and mechanisms in composite materials with piezoelectric phases have been still not clear.

In the present study, fracture toughness of 5 mol% BaTiO₃/Al₂O₃ composite for both before and after polarization was investigated under various applied electric field to discuss the toughening mechanisms. The generated cracks in the parallel or

perpendicular direction to poling were observed in detail, and compared to those for monolithic BaTiO₃.

EXPERIMENTAL PROCEDURE

2.1. Sample Preparation

Commercial barium titanate (BT-05, Sakai chemical industrial Co. Ltd.) with an average particle size of 0.5 μm and high purity alumina (Sumitomo Sekitan Kougyo, KK) powders with an average particle size of 0.2 μm were used as the starting materials. Al₂O₃ powders with 5 mol% BaTiO₃ powders (as denoted 5B95A composite in this study) were mixed by a ball milling machine with alumina balls in ethanol for 24 h. The wet slurry was then dried by a rotary evaporator. Dried powders were milled again and sieved through a 150 μm mesh screen. The mixed powders were put into a cylindrical graphite die with a diameter of 25 mm, which was on the vibration table for homogeneous packing of the powders, and then sintered with graphite punches on both sides by using a spark plasma sintering machine (Dr. sintering, SPS 1030, Sumitomo Coal Mining Co., Ltd.). The sintering was conducted at a sintering temperature of 1300°C under an applied load of 38 MPa in vacuum. The temperature was increased up to the sintering temperature at a rate of 100°C/min. After holding of 3–5 min at the sintering temperature, the d.c. power of SPS machine was shut off to let the sample rapidly cool down to 600°C in 30 min. During sintering, the linear change in shrinkage was recorded by monitoring the displacement of the sample along the pressing direction. The temperature was measured by means of an optical pyrometer focused at the middle of the graphite die surface. Rectangular bar specimens were cut from the sintered sample with a diamond saw. The specimen surfaces were then ground and polished with a 600# SiC abrasive paper and a finer diamond paste to yield a mirror-like surface suitable for the subsequent indentation test. The final dimensions of the specimens were 4 mm × 3 mm × 20 mm. BaTiO₃ monolithic ceramics were also fabricated by the same sintering procedure at 1100°C.

The relative density of the monolithic BaTiO₃ and 5B95A composite sintered by SPS were 99.99 and 94%, respectively. From the results of XRD analysis, some intermediate phases such as BaAl_{13.2}O_{20.8}, BaAl₆TiO₁₂, as well as BaTiO₃ and Al₂O₃ phases were found. Figures 1(a) and (b) show microstructures of monolithic BaTiO₃ and 5B95A composite sintered at 1300°C by SPS, respectively. Al₂O₃, intermediate and BaTiO₃ grains in the SEM micrographs (Back scattering electrons image) are black, gray and white regions, respectively. The agglomerated BaTiO₃ grains and the aggregated intermediate phases were formed at grain boundaries.

2.2. Polarization and Fracture Toughness Test

In order to remove carbon contamination on sintered samples, 5B95A composite was annealed at 1100°C before polarization. 3 × 35 mm surfaces of the specimen were polished by using an 800 mesh SiC paper and then applied silver paste as an electrode and dried in air oven at 120°C for 10 min. Polarization treatment was conducted in silicon oil at 80°C for 10 min with electric field of 1.25 kV/mm. The indentation

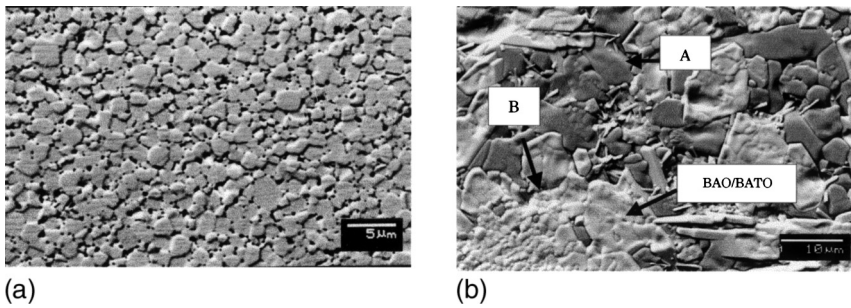


Figure 1. Scanning electron micrographs of thermal etched surface of (a) monolithic BaTiO₃ and (b) 5B95A composites (A:Al₂O₃, B:BaTiO₃, BAO/BATO: intermediate phases).

surface was parallel to the poling direction for poled specimens. The indenter was loaded on the surface perpendicular to the electrode surfaces. In this experiment, the cracks introduced by a Vickers indenter were perpendicular or parallel to the applied electric field (see Fig. 2).

The combination of electrical and mechanical loading was achieved by applying an electrical potential across the electroded specimen during indenting. Figure 3 shows sample setup for Vickers indentation test under applied electric field. To avoid additional mechanical constraints on the specimen, the electric fields were applied to the electrode surfaces by the welding contacts. Static electric fields were applied in either the same or opposite direction to the poling direction using a high voltage power supply (model HDV-40 K2 SU, Pulse Electronic Engineering, Co., Ltd.). The electric field was applied before the indenter contacted the specimen and was turned off after the indenter was lifted off the specimen.

The Vickers indentation test was conducted at room temperature using loads of 9.8 and 49 N for BaTiO₃ and 5B95A composite, respectively, for a constant duration of 15s. After unloading, the crack lengths were measured immediately. Fracture tough-

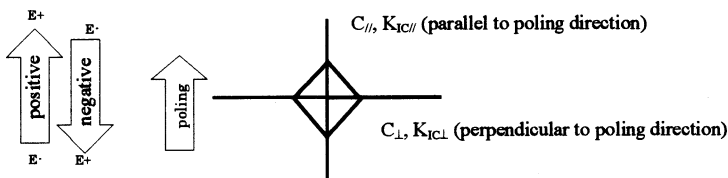


Figure 2. Schematics of directions of applied electric field and cracks

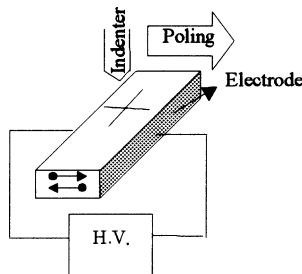


Figure 3. Schematic view of sample setup in Vickers indentation test under applied electric field.

ness was evaluated using the equation proposed by Tanaka¹⁴. At least 20 measurements were taken for each data, and the average and standard deviation were calculated.

3. RESULTS AND DISCUSSION

3.1. Fracture Toughness of Unpoled and Poled Samples

In absence of applied electric field, fracture toughness of unpoled BaTiO₃ and 5B95A composite were isotropic, where crack lengths in two orthogonal directions were almost identical. After poling, anisotropy in fracture toughness was found for both monolithic BaTiO₃ and 5B95A composite, where the crack length in perpendicular direction was longer compared to that in parallel direction (see Fig. 4). Similar behavior have been observed in some other works^{15–17}.

3.2. Fracture Toughness under Applied Electric Field

Polarization switching is known as a unique feature of piezoelectrics/ferroelectrics. A switching of 180° causes little strain and is activated by the electric field, whereas a switching of 90° results from the electric and / or stress fields and induced a sizable strain of fixed amount, with contracting along the previous polarization direction and elongation along the current one. Therefore, anisotropy of fracture toughness for ferroelectric may result from the polarization switching induced by the crack tip stress. It has been reported that fracture toughnesses along the poling direction and the normal to it are different^{6,10,15–19}.

In the present composite, since BaTiO₃ structure extends in the poling direction whereas Al₂O₃ matrix maintains its crystal structure and orientation, even after poling the residual stress would be generated in Al₂O₃ matrix. In the pervious work⁸, residual stresses were observed in the same composite as the present study.

From Fig. 5 (a) and (b), it was found that since the difference between fracture toughnesses of poled and unpoled BaTiO₃ were not significant, the relationships

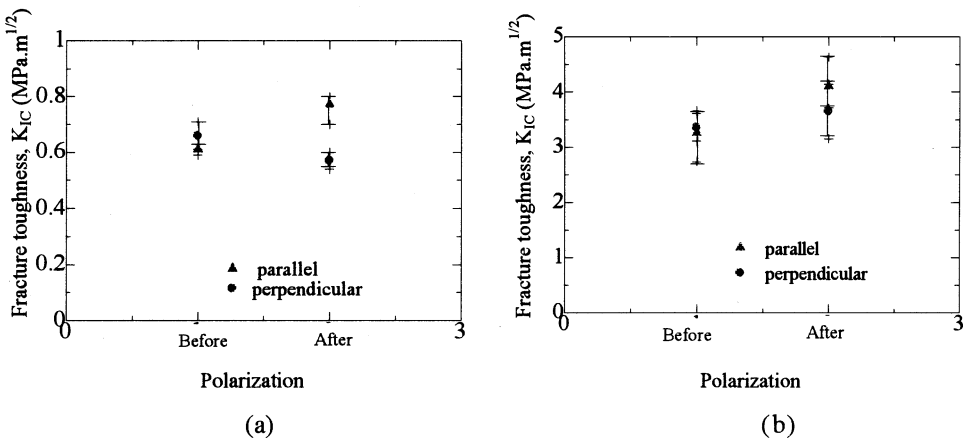


Figure 4. Fracture toughness of unpoled and poled samples in the absence of applied electric field (a) monolithic BaTiO₃ and (b) 5B95A composite.

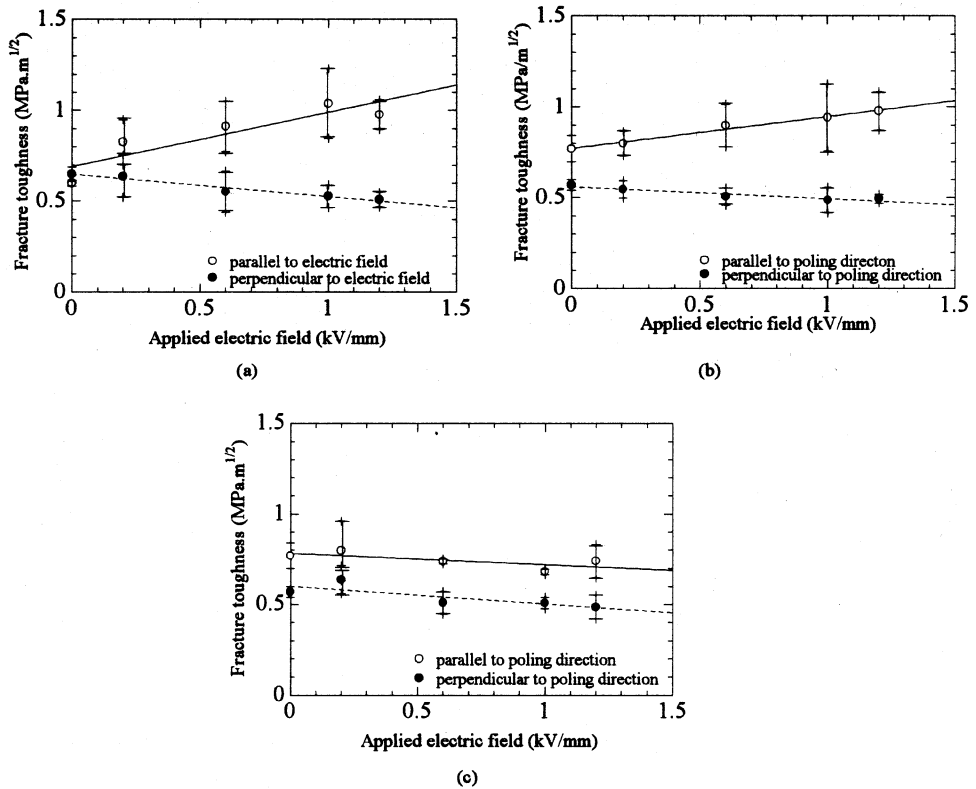


Figure 5. Fracture toughness of monolithic BaTiO₃ as a function of the applied electric field (a) Unpoled BaTiO₃ under applied electric field. (b) Poled BaTiO₃ under positive applied electric field (c) Poled BaTiO₃ under negative applied electric field.

between fracture toughness and applied electric field for unpoled and poled samples were also almost identical. Fracture toughness in the poling direction increased with increasing strength of applied electric field, while that perpendicular to the poling direction decreased with increasing strength of applied electric field. These behavior can be explained due to polarization switching: the compressive stress and tensile stress are induced by the switching in the parallel and perpendicular direction to the poling direction, respectively. The same behavior was observed in the 5B95A composite, as can be seen in Figs. 6(a) and (b).

Under negative applied electric field, both the fracture toughnesses parallel and perpendicular to the poling direction were decreased with increasing strength of applied electric field for both poled BaTiO₃ and 5B95A composite, as shown in Figs. 5(c) and 6(c). These behavior can be explained as follows: The negative applied electric field induced polarization switching of 180°, which reduced the compressive residual stress in the poling direction, which was introduced by the previous poling treatment, and increases the tensile residual stress perpendicular to the poling direction.

Improvement of fracture toughness due to in-situ application of electric field was significant compared to that due to the poling treatment. This may be explained as follows:

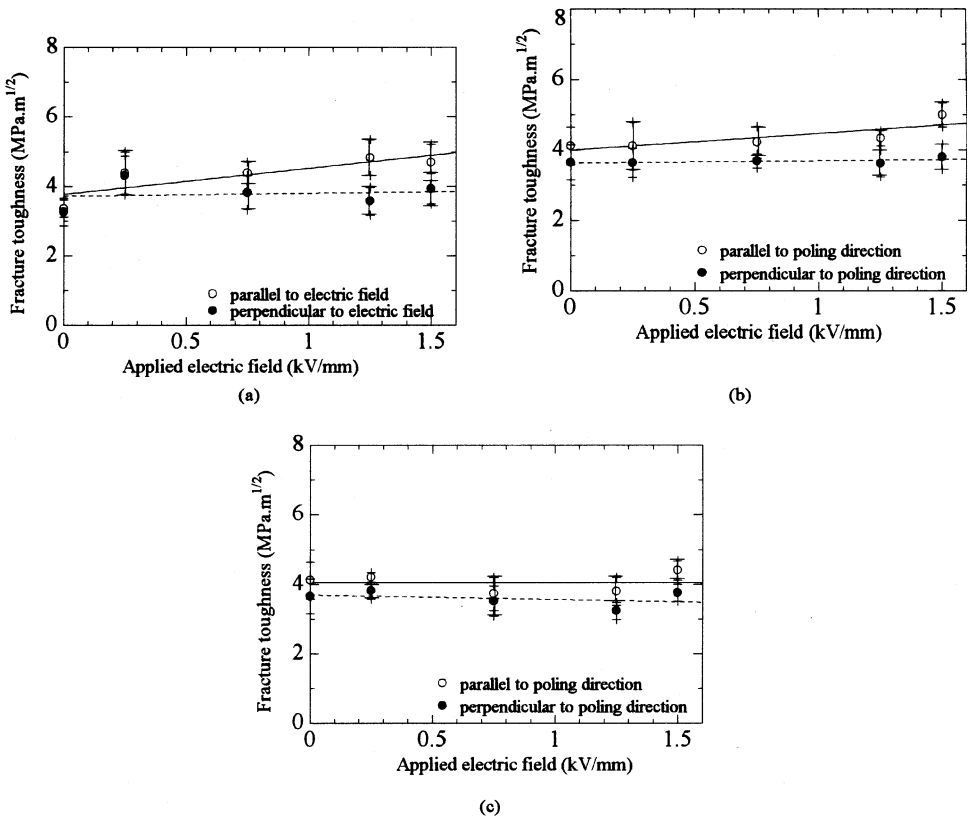


Figure 6. Fracture toughness of 5B95A composite as a function of the applied electric field (a) Unpoled 5B95A composite under applied electric field. (b) Poled 5B95A composite under positive applied electric field (c) Poled 5B95A composite under negative applied electric field

The polarization switching situation corresponding to the certain applied electric field might be maintained during crack propagation under applied electric field, while it is possible to degrade during crack propagation for the poled sample without applied electric field. Whether the electric field impedes or enhances crack propagation is still a debatable issue. From Zeng and Rajapakse's work²¹, the effects of anisotropic properties and electromechanical coupling were investigated. Based on their numerical results, it agreed with the experimental observation of this study. Another factor to be considered will be the interaction between non-uniform stress and electric field distributions near the crack tip^{20,22}. Domain switching behavior may be different between with and without applied electric field.

CONCLUSION

Fracture toughness of unpoled and poled monolithic BaTiO₃ as well as Al₂O₃-based composite with 5 mol% BaTiO₃ was evaluated under various applied electric fields. The positive applied electric field increased the fracture toughness in the parallel direction to the poling direction and decreased it in the perpendicular to the poling

direction. The negative applied electric field degraded the fracture toughness in the parallel direction and enhanced it with perpendicular direction. Improvement of fracture toughness under positive applied electric field was significant compared to that for poled sample without applied electric field. These behavior can be explained based on the polarization switching and the resultant induced residual stress.

ACKNOWLEDGEMENT

The authors wish to thank Macoho Co. for conducting spark plasma sintering, and Prof. Uematsu's laboratory in the department of chemistry, Nagaoka University of Technology, for preparing the mixed powders.

REFERENCES

1. Chen, X.M. and Yang, B.A., A new approach for toughening of ceramics, *Mater. Lett.*, 1997, 33, 237–240.
2. Chen, X.M. and Yang, B., A new approach for toughening of ceramics. *Mat. Lett.*, 1997, 33, 237–240.
3. Yang, B., Chen, X. M. and Liu, X. Q., Effect of BaTiO₃ addition on structures and mechanical properties of 3Y-TZP ceramics. *J. Eur. Ceram. Soc.*, 2000, 20, 1153–1158.
4. Yang, B. and Chen, X.M., Alumina ceramics toughened by a piezoelectric secondary phase. *J. Eur. Ceram. Soc.*, 2000, 20, 1687–1690.
5. Chen, X. M., Liu, X. Q., Liu, F. and Zhang, X. B., 3Y-TZP ceramics toughened by Sr₂Nb₂O₇ secondary phase. *J. Eur. Ceram. Soc.*, 2001, 21, 477–481.
6. Seo, S. and Kishimoto, A., Effect of polarization treatment on bending strength of barium titanate/zirconia composite. *J. Eur. Ceram. Soc.*, 2000, 20, 2427–2431.
7. Rattanachan, S., Miyashita, Y., and Mutoh, Y., Microstructure and fracture toughness of a spark plasma sintered Al₂O₃-based composite with BaTiO₃ particulates, *Journal of the European Ceramic Society*, 2003, 23[8], 1269–1276
8. Rattanachan, S., Miyashita, Y., and Mutoh, Y., Effect of Polarization on Fracture Toughness of BaTiO₃/Al₂O₃ Composites, *Journal of the European Ceramic Society*, in submitted.
9. Pak, Y.E., and Tobin, A., On electric field effects in fracture of piezoelectric materials, *ASME Mechanics of Electromagnetic Materials and Structures*, Lee, J.S., Mangin, G.A., and Shindo, Y., eds., AMD-vol1161, 1993, MD vol. 42, 51–62.
10. Lynch, C.S., Fracture of Ferroelectric and Relaxor Electro-Ceramics: Influence of Electric field, *Acta Mater.*, 1998, 46, 599–608.
11. Fu, R., and Zhang, T.-Y., Effect of Electric field on the Fracture Toughness of Poled Lead Zirconate Titanate Ceramics, *J. Am. Ceram. Soc.*, 2000, 83, 1215–1218.
12. Park, S.B., and Sun, C.T., Effect of Electric field on Fracture of Piezoelectric Ceramics, *Int. J. Fract.*, 1995, 70, 203–216.
13. Kishimoto, A., and Seo, S., Strength control of a ceramic composite by electric field, *Smart Materials*, Proceeding of SPIE, 2001, 4234, 321–327.
14. Tanaka, K., Elastic/Plastic Indentation Hardness and Indentation Fracture Toughness: the Inclusion Core Model, *J. Mater. Sci.*, 1987, 22, 1501.
15. Okazaki, K., Mechanical Behavior of Ferroelectric Ceramics, *Bull. Am. Ceram. Soc.*, 1984, 63(9), 1150–1157.
16. Pisarenko, G.G., Chushko, V.M., and Kovalev, S.P., Anisotropy of Fracture Toughness of Piezoelectric Ceramics, *J. Am. Ceram. Soc.*, 1985, 68(5), 259–265.
17. Yamamoto, T., Igarashi, H., and Okazaki, K., Internal Stress Anisotropics Induced by Electric Field in Lanthanum Modified PbTiO₃ Ceramics, *Ferroelectrics*, 1983, 50, 273–278.
18. Wang, H., and Singh, R.N., Crack propagation in piezoelectric ceramics: Effects of applied electric fields, *J. Appl. Phys.*, 1997, 81[1], 7471–7479

19. Singh, R.N., and Wang, H., Crack Propagation in Piezoelectric Materials Under Combined Mechanical and Electrical Loadings: An Experimental Study, *Adaptive Material Systems ASME*, 1995, AMD-Vol. 206/MD-Vol. 58, 85–95.
20. Schneider, G.A., and Heyer, V., Influence of the Electric Field on Vickers Indentation Crack Growth in BaTiO₃, *J. Euro. Ceram. Soc.*, 1999, 19, 1299–1306.
21. Zeng, X., and Rajapakse, R.K.N.D., Domain switching induced fracture toughness variation in ferroelectrics, *Smart Mat. Struc.*, 2001, 10, 203–211.
22. Zhu, T. and Yang, W., Toughness variation of ferroelectrics by polarization switch under non-uniform electric field, *Acta mater.*, 1997, 45[11], 4695–4702.

ROOM TEMPERATURE POST-FRACTURE TENSILE (PFT) STUDY OF TWO FIBER-REINFORCED CERAMIC MATRIX COMPOSITES WITH A “STRONG” FIBER/MATRIX INTERFACE

Rafael A. Longoria, Nicolas Du Souich,
Kenneth W. White

1. INTRODUCTION

Elevated temperature applications require materials that can maintain good mechanical properties such as strength and hardness. Ceramics have good mechanical properties at high temperature and, thus, appear to be good candidates for elevated temperature applications. However, due to their brittle nature, monolithic ceramics are unsuitable for many applications where reliability is a critical issue. In the last few years, a new class of ceramic materials has been developed and studied. It is understood that two brittle materials can show non-brittle behavior if they are properly mixed. Fiber-reinforced ceramic matrix composites (CMCs) exhibit pseudo-plastic behavior at room temperature, as well as in an elevated temperature environment. Since the fiber and the matrix are made of ceramic material, creep behavior and hazardous emissions are reduced considerably.

The first CMCs to be developed consisted of three major components: a ceramic matrix, fibers embedded in the matrix, and a tailored interface between the fiber and the matrix.¹ Although these materials show damage tolerance and non-brittle behavior, the non-oxide materials that compose the CMCs are prone to oxidation, especially when matrix cracks are present.² Lately, the development of an all-oxide CMC has captured the researchers' attention. In these oxide/oxide composites, fracture toughness is achieved through crack deflection inside the matrix. A controlled level of matrix porosity will provide suitable conditions for crack deflection while inherently impeding oxidation during high temperature service.³

2. MATERIALS

Two all-oxide composites were studied. A sol-gel derived alumina matrix composite produced by COI Ceramics that is reinforced with Nextel 720 (3M Company) fibers. The matrix porosity level is $\sim 40\%$ and the fiber volume fraction is $\sim 47\%$.⁴ The processing route is shown in Figure 1. A sintering process between 1800–2100 °F controls porosity levels. The second ceramic composite was a mullite/alumina matrix composite developed by the University of California at Santa Barbara with the same reinforcing fibers. The porosity level for this material is $\sim 40\%$ with a fiber volume fraction of $\sim 37\%$.⁵ The processing route is shown in Figure 2. A repeated precursor-impregnation process is responsible for the porosity.

3. EXPERIMENTAL PROCEDURES

Initial damage (crack) was introduced by using a Double Cantilever Beam (DCB) configuration. Aluminum fixtures were used to avoid delamination of the composites during the DCB test. Grooves on both sides of the DCB specimen assured symmetric

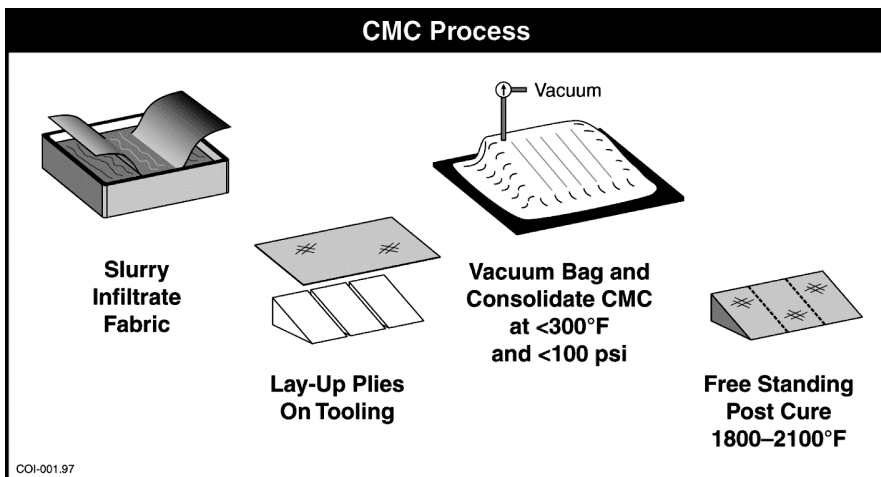


Figure 1. Processing route for the Alumina matrix composite.⁴

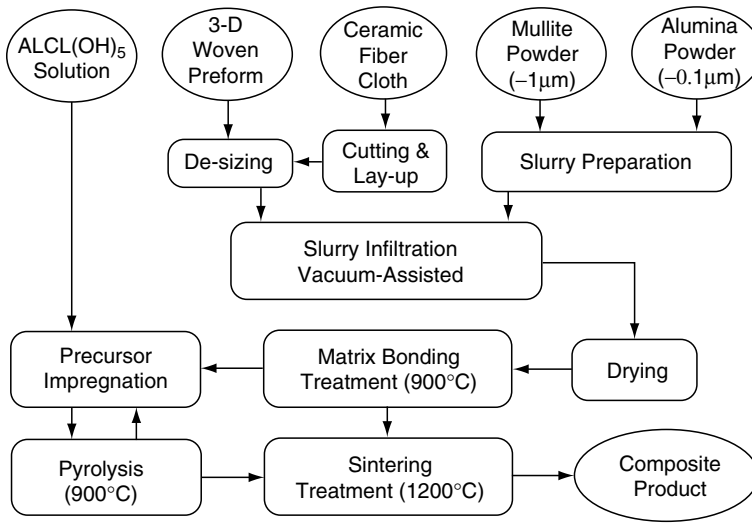


Figure 2. Processing route for the mullite/alumina matrix composite.⁵

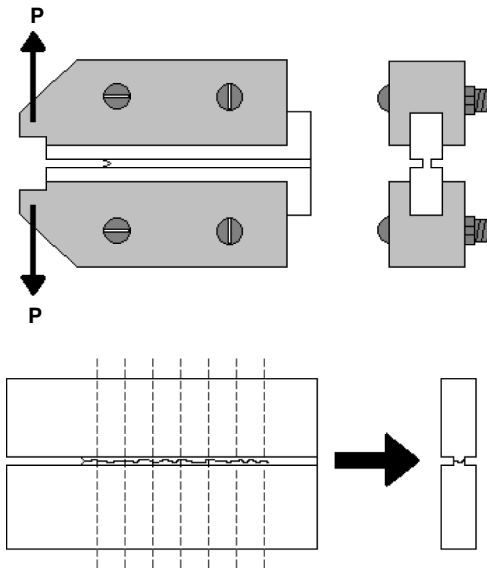


Figure 3. a) DCB testing configuration. b) PFT specimens obtained from DCB specimen.

crack propagation during the test. The DCB test was deliberately interrupted before the crack reached the opposite side of the specimen. The DCB configuration provides a wide range of crack openings. PFT specimens were obtained from the cracked DCB specimen. The initial COD characterizes each PFT specimen.^{6,7} Figure 3 shows a schematic for both the DCB configuration and the PFT specimen distribution.

PFT specimens are numbered from 1 to 8. The PFT with the smallest COD becomes PFT-1. COD measurements were performed using optical microscopy. A Static PFT test (monotonic loading) was performed on different PFT specimens. The crosshead speed was 200×10^{-6} inch/min. Cyclic PFT test required a sinusoidal

loading profile with relatively small amplitude. A suitable frequency and amplitude for the oscillation was obtained by using a piezo actuator. The increase in COD was tracked with a video extensometer for both tests.

4. RESULTS

A family of PFT curves can be obtained by plotting the Static PFT data of PFT specimens with different initial COD. The influence of characteristic (initial) COD becomes noticeable by using this type of graph. An inversely proportional bridging load with respect to initial COD is clearly observed. Furthermore, all the curves show a good agreement in the strain-softening region, proving the universality of the PFT test. Figures 4 and 5 show a family of PFT curves for the alumina composite and the mullite/alumina matrix composite, respectively.

The overlapping of curves for final stages of the separation event validates the existence of a universal strain-softening behavior (exponent), independent of the initial condition of the specimen. This observation can be corroborated by a loading-reloading static PFT test on the same specimen.

Cyclic PFT gave a better insight about the failure mechanism. Due to the nature of the PFT test, where only tensile loading is possible, the energy required to close a cycle loop arises solely from the stored elastic energy. Therefore, the existence of enough stick points with sufficient strain energy will return the crack to its initial state. This behavior is observed in Figure 6, where a PFT-2 specimen of the alumina matrix composite was subjected to one loading cycle. The maximum load was controlled to 0.9 kg.

Although, the hysteresis loop is fully close for cycle one of a PFT-2 specimen, gross slip was observed for later stages of the cyclic test. Figure 7 shows the comparison of cycle 1 between a PFT-2 specimen and a PFT-3. As the initial compliance depends on the total number of contact points, a nearly constant number of points remain between PFT-2 and PFT-3.

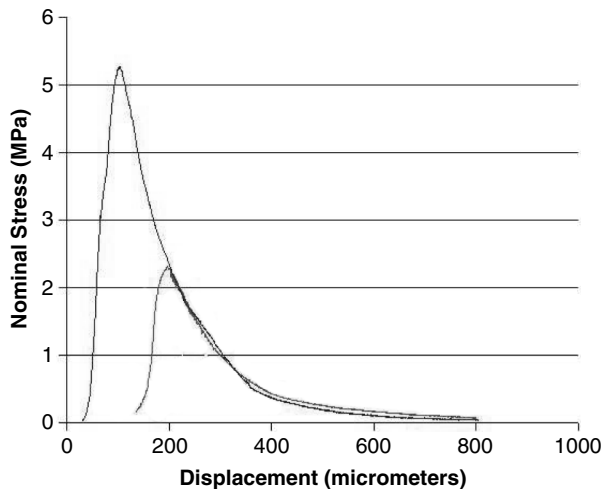


Figure 4. Family of PFT curves for the Alumina matrix composite.

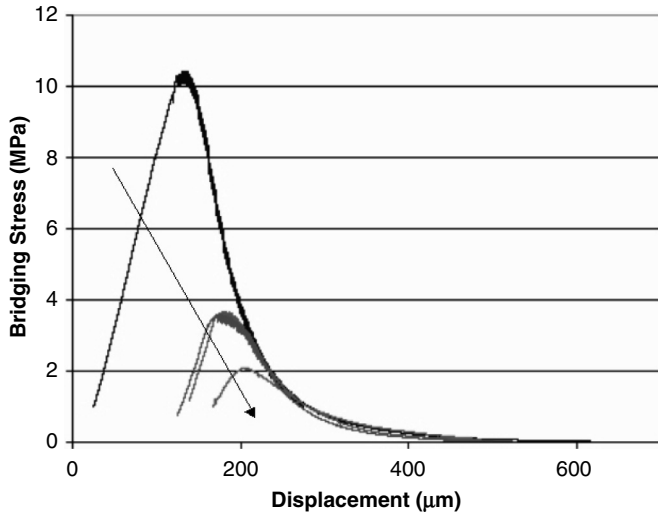


Figure 5. Family of PFT curves for the Mullite/alumina matrix composite.

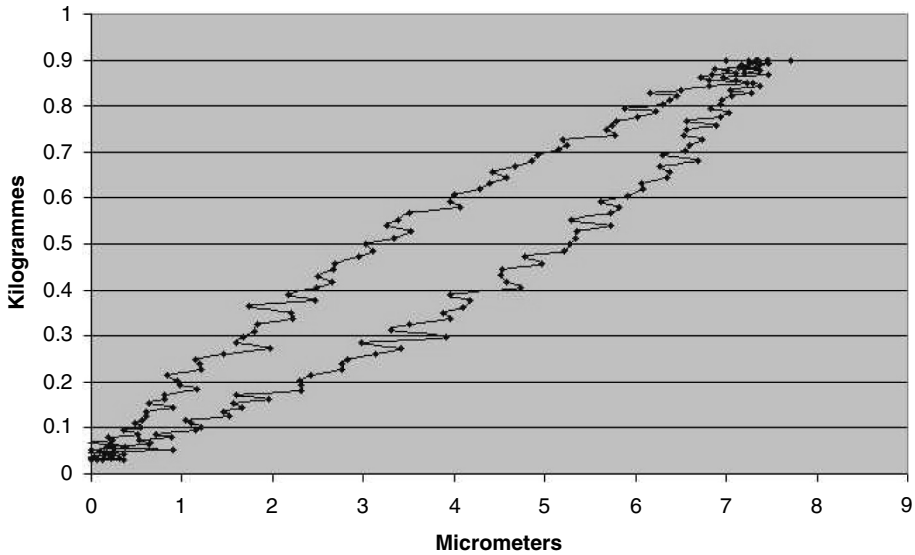


Figure 6. First cycle for a PFT-2 of the alumina matrix composite.

Although the initial compliance remains similar between the two specimens, the area fraction increases significantly. The slip-to-stick contact point ratio increases considerably for the level of damage in PFT-3. The appearance of a sharp transition point indicates that the number of stick points converted to slip contacts is large enough to induce gross slip at that load. The insufficient number of stick contact points at the maximum load yields to a non-recoverable displacement.

Figure 8 shows three subsequent cycles for a PFT-7 specimen of the mullite/alumina matrix composite. The transition point between partial slip and gross slip

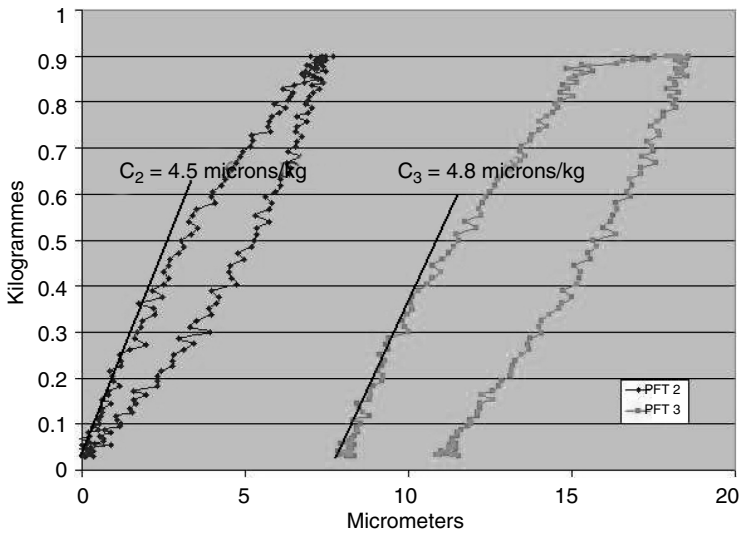


Figure 7. Comparison of cycle 1 between PFT-2 and PFT-3 specimen of the alumina matrix composite.

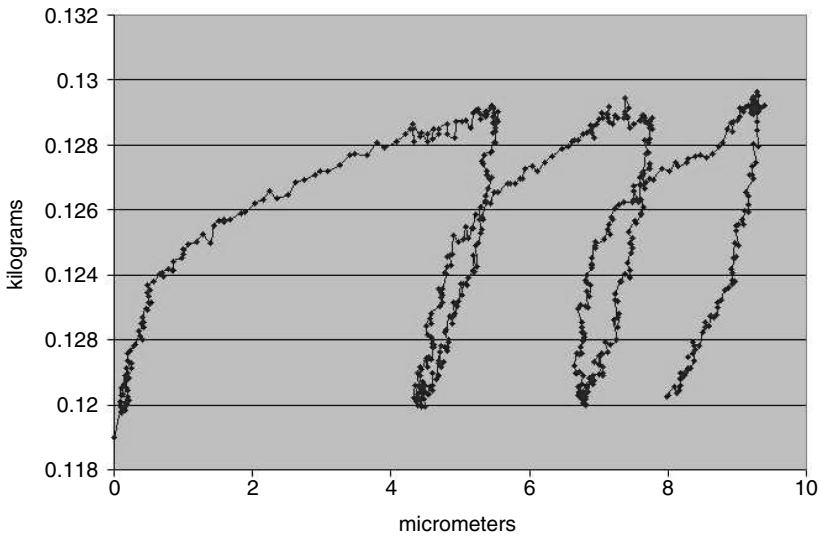


Figure 8. Three subsequent cycles for a PFT-7 specimen of the mullite/alumina composite.

occurs at a higher load at each cycle. This is an indication of a rearrangement of contact points leading to a different bridging configuration. Since new portions of fiber are sliding after gross slip, each cycle brings a slightly increased friction coefficient due to fiber/matrix interaction. There is an increasing load during gross slip for this material. This suggests an increasing fiber/matrix interaction during sliding.

Long-term fatigue behavior was also studied. The hysteresis loop after each cycle was observed to behave stochastically. As the crack opening displacement

grows, the hysteresis loop opens and closes, suggesting that after gross slip takes place, an appropriate configuration of stick points can be formed. Although interfacial wear might take place, the new portions of fiber sliding after gross slip apparently provide enough interfacial friction and contact points to fully close the hysteresis loop. This new configuration will remain active until wear diminishes the contact surfaces enough to induce gross slip again. Therefore, interfacial properties play a significant role in fiber pullout under both monotonic and cyclic loading.

SEM analysis led to the identification of different microstructural features between the two composites. The alumina matrix composite exhibited single fiber pullout after complete fiber pullout, while fiber bundle pullout dominated in the mullite/alumina composite. Comparing Figures 4 and 5 in this work, one can see a larger displacement to total failure for the alumina matrix composite than for the mullite/alumina, suggesting that fiber bundle pullout represents a more severe failure mode. Figure 9 and 10 show the fiber pullout mode for the alumina matrix and for the mullite/alumina matrix composite, respectively.

5. CONCLUSIONS

Room temperature fiber pullout under monotonic and cyclic loading was successfully investigated by using the PFT test configuration. Static (monotonic) PFT test led to the identification of a common strain-softening exponent between PFT speci-

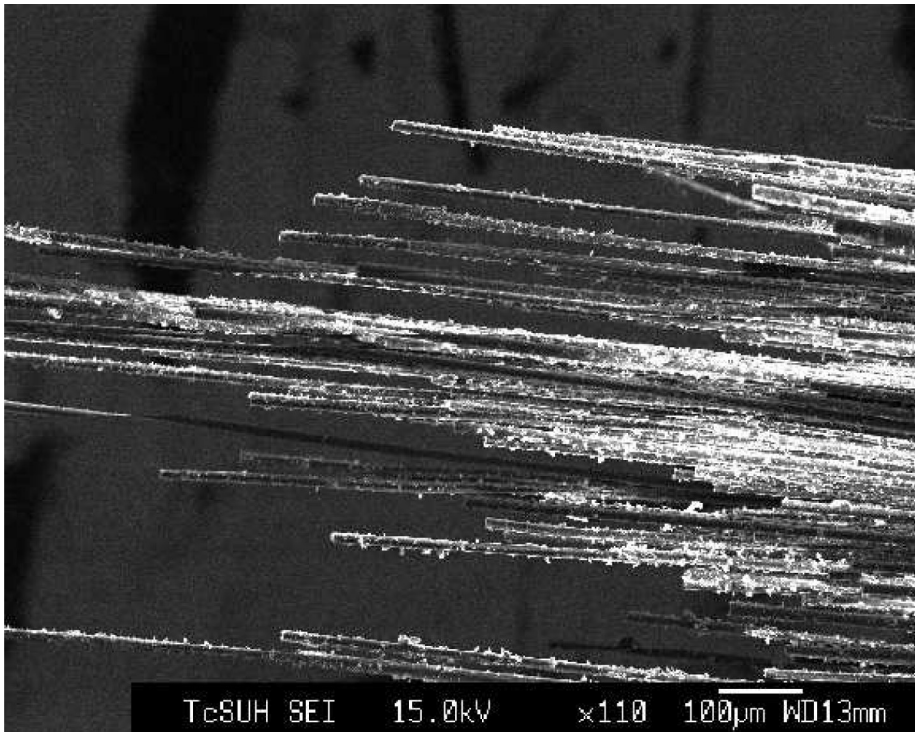


Figure 9. Single fiber pullout observed for the alumina matrix composite.

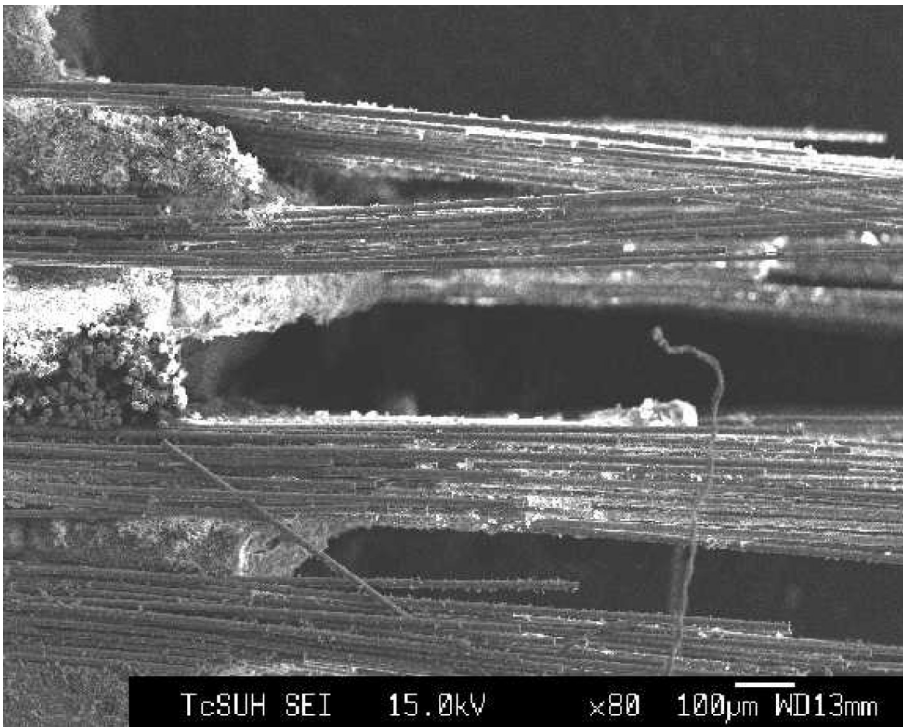


Figure 10. Fiber bundle pullout observed for the mullite/alumina matrix composite.

mens. This suggests the existence of a displacement-controlled failure mechanism for this new type of fiber-reinforced ceramic matrix composites with a strong fiber/matrix interface. An inversely proportional maximum bridging stress with respect to COD was found for both composites. Gross slip under cyclic loading was observed for both composites, suggesting a reduced number of contact points due to interfacial wear. However, the stochastic behavior of the hysteresis loops during long-term fatigue experiments suggested a reconfiguration of the fiber/matrix interacting surface after gross slip. In addition, SEM analysis led to the identification of different pullout mechanisms between composites. The data suggests bundle pullout is a more severe pullout mode.

REFERENCES

1. T. Radsick, B. Saruhan, and H. Schneider, "Damage tolerant oxide/oxide fiber laminates composites," *Journal of the European Ceramic Society* **20**, 545–550 (2000).
2. K. K. Chawla, Z. R. Xu, J. S. Ha, M. Schmucker, and H. Schneider, "Effect of BN coating on the strength of a mullite-type fiber," *Applied Composite Materials* **4**, 263 (1997).
3. W. Tu, F. F. Lange, and A. G. Evans, "Concept of a Damage-tolerant Ceramic Composite with "Strong" Interfaces," *Journal of the American Ceramic Society* **79**, 417–424 (1996).
4. <http://www.coiceramics.com/cmdevelopment.htm> COI Ceramics, San Diego, California, USA.
5. C. G. Levi, J. Y. Yang, B. J. Dalgleish, F. W. Zok, and A. G. Evans, "Processing and Performance of an All-oxide Ceramic Matrix Composite," *Journal of the American Ceramic Society* **81**, 2077–2086 (1998).

6. R. D. Geraghty, J. C. Hay, and K. W. White, "Fatigue Degradation of the Crack Wake Zone in Monolithic Alumina," *Acta Materialia* **47**, 1345–1353 (1999).
7. J. C. Hay, and K. W. White, "Crack Face Bridging Mechanisms in Monolithic MgAl₂O₄ Spinel Microstructures," *Acta Metallurgica and Materialia* **40**, 3017–3025 (1992).

A FE MODEL OF CARBON/ CARBON COMPOSITE FRACTURE

J. Ohgi, J. H. Jackson, A. S. Kobayashi, K. W. White*

ABSTRACT

Fracture behavior of carbon fiber/carbon matrix (C/C) composite was analyzed with a 2-D finite element (FE) model of a single edged notch bend (SENB) specimen subjected to a series of re-notching tests. The irregular transverse cracking in the wide frontal fracture process zone (FPZ) of the machined notch tip was represented by an idealized distribution of crack bridging stress (CBS) along an idealized straight crack. The CBS was obtained through an inverse analysis by matching the FE computed and moiré measured crack opening displacement (COD) during the re-notching process. This FE model was used to estimate the equivalent strain energy release rate, G_{eq} , and the equivalent stress intensity factor, K_{eq} , of the zig-zagged crack.

INTRODUCTION

Self similar crack growth in a fiber reinforced composite is seldom observed due to the inevitable crack deflection along debonded fibers, interply delamination as well as fabrication defects in the crack path. While the overall crack growth direction is perpendicular to the local maximum stress direction, the tortuous 3-D crack path poses an insurmountable challenge for a linear elastic fracture mechanics (LEFM) interpretation of crack growth in fiber reinforced composite. Numerous attempts

* J. Ohgi, Yamaguchi University, Department of Mechanical Engineering, Ube, 755-8611, Japan. J. H. Jackson, Idaho National Engineering and Environmental Laboratory, Idaho Falls, ID 83415, A. S. Kobayashi, University of Washington, Seattle, WA 98195. K. W. White, University of Houston, Houston, TX 77204.

have been made to quantify composite fracture through the micromechanics in this frontal process zone (FPZ) involving fiber pullout, fiber breaking, matrix cracking and interply delamination. The interaction of these micro- and macro-mechanic failure mechanisms, unfortunately, overwhelms a LEFM analysis. LEFM, however, has been used successfully in assessing the onset of crack growth of a straight machined crack with a relatively small FPZ by lumping the micro-mechanic failure modes into a single energy dissipation mechanism. This continuum approach, however, is no longer valid when the FPZ is more than ten percent of the original crack length. As an alternative, nonlinear fracture mechanics, such as J -integral, has been used to estimate the fracture resistance of fiber reinforced ceramic composite after replacing the zig-zagged crack with a “linear crack (Wang and Nair, 1998)”. Another approach is to measure directly the crack bridging stress imparted by the zig-zagged crack by the post fracture tension (PFT) method (Lucchesi, Hay and White, 1993) or indirectly by the re-notching method (White and Grimes, 1991).

This paper presents a LEFM model of the complex failure mechanism by replacing it with a postulated self-similar crack extension. The LEFM model of the frontal FPZ is assumed to be a straight cohesive zone with a crack bridging force which replaces the multifaceted failure mechanisms. The bridging force is determined by a hybrid moiré-finite element (FE) analysis. With this simplified 2-D modeling, LEFM can then be used to characterize stable crack growth in a fiber reinforced composite.

HYBRID MOIRÉ-FE ANALYSIS

Single-Edge Notch Bend (SENB) Specimen

The fracture specimen used in this proof-of-concept study is a 2-D, carbon-fiber reinforced carbon matrix (C/C) composite, single-edged notch bend (SENB) specimen with a straight notch in the T-S plane of a C/C plate. This relatively porous composite is a 12.7 mm thick plate of stacked plies of discontinuous carbon fibers impregnated with a carbon matrix as shown in Figure 1. Its bulk density is 1.54 gr/cc

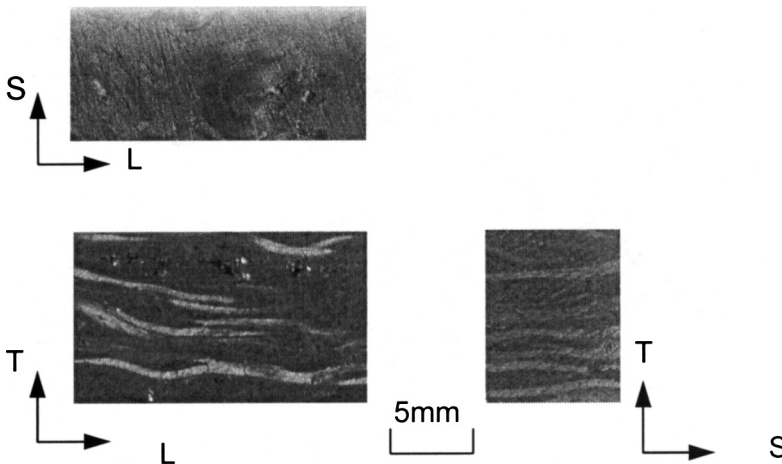


Figure 1. C/C composite.

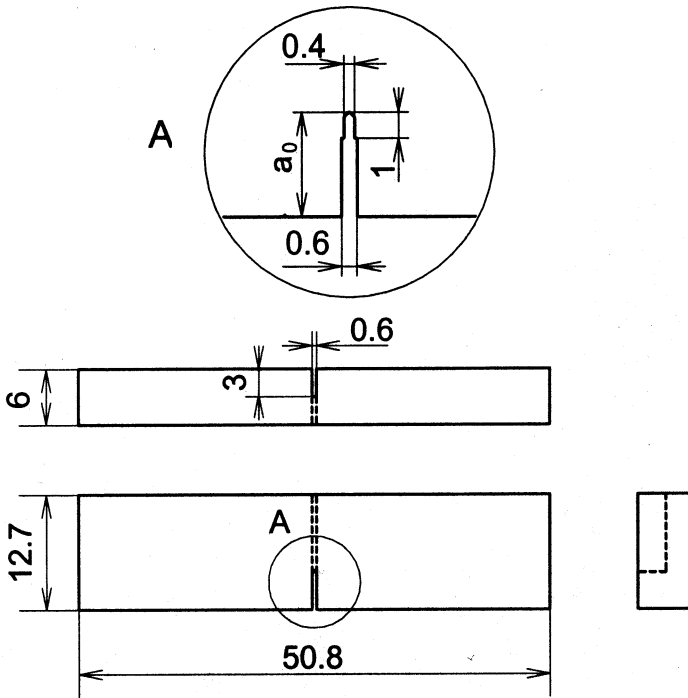


Figure 2. C/C composite SENB specimen.

with a porosity of 16%, compressive strength of 200 MPa and a fiber volume fraction of 40%.

Figure 2 shows the SENB specimen with a 50% side groove. The support span for the three-point bend fixture was 48 mm. Uniaxial tension tests in the L-T and T-L directions yielded a relatively uniform elastic modulus of $E_T = E_L = 48$ GPa. Two of the three remaining elastic modulus of $E_S = 0.67$ GPa and the shear modulus of $G_{LS} = 1.92$ GPa were obtained through an inverse analysis, discussed later, by matching the response of a finite element (FE) model of the SENB specimen with the experimentally obtained load versus load-line displacement and the load versus crack mouth opening displacement (CMOD) relations. A Poisson's ratio of $\nu = 0.05$ was obtained from Ohtake et al (1999).

Three-Point Bend Test

The C/C composite SENB specimen was subjected to a three point bend test. As illustrated in Figure 3, the crack propagated in an irregular zig-zaged pattern along the side groove and fractured in a likewise pattern. The corresponding load versus load-line displacement curve is shown in Figure 4 where Pt. A is the onset of crack growth. Extensive crack growth occurred with the maximum load at Pt. B and complete penetration of the crack through the height of the SENB specimen occurred at Pt. C. The extensive crack bridging kept the two specimen halves together through an applied load line displacement of 2 mm.

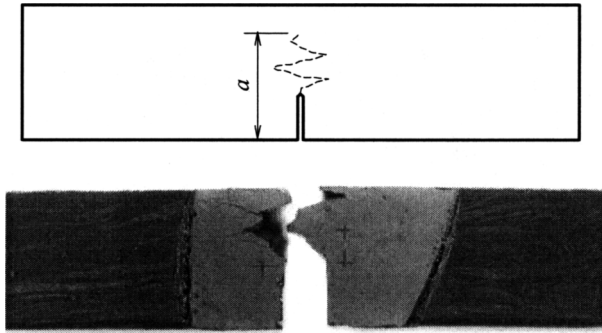


Figure 3. Crack path and fractured C/C SENB specimen.

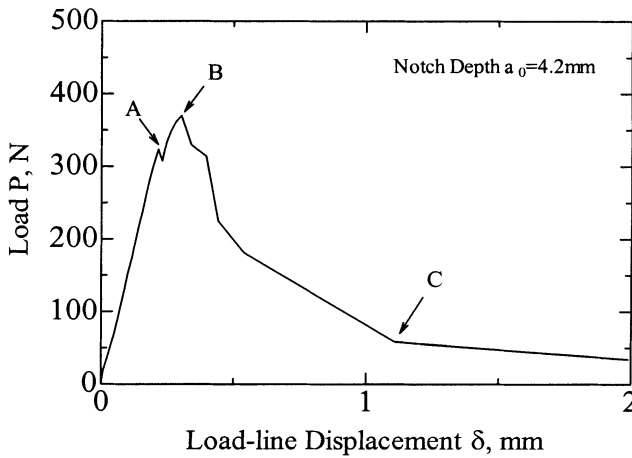


Figure 4. Load versus load-line displacement with crack growth. C/C SENB specimen.

The area under the load versus load-line displacement in Figure 4, for a given applied load line displacement, is the work of fracture. The difference in the work of fracture with an incremental increase in crack length is the work rate of fracture.

In order to assess the effect of crack bridging generated by the zig-zagged crack path, the stress intensity factor of a postulated self-similarly extended crack was calculated for various machined notch lengths, a_0 , as shown in Figure 5, using the standard LEFM formula (Srawley, 1976) of:

$$K_I = \frac{PS}{BW^{\frac{3}{2}}} \frac{3\left(\frac{a}{W}\right)^{\frac{1}{2}} \left[1.99 - \frac{a}{W} \left(1 - \frac{a}{W} \right) \left(2.15 - 3.93 \frac{a}{W} + 2.7 \frac{a^2}{W^2} \right) \right]}{2\left(1 + 2 \frac{a}{W} \right) \left(1 - \frac{a}{W} \right)^{\frac{3}{2}}} \tag{1}$$

Region A in Figures s shows that for the same total crack length, a shorter initial notch required a higher stress intensity factor for crack growth due to the longer FPZ which provided a larger crack bridging (closing) force. In Region B with a longer total crack length, this difference disappeared as the crack grew with a constant FPZ size. The increase in resistance to crack growth is shown by Figure 6, which plots the initiation stress intensity at the onset of crack growth from the machined notch tip

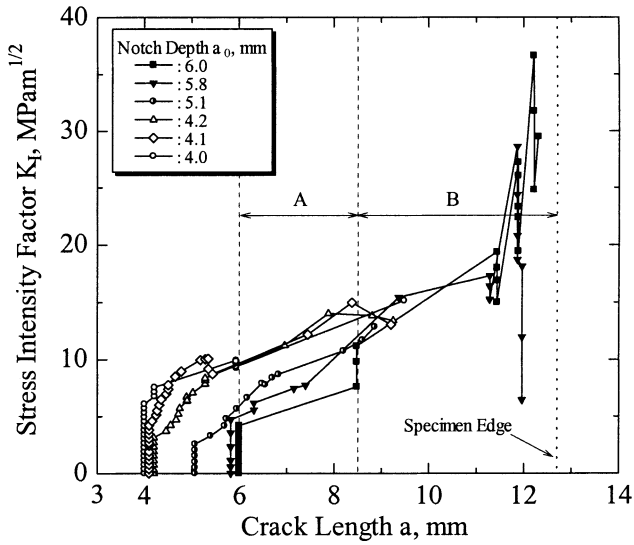


Figure 5. Stress intensity factor of a straight crack in a SENB specimen.

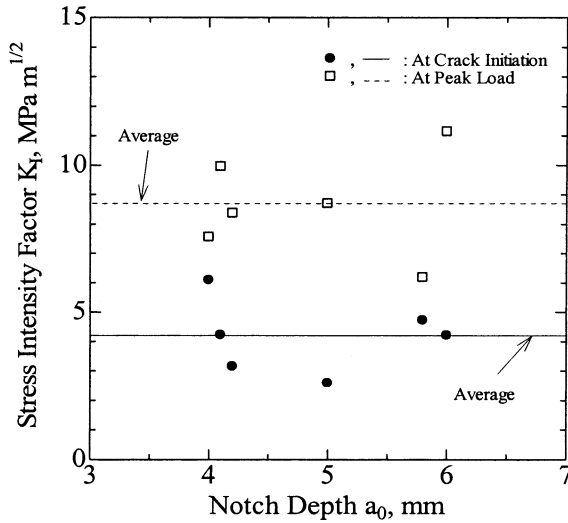


Figure 6. Stress intensity factor at crack growth initiation and maximum load.

and the stress intensity factor at maximum load in terms of an increasing notch depth.

Re-notching Test

The crack bridging stress (CBS) acting along the FPZ of a postulated self-similarly crack extension was determined by re-notching the SENB specimen. The incrementally re-notched SENB specimen was then re-loaded back to its maximum load and the load versus load-line displacement relation shown by Figure 7 was obtained. The residual load-line displacement at complete unloading in this figure is attributed to

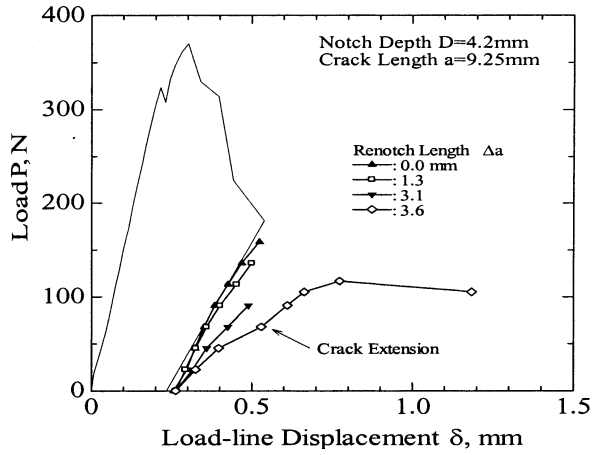


Figure 7. Load versus load-line displacement relations of re-notched SENB specimen.

the resistance of the pulled out fibers to crack closure. The area under the loading curve provided the work of fracture. The specimen compliance increased with increasing re-notch length with a total crack length of 9.25 mm.

Moiré Interferometry

The crack opening profile and the lateral displacement field during the re-notching test were determined by moiré interferometry. The moiré interferometer was configured to yield an effective grating frequency of 1,200 lines/mm for an actual grating frequency of 600 lines/mm. Moiré fringe pattern was recorded at the maximum load of each re-notching process. Figure 8 shows the actual zig-zagged FPZ and the moiré

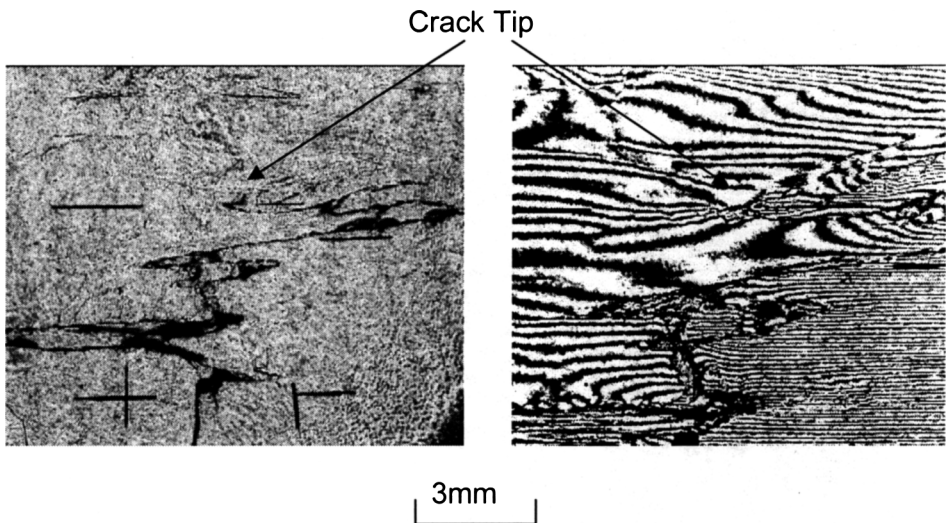


Figure 8. Actual FPZ and moiré pattern.

pattern surrounding this FPZ. The moiré data was used to determine the COD along the original machined notch and the re-notched crack as an input to the FE analysis.

Finite Element Modeling

A FE model of the SENB specimen with a straight FPZ was used to compute, through an inverse analysis, the CBS acting on the FPZ. Figure 9 shows the FE mesh which models one half of the SENB specimen. The FE analysis consisted of matching the computed and moiré COD's, through an inverse iterative process, for an assumed CBS distribution at various re-notched lengths. The final FE analysis yielded the effective stress intensity factor for the C/C SENB specimen with an idealized crack bridging stress.

RESULTS

The crack was grown to a straight crack length of 9.25 mm or 5.05 mm from the machined notch tip. This growth, Δa , as shown in Figure 9, is defined as the projected length of the zig-zagged crack path. Figure 10 shows the COD variation with re-notching. The area under the load versus load line displacement curve, which is the work of fracture, was then obtained.

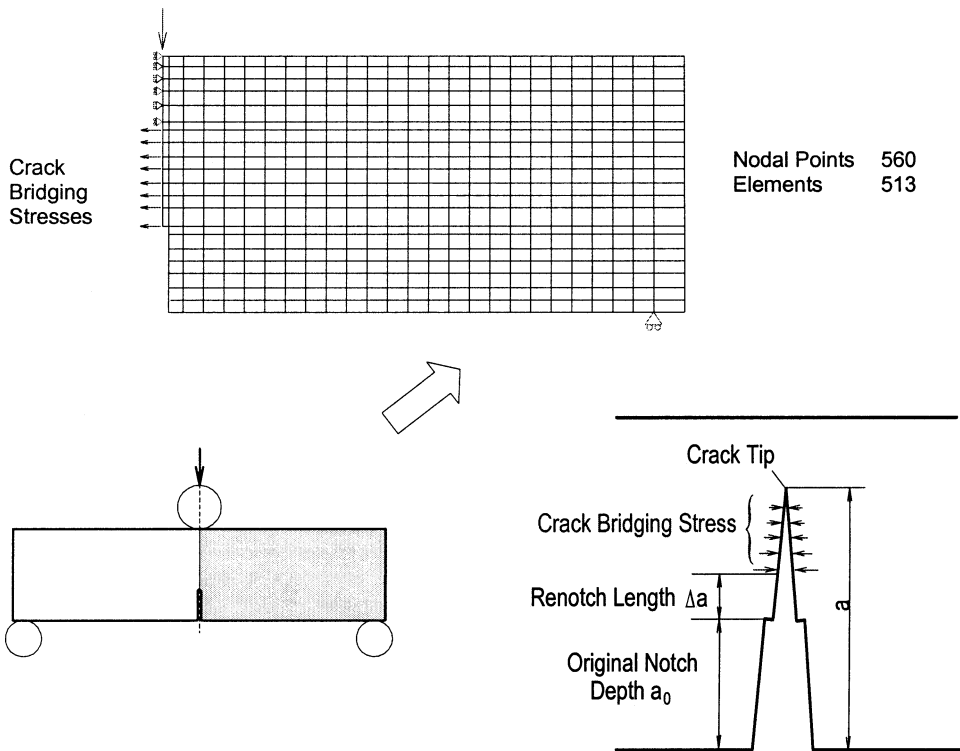


Figure 9. FE model of the re-notched SENB specimen.

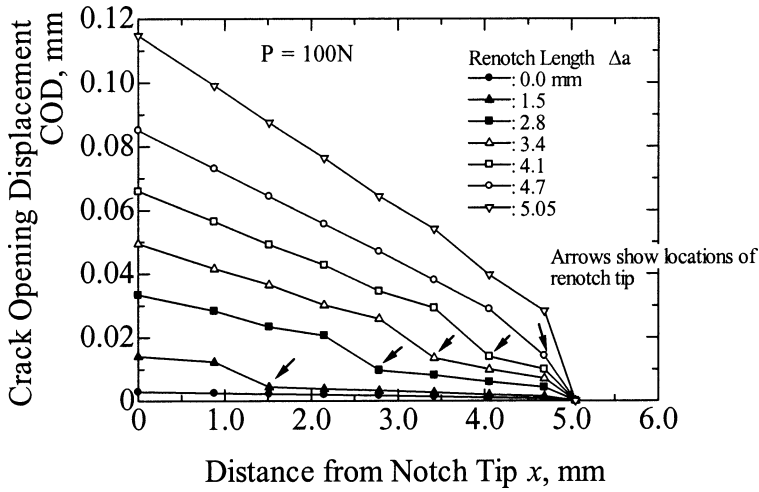


Figure 10. COD profiles.

Figure 11 shows the change in the crack bridging stresses with re-notching in the frontal FPZ. The bridging stress is largest at the machined notch tip, i.e. the location of maximum fiber pull out. The FE analysis then computed the reduction in stress intensity factor due to fiber bridging, K_c , from which the following equivalent stress intensity factor, K_{eq} , was obtained:

$$K_{eq} = K_I - K_c \tag{2}$$

$$G_{eq} = G_I - G_c \tag{3}$$

$$G_{eq} = \frac{K_{eq}^2}{E} \quad G_I = \frac{K_I^2}{E} \tag{4}$$

where the G 's are the corresponding energy release rates. From Eqs. (1)–(3),

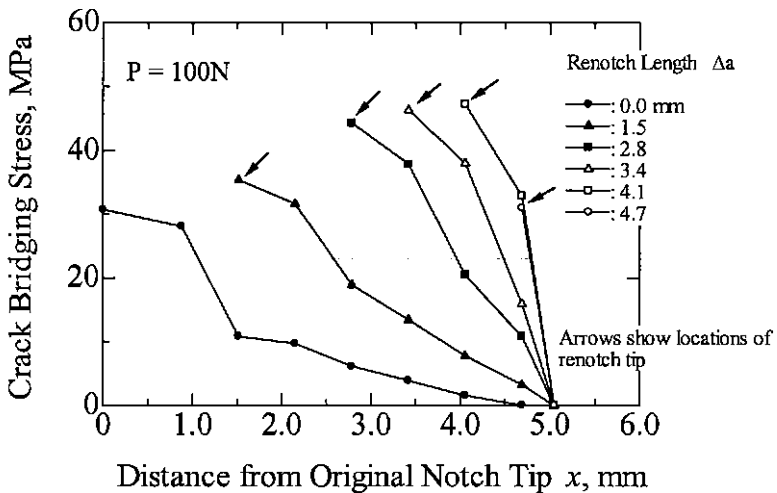


Figure 11. Crack bridging stress.

$$\frac{K_{eq}}{K_I} = \sqrt{\frac{G_{eq}}{G_I}} = \sqrt{1 - \frac{G_c}{G_I}} \tag{5}$$

$$\frac{K_c}{K_I} = 1 - \frac{K_{eq}}{K_I} = 1 - \sqrt{\frac{G_{eq}}{G_I}} = 1 - \sqrt{1 - \frac{G_c}{G_I}} \tag{6}$$

Figure 12 shows the computed reduction in stress intensity factor with the increase in re-notch length due to the crack bridging stress.

Figure 13 shows the measured work rate of fracture, G_I , is closely related to the computed stress intensity factor of the SENB specimen with crack bridging. The stress intensity factor is normalized by the modulus for an equivalent isotropic material, E_c , of:

$$1/E_c = \sqrt{\frac{A_{11}A_{22}}{2}} \left[\sqrt{\frac{A_{22}}{A_{11}} + \frac{2A_{12} + A_{66}}{2A_{11}}} \right]^{\frac{1}{2}}$$

$$A_{11} = 1/E_y = 1/0.67$$

$$A_{22} = 1/E_x = 1/48.0$$

$$A_{12} = -\nu/E_x = -0.05/48.0$$

$$A_{66} = 1/G_{xy} = 1/1.92$$

Since Figure 13 implies that $U \propto G$

$$\frac{K_c}{K_I} \approx 1 - \sqrt{1 - \frac{U_c}{U_I}} \tag{7}$$

which simplifies the computation of K_c .

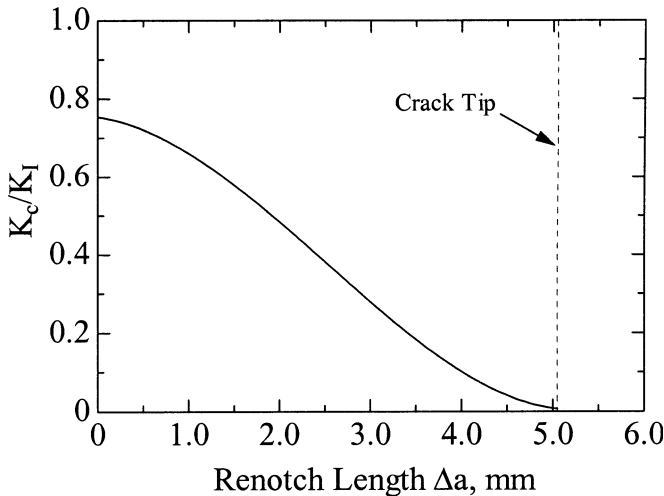


Figure 12. Reduction in bridging stress intensity factor.

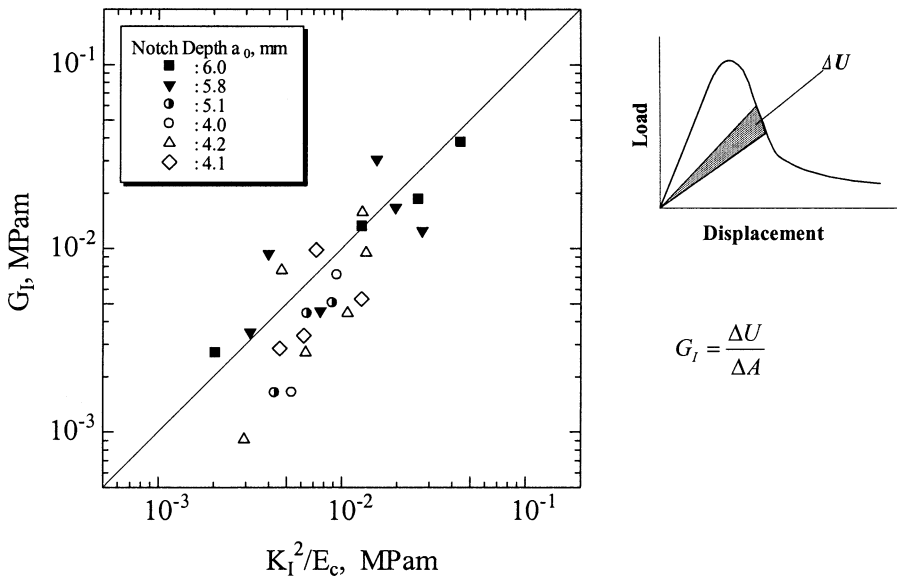


Figure 13. G_I versus K_I .

CONCLUSIONS

A hybrid experimental-numerical, inverse procedure was used to model the crack bridging stress of the tortuous crack in a C/C composite SENB specimen.

The measured work rate of fracture was found to be nearly equal to the strain energy release rate obtained from the stress intensity factor of a carbon/carbon composite SENB specimen.

ACKNOWLEDGEMENT

The work reported here is supported by an AFOSR Grant F49620-96-01-1-0143, Dr. B. Les Lee, AFOSR Program Manager.

REFERENCES

1. Y.-L. Wang and S. Nair, Toughening Behavior of a Two-Dimensional SiC/SiC Woven Composite at Ambient Temperature: II, Stress-Displacement relationship in the Crack Process Zone, *J. Am Ceram Soc.*, **81** (5), 1157–62 (1998).
2. A. J. Lucchesi, J. C. Hay and K. W. White, Characterization of Wake-Zone Traction in an Oxidation-Inhibited Carbon/Carbon Composite, *Composite Science and Technology*, **49**, 315–325 (1993).
3. K. W. White and R. E. Grimes, Effect of Fiber Architecture on High Temperature Fracture Behavior of 2-D Carbon/Carbon Composites, *Mechanics and Mechanism of Damage in Composites and Multi-Materials*, ESIS ed. D. Baptise, 33–44 (1991).
4. Y. Ohtake, S. Sato, K. Hatanaka, H. Masumoto, Y. Matsumura, Biaxial deformation behaviors of C/C composite at high temperatures, *Proc. of Int. Conf. On Advanced Technology in Experimental Mechanics '99 (ATEM '99)*, **2**, 490–495 (1999).
5. J. E. Srawley, Wide Range Stress Intensity Factor Expressions for ASTM E399 Standard Fracture Toughness Specimens, *Int. Journal of Fracture*, **12**, 475–476 (1976).

TAILORING THE COMPOSITION OF SELF-REINFORCED SILICON NITRIDE CERAMICS TO ENHANCE MECHANICAL BEHAVIOR

P. F. Becher, G. S. Painter, H. T. Lin, and M. K. Ferber*

1. ABSTRACT

Studies have shown that seeding allows for greater control of the microstructure of self-reinforced beta-silicon nitride based ceramics, which when combined with tailoring of the sintering additives can result in significant improvements in fracture toughness and strength. Similar behavior was noted in alpha-SiAlONs. In beta-Si₃N₄ ceramics in which alumina serves as one of the additives, the larger elongated reinforcing grains result from the epitaxial deposition of Si_{6-z}Al_zO₂N_{8-z} layers on the Si₃N₄ core. Structural models show that the bond strength of the interface between the SiAlON and the amorphous intergranular film increases as the Al and O contents of the SiAlON increase. This is consistent with experiments that revealed interfacial debonding was promoted when the z-value of the SiAlON epitaxial layer was reduced. Compositional tailoring that leads to enhanced interfacial debonding and an increase in the fracture toughness.

For a number of applications, creep resistance is also required in these ceramics. Recent results have been obtained in self-reinforced silicon nitride ceramics where

* P. F. Becher, G. S. Painter, H. T. Lin, and M. K. Ferber, Metals and Ceramics Division, Oak Ridge National Laboratory, P. O. Box 2008, Oak Ridge, Tennessee 37831.

controlled increases in the fraction of larger elongated reinforcing grains were found to reduce the creep rates. However, viscous flow in the amorphous intergranular films (IGF) in silicon nitride-based ceramics significantly impact their creep behavior and mechanical reliability at elevated temperatures. Recent studies of bulk Si-based oxynitride glasses have shown that increasing the nitrogen to oxygen (N:O), rare earth (RE): aluminum (Al) ratios of the glass and using smaller RE ions raise the glass viscosities. Creep models suggest that this will improve the creep resistance of the silicon nitride ceramics, which is supported by the results of creep studies. The above findings are providing a framework for designing the next generation of silicon nitride-based ceramics by microstructural and compositional tailoring.

2. BACKGROUND

As a class of materials, ceramics present an unusually complex set of both intellectual and technological challenges. One of the key issues has been the need to make ceramics tougher by devising approaches to increase the energy required to grow cracks. This would be reflected in increased fracture toughness where traditional ceramics exhibit values that are only 2 to 10% of those of metallic alloys. Even so, ceramics, such as silicon nitride, continue to find important and demanding applications including high performance bearings, turbocharged rotors, fuel igniters and machine tool inserts. The most recent important milestones achieved include the incorporation of silicon nitride ceramic as (1) hot section components for auxiliary power units produced by AlliedSignal for aircraft and industrial auxiliary turbo-power units and various components for aircraft turbine engines¹ and (2) valves in selected automotive diesel engines by Daimler-Benz.²

These are quite remarkable considering the brittle nature of ceramics and the dearth of research on high tech ceramics until ~ 30 years ago. Two major advances have given rise to these subsequent successes. These include: (1) substantial improvements in the technology to reliably fabricate ceramic components including those with complex shapes, and (2) improvements in the mechanical properties due to the evolution of a class of tougher silicon nitride ceramics that are more resistant to damage and attendant strength losses. This evolution must continue for future applications and requires a scientific basis for tailoring a wider range of tough, high strength ceramics for both room and elevated temperature applications.^a The goal must be to improve the reliability of silicon nitride components whether limited by brittle fracture, crack growth at intermediate and low temperatures, or creep- or oxidation/corrosion-induced damage that reduce the load bearing capacity or the lifetime of components. Depending on the application, all of those factors controlling the mechanical reliability may have to be considered in the tailoring of the composition and microstructure of a silicon nitride ceramic. Here we consider some of those factors that can influence the fracture and creep responses.

^a Note that the issue of the brittleness of ceramics restricting their application is not limited to structural applications. For instance, the brittleness of superconducting ceramics had to be resolved by employing them either as thin films on ductile metal wires or embedded within ductile metal casings. Thus the understanding of how to defeat the brittleness of the ceramics impacts their use in a host of applications.

3. TAILORING THE FRACTURE TOUGHNESS AND STRENGTH

For high strength-high toughness response, one now has a basis for tailoring the microstructure of silicon nitride-based ceramics. In the case of beta-silicon nitride (and β -SiAlON) ceramics, it has been established that this can be accomplished through the controlled introduction of larger elongated grains combined with the tailoring of the sintering additive composition.^{3,4} The larger elongated grains that form serve as the reinforcing elements much like whiskers in whisker-reinforced ceramics^{4,5} or fibers in fiber-reinforced ceramics.⁶ Results using these principles show that self-reinforced silicon nitride (SRSN) ceramics can have high strengths (1 to 1.4 GPa) combined with high fracture toughness (e.g., up to 11 MPa $m^{1/2}$ or at least two to three times that of commercial materials), Figure 1. Higher fracture toughness values are reported in the literature, but these often have been obtained using notched beam or related techniques, which are subject to overestimating the toughness. More rigorous measurements (e.g., double cantilever beam and similar test geometries), as used here, provide more conservative toughness values and allow one to obtain R-curve behavior.^b

However, these findings also reveal that the presence of larger elongated grains in silicon nitride is not a sufficient condition for achieving high strength and high toughness. As seen in Figure 1, careful control of the microstructure is a key here as the toughening achieved by crack bridging processes is dependent upon the size and volume fraction of these larger elongated grains. In self-reinforced ceramics, the reinforcements are generated during the sintering of the ceramic, which greatly simplifies the processing and avoids the use of expensive ceramic fibers or whiskers. The larger elongated beta-phase grains form in silicon nitride ceramics due to the presence of some beta phase in the alpha phase silicon nitride powders that are typically used. Unfortunately in this case, it is difficult, if not impossible, to regulate the size and number of the larger reinforcing grains as well as to obtain a more uniform spatial distribution of them. In fact, each of these factors must be regulated in order to achieve both high toughness and high strength. Recent studies have shown that the microstructural control can be achieved by the incorporation of a small fraction ($\sim 2\%$) of rice-shaped beta seeds into the silicon nitride powder-sintering additive mixture. The beta seeds used to date are typically $\leq 4 \mu\text{m}$ long by $\leq 1 \mu\text{m}$ in diameter; however, the optimum size (and fraction) of such seeds has not been determined as yet. The beta seeds, then, serve as the nuclei for generating well-dispersed elongated reinforcing grains with controlled size(s).^{3,9} Without the use of such a seeding method, control of the microstructure to reproducibly obtain high strength and toughness is quite difficult. Indeed, fracture strengths can be severely limited by the clustering of larger grains or formation of excessively large grains.³ In addition, clustering and lack of control of the formation of the reinforcing grains typically results in intermediate toughening effects as indicated in Figure 1.³ An important extension of these concepts has been reported in recent studies that revealed substantially increased fracture toughness (in the range of 10 MPa $\sqrt{\text{m}}$) values were also achieved in α' -SiAlON ceramics using a similar seeding approach.¹⁰

^b The recent advent of methods to introduce very sharp notches and, hence, very short ($\leq 50 \mu\text{m}$) initial crack lengths (e.g., ref. 8) will also allow us to obtain a greater understanding of the R-curve response at scales more consistent with natural flaws.

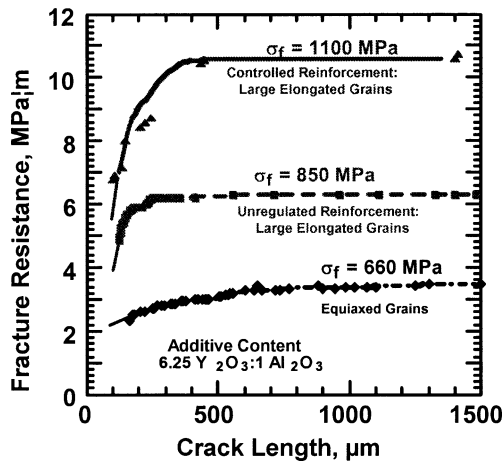


Figure 1. Very high strength and toughness values are achieved by controlled generation of large elongated β - Si_3N_4 reinforcing grains into a fine-grained β - Si_3N_4 matrix.³ The average room temperature fracture strength values, σ_f , shown above for each material were obtained in four point flexure using ASTM C1161B method.⁷

Both the growth of the reinforcing grains during sintering and their subsequent ability to act as reinforcements are controlled by the intergranular material found in silicon nitride ceramics. These intergranular films (typically < 2 nm thick) are a result of the reaction between the native oxygen in silicon nitride powders and the specific chemical additives used to promote sintering. This reaction results in the formation of a viscous glass that allows liquid phase sintering to occur and acts as a media for the growth of the elongated reinforcing beta grains. In addition, the resultant intergranular films (IGFs) affect the debonding of the reinforcing grains from the matrix material in the crack tip region.¹¹ This debonding process prevents the crack from cutting through the reinforcing grains and allows them to bridge across the crack. This is similar to what occurs in fiber-reinforced ceramics. Recent studies are revealing that the composition of the sintering additives and, hence, the IGF can be tailored to optimize the toughening effects of the elongated reinforcing grains in silicon nitride ceramics. These studies revealed that the fracture toughness of SRSN ceramics with ~ 7 wt.% additives of yttria plus alumina could be raised by $\sim 50\%$ simply by substituting more yttria in place of the alumina.¹² Theoretical calculations reveal that energetics favor Al migration to the interface from the silicate intergranular film (IGF) in polycrystalline Si_3N_4 . This migration of Al (and O) to the interface, then, leads to the growth of an epitaxial SiAlON layer on the Si_3N_4 .¹³ These calculations also show that the presence of an interfacial SiAlON layer increases the number of strong interfacial bond pairs and results in strengthening the interface, consistent with the experimental results. The tailoring of the additive composition plus the microstructure is now recognized as the critical factors in obtaining both high fracture toughness and high fracture strength.

What can we expect out of such toughened ceramics? The object must be to generate robust materials with improved mechanical properties and resistance to damage during handling or in-service. As an example, the fracture strength of toughened ceramics may become more resistant to degradation due to the severity of surface damage. One can simulate such conditions by the damage introduced by

more severe (i.e., coarser diamond grit size) surface grinding. A very significant benefit of tailoring the self-reinforced silicon nitrides can be seen in Figure 2 where the high strengths are unaffected by the severity of the surface damage.¹⁴ This itself suggests that in self-reinforced silicon nitride ceramics with controlled microstructures (e.g., eliminate wide variations in microstructures, extensive clustering of larger elongated grains and formation of excessively large grains) it should be possible to improve the flaw size distributions and, thus, the strength distributions. Indeed recent studies of tensile strength distributions of a self-reinforced silicon nitride ceramic with both a high toughness and a strong R-curve response give support for this.¹⁵ In this case, a two parameter Weibull analysis was conducted using 93 tensile strength results obtained with a toughened ($\sim 8.5 \text{ MPa}\sqrt{\text{m}}$) silicon nitride ceramic. This yielded a very high Weibull modulus of 33 by the maximum likelihood criterion (or 45 by linear regression analysis) compared to typical Weibull modulus values of ~ 10 .

4. FACTORS CONTRIBUTING TO CREEP RESISTANCE

The mechanical reliability of silicon nitride ceramics at intermediate and elevated temperatures can be dominated by both the microstructure and the intergranular phases present. For instance, recent creep studies indicate that the creep resistance increases in self-reinforced silicon nitride ceramics and can be raised by increasing the fraction of the larger elongated reinforcing grains by the beta-seeding method.¹⁶ The elongated grains apparently restrict grain boundary sliding and grain rotation during

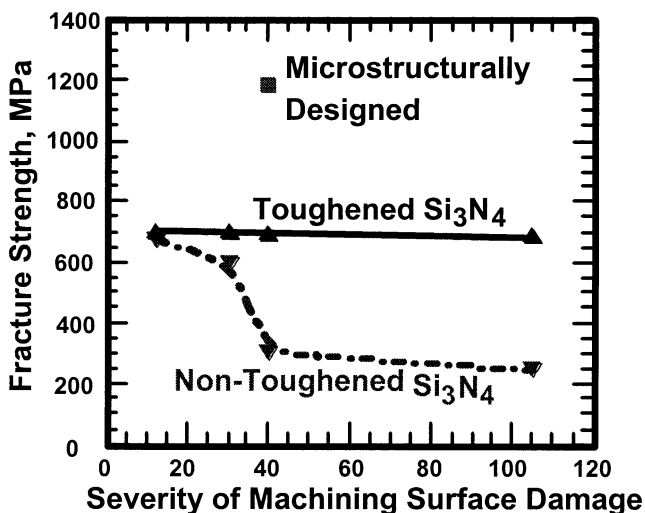


Figure 2. The self-reinforced silicon nitride ceramics exhibit fracture strengths that are not degraded by increasing the severity of surface damage while the unreinforced silicon nitrides undergo substantial strength loss. Note that the x-axis represents the size in microns of the diamond particles used in the grinding wheel used to finish the tensile surface of the four point flexure bars. In this case, the depth of the residual grinding grooves and associated damage zone as well as the size of the surface cracks generated all increase as the size of the diamond particles in the grinding wheel increases. Data for toughened and non-toughened silicon nitride are taken from Tajima.¹⁴ Data for microstructurally designed silicon nitride from ORNL studies.

creep by forming a rigid network that constrains the motion of the fine grained matrix.

In addition to the affects of reinforcing grains, amorphous intergranular films can have a substantial impact on the creep deformation of silicon nitride ceramics at elevated temperatures.^{17,18} Thus, studies of the properties of oxynitride glasses comprising these IGF films can provide directions for tailoring the sintering additives for silicon nitride to improve the mechanical reliability of these ceramics at elevated temperatures, as well as at low and intermediate temperatures. For instance, studies have shown that the glass transition temperature, which reflects a viscosity in the range of 10^{12} Pa•s, can be increased by increases in the N:O ratio, decreases in aluminum content, and substitution of smaller rare earth ions in SiREAl oxynitride glasses.¹⁹ In order to better illustrate this, it is informative to assess how the viscosity of bulk Si-based oxynitride glasses is influenced by changes in the glass composition. The trends in the shifts in the temperature-dependent viscosity with composition from recent studies of silicon oxynitride glasses containing aluminum and various rare earths²⁰ are summarized in Figure 3. As shown here, the viscosity of a 45Si30La25Al glass (composition in equivalent percent) is increased by over three orders of magnitude by replacing some of the oxygen by nitrogen. An additional ten fold increase can be obtained by replacing the La ion by the smaller Gd ion, while reducing the Al content by raising the Si (or RE) level can result in a further 100-fold increase in the glass viscosity. In this simple illustration, upwards of a million-fold increase in viscosity

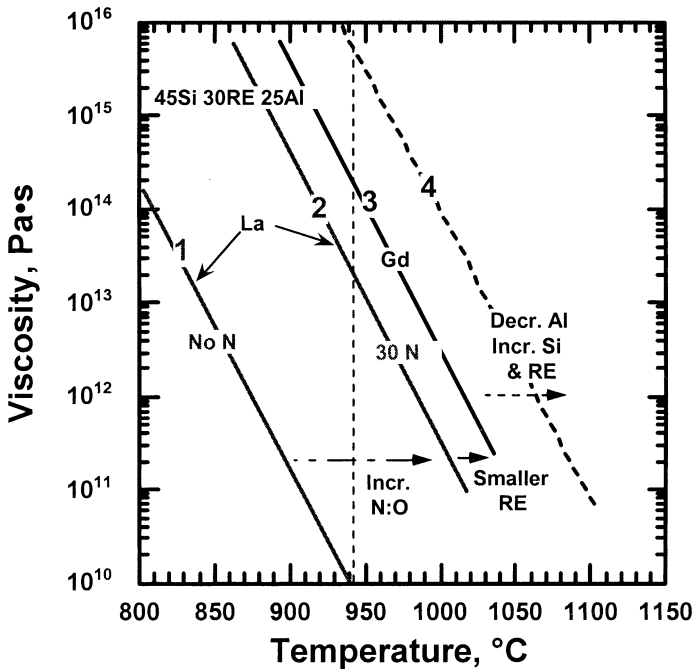


Figure 3. Modifying their composition as summarized here can raise the viscosity of SiREAl oxynitride glasses. By replacing some of the oxygen by nitrogen, the viscosity of a 45Si30La25Al glass (composition in equivalent percent) is increased by over three orders of magnitude (line 1 to line 2). Replacing the La by Gd increases the viscosity by \sim one order of magnitude (line 2 to line 3). Reducing the Al content by increasing the Si (or RE) content raises the viscosity by another two orders of magnitude.

could be achieved in the bulk glass by tailoring the composition, which should allow us to impact the creep resistance of silicon nitride ceramics.

To examine the effects that might be achieved in the ceramic by simply altering the viscosity of the IGF, a “brick wall” type model can be used to characterize the effective viscosity of the silicon nitride ceramic composed of rigid, non-deforming grains surrounded by a viscous media.¹⁷ For the simple case of an array of cubic rigid grains with a size of G with an amorphous film of a thickness (t) and a viscosity (η_o), the effective viscosity (η_{eff}) of the silicon nitride ceramic is:

$$\eta_{\text{eff}} = A \eta_o (t/G)^{-3} \quad (1)$$

where A is a constant. For the typical 1 to 2 nm thick viscous films in silicon nitride, the calculated η_{eff} values of a ceramic with a grain size of one micron can be as much as six orders of magnitude greater than the η_o values for the bulk glasses. In addition, the equilibrium thickness of the intergranular films in silicon nitride ceramics has been shown to decrease with the substitution of rare earths with smaller ionic size as densification additives.²¹ Thus, the improvement in creep resistance of the ceramic brought on by increases in bulk glass viscosities with the use of smaller rare earth additions can be augmented by the formation of thinner IGFs in the ceramic. Studies of the creep of silicon nitrides that had been fabricated using silica plus rare earth oxides revealed a decrease in creep rates with the use of smaller rare earths $\text{Sm} > \text{Gd} > \text{Dy}$.²² Recent studies of the creep response of commercial silicon nitride ceramics illustrate a similar trend for decreasing creep rates when smaller rare earths are used as densification aids with lutetium being the most effective.²³ The creep resistance of self-reinforced silicon nitrides has been found to increase by about 10-fold when the yttria to alumina ratio in the densification additives (fixed total amount) is increased,¹⁶ which is known to result in amorphous intergranular films with increased Y: Al ratios.^{12a} This is consistent with the observations of increases in glass viscosity brought about by increases in the Y: Al ratio. Obviously, other microstructural factors (e.g., presence of elongated grains, phase changes and reactions involving the test environment, and migration and crystallization of the amorphous films) will also influence the creep response of silicon nitride ceramics. However, there is considerable potential for improving the creep resistance of silicon nitride ceramics by the judicious selection of the sintering additives to control the viscosity of the amorphous intergranular films that are formed.

5. SUMMARY

Self-reinforced silicon nitride ceramics exhibiting high toughness and strength are obtained by tailoring the size and number of the bridging grains. In each material, bridging mechanisms rely on debonding of the reinforcing grains from the matrix to increase toughness. Interfacial debonding can be influenced by the nature of the intergranular films, whose composition and properties are a function of the sintering aids. In silicon nitride ceramics that use alumina as one of the sintering aids, the amorphous intergranular films surround the Si_3N_4 grains on which epitaxial SiAlON layers form. In this case, interfacial debonding is dependent on the composition of the SiAlON layer, becoming more difficult as the Al (and the O) content of the

SiAlON increases. Theoretical calculations show this results from the formation of strong Si-O, Si-N, and Al-O bonds across the glass-crystalline interface. In addition to the influence of intergranular films on fracture, the amorphous IGFs containing Si, Al, O, N, and RE will also influence the temperature dependent viscosity of the amorphous phase. Measurements of the temperature dependent viscosities of bulk glasses reveal that the viscosity increases with increase in the nitrogen to oxygen ratio, the substitution of smaller rare earth ions, and a reduction of the Al content in the film. Increasing the viscosity of glasses similar to those in the amorphous intergranular films offers a means to substantially improve the creep resistance of the ceramic and, thus, enhance its life at elevated temperatures. It is apparent that sintering additives used to promote the densification of self-reinforced ceramics can play an important role in improving both their fracture and creep resistances.

6. ACKNOWLEDGEMENT

The research was sponsored by the Division of Materials Sciences and Engineering, U. S. Department of Energy, under Contract No. DE-AC05-00OR22725 with UT-Battelle, LLC.

REFERENCES

1. M. Savitz, "Commercialization of Advanced Structural Ceramics, Part I: Patience is a Necessity," *Am. Ceram. Soc. Bulletin* **78**(1), 53–56 (1999).
2. K. Moergenthaler, private communication.
3. P. F. Becher, E. Y. Sun, K. P. Plucknett, K. B. Alexander, C-H Hsueh, H-T Lin, S. B. Waters, C. G. Westmoreland, E-S Kang, K. Hirao, and M. Brito, "Microstructural Design of Silicon Nitride with Improved Fracture Toughness, Part I: Effects of Grain Shape and Size," *J. Am. Ceram. Soc.*, **81**(11) 2821–30 (1998).
4. P. F. Becher, C. H. Hsueh, K. B. Alexander, and E. Y. Sun, "The Influence of Reinforcement Content and Diameter on the R-Curve Response in SiC Whisker-Reinforced Alumina," *J. Am. Ceram. Soc.*, **79**(2) 298–304 (1996).
5. P. F. Becher, "Microstructural Design of Toughened Ceramics," *J. Am. Ceram. Soc.*, **74**(2) 255–69 (1991).
6. A. G. Evans, "Perspective on the Development of High-Toughness Ceramics," *J. Am. Ceram. Soc.*, **73**(1) 187–206 (1990).
7. C1161-02c Standard Test Method for Flexural Strength of Advanced Ceramics at Ambient Temperature, Developed by Subcommittee: C28.01, ASTM Book of Standards, Volume: 15.01, ASTM International, West Conshohocken, PA, 2003.
8. H. Kawamoto, Y. Takigawa, K. Hiramatsu, and A. Okada, "Behavior of Crack-Grow Resistance in Toughened Anisotropic Silicon Nitride Ceramics," in *Key Engineer Materials, Vols. 175–176: Engineering Ceramics*, edited by P. Sajgalik and Z. Lences, (Trans Tech Publications, Zurich, 2000), pp. 241–252.
9. a. K. Hirao, T. Nagaoka, M. E. Brito, and S. Kanzaki, "Microstructure Control of Silicon Nitride by Seeding with Rodlike β -Silicon Nitride Particles," *J. Am. Ceram. Soc.*, **77**, 1857–62 (1994). b. K. Hirao, T. Nagaoka, M. E. Brito, and S. Kanzaki, *J. Ceram. Soc. Jpn.* **104**: 55–59 (1996).
10. J. Kim, A. Rosenflanz, and I. W. Chen, "Microstructure Control of In-Situ Toughened α' -SiAlON Ceramics," *J. Am. Ceram. Soc.*, **83**(7) 1819–21 (2000).
11. a. P. F. Becher, E. Y. Sun, C. H. Hsueh, K. B. Alexander, S. L. Hwang, S. B. Waters, and C. G. Westmoreland, "Debonding of Interfaces Between Beta-Silicon Nitride Whiskers and Si-Al-Y Oxynitride Glasses," *Acta. Metall.*, **44**(10) 3881–93 (1996). b. E. Y. Sun, P. F. Becher, C. H.

- Hsueh, G. S. Painter, S. B. Waters, S. L. Hwang, and M. J. Hoffmann, "Debonding Behavior Between β - Si_3N_4 Whiskers and Oxynitride Glasses With And Without An Epitaxial β -SiAlON Interfacial Layer," *Acta. Mater.*, **47**(9) 2777–85 (1999).
12. a. E. Y. Sun, P. F. Becher, C-H Hsueh, S. B. Waters, K. P. Plucknett, K. Hirao, and M. Brito, "Microstructural Design of Silicon Nitride with Improved Fracture Toughness, Part II: Effects of Additives," *J. Am. Ceram. Soc.*, **81**(11) 2831–40 (1998). b. P. F. Becher, G. S. Painter, E. Y. Sun, C. H. Hsueh, and M. J. Lance, "The Importance of Amorphous Intergranular Films in Self-Reinforced Si_3N_4 Ceramics," *Acta. Mater.*, **48**(12) 4493–99 (2000).
 13. G. S. Painter, P. F. Becher, and Ellen Y. Sun, "Bond Energetics at Intergranular Interfaces in Alumina-Doped Silicon Nitride," *J. Am. Ceram. Soc.*, **85**(1) 65–67 (2002).
 14. Y. Tajima and K. Urashima, "Improvement of Strength and Toughness of Silicon Nitride Ceramics," in *Tailoring of Mechanical Properties of Si_3N_4 Ceramics*, edited by M. J. Hoffmann and G. Petzow, (Kluwer Academic Publishers, Dordrecht, Netherlands, 1994), pp. 101–109.
 15. C.-W. Li, J. Wimmer and J. J. Nick, "Tensile Strength of an In-Situ Reinforced Silicon Nitride Exhibiting R-Curve Behavior," ECD meeting, January 2003, submitted to Ceramics Transactions.
 16. H. T. Lin, unpublished results.
 17. a. D. Wilkinson, "Creep Mechanisms in Multiphase Ceramic Materials," *J. Am. Ceram. Soc.*, **81**(2) 275–99 (1998). b. J. R. Dryden and D. S. Wilkinson, "Three-Dimensional Analysis of the Creep Due to a Viscous Grain Boundary Phase," *Acta. Mater.* **45**(3) 1259–73 (1997).
 18. W. E. Luecke and S. M. Wiederhorn, "A New Model for Tensile Creep of Silicon Nitride," *J. Am. Ceram. Soc.* **82**(10) 2769–78 (1999).
 19. P. F. Becher, S. B. Waters, C. G. Westmoreland, and L. Riester, "Influence of Composition on the Properties of SiREAL Oxynitride Glasses: RE = La, Nd, Gd, Y or Lu," *J. Am. Ceram. Soc.*, **85**(4) 897–902 (2002).
 20. P. F. Becher and M. K. Ferber, "The Temperature Dependent Viscosity of SiREAL-Based Glasses As a Function of N:O and RE:Al Ratios. Where RE = La, Gd, Y and Lu," to be published.
 21. C.-M. Wang, X. Pan, M. J. Hoffmann, R. M. Cannon, and M. Rühle, "Grain Boundary Films in Rare-Earth-Based Silicon Nitride," *J. Am. Ceram. Soc.*, **79**(3) 788–92 (1996).
 22. M. K. Cinibulk, G. Thomas and S. M. Johnson, "Strength and Creep Behavior of Rare-Earth Disilicate-Silicon Nitride Ceramics," *J. Am. Ceram. Soc.* **75**(8) 2050–55 (1992).
 23. a. S. M. Wiederhorn and M. K. Ferber, "Silicon nitride for gas turbines," *Current Opinion in Solid State and Mater. Sci.*, **5**: 311–16 (2001). b. F. Lofaj, S.M. Wiederhorn, G.G. Long, P.R. Jemian and M.K. Ferber, "Cavitation Creep in the Next Generation Silicon Nitride," in *Ceramic Materials and Components for Engines*, edited by J.G. Heinrich and F. Aldinger (Wiley-VCH 2001), pp. 487 to 493.

NONLINEAR FRACTURE OF A POLYCRYSTALLINE GRAPHITE – SIZE-EFFECT LAW AND IRWIN’S SIMILARITY

M. Sakai and R. Nonoyama

ABSTRACT

Nonlinear fracture of a polycrystalline graphite is examined through the studies for the test specimen size-effect on fracture toughness parameters. The fracture toughness of polycrystalline graphite significantly depends on the dimensions and the geometries of test specimens. A finite non-negligible frontal process zone dictates this size-effect law. The Bažant’s theoretical approach modified by the present authors is successfully applied to the nonlinear fracture of polycrystalline graphite, allowing an estimate of the size of frontal process zone, as well as the theoretical prediction for the size-effect law of fracture toughness. The Irwin’s similarity relationship (the equivalence between the stress-intensity derived toughness, K_c^2/E' and the potential energy-derived toughness R_c ; $K_c^2/E' = R_c$) is also studied in the present nonlinear fracture mechanics regime; R_c is always larger than K_c^2/E' , and the excess energy ($R_c - K_c^2/E'$) becomes progressively significant with the increase in the critical load P_c for the onset of main crack extension, independent of the notch/crack length of test specimen. This fact suggests that the excess energy, $R_c - K_c^2/E'$, is consumed in the region away of the

localized area including the main crack and its adjoint frontal process-zone. The microscopic considerations are made of the characteristic processes and mechanisms for the excess energy consumption in polycrystalline graphite materials.

1. INTRODUCTION

The standard test methods for the stress-intensity-derived fracture toughness K_c are very restrictive with respect to the size requirements of test specimen to assure the plane-strain condition, where the fracture process zone in front of the tip of a critical crack is extremely small in size compared to the geometrical dimensions of test specimen (thickness, width, height, and crack/notch length). Linear Elastic Fracture Mechanics (LEFM) only refers to this mechanical situation of small-size process zone. The plane-strain fracture toughness K_c thus defined in these standards is independent of the dimensions of test specimen, being supposed to be a characteristic material parameter for the resistance to failure. In LEFM-regime, Irwin demonstrated the similarity between K_c and the potential energy derived fracture toughness R_c through the relation of $R_c = K_c^2/E'$ in terms of the elastic modulus $E' [= E/(1 - \nu^2)]$ (E : Young's modulus, ν : Poisson's ratio). R_c is defined by the potential energy consumption associated with creating a unit fracture surface area at crack-tip [1–3].

Once the size of frontal process zone is not fit to the criterion of LEFM, the stress-intensity factor K_Q (apparent fracture toughness) for the critical crack significantly depends on the geometries and dimensions of test specimen. Furthermore, a finite amount of residual offset in the displacement is often observed on unloading in the load P vs. load-point displacement u diagram, due to the irreversible displacement enhanced by nonlinear mechanical processes and mechanisms in the frontal process zone [4–6]. In this non-linear fracture regime, not only the work-of-fracture γ_{wof} (total work for a static failure divided by the total areas of resultant fracture surfaces), but also the energy fracture toughness R_c do not fulfill the Irwin's similarity [$R_c (= 2\gamma_{\text{wof}}) = K_c^2/E'$]. These energy-derived toughness parameters (R_c and $2\gamma_{\text{wof}}$) are always larger than the stress-intensity-derived value of K_c^2/E' . Phase-transformation-toughened zirconia ceramics [6], numbers of refractory materials [4,5], and fiber-reinforced ceramic composites [7], by way of examples, are not subjected to the Irwin's similarity.

The test specimen size-effect on K_c and R_c is examined in the present work for a polycrystalline graphite. In particular, the excess energy consumption, $R_c - K_c^2/E'$, will be related to the size of test specimen as well as to the test conditions. It will be concluded that this excess energy is intimately related to the processes and mechanisms of microcracking and slippage of graphite basal planes that occur in the locations away of the crack-tip process zone.

2. EXPERIMENTAL DETAILS

2.1. Test Material

An isotropic polycrystalline graphite (IG-110U, Toyo Tanso Co., Osaka, Japan) was obtained for study. The microstructural characteristics of the polycrystalline graphite

are a mean size of petroleum coke grains of $15\ \mu\text{m}$, a mean pore size of $5\ \mu\text{m}$, a porosity of 15%, and a bulk density of $1.76\ \text{g/cm}^3$. Some mechanical characteristics include the young's modulus (E) of 9.0 GPa, three-point flexural strength (σ_f) of 35 MPa, and the fracture toughness (K_c) of $0.85\ \text{MPa}\sqrt{\text{m}}$. This graphite material shows rising R-curve (crack growth resistance K_R vs. crack extension Δa curve) behavior during crack extension, yielding the eventual plateau toughness of $K_c = 1.17\ \text{MPa}\sqrt{\text{m}}$ after a crack extension Δa of about 3 mm. Grain bridging in the crack-face contact region gives rise to this rising R-curve behavior [4].

2.2. Fracture Mechanics Tests

Single-edge-notched beam (SENB) specimens were used for fracture mechanics tests. The geometrical notation is shown in Figs. 1(a) and 1(b). The test specimen geometries and the dimensions employed in the present work were classified into the following two categories: (1) geometrically similar specimens with different sizes of S , W , B and a_0 , but with the same ratios of $a_0/W = 0.5$, and $S/W = 4.0$ [Fig. 1(a)], and (2) geometrically nonsimilar specimens with fixed dimensions of $S = 50.0\ \text{mm}$, $W = 12.5\ \text{mm}$ ($S/W = 4.0$), and $L = 60.0\ \text{mm}$, besides different depths of initial notch a_0 ($0.1 \leq a_0/W \leq 0.9$) and different thickness values B [see Fig. 1(b)]. The notch was machined with a 0.3mm-thick diamond wheel saw, and then extended by about 1 mm using a very thin saw made from a razor blade, yielding a resultant notch-tip radius less than $10\ \mu\text{m}$. It has been confirmed in the previous study that this tip-acuity is sufficient enough for providing the fracture toughness K_c as a characteristic material parameter [4].

Fracture mechanics tests were conducted on an Instron-type displacement controlling test machine (Sanwa Testing Machine Co., Toyohashi, Japan) under a crosshead speed of 0.05 mm/min. All the fracture tests were made in three-point flexural modes. A stable crack extension was observed for all the specimens with the relative notch depth $a_0/W \geq 0.4$. However, the crack extension was always unstable for $a_0/W < 0.4$. The apparent fracture toughness, K_Q , at the onset of crack initiation for the critical load P_c was determined by

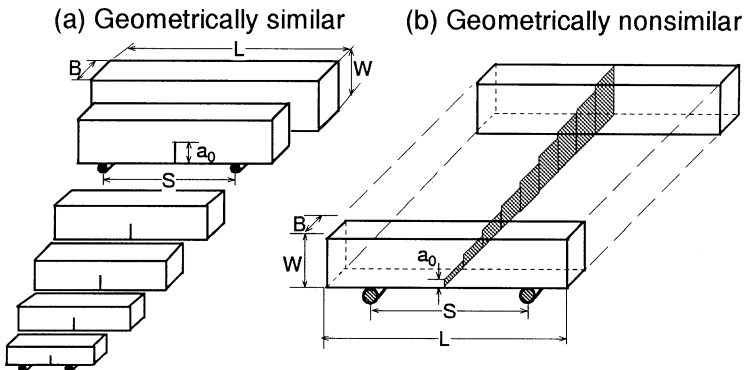


Figure 1. Test specimen geometries and dimensions for (a) geometrically similar configuration ($S = 10.0 \sim 80.0\ \text{mm}$, $W = 2.5 \sim 20\ \text{mm}$, $S/W = 4.0$, $L = S + 10$ in mm, $a_0/W = 0.5$, and $B = 5.0$ and $10.0\ \text{mm}$), and (b) geometrically nonsimilar configuration ($S = 50.0\ \text{mm}$, $W = 12.5\ \text{mm}$, $S/W = 4.0$, $L = 60.0\ \text{mm}$, $a_0/W = 0.1 \sim 0.9$, and $B = 3.0, 5.0,$ and $10.0\ \text{mm}$).

$$K_Q = \frac{P_c}{B\sqrt{W}} Y(a_0/W) \tag{1}$$

using the shape factor $Y(a_0/W)$ of the ASTM E399 formula for SENB geometry [8].

A schematic diagram for determining the potential energy-derived fracture toughness, R_c , is illustrated in Fig. 2, utilizing two specimens with different initial notch lengths a_1 and $a_2(a_1 < a_2)$.

The area, $\Delta\pi$, of the diagram (the hatched area in Fig. 2) enclosed by their loading lines (load P vs. load-point displacement u lines) to the respective critical load P_c indicates the critical energy to create an incremental crack surface $\Delta A[\equiv (a_2 - a_1)B]$. Accordingly, the energy fracture toughness R_c for the onset of crack extension is defined by the following formula [1–3,5];

$$R_c = \frac{\Delta\pi}{\Delta A} \tag{2}$$

A generalization of the concept of energy fracture toughness for linear elastic materials to that for nonlinear elastic materials leads to the path independent J-integral. Some details are given in APPENDIX.

In all the test specimens, the critical load P_c for the onset of crack extension is some-what smaller than the peak load P_{max} (see Fig. 3). The crack extension from P_c to P_{max} is always stable. Accordingly, the determination of the critical load P_c is made in a precise manner by monitoring the notch-tip on the polished side surface of each specimen through a traveling microscope ($\times 50$).

In the present fracture tests, the difference of notch depths, $a_2 - a_1$, was controlled (1.0 ± 0.1) mm, and then the energy fracture toughness R_c obtained from the procedures in Fig. 2 was assigned to the toughness of test specimen with the initial notch depth of $a_0 = (a_1 + a_2)/2$. A precise measurement of load-point displacement u

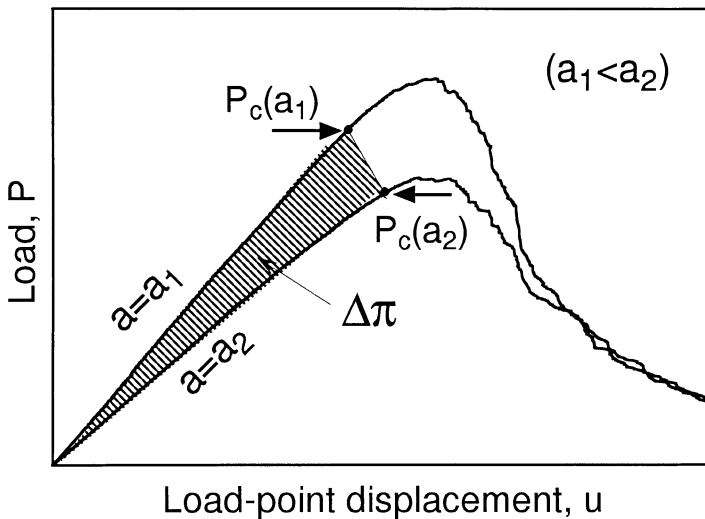


Figure 2. Procedures for determining R_c by the use of two test specimens with different notch lengths a_1 and a_2 .

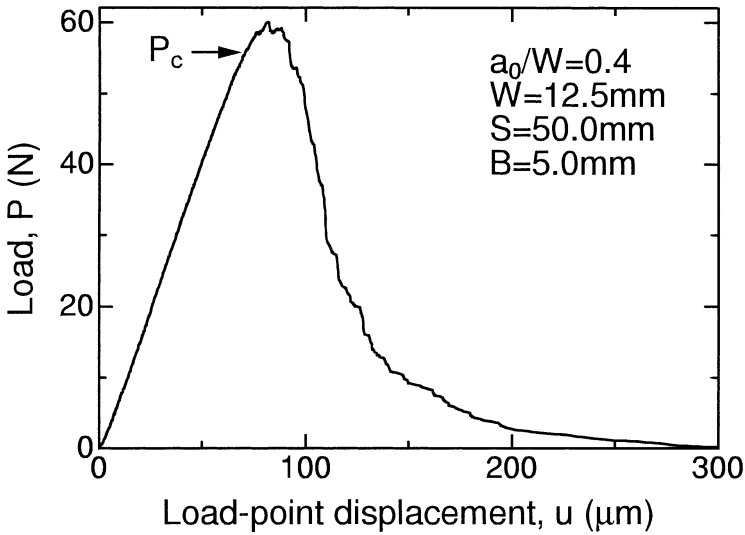


Figure 3. An example for the load P vs. load-point displacement u relation of a polycrystalline graphite. The arrow indicates the critical load for the onset of crack extension.

is substantial for the R_c -determination in the preceding procedure (Fig. 2). The load-point displacement u in three-point flexural configuration was determined in the present work by measuring the relative displacement between the inner loading point and the outer supporting points of flexure by the use of a twinning eddy-current gap detector.

3. RESULT

An example of P - u curve during a stable crack extension is shown in Fig. 3 ($a_0/W = 0.4$, $W = 12.5$ mm, $B = 5.0$ mm, and $S = 50.0$ mm). The crack extension is very stable. The critical load P_c for the onset of crack extension is marked by the arrow, indicating that the crack initiates propagation before the load P reaches the peak value. Furthermore, it must be noticed that the loading P - u line is curved (non-Hookean) at loads even smaller than the critical P_c value, implying the presence of inelastic deformation processes in loading [4].

The dependence of the apparent fracture toughness K_Q for geometrically similar test specimens [refer to Fig. 1(a)] is shown in Fig. 4 as a function of the width W . K_Q -values increase with the increase in W , eventually reaching a plateau value of $K_Q \approx 0.85 \text{ MPa}\sqrt{\text{m}}$. In contrast to the geometrically similar test specimens, the K_Q -values of geometrically nonsimilar test specimens [refer to Fig. 1(b)], as shown in Fig. 5, decrease with the increase in the relative notch depth, a_0/W . However, in the extreme of $a_0/W \downarrow 0$, the K_Q -values attain the same plateau value of $K_Q \approx 0.85 \text{ MPa}\sqrt{\text{m}}$ as that observed in Fig. 4.

The dependence of the energy-derived fracture toughness R_c for geometrically similar test specimens [Fig. 1(a)] is plotted in Fig. 6 as a function of W , along with the values of K_Q^2/E' for comparison. The similar plots for geometrically nonsimilar test

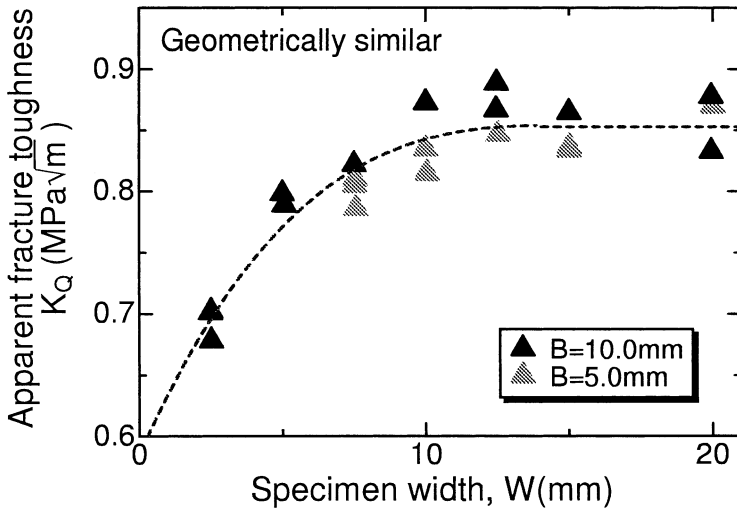


Figure 4. Dependence of the apparent fracture toughness K_Q on the width W of test specimens with geometrically similar configuration.

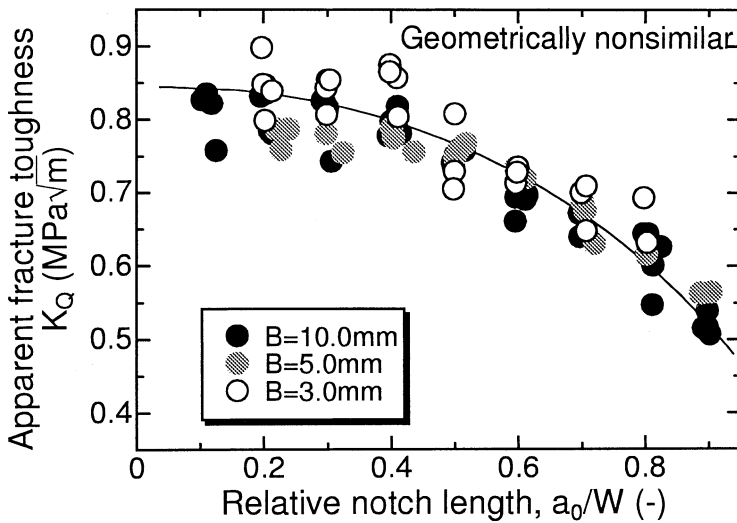


Figure 5. Dependence of the apparent fracture toughness K_Q on the relative notch depth a_0/W of test specimens with geometrically nonsimilar configuration.

specimens [Fig. 1(b)] are given in Fig. 7. A careful inspection for Figs. 6 and 7 indicates; (1) R_c is always larger than K_Q^2/E' , (2) both the toughness parameters, K_Q^2/E' and R_c , are significantly dependent on W and a_0/W ; increasing with the increase in W and with the decrease in a_0/W , and (3) the excess energy, $R_c - K_Q^2/E'$, tends to diminish and then to satisfy the Irwin's similarity with the increase in a_0/W , and with the decrease in W .

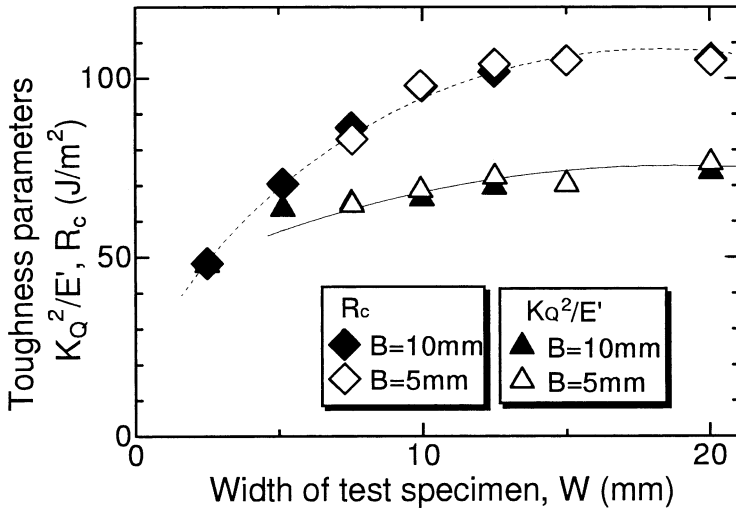


Figure 6. Dependence of the energy fracture toughness parameters, K_Q^2/E' and R_c , on the width W of test specimens in geometrically similar configuration.

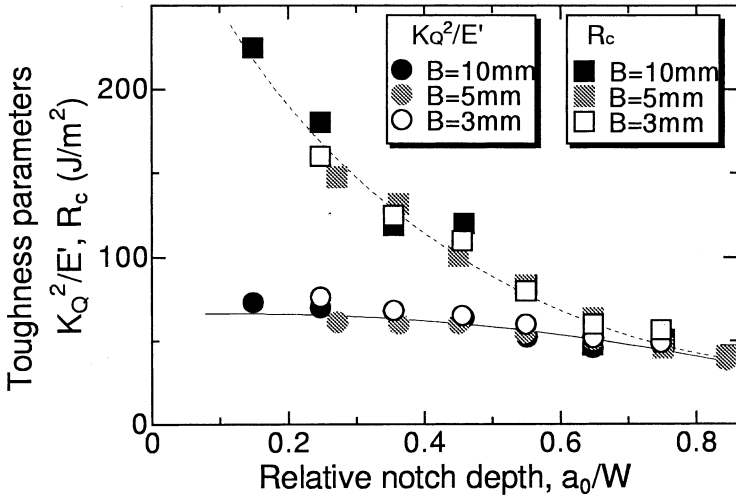


Figure 7. Dependence of the energy fracture toughness parameters, K_Q^2/E' and R_c , on the relative notch depth a_0/W in geometrically nonsimilar configuration.

4. DISCUSSION

4.1. Stress Intensity Derived Fracture Toughness K_Q -The Size-Effect Law-

The failure strength σ_c of brittle materials is given by the following general descriptions in a LEFM-regime [9–12]:

$$\sigma_c = N_W \cdot \frac{K_c}{\sqrt{W}} \tag{3a}$$

$$\sigma_c = N_a \cdot \frac{K_c}{\sqrt{a_0}} \tag{3b}$$

In these expressions, W is a characteristic length (width) of the test specimen, a_0 is a characteristic length of a crack as a fracture origin, α_0 is defined as a_0/W , and both $Y(\alpha_0)$ and $F(\alpha_0)$ are the dimensionless stress intensity factors (shape factors) of the crack. N_W is defined by $c_n/Y(\alpha_0)$ and N_a by $1/[\sqrt{\pi}F(\alpha_0)]$. The parameter c_n is a characteristic coefficient of the test specimen geometry. Equation (3a) has been utilized by Bažant, et. al. for the considerations of size-effect law of geometrically similar test specimens [9,10]. One of the present authors (MS) has applied Eq. (3b) to the discussions of the size-effect law for geometrically nonsimilar test specimens with different notch/crack lengths, and then to the discussions of R-curve studies [11,12]. It must be noticed in a fracture mechanics sense that both Eqs. (3a) and (3b) are equivalent, as pointed out by the present author [11,12].

A “finite nonnegligible fracture process zone” in front of the crack tip gives rise a deviation from the size-effect law prescribed in Eqs. (3a) and (3b). When the characteristic dimension of the frontal process zone c_f becomes significant compared to the characteristic dimensions of W and a_0 , Eqs. (3a) and (3b) must include the nonlinear contributions of the microscopic deformation and fracture in the process zone, and be modified through the replacement of the crack length a_0 with its effective value $a_{\text{eff}} (\equiv a_0 + c_f)$. This modification in Eqs. (3a) and (3b) results in the following formulae of failure strength in their intrinsic expressions;

$$\tau_c = \frac{K_Q}{\sqrt{\bar{w}}} \tag{4a}$$

with the relation of $K_Q = \sqrt{\beta/(1 + \beta)}K_c$, and

$$\hat{\tau}_c = \frac{K_Q}{\sqrt{\hat{a}_0}} \tag{4b}$$

with the relation of $K_Q = \sqrt{\hat{\beta}/(1 + \hat{\beta})}K_c$. In these equations and relationships, $\tau_c (\equiv \hat{\tau}_c) \propto \sigma_c$, $\bar{a}_0 \propto a_0$, $\bar{w} \propto W$, $\beta = \bar{w}/c_f$, and $\hat{\beta} = \bar{a}_0/c_f$. The details of the definitions and their fracture mechanics meanings were given in the literature [9–12]. The intrinsic failure strength τ_c was first introduced by Bažant, et. al [9]. It must be noticed in Eqs. (4a) and (4b) that expressions of τ_c and $\hat{\tau}_c$, the brittleness numbers β and $\hat{\beta}$, and the characteristic dimensions \bar{a}_0 and \bar{w} are, respectively, completely equivalent in a fracture mechanics sense [11]. Accordingly, the differences in the intrinsic strengths τ_c [Eq. (4a)] and $\hat{\tau}_c$ [Eq. (4b)] are only apparent [11,12].

A fracture mechanics estimate of the characteristic size of frontal process zone, c_f , can be made by recasting Eqs. (4a) and (4b) into the following equations [9–12]:

$$\frac{1}{\tau_c^2} = \frac{1}{K_c^2} \bar{w} + \frac{c_f}{K_c^2} \tag{5a}$$

for geometrically similar test specimens, and

$$\frac{1}{\tau_c^2} = \frac{1}{K_c^2} \hat{a}_0 + \frac{c_f}{K_c^2} \tag{5b}$$

for geometrically nonsimilar specimens. In Eqs. (5a) and (5b), use has been made of the equivalence of $\hat{\tau}_c \equiv \tau_c$. Equations (5a) and (5b) indicate an important advantage in the experimental estimate of the plane-strain fracture toughness K_c and the frontal zone size c_f , respectively, from the slope and from the intercept of the linear regression of $1/\tau_c^2$ vs. \bar{w} and $1/\tau_c^2$ vs. \bar{a}_0 ; their linear regressions are shown in Fig. 8 for both geometrically similar and nonsimilar specimens. All of the data fall on a single regression line with some experimental variations; yielding $K_c = 0.85 \pm 0.1 \text{MPa}\sqrt{\text{m}}$ and $c_f = 0.8 \pm 0.1 \text{mm}$. The *in situ* observation of the frontal micro-cracking zone of the present graphite material with a scanning electron microscope supports this fracture mechanics estimate of c_f [4].

Once the c_f -value was estimated, it is possible to calculate the brittleness number β ($\equiv \bar{a}_0/c_f, \bar{w}/c_f$), and then K_Q can be universally plotted against β for all the test specimens with geometrically similar and nonsimilar configurations, as illustrated in Fig. 9 in its normalized form, where the solid line indicates the theoretical prediction of $K_Q/K_c = \sqrt{\beta/(1 + \beta)}$.

4.2. Potential Energy-Derived Fracture Toughness, R_c -The Irwin’s Similarity-

4.2.1. Nonlinear Deformation and Fracture of Polycrystalline Graphite

The stress vs. strain curves (S-S curves) of various types of carbon and graphite materials have been studied in tensile, compressive, and flexural tests [13]. Most of these S-S curves are nonlinear (non-Hookean), and have a permanent residual strain after complete unloading, resulting in a hysteresis loop during a loading/unloading cycle. The apparent elastic moduli (the tangent of the loading S-S curves at the respective strain values) are always greater at small strains than at large strains. Two of the major microscopic origins of the mechanical non-linearity of carbon and

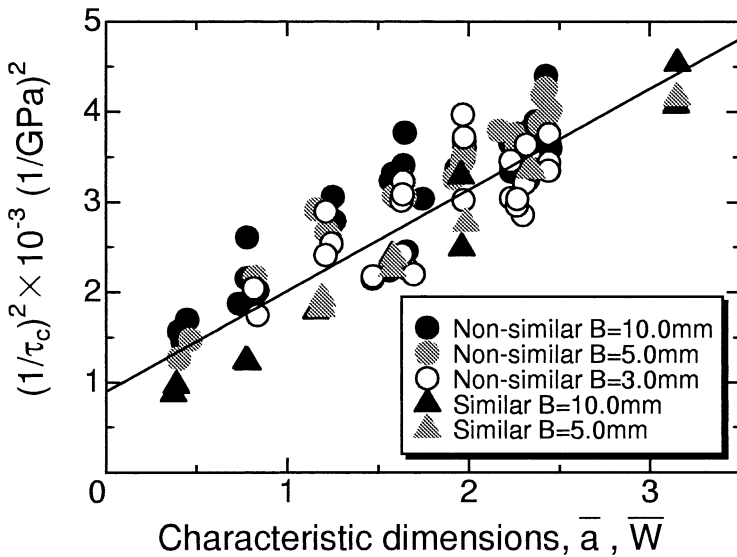


Figure 8. Linear regression of the intrinsic failure strength τ_c and the characteristic dimensions, \bar{a} and \bar{W} , of test specimen.

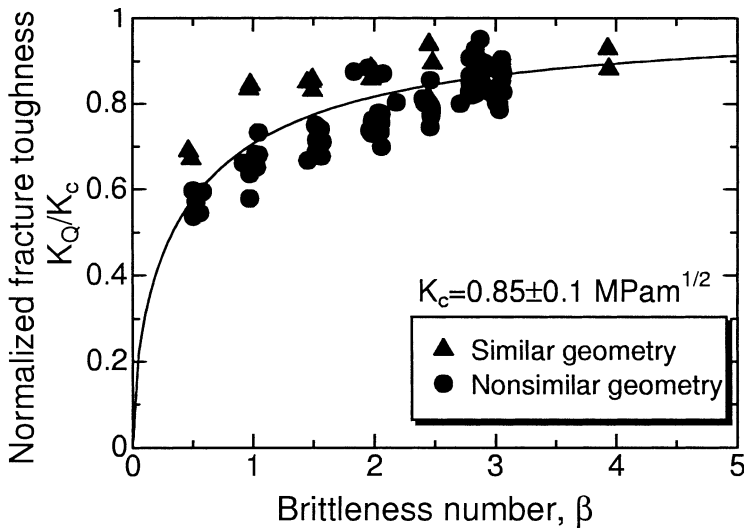


Figure 9. The universal plot of normalized fracture toughness K_Q/K_c as a function of the brittleness number β .

graphite materials include (1) dislocation-related plastic slip along graphite basal planes, and (2) stress induced microcracking [13]. Due to the significant crystallographic anisotropy of carbon and graphite materials, numerous microcracks (Mrozowsky microcracks) are induced in the carbonization and graphitization processes of these materials. These microcracks pre-existing in the material is very susceptible to applied external stresses/strains, leading to sizable stress-induced microcracking [4].

The plastic-slip always results in a nonlinear S-S curve with a finite residual strain after complete unloading. In contrast, the microcracking-induced nonlinear S-S loading curve and the subsequent unloading hysteresis do not leave a permanent residual strain after complete unloading, unless the stress-induced microcracks significantly relieve residual stresses. Crack-face bridging and interlocking also contribute significantly to the permanent residual strain after complete unloading.

4.2.2. Non-Linear Fracture with Irreversible Deformations

Burns and Swain [6], and then Sakai [4,5] examined the energy principle for the fracture with a finite amount of irreversible deformation that is associated with crack extension, yielding a residual load-point displacement δu_{ir} after an incremental crack extension of δa .

Figure 10 schematically illustrates two different types of crack extension problems for a linear elastic body (material A) and a nonlinear inelastic body (material B) with irreversible load-point displacement (δu_{ir}) after an infinitesimal crack extension δa at a constant critical load P_c . The total amount of load-point displacement δu induced by this virtual crack extension δa of the inelastic material B is given by the sum of the elastic and irreversible displacements, δu_e and δu_{ir} , i.e., $\delta u = \delta u_e + \delta u_{ir}$. This fracture mechanics consideration for residual load-point displacement affords the following modification of the Irwin's similarity [4–6]:

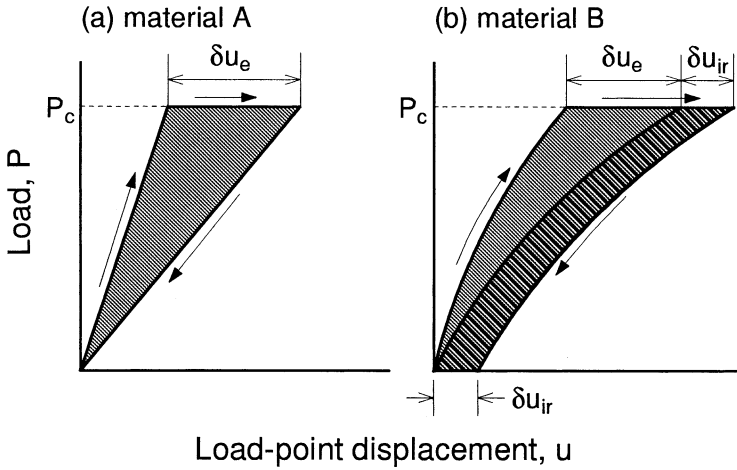


Figure 10. Load P vs. load-point displacement u diagrams for (a) a linear elastic material A, and (b) a nonlinear inelastic material B with a finite offset displacement δu_{ir} .

$$R_c = (1 + 2\eta) \frac{K_Q^2}{E'} \tag{6}$$

where η is defined by

$$\eta = \frac{\delta u_{ir}/\delta a}{\delta u_e/\delta a} \left(\equiv \frac{\delta u_{ir}}{\delta u_e} \right) \tag{7}$$

Accordingly, η stands for the fraction of irreversible load-point displacement δu_{ir} relative to the elastic displacement δu_e during a virtual crack extension of δa . The Irwin’s similarity must be modified by a factor of $1 + 2\eta$ for an inelastic body with a finite residual offset load-point displacement; Eq. (7) necessarily becomes the Irwin’s LEFM expression when $\eta = 0$ (that is, $\delta u_{ir} = 0$).

4.2.3. Deviation from the Irwin’s Similarity

In LEFM-regime, the stress-intensity-derived fracture toughness K_c (or K_Q) and the potential-energy derived fracture toughness R_c is related by the Irwin’s similarity of $R_c = K_c^2/E'$ or $= K_Q^2/E'$. The deviations from Irwin’s similarity are well demonstrated in Fig 6 for geometrically similar specimens and in Fig. 7 for geometrically nonsimilar specimens. The deviation is significantly dependent on the geometries and the dimensions (a/W and W) of test specimen. It is not well understood in the present study what kinds of microscopic processes and mechanisms dictate the size-effect laws through which quantitatively described is the deviation from the Irwin’s similarity. Burns and Swain related the finite amount of η -value of zirconia ceramics to the compressive irreversible deformations via martensitic phase-transformation in the crack-wake region behind a propagating crack [6]. In the present study for a *critical crack (not propagating crack)* of polycrystalline graphite, however, the wake-effect is not the origin for providing the finite discrepancies between R_c and K_c^2/E' observed in Figs. 6 and 7.

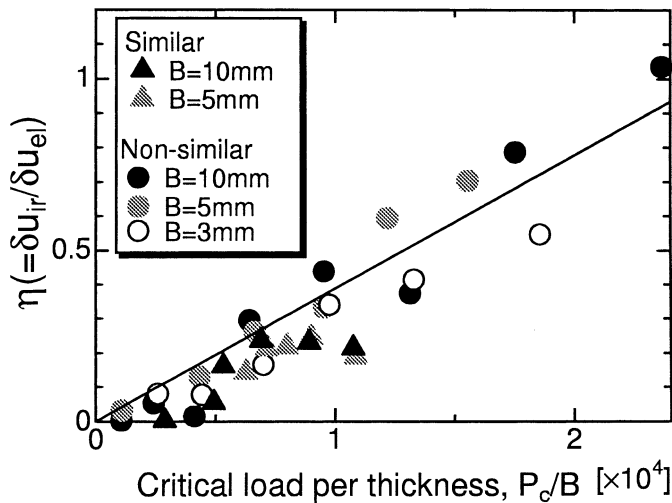


Figure 11. The nonlinear parameter η plotted against the critical load per thickness P_c/B for all the test specimens in geometrically similar and nonsimilar configurations.

As discussed in the preceding section, the deviation from the Irwin's similarity can be quantitatively expressed in a phenomenological manner by the dimensionless parameter η . The η -values of all the test specimens examined in this study are plotted in Fig. 11 against the critical load per unit thickness of test specimen, P_c/B . As clearly demonstrated in Fig. 11, there exists a strong correlation between η and P_c/B , though some experimental variations are included. This correlation implies that the deviation from the Irwin's similarity is directly enhanced by the critical load P_c applied to the specimen, being independent of the fracture mechanics requirement, "how large or small the notch/crack length is". This fact suggests that the deviation is not related to the presence of a notch or a crack itself, but is related to the stress/strain filed in the locations away of the crack-tip process zone.

Examples of the stress distributions [the normal stresses (tensile/compressive stresses) along the longitudinal direction (x -direction) of specimen] in three-point flexural configuration are shown in Fig 12 for test specimens with three different relative notch/depths ($a_0/W = 0.1, 0.5,$ and 0.9) at their respective critical loads. The numerical calculations were made in a finite element method (FEM) (ANSYS, Ver. 5.3, ANSYS, Inc., IL., USA). As clearly seen in Fig. 12, the stress-values away of the notched area are rather large both in tensile and compressive stresses for the specimen with a relatively small notch depth of $a_0/W = 0.1$, resulting from the rather large value of P_c . In contrast to the small notch depth, the specimen with a relatively large notch depth of $a_0/W = 0.9$ has none of large stresses outside the notch-tip region. This is resulted from the very smaller critical load P_c for test specimens with a larger value of a_0/W . The significant discrepancy between R_c and K_Q^2/E' for the smaller a_0/W -values and its diminishing nature for $a_0/W > 0.7$ observed in Fig. 7 have a good correlation to the stress distributions of test specimens demonstrated in Fig. 12. These FEM-results combined with the considerations for the characteristic non-linear microscopic deformation/fracture processes given in Sec. 4.2.1. may lead to a rather good understanding for the deviation from the Irwin's similarity observed in the present polycrystalline graphite. Accordingly, it may be well concluded that the

Stress distributions (σ_x) at the critical load P_c

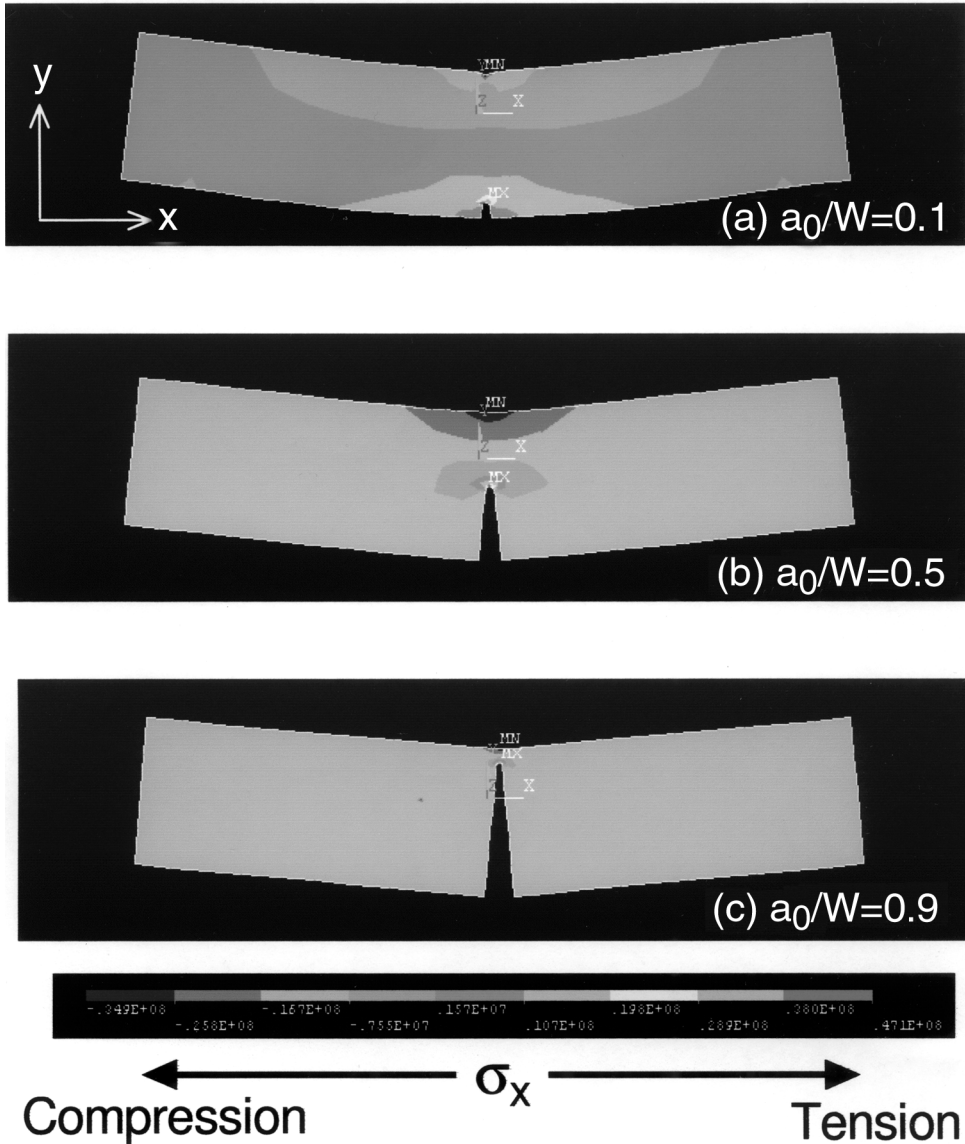


Figure 12. Numerical results of finite element analysis for the stress distribution profile (normal stresses, σ_x) of the specimens with relative notch depths of $a_0/W = 0.1, 0.5,$ and 0.9 at the respective critical loads P_c , illustrating a significant difference in the tensile/compressive distribution profiles in the locations away of the cracked region.

excess energy ($R_c - K_Q^2/E'$) is consumed in the area outside the cracked region, where the stress/strain field is large enough for operating inelastic micro-deformations and micro-fractures (i.e., plastic slippage along graphite basal planes and stress-induced microcracking).

5. CONCLUSION

Nonlinear fracture of a polycrystalline graphite was examined. Fracture mechanics test specimens (3-point flexural rectangular bars) with geometrically similar as well as non-similar configurations were utilized to measure the stress intensity-derived fracture toughness (K_c , K_Q) and the potential energy-derived fracture toughness R_c . The dependences of these toughness parameters on the geometries and dimensions allowed an estimate of the size of crack-tip frontal process zone through the considerations of the size-effect law of fracture toughness.

The Irwin's similarity relationship of $R_c = K_c^2/E'$ and the deviation from this relationship in nonlinear fracture mechanics regime were studied as functions of the dimensions and geometries of test specimens. In nonlinear fracture regime, R_c is always larger than K_c^2/E' (or K_Q^2/E'). The excess energy, $R_c - K_c^2/E'$, was experimentally expressed by an increasing function of P_c/B , independent of the magnitude of notch/crack depth, and being attributed to the energies consumed in the regions away of the cracked area. This excess energy consumption was intimately related to the characteristic microcracking in polycrystalline graphite, as well as to the intrinsic plastic slippage of graphite basal planes. These microscopic processes and mechanisms leading to the excess energy consumptions may not contribute to the resistance to main crack extension in a dead load (failure for constant loading). However, in mechanical conditions of fixed grips (failure under a constraint displacement) and of thermal strains, these microscopic deformations and fractures operating outside the cracked region may significantly enhance the mechanical relaxation of local stresses and strains at crack-tip, and then result in a sizable reduction of the driving force for the extension of main crack, contributing to toughening a cracked body.

REFERENCES

1. D. Broek, *Elementary Engineering Fracture Mechanics* (Martinus Nijhoff, Dordrecht, 1986), Chap. 5.
2. R.W. Hertzberg, *Deformation and Fracture Mechanics of Engineering Materials* (Wiley, New York, 1983), Chap. 8.
3. M.F. Kanninen and C.H. Popelar, *Advanced Fracture Mechanics* (Oxford University Press, New York, 1985), Chap. 3.
4. M. Sakai, J. Yoshimura, Y. Goto, and M. Inagaki, *J. Am. Ceram. Soc.*, **71**[8] 609–616(1988).
5. M. Sakai and R.C. Bradt, *Int. Mater. Rev.*, **38**[2] 53–78(1993).
6. S.J. Burns and M.V. Swain, *J. Am. Ceram. Soc.*, **69**[3] 226–230(1986).
7. S.M. Barinov and M. Sakai, *J. Mater. Res.*, **9**[6] 1412–1425(1994).
8. *Stress Intensity Factors Handbook, Vol. 1*, edited by Y. Murakami (Pergamon, Oxford, 1987), pp. 13–15.
9. Z.P. Bažant and P.A. Pfeiffer, *Am. Concr. Inst. Mater. J.*, **Nov.-Dec.**, 463–480(1987).
10. Z.P. Bažant and M. Kazemi, *J. Am. Ceram. Soc.*, **73**[7] 1841–1853(1990).
11. M. Sakai and H. Kurita, *Fracture of Brittle Disordered Materials: Concrete, Rock and Ceramics*, edited by G. Baker and B.L. Karihaloo (E&FN Spon, London, 1995), pp. 227–245.
12. M. Sakai and H. Kurita, *J. Am. Ceram. Soc.*, **79**[12] 3177–3184(1996).
13. B.T. Kelly, *Physics of Graphite* (Applied Science, London, 1981), Chap. 3.

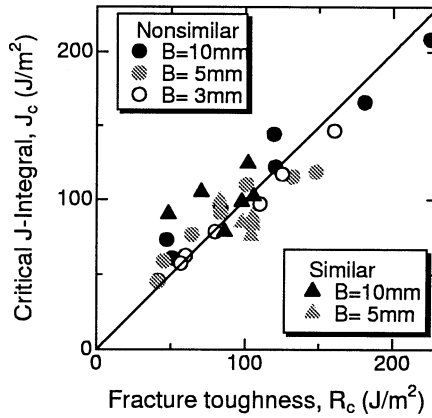


Figure 13. One-to-one correlation between J_c and R_c .

APPENDIX

Rice was the first to recognize the potential use of J-integral in elastic-plastic fracture mechanics, after Eshelby was apparently the first to derive the integral [1–3]. The J-integral of a “critical” crack, J_c , is actually equivalent to R_c defined in Eq. (2) combined with the schematic procedure in Fig. 2. For the case of a plate containing a deep notch and subjected to pure bending, Rice found that [1–3]

$$J_c = \frac{2}{bB} \int_0^{u_c} P du \tag{8}$$

where b is the length of the remaining un-notched ligament. The correlation between the R_c -values estimated in Eq. (2) and the J_c -values thus determined in Eq. (8) is shown in Fig. 13, demonstrating a rather good one-to-one correlation with some experimental variations. Accordingly, the discussions for the deviation from the Irwin’s similarity in terms of R_c , and for the dependence of η on P_c/B made in the present study are made without any essential modifications, even if we utilize the critical J-integral, J_c , instead of R_c .

FRAGMENTATION OF CERAMICS IN RAPID EXPANSION MODE

Spandan Maiti, Philippe H. Geubelle,
and Krishnan Rangaswamy¹

1. INTRODUCTION

The study of the fragmentation process goes back to more than a century, motivated primarily by problems related to mining and ore handling (Grady and Kipp, 1985). Various theories have been proposed to predict the fragmentation stress and the fragment size and distribution. But the investigations are generally case specific and relate to only a narrow set of fragmentation processes. A number of theoretical studies of dynamic fragmentation in a rapidly expanding body can be found in the literature. For example, the study summarized in (Grady, 1982) presents a model based on a simple energy balance concept between the surface energy released due to fracture and the kinetic energy of the fragments. Subsequent refinements of the energy balance model have been proposed by (Glenn and Chudnovsky, 1986), which take into account the strain energy of the fragments and specify a threshold stress below which no fragmentation occurs. These models assume that the fracture events are instantaneous and occur simultaneously. Evidently, these assumptions are quite restrictive and these models cannot take into account the transient nature of the fragmentation process after the onset of fracture in the material. A more recent model proposed by (Miller et al., 1999) however takes into account this time-dependent nature of the fragmentation event and the distribution of flaws of various strengths in the original material.

¹ Department of Aeronautical and Astronautical Engineering, University of Illinois at Urbana-Champaign, Urbana, USA.

Attempts to model the fragmentation phenomenon numerically are quite recent (Camacho and Ortiz, 1996, Miller et al., 1999), and some success has been reached through the use of cohesive modeling. Although the cohesive finite element models used so far have been shown to be effective in simulating the dynamic crack propagation in the material, they do not take into account the effect of the microstructure inherent to ceramic materials. An exception can be found in the recent work by (Espinosa et al., 1998), although the emphasis of this work is less on the fundamental problem of fragmentation and more on the numerical modeling of rod on rod impact experiments. Also, the cohesive models are sensitive to the spacing and size of the cohesive surfaces making convergence difficult to achieve.

In this paper, we study the fundamental fragmentation problem of a specimen with an inherent granular microstructure that is subjected to a rapid expansion. Of special interest are the effects of the average grain size, initial strain rate and cohesive failure model parameters (strength and toughness) on the fragmentation process.

2. NUMERICAL SCHEME

The key elements of the numerical scheme used in this study are its ability to incorporate the granular microstructure of the ceramic material, to simulate the spontaneous initiation, propagation and branching of intergranular cracks and subsequent fragmentation of the body, to account for inertial and finite kinematics effects and to capture the complex contact events taking place between the fragments.

To simulate the spontaneous dynamic motion of cracks, we use a 2-D plane strain cohesive/volumetric finite element (CVFE) scheme that has shown great success in the simulation of various dynamic fracture events in brittle media (Xu and Needleman, 1994, Camacho and Ortiz, 1996, Geubelle and Baylor, 1998). As its name indicates, the numerical method is based on the combination of conventional (volumetric) elements used to model the mechanical response of the ceramic material and interface (cohesive) elements introduced to simulate the intergranular failure process. Figure 1 schematically illustrates the CVFE concept. The volumetric elements

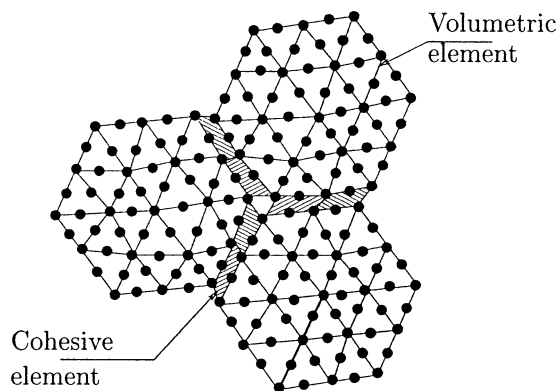


Figure 1. Schematic of the grain-based CVFE scheme, showing three grains discretized with 6-node volumetric elements and linked with 6-node cohesive elements placed along their boundary. The cohesive elements are shown in their deformed configuration: they initially have no thickness and adjacent nodes are superposed.

used in the present study are six-node triangular elements, with a constitutive response described by a linear isotropic relation between the second Piola-Kirchhoff stress tensor S and the Lagrangian strain tensor E (Geubelle and Baylor, 1998). A nonlinear kinematic description is used here to allow for possible large rotations associated with the fracture event. The cohesive elements placed along the grain boundaries are characterized by a bilinear rate-independent failure law relating the displacement jump vector (Δ) to the cohesive traction vector (T) acting across the cohesive surfaces Γ_c :

$$T_n = \frac{S}{1-S} \frac{\Delta_n}{\Delta_{nc}} \sigma_{max}, \quad T_t = \frac{S}{1-S} \frac{\Delta_t}{\Delta_{tc}} \tau_{max}, \tag{1}$$

where the subscripts n and t denote normal and tangential components, respectively, σ_{max} and τ_{max} are the tensile and shear failure strengths, while Δ_{nc} and Δ_{tc} are the critical opening and shear displacement jumps. The evolution of the damage process is quantified by the monotonically decreasing damage parameter S defined as (Geubelle and Baylor, 1998, Bi et al., 2002)

$$S = \min\left(S_{min}, \max(0, 1 - \|\tilde{\Delta}\|)\right), \tag{2}$$

where $\tilde{\Delta}$ denotes the normalized displacement jump vector

$$\tilde{\Delta} = \left\{ \begin{matrix} \tilde{\Delta}_n \\ \tilde{\Delta}_t \end{matrix} \right\} = \left\{ \begin{matrix} \Delta_n/\Delta_{nc} \\ \Delta_t/\Delta_{tc} \end{matrix} \right\}. \tag{3}$$

As the grain boundary fails, the value of S gradually decreases from an initial value close to unity to zero, point at which complete failure is achieved. The coupling between normal and tangential failure in mixed-mode situations is captured by defining S in terms of the L_2 -norm of the normalized displacement jump vector $\tilde{\Delta}$, as indicated by Equation 2 and illustrated in Figure 2.

To prevent overlapping of adjacent grains, the damage parameter S is kept to its initial value S_{init} close to unity when the normal displacement jump Δ_n becomes negative. As illustrated in Figure 2(a), this approach results in very high repulsive normal traction along the contacting surfaces. This simple explicit contact enforcement scheme along with intermittent use of more sophisticated optimization-based

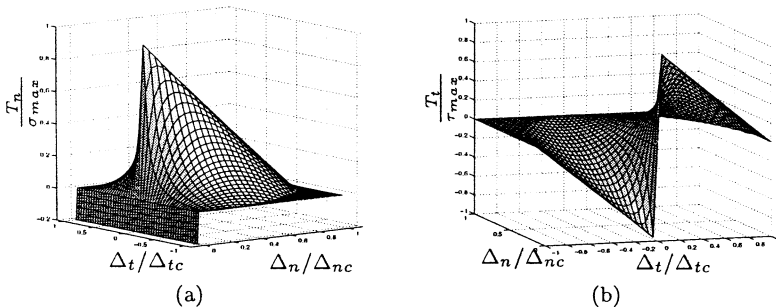


Figure 2. Cohesive failure model: variation of the normal (a) and tangential (b) components of the cohesive traction vector T with respect to the normal (Δ_n) and shear (Δ_t) crack opening displacements, showing the coupling between tensile and shear failure.

contact algorithm designed for angular fragments (Kane et al., 1999) is appropriate for the present study dedicated to fragmentation due to tension. Once the fragmentation process is complete, the overlap of the fragments does not affect the phenomena we are investigating, so no contact algorithm is invoked at this stage.

The finite element implementation is based on the principle of virtual work. Since the capture of the dynamic fracture process requires very small time steps, an explicit central difference time stepping scheme is used in this investigation, with the time step size Δt chosen as 4% of the limiting (Courant) value.

To generate the granular microstructure, a two-step discretization process is adopted. The grains are first created through a Voronoi tessellation of the ceramic specimen, leading to a relatively uniform size distribution. The grains are then discretized with 6-node triangular elements by Delaunay triangulation and 6-node cohesive elements are inserted along the grain boundaries. For more detail about the mesh generation, see (Maiti and Geubelle, 2003). To calculate the number of fragments, we have generated a graph with each grain in the domain as a node, and have computed the connected components of the graph. A breadth-first algorithm for finding the spanning forest of a graph (Nijenhuis and Wilf, 1978) is utilized for this purpose.

3. PROBLEM DESCRIPTION

Figure 3 depicts the specimen used in our fragmentation study. The specimen is rectangular with the upper and lower boundaries subjected to a constant velocity V . We assume that the specimen is in a state of rapid expansion just after an impact and thus have a constant initial strain throughout the domain. For this reason, we subject all the points of the computational domain to a linear initial velocity distribution with the magnitude equal to V at the ends of the specimen, as illustrated in Figure 3.

The material used for all the simulations is alumina, whose properties are as follows: Young's modulus $E = 400 \text{ GPa}$, Poisson's ratio $\nu = 0.27$ and density

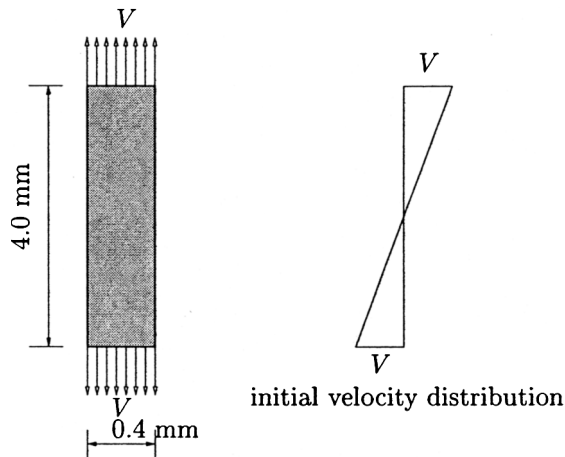


Figure 3. Geometry and initial and boundary conditions of the test specimen used in the fragmentation study.

$\rho = 3800 \text{ kg/m}^3$. The mode I and mode II fracture toughnesses are taken to be the same: 69.5 J/m^2 . The cohesive strength in the normal (σ_{max}) and tangential (τ_{max}) directions are always chosen to have the same magnitude. For most of the simulations presented hereafter, this value is varied between 0.1 and 4 *GPa*. The initial value of the damage parameter $S_{initial}$ is chosen as 0.98. Five average grain sizes are chosen for this study: 120, 100, 80, 60, and 40 μm , yielding a total of 187, 227, 369, 636 and 1406 grains, respectively. Different grain distributions for a single average size are also examined. Figure 4 shows a sample of these different grain size distributions.

In the discussion that follows, we repeatedly use the term *damage index* (DI). This parameter is defined as the ratio of failed cohesive elements to the total number of cohesive elements and is expressed in percent. As the length of all cohesive elements is almost the same, this parameter gives a good indication of the extent of fracture in the specimen.

4. RESULTS AND DISCUSSION

4.1. General Features

Let us start the result discussion by studying the general features of the fragmentation process for a specimen with an average grain size of 60 μm and a failure strength of 1 *GPa* subjected to an initial strain rate $\dot{\epsilon}$ of $0.5 \times 10^5/s$. The evolution of the DI is presented in Figure 5 for the grain distributions shown in Figure 4(b), (c) and (d). As apparent in Figure 5, the fragmentation process is not instantaneous but initiates at about 0.165 μs to end at approximately 0.25 μs . While some differences are noted between the three grain distributions giving some measure on the variability of the

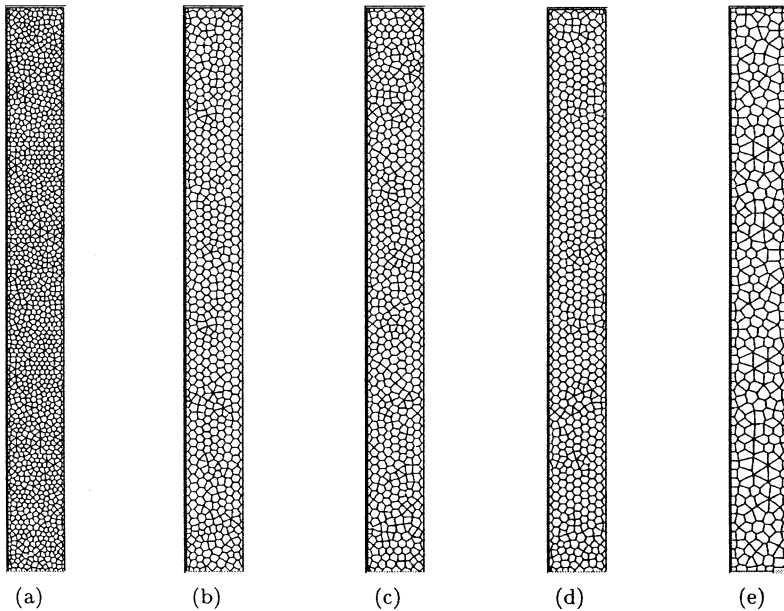


Figure 4. Granular microstructure of the sample with an average grain size of (a) 40 μm , (b-d) 60 μm and (e) 80 μm . For figures (b), (c) and (d), the average grain size is the same but the distributions are different.

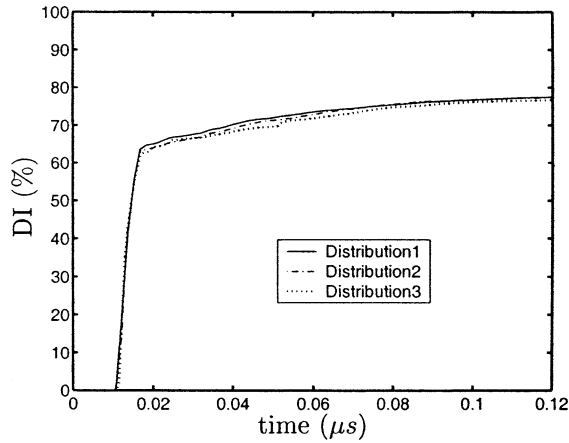


Figure 5. Evolution of the damage index with time for a specimen with an average grain size of $60 \mu\text{m}$ with the three distributions shown in Figures 4(b)–(d).

results on the microstructure, the overall behavior is very similar between the three cases. In the remainder of this paper, we use the microstructure shown in Figure 4(b).

As shown in Figure 6(a), the loading rate has a very strong influence on the initiation of fragmentation and on the final value of the damage index, i.e., on the extent of fragmentation. As $\dot{\epsilon}$ increases, the fragmentation process starts sooner and leads to more extensive damage. The dependence of initiation time on the initial strain rate is summarized in Figure 6(b) and is qualitatively similar to that presented in (Miller et al., 1999).

The evolution of the fragmentation process for a specimen with an average grain size of $60 \mu\text{m}$ and a cohesive strength of 1 GPa subjected to $\dot{\epsilon} = 3 \times 10^5 / \text{s}$ is illustrated by the four snapshots shown in Figure 7. Initially, the fragment size is relatively large and, for values of DI less than 50%, there are only a few fragments. As time progresses, however, the cracks coalesce and the number of fragments increases rapidly.

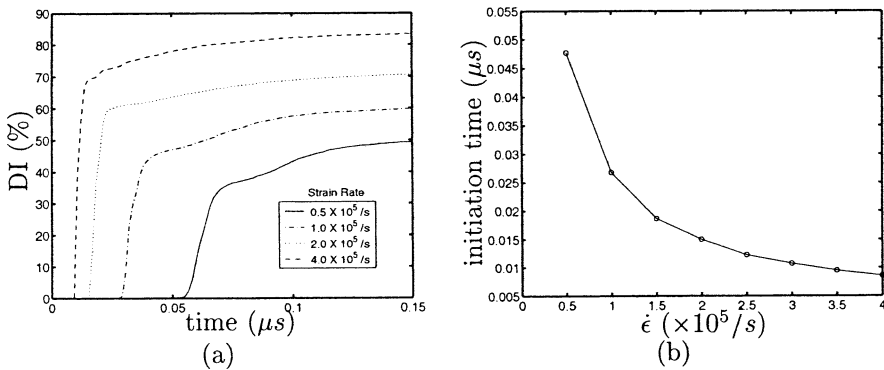


Figure 6. Effect of the initial strain rate $\dot{\epsilon}$ on the evolution of the damage index (DI) (a) and on the initiation time (b) for a ceramic specimen with an average grain size of $60 \mu\text{m}$ and a cohesive strength of 1 GPa .

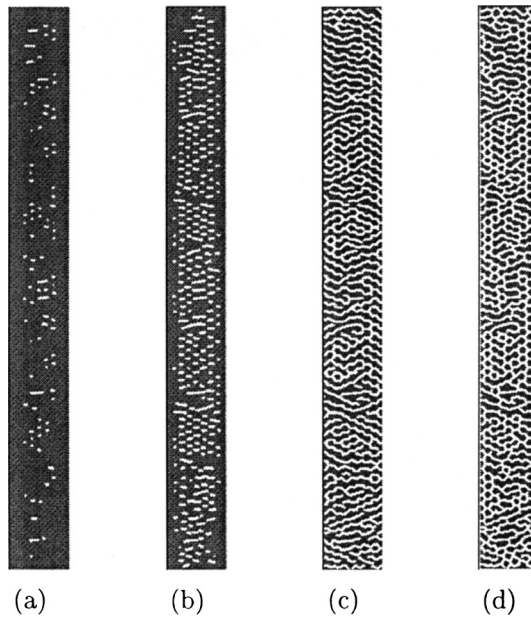


Figure 7. Snapshots of the fragmentation process for a specimen with an average grain size of $60 \mu m$ at (a) $t = 0.0116 \mu s$ (DI = 5%), (b) $t = 0.0122 \mu s$ (DI = 20%), (c) $t = 0.0168 \mu s$ (DI = 63%) and (d) $t = 0.1985 \mu s$ (DI = 79%). The cohesive strength is $1 GPa$ and $\dot{\epsilon} = 3 \times 10^5 /s$.

To quantify the evolution of the fragment size during the fragmentation process, we present in Figure 8 the cumulative distribution of fragment areas at three instants during the failure process for which DI = 63,70 and 79%. As apparent in that figure, the curves shift to the left and become steeper as fragment size decreases. The numerical distribution curve corresponding to DI = 79% is compared in Figure 9 to two models available in the literature: the so-called Mott distribution (Mott, 1947) and the linear exponential distribution (Grady and Kipp, 1985), showing better

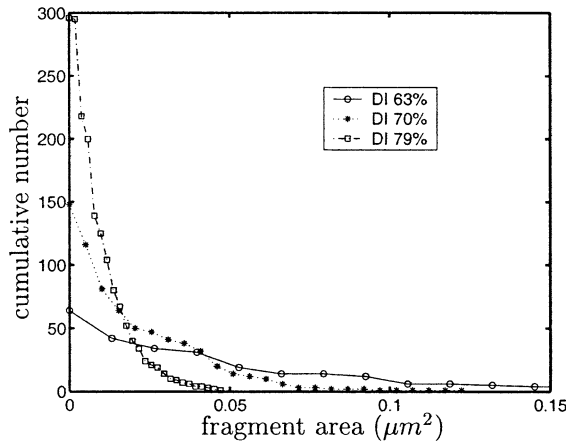


Figure 8. Cumulative distribution of fragment areas at (a) DI = 63%, (b) DI = 70% and (c) DI = 79% for the case shown in Figure 7.

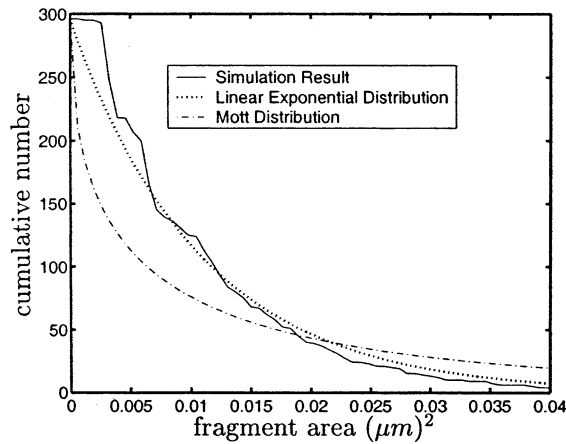


Figure 9. Fit of linear exponential distribution and Mott distribution for the curve $DI = 79\%$ shown in Figure 8.

agreement with the latter. This agreement with the linear exponential distribution is observed throughout the fragmentation process after the specimen starts breaking into multiple fragments.

4.2. Effect of Cohesive Parameters

To study the effect of the cohesive strength on the fragmentation process, a series of simulations have been performed with a range of cohesive strength values (from 0.10 to 4 *GPa*) but keeping the fracture toughness unchanged in all the cases. The average grain size is 60 μm and we assume the tensile (σ_{max}) and shear (τ_{max}) cohesive strengths to be equal.

Figure 10 shows how the cohesive strength affects the final value of the damage index, i.e., the final extent of fragmentation. Note that the failure of all cohesive

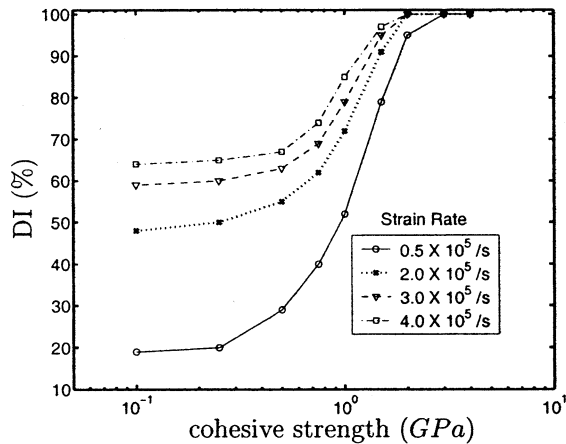


Figure 10. Variation of final damage index with cohesive strength for different initial strain rates. The average grain size is 60 μm .

surfaces is observed for high values of the strength (superior 2 *GPa*). It can thus be concluded that, for truly brittle materials with low fracture toughness and high fracture initiation stress, the fragmentation does not depend on the initial strain rate (Glenn and Chudnovsky, 1986) as the fragmentation process is always complete. The results also indicate that, as the cohesive strength is reduced, the relative portion of failed cohesive elements experiences first a sharp drop followed by a plateau for small value of the strength (less than 0.5 *GPa*). Also, as expected, final DI increases as the initial strain rate is increased, though the curves retain their general trend. The presence of the drop is to be expected: as the cohesive strength is decreased, the material reaches the fracture initiation point at earlier time for the same initial strain rate. The material has thus less time to store energy to be expended during the fracture event. But it is interesting to note the existence of a strain rate dependent lower bound for the final damage index for lower cohesive strengths.

The variation of the initiation time of the fragmentation process (i.e., time at which the first cohesive failure is detected) with respect to the cohesive strength is presented in Figure 11 for constant values of the fracture toughness. For higher values of the cohesive strength, the initiation time decreases with decreasing cohesive strength since the material points in the specimen reach the fracture initiation stress sooner. For smaller cohesive strengths, however, the trend is reversed and the initiation time increases with decreasing strength reflecting the corresponding increase of the critical displacement jump values Δ_{nc} and Δ_{lc} . As shown in Figure 11, an increase in $\dot{\epsilon}$ results in a decrease of the initiation time while keeping the nature of the curves same.

4.3. Effect of Grain Size

In this section we study the effect of the average grain size on the fragmentation process. For that purpose we have chosen specimens with five different grain sizes: 40, 60, 80, 100 and 120 μm . First, we present the effect of average grain size on the

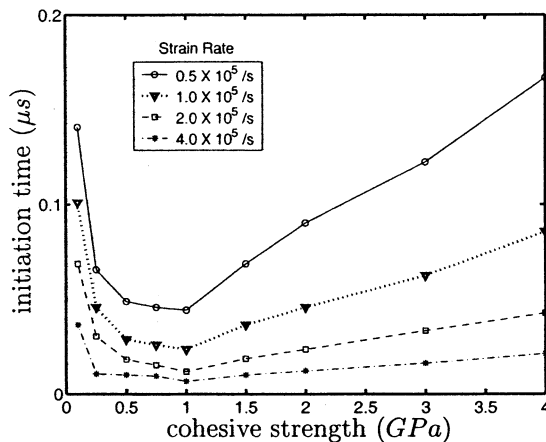


Figure 11. Variation of fragmentation initiation time with cohesive strength for different initial strain rates. The average grain size is 60 μm and the fracture toughness is kept constant.

initiation time of fragmentation. As observed in Figure 12, the grain size does not affect the initiation time, especially for high values of the initial strain rate $\dot{\epsilon}$. As the grain size decreases, the density of cohesive elements increases. But since the cohesive strength is kept constant, the time required for the cohesive traction to reach the critical value and initiate the failure process does not depend significantly on the number of available fracture paths.

The average grain size has however a strong influence on the evolution and extent of the fragmentation process, as illustrated in Figure 13, which presents the evolution of the damage index for the same five specimens as those used in Figure 12. As noted earlier, the initial phase of the fragmentation process is independent of the microstructure. However, the grain size affects the final value of the damage index, which increases as the grains become larger. This trend can be explained by the fact that the ratio of energy required for fragmentation to the energy available varies with the inverse of grain size, and hence the extent of final fragmentation increases with an

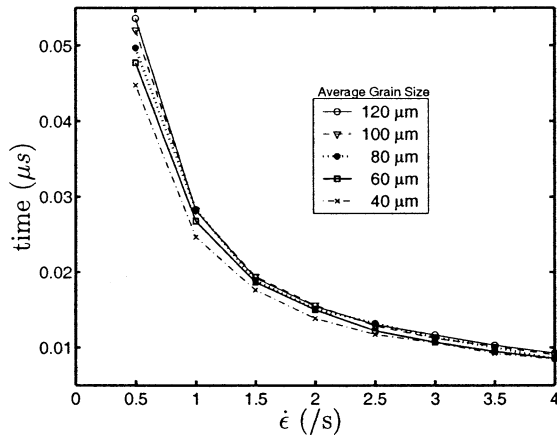


Figure 12. Variation of the initiation time with initial strain rate for different average grain sizes. The cohesive strength $\sigma_{\text{max}} = \tau_{\text{max}} = 1.0 \text{ GPa}$.

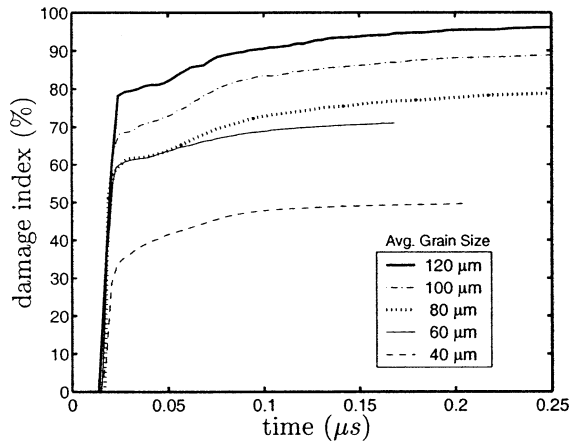


Figure 13. Evolution of damage index for different average grain size of the material. Cohesive strength $\sigma_{\text{max}} = \tau_{\text{max}} = 1.0 \text{ GPa}$ and $\dot{\epsilon} = 2 \times 10^5 / \text{s}$.

increase of average grain size. Note that, for higher cohesive strengths (in excess of 2 GPa), the damage index reaches 100% for all different grain sizes as the strain and kinetic energy stored in the system prior to the failure process is higher due to increased fragmentation initiation time.

5. CONCLUSIONS

In this paper we have studied the fragmentation process of a rapidly expanding bar using a numerical scheme relying on a grain-based mesh generation technique and a cohesive/volumetric finite element method which is able to capture dynamic intergranular fragmentation events. We have observed that the fragmentation process is not instantaneous and that the initiation time decreases drastically with the increase in initial strain rate. Also, we have shown that the cumulative frequency of the fragment area can be estimated reasonably by a linear exponential distribution throughout the fragmentation process.

6. ACKNOWLEDGEMENTS

This research project is funded by NSF through the Career Award CMS-9734473. The grain-based finite element discretizations have been obtained with the help of the mesh generation software TRIANGLE originally developed by J. R. Shewchuk.

REFERENCES

- Bi, X., Li, Z., Geubelle, P. H., and Lambros, J. (2002). Dynamic debonding and frictional push-out in model composite systems: numerical analysis. *Mech. of Mater.*, 34:433–446.
- Camacho, G. T. and Ortiz, M. (1996). Computational modeling of impact damage in brittle materials. *Int. J. Solids Structures*, 33(20–22):2899–2938.
- Espinosa, H. D., Zavattieri, P. D., and Dwivedi, S. K. (1998). A finite deformation continuum/discrete model for the description of fragmentation and damage in brittle materials. *J. Mech. Phys. Solids*, 46(10):1909–1942.
- Geubelle, P. H. and Baylor, J. (1998). Impact-induced delamination of composites: a 2-D simulation. *Composites B*, 29:589–602.
- Glenn, L. A. and Chudnovsky, A. (1986). Strain energy effects on dynamic fragmentation. *J. Appl. Phys.*, 59:1379–1380.
- Grady, D. E. (1982). Local inertial effects in dynamic fragmentation. *J. Appl. Phys.*, 53:322–325.
- Grady, D. E. and Kipp, M. E. (1985). Geometric statistics and dynamic fragmentation. *J. Appl. Phys.*, 58:1210–1222.
- Kane, C., Repetto, E. A., Ortiz, M., and Marsden, J. E. (1999). Finite element analysis of nonsmooth contact. *Comp. Meth. Appl. Mech. Engrg.*, 180:1–26.
- Maiti, S. and Geubelle, P. H. (2003). Mesoscale modeling of dynamic fracture of ceramic materials. To appear in *Comp. Meth. Engr. Sci.*
- Miller, O., Freund, L. B., and Needleman, A. (1999). Modeling and simulation of dynamic fragmentation in brittle materials. *Int. J. Fracture*, 96:101–125.
- Mott, N. F. (1947). Fragmentation of shell cases. *Proc. Royal Soc.*, A189:300–305.
- Nijenhuis, A. and Wilf, H. S. (1978). *Combinatorial Algorithms For Computers and Calculators*. Academic Press, 2nd edition.
- Xu, X.-P. and Needleman, A. (1994). Numerical simulation of fast crack growth in brittle solids. *J. Mech. Phys. Solids*, 42:1397–1434.

EXPERIMENTAL APPROACH TO MICROFRACTURE PROCESS OF CERAMICS UNDER THERMAL SHOCK

Shuichi Wakayama, Kousuke Nishino, Kouhei Kubota,
Toshiya Wada and Satoshi Kobayashi

1. INTRODUCTION

The thermal shock fracture behavior of ceramics has been investigated using traditional testing methods such as the water quench in which the critical temperature difference, where samples are subjected to severe damage, is used as the thermal shock resistance.^{1,2} Recently, new experimental methods are proposed and applied to the investigation of macroscopic crack propagation process during thermal shock fracture, based on fracture mechanics.³⁻⁵

However the characterization of microfracture process under thermal shock as well as transient thermal stress field is indispensable, since thermal shock fracture is caused by the accumulation of microscopic damages such as microcrackings under thermal stress. On the other hand, the authors investigated the microfracture process during bending tests of ceramics using AE technique.^{6,7} Especially, the critical stress for maincrack formation due to the growth and/or coalescence of microcracks was evaluated by detecting the critical increase in AE signals.

In this study, new experimental technique for the investigation of thermal shock fracture behavior, *Disk-on-Rod test*, is proposed. The temperature fields in the specimen were measured and used to calculate the 2 dimensional thermal stress field.

Shuichi Wakayama, Kousuke Nishino, Kouhei Kubota, Toshiya Wada and Satoshi Kobayashi, Department of Mechanical Engineering, Tokyo Metropolitan University, 1-1 Minami-Ohsawa, Hachioji-shi, Tokyo 192-0397, JAPAN

Furthermore, microfracture process was characterized by AE measurement. The formation of maincrack due to propagation and/or microcracks was focused in the present paper. Especially, the critical stress for maincrack formation is evaluated from obtained experimental data and compared with the results of mechanical biaxial bending tests.

2. EXPERIMENTAL PROCEDURE

2.1. Materials

The materials used in the present study were alumina ceramics (ADS-11) offered from Toshiba Ceramics Co., Ltd. The relative density and mean grain size were 97.7% and $6\ \mu\text{m}$, respectively. Disk specimens were cut from the rod materials and both surfaces were polished. The disk specimens with a diameter of 20 mm and a thickness of 0.6 mm were then obtained. In order to avoid the influence of stress corrosion cracking by water contents in materials, the specimens were dried in the vacuum at 150°C for 2 hours.

2.2. Disk-on-Rod Tests

In this study, for characterizing the thermal shock fracture process, new experimental technique, Disk-on-Rod test, was developed. An outline of the Disk-on-Rod test is shown in Figure 1. A thin disk specimen was heated to the required temperature by an infrared (IR) lamp and only the central part of disk was quenched by means of contacting with a metal rod. Since the disk specimen has a diameter of 20 mm and a thickness of 0.6 mm, and a contacting area has 4 mm diameter, 2-D thermal stress field was obtained. In order to characterize the fracture process, AE signals during thermal shock fracture were detected by an AE sensor attached on the bottom end of a metal rod, thus it was used for both coolant and wave guide.

The apparatus of Disk-on-Rod test and AE measuring system are shown in Figure 2, schematically. The heated specimen was brought down with a holder and

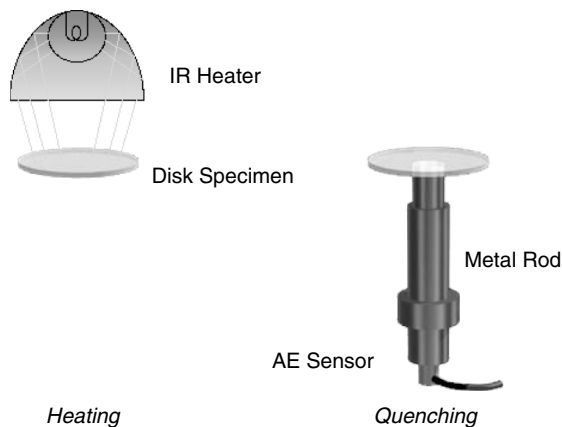


Figure 1. Outline of Disk-on-Rod Test.

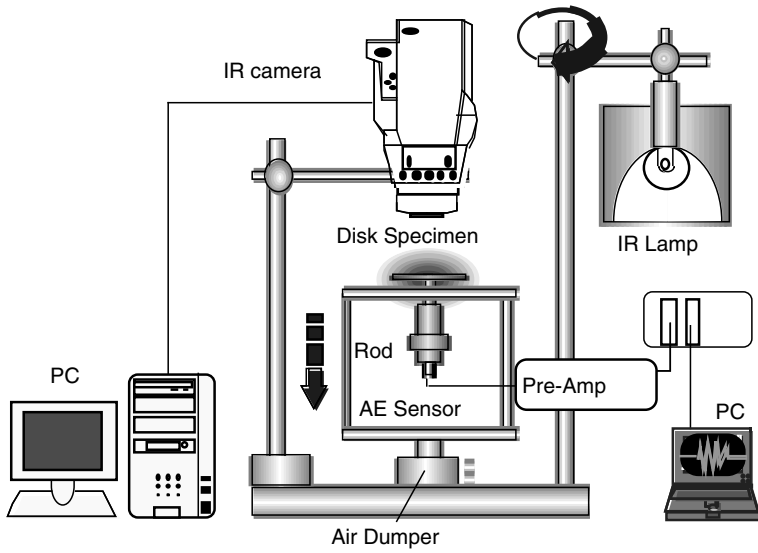


Figure 2. Schematic Diagram of Disk-on-Rod Test System.

contacted with a metal rod. For removing the generation of AE noise due to contacting, contacting speed was controlled by an air damper. And temperature distributions on disk surface were measured by a high-speed infrared camera (30 frames/s). Then thermal stress was calculated from the measured temperature distribution using FEM analysis.

An AE sensor, in which amplifier is instrumented, with resonant frequency of 180 kHz was used, then the initiations of microcracks could be detected with excellent sensitivity. The total gain of the AE system was 75 dB (main amplifier; 20 dB and pre-amplifier with sensors; 55 dB) and the threshold level was 18 μV at the input terminal of pre-amplifier.

2.3. Piston-on-Ring Tests

In order to obtain the strength under biaxial mechanical loading, Piston-on-Ring tests were carried out. The disk specimen has a same geometry as Disk-on-Rod tests. The specimen was supported by a supporting ring with a diameter of 16 mm and loaded by a loading rod with a diameter of 4 mm. Then the maximum equi-biaxial stress was obtained at the center region of specimen. According to the ASTM test standard (F394-78), the maximum qui-biaxial stress, σ_{max} , can be calculated by the following equation.

$$\sigma_{\text{max}} = \frac{3P(1 + \nu)}{4\pi t^2} \left[1 + 2 \ln\left(\frac{a}{b}\right) + \left(\frac{1 - \nu}{1 + \nu}\right) \left(1 - \frac{b^2}{2a^2}\right) \left(\frac{a^2}{R^2}\right) \right] \quad (1)$$

where P is the load, ν is the Poisson's ratio, a is the radius of supporting ring, b is the radius of loading rod, and t and R are the thickness and radius of the disk specimen, respectively.

3. EXPERIMENTAL RESULTS AND DISCUSSION

3.1 Determination of Thermal Stress

The temperature on specimen surface was measured by 1/30 s using a high-speed infrared camera system during Disk-on-Rod test and the thermal stress field was computed from the obtained 2-dimensional temperature distribution using finite element code (ANSYS; isoparametric structural shell, 2977 elements, 6082 nodes). Young's modulus (360 GPa), Poisson's ratio (0.22) and the coefficient of thermal expansion ($7.8 \times 10^{-6}/K$) were assumed as constant in the FEM analysis. The determined thermal stress fields are shown in Figure 3 (a) radial stress and (b) tangential stress. The obtained stress field was axi-symmetric according to the concentric temperature distribution. It is understood from the figure that the center of the disk is subjected to the maximum equi-biaxial stress and the stresses decrease

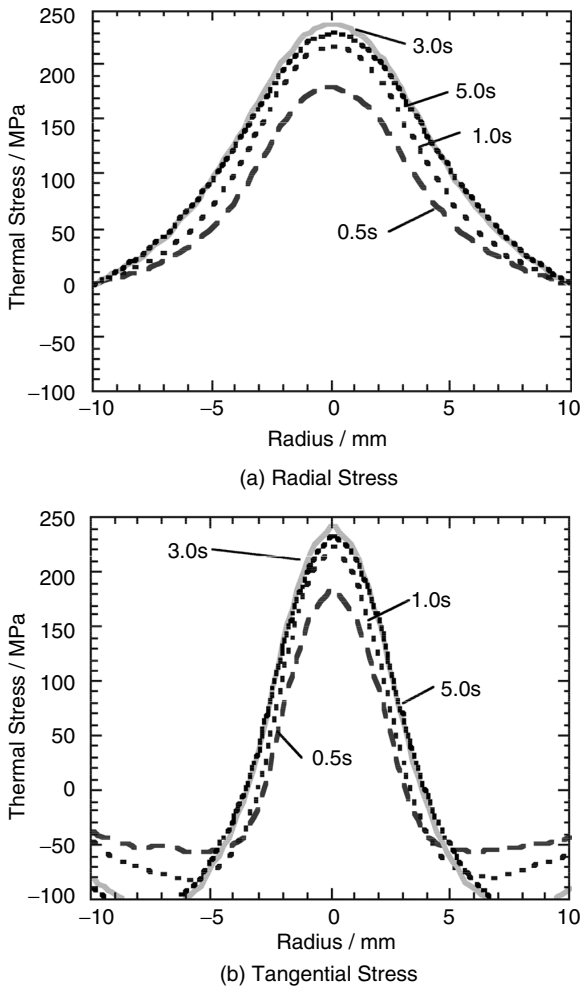


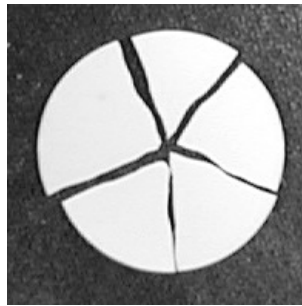
Figure 3. Thermal Stress Distribution during Disk-on-Rod Test (a) Radial Stress, (b) Tangential Stress.

to the outer region along the radial direction. It is also seen in the figure that the radial stress is tension in the whole of disk specimen, while the tangential stress is tension in the central region but compression in the outer region. Both stresses show the maximum at 3 s and decrease gradually.

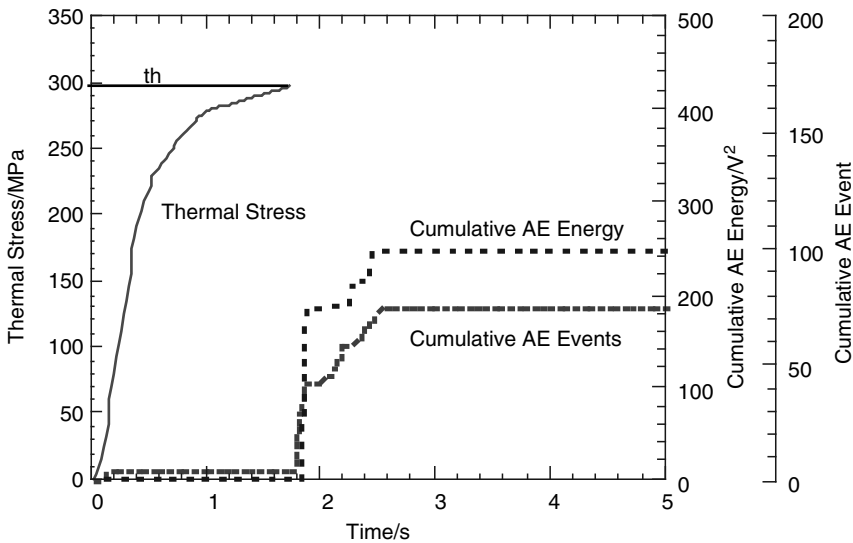
3.2 Disk-on-Rod Test

Figure 4 shows a typical result of Disk-on-Rod test. Figure 4 (a) shows the fractured specimen. The crack path observed in the figure demonstrates that the maincrack was formed at the center region, which was subjected to the maximum equi-biaxial stress, and propagated to outer region associating with slight deflections.

Maximum thermal stress at the center of specimen, cumulative AE energy and cumulative AE event are shown in Figure 4 (b). It is recognized in the figure that both cumulative AE events and energy increase remarkably at 1.8 s, continue to increase intermittently until 2.5 s and cease to generate.



(a) Fractured Specimen



(b) Thermal Stress and AE Behavior

Figure 4. Typical Results of Disk-on-Rod (a) Fractured Specimen (b) Thermal Stress and AE Behavior.

Since the formation of maincrack could be observed at the AE increasing point, it is understood that the remarkable increase in AE corresponds to the maincrack formation due to microdamage accumulation. Then the critical stress for maincrack formation during thermal shock fracture, σ_{th} , can be determined by Disk-on-Rod test. Those values ranged from 220 to 330 MPa. The instantaneous crack path was not determined definitely because of its high growth velocity. Therefore, the thermal stress analysis is no longer valid after maincrack formation because the crack path could not be introduced into finite element models.

It can be also seen in Figure 4 (b) that the AE events increase intermittently after the critical increasing. Therefore, it can be considered that the maincrack propagated into the outer region to the final fracture at 2.5 s. Furthermore, the incubation period was observed in AE generation from 1.9 to 2.1 s, which suggest the arrest and re-propagation of maincrack occurred during thermal shock fracture. Consequently, it can be concluded that the whole process associated with thermal shock fracture presented in the unified theory of Hasselman², i.e. crack initiation, arrest and propagation, can be identified during a single Disk-on-Rod test.

3.3 Piston-on-Ring Test

In order to investigate the critical stress for maincrack formation under biaxial mechanical loading, the Piston-on-Ring tests were carried out. Figure 5 shows a fractured specimen (Figure 5 (a)), and the maximum biaxial stress and AE behavior during Piston-on-Ring test (Figure 5 (b)). It is observed in Figure 5 (a) that the maincrack was initiated at the center region of the specimen subjected to equi-biaxial stress and propagated to the outer region.

In Figure 5 (b), the AE increasing point can be observed at 80 s before the final fracture at 107 s. Similarly to the previous studies,^{6,7} it is understood that the critical stress for maincrack formation under mechanical loading, σ_C , as well as bending strength, σ_B , can be determined. The critical stresses, σ_C , were evaluated as 180 – 280 MPa; they were lower than the critical stress for maincrack formation under thermal shock mentioned above.

3.4 Critical Stress for Maincrack Formation

For the quantitative comparison of the critical stress for maincrack formation under thermal shock, σ_{th} , with mechanical loading, σ_C , the volume effect of strength should be considered. According to Weibull statistics,⁸ the cumulative probability of failure of brittle materials is written in the following simplified form.

$$P = 1 - \exp[-(\sigma_R/\sigma_0)^m \bullet V_E] \quad (2)$$

The parameters m and σ_0 are the shape parameter (Weibull modulus) and the scale parameter (characteristic strength), respectively. σ_R is the maximum stress in the structure and V_E is the effective volume.

$$V_E = \int_V (\sigma/\sigma_R)^m dV \quad (3)$$

From Eq. (2), the average strength, μ , can be obtained as

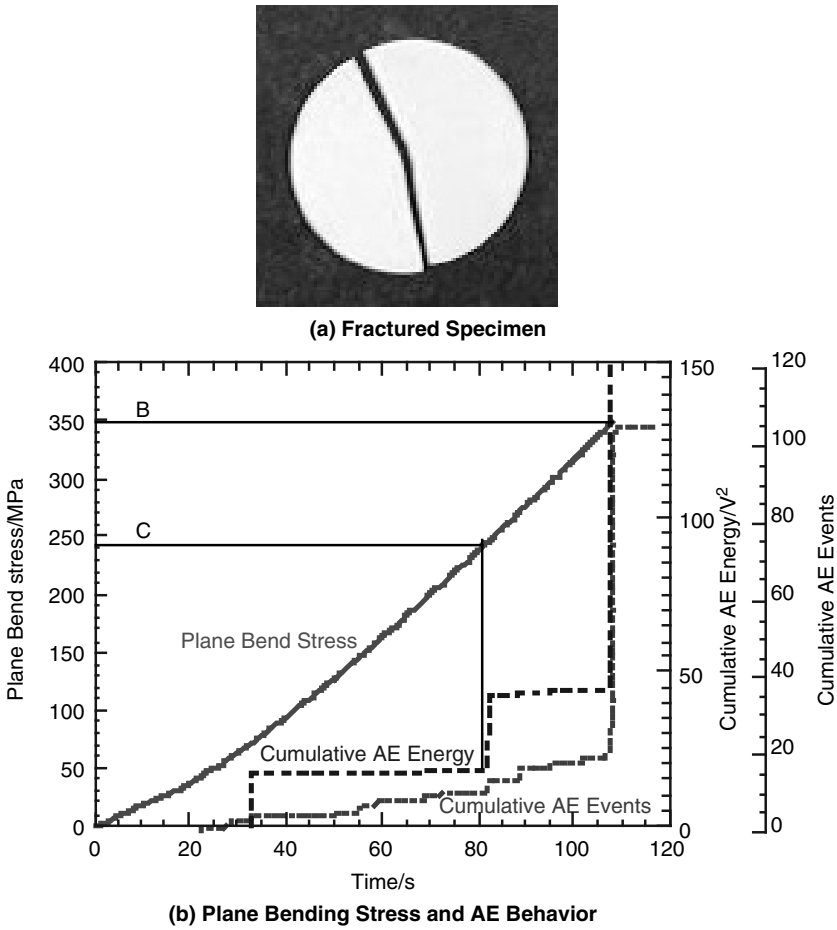


Figure 5. Typical Results of Plane Bending Test (a) Fractured Specimen, (b) Plane Bending Stress and AE Behavior.

$$\mu = \sigma_0 \bullet V_E^{-1/m} \bullet \Gamma((m + 1)/m) \tag{4}$$

where Γ is a gamma function. From Eq. (4), the volume effect of strength can be derived as

$$\mu_2/\mu_1 = (V_{E1}/V_{E2})^{1/m} \tag{5}$$

where μ_1 and μ_2 are the average strength of the structure with the volume of V_{E1} and V_{E2} , respectively.

These statistical approaches can not be applied directly to the experimental results in this study, because the fracture was occurred under biaxial stress in Disk-on-Rod tests and Piston-on-Ring tests. The statistical approaches for multiaxial stress state have been studied by several investigators.^{9,10} In order to determine the suitable equivalent stress more precisely, further investigation is needed for the widely variable stress states. However, it is considered that uniaxial statistical approach by eqs. (2)–(5) are available for the comparison of the critical stress for maincrack formation under

thermal shock, σ_{th} , with mechanical loading, σ_C , since the maincrack was formed at the center of disk specimen subjected to equi-biaxial stress in both cases.

For the first assumption, the maximum principal stress was taken as the equivalent stress in the present study. Inserting the experimental data into Eqs. (3) and (4), the average value of critical stress for maincrack formation and effective volume were calculated as 233 MPa and 4.1 mm^3 for plane bending tests, and 271 MPa and 3.4 mm^3 for thermal shock tests, respectively. On the other hand, considering the volume effect (Eq. (5)), the critical stress under thermal shock can be estimated as 238 MPa from the experimental results of plane bending tests, which is lower than the experimental results of thermal shock tests. Thermal shock tests were carried out at high temperature while plane bending tests at room temperature in air. Therefore, it is considered that the influence of stress corrosion cracking by water vapor resulted in the difference in the estimated value and experimental results.

4. CONCLUSIONS

In the present study, new experimental technique, Disk-on-Rod test, was developed and applied to the characterization of thermal shock fracture process in ceramics. The thermal stress fields were computed from temperature distributions measured by high-speed IR camera and fracture process was characterized by AE measurement, both of which are significant for understanding the thermal shock fracture behavior.

During thermal shock fracture, the maincrack was formed at the center of disk specimen subjected to maximum equi-biaxial stress and propagated into the outer region with crack deflections. The critical stress for maincrack formation was successfully determined by AE measurement and FEM analysis using the measured temperature distribution. Furthermore, those were compared with the critical stress under mechanical biaxial loading, considering the volume effect based on Weibull statistics. It was then understood that the critical stress for maincrack formation under thermal shock is higher than that under mechanical loading because of the absence of stress corrosion cracking by water vapor.

Further investigation is needed for the application to complex multiaxial stress states and the fracture mechanical analysis of crack arrest and propagation process. However, new experimental technique of thermal shock fracture (Disk-on-Rod test), by which the indispensable information for the structural application of ceramics at high temperature, was established in the present study.

ACKNOWLEDGMENT

The authors would like to thank Toshiba Ceramics Co., Ltd. for their offer of ceramic samples.

REFERENCES

1. W. D. Kingery, Factor Affecting Thermal Shock Resistance of Ceramic Materials, *J. Am. Ceram. Soc.* **38**(1), 3–15 (1955).

2. D. P. H. Hasselman, Unified Theory of Thermal Shock Fracture Initiation and Crack Propagation in Brittle Materials, *J. Am. Ceram. Soc.* **52**(11), 600–604 (1969).
3. G. A. Schneider and G. Petzow, Thermal Shock Testing of Ceramics – A New Testing Method, *J. Am. Ceram. Soc.* **74**(1), 98–102 (1991).
4. W. P. Rogers and A. F. Emery, Contact Thermal Shock Test of Ceramics, *J. Mater. Sci.* **27**(1), 146–152 (1992).
5. Y. Mizutani, N. Nishikawa and M. Takatsu, Evaluation of Thermal Shock Damage in Ceramic Disks Heated under Constant Heat Flux Conditions, *J. Ceram. Soc. Jpn.* **103**(5), 494–499 (1995).
6. S. Wakayama, T. Koji and H. Nishimura, Evaluation of Critical Stress for Microcracking in Alumina Ceramics by Acoustic emission, *Trans. Jpn. Soc. Mech. Eng.* **57**(535), 504–511 (1991).
7. S. Wakayama and H. Nishimura, Critical Stress for Microcracking in Alumina Evaluated by Acoustic Emission, *Fracture Mechanics of Ceramics*, **10**, Plenum Press, New York, 59–72 (1992).
8. W. A. Weibull, Statistical Distribution Function of Wide Applicability, *J. Appl. Mech.* **18**(3), 293–297 (1951).
9. S. B. Batdorf and J. G. Crose, A Statistical Theory for the Fracture of Brittle Structures Subjected to Polyaxial Stress States, *J. Appl. Mech.* **41**, 459–465 (1974).
10. J. Lamon, Statistical Approaches to Failure for Ceramics Reliability Assessment, *J. Am. Ceram. Soc.* **71**(2), 106–112 (1988).

FINITE ELEMENT ANALYSIS OF CRACK-PATH SELECTION IN A BRICK AND MORTAR STRUCTURE

Reza Sarrafi-Nour, Mohan Manoharan
and Curtis A. Johnson*

ABSTRACT

Many natural composite materials rely on organized architectures that span several length scales. The structures of natural shells such as nacre (mother-of-pearl) and conch are prominent examples of such organizations where the calcium carbonate platelets, the main constituent of natural shells, are held together in an organized fashion within an organic matrix. At one or multiple length scales, these organized arrangements often resemble a brick-and-mortar structure, with calcium carbonate platelets acting as bricks connected through the organic mortar phase.

The structure of natural shells and their outstanding resistance to damage and fracture have both attracted and inspired scientists from various disciplines, including material science, for a number of years. It is believed that the organized nature of the brick-and-mortar structure imparts a significant influence on the unusually high fracture resistance and work-of-fracture of the natural shells. Hence, the interaction between the growing cracks and the shell architecture is of central interest in any attempt to mimic the structure and potentially design materials based on such architectures. This work presents a finite element analysis of crack-path selection in a simple model brick-and mortar structure. The analysis relies on interface fracture mechanics concepts to gain insight into the pathological behavior of cracks propagating in such

* Ceramics and Metallurgy Technologies, General Electric Global Research Center, Niskayuna, NY 12309, USA. E-mail: sarrafi@crd.ge.com, Tel. (518) 387-5803, Fax (518) 387-7563

structures. The ratio of the strain energy release rate between the interfacial and non-interfacial crack-propagation directions is used as an indicator in evaluating the tendency towards interfacial crack growth. The strain energy release rate ratio is then evaluated as a function of elastic properties and the characteristic geometrical dimensions of the brick and the mortar phase.

1. INTRODUCTION

Natural shells are known to exhibit unique fracture resistance characteristics, inspiring materials scientists to study and to attempt mimicking their structures. Some prominent examples of natural shells include nacre [1,2] and conch [3,4]. Both conch and nacre are composed of more than 95% calcium carbonate, mostly aragonite platelets, and less than 5% of a proteinaceous material which is believed to act as a mortar or a binding matrix. In the microstructure of nacre, the calcium carbonate platelets are highly tessellated and resemble a well-organized brick-and-mortar structure at a micrometer length scale. The microstructure of conch shell is far more complex; it is laminated and consists of three distinct layers that resemble the structure of plywood [3,4]. However, at lower length scales the microstructure of conch shell also consists of lamellae and, further down, of high aspect ratio calcium carbonate platelet arrangements. At both of these levels, the structure of conch also resembles a brick and mortar structure.

It is believed that the organized nature of a brick-and-mortar structure imparts a significant influence on the unusually high fracture resistance and work-of-fracture of these natural shells. Hence, the interaction between growing cracks and these structural arrangements is of central interest in any attempts to mimic and material design based on such architectures. By examining the pathological behavior of cracks as they propagate into a structure, one can gain fundamental understanding and useful insight into such interactions. It is the goal of this article to gain such insights on cracks propagating in a brick-and-mortar structure arrangement.

2. ANALYSIS METHODOLOGY

We employ the finite element method and interface fracture mechanics concepts to parametrically examine interfacial crack path selection in a unit brick-and-mortar structure. The analysis methodology, to be described below briefly, is based on the analyses of cracks kinking into and out of a bi-material interface as discussed by He and Hutchinson [5], He et al [6,7], and Suo and Hutchinson [8].

For a crack intersecting the bi-material interface, the basis for the analysis [6,7] is the relative energy release ratio for crack propagation along the two competing directions: the bi-material interface, G_i , and penetrating into the material across the interface, G_o . Comparison between the release rate ratio, G_i/G_o and the ratio of fracture energy, Γ_i/Γ_o along the two competing directions would then establish a criterion as which direction is favored. If $G_i/G_o > \Gamma_i/\Gamma_o$ the condition for interfacial crack propagation is met before that of penetration and hence cracks would propagate along the interface. Therefore, G_i/G_o can be viewed as a measure of the tendency for interfacial path selection. When a crack is already at the bi-material interface, the

competition between further interfacial crack growth and the crack kinking out of the interface could be assessed using a similar criterion. In this case, the crack propagation process is controlled by $G_i/G_d > \Gamma_i/\Gamma_d$ [5] where the index “d” refers to the crack kinking out of an interface into the material on one side of the interface. Nevertheless, complexities would arise in adopting a unified criterion to establish the direction of the kink crack as discussed by He and Hutchinson [5]. For most material combinations and loading conditions, both the well-known $K_{II} = 0$ and G_{\max} criteria have been shown [5] to predict virtually the same direction for the kink crack. For certain material and loading combinations (in bi-material terminology when α , the first Dundurs’ parameter representing the mismatch between Young’s modulus of the two materials, is less than -0.6 and the crack kinks into the stiffer material), however, the two criteria were found to suggest substantially different kink angles, giving rise to some ambiguities. He and Hutchinson [5] suggested that under such conditions the selection of a criterion for kink directions had to be guided by experiments.

In this paper, we examine the pathological behavior of cracks propagating in model brick-and-mortar structures using the interface fracture mechanics methodology described while adopting a $K_{II} = 0$ criteria for the crack kinking out of an interface.

3. FINITE ELEMENT MODEL AND ANALYSIS

The interface crack propagation analysis was simulated in a two-dimensional brick-and-mortar model structure consisting of six brick units along the length and six brick units along the width of the model. FRANC2D [9] finite element code was used for fracture mechanics analysis due to the ease of crack insertion and propagation, and due to implementation of some interface crack propagation capabilities in the code. The finite element realization of the model and the boundary conditions are shown in Figure 1a. The finite element model was first created in ANSYS 6.0 with proper material properties assigned to the brick and mortar regions, assumed to be isotropic elastic. This model consisted of about 6,600–14,300 eight- and six-noded isoparametric plane-strain elements ($\sim 19,500$ – $41,000$ nodes) depending on the geometrical ratios of the brick and mortar regions. The crack free model was next read into FRANC2D and a crack was inserted into the model at the desired location. In one subset of the analyses, the crack was inserted along the centerline of the vertical mortar region at the mid point on one side of the model, as shown in Figure 1b, to simulate the conditions when a crack terminated at the bi-material interface. In another subset of the analyses, this crack was further propagated to the mid point along the adjacent horizontal interface between the brick and mortar region as shown in Figure 1c. (Details about crack insertion, propagation and fracture mechanics analysis using FRANC2D can be found in contributions by Bittencourt et al [10] and Wawrzynek and Ingraffea [11–13].) Further mesh refinements were employed in the models during the course of crack insertion and propagation analyses to ensure a fine mesh in the regions surrounding the crack tip. The crack tip itself consisted of a rosette of eight quarter-point elements. After the crack insertion, the total number of nodes in the models increased to some 25,000–60,000.

The energy release rates for the interface and kinked cracks were evaluated using the equivalent domain version of elastic J-integral [14]. These values were further

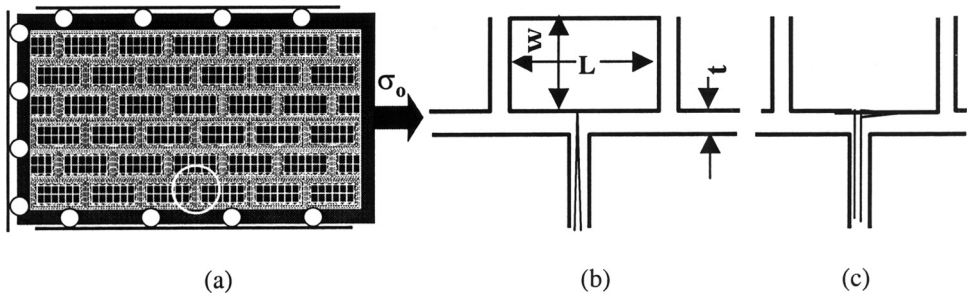


Figure 1. Finite element model and the definitions of evaluated configurations of the interface cracks: a) FE mesh with no cracks, b) the crack intercepting the interface between the brick and the mortar and c) the crack at the interface between the mortar and the brick unit. The region marked with the white circle corresponds to the location where the crack configurations (b) and (c) were analyzed.

used to calculate the G_i/G_o or G_i/G_d depending on the crack configuration. The implementation of the analysis of a crack kinking out of an interface in FRANC2D has not been documented in the past. In short, the analysis proceeds as described in the followings. When the parent crack is at an interface, the kink directions into the materials on either side of the interface are determined based on the maximum circumferential stress theory [15], a close approximation of $K_{II} = 0$ criterion, in homogenous materials. Due to difficulties involved in re-meshing the region between a shallow kink and the bi-material interface, a kink direction with an angle of less than three degrees with the bi-material interface is neglected. Otherwise, a kink crack with a length corresponding to a fixed fraction of the size of the singular elements at the tip of the parent crack would be extended from the parent crack tip. The analysis was then invoked to calculate the energy release rate of the new crack configuration. This sequence was repeated for any other potential directions including the one along the bi-material interface by recovering the original parent crack mesh configuration.

Another important quantity in interface fracture mechanics is mode mixity. The crack tip field of an interface crack is intrinsically mixed mode [8] due to the asymmetric elastic properties across the interface. Hence, mode mixity is required to fully characterize the loading conditions at the crack tip. Furthermore, the fracture toughness of an interface is known to depend on the mixed mode condition, typically observed to rise with increasing mixed mode. The degree of the mode mixity can be characterized using the definition of the complex interface stress intensity factor $K = iK_1 + K_2$ after He and Hutchinson [5]:

$$\varphi = \tan^{-1} \left(\frac{\text{Im}[K]}{\text{Re}[K]} \right) \tag{Eq.(1)}$$

where φ is the mode mixity or phase angle, and $\text{Im}[K]$ and $\text{Re}[K]$ are the imaginary and real components of the stress intensity factor describing the stress field at the tip of the interface crack:

$$\sigma_{22} + i\sigma_{12} = \frac{K_1 + iK_2}{\sqrt{2\pi r}} r^{i\varepsilon} \tag{Eq.(2)}$$

In Eq. (2), σ_{22} and σ_{12} are normal shear stresses ahead of the crack tip, r is the distance from the crack tip and ε is the so-called oscillation index, which is related to

the second Dundurs' elastic mismatch parameter β (see the appendix for the definition of Dundurs' parameters):

$$\varepsilon = \frac{1}{2\pi} \ln \frac{(1 - \beta)}{(1 + \beta)} \quad \text{Eq.(3)}$$

Various techniques, such as interaction integral [16] and direct K solution using enriched finite elements [17], have been used to calculate K_2/K_1 ratio for an interface crack. Here, we used the near-tip asymptotic displacement field solution of Hutchinson and Su [8] to calculate the K_2/K_1 ratio, and hence φ , from the displacements of the quarter-point nodes behind the crack tip. The required derivations are brought in the Appendix. An independent comparison between φ results from a direct K solution using enriched finite elements¹ and those obtained by inserting the displacement results from FRANC2D into the equation derived in the Appendix were found to agree within 1–3%.

4. RESULTS AND DISCUSSIONS

Examples of the variation of energy release rate and mode mixity in reference to crack-tip positions depicted in Figure 1b and Figure 1c are shown in Figure 2 for two different ratios of mortar thickness, t , to brick with, W , at a constant aspect ratio of the bricks, L/W . Two key observations could be made from the data. First, at the onset of the crack propagation along the horizontal boundaries, there was a transition region where both G_i/G_d and the mixity of the interface crack passed through minimums. A closer examination of the data indicated that the minima of both G_i/G_d and the mixity were located at a distance of $\sim t/2$ from initial crack tip position, the mid-point of the vertical mortar region. Second, both the release rate ratio and mode mixity along the interface tended to rise towards a plateau as the crack tip reached the mid point of the horizontal boundary. In addition, while the release rate ratio showed a strong dependence on t/W , the mixity appeared to be far less sensitive to t/W (at least for the combination of the geometrical and material properties of the models examined).

Any attempts to mimic such natural structural arrangements using ceramic materials needs further understanding of how the geometrical ratios and material properties may contribute/control the crack path selection process in such structures. One could approach such evaluations through a full parametric study of the problem. However, given the number of iterations and numerical efforts involved, a response-surface-methodology-based approach is more practical [18].

We employed such an approach to evaluate the effects of the aspect ratio of the brick units, the thickness of the mortar phase and the elastic properties of each phase. Guided by the preliminary analyses, the study was carried out for two particular crack tip locations, i.e., the crack configuration shown in Figure 1b and after crack propagation along the brick and mortar interface by $2x/L = 0.5$ (Figure 2). The selection of this second configuration was primarily driven by the plateau behavior

¹ FRANC2D Finite Element Code for 2D and Axisymmetric Fracture Analysis, General Electric Global Research, Niskayuna, NY

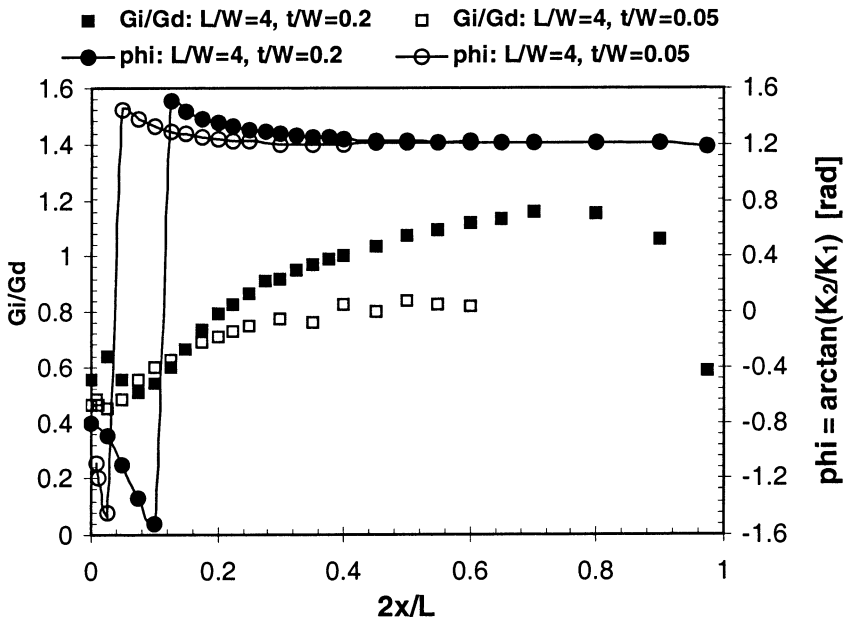


Figure 2. Variation of energy release ratio and mixity as function of position of crack tip at the brick-mortar layer interface, $E_b = 320$ GPa, $E_m = 20$ GPa, $\nu_b = \nu_m = 0.25$. Note that the energy release ratio values at $2x/L = 0$ represent G_i/G_o , the energy release ratio between interfacial and penetrated crack paths.

suggested by the mixity results (Figure 2) and by an apparent steady-state behavior of G_i/G_d for small t/W values (Figure 2) at this location. The range of elastic properties considered in the analysis was selected based on the properties of ceramic materials of interest for structural applications. Table 1 summarizes the geometrical and material properties considered.

A design-of-experiment software package² was used to generate the design³ points that were suitable for a quadratic response surface analysis of the design space with proper constraints on the variables. A constraint imposed while generating the design matrix was that the modulus of the brick had to be always greater than the modulus of the mortar phase. The resulting design matrix consisted of 39 independent runs where the variables were changed systematically within their selected range. Finite element analyses were carried out for the two crack configurations using the sets of variables at each design point and the results (calculated

Table 1. Material and geometrical properties used in the parametric study.

| Parameter | Range |
|--|----------------|
| Elastic modulus of brick, E_b , and mortar, E_m | 20 GPa-700 GPa |
| Poisson's ratio of bricks, ν_b , and mortar, ν_m | 0.1-0.3 |
| Length-to-Width ratio, L/W , of bricks | 2-10 |
| Ratio of the mortar thickness to brick width, t/W | 0.05-0.5 |

² Design Expert Version 6.0, Stat-Ease Inc., Minneapolis, MN

³ D-Optimal, Response Surface Design, Design Expert Version 6.0

energy release rate ratios and mixities) were analyzed using the same design-of-experiment software package to obtain quadratic response surfaces for both the energy release rate and mixity as a function of the design variables (Table 1). The response surface functions obtained are illustrated in Figs. 3–5 for two different combinations of elastic moduli of the brick and the mortar phases. It is to be kept in mind that the response surface functions here are “best-fit” functions obtained by regression analysis of the data with respect to the selected variables within their specific domains. All the fit functions shown here had R-squared statistics of about > 0.93 , except for the fit function (not shown here) to the mixity results of the interface crack tip at $2x/L = 0.5$.

As seen from the surface plots in Figure 3 and Figure 4, the energy release rate ratio is strongly influenced by the aspect ratio of the brick and the mortar units. The positive influence of the elastic mismatch across the interface on the energy release rate ratio was expected based on the previous studies of interface cracks [5–8]. It was also interesting to note that the results shown in Figure 3 suggested that a combination of high aspect ratio bricks with high elastic mismatch between the brick and mortar would require a thin mortar layer in order to achieve high release rate ratio. This could mean that for such combinations of geometry and material properties a thin mortar layer would better facilitate crack deflection into the brick and mortar interface. In contrast, when the crack has grown into the interface between the brick and mortar layer, the energy release ratio appeared to become far less sensitive to the thickness of the mortar layer and increased monotonically with increasing thickness for all values of the aspect ratios of the bricks.

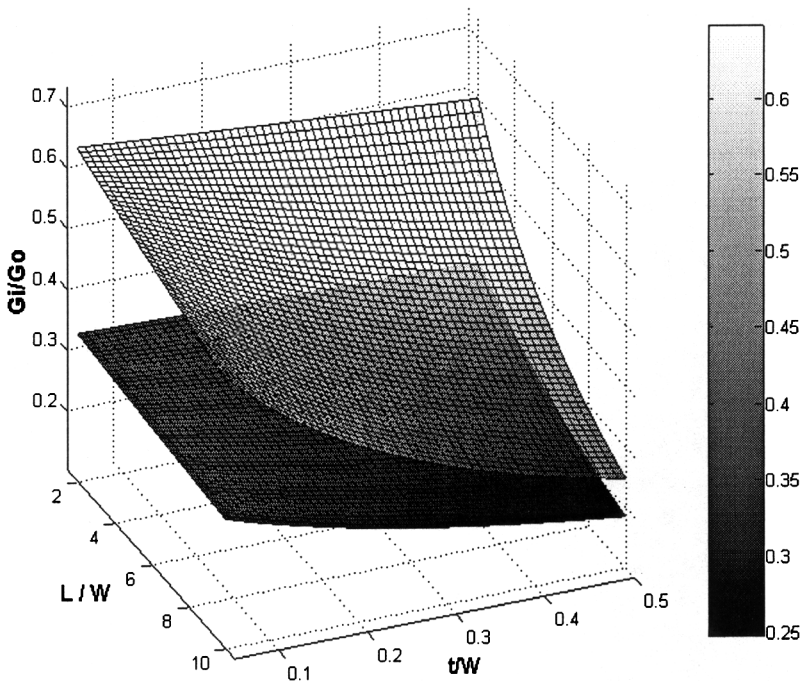


Figure 3. Variation of energy release ratio of interfacial versus penetrated crack as a function of the aspect ratio of the brick and thickness ratio of the mortar units for crack configuration in Figure 1b. Upper surface: $E_b = 400\text{GPa}$, $E_m = 20\text{GPa}$. Lower surface: $E_b = 400\text{GPa}$, $E_m = 100\text{GPa}$. $\nu_b = \nu_m = 0.2$

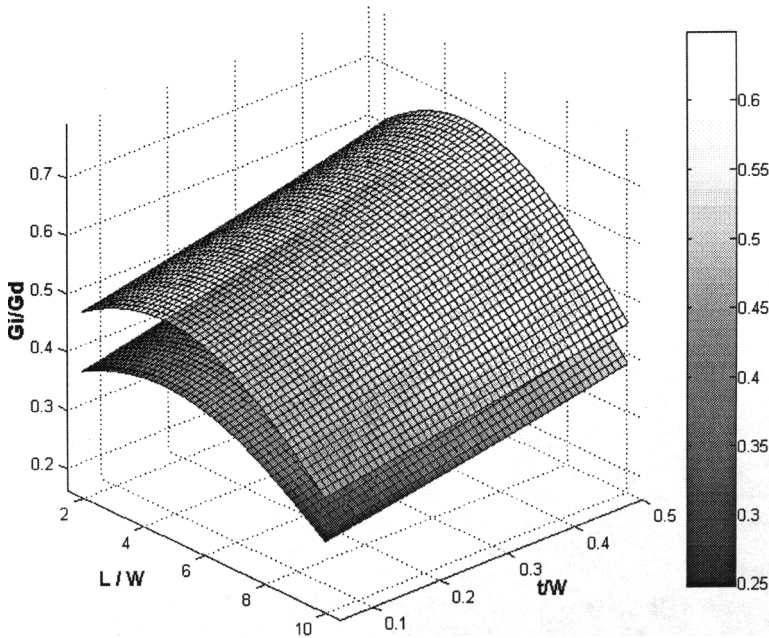


Figure 4. Variation of energy release ratio of interfacial versus deflected crack as a function of the aspect ratio of the brick and thickness ratio of the mortar units for interface crack configuration shown in Figure 1c. Upper surface: $E_b = 400\text{GPa}$, $E_m = 20\text{GPa}$. Lower surface: $E_b = 400\text{GPa}$, $E_m = 100\text{GPa}$. $\nu_b = \nu_m = 0.2$

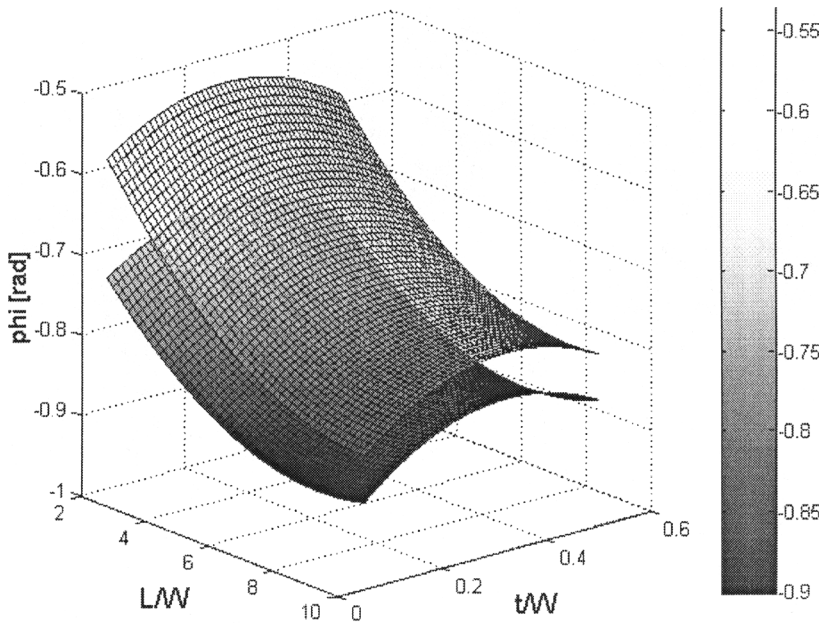


Figure 5. Variation of mixity of the interface crack at the onset of the deflection into the interface between the brick and mortar layers as a function of the aspect ratio of the brick and the thickness ratio of the mortar units. Upper surface: $E_b = 400\text{GPa}$, $E_m = 20\text{GPa}$. Lower surface: $E_b = 400\text{GPa}$, $E_m = 100\text{GPa}$. $\nu_b = 0.2$, $\nu_m = 0.3$

It is noteworthy that when the elastic mismatch between the bricks and the mortar layer was low, the energy release ratio of the crack configuration deflecting into an interface (Figure 3) gave a value of ~ 0.2 – 0.3 . This was consistent with earlier suggestions related to the requirements for the interface toughness ratio in reinforced ceramics. In earlier studies, Evans [19] suggested the toughness ratio between the interface and matrix had to be ≤ 0.25 in order to achieve toughening; Becher [20] suggested that the toughness ratio between the interface and the reinforcement needed to be $\sim 1/6$ [20] in order to ensure debonding at the interface between the bridging ligament and the matrix.

The results shown in Figure 4, where the crack has already grown into the interface between the brick and mortar layer, suggested that the energy release rate ratio increased monotonically with increasing thickness of the mortar layer. However, the aspect ratio of bricks appeared to have a stronger influence on the energy release ratio.

5. SUMMARY AND CONCLUSIONS

Based on interface fracture mechanics of brittle solids, the conditions of crack growth into or out of an interface between two dissimilar materials can be assessed by evaluating the ratio of energy release rate for crack propagating along the two competing directions. A finite element implementation of this concept was employed to evaluate the ratio of the energy release rate of cracks growing into and out of the interface between two dissimilar materials in a brick-and-mortar structure. A parametric study was carried out to examine the effect of both the geometrical and elastic properties of brick and mortar units on the energy release rate ratio between the interface crack and the competing kink-out or penetrating cracks. Consistent with earlier studies of interface cracks, elastic mismatch between the brick and mortar units was found to influence the energy release ratio strongly. The results also indicated a strong influence of geometrical characteristics. In the case of the crack configuration at the brick-mortar interface, a combination of high aspect ratio of bricks, low thickness of the mortar and high elastic mismatch appeared to achieve the highest energy release ratio. The results for the crack configuration already grown into the interface between the brick and mortar layer suggested a mild and monotonic increase in energy release ratio with increasing thickness of the mortar layer. However, in this case the energy release ratio appeared to be more sensitive to the aspect ratio of the bricks.

5. ACKNOWLEDGEMENTS

Ahmet Kaya, GE Global Research is acknowledged for useful and stimulating discussions, and for running comparative analysis in FRAC2D to verify the mixity calculations. Bruce Carter, GE Power Systems, and Paul Wawrzynek, Cornell Fracture Group, are acknowledged for their efforts to improve the interface fracture routines and to increase the problem-size capability of FRANC2D in order to accommodate analysis of large models.

REFERENCES

1. J.D. Currey, Proc. R. Soc. London, Ser. B, 196, 443 (1977)
2. R.Z. Wang, Z. Suo, I.A. Aksay and A. G. Evans, J. Mater. Res., 16 [9] 2485–2493 (2001)
3. S. Kamat, X. Su, R. Ballarini and A.H. Heuer, Nature, 405 [29] 1036–1040 (2001)
4. L.T. Kuhn-Spearing, H. Kessler, E. Chateau, R. Ballarini, A.H. Heuer and S.M. Spearing, J. Mat. Sci., 31, 6583–6594 (1996)
5. M-Y. He, J.W. Hutchinson, Trans. ASME, 56, 270–278 (1989)
6. M-Y. He, A. Bartlett, A.G. Evans and J.W. Hutchinson, J. Am. Ceram. Soc., 74 [4] 767–71 (1991)
7. M-Y. He, A.G. Evans and J.W. Hutchinson, Int. J. Solids Struct., 31 [24], 3443–3455 (1994)
8. J.W. Hutchinson, Z. Suo, Adv. Appl. Mech., 29, 63–191 (1992)
9. P. Wawrzynek and A.R. Ingraffea, NASA Contractor Report 4572, Cornell University (1994).
10. T. Bittencourt, P.A. Wawrzynek and A.R. Ingraffea, Eng. Fract. Mech., 55 [2] 321–334 (1996)
11. P.A. Wawrzynek and A.R. Ingraffea, Theo. Appl. Fract. Mech., 8, 137–150 (1987)
12. Ibid, Eng. With Computers, 3, 13–20 (1987)
13. Ibid, Finit. Elem. Anal. Des., 5, 87–96 (1989)
14. R.H. Dodds, Jr. P.M. Vargas, Report, University of Illinois at Urbana-Champaign, Dept. of Civil Engineering (1988)
15. F. Erdogan and G. Sih, ASME J. Bas. Eng., 85, 519–527 (1963)
16. L. Banks-Sills, N. Travitzky, D. Ashkenazi and R. Eliasi, Int. J. Fract., 99, 143–160 (1999)
17. H.F. Nied and A.C. Kaya, General Electric Technical Report, 92CRD028
18. R.H. Myers, D.C. Montgomery, “Response Surface Methodology: Process and Product Optimization using Designed Experiments,” Wiley-Interscience Publication, New York (1995).
19. A.G. Evans, “Perspective on the Development of High Toughness Ceramics,” J. Am. Ceram. Soc., 73 [2] 187–206 (1990)
20. P.F. Becher, “Microstructural Design of Toughened Ceramics,” J. Am. Ceram. Soc., 74 [2] 255–69 (1991).

APPENDIX

A.1. DUNDURS’ ELASTIC PARAMETERS

A wide class of elastic plane problems related to bimetals depends on only two non-dimensional combinations of the elastic moduli known as Dundurs’ parameter α and β :

$$\alpha = \frac{G_1(K_2 + 1) - G_2(K_1 + 1)}{G_1(K_2 + 1) + G_2(K_1 + 1)} \quad \text{Eq.(A1)}$$

$$\beta = \frac{G_1(K_2 - 1) - G_2(K_1 - 1)}{G_1(K_2 + 1) + G_2(K_1 + 1)} \quad \text{Eq.(A2)}$$

where G and K are the shear and bulk moduli and the indices 1 and 2 refer to materials 1 and 2 on either side of a bimaterial interface.

A.2. CALCULATION OF THE MIXITY AT THE TIP OF AN INTERFACE CRACK

The near-tip asymptotic displacement field of a crack at the interface between two isotropic elastic solids after Hutchinson and Suo reads:

$$\delta_2 + i\delta_1 = \frac{8(K_1 + iK_2)}{E_*(1 + 2i\varepsilon) \cosh(\pi\varepsilon)} \sqrt{\frac{r}{2\pi}} r^{i\varepsilon} \tag{Eq.(A3)\#}$$

where $\delta_i = u_i(r, \theta = \pi) - u_i(r, \theta = -\pi)$ are the crack surface displacements at distance r behind the crack. Replacing: $1 + 2i\varepsilon \cosh(\pi\varepsilon) = 1 + iA$, $r^{i\varepsilon} = \text{Cos}(\varepsilon \ln(r)) + i \text{Sin}(\varepsilon \ln(r))$, $\varepsilon \ln(r) = y$ and $B = (8/E_*)(r/2\pi)^{1/2}$ and rewriting Eq. A3 after some manipulations gives:

$$\frac{\delta_1}{\delta_2} = \frac{K_1(\text{Sin}(y) - A\text{Cos}(y)) + K_2(\text{Cos}(y) + A\text{Sin}(y))}{K_1(\text{Cos}(y) + A\text{Sin}(y)) - K_2(\text{Sin}(y) - A\text{Cos}(y))} \tag{Eq.(A4)}$$

Eq. A4 can be further simplified by dividing both the nominator and the denominator on the right-hand side by $K_2[\text{Sin}(y) - A\text{Cos}(y)]$ to give:

$$\frac{\delta_1}{\delta_2} = \frac{\frac{K_1}{K_2} + \frac{\text{Cos}(y) + A\text{Sin}(y)}{\text{Sin}(y) - A\text{Cos}(y)}}{\frac{K_1}{K_2} \frac{\text{Cos}(y) + A\text{Sin}(y)}{\text{Sin}(y) - A\text{Cos}(y)} - 1} \tag{Eq.(A5)}$$

Using the abbreviations $g = (\text{Cos}(y) + A\text{Sin}(y))/(\text{Sin}(y) - A\text{Cos}(y)) =$ and $f = \delta_2/\delta_1$, further rearrangement of Eq. A5 gives

$$\frac{K_2}{K_1} = \frac{f \cdot g - 1}{f + g} \tag{Eq.(A6)}$$

and, hence, $\phi = \tan^{-1}(K_2/K_1)$.

Table A1 shows the verification of the mixity values calculated based on Eq. A6 using near-tip displacement solutions from finite element analysis. The crack config-

Table A1. Verification of Eq. A6 using finite element Enriched-Element Solution[#]
 $\tan^{-1}(K_2/K_1) = -1.0537$ radian.

| Distance from the crack tip, r | ΔU_x | ΔU_y | $\tan^{-1}(K_2/K_1)$ [rad] from Eq. (A6) |
|----------------------------------|--------------|--------------|--|
| FRAC2D* | | | |
| 0.005504 | -1.4809E-05 | 5.3778E-05 | -1.0660 |
| 0.011007 | -2.6683E-05 | 7.3379E-05 | -1.0702 |
| 0.023603 | -4.7940E-05 | 10.2779E-05 | -1.0744 |
| 0.037788 | -6.7124E-05 | 12.3337E-05 | -1.0848 |
| FRANC2D (quarter-point node) | | | |
| 0.002232 | -6.7927E-06 | 3.5325E-05 | -1.0860 |
| 0.003348 | -1.0014E-05 | 4.2355E-05 | -1.0843 |
| 0.008928 | -2.3735E-05 | 6.6502E-05 | -1.0871 |

[#] $E_b = 320\text{GPa}$, $E_m = 20\text{GPa}$, $\nu_b = \nu_m = 0.25$
 * FRAC2D mesh consists of enriched elements at the crack tip and cubic elements elsewhere

[#] It can be seen in Eq. A1 that the classical definition of interface stress intensity factors includes the complex oscillatory term $(\text{length})^{i\varepsilon}$. Therefore, the stress intensity factor unit in this case is not simply $(\text{stress}) \times (\text{length})^{1/2}$ but $(\text{stress}) \times (\text{length})^{1/2} \times (\text{length})^{i\varepsilon}$. As suggested by Rice, the complex stress intensity factor K can be rotated in such a manner to reduce to the conventional form using $K' = KL^{i\varepsilon}$. In this case, L is a characteristic length (chosen arbitrarily) of the interface crack problem. This will allow one to define a phase angle in the rotated coordinates by using $\phi' = \phi + \varepsilon \ln(L)$.

uration analyzed was the same as shown in Fig. 1c. The K_2/K_1 at the crack tip was calculated in FRAC2D through a direct solution of the stress intensity factors K_1 and K_2 using enriched finite elements.

INVESTIGATION OF CRACK GROWTH PROCESS IN DENSE HYDROXYAPATITE USING THE DOUBLE TORSION METHOD

C. Benaqqa^{1,2}, J. Chevalier¹, M. Saâdaoui²,
and G. Fantozzi¹

ABSTRACT

In this work, double torsion tests were performed to investigate slow crack growth behavior of dense hydroxyapatite materials. Crack rate, V , versus stress intensity factor, K_I , laws were obtained for different environments and processing conditions. Stress assisted corrosion by water molecules in oxide ceramics is generally responsible for slow crack growth. The different propagation stages obtained here could be analyzed in relation to this process. The presence of a threshold defining a safety range of use was also observed. Hydroxyapatite ceramics appear to be very sensitive to slow crack growth, crack propagation occurring even at very low K_I . This can be explained by the fact that their contain hydroxyl groups (HAP: $\text{Ca}_{10}(\text{PO}_4)_6(\text{OH})_2$), favoring water adsorption on the crack surface and thus a strong decrease of surface energy in the presence of water. This study demonstrates that processing conditions must be carefully controlled, specially sintering temperature, which plays a key role on V - K_I laws. Sintering at 50°C above or below the optimal temperature, for example, may shift the V - K_I law towards very low stress intensity factors. The influence of ageing is finally discussed.

¹ G.E.M.P.P.M. (U.M.R. C.N.R.S. 55 10) I.N.S.A. de Lyon, 69621 Villeurbanne Cedex France

² L.E.R.S.I.M. Ecole Mohammadia d'Ingénieurs, Rabat, Morocco

1. INTRODUCTION

Bio-active hydroxyapatite ceramics (HAP), are widely used as coatings on femoral stems or acetabular cups and as bone substitutes, because they induce growth and bonding of the bone on their surface [1]. For these ceramics, biological properties are of prime interest. However, their mechanical properties must not be neglected. Depending on the site where bio-active ceramics are implanted, non negligible stresses may appear in the biomaterial. In addition to the sudden failure of the ceramics, which takes place for a stress intensity factor reaching the toughness, K_{IC} , it is essential to consider also the so-called “*Subcritical Crack Growth*” which corresponds to a crack propagation for stress intensity factors, K_I , lower than K_{IC} in particular in corrosive environments. The propagation of the preexisting natural defects occurs at low rates (*slow crack growth*), and causes delayed failure of ceramics when the flaw size reaches a critical value. The sensitivity of ceramics to the slow crack growth is one of their major limitations. It is thus very important to understand the mechanisms which are involved and to determine with precision the crack propagation laws in order to predict the lifetime of these materials for a given application.

Few interest has been paid to this behavior in hydroxyapatite ceramics, despite its importance for long term success. Some investigations have shown that hydroxyapatite ceramics were sensitive to slow crack growth and fatigue, mainly by so-called static or dynamic fatigue tests [2,3]. In these studies, Hydroxyapatite was shown to present reduced lifetime under stress. Static and dynamic fatigue are indirect methods, since they do not allow the real measurement of crack rates for a given applied load. They only show the evidence of fatigue effects. In contrast, the double torsion is used here as a direct method of crack growth characterization because it can allow the real determination of the crack growth rate, V , versus the applied stress intensity factor, K_I , over a wide range of crack velocities, from 10^{-12} to 10^{-2} m/s [4].

The entire V - K_I diagram should be used for lifetime prediction, and the aim of this study is to characterize the V - K_I law of this material using the double torsion method. Emphasis is given to the role of processing conditions and of ageing on the entire V - K_I law, which to the knowledge of the authors has not been studied in previous works.

2. EXPERIMENTAL PROCEDURE

2.1. Material

A pure atomized hydroxyapatite powder was supplied by Coating Industry (France). Specimens were processed by uniaxial pressing at 20 MPa followed by cold isostatic pressing at 200 MPa. The green compacts reached about 55% of the theoretical density (3.16 g/cm^3). They were then sintered in air at different temperatures (from 1000°C to 1400°C) for three hours.

Grain size and morphology were examined by Scanning Electron Microscopy (*SEM*) and the mean grain size was evaluated from the linear intercept method according to the ASTM E112 standard¹. Densities were determined by the Archime-

¹ American Society Testing and Materials, West Conshohocken, PA

des method using water as the immersion medium. The evolution of the density and the microstructure versus sintering temperature are shown in figure 1. In agreement with previous studies [2, 3, 5, 6], full density is hardly obtained by natural sintering in air. However, 1200°C allows to reach 98% of theoretical density. The evolution of the grain size versus sintering temperature initially shows a slight increase, followed by a strong acceleration above 1250°C. Hardness measurements were conducted at low loads (200 g) for the same range of temperatures. They are shown in figure 2 and compared to density values. The two curves clearly show the same behavior, with an increase until 1200°C before reaching a plateau. 1200°C can be considered as the optimum sintering temperature, since densification is nearly achieved and grain size is limited.

From this preliminary results, three model materials were chosen for crack propagation studies: sintered 3 hours at 1200°C (a priori optimum properties), 1150°C (lower density) and 1250°C (coarsening of the grain size).

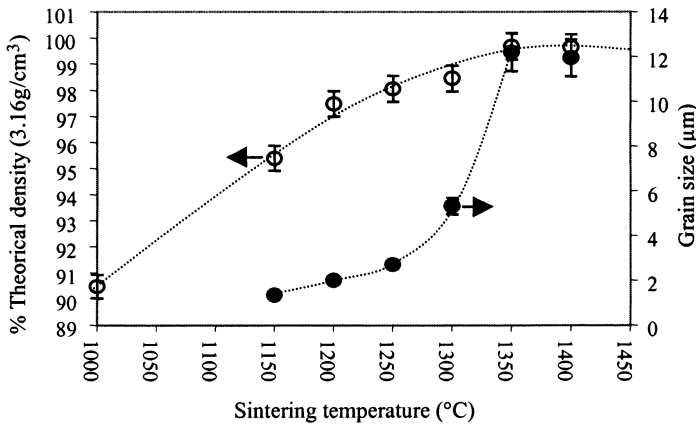


Figure 1. Evolution of density and grain size of HAP with sintering temperature.

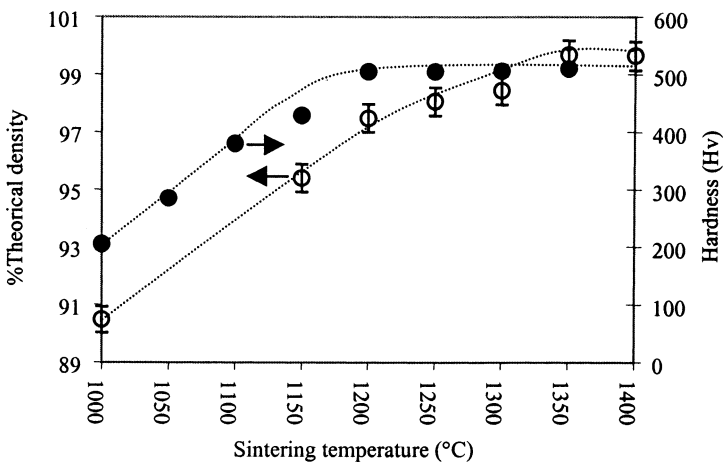


Figure 2. Evolution of relative density and vickers hardness of HAP with temperature.

2.2. Double Torsion Technique

The double torsion specimens, consisting of plates of dimensions $40 \times 20 \times 3 \text{ mm}^3$, and the loading configuration, are shown in figure 3. Specimens were thicker than we use generally for testing monolithic ceramics (2 mm) [4, 7–9]. Indeed, hydroxyapatite is very brittle, with a toughness on the order of $1 \text{ MPa}\sqrt{\text{m}}$ [10], thus 3 mm thickness was necessary to work under reasonable loads. The tensile surface of sintered samples was polished with a series of diamond pastes down to a final polish of $3 \mu\text{m}$ in order to observe the crack with a precision of $\pm 2 \mu\text{m}$. A notch of length $a_0 = 8 \text{ mm}$ and root $\rho = 0.1 \text{ mm}$ was machined with a diamond saw and an indentation was performed at low load (300 g) in order to initiate a small natural crack. Subsequent precracking was performed by loading the specimens at low rate in order to induce a sharp crack of initial length $a_i = 12 \text{ mm}$.

Generally, it is admitted that the stress intensity factor, K_I , is independent of the crack length, and given by:

$$K_I = \frac{W_m}{U^2} \left(\frac{3(1+\nu)}{W \cdot \psi} \right)^{1/2} \cdot P \quad (1)$$

where P is the load, W_m the span, U and W the width and the thickness of the specimen, ν the Poisson ratio (taken here as equal to 0.3), and ψ a calibration factor [11].

To obtain accurate crack growth measurement of the $V-K_I$ curves, it has been recently argued that a correction factor should be introduced in the conventional expression of K_I [4]. Thus, the following more realistic expression of K_I was used:

$$K_I = \frac{W_m}{U^2} \left(\frac{3(1+\nu)}{W \cdot \psi} \right)^{1/2} \cdot P \left(\frac{a}{a_0} \right)^{0.17} \quad (2)$$

where a_0 and a are respectively the notch and the crack lengths.

Crack velocity versus stress intensity factor ($V-K_I$) curves were obtained by two general tests, so called “constant loading” and “relaxation” tests [4]. In the load relaxation method, the pre-cracked specimen was subjected to fast loading, followed by subsequent stopping of the crosshead at a certain displacement. Hence, the crack propagation resulted in a load relaxation and the load versus time curve allows the determination of the $V-K_I$ curve with a single experiment, for crack rates down to 10^{-7} m/s [4]. The stress intensity factor can be calculated from expression (2) pro-

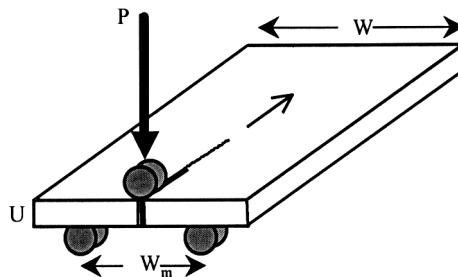


Figure 3. Double Torsion specimen and loading configuration.

vided the crack length is known. Both crack length and crack rate can be calculated from the compliance and the compliance rate at each time of the load relaxation curve. More details concerning this method can be found elsewhere [12–14].

To obtain lower crack rates, an alternative method (so called *constant loading test*) was used. The specimen is subjected to a static load under a prescribed duration, Δt . The crack length is measured via optical microscopy, with a precision of $\pm 2 \mu\text{m}$, and V is defined as the ratio of crack increment, Δa , to the duration, Δt ($V = \Delta a / \Delta t$). By conducting experiments under different loads, it is therefore possible to obtain different points of the V - K_I diagram. This technique presents the advantage of allowing very low velocities in order to investigate the presence of a threshold stress intensity factor value below which crack propagation does not occur [9, 12].

2.3. Influence of Environment and Ageing on Slow Crack Growth

In order to understand the crack propagation mechanisms in HAP, and in particular the role of water, relaxation tests were conducted on the same specimen at room temperature in three different media, namely in ambient air, liquid water and silicon oil (Rhodorsil 710, Rhône Poulenc, France). To obtain reproducible results in liquid environments, precracked specimens were cleaned by ultrasonic cleaner in acetone and then in ethyl alcohol for 5 minutes to insure a perfectly clean crack path. They were subsequently put in a desiccator under 10^{-2} hPa vacuum for 1 hour and dropped into the test liquid environment while vacuum was maintained for an additional hour. They were further transferred to the testing jig without any contact with ambient atmosphere. This procedure insures perfect wettability of the liquid along the crack path. In order to increase the significance of the results, three successive relaxation curves were conducted on the same specimen, first in air, then in water and oil. This ensures that no variation occurs from one sample to another.

Ageing was performed in a thermostated bath at 37°C . Specimens were left during 6 weeks, then tested in air by means of the relaxation technique. 6 weeks may correspond roughly to the time necessary for bone healing to occur *in-vivo* [15]. Although these ageing tests are conducted *in-vitro*, they could give a first idea of the stability of HAP properties in an immersed media.

3. RESULTS AND DISCUSSION

3.1. V - K_I Diagram

The V - K_I diagram determined in air for a dense hydroxyapatite with a grain size of $2 \mu\text{m}$ (sintered at 1200°C for 3 hours) is given in figure 4 for crack velocities from 10^{-10} m/s to 10^{-2} m/s. The results show that crack propagation takes place well below the toughness (about $0.9 \text{ Mpa}\sqrt{\text{m}}$), over a wide range of crack velocity: Hydroxyapatite is thus very sensitive to crack growth. The overall curve presents three different stages, which are generally observed in oxide ceramics [12]. Each stage can be fitted by a single relation, between the crack speed, V , and the stress intensity factor, K_I , [7, 8, 16, 17], on the form:

$$V = AK_I^n \quad (3)$$

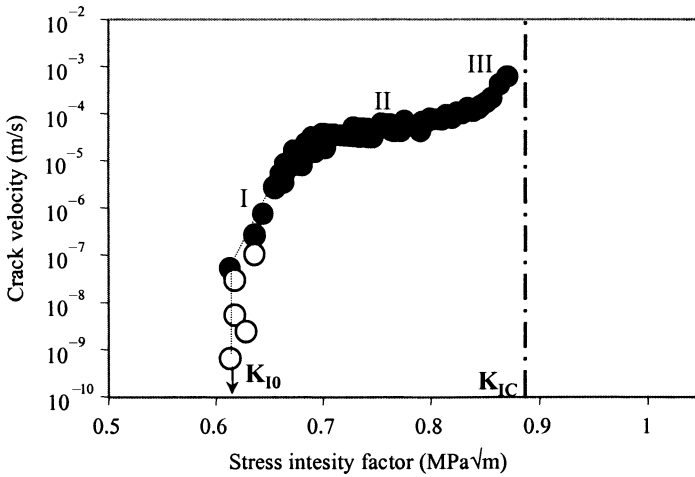


Figure 4. V - K_I diagram of HAP in air obtained by: ● Relaxation test and ○ Constant loading test.

where A and n are constants which correspond to each stage. They are given in table I. They can be used for lifetime prediction. In particular, stage I has a primordial practical importance since low crack rates ($V < 10^{-4}$ m/s) rule the lifetime of the pieces in service. This region is attributed to the reaction kinetic between water and the ceramic bonds [12] : this is the rate of the reaction kinetic which drives the crack velocity. Stage II occurs in air, when the transport of moisture from the crack mouth to the crack tip noticeably reduces the crack velocity: in this stage, the crack rate is controlled by the diffusion of the water molecules to the reaction site. The crack velocity is a weak function of the stress intensity factor (low n value). A third stage occurs for even higher crack rates (region III), when the crack rate exceeds the molecules transport rate. In this case, the fracture of ceramic bonds occurs without reaction with environmental species. Thus, this stage corresponds to the vacuum conditions. Region II of crack propagation is often considered as a connecting branch between fracture of ceramic bonds by water (region I) and fracture under vacuum conditions (region III).

It must be noted that stage I was not completely described by relaxation tests and that no threshold could be obtained. This was done by constant loading tests. The threshold, K_{I0} , is the most important parameter in practice because it defines a perfectly sure field of work. It is seldom defined clearly in the case of polycrystalline ceramics, due to the experimental difficulty and duration of tests. Our results show that crack rates tend to zero for a stress intensity factor around $K_{I0} = 0.6$ MPa√m. The ratio of threshold to toughness K_{I0}/K_{IC} is low, showing that hydroxyapatite is very sensitive to subcritical crack growth.

Table 1. Crack growth parameters for hydroxyapatite.

| | Stage I | Stage II | Stage III |
|----------------------------------|------------------|---------------------|-----------|
| $A(K_I \text{ in } MPa\sqrt{m})$ | $3.3 \cdot 10^4$ | $3.6 \cdot 10^{-4}$ | 0.8 |
| n | 55 | 7 | 52 |

The presence of three stages, noted I, II and III on the figure and of a threshold stress intensity factor, strongly suggests that stress corrosion by water molecules is the key mechanism for crack propagation [12, 18]. Its spreading over a large range of K_I shows the detrimental effect of stress corrosion by water on the crack resistance. Hydroxyapatite ceramics contain hydroxyl groups (chemical formulae: $\text{Ca}_{10}(\text{PO}_4)_6(\text{OH})_2$), favoring water adsorption on the crack surface and thus a strong decrease of surface energy in the presence of water. Some surface energy measurements are available in the literature [3]. They show that the ratio of surface energy in the presence of water to that under vacuum condition is low, which agrees with our measurements, since K_{I0} and K_{IC} refer respectively to the surface energy in air and in vacuum [12].

Results of successive relaxation tests on the same specimen in different media are shown in figure 5. Only one stage is present in both liquids. For oil, this unique stage is superimposed to the third stage of the $V-K_I$ law in the air, which proves that this stage corresponds well to the conditions of vacuum. In the case of water, the slope of the $V-K_I$ diagram is very close to that of the primary stage in air. This proves the effect of water activity and concentration on crack rate and surface energy. From these results, it can indeed be anticipated that the threshold in water should be less than $0.4 \text{ MPa}\sqrt{\text{m}}$. This can already question about the use of this material under significant loading. Using the well known equation:

$$K_I = \sigma \cdot \sqrt{\pi \cdot a} \quad (4)$$

One obtains that a defect of only $20 \mu\text{m}$ will propagate slowly under a stress of 50 MPa and lead to delayed failure.

Some results were already available in the literature concerning the stress exponents of equation (3). The effects of environment on dynamic fatigue resistance of hydroxyapatite ceramics were investigated by Raynaud et al. [6]. They found that the crack propagation exponent decreased from 22.5 ± 2 in air to 10 ± 4 in Ringer's solution for dense materials. Wakamatsu et al. [19] gave a constant fatigue parameter $n = 19$ for sintered hydroxyapatite in 37°C distilled water. Values obtained with these indirect methods (e.g. dynamic fatigue) are only average values, whereas double

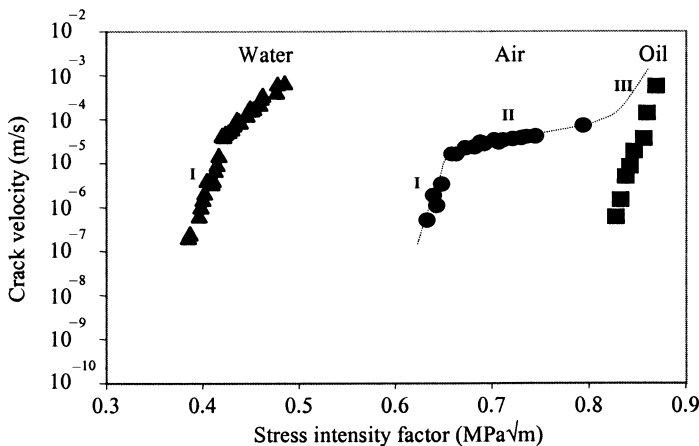


Figure 5. $V-K_I$ diagram of HAP in three media obtained on the same specimen.

torsion test (direct method) allows measurement of the real parameters A and n for each propagation stage. These averages take into account the three stages of crack propagation, but the importance of stage I is often minor and difficult to control. Unfortunately, in industrial applications, where the components have to support stresses for long duration, stage I is much more important than stages II and III. Therefore, such indirect methods cannot be used to predict the lifetime of pieces.

3.2. Microstructure–Mechanical Properties Relation

The results of crack propagation in air for the three selected sintering temperatures (1150°C, 1200°C and 1250°C) obtained by the relaxation method are shown in figure 6. In agreement with our first preliminary results, 1200°C is the optimal sintering temperature, since it corresponds to the highest crack resistance. Few degrees above or below this optimal sintering temperature lead to a shift of the V - K_I diagram towards weak stress intensity factor. This is particularly crucial for the material sintered at 1250°C, which exhibits a very poor crack resistance.

The mode of fracture can easily explain these results: figure 7 shows that 1200°C corresponds clearly to a transition from inter- to trans-granular failure. In ceramics, this transition corresponds generally to a strong decrease of crack resistance. However, it occurs often for grain sizes coarser than several dozen microns. In the case of HAP, this transition corresponds to a very low grain size (about 2 μm). The fact that the material sintered at 1150°C exhibited a slightly lower crack resistance than that sintered at 1200°C is explained by the fact that complete densification is not reached. Table II shows Young's modulus values for these three materials, measured by a resonance frequency method. As reported in the literature [3], 1200°C corresponds again to a maximum. Below this temperature, Young's modulus is lower, due to the presence of residual porosity. Above, the fall of Young's modulus can traduce micro-cracking [20]. Indeed, during cooling, residual stresses due to the anisotropy of grains can be sufficient to promote crack growth, since both toughness and threshold are low.

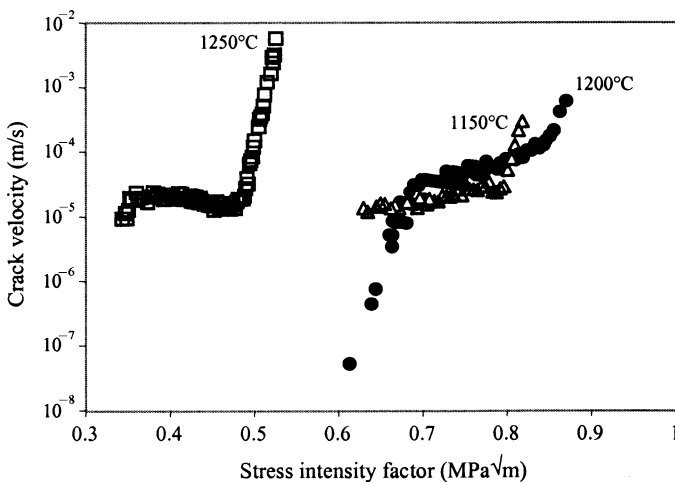


Figure 6. $V - K_I$ laws of hydroxyapatite in air for three different sintering temperature, obtained by the relaxation test.

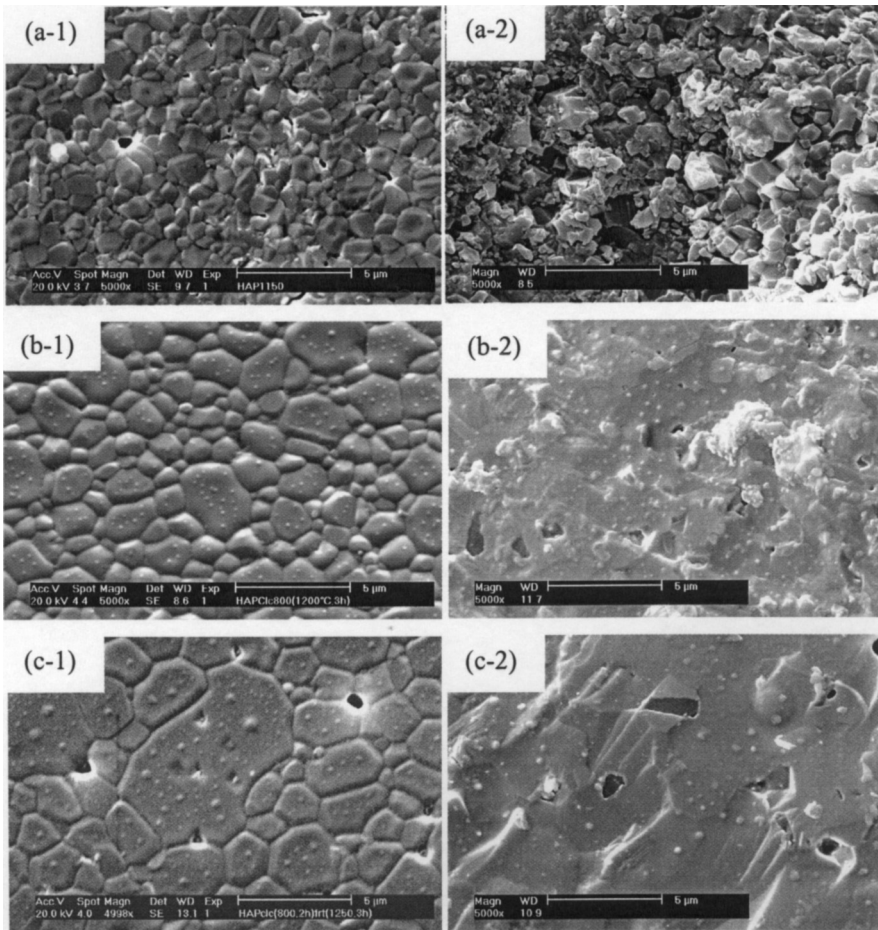


Figure 7. SEM images of HAP sintered at different temperatures ((a) 1150°C, (b) 1200°C, (c) 1250°C): etched surfaces (1) and fracture surfaces (2).

Table 2. Young's modulus evolution with different sintering temperature of HAP.

| Sintering temperature (°C, 3h) | 1150 | 1200 | 1250 |
|--------------------------------|---------|---------|-----------|
| Young's modulus (GPa) | 104 ± 2 | 112 ± 2 | 106.5 ± 2 |

3.3. Influence of ageing on $V - K_I$ laws

In order to investigate the influence of ageing on crack resistance of HAP, two relaxations were performed on the same specimen before and after ageing, as shown in figure 8. The results show a strong decrease of the toughness and a shift of the overall $V - K_I$ curve towards lower stress intensity factors. Such decrease of the mechanical properties of hydroxyapatite has been already observed in the literature. Raynaud et al. [2] argued that ageing occurred by a progressive attack of the grain boundaries by water and apparition of pores. This is confirmed in our study: ageing was followed by a decrease of the density from 98% down to 95%. It is interesting to

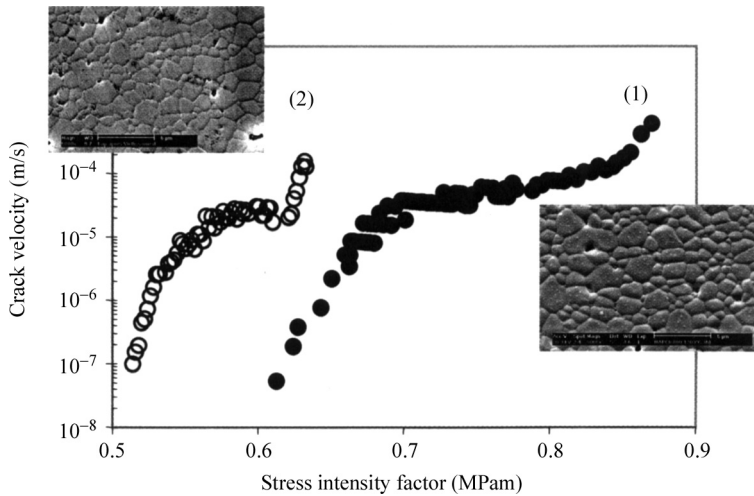


Figure 8. $V - K_I$ laws and SEM micrographs of HAP before (1) and after (2) ageing water at 37°C during 6 weeks.

note that the second stage is much more limited after ageing than before. It must be kept in mind that stage II corresponds to a saturation of crack velocity limited by the diffusion of water molecules. In the case of aged materials, water can be adsorbed at the surface, giving rise to higher diffusion rate to the crack tip.

4. CONCLUSION

This study shows the strong sensitivity of hydroxyapatite to slow crack growth, due to stress corrosion by water, resulting in a spectacular fall of crack resistance in the presence of humidity or after ageing in water. The presence of a threshold is observed in air. However, in water, this threshold is lower than $0.4 \text{ MPa}\sqrt{\text{m}}$, which is exceptionally low. Another important issue raised here is the narrow range of sintering temperatures giving acceptable mechanical properties. In particular, sintering temperatures above 1200°C lead to a dramatic decrease of crack resistance due to transgranular failure and micro-cracking.

ACKNOWLEDGMENTS

Coating Industries and Région Rhône-Alpe are acknowledged for their help and financial support ('programme MIRA' and 'Thématiques prioritaires').

REFERENCES

1. Hardouin P, Chopin D, Devyver B, Flautre B, Blary MC, Guigui P, Anselme K. *J Mater Sci-Mater Med* 1991; 3:212-218.

2. Raynaud S, Champion E, Bernache-Assolant D. *Bioceramics* 1997; 10:75–78.
3. De With G, Van Dijk J. A., Hattu N, Prijs K. *J Mater Sci* 1981; 16:1592–1598.
4. Chevalier J, Saïdaoui M, Olagnon C, Fantozzi G. *Ceramics Inter* 1996; 22:171–177.
5. Muralithran G, Ramesh S. *Ceramics Int* 2000; 26:221–230.
6. Raynaud S, Champion E, Bernache-Assolant D, Tetard D. *J Mater Scien : Mater. in medicine* 1998; 9:221–227.
7. Chevalier J, Olagnon C, Fantozzi G, *J Am Ceram Soc* 1999; 82, n°11:3129–3138.
8. Ebrahimi M. E, Chevalier J, Fantozzi G. *J Mater Res* 2000; 15, n°1:142–147.
9. Chevalier J, Olagnon C, Fantozzi G, Cales B. *Ceramics International* 1997; 23:263–266.
10. Gautier S, Champion E, Bernache-Assolant D. *4th Euroceramics* 1995; 8:201–208.
11. Plekta B. G, Fuller E. R, Koepke B. G. *ASTM Spec tech publ* 1979; 678:19–38.
12. Lawn B. *Fracture of Brittle Solids* : 2nd Edition, Cambridge University Press 1993:378 p.
13. Ciccotti M, Gonzato G, Mulargia F. *Int J of Rock Mechanics & Mining Sciences* 2000; 37:1103–1113.
14. Williams D. P, Evans A. G. *J. Test Eval* 1973;1, n°4:264–270.
15. Poitout D. *Biomécanique orthopedique*. Paris : Masson 1987:203 p.
16. Rhanim H, Olagnon C, Fantozzi G, Torrecillas R, *J Europ Cer Soc* 1997; 17:85–89.
17. Fett T, Munz D. *Fracture mechanical of ceramics* 1992; 9:219–233.
18. Wan K, Lathabai S, Lawn B. *J Europ Ceram Soc* 1990; n°6:259–268.
19. Wakamatsu N, Goto T, Adachi M, Imura S et al. *J Japanese Soc for Dental Mater And Devices* 1990; 9:178–188.
20. Halouani R, Bernache-Assolant D, Champion E, Ababou A. *J Mater Sci* 1994; 5:563–568.

CRACK PROPAGATION BEHAVIOR OF ALUMINA WITH DIFFERENT GRAIN SIZES UNDER STATIC AND CYCLIC FATIGUE

H. El Attaoui^{1, 2}, M. Saadaoui², J. Chevalier¹
and G. Fantozzi¹

ABSTRACT:

Crack propagation in high purity alumina ceramics with different grain sizes was investigated with the Double Torsion method during static and cyclic fatigue. Slow crack growth in alumina is due to stress corrosion by water molecules at the crack tip. However, the microstructure plays a significant role on $V-K_I$ laws (crack velocity versus stress intensity factor) under static loading: the higher the grain size, the larger the crack resistance. This increase in crack resistance with grain size is easily attributed to crack bridging mechanisms. A compliance function, based on the variation of compliance with bridging stresses, is applied here to quantify the amount of crack bridging. It is shown experimentally that the reinforcement due to crack bridging is proportional to the compliance function. Under cyclic fatigue, a reduction of crack bridging is observed, followed by a decrease of the compliance function. During crack propagation under cyclic loading, the compliance is affected by the frictional degradation of bridges (due to repeated unloading and loading). The amount of frictional degradation versus number of cycles is followed for different loading conditions. At low loads, the crack rate is initially equal to zero, but crack bridging

¹ G.E.M.P.P.M. (U.M.R. C.N.R.S. 55 10) I.N.S.A. de Lyon, 69621 Villeurbanne Cedex France

² L.E.R.S.I.M. Ecole Mohammadia d'Ingénieurs, Rabat, Morocco

decreases monotonically with the number of cycles. After an 'incubation' period, crack propagation initiates and new bridges are formed. This leads further to an equilibrium between crack shielding degradation and crack shielding accumulation. The equilibrium condition is obtained more rapidly for higher loads. In any case, the crack resistance at the equilibrium is always lower than that obtained under monotonic loading. This is particularly significant for coarse grain microstructures: the higher the crack resistance under monotonic loading, the higher the degradation under cyclic loading. This implies, that it is inappropriate to incorporate directly V - K_I curves obtained from monotonic loading into a cyclic fatigue analysis because of the reduction in crack-tip shielding.

1. INTRODUCTION

For most ceramics, the presence of a reactive environment causes crack to grow at subcritical stress levels. This phenomenon is commonly referred to static fatigue or delayed failure [1–4]. The basic mechanism for this slow crack growth is the stress-enhanced chemical interaction between environmental species (especially water) and the crack tip bonds. As a general trend, slow crack growth is described on the basis of V (crack velocity) versus K_I (stress intensity factor) diagrams. These diagrams generally exhibit three different stages [5]. In the first stage (Region I, for low velocities), crack propagation is limited by the thermally activated reaction kinetic between the ceramic and water molecules. Region II, at intermediate velocities, depends on environment, but is much less sensitive to K_I . This region is often attributed to gaseous diffusion along the crack interface. Region III, for high velocities represents the fracture of ceramic bonds without the need of environmental species.

Polycrystalline ceramics generally offer greater crack resistance than single crystals, and this effect is more pronounced for ceramics with coarse microstructure [4, 6, 7]. This is due to reinforcement mechanisms which increase the energy needed for crack propagation. In alumina, this reinforcement (often denoted as an 'R-Curve' behavior) has been clearly attributed to crack bridging [8–11]. Different studies have shown the influence of R-Curve on V - K_I laws obtained under static loading. An increase of crack resistance is followed by a shift of the V - K_I plot towards high values of K_I [4]. Moreover, the slope of the curve is apparently higher for coarse grain alumina. However, if the R-Curve effect is subtracted from the experimental results, a unique V - $K_{I\text{tip}}$ (crack velocity versus stress intensity factor at the crack tip) law is obtained for all alumina ceramics, independently of the grain size. This means that the crack growth mechanism (stress corrosion by water molecules) is the same at the crack tip and that the apparent change of the V - K_I law with grain size is a direct effect of crack bridging.

In the eighty's, great effort was focused to the development of ceramics with high crack resistance, to increase their reliability [12]. However, it was quickly recognised that ceramics, which exhibited stable crack growth resistance behavior were also generally susceptible to cyclic fatigue effects [13, 14]. There is now a common belief that this effect is related to the same crack bridging mechanism, which makes possible the stable crack growth in these materials. In other words, this means that crack bridging in alumina can be degraded under alternate loading

[6, 15, 16]. Under cyclic loading, the crack-tip shielding effect from existing bridges is reduced owing to the damage of these bridges under cyclic loading. Jacobs and Chen [17] hypothesised that the fatigue behavior was the result of an equilibrium between degradation and the creation of new bridging sites with crack propagation. The creation of new bridging sites is governed by the growth of the crack, whereas the deterioration is function of repeated frictional degradation.

In a recent work, the authors have applied a procedure, which allows for bridging stress determination and R-Curve evaluation from compliance data [18–21]. This is the aim of this work to apply this approach to the overall crack propagation behavior of alumina, under both static and cyclic loading. The idea is to follow the evolution of crack resistance of different alumina ceramics for different conditions of loading.

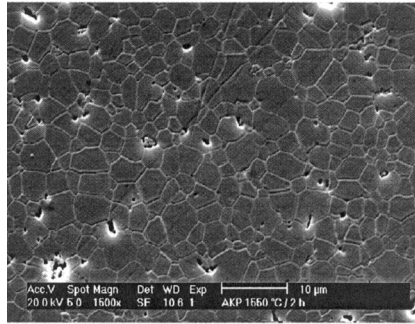
2. EXPERIMENTAL PROCEDURE

2.1. Samples Preparation

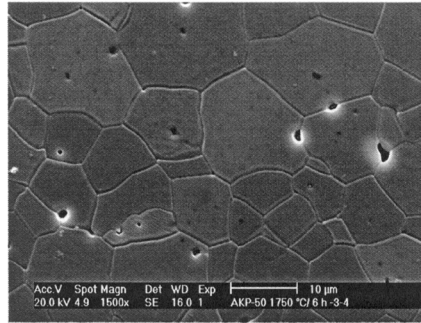
An ultrapure (>99.99 %) α -alumina powder (AKP50, Sumitomo, Tokyo, Japan), with an initial crystallite size of 0.2 μm , was used as starting material. A two-step process was applied for powder compaction: after uniaxial pressing at 40 MPa, the powder was cold isostatically pressed at 350 MPa. The green density was about 52% theoretical density. Specimens were sintered in air for various times and temperatures between 1550°C and 1750°C with heating and cooling rates of 5°C/min. In order to avoid any contamination, the green compacts were placed in high-purity alumina crucibles, elaborated from the same powder, and filled with the same alumina powder. The sintered samples were cut and polished with a series of diamond pastes down to a final polish of 1 μm . Several specimens from each heat treatment were thermally etched in order to reveal the microstructures. Grain size and morphology were examined by scanning electron microscopy (SEM) on thermally etched surfaces (Fig. 1). The grain size given in table 1 are obtained from the linear intercept method. Densities were measured using the Archimede method using distilled water as the medium. An uniform equi-axed structure was available even for high sintering temperature, because of the care taken during processing (absence of contamination).

2.2. Double Torsion Method

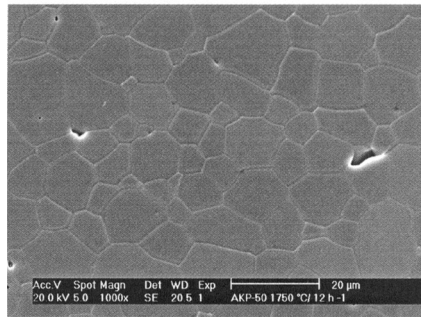
The Double Torsion (DT) method was used to obtain crack propagation laws under static and cyclic loading conditions, and to evaluate the amount of R-Curve under any specific condition. The geometry of the DT specimens, test method and loading configuration can be found in preceding works [3, 4, 22, 23]. Specimens consisted of plates with dimensions of 40 mm \times 20 mm \times 2 mm. The tensile surface was polished down to 1 μm , to observe the crack with a precision of $\pm 2 \mu\text{m}$. A notch of dimension $a_0 = 8$ mm and root $\rho = 0.15$ mm was machined with a diamond saw. The specimens subsequently were heat-treated in air at 1400°C for 20 min, to anneal residual grinding stresses. Then an indentation was performed at low load (5 kg) in order to initiate a small natural crack. Subsequent precracking was performed by loading the specimens at a low rate, to induce a sharp crack with an initial length $a_i = 10$ mm.



AKP4



AKP14



AKP19

Figure 1. SEM microstructures of alumina ceramics.

Table 1. Sintering temperatures and physical properties of alumina ceramics.

| Nomenclature | Sintering temperature | Sintering time | % theoretical density | Mean grain size (μm) |
|--------------|-----------------------|----------------|-----------------------|-----------------------------------|
| AKP4 | 1550 °C | 2 h | 97.4 | 4.2 μm |
| AKP14 | 1750 °C | 6 h | 98.9 | 14.1 μm |
| AKP19 | 1750 °C | 12 h | 99.3 | 19.8 μm |

The DT configuration is known for giving stress intensity independent of crack length. However, it has been recently demonstrated that K_I was slightly dependent on the crack length [2]. Therefore in order to obtain accurate $V-K_I$ curves, a correction factor needs to be introduced in the conventional expression of K_I . This correction is expressed with the following empirical equation [2]:

$$K_I = HP(a/a_0)^{6/32} \quad (1)$$

Where K_I is the stress intensity factor, P is the applied load, H is the geometry factor in DT configuration, a is the total crack length, and a_0 is the notch length.

2.3. Static Fatigue Experiments: Load relaxation Curves, Compliance Data and R-Curves

Relaxation test [2,4] were used to obtain V- K_I curves under monotonic loading: the pre-cracked specimens were loaded at a constant rate of 0.3 mm/min, followed by subsequent stopping of the crosshead at a given displacement, when crack starts to propagate. The load versus time (P versus t) curve theoretically allows easily the determination of the V- K_I curve. However, to be perfectly correct, this determination necessitates the knowledge of the crack length at each time of the relaxation (see eqn. 2 for K_I determination). Thus calibration curves were first conducted in order to connect crack length and compliance. They were done on one specimen for each alumina. For these particular specimens, several loading until crack propagation – unloading - optical measurement of crack length – were conducted, which enable to obtain the variation of compliance versus crack length. During load relaxation, the variation of the compliance with time can be monitored from the value of the displacement applied to the specimen and from the variation of the load versus time. R-Curves were also obtained with the calibration specimens, since the load necessary for crack propagation, hence K_R and the crack length were measured for each loading–unloading sequence.

2.4. Cyclic Fatigue Experiments

Tests were performed at a frequency of 10 Hz under load control using a sine wave form. For all the tests, the load ratio was fixed to $R = P_{\min}/P_{\max} = 0.1$. Crack length was measured optically at regular intervals to obtain the crack rate for a given applied maximum stress intensity factor $K_{I\max}$. Compliance was also measured at regular intervals.

3. RESULTS AND DISCUSSION

3.1. Crack Propagation Under Static Loading

3.1.1. Compliance Analysis and R-Curves

Figure (2) represents the compliance of DT specimens versus crack length for the three alumina ceramics. They are compared to the theoretical ‘expected’ evolution based on the hypothesis of two independent beams [24]. On the one hand, the discrepancy between theoretical variation of compliance with crack length is insignificant for fine grain alumina. On the other hand, it becomes important for the alumina with large grain size. This result was already noted in previous works [4]. This means that the two beams constituting the DT specimens cannot be considered as independent, since crack bridging occurs to close the crack in coarse grain alumina, leading to lower compliance.

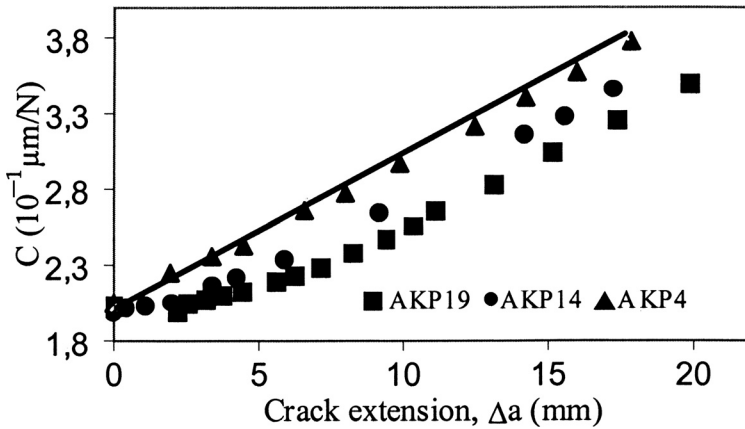


Figure 2. Compliance of the DT specimen versus crack length, for tree alumina ceramics. Solid line represents the theoretical evolution.

A compliance function $\phi(\Delta a)$ has been recently proposed to give an insight into the crack bridging stresses along the crack wake [18–20]. It was successfully adopted by different authors to evaluate the bridging stress / crack opening displacement relationship in alumina based materials. This function considers the difference between the real compliance of the specimen C_{real} and the theoretical compliance C_{th} , which can be calculated from theoretical purely elastic models or measured with notches. It is argued that because of the effect of bridging stresses on crack opening displacement, $C_{real} < C_{th}$. This inequality results from crack-interface bridging stresses, which cause C_{real} to be less than the ideal elastic compliance. In other word, the inequality $C_{real} < C_{th}$ can provide a measurement of the bridging stress influence. A compliance function, $\phi(\Delta a)$, is defined [18]. It increases from zero to a given value and shows a plateau when the bridging zone is fully developed:

$$\phi(a) = \frac{C_{th}(a)}{\frac{\partial C_{th}}{\partial a}} \left(\frac{C_{th}(a)}{C_{real}(a)} - 1 \right) \tag{2}$$

This function is null for ceramics without bridging $C_{real} = C_{th}$. It is plotted in figure (3) for the three alumina ceramics and compared to the evolution of K_R versus a (measured on the same specimens). The two type of curves show exactly the same shape (an initial increase due to the extension of the crack bridging zone, followed by a plateau corresponding to a saturation). From these results, it can be argued that the compliance function is proportional to the amount of crack shielding $\Delta K_R = K_R(a) - K_0$, where K_0 is the initiation crack resistance, without bridging reinforcement. Experimentally, we obtain:

$$\phi(a) = C_s \cdot \Delta K_R(a)$$

with $C_s = 2,1 \text{ mm/MPa}\sqrt{\text{m}}$.

Thus, the compliance function can be a useful tool to quantify the amount of reinforcement due to crack bridging. It will be used in the next section on cyclic fatigue.

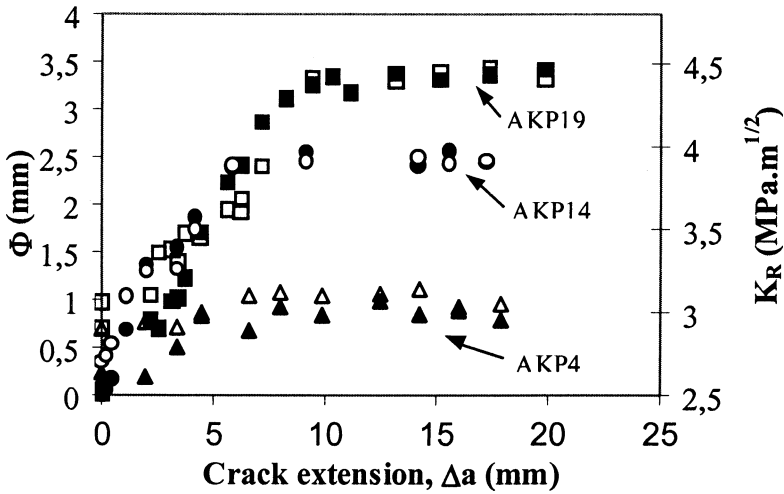


Figure 3. R-curves (open symbols) and ϕ functions (solid symbols) for three alumina ceramics AKP4, AKP14 and AKP19.

3.1.2. *V-K_I and Reinforcement Curves under Static Loading*

Figure (4) represents the $V-K_I$ curves obtained from the relaxation method. As already reported, the three curves exhibit three distinct stages, attributed to the stress corrosion mechanism cited in the introduction [2, 4]. The three curves are different, while the same powder was used as the starting material. The higher the grain size, the higher the slope of the $V-K_I$ diagram. This is obviously related to reinforcement mechanism that act to shield the crack for large grain size (see for example figure 5). The fracture toughness, K_{IC} , deduced from figure (4) by taking K_{IC} as the K_I value needed to propagate the crack above 10^{-3} m/s, is about the same for the three material, around $4.5 \text{ MPa}\sqrt{\text{m}}$, indicating independence of the grain size. Indeed, this critical stress intensity factor corresponds to the initiation of the relaxation test

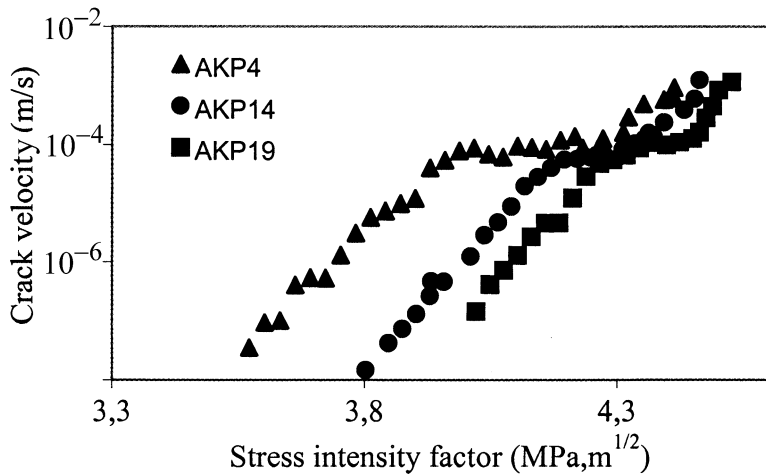


Figure 4. Crack-velocity diagram for three alumina ceramics AKP4, AKP14 and AKP19 under static fatigue.

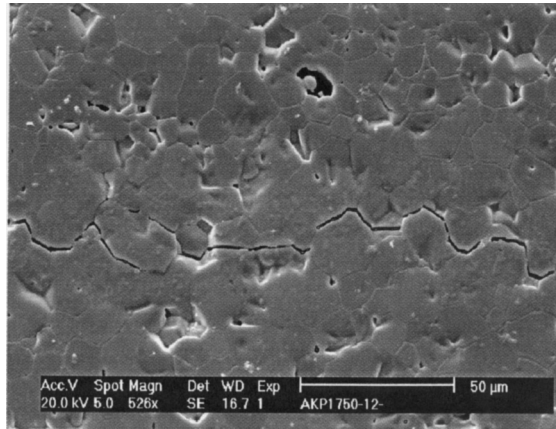


Figure 5. Crack bridging in coarse-grained AKP19 alumina.

for small crack lengths (after pre-cracking only), where crack bridging interactions are not developed yet. In contrast, the minimum stress intensity factor that leads to measurable crack propagation during relaxation, is higher in coarse-grained alumina than that in fine-grained alumina. This was discussed in the preceding issue of *Fracture Mechanics of Ceramics* [25]. In particular, it was shown that an intrinsic crack propagation law, $V-K_{I\text{tip}}$ (crack rate versus stress intensity factor at the crack tip) could be obtained by considering that:

$$K_{I\text{tip}}(a) = K_I - \Delta K_R(a) \quad (3)$$

This means that the crack growth mechanism is basically the same, the difference in $V-K_I$ diagram lying in the crack bridging mechanism. The question that can be risen at this stage is the influence of cyclic fatigue on crack bridging degradation, especially for the alumina with the larger grain size (AKP19).

3.2. Crack propagation under Cyclic Loading.

3.2.1. Crack Bridging Degradation under Alternate Loading

Crack bridging degradation was studied here by the means of the compliance function. A series of DT tests was conducted to observe the drop in crack bridging during a transient regime between static and cyclic fatigue. The samples were first loaded under monotonic loading, and the $\phi(a)$ function measured until it reaches the plateau value (maximum K_R value). They were subsequently subjected to cyclic mode under a maximum load lower than one reached at the end of the static fatigue. The ratio between the load under cyclic fatigue and static fatigue will be called R_f . For most of the test, R_f was chosen to induce no crack propagation initially under cyclic fatigue. Thus, the compliance function could be monitored first as a function of the number of cycles, without any crack propagation. Generally, after a given amount of cycles, the crack started to grow in a slow manner and the ϕ function could be monitored as a function of the crack size. An example of this method is given in figure (6), for AKP19, and for $R_f = 0.85$. The sample is first loaded to obtain

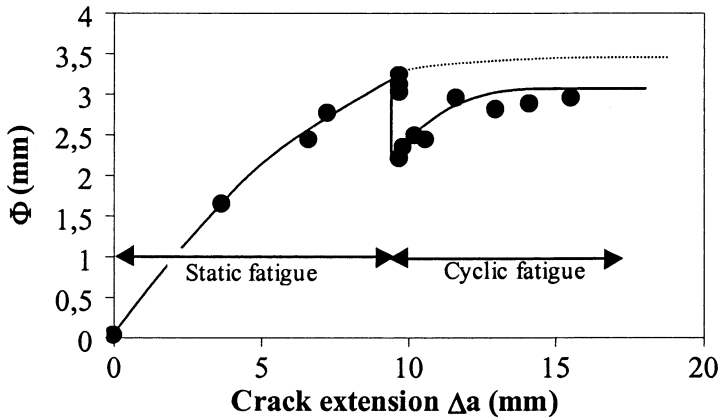


Figure 6. ϕ -curves under static fatigue then under cyclic fatigue ($R_f = 0.85$) for AKP19.

a fully bridged crack, then loaded under cyclic fatigue. The results show a dramatic decrease of the compliance function at a constant crack size. This means that crack bridging degradation occurs. When crack-bridging degradation is larger enough to promote slow crack growth ($K_{I\text{tip}}$ larger than the threshold stress intensity factor K_{I0}), the crack starts to grow. This is followed by a subsequent increase of the compliance function. The function tends to an equilibrium after a given amount of crack extension. Jacobs and Chen [17] have claimed for an equilibrium crack rate under cyclic fatigue, corresponding to a balance between frictional crack bridging degradation and accumulation due to crack growth (creation of new bridges). This equilibrium is assessed in this experiment. Fatigue crack growth was observed in this experiment only after $N_c = 100000$ cycles. This means that an ‘incubation’ is needed for the crack to grow under this load level. This incubation period correspond to the duration needed for the mechanical fatigue to degrade bridging enough to obtain $K_{I\text{tip}} > K_{I0}$.

Another experiment was conducted on the same alumina, but for a lower R_f ratio ($R_f = 0.7$). For this experiment, crack propagation initiated after an incubation of 2 million cycles. The two experiments are compared figure (7) in a ϕ versus number of cycles diagram. Figure (7) shows that the bridging degradation (traduced here by the drop of the ϕ function) is slower for low R_f value, but reached a maximum which is higher.

It must be kept in mind that during mechanical fatigue, before any crack reinitiation, ΔK_R decreases with the number of cycles. Thus, it is easy to understand that the amount of crack bridging degradation must be important for low K_I values for crack to re-start, while it is smaller for high K_I values. When the crack re-propagate, it grows at a higher rate for high load, which in turns leads to a lower crack bridging degradation at the equilibrium. In the hypothesis that the ϕ function is always proportional to the crack bridging reinforcement, one can calculate the amount of degradation due to cyclic fatigue just before crack repropagation and at the crack rate equilibrium. The values are compiled in table 2. These experimental results show clearly that both the frictional degradation of bridged sites and the accumulation of new ones during cyclic fatigue influence the ϕ -curve. The ϕ function thus appears to be an ideal tool to quantify the amount of crack bridging during

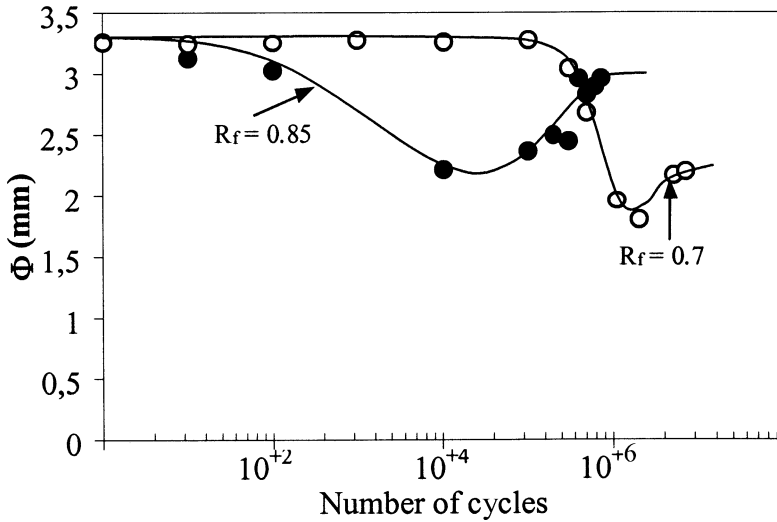


Figure 7. ϕ function versus number of cycles for two load ratios ($R_f=0.7$, and $R_f=0.85$)

Table 2. Crack bridging degradation under cyclic fatigue.

| R_f ratio | Maximal K_R degradation By cyclic fatigue (before crack re-initiation) | Equilibrium degradation |
|-------------|---|----------------------------|
| 0.7 | 0.7 MPa \sqrt{m} | 0.5 MPa \sqrt{m} |
| 0.85 | 0.5 MPa \sqrt{m} | 0.15 MPa \sqrt{m} |

static fatigue or the amount of degradation during cyclic fatigue. It will help us to discuss the cyclic fatigue diagrams presented below.

3.2.2 Crack Velocities under Cyclic Loading

The crack velocity versus $K_{I,max}$ curves obtained during cyclic loading are represented in Fig. 8. For comparison, the results under static loading also are included in the figure. For AKP4, the $V-K_{I,max}$ diagram corresponds roughly to that obtained under static loading conditions. This might suggest that no cyclic fatigue degradation occurs in this fine grain material. However, the evaluation of the degradation caused by cyclic loading from the direct comparison of $V-K_I$ and $V-K_{I,max}$ is not completely correct. The crack velocity per second that would occur if there were no specific cyclic mechanism must be evaluated. This calculation can be done easily via integration of the slow crack growth velocity that is measured under static stress over the cycling stress [2]. The result of this calculation is also plotted in figure (8) (dotted line). From the comparison of the calculated cyclic crack growth and that obtained experimentally, it is shown here that a small, but significant amount of cyclic fatigue degradation is observed. The degradation is about 0.1 MPa \sqrt{m} . Even for this material, a small amount of bridging was noted. This leads to the observed cyclic fatigue sensitivity.

The degradation is very important for AKP19. The crack rates measured under cyclic loading are several orders of magnitude higher than calculated from static

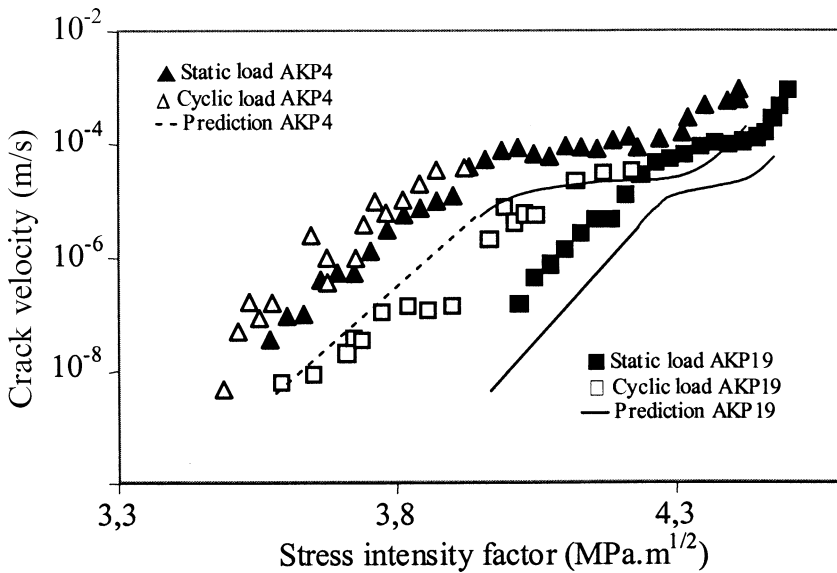


Figure 8. Crack velocity versus stress intensity factor K_I or $K_{I,max}$ for AKP4 and AKP19, under both static and cyclic fatigue.

fatigue results (single line in figure (8)). The degradation is more pronounced for low crack rates. This leads to a slope of the crack rate versus $K_{I,max}$ diagram which is lower than under static loading conditions. Again, we must remember that cyclic fatigue crack rate corresponds to an equilibrium between crack bridging accumulation (by crack propagation) and damage (frictional degradation). At low loads, the ratio of frictional degradation to accumulation is high, leading to higher cyclic fatigue effects. These results highlight the fact that cyclic fatigue degradation is more detrimental around the threshold stress intensity factor and that design of ceramic structure must include this aspect. From our experimental results for low crack rates, it seems that a major part of the benefit of crack bridging under static loading is degraded during cyclic fatigue. The threshold stress intensity factor of AKP4 and AKP19 under cyclic fatigue appears to be roughly the same. These results must be confirmed with experiments for still lower crack rates, but could have an important practical impact.

It is interesting to note that crack bridging degradation obtained with the ϕ -function analysis (see table 2) are in perfect agreement with the latter results. For the lowest crack rates, the cyclic fatigue degradation is on the order of $0.5 \text{ MPa}\sqrt{\text{m}}$.

4. CONCLUSION

The crack-propagation behavior of alumina was investigated under static and cyclic loading condition. A compliance analysis has been successfully applied to the determination of crack bridging reinforcement and its degradation during fatigue. The crack velocities increase under alternative stresses is important for coarse grain alumina. A major part of crack bridging occurring during quasi-static testing can

be degraded under alternative stresses. This result shows that the importance of cyclic-fatigue degradation is strongly related to the toughening under static loading (R-curve behaviour). It should be kept in mind that the cyclic fatigue degradation is more pronounced for low crack rates, i.e. it is maximum around the threshold stress intensity factor K_{10} . An incubation period of several million cycles can be required for crack initiation. This aspect should be kept in mind in terms of structural design.

ACKNOWLEDGMENT

Région Rhône-Alpe is acknowledged for financial support ('programme MIRA').

REFERENCES

1. Michalske T. A, Freiman S. W, J Am Ceram Soc 1983; 66, n°4:284–288.
2. Chevalier J, Olagnon C, Fantozzi G, J Am Ceram Soc 1999; 82, n° 11:3129–3138.
3. Chevalier J, Saïdaoui M, Olagnon C, Fantozzi G. Ceramics Inter 1996; 22:171–177.
4. Ebrahimi M. E, Chevalier J, Fantozzi G. J Mater Res 2000; 15, n°1:142–147.
5. Wan K. T, Lathabais S, and Lawn B. R, J Eur Ceram Soc 1990; 6, n°4:259–268.
6. Guiu F, li M, Reece M.J, J Am Ceram Soc 1992; 75, n°11:2976–2984.
7. Chantikul P, Bennison S. J, Lawn B. R, J Am Ceram Soc 1990; 73, n°8:2419–2427.
8. Swain M V, J Mater Sci Letters 1986, 15:1313–1315.
9. Steinbrech R. W, Reichl A., Schaarwachter W, J Am Ceram Soc 1990; 73, n°7:2009–2015.
10. Swanson P. L, Fairbanks C. J, Lawn B. R, Mai Y. W, Hockey B. J, J Am Ceram 1987; 70, n°4: 279–289.
11. Mai Y. W, Lawn B.R, J Am Ceram Soc 1987; 70, n°4:289–294.
12. Kendall K, Alford N. McN, Tan S.R, Birchall J.D, J Mater Res 1986; 1, n°1:120–23.
13. Lathabais S, Rodel J, Lawn B.R, J Am Ceram Soc 1991; 74, n°6:1340–1348.
14. Fett T, Munz D, J Mater Sci Letters 1993; 12 : 352–354.
15. Gilbert C. J, Dauskardt R. H, Ritchie R. O, Ceram Inter 1997, 23:413–418.
16. Gilbert C. J, Han Y. S, Kim D. K, Ritchie R. O, Ceram Inter 2000, 26:721–725
17. Jacobs D. S, Chen I. W, J Am Ceram Soc 1995; 78, n°6:513–520.
18. Hu X, Mai Y. W, J Am Ceram Soc 1992; 75, n°6:848–853.
19. Mai Y. W, Lawn B. R., J Am Ceram Soc 1987; 70, n°4:289–294.
20. Hu X, Mai Y. W, J Eur Ceram 1992; 9:213–217.
21. Lutz H. F, Hu X, Mai Y. W, J Eur Ceram 1992; 9:133–142.
22. Lawn B. Fracture of Brittle Solids : 2nd Edition, Cambridge University Press 1993:378 p.
23. Williams D. P, Evans A. G. J. Test Eval 1973; 1, n°4:264–270.
24. Bousuge M, Inghels E, Lamon J, Rev Int Hautes Temp Refract 1982; 19:185–206.
25. Ebrahimi M. E, Chevalier J, Fantozzi G. Fracture Mechanics of Ceramics Vol 13:273–286.

EFFECTS OF PORE/ GRAIN-SIZE INTERACTION AND POROSITY ON THE FRACTURE OF ELECTROCERAMICS

Chunsheng Lu, Robert Danzer, and Franz Dieter Fischer*

ABSTRACT

The strength of brittle materials decreases as the size of specimens increases, and this so-called size effect can be described by the Weibull statistical fracture theory. Recent experiments on the fracture strength of electroceramics, however, have shown that it is not always so. Electroceramics, such as zinc oxide (ZnO) applied for varistors, are mainly designed with respect to electrical rather than mechanical properties, and thus they usually contain a high degree of porosity which may act as the origin of fracture. It is suspected that the complex nature of defect-microstructure interaction and the high density of porosity are possible reasons for this insensitivity to strength scaling. In order to verify this hypothesis, more generally, to deliberate the scaling behavior of the fracture strength of electroceramics containing high densities of flaws, the effects of pore/grain-size interaction and porosity on the fracture strength in ZnO ceramics are investigated based on the finite element analysis. The numerical results show that the fracture strength is more influenced by the pore/grain-size interaction than only by the size of a pore or its shape although the stress singularity of sharp

* Chunsheng Lu, Institut für Struktur- und Funktionskeramik, Montanuniversität Leoben, A-8700 Leoben, Austria; and LNM, Institute of Mechanics, Academia Sinica, Beijing 100080, China. Robert Danzer, Institut für Struktur- und Funktionskeramik, Montanuniversität Leoben, A-8700 Leoben, Austria. Franz Dieter Fischer, Institut für Mechanik, Montanuniversität Leoben, A-8700 Leoben, Austria.

grooves around a pore is closely related to their angles. As a consequence the pore/grain-size interaction will increase the fracture probability of small pores, and lead to a homogenization of critical flaw sizes. Furthermore, the finite element analysis exhibits that the high degree of porosity, especially the heterogeneous distribution and the clustering of pores, could be conducive to further homogenization of critical crack sizes. This implies that the fracture strength of ZnO ceramics is insensitive to the size of specimens, which has been corroborated by recent experiments using specimens with various effective volumes.

INTRODUCTION

Ceramics have been widely applied in engineering for their excellent resistance to heat, corrosion, and wear. Unfortunately ceramics also are very sensitive to flaws and have a disposition to brittle failure. Their strengths vary unpredictably from component to component even if a set of nominally identical specimens are tested under the same conditions. In general the strength of brittle materials decreases as the size of specimens increases, and this so-called size effect can be well described by the Weibull statistical fracture theory.¹⁻⁵ Recent experiments on the fracture strength of electroceramics, however, have shown that it is not always so. The strength of zinc oxide (ZnO) ceramics, applied for varistors, is still found to scatter, but the size of specimens has no evident influence on their mean strengths.⁶⁻¹⁰ The latter is obviously in conflict with the Weibull statistical theory.

Extensive fractographic investigations for the fracture surfaces of ceramics have shown that fracture usually originates from pre-existing defects, which may arise from their intrinsic structures or imperfect processing.¹¹⁻¹³ In most cases the fracture strength of ceramics, similar to other brittle materials, is controlled by the local properties of critical flaws or microstructures such as size, shape and orientation etc. For example the grain size has a clear effect on the fracture strength of ceramics, which can be represented in the form of the Orowan-Petch relationship.¹⁴⁻¹⁸

As is well known, electroceramics are mainly designed with respect to electrical rather than mechanical properties, and thus they usually contain a high degree of porosity which might act as the origin of fracture. Although mechanical properties including elastic moduli, strength, and toughness usually decrease with increasing porosity, it is suspected that the complex nature of defect-microstructure interaction and high density of porosity of flaws are possible reasons for the insensitivity to strength scaling in ZnO ceramics.⁶⁻⁸ In order to verify this hypothesis, more generally, to investigate the scaling behavior of the strength of electroceramics containing high densities of flaws, the effects of pore/grain-size interaction and porosity on the fracture strength in ZnO ceramics are investigated in this paper.

STRENGTH DISTRIBUTION AND SIZE EFFECT

It is often supposed that a small volume in a brittle material is like a chain of many links, and if any link breaks, then the whole material will fail. Based on this weakest link principle and an empirical power law distribution function for the size of

defects,⁵ the cumulative failure probability of a brittle material subjected to an applied stress σ , i.e., the Weibull strength distribution, can be represented as

$$F(\sigma, V) = 1 - \exp \left[-\frac{V}{V_0} \left(\frac{\sigma}{\sigma_0} \right)^m \right] \tag{1}$$

where V is the volume of a specimen, V_0 the reference volume, σ_0 the characteristic strength, and m the Weibull modulus which is a measure of the scatter of strength data.

The size effect is a direct consequence of the Weibull distribution. In other words, the larger the specimen, the higher the probability to find a large and critical defect and the smaller the mean strength of the corresponding sample.⁷⁻⁹ This size effect can be described as

$$V_{\text{eff},1} \sigma_{\text{max},1}^m = V_{\text{eff},2} \sigma_{\text{max},2}^m \tag{2}$$

if we suppose two specimens with different effect volumes as well as the same probability of failure, where V_{eff} is the effective volume subjected to the maximum stress σ_{max} . This provides us with another experimental procedure to check out the Weibull distribution.

Recently, fracture strengths of three ceramic materials, i.e., silicon nitride (Si_3N_4), silicon carbide (SiC), and ZnO, have been tested.⁶⁻⁹ As illustrated in Figure 1, for Si_3N_4 and SiC ceramics, the mean strength decreases with the increase of effective volume (as described by the Weibull theory, see arrows in Figure 1). In the case of ZnO ceramics, the mean strength of specimens with various effective volumes almost keeps to be a constant. This is in conflict with the Weibull theory. Further more detailed studies on the distribution of strength data, in terms of the Akaike information criterion, showed that the normal distribution may be a preferred choice in the case of ZnO ceramics.^{9,19}

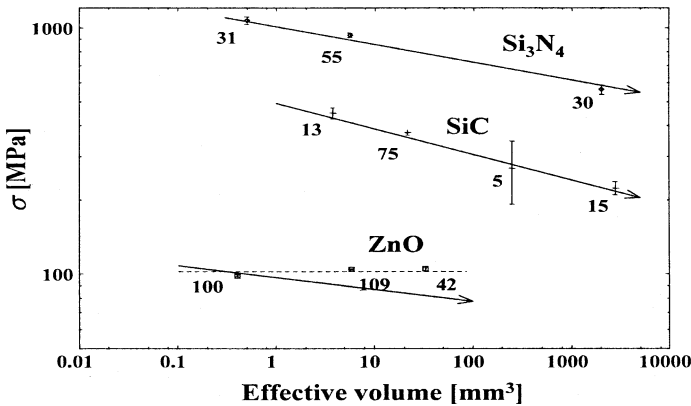


Figure 1. Experimental results of the dependence of mean strengths for three ceramics on the effective volumes, where numerals are the number of experiments, and error bars refer to 90% confidence band (the higher the number of tests, the smaller the scatter of data). Solid arrow lines, with the slope of $-1/m$, indicate the size effect extrapolated by the Weibull distribution (here the Weibull moduli m determined by the sample with the single size and the largest specimens, 55 for Si_3N_4 , 75 for SiC and 109 for ZnO) are 13.89, 9.62, and 20.92 for Si_3N_4 , SiC and ZnO respectively). The dashed line indicates the arithmetic mean strength $\sigma = 102.37$ MPa of the sample with the largest specimens.

Strictly speaking, the conditions made to get the Weibull distribution are not always correct or necessary in real applications. Based on as few assumptions as possible, a general strength distribution can be derived as

$$F(\sigma, V) = 1 - \exp[-\langle N_c(\sigma, V) \rangle] \quad (3)$$

where $\langle N_c(\sigma, V) \rangle$ is the expectation value of critical defects. So obviously the Weibull distribution is only a special case of this general strength distribution function.²⁰⁻²³ This could provide us with some hints for the explanation of experimental discoveries, however more investigation on the relationship between fracture strength and microstructures should be made.

MICROSTRUCTURES AND DEFECTS

Recent experiments on electroceramic components, such as high power varistors and positive temperature coefficient (PTC) switching components, show that fracture starts at internal flaws which could be traced back to green bodies or powder agglomerates.¹¹⁻¹³ Due to the trend to increase power densities in electrical devices, the mechanical loads subjected to these components increase, and problems with insufficient mechanical strength get more and more severe. It is surprising that, however, relatively few investigations exist about the mechanical failure of electroceramics.^{24,25}

The real configuration of flaws in ZnO ceramics is very complex. Maybe the intrusions formed by the impingement of neighboring grains can be described by a Saturn-ring like cracks around a pore. Based on fractographic evidence, a model for brittle fracture has to include the interaction of two different defect populations: intrinsic defects on the microstructural level such as grain boundaries are considered as nucleation sites for microcracks, whereas processing defects such as pores or inclusions act as stress concentrators.¹⁵⁻¹⁸ In a first approximation, a typical flaw in ZnO ceramics is represented by a pore with cusps or sharp grooves, as illustrated in Figure 2(a). Here there are three characteristic length scales: the pore radius R , the grain radius r , and the notch depth c (or the groove angle θ). If $\theta = 0$, the notch depth c can be determined by the simple relationship, $c = \sqrt{R(R + 2r)} - R$, that is to say, there are just two independent parameters, and the sharp groove is similar to a crack with curved faces. In the case of ZnO ceramics, the mean radius R of pores is in the range of 50 to 100 μm , and the radius r of grains is about in the range of 2 to 10 μm .¹¹⁻¹³ The mechanical properties of ZnO ceramics are: the elastic modulus $E = 100$ GPa and the Poisson ratio $\nu = 0.36$.^{25,26}

It is worth noting that the porosity in ZnO ceramics is high to about 5 vol.%. Due to the heterogeneous distribution of defects there often exist clusters formed by a lot of pores, as illustrated in Figure 2(b), and even the clustering of sub-clusters. Thus the interaction (the stress shielding or intensification) between pores or clusters may play an important role in determining the fracture strength of ZnO ceramics.

FINITE ELEMENT ANALYSIS

In the following analysis, the stress fields and stress intensity factors for a single pore with sharp grooves or its clusters were evaluated using the finite element program

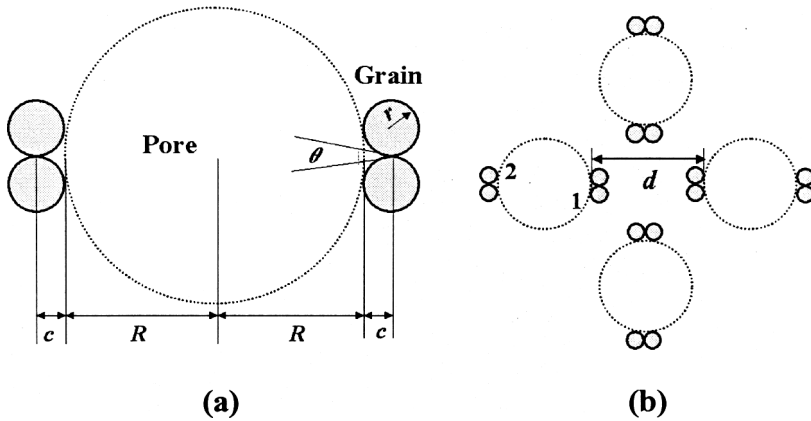


Figure 2. Schematic two-dimensional representation of defects in ZnO ceramics. (a) A single pore with cusps or sharp grooves formed by neighboring grains, and (b) a typical cluster formed by several pores due to heterogeneous distribution of defects, where d is the internal distance of the cluster, and the numbers 1 and 2 indicate the inner and outer cracks respectively.

ABAQUS/Standard V.5.8 (Hibbitt, Karlsson and Sorensen Inc., 1998), and meshing was mainly carried out with the preprocessor code PATRAN V.9.0 (MacNeal-Schwendler Corp., 1998).

Stress Singularity of a Sharp Groove

As illustrated in Figure 2(a), for the sake of simplicity, let the radii of a pore and grains surrounding the pore be constants, the different notch angles can be obtained via the change of the depth from the groove tip. The cases for every ten-degree interval were chosen, and the stress fields in the vicinity of a sharp groove were calculated. The results show that the stress singularity takes the form $\sigma \propto r^{-\alpha}$, where the singularity order α is closely related to the angle θ of the groove, and changes from 0.5 ($\theta = 0^\circ$) to 0 ($\theta = 180^\circ$), see Figure 3. The detail structure of the groove-tip stress field differs from that of a common crack. Specifically, this singularity still exists under compression loading. The difference with the Williams' analytical result reflects the influence of groove shapes.²⁷ As we expected, the singularity order $\alpha = 0.5$ if $\theta = 0$, and the groove reduces to a crack-like sharp notch. In fact such a sharp notch is often developed due to the surface energy minimization of grains.

Effect of Pore/Grain Size Interaction on Fracture

The stress intensity factors for a two-dimensional multicroack system, as illustrated in Figure 2, are calculated applying the energy release rate or contour integral J . It is worth noting that the crack (i.e., sharp groove) faces are curved, and a positive stress intensity factor also exists in the case of global compressive loading. Since J values can be obtained only for planar cracks, the normal to the crack faces that lie within the domains used for the contour integrals must be specified in the calculation. The stress intensity factor can be calculated by

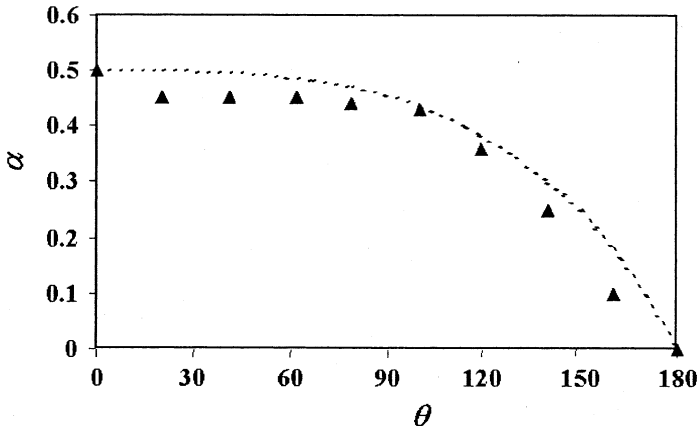


Figure 3. The stress singularity exponent α in the vicinity of a sharp groove vs. its angle θ . For comparison the Williams' analytical result for a sharp notch is also plotted (the dotted line).

$$K = \sqrt{\frac{JE}{1 - \nu^2}} \tag{4}$$

Three kinds of pores with sharp grooves formed by various grain sizes were investigated. Numerical results of the normalized stress intensity factor, K/K_0 , versus the ratio of grain and pore sizes, r/R , are summarized in Figure 4. Here we define the stress intensity factor for a crack with the length $R + c$ as a reference value, i.e., $K_0 = \sigma\sqrt{\pi(R + c)}$, where σ is the nominated stress used in the calculation. It is obvious to see that the normalized stress intensity factor is related to the ratio of grain and pore sizes. It is interesting to note that the normalized stress intensity factor for small pores is greater than that for big pores. In other words, there is a trend to make the distribution of critical flaw sizes be more homogeneous.

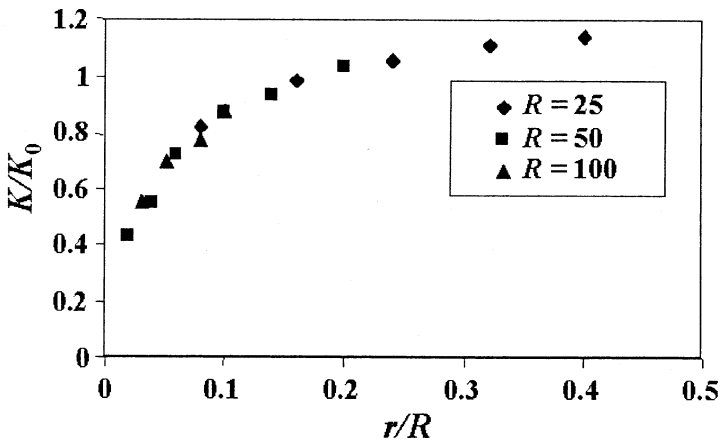


Figure 4. The normalized stress intensity factor vs. the ratio of grain and pore sizes. Here three kinds of pores with radius $R = 25 \mu\text{m}$, $50 \mu\text{m}$, and $100 \mu\text{m}$ were calculated. The depth of a sharp groove c can be determined by the simple geometrical relationship, $c/R = \sqrt{1 + 2r/R} - 1$. For more details of the model, see Figure 2(a).

The real configuration of a pore in ZnO ceramics is much more complex than that we supposed in this simple model. One may argue that at least two or more grooves should be used to simulate the irregular notch formed by grains surrounding a pore. Further numerical analysis for a more realistic model, in which three sharp grooves were introduced, showed that the stress intensity factor at the middle groove tip decreases due to the influence of other neighboring grooves, but the influence region is limited. Compared to the influence of the ratio of grain and pore sizes discussed above, it is less important and will be omitted.

Effect of Porosity on Fracture

As is well known, the interaction between defects is sensitive to the details of their geometrical arrangement. Especially if mechanical properties such as fracture strength discussed here are closely related to local rather than average properties, it is not easy to get a deterministic relationship.²⁸⁻³¹ Next, in order to qualitatively understand the possible influence of the high degree of porosity to fracture strength of ZnO ceramics, two typical cases are studied: one being a single cluster as illustrated in Figure 2(b) and the other a periodic distribution of the single cluster.

As shown in Figure 5, shielding for the inner crack, i.e. the crack 1 in Figure 2(b), will be effective if the distance between pores approach to a certain threshold. The stress intensity factor of the inner crack decreases when the ratio d/R is about equal to two, which is approximately equal to the 5 vol.% for pores uniformly distributed in the specimen. Although the stress intensity factor of the outer crack, i.e., crack 2 in Figure 2(b), increases, the corresponding region is much smaller than that the stress intensity factor decreases.

Due to heterogeneous distribution of microstructures and defects, the aggregation of defects is often found in specimens. The main reason can be a multi-modal powder size distribution. Here the clustering behavior is modeled by a periodic array of clusters with distance D . The shielding effect discussed above is more clear, as shown in Figure 6. The normalized stress intensity factors of both inner and outer

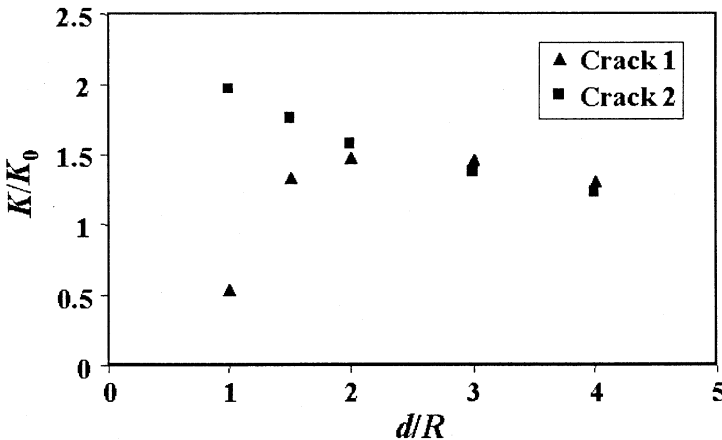


Figure 5. The normalized stress intensity factor vs. the ratio of cluster and pore sizes for a single cluster of pores. For more details of the model, see Figure 2(b).

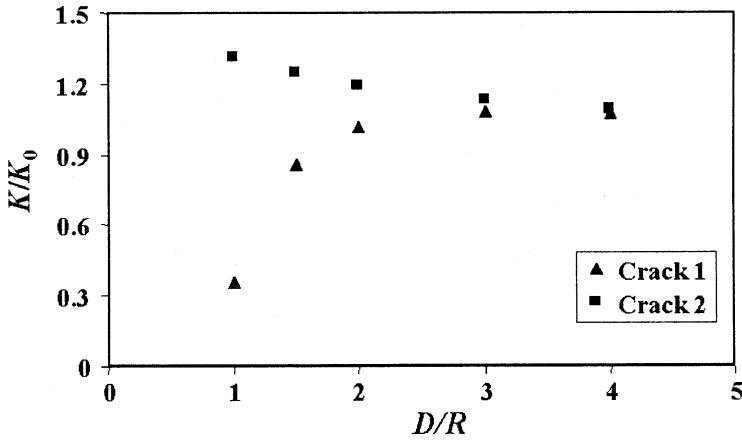


Figure 6. The normalized stress intensity factor vs. the ratio of cluster and pore size for clustering with a periodic distribution, where D indicates the distance between two clusters. For more details of the model, see Figure 2(b).

cracks decrease. This means that clustering will further increase the homogeneities of critical flaw sizes, at least for this special defect configuration in ZnO ceramics.

DISCUSSION

The absence of the size effect discovered from experiments on the fracture strength of ZnO ceramics manifests a deviation from the Weibull distribution. The other distribution such as normal or lognormal distribution might be used in the analysis of strength data, which has been corroborated by further statistical analysis. As discussed above, the grain size has a clear effect on the fracture strength of ZnO ceramics. It is usually found that grain size distributions measured are approximately log-normally distributed.³²

Contrary to Si_3N_4 and SiC ceramics where crack-like flaws are sparsely distributed, flaws in ZnO ceramics, i.e. pores with sharp grooves, are determined by many independent and random factors such as size, location, even the degree of porosity etc. Thus it is not surprising that strength data yield the Weibull distribution in Si_3N_4 and SiC ceramics, but it is not so in ZnO ceramics. The probability of a flaw as becoming critical in ZnO ceramics may be described $p = \prod p_i$, where p_i denotes the probability of i th possible factor. So taking logarithms of both sides we have $\log p = \sum p_i$. Since the p_i are independent random variables, the central limit theorem is applicable, and $\log p$ has a normal distribution just as we expected.

Finally it is worth noting that the results obtained here are based on a two-dimensional model. The three-dimensional configuration of defects in ZnO ceramics could be described by a spherical pore with some kind of sharp cracks, such as a circumferential crack, a semicircular crack and a circular crack.¹⁵⁻¹⁸ The numerical analysis of three-dimensional model is much more complex since we need to consider the special configuration of defects and their arrangement, but it is worthwhile to be investigated.

CONCLUSIONS

Based on both experiments of fracture strength and numerical analysis of the effects of pore/grain-size interaction and porosity on fracture strength in ZnO ceramics, the following conclusions can be drawn:

- (1) The Weibull distribution could be widely used in the analysis of strength data and size effect. Recent experiments on the fracture strength of electroceramics, however, have shown that it is not always so. The strength distribution may be the normal, or other distributions rather than the Weibull distribution are valid due to the influence of many independent and random factors.
- (2) The stress singularity of a sharp groove formed by grains around a pore is closely related to its angle.
- (3) The fracture strength in ZnO ceramics is more influenced by the ratio of pore and grain sizes or pore/grain-size interaction than only by the size of critical pores. As a consequence the pore/grain-size interaction increases the fracture probability of small pores and decreases the fracture probability of large pores. It leads to a homogenization of the critical flaw sizes.
- (4) The high degree of porosity, especially the heterogeneous distribution and clustering of pores, could be conducive to further homogenization of critical crack sizes in ZnO ceramics.

ACKNOWLEDGMENTS

This work was supported by the Lise Meitner Program of Austrian Science Fund (FWF) under project numbers M587 and M662. We are grateful to Prof. F. G. Rammerstorfer and Dr. H. J. Böhm for many valuable discussions.

REFERENCES

1. B. R. Lawn, *Fracture of Brittle Solids*, 2nd ed. (Cambridge University Press, Cambridge, 1993).
2. J. B. Wachtman, *Mechanical Properties of Ceramics* (John Wiley & Sons Inc., New York, 1996).
3. Z. P. Bažant and J. Planas, *Fracture and Size Effect in Concrete and Other Quasibrittle Materials* (CRC Press, Boca Raton, 1998).
4. R. W. Rice, *Mechanic Properties of Ceramics and Composites* (Marcel Dekker Inc., New York, 2000).
5. W. Weibull, A statistical distribution function of wide applicability, *J. Appl. Mech.* **18**, 293–297 (1951).
6. T. Lube, M. Manner, and R. Danzer, The miniaturization of the 4-point-bend test, *Fatigue Fract. Eng. Mater. Struct.* **20**, 1605–1616 (1997).
7. R. Danzer and T. Lube, Fracture statistics of brittle materials: It does not always have to be Weibull statistics, in: *Ceramic Materials and Components for Engines*, edited by K. Niihara et al. (Japan Fine Ceramics Association, Tokyo, 1998), pp. 683–688.
8. R. Danzer, Mechanical behavior and reliability of ceramics, in: *Ceramics: Getting into the 2000's*, edited by P. Vincenzini (Techna Srl., Faenza, 1999), pp. 379–386.
9. C. Lu, R. Danzer, and F. D. Fischer, Fracture statistics of brittle materials: Weibull or normal distribution, *Phys. Rev. E* **65**, 067102 (2002).

10. C. Lu, R. Danzer, and F. D. Fischer, Fracture statistics of brittle materials: How to choose a better distribution function, in: *Fracture Mechanics Beyond 2000*, Vol. 2, edited by A. Neimitz et al. (EMAS Publishing, Warley, 2002), pp. 395–400.
11. R. Danzer, Mechanical failure of advanced ceramics: The value of fractography, *Key Eng. Mater.* **223**, 1–18 (2002).
12. P. Supancic, Fracture and fractography of electroceramics, *Key Eng. Mater.* **223**, 69–78 (2002).
13. R. Danzer and P. Supancic, Mechanical failure and mechanical design of electroceramics components, in: *Proceeding of the 27th Annual Cocoa Beach Conference and Exposition of Advanced Ceramics & Composites*, (Cocoa Beach, Florida, 2003).
14. R. W. Rice and D. Lewis, Limitation and challenges in applying fracture mechanics to ceramics, in: *Fracture Mechanics of Ceramics*, Vol. 5, edited by R. C. Bradt, A. G. Evans, D. P. H. Hasselman, and F. F. Lange (Plenum Press, New York, 1983), pp. 659–676.
15. A. Zimmermann and J. Rödel, Generalized Orowan-Petch plot for brittle fracture, *J. Am. Ceram. Soc.* **81**, 2527–2532 (1998).
16. A. Zimmermann, M. Hoffman, B. D. Flinn, R. K. Bordia, T.-J. Chuang, E. R. Fuller Jr., and J. Rödel, Fracture of alumina with controlled pores, *J. Am. Ceram. Soc.* **81**, 2449–2457 (1998).
17. A. Zimmermann and J. Rödel, Fracture statistics based on pore/grain-size interaction, *J. Am. Ceram. Soc.* **82**, 2279–2281 (1999).
18. A. Zimmermann, M. Hoffman, T. Emmel, D. Gross, and J. Rödel, Failure of metal-ceramic composites with spherical inclusions, *Acta Mater.* **49**, 3177–3187 (2001).
19. C. Lu, R. Danzer, and F. D. Fischer, Influence of threshold stress on the estimation of the Weibull statistics, *J. Am. Ceram. Soc.* **85**, 1640–1642 (2002).
20. R. Danzer, A general strength distribution function for brittle materials, *J. Eur. Ceram. Soc.* **10**, 461–472 (1992).
21. R. Danzer and T. Lube, New Fracture statistics for brittle materials, in: *Fracture Mechanics of Ceramics*, Vol. 11, edited by R. C. Bradt et al. (Plenum Press, New York, 1996), pp. 425–439.
22. R. Danzer, F. D. Fischer, and W. Y. Yan, Application of probabilistic fracture mechanics to a dynamic loading using the example of a dynamic tension test for ceramics, *J. Eur. Ceram. Soc.* **20**, 901–911 (2000).
23. R. Danzer, T. Lube, and P. Supancic, Monte Carlo simulations of strength distributions of brittle materials – type of distribution, specimen and sample size, *Z. Metallkd.* **92**, 773–783 (2001).
24. A. Vojta and D. R. Clarke, Electrical-impulse-induced fracture of zinc oxide varistor ceramics, *J. Am. Ceram. Soc.* **80**, 2086–2092 (1997).
25. M. Lengauer, D. Rubeša, and R. Danzer, Finite element modeling of the electrical impulse induced fracture of a high voltage varistor, *J. Eur. Ceram. Soc.* **20**, 1017–1021 (2000).
26. J. F. Shackelford, W. Alexander, and J. S. Park, *Materials Science and Engineering Handbook* (CRC Press, Boca Raton, 1994).
27. M. L. Williams, Stress singularities resulting from various boundary conditions in angular corners of plates in extension, *J. Appl. Mech.* **19**, 526–528 (1952).
28. M. Kachanov, Elastic solids with many cracks and related problems, *Adv. Appl. Mech.* **30**, 259–445 (1994).
29. M. Kachanov, Solids with cracks and non-spherical pores: proper parameters of defect density and effective elastic properties, *Int. J. Fracture* **97**, 1–32 (1999).
30. C. Lu, D. Vere-Jones, and H. Takayasu, Avalanche behavior and statistical properties in a micro-crack coalescence process, *Phys. Rev. Lett.* **82**, 347–350 (1999).
31. E. B. Shields, Fracture prediction of hole patterns with multiple cracks using the finite element method, *Int. J. Fatigue* **23**, 13–20 (2001).
32. E. Bennett, L. Lay, R. Morrell, and B. Roebuck, *Microstructural Measurements on Ceramics and Hardmetals* (Measurement Good Practice Guide No. 21, National Physical Laboratory, London, 1999).

FRACTURE BEHAVIOUR OF PLASMA SPRAYED THERMAL BARRIER COATINGS

Jürgen Malzbender, Takashi Wakui, Egbert Wessel, and Rolf W. Steinbrech^{*}

1. INTRODUCTION

Thermal barrier coatings (TBCs) of plasma sprayed yttria stabilised zirconia (YSZ) are increasingly utilised for heat exposed components of advanced gas turbines^{1,2}. An important reason for the application of zirconia coatings is the low thermal conductivity of this ceramic material which is further diminished in a TBC by the high concentration of spraying induced microstructural defects, e.g. crack-shaped defects between and within the spraying splats. Thus with TBCs on gas cooled turbine components stiff temperature gradients can be realised as an important prerequisite for an increased thermal efficiency of the energy conversion process.

However, the same spraying defects also provide sources of TBC fracture under mechanical loading and cyclic thermal exposure during the operation of the turbines. In principle, segmentation and delamination fracture of the TBC can be distinguished with cracks orientated perpendicular and parallel to the lamellar microstructure.

The vertical segmentation cracks improve the in-plane strain tolerance of the TBC and are at present deliberately introduced in some of the advanced industrial coatings. Contrary, delamination is highly unfavourable since large scale spallation of the TBC would terminate the service life of the component. Accordingly, any further improvement of the plasma sprayed TBCs with respect to easier segmentation and more difficult delamination requires in-depth understanding of the fracture

^{*} Jürgen Malzbender, Takeshi Wakui, Egbert Wessel and Rolf W. Steinbrech, Institute for Materials in Energy Systems (IWV2), Research Centre Juelich, 52428 Juelich, Germany

behaviour. In particular, experimental methods to quantify the respective fracture resistances and to study the microstructural crack growth mechanisms are of interest.

From the experimental point of view the toughness (resistance) domain is still minimally encompassed³ due to the difficulty to analyse quantitatively the fracture behaviour of TBCs in the actual thickness (few hundred microns) applied for gas turbine components. Indeed, many of the fracture mechanics approaches that have been carried out in recent years focus on long crack fracture behaviour in thick coatings.

In this respect the fracture experiments of Damani and Lutz⁴, who measured the toughness of air plasma sprayed bulk alumina prepared from free-standing, thick-walled tubes, may be taken as a baseline. Using CT and SENB specimens they obtained for as sprayed material long crack toughness values of $\sim 1.4 \text{ MPam}^{1/2}$ and $\sim 0.4 \text{ MPam}^{1/2}$ in segmentation and delamination orientation, respectively. Essentially flat R-curve behaviour of the as sprayed material changed into a sharply rising R-curve after heat treatment at 1550°C .

Toughness values of segmentation cracks in the same order of magnitude $\sim 1 \text{ MPam}^{1/2}$ were also measured by Choi et al.⁵ in SEVNB tests after separation of thick (6mm) plasma sprayed TBC ($\text{ZrO}_2\text{-8wt\% Y}_2\text{O}_3$). The toughness was the same at room temperature and 800°C . Long crack toughness data referring to attached YSZ coatings (0.87 mm thick) have been reported by Thurn et al.⁶. Bending tests with the un-notched TBC in tension revealed pronounced R-curve behaviour during controlled propagation of segmentation cracks. In as sprayed condition the segmentation toughness increased from 0.2 to $1.3 \text{ MPam}^{1/2}$ over $500 \mu\text{m}$ of crack extension, equivalent to a crack resistance range between 10 N/m and 180 N/m. With increasing annealing temperature the R-curve shifted towards higher toughness. Considering the maximum tensile stress in the specimen the authors defined a fracture toughness value of $1.1 \text{ MPam}^{1/2}$.

Mechanical delamination studies with long cracks are more difficult to carry out, since they bear the problem of appropriate loading of the TBC. Typically the TBC is sandwiched by gluing on the TBC surface a metallic extension bar for load application.

Thurn et al.⁶ used such symmetric composite specimens with intermediate TBC in the shape of bend bars. The delamination crack was propagated from a notch in the TBC adjacent to the interface with the bond coat. The work of fracture as averaging crack resistance was about 80 N/m, which is 30% lower than the respective value of segmentation. Anderson⁷ obtained with specimens in DCB geometry a critical energy release rate of $\sim 17 \text{ N/m}$ ($\sim 0.68 \text{ MPam}^{1/2}$). Shaw et al.⁸ used a chevron notched sandwich specimen and determined from the maximum load of the delamination test a critical energy release rate of 16 N/m. Failure occurred in all studies within the TBC (white failure). Much higher crack resistance values were reported from delamination studies with a testing geometry after Charalambides et al.⁹, which provides a value for the steady state resistance of long cracks. Oechsner¹⁰ determined crack resistance values of 100 and 200 N/m for an interface roughness R_A of 4.5 and $12 \mu\text{m}$, respectively. For the smoother interface the fracture resistance remained essentially unaffected by heat treatment, i.e. the thickness of the thermally growing oxide scale (TGO) had no influence, whereas in the case of a rougher interface a decrease was measured with increasing TGO thickness.

Efforts to measure the resistance of short cracks in delamination orientation are limited and typically rely on indentation cracking. Bartlett and Dal Maschina¹¹ used a Vicker's tip with 10 N load to generate near interface cracking in the TBC. Unaffected by heat treatment the measured toughness was in the range of 1.5–1.9 MPam^{1/2} equivalent to 15–25 N/m with the reported elastic modulus of 130 GPa. Using the same indentation method Rabiei and Evans¹² determined a short crack toughness of 0.7 MPam^{1/2}, equivalent to a crack resistance of 50 N/m, if a low TBC stiffness of ~10 GPa is assumed.

Although a comparison of the results from the different groups has definitively limitations, since different processing parameters and microstructures of the tested TBCs must be assumed, some general trends can be deduced. It appears that segmentation cracks experience a higher material resistance than the cracks causing delamination. The segmentation cracks also tend to exhibit pronounced R-curve behaviour when growing from the initial defect size to the long crack configuration. The delamination cracks propagated in all the reported mechanical tests within the TBC and the crack path was typically observed to be close to the interface with the bond coat. However, controversial results exist with respect to long crack resistance data and the R-curve behaviour proposed for delamination by Evans et al.³ has not really been demonstrated. Also the initial stages of delamination due to growth of the existing microstructural TBC defects have not been analysed in detail.

It is the aim of the present work to contribute to the still limited experimental body of fracture characterisation of plasma sprayed TBCs with controlled crack propagation studies which cover the size scale between the initial microcrack length and the final length of long cracks. The presented fracture results are restricted to as sprayed TBC at room temperature with particular focus on two aspects: i) crack length dependent fracture resistance is determined to further elaborate the R-curve behaviour of segmentation cracks as well as to demonstrate the same effect for delamination and ii) the observed toughening is attributed to the microstructural features of crack path selection and crack surface interaction. Bending geometries are used to propagate the cracks in thick stand-alone and thin attached TBCs. As exception, the long delamination cracks were propagated by wedge opening loading (WOL). Thus gluing of extension bars on the TBC surface could be avoided. In order to achieve a correlation with microstructure the crack growth is monitored in-situ with optical and scanning electron microscopy.

2. EXPERIMENTAL

2.1. Material

Zirconia stabilised with ~8 wt.% zirconia was used as coating material for processing of the TBC specimens. All atmospheric plasma spraying (APS) was carried out by the processing group of the Institute for Materials and Processes in Energy Systems (IWV1) at the Research Centre Juelich.

Due to the plasma spraying process the TBC comprises a characteristic microstructure, which is conveniently recognised on through-thickness fracture surfaces. The SEM micrograph of Fig. 1 reveals the lamellar alignment of the spraying splats. Within the individual splats columnar, sub-micron diameter grains are visible.

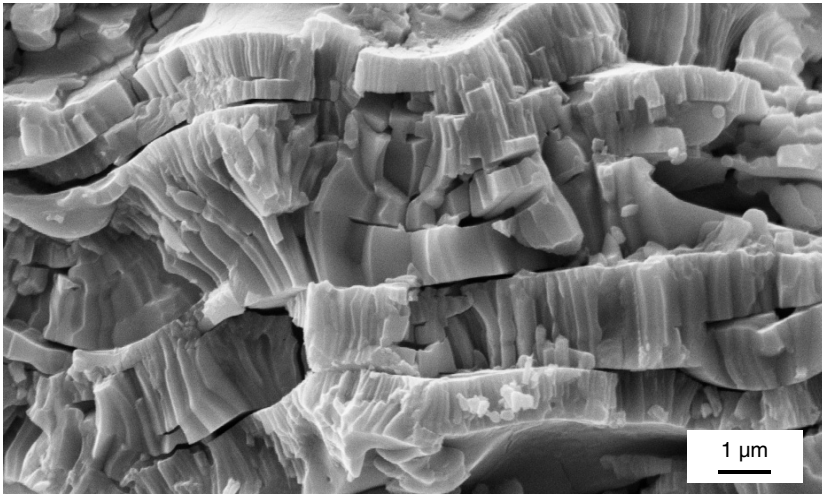


Figure 1. Fracture surface of air plasma sprayed TBC with lamellar microstructure. The spraying splats consist of sub-micron grains. Crack-shaped defects exist between and within the spraying splats (inter- and intra-splat cracks).

Moreover, crack-shaped defects exist between and within the splats, hereafter termed as inter- and intra-splat cracks, respectively.

2.2. Specimen Preparation

The geometrical configuration of the TBC in the thermal barrier system of a gas turbine component was adapted by spraying thin TBC ($\sim 300 \mu\text{m}$) on larger plates of Ni-super alloy substrate with a NiCoCrAlY bond coat.

The multilayer composite plate was machined into bend bars (see Table 1) using a diamond saw for the ceramic TBC and spark erosion for the metal.

Thick TBCs (2–3 mm) were obtained by plasma-spraying the YSZ on a mild steel substrate plate. The substrate was then dissolved using hydrochloric acid and the remaining TBC layer was cut into bend bars and small rectangular blocks for wedge opening tests.

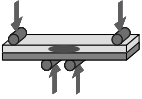
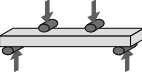
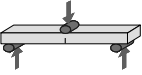
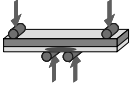
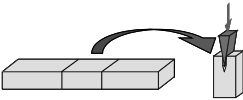
In order to facilitate in-situ microscopic observation of the controlled crack growth, one side face of each specimen was mirror polished ($1 \mu\text{m}$ final diamond paste).

Some of the stand-alone thick TBC bend bars as well as all WOL specimens were notched using the razor-blade method¹³ to obtain a sharp notch tip.

2.3. Testing Procedure

The specimens were tested in miniaturised mechanical testing equipment mounted on the stages of optical and scanning electron microscopes to monitor the crack propagation in-situ on a side face of the specimens. The 4-point bending tests of attached TBC were carried out either with the TBC under tension or under compression. Stand-alone TBCs were tested in 4-point (un-notched) and 3-point (notched) bending (see Table 1).

Table 1. Testing and specimen geometries used for fracture characterisation of APS-TBC.

| Testing Geometry | Specimen Size | TBC | | |
|------------------|---|--|-------------------|-------------------------------|
| | | Thickness | State | |
| Segmentation |  | $(1.5 \times 3 \times 45)\text{mm}^3$ | 300 μm | attached / tension |
| |  | $(2 \times 3 \times 45)\text{mm}^3$ | 2 mm | separated / tension |
| |  | $(2 \times 3 \times 45)\text{mm}^3$ | 2 mm | separated / notched / tension |
| Delamination |  | $(1.5 \times 3 \times 45)\text{mm}^3$ | 300 μm | attached / compression |
| |  | $(2.4 \times 3 \times 4.5)\text{mm}^3$ | 2.4 mm | separated / wedge opening |

Growth of cracks in segmentation orientation was achieved by bending tests with the TBC under tension. For delamination cracking two different methods were applied. The first stage of growth related with the extension of the initial inter-splat cracks was studied in bending tests with the TBC under compression. Long delamination cracks were propagated in the thick stand-alone TBCs by loading the notched specimens with a wedge (17.5° angle). Details of the testing method will be reported elsewhere¹⁴.

In all cases (bending and WOL tests) controlled crack growth could be obtained. The load was applied stepwise to take micrographs of the resulting crack extension. After the fracture tests a frame by frame comparison of the micrographs was performed to correlated crack length with the mechanically measured load and deflection.

The sequences of in-situ taken micrographs were also used to evaluate the displacement occurring in the vicinity of the propagating crack. The determination of the strain was based on commercial software UNIDAC (universal deformation analysis by means of correlation, Chemnitzer Werkstoffmechanik GmbH). The software program permits a comparison of the displacement and strain after various increments of crack growth based on the analysis of the image contrast¹⁵. The grey-scale analyses were performed in the following sequence: i) digital image acquisition

ii) image analysis of the digitised grey-scale picture and iii) interpretation of the displacement vector field.

2.4. Crack Resistance Determination

The variety of testing geometries for the attached and separated TBCs as well as the distinction between micro-cracks and long cracks (Table 1) made different methods of crack resistance determination necessary.

2.4.1. Stand-alone TBC

The crack resistance R was determined from the balance with the critical crack driving force (G_{IC}) using a compliance approach

$$G_{IC} = \frac{P^2}{2B} \frac{dC}{da} = R \quad (1)$$

where P is the applied load, B the specimen width and C the compliance which depends on crack length a .

The compliance functions (dC/da) used in the present study for segmentation crack growth in stand-alone TBCs referred to Moon et al.¹⁶ (4-point bending) and Knehans et al.¹⁷ (notched, 3-point bending).

In the case of long cracks propagated in delamination orientation by the WOL procedure Th. Fett¹⁸ provided the compliance function:

$$C = \frac{8 \cdot a^3}{B \cdot H^3 \cdot E} \cdot \lambda(\alpha) \quad (2)$$

with

$$\lambda(\alpha) = -99.01\alpha^5 + 332.24\alpha^4 - 446.1\alpha^3 + 303.23\alpha^2 - 107.21\alpha + 18.06 \quad (3)$$

where α is the normalised crack length with respect to specimen height.

2.4.2. Attached TBC

Resistance of the segmentation crack in the attached TBC of the composite specimen was derived from the general relationship for stress intensity

$$K_I = Y\sigma_0\sqrt{\pi a} \quad (4)$$

where σ_0 is the stress, which the crack experiences. The crack-shape parameter Y depends on the ratio of crack length to specimen thickness and the loading configuration.

In principle, a crack in the TBC leads to a different specimen deflection at a particular ratio of crack length compared to isotropic material behaviour in a bending test. However, the analysis simplifies for short cracks since then Y is essentially independent of specimen thickness and loading configuration. In the case of the thermal barrier coatings analysed in this investigation the ratio of crack length to total specimen thickness was ~ 0.2 . An additional factor that has to be

taken into consideration is the change in stress intensity as the segmentation crack approaches the metallic bond coat and substrate, which can be evaluated using finite element simulation¹⁹. Taking the actual crack configuration in the attached TBC into account, Y is replaced by F_σ , which depends on the ratio of the stiffness values. Estimating $E_{\text{TBC}}/E_{\text{substrate}} \sim 0.1$ the parameter F_σ can be approximated by¹⁹

$$F_\sigma = 1.3 - 0.779(a/t) \quad (5)$$

where t is the specimen thickness. Application of equation (4) requires also knowledge of the average stress σ_0 acting on the crack:

$$\sigma_0 = \int_{a=0}^{a_{\max}} \sigma_a da / a_{\max} \quad (6)$$

The stress σ_a can be determined from the sum of the residual stress²⁰ and the applied stress due to bending moment, where in the latter case the formulas for the bending of multi-layered composites have to be used²¹. Finally, using the Irwin relationship $G_I = K_I^2/E$ the toughness was converted into crack resistance.

Assumptions had also to be made with respect to the fracture mechanics treatment of the inter-splat cracks which showed extension upon compressive loading of the TBC in bending. As will be shown in section 3.2, favourably orientated inter-splat cracks were observed to grow under the applied compressive bending stress similar to the “wing-cracks” reported and analysed by Ashby and Hallam²². The concept requires the existence of an initial crack inclined with respect to the compressive stress. The resulting shear forces cause mode I crack opening in the “wing” portions of the crack, which thereby grow parallel to the compressive stress field. Statistical evidence for this crack growth mechanism in TBCs still needs to be demonstrated, but strong support for the effect is also found in the studies of Trice and Faber²³, who tested hollow cylindrical specimens of free-standing plasma sprayed alumina under compression. The crack resistance of “wing-cracks” can be computed from the initial crack length $2a$ and the extension of the wing portion Δc under the influence of a compressive stress σ according to²²

$$R = -\frac{2}{E\pi^2} D_0 \left(\frac{\Delta c}{a} + \frac{1}{\sqrt{2}} \right) \cdot \sigma^2 \pi a \quad (7)$$

The parameter D_0 reflects the initial level of damage, $D_0 = \pi a^2 N_A$, where N_A is the number of cracks per unit area, $N_A = (2h \cdot (\Delta c + a))^{-1}$ and h is the height of the splats. Note that again the contribution of the residual stress has to be taken into account.

3. RESULTS AND DISCUSSION

The two modes of macro-cracking that occur in bending tests in case of large specimen deformation with attached TBC are shown in Fig. 2. With the TBC under tension almost equidistant segmentation cracks develop (Fig. 2a). The ratio of crack distance to TBC thickness is about $\Gamma \approx 2.25$ which is in fair agreement with

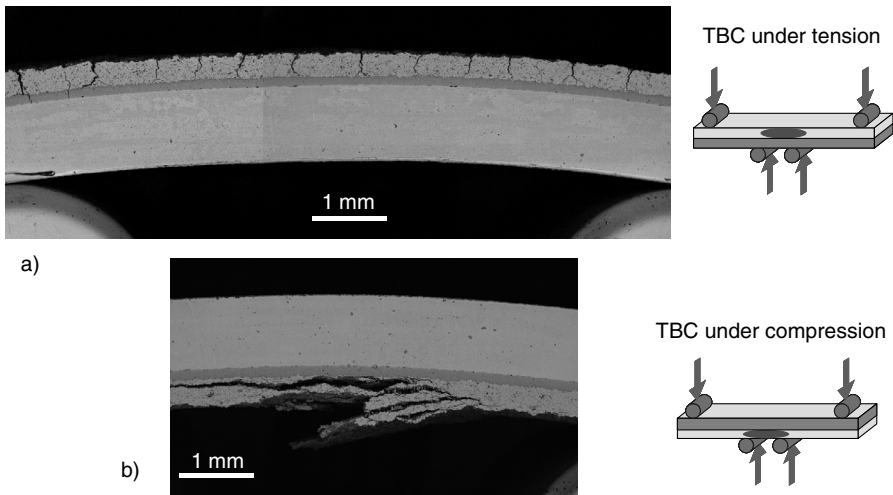


Figure 2. Bending tests with attached TBC in tension (a) and compression (b). Micrographs from fracture experiments carried out in SEM with in situ side face observation.

the theoretical value of $F_{theo} \approx 2.5$ reported in literature for coatings and thin surface films²⁴.

Under compression damage by delamination cracking is prominent (Fig. 2b). Fracture processes initiate near the free TBC surface where the highest compressive stress exists. Damage and buckling then progresses by cracking on parallel planes in an uncontrolled manner through the TBC towards the interface with the bond coat. The complexity of the failure sequence and the dependence of new delamination from the previous fracture events does not allow a quantitative toughness characterisation. The WOL tests with the growth of a single delamination crack in a stand-alone TBC provide an experimentally better defined alternative.

3.1. Segmentation Cracking

Micrographs of segmentation cracks in the three tested bending/material variants are shown in Fig. 3. In each case the segmentation crack exhibits a tortuous crack path.

The crack resistance in the attached TBC of the composite specimen increases significantly with crack extension (Fig. 4). The apparent R-curve reaches values up to 300 N/m. First crack extension is observed at low TBC resistance (~ 10 N/m), which is indicative of the weak bonding within and between the spraying splats. The apparent crack resistance reduces, if the compressive residual stress in the TBC is taken into account and subtracted from the measured values. For the given layer geometry and the involved materials of the composite specimen the TBC possesses a residual compressive stress in the order of 50 MPa²⁰. The slope of the R-curve decreases by almost a factor of three. Having made the residual stress correction, the R-curve result of the attached TBC can be compared with those of the stand-alone TBCs (Fig. 5). All testing variants reveal a rising R-curve which follows the same master-curve. Moreover the results agree well with the R-curve reported by Thurn et al.⁶ for the free-standing APS-TBC.

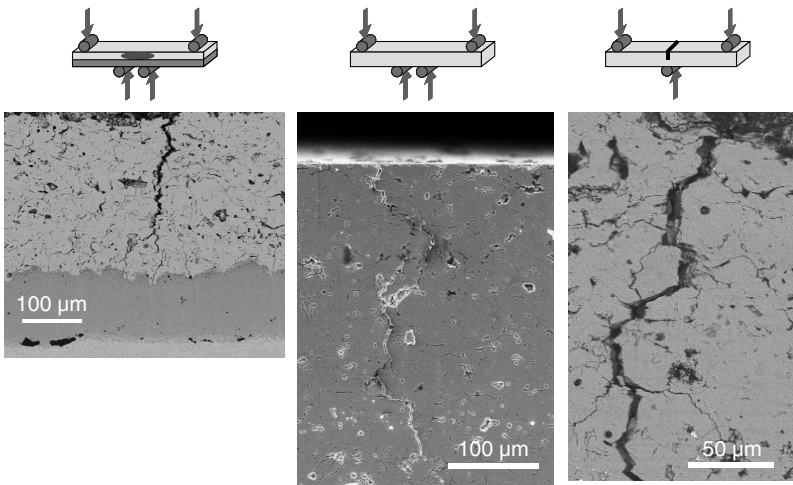


Figure 3. Controlled propagation of segmentation cracks in bending tests with attached (left) and stand-alone TBC.

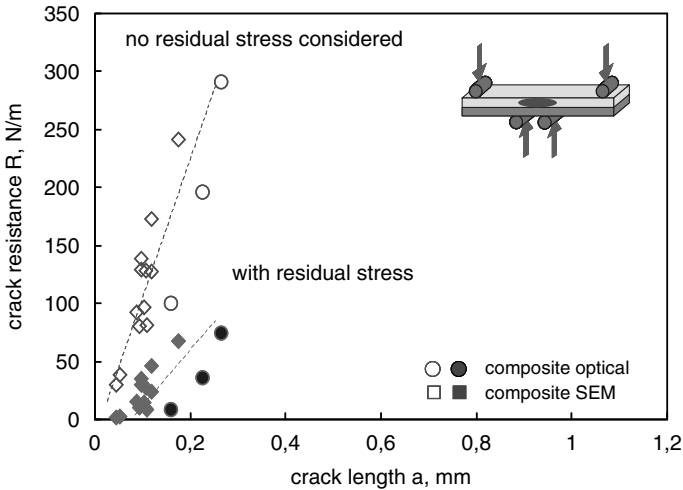


Figure 4. Influence of compressive residual stress on resistance behaviour of segmentation cracks in attached TBC.

Fig. 5 also displays a distinct difference in the initial resistance values of the cracks developing from the microstructural defects in the TBC and those starting from an artificial notch tip. The higher initial crack resistance of the notched TBC might be related to the formation of a non-uniform crack front. Crack front segments with local shifts in delamination plane due to microstructural heterogeneities may generate a spatially dispersed crack front which causes a higher apparent toughness.

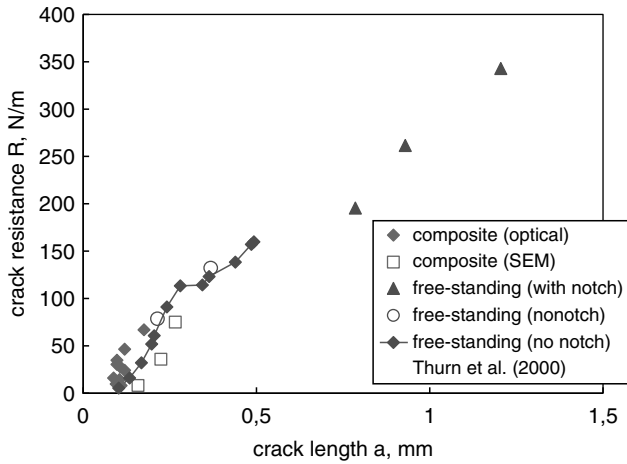


Figure 5. R-curve results for segmentation cracks in attached and stand-alone TBCs. For comparison R-curve of attached TBC corrected from the influence of residual stress.

3.2. Delamination Cracking

In the bending tests with the attached TBC under compression, special attention was given to fracture events along the interface between bond coat and TBC. According to results of FEM modelling^{3,25} the undulated interface between bond coat and TBC, in combination with the thermal mismatch of both materials, should give rise to local tensile residual stresses perpendicular to the interface. However, the in-situ observations revealed no preferred growth of cracks along the interface or in the TBC next to the interface (Fig. 6). But limited growth of some inter-splat cracks could be observed in the TBC before “macroscopic” delamination damage occurred. The growth of the inter-splat cracks happened unpredictable with respect to location and was only detected by post experimental inspection of the sequence of SEM micrographs. As an example Fig. 7 shows in comparison with the initial load-free situation the extension of an inter-splat crack after applying a (horizontal compressive force of 150 N.

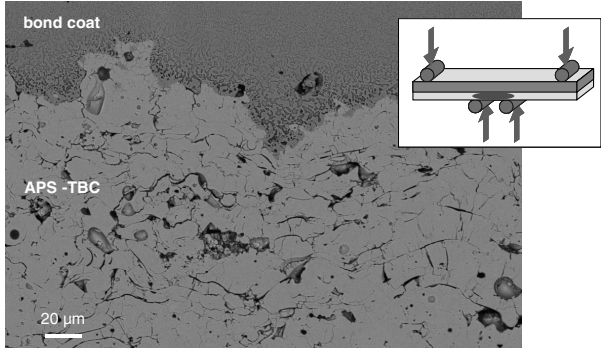


Figure 6. Attached TBC under compression in bending test. No preferential delamination was observed near interface to the bond coat.

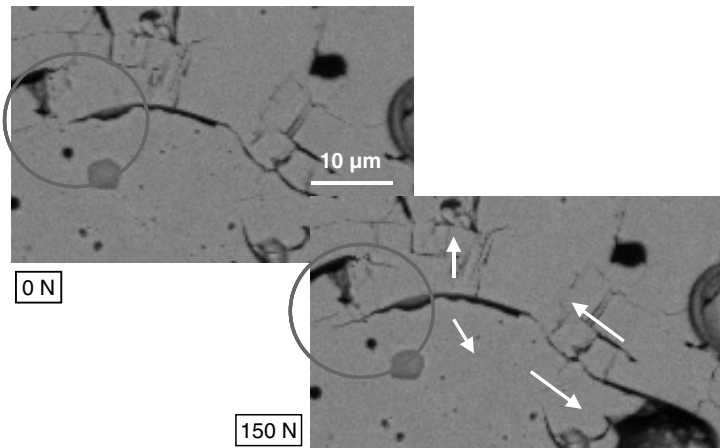


Figure 7. Magnified section of TBC area from Figure 6. Extension of inter-splat crack by horizontal compressive bending stress. Arrows indicate displacements analysed from grey-scale analysis. Crack opening behaviour similar to “wing crack” model²².

Considering all analysed examples the stable crack growth of the inter-splat cracks was in the order of 5–10 μm before the experiment had to be terminated, since the higher applied bending stress near the TBC surface caused the above described macroscopic delamination damage (Fig. 3). Examination of the load triggered displacements in the vicinity of the inter-splat crack in Fig. 7 reveals shear effects and crack closure in the central (inclined) portion as well as crack opening and extension in the “wing” portion.

The average directions of displacement obtained from the grey-scale analysis are visualised by arrows in Fig. 7. Evaluation of the mode I crack resistance based on equation (7) yields a steep rising crack resistance behaviour with values between 3 N/m at the beginning and 26 N/m after the limited amount of crack extension at the end of the experiment. The analysis includes the supporting impact of the residual compressive stress. Interestingly the average crack resistance ~ 13 N/m is only slightly lower than the short crack results reported by Bartlett and Dal Maschio¹² from indentation tests.

Fig. 8 displays the inter-splat crack resistance together with the results of the long delamination cracks propagated in the WOL specimens¹⁴. The crack length dependent resolution of the long crack resistance shows unambiguously R-curve behaviour. Starting from $R_0 \sim 100$ N/m the R-curve saturates in a plateau resistance which is about 50% higher. Compared to the resistance level determined for the inter-splat cracks (average value ~ 13 N/m) a fairly large gap in the data exists. The higher resistance of the long delamination cracks probably reflects a more tortuous crack path consisting of inter- and intra-splat sections. In addition the high starting value of the long crack R-curve can be explained again by assuming a non-planar, kinked crack front formation from the notch tip. Interestingly the average resistance values of the WOL tests are in the same order of magnitude like the long crack delamination data reported by Thurn et al.⁶ ($R_{\text{WOL}} \sim 90$ N/m) and Oechsner¹⁰ (~ 150 N/m $< R < \sim 200$ N/m).

Summarising, the fracture toughness values for segmentation and delamination cracks obtained with the as sprayed TBC in the present study two results have to be

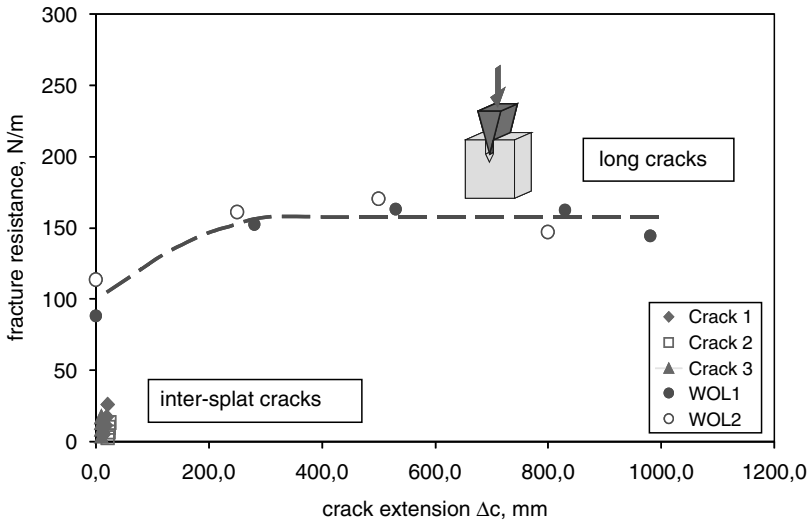


Figure 8. Crack resistance of inter-splat cracks and R-curve from extension of long delamination cracks in WOL tests¹⁴.

emphasised: i) both crack types showed R-curve behaviour and ii) although the R-curves might be different in slope and plateau value, there was no pronounced difference in the initial and average crack resistance level.

3.3. Crack Path Selection and Toughening Mechanisms

Fig. 9 displays the side-face of a notched stand-alone TBC specimen before loading and after growth of the segmentation crack. Obviously the macro-crack selects and combines essentially the suitable segments from the pre-existing pattern of inter- and intra-splat cracks and thus the segmentation crack path comprises of segments of these micro-defects^{26,27}.

The same holds for the delamination crack which is also composed of segments of inter- and intra-splat cracks. From the surface observation and crack path studies it appears that only little additional fracture at the crack tip is required to obtain the macroscopic segmentation and delamination configuration. However, the sequence of inter- and intra-splat cracks generates a tortuous crack surface with sharp deflections on the microstructural level. Upon crack opening such serrated crack surfaces frequently develop contact sites and friction²⁸.

Examples of microstructural crack deflection are shown in Fig. 10 for the different crack orientations²⁷. In Fig. 10a an intact spraying splat deflects a segmentation crack, in Fig. 10b the delamination crack bounces between the two interfaces with the adjacent splats, leaving a serrated fracture surface.

Implications of cracks surface contact are observed also on a larger scale in the crack wake. The crack bridging yields formation of a new side path behind the actual tip of a segmentation crack. Obviously the tortuous crack surfaces provide sufficient contact bridging to shield the apparent crack tip, a toughening mechanism frequently observed in ceramics with R-curve behaviour^{28,29}.

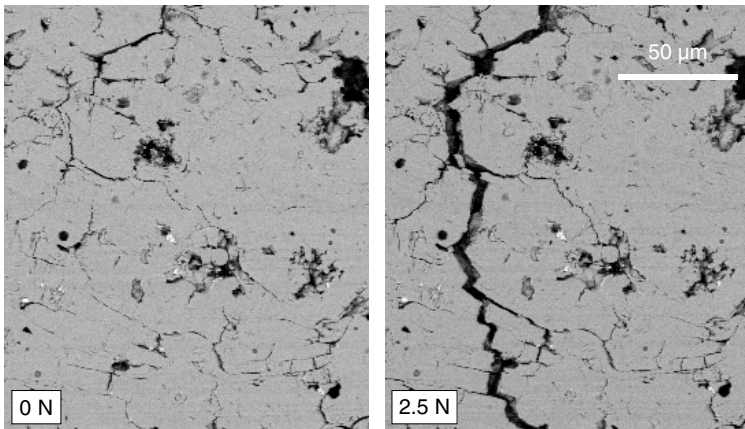


Figure 9. Tortuous segmentation crack path. Macro-crack follows pre-existing pattern of intra- and inter-splat micro-cracks.

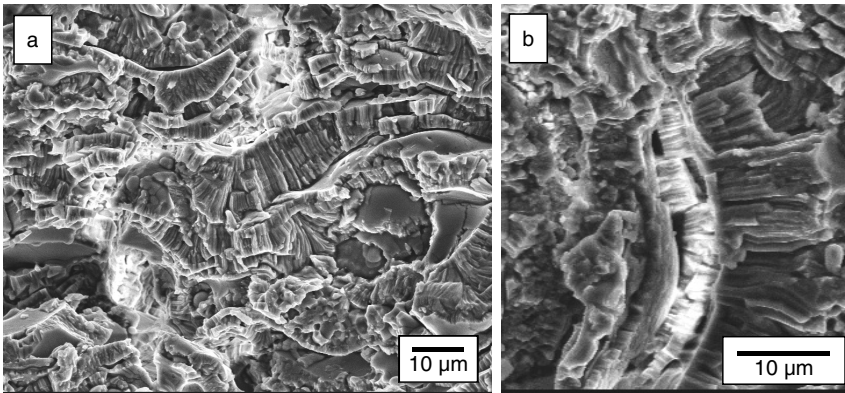


Figure 10. Crack deflection mechanisms in TBC. a) Segmentation crack deflects on intact spraying splat. b) Delamination crack bounces between surfaces of thin spray splat. Crack propagation from top to bottom.

However, it should be emphasised that grey scale analysis in the vicinity of segmentation cracks also revealed displacement activities caused by side cracks and crack branching, depending on the heterogeneities in the lamellar TBC microstructure.

4. CONCLUSIONS

The controlled crack growth studies of segmentation and delamination cracks in plasma sprayed TBCs revealed an increase of crack resistance with crack extension. This R-curve behaviour could be measured in the case of segmentation from short to long crack configuration using un-notched, stand-alone TBCs. The observed permanent increase in crack resistance was attributed to the limited TBC thickness in spraying direction. Propagation of long cracks in delamination orientation showed also R-curve behaviour with plateau values in the order of 150 N/m.

The macro-crack path followed in both orientations the pre-existing pattern of inter- and intra-splat cracks. The sharp deflections in the microcrack mode generate a tortuous crack path which gives rise to crack surface interaction and thereby provides a source of toughening. However, depending on the microstructural heterogeneities of the APS-TBC and local weak adherence of spraying splats also crack branching and side crack activities in a process zone around the macro-crack were observed.

Thus it seems premature to further quantify the measured R-curve behaviour and to describe the toughening effect in a model. Yet an important conclusion can be drawn from the present study. Tailoring plasma sprayed TBCs with low crack resistance for segmentation cracks and high delamination resistance should focus on a reduction of the density of inter-splat microcracks. Variation of the spraying parameters has the potential to systematically change APS-TBCs with respect to the ratio of inter- and intra-splat defects in the lamellar microstructure.

5. ACKNOWLEDGEMENTS

The authors would like to thank R. Vassen for providing the APS-TBC coatings, J. Mönch for experimental support and B. Mukherjee for contributing WOL-results. The encouraging and stimulating support of L. Singheiser throughout the work is gratefully acknowledged.

6. REFERENCES

1. J.T. DeMasi - Marcin, D.K. Gupta, Protective coatings in the gas turbine engine, *Surface and Coating Technology* 68/69 (12) 1–9(1994)
2. N.P. Padture, M. Gell, E.H. Jordan, “Thermal barrier coatings for gas turbine engine applications”, *Science*, Vol. 296, 280–84 (2002)
3. A.G. Evans, D.R. Mumm, J.W. Hutchinson, G.H. Meier, F.S. Petit, Mechanisms controlling the durability of thermal barrier coatings, *Progress in Materials Science* 46 (2001) 505–535
4. R.J. Damani, E.H. Lutz, Microstructure, strength and fracture characteristics of a free-standing plasma sprayed alumina, *Journal European Ceramic Society* 17 (1997) 1351–1359
5. S.R. Choi, D. Zhu, R.A. Miller, High temperature slow crack growth, fracture toughness and room temperature deformation behaviour of plasma-sprayed $ZrO_2 - 8wt\%Y_2O_3$, *Ceram. Eng. Sci. Proc.*, Vol. 19, 1998, 293–301
6. G. Thurn, G.A. Schneider, H.A. Bahr, F. Aldinger, Toughness anisotropy and damage behaviour of plasma sprayed ZrO_2 thermal barrier coatings, *Surface and Coatings Technology* 123 (2000) 147–58.
7. C.A. Anderson, Thermal stress fracture of ceramic coatings, in *Fracture Mechanics of Ceramics*, Ed. R.C. Bradt, D.P.H. Hasselman, F.F. Lange, A.G. Evans, Vol. 6, Plenum Press. New York, 1983, 497–510
8. L.L. Shaw, B. Barber, E.H. Jordan, M. Gell, Measurement of the interfacial fracture energy of thermal barrier coatings, *Scripta Materialia*, Vol. 39, No. 10, pp. 1427–1434, 1998
9. P.G. Charalambides, J. Lund, A.G. Evans, R.M. McMeeking, A test specimen for determining the fracture resistance of bimaterial interfaces, *J. Appl. Mechanics*, 56 (1989) 77–82
10. M. Oechsner, A contribution to life prediction of ceramic thermal barrier coatings, (Thesis, in German), *Fortschritt-Berichte VDI-Verlag, Duesseldorf, Series 18, No. 263*, 2001
11. A.H. Bartlett, R. Dal Maschio, Failure mechanisms of zirconia-8wt% yttria thermal barrier coatings, *J. Am. Ceram. Soc.*, 78 [4] 1018–24, 1995
12. A. Rabiei, A.G. Evans, Failure mechanisms associated with the thermally grown oxide in plasma-sprayed thermal barrier coatings, *Acta mater.* 48 (2000) 3963–3976

13. J. Kübler, Fracture toughness of ceramics using the SEVNB Method: Preliminary results, *Ceram. Eng. Sci. Proc.*, 18, 1997, 155–162
14. B. Mukherjee, R.W. Steinbrech, Fracture behaviour of long delamination cracks in thermal barrier coatings, to be published
15. E. Kieselstein, B. Seiler, M. Dost, E. Than, Characterization of composites by measuring the optical displacement via UNIDAC, (in German) *Technisches Messen* 69 [10], 412 (2002)
16. R. Moon, K. Bowman, K. Trumble, J. Roedel, Comparison of R-curves from single-edge V-notch-beam (SEVB) and surface-crack-in flexure (SCF) fracture-toughness test methods on multilayered alumina-zirconia composites, *J. Am. Ceram. Soc.* 83 [2] 445–47 (2000)
17. F. Deuerler, R. Knehans, R.W. Steinbrech, Testing methods of R-curve behaviour of Al_2O_3 , *Journal de Physique*, 1986, CI-617–621
18. Th. Fett, private communication
19. Th. Fett, D. Munz, Stress intensity factors and weight functions, *Computational Mechanics Publ.*, Billerica, Massachusetts, 1997
20. G. Blandin and R.W. Steinbrech, “Thermomechanical behaviour of plasma-sprayed multilayer composites for thermal barriers” (in German), Juel-Report 3954, Forschungszentrum Juelich, Germany (2002)
21. J. Malzbender, R.W. Steinbrech, Mechanical methods to determine the compliances within multilayered composites, *J. Mater. Res.* 18 [6] (2003)
22. M.F. Ashby, S.D. Hallam, The failure of brittle solids containing small cracks under compressive stress state, *Acta metall.* 34 (1986) 497–510
23. R.W. Trice, D.W. Prine, K.T. Faber, Deformation mechanisms in compression-loaded stand-alone plasma-sprayed alumina coatings, *J. Am. Ceram. Soc.*, 83 [12] 3057–64 (2000)
24. S.R. Kim, J.A. Nairn, Fracture mechanics analysis of coating/substrate systems. Part I: Analysis of tensile and bending tests, *Eng. Fracture Mechanics*, 65 (2000) 573–579
25. M. Ahrens, R. Vassen, D. Stöver, Stress distributions in plasma-sprayed thermal barrier coatings as a function of interface roughness and oxide scale thickness, *Surface and Coatings Technology* 161 (2002) 26–35
26. R.W. Steinbrech, “Thermomechanical behaviour of plasma sprayed thermal barrier coatings”, *Ceramic Eng. Sci. Proc.* 23 (2002) 379
27. E. Wessel, R.W. Steinbrech, Crack propagation in plasma sprayed ceramic, *Key Engineering Materials*, Vol. 223 (2002) 55–60
28. R.W. Steinbrech, Toughening mechanisms for ceramic materials, *J. Europ. Ceram. Soc.* 10 (1992) 131–142
29. A.G. Evans, Perspective of the development of high toughness ceramics, *J. Am. Ceram. Soc.* 73 (1990) 187–206

PARTICLE IMPACT DAMAGE AND POINT LOAD-INDUCED FRACTURE BEHAVIOR IN ZIRCONIA PLASMA SPRAY COATING FILM

Yoshio Akimune, Kazuo Matsuo, Tatsuo Sugiyama, Hiro Yoshida, Satoshi Sodeoka, Satoshi Shimizu*

ABSTRACT

This study concerns the method for examining the load conditions and evolving stress related to debonding at the coat-substrate interface to identify the responsible factors, by indenting a ceramic coated specimen with a spherical indenter either through impact or quasi-statically under static loading. The morphology of cracks induced by the impact of a foreign object on to specimens of inconel substrate with thermo-resistive coating of zirconia sprayed by two different methods was studied in comparison with the indentation test results by a spherical indenter under static loading. Consequently, the load conditions for coat fracture and debonding at the coat-substrate interface were successfully identified in a plasma spray specimen.

INTRODUCTION

The heat-resistant coating technology has been expected to be utilized for protecting the surface of metal blade in the gas turbine. The gas turbine is one of main devices in

National Institute of Advanced Industrial Science and Technology

1-1-1 Umezono, Tsukuba-city, 305-8568Japan

* 1, Natsushima, Yokosuka-city, 237-0061 Japan

the thermal power generation, to be used with various kinds of fuel, such as heavy oil and kerosene, and in the presence of combustion residuals and corrosive atmosphere. Troubles in the coated turbine blade involve point load-induced damages resulting from the impact of oxide scale which cause coating delamination and substrate fractures. This problem is to be resolved as quickly as possible¹.

Works to evaluate mechanical properties of ceramics protective coating for turbine blade include damage analysis through the finite element method and experimental results by A.S. Kobayashi et al.¹, particle impact experiment with ceramics film deposited on silicon nitride through CVD by Y. Akimune et al.², analysis of crack development after the indentation with a spherical indenter by J.B. Davis et al.³. Evaluation of damage morphology with stress-strain curve of coating film in a quasi-static testing for point load by A. Pajares et al.⁴⁻⁵, S. Wuttiphan et al.⁶, M. Swain and J. Mencik⁷ as well. In these papers, analysis of relationship between the mechanical behaviors of film and substrate under high speed and quasi-static point loads are not dealt with. The theoretical analysis has been conducted by Hertz⁸, and followed by those by S. P. Timoshenko and J. N. Goodier⁹ and by K. L. Johnson¹⁰. Studies on damages in ceramic materials using a spherical indenter are reviewed by B.R. Lawn¹¹. On the other hand, it seems to be important to set up a quasi-static evaluation technique to assess the fracture events caused by foreign object damage in the actual turbine blade at the time of depositing protective film.

The present study concerns a test for the purpose of proposing the optimum indentation test method for assessing foreign object damage in heat resistant coating film prepared through two spraying methods: atmospheric pressure plasma spray and pressurized plasma spray. In the experiment, the film fracture and surface delamination were observed after the high speed impact with particles, and quasi-static indentation test with a spherical indenter, for a specimen consisting of inconel 600 substrate with a bond coat on the surface and an additional deposit of zirconia spray film, prepared through either of two methods.

1. EXPERIMENTAL PROCEDURES

2.1. Specimens

The specimen was composed of inconel 600 substrate, 8wt% stabilized zirconia (METECO204NS-G) as spray material, and NiCoCrAlY alloy (AMDRY-1) as intermediate bond coat. The top coat is sprayed either with atmosphere or with pressurized argon (200 kPa Ar), to form zirconia film of 200 μm thickness.

Specimen designation:

A: atmospheric pressure plasma spray (film thickness: 200 μm)

H: Ar pressurized plasma spray (film thickness: 200 μm)

Inconel 600 (substrate), thickness: 3 mm

2.2. Plasma Spray Conditions

The heat resistant coat was sprayed either by atmospheric spraying or by Ar pressurized spraying. Conditions for the experiment are summarized in Table 1.

Table 1. A summary of spray conditions.

| | Bond Coat | Atmospheric pressure plasma Spray | Pressurized plasma Spray |
|--------------------|--|--|--|
| Top coat materials | NiCoCrAlY (AMDRY365-1) | 8 wt% Y ₂ O ₃ Stabilized ZrO ₂ (METCO204NS-G) | 8 wt% Y ₂ O ₃ Stabilized ZrO ₂ (METCO204NS-G) |
| Atmosphere | Argon | Atmosphere | Argon |
| Pressure | 10 kPa | Atm. pressure | 200 kPa |
| Spray distance | 300 mm | 100 mm | 100 mm |
| Gas flow | Ar: 50 L/min. H ₂ : 9 L/min. | Ar: 42 L/min. H ₂ : 10 L/min. | Ar: 50 L/min. H ₂ : 5 L/min. He: 10 L/min. |
| Powder feed | 25 g/min. | 4.8 g/min. | 5.2 g/min. |

2.3. Testing Method

(1) Foreign Object Impact Test^{12,13}

A high-speed impact test system with an electron thermal (ET) gun is illustrated in Fig. 1. First, a substrate with coating film is mounted on a specimen holder. The specimen is to be mounted mechanically in line with the ET gun and the solenoid coils. Then, a spherical magnet of samarium-cobalt (Sm₂Co₁₇, density: 8.4 g/cm³, hardness: 5.4 GPa, Young's modulus: 151 GPa, strength 118 MPa) is mounted in a plastic sabot as a simulated foreign object.

The sabot is blasted off by the pressure of aluminum vapor, generated explosively by applying 10 kV/50 kA power (electrical energy: 2.5 kJ) to an aluminum foil. The sabot is halted at a stopper located at the muzzle, and the samarium-cobalt magnet alone is shot through the two coils (100mm separation) to hit the target specimen. The flight speed of the magnet sphere is calculated from the time difference

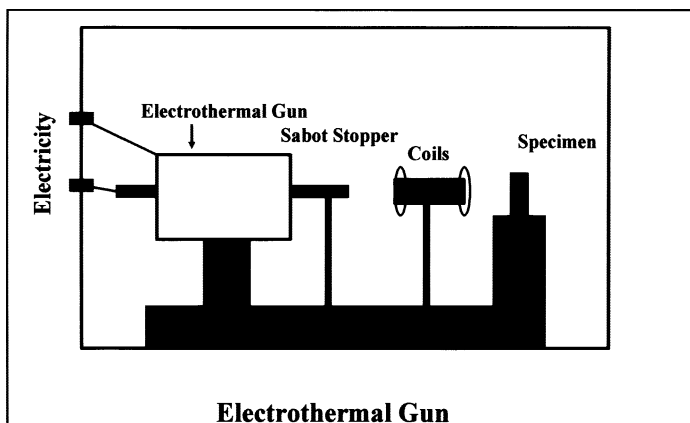


Figure 1. An overall view of the high speed impact testing system.

in rise-time of electromotive force induced as it passes through the coils. The impact velocity in the experiment was around 500 to 600 m/s.

(2) *Static Indentation Test*¹⁴

A spherical indenter is pressed into the film at a constant speed of 0.05mm/min and released. With load (P) and impression depth (h) measured, the stress-strain curve was calculated by using a theoretical formula. The loading and unloading session was repeated three times at a same rate. Owing to the mechanical design for reversing the crosshead of the testing machine, the indenter was held for 1 second or so at the top and bottom positions.

The specimen was processed by cutting to a size of about 15 mm square and polished with abrasive (Buehler's Colloidal Silica). With a point load indentation device mounted on an INSTRON strength test machine(#4487), as shown in Fig. 2, a spherical indenter (materials: WC, indenter diameter: 1, 2 and 4 mm) was loaded and unloaded continuously up to the maximal load of 1 kN at a rate of 0.05 mm/min at the room temperatures to measure the indent depth.

(3) *Damage Observation*

The impact impression of the shot was observed under an optical microscope. After the macro-indentation test, a part of specimen surrounding the indentation was cut out, embedded in epoxy-resin, sectioned and had the sectional face ground and polished with abrasive (Buehler's Colloidal Silica). The surface was observed under the optical microscope in the bright field and through the differential interference, a scanning electron microscope (SEM:Hitachi s-4000), and an electron probe surface analyzer (EPSA:Elionix ERA8000).

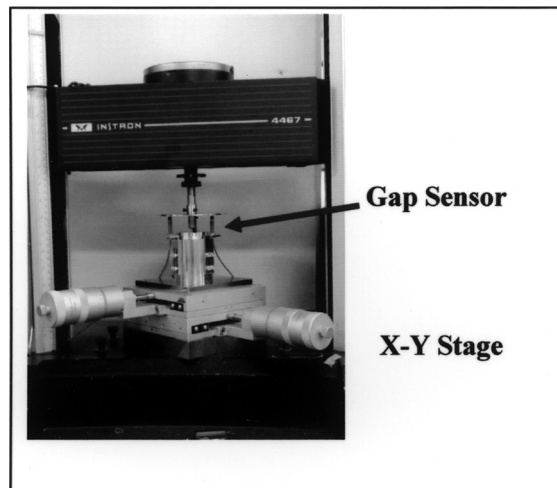


Figure 2. An overall view of quasi-static indentation testing system.

3. RESULTS AND DISCUSSION

3.1. Foreign Object Impact Test

(1) Surface Observation

In the impact test, a spherical particle was shot onto the surface of atmospheric pressure plasma spray coat specimen. At shooting speeds of 550 m/s and 620 m/s, no radial crack was seen at the point of impact unlike the data in the literature², though spray coating film fell out of the surface immediately below the impact point (Fig. 3). The observation with an EPSA, shown in Fig. 4, gave a removal of spray materials immediately below the impact point and a buildup in its periphery. In case of substrate only, similar morphology of crater and ridge was observed due to plastic deformation⁴⁻⁵.

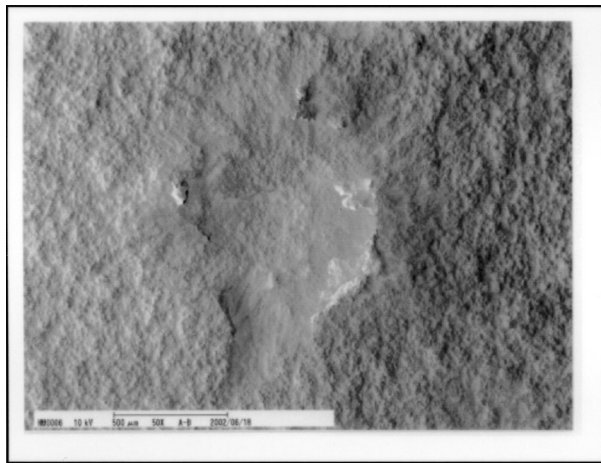


Figure 3. Surface fracture on atmospheric plasma spray specimen.

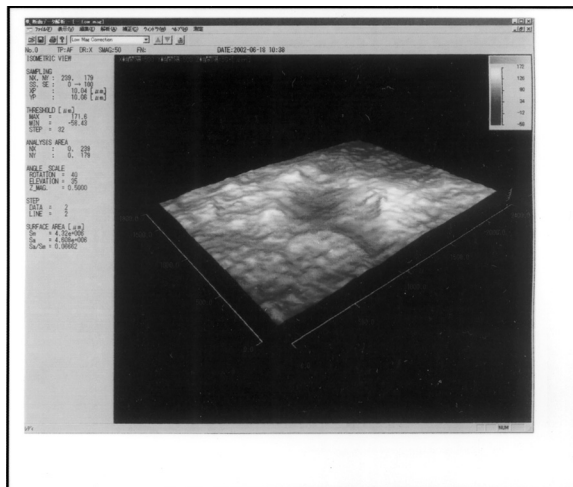


Figure 4. 3D analysis of surface fracture on atmospheric plasma spray specimen.

When a spherical particle was shot onto the surface of a specimen coated by pressurized plasma spray, the removal of spray coating film from the surface was seen just below the impact point for both 550 m/s and 540 m/s, as in case of atmospheric pressure spray coating film, but none of radial cracks were recognized from the impact point (Fig. 5). The observation under the EPSA, shown in Fig. 6, revealed slight crater immediately below the impact point and buildup surrounding it, definitely out of rough surface of spray coating.

(2) Cross-Sectional Observation

(i) atmospheric pressure plasma spray specimen

With a specimen using inconel 600 substrate, the cross-sectional view showed crater and slight ridge caused by plastic deformation immediately below the impact site (Fig. 7). In case of impact with 1 mmφ particle, minor cracks and separation from

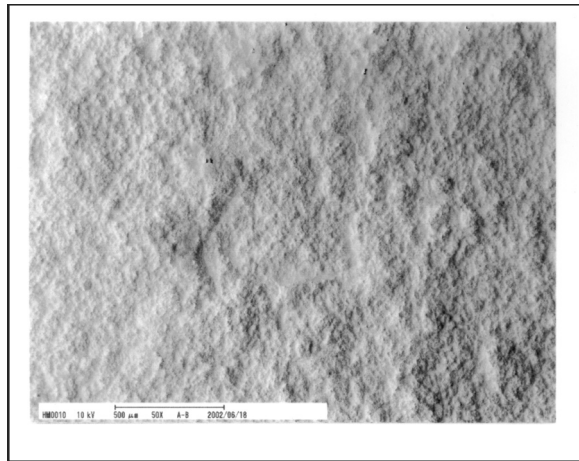


Figure 5. Surface fracture on pressurized plasma spray specimen.

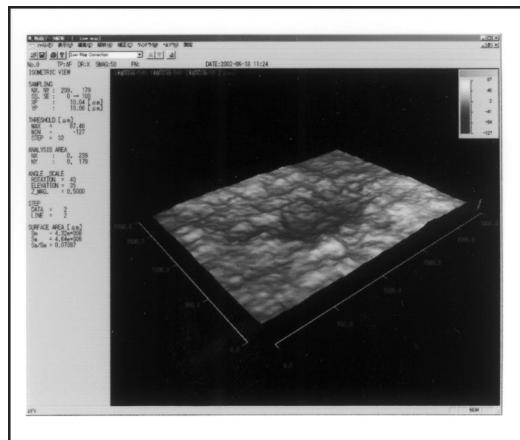


Figure 6. 3D analysis of surface fracture on pressurized plasma spray specimen.

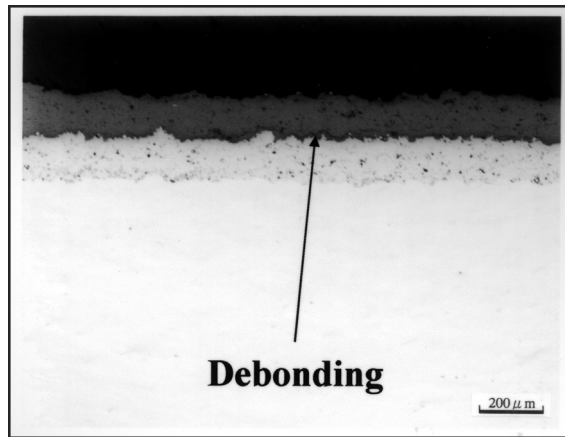


Figure 7. Cross-section of an atmospheric plasma spray specimen.

bond coat were observed with very little plastic deformation of substrate. The separation of coating film may be attributed to change in the direction of stress at the time of unloading following the fracture of the spherical particle. As the particle is made from sintered intermetallic compounds, with low strength, the fracture of the sphere was thought to occur when the stress within the sphere exceeded its strength at the moment of indenting the spray coat film. Consequently, the impact force was dissipated by fracturing, before inducing plastic deformation in the substrate and the bond coat. In this process, the vertical stress direction from the coating to the substrate was reversed to cause lateral crack due to by stress direction change¹⁵.

(ii) *pressurized plasma spray specimen*

In case of pressurized plasma spray specimen, different kinds of damage were observed, such as Hertz cone crack caused by impact loading in the spray coating film, lateral cracks caused by unloading due to fracture of sphere, and debonding (Fig. 8) from the bond coat extending radially from the tip of Hertz cone crack⁸⁻¹⁰,

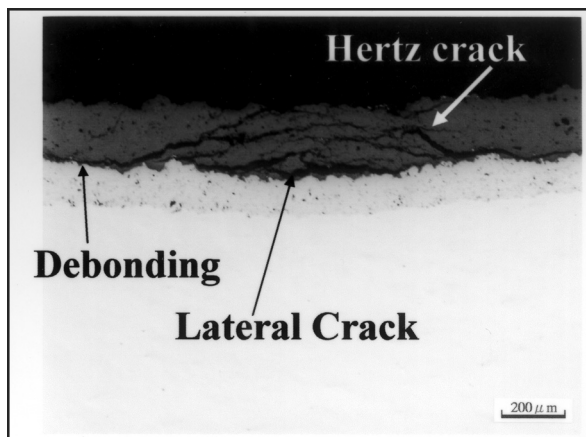


Figure 8. Cross-section of a pressurized plasma spray specimen.

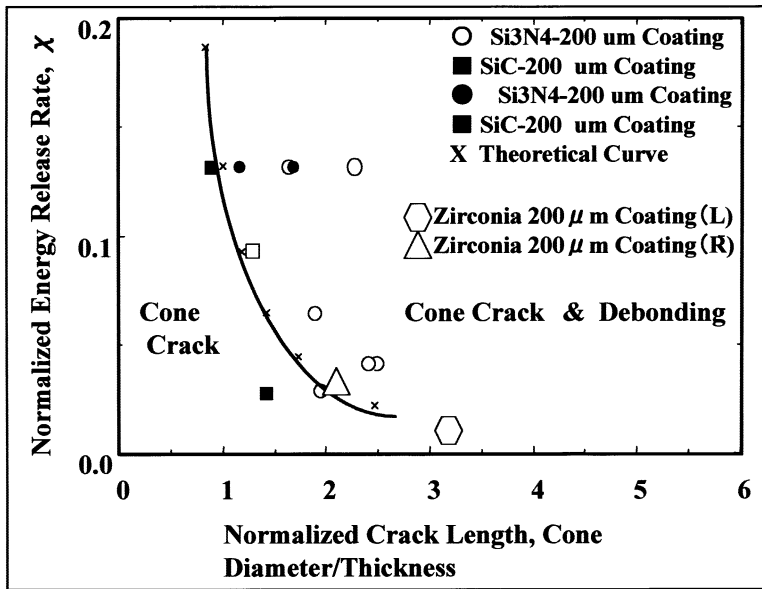


Figure 9. A crack-vs-debonding diagram (χ -R/h).

and a distinct plastic deformation of the substrate. These effects are a combination of Hertz cone cracks generation with debonding. In the crack map proposed by Davis et al.³, where normalized energy release rate $\chi = 1.30/\pi^2 \times \tan^2 \beta$ is plotted against normalized crack length, that is, cone crack radius R divided by coating film thickness h, the experimental data, $\chi = 0.0127$ and 0.305 (left side crack and right side crack, respectively) and $R/h = 3.2$ and 2.08 , (left side crack and right side crack, respectively), falls in an area where Hertz cone cracks coexist with debondings running from the cone crack tip in the radial direction and an area where Hertz cone crack, in agreement with data in the reference², (Fig. 9). The fracture proceeds in the following way: the load brought about by the impact of the particle induces cone cracks, which grow in the radial direction along the bond coat interface. As the load is eliminated by the fracture of the sphere, debonding occurs immediately below the cone crack¹⁵. This debonding is caused by the reversal of stress direction, through a mechanism entirely different from that for debonding in the growing phase of cone cracks³.

The difference in impact fracture behavior in two coating methods is thought to be related to the different yielding process in two coating films. The residual penetration depth in the coating films revealed impact damage behavior change which resulted in stress change under impact site.

3.2. Quasi-Static Indentation Test

(1) Continuous Load/Unload Test¹⁴

An load/unloading curve with an atmospheric plasma spray-coated specimen (A) is shown in Fig. 10, and a stress-strain curve by the indentation method in Fig. 11. In the latter curve, the initial slope, corresponding to the Young's modulus of materials, was different when using a spherical indenter of diameter 1 mm from that using

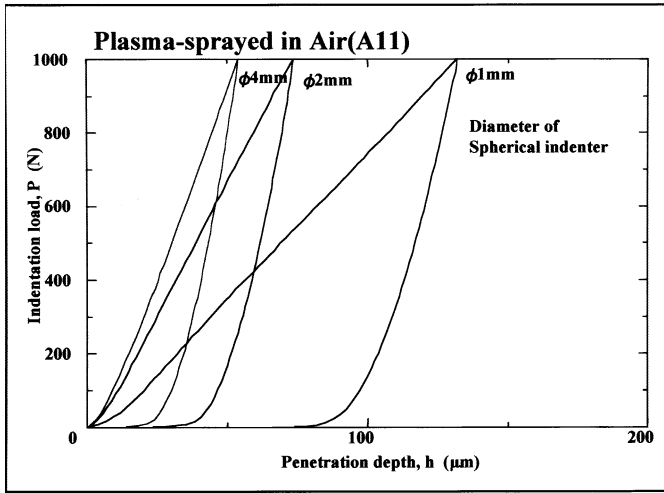


Figure 10. Load-unload curve with spherical indenter.

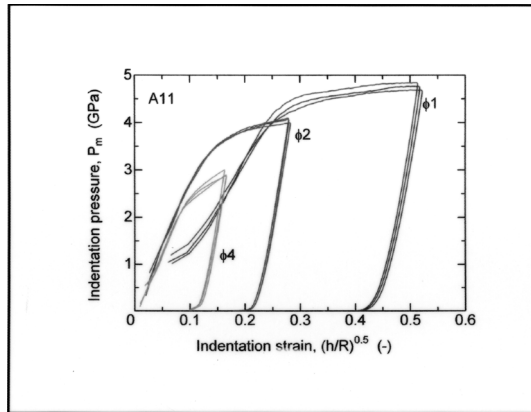


Figure 11. Stress-strain curve for the indentation testing.

indenters of other sizes, for all the specimens. This may be attributed to the fluctuation in the thickness of bond coat and top coat, and it seems necessary to take adequate caution when interpreting the results with 1 mmφ indenter.

It is evident that the yield stress (P_m) represented by a point of inflection from the initial slope tends to increase with the diameter of indenter. The similar tendency is recognized with the substrate (Inconel 600), suggesting that the difference in the elastic-plastic behavior or fracture morphology of spray film is responsible, dependent on the plastic deformation of substrate. While there is little difference in yield stress between atmospheric pressure plasma spray specimen (A) and argon pressurized plasma spray specimen (H), the subsequent behavior of the latter specimen is more inferior, suggesting that the pressurized plasma spray gives coating of poorer tolerance to fractures.

Note that the calculation of P_m by equation (1).

$$P_m = P_y / \pi R h \tag{1}$$

$$P = k_e h^{3/2}: \text{relation of pressure to indent depth} \quad (2)$$

$$K_e = 4/3 \sqrt{(RE^*)}^{1/2} \text{ composite Youngs modulus} \quad (3)$$

$$1/E^* = (1 - \nu^2)/E + (1 - \nu_i^2)/E_i$$

where P_m :Yield contact pressure, P_y :yield load, h_y :penetration dept, R :sphere radius, E_i :Young's modulus of indenter(WC:534 GPa), ν_i : Poisson's ratio of indenter(WC:0.28)

(2) Surface Observation

Examples of surface observation of the impression after the load/unload test with atmospheric plasma spray and pressurized plasma spray coating are shown in Figs. 12, respectively. In specimens with thin spray coat film, a lot of ring cracks are seen on the surface, while in those with thick film, the number of cracks is not so many. In the pressurized plasma spray coat specimen, circular depression is seen not only at the indent impression but also in its surrounding. This may be interpreted in this way: in consideration of after-yield behavior in the indentation test, if the spray film is subjected to a force greater than the yield stress of materials in the process of the load/unload test, micro-cracks grow to enlarge apparent radius of the indenter, reducing the contact pressure and making the after-yield behavior flatter.

(3) Cross-Sectional Surface

The cross-sections of impression for different combination of specimen and indenter size are shown in from Figs. 13 to Fig. 16. For the observation of plastic zone immediately below the impression^{4,5}. While there was little distinction in the fracture of spray film and the formation of plastic zone in different specimens, they presented clear differences depending on the indenter size. In case of indenter 1 mm ϕ , the fracture of Hertz cone crack⁸ occurred rather than interfacial debonding^{4,5}. As the indenter size increased, the fracture tended to turn closer to the interfacial debonding. With smaller indenter, the indentation pressure is greater, to produce plastic deformation in the substrate. With 1 mm ϕ indenter, plastic deformation occurred in proportion to the size of damage area, while with 4 mm ϕ indenter, the plastic

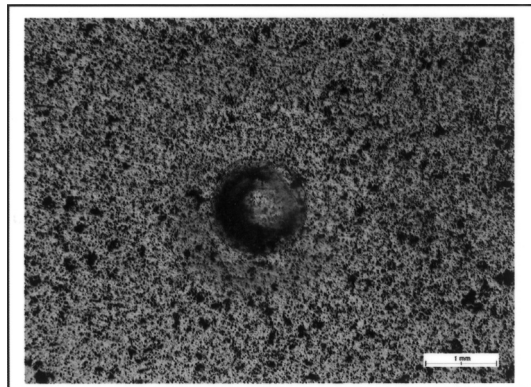


Figure 12. Impression (pressurized plasma spray, indenter 4 mm ϕ).

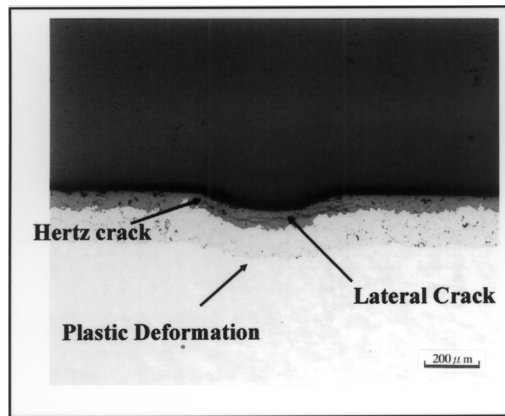


Figure 13. Cross-section of impression (atmospheric plasma spray, indenter 1 mm ϕ).

deformation occurred in a limited area only. On the basis of the observation of fracture and debonding, it was shown that both specimens had hard coat film, presenting elastic response with Hertz cone cracks in the earlier phase, and later, shifting to elastic-plastic behavior. For this reason, when unloaded, the stress field changed so as to cause lateral cracks and debonding, at the top coat/bond coat interface¹⁵. That is, loading accumulates elastic strain energy at the bond coat and the substrate, which is released as repulsive force, and as the stress acts vertically to the surface of bond coat, debonding occurs at the interface between the top coat and the bond coat.

3.3. Comparison of Spray-Coating Method on Static Indentation

With specimens prepared in different ways, the results of quasi-static testing using spherical indenters of different diameters and those of fracture observation after impact tests using 1 mm ϕ spherical particle were compared.

When an atmospheric spray specimen was subjected to a quasi-static test with an indenter of 1 mm ϕ , both the substrate and the bond coat were affected with marked plastic deformation, and in particular, the substrate underwent so drastically that the limit of elastic-plastic deformation was stepped over to present a porous zone with concentrated cracks. As the indenter size grew, the area of plastic deformation in the substrate and the bond coat was reduced, to present Hertz cone cracks in the cross-section. In addition to Hertz cone cracks, a number of cracks were seen in parallel to the substrate, which were thought to have occurred when the load was eliminated. With an indenter of 4 mm ϕ , the area of plastic deformation was reduced further, and lateral cracks were observed as the load was eliminated. Debonding between the bond coat and the substrate was observed only with the 4-mm indenter. Comparing to impact tests results(Fig. 7), quasi-static tests(Fig. 14) can reproduce similar fracture behavior.

In case of pressurized plasma spray specimens, marked plastic deformation occurred in the substrate and the bond coat with 1 mm ϕ indenter, and in the substrate, a porous zone with concentrated cracks as well as lateral cracks were observed, stepping over the region of elastic-plastic deformation. As the indenter size grew, the area of plastic deformation in the substrate and the bond coat was

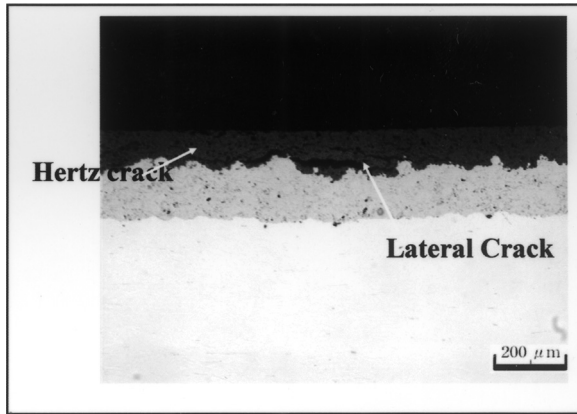


Figure 14. Cross-section of impression (atmospheric plasma spray, indenter 4 mmφ).

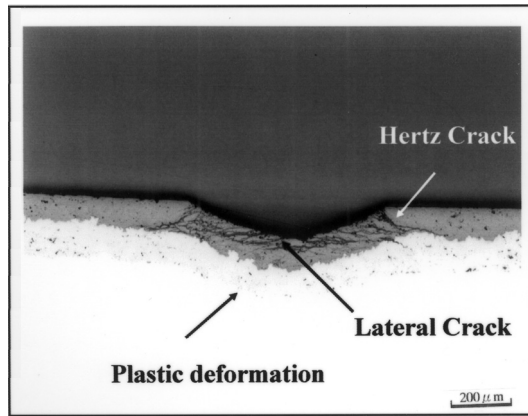


Figure 15. Cross-section of impression (pressurized plasma spray, indenter 1 mmφ).

reduced, and Hertz cone cracks were seen in the cross-section. As in case of atmospheric spray specimen, a number of lateral cracks occurred besides Hertz cone cracks, which were thought to have been produced when the load was eliminated. When a 4 mmφ indenter was used, the area of plastic deformation was reduced further, but cone cracks under the load and lateral cracks without load were observed. Comparing to impact tests results (Fig. 8), quasi-static tests (Fig. 16) can reproduce Hertz cracks and debonding under impact site but debonding from Hertz cone crack tip.

4. CONCLUSION

The morphology of cracks induced by the impact of a foreign object on to specimens of inconel substrate with thermal-resistive coating of zirconia sprayed by two different methods was studied in comparison with the indentation test results by a spherical indenter under static loading.

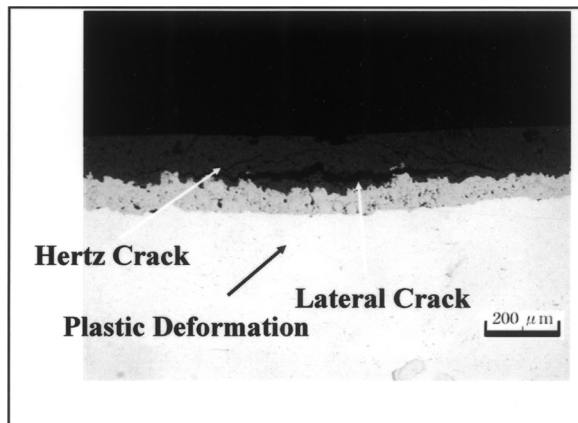


Figure 16. Cross-section of impression (pressurized plasma spray, indenter 4 mm ϕ).

In the impact test, for an atmospheric pressure plasma spray specimen, in case of impact with 1 mm ϕ particle, Hertz cone crack and separation from bond coat were observed, with very little plastic deformation of substrate. On the otherhand for pressurized plasma spray specimen, different kinds of damage were observed, such as Hertz cone crack caused by loading in the spray coat, lateral cracks caused by unloading due to fracture of impact sphere, and debonding from the bond coat extending radially from the tip of Hertz cone crack at impact loading, and a minor plastic deformation of the substrate.

On the basis of the observation of fracture and debonding for quasi-static indentation, crack morphologies in an atmospheric pressure plasma spray specimen were reproduced with 4 mm indenter. In the case of pressurized plasma spray specimen, crack morphologies were also reproduced with 4 mm indenter except debonding from cone crack tip.

ACKNOWLEDGEMENT

This work was performed as a part of the Nanostructure Coating Project carried out by the New Energy and Industrial Technology Development Organization.

REFERENCES

1. B. M. Liaw, A. S. Kobayashi, A. F. Emery, and J. J. Du, "Impact Damage Model of Ceramic Coating"; pp. 187–96 in *Fracture Mechanics of Ceramics*. Vol. 7. Edited by R. C. Bradt, A. G. Evans, D. P. H. Hasselman, and F. F. Lange. Plenum Press, New York, 1986.
2. Y. Akimune, T. Akiba, N. Hirotsuki, and T. Izumi, "Impact damage behavior of CVD coated silicon nitride for gas turbine," *J. Mat. Science*. 29, 3243–47 (1994).
3. J. B. Davis, H. C. Cao, G. Bao, and A. G. Evans, "The Fracture Energy of Interfaces: an Elastic Indentation Technique," *Acta metall. mater.* Vol. 39. No. 5. pp. 1019–1024. (1991).
4. A. Pajares, L. Wei, and B. R. Lawn, "Contact Damage in Plasma-Sprayed Alumina-Based Coatings," *J. Am. Ceram. Soc.*, 79 [7] 1907–14 (1996).

5. A. Pajares, L. Wei, B. R. Lawn, N. P. Padture, C. C. Berndt, "Mechanical Characterization of Plasma Sprayed Ceramic Coatings on Metal Substrates by Contact Testing," *Materials Science and Engineering*, **A208** 158–165 (1996).
6. S. Wuttiphphan, A. Pajares, B. Lawn, C. C. Berndt, "Effect of substrate and bond coat on contact damage in zirconia-based plasma-sprayed coatings," *Thin Solid Films*, **293** 251–260 (1997).
7. M. V. Swain, J. Menčík, "Mechanical Property Characterization of Thin Films Using Spherical Tipped Indenters," *Thin Solid Films*, **253** 204–211 (1994).
8. H. R. Hertz, Hertz's Miscellaneous Papers; Chs. 5 and 6., Macmillan, London, 1896
9. S. P. Timoshenko, J. N. Goodier, "Theory of Elasticity – third edition-," *McGraw-Hill Book Company*, 409–415.
10. K. L. Johnson, "Contact Mechanics" *Cambridge University Press*, 84–106.
11. B. R. Lawn, "Indentation of Ceramics with spheres: A Century after Hertz," *J. Am. Ceram. Soc.*, **81**[8]1977–94 (1998).
12. H. Yoshida, S. Kano, Y. Hasegawa, T. Shimamori, and M. Yoshida, "Particle impact phenomena of silicon nitride ceramics," *Philosophical Magazine A*, 1996, Vol74, No.5, 1287–1297.
13. H. Yoshida, Y. Hoshi, K. Uematsu, and Y. Kitazawa, "A single, small particle launch system by electro-thermal gun and micro-sabot," *Rev. Scientific. Instrument*, 68(1), (1997)
14. S. Shimizu, PhD Dissertation, Toyoshashi Institute of Technology (in Japanese)(2001)
15. D. B. Marshall, B. R. Lawn, and A. G. Evans, "Elastic/Plastic Indentation Damage in Ceramics : The Lateral Crack System," *J. Am. Ceram.Soc.*,65 [11] 561–566(1982).

MODE I, MODE II, AND MIXED-MODE FRACTURE OF PLASMA-SPRAYED THERMAL BARRIER COATINGS AT AMBIENT AND ELEVATED TEMPERATURES

Sung R. Choi, Dongming Zhu, and Robert A. Miller*

The mixed-mode fracture behavior of plasma-sprayed ZrO_2 -8 wt% Y_2O_3 thermal barrier coatings was determined in air at 25 and 1316°C in asymmetric four-point flexure with single edge v-notched beam (SEVNB) test specimens. The mode I fracture toughness was found to be $K_{Ic} = 1.15 \pm 0.07$ and $0.98 \pm 0.13 \text{ MPa}\sqrt{\text{m}}$, respectively, at 25 and 1316°C. The respective mode II fracture toughness values were $K_{IIc} = 0.73 \pm 0.10$ and $0.65 \pm 0.04 \text{ MPa}\sqrt{\text{m}}$. Hence, there was an insignificant difference in either K_{Ic} or K_{IIc} between 25 and 1316°C for the coating material, whereas there was a noticeable distinction between K_{Ic} and K_{IIc} , resulting in $K_{IIc}/K_{Ic} = 0.65$ at both temperatures. The empirical mixed-mode fracture criterion best described the coatings' mixed-mode fracture behavior among the four mixed-mode fracture theories considered. The angle of crack propagation was in reasonable agreement with the minimum strain energy density criterion. The effect of the directionality of the coating material in on K_{Ic} was observed to be insignificant, while its sintering effect at 1316°C on K_{Ic} was significant.

* Sung R. Choi, Ohio Aerospace Institute, Brook Park, Ohio 44142. Dongming Zhu, U.S. Army Research Laboratory, Glenn Research Center, Cleveland, Ohio 44135. Robert A. Miller, NASA Glenn Research Center, Cleveland, Ohio 44135.

1. INTRODUCTION

Thermal barrier coatings (TBCs) have attracted increasing attention for advanced gas turbine and diesel engine applications due to their ability to provide thermal insulation to engine components.¹⁻³ The merits of using the ceramic thermal barrier coatings are well recognized and include the potential increase in engine operating temperature with reduced cooling requirements, resulting in significant improvement in thermal efficiency, performance, and reliability. Plasma-sprayed zirconia-based ceramics are one of the most important coating materials in light of their low thermal conductivity, relatively high thermal expansivity, and unique microstructure as a result of the plasma spraying process. However, the limited durability of thermal barrier coatings under severe thermal and mechanical loading conditions encountered in heat engines remains one of the major problems. As a result, the development of thermal barrier coatings requires a better understanding of both thermal and mechanical behavior of the coating materials to ensure life and reliability of the related components.

It has been suggested that the important limiting factor encountered in thin plasma-sprayed thermal barrier coatings is the relatively low fracture energy of the coating in planes close to and parallel to the interface. Various efforts have been made to determine mode I 'interfacial' fracture toughness of the coatings in the vicinity of the interface using various techniques such as the indentation method, debonding technique, three- or four-point flexure delamination technique, and compact tension test method.⁴⁻⁶ Failure of the thick thermal barrier coatings has been observed within the bulk of the coating material, independent of any delamination that typically occurs at the interface of a thin coating and a substrate.⁷ There have been efforts to determine mode I fracture toughness of thick thermal barrier coatings at ambient and elevated temperatures. In fact, the majority of data on fracture toughness of both thin and thick coating materials have been determined under mode I loading. However, rarely are structural components or coatings subject to pure mode I loading. This is particularly true for thermal barrier coatings that encounter complex thermal and mechanical loading in engine operations. Recently, Callus and Berndt⁸ used a pure-shear technique to determine the interfacial critical mode II strain energy release rate of some thin coatings. Their data, however, were only for *ambient* temperature. Mixed-mode data on either thin or thick coatings are rarely available in the literature at *elevated* temperatures, despite an important fact that mechanical behavior of coating materials should not be based solely on ambient-temperature properties. Dense oxide ceramics (such as zirconia) have exhibited significant changes in mechanical properties such as strength, fracture toughness, and slow crack growth when temperature is increased above 800 to 1000°C.⁹

The objective of this work was to determine modes I and II fracture toughness and mixed-mode fracture behavior of free-standing thermal barrier coatings of plasma-sprayed $\text{ZrO}_2\text{-}8 \text{ wt}\% \text{ Y}_2\text{O}_3$ at an *elevated* temperature of 1316°C in air. The choice of this temperature was based on a typical target temperature of aerospace gas turbine applications. These same properties were also determined at ambient temperature (25°C). An asymmetric four-point flexure test technique was used at both temperatures in conjunction with single-edge-v-notched beam (SEVNB) test specimens, which yielded simplicity in both specimen and crack preparation and in test procedure. Fracture locus, ranging from mode I to mode II, was determined. Several mixed-mode fracture criteria were analyzed based on experimental data on mode I

and mode II stress intensity factors as well as on crack propagation angles. The mixed-mode fracture behavior of the coatings was compared with that of typical advanced structural ceramics in terms of mixed-mode fracture theories. The effects of sintering and the material's directionality on mode I fracture toughness at ambient temperature were also characterized.

2. EXPERIMENTAL PROCEDURES

2.1. Material

The ZrO₂-8 wt% Y₂O₃ powder with an average particle size of 60 μm, was first plasma-sprayed on a graphite substrate measuring 150 by 100 by 6.5 mm to a thickness of about 6 mm, using a Sulzer-Metco ATC-1 plasma coating system with an industrial robot. The plasma-spray conditions can be found elsewhere.¹⁰ A free standing, plasma-sprayed ceramic billet was then obtained by burning away the graphite substrate at 680°C in air for 24 h. The billet was machined into the final, rectangular flexure test specimen with nominal dimensions of 3 by 4 by 50 mm, respectively, in width, depth, and length. The 3-mm-wide face of flexure test specimens corresponded to the plane perpendicular to the plasma spraying direction. Major physical and mechanical properties of as-sprayed coating material including hardness, fracture toughness, and strength have been determined previously at ambient temperature^{11,12} and are presented in Table 1. Figure 1 shows a typical fracture surface and a polished surface showing the microstructure of as-processed coatings, in which large amounts of microcracks and pores are characterized in conjunction with a unique platelet structure.

2.2. Mixed-Mode Fracture Testing

2.2.1. Preparation of Sharp Precracks

Sharp v notches were introduced in flexure test specimens, using the single-edge-v-notched-beam method.¹³ This method utilizes a razor blade with diamond paste to

Table 1. Typical Physical and Mechanical Properties of Plasma-Sprayed ZrO₂-8 Wt% Y₂O₃ Thermal Barrier Coatings at Ambient Temperature.^{11,12}

| Density, g/cm ³ | Elastic modulus ^a (in compression), <i>E</i> , GPa | Fracture toughness, ^b <i>K</i> _{IC} , MPa√m | Strength | | |
|----------------------------|---|---|-------------------------|------------------------|---------------------------------------|
| | | | Type of test | Number of specimens | Average strength, ^b MPa |
| 5.22 | 34 | 1.0(0.1) | Tension | 10 | 10 (2) |
| | | | Trans-thickness tension | 10 | 11(1) |
| | | | compression | 10 | 324(72) |
| | | | Four-point flexure | 20 | 32(6) |
| | | | Biaxial flexure | 10 | 40(4) |

^a The value of *E* is estimated from the starting point of the stress-strain curve.¹¹

^b The number in parenthesis represents the ± 1.0 standard deviation.

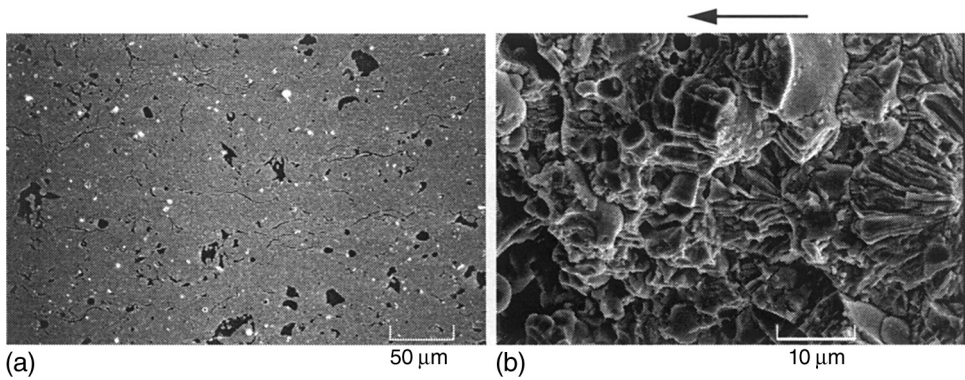


Figure 1. Typical microstructures of plasma-sprayed ZrO_2 -8 wt% Y_2O_3 thermal barrier coatings. (a) Polished surface. (b) Fracture surface. Arrow indicates plasma-spray direction.

introduce a sharp root radius by tapering a saw cut. Sharp v-notch radii ranging from 4 to 6 μm have been successfully obtained for alumina, glass ceramic, silicon nitride, zirconia, and silicon carbide ceramics.¹³ A starter straight-through notch 0.6 mm deep and 0.026 mm wide was made on the 3-mm-wide face of the test specimens. A steel razor blade was put into the starter notch sprinkled with diamond paste with a particle size of 9 μm . Typically, a load of about 10 N was applied through the razor blade with a stroke rate (back-and-forth motion) of 1 Hz and a stroke distance of about 13 mm in a specially designed polishing machine.¹¹ The final notch depth and root radius were 2.0 mm and 20 to 50 μm , respectively, resulting in the crack size-to-specimen depth ratio of 0.5 ($= a/W$). The coating material resulted in less sharpness in root radius due to its porous and microcracked nature, compared to typical dense ceramics. However, it has observed that the sharpness ranging from 20 to 50 μm was sufficient to give a consistent and accurate value of fracture toughness of the coating material.¹¹ Note that the through-the-thickness sharp notches thus prepared were aligned parallel with respect to the plasma spraying direction.

Other methods to generate sharp cracks to estimate fracture toughness, such as the single-edge-precracked-beam (SEPB)¹⁴ and the indentation techniques, were not feasible for the coating material: The indentation response was poor because of the material's significant porosity, microcracks, and 'softness,' so that well-defined indentation cracks were not achieved. This indicates that microindentation techniques may not be appropriate for plasma-sprayed coating materials whose pore and microcrack sizes in some cases are much greater than microindentation cracks, and as a result, a continuum approach is no longer valid.¹¹ Also note that cracks produced by this SEVNB method were very uniform in their crack-front geometry and very consistent in size with high reproducibility from specimen to specimen. This gives rise to very little scatter in or a small coefficient of variation in the values of fracture toughness, a notable advantage of the SEVNB method over other methods.

2.2.2. Asymmetric Four-Point Flexure Testing

The sharp v-notched flexure test specimen was loaded in asymmetric four-point flexure as shown in figure 2. The ratio of mode I to mode II stress intensity factor

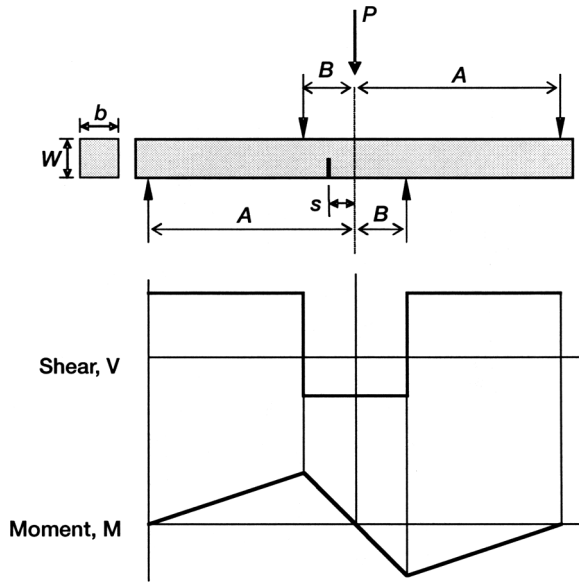


Figure 2. Schematic of asymmetric four-point flexure geometry with accompanying shear force and bending moment diagrams.

(SIF), K_I/K_{II} , was varied by varying the distance of the precrack from the center plane, s , as shown in the figure. When the precrack was centered with respect to the loading point ($s = 0$), the precrack was subjected to pure mode II loading. As s was increased, K_I/K_{II} also increased. The stress intensity factors, K_I and K_{II} , are expressed as

$$K_I = \sigma(\pi a)^{1/2} F_I \left(\frac{a}{W} \right) \tag{1}$$

$$K_{II} = \tau(\pi a)^{1/2} F_{II} \left(\frac{a}{W} \right) \tag{2}$$

where σ is the applied (remote) normal stress, τ is the applied (remote) shear stress, a is the crack size, and W is the specimen depth. F_I and F_{II} are crack geometry factors in modes I and II, respectively. The normal and shear stresses are given from the elementary beam theory by

$$\sigma = \frac{A - B}{A + B} \left(\frac{6sP}{bW^2} \right) \tag{3}$$

$$\tau = \frac{A - B}{A + B} \left(\frac{P}{bW} \right) \tag{4}$$

where A and B are distances from a load point as defined in figure 2, b is the specimen width, and P is the applied force. The values of $A = 10$ mm and $B = 5$ mm were typically used, but in some cases (K_{IIC} at RT) values of $A = 12$ and $B = 6$ mm were used for comparison and verification. The test specimen's cross section was $W = 4$ mm and $b = 3$ mm.

Several different expressions of F_I and F_{II} were suggested by Suresh et al.,¹⁵ Wang et al.,¹⁶ and He and Hutchinson¹⁷ for the case of through-the-thickness crack, and their respective results of F_I and F_{II} are illustrated in figure 3. As seen from the figure, no significant difference in F_I and F_{II} between the solutions was found, particularly when a/W is between 0.35 and 0.50. The solution by He and Hutchinson¹⁷ that provided a convenient polynomial expression was used in here, and is given as follows:

$$F_I\left(\frac{a}{W}\right) = 1.122 - 1.121\left(\frac{a}{W}\right) + 3.740\left(\frac{a}{W}\right)^2 + 3.873\left(\frac{a}{W}\right)^3 - 19.05\left(\frac{a}{W}\right)^4 + 22.55\left(\frac{a}{W}\right)^5 \text{ for } \frac{a}{W} \leq 0.7 \tag{5}$$

$$F_{II}\left(\frac{a}{W}\right) = 7.264 - 9.37\left(\frac{a}{W}\right) + 2.74\left(\frac{a}{W}\right)^2 + 1.87\left(\frac{a}{W}\right)^3 - 1.04\left(\frac{a}{W}\right)^4 \text{ for } 0 \leq \frac{a}{W} \leq 1 \tag{6}$$

Note that Eq. (5) was quoted from Murakami's¹⁸ and was almost identical to Sawley and Gross' solution¹⁹ up to $a/W = 0.7$, as seen in the figure. Also note that the difference in F_I and F_{II} between solutions in the range of $a/W = 0.4$ to 0.5 was negligible, resulting in

$$F_I \approx F_{II} \tag{7}$$

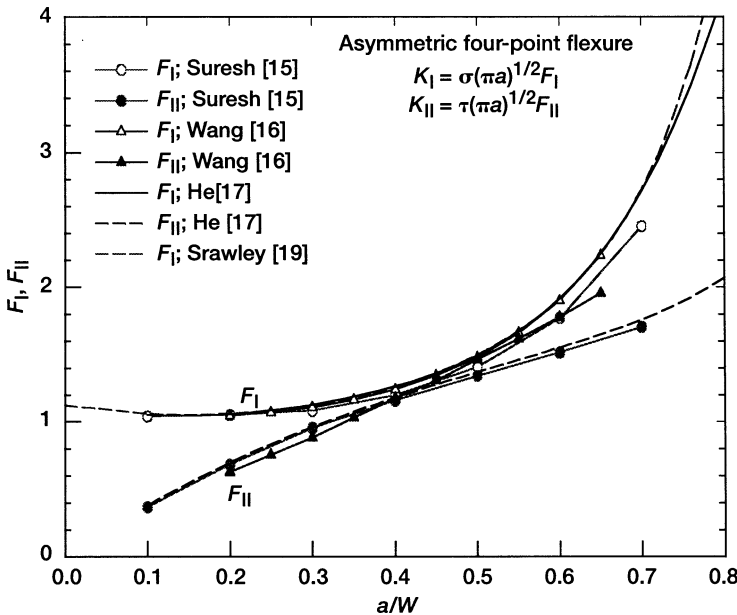


Figure 3. Various solutions of crack geometry factors F_I and F_{II} applied in the asymmetric four-point flexure configuration.

Hence, in the case of $a/W = 0.4$ to 0.5 , the K_{II}/K_I ratio (or called ‘mixity’) can be simplified from Eqs. (1)–(4) and (7) as follows:

$$\frac{K_{II}}{K_I} = \frac{WF_{II}}{6sF_I} \approx \frac{W}{6s} \tag{8}$$

$$\beta = \tan^{-1} \left(\frac{K_{II}}{K_I} \right) \approx \tan^{-1} \left(\frac{W}{6s} \right) \tag{9}$$

where β is the mixity angle. The angle β was also called the “equivalent crack angle” by Maccagno and Knott²⁰ for situations which do not actually use the inclined crack configuration. The ratio of crack size to specimen width used in this work was chosen to be $a/W = 0.5$ so that Eq. (8) or (9) could be conveniently used. The values of $s = 0$ to 3.6 mm were selected to give uniformly distributed β between pure mode I ($\beta = 0^\circ$) and pure mode II ($\beta = 90^\circ$) based on Eq. (9). Pure mode I fracture toughness K_{Ic} was determined using a symmetric four-point flexure fixture with 10-mm inner and 20-mm outer distances.

All testing was performed in displacement control using a SiC flexure fixture with an actuator speed of 0.5 mm/min of an Instron electromechanical test frame (Model 8562, Instron, Canton, MA). Testing was conducted at 25 and 1316°C in air. Each test specimen in elevated-temperature testing was held for thermal equilibration for about 20 min prior to testing. At room temperature, four and nine specimens were tested for K_{Ic} and K_{IIc} , respectively, whereas at 1316°C, four specimens were examined for each test. There were nine mixity values associated with the specimens tested at 25°C, and four mixity values associated with those tested at 1316°C. Typically, two or three specimens of each mixity value were tested. After testing, the crack size of each tested specimen was determined optically from its fracture surface based on the three-point measurements in accordance with test standard ASTM C1421.¹⁴ The crack propagation angles were also determined.

2.3. Effects of Sintering and Material Directionality

In order to determine the effect of sintering on mode I fracture toughness of the coating material, additional fracture toughness testing was carried out at ambient temperature using the test specimens annealed at 1316°C in air for 5, 20, 100, and 500 h. The sharp v-notches were introduced in the annealed specimens using the

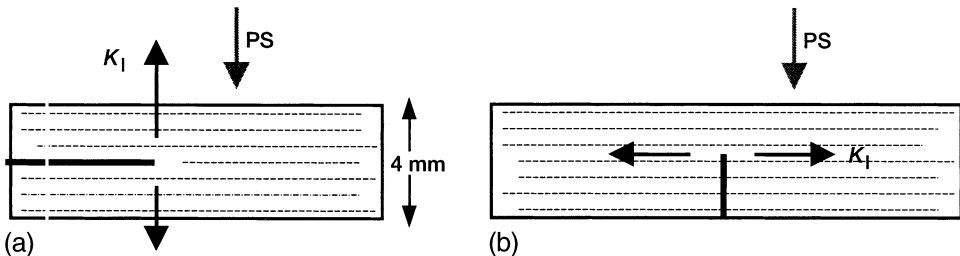


Figure 4. (a) A schematic geometry of double-cantilever-beam (DCB) test specimens used to determine K_{Ic} in the plane perpendicular to the plasma-sprayed (PS) direction. (b) ‘Regular’ fracture toughness testing by the SEVNB method with crack planes parallel to the plasma-spraying direction is shown for comparison.

same technique described in section 2.2.1. The test fixture, test frame, and test procedure used were the same as those used in the aforementioned ‘regular’ fracture toughness testing. Fracture surfaces were also examined via SEM with respect to annealing time to see any change in microstructure and morphology.

Mode I fracture toughness (K_{Ic}) of as-sprayed coating material was also evaluated at ambient temperature in the plane perpendicular to the plasma-sprayed direction (that is, within the ‘layered’ direction) using the double cantilever beam (DCB) method. A sharp v notch was introduced in the center plane of the 4-mm-wide face of each flexure test specimen with a crack length of about 6 mm (see fig. 4). Fracture toughness was calculated based on the formula by Murakami.¹⁸ A total of three DCB specimens were tested. This additional fracture testing was to determine directionality of the material in response to fracture toughness relative to the plasma-spraying direction.

3. RESULTS AND DISCUSSION

3.1. Test Results

The results of the mode I, mode II, and mixed-mode fracture testing for the coating material at both 25 and 1316°C are presented as K_{II} versus K_I in figure 5. Each point represents a single datum, and the values K_{Ic} and K_{IIc} represent the average of four and eight measurements, respectively, at 25°C and the average of four measurements for each at 1316°C. The effect of test distance on K_{IIc} at 25°C was found to be insignificant: $K_{IIc} = 0.74 \pm 0.1$ and 0.69 ± 0.09 MPa√m, respectively, for A/B values of 10/5 and 12/6 mm (see fig. 2). Hence, the 10/5-mm distances were exclusively used

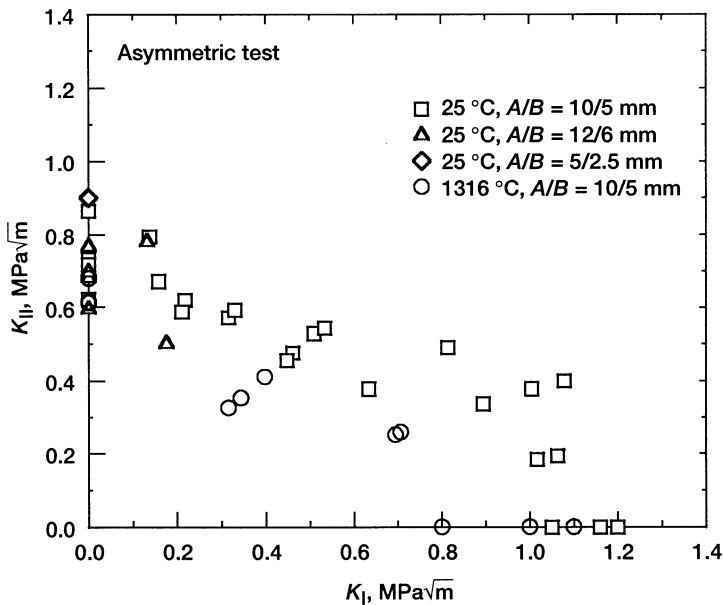


Figure 5. A summary of K_{II} versus K_I for mode I, mode II, and mixed-mode fracture of plasma-sprayed ZrO_2 -8 wt% Y_2O_3 thermal barrier coatings at both 25 and 1316°C in air.

throughout the mixed-mode test program. At 25°C, $K_{Ic} = 1.15 \pm 0.07$ and $K_{IIc} = 0.73 \pm 0.10 \text{ MPa}\sqrt{\text{m}}$, and at 1316°C, $K_{Ic} = 0.98 \pm 0.13$ and $K_{IIc} = 0.65 \pm 0.04 \text{ MPa}\sqrt{\text{m}}$. Note that the values of K_{IIc} were 37 and 34 percent lower than those of K_{Ic} at 25 and 1316°C, respectively. It has been reported that for some dense ceramics K_{IIc} was greater than K_{Ic} , presumably attributed to the frictional interaction between the two crack planes.²¹ However, the previous studies on advanced (dense) ceramics including silicon nitrides, alumina and zirconia^{22,23} showed a different result that K_{IIc} was almost identical to K_{Ic} for a given material, indicative of an insignificant frictional effect on K_{IIc} by either coarse grained or fine grained ceramics. The coating material, however, did not exhibit a similar value in both K_{IIc} and K_{Ic} but rather yielded a lower value in K_{IIc} than in K_{Ic} at both 25 and 1316°C. It is believed that because of the porous, microcracked, ‘soft’ nature the coating material, there would not have been any significant frictional contribution to K_{IIc} . Furthermore, the coating material would be easier to shear (mode II) than to cleave (mode I), probably because of its unique platelet structure formed by plasma-spraying process, which results in low K_{IIc} compared with K_{Ic} . The difference between K_{IIc} and K_{Ic} for various ceramics and brittle materials will be described in more detail in a next section.

As shown in figure 5, because $K_{IIc} < K_{Ic}$, the overall K_{II} versus K_{I} relation is represented by an ellipse at either 25 or 1316°C with K_{Ic} being a major axis. For a given mixity angle ranging from $\beta = 0$ to 90° , $K_{EQ} = (K_I^2 + K_{II}^2)^{1/2}$ was lower at 1316°C than at 25°C, probably because of a somewhat softening effect at elevated temperature. The values of K_{Ic} and K_{IIc} were decreased by 15 and 11 percent, respectively, when temperature was increased from 25 to 1316°C. However, this decrease was marginal, as can be seen in a summary of K_{Ic} as a function of temperature in figure 6, in which the K_{Ic} data previously determined¹¹ at 25 and

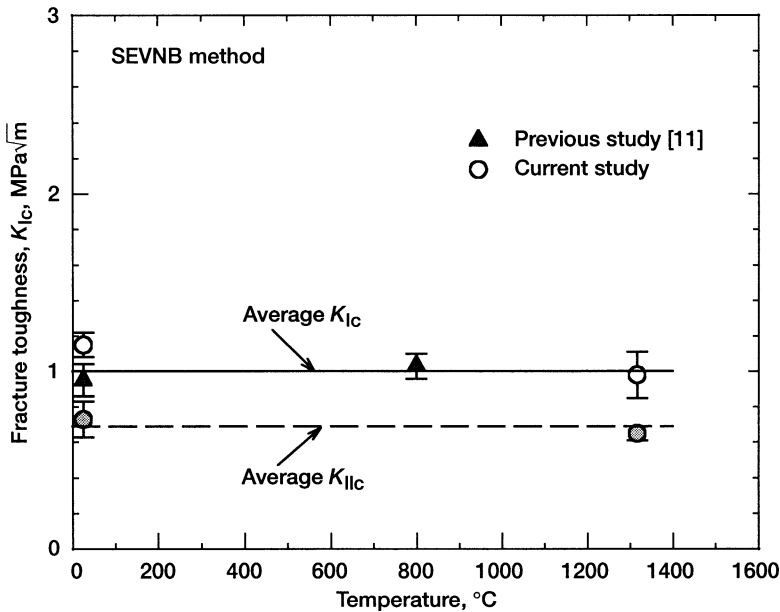


Figure 6. Fracture toughnesses of K_{Ic} and K_{IIc} as a function of temperature for plasma-sprayed $\text{ZrO}_2\text{-8 wt\%Y}_2\text{O}_3$ thermal barrier coatings. The previous K_{Ic} data¹¹ were included. Error bars represent ± 1.0 standard deviation.

800°C by the SEVNB method were included with the current data. K_{Ic} remains statistically invariable with an average of $K_{Ic} = 1.0 \pm 0.1 \text{ MPa}\sqrt{\text{m}}$, regardless of test temperature up to 1316°C. The same would be true for $K_{IIc} (= 0.69 \text{ MPa}\sqrt{\text{m}})$ as depicted in the figure, notwithstanding the lack of intermediate-temperature data. The insensitivity of K_{Ic} to temperature was also observed in a similar but dense (hot-pressed) 10 mol% yttria-stabilized zirconia (10-YSZ) in which fracture toughness of the material—evaluated in air by the same SEVNB method—was almost unchanged ($K_{Ic} = 1.6\text{--}1.8 \text{ MPa}\sqrt{\text{m}}$) from 25 to 1000°C.⁹

Figure 7 shows typical examples of crack propagation with different mixities ranging from pure mode II ($K_I/K_{II} = 0$) to pure mode I ($K_I/K_{II} = \infty$). The angle of crack propagation θ_c was defined as an angle of the crack plane propagated with respect to the original precrack plane. The direction of crack plane propagated was in most cases straight with some exceptions such as tortuous or not-straight paths. The angle of crack propagation was greatest in pure mode II, and decreased with increasing K_I/K_{II} reaching to $\theta_c = 0$ in pure mode I. A summary of experimental data on the angle of crack propagation as a function of K_I/K_{II} determined at both 25 and 1316°C is depicted in figure 8. The overall trend of the angle of crack propagation was that θ_c initially decreased quickly with increasing K_I/K_{II} and then decreased monotonically at $K_I/K_{II} > 3$. No significant difference in θ_c between 25 and 1316°C was observed. It is noted that the scatter in θ_c , for example, $\theta_c = 45$ to 70° at $K_I/K_{II} = 0$ (pure mode II), seemed more appreciable in the coating material than in dense advanced ceramics,²² which exhibited a typical scatter of about 15° .

Analysis of fracture surfaces revealed no explicit difference in the fracture morphology of the pure mode I, mixed-mode, or pure mode II specimens. However, it should be mentioned that unlike dense ceramics the coating material has provided a challenging subject on fractography because of its unique open and microcracked platelet

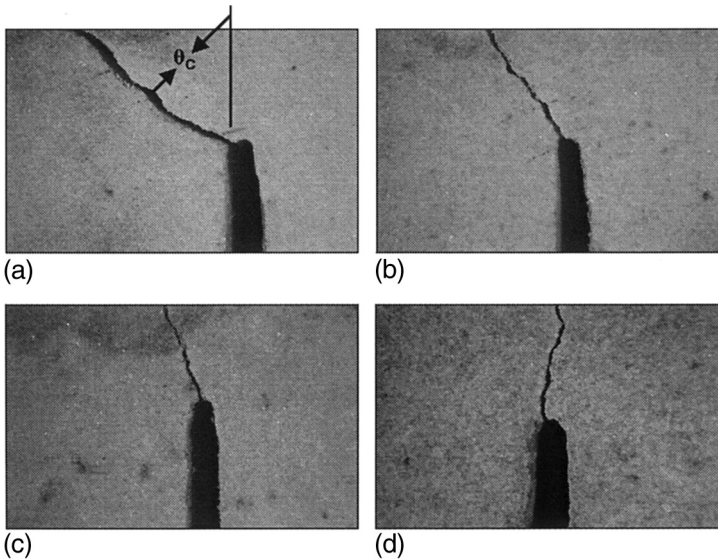


Figure 7. Typical examples of specimens showing angles of crack propagation with respect to K_I/K_{II} of plasma-sprayed $\text{ZrO}_2\text{-}8 \text{ wt}\% \text{ Y}_2\text{O}_3$ thermal barrier coatings: (a) pure mode II; $K_I/K_{II} = 0$, (b) $K_I/K_{II} = 2.7$, (c) $K_I/K_{II} = 5.5$, and (d) pure mode I; $K_I/K_{II} = \infty$.

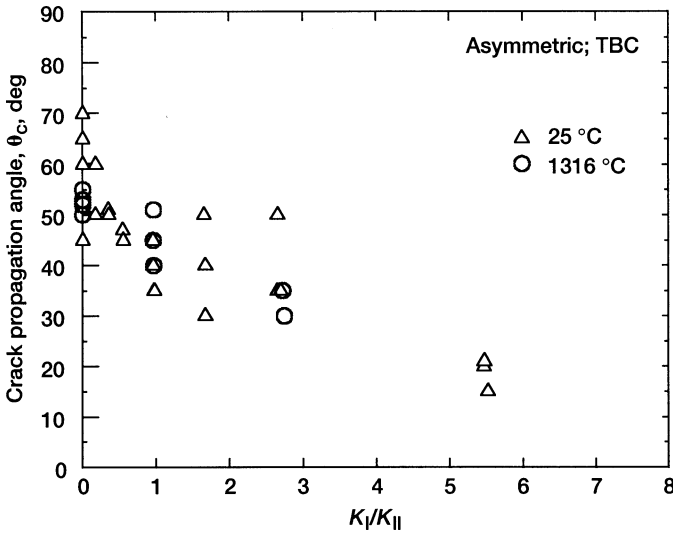


Figure 8. Crack propagation angles as function of K_I/K_{II} of plasma-sprayed ZrO_2 -8 wt% Y_2O_3 thermal barrier coatings determined in asymmetric four-point flexure at both 25 and 1316°C in air.

microstructure. The origin or nature of strength-controlling flaws in the coating material has rarely been identified with any traditional means of fractography (optical and/or SEM) that would be otherwise sufficient for the case of dense ceramics.¹² An improved means of fractography is required to better distinguish fracture morphologies in response to different modes of fracture of the coating material.

3.2. Consideration of Mixed-Mode Fracture Criteria

3.2.1. Considered Criteria

As shown from the crack propagation angles in figure 8, mixed-mode fracture does not take place in the same plane as the original crack. This noncoplanar crack propagation requires different fracture criteria, typically a combination of the driving forces K_I and K_{II} together with K_{Ic} and K_{IIc} . The mixed-mode fracture criteria for an isotropic, homogeneous material can be broadly categorized in four areas and will be briefly described then compared with experimental results.

3.2.1a. *maximum principal stress criterion.*²⁴ this criterion assumes that a crack at instability propagates in the direction normal to the maximum principal stress direction. the instability condition is given by the following relationship:

$$K_{Ic} - K_I \cos^3 \frac{\theta_c}{2} + 3K_{II} \cos^2 \frac{\theta_c}{2} \sin \frac{\theta_c}{2} = 0 \tag{10}$$

The angle of crack propagation θ_c is a function of K_I/K_{II} and is given by

$$\theta_c = 2 \tan^{-1} \left\{ \frac{K_I}{4K_{II}} \pm \frac{1}{4} \left[\left(\frac{K_I}{K_{II}} \right)^2 + 8 \right]^{1/2} \right\} \tag{11}$$

In case of pure mode II, the following relations can be obtained from Eqs. (10) and (11):

$$\theta_c = 70.53^\circ, \frac{K_{IIc}}{K_{Ic}} = 0.8662 \tag{12}$$

3.2.1b. *minimum strain energy density criterion.*²⁵ This criterion assumes that crack propagation would take place in the direction along which the strain energy density is minimum. this assumption gives rise to the following mixed-mode fracture criterion

$$K_{Ic}^2 - \frac{1}{2(\kappa - 1)} [a_{11}K_I^2 + 2a_{12}K_IK_{II} + a_{22}K_{II}^2] = 0 \tag{13}$$

where

$$\begin{aligned} a_{11} &= (1 + \cos \theta_c)(\kappa - \cos \theta_c) \\ a_{12} &= \sin \theta_c(2 \cos \theta_c - \kappa + 1) \\ a_{22} &= (\kappa + 1)(1 - \cos \theta_c) + (1 + \cos \theta_c)(3 \cos \theta_c - 1) \end{aligned}$$

with

$$\begin{aligned} \kappa &= 3-4\nu \text{ for plain strain} \\ \kappa &= (3 - \nu)/(1 + \nu) \text{ for plain stress} \end{aligned}$$

where ν is Poisson’s ratio. The angle of crack propagation, θ_c , is given by

$$(\kappa - 1) \sin \left(\theta_c - 2 \tan^{-1} \frac{K_I}{K_{II}} \right) - 2 \sin \left[2 \left(\theta_c - \tan^{-1} \frac{K_I}{K_{II}} \right) \right] - \sin 2\theta_c = 0 \tag{14}$$

In case of pure mode II, the following relations can be obtained from Eqs. (13) and (14):

$$\theta_c = \cos^{-1} \left(\frac{\kappa - 1}{6} \right), \frac{K_{IIc}}{K_{Ic}} = \left[\frac{2(\kappa - 1)}{a_{22}} \right]^{1/2} \tag{15}$$

3.2.1c. *maximum energy release rate criterion.* this criterion assumes that a crack with an infinitesimally small kink at an arbitrary direction propagates in the direction along the maximum strain energy release rate.^{26,29} many investigators keeps that the strain energy release rate, g , can be expressed in terms of K_I and K_{II} as follows:

$$G = c_{11}K_I^2 + c_{12}K_IK_{II} + c_{22}K_{II}^2 \tag{16}$$

where c_{11} , c_{12} , and c_{22} are coefficients. Hyashi and Nemeat-Nasser²⁸ determined numerically the coefficients and the direction of maximum G as a function of K_I/K_{II} . Palaniswamy and Knauss²⁷ proposed an approximated mixed-mode fracture criterion on the maximum energy release rate as follows (that was also used by Suresh et al.¹⁵)

$$\frac{K_I}{K_{Ic}} + \frac{3}{2} \left(\frac{K_{II}}{K_{Ic}} \right)^2 = 1 \quad (17)$$

where for pure mode II the approximation leads to

$$\theta_c = 77.4^\circ, \quad \frac{K_{IIc}}{K_{Ic}} = 0.817 \quad (18)$$

The fracture criterion and the crack propagation angle on the maximum G were used based on Eqs. (16) and (17) in this work.

3.2.1d. empirical criterion.^{30,31} The empirical fracture criterion can be expressed by the following generalized, simplified form

$$\left(\frac{K_I}{K_{Ic}} \right)^p + \left(\frac{K_{II}}{\gamma K_{Ic}} \right)^q = 1 \quad (19)$$

where p and q are parameters (typically $p, q = 1 - 2$) to be determined from experimental data through a curve fitting, and

$$\gamma = \frac{K_{IIc}}{K_{Ic}} \quad (20)$$

with $0 < \gamma < 2$, an experimentally determined value. Despite the lack of its theoretical frame work in some cases, the empirical fracture criterion can still provide a much simplified representation (as database, too) of mixed-mode behavior of a material particularly when other (preceding) fracture criteria do not describe reasonably well the actual material's behavior under mixed mode. The maximum G criterion (Eq. 15) or the coplanar crack propagation criterion,³² in fact, is one particular type of the empirical fracture criterion in its form.

3.2.2. Comparison with Experiment

Figure 9 compares the afore-reviewed four different mixed-mode fracture criteria with the experimental data (that were presented in fig. 5), where K_{II} normalized with respect to K_{Ic} , K_{II}/K_{Ic} , was plotted as a function of K_I/K_{Ic} for both 25 and 1316°C data. The prediction for the minimum strain energy density criterion was made using a value of $\nu = 0.2$. Neither the maximum principal stress nor the minimum strain energy density nor the maximum energy release rate criterion was in reasonable agreement with the experimental data. Only the empirical criterion was in good agreement with both ambient and elevated-temperature data, resulting in the following parameters:

$$\begin{aligned} p = 1; q = 2; \gamma = 0.65 & \quad \text{for } 25^\circ\text{C} \\ p = 1; q = 1.3; \gamma = 0.65 & \quad \text{for } 1316^\circ\text{C} \end{aligned} \quad (21)$$

Previous studies on dense ceramics such as silicon nitrides and alumina²² and ceria-doped zirconia²³ showed that the minimum strain energy density criterion resulted in best agreement among the mixed-mode criteria mentioned above, as that was the case in another study of alumina by Suresh et al. as well.¹⁵ Hence, there exists a

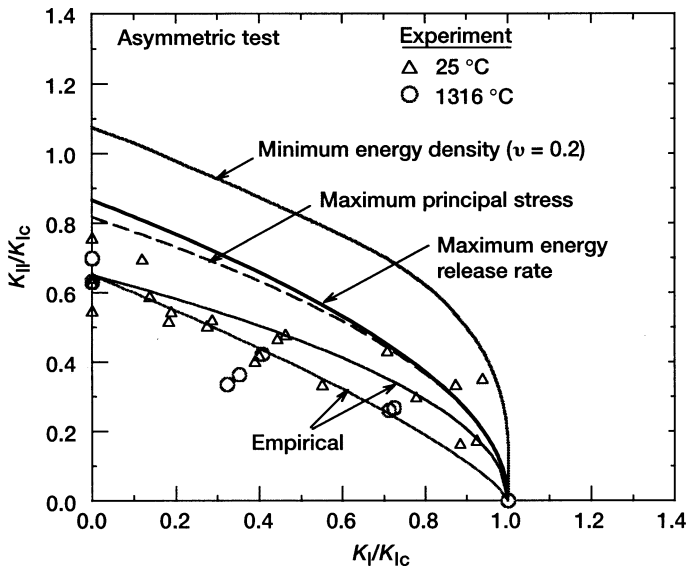


Figure 9. Plots of K_{II}/K_{Ic} as a function of K_I/K_{Ic} for mixed-mode fracture criteria and experimental data determined for plasma-sprayed ZrO₂-8 wt% Y₂O₃ thermal barrier coatings. ν is Poisson's ratio.

remarkable contrast in mixed-mode behavior between the dense and the porous TBC ceramics. The unique nature of the coating material—possessing porosity, microcracks, and platelet microstructure—might have been responsible for the ability to distinguish its unique mixed-mode fracture pattern, as this is not the case for dense ceramics. As also seen from figure 9, the three mixed-mode fracture criteria—the maximum principal stress, minimum strain energy density, and maximum energy release rate criteria—predict the values of $K_{IIc}/K_{Ic} = 0.8$ to 1.1. The poor agreement with these three fracture criteria was, therefore, due to the lower values of K_{IIc}/K_{Ic} that were around 0.65 for the coating material at both temperatures. Hence, the value of K_{IIc}/K_{Ic} is the parameter with the largest influence on the degree of agreement with the prediction of the fracture pattern. In case of $K_{IIc}/K_{Ic} \approx 1$, statistically reasonable agreement would be found in any of the major mixed-mode fracture criteria mentioned. The dense ceramics examined in previous studies^{22,23} all exhibited a value close to $K_{IIc}/K_{Ic} \approx 1$. Comparison of K_{IIc}/K_{Ic} among other brittle materials will be presented and discussed below.

The data on crack propagation angle shown in figure 8 were compared with the predictions made with the three mixed-mode fracture criteria, and the results are presented in figure 10. The minimum strain energy density criterion overall seemed to yield a better prediction compared with the other two criteria. However, because of somewhat significant scatter in θ_c as well as little difference in prediction between the criteria, it is difficult to state which criterion gives the best agreement with the experimental data. Note that a significant discrepancy was found particularly in the region close to pure mode II, e.g., $K_I/K_{II} < 1$. This discrepancy predominant in the region of $K_I/K_{II} < 1$ was also observed in the previous studies with silicon nitrides and alumina²² and other grade alumina by Suresh et al.¹⁵ By contrast, this discrepancy seemingly unique in ceramics was not found in amorphous glassy polymer PMMA (polymethylmethacrylate) mixed-mode tested in either asymmetric

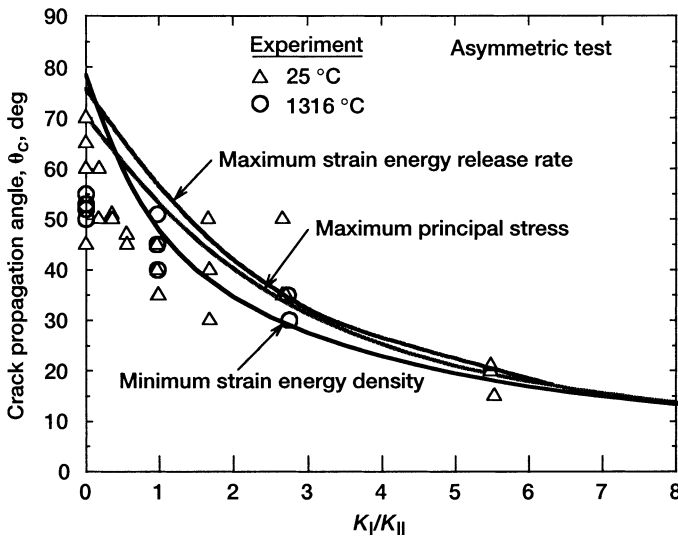


Figure 10. Plots of crack propagation angle as a function of K_I/K_{II} for mixed-mode fracture criteria and experimental data determined for plasma-sprayed ZrO_2 -8 wt% Y_2O_3 thermal barrier coatings.

four-point flexure²³ or uniaxial tension²⁵ configuration. A good agreement of propagation angle with the fracture criteria (as well as little scatter in θ_c) in a wide range of K_I/K_{II} close to pure mode II was also found in steel tested in asymmetric four-point flexure at -196°C to induce brittle fracture.³³

As previously mentioned, the overall locus of mixed-mode fracture (in K_{II} versus K_I , or K_{II}/K_{Ic} versus K_I/K_{Ic} relation) is mainly controlled by the value of K_{IIc}/K_{Ic} ; hence, the ratio of mode II fracture toughness to mode I fracture toughness is a very important measure of a material in terms of its response to mixed-mode fracture. With this in mind, a summary of data on K_{IIc}/K_{Ic} for various brittle materials compiled by Munz and Fett³¹ as well as data on dense ceramics from previous studies^{22,23} was used and compared with the TBC data obtained in this work, as shown in figure 11. The values of K_{IIc}/K_{Ic} for the dense ceramics two silicon nitrides (one with fine and one, elongated grains), coarse grained alumina,²² and ceria-doped tetragonal zirconia polycrystal (Ce-TZP),²³ all tested in asymmetric four-point flexure using *naturally* sharp precracks, are invariably around $K_{IIc}/K_{Ic} = 1$ and are much greater than those of the TBC ($K_{IIc}/K_{Ic} \approx 0.65$). Except for this comparison, a large variation of K_{IIc}/K_{Ic} varying from 0.6 to 2.0 is noted depending on materials, test specimens, notch or initial crack preparations, and even investigators, etc. As a result of this significant variation, a reasonably unified trend on the value of K_{IIc}/K_{Ic} cannot be made for the materials provided. However, it should be noted that the value of K_{IIc}/K_{Ic} for the TBC evaluated in this work is still at the lower end of the data pool. One thing to note is that test technique must be technically sound, particularly in the areas of specimen configuration and precrack preparation. A diametral compression technique, for example, would be in danger to overestimate greater K_{IIc} as a result of frictional constraint between the two crack faces by the existence of compressive stress therein.²² Use of sharp precracks using an appropriate method such as single edge precrack beam (SEPB) method¹⁴ or SEVNB method as used in this work is also crucially important to obtain as accurate fracture toughness as possible.

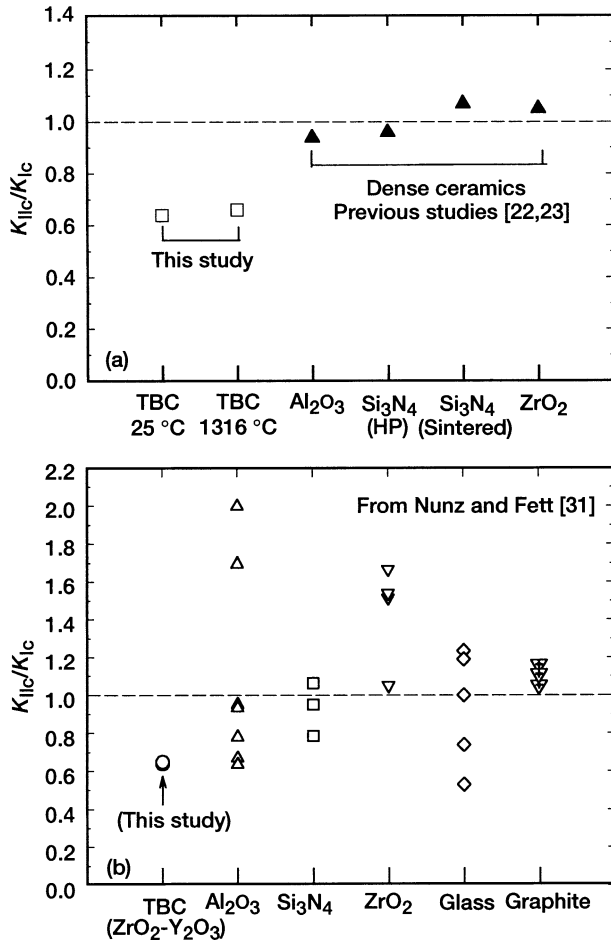


Figure 11. Comparisons of K_{IIc}/K_{Ic} of plasma-sprayed ZrO_2 -8 wt% Y_2O_3 thermal barrier coatings with other advanced monolithic ceramics and brittle materials at ambient temperature. (a) Comparison with previous studies^{22,23}. (b) Comparison with data compiled by Munz and Fett³¹.

3.3. Effect of Directionality

To determine a possible effect of the material’s directionality on fracture toughness, mode I fracture toughness testing for the coating material was performed by the DCB method in the direction perpendicular to the plasma-sprayed direction, as mentioned in the Experimental section. The value of fracture toughness was found to be $K_{Ic} = 1.04 \pm 0.05 \text{ MPa}\sqrt{\text{m}}$. This value of K_{Ic} was very similar to that of $K_{Ic} = 1.15 \pm 0.07 \text{ MPa}\sqrt{\text{m}}$ determined in the direction parallel to plasma-spraying direction. Hence, the directionality of the coating material in response to mode I fracture toughness was insignificant. The previous studies showed that even the tensile strength of the coatings with different vintages was almost independent whether the plasma-spraying direction which was either perpendicular or parallel. Therefore, a notion that mechanical properties of TBC would be *strongly* dependent on the direction of plasma spraying may not be supported and generalized, based on the fracture toughness testing in this study and the strength testing in previous studies.¹²

3.4. Effect of Sintering

Figure 12 shows the results of mode I fracture toughness testing for the coating material annealed at 1316°C in air with annealing times ranging from $t = 0$ (as-sprayed) to 500 h. Fracture toughness increased significantly at $t = 5$ h, increased monotonically to $t = 100$ h, and then reached a plateau at $t = 500$ h with a value of $K_{Ic} = 2.6 \pm 0.2 \text{ MPa}\sqrt{\text{m}}$, about a 120 percent increase from $t = 0$. This increase in K_{Ic} was attributed to a sintering effect.⁶ Figure 13 shows typical fracture surfaces of specimens tested, subjected to annealing for $t = 0$ and 100 h. The sintering effect was manifest by the evidence of significant grain growth for the specimen annealed for $t = 100$ h. It has been shown that sintering gives rise to an increase not only in fracture toughness but in elastic modulus, strength, and thermal conductivity of the coating material.^{34,12,6} Although not performed in this work, it is expected that K_{IIc} in response to sintering would follow a trend similar to K_{Ic} . Therefore, evaluation of K_{IIc} as a function of annealing time at 1316°C is an immediate task for future study. Since a change in mechanical properties (and physical properties as well) would occur inevitably upon sintering, particularly in a short period of time, a continuous use of as-sprayed mechanical data in elevated-temperature applications would give an over-conservative estimate, leading to erroneous results in reliability and/or life predictions of components.

3.5. Other Considerations

Finally, it should be mentioned that the coating material has shown nonlinearity and hysteresis in its stress-strain relation, irrespective of loading configuration: tension, uniaxial or biaxial flexure, or compression.¹² A typical result showing such nonlinearity and hysteresis exhibited in compression by the as-sprayed $\text{ZrO}_2\text{-Y}_2\text{O}_3$ coatings is presented in figure 14. This nonlinearity in constitutive relation was due to the coatings' unique microstructure (porosity, microcracks, and platelets) and diminished upon annealing to a degree depending on annealing time and temperature.

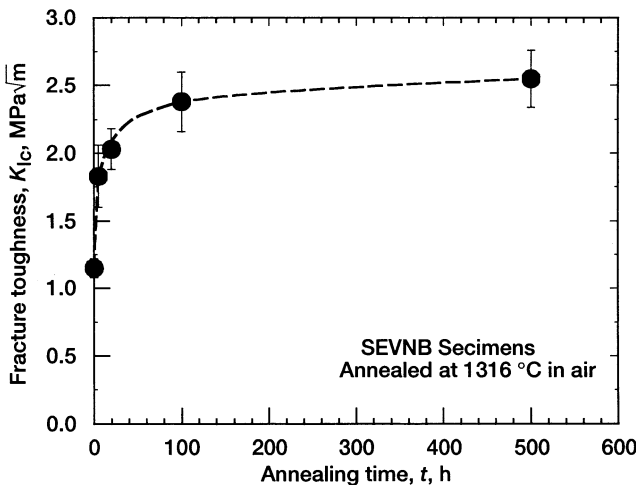


Figure 12. Result of fracture toughness as a function of annealing time for plasma-sprayed $\text{ZrO}_2\text{-8 wt}\% \text{ Y}_2\text{O}_3$ thermal barrier coatings annealed at 1316°C in air.

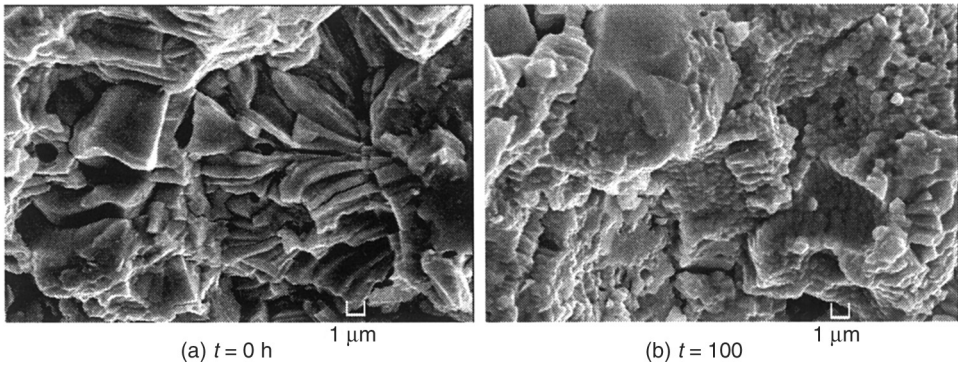


Figure 13. Comparison of fracture surfaces of fracture toughness-tested specimens of plasma-sprayed $ZrO_2-8\text{ wt}\%Y_2O_3$ thermal barrier coatings. (a) As-sprayed. (b) Annealed in air at 1316°C for 100 h.

A question arises as to whether linear elastic fracture mechanics (LEFM) approach could be applicable to this nonlinear, elastic, as-sprayed coating material. The degree of nonlinearity was more significant when the level of applied stress was increased. In most cases, however, fracture force employed in fracture toughness testing was relatively low (with about one tenth of the peak force in figure 14), and in this case the nonlinearity became negligibly small. As a result, an LEFM approach (a continuum approach as well) would be justified at least in fracture toughness testing for the as-sprayed coating material.

4. CONCLUSIONS

A full range of mixed-mode fracture behavior covering mode I and mode II for plasma-sprayed $ZrO_2 - 8\text{ wt}\% Y_2O_3$ thermal barrier coating was determined in air at

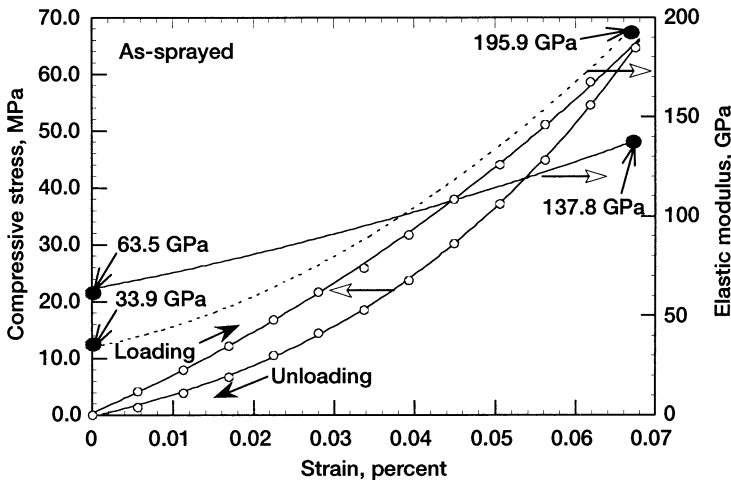


Figure 14. Typical stress-strain curve for plasma-sprayed $ZrO_2-8\text{ wt}\% Y_2O_3$ thermal barrier coatings in compression¹¹.

25 and 1316°C in asymmetric four-point flexure in conjunction with the single edge v-notched beam (SEVNB) method. The following conclusions were made:

1. The mode I fracture toughness was found to be $K_{Ic} = 1.15 \pm 0.07$ and $0.98 \pm 0.13 \text{ MPa}\sqrt{\text{m}}$, respectively, at 25 and 1316°C. The respective mode II fracture toughness was $K_{IIc} = 0.73 \pm 0.10$ and $0.65 \pm 0.04 \text{ MPa}\sqrt{\text{m}}$. Hence, the coating material exhibited an insignificant difference in either K_{Ic} or K_{IIc} between 25 and 1316°C, whereas it exhibited noticeable difference between K_{Ic} and K_{IIc} , resulting in $K_{IIc}/K_{Ic} = 0.65$ at both temperatures.
2. The empirical mixed-mode fracture criterion was in best agreement with the coating's mixed-mode fracture behavior among the four mixed-mode fracture theories considered. The angle of crack propagation was in reasonable agreement with the minimum strain energy density criterion.
3. The mode I fracture toughness of the coating material at 25°C was almost irrespective of the plane either parallel (typical) or perpendicular to plasma spraying direction so that the coating's directionality in response to K_{Ic} was insensitive.
4. Sintering at 1316°C in air showed a significant influence on mode I fracture toughness, giving rise to an increase in K_{Ic} at the plateau region by 120 percent when the coatings were annealed for the duration of 500 h.

REFERENCES

1. R. A. Miller, "Current Status of Thermal Barrier Coatings—An Overview," *Surface and Coating Technology*, **30**, 1–11 (1987).
2. R. A. Miller, "Thermal Barrier Coatings for Aircraft Engines—History and Direction," pp. 17–34 in NASA CP-3312 (Ed. W.J. Brindley), National Aeronautics and Space Administration, Glenn Research Center, Cleveland, OH (1995).
3. T. M. Yonushonis, "Thick Thermal Barrier Coatings for Diesel Components," NASA CR-187111, National Aeronautics and Space Administration, Glenn Research Center, Cleveland, OH (1991).
4. Y. C. Tsui, T. W. Clyne, *Proc. 9th Nat. Thermal Spray Conf.*, Cincinnati, OH (1996).
5. L. L. Shaw, B. Barber, E. H. Jordan, and M. Gell, *Scr. Mater.*, **39**, 1427–1434 (1998).
6. G. Thurn, G. A. Schneider, H. A. Bahr, and F. Aldinger, "Toughness Anisotropy and Behavior of Plasma Sprayed ZrO₂ thermal Barrier Coatings," *Surf. Coat. Tech.*, **123**, 147–158 (2000).
7. K. F. Wesling, D. F. Socie, and B. Beardsley, "Fatigue of Thick Thermal Barrier Coatings," *J. Am. Ceram. Soc.*, **77**[7] 1863–1868 (1994).
8. P. J. Callus and C. C. Berndt, "Relationship between the Mode II Fracture Toughness and Microstructure of Thermal Spray Coatings," *Surf. Coat. Tech.*, **114**, 114–128 (1999).
9. S. R. Choi and N. P. Bansal, "Strength and Fracture Toughness of Zirconia/Alumina Composites for Solid Oxide Fuel Cells," *Ceram. Eng. Sci. Proc.*, **23**[3] 741–750 (2002); "Processing and Mechanical Properties of Various Zirconia/Alumina Composites for Fuel Cells Applications," NASA/TM—2002-211580, National Aeronautics and Space Administration, Glenn Research Center, Cleveland, OH (2002); also presented at CIMTEC 2002 Conference, paper no. G1:P03 (to be published in the proceedings), June 14–18, 2002, Florence, Italy.
10. D-M. Zhu and R. A. Miller, "Influence of High Cycle Thermal Loads on Thermal fatigue Behavior of Thick Thermal Barrier Coatings," NASA Technical paper 3676 (also in Army Laboratory Technical Report ARL-TR-1341), National Aeronautics and Space Administration, Glenn Research Center, Cleveland, OH (1997).
11. S. R. Choi, D-M. Zhu, and R. A. Miller, "High-Temperature Slow Crack Growth, Fracture Toughness and Room-Temperature Deformation Behavior of Plasma-Sprayed ZrO₂ – 8 wt% Y₂O₃," *Ceram. Eng. Sci. Proc.*, **19**[4] 293–301 (1998).

12. S. R. Choi, D-M. Zhu, and R. A. Miller, "Deformation and Strength Behavior of Plasma-Sprayed $ZrO_2 - 8 \text{ wt}\% Y_2O_3$ Thermal Barrier Coatings in Biaxial Flexure and Trans-Thickness Tension," *Ceram. Eng. Sci. Proc.*, **21**[4] 653–661 (2000).
13. J. Kübler, (a) "Fracture Toughness of Ceramics Using the SEVNB Method: Preliminary Results," *Ceram. Eng. Sci. Proc.*, **18**[4] 155–162 (1997); (b) "Fracture Toughness of Ceramics Using the SEVNB Method; Round Robin," VAMAS Report No. 37, EMPA, Swiss Federal Laboratories for Materials Testing & Research, Dübendorf, Switzerland (1999).
14. ASTM C 1421 "Test Method for Determination of Fracture Toughness of Advanced Ceramics at Ambient Temperature," *Annual Book of ASTM Standards*, Vol. 15.01, American Society for Testing and Materials, West Conshohocken, PA (2002).
15. S. Suresh, C. F. Shih, A. Morrone, and N. P. O'Dowd, "Mixed-Mode Fracture Toughness of Ceramic Materials," *J. Am. Ceram. Soc.*, **73**[5] 1257–1267 (1990).
16. K. J. Wang, H. C. Lin, and K. Hua, "Calculation of Stress Intensity Factors for Combined Mode Bend Specimens," pp. 123–133 in *Advances in Research on the Strength and Fracture of Materials*, Vol. 4, Edited by M. D. R. Taplin, ICF4, Waterloo, Canada (1977).
17. M. Y. He and J. W. Hutchinson, "Asymmetric Four-Point Crack Specimen," *J. Appl. Mech.*, **67**, 207–209 (2000).
18. Y. Murakami (ed.), *Stress Intensity Factors Handbook*, Vol. 1, p. 16, Pergamon Press, New York (1987).
19. J. E. Srawley and B. Gross, "Side-Cracked Plates Subjected to Combined Direct and Bending Forces," pp. 559–579 in *Cracks and Fracture*, ASTM STP 601, American Society for Testing and Materials, Philadelphia (1976).
20. T. M. Maccagno and J. F. Knott, "The Fracture Behavior of PMMA in Mixed Modes I and II," *Eng. Fract. Mech.*, **34**[1] 65–86 (1989).
21. D. K. Shetty, A. R. Rosenfield, and W. H. Duckworth, "Mixed-Mode Fracture of Ceramics in Diametral Compression," *J. Am. Ceram. Soc.*, **69**[6] 437–443 (1986).
22. V. Tikare and S. R. Choi, "Combined Mode I and Mode II Fracture of Monolithic Ceramics," *J. Am. Ceram. Soc.*, **76**[9] 2265–2272 (1993).
23. V. Tikare and S. R. Choi, "Combined Mode I-Mode II Fracture of 12-mol-%-Ceria-Doped Tetragonal Zirconia Polycrystalline Ceramic," *J. Am. Ceram. Soc.*, **80**[6] 1624–1626 (1997).
24. F. Erdogan and G. C. Sih, "On the Crack Extension in Plates under Plane Loading and Transverse Shear," *J. Basic Eng.*, **85**, 519–527 (1963).
25. G. C. Sih, "Strain-Energy-Density Factor Applied to Mixed Mode Crack Problems," *Int. J. Fracture*, **10**[3] 305–321 (1974).
26. R. J. Nuismer, "An Energy Release Rate Criterion for Mixed Mode Fracture," *Int. J. Fracture*, **10**[3] 305–321 (1974).
27. K. Palaniswamy and W. G. Knauss, "On the Problem of Crack Extension in Brittle Solids under General Loading," pp. 87–148 in *Mechanics Today*, Vol. 4, Edited by S. Nemat-Nasser, Pergamon Press, New York (1978).
28. K. Hyashi and S. Nemat-Nasser, " " *J. Appl. Mech.*, **48**, 520–524 (1981).
29. Y. Ueda, K. Ikeda, T. Yoa, and M. Aoki, "Characteristics of Brittle Fracture under General Combined Modes Including Those under Biaxial Tensile Loads," *Eng. Fract. Mech.*, **18**[6] 1131–1158 (1983).
30. D. K. Shetty, "Mixed-Mode Fracture Criteria for Reliability Analysis and Design with Structural Ceramics," *J. Eng. Gas Turbine Power*, **109**[7] 282–289 (1987).
31. D. Munz and T. Fett, *Ceramics*, pp. 45–49, Springer-Verlag, Berlin, Germany (1999).
32. P. C. Paris and G. C. Sih, "Stress Analysis of Cracks," ASTM ATP 381, pp. 30–81, American Society for Testing and Materials, Philadelphia, PA, 1965.
33. T. M. Maccagno and J. F. Knott, "The Low Temperature Brittle Fracture Behavior of Steel in Mixed Modes I and II," *Eng. Fract. Mech.*, **38**[2–3] 111–128 (1991).
34. D-Z. Zhu and R. A. Miller, "Thermal Conductivity and Elastic Modulus Evolution of Thermal Barrier Coatings under High Heat Flux Conditions," NASA/TM—1999-209069, National Aeronautics and Space Administration, Glenn Research Center, Cleveland, OH (1999).

MODELING OF FRACTURE IN FERROELASTIC CERAMICS

Chad M. Landis*

1. INTRODUCTION

Ferroelectric ceramics are used in applications ranging from actuators and sensors to ultrasonic motors. A significant shortcoming of these materials in structural applications is their inherent brittleness. Specifically, most ferroelectrics have fracture toughness levels on the order of $K_{Ic} = 1 \text{ MPa}\sqrt{\text{m}}$. The characteristic of ferroelectric ceramics that makes them useful as smart materials is their ability to deform and change polarization irreversibly by the mechanism of domain switching. In a manner akin to transformation toughening, domain switching leads to R-curve behavior and toughness enhancement during crack growth in ferroelectrics. Hence, an understanding of the dissipation due to domain switching and the fracture mechanics governing these materials is crucial for the efficient design of ferroelectric devices.

As an initial investigation, this chapter will focus on fracture in unpoled ferroelectric ceramics under mechanical loading. Note that in the absence of electrical loading, unpoled ferroelectrics remain unpoled. Hence, unpoled ferroelectrics loaded mechanically exhibit purely ferroelastic response; i.e. irreversible straining as a result of applied stress. Experimental investigations on unpoled ferroelectric ceramics by Meschke et al. (2000) and Oates et al. (2003) have found toughness enhancements in the range of $\Delta K_{Ic} = 40\text{--}100\%$ of the initiation toughness, which corresponds to $\Delta G_c = 100\text{--}300\%$. Here ΔK_{Ic} represents the difference in the steady state and initiation levels of fracture toughness during crack propagation. Generally, this toughness enhancement has been attributed to ferroelastic domain switching near the crack tip.

A number of theoretical investigations of switch toughening have been carried out (Zhu and Yang (1997), Yang and Zhu (1998), Reece and Guiu (2002), and Kreher (2002)) which follow the approximate methods used to analyze transform-

* Department of Mechanical Engineering and Materials Science, MS 321, Rice University, P.O. Box 1892, Houston, TX 77251, landis@rice.edu

ation toughening developed by McMeeking and Evans (1982) and Budiansky et al. (1983). With the exception of the work of Kreher (2002), the models applied above assume that domain switching near the crack tip occurs as a discrete transformation. More specifically for the case of pure ferroelasticity, switching is assumed to occur at a well defined level of stress. Once this level of stress is achieved the material accumulates a finite pre-determined level of irreversible strain. The switch is all or none, and there is no partial transformation allowed. Finally, once the switch occurs the irreversible strain cannot be reverse-switched or reoriented; it is locked into the material. This is an approximation to the actual ferroelastic constitutive behavior. In reality, switching takes place over a range of stress levels, transformation is limited by kinematic and equilibrium constraints, and strain reorientation can occur. The previously stated approximations have been used for at least two reasons. First, for most switching criteria the model can be solved analytically. Second, until very recently, no multi-axial incremental constitutive law for ferroelastic switching has been available to analyze this problem.

In this work the newly developed constitutive law of Landis (2003a) for ferroelastic switching is applied to the ferroelastic cracking problem. Some characteristics of the ferroelastic behavior of ferroelectric ceramics include asymmetry in the levels of attainable irreversible strain in tension versus compression, Fett et al. (1998) and Fett and Thun (1998), a Bauschinger effect upon reverse loading, and reorientation of the irreversible strain with reorientation of the applied stress. Due to the highly non-proportional loading experienced by material elements near a passing crack tip, the effects of unloading and strain reorientation are significant in the determination of the quantitative effects of domain switching on the toughness of ferroelastic materials. The constitutive law to be used here is cast in incremental form and captures all of the features described above.

The remainder of the chapter is organized as follows. Section 2 presents the constitutive law used to describe polycrystalline ferroelastic materials. Section 3 presents the fracture model, including the finite element method implemented to determine the fields near a steadily growing crack and the crack tip energy release rate. Results for the toughness enhancement predicted by the model will also be presented in this section. Finally, Section 4 will be used to discuss the results and their comparison to experimental observations.

2. CONSTITUTIVE LAW FOR FERROELASTIC SWITCHING

The nonlinear constitutive response of ferroelastic ceramics is a result of the mechanism of domain switching. The crystal structure of many ferroelectrics of technological interest is tetragonal. Single crystals of ferroelectric material are divided into domains where each domain has a single crystallographic variant. Within a single variant the orientation of the *c*-axis of the unit cells is identical. Domains of different variants are separated by domain walls, and domain switching proceeds in an incremental fashion by the motion of these domain walls. Since the volume of the variants on either side of a domain wall is identical, domain switching can only result in irreversible shear strains. Note here that we are concerned with ferroelasticity and hence 90° degree switching only, since 180° degree switching does not lead to irreversible strains. A more detailed discussion of domain switching and the consti-

tive behavior of single crystals can be found in Huber et al. (1999), Kamlah (2001), or Landis (2003a). Here we are interested in the behavior of ferroelastic *polycrystals* and a phenomenological constitutive description that can be readily implemented within finite element computations.

In order to maintain simplicity, isotropic elastic response and linear kinematics will be assumed such that the stress-strain relations can be written as

$$\varepsilon_{ij} = \frac{1+\nu}{E}\sigma_{ij} - \frac{\nu}{E}\sigma_{kk}\delta_{ij} + \varepsilon_{ij}^r \quad (2.1)$$

Here, ε_{ij} and σ_{ij} are the Cartesian components of the infinitesimal strain tensor and Cauchy stress tensor, ν is the Poisson's ratio and E is the Young's modulus. Also, ε_{ij}^r are the Cartesian components of the remanent strain tensor. The remanent strain is the irreversible strain and can also be referred to as the plastic strain. In all cases discussed in this paper, the datum for remanent strain is the state of the material as cooled from above the Curie temperature. In such a state, all possible domain orientations are equally likely.

The purpose of the nonlinear constitutive law is to provide the evolution of the remanent strain history given the stress or total strain history. Consistent with the facts that domain switching gives rise to deviatoric strains and ferroelastic ceramics exhibit kinematic hardening effects, it is assumed that the material responds elastically within a switching (yield) surface Φ described by

$$\Phi = \frac{3}{2}(s_{ij} - s_{ij}^B)(s_{ij} - s_{ij}^B) - \sigma_0^2 = 0. \quad (2.2)$$

If the stress state is on the switching surface and the load increment induces remanent straining, then the remanent strain increment is normal to the switching surface such that

$$\dot{\varepsilon}_{ij}^r = \lambda(s_{ij} - s_{ij}^B) \quad (2.3)$$

Here s_{ij} are the components of the stress deviator such that $s_{ij} = \sigma_{ij} - \delta_{ij}\sigma_{kk}/3$, s_{ij}^B are the components of the deviator of the back stress tensor σ_{ij}^B , σ_0 is the initial switching (yield) strength of the material in tension or compression, and λ is the as yet undetermined plastic multiplier.

The back stress tensor leads to kinematic hardening and must be used to enforce the remanent strain saturation conditions. The approach used to determine the back stresses is based on the assumption that the internal state of the ferroelastic material is completely characterized by the components of the remanent strain tensor, Cocks and McMeeking (1999) and Landis (2002). This assumption leads to the identification of a remanent potential, $\Psi^r(\varepsilon_{ij}^r)$, such that the back stresses are derived from the potential in the following manner

$$\sigma_{ij}^B = \frac{\partial \Psi^r}{\partial \varepsilon_{ij}^r} \quad (2.4)$$

In order to complete the constitutive theory, the form of Ψ^r must be specified. As previously noted, ferroelectric ceramics exhibit an asymmetry in the attainable

levels of remanent strain in tension versus compression. Specifically, micromechanical simulations by Frölich (2001) and Landis (2003a) suggest that the ratio of remanent strain possible in tension to that possible in compression is 1.37:1. Furthermore, this theoretical value is in the same range as the ratio of the maximum poling remanent strain to the maximum compressive remanent strain due to stress depolarization measured in PLZT by Lynch (1996), and in PZT by Fang and Li (1999). Unfortunately, knowledge of the saturation strains in axisymmetric tension and compression do not provide the complete range of saturation conditions for other multi-axial remanent strain states.

By implementing the micromechanical model of Huber et al. (1999), Landis (2003a) was able to map out the full range of remanent strain saturation states. Figure 1 illustrates the remanent strain states that are possible in a ferroelastic polycrystal comprised of unpoled randomly oriented single crystal grains with tetragonal crystal structure. Remanent strain states that are below the curve are possible in the material, while those above the curve are unattainable. The following procedure has been proposed by Landis (2003a) to determine when saturation is approached. First, since the remanent strain due to domain switching is volume conserving, the following two remanent strain invariants can be used to describe any multi-axial remanent strain state.

$$J_2^e = \left(\frac{2}{3}e_{ij}^r e_{ij}^r\right)^{1/2} \quad \text{and} \quad J_3^e = \left(\frac{4}{3}e_{ij}^r e_{jk}^r e_{ki}^r\right)^{1/3} \tag{2.5}$$

Here, e_{ij}^r is the remanent strain deviator, $e_{ij}^r = \varepsilon_{ij}^r - \delta_{ij}\varepsilon_{kk}^r/3$. Due to volume conservation, the introduction of the remanent strain deviator appears to be unnecessary. However, the potential Ψ^r will be described with these two invariants, and the

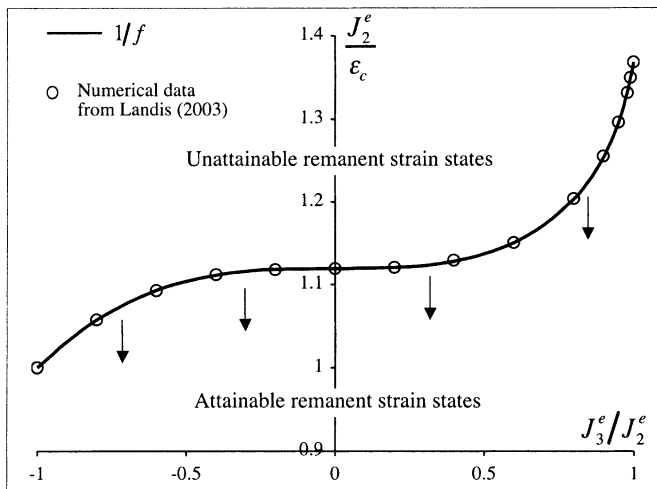


Figure 1. The remanent strain saturation curve dividing remanent strain space into regions that are attainable and unattainable by a polycrystal assembled from randomly oriented tetragonal single crystals. Only remanent strain states below the curve are attainable by such a material. The dots are numerical results from Landis (2003a) obtained using a micromechanical self-consistent model, and the line is one divided by the function f given in Eqs. (2.7) and (2.8). The remanent strain invariants J_2^e and J_3^e are defined in Eq. (2.5) and the results are normalized by the saturation strain in axisymmetric compression ε_c .

derivatives of Ψ^r with respect to ε_{ij}^r will be affected by the distinction between the remanent strain and its deviator. With the definition of these two invariants, a full range of remanent strain saturation states can be probed by allowing the ratio of J_3^e/J_2^e to vary from -1 (axisymmetric contraction) to 0 (pure shear) to 1 (axisymmetric extension).

Now, define a strain-like variable $\bar{\varepsilon}$ as

$$\bar{\varepsilon} = J_2^e f(J_3^e/J_2^e) \tag{2.6}$$

where

$$f\left(\frac{J_3^e}{J_2^e}\right) = -0.0965\left(\frac{J_3^e}{J_2^e}\right)^3 + 0.01\left(\frac{J_3^e}{J_2^e}\right)^6 + 0.8935, \text{ for } \left(\frac{J_3^e}{J_2^e}\right) < 0 \tag{2.7}$$

and

$$f\left(\frac{J_3^e}{J_2^e}\right) = -0.1075\left(\frac{J_3^e}{J_2^e}\right)^3 - 0.027\left(\frac{J_3^e}{J_2^e}\right)^6 - 0.028\left(\frac{J_3^e}{J_2^e}\right)^{21} + 0.8935, \text{ for } \left(\frac{J_3^e}{J_2^e}\right) \geq 0 \tag{2.8}$$

Here, f is a functional fit to the numerical results obtained from the micromechanical computations described in Landis (2003a). This fit is illustrated in Figure 1. When the remanent strain level characterized by $\bar{\varepsilon}$ reaches the compressive saturation level, ε_c , the remanent strain will be saturated. In other words, the only possible remanent strain states in the material are those that satisfy $\bar{\varepsilon} \leq \varepsilon_c$. Hence, in order to prohibit remanent strain states characterized by $\bar{\varepsilon} > \varepsilon_c$, the remanent potential Ψ^r must increase without bound as $\bar{\varepsilon} \rightarrow \varepsilon_c$.

Two final considerations were used to establish the functional form for Ψ^r . First, the potential should yield smooth stress versus strain behavior as the remanent strain goes through zero. Second, the functional form should be simple so that a parametric study can be readily performed within the fracture model. These criteria have been implemented to make the following choice for the remanent potential,

$$\Psi^r = \frac{1}{2} H_0 \varepsilon_c \left[\frac{J_2^e}{\varepsilon_c} \exp\left(\frac{m}{1 - \bar{\varepsilon}/\varepsilon_c}\right) \right]^2 \tag{2.9}$$

Here, H_0 is a characteristic level of back stress that primarily affects the initial slope of the uniaxial stress versus remanent strain curve, and m is another hardening parameter that controls how abruptly the strain saturation conditions are reached. Figure 2a illustrates the predictions of the effective stress versus the effective remanent strain from the constitutive law for uniaxial compression, pure shear strain, pure shear stress and uniaxial tension. It is interesting to note that the shear strain and shear stress curves do not coincide. This feature is due to the fact that the material can strain more in tension than in compression, and has been confirmed in micro-mechanical simulations. Figure 2b illustrates the uniaxial stress versus remanent strain hysteresis curves for two sets of the material parameters H_0 and m .

With the remanent potential specified, it is possible to derive the back stresses and finally solve for the plastic multiplier yielding the incremental form of the constitutive law. For the implementation within the finite element model presented

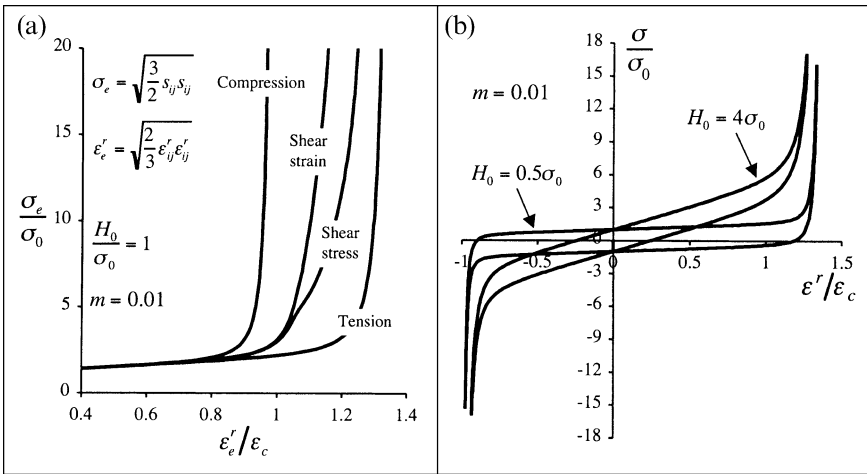


Figure 2. (a) Effective stress versus effective remanent strain curves for the model material described in Section 2 in uniaxial compression, pure shear strain, pure shear stress and uniaxial tension tests. (b) Uniaxial stress versus remanent strain hysteresis loops for the model material illustrating the effect of the hardening parameter H_0 . In both cases notice the asymmetry in the remanent strains that can be achieved in tension versus compression.

in the next section, a backward Euler integration scheme was developed such that the switching surface of Eq. (2.2) and the flow rule of Eq. (2.3) are satisfied at the end of the increment.

3. THE FRACTURE MODEL

Throughout this paper it is assumed that applied loading is small enough such that the height of the switching zone around the crack is small compared to the length of the crack or any other specimen length dimension. Furthermore, only stress fields symmetric with respect to the crack plane will be analyzed, i.e. mode I loading. As discussed by Rice (1968), under these conditions a small scale switching analysis can be performed on a semi-infinite crack with the remote applied stress field being that of the mode I asymptotic elastic K-field,

$$\begin{Bmatrix} \sigma_{11} \\ \sigma_{22} \\ \sigma_{12} \end{Bmatrix} \rightarrow \frac{K_I}{\sqrt{2\pi r}} \cos \frac{\theta}{2} \begin{Bmatrix} 1 - \sin \frac{\theta}{2} \sin \frac{3\theta}{2} \\ 1 + \sin \frac{\theta}{2} \sin \frac{3\theta}{2} \\ \sin \frac{\theta}{2} \cos \frac{3\theta}{2} \end{Bmatrix} \text{ as } r \rightarrow \infty \quad (3.1)$$

Here K_I is the remote applied mode I stress intensity and r and θ are polar coordinates centered on the crack tip. Under plane strain conditions, K_I is related to the remote applied energy release rate G by

$$G = \frac{1 - \nu^2}{E} K_I^2 \quad (3.2)$$

Consider stable crack growth conditions such as a double cantilever beam specimen loaded by forcing a wedge along the crack growth direction. Initially the

crack tip is stationary. As the loading is increased from zero, a localized zone of domain switching surrounds the crack tip. The characteristic size of this switching zone, R_s , is given as

$$R_s = \frac{1}{3\pi} \left(\frac{K_I}{\sigma_0} \right)^2 = \frac{1}{3\pi} \frac{GE}{(1 - \nu^2)\sigma_0^2}. \tag{3.3}$$

The crack tip will remain stationary and the switching zone size will continue to grow until some criterion for crack growth is met. In this paper, it is assumed that crack growth occurs when the crack tip energy release rate, G_{tip} , reaches a material specific critical level of G_0 .

Given this crack growth criterion and assuming that any non-proportional loading effects near a stationary crack in these materials can be neglected, the path-independence of the J -integral implies that $G_{tip} = G$ prior to crack growth and crack growth will commence when $G = G_0$. This point corresponds to the crack growth initiation toughness on the R-curve for the material in consideration. Then, when the crack advances, material elements near the crack tip will unload or load in a non-proportional manner resulting in dissipated energy that must be supplied by the external loading in order to maintain crack growth. Hence, after initiation K_I and G must continue to increase until steady growth conditions are met. This behavior corresponds to the rising portion of the R-curve and occurs over a crack growth range of a few times the maximum switching zone height. After a considerable amount of crack growth, the switching zone and wake of switched material become well-developed and crack growth continues at a constant level of K_I or G . This corresponds to the plateau on the R-curve where steady state crack growth occurs. The constant level of applied energy release rate during steady crack growth will be denoted as G_{ss} .

The analysis presented in this paper will focus only on the toughening due to domain switching during the steady crack growth conditions described above. Under steady growth conditions, all increments of field quantities can be related to derivatives with respect to the x_1 coordinate direction by

$$\dot{\phi} = -\dot{a} \frac{\partial \phi}{\partial x_1} \tag{3.4}$$

Here, ϕ is any scalar field quantity such as a Cartesian component of stress or strain, and \dot{a} is the increment of crack advance in the x_1 direction. Finally, Hutchinson (1974) derived the following path-independent integral that can be used to determine the crack tip energy release rate G_{tip} during steady crack growth,

$$G_{tip} = I \equiv \int_{\Gamma} (Un_1 - \sigma_{ij}n_j u_{i,1}) ds \tag{3.5}$$

where Γ is a counterclockwise directed contour encircling the crack tip, n_i are the components of the unit normal directed to the right along the contour, u_i are the components of the displacement vector, and U is the history dependent stress work density at a material point defined by

$$U = \int_0^{\epsilon} \sigma_{ij} d\epsilon_{ij} \tag{3.6}$$

In order to determine the amount of switch toughening that can occur in a given material, the stress and strain fields near a steadily growing crack must be computed. Due to the complex nonlinear character of the ferroelastic constitutive law described in Section 2, these fields cannot be determined analytically; instead, they will be computed numerically with the finite element method. The numerical model to be used here was originally developed by Dean and Hutchinson (1980) and has been used by numerous authors to investigate steady crack growth in dissipative materials including conventional elastic-plastic, strain-gradient plastic, and visco-plastic materials among others. The basic idea of the formulation is that the finite element mesh is fixed to the crack tip and the material moves through the mesh from $x_1 = \infty$ to $x_1 = -\infty$. The virtual work expression used to derive the finite element method is

$$\int_V \delta \varepsilon_{ij} C_{ijkl} \varepsilon_{kl} dV = \int_S \delta u_i T_i dS + \int_V \delta \varepsilon_{ij} C_{ijkl} \varepsilon_{kl}^r dV \tag{3.7}$$

where S is the boundary of the volume V , C_{ijkl} are the Cartesian components of the isotropic elastic stiffness tensor that can be written in terms of E and ν , and the tractions acting on the boundary S are given as $T_i = \sigma_{ji} n_j$. These tractions are determined from the stress field of Eq. (3.1).

After insertion of the appropriate finite element interpolations, the left-hand side of this equation yields a standard linear elastic stiffness matrix dotted with the vector or unknown nodal displacements. The first term on the right is a vector of applied forces, and the last term is a residual body force vector that accounts for the remanent strain in the volume. An iterative procedure is applied to solve the nonlinear steady crack growth problem. Initially it is assumed that the remanent strain at every point in the body is zero. Hence, the body force vector due to the remanent strains is zero and the linear elastic asymptotic crack tip field solution is recovered. With this solution, the constitutive law of Section 2 is integrated along streamlines of constant height above the crack plane from the right edge of the finite element mesh to the left. This integration yields a new approximation for the distribution of remanent strains. The residual body force vector is recomputed and a new nodal displacement solution is calculated. Again, the constitutive law is integrated along streamlines to obtain a new distribution of remanent strains and the procedure is repeated until the solution achieves a suitable level of convergence.

Within this model for fracture in ferroelastic materials, dimensional analysis dictates that all field quantities, for example the stresses, will be of the form

$$\frac{\sigma_{ij}}{\sigma_0} = \bar{\sigma}_{ij} \left(\frac{x}{R_s}, \frac{y}{R_s}, \frac{\varepsilon_c E}{\sigma_0}, \frac{H_0}{\sigma_0}, m, \nu \right) \tag{3.8}$$

where $\bar{\sigma}_{ij}$ are dimensionless functions of the normalized spatial coordinates parameterized by the normalized material quantities. Also note that here R_s is the characteristic size of the switching zone given by Eq. (3.3) when $G = G_{ss}$. Furthermore, the relative toughening ratio will only depend on the dimensionless material parameters, i.e.

$$\frac{G}{G_{tip}} = \frac{G_{ss}}{G_0} = \bar{G} \left(\frac{\varepsilon_c E}{\sigma_0}, \frac{H_0}{\sigma_0}, m, \nu \right) \tag{3.9}$$

Equation (3.9) reinforces that in this model, crack growth occurs when the crack tip energy release rate, G_{tip} , reaches some material specific critical level G_0 .

3.1. Results

Prior to presenting results for the toughening ratio, some features of the distributions of stress and remanent strain fields will be given. Due to the mode I symmetry of the problem only the upper half plane needs to be analyzed. Figure 3 is a contour plot of the effective strain distribution near a steadily growing crack in a ferroelastic material. As a material point approaches the crack tip from the right, switching commences as it enters the active switching zone. Very close to the crack tip the remanent strain of such a material point will accumulate, reorient as the crack tip passes and eventually the material point will unload elastically. The active switching zone is the region where remanent strain is accumulating or reorienting, while in the unloaded wake the remanent strain distributions are uniform in the x -direction. The shape of the active switching zone is very similar to the shape of the active plastic zone near a steadily growing crack in an elastic-perfectly plastic material, Dean and Hutchinson (1970), Landis et al. (2000). One significant difference between the active zones in these two types of materials is that in the ferroelastic material the unloaded elastic sector behind the crack tip actually lies along the crack faces, while the same feature in the perfectly plastic material is tilted away from the crack faces. Another difference between the ferroelastic and perfectly plastic material is that remanent strains in the ferroelastic material are bounded, while plastic strains in the perfectly plastic material are unbounded.

Due to this strain saturation effect, the stresses near the crack tip in the ferroelastic material increase severely. In fact, the numerical results suggest that very close to the crack tip the stresses have a $1/\sqrt{r}$ radial dependence. Hence the crack tip stress intensity factor $K_{I\text{tip}}$ can be defined such that on the plane ahead of the crack tip

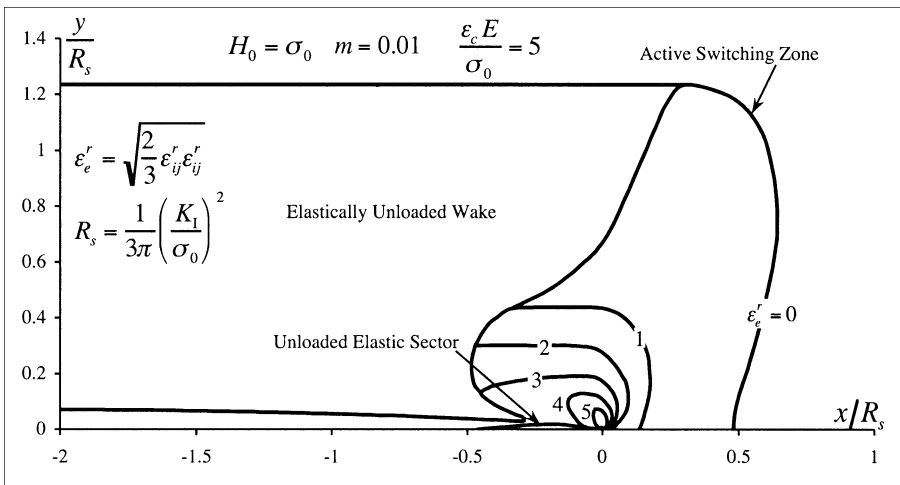


Figure 3. The distribution of effective remanent strain near a growing crack in a ferroelastic material. The active switching zone, elastically unloaded wake, and unloaded elastic sector behind the crack tip are each denoted on the illustration. The material law is given in Section 2, and the material parameters for this computation are $\epsilon_c E / \sigma_0 = 5$, $H_0 = \sigma_0$, $m = 0.01$ and $\nu = 0.25$.

$\sigma_{yy} \rightarrow K_{I\text{tip}}/\sqrt{2\pi r}$ as $r \rightarrow 0$. However, the results also suggest that angular dependence of the stress field asymptotically close to the crack tip is *not* equivalent to the asymptotic field for an isotropic elastic solid. The discrepancy between the ferroelastic asymptotic field and the isotropic elastic asymptotic field is most pronounced for low values of H_0/σ_0 and large values of $\varepsilon_c E/\sigma_0$. Figure 4a plots the angular dependence of the stresses near a growing crack tip in a ferroelastic material with properties $\varepsilon_c E/\sigma_0 = 3$, $H_0 = 0.1\sigma_0$, $m = 0.01$ and $\nu = 0.25$. Notice that the $1/\sqrt{r}$ radial dependence of the stresses has been accounted for in the normalization. Furthermore, since the stresses do not follow the isotropic asymptotic field, the relationship between G_{tip} and $K_{I\text{tip}}$ is *not* given by Eq. (3.2). This then implies that $G/G_{\text{tip}} \neq (K_I/K_{I\text{tip}})^2$. Specifically, for these material parameters, $G/G_{\text{tip}} = 3.02$ whereas $K_I/K_{I\text{tip}} = 2.25$. For comparison, if the hardening parameter is changed to $H_0 = 10\sigma_0$, then the stress field is very close to the isotropic asymptotic field (the σ_{xx} component falls noticeably but just slightly below the isotropic curve) and $G/G_{\text{tip}} = 1.29$ with $K_I/K_{I\text{tip}} = 1.20$. A similar approach of the asymptotic ferroelastic stresses to the isotropic elastic asymptotic fields occurs as $\varepsilon_c E/\sigma_0 \rightarrow 0$, which is to be expected.

Figure 4b plots the angular dependence of the remanent strains near the growing crack tip in the same material described above. Note on Figure 4b that the saturation strain variable $\bar{\varepsilon}$ is very close to ε_c over the entire angular range, denoting that the material is in fact near saturation close to the crack tip. However, the remanent strain components are not uniform, indicating that remanent strain reorientation does occur around a growing crack.

The primary goal of this fracture model is to determine how the steady state toughness enhancement in ferroelastic materials, G_{ss}/G_0 , depends on the material properties. Eq. (3.9) identifies the material properties in question and ranks them in order of significance. Poisson’s ratio ν will be shown to have a very weak influence over the toughness enhancement. The two hardening parameters, H_0/σ_0 and m , have a much stronger influence on G_{ss}/G_0 , and it will be shown that as the hardness of the

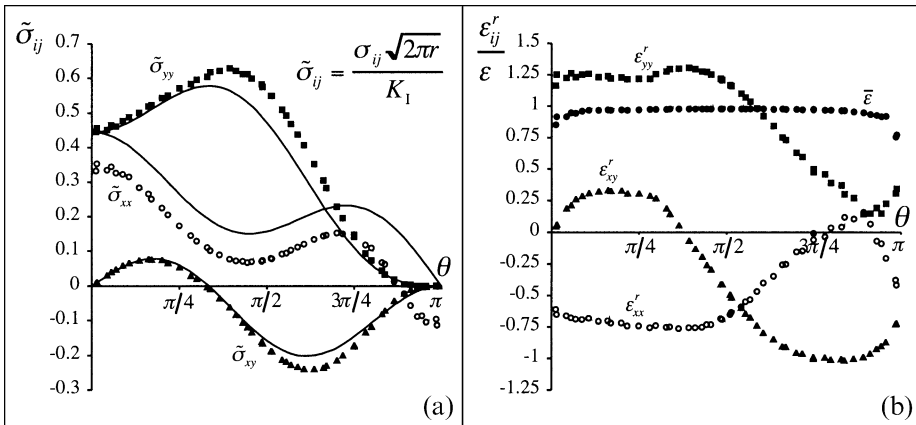


Figure 4. (a) The angular distribution of the stresses very close to the crack tip. The dots are numerical results for a material with $\varepsilon_c E/\sigma_0 = 3$, $H_0 = 0.1\sigma_0$, $m = 0.01$ and $\nu = 0.25$, and the solid lines are the result for an isotropic elastic solid. Note that the $1/\sqrt{r}$ radial dependence has been accounted for within the normalization. (b) The angular distribution of remanent strains very close to the crack tip from the same computation. The numerical results plotted in both figures are for all integration stations within the radial range $8 \times 10^{-3} R_s < r < 1.3 \times 10^{-2} R_s$.

material increases then the toughness enhancement decreases. Finally, the most fundamental material parameter that has been identified in all transformation toughening models is $\epsilon_c E/\sigma_0$. Explicitly, this is the ratio of the irreversible strain to the characteristic elastic strain in the material. However, if this ratio is rearranged as $(\sigma_0 \epsilon_c)/(\sigma_0^2/E)$, then it can also be interpreted as the ratio of the characteristic level of dissipated to stored energy in the material. Results for the dependence of G_{ss}/G_0 on $\epsilon_c E/\sigma_0$ will be given presently.

Figure 5 plots G_{ss}/G_0 versus $\epsilon_c E/\sigma_0$ for a range of initial hardening values H_0/σ_0 with $m = 0.01$ and $\nu = 0.25$. The first observation to make about this plot is that the toughness enhancement increases monotonically as the saturation level of irreversible remanent strain increases. Larger saturation strains imply that the material can dissipate more energy, which in turn implies higher fracture toughness. A second feature illustrated on this plot is the dependence on the hardening parameter H_0/σ_0 . As shown in Figure 2b, increasing levels of H_0/σ_0 induce higher stresses in the material that are required to reach given levels of remanent strain. Figure 5 illustrates that there is a relatively strong dependence of the toughness enhancement on the initial hardness. Hence, the actual shape of the stress strain curve in these materials is important when making a quantitative determination of the fracture toughness.

Finally, it is worth noting that these toughness curves are relatively straight at low levels of $\epsilon_c E/\sigma_0$. Therefore, the initial slope of these curves when $\epsilon_c E/\sigma_0 = 0$ provides a useful measure of the toughness enhancement. Specifically, the toughening parameter α is defined as

$$\alpha = \frac{\sigma_0}{G_0 E} \left. \frac{\partial G_{ss}}{\partial \epsilon_c} \right|_{\epsilon_c=0} \tag{3.10}$$

Figure 6 plots the toughening parameter α as a function of H_0/σ_0 for ranges of Poisson’s ratio and the second hardening parameter m . The insert plots hysteresis

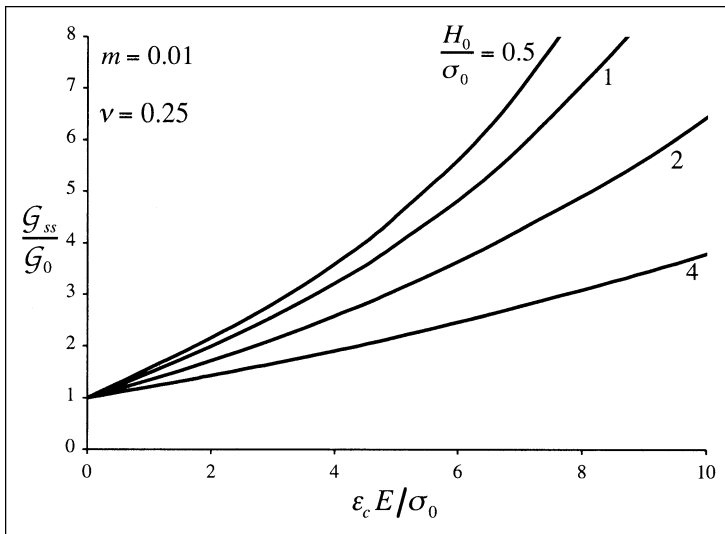


Figure 5. The toughness enhancement, G_{ss}/G_0 , during steady crack growth in a ferroelastic material as a function of the saturation strain level, $\epsilon_c E/\sigma_0$, for a range of initial hardening values, H_0/σ_0 .

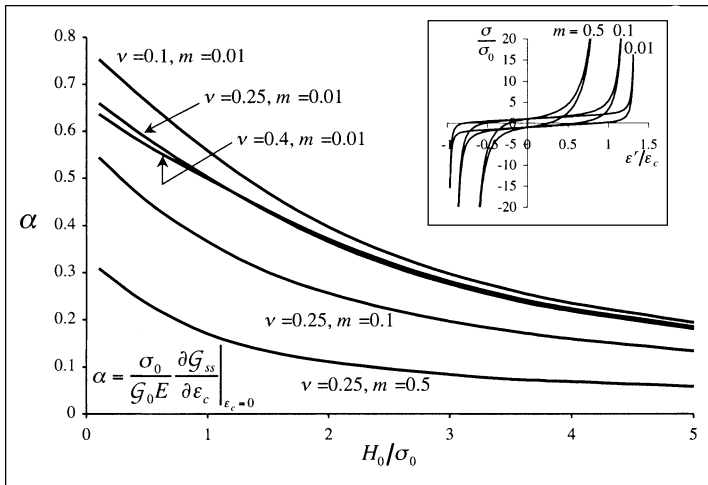


Figure 6. The initial slope of the toughness ratio versus the relative saturation strain, α , as a function of the initial hardening H_0/σ_0 , for a range of Poisson's ratio and m . The insert plots hysteresis loops in order to illustrate the dependence of the stress-strain behavior on m .

loops for a few values of m and a single value of $H_0/\sigma_0 = 1$. First notice that α is only weakly dependent on Poisson's ratio, and this dependence is very weak for the range of $0.25 < \nu < 0.4$. The toughness enhancement has a stronger dependence on the hardening parameter m . However, note from the insert that increasing m drastically increases the stress levels near strain saturation. Effectively, large m values reduce the saturation strain of the material. It is likely that most materials are characterized within the range of $0 < m < 0.1$.

In summary, results from numerical computations of the stress and strain fields and the toughness enhancement during steady crack growth in ferroelastic materials have been presented. The computations illustrate a few interesting features and confirm some intuitive hypotheses about the solution. First, the near tip stresses appear to recover a $1/\sqrt{r}$ singular form, however the radial dependence of these stresses is not the same as those for an isotropic elastic material. It was also shown that the distributions of remanent strain are not trivial and do reorient as the crack tip passes. Lastly, as would be expected, the steady state toughness of the material increases as the relative saturation strain increases, and decreases as the hardness of the material increases.

4. DISCUSSION

The steady state fracture toughness enhancement in ferroelastic ceramics has been computed accurately by implementing a micromechanically verified phenomenological constitutive law to describe the continuum material response. The constitutive law is able to account for most of the features of ferroelastic deformation, including the asymmetry in tensile versus compressive remanent strains and the Bauschinger effect. This constitutive law was implemented within the finite element method to determine the fields near a steadily growing crack. Crack growth was assumed to occur at a critical level of the crack tip energy release rate. The most significant material features

that control the level of toughening in these materials have been identified as the relative saturation strain level and the shape of the uniaxial stress-strain curve.

It is worth noting that the assumptions implemented within transformation toughening-type analyses have not been used in this model. Specifically, the remanent strain is allowed to vary and change within the switching zone near the crack tip. Figure 4b illustrates how the remanent strain components vary near the crack tip and well into the region where strain saturation is achieved. This figure emphasizes the fact that the stress fields near a growing crack tip act to reorient the remanent strain in the material. This reorientation of the remanent strain is a dissipative process and influences the toughness enhancement due to switching. Transformation toughening models that assume a “locked in” switching strain simply cannot account for this feature of the problem. While these transformation toughening models can give estimates of the toughness enhancement due to switching, material features such as the initial hardening ratio H_0/σ_0 do not enter into these types of models. Hence, qualitative determinations of the effects of such parameters cannot be ascertained from transformation toughening models. A more detailed discussion of transformation toughening switching models, their limitations, and a comparison to the results from the finite element computations performed in this work are included in Landis (2003b).

Due to the inherent brittleness of ferroelastic ceramics, there is a dearth of detailed experimental measurements on their full range of uniaxial stress-strain behavior. In tension, the material fractures before strain saturation can be achieved. Hence, most experiments in the literature are carried out in compression. This is unfortunate since even a partial hysteresis loop would be very useful for the determination of the switching strength. Specifically, the width of the hysteresis loop is approximately $2\sigma_0$. In order to obtain information from the uniaxial compressive stress-strain curve, the following observations are made. The elastic modulus should be taken as the initial slope of the *unloading* portion of the stress-strain curve. The compressive saturation strain is at least the strain extrapolated back to zero stress using this initial unloading slope. If the stress-strain behavior is measured on an electrically *poled* sample, then the nonlinear strain range is approximately $2.37\varepsilon_c$. Finally, the slope of the switching portion of the stress-strain curve is approximately equal to H_0/ε_c . Applying these considerations to the data available in the literature, it was found that PZT materials have properties in the range $\varepsilon_c E/\sigma_0 \approx 3 - 7$ and $H_0/\sigma_0 \approx 1$, Schäufele and Härdtl (1996), and PLZT has properties near $\varepsilon_c E/\sigma_0 \approx 5$ and $H_0/\sigma_0 \approx 1$, Lynch (1996). Applying these material properties to the model computations of Section 3 the predicted steady state toughness enhancement for these materials is in the range of $G_{ss}/G_0 \approx 2.5 - 5.8$ or $\Delta K_1 \approx 60 - 140\%$. As mentioned in the Introduction, experimental investigations on unpoled ferroelectric ceramics by Meschke et al. (2000) for barium titanate and Oates et al. (2003) for PZT, have found toughness enhancements in the range of $\Delta K_{Ic} = 40 - 100\%$ of the initiation toughness. Hence, the model yields prediction in the appropriate range. A more critical experimental comparison can only be made if both fracture data and detailed stress-strain measurements are obtained for the same material.

ACKNOWLEDGEMENT

The author would like to acknowledge support from the Army Research Office contract DAAD19-02-1-0241.

REFERENCES

- Budiansky, B., Hutchinson, J. W. and Lambropoulos, J. C., 1983, Continuum theory of dilatant transformation toughening in ceramics, *International Journal of Solids and Structures* **19**:337–355.
- Cocks, A.C.F. and McMeeking, R.M., 1999, A phenomenological constitutive law for the behavior of ferroelectrics, *Ferroelectrics* **228**:219–228.
- Dean, R.H. and Hutchinson, J.W., 1980, Quasi-static steady crack growth in small scale yielding. In *Fracture Mechanics*, ASTM-STP 700, 383–405.
- Fang, D. and Li, C., 1999, Nonlinear electric-mechanical behavior of a soft PZT-51 ferroelectric ceramic, *Journal of Materials Science* **34**:4001–4010.
- Fett, T., Müller, S., Munz, D., Thun G., 1998, Nonsymmetry in the deformation behavior of PZT, *Journal of Materials Science Letters* **17**:261–265.
- Fett, T. and Thun, G., 1998, Nonsymmetric deformation behavior of lead zirconate titanate determined in bending tests, *Journal of the American Ceramic Society* **81**:269–272.
- Frölich, A., 2001, Mikromechanisches modell zur ermittlung effektiver materialeigenschaften von piezoelektrischen polykristallen, Dissertation Thesis, Universität Karlsruhe, Germany.
- Huber, J.E., Fleck, N.A., Landis, C.M. and McMeeking, R.M., 1999, A constitutive model for ferroelectric polycrystals, *Journal of the Mechanics and Physics of Solids* **47**:1663–1697.
- Hutchinson, J.W. 1974, On steady quasi-static crack growth, Harvard University Report, Division of Applied Sciences, DEAP S-8.
- Kamlah, M., 2001, Ferroelectric and ferroelastic piezoceramics – modeling and electromechanical hysteresis phenomena, *Continuum Mechanics and Thermodynamics* **13**:219–268.
- Kreher, W., 2002, Influence of domain switching zones on the fracture toughness of ferroelectrics, *Journal of the Mechanics and Physics of Solids* **50**:1029–1050.
- Landis, C.M., Pardoën, T. and Hutchinson, J.W., 2000, Crack velocity dependent toughness in rate dependent materials, *Mechanics of Materials* **32**:663–678.
- Landis, C.M., 2002, Fully coupled, multi-axial, symmetric constitutive laws for polycrystalline ferroelectric ceramics, *Journal of the Mechanics and Physics of Solids* **50**:127–152.
- Landis, C.M., 2003a, On the strain saturation conditions in polycrystalline ferroelastic ceramics, to appear in *Journal of Applied Mechanics*.
- Landis, C.M., 2003b, On the fracture toughness of ferroelastic materials, submitted to *Journal of the Mechanics and Physics of Solids*.
- Lynch, C.S., 1996, The effect of uniaxial stress on the electro-mechanical response of 8/65/35 PLZT, *Acta Materialia* **44**:4137–4148.
- McMeeking, R.M. and Evans, A.G., 1982, Mechanics of transformation toughening in brittle materials, *Journal of the American Ceramic Society* **65**:242–246.
- Meschke, F., Raddatz, O., Kolleck, A., and Schneider, G.A., 2000, R-curve behavior and crack-closure stresses in barium titanate and (Mg, Y)-PSZ ceramics, *Journal of the American Ceramic Society* **83**:353–361.
- Oates, W.S., Lynch, C.S., Rödel, J., Lupascu D. and Aulbach, E., 2003, Investigation of subcritical crack growth in lead zirconate titanate, submitted to the *Journal of the American Ceramic Society*.
- Reece, M.J. and Guiu, F., 2002, Toughening produced by crack-tip-stress-induced domain reorientation in ferroelectric and/or ferroelastic materials, *Philosophical Magazine* **A82**:29–38.
- Rice, J.R., 1968, A path independent integral and the approximate analysis of strain concentration by notches and cracks, *Journal of Applied Mechanics* **35**:379–386.
- Schäufele, A.B. and Härdtl, K.H., 1996, Ferroelastic properties of lead zirconate titanate ceramics, *Journal of the American Ceramic Society* **79**:2637–2640.
- Yang, W. and Zhu, T., 1998, Switch toughening of ferroelectrics subjected to electric fields, *Journal of the Mechanics and Physics of Solids* **46**:291–311.
- Zhu, T. and Yang, W., 1997, Toughness variation of ferroelectrics by polarization switch under non-uniform electric field, *Acta Materialia* **45**:4659–4702.

STRENGTH AND RELIABILITY OF LEAD ZIRCONATE TITANATE CERAMICS

Chad S. Watson[‡]

ABSTRACT

The influences of temperature and processing conditions (unpoled or poled-depoled) on strength, Weibull parameters and the stress-strain behavior of tin-modified lead zirconate titanate (PSZT) were evaluated in four-point bending. PSZT exhibited temperature-dependent non-linear and non-symmetric stress-strain behavior. A result of temperature dependent non-linearity was an apparent reduction in the flexural strength of PSZT as temperature increases. At room temperature the average stress in the outer-fiber of bend bars was 84 MPa, whereas, for specimens tested at 120°C the average failure stress was only 64 MPa. The load-carrying capacity, however, did not change with temperature, but the degree of deformation tolerated by PSZT prior to failure increased with temperature.

1. INTRODUCTION

Partially electroded ferroelectric devices that are heated to enhance dipole alignment under the influence of an electric field develop differential strains at the electrode edge. Strain incompatibilities at the electrode boundary can result in stresses large enough to initiate cracks from nearby flaws.¹⁻³ Similarly, multilayer actuators, which

[‡] Chad S. Watson, Ceramic Materials Department, Sandia National Laboratories, Albuquerque, NM 87185

are composed of several layers of partial internal electrodes, can develop stresses during switching operations that are high enough to generate cracks at electrode boundaries, thus limiting the effective lifetime of the device.⁴ The reliability of partially electroded ferroelectrics can be improved by using thinner layers, which effectively reduces the volume of material exposed to high tensile stresses around the electrode edge during poling.^{1,2} Another reliability enhancement technique includes the use of a pre-conditioning step prior to polarizing the electroded volume. By polarizing and then depolarizing the entire ferroelectric element, the domains in the material, instead of being randomly oriented, are now aligned “parallel” to the applied field. As a result, the strain differential between the electroded and unelectroded area can be reduced; for example, from $\sim 800 \mu\epsilon$ to only $200 \mu\epsilon$ in the ϵ_{31} direction for tin-modified lead zirconate titanate.³

Ferroelectric devices are frequently exposed to elevated temperatures during processing or while in operation, which could potentially degrade component integrity. For instance, the mechanical properties of ferroelectrics can vary as temperature is increased due to phase transformations, domain wall movement, residual stress changes, microcracking or other mechanisms. Research relating the effect of temperature on the mechanical properties of ferroelectrics indicates a reduction in strength^{5,6} and fracture toughness⁷ as the applied temperature approaches the Curie temperature. The potential for temperature-dependent mechanical degradation of ferroelectrics needs to be addressed to establish a more complete understanding of component reliability. To this end, the effects of temperature on the stress-strain behavior and flexural strength of tin-modified lead zirconate titanate (PSZT) have been examined. In addition, Weibull strength parameters were determined for unpoled and poled-depoled specimens at room temperature.

2. EXPERIMENTAL PROCEDURE

Sintered PSZT [$\text{Pb}_{0.99}(\text{Sn}_{0.13}\text{Zr}_{0.82}\text{Ti}_{0.05})_{0.98}\text{Nb}_{0.02}\text{O}_3$] ceramics were prepared using conventional mixed oxide techniques (Alliant Corporation, New Hope, MN). Bend bars were sliced and ground from sintered billets and finished with a 600 grit diamond wheel to dimensions of $3 \text{ mm} \times 4 \text{ mm} \times 45 \text{ mm}$. Analogous to the procedures used to fabricate PSZT partially electroded components, all of the bend bars were thermally cleaned at 825°C . At this point, the bend bars were in the unpoled state, i.e., the domains in the material were assumed to be randomly oriented. Some of these unpoled bend bars were saved after thermal cleaning for mechanical property measurements. The remaining bend bars were processed through the pole-depole state. A temporary silver electrode was applied to the top and bottom surfaces of the bend bars and dried at 71°C . After the temporary electrode was dried and the bend bar cooled to room temperature, it was subjected to a pole-depole process. For this process, the bend bars were polarized in dielectric fluid (Fluorinert FC77, 3M Corp., Minneapolis, MN) at room temperature to 32 kV/cm ; whereupon, the electric field was reversed until negligible charge was stored. After pole-depole the temporary electrode was removed by rinsing in acetone. A schematic illustrating the experimental configuration of the bend bars with respect to the poling-depoled direction and loading conditions is shown in Fig. 1.

The stress-strain behavior and flexure strength of PSZT were measured in four-point bending at $23, 75, 86, 100$ and 120°C . For the $75, 86$ and 100°C runs, the

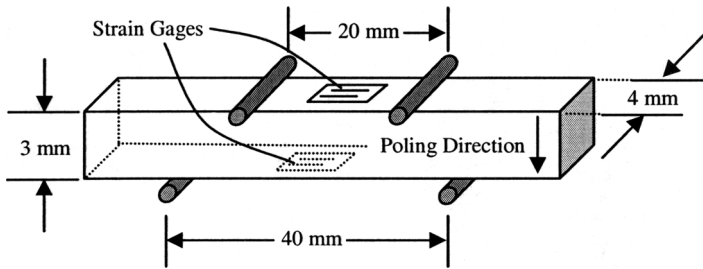


Figure 1. Schematic of bend bar geometry, polarization direction and strain gage placement.

samples were taken to 105°C and held at temperature for 15 min and then cooled to their respective test temperature at 3°C/min and held at temperature for 15 min prior to testing to minimize thermal gradients in the material. These heating and cooling cycles (3°C/min ramp rates and 15 min holds) are analogous to those used for hot poling PSZT components. An MTS 810 Universal Testing Machine and a MTS Environmental Chamber (MTS Systems Corporation, Minneapolis, MN) were used to mechanically load the specimens at temperature. Strength was measured according to ASTM C1161-02c.⁸ Weibull parameters for unpoled and poled-depoled PSZT were determined from room temperature strength measurements.

To evaluate the stress-strain behavior of PSZT, load-strain and load-deflection measurements were performed at each temperature condition. Tensile and compressive strains that developed while loading to failure were determined for two specimens at each temperature with the use of strain gauges with pre-attached leads (Type CEA-06-062UW-350, Measurements Group, Inc.; Raleigh, NC). The gauges were affixed to the compression and tension face of the bend bars with adhesive (M-Bond 600; Measurements Group, Inc.; Raleigh, NC) and cured at 100°C for four hours. Deflection measurements were made on eight specimens at each temperature utilizing an extensometer (MTS Systems Corporation, Minneapolis, MN). The deflection data was converted to strain (ϵ),

$$\epsilon = \frac{6Wh}{L^2} \quad (1)$$

where W is the magnitude of bar deflection, h is bar thickness and L is the distance between the outer supports.

Representative SEM micrographs of a polished and chemically etched PSZT specimen and of a typical fracture surface are shown in Figs. 2a & b, respectively.

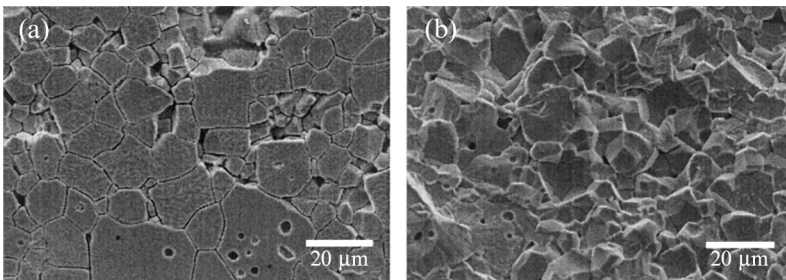


Figure 2. SEM images of (a) polished and chemically etched PSZT and (b) of a typical fracture surface.

PSZT microstructures consist of equiaxed grains with a bimodal grain size distribution. Some intragranular porosity within the larger grains is evident. The grain pullout is an artifact of polishing. PSZT fractures in both an intergranular and transgranular mode. Typically, the larger grains fail transgranularly while smaller grains fail intergranularly.

3. RESULTS AND DISCUSSION

3.1. Non-Linear Stress-Strain Behavior and True Flexural Strength

Based on the load-strain and load-deflection measurements, PSZT exhibits non-linear stress-strain behavior. A plot of linear-elastically computed stress (or engineering stress) versus strain for poled-depoled specimens tested at room temperature, 75, 86, 105 and 120°C is shown in Fig. 3. Deviations from linear-elastic behavior initiate at a nominal stress level of approximately 20–30 MPa for specimens tested at room temperature and 10–20 MPa for specimens tested at an elevated temperature. Furthermore, the extent of non-linearity increases as the testing temperature increases. Conversion of the load-strain data to the true stress-strain behavior was achieved by implementing the approach first described by Nadai⁹ and adapted by Chen et al.¹⁰ The true compressive (σ_c) and tensile stresses (σ_t) were calculated as follows:

$$\sigma_c = \frac{2M(\varepsilon_t - \varepsilon_c)}{\varepsilon_c b h^2} - \frac{\partial M}{\partial \rho} \frac{1}{\varepsilon_c b h} \quad (2)$$

$$\sigma_t = \frac{2M(\varepsilon_t - \varepsilon_c)}{\varepsilon_t b h^2} - \frac{\partial M}{\partial \rho} \frac{1}{\varepsilon_t b h} \quad (3)$$

where M is the applied bending moment, ε_c and ε_t are the compressive and tensile strains respectively, b is the width of the bend bar, and ρ is radius of curvature given by

$$\rho = \frac{h}{\varepsilon_t - \varepsilon_c} \quad (4)$$

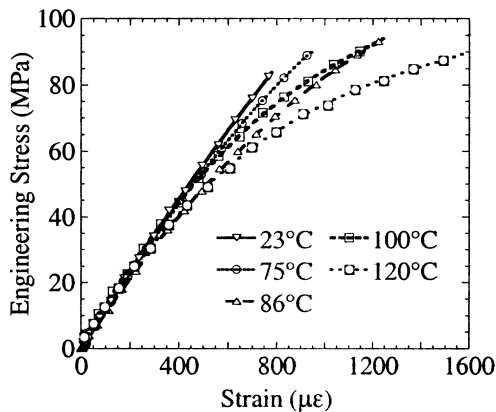


Figure 3. Tensile stress-strain curves to failure for PSZT four-point bend specimens at 23, 75, 86, 100 and 120°C assuming linear-elasticity.

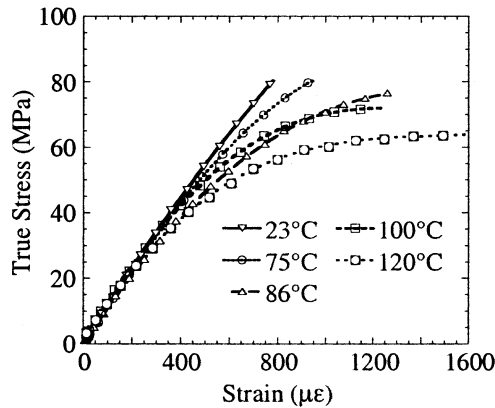


Figure 4. Conversion of load-strain data to the true tensile stress-strain curves to failure for PSZT four-point bend specimens at 23, 75, 86, 100 and 120°C.

The true stress versus strain curves are shown in Fig. 4. These curves are derived from the same load-strain data as the engineering stress-strain curves in Fig. 3. It is evident that as the temperature increases, the amount of deformation supported by the material to failure also increases. For example, the specimen tested at room temperature failed at a strain of $\sim 800 \mu\epsilon$, whereas, the specimen tested at 120°C deformed twice as much at failure ($\sim 1600 \mu\epsilon$). This additional deformation is most likely the result of a higher percentage of domains switching in response to the applied load. The reproducibility of the stress-strain measurements is shown in Fig. 5 where the true tensile stress-strain traces of two strain-gauged specimens at each temperature follow similar curves. Assuming the remaining eight bend bars that were tested to failure without a strain gauge at each temperature exhibit a similar stress-strain response, then the true failure stress for each specimen can be determined. Because strain-gauge measurements can be cumbersome, strain development can also be assessed from deflection measurements using an extensometer. However, extensometers do not provide the same sensitivity as strain-gauges. In addition, contributions from non-symmetry are not measured with an extensometer. Nonetheless, the true strength can be ascertained, but non-symmetry contributions are assumed negligible and strain resolution is compromised. The true failure stress of specimens loaded to failure without strain-gauges was determined by converting load-deflection measurements made with an extensometer to the true failure stress following Gogotsi,¹¹

$$\sigma_t = \frac{3a}{bh^2} \left(P + \frac{\epsilon}{2} \cdot \frac{dP}{d\epsilon} \right) \quad (5)$$

where a is the distance between the inner supports, P is the load, and ϵ is the tensile strain (calculated using Eq. 1) experienced by the material during flexure. A small portion of the load-deflection data (three out of eight poled-depoled specimens at 23°C and one out of eight poled-depoled specimens at 120°C) was taken from measurements made with the LVDT of the mechanical testing machine. In addition, the strains measured with the two strain-gauge experiments at each temperature were also included in the extensometer data set, as a result, a total of ten specimens were

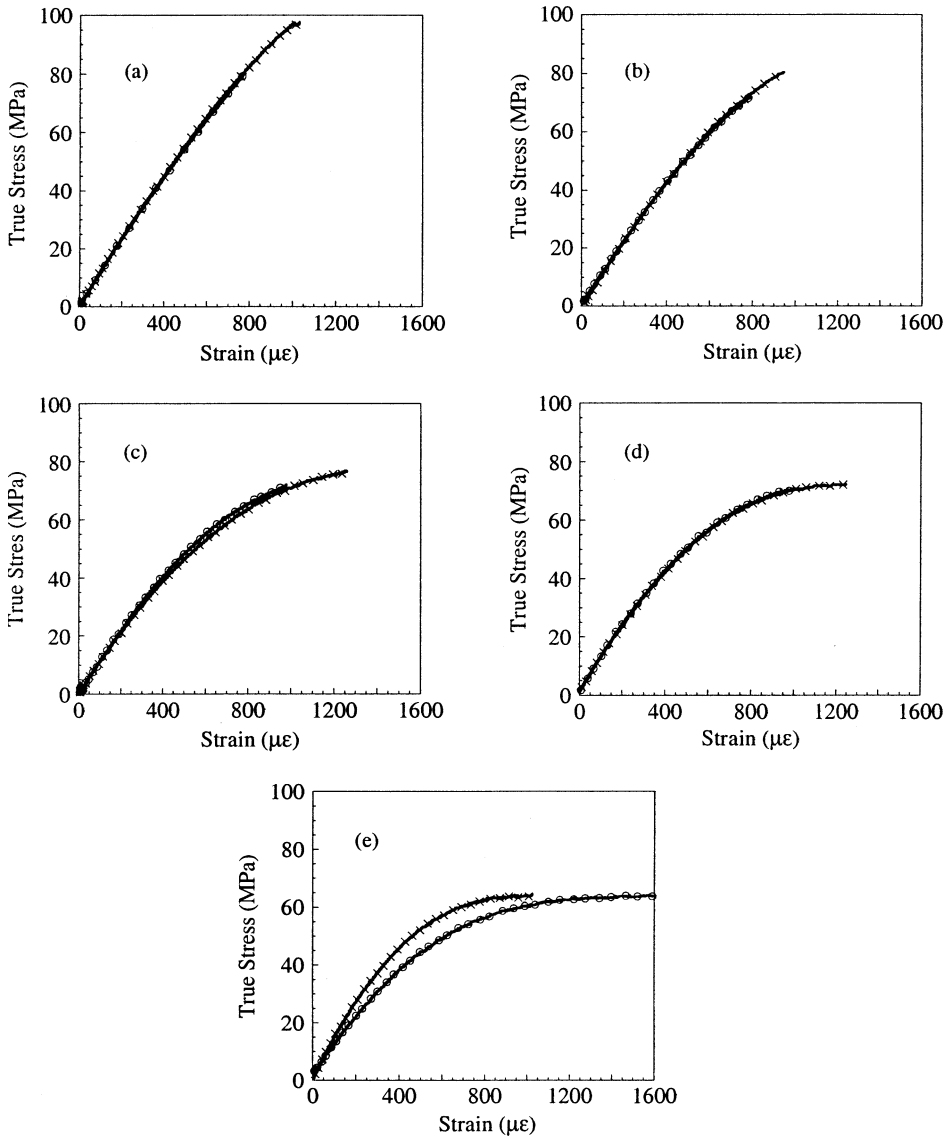


Figure 5. True tensile stress-strain curves to failure of two different strain-gauged PSZT four-point bend specimens at (a) 23, (b) 75, (c) 86, (d) 100 and (e) 120°C.

averaged to determine the true failure stress using Eq. 5. The results are given in Table 1 and shown in Fig. 6. In addition, the average load at failure, linear elastic or engineering stress, and the average true failure stress based on the stress-strain response of the two strain-gauged specimens, 10 specimens per temperature, is shown in Table 1 and Fig. 6. The true failure stresses, as calculated from the strain-gauge and displacement techniques, are typically within 3%. As shown in Fig. 6, the average true stresses for both measurement techniques follow the same trend: the true failure stress decreases with increasing temperature. At room temperature, the true failure stress as calculated using the strain gauge technique is 84.3 MPa and decreases significantly to

Table 1. Mechanical Property Measurements with 95% Confidence Intervals.

| Temperature | Failure Load (N) | Engineering Failure Stress (MPa) | True Failure Stress (MPa) – Strain Gauges | True Failure Stress (MPa) – Extensometer |
|-------------|------------------|----------------------------------|---|--|
| 23°C* | 103.9 ± 6.3 | 86.0 ± 5.3 | 83.9 ± 6.7 | 82.2 ± 4.6 |
| 23°C | 106.2 ± 8.3 | 88.0 ± 6.9 | 84.3 ± 6.1 | 82.3 ± 5.1 |
| 75°C | 110.9 ± 5.7 | 91.7 ± 4.5 | 82.1 ± 3.1 | 82.0 ± 3.5 |
| 86°C | 105.7 ± 5.6 | 87.7 ± 4.6 | 73.9 ± 2.3 | 76.8 ± 2.9 |
| 100°C | 108.0 ± 3.6 | 89.5 ± 2.8 | 71.6 ± 0.7 | 72.7 ± 1.8 |
| 120°C | 100.7 ± 4.3 | 83.8 ± 3.5 | 63.7 ± 0.7 | 65.4 ± 2.1 |

* Unpoled Specimen

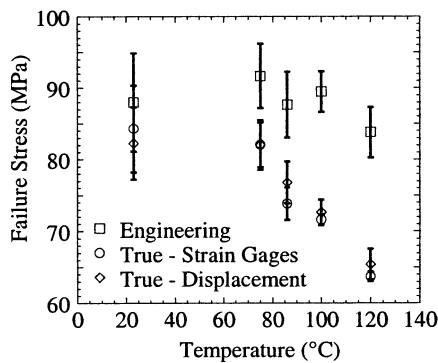


Figure 6. Average engineering and true (strain gauge and displacement technique) failure stress with 95% confidence intervals from room temperature to 120°C.

63.7 MPa by 120°C. However, if we were to assume that the material behaved linearly elastically, the true failure stress would have been overestimated by $\sim 4\%$ at room temperature and $\sim 24\%$ at 120°C. The increase in the difference between the engineering stress and the true failure stress as temperature increases is because non-linearity increases with temperature. Although the true failure stress decreases with temperature, the load-carrying capacity of PSZT does not differ significantly with 95% confidence. The average load at failure is between 100.7 and 110.9 N over the entire temperature range. Thus, the material is able to support similar loads prior to failure while also being able to support a higher degree of deformation as temperature increases. Intuitively, this suggests that at elevated temperatures PSZT is able to alleviate mechanically induced stresses by deforming.

At room temperature, soft PZT-based materials can exhibit non-linear and non-symmetric behavior.¹² To fully complement strength data, it is recommended that when flexural strength measurements of ferroelectrics are reported that the stress-strain behavior of the material also be included. Otherwise, without full disclosure of stress-strain behavior, the predicted strength of the material, as that calculated from linear-elastic fracture mechanics can lead to a systematic over-estimation of strength. Indeed, the most appropriate method for reporting strength data without strain-gauge or deflection measurements is load at failure. With this disclosure, at least the load-carrying capacity of the material is identified.

3.2. Stress-Strain Behavior of Unpoled and Poled-Depoled PSZT

A distinct difference in the stress-strain response of unpoled and poled-depoled PSZT, as measured with strain gauges, is shown in Fig. 7. Poled-depoled PSZT exhibits additional non-linearity. This trend would most likely continue until the Curie temperature is reached. Presumably, the difference in the non-linearity is the result of the formation of 180° domains parallel to the applied electric field (or as close as crystallographically possible) during the polarization and depolarization step. Because domains attempt to align parallel to the direction of maximum principal stresses in tension, which is perpendicular to the polarization-depolarization direction, a higher percentage of domains in the poled-depoled specimen are available for switching. For the unpoled specimen, domains are randomly oriented, thus certain percentages are already parallel or nearly parallel to the direction of maximum principal stresses; therefore, fewer domains are available for switching during loading.

3.3. Non-Symmetrical Stress-Strain Behavior

PSZT, as with similar soft ferroelastics, exhibits non-symmetric stress-strain behavior.¹² Non-symmetry was negligible at room temperature for PSZT but at elevated temperatures non-symmetry was evident (Fig. 8a-e). However, because of strain-gauge misalignment, poor strain-gauge adhesion, or statistical variations in data, not all of the elevated temperature stress-strain tests revealed significant non-symmetrical behavior.¹³ Non-symmetry refers to deviations in the stress-strain response in tension as compared to compression. In response to tension, domains align parallel to the principal stress direction, and in compression domains align perpendicular to the principal stress direction. As a result, at the same loading level, above which non-linearity has developed, the resulting strain in a specimen poled perpendicularly to the maximum principal direction (or for an unpoled specimen) is greater in tension than in compression. As a consequence the outer-fiber stress of a perpendicularly poled or unpoled specimen tested in flexure is greater in compression than in tension. Comparisons of non-symmetry obtained through flexure testing to measurements made from uniaxial compression and tension tests follow the same trends.¹² But by applying strain gauges on the compression and tension faces of bend bars, non-symmetry can be

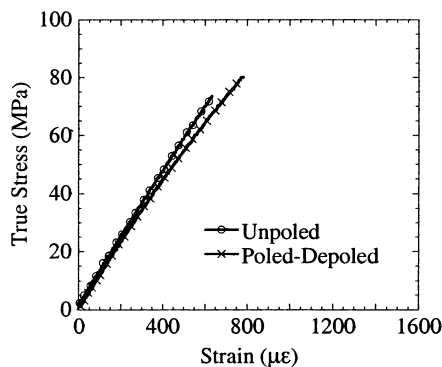


Figure 7. True tensile stress-strain behavior (strain gauge technique) of unpoled and poled-depoled PSZT at room temperature.

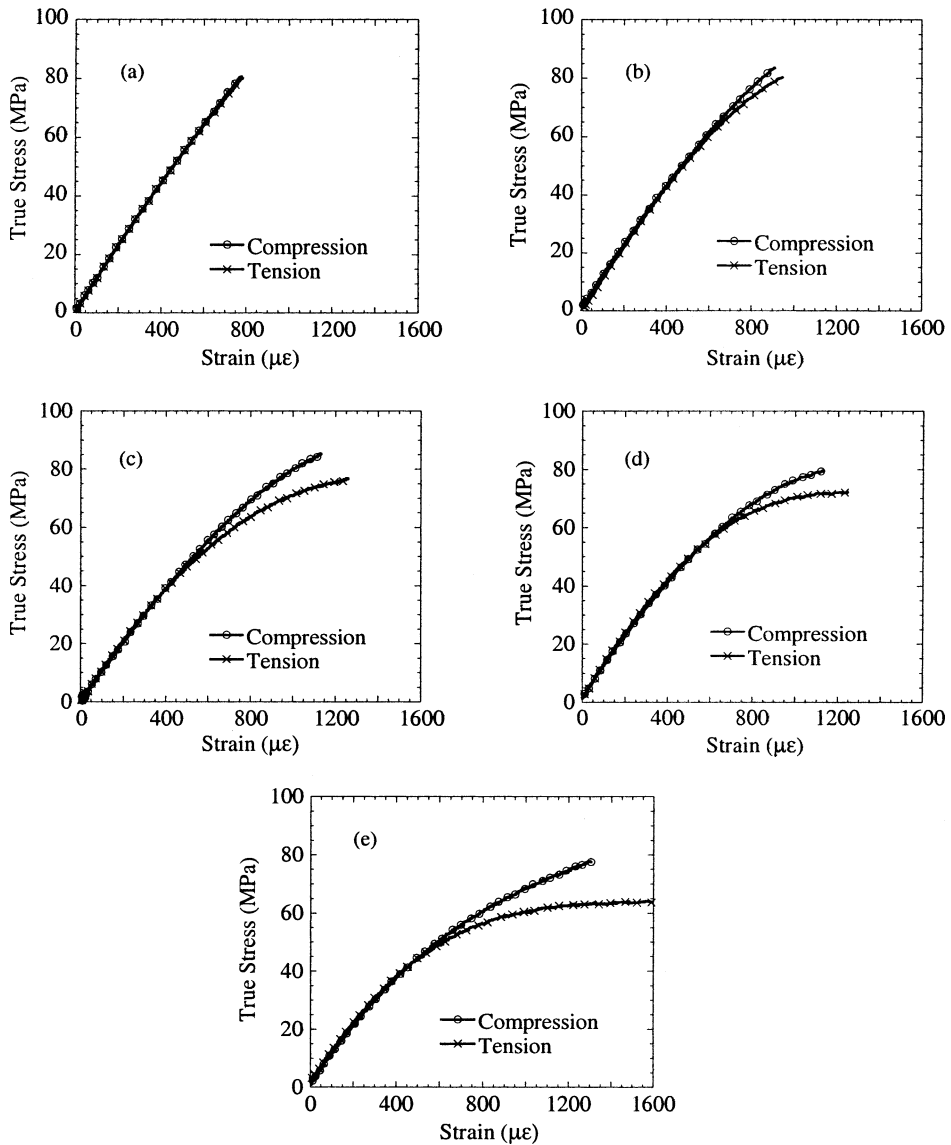


Figure 8. Non-symmetry is evident by comparing the tension and the compressive stress-strain curves to failure for PSZT four-point bend specimens at (a) 23, (b) 75, (c) 86, (d) 100 and (e) 120°C.

ascertained.¹⁴ In doing so, the intrinsic variability of material properties can be avoided because both the compression and tension response can be determined for the same test specimen instead of two independent test specimens needed for compression and tension tests.

3.4. Weibull Statistics

Ceramic components are susceptible to failure at stresses much lower than predicted from theoretical strength calculations because of stress concentrations at surface or

volume flaws, where the location and size of these strength-limiting flaws are randomly distributed. Flaw types and their distributions are processing and handling history dependent, and can vary significantly for ceramic components processed from nominally the same source. Weibull statistics, which are based on weakest link theory, can be employed to estimate the probability of failure for a particular material at a given stress level. An indirect measurement of component reliability can be obtained from the Weibull modulus: a descriptor relating the strength distribution (thus failure-initiating flaw distribution) within the material. A low Weibull modulus is indicative of a material that exhibits a wide range of failure strengths, and thus has a higher probability of failure at a lower stress level than a material exhibiting a higher Weibull modulus. Knowledge of PSZT Weibull parameters is needed to have a more intimate understanding of the effect processing and fabrication conditions have on flaw distributions and ultimately component reliability. As such, Weibull strength parameters¹⁵ of unpoled and poled-depoled PSZT were determined.

A total of 44 specimens was tested, per processing condition (unpoled or poled-depoled), to failure in 4-point bending. The true failure stress was determined based on the stress-strain results of unpoled and poled-depoled specimens. The strength distribution was characterized using a two-parameter Weibull distribution and maximum likelihood estimators for Weibull modulus (*m*) and characteristic strength (σ_0)

$$P_f = 1 - \exp \left[- \left(\frac{\sigma}{\sigma_0} \right)^m \right] \tag{6}$$

where P_f is the probability of fracture (Fig. 9). Fractographic examinations of a portion of the fracture surfaces indicated that both unpoled and poled-depoled PSZT contained multiple flaw distributions; however, Weibull strength parameters were not estimated with the use of censored data analysis techniques.¹⁵ Consequently, significant statistical bias in the estimated Weibull strength parameters is possible. The Weibull modulus for the specimens tested in the unpoled condition was 17 with a characteristic strength of 90.9 MPa. The strengths ranged from 70.9 to 99.8 MPa with an average strength of 88.2 ± 6.2 MPa (one standard deviation). The poled-depoled specimens exhibited a Weibull modulus of 13.2, a characteristic strength of 92.1 MPa, and an average strength of 88.4 ± 8.8 MPa (one standard deviation) where the strength values ranged from 67.0 to 102.7 MPa. The apparently lower

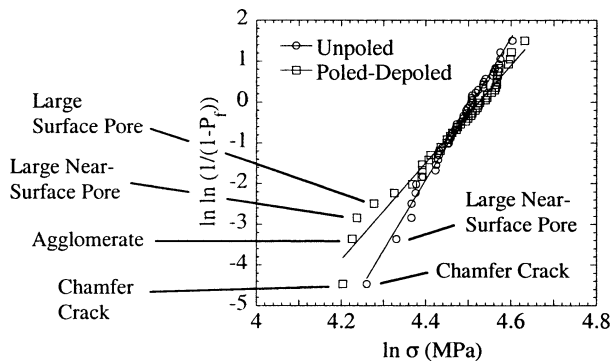


Figure 9. Weibull plots of strength of unpoled and poled-depoled PSZT. Measurements were made at room temperature on 44 specimens per processing condition.

Weibull modulus of poled-depoled PSZT is indicative of a material containing a wider flaw distribution compared to unpoled specimens, thus, the pole-depole process could potentially reduce component reliability. If there is a true difference in Weibull moduli it may be attributed to the additional handling required for the pole-depole step. This includes (i) the application of temporary silver electrodes to the top and bottom surfaces of the bend bars, (ii) drying of these electrodes at 71°C, (iii) polarization and depolarization in dielectric fluid, (iv) removal of the temporary electrodes with acetone and (v) transportation of specimens between each step. Also, the polarization and then depolarization step could potentially degrade the mechanical properties^{16–18} of some specimens as a result of the high electric fields (32 kV/cm) required for this procedure, by creating new flaws or by making intrinsic failure-initiating flaws more severe. Despite the additional handling and processing steps experienced by poled-depoled specimens, the Weibull moduli are remarkably similar. Fractography revealed that the lowest strength specimens, unpoled or poled-depoled, typically failed from similar flaws (Fig. 9). Perhaps a higher number of these gross flaws happened to be sampled for the poled-depoled specimens. Accordingly, statistical sampling may have a significant effect on the calculated Weibull moduli and care should be taken when interpreting the results. From this analysis, the poled-depoled specimens have a slightly lower Weibull modulus than unpoled PSZT. The calculated difference in the Weibull moduli may be attributed to the statistical nature of sampling or the additional processing steps experienced by poled-depoled PSZT.

3.5. Fractography

Fracture surfaces were examined to determine failure origins and the type of flaws that initiated failure at low stress levels for both unpoled and poled-depoled specimens (Fig. 9). Examination of fracture surfaces revealed that the majority of failures originated from large grain clusters (Fig. 10a), surface or near-surface pores (Fig. 10b) or large grain clusters and surface or near-surface pores (Fig. 10c). The weakest specimens, however, failed from very large surface or near-surface pores (Fig. 10d), agglomerates (Fig. 10e) or from large pre-existing cracks located near chamfers.

The reliability of ceramic materials is highly dependent on the presence of handling or machining damage and/or processing flaws. Several of the low strength specimens failed from pre-existing cracks at the chamfer that may have formed as the result of handling or machining damage. Care must be taken to ensure that the handling and machining of PSZT specimens is innocuous, thus reducing the probability of a large pre-existing crack inducing failure, and increasing the reliability of the component. The reliability of ceramic materials, however, will always be subject to processing and fabrication history as well as handling damage. For instance, the microstructure of ceramics, which is processing history dependent, can be the strength-limiting factor. Microstructural subtleties, such as, abnormally large grains, porosity, agglomerates and/or the presence of second phases can have a significant influence on failure probabilities. Both Figs. 10d & 10e show microstructural features (failure origins) representative of low strength samples. Closer examination of Fig. 10d reveals that, besides the large pore, there is a difference in grain size around the pore compared to that found in the bulk of the material (Fig. 11a). This microstructural feature can certainly be a contributor to the low failure stress. In addition,

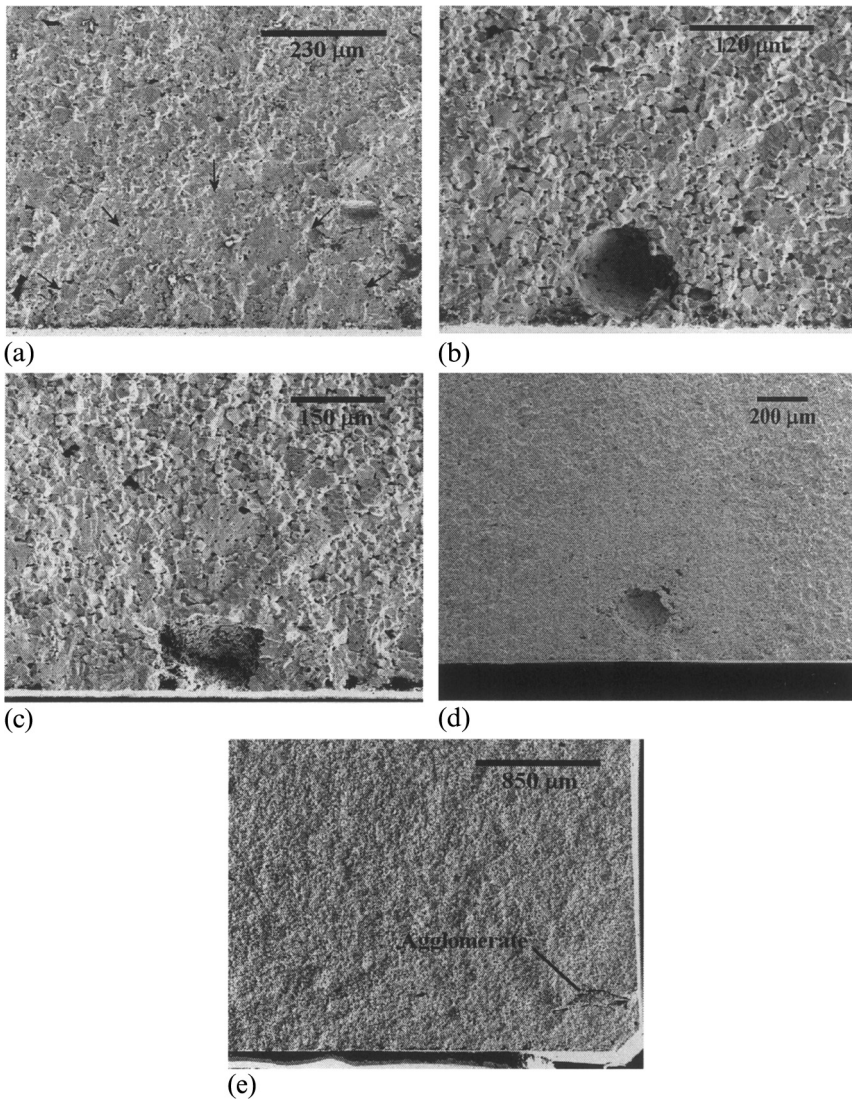


Figure 10. SEM images of fracture surfaces showing (a) clusters of large grains in combination with possible machining damage as the failure origin (fractured at 91.5 MPa), (b) a near-surface pore in combination with possible machining damage (fractured at 86.1 MPa), (c) a failure origin consisting of a combination of large grains and a surface pore (92.5 MPa), (d) a fracture surface where a large near-surface pore initiated failure at a stress of 72.1 MPa, and (e) an agglomerate where failure initiated at a stress level of 69.2 MPa.

the failure-initiating flaw shown in Fig. 10e appears to be a large agglomerate. At higher magnification, there is noticeable separation between the agglomerate and the bulk (Fig. 11b). The cracks associated with the agglomerate led to a very low failure stress (69.2 MPa). Both of these flaws are processing dependent and can be eliminated by modifying processing parameters. Thus, with the use of Weibull statistics the flaw size distribution can be determined and in combination with fractography, failure-initiating flaws can be identified and processing modifications can be implemented to

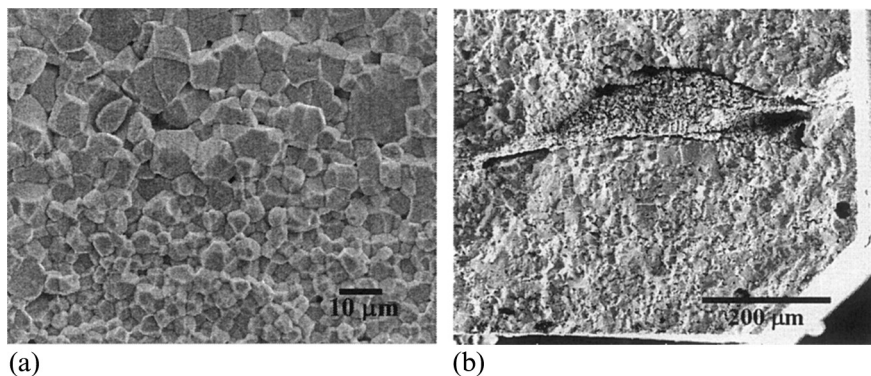


Figure 11. SEM images of (a) a fracture surface showing a distinct boundary between small and large grains where the small grains surround a large pore (Fig. 10d) and (b) a large processing flaw (agglomerate) that was responsible for failure (Fig. 10e).

reduce or eliminate these severe flaws. In addition, the reliability of PSZT components can be estimated using computer programs, such as CARES/LIFE¹⁹ or FAIL-PROB,²⁰ which incorporate Weibull strength statistics into the predicted stress distribution of the component.

4. CONCLUSIONS

Failure stress and the stress-strain behavior of PSZT were determined as a function of temperature (23,75,86,100 and 120°C). The strength of PSZT decreased with temperature. Strength measurements were carried out with the use of strain gauges and an extensometer in order to evaluate the true stress-strain behavior. PSZT underwent non-linear and non-symmetric stress-strain behavior, which was more predominant at elevated temperatures. A comparison of the strain gauge and extensometer techniques indicates only a slight difference (~3%) in the calculated true failure stress. Both measurement techniques indicate a significant reduction in the outer-fiber stress at failure as temperature increased. The implications of this are that if the assumption of linear-elasticity was used a systematic overestimation in the failure stress would result. The load-carrying capacity of PSZT did not change as a function of temperature, but the extent of deformation did increase with temperature. The Weibull parameters of PSZT indicated that poled-depoled specimens have a slightly higher probability of failure at a particular stress level (thus lower reliability) than unpoled PSZT. Thorough examinations of the fracture surfaces suggested that the lower Weibull modulus of poled-depoled PSZT may be attributed to sampling or differences resulting from additional processing steps.

5. ACKNOWLEDGMENTS

Technical contributions by Michael Hutchinson, George Burns, Bonnie Mckenzie, John Laing, Roger Moore, Pin Yang and Jill Glass are gratefully acknowledged. Sandia is a multiprogram laboratory operated by Sandia Corporation, a Lockheed

Martin Company, for the United States Department of Energy's National Nuclear Security Administration under Contract DE-ACO4-94-AL85000.

REFERENCES

1. S. L. dos Santos e Lucato, D. C. Lupascu, M. Kamlah, J. Rödel, and C. S. Lynch, "Constraint-Induced Crack Initiation at Electrode Edges in Piezoelectric Ceramics," *Acta Mater.*, **49**[14] 2751–2759 (2001).
2. S. L. dos Santos e Lucato, D. C. Lupascu and J. Rödel, "Crack Initiation and Crack Propagation in Partially Electroded PZT," *J. Eur. Ceram. Soc.*, **21** 1425–1428 (2001).
3. R. H. Moore, G. R. Burns, S. N. Burchett, S. J. Glass, M. A. Hutchinson, T. W. Scofield, M. E. Stavig, C. S. Watson, and P. Yang, "Polarization Induced Cracking in Partially Electroded PSZT Ceramic," *Ceram. Trans.*, **136** 105–116 (2003).
4. A. Furuta and K. Uchino, "Dynamic Observation of Crack-Propagation in Piezoelectric Multilayer Actuators," *J. Am. Ceram. Soc.*, **76** [6] 1615–1617 (1993).
5. R. F. Cook, S. W. Freiman, and B. R. Lawn, "Fracture of Ferroelectric Ceramics," *Ferroelectrics*, **50** 267–272 (1983).
6. R. Fu and T. Y. Zhang, "Influences of Temperature and Electric Field on the Bending Strength of Lead Zirconate Titanate Ceramics," *Acta Mater.*, **48** [8] 1729–1740 (2000).
7. K. Mehta and A. V. Virkar, "Fracture Mechanisms in Ferroelectric-Ferroelastic Lead Zirconate Titanate [Zr-Ti = 0.54-0.46] Ceramics," *J. Am. Ceram. Soc.*, **73** [3] 567–574 (1990).
8. "Standard Test Method for Flexural Strength of Advanced Ceramics at Ambient Temperatures," *ASTM Designation C1161–02c*, American Society for Testing and Standards, West Conshohocken, Pennsylvania.
9. A. Nadai, *Theory of Flow and Fracture of Solids*, Vol. 1; Ch. 22. McGraw-Hill, New York, 1950.
10. W. Chen, D. C. Lupascu, J. Rödel, and C. S. Lynch, "Short Crack R-curves in Ferroelectric and Electrostrictive PLZT," *J. Am. Ceram. Soc.*, **84** [3] 593–597 (2001).
11. G. A. Gogotsi, "The Problem of the Classification of Low-Deformation Materials Based on the Features of Their Behavior Under Load," *Strength Mater. (Engl. Transl.)*, **9** [1] 77–83 (1977).
12. T. Fett, S. Muller, D. Munz, and G. Thun, "Nonsymmetry in the Deformation Behaviour of PZT," *J. Mater. Sci. Lett.*, **17** [4] 261–265 (1998).
13. C. S. Watson, "Mechanical Behavior, Properties and Reliability of Tin-Modified Lead Zirconate Titanate," *Sandia National Laboratories Report*, SAND2003–2422 (2003).
14. T. Fett, D. Munz, and G. Thun, "Nonsymmetric Deformation Behavior of Lead Zirconate Titanate Determined in Bending Tests," *J. Am. Ceram. Soc.*, **81** [1] 269–272 (1998).
15. "Standard Practice for Reporting Uniaxial Strength Data and Estimating Weibull Distribution Parameters for Advanced Ceramics," *ASTM Designation C1239–00*, American Society for Testing and Standards, West Conshohocken, Pennsylvania.
16. A. G. Tobin and Y. E. Pak, "Effect of Electric Fields on Fracture Behavior of PZT Ceramics," *Proc. SPIE -Int. Soc. Opt. Eng.*, **1916** 78–86 (1993).
17. K. D. McHenry and B. G. Koepke, "Electric Field Effects on Subcritical Crack Growth in PZT"; pp. 337–352 in *Fracture Mechanics of Ceramics*, Vol. 8. Edited by F. F. Lange. Plenum Press, New York, 1983.
18. S. B. Park and C. T. Sun, "Fracture Criteria for Piezoelectric Ceramics," *J. Am. Ceram. Soc.*, **78** [6] 1475–1480 (1995).
19. N. N. Nemeth, L. M. Powers, L. A. Janosik, and J. P. Gyekenyesi, "CARES/Life Ceramics Analysis and Reliability Evaluation of Structures," *Users and Programmers Manual*, NASA TM-106316.
20. G. W. Wellman, "FAILPROB—A Computer Program to Compute the Probability of Failure of a Brittle Component," *Sandia National Laboratories Report*, SAND2002–0409 (2002).

STANDARD REFERENCE MATERIAL 2100: FRACTURE TOUGHNESS OF CERAMICS

George D. Quinn,^a Kang Xu,^b Robert Gettings,^c Jonathan A. Salem,^d and Jeffrey J. Swab^e

ABSTRACT:

Standard Reference Material (SRM) 2100 is the first reference material in the world for the property fracture toughness for any class material. The SRM is for fracture toughness of ceramics and may be used with any ceramic fracture toughness test method, but is best suited for methods that use beams in bending. The SRM complements ASTM, ISO, CEN and national fracture toughness standards. This paper describes SRM 2100 and its creation.

1. INTRODUCTION

Standard Reference Material (SRM) 2100 is intended for verification of ceramic fracture toughness testing procedures. It may be used with any fracture toughness test procedure. It may also be used in conjunction with standard test methods from American Society for Testing and Materials (ASTM), the International Organization

^a Ceramics Division, Stop 852, National Institute of Standards and Technology, Gaithersburg, MD 20899.

^b Praxair Technology Center, 175 East Park Dr. , Tonawonda, NY 14150.

^c Formerly with the Standard Reference Materials Program Office, National Institute of Standards and Technology, Gaithersburg, MD 20899.

^d Life Prediction Branch, Structures Division, MS 49-7, NASA-Glenn Research Center, Cleveland, OH 44135.

^e Weapons and Materials Research Directorate, U.S. Army Research Laboratory, Aberdeen Proving Ground, MD, 21005.

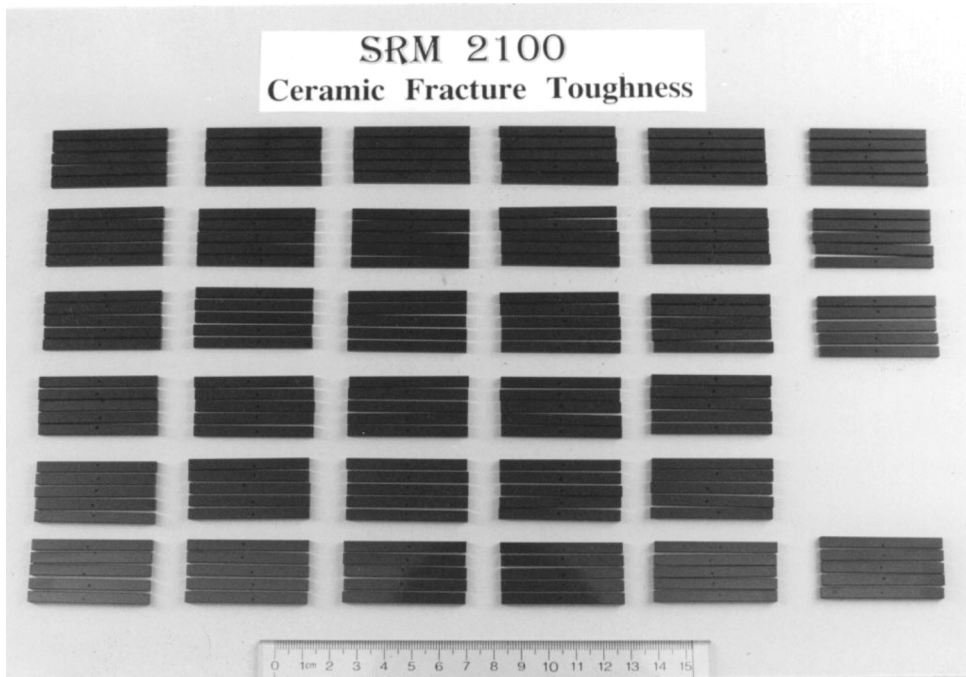


Figure 1. SRM 2100 comprises groups of five hot-pressed silicon nitride test pieces.

for Standards (ISO), the European Committee on Standardization (CEN) or Japanese Industrial Standards Association (JIS). The SRM is a set of five unprecracked ceramic test specimens cut from a single billet (plate) of hot-pressed silicon nitride (HPSN), Norton grade NC 132^{f,g} as shown in Figure 1. A considerable experience base exists for this particular grade of silicon nitride and it was featured in an international fracture toughness round robin described below.

ASTM C 1421 for advanced ceramics¹ includes three related test method procedures as illustrated in Figure 2. The three methods are the surface crack in flexure (SCF), precracked beam (PB) [also known as single-edge precracked beam (SEPB)], and chevron notch in bending (CNB) methods. The content and development of C 1421 and its precursor, ASTM PS 070-97^h are documented elsewhere [2,3,4,5]. The SRM may also be used with three ISO standard test methods that are under development in Technical Committee TC 206, based on the SEPB,⁶ SCF,⁷ and CNB⁸ methods. It may also be used with a draft CEN standard⁹ that features SCF, CNB, SEPB, and single edge-V-notched beam methods, as well as JIS R 1607 which has the SEPB method.¹⁰

^f St. Gobain-Norton Co., Worcester, MA. NC 132 is no longer available from the manufacturer.

^g Certain commercial materials or equipment are identified in this paper to specify adequately the experimental procedure. Such identification does not imply endorsement by the National Institute of Standards and Technology nor does it imply that these materials or equipment are necessarily the best for the purpose.

^h ASTM PS 070-97 was a Provisional Standard adopted in April 1997 by Committee C-28. It was converted to the full consensus standard C 1421 in April 1999.

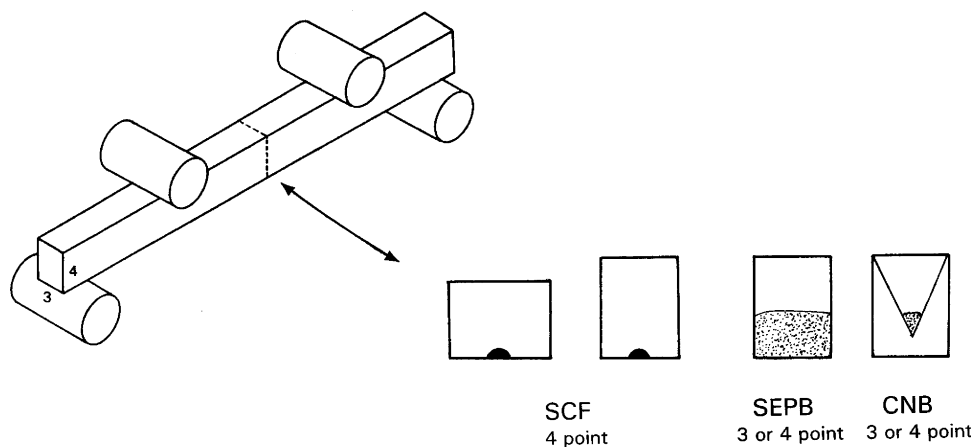


Figure 2. The three test methods in ASTM Standard C 1421. JIS R 1607 has only the SEP, whereas ISO and CEN will include all three methods.

2. BACKGROUND

A substantial amount of work on fracture toughness testing methodologies and materials characterization was performed in the 1970's, much of it motivated by potential ceramic heat engine applications. Nevertheless, there was considerable confusion and conflicting fracture toughness data in the 1980's. A 1981 report associated with a project to prepare a handbook of ceramic property data stated:¹¹

“Although a limited amount of fracture toughness information is present in the ceramic literature, it was decided . . . not to include such data. The reason for this is the nebulous and sometimes controversial nature of this property and the test methods used to obtain it.”

A 1980 National Materials Advisory Board report even had discussion of whether K_{Ic} was an intrinsic, bulk property of a ceramic.¹² One 1984 mechanical properties review paper concluded:¹³

“Fracture toughness (K_{Ic}) is a critical property of interest to a designer since it is a direct measure of the intrinsic resistance to crack propagation or fracture. There is a respectable amount of published data on fracture toughness, but much of it is contradictory and unreliable. . . .{Results from} large-cracked fracture mechanics specimens often do not relate well to component failure from small natural defects. . . . Unfortunately, no analysis or technique is emerging as a leading candidate and there appears to be little chance a standard method will be available in the near future.”

The advent of the Vickers indentation crack length techniques in the mid to late 1970's was a major distraction. It was not until 1991 that a concerted effort to refine and standardize technically rigorous fracture toughness test methods was resumed in ASTM Committee C-28, Advanced Ceramics. Work on the reference material began at National Institute of Standards and Technology (NIST) in May 1997 shortly after the ASTM Provisional Standard PS 070-97 was approved in April 1997.

We first contemplated creating a fracture toughness reference material in late 1994 after the completion of a very successful Versailles Advanced Materials and Standards (VAMAS) international round robin. VAMAS is a prestandardization collaboration program between the G-8 countries and the European Community.

Technical Working Area 3, Structural Ceramics, has conducted thirteen major round robins over the course of 13 years, including five round robins and 4,500 experiments on fracture toughness alone.¹⁴ The 1993 to 1994 round robin featured the surface crack in flexure (SCF) method. Twenty laboratories around the world obtained very consistent results on test specimens from a single billet (designated “E”) of the NC 132 HPSN.^{15,16,17} A grand mean fracture toughness of $4.59 \text{ MPa}\sqrt{\text{m}} \pm 0.37 \text{ MPa}\sqrt{\text{m}}$ was obtained from 107 experiments from all laboratories as shown in Figure 3. Eliminating results from one laboratory improved the data to a mean of $4.56 \text{ MPa}\sqrt{\text{m}}$ with a standard deviation of $0.32 \text{ MPa}\sqrt{\text{m}}$ for 102 valid experiments. The test method precision was evaluated using ASTM E 691-92, Practice for Coordinating an Interlaboratory Study to Determine the Precision of a Test Method. The within-laboratory precision (repeatability standard deviation) was $0.24 \text{ MPa}\sqrt{\text{m}}$, or a coefficient of variation of only 5.4 %. The between-laboratory precision (reproducibility standard deviation) was $0.31 \text{ MPa}\sqrt{\text{m}}$, or a coefficient of variation of only 6.8 %. Some laboratories tried other methods such as the chevron notch in bending test on spare test specimens furnished as part of the round robin and they obtained results that agreed with the SCF outcomes.

The VAMAS round robin results matched other NC 132 silicon nitride data from many laboratories over the course of 25 years. Table 1 shows the tabulation of thirty-eight values of fracture toughness for this material using methods as diverse as double cantilever beam, double torsion, SCF, SEPB, CNB, short bar chevron notch, and fractographic evaluations using NC 132’s natural flaws. Data by the Vickers indentation crack length and single-edge notched beam are not included since such data is unreliable. The SCF, CNB and SEPB methods usually yielded results from $4.3 \text{ MPa}\sqrt{\text{m}}$ to $4.8 \text{ MPa}\sqrt{\text{m}}$. NC 132’s uniform creep and static fatigue resistance had been noted previously.^{19,42}

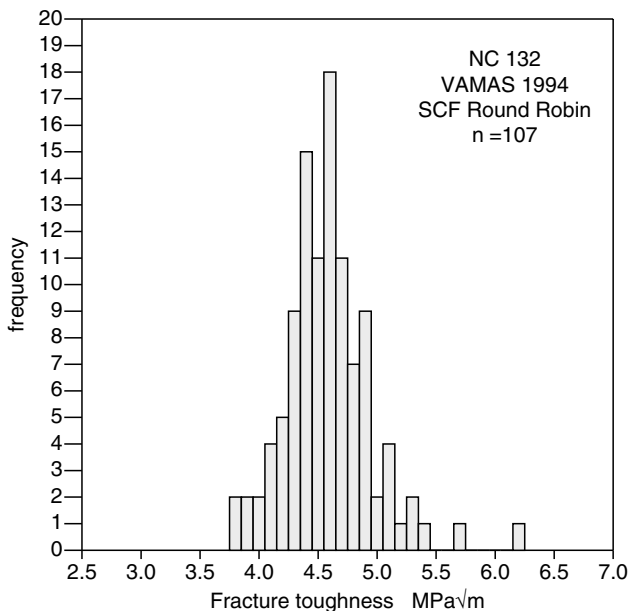


Figure 3. Histogram of all 107 results obtained for the HPSN in the VAMAS SCF round robin.

Table 1. Fracture toughness ($\text{MPa}\sqrt{\text{m}}$) for NC-132 silicon nitride.

| Mean K_{Ic} | S. dev. | Method | n | Source (Ref.) |
|---------------|---------------|--------------------------|-----|----------------------------------|
| 4.59 | 0.37 | SCF | 107 | VAMAS Round Robin (15,16) |
| 4.65 | 0.10 | SCF | - | Petrovic et al. ** (18) |
| 4.64 | 0.25 | SCF | 4 | Quinn and Quinn ** (19) |
| 4.48 | 0.07 | SCF | 4 | " |
| 4.33 | 0.37 | SCF | 3 | " |
| 4.39 | 0.19 | SCF, lab ambient | 3 | Swab and Quinn (20) |
| 4.32 | 0.29 | SCF, dry nitrogen | 5 | " |
| 4.64 | 0.4 | SCF | 5 | Tikare and Choi (21) |
| 5.25*** | - | SCF | 4 | Gonczy and Johnson (22) |
| 4.67 | 0.3 | SEPB | 7 | Tikare and Choi (21) |
| 4.54 | 0.12 | SEPB | 5 | Bar-on, Baratta, and Cho (23) |
| 4.21 | 0.12 | SEPB | 10 | " |
| 4.5 | 0.4 | SEPB | 3 | Salem, Shannon and Jenkins (24) |
| 4.60 | 0.30 | SEPB | - | Salem and Choi (25) |
| 4.68 † | 0.19 | CN-Short Bar | 35 | Salem and Shannon (26) |
| 4.85 † | - | CNB | 4 | Salem, Shannon and Jenkins (24) |
| 4.64 † | ≈ 0.2 | CN-Short Bar | 13 | Bubsey, Shannon, and Munz * (27) |
| 4.72 | - | CN-Short Bar | 7 | " |
| 4.71 \perp | - | CN-Short Bar | 9 | " |
| 4.85 \perp | - | CNB | 2 | " |
| 4.85 \perp | - | CNB | 2 | " |
| 4.42 | 0.14 | CNB | 2 | VAMAS Round Robin (15) |
| 4.5-5.0 | - | Natural Flaws | 6 | Quinn and Quinn (19) |
| 4.58 † | 0.10 | Vickers Indent. Strength | 4 | Kübler (28) |
| 4.9 † | - | Vickers Indent. Strength | - | Salem and Choi (29) |
| 4.1 † | - | Vickers Indent. Strength | | Tikare and Choi (30) |
| 5.2 | - | Double torsion | 4 | Annis and Cargill (31) |
| 4.9 | - | Double torsion | - | Evans and Charles (32) |
| 4.1 | 0.21 | Double torsion | 4 | Govila (33,34) |
| 5.8 | 0.74 | Double torsion | 3 | Quinn (35) |

(continued)

Table 1. Fracture toughness ($\text{MPa}\sqrt{\text{m}}$) for NC-132 silicon nitride (*Cont'd*).

| Mean K_{Ic} | S. dev. | Method | n | Source (Ref.) |
|-------------------|---------|--------------------------|----|-----------------------------------|
| 4.24 | 0.30 | Double torsion | - | Bansal and Duckworth (36,37) |
| 3.9–5.0 | - | Double torsion | - | Bansal and Duckworth (39) |
| 4.80 | 0.09 | Double torsion | - | Tressler, Yonushonis, Meiser (38) |
| 4.93 | 0.31 | Double Torsion | - | Bourne and Tressler (39) |
| 4.20 | 0.15 | Fracture Mirror Analysis | - | Bansal and Duckworth (36,37) |
| 5.4 | - | Fracture Mirror Analysis | - | Bansal and Duckworth (40) |
| 4.0 \perp - 5.0 | - | Double Cantilever Beam | - | Bansal and Duckworth (40) |
| 4.0 \perp | - | Double Cantilever Beam | 30 | Freiman et al. (41) |

* Several chevron geometries and orientations.

** Several annealing conditions (air or inert atmospheres).

*** Annealed in air and cracks were probably healed.

- Not reported

\perp Perpendicular to the HP direction

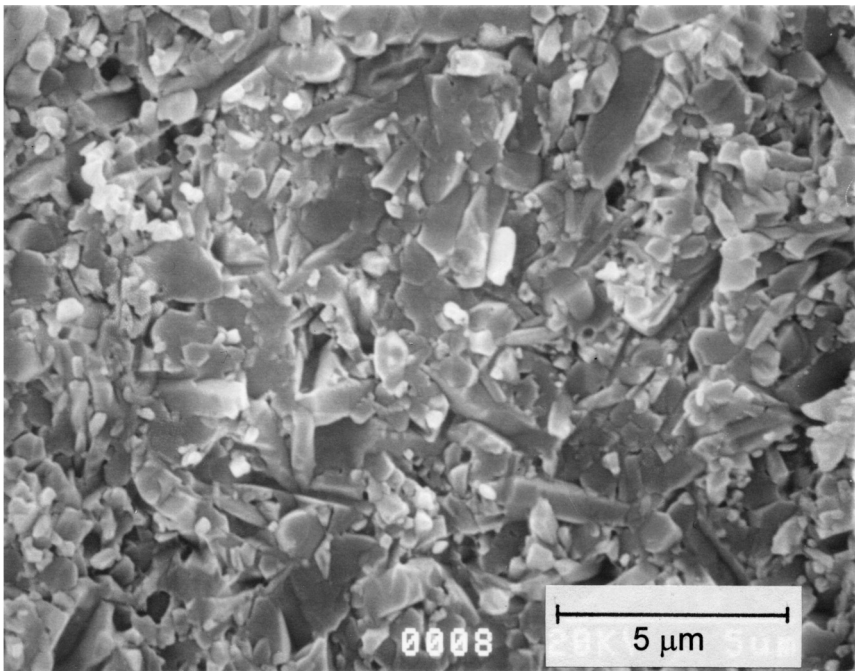
† Flat R-curve

These positive results prompted us to investigate the NC 132 further. Fracture toughness test specimens were prepared from six separate billets of NC 132. One thousand one hundred and thirty-one test specimens were prepared. Two hundred thirty-seven experiments were conducted. Eventually five hundred and thirty-seven specimens from three billets (C, G, D) were accepted for SRM 2100, and four hundred sixty-four specimens from billets (A, H, and 4) were rejected and set aside as will be discussed below.

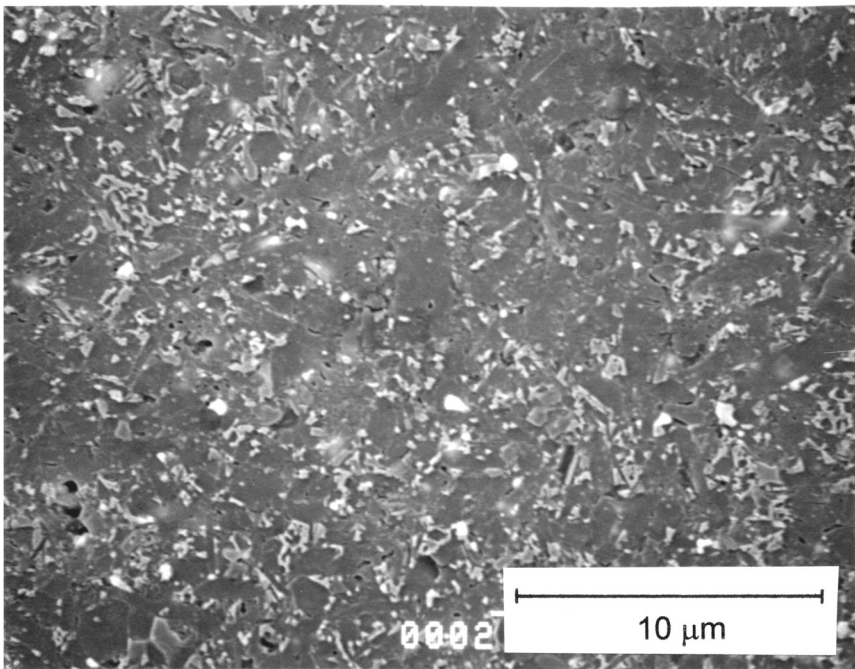
3. THE SRM MATERIAL

This 1970–1980's vintage material⁴³ which was hot-pressed with a small amount $\approx 1\%$ mass fraction of a magnesia-based sintering aid is composed of slightly elongated beta phase silicon nitride grains with a maximum size of about $3\ \mu\text{m}$ as shown in Figure 4. A small amount of amorphous second phase resides in small triple point pockets or as very thin layers between the silicon nitride grains. Very fine tungsten carbide or tungsten silicide inclusions are dispersed throughout the bulk and were picked up during ball milling of the starting powders. The material is fully dense and has a density $3.22\ \text{g}/\text{cm}^3$ to $3.26\ \text{g}/\text{cm}^3$, which is slightly greater than the theoretical density of silicon nitride because of the tungsten compounds in the material. This HPSN was originally fabricated in the form of billets (plates) of nominal size $158\ \text{mm} \times 158\ \text{mm} \times 20\ \text{mm}$ to $30\ \text{mm}$ thick as illustrated in Figure 5. NC 132 fractures in a mixed transgranular and intergranular mode at room temperature. It has a flat R-curve (whereby crack growth resistance is independent of crack size)^{24, 26–30} and is highly resistant to environmentally-assisted slow crack growth at room temperature. Consequently, different test methods should produce identical fracture toughness results.

NC 132 is no longer made by the manufacturer, so test specimens were prepared from six billets that were on hand. From the six billets, only three labeled “C”, “G”,



(a)



(b)

Figure 4. Microstructure of the silicon nitride. (a) shows a fracture surface and is from the inside of a SCF precrack; (b) is a polished and plasma etched section.

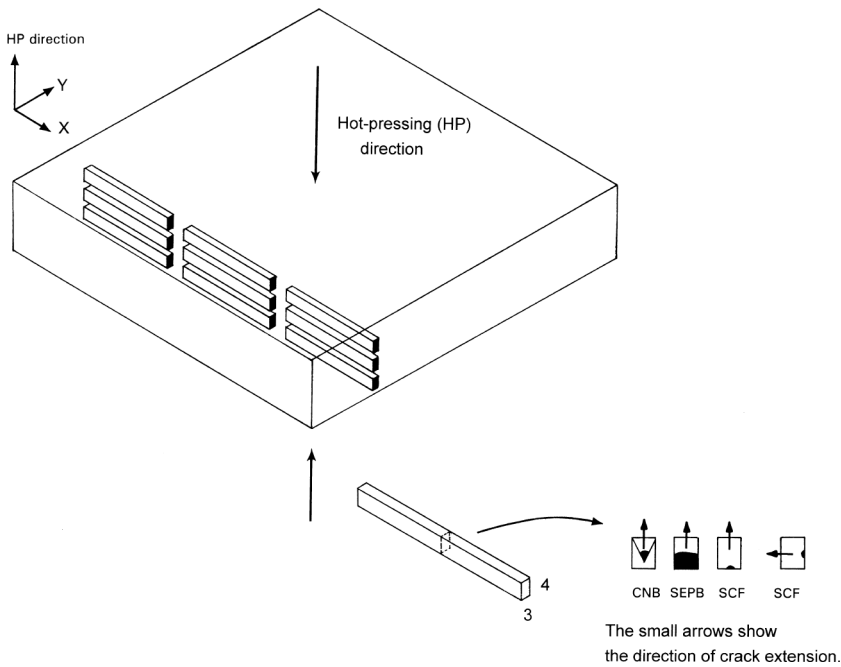


Figure 5. All test pieces were cut from the billet in the same orientation. The test specimen cross section plane is parallel to the direction of hot pressing. The small arrows on the cross section planes show the direction of crack propagation. The fracture toughness is certified only for crack planes parallel to the hot pressing direction.

and “D” for short, were actually used for the SRM. The test specimens in each SRM kit are all randomized from one billet whose identity is listed on the accompanying certificate and scribed onto an end face of each test specimen. SRM 2100 is made up exclusively of test specimens from billet C. When SRM 2100 is expended, test specimens from billets G and D will be used for SRM 2100A and SRM 2100B.

Three additional billets, “H,” “A,” and “4” were also evaluated but were ultimately rejected for the SRM. Billets A and 4 had excessive variability in fracture toughness that was traced to a material inhomogeneity that manifested itself on the test specimen surfaces as a faint patchwork mottling. Such mottling, commonly detected in HPSN’s with rare earth oxide sintering additives, has even been reported in magnesia-doped NC 132. In the case of NC 132, it is associated with elemental silicon from a thermal decomposition of the silicon nitride.⁴⁴ Billet A also had an aberrant amount of aluminum detected by x-ray fluorescence analysis in one chemical analysis sample. Billet H was rejected since, unlike the other billets, there was evidence of environmentally-assisted slow crack growth in the SCF and SEPB test specimens. Billet H also had a blistered appearance on one hot-pressed surface. Specimens tested in laboratory air produced different lower K_{Ic} ’s than specimens tested in dry-nitrogen gas environment. Halos around the SCF precracks, which are signs of stable crack extension,⁴⁵ were detected in the SCF specimens. The source of the environmental sensitivity in billet H was traced to a slightly greater glassy boundary phase content as detected on polished micrographs, but strangely, not from the chemical analysis.

Tables 2 and 3 show chemical and density data for the billets. Carbon was determined by a direct combustion infrared detection method, and oxygen by a direct inert gas fusion-thermal conductivity method.ⁱ The other elements were measured by x-ray fluorescence at NIST. X-ray diffraction revealed only β - Si_3N_4 , some $\text{Si}_2\text{N}_2\text{O}$, and WSi_2 . No α - Si_3N_4 was detected. The manufacturer's densities were taken either from the billet identification label or a chalk written marking the manufacturer applied to the as-pressed billets. We also measured the density of five or more bend bars taken at random after the billets were cut up. Density was computed from the mass (measured to 0.001 g) and the geometric dimensions of these well-defined prisms. Bar lengths were measured to 0.01 mm with a digital caliper and the cross section dimensions to within 0.002 mm with a vernier micrometer. All four chamfers sizes were measured and a correction made to the bar geometry. In this manner, the density of a bar could be measured to within 0.002 g/cm³. Table 3 shows that the densities were very uniform. On the other hand a 2 mm thickness taper was detected in billet D and the variability in bend bar density is greater.

NC 132 silicon nitride was one of the most studied advanced ceramic materials of all time. Its fracture toughness is representative of many ceramics whose fracture

Table 2. Chemical analysis (mass fraction in percent) for the several billets.

| Billet | C | O | Al | Ca | Co | Fe | Mg | W |
|--------|-----|-----|-----|-----|-----|-----|----|-----|
| C | .45 | 2.8 | .3 | .02 | .13 | .22 | .5 | 2.0 |
| G | .45 | 3.0 | .4 | ND | .12 | .31 | .5 | 1.9 |
| H | .41 | 2.4 | .4 | .04 | .13 | .27 | .5 | 1.7 |
| A | .39 | 4.6 | 6.7 | .01 | .15 | .25 | .4 | 2.3 |
| E* | 1.1 | 3.3 | - | - | - | - | - | |

- Not measured

ND Measured, but not detected

* VAMAS SCF Round Robin

Table 3. Densities (g/cm³) of the NC 132 billets.

| Billet | Manufacturer's density | NIST density |
|--------|------------------------|---------------|
| C | - | 3.225 ± 0.002 |
| D | - | 3.233 ± 0.004 |
| G | 3.23 | 3.207 ± 0.002 |
| H | - | 3.233 ± 0.002 |
| A | 3.21 | 3.188 ± 0.002 |
| 4 | - | 3.194 ± 0.002 |
| E | - | 3.227 ± 0.001 |

* VAMAS SCF round robin

- Not available

ⁱ Tests performed by Leco Corp., St. Joseph, MI.

toughness values lie in the range of 1.0 MPa√m to 10.0 MPa√m. Although it is obsolete, the material is relevant since derivatives are produced commercially today for use in seal and bearing applications around the world. NC 132 has the fracture toughness of a fully dense, fine beta silicon nitride grain material with slight grain elongation, and only a small amount of boundary phase, and which has mixed trans- and intergranular fracture mode.

Some consideration was given to using sintered α -silicon carbide^j as a fracture toughness reference material. It also has a flat R-curve and does not experience slow crack growth at room temperature.⁴⁶ It was a mature engineering grade structural ceramic that was the focus of many studies. One team went so far as to declare in 1989 its true fracture toughness was 3.0 MPa√m.⁴⁶ We did not use it for several reasons. Tabulations of fracture toughness data for α -SiC in the 1990's still showed some variability. It is now known that some of the variability was in the test methods and not the material. On the other hand, we have now confirmed that there were batch-to-batch variations in fracture toughness.^{5,47} The fracture toughness varied from 2.6 MPa√m to 2.9 MPa√m depending upon the batch. There was also some concern that chevron notch beam testing may have been a little more difficult for many users, since it is more difficult to achieve stable crack extension due to α -SiC's high elastic modulus and low fracture toughness. The decisive factor was our familiarity with NC 132 from the international round robin which gave us an experience base to expand upon on.

4. TEST METHODS USED FOR THE SRM

4.1. Specimen Preparation

A large sample set of representative flexural test specimens from each of the billets was tested at NIST by the SCF and PB (SEPB) methods in accordance with C 1421 unless otherwise noted. In addition, a few test specimens from billets C and H were tested by the CNB method at NIST and at National Aeronautics and Space Administration (NASA)-Glenn Center. As we will show, fracture toughness was independent of test method. A substantial number of additional experiments using nonstandardized procedures were conducted but were not used for the SRM database. Data from these dozens of supplemental experiments were very important for establishing the robustness of the individual test methods and for confirming the tolerances and procedures in the ASTM and ISO standards.

One of the advantages of the three methods in C 1421 is that they all use a simple bend bar. Each 3 mm × 4 mm × 45 mm to 47 mm bar test specimen was prepared in accordance with the generic ("standard") preparation procedure specified in the flexural strength standards MIL STD 1942 MR,⁴⁸ ASTM C 1161,⁴⁹ and ISO 14704.⁵⁰ One 4 mm wide face was finished with a 900 grit wheel (finer than is normally required) to produce a flat and smooth surface for the Knoop indentation in the SCF test method. The four long edges of the test specimens were chamfered in accordance with requirements for the surface crack in flexure (SCF) and precracked beam (SEPB) test methods.

^j Hexoloy SA grade, St. Gobain - Carborundum, Co., Niagara Falls, NY.

All test specimens were cut with their 45 mm length axis perpendicular to the hot pressing direction as shown in Figure 5. The certified fracture toughness is valid only for cracks in planes that are parallel to the hot-pressing direction. Cracks may be initiated or propagated from either the 3 mm wide or the 4 mm wide test specimen surfaces. The fracture toughness is *not* certified for cracks propagated on planes parallel to the billet's 152 mm \times 152 mm faces, since these other planes may have lower fracture toughness, due to a preferred orientation of the elongated beta silicon nitride grains that tend to be aligned in the plane, normal to the hot-pressing direction. The outer 6 mm of the billet sides was sliced off and not used since it became evident that the fracture toughness was a little greater in these regions. (For example, in billet C, the average fracture toughness for 5 SCF tests was $4.90 \text{ MPa}\sqrt{\text{m}} \pm 0.16 \text{ MPa}\sqrt{\text{m}}$.) X-ray radiographs of the billets revealed slight density gradients in the edges.

Groups of five test specimens were precracked and then fractured in a single session. Fracture testing was in laboratory ambient conditions (20 °C to 25 °C; relative humidities, 30 % to 72 %). Some sets were tested in dry-nitrogen gas for comparison, in order to ascertain whether environmentally-assisted slow crack growth might have been active. No such slow crack growth was detected in test specimens from billets C, G, or D and environment had no effect. Slow crack growth was active in some test specimens from billet H.

Conventional flexural strength (bend) fixtures with 20 mm \times 40 mm spans usually were used. Some broken halves were retested in the PB (SEPB) configuration in either three- or four-point flexure strength fixtures with a shorter 16 mm or 20 mm outer span. Fixtures were of either the semi-articulating or fully-articulating styles and were in accordance with C 1421 and the well-known standard flexural strength test standards C 1161 and MIL STD 1942. These standards have requirements for fixture alignment and articulation, and loading rollers that are free to rotate in order to eliminate frictional errors.

4.2. Surface Crack in Flexure (SCF) Precracking and Testing

The SCF method, also known as the "controlled flaw" method, is a development of early work by Petrovic and colleagues.^{18,51} This method utilizes a Knoop hardness indenter to create a single micro surface precrack such as shown in Figure 6. In brittle ceramic materials and glasses, the indentation causes a very deep semi-elliptical crack to open up underneath the hardness indentation. The crack is much deeper than the indentation. Crack orientation may be controlled by orienting the Knoop indentation axis. The indentation and its residual stresses must be removed by polishing or hand grinding after indentation. The specimen is then fractured in a conventional flexural strength fixture. Fractographic techniques are used to detect and measure the precrack on the fracture surface after test specimen fracture. Fracture toughness is computed from the maximum stress (or maximum load) at fracture, the crack size, and the stress intensity factor solution. The precrack size must be measured for each test specimen. The stress intensity shape factor should be individually calculated for each test specimen. Additional details are in the literature^{15-17,52} and ASTM C 1421 and ISO 18756.

Most of the SRM 2100 SCF database was generated with a 24.5 N (2.5 kgf) indentation force. This is less than the 49.0 N recommended in C 1421, but the VAMAS round robin showed that the smaller force was suitable. Less material had to be removed by hand grinding around the smaller precrack. Cracks were usually

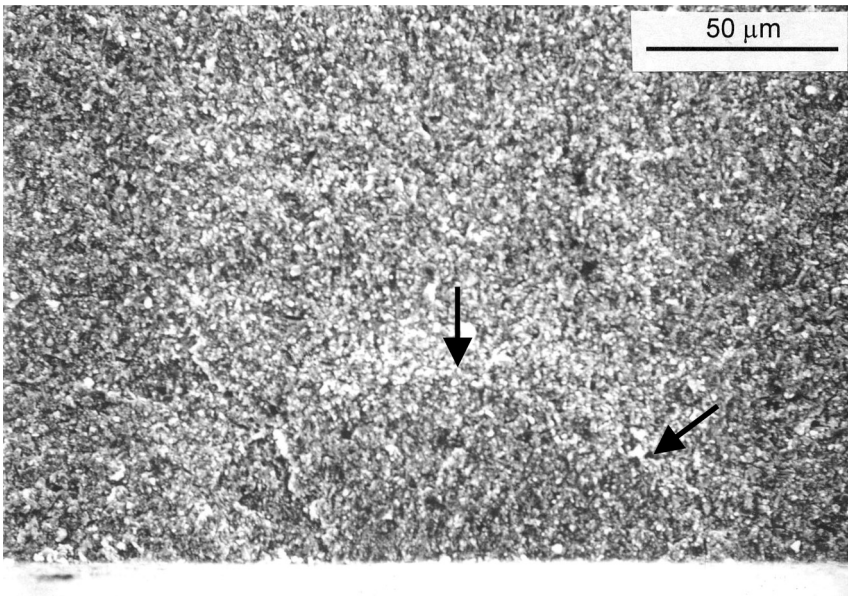


Figure 6. SEM photograph of SCF precrack at about 500X original magnification. The boundary is clear on the top and right side (arrows), but can be easily extrapolated along the left side. Some precracks were easier than this one to detect, and some were harder. The precrack is tilted at a slight angle relative to the final fracture plane which accounts for the lighter contrasting features around the top.

put into a $4\text{ mm} \times 45\text{ mm}$ flat face. Semielliptical precracks were approximately $50\text{ }\mu\text{m}$ deep \times $150\text{ }\mu\text{m}$ wide after hand grinding removal of the indentation and residual stress zone. The hand polishing/grinding was done in stages in order to remove $23\text{ }\mu\text{m}$ to $25\text{ }\mu\text{m}$ of material, the necessary amount for these 24.5 N indentations. The first $10\text{ }\mu\text{m}$ to $15\text{ }\mu\text{m}$ of material was removed with a dry $30\text{ }\mu\text{m}$ diamond-impregnated abrasive grit wheel on a low speed 200 mm diameter rotary polishing-grinding machine with light finger pressure. The final $10\text{ }\mu\text{m}$ – $15\text{ }\mu\text{m}$ was removed by more delicate hand sanding-grinding with round sheets of dry 240 grit silicon carbide abrasive paper, also mounted on the low speed rotary polishing machine. The removal was done in many small steps and the test specimen thickness dimension W was closely monitored with a hand micrometer with a resolution of 0.002 mm . Care was taken not only to remove the prescribed material, but also to keep the cross section as even as possible. One sample set was also evaluated with indentations implanted into the narrower 3 mm wide face, but the outcomes were the same. A few test specimens from billet C had the indentation and residual stress damage zone machined off by surface grinding with a diamond wheel rather than by hand grinding.

SCF test specimens were only done in four-point loading since it is very difficult to align the tiny precrack with the middle load roller in three-point loading.

The long edges were chamfered 0.08 mm to 0.13 mm in accordance with C 1421 in order to eliminate the chance that a chip or edge cracks would cause fracture. Although small, these chamfers reduce the cross-sectional area and the second moment of inertia of the cross section about the test specimen neutral axis. All four chamfers were measured for each test specimen using a stereo binocular microscope with a precision traversing stage with a resolution of 0.001 mm . An average

chamfer size was computed for each group of five test specimens and a single correction factor computed for the set. The fracture toughness was corrected (0.7 % to 1.0 %) for the change in the moment of inertia as directed in C 1421.

After fracture every precrack was photographed with a scanning electron microscope (SEM), often with paired stereo photos, at magnifications from 200 X to 500 X. If there was any doubt about an interpretation, the second fracture half was also examined and photographed. An SEM length calibration standard was photographed in both the horizontal and vertical orientations with each set of test specimens under examination (usually five at a time) in order to correct for the magnification distortions or errors. The magnification correction was usually 3 % to 5 %, but sometimes as large as 8 %. Users of the SRM 2100 need not resort to these precautions and simpler SEM or optical microscopy techniques are effective in finding and measuring the precracks, with only a small loss of precision or accuracy, but magnification checks are a wise precaution, even in routine work.

It is beyond the scope of this paper to cover all details, but a remarkable interaction between the calculated stress intensity shape factor and the measured crack size was beneficial in mitigating errors or uncertainties in the crack size interpretation or measurements.^{15,17} The stress intensity shape factor for a semi-elliptical surface crack depends upon the precrack depth and width, and the test specimen cross-section size. The Newman-Raju stress intensity factors (Y) for surface cracks in beams in bending⁵³ were used in accordance with C1421. For the SRM test specimen geometries, it was discovered that a slight measurement error of the precrack size (depth or width) was offset by a compensating error in the computed Y factor. That is to say, a +10 % error in a precrack depth measurement also led to a $\approx -5\%$ error in the calculated stress intensity shape factor. The computed fracture toughness depends upon the square root of the crack size and linearly with the Y factor.

The success rate in conducting the SCF experiments was of the order 90 % or more. That is to say, for each set of five test specimens, we usually obtained four or five valid outcomes. An invalid test usually corresponded to the precrack being too irregular or too difficult to mark precisely.

4.3. Precracked Beam (SEPB) Precracking and Testing

This variant of the single-edge notched beam test uses a bridge precracker to pop in a sharp precrack from a starting notch or indentation flaw.⁵⁴ A bridge precracker was used to pop in a 0.45 W to 0.55 W deep precrack, where the test specimen thickness, W, was 4 mm. Figure 7 shows some specimens. A single 98 N (10 kgf) Knoop indentation was used to produce a starter flaw in a ground 3 mm wide face. The indented test specimen was carefully centered in the bridge anvil. With a 6 mm bridge anvil gap, pop-in loads were between 8,000 N and 11,000 N. A simple stethoscope attached to the bridge precracker was used to detect the pop-in, which was heard as a faint snap in this material.

Four-point loading with 20 mm \times 40 mm spans was usually used with exceptions noted below. Fracture loads were small (50 N to 120 N) and depended upon the testing configuration and precrack size, so care was exercised in handling and preloading the test specimens. No correction for test specimen chamfers is necessary or appropriate for the SEPB test. After fracture, precracks were measured with a precision traversing stage with a resolution of 0.001 mm under a stereo binocular

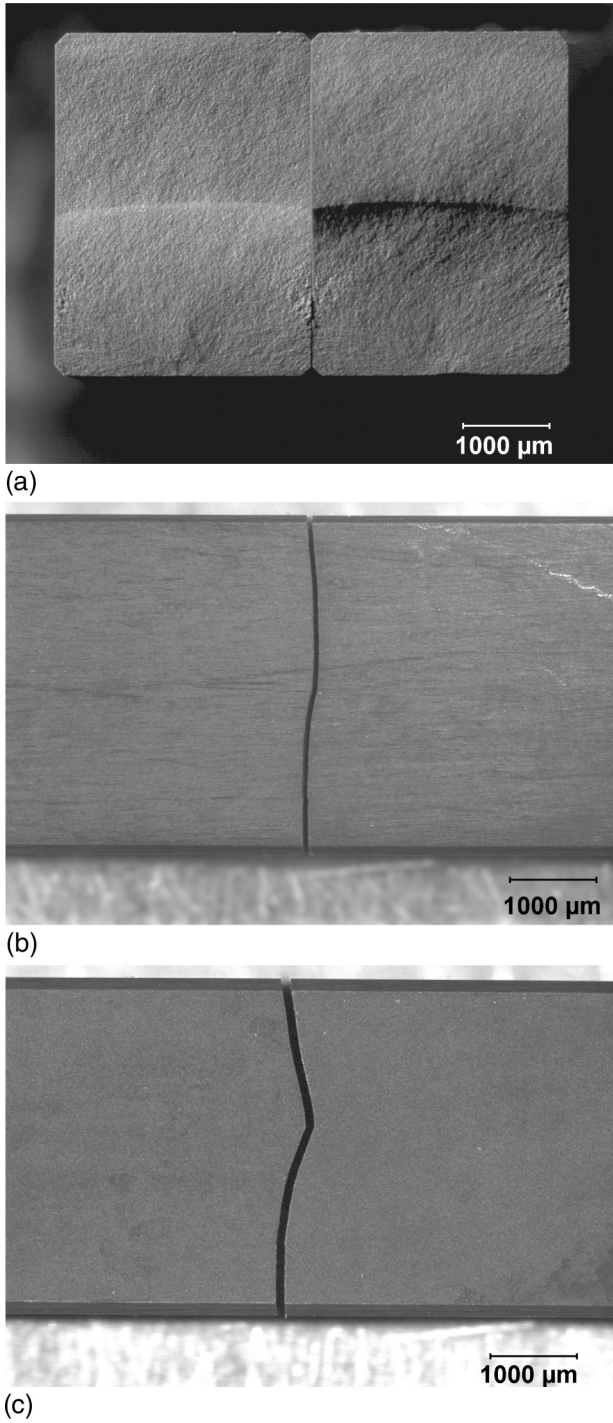


Figure 7. SEPB specimens. (a) shows fracture surfaces for one specimen. (b) and (c) show side views of two different specimens. In each case the crack ran from bottom to top. Specimen height was 4 mm in each case.

microscope at 16X to 40X magnification. The precrack boundary was quite obvious on the fracture surfaces of this fine-grained, fully-dense material as shown in Figure 7a. Dye penetration was unnecessary.

Some test specimen halves from SEPB or SCF trials were retested. They were precracked again and tested on 10 mm × 20 mm four-point flexure fixtures, or on three-point flexure fixtures with a 16 mm span. Three-point loading with 16 mm span with a 4 mm tall specimen is a traditional configuration that is a scaled down version of the notched beam test in ASTM E 399 for fracture toughness of metals.⁵⁵ Only a very few tests were done in our work with this configuration since it was very difficult to align the SEPB precrack with the middle roller in the bend fixture. As will be shown below, there was no difference in outcomes for full-size specimens versus their halves. The reject rate for the three-point configuration was greater, however, due to crack twisting and alignment problems.

Precrack pop in and final fracture angles were measured on both sides of every specimen. We used the angle from the side with the greatest deviation from a straight crack to determine whether the fracture met the requirements of the ASTM, JIS, or ISO standards. Figure 7b shows a specimen with acceptable precrack and final propagation angles. Figure 7c shows a specimen that just barely passed the specifications, but which was rejected due to the sharp jog at the intersection of the precrack and the final crack plane. Test specimens outcomes were rejected if *either* the precrack or the final fracture crack was tilted too much.^k Eighty-six percent of billet C test specimens were accepted, eighty-one percent from billet G, and one hundred percent from billet D. Every test specimen passed the precrack depth evenness criterion of standards ASTM C 1421, JIS R 1607, and ISO 15732.

4.4. Chevron Notched Beam (CNB) Testing

A limited number of specimens from billets C and H were tested by the chevron notch method.⁵⁶ SRM 2100 specimens may be used with C 1421 configurations “A” or “D.” Specimens with “A” type notches were prepared by a professional machine shop to the tolerances in C 1421. Figure 8 shows an example. The notch width was less than 0.25 mm and was carefully machined to ensure that each side of the notch lined up well as shown in Figure 8b. The notch tip in the A configuration is 0.80 mm from the specimen end. This configuration was chosen since it has the most amount of stable crack extension and the lowest crack velocity, and hence, stability can be more readily detected. Two specimens from billet C were tested at NIST, but we initially were uncertain as to whether stable fracture had occurred. We later confirmed that these two tests were indeed valid. Ten other billet C specimens were tested at NASA-Glenn and eight valid outcomes were obtained. Stability was verified either by back face strain gages or by displacement transducers contacting the specimen. Instability was due to a chevron notch-tip having been chipped during machining in one case; and residual glue from strain gaging accidentally being in the notch. Several specimens were tested in three-point loading, but no meaningful difference in three-versus four-point results was detected. The NIST and NASA-Glenn results con-

^k ASTM C 1421 and the ISO 15732 differ on this point. The former specifies an allowable final fracture misalignment, whereas the latter specifies an allowable precrack misalignment. We rejected a datum for the SRM if it failed either criterion.

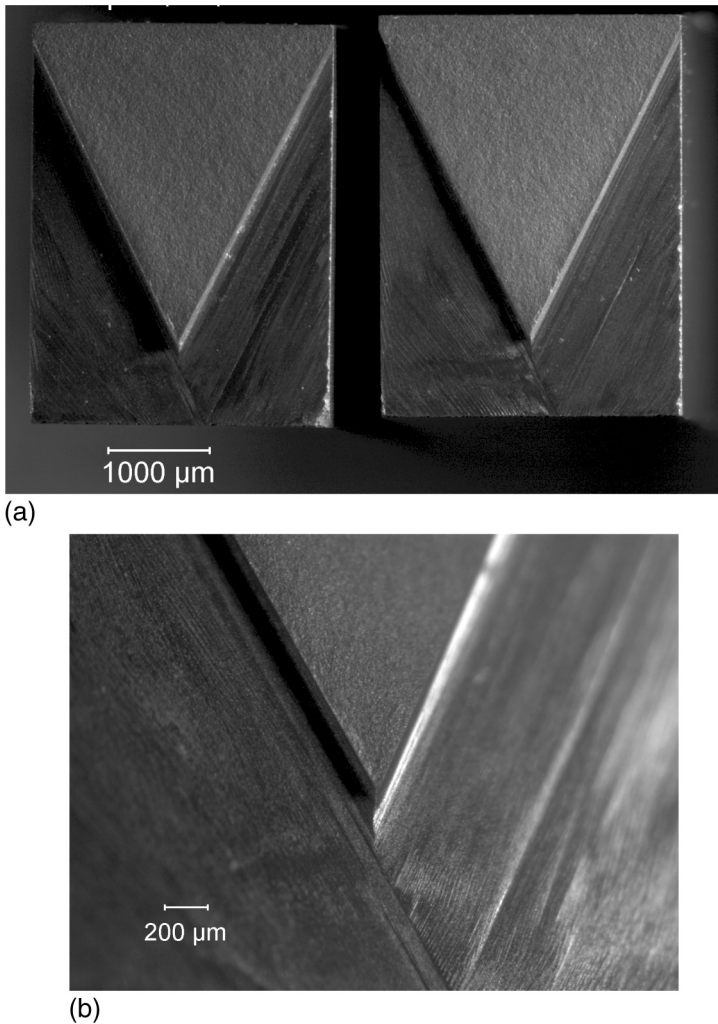


Figure 8. Chevron notch specimen, configuration “A”. (a) shows matching halves. (b) shows a close-up of one tip with the piece tilted to show how well the two sides of the chevron meet.

curred. Stress intensity factor coefficients (Y_{\min}^*) for the four-point specimens were calculated on the basis of a straight-through crack assumption (STCA) model.

5. RESULTS

Table 4 and Figure 9 show the results by test method. The results for all data usually were in extraordinary agreement within a given billet. An analysis of variation analysis confirmed that the mean fracture toughness varied between billets, however. Fracture toughness results for billets C and D are statistically significantly different than the results for billet G. The source of the differences between billets is subtle, but may be due to slight variations in the densities of the billets and to slight variations in the secondary phase content.

Table 4. Fracture toughness data for hot-pressed silicon nitride billets C, D, and G by the three test methods in ASTM C 1421-99. SRM 2100 uses test specimens from billet C.

| Billet | Method | Mean MPa√m | Std. Dev. MPa√m | Number of outcomes |
|--------------|--------|--------------------------|--------------------------|----------------------|
| C (SRM 2100) | SCF | 4.56 (4.58) ^a | 0.13 (0.16) ^a | 17 (26) ^a |
| C (SRM 2100) | CNB | 4.58 | 0.12 | 10 |
| C (SRM 2100) | SEPB | 4.58 | 0.10 | 19 |
| D | SCF | 4.53 | 0.22 | 19 |
| D | SEPB | 4.46 | 0.24 | 18 |
| G | SCF | 4.29 | 0.19 | 15 |
| G | SEPB | 4.27 | 0.16 | 17 |

^a SCF values in parenthesis include nine SCF test specimens wherein the damage zone and residual stresses were removed by machine grinding and not by hand.

Fifty-eight specimens from billet C were expended. Some halves were retested as SEPB experiments with shorter span flexure fixtures. Altogether, 75 experiments were conducted on billet C test specimens from which the SRM 2100 database of 46 outcomes was constructed. An additional 234 test specimens were available for SRM distribution from which 46 kits of 5 test specimens were prepared.

A discussed previously, nine additional SCF test specimens from billet C had the indentation and residual stresses removed by a surface grinder as opposed to the usual hand grinding with abrasive papers. These experiments confirmed that although almost identical mean fracture toughness was obtained (4.63 MPa√m), the standard deviation was considerably larger (0.26 MPa√m). The effect of adding these nine test specimens to the other forty-six SCF outcomes is shown in the bracketed data entries in the first line of Table 4 as well as in the open bars in Figure 9. The precracks were more irregular than those from hand grinding. Apparently machine grinding altered the indentation precracks and possibly propagated portions of the crack front. It was also difficult to guarantee that each test specimen had the correct amount of material removed with machine grinding since test specimens were mounted together and ground simultaneously.

Thirty-six test specimens from billet G were tested and produced a database of 32 valid experiments, leaving 215 test specimens available for the SRM. The billet G specimens had a 6.4 % lower fracture toughness than billet C, but the scatter was very small. Testing G specimens in dry nitrogen had no effect. Table 3 shows that this billet had a slightly lower density (0.5 % to 0.8 %) than billets C and D.

Twenty-five test specimens from billet D were tested and produced 37 test results. Many SCF and SEPB fragments halves were retested as short SEPB specimens to minimize the number of specimens expended from this smaller than normal batch. Billet D had somewhat greater variability than the other two billets, yet on average it had a similar fracture toughness as billets C and billet E (used in the VAMAS round robin). The cause for the increased variability in billet D could not be conclusively identified, but two of the SCF test pieces that had low fracture toughnesses (4.02 MPa√m and 4.19 MPa√m) also produced low fracture toughnesses when their halves were retested as miniature SEPB specimens (as described below).

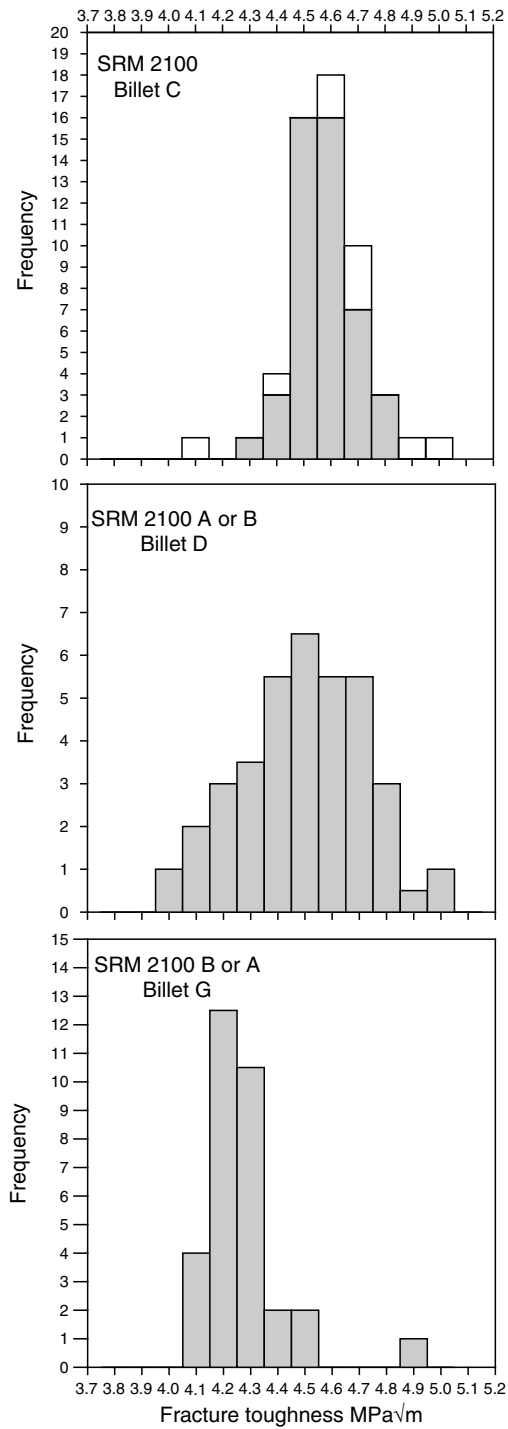


Figure 9. Results for billets C, D and G.

The SCF precracks for these two specimens may have had slight halos suggesting that slow crack growth had occurred in these two specimens. Such halos were not detected in the other billet D specimens. It is possible that the variability may be from some regions in the billet that have slight sensitivity to slow crack growth. Although this billet had a high density, it was tapered and had a slightly greater density variation than the other billets. Only ninety specimens remain for the SRM since parts of this billet had been used for other studies.

As previously noted, groups of five specimens were usually tested, the same number that is included in a SRM 2100 kit. The mean fracture toughness for sets of five test specimens also usually agreed within 1 % to 2 %, irrespective of test method. Even the standard deviations for groups of five test specimens were consistent.

We investigated the data consistency further by conducting SEPB tests on the fragments of some broken SCF and SEPB specimens from billets D and C. The halves were tested on shorter 10 mm × 20 mm four-point or 16 mm span three-point fixtures. Table 5 shows the results. Most of the miniature specimen outcomes

Table 5. Results for repeat tests using the halves of previously broken billet D and C specimens. In some instances, both halves were retested and double entries are noted in the right column. All tests were in four-point loading unless otherwise noted.

| Billet | Full Sized Specimen Test Method, K_{Ic} , $\text{MPa}\sqrt{\text{m}}$ | Half Sized Specimen Test Method, K_{Ic} , $\text{MPa}\sqrt{\text{m}}$ |
|--------|--|--|
| D | SCF 4.02 | SEPB 4.10 |
| D | SCF 4.19 | SEPB 4.16 |
| D | SCF 4.61 | SEPB 4.72 |
| D | SCF 4.80 | SEPB 4.71 |
| D | SCF 4.24 | SEPB 4.13 |
| D | SCF 4.44 | SEPB 4.35 |
| D | SCF 4.44 | SEPB 4.16 |
| D | SCF 4.44 | SEPB 4.56 |
| D | SCF 5.04 | SEPB 4.85 |
| D | SCF 4.37 | SEPB 4.79 |
| D | SCF 4.68 | SEPB 4.10 |
| D | SEPB 4.47 | SEPB 4.39 and 4.29 |
| D | SEPB 4.60 | SEPB 4.60 and 4.75 |
| C | SEPB 4.39 | SEPB 4.56 and 4.50 |
| C | SEPB 4.69 | SEPB 4.60 and 4.63 |
| C | SEPB 4.46 | SEPB 4.61 and 4.55* |
| C | SEPB 4.72 | SEPB 4.46 |

* 3-point flexure

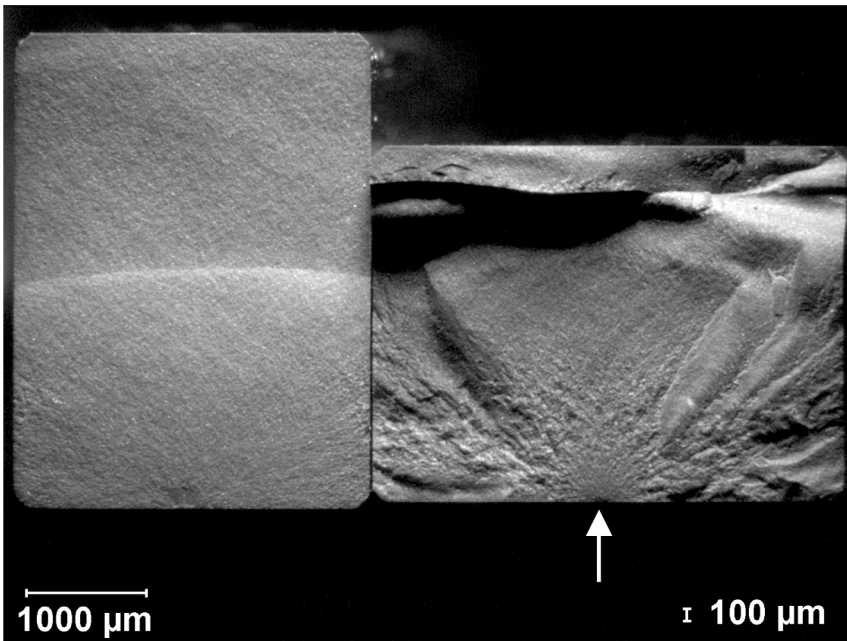


Figure 10. Matching fracture surfaces for a single SRM 2100 test specimen. The specimen was first tested by the SCF method and produced the fracture surface on the right. It is common to put the semielliptical surface flaw into the wider face. The precrack is just barely visible (arrow) at this magnification within the fracture mirror. This fracture surface has all the normal characteristics of a strength test fracture surface. One half of the broken specimen was retested in the SEPB configuration as shown on the left. The precrack extends half way into the test piece. The lower fracture load for the SEPB configuration creates a much smoother fracture surface.

matched the full sized beam outcome within $0.1 \text{ MPa}\sqrt{\text{m}}$. Figure 10 shows two fracture surfaces from one such test set and illustrates the dramatic difference in precrack styles and fracture modes. The SCF full sized specimens on the right side has a tiny $51 \mu\text{m}$ deep semielliptical crack that is just barely visible in the middle of the fracture mirror. One half of the specimen was retested in the SEPB configuration with a $\approx 2 \text{ mm}$ deep precrack shown on the left.

The remarkable within-billet and between-method data consistency confirms that the C 1421 test methods have been optimized to the extent that *genuine material variability* (billet-to-billet, or batch-to-batch) can now be discerned.

The comprehensive certificate that accompanies each SRM 2100 set lists the fracture toughness for the set as well as the uncertainty associated with the estimate. For each billet the mean fracture toughness and the scatter in results as measured by the three test methods were statistically indistinguishable. The data were therefore pooled for each billet. The certified average fracture toughness in Table 6 is the grand mean of the pooled NIST database. The uncertainty U_1 (with the subscript 1) is a 95 % prediction uncertainty for a **single** future observation and is based on the results of the NIST observations from the same normally-distributed population.⁵⁷ The uncertainty U_m (where the subscript m denotes the mean) is a 95 % confidence interval for the **mean of five** future observations, also based on the results of the NIST independently and randomly selected observations. The expanded uncertain-

Table 6. Certified fracture toughness values. The uncertainties are at the 95% confidence interval. The numbers in parenthesis is the uncertainty expressed as a percentage of the mean fracture toughness.

| Billet | Grand Mean K_{Ic} MPa \sqrt{m} | Grand Std. Dev. MPa \sqrt{m} | n | Uncertainty, U_1 , Single specimen MPa \sqrt{m} (%) | Uncertainty, U_m , Mean of 5 specimens MPa \sqrt{m} (%) |
|--------------|---------------------------------------|-----------------------------------|----|---|---|
| C (SRM 2100) | 4.572 | 0.112 | 46 | 0.228 (5.0 %) | 0.106 (2.3 %) |
| G | 4.268 | 0.148 | 32 | 0.307 (7.2 %) | 0.145 (3.4 %) |
| D | 4.495 | 0.232 | 37 | 0.477 (10.6 %) | 0.224 (5.0 %) |

ties, U , represent the combined effects of material inhomogeneity and within-laboratory components of uncertainty and were calculated from:

$$U = t \left(\frac{1}{m} + \frac{1}{n} \right)^{1/2} s \quad (1)$$

where s is the grand NIST sample standard deviation, $m = 1$ for a single test specimen, or $m = 5$ for the SRM kit sample size, n is the NIST sample size and t is the Student's t parameter ($= 2$) for a 95 % confidence interval and the appropriate degrees of freedom, $(n - 1)$. Table 6 shows that the smallest uncertainties are associated with billet C since the database was larger and the standard deviation smaller than for the other two billets. Once all the SRM 2100 kits have been distributed, then SRM's 2100A and 2100B will be available using the billet G and D test specimens.¹

6. REFINEMENTS TO C 1421

Findings from the SRM 2100 project were helpful during the drafting of ASTM C 1421. In the paragraphs below, we give examples where lessons learned from the SRM work aided setting the specifications and tolerances for the test methods.

A key issue with any fracture test method is the choice of proper stress intensity factor coefficients. Accurate stress intensity factor coefficients are particularly of concern for the CNB test specimen. This is mainly a result of its 3-dimensional nature and the use of approximate solutions from the Slice and Straight-through-crack-assumption (STCA) models. One key parameter is α_1 , which is the normalized dimension for the location of the end of the chevron on both sides of the specimens. An α_1 of 1.0 (configurations A, B, D in C 1421) means that the ends of the chevron merge exactly with the side face and the back face of the test pieces. The Provisional Standard PS070-97 used the stress intensity factor coefficients from the Slice model for configurations A, B, C and D. During the conversion of this standard to the full consensus standard C 1421, this matter was investigated more carefully. In order to determine the best stress intensity factor coefficient function for ASTM C 1421, the Slice and STCA models were compared to finite element analyses (FEA) and boundary element analyses (BEA) solutions.⁵⁸ It was determined that the STCA is a good

¹ The price per kit is \$350 in the year 2003. The price covers the cost of fabricating the specimens, SRM project overhead costs, as well as a small fraction of the preliminary research costs.

approximation to the BEA for geometries with $\alpha_1 = 1.0$), but a poor approximation for geometries with $\alpha_1 < 1$ (e.g., configuration C in C 1421). In the latter case the Slice model is a better but less than ideal approximation. (FEA results are currently the best solution.) It is now believed that the STCA model is more accurate (by 5 - 10 percent) than the slice model for configurations A, B, and D. C 1421 changed the formulation for Y_{\min}^* to the STCA model for test configurations A, B, and D, and retained the Slice model solution for configuration C. This was an important change. The decision was reinforced by our SRM 2100 data. We compared calculated fracture toughness results with both solutions for the SRM 2100 "A" configuration specimens. Better agreement with the SCF and SEPB data was achieved with the STCA model, thus reinforcing the analytical findings.

One key issue with the SEPB test is the straightness of the precracks and final fracture planes. Ideally the precracks should pop in reasonably straight and then should propagate directly to the back specimen face during final fracture. In practice, precracks often pop in at an angle as illustrated in Figures 7 and 11. Many precracks are curved. We initially measured the angle at the tip, $\theta_{\text{precrack,tip}}$, to check the deviations, but we realized this would be impractical for routine work. Instead we used a chord angle, θ_{precrack} , as shown in Figure 11a. Final fracture may progress along a different angle, θ_{final} . The slight shift in precrack and final fracture angle actually is helpful in determining the depth of the precrack on the fracture surface. How much of an angular departure from the ideal plane is acceptable? ASTM C 1421 differs from ISO 15732 and JIS R 1607 on this point. ASTM C 1421 sets an allowable *final fracture* misalignment, whereas the latter two specify an allowable *precrack* misalignment. JIS 1607 allows a maximum 10° precrack deviation for three-point loading. ISO 15732 allows 10° for four-point loading, but only 5° for three-point loading. (The tightening of this tolerance in ISO 15732 as compared to JIS 1607 was driven by fear that a 10° tilted crack would be very hard to properly line up in a three-point bend fixture, especially one with a 16 mm span.) In contrast, C 1421 sets a 10° limit on the *final* fracture plane for four-point fracture and only 5° for three-point loading. All these tolerances were chosen on the basis of prior work, but the SRM 2100 data provided a useful check. The precrack and final crack angles were measured to within 0.5° on both sides of each SRM 2100 specimen. We rejected a datum for the SRM database if it failed either a precrack or final fracture tolerance. Figure 11 shows the results for all SEPB tests for billets C, D, and G and includes data rejected for SRM 2100. The fracture toughness values were normalized by the billet mean value to put the data on a common basis. Most of the data is from four-point flexure. Several points may be made. First, we usually had no trouble obtaining good precracks and straight crack propagation and most cracks were well below the 10° limits. Second, the trends do not show a dramatic change at 10° for either angle. Data may be slightly more scattered at $> 10^\circ$ and may have a slight trend of increasing fracture toughness. In summary, our SRM 2100 work indicates the tolerances chosen for the world standards are reasonable and conservative.

Lessons learned from the SCF experiments also aided the drafting of the test method standards ASTM C1421 and ISO 18756. We confirmed that it did not matter whether the tiny Knoop precrack was implanted in the narrow 3 mm face or the wider 4 mm face. The formal test standards allow both indentation and loading configurations. Slight (0.5 % - 1.0 %) discrepancies in our SCF outcomes early in the project were traced to the size of the chamfers in some of the preliminary bend bar sets. Bend

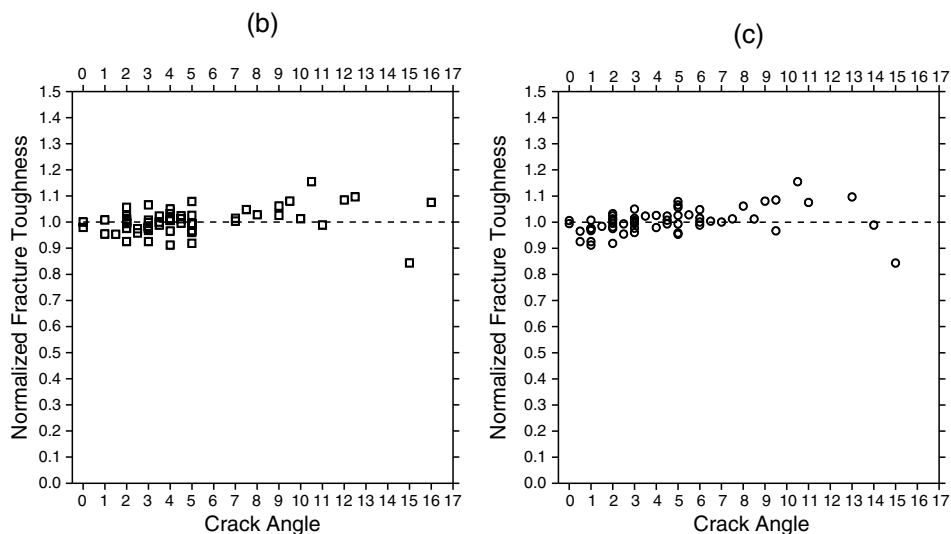


Figure 11. The effect of SEPB crack angles upon the fracture toughness for all billet C, D, and G data. Fracture toughness is normalized for the billet average in each case. (b) shows the effect of the precrack pop in angle, θ_{precrack} ; and (c) shows the effect of the final crack angle, θ_{final} .

bars and fracture toughness specimens often have chamfers applied to the edges in order to eliminate chipping or machining damage. This must not be overdone, however, lest the cross section of the beam be altered too much. The relationship is not linear: removing 1 % of the material from the cross section by using 45° chamfered edges has a 2.8 % effect on stresses due to the change of the second moment of inertia of the cross section. Hence the flexural strength standards have tolerances on the size of the chamfers. The maximum 45° chamfer size is 0.15 mm maximum for a $3\text{ mm} \times 4\text{ mm}$ bend bar. The SCF method is in essence a strength test with a well-defined tiny flaw. Once the bending stresses were corrected for the chamfers, we were amazed to see an appreciable diminishment in the SRM 2100 data variability. The small discrepancies diminished or disappeared altogether. ASTM C 1421 and ISO 18756 have tolerances for allowable chamfer sizes. The latter standard even includes correction factors for specimens with oversized chamfers.^m

Although at NIST we find it easy to remove the Knoop SCF indentation and its residual stress damage zone with a diamond abrasive disk or abrasive SiC papers, some users prefer to do this step via surface grinding with a grinding machine. Our SRM 2100 work showed this is acceptable, except that it is difficult to verify each specimen has had the correct amount of material removed. There also is a risk that the precrack may be enlarged or disturbed by the machine grinding. There are some hard and tough ceramics where it would be impractical to remove the requisite material by hand grinding or polishing and it is valuable to know that machine grinding is acceptable if precautions are taken. With practice with the SRM 2100 specimens, we became adept at controlling the exact amount of material that was removed and ensuring that the hand ground surface remained reasonably flat and

^m Such chamfers corrections are not appropriate for the SEPB or CNB tests, however.

not crowned. It is routine to control the amount removed to within 2 μm to 4 μm . It was even possible to tailor the shape of the semielliptical precrack so that the maximum stress intensity shape factor was either at the deepest part of the crack, or was approximately constant around the flaw periphery. The Y factors for the deepest point were usually 1.3 to 1.5. At the surface, the Y factors were 1.25 to 1.30. Precracking is an important step in most fracture toughness tests and it was reassuring that we had good control and were the “masters” of the SCF precracks.

Anyone who has ever tried the SCF method has worried about how well they need to discern the SCF precrack. The more Knoop precracks we prepared, the more we recognized some of the nuances of their shapes and boundaries. In some cases the full boundary was not clear (e.g. the left side of the precrack in Figure 6), but we realized that reasonable extrapolations of the precrack boundary could be made with no sacrifice in data quality. On the basis of the SRM 2100 work as well as studies on other materials, we determined that reasonable estimates of the crack size and shape may be made if two-thirds of the boundary is visible. A specification to this effect is incorporated in C 1421. Users also often worry about how precisely they need to measure the tiny precrack. We discovered to our delight that measurements do not have to be especially precise! We frequently made a best estimate of precrack size and computed toughness, but then checked what the effect would be if we added 10 μm to a dimension. Much to our surprise, the effect on computed toughness was often negligible. This is due to the dependence of fracture toughness on the square root of crack size, so uncertainties in the size measurement are diminished in the calculated fracture toughness. Furthermore, as discussed previously, there is a serendipitous interaction of the computed Y factor with errors in the crack size measurements: errors in the latter are offset by compensating errors in the former. On the other hand, it is *not* sufficient to measure an average stress intensity shape factor Y for a group of specimens. Each specimen should have its precrack measured and its own Y calculated. Both C 1421 and ISO 18756 are explicit on this point.

So in summary, detailed “nuts and bolts” work with the SRM 2100 specimens for these methods led us to appreciate which details are important for ensuring accurate and precise fracture toughness measurements, and which details are not important.

7. APPLICATIONS OF SRM 2100

7.1. General

SRM 2100 may be used a variety of ways. The most obvious usage will be to help engineers, researchers, and technicians confirm that their SEPB, SCF, or CNB procedures are sound. Our use of NC 132 in the 1994 to 1995 VAMAS SCF round robin exemplifies this. Most users obtained good results on specimens from billet E. In the few instances where problems occurred, and data was atypical or deviant, it was usually possible to review the testing procedure and find the origin of the discrepancy.

We do not recommend that the five specimens in an SRM 2100 kit be given immediately to a novice. Less expensive practice specimens should be used first until the tester has some familiarity with the test method. Once the tester is familiar with

the test procedure and some of its nuances, then the SRM 2100 specimens may be used to check for accuracy and precision.

As time goes on, we hope the user community will benefit from the test method refinements. More and more examples of consistent fracture toughness data are now starting to appear in the literature. References 59 and 47 show remarkable consistency of SCF, CNB and SEPB data for a toughened silicon nitride and a sintered silicon carbide, respectively. SRM 2100 is available to support ISO and the European Community fracture toughness standards. The reference material should facilitate specifications writing and trade. The paragraphs below give some examples of the utility of SRM 2100.

7.2. Facilitating the refinement and adoption of new methods

SRM 2100 should facilitate the introduction of new alternative test methods. For example, a popular method that may be adopted in the European Community standard is the single-edge V-notched beam (SEVNB)^{60,61} procedure. SEVNB refines the older SENB method by sharpening the saw cut slit with a common single edge or shaving razor blade and fine diamond paste.⁶² NIST and the Swiss Federal Research Laboratory (Dubendorf, Switzerland) both tested sets of SRM 2100 specimens with the results shown in Table 7. They confirm that the SEVNB results were consistent but underestimated the certified fracture toughness by 5 %, a difference that was statistically significant at the 99.9 % level using the Student's t-test to compare the means. It is believed that notch root issues account for the difference, and indeed, fractographic examinations of the notch root of this and other ceramics often show that the notch root has a "start up zone" of the order of $\approx 100 \mu\text{m}$. Addition of this to the initial crack lengths brings the SEVNB results into better agreement with the certified values. Although the SEVNB notch is very sharp, it is still not as sharp as a bona fide crack. Other experience with the SEVNB method confirm that SEVNB results are usually within 5 % to 10 % of results obtained with sharp crack, standardized fracture mechanics test methods. This 5 % to 10 % discrepancy should be resolved before the SEVNB method is formalized.

7.3. Materials Specifications

New ceramic material specifications may incorporate fracture toughness characterization. One example is the new ASTM Standard F 2094 –01 for silicon nitride ball bearings.⁶³ Three grades of bearing balls are specified in this standard and fracture

Table 7. Comparison of SEVNB results to standard test methods results. Each entry has the mean and standard deviation fracture toughness in $\text{MPa}\sqrt{\text{m}}$, and the number of test specimens is in parenthesis.

| Billet | SEVNB data | C 1421 data Methods |
|--------------|--------------------------------|--|
| C (SRM 2100) | 4.34 ± 0.19 (5) This paper | 4.57 ± 0.11 (46) SCF, SEPB, CNB This paper |
| E | 4.36 ± 0.08 (6) Ref. 62 | 4.59 ± 0.37 (107) SCF VAMAS round robin, Refs. 15–17 |

toughness is one of the key determinants whether a bearing grade material is Class I ($K_{Ic} \geq 6.0$), Class II ($K_{Ic} \geq 5.0$), or Class III ($K_{Ic} \geq 5.0$).ⁿ

A time goes on, more specifications like this may be crafted, possibly for biological materials such as surgical implants. Several ASTM standards for alumina and zirconia materials for surgical implants are on the books, but only require flexural strength, elastic modulus, and hardness at the moment.

8. WHAT IS THE REAL FRACTURE TOUGHNESS?

The SRM 2100 results are reassuring in the sense that they are extraordinarily consistent and independent of test method. Claims of ceramic fracture toughness measurements that were accurate and precise to within a few percent were unheard of in the 1980's and early 1990's. It would seem that the experimental errors now have been "wrung out" of the individual test methods to the extent that the methods are reliable and the test method uncertainties are of the order of a few percent. The scatter of the SRM data base (Table 6) is smaller than the scatter in the VAMAS round robin (Table 1). This is not surprising since the round robin scatter included material variability, within-laboratory test method uncertainty, plus the between-laboratory method uncertainties.

Our SRM results are also consistent with 30 years of test data from a variety of sources (Table 1). Indeed, our experience with the six billets studied for the SRM as well as billet E, and data from the old stress rupture and fracture map work cited earlier, suggests that NC 132 actually did have billet-to-billet variability after all. Other investigators have commented on variability between and within billets, but often furnished no concrete data or stated that the variation could not be correlated with any observable microstructural variations or inhomogeneities.^{40,64,65,66,67,68}

We conclude that the fracture toughness for NC 132 is $4.6 \text{ MPa}\sqrt{\text{m}}$ for fully dense plates. This fracture toughness was attained in the billets that had the full density of 3.23 g/cm^3 . Although billet D had this density, it also had greater scatter since the billet had a small taper after hot pressing and some density gradients. Billet G had a slightly lower density ($\approx 0.5 \%$) and, in turn, a 6.4% reduced fracture toughness compared to billet C. We also detected a slightly greater boundary phase content from the microstructural analysis, but this was not confirmed by the chemical analysis. So in summary, it seems that slight density, microstructural, and chemical variations have measurable effects upon fracture toughness, and that the refined fracture toughness tests methods can now discern the effect.

Is the fracture toughness of hot-pressed silicon nitride, grade NC 132 independent of crack size? Does a $40 \mu\text{m}$ deep crack have the same fracture resistance as a 2.5 mm long crack? Our data suggests the fracture toughness is indeed invariant over this range. Tiny $40 \mu\text{m}$ deep SCF precracks showed no significant signs of stable crack extension on the fracture surfaces,^o nor did the larger 2.5 mm cracks in SEPB

ⁿ The standard unfortunately also included a Vickers indentation crack length method as an alternative to estimate fracture resistance. The measured property in that instance is deemed as "indentation fracture resistance" and not a genuine fracture toughness.

^o An important exception was for billet H specimens wherein cracks did have stable crack extension, but from environmentally- assisted slow crack growth and not from a rising R-curve behavior. Specimens tested in inert atmosphere did not have any stable extension.

specimens. The natural inherent flaws in this material are of the order of 15 μm to 35 μm in size (depth of a surface crack or radius for an internal flaw). Perhaps there is an ultimate short crack, tip fracture toughness (crack size $\approx 0 \mu\text{m}$) which may be as low as 1.5 $\text{MPa}\sqrt{\text{m}}$ to 2.5 $\text{MPa}\sqrt{\text{m}}$ for tiny cracks in dense polycrystalline silicon nitrides. If the toughness is this low, then the R-curve must come up very quickly with increasing crack size or extension. Any other trend could not account for our observations and those of other investigators over the years who have deduced this material does indeed have a flat R-curve.^{24,26-30}

Our work has shown that for *all practical purposes* the fracture toughness of this simple MgO-doped hot-pressed, dense silicon nitride, with mixed trans- and intergranular fracture, and with slightly elongated grains of the order of 1 μm to 3 μm in size, is invariant with crack size (40 μm to 2.5 mm) and is 4.3 $\text{MPa}\sqrt{\text{m}}$ to 4.6 $\text{MPa}\sqrt{\text{m}}$ depending on the billet and its density.

It is ironic that fracture toughness test methods for ceramics, which are bona fide brittle materials, have come so late to the scene. JIS R 1607 arrived in 1990, ASTM C 1421 in 1999, and the ISO and CEN standards in 2003. This is 20 - 33 years after ASTM E 399 was first adopted for metals in 1970. So although ceramists were late, we need not include in our standards the singularly pessimistic statement in E 399:^P

“There is no accepted “standard” value for the plane strain fracture toughness of any material. In the absence of such a value, any statement concerning bias is not meaningful.”

Our reply is simple. There now is a reference material with a certified fracture toughness. The following quote is taken directly from the NIST Certificate that comes with every SRM 2100 kit:

“This SRM is intended for the verification of fracture toughness testing procedures and consists of a set of 5 hot-pressed silicon nitride flexure specimens . . . The certified fracture toughness is 4.572 $\text{MPa}\sqrt{\text{m}}$ and the uncertainty at the 95% confidence interval for a single specimen is 0.228 $\text{MPa}\sqrt{\text{m}}$, and for the mean of five specimens, is 0.106 $\text{MPa}\sqrt{\text{m}}$.”

9. CONCLUSIONS

The first reference material in the world for the property fracture toughness has been created in tandem with ASTM C 1421. Both were completed within months of each other in mid-1999. The fact that multiple test methods produce virtually identical results strongly validates the ASTM and ISO standard test methods for ceramics. Methods for measuring fracture toughness have been optimized to the extent that genuine material differences may now be discerned. This meets one goal of any standard: to enable the user to measure the desired property with good accuracy and precision.

The 115 valid results in Table 2 (out of 152 total experiments) that constitute the SRM database on billets C, G, and D are supported by years of work and hundreds of additional fracture toughness experiments on NC 132. Altogether, 582 fracture toughness experiments on this particular material have been conducted over the last eight years in our ceramic fracture toughness standardization program. One hundred and seven kits are available for sale. Forty-six are from billet C for SRM 2100.

^P Precision and Bias paragraph 11.3.

Eighteen and forty-three kits from billets D and G, respectively, will be used for SRM's 2100A and 2100B.

It is hoped that the ceramic community will begin using the new standard methods, but this will probably be a gradual process. Rudimentary indentation methods will continue to have some allure, no matter how dubious the quality of the data. Hopefully the ceramic community will recognize the value of refined standard test methods and the methods will restore some long overdue credibility to ceramic fracture toughness data.

ACKNOWLEDGMENTS

Nien-Fan Zhang of the NIST Statistical Engineering Division assisted with the statistical interpretations. John Sieber of the Chemistry Division furnished the x-ray fluorescence data. Michael Foley of St. Gobain/Norton contributed with helpful consultations. The U. S. Department of Energy, Office of Transportation Technologies, Heavy Vehicle Propulsion Systems Materials Program is acknowledged for its support of the SCF test method development under contract DE-AC05-840R21400 with Martin Marietta Energy Systems, Inc.

REFERENCES

1. ASTM C 1421-99, Standard Test Method for Determination of Fracture Toughness of Advanced Ceramics at Ambient Temperature," Annual Book of Standards, Vol. 15.01, ASTM, West Conshohocken, PA, 1999.
2. G. D. Quinn, J. A. Salem, I. Bar-On, and M. J. Jenkins, The New ASTM Fracture Toughness of Ceramics Standard: PS 070-97, *Ceramic Engineering and Science Proceedings*, **19** (3) 565-578 (1998).
3. G. D. Quinn, I. Bar-On, M. G. Jenkins, and J. A. Salem, Fracture Toughness Standards Test Method C 1421-99 for Advanced Ceramics, *Korean Journal of Ceramics*, **4** (4) 311-322 (1998).
4. I. Bar-On, G. D. Quinn, J. A. Salem, and M. J. Jenkins, Fracture Toughness Standard Test Method C 1421-99 for Advanced Ceramics, pp. 315-335 in *Fatigue and Fracture Mechanics, Vol. 32*, ASTM STP 1406, ed. R. Chona, American Society for Testing and Materials, West Conshohocken, PA, 2001.
5. J. A. Salem, G. D. Quinn, and M. J. Jenkins, Measuring the Real Fracture Toughness of Ceramics: ASTM C1421, this volume.
6. ISO 15732, Fine Ceramics (Advanced Ceramics, Advanced Technical Ceramics) – Test Method for Fracture Toughness at Room Temperature by Single Edge Precracked Beam (SEPB) Method, International Organization for Standards, Geneva, 2003.
7. ISO 18756, Fine Ceramics (Advanced Ceramics, Advanced Technical Ceramics) – Determination of Fracture Toughness of Monolithic Ceramics at Room Temperature by the Surface Crack in Flexure (SCF) Method, ISO Geneva, 2003.
8. ISO xxxxx, draft, Fine Ceramics (Advanced Ceramics, Advanced Technical Ceramics) – Test Method for Fracture Toughness of Monolithic Ceramics at Room Temperature by Chevron Notched Beam (CNB) Method, ISO, Geneva, 2003.
9. PrENV xxx, European Standard, Advanced Technical Ceramics – Monolithic Ceramics – Fracture Toughness – Parts 1-5, European Committee for Standardization, Brussels, 2003.
10. Japanese Industrial Standard R 1607-1990, Japanese Standards Association, Tokyo, February, 1990.
11. D. C. Larsen, J. W. Adams, and S. A. Bortz, Survey of Potential Data for Design Allowable MIL-Handbook Utilization for Structural Silicon-Based Ceramics, final report on IITRI/AMMRC Contract DAAG46-79C-0078, U.S. Army Materials and Mechanics Research Center, Watertown, MA, Dec. 1981.
12. *Reliability of Ceramics for Heat Engine Applications*, National Materials Advisory Board Report, NMAB-357, Nat. Acad. of Sci., Washington, DC, 1980.

13. G. D. Quinn, Properties Testing and Materials Evaluation, *Ceramic Engineering and Science Proceedings*, **5** (5–6) 298–311 (1984).
14. G. D. Quinn, VAMAS After Twelve, *Bulletin of the American Ceramic Society*, **78** (7) 78–83 (1999).
15. G. D. Quinn, J. J. Kübler, and R. J. Gettings, Fracture Toughness of Advanced Ceramics by the Surface Crack in Flexure (SCF) Method: A VAMAS Round Robin, *VAMAS Technical Report #17*, National Institute of Standards and Technology, Gaithersburg, MD 20899, June, 1994.
16. G. D. Quinn, R. J. Gettings, and J. J. Kübler, Fracture Toughness of by the Surface Crack in Flexure (SCF) Method: Results of the VAMAS Round Robin, *Ceramic Engineering and Science Proceedings*, **15** (5) 846–855 (1994).
17. G. D. Quinn, R. J. Gettings, and J. J. Kübler, Fracture Toughness of Ceramics by the Surface Crack in Flexure (SCF) Method, *Fracture Mechanics of Ceramics, Vol.11*, eds. R. C. Bradt, D. P. H. Hasselman, D. Munz, M. Sakai, and V. Yashevchenko, (Plenum, NY, 1996), pp. 203–218.
18. J. J. Petrovic, L. A. Jacobson, P. K. Talty, and A. K. Vasudevan, Controlled Surface Flaws in Hot-Pressed Si₃N₄, *J. Am. Ceram. Soc.*, **58** (3–4) 113–116 (1975).
19. G. D. Quinn and J. B. Quinn, Slow Crack Growth in Hot-Pressed Silicon Nitride, in “*Fracture Mechanics of Ceramics*, Vol. 6, eds. R. C. Bradt, A. G. Evans, D. P. H. Hasselman, and F. F. Lange, (Plenum, NY, 1983) pp. 603–636.
20. J. J. Swab and G. D. Quinn, unpublished results, billet P, 1997.
21. V. Tikare and S. R. Choi, Combined Mode I and Mode II Fracture of Monolithic Ceramics, *J. Am. Ceram. Soc.*, **76** (9) 2265–2272 (1993).
22. S. T. Gonczy and D. L. Johnson, Impact Fracture at High Temperature, in *Fracture Mechanics of Ceramics, Vol. 3*, eds. R. C. Bradt, D. P. H. Hasselman, and F. F. Lange, (Plenum, NY, 1978) pp. 495–506.
23. I. Bar-on, F. I. Baratta, and K. Cho, Crack Stability and Its Effect on Fracture Toughness of Hot-Pressed Silicon Nitride Beam Specimens, *J. Am. Ceram. Soc.*, **79** (9) 2300–2308 (1996).
24. J. A. Salem, J. L. Shannon, Jr., and M. Jenkins, Some Observations in Fracture Toughness and Fatigue Testing with Chevron-Notched Specimen, in *Chevron-Notch Fracture Test Experience: Metals and Non-Metals*, ASTM STP 1172 eds. K. R. Brown and F. I. Baratta, (ASTM, Phil., PA, 1992) pp. 9–25.
25. J. A. Salem and S. R. Choi, Toughened Ceramics Life Predictions Project, in *Propulsion System Materials Program Bimonthly Technical Progress Report*, DOE Office of Transportation Technologies, Dec. 1995 – Jan. 1996, ORNL, Oak Ridge, TN, 1996, pp. 180–187.
26. J. A. Salem, and J. L. Shannon, Jr., Fracture Toughness of Si₃N₄ Measured With Short Bar Chevron-Notched Specimens, *J. Mat. Sci.*, **22** 321–324 (1987).
27. R. T. Bubsey, J. L. Shannon, Jr. and D. Munz, Development of Plane Strain Fracture Toughness Test for Ceramics Using Chevron Notched Specimens, in *Ceramics for High Performance Applications III, Reliability*, (Plenum, NY, 1983), pp. 753–771.
28. J. J. Kübler, Unpublished research.
29. J. A. Salem and S. R. Choi, Toughened Ceramics Life Prediction, pp. 220–234 in *Ceramics Technology Project Bimonthly Progress Report*, Oct.-Nov. 1991, Oak Ridge National Laboratory, Oak Ridge, TN, 1991.
30. V. Tikare and S. Choi, Influence of the Si₃N₄ Microstructure on its R-curve and Fatigue Behavior, *Cer. Eng. Sci. Proc.*, **12** (7–8) 1437–1447 (1991).
31. C. G. Annis and J. S. Cargill, Impact Fracture of Ceramics at High Temperature, in *Fracture Mechanics of Ceramics, Vol. 4*, eds. R. C. Bradt, D. P. H. Hasselman and F. F. Lange, (Plenum, NY, 1978), pp. 737–744.
32. A. G. Evans and E. A. Charles, Fracture Toughness Determinations by Indentation, *J. Am. Ceram. Soc.*, **59** (7–8) 371–372 (1976).
33. R. K. Govila, Material Parameters for Life Prediction in Ceramics in *Ceramics for High Performance Applications III, Reliability*, (Plenum, NY, 1983), pp. 535–567.
34. R. K. Govila, Indentation Precracking and Double Torsion Methods for Measuring Fracture Mechanics Parameters in Hot-pressed Si₃N₄, *J. Am. Ceram. Soc.*, **63** (5–6) 319–326 (1980).
35. G. D. Quinn, Unpublished results.
36. G. K. Bansal and W. H. Duckworth, Effects of Specimen Size on Ceramic Strength, in *Fracture Mechanics of Ceramics, Vol. 3*, eds. R. C. Bradt, D. P. H. Hasselman, and F. F. Lange, (Plenum, NY, 1978), pp. 189–204.
37. G. K. Bansal and W. H. Duckworth, Fracture Toughness of Hot-Pressed Si₃N₄, *Am. Ceram. Soc. Bull.*, **14** 254, 1984.

38. R. E. Tressler, T. M. Yonushonis, and M. D. Meiser, Crack Propagation in Molten Salt Corrosion of Si_3N_4 , private communication, 1976.
39. W. C. Bourne and R. E. Tressler, "Alteration of Flaw sizes and K_{Ic} 's of Si_3N_4 Ceramics by Molten Salt Exposure," in *Fracture Mechanics of Ceramics, Vol. 3*, ed. R. C. Bradt, D. P. Hasselman, and F. F. Lange, (Plenum, NY, 1978), pp. 113–124.
40. G. K. Bansal and W. H. Duckworth, Fracture Surface Energy Measurements by the Notched Beam Technique, in *Fracture Mechanics Applied to Brittle Materials*, ASTM STP 678, ed. S. W. Freiman, (ASTM, Philadelphia, PA, 1979), pp. 38–46.
41. S. W. Freiman, A. Williams, J. J. Mecholsky, Jr., and R. W. Rice, Fracture of Si_3N_4 and SiC, in *Ceramic Microstructures 1976*, eds. R. M. Fulrath and J. A. Pask, (Westview Press, Boulder, Co, 1977), pp. 824–834.
42. G. D. Quinn, Fracture Mechanism Maps for Advanced Structural Ceramics, Part I, Methodology and Hot Pressed Silicon Nitride, *Journal of Materials Science*, Vol. 25, 1990, pp. 4361–76.
43. M. L. Torti, Processing Hot Pressed Silicon Nitride for Improved Reliability: HS 110 to NC 132, *Ceramics for High Performance Applications, III Reliability*, eds., E. Lenoe, R. N. Katz, and J. J. Burke, (Plenum, NY, 1983), pp. 261–273.
44. D. R. Clarke, A Large Scale Processing Inhomogeneity in Silicon Nitride Ceramics and Its Effect on Oxidation, *Materials Science Forum*, **47** (Trans Tech. Publ., Switzerland, 1989), pp. 110–118.
45. J. J. Swab and G. D. Quinn, Effect of Precrack "Halos" on K_{Ic} Determined by the Surface Crack in Flexure Method, *J. Am. Ceram. Soc.*, **81** (9) 2261–2268 (1998).
46. A. Ghosh, M. G. Jenkins, K. W. White, A. S. Kobayashi, and R. C. Bradt, Elevated-Temperature Fracture Resistance of a Sintered α -Silicon Carbide, *J. Am. Ceram. Soc.*, **72** [2] 242–47 (1989).
47. G. D. Quinn and J. A. Salem, Effect of Lateral Cracks Upon Fracture Toughness Determined by the Surface Crack in Flexure Method, *J. Am. Ceram. Soc.*, **85** (4) 873–80 (2002).
48. MIL STD 1942 (MR) Flexural Strength of High Performance Ceramics at Ambient Temperature, U. S. Army Materials Technology Laboratory, Watertown, MA, Nov. 1983.
49. ASTM C 1161, Test Method for Flexural Strength of Advanced Ceramics at Ambient Temperature, *Annual Book of Standards*, Vol. 15.01, ASTM, West Conshohocken, PA, 2002.
50. ISO 14704, Fine (Advanced, Advanced Technical) Ceramics - Determination of Flexural Strength at Room Temperature, International Organization for Standards, Geneva, 2002.
51. J. J. Petrovic, and M. G. Mendiratta, Fracture from Controlled Surface Flaws, *Fracture Mechanics Applied to Brittle Materials*, ASTM STP 678, ed. S. Freiman, (ASTM, West Conshohocken, PA, 1979), pp. 83–102.
52. G. D. Quinn, R. J. Gettings, and J. J. Kübler, Fractography and the Surface Crack in Flexure (SCF) Method for Evaluating Fracture Toughness of Ceramics, *Fractography of Glasses and Ceramics, Ceramic Transactions*, **64**, (American Ceramic Society, Westerville, OH, 1996), pp. 107–144.
53. J. C. Newman, Jr., and I. S. Raju, An Empirical Stress-Intensity Factor Equation for the Surface Crack, *Engineering Fracture Mechanics*, **15** (2) 185–92 (1981).
54. T. Nose and T. Fuji, Evaluation of Fracture Toughness for Ceramic Materials by a Single-Edge-Precracked-Beam Method, *Journal of the American Ceramic Society*, **71** (5) 328–333 (1988).
55. ASTM E 399–90, Standard Test Method for Plane-Strain Fracture Toughness of Metallic Materials, *Annual Book of Standards*, Vol. 3.01, ASTM, West Conshohocken, PA, 1990.
56. J. A. Salem, J. L. Shannon, Jr., and M. G. Jenkins, Some Observations in Fracture Toughness and Fatigue Testing with *Chevron-Notched Specimen*, *Chevron-Notch Fracture Test Experience: Metals and Non-Metals*, ASTM STP 1171, eds. K. R. Brown and F. I. Baratta, (American Society for Testing and Materials, West Conshohoken, PA, 1992), pp. 9–25.
57. G. Hahn, and W. Meeker, *Statistical Intervals: A Guide for Practitioners*, Wiley, NY, 1991.
58. J.A. Salem, L.J. Ghosn, M.G. Jenkins, and G.D. Quinn, Stress Intensity Factor Coefficients for Chevron-Notched Flexure Specimens and Comparison of Fracture Toughness Methods, *Ceramic Engineering and Science Proceedings*, **20** (3) 503–512 (1999).
59. G. D. Quinn, J. J. Swab, and M. J. Motyka, Fracture Toughness of a Toughened Silicon Nitride by ASTM C 1421, to be publ. *J. Am. Ceram. Soc.*, 2003.
60. J. J. Kübler, Fracture Toughness of Ceramics Using the SEVNB Method: First Results of a Joint VAMAS/ESIS Round Robin, *Ceramic Engineering and Science Proceedings*, **20** (3) 495–502 (1999).
61. J. J. Kübler, Fracture Toughness of Ceramics Using the SEVNB Method; Round Robin, VAMAS Report No. 37, Swiss Federal Laboratories for Materials Testing and Research, Dübendorf, Switzerland, 2000.

62. J. J. Kübler, Fracture Toughness of Ceramics Using the SEVNB Method: Preliminary Results, *Ceramic Engineering and Science Proceedings*, **18** (4) 155–162 (1997).
63. ASTM F 2094–1, Standard Specification for Silicon Nitride Bearing Balls, Annual Book of Standards, Volume 14.02, ASTM, West Conshohocken, PA, 2001.
64. K. D. McHenry, T. Yonushonis, and R. E. Tressler, Low-Temperature Subcritical Crack Growth in SiC and Si₃N₄, *J. Am. Ceram. Soc.*, **59** (5–6) 262–263 (1976).
65. K. Jakus, J. E. Ritter, Jr., and J. P. Fahey, Effect of Billet Difference on the High-Temperature Strength of Hot-Pressed Silicon Nitride, *J. Am. Ceram. Soc.*, **65** (9) C143–C144 (1982).
66. M. E. Gulden and A. G. Metcalfe, Stress Corrosion of Silicon Nitride, *J. Am. Ceram. Soc.*, **59** (9–10) 391–396 (1976).
67. D. G. Miller, C. R. Booher, Jr., R. J. Bratton, “Brittle Materials Design, High Temperature Gas Turbine Stator Vane Development and Static Rig Tests, Westinghouse Final Report, U. S. Army Materials and Mechanics Research Center, Watertown, MA, Technical Report, AMMRC CTR 76–32, Volume II, page 224, 1976.
68. D. W. Richerson and T. M. Yonushonis, Properties of Silicon Nitride Rotor Blade Materials, pp. 193–217 in *Ceramic Gas Turbine Demonstration Program Review*, Castine MA, Metals and Ceramics Research center, Battelle Columbus Technical Report, MCIC 78–36, March 178.

MEASURING THE REAL FRACTURE TOUGHNESS OF CERAMICS: ASTM C 1421

Jonathan Salem,¹ George Quinn,² and Michael Jenkins³

ABSTRACT

ASTM C 1421 “Standard Test Methods for Determination of Fracture Toughness of Advanced Ceramics at Ambient Temperature” is a high-quality, technically-rigorous, full-consensus standard that may have finally answered the question, “What is the ‘real’ fracture toughness of ceramics?” This document was eight years in the actual standardization process (although an estimated two decades of preparation work may have preceded the actual standardization process). Three different types of notch/crack geometries are employed in flexure beams: single edge pre-cracked beam (SEPB); chevron-notched beam (CNB), and surface crack in flexure (SCF). Extensive experimental, analytical, and numerical evaluations were conducted in order to mitigate interferences that frequently lower the accuracy of fracture toughness test results. Several round robins (e.g., Versailles Advanced Materials and Standards {VAMAS}) verified and validated the choice of dimensions and test parameters included in the standard. In addition, the standard reference material NIST SRM 2100 was developed and can be used in concert with ASTM C 1421 to validate a fracture toughness test setup or test protocol.

¹ Materials Research Engineer, NASA Glenn Research Center at Lewis Field, Life Prediction Branch, 21000 Brookpark Road, MS 49-7, Cleveland, OH 44135. jsalem@grc.nasa.gov.

² Research Scientist, National Institute for Standards and Technology, Ceramics Division, 100 Bureau Drive, Stop 852, Gaithersburg, MD 20899-852.

³ Professor and Chair, Department of Mechanical Engineering, University of Detroit Mercy, Engineering Bldg, 4001 W. McNichols Rd, P.O. Box 19900, Detroit, MI 48219-0900.

1. INTRODUCTION

A wide variety of test configurations and specimen geometries have been used to determine the fracture toughness of ceramic materials. A variety of definitions exist for fracture toughness: for example, “a generic term for measures of resistance to crack extension” [1], or “a measure of the ease of crack propagation through a material” [2]. In terms of standardization, the definitions typically boil down to a well defined operational procedure as stated in the discussion following one definition: “. . . the value of stress-intensity factor designated K_{Ic} as measured using the operational procedure specified in this test method” [3]. The need for an operational rather than theoretical definition is used in standardization in order to avoid interferences and pitfalls that can occur in many popular and widely used test specimens.

Interferences must be minimized if accurate, repeatable results are to be ensured. Standards developed by full consensus bodies, such as the American Society for Testing and Materials (ASTM) and ISO (International Organization for Standardization), not only put data measurement on a common basis, but attempt to improve the metrology of the result by controlling such interferences. A standard sets up rigorous guidelines that will identify and avoid the occurrence of interferences during data generation. For fracture toughness testing, interferences include the lack of stable crack extension, stress corrosion, crack growth resistance, stress intensity factor solution accuracy, crack length measurement, crack shape, residual stresses, and alignment of the crack with the fixture. In addition, fracture toughness tests performed by using beams tend to encounter the interferences associated with flexural strength testing, such as nonparallelism, twist, friction, and bevel effects. The severity of the interferences varies with the particular test method.

Recently, a full consensus standard for the “Determination of Fracture Toughness of Advanced Ceramics at Ambient Temperature” was developed and published under the auspices of ASTM [4]. During development of the standard test method, typical interferences were addressed, and when possible each error was kept to $\sim 2\%$ or less. In addition to development of the standard, several round robin exercises were run [5–9], and a standard reference material was developed [10]. Additional work on fracture toughness standardization should include a method(s) for elevated temperature testing, very thin shapes such as fuel cell electrolyte membranes, and miniaturized test specimens.

2. THE STANDARD METHODS

The standard allows three tests methods: the chevron notch beam (CNB), the single-edge-precracked-beam (SEPB), and the surface-crack in flexure (SCF). Three test methods are allowed because no one method provides valid test results for the variety of ceramics being developed. All the test methods use 3- or 4-point flexure to test rectangular cross sections such as the common 3 mm by 4 mm test section used in flexural strength testing of ceramics [11]. More importantly, all have a well defined loading configuration, a well defined crack, and an accurate stress intensity factor coefficient solution. Some allowances are made for other cross sections because adequate results can be obtained from such sections.

Despite the commonality of bend testing a rectangular cross section, the methods differ substantially in terms of the size, shape and development of the cracks used, as illustrated in Figure 1. The SEPB uses a large, straight-through precrack that

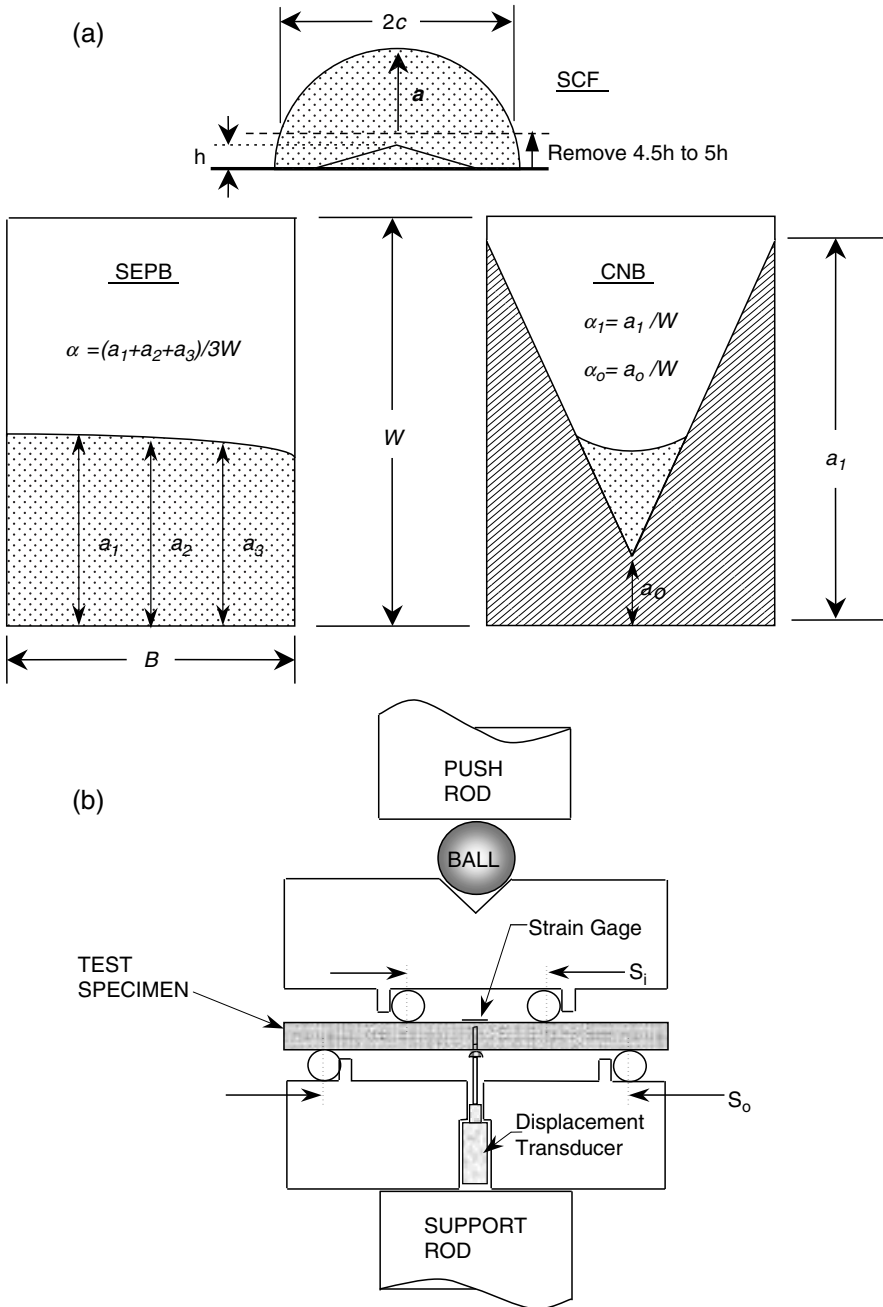


Figure 1. (a) Crack configurations allowed in ASTM C 1421. (b) Example of a test specimen in four-point loading.

is rapidly formed from a small Vickers indentation or a shallow machined notch. The CNB uses a 3-dimensional crack that is generated stably during fracture testing of the section. The SCF uses a semi-elliptical precrack generated by removing a portion of a Knoop indentation precrack.

All the methods fulfill the fundamental requirement that a sharp, real crack be used to detect the onset of crack extension. Ideally this extension should be stable, and it generally has been shown to be for both the CNB and SEPB methods. The definitions of sharp and real differ somewhat from those used for metals. For metals, a sharp, real crack is generated with low stress intensity cyclic fatigue [3] and a minimal amount of plasticity. Because plasticity is generally minimal in ceramics, sharp cracks can usually be developed with monotonic loading.

In this paper, rather than recite the specifications in C 1421, we have chosen instead to focus on some of the key interferences in fracture toughness testing and how they were dealt with in C 1421.

3. THE INTERFERENCES

3.1. Stability

A basic requirement for a valid experiment with the CNB specimen is stable crack extension. Unstable crack extension, which may occur in test pieces with poorly prepared notches, typically causes the test piece to be overloaded and leads to overestimates of fracture toughness. Generally, notch width between 0.25 and 0.30 mm at any point on the specimen surface is available from commercial machine shops. Larger notch thickness is acceptable provided that stable crack extension occurs. The offset between the notch planes is particularly critical. For alpha silicon carbide, notch widths of 0.225 to 0.250 mm with an offset less than 0.030 mm were consistently stable. For sapphire, notch widths of 0.300 to 0.325 mm with notch offsets of 0.075 to 0.110 mm were consistently unstable. However, notch widths of 0.250 to 0.300 mm with offsets of 0.025 to 0.075 mm were stable. Wider notches may allow for more total offset.

On the other hand, there may be instances when seemingly unstable fractures are in fact valid stable fractures. The inability to adequately detect stable crack extension results in the appearance of an unstable test and the presumption of an invalid result. A variety of methods have been used to verify stability such as load-point displacement (LPD) as determined from the linear variable differential transducer (LVDT) used to control the test system actuator; center-point displacement (CPD) as determined using an LVDT or capacitance extensometer placed in or near the flexure fixture; a time record as generated with an XY recorder; or strain as monitored with a strain gage centered about the crack plane on the compressive or back-face of the test specimen [12,13]. In addition, laser extensometers have also been used [14].

Generally, actuator displacement or time-sweeps are only marginally adequate for detecting specimen stability. Success depends upon the choice of scales, the test system "noise" levels, and the fracture behavior of the material. Locally placed extensometers and strain gages are usually excellent. Figure 2.2 shows load as a function of various detection methods for α -SiC.

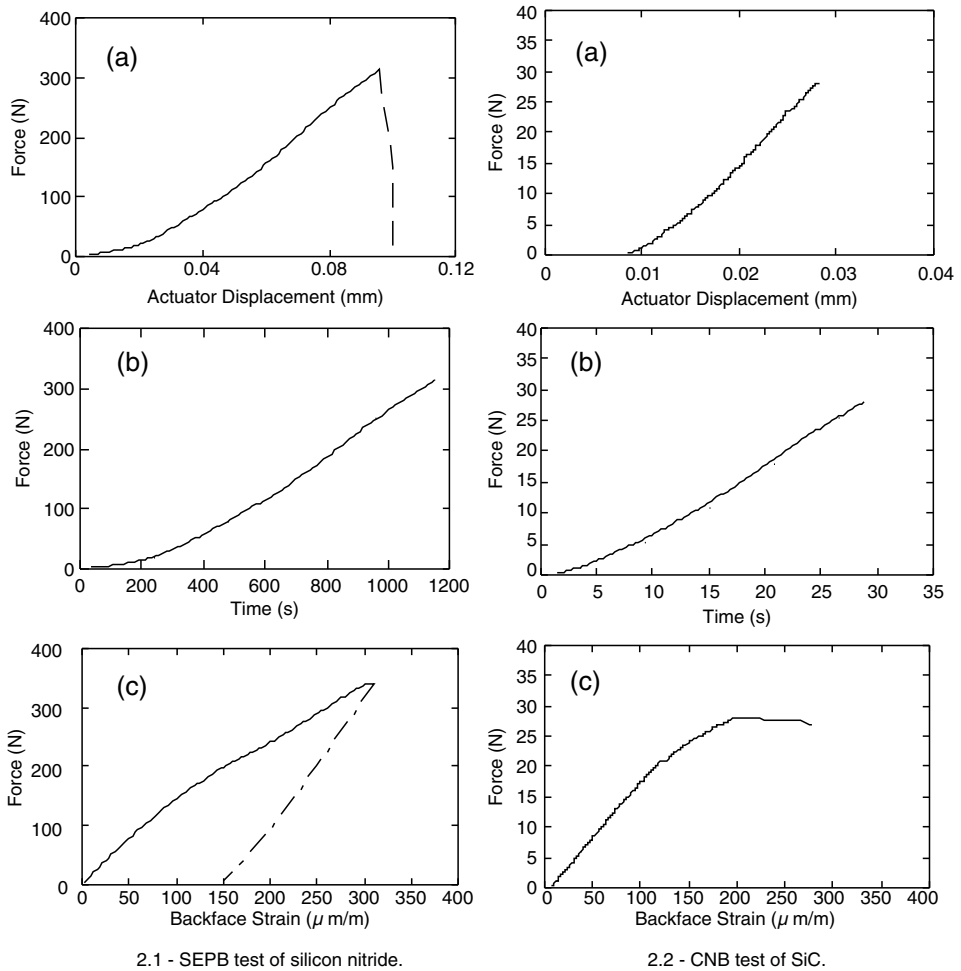


Figure 2. Plots of (a) force vs. time, (b) force vs. actuator displacement, and (c) force vs. back face strain for silicon nitride tested using the SEPB (2.1) and silicon carbide tested using the CNB (2.2). In both cases stable crack extension occurred as evidenced by the nonlinearity near maximum load in the BFS plots 2.1(c) and 2.2(c). The other methods did not detect the crack extension.

For the SEPB test specimen, stability is not required, however, the lack of stability can [15] result in overloading and slightly increase the measured fracture toughness. Actuator displacement is inadequate for detecting test stability even with a digitally controlled electro-mechanical system (e.g. Instron 8562⁴) using relatively sophisticated zero shift suppression and range (amplification) capability. Locally placed extensometers are only marginally adequate whereas back face strain (BFS) is excellent for detecting stability, as shown in Figure 2.1.

In addition, excessive stability in the SEPB can create problems because the precrack length is used to calculate the fracture toughness. If the crack extends significantly, the measured maximum load might not correspond reasonably with the precrack length, and lower, apparent fracture toughness will result. This is in part due to the current operational procedure of C 1421, which uses maximum load and

precrack length to calculate the SEPB fracture toughness, K_{Ipb} . Ideally, the calculation should be based on the load and the crack size corresponding to the onset of crack extension. Generally, most ceramic materials exhibit sufficient but not excessive stability when tested in four-point flexure [13]. The only notable exception is when the precracks are very twisted [16]. Such cracks tend to exhibit complete instability or alternatively, jumps followed by unstable failure as detected with back-face strain. The stability exhibited in four-point flexure probably results because of factors such as stress corrosion, crack shape, and crack growth resistance.

However, it is notable that limited experimental work indicated that four-point flexure is unstable and results in an overestimate of the SEPB fracture toughness as compared to three-point results [17]. That finding may merely have been due to a failure to detect stability (the actuator displacement was used), and excess extension or other differences in the comparative three-point tests. A comparison of fracture toughness calculated with the C 1421 procedure (maximum load and precrack length) and the use of the precrack length and load corresponding to 2% crack extension, as done in ASTM E 399, indicated little practical difference for four-point flexure [13], as shown in Table 1. Although the standard allows user to choose either configuration, it is recommended that four-point flexure be used because it avoid errors associated with aligning the crack and load-point.

Stability is not normally an issue with the SCF test. The fractures usually are unstable unless unusual precautions are taken, or the material has a very steep R-curve.

3.2. Stress Corrosion

Many ceramics and glasses exhibit slow crack growth or stress corrosion. This interferes with fracture toughness measurements because the results become a function of the test environment used and stress-intensity rate applied. Slow crack growth occurs at stress intensities less than the critical stress intensity, and any such crack extension may cause the measured fracture toughness to underestimate the fracture toughness obtained in an inert environment. An example of the significance of the effect for an alumina is shown in Table 2 [16]. To mitigate the interference, the choice

Table 1. Stress intensity factors and standard deviations calculated with various operational procedures [13]. Units are $\text{MPa}\sqrt{\text{m}}$ and uncertainties are one standard deviation.

| Material ⁴ {number of tests} | Maximum load and optical precrack length (C 1421 procedure) | 2% extension load and optical precrack length (E 399 procedure) | Maximum load and crack length estimated from BFS |
|---|---|---|---|
| Glass {4} | 0.70 ± 0.01 | 0.70 ± 0.01 | 0.70 ± 0.04 |
| Si_3N_4 (GN-10) {6} | 5.42 ± 0.17 | 5.38 ± 0.20 | 5.73 ± 0.12 |
| $\text{Si}_3\text{N}_4/\text{SiC}_{\text{Wiskers}}$ {3} | 6.62 ± 0.17 | 6.56 ± 0.16 | 6.48 ± 0.03 |
| Si_3N_4 (AS800) {4} | 7.52 ± 0.34 | 7.38 ± 0.33 | 7.53 ± 0.49 |
| Si_3N_4 (NKK) {4} | 10.3 ± 0.6 | 10.2 ± 0.6 | 10.1 ± 0.4 |

⁴ Certain commercial materials or equipment are identified in this paper to specify adequately the experimental procedure. Such identification does not imply endorsement by the National Institute of Standards and Technology or the National Aeronautics and Space Administration nor does it imply that these materials or equipment are necessarily the best for the purpose.

Table 2. Effect of test environment on the measured fracture toughness \pm one standard deviation for ALSIMAG 614 alumina [16]. The number of tests is given in parentheses.

| Test Specimen Configuration | Test Environment | | |
|-----------------------------|---------------------|---------------------|------------------------------------|
| | Water | Air | Silicone Oil or Dry N ₂ |
| $K_{Ivb}(A)$ MPa \sqrt{m} | 2.75 \pm 0.01 (4) | 3.19 \pm 0.07 (7) | 3.37 \pm 0.05 (4) |
| K_{Isc} MPa \sqrt{m} | - | 3.18 \pm 0.10 (5) | 3.47 \pm 0.12 (4) |

of test environment should be tied to the application if possible. For example, in the calculation of slow crack growth parameters from “dynamic” fatigue or “static” fatigue data, the fracture toughness in an inert environment is combined with the inert strength to indirectly estimate the initial flaw size distribution of the test specimens. However, for field applications, a value measured in an environment such as air may be more realistic, depending upon the loading conditions and crack velocity expected at failure.

Very fast loading rates have been used to eliminate environmental effects in strength testing of ceramics. However, the use of fast rates for SEPB and CNB specimens is generally impractical because the specimens are more likely to be overloaded and unstable. An inert environment should be used instead to eliminate the environmental effects. In order to determine the presence and significance of environmental effects, C 1421 recommends testing either in several environments (e.g. oil and water) or at very different rates. One caution in using slow rates for testing is that the correspondence between the optically measured precrack and the maximum load may be lost, and although an effect will be indicated, the measured value may not be accurate.

SCF precracks are especially sensitive to stable crack extension from environmental effects. Reference 18 shows examples for alumina and several other ceramics. C 1421 recommends that the precracks be examined for fractographic evidence of stable extension and if it is detected, the critical crack size should be used for the fracture toughness calculation. Testing in inert atmospheres is effective in eliminating the interference in SCF testing.

3.3. Crack Growth Resistance

Ceramics such as coarse grained aluminas, *in situ* toughened silicon nitrides, and transformation toughened zirconias exhibit an increase in the measured stress intensity factor as a function of crack extension. This behavior is commonly referred to as crack growth resistance or R-curve behavior. This phenomenon affects fracture toughness measurements because many components are expected to fail with relatively short crack lengths (< 0.5 mm) whereas many fracture toughness measurements are performed with longer crack extensions and/or precrack lengths. Thus the point of determination of fracture resistance on the crack growth curve does not have similitude with the applications. Another disconnect between applications and many methods is the existence of cyclic loading during formation of the crack. Cyclic loading tends to break down the toughening mechanisms exhibited by some materials and thus renders the mechanisms less effective in applications.

To address these interferences, test specimens could be prepared with fatigue precracking and the measurements made at small, defined crack extensions. However, the additional effort is significant and was considered too substantial for the first version of the standard. Instead, the effort was focused upon consistency and accuracy between several methods for materials exhibiting little crack growth resistance. C 1421 provides warnings to alert the user to this interference.

It should be noted that both the CNB and SEPB test methods do produce very similar results for *in situ* toughened silicon nitrides despite the differences in the formation, growth and size of the crack. The CNB grows a crack monotonically ~ 0.86 mm during the test whereas as the SEPB uses a ~ 2 mm precrack that is subsequently failed with monotonic loading that typically involves $\sim 5\%$ crack extension [13]. Table 3 compares results from these relatively different methods for several *in situ* toughened silicon nitrides. The agreement is surprisingly good. The SCF method is difficult to apply to coarse grained materials because the precrack becomes difficult to delineate. This is particularly unfortunate because the SCF method should provide fracture resistance values more akin to those developed in real applications.

For alumina with a $5\ \mu\text{m}$ average grain size, the effects of compressive or tensile fatigue precracking versus monotonic precracking via large chevron-notch short bar (CNSB) specimens shows the fatigued test specimens to have lower values that were not a function of crack length for very long cracks [21]. Comparison of the data using student's *t* distribution indicated a statistically significant difference between monotonically grown long cracks ($3.93\ \text{MPa}\sqrt{\text{m}}$ for an extension of 16 mm) and fatigue induced long cracks ($3.56\ \text{MPa}\sqrt{\text{m}}$ for extensions between 3 and 30 mm) at better than 99% confidence, implying that the best approach is to keep crack length as short as possible while employing good metrology, regardless of the precracking method, as shown in Table 4. Thickness effects, which play a role in the plasticity and degree of plane strain developed, could not be detected in testing of relatively thick alumina test specimens, as shown in Table 5. Thus the small section sizes used in ASTM C 1421 are likely reasonable, however, additional testing of very thin sections should be performed.

Table 3. Fracture toughness of *in situ* toughened silicon nitrides as measured by the methods specified in ASTM C 1421. Results in any row are for the same billet and have identical test orientation except as noted. The number of tests is given in parenthesis. Exceptions to criteria for validity are given in the footnotes.

| Material | $K_{Ivb} (A)^1\ \text{MPa}\sqrt{\text{m}}$ | $K_{Ipb}\ \text{MPa}\sqrt{\text{m}}$ | $K_{Isc}\ \text{MPa}\sqrt{\text{m}}$ |
|-----------------------------|--|--------------------------------------|--------------------------------------|
| NKK | $10.43 \pm 0.48 (5)^2$ | $10.29 \pm 0.63 (3)$ | Unmeasurable ³ |
| AS440 | $7.16 \pm 0.27 (5)$ | $7.3 \pm 0.3 (7)^4$ | - |
| AS800 (light) | $7.40 (1)$ | $7.60 \pm 0.20 (4)$ | - |
| AS800 (dark) | $6.90 \pm 0.09 (4)$ | $7.17 \pm 0.20 (5)$ | - |
| PY6 | $6.30 \pm 0.03 (5)$ | $6.19 \pm 0.01 (2)^5$ | - |
| SRBSN 147-31 N ⁵ | $5.28 \pm 0.17 (5)$ | $5.59 \pm 0.22 (14)$ | $5.58 \pm 0.24 (16)$ |

1. Geometry *A* of ASTM C 1421.

2. Geometry *D* tested at 0.1 mm/min.

3. Not measurable due to a coarse grain structure that masked the crack size.

4. See ref. 19. Inner and outer spans of 10 and 18 mm were used.

5. Inner and outer spans of 10 and 18 mm were used. 6. See ref. 20.

Table 4. Effect of precracking method on the measured fracture toughness of ALSIMAG 614 alumina [21].

| Test Method | Precracking Method | Precrack Size or Extension mm | Number of Tests | Fracture Toughness MPa√m |
|--|------------------------------------|-------------------------------|-----------------|--------------------------|
| <i>ASTM C 1421 Methods:</i> | | | | |
| CNB | Monotonic | 0.86 | 7 | 3.19 ± 0.07 |
| SEPB | Monotonic | 1–3 | 13 | 3.09 ± 0.17 |
| SCF | Monotonic | 0.21–0.42 | 5 | 3.18 ± 0.10 |
| <i>Long Cracks by Monotonic Crack Extension:</i> | | | | |
| CNSB ¹ | Monotonic | 6.3 | 20 | 3.67 ± 0.05 |
| CNSB | Monotonic | 15 | 3 | 3.93 ± 0.04 |
| DT ² | Monotonic | — | — | 3.84 ± 0.05 |
| <i>Long and Short Cyclic Fatigue Precracks:</i> | | | | |
| CNSB ³ | Tension/Tension | 3–30 | 17 | 3.56 ± 0.12 |
| CNSB ³ | Tension/Tension Dry N ₂ | 7–9 | 5 | 3.90 ± 0.08 |
| SNSB ⁴ | Compression/Compression | 0.1–0.5 | 11 | 3.52 ± 0.07 |

1. Chevron-notch short bar (CNSB).
2. Double torsion. See ref. 22.
3. Fatigued as a CNSB to the extension listed, and then machined into a straight-notch short bar (SNSB) and fractured.
4. Fatigued in compression as a straight-notch short bar (SNSB).

Table 5. Effect of test specimen thickness on the measured fracture toughness of ALSIMAG 614 alumina. The number of tests is given in parentheses [21].

| | | | |
|---|-----------------|----------------|-----------------|
| <i>Tension-Tension Fatigue Precracked, Tested in N₂:</i> | | | |
| Test Specimen Thickness, mm | 7.6 | 12.7 | 17.8 |
| Fracture Toughness, MPa√m | 3.92 ± 0.13 (2) | 3.90 ± – (1) | 3.88 ± 0.10 (2) |
| <i>Compression-Compression Fatigue Precracked, Tested in Air:</i> | | | |
| Test Specimen Thickness, mm | 5 | 10 | — |
| Fracture Toughness, MPa√m | 3.53 ± 0.08 (6) | 3.51 ± 0.07(5) | — |

Crack growth resistance curves measured with short and long crack techniques might be expected to measure different ranges of the R-curve depending the extension and area of the cracked region. Figure 3a shows R-curves measured with the indentation strength technique [23] and with chevron-notch short bar test specimens [24]. For comparison, the values of K_{Ipb} , K_{Ivb} , and K_{Isc} are included in the plot. The R-curves generated with short and long cracks not only cover the same range of fracture resistance, but start just below the fracture toughness values generated with C 1421. The IS data show a sharply increasing R-curve trend, which is not reflected in the other data. The IS trend is probably due to an artificial stabilizing influence of the

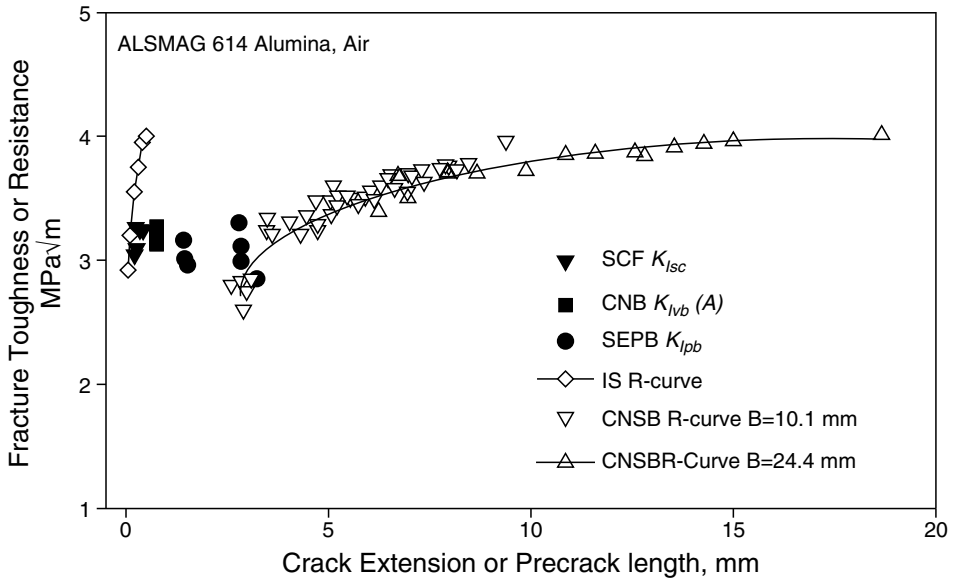


Figure 3a. Crack growth resistance curves from indentation strength (IS) [23] and chevron-notch short bar methods [24] compared to fracture toughness values via C 1421. For the PB and SCF methods, the precrack length is plotted. For the CNB method, the crack extension to maximum load is plotted.

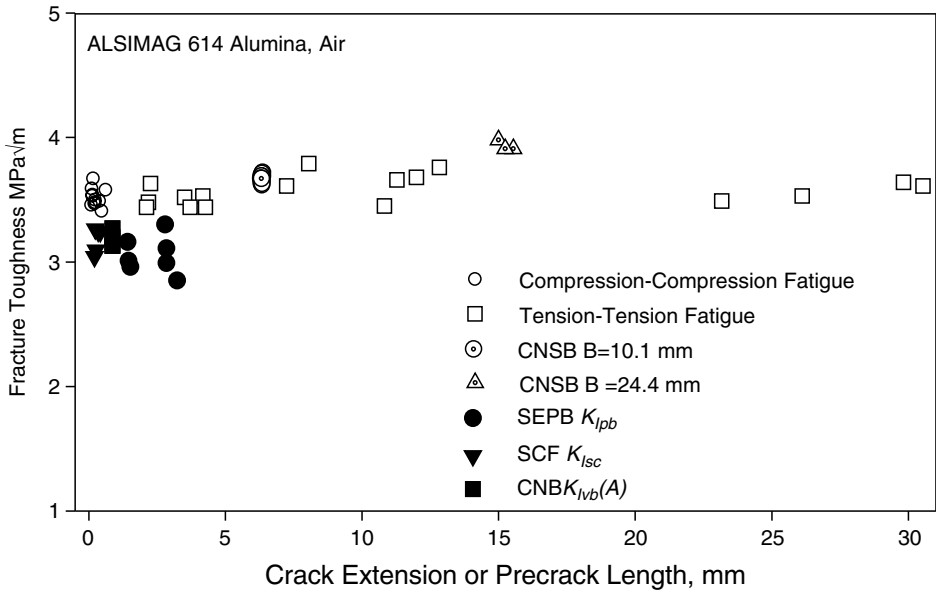


Figure 3b. Fracture toughness measured after fatigue precracking compared to fracture toughness values via C 1421. For the PB, SCF, and fatigue methods, the precrack length is plotted. For the CNB method, the crack extension to maximum load is plotted.

residual stress field associated with the Vickers indentation. Some recent studies [25, 26] have shown that by varying the SCF precrack size by using a range of indentation loads, it may be possible to gain a sense of whether the calculated fracture toughness depends on crack size and whether R-curve phenomena are active.

Table 6. Effect of texture on the measured fracture toughness of ALSIMAG 614 alumina. The number of tests is given in parentheses [24].

| Processing Method | Test Orientation: | | |
|-------------------|-------------------|-------------|-------------|
| | RC | LC | RL |
| Extruded | 4.94 ± 0.37 | 3.63 ± 0.21 | 3.99 ± 0.12 |
| Isopressed | 3.69 ± 0.05 | 3.64 ± 0.03 | 3.68 ± 0.02 |

Interestingly, the fracture toughness measured with fatigue precracked specimens appears to be higher than that measured with C 1421 techniques, as shown in Figure 3b. Thus C 1421 provides values on the lower end of the R-curve without fatigue precracking.

Texture due to the manufacturing process can also influence the crack growth resistance and fracture toughness as shown in Table 6 [24]. Alignment of pores and elongated grains produces both crystallographic texture and macro-textures that influence the measured properties.

3.4. Stress Intensity Factor Coefficients

Accurate stress intensity factor coefficients (SCIF) are particularly of concern for the CNB test specimen. This is mainly a result of its 3-dimensional nature and the use of approximate solutions such as the Slice and straight-through-crack-assumption (STCA). In order to determine the best SIFC function, the Slice and STCA models were compared to finite element analyses (FEA) and boundary element analyses (BEA) solutions [16]. The STCA is a good approximation to the BEA for geometries (see Figure 1) with $\alpha_1 = 1.0$ (which include configurations *A*, *B*, *D* in C 1421), but a poor approximation for geometries with $\alpha_1 < 1$ (such as configuration *C* in C 1421) as shown in Figure 4 and summarized in Table 7. For geometries with $\alpha_1 < 1$ the Slice is a better but less than ideal approximation, and FEA results are currently the best solution.

For the SEPB test specimen, good SIFC's are available for configuration similar to those used in testing of metallic materials. However, ceramics are frequently tested in shorter sections that alter the span-to-depth ratio and thereby affect the SIFC. In order to allow a wider range of span-to depth ratios, previously unpublished solutions generated at the Materials Technology Laboratory, Watertown, Massachusetts [27] were reviewed and added to C 1421.

For the SCF, the SIFC, *Y*, for semicircular and semi-elliptical surface cracks in bending are from the empirical equations developed by Newman and Raju [28]. The Newman-Raju formulas [28] for *Y* are widely accepted and have estimated accuracies of a few percent. The SIFC depends upon the ratio of *a* to *c*, the cross section size relative to *a* and *c*, and the presence of bending. The *Y* factor is not constant and varies along the precrack boundary. It is important to use the maximum value of *Y*, which will either be at the deepest point of the precrack, or where the precrack intersects the surface.

Fracture from the deepest point of the precrack is preferred and can be promoted by polishing sufficient material off the test specimen so as to make the precrack a shallow semi-ellipse. In some materials (e.g., those with clear markings

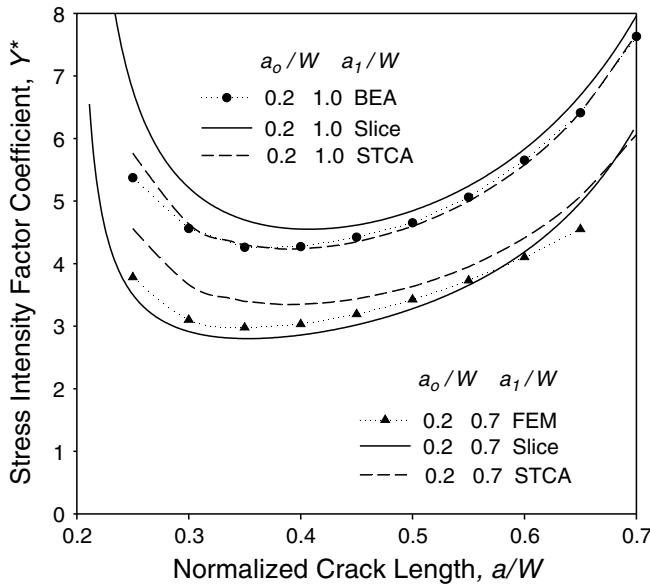


Figure 4. Stress intensity factor coefficient Y^* for CNB test geometries A and C of ASTM C 1421 as calculated with the Slice, STCA, and FEA/BEA methods.

Table 7. Comparison of minimum stress intensity factor coefficients, Y_{min}^* , from BEA and FEA methods, and the Slice and STCA approximations.

| α_o | α_1 | B/W | S_1, mm | S_o, mm | Numerical Methods | Slice | % Diff. | STCA | % Diff. |
|------------|------------|-------|-----------|-----------|---------------------------|-------|---------|-------|---------|
| 0.2 | 0.7 | 0.5 | 0 | 40 | 2.850 (FEA) | 2.695 | -5.4 | 3.216 | 12.8 |
| 0.2 | 0.7 | 0.5 | 20 | 40 | 2.979 (FEA) | 2.801 | -6.0 | 3.347 | 12.3 |
| 0.2 | 1.0 | 0.5 | 20 | 40 | 4.240 (BEM) | 4.549 | 7.3 | 4.233 | -0.2 |
| 0.25 | 1.0 | 1.0 | 20 | 40 | 4.719 (FEA ¹) | 5.061 | 7.3 | 4.690 | -0.6 |
| 0.37 | 0.8 | 1.0 | 0 | 7.3 | 4.540 (FEA ²) | 4.527 | 0.3 | 4.962 | 9.3 |
| 0.44 | 1.0 | 1.0 | 0 | 38 | 6.910 (FEA ³) | 7.514 | 8.7 | 7.147 | 3.4 |

1. See Ref. 29. 2. See Ref. 30. 3. See Ref. 31.

on the fracture surfaces) it has been possible to confirm that fracture initiated from the point of the periphery where Y was maximized. One notable conclusion of one of the VAMAS round robins [5] was that the computed fracture toughness was insensitive to the exact precrack boundaries marked, because the computed fracture toughness was not sensitive to the precrack size measurement! This is partly due to the dependence of the fracture toughness on the square root of the crack size. Thus, a 10% error in crack size is diminished to a 5% error in fracture toughness. A serendipitous outcome was the offsetting influence of Y on the errors due to crack size measurements. For example, if the crack depth, a , is overestimated, the corresponding calculated Y is underestimated.

3.5. Residual Stresses

Residual stresses affect the fracture toughness tests in C 1421 in different ways. For the CNB test specimen, residual stresses associated with grinding of the chevron notch have been anecdotally associated with unstable fracture from the notch tip. For the SEPB test specimen, residual stresses associated with indentation used to form the precrack have been demonstrated to lower fracture toughness measurements because the crack is wedged open by an additional, unmeasured stress intensity. Figure 5 illustrates the effect for a silicon nitride, and implies that indentation loads should be less than 100 N for silicon nitrides [32]. For α -SiC, which is relatively hard, the removal of 50 N indentations by lapping resulted in comparable values to those measured without lapping ($2.52 \pm 0.11 \text{ MPa}\sqrt{\text{m}}$ vs. $2.58 \pm 0.08 \text{ MPa}\sqrt{\text{m}}$) [33].

C 1421 recommends that if residual stresses from the indentation are suspected, the indentations may be removed by polishing or hand grinding. Annealing may be used provided that the crack tip is neither blunted nor the crack tip/planes “healed.”

For the SCF test method, residual stresses around the Knoop precrack affect the measured fracture toughness and thus have been studied in some detail. The stresses are minimized or eliminated by removing the indentation and surrounding material by using hand polishing or machine grinding to a depth of 4.5 h to 5.0 h (where $h = d/30$ in Figure 1). Most studies on silicon nitride imply that as little as 3h is sufficient [34–36], however for SiC, recent studies comparing SCF, CNB, and SEPB results indicate that more removal may be necessary to eliminate lateral cracks, as shown in Figure 6 [37].

3.6 Crack Length Measurement

The measurement of crack length has been identified as a major source of error in fracture testing of metallic materials [38]. In ceramics, crack length measurement is particularly difficult for a number of reasons: the small specimens typically used; the

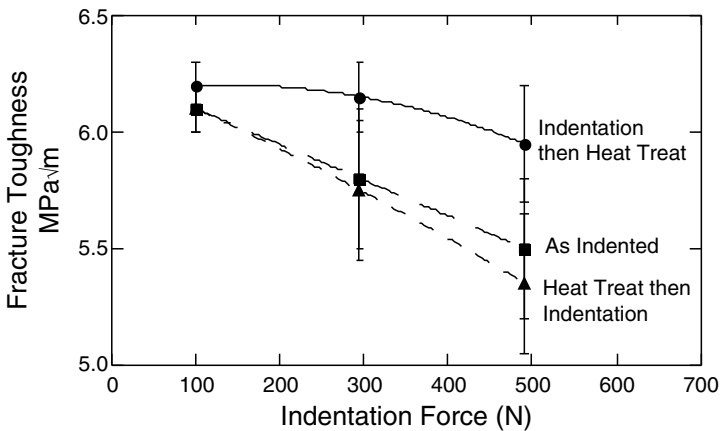


Figure 5. SEPB fracture toughness of for hot pressed silicon nitride as a function of indentation force without and with heat treatments [32].

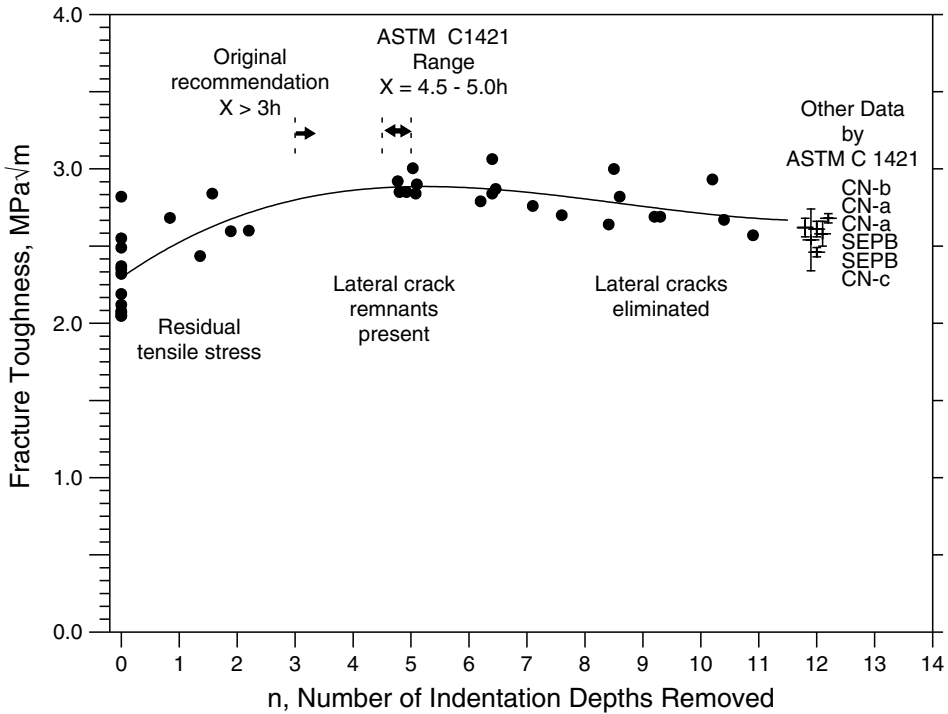


Figure 6. SCF, CNB and SEPb fracture toughness test results for specimens from one lot of alpha silicon carbide [37]. SCF fracture toughness values overestimate the correct value if the amount removed, at $X = nh$, is insufficient to remove lateral cracks that interfere with the main precrack.

semi-opaque nature of many glass-based ceramics; the lack of plastic deformation at the crack tip which results in poor definition of the crack front; and the high elastic moduli and low fracture toughnesses that result in small crack opening displacements.

The CNB test specimen does not require crack length measurement, thereby providing some convenience to the user. However the SEPb and SCF test methods require quality measurements if accurate fracture toughness estimates are expected. For the SEPb test specimen, the precrack front is very difficult to delineate unless it leaves a crack arrest line. An arrest line is easily detected if the crack tip turns out of plane or is hooked, thereby making the precrack and fast fracture plane non-coplanar, as shown in Figure 7. In one study, some cracks were so planar that the front could not be detected with conventional optical microscopy [12]. In such cases, the use of dye penetrants have been successful as shown in Figure 8, however, in some cases penetrants tend to bleed on the fracture surface and the measurements must be made immediately. Dye penetrants must be used with caution as they may cause environmentally assisted crack growth.

Another simple and sensitive technique that can be used to measure crack length and extension in both the CNB and SEPb techniques is the back-face strain gage (BFSG). It has been used previously in metallic compact tension specimens [39], and in fracture toughness testing of ceramic flexure specimens [12, 13]. Figure 9 shows a strain gage mounted on the back-face of a flexure specimen and Figure 10 show the

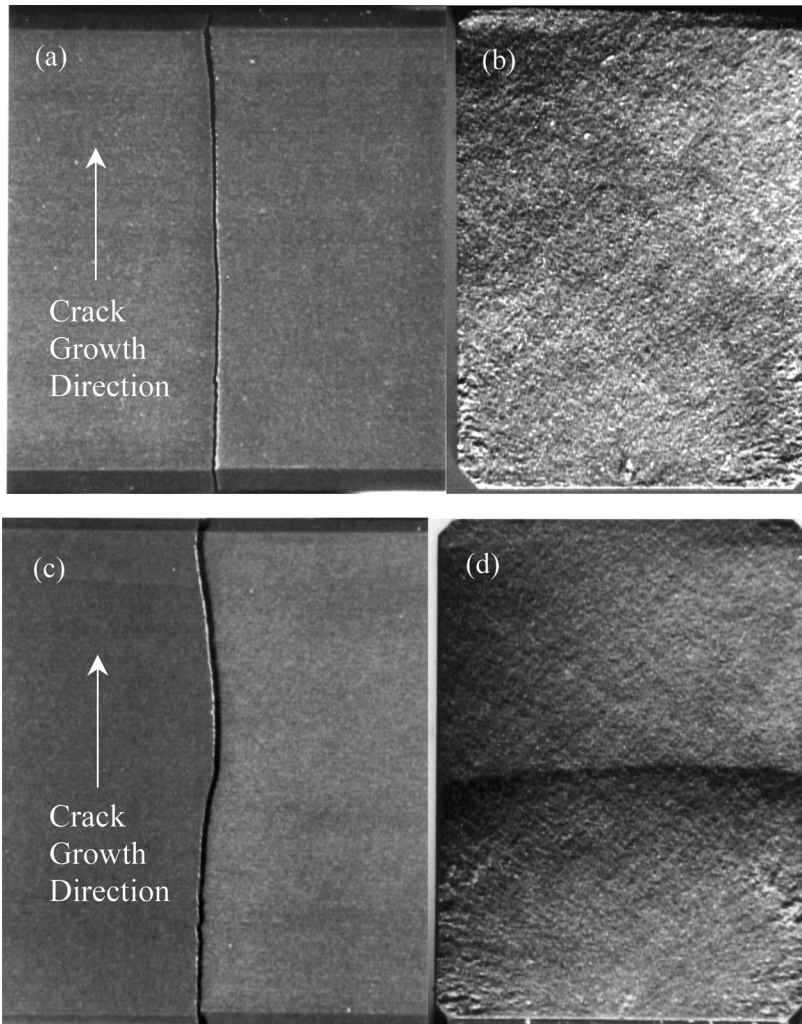


Figure 7. Effect of precrack shape on optical visibility: (a) and (b) are side and top views of a coplanar precrack and failure plane; (c) and (d) are views of a precrack with a hooked tip [12].

correlation between measurements made with BFS and optical microscopy for glass, silicon nitrides, and α - SiC.

The SCF method uses a very small precrack introduced by a Knoop indenter. This method of relying on the material's brittleness to cause small surface precracks to form underneath an indentation is unique to ceramics. The precrack is small and on the order of real flaws in ceramics. Thus, fractographic techniques, and some care and skill, are needed to see and measure the size of the precrack. Both the cracks depth and the width must be measured for the SCF precrack. Crack detection and the size measurement is aided by purposely tilting the test specimen $1/2^\circ$ relative to the indenter so that the precrack and fast fracture regions are not coplanar. As a result, the precrack in some materials is easy to discern, even with a low power stereo binocular microscope. In other materials, a careful examination with a scanning

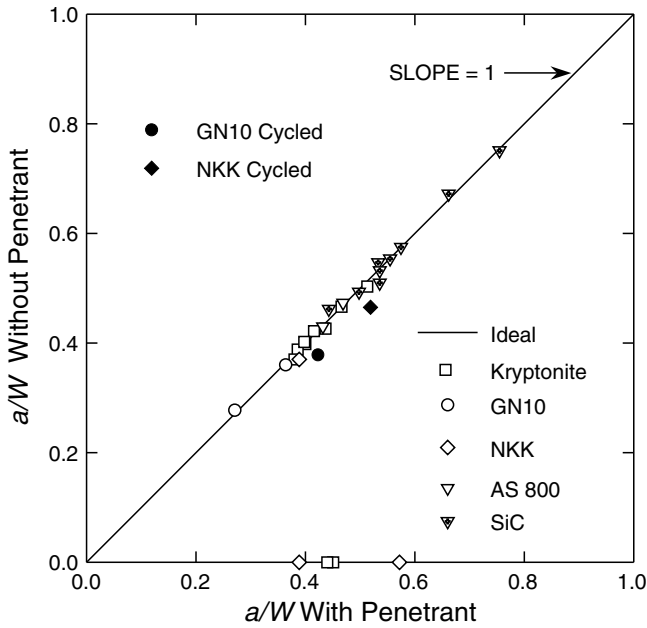


Figure 8. Normalized crack length in SEPB test specimens as measured with and without penetrant [12]. Data points on the x-axis were not measurable without using dye penetrant.

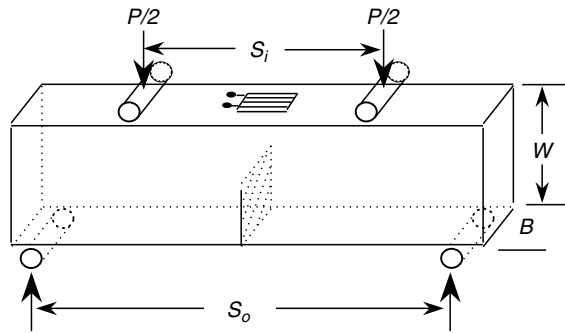


Figure 9. Illustration of a strain gage mounted on the back-face of a four-point flexure specimen.

electron microscope may be necessary. A variety of features, including color, contrast, brightness, ridge or rim lines, halos, and micro hackle line redirection help to discern the precracks, as shown in Figure 11 [40,41]. Stereo scanning electron microscope (SEM) photo pairs may be the best solution in very difficult materials. Dye penetration techniques may also be useful. A detailed and well-illustrated discussion of fractographic techniques to detect SCF precracks has been presented [36] and C 1421 has a detailed appendix on this topic. As discussed above in the Stress Intensity Factor Coefficient section, the calculated SCF fracture toughness is surprisingly insensitive to the precision of the crack size measurement.

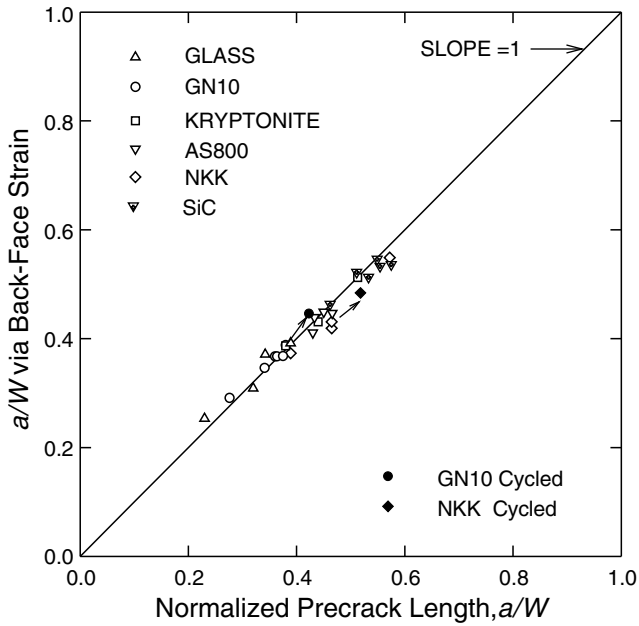


Figure 10. Comparison of precrack lengths in SEPB test specimens as determined by optical measurements and by the initial compliance as measured with back-face strain [13].

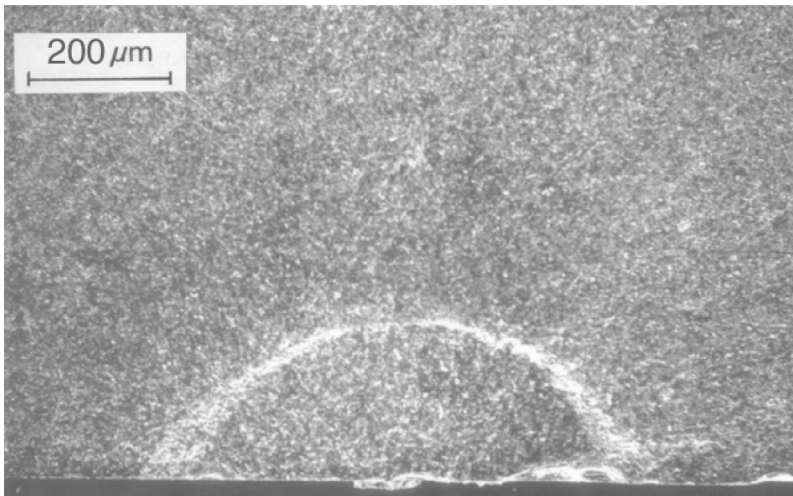


Figure 11. Example of a SEM photograph of a precrack generated in 99.9% sintered alumina with the SCF method.

3.7. Crack Shape

Crack shape can be a problem in the SEPB test method if the precracks hook or twist excessively because the fixture or indentation was not accurately aligned. The effect of hook angle on measured toughness is shown in Figure 12. Little trend can be seen. Currently, the standard recommends keeping the angle below 10°, however, this may be conservative based on currently available data.

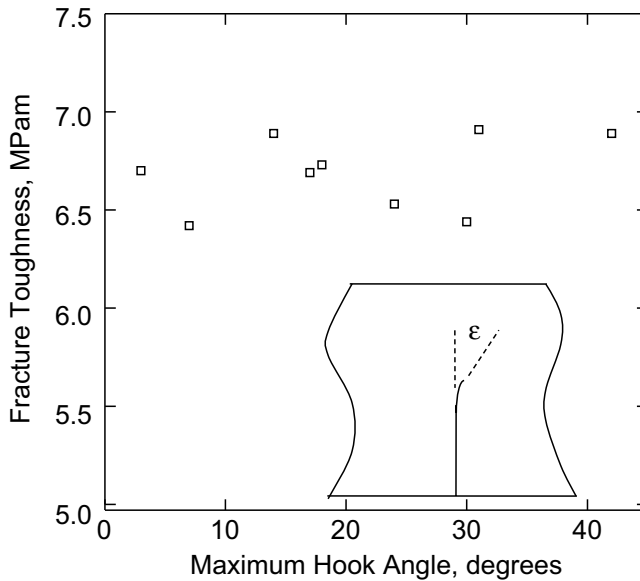


Figure 12. Fracture toughness as a function of hook angle for the SEPB test on silicon nitride [13].

As discussed in the section on Stability, crack twist appears to effect crack growth and stability. For example, during testing of ADS96R alumina, two test specimens with relatively twisted cracks exhibited no stable crack extension and greater fracture toughness values (3.96 and 4.00 MPa√m vs. 3.63, 3.68 and 3.83 MPa√m for the planar cracks). Similar behavior was exhibited by the α -SiC test specimens: Twisted cracks exhibited crack jumps followed by unstable failure and greater fracture toughness values (2.74 and 2.72 MPa√m vs. 2.58 ± 0.08 MPa√m for four tests). More systematic study of such effects are needed. Currently, the standard mitigates the issue by recommending that twist angle be less than 10° .

A semi ellipse is used to model the SCF precrack created by Knoop indentation. In reality, the subsequent hand polishing or grinding to eliminate residual stress truncates the semicircle or semi-ellipse precrack shape. Approximating the crack by a semi ellipse is satisfactory if the maximum stress intensity is at the deepest portion of the precrack, but is less satisfactory if the maximum Y is at the surface. The initial test piece tilt ($1/2^\circ$) during indentation causes precracks to pop in at angles from 0 to $2-3^\circ$ off perpendicular and greatly enhances the visibility of the precracks on the fracture surfaces. Specimen tilt angles greater than 2° are unsatisfactory, however, because the precracks often pop in 5° or more off perpendicular. This is felt to be excessive, especially since Mode II loading may be introduced to the crack and the stress intensity factor coefficients, Y might be affected as discussed in appendix 5 of the VAMAS Round Robin report [8]. For precrack tilt angles up to 5° , the influence on Y is negligible.

C 1421 recommends that SCF precrack be prepared to force the maximum Y factor to be at the deepest part of the precrack. Complications arise if, on the other hand, the maximum Y is at the intersection of the precrack with the test piece surface. The complications include local perturbations of the crack front, uncertainties about

the ellipse approximation to the truncated semicircle or semi ellipse, possible interactions with surface damage, and uncertainties associated with the Newman-Raju solutions at that site. For most ceramics, the amount of material that must be removed to eliminate the residual indentation stresses is only about three times the indentation depth. This usually leaves a nearly semicircular precrack, however, which still has a maximum Y at the test piece surface. Removal of 4.5 to 5.0 times the indentation depth creates a shallower precrack ($\approx 0.6 - 0.8$ aspect ratio, depth to half width) and shifts the maximum Y to the deepest part of the precrack as desired.

3.8. Method to Method Variation

Because the cracks used in the standardized methods are so different, substantially different results might be expected, even for fairly well behaved materials. Table 8 compares results from the three methods and demonstrates that very comparable results can be obtained with good metrology. In most cases, the results are within a few percent, and in the cases of discrepancy, the variations are usually the result of different billets being used. In the case of α -SiC, the presence of lateral cracks has also caused differences. If the lateral cracks are not removed, then the measured fracture toughness increased from 2.76 ± 0.08 and 2.64 ± 0.05 MPa \sqrt{m} for the JAS and UW billets to 2.86 ± 0.03 and 3.01 ± 0.35 MPa \sqrt{m} , respectively [37].

Table 8. Fracture toughness and standard deviation measured by the methods specified in ASTM C 1421. Results in any row are for the same billet and have identical test orientation except as noted. The number of tests is given in parenthesis. Exceptions to criteria for validity are given in the footnotes.

| Material | $K_{Ivb}(A)$ MPa \sqrt{m} | K_{Ipb} MPa \sqrt{m} | K_{Isc} MPa \sqrt{m} |
|-----------------------------|----------------------------------|-------------------------------------|-----------------------------------|
| α -SiC (JAS) | 2.61 ± 0.05 (6) | 2.58 ± 0.08 (4) ¹ | 2.76 ± 0.08 (4) ² |
| α - SiC (UW) | 2.62 ± 0.06 (6) | 2.54 ± 0.20 (3) ¹ | 2.64 ± 0.05 (4) |
| ADS96R | 3.56 ± 0.03 (5) | 3.71 ± 0.10 (3) | - |
| ALSIMAG 614 ⁴ | 3.19 ± 0.06 (7) | 3.09 ± 0.17 (13) ^{1,3} | 3.18 ± 0.10 (5) |
| ALSIMAG 614 ⁶ | 3.13 ± 0.03 (4) ⁵ | 2.98 ± 0.06 (4) ^{1,7} | - |
| NC132 ⁸ SRM 2100 | 4.58 ± 0.12 (10) | 4.58 ± 0.10 (19) | 4.56 ± 0.13 (17) |
| NT154 | 5.18 ± 0.11 (5) | 5.21 ± 0.02 (5) | 5.80 ± 0.23 ⁹ (5) |
| SN260 | 5.19 ± 0.06 (5) | 5.13 ± 0.15 (4) ¹⁰ | - |
| SiAlON | - | 2.45 ± 0.09 (6) | 2.55 ± 0.05 (4) ¹¹ |

1. Different billet from the same material batch as the CNB geometry A specimens.
2. See ref. 37.
3. See ref. 21
4. Processed by isopressing.
5. $B = 4.06$ mm, $W = 5.08$ mm, $\alpha_o = 0.2$ and $\alpha_1 = 1$ with inner and outer spans of 12.7 and 38.1 mm.
6. Processed by drypressing – mild texture was present.
7. A single 30 kg indentation was used as the PB starter crack.
8. Billet “C” of SRM 2100 in ref. 10.
9. Different material lot. Strong lot to lot variation has been reported.
10. A single 20 kg indentation was used as the PB starter crack. Test spans of 10 and 18 mm.
11. Two of the data points were measured by Westmorland Mechanical Testing, Youngstown, PA.

4. STANDARD REFERENCE MATERIAL

For researchers with little experience in measuring fracture toughness via the methods in C 1421, valuable experience and the adequacy of a test setup can be verified by performing tests on material of a known fracture toughness. Such a material has been prepared and made available by the National Institute of Standards and Technology [10].

Standard Reference Material (SRM) 2100 is the first reference material in the world for the property of fracture toughness for any class of material. Although SRM 2100 may be used with any credible fracture toughness test method, it was optimized for those that use beams in bending such as in C 1421.

A package of SRM 2100 consists of a set of five hot pressed silicon nitride beams cut from a single billet. The billet was originally fabricated in the form of plates 158 mm \times 158 mm \times 20 to 30 mm thick. SRM 2100 is a very consistent material from a mechanical properties standpoint, owing to its uniform microstructure ($\sim 3 \mu\text{m}$ grain size) and small amount of sintering aid ($\sim 1\%$ mass fraction magnesium oxide). The material is fully dense with a density slightly greater than theoretical for β silicon nitride because of very fine tungsten carbide inclusions.

In developing the SRM data base, a large sample set of representative flexure test specimens (3 mm \times 4 mm \times 47 mm) from each of three billets of the material were prepared in accordance with the procedures of C 1161 [11] and C 1421. The test specimens were cut from the billets with their long axis perpendicular to the hot pressing direction, and thus the certified fracture toughness of SRM 2100 is for cracks propagated parallel to the 3 \times 4 mm cross section.

Fracture testing was in laboratory conditions using semi to fully-articulating flexure fixtures. Four-point flexure fixtures with 20 mm and 40 mm inner and outer spans, respectively were used to test the full length SCF, SEPB and CNB test specimens. In some instances, broken halves of test specimens were retested in three- and four-point flexure per the SEPB method.

Table 8 summarizes the fracture toughness results for one billet. Within a given billet, the fracture toughness results were in good agreement. The consistent results confirm that the test methods of C 1421 have been refined to the extent that genuine material variability (e.g., billet to billet, batch to batch) can be discerned, thus fulfilling one goal of a good standard: to provide tools to measure the desired property with good accuracy and precision.

5. SUMMARY AND CONCLUSIONS

ASTM C 1421 provides detailed guidance for a quality determination of the fracture toughness of ceramic materials. The sources of error addressed in the standard include stability, stress corrosion, crack growth resistance, stress intensity factor solution accuracy, crack length measurement, crack shape, residual stresses, and alignment of the crack with the fixture. Many of these have been sufficiently addressed as demonstrated by the comparable results for a wide variety of ceramics. For situations in which the interferences are problematic, C 1421 gives recommendations and a choice of three methods to address the issue. The contribution of any individual interference to the measured fracture toughness has generally been kept

below $\sim 2\%$. Use of the standard should avoid significant errors in the measurement of fracture toughness.

ACKNOWLEDGEMENT

The authors thank the Low Emission Alternative Power Project for funding.

REFERENCES

1. ASTM C 1145-01, "Standard Terminology of Advanced Ceramics," *Annual Book of Standards*, Vol. 15.01 (American Society for Testing and Materials, West Conshohocken, Pennsylvania, 2001).
2. A. Dodd and D. Murfin, *Dictionary of Ceramics* (The Institute of Materials, London, 1994).
3. ASTM E 399-90, "Standard Test Method for Plane Strain Fracture Toughness of Metallic Materials," *Annual Book of Standards*, Vol. 03.01 (American Society for Testing and Materials, West Conshohocken, Pennsylvania, 2001) pp. 434-464.
4. ASTM C 1421, "Standard Test Method for Determination of Fracture Toughness of Advanced Ceramics at Ambient Temperatures" *Annual Book of Standards*, Vol. 15.01 (American Society for Testing and Materials, West Conshohocken, PA, 2001) pp. 641-672.
5. H. Awaji, J. Kon, and H. Okuda, "The VAMAS Fracture Toughness Test Round Robin on Ceramics," VAMAS Report #9, Japan Fine Ceramic Center, Nagoya, Japan, 1990.
6. G. Quinn, J.A. Salem, I. Bar-on, K. Chu, M. Foley, and H. Fang, "Fracture Toughness of Advanced Ceramics at Room Temperature," *Journal of Research of National Institute of Standards and Technology*, Vol. 97, No. 5, 579-607 (1992).
7. M. Mizuno, and H. Okuda, "VAMAS Round Robin on Fracture Toughness of Silicon Nitride at High Temperature," VAMAS Technical Report 16 (Japan Fine Ceramics Center, Nagoya, Japan, 1993).
8. G.D. Quinn, J.J. Kübler, and R.J. Gettings, "Fracture Toughness of Advanced Ceramics by the Surface Crack in Flexure Method, A VAMAS Round Robin," VAMAS Technical Report #17 (National Institute of Standards and Technology, Gaithersburg, MD, 1994).
9. G. D. Quinn, "The Fracture Toughness Round Robins in VAMAS: What We Have Learned," in *Fracture Resistance Testing of Monolithic and Composite Brittle Materials, ASTM STP 1409*, edited by J. A. Salem, G. D. Quinn, and M. G. Jenkins (ASTM, West Conshohocken, PA, 2002) pp. 107-126.
10. G.D. Quinn, K. Xu, J.A. Salem, and J.J. Swab, "SRM 2100: The World's First Fracture Toughness Reference Material," Published in this proceeding.
11. ASTM C 1161-96, "Standard Test Method for Flexural Strength of Advanced Ceramics at Ambient Temperature," *Annual Book of Standards*, Vol. 15.01 (American Society for Testing and Materials, West Conshohocken, Pennsylvania, 1999) pp. 309-315.
12. J. A. Salem, L. J. Ghosn, and M. G. Jenkins, "A Strain Gage Technique to Measure Stable Crack Extension in Ceramics," in *Post Conference Proceedings of the 1997 SEM Spring Conference on Experimental Mechanics* (Society for Experimental Mechanics, Bethel, Connecticut, 1997) pp. 1-8.
13. J.A. Salem, L.J. Ghosn, and M. Jenkins, "Back-Face Strain as A Method for Monitoring Stable Crack Extension," in *Ceramic Engineering and Science Proceedings*, Vol. 19, Issue 3-4, (Am. Ceramic Soc, Westerville, OH, 1998) pp. 587-594.
14. M.G. Jenkins, M.K. Ferber, A. Ghosh, and J. Peussa and J.A. Salem "Chevron-Notch, Flexure Tests For Measuring the Elevated Temperature Fracture Resistance's of Structure Ceramics," in *Chevron - Notch Test Experience: Metals and Non-Metals*, ASTM STP 1172, edited by K. R. Brown & F. I. Baratta (American Society for Testing and Materials, Philadelphia, Pennsylvania, 1992) pp. 159-177.
15. F.I. Baratta, and W.I. Dunlay, "Crack Stability in Simply Supported Four-Point and Three-Point Loaded Beams of Brittle Materials," *Mechanics of Materials*, **10**, 149-159 (1990).
16. J.A. Salem, L.J. Ghosn, M.G. Jenkins, and G.D. Quinn, "Stress Intensity Factor Coefficients for Chevron-Notched Flexure Specimens and Comparison of Fracture Toughness Methods," *Ceramic Engineering and Science Proceedings*, Vol. 20, No. 3, 503-512 (1999).

17. I. Bar-on, F.I. Baratta, and K. Cho, "Crack Stability and its Effect on Fracture Toughness of Hot Pressed Silicon Nitride Beam Specimens," *Journal of American Ceramic Society*, Vol. 79, No. 9, 2300–2308 (1996).
18. J. J. Swab and G. D. Quinn, "Effect of Precrack "Halos" on K_{Ic} Determined by the Surface Crack in Flexure Method," *ibid.*, 81 [9] 2261–2268 (1998).
19. V. Tikare and S.R. Choi, "Combined Mode I and Mode II Fracture in Monolithic Ceramics," *J. Am. Ceram. Soc.*, 76 [9], 2265–72 (1993).
20. G. D. Quinn, J. J. Swab, and M. J. Motyka, "Fracture Toughness of a Toughened Silicon Nitride by ASTM C 1421," *ibid.*, 86 [6] pp. 1043–1045 (2003).
21. J.A. Salem, M.G. Jenkins, M.K. Ferber, and J.L. Shannon, Jr., "Effects of Pre-cracking Method on Fracture Properties of Alumina," in *Proceedings of Society of Experimental Mechanics Spring Conference on Experimental Mechanics*, Milwaukee, Wisconsin, June 10–13, (Society for Experimental Mechanics, Bethel, Connecticut, 1991) pp. 762–769.
22. G.K. Bansal and W. Duckworth "Comments on "Subcritical Crack Extension and Crack Resistance in Polycrystalline Alumina,"" *J. Mat. Sci. Letters*, No. 13, pp. 215–216, (1978).
23. J.A. Salem, J.L. Shannon, Jr., and M.G. Jenkins, "Some Observations in Fracture Toughness Testing with Chevron-Notched Specimens," in *Chevron-Notch Fracture Test Experience: Metals and Non-Metals*, ASTM STP 1172, edited by K.R. Brown and F.I. Baratta (American Society for Testing and Materials, West Conshohocken, PA, 1992) pp. 9–25.
24. J.A. Salem, J.L. Shannon, Jr. and R.C. Bradt, "Crack Growth Resistance of Texture Alumina," *Journal of the American Ceramic Society*, 72, [1], 20–27 (1989).
25. T. Fett, D. Munz, and G. Thun, "Fracture Toughness and R-Curve Behavior of PZT," Research Center, Karlsruhe, Technical Report KZKA 6058, July 1998.
26. K. Yasuda, T. Taguchi, J. Tatami, and Y. Matsuo, "Estimation of Short Crack R-Curves of Polycrystalline Ceramics by Surface Crack in Flexure Method," pp. 115–120 in *Improved Ceramics Through New Measurements, Processing and Standards*, Ceramic Transactions, vol. 133, (2002).
27. C.P. Freese, Unpublished Research, ARL, Watertown, MA.
28. J.C. Newman, Jr., and I.S. Raju, "An Empirical Stress-Intensity Factor Equation for the Surface Crack," *Engineering Fracture Mechanics*, Vol. 15, No. 1–2, 185–192 (1981).
29. J. Joch, J. Zemankova and J. Kazda, "Analysis of a Chevron-Notch Four-Point-Bend Specimen by the Three-Dimensional Finite-Element Method," *Comm. Am. Ceram. Soc.*, C154 - C155, March (1988).
30. R. Kolhe, C.Y. Hui, A.T. Zehnder, Effects of Finite Notch Width on the Fracture of Chevron-Notched Specimens," *International Journal of Fracture*, 94 (2): 189–198 (1998).
31. M.G. Jenkins, A.S. Kobayashi, K.W. White and R. Bradt, "A 3-D finite Element Analysis of a Chevron-notched, Three-Point Bend Fracture Specimen for Ceramic Materials," *Int. J. Fract.* 34, 281–295 (1981).
32. N. Murayama, S. Sakaguchi, and F. Wakai, "Evaluation of Fracture Toughness using SENB Specimens with Precrack Produced by Growing Microcrack Around Vickers Indent," *Journal of Ceramic Society of Japan, International Editions*, Vol. 95, pp. 980–982 (1987).
33. J.A. Salem, unpublished work.
34. G.D. Quinn, R.J. Getting, and J.J. Kübler, "Fracture Toughness of Ceramics by the Surface Crack in Flexure (SCF) Method," in *Fracture Mechanics of Ceramics*, Vol. 11, edited by R.C. Bradt, D.P.H. Hasselman, D. Munz, M. Sakai, and V. Yashevechenko (Plenum Press, New York, NY, 1996), pp. 203–218.
35. J.J. Petrovic, R.A. Dirks, L.A. Jacobson, and M.G. Mendiratta, "Effect of Residual Stress on Fracture from Controlled Surface Flaws," *J. of Am. Ceram. Soc.*, 59 [3–4] 177–178 (1976).
36. G.D. Quinn, R.J. Gettings, and J.J. Kübler, "Fractography and the Surface Crack in Flexure (SCF) Method for Evaluating Fracture Toughness of Ceramics," *Fractography of Glasses and Ceramics*, Ceramic Transactions, Vol. 64, American Ceramic Society, Westerville, OH, 1996, pp. 107–144.
37. G.D. Quinn and J.A. Salem, "Effect of Lateral Cracks on Fracture Toughness Determined by the Surface-Crack-in-Flexure Method," *J. Am. Ceram. Soc.*, 85 [4] 873–880 (2002).
38. W.G. Clark, and S.J. Hudak, *J. Testing and Eval.*, Vol. 3, No. 6, 454–476 (1975).
39. W.F. Deans, and C.E. Richards, "A Simple and Sensitive Method of Monitoring Crack Extension and Load in Compact Fracture Mechanics Specimens Using Strain Gages," *J. Testing and Eval.*, Vol. 7, No. 3, 147–154 (1979).

40. G.D. Quinn, R.J. Gettings, and J.J. Kübler, "Fractography and the Surface Crack in Flexure (SCF) Method for Evaluating Fracture Toughness of Ceramics," *Fractography of Glasses and Ceramics*, Ceramic Transactions, Vol. 64, (American Ceramic Society, Westerville, OH, 1996), pp. 107–144.
41. J.J. Swab, and G.D. Quinn, "Investigation of 'Halos' Associated with Fracture Toughness Pre-cracks," *Ceramic Engineering and Science Proceedings*, Vol. 18, No. 4, 1997, pp. 173–182.
42. A. Ghosh, M.G. Jenkins, K. W. White, A.S. Kobayashi, and R. Bradt, "Elevated Temperature Fracture Resistance of a Sintered α -Silicon Carbide," *J. Am. Ceram. Soc.*, Vol. 77, No. 2, 242–247, (February 1989).
43. D. Munz, R.T. Bubsey, and J.E. Srawley, "Compliance and Stress Intensity Coefficients for Short Bar Specimens with Chevron-notches," *Int. J. Fract.*, Vol. 16, No. 4 359–374 (1980).

PREDICTING THE RELIABILITY OF BRITTLE MATERIAL STRUCTURES SUBJECTED TO TRANSIENT PROOF TEST AND SERVICE LOADING

Noel N. Nemeth,¹ Osama M. Jadaan,² Tamas Palfi,³
and Eric H. Baker⁴

1. INTRODUCTION

Brittle materials today are being used, or considered, for a wide variety of high tech applications that operate in harsh environments, including static and rotating turbine parts, thermal protection systems, dental prosthetics, fuel cells, oxygen transport membranes, radomes, and MEMS. Designing brittle material components to sustain repeated load without fracturing while using the minimum amount of material requires the use of a probabilistic design methodology. The NASA CARES/*Life*¹ (Ceramic Analysis and Reliability Evaluation of Structures/*Life*) code provides a general-purpose analysis tool that predicts the probability of failure of a ceramic component as a function of its time in service. This capability includes predicting the time-dependent failure probability of ceramic components against catastrophic

¹ Research Engineer, Life Prediction Branch, NASA Glenn Research Center, Brookpark, OH, 44135

² Professor, College of Engineering, Mathematics, and Science, University of Wisconsin-Platteville, WI, 53818

³ Ph. D. Student, Budapest University of Technology and Economics, Budapest, Hungary

⁴ Research Engineer, Connecticut Reserve Technologies, 2997 Sussex Court, Stow, OH, 44224

rupture when subjected to transient thermomechanical loads (including cyclic loads). The developed methodology allows for changes in material response that can occur with temperature or time (i.e. changing fatigue and Weibull parameters with temperature or time). For this article an overview of the transient reliability methodology and how this methodology is extended to account for proof testing is described. The CARES/*Life* code has been modified to have the ability to interface with commercially available finite element analysis (FEA) codes executed for transient load histories. Examples are provided to demonstrate the features of the methodology as implemented in the CARES/*Life* program.

NOMENCLATURE

| | |
|---------------------------------|--|
| A | = slow crack growth coefficient (A_1 – power law, A_2 – Walker law) |
| A_e | = effective area |
| a | = crack length |
| B | = slow crack growth material parameter |
| \bar{C} | = Shetty shear sensitivity constant |
| CARES | = Ceramics Analysis and Reliability Evaluation of Structures |
| f_c | = cyclic frequency |
| FEA | = Finite Element Analysis |
| K_i | = Stress intensity factor ($i = I, II, III$ for modes I, II, or III, respectively) |
| K_{Ic} | = critical mode I stress intensity factor (fracture toughness) |
| K_{Ieq} | = equivalent mode I stress intensity factor from applied effective stress |
| $\overline{K}_{Ieq,cyclic,max}$ | = maximum mode I equivalent stress-intensity factor over a cycle |
| k_B | = normalized Batdorf crack density coefficient |
| m | = Weibull modulus (scatter parameter) |
| N | = slow crack growth exponent |
| P_{fa} | = attenuated probability of failure from proof test and service load |
| P_f | = probability of failure ($P_f = 1 - P_s$) |
| $P_s(t_f)$ | = probability of survival at time $t = t_f$ |
| P_{Sa} | = attenuated probability of survival from proof test and service load |
| P_{Si} | = probability of survival from proof test and service load |
| P_{Sp} | = probability of survival from proof test |
| Q | = Walker law R-ratio sensitivity exponent |
| R | = R-ratio; ratio of minimum stress divided by maximum cyclic stress |
| S | = surface area based property (indicates surface flaw analysis) |
| SCG | = Slow Crack Growth |
| T | = temperature |
| t | = time |
| t_{min} | = service time after proof test where no failure should occur |
| $t_{min,1,eff}$ | = effective service time after proof test where no failure should occur for an applied static stress of $\sigma_{Ieq,1,Tmax,p}$ based on the properties of time step 1 |
| $t_{p,1,eff}$ | = effective proof test time for an applied static stress of $\sigma_{Ieq,1,Tmax,p}$ based on the properties of time step 1 |

| | |
|------------------------------|---|
| $t_{q,1,eff}$ | = effective time for an applied static stress of $\sigma_{Ieq,1,Tmax,p}$ based on the properties of time step 1 for all time steps (service and proof test) |
| t_p | = proof test time |
| t_q | = total time in proof testing and service |
| V | = volume, or volume based property (indicates volume flaw analysis) |
| V_e | = effective volume |
| Y | = crack geometry correction factor |
| x,y,z | = represents a location in the body of the structure |
| Z | = number of load blocks or number of cycles |
| Z_e | = number of service load blocks or number of cycles |
| Z_p | = number of proof test load blocks or number of cycles |
| Δ | = increment or difference |
| Δt_j | = duration of time step j |
| σ_f | = represents the peak stress in a component |
| σ_{Ieq} | = equivalent mode I far-field stress |
| $\sigma_{Ieq,j}$ | = equivalent mode I far-field stress during the step j |
| $\sigma_{Ieq,k,Tmax}$ | = maximum transformed stress over k time steps (using the properties of step k) |
| $\sigma_{Ieq,\kappa,Tmax}$ | = maximum transformed stress over κ steps (using the properties of step κ) |
| $\sigma_{Ieq,\zeta,Tmax}$ | = maximum transformed stress over ζ time steps (using the properties of step ζ) |
| $\sigma_{Ieq,1,Tmax,e}$ | = maximum transformed stress over the service load time steps (using the properties of step 1) |
| $\sigma_{Ieq,1,Tmax,p}$ | = maximum transformed stress over the proof test time steps (using the properties of step 1) |
| $\sigma_{Ieq,\kappa,Tmax,e}$ | = maximum transformed stress over the proof test time steps (using the properties of step κ) |
| $\sigma_{Ieq,\zeta,Tmax,e}$ | = maximum transformed stress over the service load time steps (using the properties of step ζ) |
| σ_n | = applied far-field stress normal to a crack face |
| σ_0 | = Weibull scale parameter |
| σ_{0B} | = Weibull scale parameter incorporating the effect of \bar{k}_B |
| σ_θ | = characteristic strength (value of σ_f where 63.21% of specimens fail) |
| τ | = applied far-field shear stress on a crack face |
| Ψ | = represents a location (x,y,z) and crack orientation (α,β) |
| $d\Omega$ | = $\sin \alpha d\alpha d\beta$ |

2. BACKGROUND

Ceramic materials display a stochastic strength response because of the combination of brittleness and the random nature of the size, orientation, and distribution of inherent microscopic flaws. In addition, the ability of ceramic structures to sustain loads degrades over time due to a variety of effects such as slow crack growth (SCG), cyclic fatigue, creep, and oxidation. Life prediction codes such as CARES/Life,¹ CERAMIC/ERICA², and STAU³ are available and have been demonstrated to

be successful in predicting the probability of ceramic components failing from spontaneous catastrophic rupture when these components are subjected to multiaxial loading and SCG conditions. For the CARES/*Life* code this includes a generalized approach that enables the calculation of component failure probability when loading and temperature varies over time. This capability is referred to as transient reliability analysis and can be used to predict component reliability (probability of survival) for situations such as thermal shock, startup and shutdown conditions in heat engines, and cyclic loading. This computational methodology is an extension to the work of Paluszny and Nichols,⁴ Stanley and Chau⁵ and Ziegler.⁶

For the CARES/*Life* program the transient reliability analysis methodology is developed with the following capabilities:

- a) Fast-fracture transient analysis (reliability analysis without SCG).
- b) SCG transient modeling with SCG and Weibull parameters (including the shape parameter, m) allowed to vary with temperature.
- c) Computationally efficient algorithm to compute reliability for cyclic loading.
- d) Cyclic fatigue modeling using a combined SCG and Walker fatigue law.
- e) Transient proof test capability.

Three example problems are shown; 1) A disk in thermal shock to illustrate fast-fracture transient analysis, 2) a diesel engine exhaust valve to contrast predictions for cyclic loading and proof testing, and 3) the hypothetical effect of changing Weibull and fatigue parameters over time on the reliability of alumina flexure bars in static fatigue.

3. METHODOLOGY

The detailed development of the transient reliability methodology for SCG has been described previously^{7,8} and will not be repeated here. Instead a highlight of these equations will be presented as well as a proposed relation for transient proof testing.

The CARES/*Life* software describes the probabilistic nature of material strength using the Weibull cumulative distribution function.⁹ For uniaxially stressed components the 2-parameter Weibull distribution for volume residing flaws describes the component *fast-fracture* failure probability, P_{fV} , as

$$P_{fV} = 1 - \exp \left[- \frac{1}{\sigma_0^{mv}} \int_V \sigma(x,y,z)^{mv} dV \right] \quad (1)$$

where V is the volume, terms that are a function of volume have V in the subscript, $\sigma(x,y,z)$ is the uniaxial stress at a point location in the body, and m and σ_0 are the shape and scale parameters of the Weibull distribution, respectively. The shape parameter is a (unitless) measure of the dispersion of strength while the scale parameter is the characteristic strength of a unit volume of material in uniaxial tension and has units of stress \cdot volume^{1/ m} . An analogous equation based on surface area can be shown for flaws that exclusively reside on the component surface. However, for the sake of brevity this paper is restricted to showing volume flaw based relations only.

Determination of the Weibull parameters comes from rupture experiments of specimens in simple tension or flexure. Regression techniques such as least squares and maximum likelihood have been developed that can determine these parameters from a simplified form of Eq. (1);

$$\begin{aligned}
 P_{fV} &= 1 - \exp \left[- \int_V \left(\frac{\sigma(x, y, z)}{\sigma_f} \right)^{m_V} dV \left(\frac{\sigma_f}{\sigma_{0V}} \right)^{m_V} \right] \\
 &= 1 - \exp \left[- \left(\frac{\sigma_f}{\sigma_{0V}} \right)^{m_V} \right] = 1 - \exp \left[- V_e \left(\frac{\sigma_f}{\sigma_{0V}} \right)^{m_V} \right]
 \end{aligned}
 \tag{2}$$

where σ_f is the peak stress in the specimen, σ_{0V} is the specimen characteristic strength, and V_e is known as the effective volume.

To predict component reliability for multiaxial stress states the Batdorf theory^{10,11} is used. Batdorf theory combines the weakest link theory with linear elastic fracture mechanics. It includes the calculation of the combined probability of the critical flaw being within a certain size range and being located and oriented so that it may cause fracture.

Slow crack growth refers to the stable extension of a crack over time. It results from the combination of stress at the crack tip and chemical attack such that chemical bonds break and the crack tip extends. At high temperatures it can also occur from the action of stress and the loosening of viscous phases such that material at the crack tip displaces. The crack length, a , as a function of time, t , can be expressed as a power law¹² with the following form

$$\frac{da(\Psi, t)}{dt} = A(x, y, z, t) K_{Ieq}^{N(x, y, z, t)}(\Psi, t)
 \tag{3}$$

where K_{Ieq} is the equivalent mode I stress intensity factor from the applied effective stress, (Ψ, t) denotes a term that is a function of Ψ (indicating a location (x,y,z) and crack orientation described by angles α , and β) and t , and A and N are material parameters that depend on the temperature and environment and hence become a function of time and location but not orientation.

To take into account the time dependence of loading and material response, the stress history for each finite element i is discretized into short time steps (Δt_j) during which the stress and material parameters are assumed to remain constant over that time step interval. For a specific time step j , the applied equivalent stress in element i is given by $\sigma_{Ieq, j}$, the temperature T_j , the scale parameter σ_{0Vj} , the Weibull modulus m_{Vj} , the fatigue constant B_{Vj} , and the fatigue exponent N_{Vj} . At time Zt_k (for k time steps per cycle over Z number of cycles) the component survival probability, using the Batdorf approach, can be expressed in it's most computationally efficient form as⁸

$$\begin{aligned}
 P_{SV}(Zt_k) &= \exp \left\{ - \sum_{i=1}^n \frac{V_i}{4\pi} \int_{\Omega} \left[\dots \left[\left(\frac{\sigma_{Ieq, k, T} \max}{\sigma_{0BVk}} \right)^{N_{Vk}-2} + \right. \right. \right. \\
 &\quad \left. \left. \frac{\sigma_{Ieq, k}^{N_{Vk}} Z \Delta t_k}{\sigma_{0BVk}^{N_{Vk}-2} B_{Vk}} \right]_k \frac{m_{Vk}(N_{Vk}-2)}{m_{Vj}^{m_{Vk}(N_{Vk}-2)}} + \frac{\sigma_{Ieq, j}^{N_{Vj}} Z \Delta t_j}{\sigma_{0BVj}^{N_{Vj}-2} B_{Vj}} \right]_j \frac{m_{Vj}(N_{Vj}-2)}{m_{V1}^{m_{Vj}(N_{Vj}-2)}} + \dots + \frac{\sigma_{Ieq, 1}^{N_{V1}} Z \Delta t_1}{\sigma_{0BV1}^{N_{V1}-2} B_{V1}} \right]_1 \frac{m_{V1}}{m_{V1}^{m_{V1}-2}} d\Omega \Big\}
 \end{aligned}
 \tag{4}$$

where, in Eq. (4) $j = (k-1)$, $i = (j-1) = (k-2)$ and

$$\sigma_{0BVj} = \left(\frac{\sigma_{0Vj}}{[\bar{k}_{BVj}]^{1/m_{Vj}}} \right) \tag{5}$$

$$B_{Vj} = \frac{2}{A_j Y^2 K_{IC,j}^{N_{Vj}-2} (N_{Vj} - 2)} \tag{6}$$

Most of the terms in these equations are functions of Ψ and t . The fatigue parameter B has units $\text{stress}^2 \times \text{time}$. Y is the crack geometry correction factor, K_{IC} is the critical mode I stress intensity factor, and $d\Omega = \sin \alpha d\alpha d\beta$. The term $\sigma_{Ieq,k,T \max}$ represents the effective stress examined over k time steps (entire load history) which yields the highest fast-fracture failure probability⁵⁻⁸. It can be computed by

$$\sigma_{Ieq,k,T \max} = \text{Max}(\sigma_{Ieq,1,k}, \sigma_{Ieq,2,k}, \dots, \sigma_{Ieq,i,k}, \dots, \sigma_{Ieq,k,k}) \tag{7}$$

where

$$\sigma_{Ieq,i,k} = \sigma_{0BVk} \left(\frac{\sigma_{Ieq,i}}{\sigma_{0BVi}} \right)^{\frac{m_{Vj}}{m_{Vk}}} \tag{8}$$

and $\sigma_{Ieq, i, k}$ is the transformed stress during time step i , using the properties of time step k .

For non-cyclic loading where the entire load history is made up of one transient cycle, Z is set equal to 1 in Eq. (4). In this case no approximation is used in the analysis and the solution yields the most accurate results. Equation (4) was developed based on an approach of using flaw strength and maintaining compatibility of failure probability between discrete time steps. This methodology allows for the introduction of a variable Weibull modulus as a function of time or temperature. The effective stress $\sigma_{Ieq, j}$ represents an equivalent normal stress on the crack face caused by the combined action of the normal stress $\sigma_{n, j}$ and the shear stress τ_j on the crack face, oriented normal to angles α and β – which define the orientation of the flaw. A mixed-mode fracture criterion and an assumed crack shape define the relationship for the equivalent stress. A parameter, \bar{C} , known as the Shetty shear-sensitivity coefficient¹³, is used in CARES/*Life* to weight the contribution of τ_j relative to $\sigma_{n,j}$ for the equivalent stress. Shetty¹³ has found this parameter to range between $0.80 \leq \bar{C} \leq 2.0$. As \bar{C} increases, the response becomes progressively more shear insensitive. The term \bar{k}_{BVj} in Eq. (5) is the normalized Batdorf crack density coefficient for volume flaws. It is used in the reliability equation for compatibility purposes. It insures that the multiaxial Batdorf theory collapses to the basic uniaxial Weibull equation (Eq. 1) when a uniaxial stress state is applied for a single time step solution. It needs to be clarified that for increased numerical accuracy CARES/*Life* further subdivides each of the elements into their constituent Gaussian integration points and performs calculations in Eqs. (4)-(8) based on these values.

3.1. Combined Fatigue and SCG Behavior

Equation (4) for component reliability is based on the power law shown in Eq. (3). This equation is affected by the shape of the cyclic wave form and is predicted to be

less damaging than static loading - when the static load is the peak stress of the wave form applied over the same service time as the cyclic load. Glasses seem to follow this behavior well, while polycrystalline materials may show more complex behavior under cyclic loading. Damage from cyclic loading can be caused by a variety of effects, such as debris wedging or the degradation of bridging ligaments, but essentially it is based on the accumulation of some type of irreversible damage that tends to enhance the crack growth. To empirically account for cyclic effects the CARES/*Life* program has implemented the Walker law¹⁴, which traditionally has been used for metal fatigue, superimposed with the power law¹⁵

$$\frac{da(\Psi, t)}{dt} = A_{1V}(x, y, z, t)K_{Ieq}(\Psi, t)^{N_V(x, y, z, t)} + f_c A_{2V}(x, y, z, t)K_{Ieq, cyclic_{max}}(\Psi, t)^{N_V(x, y, z, t) - Q_V(x, y, z, t)} \Delta K_{Ieq}(\Psi, t)^{Q_V(x, y, z, t)} \tag{9}$$

where A_1, A_2, N , and Q are material constants which depend on temperature, $K_{Ieq}(\Psi, t)$ is mode I equivalent stress-intensity factor at location/orientation Ψ , $K_{Ieq, cyclic_{max}}(\Psi, t)$ is the maximum mode I equivalent stress-intensity factor (*i.e.*, the maximum value of K_{Ieq} over the cycle at location/orientation Ψ), $\Delta K_{Ieq}(\Psi, t)$ is the range of mode I equivalent stress-intensity factor at Ψ , and f_c is the frequency. A methodology for estimating these parameters from cyclic fatigue specimen rupture data is described in Rahman¹⁵. The values of A_1, A_2, N , and Q in Eq. (9) depend on location x, y, z and time t . It is assumed that $da(\Psi, t)/dt$ is continuous at fractions of a cycle, that is, it is assumed that $da(\Psi, t)/dt$ could be computed for non-integer (real number) cycle counts. The advantage Eq. (9) has over the Walker law for ceramic materials is that when the range of the stress intensity factor ΔK_{Ieq} is zero, crack growth is not predicted to be zero in the presence of a static load. Following the same derivation methodologies from Jadaan et al.⁷ and Nemeth et al.⁸ an equation similar to Eq. (4) can be constructed

$$P_{SV}(Zt_k) = \exp \left\{ - \sum_{i=1}^n \frac{V_i}{4\pi} \left[\int_{\Omega} \left[\left(\frac{\sigma_{Ieq,k,T_{Max}}}{\sigma_{0BVk}} \right)^{N_{Vk}-2} + \frac{\sigma_{Ieq,k}^{N_{Vk}} \left\{ 1 + \left(\frac{\sigma_{Ieq,k,T_{Max}}}{\sigma_{Ieq,k}} \right)^{N_{Vk}} f_c \left(\frac{A_2}{A_1} \right)_{Vk} (1-R)^{Q_{Vk}} \right\} Z \Delta t_k}{\sigma_{0BVk}^{N_{Vk}-2} B_{Vk}} \right]^k \frac{m_{Vj}(N_{Vj}-2)}{m_{Vj}(N_{Vj}-2)} \right. \right. \\ \left. \left. + \frac{\sigma_{Ieq,j}^{N_{Vj}} \left\{ 1 + \left(\frac{\sigma_{Ieq,j,T_{Max}}}{\sigma_{Ieq,j}} \right)^{N_{Vj}} f_c \left(\frac{A_2}{A_1} \right)_{Vj} (1-R)^{Q_{Vj}} \right\} Z \Delta t_j}{\sigma_{0BVj}^{N_{Vj}-2} B_{Vj}} \right]^j + \dots \right. \\ \left. + \dots \frac{\sigma_{Ieq,l}^{N_{Vl}} \left\{ 1 + \left(\frac{\sigma_{Ieq,l,T_{Max}}}{\sigma_{Ieq,l}} \right)^{N_{Vl}} f_c \left(\frac{A_2}{A_1} \right)_{Vl} (1-R)^{Q_{Vl}} \right\} Z \Delta t_l}{\sigma_{0BVl}^{N_{Vl}-2} B_{Vl}} \right]^1 \frac{m_{Vl}}{(N_{Vl}-2)} d\Omega_j \right\} \tag{10}$$

where R is the R -ratio, shown below as a function of Ψ and t

$$R(\Psi, t) = \frac{\sigma_{\text{Ieq,cyclic}_{\min}}(\Psi, t)}{\sigma_{\text{Ieq,cyclic}_{\max}}(\Psi, t)} \quad (11)$$

There are limitations associated with Eq. (10) and its implementation in *CARES/Life*. The first is that the equation represents an averaging of properties over the cycle. There is no weighting given to whether the time step is at the peak or trough of the cycle – all time steps are weighted equally regarding their damage contribution. Thus, Eq. (10) is not a true thermomechanical fatigue methodology for brittle material transient reliability analysis. It is however accurate when parameters are constant over the cycle. In *CARES/Life* $R(\Psi, t)$ is calculated by examining all the time steps.

3.2. Proof Testing

Prior to placing a ceramic component in service, confidence that it will perform reliably is usually demonstrated through proof testing. Ideally, the boundary conditions applied to a component under proof testing simulate the conditions that the component would be subjected to in service. Additionally the proof test loads are designed to be appropriately greater in magnitude over a fixed time interval t_p . After proof testing, the survived component is placed in service with greater confidence in its integrity and a predictable minimum service life, t_{\min} , where no failure should theoretically occur.

The attenuated probability of failure, P_{fav} , of a component surviving proof testing over time t_p and subjected to operational (service) loading over a time interval t_e is

$$P_{\text{fav}}(t_q) = 1 - P_{\text{Sav}}(t_q) = 1 - \frac{P_{\text{SV}}(t_q)}{P_{\text{SV}}(t_p)} \quad (12)$$

where $t_q = (t_p + t_e)$. The term $P_{\text{SV}}(t_p)$ is the probability of survival of a component subjected to a proof test over a time interval denoted by t_p . The term $P_{\text{SV}}(t_q)$ is the probability of survival of a component subjected to a proof test over time interval t_p and service loading over time interval t_e . The reliability of the survived component increases as the ratio of the proof test stress to the service stress increases.

In the *CARES/Life* program the computation associated with Eq. (12) is not performed at the component level, but rather at Ψ - a given x,y,z location and flaw orientation α, β . This allows that the proof test loading does not have to exactly simulate the service loading. For example, the attenuated failure probability can be computed for the case when proof test load and the service load are applied in different directions. Further details of this methodology are described in Nemeth et al.¹ and the extension to transient reliability analysis is subsequently described herein. This methodology is developed by taking the transient loading condition (at Ψ) and re-casting it as an equivalent static stress applied over an equivalent time. The equivalent static stress is set equal to the peak stress found over the duration of the proof test. The weakest flaw that could survive the proof test (at Ψ) is assumed to be of strength just greater than the peak proof test stress (i.e. the strength of the weakest

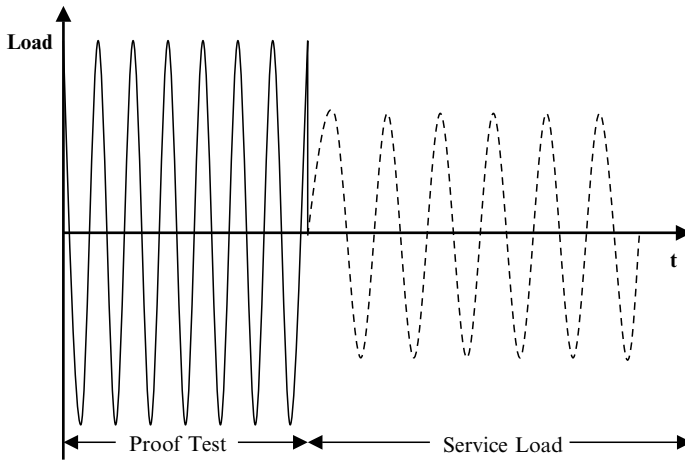


Figure 1. Schematic diagram of proof test and service loading versus time.

flaw at time $t = t_p$ just exceeds the peak stress seen over the proof test). Therefore this methodology does not consider a circumstance where the weakest flaw that could survive the proof test could be lower in strength than the peak proof test load at the end of the proof test (at time $t = t_p$). This limitation should be acceptable since typically the proof test is of short duration (such that SCG is minimized) and unloading is performed quickly after peak load is attained (again so that SCG is minimized) so that a component surviving the proof test with a weakest flaw (at Ψ) with a strength (significantly) less than the peak stress is not possible.

The loading history for the proof test is denoted by Z_p , which represents the number of proof test cycles, and for the service history Z_e represents the number of service load cycles. The equation for the survival probability for the proof test, $P_{SV}(t_p)$, is straightforward and is identical to Eq. (4), except shown here with different subscripts representing the proof test conditions. The component survival probability $P_{SV}(t_p)$ for the proof test condition is

$$P_{SV}(t_p) = \exp \left\{ - \sum_{i=1}^n \frac{V_i}{4\pi} \int_{\Omega} [X_p(\Psi)]_1^{\frac{m_{V1}}{N_{V1}^2}} d\Omega_i \right\} \tag{13}$$

where (in it's most computationally efficient form)

$$X_p(\Psi) = \left\{ \left[\dots \left[\left(\frac{\sigma_{Ieq,\kappa,T \max}}{\sigma_{0BV\kappa}} \right)^{N_V \kappa^{-2}} + \frac{\sigma_{Ieq,\kappa}^{N_V \kappa} Z_p \Delta t_{\kappa}}{\sigma_{0BV\kappa}^{N_V \kappa - 2} B_{V\kappa}} \right]_{\kappa}^{\frac{m_{V\kappa}(N_V(\kappa-1)-2)}{m_{V(\kappa-1)}(N_V\kappa-2)}} + \frac{\sigma_{Ieq,(\kappa-1)}^{N_V(\kappa-1)} Z_p \Delta t_{(\kappa-1)}}{\sigma_{0BV(\kappa-1)}^{N_V(\kappa-1)-2} B_{V(\kappa-1)}} \right]_{\kappa-1}^{\frac{m_{V(\kappa-1)}(N_V(\kappa-2)-2)}{m_{V(\kappa-2)}(N_V(\kappa-1)-2)}} + \dots + \frac{\sigma_{Ieq,1}^{N_{V1}} Z_p \Delta t_1}{\sigma_{0BV1}^{N_{V1}-2} B_{V1}} \right]_1^{\frac{m_{V1}(N_V\kappa-2)}{m_{V\kappa}(N_{V1}-2)}} \right\} \tag{14}$$

The proof test time steps are from 1 to κ for the first cycle of loading and a total of κZ_p time steps are involved with the proof test.

The service loading time steps for the first cycle of service loading are counted from $\kappa + 1$ to ζ . The authors chose this numbering scheme because they assume that from the transient finite element analysis the first κ time steps are for the proof test and that the service loading time steps number from $\kappa + 1$ to ζ . Running more than one cycle (or load block) of loading for the proof test and service loading in the transient finite element analysis is unnecessary (its redundant). Therefore a total of $(\zeta - \kappa)Z_e$ time steps are involved with the service loading. The overall component survival probability, $P_{SV}(t_q)$, for the combination of the proof test and the service loading is

$$P_{SV}(t_q) = \exp \left\{ - \sum_{i=1}^n \frac{V_i}{4\pi} \int_{\Omega} [X_q((\Psi))]_i^{\frac{m_{V1}}{N_{V1}-2}} d\Omega \right\} \tag{15}$$

where (in its most computationally efficient form)

$$\begin{aligned} X_q(\Psi) = & \left\{ \left[\dots \left[\left[\dots \left[\left[\left(\frac{\sigma_{Ieq,\zeta,T \max}}{\sigma_{0BV\zeta}} \right)^{N_{V\zeta}-2} + \frac{\sigma_{Ieq,\zeta}^{N_{V\zeta}} Z_e \Delta t_{\zeta}}{\sigma_{0BV\zeta}^{N_{V\zeta}-2} B_{V\zeta}} \right]_{\zeta}^{\frac{m_{V\zeta}(N_{V(\zeta-1)}-2)}{m_{V(\zeta-1)}(N_{V\zeta}-2)}} \right. \right. \right. \\ & + \frac{\sigma_{Ieq,(\zeta-1)}^{N_{V(\zeta-1)}} Z_e \Delta t_{(\zeta-1)}}{\sigma_{0BV(\zeta-1)}^{N_{V(\zeta-1)}-2} B_{V(\zeta-1)}} \Big]_{\zeta-1}^{\frac{m_{V(\zeta-1)}(N_{V(\zeta-2)}-2)}{m_{V(\zeta-2)}(N_{V(\zeta-1)}-2)}} + \dots + \frac{\sigma_{Ieq,(\kappa+1)}^{N_{V(\kappa+1)}} Z_e \Delta t_{(\kappa+1)}}{\sigma_{0BV(\kappa+1)}^{N_{V(\kappa+1)}-2} B_{V1}} \Big]_{(\kappa+1)}^{\frac{m_{V(\kappa+1)}(N_{V\kappa}-2)}{m_{V\kappa}(N_{V(\kappa+1)}-2)}} \\ & + \frac{\sigma_{Ieq,\kappa}^{N_{V\kappa}} Z_p \Delta t_{\kappa}}{\sigma_{0BV\kappa}^{N_{V\kappa}-2} B_{V\kappa}} \Big]_{\kappa}^{\frac{m_{V\kappa}(N_{V(\kappa-1)}-2)}{m_{V(\kappa-1)}(N_{V\kappa}-2)}} + \frac{\sigma_{Ieq,(\kappa-1)}^{N_{V(\kappa-1)}} Z_p \Delta t_{(\kappa-1)}}{\sigma_{0BV(\kappa-1)}^{N_{V(\kappa-1)}-2} B_{V(\kappa-1)}} \Big]_{\kappa-1}^{\frac{m_{V(\kappa-1)}(N_{V(\kappa-2)}-2)}{m_{V(\kappa-2)}(N_{V(\kappa-1)}-2)}} \\ & + \dots + \frac{\sigma_{Ieq,1}^{N_{V1}} Z_p \Delta t_1}{\sigma_{0BV1}^{N_{V1}-2} B_{V1}} \Big]_1 \left. \right\} \tag{16} \end{aligned}$$

The proof test time steps are from 1 to κ and the service time steps are from $\kappa + 1$ to ζ . Substituting Eq. (13) and Eq. (15) into Eq. (12) yields the expression for the attenuated survival probability

$$P_{SAV}(t_q) = \exp \left\{ - \sum_{i=1}^n \frac{V_i}{4\pi} \int_{\Omega} \left([X_q(\Psi)]^{\frac{m_{V1}}{N_{V1}-2}} - [X_p(\Psi)]^{\frac{m_{V1}}{N_{V1}-2}} \right) H(\Psi) d\Omega \right\} \tag{17}$$

The Heaviside function $H(\Psi)$ in Eq. (17) was originally used in Nemeth et al.¹ for static (non-time-varying loads) loads and constant Weibull and fatigue parameters. Its use here requires expressing variables in terms of equivalent peak static loads and equivalent times. Equivalent time is the comparable time interval for a static applied load that has the same amount of crack growth (or same reliability) as the transient load (load varying with time) situation. The Heaviside function $H(\Psi)$ in Eq. (17) is used where

$$\begin{aligned} H(\Psi) &= 1; \quad \sigma_{Ieq, 1, T \max, e}(\Psi) \geq \sigma_{Ieq, 1, T \max, p}(\Psi) \\ \text{Or, if } \sigma_{Ieq, 1, T \max, e}(\Psi) &< \sigma_{Ieq, 1, T \max, p}(\Psi) \text{ then} \\ H(\Psi) &= 1; \quad t_{\min, 1, eff}(\Psi) < t_{q, 1, eff}(\Psi) - t_{p, 1, eff}(\Psi) \\ H(\Psi) &= 0; \quad t_{\min, 1, eff}(\Psi) \geq t_{q, 1, eff}(\Psi) - t_{p, 1, eff}(\Psi) \end{aligned} \tag{18}$$

The Heaviside function accounts for $t_{\min,1,\text{eff}}(\Psi)$, the minimum effective service time interval in which reliability can not decrease based on the properties of time step 1. It is obtained by satisfying the condition $P_{SV}(t_q) = P_{SV}(t_p)$ locally at Ψ . For the whole component $t_{\min,1,\text{eff}}$ denotes the minimum value of $t_{\min,1,\text{eff}}(\Psi)$ when evaluated for all Ψ . If at any location the component proof test stress level is less than the service stress level, then an assured minimum effective lifetime $t_{\min,1,\text{eff}}$ does not exist and the component can not be assumed to survive for any given time during service loading. Note that t_{\min} as used here would denote the real time equivalent of $t_{\min,1,\text{eff}}$ for the transient loading condition. The equations for $t_{\min,1,\text{eff}}$ are described in the subsequent sections. $t_{p,1,\text{eff}}$ is the effective proof test time for an applied static stress of $\sigma_{\text{Ieq},1,T_{\text{max},p}}$ based on the properties of time step 1, and $t_{q,1,\text{eff}}$ is the effective time for an applied static stress of $\sigma_{\text{Ieq},1,T_{\text{max},p}}$ based on the properties of time step 1 for all time steps (service and proof test).

The subscript 1 in Eq. (18) indicates values transformed to equivalent values based on the properties of time step 1. $\sigma_{\text{Ieq},\kappa,T_{\text{max}}}$ is the maximized fast-fracture stress for the first $\kappa Z_{p,\text{Total}}$ time steps (the proof test time steps) expressed in terms of the properties of time step κ . The maximization procedure is identical to that described previously (see Eq. 7 and Eq. 8) except that the maximization is performed only over the proof test time steps 1 to κ . $\sigma_{\text{Ieq},1,T_{\text{max},p}}$ can be computed by

$$\sigma_{\text{Ieq},1,T_{\text{max},p}} = \text{Max}(\sigma_{\text{Ieq},1,1}, \sigma_{\text{Ieq},2,1}, \dots, \sigma_{\text{Ieq},i,1}, \dots, \sigma_{\text{Ieq},\kappa,1}) \tag{19}$$

where

$$\sigma_{\text{Ieq},i,1} = \sigma_{0BV1} \left(\frac{\sigma_{\text{Ieq},i}}{\sigma_{0BV_i}} \right)^{\frac{m_{V1}}{m_{V_i}}} \tag{20}$$

and $\sigma_{\text{Ieq},i,1}$ is the transformed stress during time step i , using the properties of time step 1. Similarly for the service loading time steps;

$$\sigma_{\text{Ieq},1,T_{\text{max},e}} = \text{Max}(\sigma_{\text{Ieq},(\kappa+1),1}, \sigma_{\text{Ieq},(\kappa+2),1}, \dots, \sigma_{\text{Ieq},(\kappa+i),1}, \dots, \sigma_{\text{Ieq},\zeta,1}) \tag{21}$$

To solve for $t_{p,1,\text{eff}}(\Psi)$ the proof test equation (Eq. 13) is re-expressed as an equivalent static load $\sigma_{\text{Ieq},1,T_{\text{max},p}}(\Psi)$ applied over an equivalent time $t_{p,1,\text{eff}}(\Psi)$

$$P_{SV}(t_p) = \exp \left\{ - \sum_{i=1}^n \frac{V_i}{4\pi} \int_{\Omega} \left[\left(\frac{\sigma_{\text{Ieq},1,T_{\text{max},p}}}{\sigma_{0BV1}} \right)^{N_{V1}-2} + \frac{\sigma_{\text{Ieq},1,T_{\text{max},p}}^{N_{V1}} t_{p,1,\text{eff}}}{\sigma_{0BV1}^{N_{V1}-2} B_{V1}} \right]^{\frac{m_{V1}}{N_{V1}-2}} d\Omega \right\} \tag{22}$$

And equating Eq. (22) and Eq. (13) results in

$$t_{p,1,\text{eff}} = \frac{\sigma_{0BV1}^{N_{V1}-2} B_{V1}}{\sigma_{\text{Ieq},1,T_{\text{max},p}}^{N_{V1}}} \left[X_p(\Psi) - \left(\frac{\sigma_{\text{Ieq},1,T_{\text{max},p}}}{\sigma_{0BV1}} \right)^{N_{V1}-2} \right] \tag{23}$$

To solve for $t_{q,1,\text{eff}}(\Psi)$ the combined proof test and service load reliability equation (Eq. 16) is re-expressed as an equivalent static load $\sigma_{\text{Ieq},1,T_{\text{max},p}}(\Psi)$ applied over an equivalent time $t_{q,1,\text{eff}}(\Psi)$

$$P_{SV}(t_q) = \exp \left\{ - \sum_{i=1}^n \frac{V_i}{4\pi} \int_{\Omega} \left[\left(\frac{\sigma_{\text{Ieq},1,T_{\text{max},e}}}{\sigma_{0BV1}} \right)^{N_{V1}-2} + \frac{\sigma_{\text{Ieq},1,T_{\text{max},p}}^{N_{V1}} t_{q,1,\text{eff}}}{\sigma_{0BV1}^{N_{V1}-2} B_{V1}} \right]^{\frac{m_{V1}}{N_{V1}-2}} d\Omega \right\} \tag{24}$$

And equating Eq. (24) and Eq. (15) assuming $\sigma_{Ieq,1,Tmax,p} > \sigma_{Ieq,1,Tmax,e}$, results in

$$t_{q,1,eff} = \frac{\sigma_{0BV1}^{N_{V1}-2} B_{V1}}{\sigma_{Ieq,1,Tmax,p}^{N_{V1}}} \left[X_q(\Psi) - \left(\frac{\sigma_{Ieq,1,Tmax,e}}{\sigma_{0BV1}} \right)^{N_{V1}-2} \right] \quad (25)$$

It is important to point out that the term for final strength in Eq. (24) is $\sigma_{Ieq,1,Tmax,e}$ and not $\sigma_{Ieq,1,Tmax,q}$. This condition is necessary since the final strength must be $\sigma_{Ieq,1,Tmax,e}$ when $\sigma_{Ieq,1,Tmax,p} > \sigma_{Ieq,1,Tmax,e}$ - where $\sigma_{Ieq,1,Tmax,p} > \sigma_{Ieq,1,Tmax,e}$ is a stipulation of Eq. (18) in order for $t_{min,1,eff}(\Psi)$ to exist. However, this violates the fast-fracture condition (when there is no SCG) that failure probability can not decrease over time. Equating Eq. (24) and Eq. (22) results in

$$t_{min,1,eff}(\Psi) = \frac{B_{V1}}{\sigma_{Ieq,1,Tmax,p}^2(\Psi)} \left[1 - \left(\frac{\sigma_{Ieq,1,Tmax,e}(\Psi)}{\sigma_{Ieq,1,Tmax,p}(\Psi)} \right)^{N_{V1}-2} \right] \quad (26)$$

where

$$t_{min,1,eff}(\Psi) = t_{q,1,eff}(\Psi) - t_{p,1,eff}(\Psi) \quad (27)$$

To make Eq. (26) and Eq. (27) true (solving for the equality in Eq. 27) requires iteratively finding the value of the service time t_e that satisfies the equality, however, this is computationally intensive. Fortunately, in order to perform the attenuated reliability analysis for the component only the sign of the inequality in Eq. (18) needs to be established locally at Ψ . This means that iteration is not necessary. Instead Eq. (26) is used to establish $t_{min,1,eff}(\Psi)$, which is used on the left-hand side of the inequality in Eq. (18). The right-hand side of the inequality in Eq. (18) is determined by computing $t_{q,1,eff}(\Psi)$ from Eq. (25) and $t_{p,1,eff}(\Psi)$ from Eq. (23).

For computational efficiency in the CARES/Life program the term for X_q in Eq. (25) is evaluated with $\sigma_{Ieq,1,Tmax,p}$ instead of $\sigma_{Ieq,1,Tmax,e}$. This is conservative and avoids having to evaluate X_q twice - once for Eq. (16) using $\sigma_{Ieq,1,Tmax,p}$ and once for Eq. (25) using $\sigma_{Ieq,1,Tmax,e}$.

4. EXAMPLES

4.1. Example 1: Thermal Shocked Disk In Fast-Fracture

In this example the fast-fracture reliability response of a laser induced thermal shocked disk made of silicon nitride is examined. The purpose is to see if the strength response of the disks from rupture data of simple beams in uniaxial flexure can be predicted. Also the transient fast-fracture reliability predictions of the disk versus the instantaneous fast-fracture reliability predictions of a given time step will be compared in order to verify the correctness and accuracy of the numerical algorithm. This example is derived from an international study¹⁶ involving laboratories from Germany, Japan, and the United States. Phase I of that study worked to develop and verify thermal up-shock techniques in which a disk specimen was centrally heated to fracture by an appropriate heating source, including laser, quartz lamp, shaped heating element, and gas torch. Phase II of the study involved a round-robin between

the three countries testing thermal fracture stress for two silicon nitrides, Allied-Signal's AS800 and Kyocera's SN282. For this example disk results from the Siemens AG organization, as provided by Rettig,¹⁷ for the SN282 material was used. These disks were tested using the laser irradiation technique described by Kirchoff¹⁸ and Rettig.¹⁹ Three-point flexure bar data that was provided by Ferber²⁰ was also used.

Thin disks 20 mm in diameter and 0.3 mm thick were centrally heated by a 800 W laser working in continuous wave mode. A large centrally heated area and a steep temperature gradient near the edge was created, which yielded high tensile stresses near the edge. The specimens were rapidly heated so that fracture would occur in less than a second. The temperature versus time response across the disk was measured with a fast scanning pyrometer. The heating time and the thinness of the disk were chosen such that through-thickness temperature gradients (and hence bending stresses) were negligible. Further details regarding the experimental set-up are found in Ferber et al.,¹⁶ Kirchoff et al.,¹⁸ and Rettig.¹⁹

A total of 15 disks were fractured. The time of rupture and the radius corresponding to the location of fracture was recorded for each specimen. Fracture stresses were computed by the study participants using the temperature profile at the instant of fracture, temperature dependent elastic modulus and thermal expansion coefficient, and integral equations from standard elasticity theory. Some of the disks were cut into three-point flexure specimens in order to independently quantify the strength characteristics. Fourteen of these flexure specimens were tested at room temperature with average size of 0.30 mm thick, 3.25 mm width, 15.00 mm long with a support span of 9.44 mm. The specimen edges were not beveled.

In order to perform the CARES/*Life* reliability analysis an ANSYS finite element model of the disk was prepared. The model comprised a 90° slice of the disk and spanned 1/2 the thickness (1/8 of the disk is modeled). Solid elements were used in the model. The disk was not constrained (other than to prevent rigid body motion) and thus was freely allowed to expand. Temperature dependent thermal expansion and elastic modulus values from Ferber et al.¹⁶ were used. The thermal loading profiles versus time for two specimens (designated as #3 and #9) as supplied by Rettig¹⁷ were used for the thermal loading. The temperatures were assumed constant through the thickness. Specimen #3 had the highest time to failure of 0.65 seconds and, hence, the highest reported fracture strength of 430 MPa from Ferber.¹⁶ Specimen #9 had an intermediate fracture strength of 340 MPa from Ferber.¹⁶ Figure 2 shows the transient thermal profile for specimen #3. Figure 3 shows the specimen #3 transient stress analysis results from the FEA. This figure shows the tangential (circumferential) stresses versus distance from the disk center. The tangential stresses are compressive near the disk center and become tensile towards the disk edge. The radial stresses are compressive over the entire disk and are not shown. The FEA analysis for specimen #3 consisted of 27 time steps ranging from 0.0 to 0.65 seconds, while the analysis for specimen #9 consisted of 15 time steps ranging from 0.0 to 0.35 seconds. The FEA transient tangential stress results compared very well with the numerical calculations performed by the Siemens group.

For the CARES/*Life* reliability analysis the Weibull parameters obtained from the three-point flexure bars were used to predict the strength response of the disks. Utilizing Eq. (2) with maximum likelihood analysis and assuming volume flaws a Weibull modulus $m_V = 11.96$, a characteristic strength $\sigma_{\theta V} = 612.7 \text{ MPa}$, and a Weibull scale parameter $\sigma_{0V} = 453.8 \text{ MPa} \cdot \text{mm}^{3/m}$ was obtained for the flexure

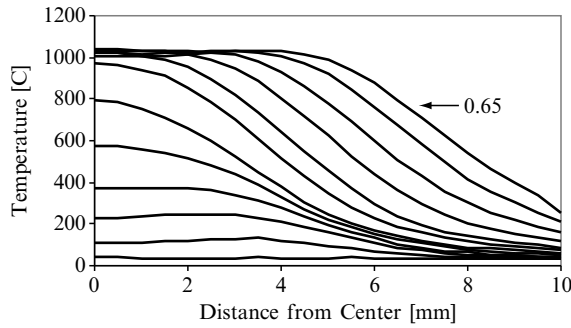


Figure 2. Disk specimen #3 transient thermal profile. Time steps range from 0.0 to 0.65 seconds. Not all time steps are shown.

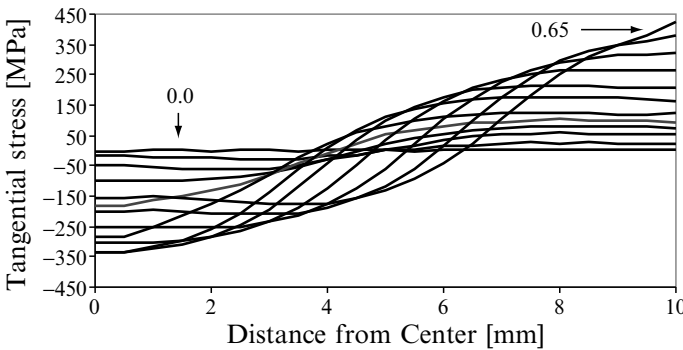


Figure 3. Disk specimen #3 transient tangential stress profile. Time steps range from 0.0 to 0.65 seconds. Not all time steps are shown.

bars tested at room temperature. Using these values of m_V and σ_{0V} and the results of the FEA with Eq. (4), the transient reliability response of the disk was calculated. For fast-fracture transient analysis, the time increment terms Δt can be set to zero and only $\sigma_{Ieq,k,Tmax}$ has to be determined. Since only one set of Weibull parameters at one temperature are used, $\sigma_{Ieq,k,Tmax}$ in this case is simply the maximum effective stress at Ψ of all time steps used in the analysis.

Material strength of ceramics (and hence Weibull and fatigue parameters) are known to be temperature dependent. Ferber¹⁶ shows this relationship for SN282, where average strength gradually lowers as temperature increases. However, this dependency is not considered in this analysis since only room temperature results were available for the bars cut from the disks. The authors believe this is still satisfactory since from Figure 2 the temperatures near the edge of the disk (where fracture is most likely to occur) are relatively low such that deviation of material properties from room temperature values should be limited.

Figure 4 shows the predicted failure probability versus time for specimens #3 and #9. These results are obtained using volume based analysis with the Batdorf multiaxial methodology, a Griffith crack and $\bar{C} = 0.82$. The plot shows straight line segments connecting the failure probability predictions for the various time steps. Each time step is based on analysis results from the experimentally measured temperature profile. The solid line shows the results of the transient analysis from Eq. (4),

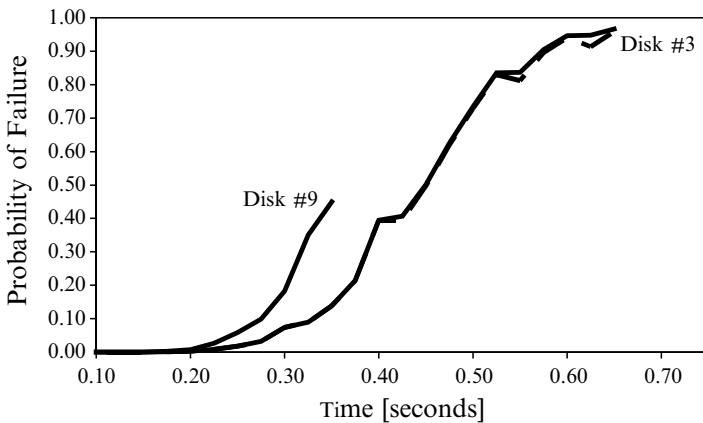


Figure 4. Failure probability as a function of time for disk specimens #3 and #9. Solid line is transient fast-fracture prediction and dotted line is fast-fracture prediction for a particular time step.

while the dotted line is results from fast-fracture analysis of the individual time steps. Notice that the dotted line occasionally shows a lower failure probability than a previous time step, while the solid line for the transient analysis correctly does not show this trend. Also, there is a close correlation between the transient fast-fracture results (solid line) and the single-time-step fast-fracture results (dotted line), increasing confidence of the validity of the transient solution algorithm. The solid line and the dotted line of disk #9 are virtually coincident. Disk #3 and disk #9 truncate at different failure probabilities because each failed at a different maximum stress σ_f . Another interesting observation is that disk #3 and disk #9 appear to have somewhat different failure probability responses versus time.

Figure 5 shows the predicted failure probability response of the disk versus the maximum stress σ_f in the disk. The experimentally obtained fracture stresses are overlaid for comparison. The curve for the three-point flexure bar results represents a line of best fit to the data as previously described ($m_V = 11.96$, and $\sigma_{\theta V} = 612.7 \text{ MPa}$) that was used to obtain the Weibull parameters used for the disk reliability analysis ($m_V = 11.96$, and $\sigma_{0V} = 453.8 \text{ MPa} \cdot \text{mm}^{3/m}$). The solid curve for the disk represents predictions based on the analysis of disk #3, while the more difficult to see dotted curve is the prediction from disk #9. Notice that the disk #9 results truncate around $P_f = 0.45$ consistent with Figure 4. The curves for disk #3 and #9 follow nearly the same path in Figure 5, unlike the results shown in Figure 4. A striking observation about figure 5 is the difference in median strength between the disk and the three-point flexure bar. This primarily represents the “Weibull size-effect” – meaning that a component with a larger amount of volume under high stress will have a lower average strength than a component with a smaller amount of volume under high stress, and is a direct consequence of Eq. (2).

Another interesting item worth commenting on is the significant difference between the Weibull modulus m_V for the three-point flexure bar rupture data ($m_V = 11.96$, $\sigma_{\theta V} = 612.7 \text{ MPa}$) and that of the thermal shocked disk ($m_V = 6.91$, $\sigma_{\theta V} = 345.9 \text{ MPa}$) experimental rupture data (shown in Figure 5) as determined by CARES/Life maximum likelihood parameter estimation. Least squares regression (using an Excel spreadsheet) on the CARES/Life disk predictions

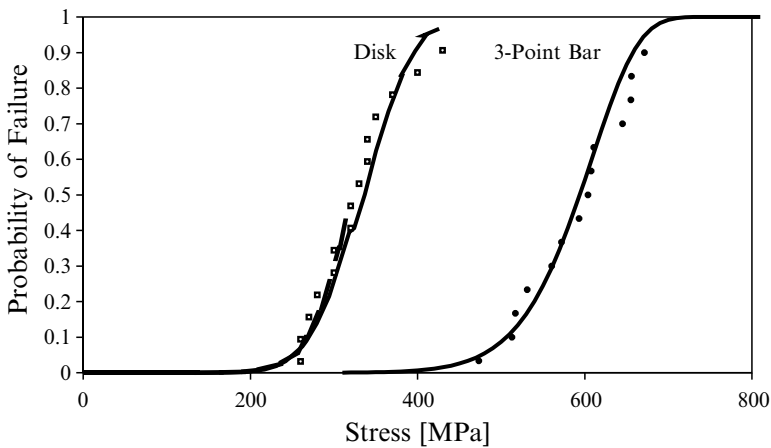


Figure 5. Predicted failure probability of disk versus stress, σ_f , using the Weibull parameters estimated from the 3-point flexure bar data. Solid line is for specimen #3 and dotted line is specimen #9. Experimental rupture data also shown.

curves shown in Figure 5 yields a Weibull modulus $m_V = 8.72$. This result is worthy of note because under usual circumstances the Weibull modulus for the test specimen and the designed component are presumed to be the same given that they are sampling similar flaw populations and that the effective volume V_e stays constant. Meaning, under usual circumstances, the Weibull modulus obtained from regression of the predicted disk failure probability curve versus strength would be 11.96 - the same value as the three-point flexure specimen data. The fact that in this case the Weibull moduli between the predicted desk response curve and the flexure bar data are significantly different can be understood by examining Figure 3. In the figure notice that as time increases, the amount of volume under high tensile stress significantly decreases. This has the effect of decreasing the effective volume V_e with time, and through the size effect, increasing predicted failure stress σ_f . The overall effect of this changing effective volume over time is to decrease the observed (apparent) Weibull modulus for the thermally shocked disks based on σ_f . The fact that CARES/*Life* predicts that the Weibull modulus obtained from the failure probability versus σ_f curve reduces to 8.7 compared to the flexure bar value of 12.0, compares favorably to the to the experimental disk result of 6.9. In other words, some of the discrepancy in the Weibull modulus values between the experimental disk and flexure bar results can be explained as a consequence of the transient thermal loads and how they influence the stress distribution in the disk as a function of time. The difference therefore is not necessarily indicative of some error or inconsistency. The remainder of the difference can be explained as natural statistical variation (within 90% confidence bounds).

The excellent correlation in Figure 5 to experimental results must be considered within the context of the underlying statistics, given that the effective volumes V_e between the three-point bend bar and the disk is large and sensitive to the value chosen for the Weibull modulus m_V . Because of the relative small number of samples tested (in this case 14 flexure specimens) and the large size effect, using Weibull parameters based on 90% confidence intervals from the three-point flexure bar data could shift the disk predictions significantly to the left and right of the experimental

data. In general a good design practice would be to avoid large size-effect scalings between specimens and components unless experimental data exists for both specimen and component such that data pooling practices can be taken advantage of to obtain a set of best-fit Weibull parameters.

4.2. Example 2: Diesel Exhaust Valve In Cyclic Loading

This example, involving a heavy-duty diesel ceramic exhaust valve (Corum et al.²¹), was selected to contrast failure probability predictions for power law, Walker law and a proof test condition. The valves were made of NT-551 silicon nitride material. Table 1 contains a summary of the Weibull and SCG parameters obtained from four-point flexure bars at three different temperatures (Andrews et al.²²). CARES/Life was used to obtain these parameters using the raw data listed in Andrews et al.²². Data to obtain values for the Walker law parameters did not exist, so assumed values for Q_V and A_2/A_1 were used.

Fifteen valves were engine tested without failure. These valves consisted of seven longitudinally machined valves and eight transversely machined valves. The transversely machined valves had been engine tested for 1000 hours while the longitudinally machined valves had been engine tested for 166 hours. These valves were subsequently tested in fast-fracture in order to examine their retained strength. The mode of failure for both valve-machining orientations was found to be volume induced.

Since all engine-tested valves failed due to volume flaws, the valve’s transient reliability was based on volume analysis. Figure 6 shows the pressure variation as a function of time during a typical combustion cycle of 0.0315 seconds. The pressure is applied to the valve’s face and other exposed surfaces within the cylinder. The maximum attained pressure during the combustion cycle was estimated to be 15.85 MPa (Corum et al.²¹). A 445 N (100 lb) force due to spring preload is applied to the valve stem when it is in the open position. At the moment the valve closes an impact force of 1335 N (300 lb) is applied to the valve stem. In addition, thermal stresses due to the temperature distribution in the valve are superposed to the mechanical stresses.

Figure 7 shows the approximate mean thermal profile in the valve. Steady-state thermal analysis using ANSYS FEA code was conducted to compute these temperatures. This figure shows that the temperature is maximum near the valve face and decays towards the valve seat and stem.

Transient reliability analysis (using Eq. 4 and Eq. 10) was conducted by dividing the load history into 29 time steps. During each step, the load was assumed constant. The loads corresponding to these time steps were modeled within the ANSYS FEA

Table 1. NT551 fast fracture and SCG material properties.

| T(°C) | m_V | $\sigma_{0V}(\text{MPa} \cdot \text{mm}^{3/m})$ | $\sigma_0(\text{Mpa})$ | N_V | $B_V(\text{MPa}^2 \cdot \text{sec})$ | Q_V | A_2/A_1 |
|-------|-------|---|------------------------|-------|--------------------------------------|-------|-----------|
| 20 | 9.4 | 1054 | 806 | 31.6 | 5.44e5 | 3.2 | 0.65 |
| 700 | 9.6 | 773 | 593 | 86.5 | 1.12e4 | 3.2 | 0.65 |
| 850 | 8.4 | 790 | 577 | 18.5 | 1.13e6 | 3.2 | 0.65 |

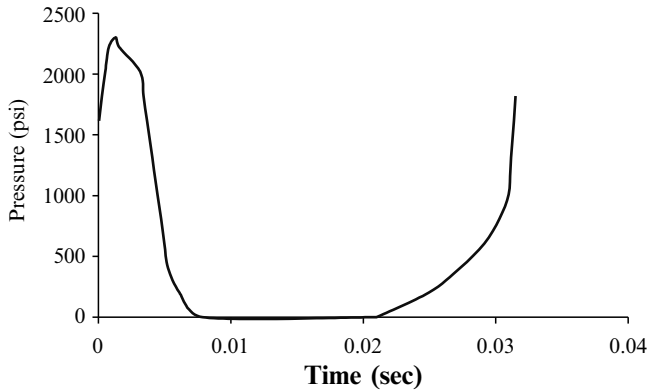


Figure 6. Pressure variation applied to the face of a ceramic valve during a typical engine combustion cycle.

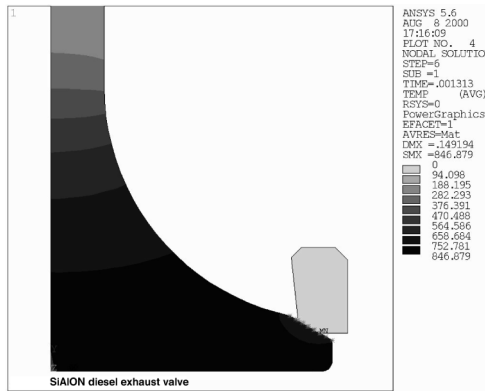


Figure 7. Mean thermal profile of the valve.

program, which yielded the stress results for these 29 time steps (stress history). Figure 8 highlights the first principal thermomechanical stress distribution in the valve at the moment of maximum applied pressure (at time step 6). From the figure it is apparent that the maximum stress location is at the valve radius, which is in agreement with the FEA results of Corum et al.²¹.

The valve’s stress history and other relevant terms (temperature, volume, material properties, element number, etc.) were subsequently read into CARES/Life. Figure 9 shows the predicted failure probability as a function of the number of cycles for various scenarios. None of the tested valves failed, 8 of the 15 of which were tested to 1000 hours (which corresponds to approximately 1.1×10^8 cycles). Thus the failure rate of the tested valves was less than 1 out of 8 at 1000 hours of operation. From Figure 9 it can be seen that in fast-fracture (at one cycle with no SCG) about 5 out of 100,000 valves are predicted to fail from the loading. With SCG and the power law about 20 out of 100,000 valves fail after 1000 hours operation. If we conservatively assume that a worst-case load (time step 6) is applied over the whole engine cycle (static loading), then about 40 out of 100,000 valves fail after 1000 hours. Using the combined Walker – power law with the hypothetical parameters from Table 1 this rate increases to 70 out of 100,000 valves at 1000 hours. All of these rates were well

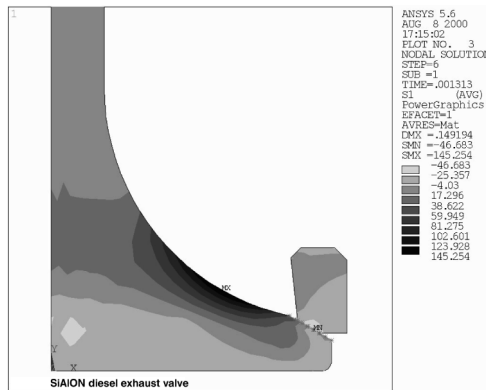


Figure 8. First principal stress distribution in the valve at the moment of maximum applied pressure (MPa).

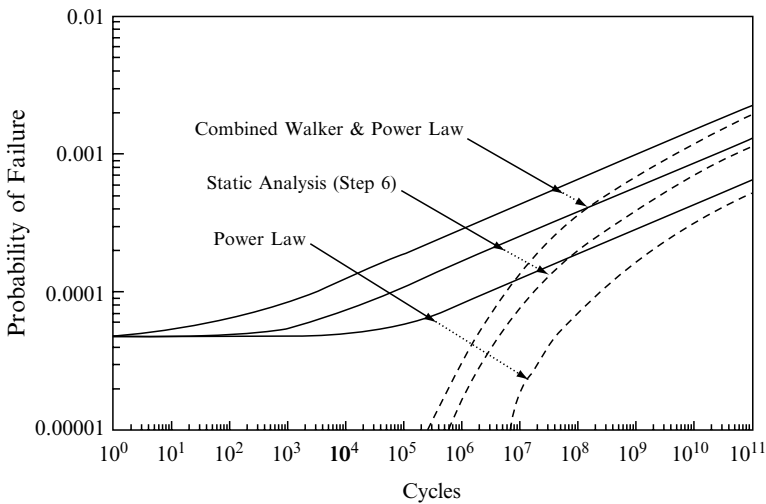


Figure 9. Failure probability versus cycles for proof test (dotted lines) and non-proof-test (solid lines) conditions for a static load, power law, and combined law.

below what was experimentally observed. These three scenarios were presented in order to contrast the predictions. The power law with cyclic loading predicts the least damage. The static loading scenario is predicted to be more damaging at double the rate of the cyclic loading. The combined Walker-power law predicts the most damage due to the enhanced cyclic fatigue effect.

Since the effect of cyclic loads is unknown, a more conservative assumption is to assume static loading, however even this assumption can be un-conservative.

To reduce the predicted failure rate even further, proof testing can be applied to prevent the weakest components (those with the highest likelihood of failing) from being placed into service. Figure 9 also shows the predicted results for the three various scenarios for an applied proof test of 10,000 cycles at a factor of 1.1 of the service loading (dotted lines in the figure). Increasing the proof test load reduces the attenuated probability of failure even further.

4.3. Example 3: Alumina In Static Fatigue - Material Properties Changing With Time

In this example it is examined how the reliability response of a vitreous bonded alumina is hypothetically affected by Weibull and fatigue parameters that change over time. The two scenarios that are presented are strictly based on curve fitting the data. The authors do not have the sufficient information necessary to physically specify which parameters are really responsible for the change in material response with time. However, the point of this analysis is to present an analytical model which potentially can explain the nonlinear and changing rupture behavior of the material given that the physical parameters that are responsible for the changing material behavior are known. This capability is potentially useful in modeling materials with changing composition (or changing physics of crack growth), including oxidation and crack blunting/healing phenomena.

The data for the example was obtained from Quinn²³ and consists of rupture lives of alumina four-point flexure bars in static fatigue (loading at a constant stress level over time). The specimens had average dimensions of 2.2 mm height, 2.8 mm width, a load span of 19.0 mm, and a support span of 38.0 mm. This data set was chosen from the literature because of its “non-ideal” behavior and the careful experimental technique reported by the author, which reduces the likelihood that equipment and measurement errors significantly affected the results. The rupture data for the individual specimens is shown in Figure 10. Testing was performed at 1000°C. The report stated that very little creep deformation was detected, and although fractography was attempted, it did not reveal the source of the strength limiting flaws.

Two trends make this data non-ideally behaved: 1) dramatically increased scatter at lower applied stresses, and 2) pronounced nonlinear behavior in the stress rupture data as the applied stresses became lower (the strength data shifted to the right which signified that the lives became longer than would have been predicted if the standard power law was applicable). An ideally behaved data set would show a

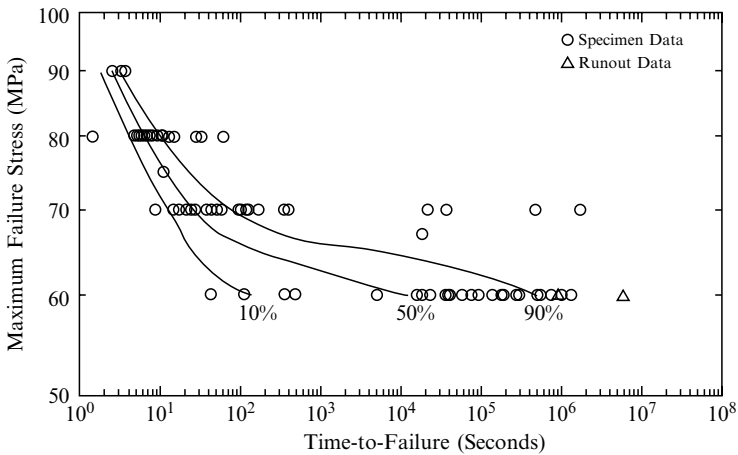


Figure 10. Affect on failure probability of changing fatigue exponent, N, with the log of time from Table 2 on static fatigue rupture data of an alumina at 1000° C.

straight line trend indicating that the fatigue exponent is constant, also the scatter band would appear with a constant width versus the applied stress indicating the Weibull modulus is constant.

A confirmatory piece of evidence that material properties were changing with time was obtained by performing static rupture experiments on specimens that were annealed (at no load) for either 1 or 24 hours at a temperature of 1050°C. The outcome of these treatments (not shown herein) was that life dramatically increased versus exposure time for an applied stress level (Quinn²³). Quinn²³ indicated that the observed behavior is probably due to the partial devitrification of the material’s glassy phase, resulting in an increased viscosity of the phase and a material with improved creep and stress rupture behavior. Quinn cites Wiederhorn et al.²⁴ to support this, although he concedes that crack blunting, healing, or residual stress changes could also be operative.

The data of Quinn defies the conventional modeling approach since the material properties could be changing over time. To account for this the authors show what happens when Weibull and fatigue parameters change with time for two cases; (1) changing the fatigue exponent N and the Weibull modulus m over time, and (2) changing the Weibull parameters (m and σ_0) over time. Tables 2 and 3 show the sets of parameters chosen to demonstrate these scenarios. Given the fact that no established parameter estimation techniques currently exist for this type of non-ideally behaved data, these parameters were iteratively selected to fit the data. Table 2 contains a set of parameters versus time where the fatigue exponent, N , and the Weibull modulus, m , were varied to yield an improved fit to the data. Table 3 shows a set of parameters where the Weibull modulus, m , is varied while the fatigue exponent, N , is kept relatively constant. Note that in both cases the scale parameter σ_0 is dependent on the Weibull modulus, and B is dependent on the fatigue exponent as well as the Weibull parameters. When applying these parameter sets within a reliability analysis, the Weibull and fatigue parameters are linearly interpolated with the log of time within the time spans listed in the tables and are held constant outside of the time span.

Because of the simplicity of the four-point specimen loading and geometry, results from FEA were not needed for the reliability analysis. Instead, a closed form expression for the effective area, A_e , was used to evaluate the integral of Eq.

Table 2. Weibull and fatigue parameters associated with Figure 10.

| t (seconds) | m_s | $(\sigma_{0s})(\text{MPa} \cdot \text{mm}^{2/m})$ | N_s | $B_s(\text{MPa}^2 \cdot \text{sec})$ |
|-------------|-------|---|-------|--------------------------------------|
| 1.6 | 29.4 | 156.8 | 6.7 | 2711.1 |
| 31.6 | 15.8 | 152.7 | 13.2 | 9707.7 |
| 1.0e5 | 13.1 | 127.3 | 36.4 | 2276.2 |

Table 3. Weibull and fatigue parameters associated with Figure 11.

| t (seconds) | m_s | $(\sigma_{0s})(\text{MPa} \cdot \text{mm}^{2/m})$ | N_s | $B_s(\text{MPa}^2 \cdot \text{sec})$ |
|-------------|-------|---|-------|--------------------------------------|
| 1.6 | 29.4 | 165.8 | 6.7 | 2711.1 |
| 31.6 | 7.4 | 263.3 | 8.0 | 2395.9 |
| 316.2 | 4.5 | 870.1 | 9.0 | 10,389.0 |

(2) for a surface flaw failure mode (Nemeth et al.²⁵). An effective area of 58.0 mm² was calculated based on a Weibull modulus value of 7.7. This value was chosen because sensitivity analysis using Eq. (2) indicated that the maximum error in strength for a given failure probability would be 1% or less for Weibull modulus values ranging between 5.0 and 30.0. This level of error is negligible for the illustrative purposes of this example. To model the transient material response 10 time steps are used per decade of the log of the time. Hence 10 time steps are used between 1 and 10 seconds, while 20 time steps are used between 1 and 100 seconds. The time steps are log increments of time – that is, they would appear as equally spaced increments in Figure 10 with 10 steps per decade.

Figure 10 shows the predicted 10%, 50%, and 90% failure probability iso-lines for the parameters shown in Table 2, while Figure 11 shows 1%, 10%, 30%, 50%, 70%, 90%, and 99% failure probability iso-lines for the parameters shown in Table 3. Neither plot represents an optimized set of fitted parameters. As previously stated no established parameter estimation techniques currently exist for this type of non-ideally behaved data. Parameters were obtained by segregating portions of the data and performing parameter estimation as described in Nemeth et al.¹ for the four-point bending bar specimen as well as further refinements by trial-and-error. Figure 10 shows that the curvature in the data can be captured by changing the fatigue exponent, *N*, however, accounting for the change in scatter still required modifying the Weibull modulus, *m*. Figure 11 is interesting because a satisfactory fit to the data can be obtained primarily by changing the Weibull modulus and scale parameter only (*B* is changing mainly in response to these parameters). The “kink” shown in the failure probability iso-lines between 10 and 100 seconds is not purposely modeled – that is, parameter values were not specifically selected to obtain this response. The “outlier” rupture data (data that appears to be not part of, or not consistent with, the main body of data) at long times to failure at 70 MPa and the “outlier” data at short times to failure at 60 MPa are better accounted for in this model compared to Figure 10. That is, data that visually appears as “outliers” are actually consistent with the

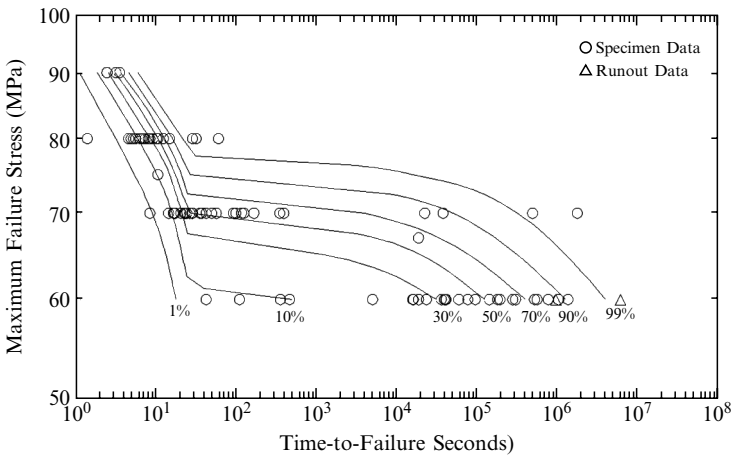


Figure 11. Affect on failure probability of changing Weibull modulus, *m*, with the log of time from Table 3 on static fatigue rupture data of an alumina at 1000°C.

flaw population failure probability response – in other words they are predicted to be there.

The modeling assumptions that produced the results in Figure 11 reasonably capture all of the trends in the data as well as or better than the approach used in Figure 10. Also, both approaches required changing the Weibull modulus m to account for the range of scatter. A changing Weibull modulus could be indicative of new flaw generation, or it could be indicative of changes of the physics of crack growth associated with R-curve behavior. On the other hand a changing fatigue exponent with time is consistent with crack blunting/healing phenomena, where the crack velocity relationship in Eq. (3) is changing with time. In this case further tests on the material would be needed to understand the underlying mechanism that was driving the SCG behavior.

5. CONCLUSIONS

A methodology for computing the transient reliability in ceramic components subjected to fluctuating thermomechanical loading was developed and incorporated into the CARES/*Life* code. This enables CARES/*Life* to be used to predict component reliability for situations such as thermal shock, startup and shutdown conditions in heat engines, and cyclic loading. The methodology accounts for varying material response, whether due to temperature or environmental changes by allowing Weibull and fatigue parameters to vary over the loading history. Examples demonstrating the viability of the technique for fast-fracture, cyclic loading, and proof testing, were presented.

6. ACKNOWLEDGEMENTS

We would like to thank Dr. Uwe Rettig and Dr. Matt Ferber for providing data from the IEA study on thermally shocked disks, and Dr. John Gyekenyesi for his support and technical direction over the years. We also thank Debbie Haught, DOE office of Industrial Technologies, and Carol Ginty, manager, NASA Hot Propulsion Components program.

REFERENCES

1. N. N. Nemeth, L. M. Powers, L. A. Janosik, and J. P. Gyekenyesi, Time-Dependent Reliability Analysis of Monolithic Ceramic Components Using the CARES/LIFE Integrated Design Program, *Life Prediction Methodologies and Data for Ceramic Materials, ASTM STP 1201*, C. R. Brinkman, and S. F. Duffy, Eds., American Society for Testing and Materials, Philadelphia, 1993, pp. 390–408.
2. A. D. Peralta, D. C. Wu, P. J. Brehm, J. C. Cuccio, and M. N. Menon, Strength Prediction of Ceramic Components Under Complex Stress States, Allied Signal Document No. 31–12637, 1995.
3. A. Heger, Stau Programm Berechnung,” Ph. D. Thesis, Karlsruhe University, Karlsruhe, Germany, 1991.
4. A. Paluszny, and P. F. Nicholls, “Predicting Time-Dependent Reliability of Ceramic Rotors, *Ceramics for High Performance Applications-II*, J. Burke, E. Lenoe, and N. Katz, Eds., Brook Hill, Chesnut Hill, Massachusetts, 1978.
5. P. Stanley, and F. S. Chau, A Probabilistic Treatment of Brittle Fracture Under Non-monotonically Increasing Stresses, *International Journal of Fracture*, Vol. 22, 1983, pp. 187–202.

6. C. Ziegler, Bewertung der Zuverlässigkeit Keramischer Komponenten bei zeitlich veränderlichen Spannungen und bei Hochtemperaturbelastung, Ph.D. Thesis, Karlsruhe University, Karlsruhe, Germany, 1998.
7. O. M. Jadaan, and N. N. Nemeth, Transient Reliability of Ceramic Structures, *Fatigue & Fracture of Engineering Materials and Structures*, Vol. 24, 2001, pp. 475–487.
8. N. N. Nemeth, and O. M. Jadaan, Transient Reliability of Ceramic Structures For Heat Engine Applications, Proceedings of the 5th Annual FAA/Air Force/NASA/Navy Workshop on the Application of Probabilistic Methods to Gas Turbine Engines, June 11–14, 2001, Westlake Ohio.
9. W. A. Weibull, A Statistical Theory of the Strength of Materials, *Ingeniörs Vetenskaps Akademiens Handlingar*, No. 151, 1939.
10. S. B. Batdorf, and J. G. Crose, A Statistical Theory for the Fracture of Brittle Structures Subjected to Nonuniform Polyaxial Stresses, *Journal of Applied Mechanics*, Vol. 41, No. 2, June 1974, pp. 459–464.
11. S. B. Batdorf, and H. L. Heinisch Jr., Weakest Link Theory Reformulated for Arbitrary Fracture Criterion. *Journal of the American Ceramic Society*, Vol. 61, No. 7–8, 1978, pp. 355–358.
12. S. M. Wiederhorn, Subcritical Crack Growth in Ceramics, *Fracture Mechanics of Ceramics*, R. C. Bradt, D. P. H. Hasselman, and F. F. Lange, Eds., Vol. 2, Plenum Press, New York, NY, 1974, pp. 613–646.
13. D. K. Shetty, Mixed-Mode Fracture Criteria for Reliability Analysis and Design with Structural Ceramics, *Journal of Engineering Gas Turbines & Power*, Vol. 109, No. 3, July 1987, pp. 282–289.
14. K. Walker, Effects of Environmental and Complex Load History on Fatigue Life, ASTM STP 462, American Society for Testing and Materials, Philadelphia, PA., 1970, pp. 1.
15. S. Rahman, N. N. Nemeth, and J. P. Gyekenyesi, Life Prediction and Reliability Analysis of Ceramic Structures Under Combined Static and Cyclic Fatigue, 1998 ASME Turbo Expo-Land, Sea, and Air, Stockholm Sweden, June 2–5, 1998, Paper No. 98-GT-569.
16. M. Ferber, G. Kirchoff, T. Hollstein, R. Westerheide, U. Bast, U. Rettig, and M. Mineo, Thermal Shock Testing of Advanced Ceramics – Subtask 9. International Energy Agency Implementing Agreement For a Programme of Research and Development on High Temperature Materials for Automotive Engines, prepared for The Heavy Vehicle Propulsion System Materials Program Oak Ridge National Laboratory for the U.S. Department of Energy, M00-107208, March 2000.
17. U. Rettig, Personal communication, August, 2002.
18. G. Kirchoff, M. Holzherr, U. Bast, and U. Rettig, Thermal Shock and Thermal Cycling Behavior of Silicon Nitride Ceramics, Proceedings of the International Conference on Silicon Nitride-Based Ceramics, October 4–6, 1994, Stuttgart, Germany. Published by Trans Tech Publications Ltd, Switzerland, in *Key Engineering Materials*, Vol. 89–91, 1994, pp. 605–610.
19. U. Rettig, Laserschock-Meßmethode – Ein Quantitatives Verfahren Zur Charakterisierung Der Temperature-Wechselbeständigkeit Hochfester Keramischer Werkstoffe, Eingereicht an der Fakultät Maschinenwesen der Technischen Universität Dresden zur Erlangung der Würde Eines Doktors der Ingenieurwissenschaften (Dr.-Ing.), October 16, 1997.
20. M. Ferber, Personal communication, July, 2002.
21. J. Corum, R. Battiste, R. Gwaltney, and C. Luttrell, Design Analysis and Testing of Ceramic Exhaust Valve for Heavy Duty Diesel Engine, Oak Ridge National Laboratory, ORNL/TM-13253, 1996.
22. M. A. Andrews, A. A. Wereszczak, T. P. Kirkland, and K. Breder, Strength and Fatigue of NT551 Silicon Nitride and NT551 Diesel Exhaust Valves, Oak Ridge National Laboratory, ORNL/TM-1999/332, 1999.
23. G. D. Quinn, Delayed Failure of a Commercial Vitreous Bonded Alumina, *Journal of Materials Science*, Vol. 22, 1987, pp. 2309–2318.
24. S. M. Wiederhorn, B. Hockey, K. Krause Jr., and K. Jakus, Creep and Fracture of a Vitreous-Bonded Aluminum Oxide, *Journal of Material Science*, Vol. 21, 1986, pp. 810.
25. Nemeth, N. N., Powers, L. M., Janosik, L. A., and Gyekenyesi, J. P., “Ceramics Analysis and Reliability Evaluation of Structures Life Prediction Program Users and Programmers Manual.” NASA Glenn Research Center, 1993.

ESTIMATION AND SIMULATION OF SLOW CRACK GROWTH PARAMETERS FROM CONSTANT STRESS RATE DATA

J. A. Salem and A. S. Weaver¹

ABSTRACT

Closed form, approximate functions for estimating the variances and degrees-of-freedom associated with the slow crack growth parameters n , D , B , and A^* as measured using constant stress rate (“dynamic fatigue”) testing were derived by using propagation of errors. Estimates made with the resulting functions and slow crack growth data for a sapphire window were compared to the results of Monte Carlo simulations.

The functions for estimation of the variances of the parameters were derived both with and without logarithmic transformation of the initial slow crack growth equations. The transformation was performed to make the functions both more linear and more normal.

Comparison of the Monte Carlo results and the closed form expressions derived with propagation of errors indicated that linearization is not required for good estimates of the variances of parameters n and D by the propagation of errors method. However, good estimates variances of the parameters B and A^* could only be made when the starting slow crack growth equation was transformed and the coefficients of variation of the input parameters were not too large. This was partially a result of the skewed distributions of B and A^* . Parametric variation of the input

¹ Jonathan A. Salem, NASA Glenn Research Center at Lewis Field, Life Prediction Branch, 21000 Brookpark Road, MS 49-7, Cleveland, OH 44135. jsalem@grc.nasa.gov. Aaron S. Weaver, NASA Glenn Research Center at Lewis Field, Life Prediction Branch, 21000 Brookpark Road, MS 49-7, Cleveland, OH 44135.

parameters was used to determine an acceptable range for using closed form approximate equations derived from propagation of errors.

1. INTRODUCTION

Slow crack growth (SCG) parameters for glasses and ceramics are determined by either strength-based or fracture mechanics based test methods. Strength-based methods employ smooth test specimens, such as flexural beams or tensile specimens, and estimate SCG material parameters from strengths measured over different time intervals. Loading is generally done in a static fashion (i.e., “static fatigue”) or in a continuously increasing fashion (i.e., “dynamic fatigue”). The strength-based methods are practical because the tests are simple, inexpensive, and usually accomplished quickly.

Strength-based methods directly sample the preexisting flaw distribution within or on the surface of the test specimens. Thus the cracks develop from at least some of the same sources that are expected to cause failure in a component manufactured in a similar fashion from the same material. Only the strength-based approaches have been standardized [1–5], and, as a result of the critical nature of flight hardware, data for design of such components is generally generated with standardized test methodologies.

The disadvantage of strength-based methods is that the SCG results are subject to the scatter inherent in the strength distribution of the material. Thus the estimation of SCG parameters from strength data can result in poor statistical reproducibility, and an estimate of the parameter variances is very necessary to the design process. In this respect, fracture mechanics based approaches, which usually exhibit lower scatter, in combination with strength-based approaches might yield the most confidence.

Closed form, approximate standard deviation functions for the SCG parameter B were previously derived for both the “static” and the “dynamic” loading cases [6–9], and the accuracy of the solutions were confirmed to some extent via Monte Carlo simulations [8]. Varying degrees of success have been reported in using the approximate solutions for the design of flight hardware [10,11].

The variance equations derived previously are very general and were determined prior to standardization of the associated test methodologies. Thus the functions are not particularly convenient for making rapid estimates from the SCG parameters derived with current testing standards [3]. Therefore, convenient closed form expressions were derived in terms of the SCG parameters determined with one of the standard methods [3] and the resulting functions were compared to Monte Carlo simulations. In addition to deriving a variance function for the logarithm of the parameter B as done previously [7], functions for the variance of the parameter A^* and its degrees-of-freedom were derived. The functions are needed for input to the computer code FLAGRO [12].

2. DERIVATION OF CLOSED FORM FUNCTIONS

One straightforward method for determining the standard deviation (i.e., the square root of the variance) associated with a dependent variable is the *generation of system*

moments or the law of propagation of errors (POE). It is based on a Taylor series expansion of the dependent variable about the means of the independent variables. A specific knowledge of the component distributions is not necessary for application of the technique. The expansion is usually truncated at the first term, and thus the functions being analyzed need to be relatively linear and the CV's (coefficients of variation; i.e., the standard deviation divided by the mean) of the independent variables should not be too large. A rule-of-thumb that the CV's not exceed ~10% has been recommended [13]. Such a CV is relatively small for strength distributions of many ceramics, and corresponds to a 2-parameter Weibull modulus of ~12. For nonlinear functions, the results can be improved by transforming the function to a more linear space. This results in standard deviation parameters in the transformation space (e.g., standard deviation of the logarithm of B , $SD_{\ln B}$, rather than the standard deviation of B , SD_B). In addition, for functions with small first derivatives in the range of interest (e.g. large values of n), higher order terms in the expansion cannot readily be ignored [14] and POE may become inaccurate. If the input variables are normal, then POE estimates are approximately normal [14]. Thus, any transformation should simultaneously accomplish two goals: more linear functions in specific independent variables, and more normally distributed independent and dependant variables. The law of propagation of errors implies that the estimated value and the associated standard deviation of a system can be estimated from [15]:

$$E(y) = f(E(x_1), E(x_2), \dots E(x_m)) + \frac{1}{2} \sum_{i=1}^m \frac{\partial^2 y}{\partial x_i^2} SD_{x_i}^2 + \sum_i \sum_{j < i} \frac{\partial^2 y}{\partial x_i \partial x_j} Cov(x_i, x_j) \quad (1)$$

and

$$SD_y \approx \sqrt{\sum_{i=1}^m \left(\frac{\partial y}{\partial x_i}\right)^2 SD_{x_i}^2 + 2 \sum_i \sum_{j < i} \left(\frac{\partial y}{\partial x_i}\right) \left(\frac{\partial y}{\partial x_j}\right) Cov(x_i, x_j) + \dots} \quad (2)$$

where $E(x_i)$ is the expected value of variable x_i (i.e. the mean), SD_{x_i} is the standard deviation of variable x_i , and $Cov(x_i, x_j)$ is the covariance between x_i and x_j . Any number of higher order terms can be included in estimates of the standard deviations; however, estimation of the moments associated with them is cumbersome, and terms greater than second order in equation (2) are frequently dropped for convenience. Also, the second term in equation (1) is usually dropped. This makes transformation an appealing approach for improving the accuracy of the technique.

2.1. Constant Stress Rate Testing

For most ceramics and glasses, the slow crack growth rate above the slow crack growth limit is expressed by the following power-law relation:

$$v = \frac{da}{dt} = AK_I^n = A^* \left[\frac{K_I}{K_{IC}} \right]^n \quad (3)$$

where v , a and t are crack velocity, crack size and time, respectively. A and n are the material/environment dependent SCG parameters and K_I and K_{IC} are, respectively,

the Mode *I* stress intensity factor and the critical stress intensity factor or fracture toughness of the material.

For constant stress rate or “dynamic fatigue” testing, the corresponding fracture or fatigue strength, σ_f , is expressed as a function of stress rate, $\dot{\sigma}$, as follows [16]:

$$\sigma_f = [B(n + 1)\sigma_i^{n-2}\dot{\sigma}]^{1/(n+1)} \tag{4}$$

where σ_i is the expected value of the inert strength and B is a parameter associated with A , n , fracture toughness, and the geometry correction factor, Y , for the stress intensity factor:

$$B = \frac{2K_{Ic}^{2-n}}{AY^2(n-2)} = \frac{2K_{Ic}^2}{A^*Y^2(n-2)}. \tag{5}$$

The American Society for Testing and Materials (ASTM) approved a full-consensus standard [3] for estimating the parameters n and D from equations (4) and (6). However, several design codes [12,17] require not only the parameter n , but either the fatigue parameter B or A as defined in equations (5) and (3). Further, as mentioned previously, the standard deviations of these parameters are necessary in estimating confidence intervals on SCG predictions and it is convenient to calculate the parameters and standard deviations directly from the regression statistics of the linearized form of equation (4) as defined by the ASTM standard [3].

In the ASTM standard, estimates of the SCG parameters are determined from the slope, α , and the intercept, β , of a plot of $\log_{10} \sigma_f$ versus $\log_{10} \dot{\sigma}$ by writing equation (4) as

$$\log_{10} \sigma_f = \frac{1}{n+1} \log_{10} \dot{\sigma} + \log_{10} D \tag{6}$$

where

$$\log_{10} D = \frac{1}{n+1} \log_{10} [B(n+1)\sigma_i^{n-2}]. \tag{7}$$

In the linear regression analysis, the dependent variable is $\log_{10} \sigma_f$ and the independent variable is $\log_{10} \dot{\sigma}$.

2.2. Parameters Determined Without Transformation

For constant stress-rate or “dynamic fatigue” testing, application of equations (1) and (2) without transformation gives the resulting SCG parameters:

$$\text{Estimated } n: \quad n = \frac{1}{\alpha} - 1 \tag{8}$$

$$\text{Estimated Standard Deviation of } n: \quad SD_n \approx \frac{SD_\alpha}{\alpha^2} \tag{9}$$

$$\text{Estimated } D: \quad D = 10^\beta \tag{10}$$

$$\text{Estimated Standard Deviation of } D: \quad SD_D \approx (ln10)(SD_\beta)(10^\beta) \tag{11}$$

Estimated B :

$$B = \frac{\alpha 10^{\beta/\alpha}}{(\sigma_i)^{\frac{1}{\alpha}-3}} \tag{12}$$

Estimated Standard Deviation of B :

$$SD_B \approx \frac{B}{\alpha} \sqrt{Q^2 \frac{SD_\alpha^2}{\alpha^2} + (\ln 10)^2 SD_\beta^2 + (1 - 3\alpha)^2 \frac{SD_{\sigma_i}^2}{\sigma_i^2} + 2Q \log 10 \frac{Cov(\alpha, \beta)}{\alpha}} \tag{13}$$

$$\text{where } Q = \alpha - \beta \ln 10 + \ln \sigma_i.$$

The statistics for parameter A^* corresponding to equation (3) can be calculated from

$$A^* = \frac{2K_{Ic}^2 (\sigma_i)^{\frac{1}{\alpha}-3}}{10^{\beta/\alpha} (1 - 3\alpha) Y^2} = \frac{2K_{Ic}^2}{B(n - 2) Y^2} \tag{14}$$

and

$$SD_{A^*} \approx A^* \sqrt{4 \frac{SD_{K_{Ic}}^2}{K_{Ic}^2} + \left(Q - \frac{\alpha}{1 - 3\alpha}\right)^2 \frac{SD_\alpha^2}{\alpha^4} + \frac{(\ln 10)^2}{\alpha^2} SD_\beta^2 + \left(\frac{1}{\alpha} - 3\right)^2 \frac{SD_{\sigma_i}^2}{\sigma_i^2} + \frac{2 \ln 10}{\alpha^3} \left(Q - \frac{\alpha}{1 - 3\alpha}\right) Cov(\alpha, \beta)}. \tag{15}$$

The use of equation (2) for deriving standard deviation functions assumes that a single term in the Taylor series expansion is sufficient. In addition, it was assumed that only the regression parameters α and β are correlated, and that the estimated parameters can be substituted for the expected values. The ‘‘hats’’ and ‘‘bars’’ used to indicate ‘‘estimate’’ and ‘‘mean’’ (e.g., $\hat{\beta}$ and $\bar{\sigma}_i$) have not been included for brevity.

The derivations of equations (12) and (14) only consider the first term in equation (1). If all three terms of (1) are retained, the following functions are obtained:

$$B = \frac{\alpha 10^{\beta/\alpha}}{2\sigma_i^{\frac{1}{\alpha}-3}} \left[2 + \frac{(\ln 10)^2 SD_\beta^2}{\alpha^2} + (\beta^2 (\ln 10)^2 - 2\beta \ln 10 \cdot \ln \sigma_i + (\ln \sigma_i)^2) \frac{SD_\alpha^2}{\alpha^4} + \left(\frac{1}{\alpha} - 2\right) \left(\frac{1}{\alpha} - 3\right) \frac{SD_{\sigma_i}^2}{\sigma_i^2} + 2 \ln 10 \cdot (\ln \sigma_i - \beta \ln 10) \frac{Cov(\alpha, \beta)}{\alpha^3} \right] \tag{16}$$

and

$$A^* = \frac{K_{Ic}^2 \sigma_i^{\frac{1}{\alpha}-3}}{10^{\beta/\alpha} \cdot (1 - 3\alpha) Y^2} \left\{ 2 + \frac{2 \cdot SD_{K_{Ic}}^2}{K_{Ic}^2} + \frac{(\ln 10)^2 \cdot SD_\beta^2}{\alpha^2} + \left[\left(\frac{1}{\alpha} - 3\right)^2 - \left(\frac{1}{\alpha} - 3\right) \right] \frac{SD_{\sigma_i}^2}{\sigma_i^2} + \left[\frac{(\beta \ln 10 - \ln \sigma_i)^2}{\alpha^2} + \frac{4 \cdot (\ln \sigma_i - \beta \ln 10)}{\alpha} + \frac{2}{(1 - 3\alpha)^2} + \frac{2 \cdot (\beta \ln 10 - \ln \sigma_i)}{\alpha \cdot (1 - 3\alpha)} - \frac{4}{1 - 3\alpha} + 2 \right] \frac{SD_\alpha^2}{\alpha^2} + 2 \cdot \left(2 \cdot \ln 10 - \frac{\beta (\ln 10)^2}{\alpha} + \frac{\ln 10 \cdot \ln \sigma_i}{\alpha} - \frac{\ln 10}{1 - 3\alpha} \right) \cdot \frac{Cov(\alpha, \beta)}{\alpha^2} \right\} \tag{17}$$

2.3. Parameters Determined with Transformation

Equation (1) becomes exact in the case of the dependent variable being a linear function of the independent variables. Equations (12) and (14) were transformed by equating the logarithms of each side:

$$\ln B = \ln \alpha + \frac{\beta}{\alpha} \ln 10 - \left(\frac{1}{\alpha} - 3\right) \ln \sigma_i \tag{18}$$

and

$$\ln A^* = \ln 2 + 2 \ln K_{Ic} - \frac{\beta}{\alpha} \ln 10 + \left(\frac{1}{\alpha} - 3\right) \ln \sigma_i - 2 \ln Y - \ln(1 - 3\alpha) \tag{19}$$

For the purposes of differentiation, the equations were taken as linear in α , β , $\ln K_{Ic}$, and $\ln \sigma_i$. If all the terms in equation (1) are used to estimate the parameters, then

$$\begin{aligned} \ln B = & \ln \alpha + \frac{\beta}{\alpha} \ln 10 - \left(\frac{1}{\alpha} - 3\right) \ln \sigma_i + \left(\frac{\beta \ln 10 - \ln \sigma_i}{\alpha} - \frac{1}{2}\right) \frac{SD_{\alpha}^2}{\alpha^2} - \ln 10 \\ & \times \frac{Cov(\alpha, \beta)}{\alpha^2} \end{aligned} \tag{20}$$

and

$$\begin{aligned} \ln A^* = & \ln 2 + 2 \ln K_{Ic} - \ln \alpha - \frac{\beta}{\alpha} \ln 10 + \left(\frac{1}{\alpha} - 3\right) \ln \sigma_i - 2 \ln Y - \ln\left(\frac{1}{\alpha} - 3\right) \\ & + \left(\frac{1}{2} - \frac{\beta \ln 10 - \ln \sigma_i}{\alpha} - \frac{1}{1 - 3\alpha} + \frac{1}{2(1 - 3\alpha)^2}\right) \frac{SD_{\alpha}^2}{\alpha^2} + \ln 10 \frac{Cov(\alpha, \beta)}{\alpha^2} \end{aligned} \tag{21}$$

Application of equation (2) to (18) and (19) gives

$$\begin{aligned} SD_{\ln B} \approx & \frac{1}{\alpha} - \sqrt{Q^2 \frac{SD_{\alpha}^2}{\alpha^2} + (\ln 10)^2 SD_{\beta}^2 + (1 - 3\alpha)^2 SD_{\ln \sigma_i}^2 + 2Q \ln 10 \frac{Cov(\alpha, \beta)}{\alpha}} \tag{22} \\ SD_{\ln A^*} \approx & \frac{1}{\alpha} \sqrt{4\alpha^2 SD_{\ln K_{Ic}}^2 + \left(Q - \frac{\alpha}{1 - 3\alpha}\right)^2 \frac{SD_{\alpha}^2}{\alpha^2} + (\ln 10)^2 SD_{\beta}^2 + (1 - 3\alpha)^2 SD_{\ln \sigma_i}^2} \\ & + 2 \ln 10 \left(Q - \frac{\alpha}{1 - 3\alpha}\right) \frac{Cov(\alpha, \beta)}{\alpha} \end{aligned} \tag{23}$$

The estimated standard deviations of $\ln A^*$ and $\ln B$ differ from the estimated standard deviations of A^* and B nominally by factors of A^* and B , respectively.

3. MONTE CARLO SIMULATION

The computing power available today makes Monte Carlo simulation an appealing technique for parameter estimation. In this technique, values for the independent variables are chosen at random from specified distributions and a value of the

dependant parameter is calculated. Thus, knowledge of, or assumptions about the distributions of the independent parameters is required. The technique is repeated a large number of times, and the statistics of the resultant data pool are calculated. The simulations in this work were repeated 50,000 times in order to insure a reasonable sample size at common probability limits.

3.1. Input Data

Data for input to the simulation came from fracture toughness, inert strength, and constant stress rate SCG testing of sapphire for a window application [18]. Linear regression of the data according to equation (6) resulted in the parameters in Table 1. The distributions of α , β and K_{Ic} were assumed to be normal. Although the distribution of α is treated as normal, values less than zero are physically unrealistic as they imply no stress corrosion, and the distribution could be truncated for values less than zero. Additionally, values of greater than ~ 0.1 imply that the assumption of $n > \sim 10$ used in derivation of the slow crack growth laws [16] is violated. To determine the significance of truncation, Monte Carlo runs were performed with and without truncation of the distribution of α below 0.01 and below zero. No differences were noted in the estimates and standard deviations. Truncation was not performed in subsequent runs. In addition to the SCG and fracture toughness data, inert strength data was generated by testing in high purity dry nitrogen. The strength data was fit to both 2-parameter and 3-parameter Weibull distributions. The resultant parameters are summarized in Table 2.

3.2. Estimation of Covariance

The dependence of the value of β upon the value for α was included in the Monte Carlo simulations by using a closed-form covariance term. Many existing computer codes calculate regression statistics such as the standard error of the parameters (i.e. the square root of the variances). Thus the covariance, $Cov(\alpha, \beta)$, can easily be calculated from

Table 1. Estimated means and standard deviations used for normal distributions.

| Parameter | Mean | Standard Deviation | Coefficient of Variation, % |
|---|---------|--------------------|-----------------------------|
| Estimated slope, α | 0.05341 | 0.00367 | 6.9% |
| Estimated intercept, β | 2.9131 | 0.00654 | 0.2% |
| Fracture toughness, $K_{Ic}, MPa\sqrt{m}$ | 2.51 | 0.12 | 4.8% |
| Geometry Correction, Y | 1.951 | 0 | 0 |
| Inert Strength, σ_i , MPa | 1108 | 93.5 | 8.4% |

Table 2. Weibull parameters for inert strength distributions.

| Inert Strength Weibull Parameters | Threshold Strength, MPa σ_{th} | Characteristic Strength, MPa σ_{θ} | Weibull Modulus m |
|-----------------------------------|---------------------------------------|--|---------------------|
| Two Parameter | 0 | 1148.8 | 14.6 |
| Three Parameter | 738.2 | 359.0 | 3.89 |

$$Cov(\alpha,\beta) = -V(\alpha)\overline{\log\dot{\sigma}} \tag{24}$$

where $V(\alpha)$ is the variance of the regression slope (i.e. the standard error squared), and $\overline{\log\dot{\sigma}}$ is the mean of the log of the stressing rates applied. Note that the ASTM standard [3] uses base 10 logarithms for plotting and regression, and thus equation (24) uses base 10. The covariance between the two can also be found from [7,8]:

$$Cov(\alpha,\beta) = -\frac{\sigma^2}{\Delta(\log\dot{\sigma})} \sum \log\dot{\sigma}_j \tag{25}$$

where:

$$\Delta(\log\dot{\sigma}) = J \sum_{j=1}^J (\log\dot{\sigma}_j)^2 - \left(\sum_{j=1}^J \log\dot{\sigma}_j \right)^2 \tag{26}$$

and σ is the standard error of regression, $\dot{\sigma}_j$ is the j^{th} value of stressing rate, and J is the number of data points.

4. RESULTS

4.1. Results without Transformation

The distributions for n , D , B , and A^* from the Monte Carlo simulation are shown in Figures 1-4. The distributions for n and D are relatively symmetric, whereas the distributions for B and A^* are extremely skewed to the left.

The estimates of the parameters n , D , B , and A^* and their variances from the Monte Carlo simulation are compared to the functions that were derived with the law of propagation of errors in Tables 3-6. This comparison shows good agreement between the closed-form estimates and the Monte Carlo results for the parameters n and D , as summarized in Table 3.

For B and A^* , the POE solutions and the Monte Carlo simulation agree only when median values are calculated from the Monte Carlo data. This is a result of the distributions of A^* and B being very skewed. The skewness is the result of the highly nonlinear nature of the functions and the associated sensitivity to small variations in the material properties, especially the inert strength. Note that the median values from the 3-parameter Monte Carlo match well with the POE solutions when the mean inert strength is used in the closed form solutions, and that the median values

Table 3. Comparison of estimates for parameters n and D .

| Parameter | Monte Carlo | Monte Carlo (repeat run) | POE Estimate |
|--------------|-------------|--------------------------|--------------|
| n_{mean} | 17.81 | 17.81 | 17.72 |
| n_{median} | 17.76 | 17.72 | |
| SD_n | 1.285 | 1.306 | 1.286 |
| D_{mean} | 819.2 | 818.7 | 818.7 |
| D_{median} | 818.9 | 818.5 | |
| SD_D | 12.34 | 12.32 | 12.34 |

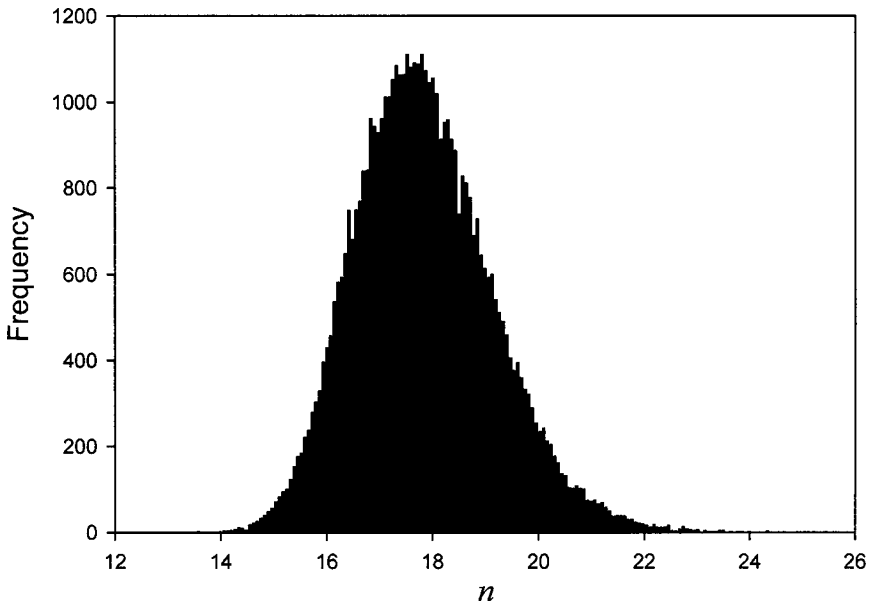


Figure 1. Histogram for slow crack growth parameter n from Monte Carlo simulation based on constant stress rate testing of sapphire in water.

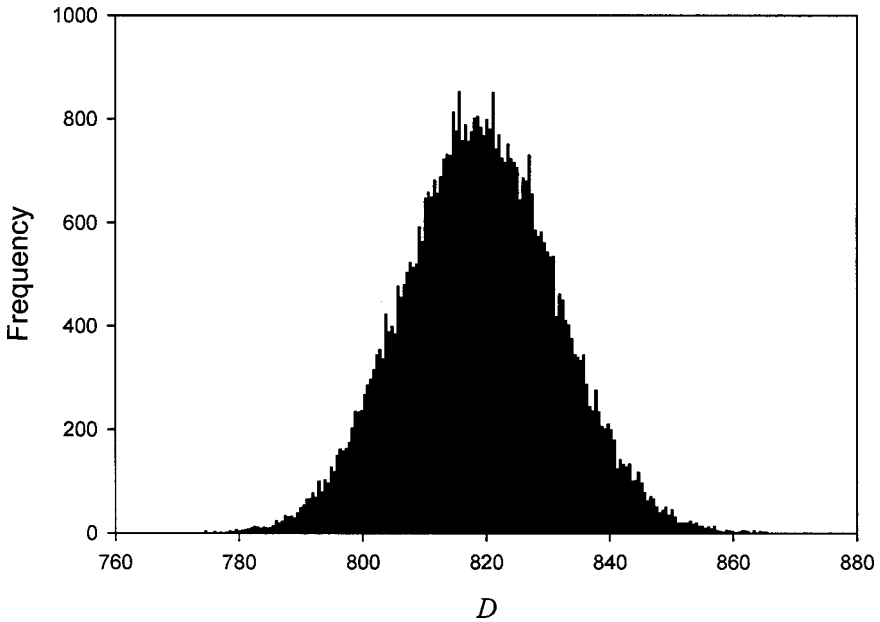


Figure 2. Histogram for slow crack growth parameter D from Monte Carlo simulation based on constant stress rate testing of sapphire in water.

of the 2-parameter Monte Carlo match well with the POE solutions when the median inert strength is used with the POE solutions. This occurs because the 3-parameter Weibull distribution is relatively symmetric, whereas the two-parameter Weibull

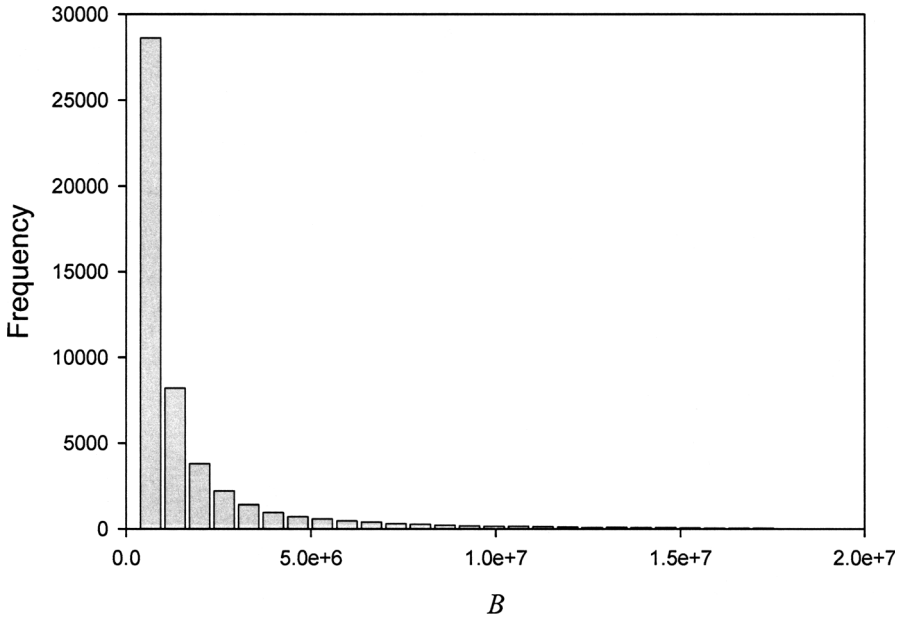


Figure 3. Histogram for slow crack growth parameter B from Monte Carlo simulation based on constant stress rate testing of sapphire in water.

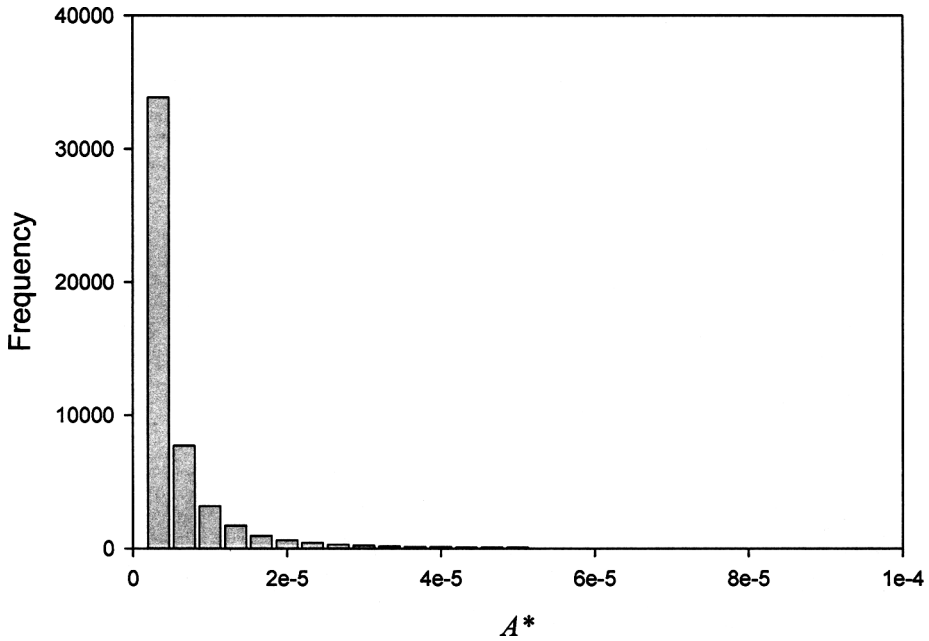


Figure 4. Histogram for slow crack growth parameter A^* from Monte Carlo simulation based on constant stress rate testing of sapphire in water.

distribution exhibits a large shape parameter and a more skewed distribution. In general, the standard deviations from the two approaches do not agree.

4.2. Results with Transformation

The results in Tables 4 and 5 indicate that POE estimates for B and A^* are not acceptable without transformation. The resultant distributions for $\ln B$ and $\ln A^*$ are shown in Figures 5 and 6, and the results from POE and Monte Carlo simulations are compared in Tables 6 and 7. Logarithmic transformation of the SCG equation brings the two methods into good agreement. As seen earlier, the Monte Carlo simulation using a three-parameter Weibull distribution compares well with POE results that use the mean value of the inert strength. And the Monte Carlo simulation using a two-

Table 4. Comparison of POE and Monte Carlo estimates for parameter B .

| Parameter | POE (mean σ_i) ¹ | POE (median σ_i) ² | Monte Carlo 3-parameter Weibull | Monte Carlo 2-parameter Weibull |
|--|--|--|---------------------------------------|---------------------------------------|
| <i>Parameter via eq. (12); SD via eq. (13) without the Cov term:</i> | | | | |
| B_{mean} | 251,203 | — | 742,130 | 251,011 |
| B_{median} | — | 219,009 | 248,387 | 204,666 |
| SD_B | 359,656 | 312,025 | 1,695,835 | 20,138,202 |
| <i>Parameter via eq. (12) plus a Cov term; SD via eq. (13):</i> | | | | |
| B_{mean} | 268,650 | — | 807,512 | 1,872,491 |
| B_{median} | — | 234,651 | 264,832 | 236,521 |
| SD_B | 373,709 | 324,638 | 1,838,818 | 32,624,604 |
| <i>Parameters with both second order terms (eq 16):</i> | | | | |
| B_{mean} | 513,825 | — | 1,730,407 | 5,709,024 |
| B_{median} | — | 444,878 | 512,423 | 443,339 |

- 1. Mean value of $\sigma_i = 1108.05$ MPa.
- 2. Median value of $\sigma_i = 1117.8$ MPa

Table 5. Comparison POE and Monte Carlo results for parameter A^* .

| Parameter | POE (mean σ_i) ¹ | POE (median σ_i) ² | Monte Carlo 3-parameter Weibull | Monte Carlo 2-parameter Weibull |
|--|--|--|---------------------------------------|---------------------------------------|
| <i>Parameter via eq. (14); SD via eq. (15) without the Cov term:</i> | | | | |
| A^*_{mean} | 8.381E-07 | — | 2.175E-06 | 1.863E-06 |
| A^*_{median} | — | 9.613E-07 | 8.494E-07 | 9.618E-07 |
| SD_{A^*} | 1.1836E-06 | 1.349E-06 | 4.721E-06 | 3.112E-06 |
| <i>Parameter via eq. (14) plus a Cov term; SD via eq. (15):</i> | | | | |
| A^*_{mean} | 9.047E-07 | — | 2.782E-06 | 2.071E-06 |
| A^*_{median} | — | 1.040E-06 | 9.223E-07 | 1.042E-06 |
| SD_{A^*} | 1.222E-06 | 1.395E-06 | 8.180E-06 | 3.644E-06 |
| <i>Parameters with both second order terms (eq. 17):</i> | | | | |
| A^*_{mean} | 1.712E-06 | — | 4.662E-06 | 4.003E-06 |
| A^*_{median} | — | 1.957E-06 | 1.707E-06 | 1.947E-06 |

- 1. Mean value of $\sigma_i = 1108.05$ MPa.
- 2. Median value of $\sigma_i = 1117.8$ MPa

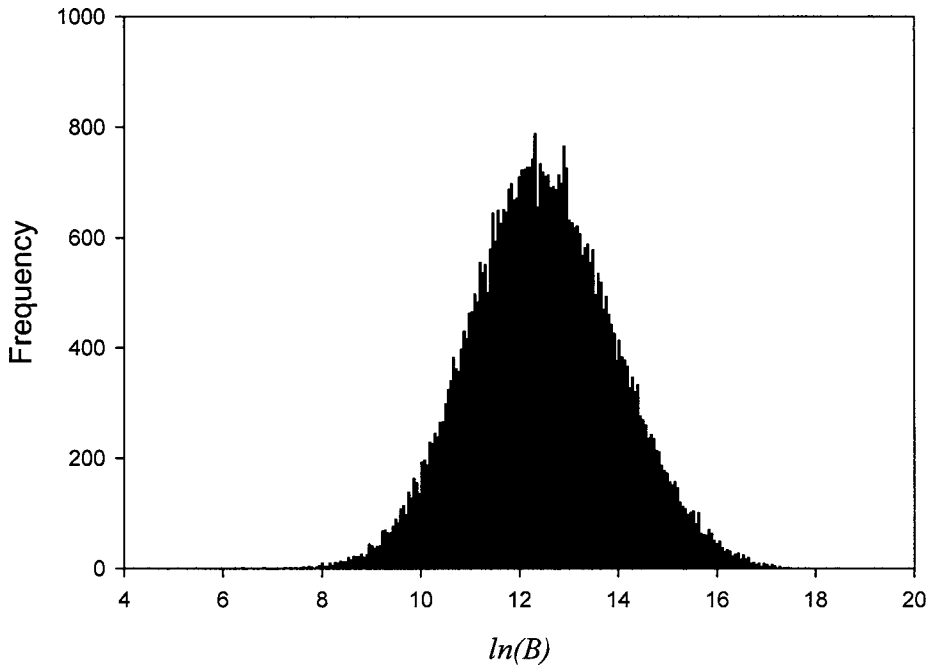


Figure 5. Histogram for slow crack growth parameter $\ln(B)$ from Monte Carlo simulation based on constant stress rate testing of sapphire in water.

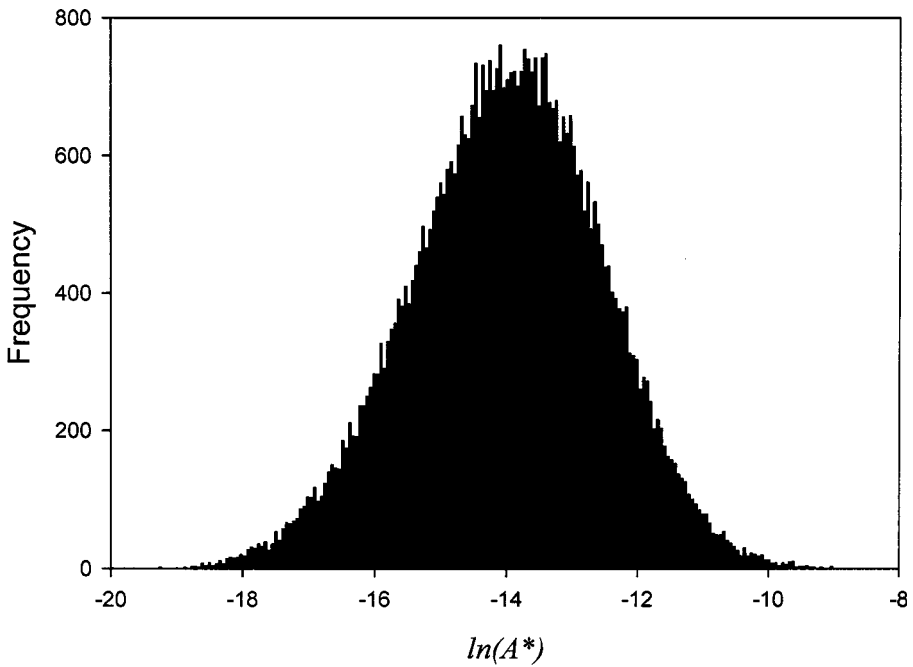


Figure 6. Histogram for slow crack growth parameter $\ln(A^*)$ from Monte Carlo simulation based on constant stress rate testing of sapphire in water.

Table 6. POE and Monte Carlo results for parameter $\ln(B)$.

| Parameter | POE (mean σ_i) ¹ | POE (median σ_i) ² | Monte Carlo 3-parameter Weibull | Monte Carlo 2-parameter Weibull |
|--|--|--|---------------------------------------|---------------------------------------|
| <i>Parameter via eq. (18); SD via eq. (22) without the Cov term:</i> | | | | |
| $\ln(B)_{mean}$ | 12.43 | — | 12.46 | 12.45 |
| $\ln(B)_{median}$ | — | 12.30 | 12.44 | 12.32 |
| $SD_{\ln(B)}$ | 1.452 | 1.456 | 1.518 | 1.553 |
| <i>Parameter via eq. (18) plus a Cov term; SD via eq. (22):</i> | | | | |
| $\ln(B)_{mean}$ | 12.42 | — | 12.43 | 12.43 |
| $\ln(B)_{median}$ | — | 12.28 | 12.41 | 12.30 |
| $SD_{\ln(B)}$ | 1.507 | 1.512 | 1.511 | 1.563 |
| <i>Parameters with both second order terms (eq. 20):</i> | | | | |
| $\ln(B)_{mean}$ | 12.39 | — | 12.43 | 12.43 |
| $\ln(B)_{median}$ | — | 12.25 | 12.41 | 12.30 |

1. Mean value of $\sigma_i = 1108.05$ MPa 2. Median value of $\sigma_i = 1117.8$ MPa

Table 7. POE and Monte Carlo results for parameter $\ln(A^*)$.

| Parameter | POE (mean σ_i) ¹ | POE (median σ_i) ² | Monte Carlo 3-parameter Weibull | Monte Carlo 2-parameter Weibull |
|--|--|--|---------------------------------------|---------------------------------------|
| <i>Parameter via eq. (19); SD via eq. (23) without the Cov term:</i> | | | | |
| $\ln(A^*)_{mean}$ | -13.99 | — | -14.02 | -14.01 |
| $\ln(A^*)_{median}$ | — | -13.85 | -14.00 | -13.87 |
| $SD_{\ln(A^*)}$ | 1.449 | 1.451 | 1.488 | 1.524 |
| <i>Parameter via eq. (19) plus a Cov term; SD via eq. (23):</i> | | | | |
| $\ln(A^*)_{mean}$ | -13.98 | — | -13.99 | -13.99 |
| $\ln(A^*)_{median}$ | — | -13.84 | -13.97 | -13.85 |
| $SD_{\ln(A^*)}$ | 1.478 | 1.482 | 1.480 | 1.534 |
| <i>Parameters with both second order terms (eq. 21):</i> | | | | |
| $\ln(A^*)_{mean}$ | -13.95 | — | -13.99 | -13.99 |
| $\ln(A^*)_{median}$ | — | -13.81 | -13.97 | -13.85 |

1. Mean value of $\sigma_i = 1108.05$ MPa 2. Median value of $\sigma_i = 1117.8$ MPa

parameter Weibull distribution matches the closed form results calculated with the median inert strength. The addition of the second order terms in equation (1) lowered the estimated B and A^* by $\sim 4\%$. Generally the standard deviations from POE are $\sim 5\%$ smaller than those from Monte Carlo.

It is noteworthy that the value of B estimated in log space (i.e. for $\ln B = 12.43$, $B = 250,196$) either with or without the second order terms of equation (20) is very similar to the direct estimate of B (251,203) only when the second order terms are not included in the direct estimate. If the second order terms are included, the direct estimate of B becomes twice as large (251,203 vs. 513,825). Evidently, the

best estimates of B and A^* without linearization are generated by using the initial algebraic formula and Cov .

4.3. Generation of Confidence Bands

For a small data set (<40), probability limits are placed on parameters by using the Student’s t distribution:

$$B_{\substack{Upper \\ Lower}} = EXP[\ln B \pm t(SD)]. \tag{27}$$

Calculation of t requires the DOF (degrees of freedom) ϕ , which is not readily estimated for a complex system. Welch [19] gave a formula for estimating the DOF when multiple components of variation are involved in comparison of two values. Jacobs and Ritter [8] generalized the Welch formula for estimation of the DOF of populations with different variances:

$$\frac{[SD_S^2]^2}{\phi_S} = \sum_i \frac{[SD_i^2]^2}{\phi_i} \tag{28}$$

where ϕ_S represents the DOF for the system variable of interest, SD_i represents the component of variation contributed to the system by variable i , and ϕ_i represents the DOF of the components adding variation to the system. For SCG parameters, the two components adding variation are the inert strength and the regression parameters α and β . Application of (28) to (22) leads to

$$\begin{aligned} \frac{[SD_{\ln B}^2]^2}{\phi_{\ln B}} &= \frac{1}{\phi_{\ln \sigma_i}} \left[\frac{(1 - 3\alpha)^2}{\alpha^2} SD_{\ln \sigma_i}^2 \right]^2 + \\ &\frac{1}{\phi_{\alpha\beta}} \left[Q^2 \frac{SD_\alpha^2}{\alpha^4} + \ln 10^2 \frac{SD_\beta^2}{\alpha^2} + 2Q \ln 10 \frac{Cov(\alpha, \beta)}{\alpha^3} \right]^2 \end{aligned} \tag{29}$$

and results in 47 DOF in $SD_{\ln B}$ base on 14 data points in inert strength ($\phi_{\sigma_i} = 13$) and 41 data points in the regression ($\phi_{\alpha\beta} = 39$). Application of equation (28) to equation (23) leads to

$$\begin{aligned} \frac{[SD_{\ln A}^2]^2}{\phi_{\ln A}} &= \frac{1}{\phi_{\ln K_{Ic}}} [4SD_{\ln K_{Ic}}^2]^2 + \frac{1}{\phi_{\ln \sigma_i}} \left[\frac{(1 - 3\alpha)^2}{\alpha^2} SD_{\ln \sigma_i}^2 \right]^2 + \\ &\frac{1}{\phi_{\alpha\beta}} \left[\left(Q - \frac{\alpha}{1 - 3\alpha} \right)^2 \frac{SD_\alpha^2}{\alpha^4} + 2\ln 10^2 \frac{SD_\beta^2}{\alpha^2} + 2\ln 10 \left(Q - \frac{\alpha}{1 - 3\alpha} \right) \frac{Cov(\alpha, \beta)}{\alpha^3} \right]^2 \end{aligned} \tag{30}$$

If, however, sufficiently large data sets are used, then the normal distribution can reasonably be assumed, and two standard deviations correspond to 95% confidence, etc:

$$B_{\substack{Upper95\% \\ Lower95\%}} = EXP[\ln B \pm 2SD_{\ln B}]. \tag{31}$$

Table 8. POE and Monte Carlo 95% probability limits for parameter B based on equations (18), (20), (22) and (27).

| | POE (mean σ_i) ¹ | POE (median σ_i) ² | Monte Carlo 3-parameter Weibull | Monte Carlo 2-parameter Weibull |
|---|--|--|---------------------------------------|---------------------------------------|
| <i>Parameters via eq. (18); SD via eq. (22) without the Cov term:</i> | | | | |
| Lower Bound | 12,258 | 10,601 | 13,202 | 16,448 |
| Upper Bound | 5,147,885 | 4,519,110 | 5,003,181 | 8,361,753 |
| <i>Parameters with second order terms (eq. 20); SD via eq. (22):</i> | | | | |
| Lower Bound | 10,485 | 9,038 | 14,885 | 18,528 |
| Upper Bound | 5,540,317 | 4,871,973 | 5,1278,769 | 8,509,182 |

1. Mean value of $\sigma_i = 1108.05$ MPa. 2. Median value of $\sigma_i = 1117.8$ MPa

Table 9. POE and Monte Carlo 95% probability limits for parameter A^* based on equations (19), (21), (23) and (27).

| | POE (mean σ_i) ¹ | POE (median σ_i) ² | Monte Carlo 3-parameter Weibull | Monte Carlo 2-parameter Weibull |
|---|--|--|---------------------------------------|---------------------------------------|
| <i>Parameters via eq. (19); SD via eq. (23) without the Cov term:</i> | | | | |
| Lower Bound | 3.750×10^{-8} | 4.276×10^{-8} | 4.286×10^{-8} | 2.567×10^{-8} |
| Upper Bound | 1.873×10^{-5} | 2.160×10^{-5} | 1.459×10^{-5} | 1.163×10^{-5} |
| <i>Parameters with second order terms (eq. 21); SD via eq. (23):</i> | | | | |
| Lower Bound | 3.661×10^{-8} | 4.166×10^{-8} | 4.438×10^{-8} | 2.637×10^{-8} |
| Upper Bound | 2.075×10^{-5} | 2.405×10^{-5} | 1.665×10^{-5} | 1.328×10^{-5} |

1. Mean value of $\sigma_i = 1108.05$ MPa. 2. Median value of $\sigma_i = 1117.8$ MPa

Probability limits calculated on the parameters with equation (29) and from the Monte Carlo data are summarized in Tables 8 and 9. The POE and Monte Carlo 3-parameter results agree reasonably. However, the 2-parameter Monte Carlo results are less conservative (failure time is proportional to B) and result in larger values for B and smaller values for A^* . This appears to result from a more skewed distribution of $\ln B$ that results in larger 95% values. Use of the median strength in the POE gives the most conservative result (i.e. the smallest B and largest A^* values). It is noteworthy that the standards for determining the inert strength and the SCG parameters recommend using 30 and 40 test specimens, respectively. Thus equation (31) is likely sufficient for most purposes. As the least value of B will produce the shortest life, a one-sided limit may be more appropriate in design than the two-sided limits presented in Tables 8 and 9.

4.4. Range of Applicability for POE

To determine the effect of input variance on the accuracy of the equations derived from POE, the CV 's of α , β , and σ_i were varied above that observed, and the standard deviation of $\ln B$ was calculated. In order to calculate the $SD_{\ln B}$, the

Table 10. Ratio of $SD_{\ln B}$ as calculated from POE via equation (22) and Monte Carlo simulation with $m \approx 1.2/CV$.

| $SD_{B(POE)}/SD_{B(MC)}$ $CV_{\sigma_i} \rightarrow \sim m$ | $CV_\alpha = 10\%$ $CV_\beta = 0.5\%$ | 10% | 20% | 20% |
|--|--|------|------|------|
| 10 $\rightarrow m \approx 12$ | 0.94 | 0.92 | 0.82 | 0.77 |
| 15 $\rightarrow m \approx 8$ | 0.96 | 0.94 | 0.87 | 0.82 |
| 20 $\rightarrow m \approx 6$ | 1.00 | 0.98 | 0.91 | 0.87 |
| 30 $\rightarrow m \approx 4$ | 0.98 | 0.97 | 0.91 | 0.89 |

Table 11. Ratio of $SD_{\ln B}$ as calculated from POE via equation (22) and Monte Carlo simulation with $m \approx 1.2/CV$. Calculations are for an alumina [21] with $n = 47.3$, $\alpha = 0.0207 \pm 0.0020$, $\beta = 2.2747 \pm 0.0048$, a median inert strength of 278.6 MPa, and a mean inert strength of $\sigma_i = 277.0 \text{ MPa} \pm 12$.

| $SD_{B(POE)}/SD_{B(MC)}$ $CV_{\sigma_i} \rightarrow \sim m$ | $CV_\alpha = 10\%$ $CV_\beta = 0.25\%$ | 10% | 15% | 15% |
|--|---|------|------|------|
| 10 $\rightarrow m \approx 12$ | 0.99 | 0.98 | 0.95 | 0.92 |
| 15 $\rightarrow m \approx 8$ | 1.00 | 0.99 | 0.96 | 0.95 |
| 20 $\rightarrow m \approx 6$ | 1.00 | 0.98 | 0.97 | 0.95 |
| 30 $\rightarrow m \approx 4$ | 0.98 | 0.98 | 0.96 | 0.96 |

standard deviation of $\ln \sigma_i$ is needed. This was calculated from a Monte Carlo simulation that used the characteristic strength and a 2-parameter Weibull modulus corresponding to the desired CV as calculated with the approximation $m \approx 1.2/CV$ [7, 20]. The strength data resulting from the Monte Carlo simulation was converted to $\ln \sigma_i$ and the corresponding $SD_{\ln \sigma_i}$ was calculated.

The ratio of the standard deviations from the POE and the Monte Carlo approaches are compared in Table 10. Generally, the POE method produced smaller values that were within $\sim 15\%$ of those from Monte Carlo. As might be expected, better comparisons occur for small CV 's of α and β . Surprisingly, the best results occur for large and intermediate standard deviations of the inert strength. This may be the result of the logarithmic transform being excessive.

To investigate the applicability of the equations for larger n values, the sensitivity for an alumina with $n = 47$ [21] was determined. The distribution α of was truncated for values of $\alpha \leq 0.008$. Again, relatively good comparisons were obtained. However, it is noteworthy that the material had a large Weibull modulus (~ 25) and low CV_α and CV_β . Despite the small initial CV 's, the size of the estimated $SD_{\ln B}$ relative to tends to become quite large as the input CV for the inert strength is increased to values common for ceramics, and the mean and median values of $\ln B$ as calculated via Monte Carlo tend to diverge. For example, with $CV_\alpha = 15\%$, $CV_\beta = 0.5\%$, and $CV_\sigma = 30\%$, equations (18) and (20) give $\ln B = -5.67$ and $\ln B = -6.14$ respectively with the mean strength, and $\ln B = -5.93$ and $\ln B = -6.41$ respectively with the median strength. Whereas Monte Carlo simulation is much less conservative, giving a mean value of $\ln B = -0.46$ and a median $\ln B = -2.21$. In this case, despite the transformation to logarithmic space, the distributions of $\ln A^*$ are skewed as compared to those for $n = 18$. More investigation with large values of n is needed.

5. CONCLUSIONS

Two methods were used to approximate variances of SCG data: Propagation of errors and Monte Carlo simulation. Transformation of the functions describing the parameters is necessary to reasonably predict the standard deviations of parameters $\ln B$ and $\ln A^*$. The addition of a covariance term slightly improved estimations of the standard deviations of $\ln(B)$ and $\ln(A^*)$ for two cases considered ($n = 18$ and $n = 47$).

The addition of second order terms made little difference for POE estimation of the parameters $\ln(B)$ and $\ln(A^*)$ for sapphire with $n = 18$. For an alumina with $n = 47$, the differences were significant, and the POE estimates of $\ln B$ and $\ln A^*$ tended to be very conservative relative to Monte Carlo simulations.

Propagation of errors is a useful approximation for estimating variances of slow crack growth parameters, however, it is an approximation that results in estimates within $\sim 15\%$ of Monte Carlo simulations for the range of variances commonly encountered in SCG testing of ceramics. Further study with large n values is needed. Equations (8), (11), (22), and (23) provide reasonably accurate functions for determining standard deviations of slow crack growth parameters determined from constant stress rate testing. For very critical applications, it may be more appropriate to use Monte Carlo or Bootstrap simulations, especially considering the availability of computing power.

REFERENCES

1. DD ENV 843-3: Advanced Technical Ceramics – Monolithic Ceramics – Mechanical Properties at Room Temperature; Part 3: Determination of Subcritical Crack Growth Parameters from Constant Stressing Rate Flexural Strength Tests. *British Standards Institution* (London, United Kingdom, 1997).
2. JIS R 1621-95 “Testing Method for Bending Fatigue of Fine Ceramics,” *Japanese Standards Association* (Minatoku, Tokyo, Japan, 1996).
3. ASTM C 1368-01 “Standard Test Method for Determination of Slow Crack Growth Parameters of Advanced Ceramics by Constant Stress-Rate Flexural Testing,” *American Society for Testing and Materials Annual Book of Standards*, Vol. 15.01, pp. 616-624 (ASTM, West Conshohocken, PA, 2000).
4. JIS R 1632-98 “Test Methods for Static Bending Fatigue of Fine Ceramics,” *Japanese Standards Association* (Minato-ku, Tokyo, Japan, December 1998).
5. ASTM C1361-96 “Constant Amplitude, Axial, Tension-Tension Cyclic Fatigue of Advanced Ceramics at Ambient Temperatures.” *American Society for Testing and Materials Annual Book of Standards*, Vol. 15.01, pp. 581-588 (ASTM, West Conshohocken, PA, 2000).
6. S.M. Wiederhorn, E.R. Fuller Jr., J. Mandel, A.G. Evans, “An Error Analysis of Failure Prediction Techniques Derived from Fracture Mechanics,” *J. Am. Ceram. Soc.* **59**(9-10) 403-411 (1976).
7. J.E. Ritter, Jr., N. Bandyopadhyay, and K. Jakus, “Statistical Reproducibility of the Dynamic and Static Fatigue Experiments,” *Am. Ceram. Soc. Bull.* **60**(8), 798-806 (1981).
8. D.F. Jacobs, J.E. Ritter, Jr., “Uncertainty in Minimum Lifetime Predictions,” *J. Am. Ceram. Soc.*, **59**(11-12), 481-487 (1976).
9. J.A. Salem, M.J. Jenkins and D. Keller “Estimating Standard Deviations of Fatigue Parameters For Ceramics Exhibiting Slow Crack Growth,” *Journal Material Science Letters* **19**, 2213-2214, (2000).
10. J.E. Ritter, Jr., Private communication, University of Massachusetts, Amherst, MA, July 2000.
11. E. R. Fuller, Jr., Private communication, National Institute of Standard and Testing Gaithersburg, MD, May 2000.
12. “Fatigue Crack Growth Program NASA/FLAGRO 2.0,” JSC 22267A, NASA Johnson Space Flight Center, (Houston, TX, May 1994).

13. J. Mandel, *The Statistical Analysis of Experimental Data* (Interscience Publishers, New York, 1964).
14. E.B. Haugen, *Probabilistic Mechanical Design*, (John Wiley and Sons, 1980).
15. G.J. Hahn, S.S. Shapiro, *Statistical Models in Engineering* (John Wiley & Sons, New York, 1994).
16. J.E. Ritter, Jr., "Engineering Design and Fatigue Failure of Brittle Materials," in *Fracture Mechanics of Ceramics*, Vol. 4, ed. by R. C. Bradt, D. P. H. Hasselman, and F. F. Lange, (Plenum Publishing Co., New York, 1978) pp. 661–686.
17. N.N. Nemeth, L.M. Powers, L.A. Janosik, and J.P. Gyekenyesi, "Durability Evaluation of Ceramic Components Using CARES/LIFE," *Trans. of the ASME*, **118**, 150–158 (1994).
18. J. Salem, L. Powers, R. Allen and A. Calomino, "Slow Crack Growth and Fracture Toughness of Sapphire for a Window Application," in *Window and Dome Technologies and Materials VII*, Vol. 4375, ed. by R.W. Tustison, (SPIE, Bellingham, WA, 2001) pp. 41–52.
19. B.L. Welch, "The Generalization of 'Student's' Problem When Several Different Population Variances are Involved," *Biometrika* **34**, 28–34 (1947)
20. W. Nelson, *Applied Life Data Analysis* (John Wiley & Sons, 1982).
21. J.A. Salem and M.G. Jenkins, "The Effect of Stress Rate on Slow Crack Growth Parameters" in *Fracture Resistance Testing of Monolithic and Composite Brittle Materials, ASTM STP 1409*, ed. By J.A. Salem, G.D. Quinn and M.G. Jenkins (American Society for Testing and Materials, West Conshohocken, Pennsylvania, January, 2002) pp. 213–227.

ON INTEGRITY OF FLEXIBLE DISPLAYS

Piet C.P. Bouten*

1. INTRODUCTION

Nowadays two display types are dominant in the display market: the bulky cathode ray tube (CRT) and liquid crystal displays (LCD). Both types use glass as substrate material. The LCD display is the dominant player for mobile applications, in for instance mobile phones and portable computers. In the development of displays and their applications a clear interest exists to replace the rigid rectangular display cells by free-shaped, curved or even roll-up cells. These types of applications require flexible displays.

Different types of flexible displays have been presented recently.¹ Section 2 gives a short introduction to these display types. To realize the flexible displays, flexible substrate materials such as thin glass,² metal foil,³ and/or polymer are used as substrate materials instead of rigid (rectangular) glass sheets. Requirements for (polymer) substrates, used to realize flexible displays are treated in section 3. To fulfill the requirements, functional brittle layers are applied on the polymer substrates.

Various types of failures encountered in flexible displays are presented in section 4. Dominant failure types are related to the application of thin brittle layers on polymer substrates. An example of such a failure type, the tensile failure of a brittle ITO layer on a polymer substrate, is presented in more detail in section 5. This example shows that formalisms, used in scaling laws and reliability predictions for the (standard) glass displays are not (completely) valid for flexible displays. In the final discussion the need for scaling laws and reliability models for flexible displays is emphasized.

* Piet C.P. Bouten, Philips Research Laboratories, 5656AA Eindhoven, The Netherlands.

2. TYPES OF FLEXIBLE DISPLAYS

Slikkerveer¹ defines a flexible display as “a flat panel display made using thin, flexible substrates, where the substrate can be bent to a radius of curvature of some centimetres without loss of functionality.” An example of a flexible display is given in figure 1. This display, a flexible CTLC (Cholesteric Texture Liquid Crystal) cell, is only 250 μm thick and can be bent down to a radius of two centimeter while operating.⁴ The size of the presently shown display cell is 150*125 mm².

Four application areas are recognized for flexible displays:

1. Flat displays. In this area the main points are the ruggedness of the cell, the low weight and the freedom to use non-rectangular devices.
2. Curved displays. The display is used at a constant, predefined, curvature, for instance on a (curved) surface of a handheld device.
3. Displays on flexible devices. The display bends as the substrate bends. An example is a display in a smartcard.
4. Roll-up displays. These displays are frequently rolled and unrolled during application.

In application areas 2–4 the display cells are mechanical loaded on purpose. In the second application area it is loaded once when bending the cell in its final shape. Areas 3 and 4 require more loading cycles. Not only functional requirements on the display performance (the image quality), but also structural requirements on the display construction and the materials are needed.

Many presently used flat panel displays with glass substrates, such as LCD cells in a mobile phone, are used in constructions that prevent loading of the display cell. Excessive loading of these cells leads to glass failure. In mobile phones, for instance, display cells are always incorporated at a certain depth in the body to prevent glass fracture in a drop test. At this point the flexible displays differ clearly from the

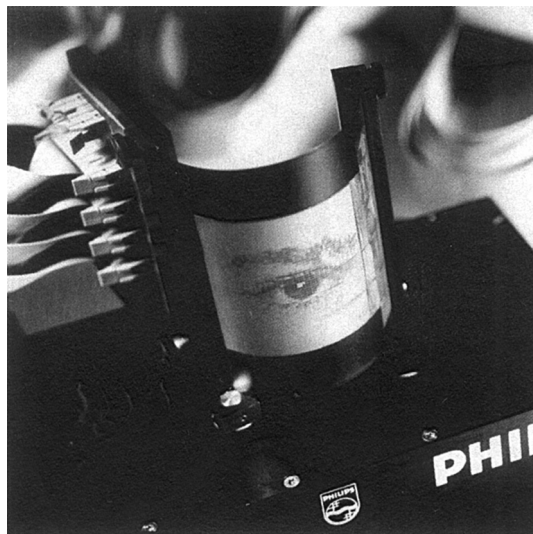


Figure 1. A flexible liquid crystal display.

presently used glass-based flat panel displays. To bend the display, a mechanical load has to be applied on the cell. This load leads to a stress distribution in the display. Upon bending the inner surface is loaded in compression and the outer surface in tension. Knowledge about the acceptable stresses and/or strains of the various display parts is required for reliability modeling.

Flexible displays require not only thin, flexible substrates, but also thin display effects. In most flat panel display the display effect is sandwiched between two substrates. Patterned electrodes on both substrates are used for localized addressing. Three thin display effects are mentioned here:

- (3) The liquid crystalline material in a LCD display acts as a light switch. The thickness of this layer is 1–10 μm . LCD displays require accurate cell gap control. This can be achieved with flexible substrates (fig. 1).⁴
- (3) The OLED (organic light emitting) displays use light emitting organic molecules. They are incorporated in a very thin ($< 1 \mu\text{m}$) functional stack. The functional display layer is extremely sensitive to water and oxygen. This sets tough requirements to water and oxygen permeation rates of the substrates.⁵
- (3) Electrophoretic displays, for instance an E-ink display,³ use colored charged particles and a colored liquid. They are encapsulated in an about 50 μm thick polymer film.

High performance displays, such as color displays on mobile phones and computer screens, require high image refresh rate in combination with high display brightness. The patterned electrode structures in these “active matrix” devices⁴ contain electronic switches in the display area. High performance active matrix devices are silicon-based.

3. SUBSTRATES

Various types of flexible displays sets different requirement to the substrates. In general, the display substrates need to be transparent and of good optical quality. During display processing, they must withstand a number of chemicals, such as organic solvents and/or strong acids/bases. Although frequently the process temperature can be lowered relative to that of glass, the substrates should be able to withstand temperatures between 150°C and 300°C. The maximum temperature determines to a large extent the selection of the base substrate material. To give an example: the deposition of polycrystalline silicon for high performance active matrix displays requires a maximum process temperature of about 275°C.⁶ This temperature requirement limits the substrate selection seriously.

Properties of base polymer films are often not appropriate for display production processes and display applications. Important parameters, like permeability and solvent resistance are inferior to those of glass. To improve the performance of the polymer sheets, several coatings are applied on a base polymer film (fig. 2). Functional coatings like a solvent-resistant and/or scratch resistant coating are either polymer-based or a combined organic/inorganic system. These layers are a few microns thick. Other functional coatings are thin ($< 150 \text{ nm}$) fully inorganic layers. So is the transparent conductor ITO (Indium Tin Oxide) used as electrode material. A hermetic transparent permeation barrier is required to guarantee sufficient lifetime

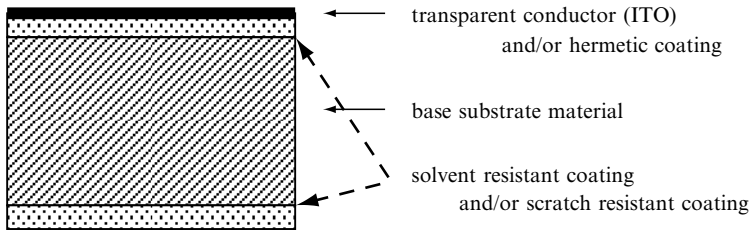


Figure 2. A schematic representation of the cross section of a flexible display substrate.

for the OLED cells. The low water permeation rate ($< 10^{-6}$ gr/m²/day) can only be realized when (transparent) inorganic layers are applied on the polymer substrate.

To achieve sufficient flexibility for the device, the selected substrate thickness is in the 50–200 μm range. Due to thermal expansion differences of the layers, a stress distribution will be present over the thickness of the multi-layer substrate. This leads to warping of the freestanding film. Processing of strongly warped films is not preferred.

The thin (< 150 nm) inorganic (brittle) layers have in general a significantly smaller failure strain than the base substrate material. They limit seriously the allowed deformations of the substrates and the cells. Failure of these brittle layers is a serious point of concern in the discussion on integrity of flexible displays. In the next section attention will be paid to several failure mechanisms, observed in flexible display cells and substrates. In section 5, some aspects on the failure of an ITO layer are described in more detail.

4. FAILURE TYPES

A complex interplay between residual stress distribution, cohesive and adhesive properties of the various layers in the stack, and the location of a critical defect determine how a crack proceeds in a product. Some examples of evolving cracks will be given.

In the previous section it is indicated that the basic substrates require processing at temperatures above 150°C. The substrates therefore should have a high glass transition temperature. The highly transparent substrates are amorphous or semi-crystalline. At ambient temperatures, they are in the glassy state. This can also be seen from the failure behavior. Figure 3 shows a strongly bent flexible LCD display. In the LCD display a cell gap between the two substrates is filled with the liquid crystalline material. A crack has started at the lower cutting edge of the upper substrate and runs in the strongly curved substrate, loaded in tension. Around the crack the gap between the substrates increased, and the LC material is withdrawn. The crack was initiated at an edge defect. This mechanism is similar to that observed in glass sheets. The quality of the cutting edge determines the failure strain. The sample shows a dominant brittle failure behavior for the polymer substrate.

At ambient conditions usually a biaxial compressive stress is present in the brittle top layer of the substrate. At high biaxial stresses a characteristic delamination pattern, the “telephone cord” structure is frequently observed.⁷ Figure 4 shows an AFM image of this structure, observed for an ITO layer on a polymer substrate. From the characteristic sizes an estimate for the adhesion quality can be obtained.

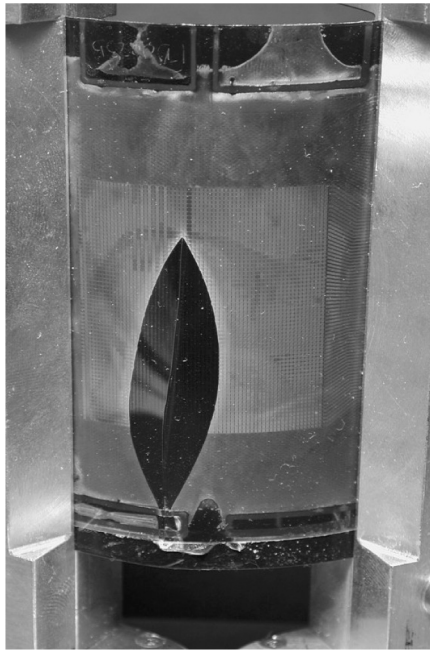


Figure 3. Edge failure of the upper substrate of a flexible LCD cell upon bending.

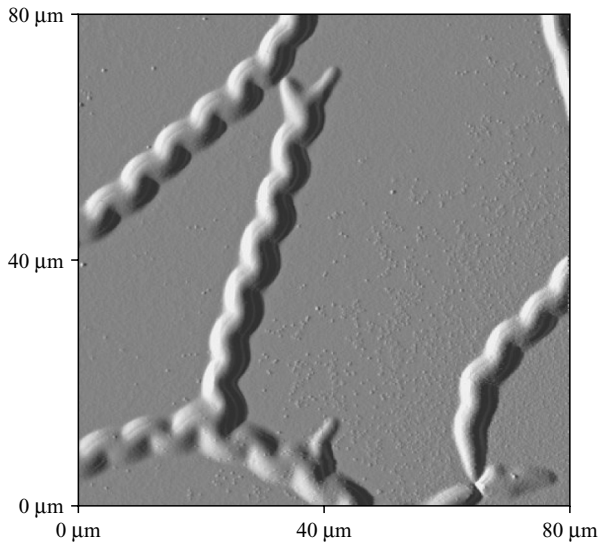


Figure 4. “Telephone cord” type delamination pattern due to biaxial compressive stress in the top layer.

A seal line is used to connect both substrates in the construction of flexible display cells, for instance at the circumference of the cell. Upon bending serious stress concentrations occur at the mechanically loaded seal line. This may lead to preferential failure near this seal line. of the some layers on the substrate. Figure 5 shows crack patterns in the ITO layer on top of a substrate at a location where the seal line is removed. The ITO layer is partly removed with the seal line.

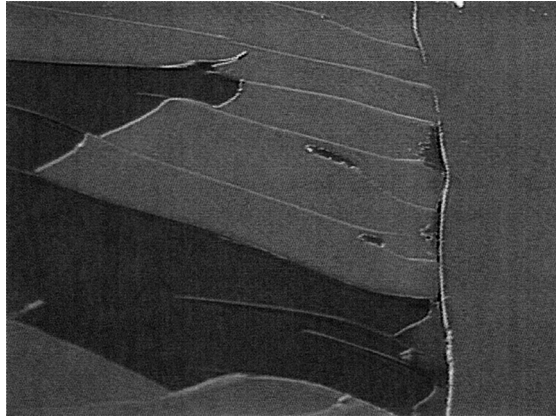


Figure 5. Crack patterns in the ITO layer at the location of the removed seal line (left).

A more detailed experimental study on the propagation of cracks in the multi-layer structure of model substrates for flexible displays⁸ clearly shows an interaction of the cracks in the brittle layer and cracks in a polymer hard-coat layer.

5. ITO TESTING

We will now focus on the failure of the transparent conductor (ITO). A tensile test is used in combination with resistance measurements^{9, 10} to determine the critical failure strain of the brittle transparent conductor (ITO) on the polymer substrate. The strain, determined directly from the displacement of the clamps⁹ is systemically too high. To circumvent this problem the displacement can be measured on the sample.¹⁰

The two point bending test,¹¹ schematically represented in figure 6, has no clamping problems. A rectangular sample of the film (length 80 mm, width 15 mm) is placed between two parallel plates. At the location with the lowest curvature radius,

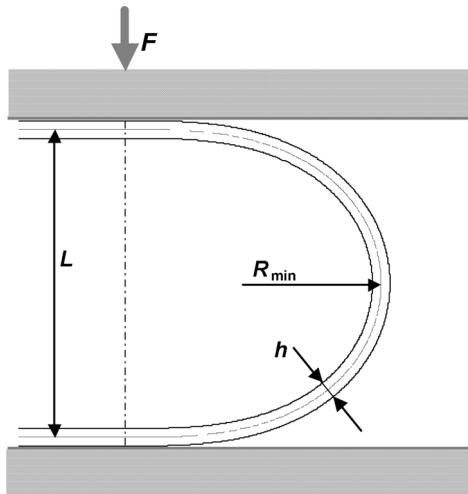


Figure 6. Geometry of the two point bending test.

R_{min} , the largest tensile strain is present at the outer surface. For a symmetrical sample the strain at this location is $\epsilon_{max} = 1.198 h/L$, where h is the sample thickness and L the distance between the neutral lines. The faces of the clamps isolate the sample electrically from the machine frame. In the test the resistance of the ITO layer is determined as a function of the distance L_o between the plates ($L_o = L + h$). The crosshead velocity of the universal testing machine (Instron 5566) during the test is 10 mm/min. The relative resistance increase $\Delta R/R$ is represented as a function of maximum tensile strain ϵ_{max} in figure 7. The curves, represented in this figure are measured on samples of the same width (15 mm). One sample has a uniform ITO layer over the full width. On the other samples a single ITO line of a defined width is etched.

Up to a certain strain level the resistance is constant. Above this strain an increase in the resistance is observed. The strain corresponding to a 10% resistance increase is used as a critical strain. The significant increase of the resistance is due to the development of cracks in the ITO layer normal to the conductive path. The shape of the curve in figure 7 depends on the ITO line width. A sudden resistance increase is observed for narrow lines, a more gradual increase for the wider lines.

Figure 8 shows the edges of the ITO layer. The cracks, visible in the upper sample surface (uniform ITO layer on top), are due to the cutting process. The cracks are present in a zone near the sample edges that is approximately 200 μm wide. The

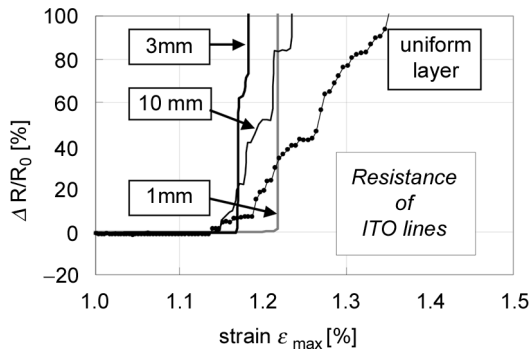


Figure 7. The increase in resistance of ITO layers as a function of the maximum applied strain. ITO lines of different width are tested.

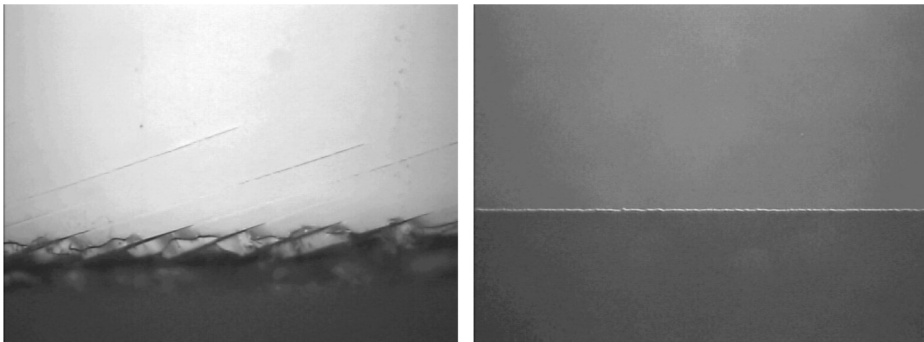


Figure 8. ITO edge of cut sample (left) and etched ITO line (right).

etched ITO layer shows no edge cracks. The crack onset strain for the etched lines and the sample with the uniform ITO layer is nearly similar, about 1.2% for the tested samples. The presence of the edge cracks has no significant effect on the on the critical failure strain of the thin layers.

To get information on the failure strain distribution, larger series of samples are tested in three batches. For one substrate type, samples with a uniform ITO layer and samples with etched narrow ITO lines are measured. For a second sample type only a uniform ITO layer is investigated. Details of the tests are given in table 1.

Experiments on narrow single ITO lines show at a critical failure strain a sudden increase of the resistance, in most cases to infinity. This effect is used to reduce the number of tested samples: Six samples with ten parallel 0.75 mm wide ITO lines at 1.0 mm pitch are etched. The resistance of these ten parallel lines is measured as a function of the plate distance L_o . Failure of a single ITO line is recorded as a step in the resistance-strain curve. From the six samples 60 line failures are recorded.

The data are represented in a two parameter Weibull distribution: $P = 1 - \exp(-\epsilon/\epsilon_o)^m$. Figure 9 shows the experimental data of substrate II in a Weibull graph. The experimental failure strain ϵ_{max} and the failure probability P are represented on the axes. The slope m and the characteristic strain ϵ_o (at 63 % failure probability) are obtained from a fit on the experimental data. The fit constants for the 3 tests are included in table 1.

Table 1. Characteristic failure strains obtained from a Weibull analysis on 3 sets of samples.

| Sample type | h [μ m] | ITO layer | # samples | Weibull | |
|-------------|--------------|----------------|-----------|------------------|----|
| | | | | ϵ_o [%] | m |
| I | 130 | Lines, 0.75 mm | 60 | 1.17 ± 0.02 | 20 |
| I | 130 | Uniform | 30 | 1.24 ± 0.02 | 20 |
| II | 100 | Uniform | 36 | 1.46 ± 0.02 | 40 |

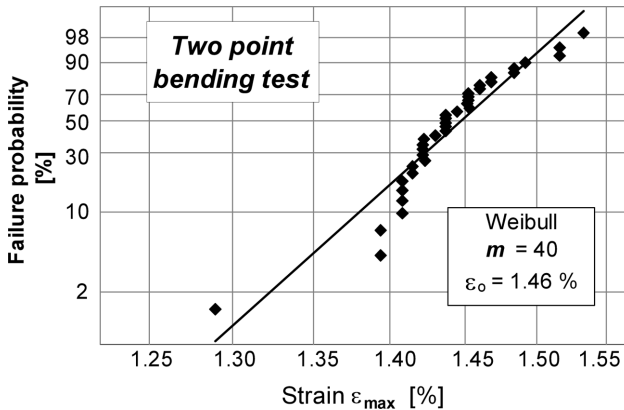


Figure 9. Weibull graph for the critical failure strain of sample II.

6. DISCUSSION

6.1 Failure of Brittle Layers

In the sections 4 and 5 a variety of failure modes for flexible displays is presented. Knowledge of at least the dominant failure modes is required for the development of reliability models and scaling rules. These types of models, applied to brittle materials, like glass and ceramics, use weakest link statistics, in many cases Weibull statistics.

In the previous section Weibull statistics is used to describe the critical failure strain of a brittle conductive layer (ITO) on a polymer substrate. During the test the polymer substrate behaves completely elastic¹¹. The results, obtained by tensile loading of the brittle layer on the substrate differs significantly from the behavior of (bulk) brittle materials:

- (3) The presence of large edge cracks does not affect the critical strain of the thin layer. Nearly identical failure strains are obtained for the smooth etched ITO lines with straight crack-free edges and uniform ITO layers with heavy damaged ITO edges.
- (3) The critical failure strain of the uniformly coated sample (1.24 %) is even slightly higher than that of the ITO lines (1.17%). This is not expected when a distribution of weakest spots in the surface area is responsible for the failure behavior. The tested ITO area is larger for the stronger sample.
- (3) The length of the ITO edges, tested in the two point bending test, is similar for the uniform ITO layer and the etched ITO line. The difference in crack density at the ITO edges is not responsible for the larger critical failure strain of the uniform ITO layer.
- (3) Identical strength distributions ($m = 20$) are obtained for the same substrate type (I, table I). For the other substrate type a significantly higher failure strain (1.46 %) and a Weibull modulus $m = 40$ are reported. These differences reflect the different deposition conditions.
- (3) High Weibull moduli ($m = 20$) are only obtained in bulk materials characterization with well-defined process conditions. They are observed, for instance, when well defined surface damage is applied, for instance with powder blasting.¹² A Weibull modulus $m = 40$ is only obtained for quite deterministic stress levels, for instance with the intrinsic strength of glass fibers.¹³

Crack initiation and crack propagation are two clearly different phenomena in the mechanics of thin layers on substrates⁷. The experiments on the ITO layer indicate that not the crack initiation but the crack propagation dominates the critical failure strain of the ITO layers. The fact that the poor quality of the ITO edge of the uniformly coated sample does not affect the failure strain clearly supports the propagation-controlled mechanism. A well-defined crack propagation threshold leads to a high Weibull modulus ($m = 20$). The level of this threshold is determined by layer properties, like internal stress, layer thickness and adhesion to the substrate.

Leterrier¹⁴ et al. studies the crack evolution of brittle silicon oxide coatings on polymer substrates with the fragmentation test. The number of cracks is counted as a function of the applied strain. The evolution of the crack density in a sample just above the crack onset strain is described with Weibull statistics. Weibull moduli

2.5 m 12 are reported. This is significantly lower than the m 20 obtained from our tests with, using resistance measurement on ITO. It is noted in this respect that the phenomena might be slightly different. Leterrier reports on the appearance of cracks within a limited area, observed with a microscope. The cracks may have a limited length. A significant increase of the resistance of an ITO layer is expected either with a large amount of small cracks in the layer, or a crack over nearly the full layer width. The differences in Weibull moduli might be related to differences in crack *initiation* or crack *propagation* limits.

For narrow lines a sudden increase of the resistance is observed; for wider lines a more gradual increase is measured. In a model description⁹ of the resistance increase in the tensile test, the presence of conducting material in the crack is assumed to be responsible for the gradual resistance increase. This model does not account for the presently observed line width dependence of the resistance increase.

In the present set of experiments, with 0.75 mm wide ITO lines, the sudden increase in resistance and the well-defined, propagation controlled critical failure strain is obtained. In many applications in electronics industry significantly smaller details are present. For active matrix addressed displays, for instance, transistors and connection lines significantly smaller than 100 μm are applied. When the size of the cracks, initiated for instance around a defect, have a stable size, comparable to the size of the component, crack initiation-controlled mechanisms and not the propagation control may govern the resistance of the lines.

Cracks in a (oxygen and/or water) barrier coating degrade the performance of the hermetic coating. For this reason, crack initiation is expected to be a dominant failure mechanism for the performance of OLED displays, requiring hermetic coatings.

6.2 Reliability Models

Glass is the dominant substrate material in the display industry. The brittle failure behavior of glass is exploited in production processes, and taken into account in applications. Knowledge of the failure behavior, and the mechanisms leading to failure, is quite important in the production of reliable products. An appropriate combination of stress distributions, failure statistics and crack extension models is used in reliability models for brittle materials.

This type of modeling is also required for new products, entering the market. Flexible displays are nowadays quite appealing, both due to their flexibility and the robustness of the cell. From fracture mechanical point of view, the base polymer substrate has certainly a higher failure strain than a glass substrate. The limiting strain for the substrate can be related to the onset to non-elastic deformations or to brittle failure behavior, thus the presence of large cracks.

The substrate is a multi-layer stack. Cohesive and/or adhesive failure of one of the layers might lead to cell failure. Section 5 describes the loss of conduction of a tensile loaded ITO layer. It is strongly related to the crack evolution in the brittle layer. Brittle functional layers seriously limit the applicable deformations of the flexible display cell. The allowable deformation of the presently tested ITO layer is slightly above 1%.

The critical strain of the presently tested brittle ITO layer is determined with relatively small samples in a short lasting test in ambient conditions. For the prediction of the reliability of a real product, tests under more severe conditions and at

longer timescales are required. This requires knowledge of the behavior of different materials as a function of time and temperature. For polymeric materials, incorporation of time-dependent deformation behavior, like creep and relaxation or plastic deformation, might be necessary. For thin brittle layers phenomena like slow crack might contribute to a lowering of the critical strain.

Apart from these phenomena, stress concentrations due to display constructions might seriously lower the applicable safe deformation. Near a seal line, for instance, preferential failure might occur (figure 4). All these factors result in a different, and probably significant lower, safe critical strain.

A large variety of mechanisms is responsible for the failure of a flexible displays. Production and market introduction of complete new products like flexible displays requires knowledge of the critical failure mechanisms. This knowledge is necessary to development reliability models.

7 CONCLUSIONS

Different failure modes for flexible display substrates are presented. Brittle layers, such as inorganic permeation barriers and transparent conductors (ITO) fail at strain levels of about 1%. They predominantly limit the allowable substrate deformation.

The critical failure strain of the conducting ITO layer does not depend on the presence of cracks in this layer. This is not in agreement with models used to predict the reliability of (bulk) ceramics.

During production, application and use of flexible displays, mechanical load is exerted on the substrates and the display cell. A good understanding of the different possible failure mechanisms is required in the development of flexible displays towards a reliable product. Appropriate reliability models are presently not available for flexible displays.

8. ACKNOWLEDGEMENT

The author acknowledges Judith de Goede and Jeroen Alberts for their contributions to the experimental work. Part of the work is done within the IST program (IST-2001-34215 FlexLED) of the European Community.

REFERENCES

1. P.J. Slikkerveer, Bending the Display Rules, Options and Challenges for Flexible, Proc. EuroDisplay 2002, Nice, 1–4 oct. 2002, pp 273–276.
2. A. Weber, S. Deutschbein, A. Plichta and A. Habeck, Thin Glass-polymer Systems as Flexible Substrates for Displays, SID 02 digest, Boston, 21–23 may 2002, pp. 53–55
3. P. Kazlas, A. Ritenour, J. Au, Y. Chen, J. Goodman, R. Paolini and H. Gates, Card-size Active-matrix Electronic Ink Display, Proc. EuroDisplay 2002, Nice, 1–4 oct 2002, pp 260–262.
4. P. Slikkerveer, G. Nisato, N. Kooyman, P. Cirkel and P. Bouten, A Fully Flexible, Cholesteric LC Matrix Display, SID '02 digest, Boston 21–23 may 2002, pp 27–29.
5. G. Nisato, P.C.P. Bouten, P.J. Slikkerveer, W.D. Bennett, G.L. Graff, N. Rutherford and L. Wiese, Evaluating High Performance Diffusion Barriers: the Calcium Test, Proc. IDW '01, Nagoya, 16–19 oct 2001, pp 1435–1438.

6. N. Young, M.J. Trainor, D.T. Murley, D.J. McCulloch and R.J. Wilks, LPTS for AMLCD on Glass and Polymer Substrates, Proc. IDW '99, 1999
7. J.W. Hutchinson and Z. Suo, Mixed Mode Cracking in Layered Materials, *Adv. Appl. Mech.*, 29 (1992) pp. 63–191.
8. Y. Leterrier, C. Fischer, L. Médico, F. Demarco, J.-A. E. Månson, P.C.P. Bouten, J. de Goede, G. Nisato and J.A. Nairn, Mechanical Properties of Transparent Functional Thin Films for Flexible Displays, Proc. Soc. Vacuum Coaters, 46th annual conference, San Francisco, may 2003, to be published.
9. D. R. Cairns, R. P. Witte II, D. K. Sparacin, S. M. Sachsmann, D. C. Paine, and G. P. Crawford, Strain-dependent Electrical Resistance of Tin-doped Indium Oxide on Polymer Substrates, *Appl. Phys. Lett.* 76 (2000) 1425–1427
10. Y. Leterrier, L. Médico, F. Demarco, J.-A. E. Månson, M. Escola-Figuera, M. Kharazzi-Olson and U. Betz, Mechanical Integrity of Transparent Conductive Oxide Film for Flexible Polymer-based Displays, submitted to *Thin Solid Films*.
11. P.C.P. Bouten, Failure test for brittle conductive layers on flexible display substrates, Proc. EuroDisplay 2002, Nice, 1–4 oct 2002, pp 313–316.
12. P.J. Slikkerveer, P.C.P. Bouten, F.H. in 't Veld and H. Scholten, Erosion and damage by sharp particles, *Wear* 217 (1998) 237–250.
13. C.R. Kurkjian and U.C. Paek, Single-valued Strength of “Perfect” Silica Fibers, *Appl. Phys. Lett.* 42 (1983) 251–253.
14. Y. Leterrier, J. Andersons, Y. Pitton and J.-A. E. Månson, Adhesion of Silicon Oxide Layers on Poly(ethylene terephthalate). II: Effect of Coating Thickness on Adhesive and Cohesive Strengths, *J. Polym. Phys.* 35 (1997) 1463–1472.

FRACTURE OF CONDUCTIVE CRACKS IN POLED AND DEPOLED PZT-4 CERAMICS

Tong-Yi Zhang*

ABSTRACT

The present work reports experimental results on the fracture behavior of conductive cracks or deep conductive notches in poled and depoled PZT-4 ceramics. The fracture tests were conducted with compact tension specimens under purely mechanical loading, purely electrical loading and combined mechanical and electrical loading. Finite element calculations were carried out to obtain the energy release rate, the stress intensity factor and the intensity factor of electric field strength of the specimens. The results show that the critical energy release rate under purely either electrical or mechanical load is a constant, independent of the ligament length of the specimens. However, for both the poled and depoled ceramics, the electrical fracture toughness in terms of the critical energy release rate is much higher than the mechanical fracture toughness. The highly electrical fracture toughness arises from the greater energy dissipation around the conductive sharp notch tip under purely electrical loading, which is impossible under mechanical loading in the brittle ceramics. Furthermore, the critical energy release rate under combined electrical and mechanical loading depends on the weight of the electrical load in comparison with the mechanical load. We normalize the critical stress intensity factor by the critical stress intensity factor under purely mechanical loading and normalize the critical intensity factor of electric field strength by the critical intensity factor of electric field strength under purely electrical loading. Then, a quadratic function describes the relationship between the normalized critical stress intensity factor and the normal-

* Department of Mechanical Engineering, Hong Kong University of Science and Technology, Clear Water Bay, Kowloon, Hong Kong, China, E-mail: mezhang@ust.hk

ized critical intensity factor of electric field strength. This quadratic function may serve as a failure criterion for conductive cracks in piezoelectric ceramics.

KEYWORDS

fracture, piezoelectric and dielectric ceramics, conducting cracks, dielectric discharge

1. INTRODUCTION

Ferroelectric ceramics have become preferred materials for a wide variety of electronic and mechatronic devices due to their pronounced dielectric, piezoelectric, and pyroelectric properties. Aging, fatigue and electrical and/or mechanical breakdown of the materials cause device failures, which are considered seriously in the design of ferroelectric devices. Ferroelectric ceramics are brittle and susceptible to cracking at all scales from domains to devices. Because of the importance of electrical and mechanical reliability of these devices, there has been tremendous interest in studying the fracture behavior of such materials. Zhang *et al.* (2002) provide an overview on fracture of piezoelectric ceramics with summarizing current knowledge of the fracture of piezoelectric ceramics. Their attention is confined to fracture mechanics studies, yet experimental results are also examined for comparison with theoretical predictions. Zhang (2002) reviewed the experimental observations on the effects of static electric field on the fracture behavior of piezoelectric ceramics.

Internal electrodes have widely been adopted in electronic and electromechanical devices made of ferroelectric ceramics. These embedded electrodes may naturally function as pre-conductive cracks or notches, which may lead to failure of these devices under electric and/or mechanical loads. Figure 1 schematically shows the similarity between a conductive crack under electrical loading and a normal crack under mechanical loading. To ensure that the electric field inside the conductive crack remains zero, electric charges in the conductive crack surfaces must rearrange themselves to produce an induced field that has the same magnitude as the applied one but with the opposite sign. As a result, the charges in the upper and lower crack surfaces near the crack tip have the same sign, as shown in Fig. 1. The charges with the same sign repel each other and then have a tendency to propagate the crack. The contour-independent *J*-integral used in fracture mechanics can also apply to conductive cracks (Zhang *et al.*, 1998; Garboczi, 1988; McMeeking, 1987) and the *J*-

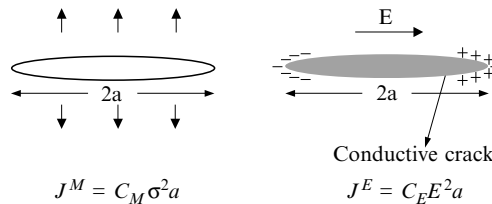


Figure 1. A comparison of a normal crack loaded by uniform mechanical stress, σ , and a conductive crack loaded by uniform electrical field, E , where J^M and J^E denote, respectively, the mechanical and electrical *J*-integrals, and $C_M = \pi / Y^*$ and $C_E = \pi \kappa / 2$.

integral results for the purely mechanical and electrical loadings are illustrated in Fig. 1 correspondingly. It is therefore of practical importance and academic significance to study the fracture mechanics and failure behavior of conductive cracks in ferroelectric ceramics.

Lynch *et al.* (1995) carried out indentation fracture tests on electroded surfaces submerged in electrically conducting NaCl solution and in distilled water. In both cases, tree-like damage grew from the indented electrode under the cyclic electric field. Heyer *et al.* (1998) studied the electromechanical fracture toughness of conductive cracks in PZT-PIC ceramics. They conducted four-point bending tests on pre-notched bars, in which the poling direction was toward the jig surface and the notch was filled with NaCl solution to make the crack conducting. Wide scattering results were obtained under a large applied electric field of $|K_E| > 50kV/m^{1/2}$, where K_E is the applied electric intensity factor. The critical stress intensity factor increased as the applied intensity factor of the electric field strength changed from $30kV/m^{1/2}$ to $-90kV/m^{1/2}$. When the applied electric intensity factor was relatively small, within the range of $-15kV/m^{1/2}$ to $15kV/m^{1/2}$, they could explain the experimental data using a domain-switching-based model. Using compact tension samples with conductive notches, Fu, Qian and Zhang (2000) have performed extensive fracture tests on lead zirconate titanate (PZT-4) ceramics under purely electrical or mechanical loading. The experimental results indicate that both the purely electric and mechanical fields can propagate conductive cracks (notches) and fracture the samples. Under purely electric loading, there exists a critical energy release rate at fracture, which is named the electric fracture toughness. The electric fracture toughness is much larger than the mechanical fracture toughness, which is the critical energy release rate at fracture under purely mechanical loading. Like the mechanical fracture toughness, the electric fracture toughness is a material property, which is defined as the resistance of a material against fracture or as the energy per unit area absorbed by the material as the crack propagates. Fu *et al.* (2000) attributed the high electric fracture toughness to electrical plastic deformation.

To clarify whether the failure of conductive cracks in poled PZT ceramics was induced by the piezoelectric effect, Wang and Zhang (2001) thermally depoled the ceramics and demonstrated that electric fields could fracture depoled lead zirconate titanate (PZT-4) ceramics. Thus, the concepts of fracture mechanics can be applied to the failure of conductive cracks in macroscopically dielectric ceramics and the electrical fracture toughness exists for dielectric ceramics. Like the case for poled PZT-4 ceramics, the electrical fracture toughness for the depoled PZT-4 ceramics is also much higher than the mechanical fracture toughness of the same depoled PZT-4 ceramics. The highly electrical fracture toughness arises from the greater energy dissipation around the conductive crack tip under purely electric loading, which is impossible under mechanical loading in the brittle depoled ceramics.

The present work summarizes the experimental results of the failure behavior of electrically conductive cracks in depoled (Wang and Zhang, 2001) and poled (Fu *et al.*, 2000) PZT ceramics under purely electrical or mechanical loading. Furthermore, the failure behavior of conductive cracks in depoled PZT ceramics under combined electrical and mechanical loading and the charge-free zone model (Zhang *et al.*, 2003) are also briefly introduced here.

2. EXPERIMENTAL PROCEDURE

The material used in this study was lead zirconate titanate ceramics (PZT-4, Morgan Matroc). Pre-notched or cracked compact tension (CT) samples were adopted in the fracture tests under purely mechanical, purely electric and mixed mechanical and electric loads. All samples had width $2w_1 = 10\text{mm}$, height $w_0 = 10\text{mm}$ and thickness $b = 3\text{mm}$. A pre-notch or crack was cut in each sample with a 0.15mm thick diamond saw parallel to the poling direction for the poled ceramics, and further sharpened by a 0.12 mm diameter wire saw. After the cutting, the samples were cleaned ultrasonically in distilled water for a few minutes. For conductive cracks, silver paint was filled into the notch (crack) to make it function as an electrode. The silver paint is a viscous solution and solidifies at room temperature quickly. The refilling technique, which meant that filling was conducted again after the preceding filling and solidification, was adopted to ensure the notch was fully filled. The refill was continuing until that no obvious shrinkage was observed by naked eyes. In this case, the electrode in the sample was perfect, which was proofed by investigating the fracture surface. Figure 2 schematically shows the sample geometry and the loading condition. Regarding electric loading, we applied a DC voltage and manually increased its magnitude until the sample failed. For poled PZT ceramics, positive and negative electric fields, which were respectively parallel and anti-parallel to the poling direction, were applied in the tests.

The fracture tests were carried out under a constant voltage mode or a constant mechanical load mode with a homemade loading apparatus. In the constant voltage mode, a constant voltage was applied first, then, the mechanical load was gradually increased until the sample fractured, while in the constant mechanical load mode, a constant mechanical load was applied first, following by a gradual increasing of the applied electric voltage until the sample fractured. Positive and negative electric fields were applied in both loading modes. To avoid electric sparking, the samples were put into the silicone oil during tests under purely electric loading or covered by a thick layer of silicone grease under combined loading. All tests were implemented at room temperature. At least ten samples were repeatedly tested for each loading condition under combined mechanical and electrical loading and 30 samples were tested under the purely electrical loading.

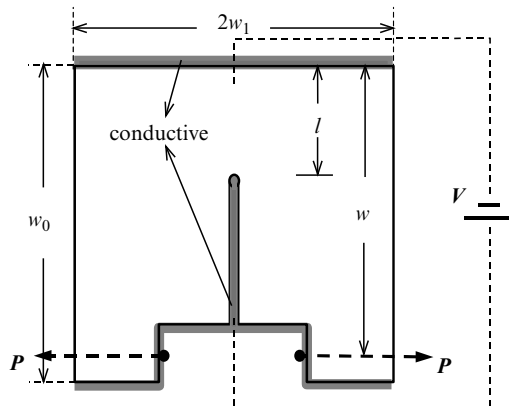


Figure 2. Sample geometry and loading condition.

The depoling was achieved by thermally annealing the PZT-4 ceramics at 400 °C for 40 minutes and then cooling them down in the furnace to room temperature (Wang and Zhang, 2001). After depoling, the ceramics lost piezoelectricity and became macroscopic dielectrics that were isotropic in elasticity and dielectricity. No detectable piezoelectric constants in the depoled ceramics were measured with the piezo d_{33} tester with 1% accuracy (Pennebaker, Model 8000). The isotropic dielectric constants were measured using an impedance analyzer (Hewlett Packard, 4192A Lf) at the standard frequency of 1M Hz. The mean value of the dielectric constants with the standard deviation was $\kappa = 9.794 \pm 0.205 \times 10^{-9} C/Vm$. The elastic constant and Poisson ratio were measured by compressive tests using strain gauges on a universal testing machine (MTS Sintech 10/D). The means of the elastic constant and the Poisson ratio were, respectively, $Y = 25.3 \pm 0.34 GPa$ and $\nu = 0.38 \pm 0.006$ for the depoled ceramics.* Pre-notched (or pre-cracked) compact tension samples were adopted for fracture tests under purely mechanical and purely electrical loads. The depoled samples were prepared in the same way as that for the poled sample such that the sample geometry and the loading condition for the depoled samples were also the same as that for the poled samples, as shown in Fig. 2.

3. ENERGY RELEASE RATE AND INTENSITY FACTORS

Finite element calculations were conducted to have the energy release rate for the used sample geometry and loading condition. The energy release rate is equivalent to the contour-independent J -integral in the linear electro-mechanics (Cherepanov, 1979; Zhang *et.al.*, 2002), which is given by

$$G = J = \int_{\Gamma} (hn_1 - \sigma_{ij}n_j u_{i,1} + D_i E_1 n_i) d\Gamma, \quad i, j = 1, 2, 3, \quad (1)$$

where $h = \sigma_{ij}\epsilon_{ij}/2 - D_i E_i/2$ is the electric enthalpy per unit volume, Γ is an integration contour around the crack tip, and \mathbf{n} is the unit out normal vector to the contour. In the finite element calculation of J -integral, we used the commercial software ABAQUS and the eight-node plane strain piezoelectric elements.

For the poled PZT ceramics, the following material constants were used in the calculations.

Elastic compliance($10^{-12}m^2/N$):

$$s_{11} = 12.37, \quad s_{12} = -3.97, \quad s_{13} = -5.52, \quad s_{33} = 16.11, \quad s_{44} = 39.06;$$

Piezoelectric constants($10^{-10}m/V$):

$$d_{31} = -1.35, \quad d_{33} = 3.00, \quad d_{15} = 5.25;$$

Dielectric constants($10^{-8}C/Vm$):

$$K_{11} = 1.31, \quad K_{33} = 1.15;$$

* The late test results showed that the average Young's modulus and the average Poisson ratio were $Y = 51 GPa$ and $\nu = 0.43$, respectively, for the depoled ceramics (Zhang *et al.*, 2003). The discrepancy might be caused by the mechanically nonlinear behavior of the depoled ceramics.

where the subscript “3” denotes the poling direction and N , m , V , and C represent, respectively, Newton, Meter, Volt, and Coulomb. For the depoled ceramics, the material constants used in the calculations were mentioned above. The conductive crack is modeled by using a large dielectric constant (10^9 times of K_{33}) of the medium inside the crack. The FEA results provide two equations to calculate the energy release rate, G_I^M or G_I^E , under the purely mechanical or electrical loading for the samples with ligaments ranging from 2.5 mm to 4.5 mm:

$$G_I^M = \frac{P^2}{b^2 w_1 Y_{11}} \left[4.287 - 35.944 \left(\frac{l}{w} \right) + 118.629 \left(\frac{l}{w} \right)^2 - 178.729 \left(\frac{l}{w} \right)^3 + 102.704 \left(\frac{l}{w} \right)^4 \right] \times 10^3, \quad (2)$$

$$G_I^E = \frac{K_{33} V^2}{w} \left[10.278 - 63.719 \left(\frac{l}{w} \right) + 185.213 \left(\frac{l}{w} \right)^2 - 266.316 \left(\frac{l}{w} \right)^3 + 151.755 \left(\frac{l}{w} \right)^4 \right], \quad (3)$$

where $Y_{11} = 1/s_{11}$, b is the sample thickness and, G , P , and V are, respectively, in units of N/m, N and kV, and all geometry parameters are in meters.

We calculated the intensity factors from the J-integral by assuming that the relationship between the intensity factors and the J-integral for the used CT samples was the same as that in an infinite body (Wang, 2003). In this case, the intensity factors are expressed in terms of

$$K_I^\sigma = \frac{P}{b\sqrt{w}} f_1 \left(\frac{a}{w} \right), \quad K_I^E = \frac{V}{\sqrt{w}} f_2 \left(\frac{a}{w} \right). \quad (4)$$

We regressed seven sets of calculated results corresponding to the different ligaments and then had the geometry functions f_1 and f_2 in the following forms,

$$\begin{aligned} f_1(t) &= -5.608 + 66.5151t - 43.373t^2 - 139.197t^3 + 226.173t^4, \\ f_2(t) &= 10.500 - 81.457t + 254.772t^2 - 338.301t^3 + 167.191t^4, \end{aligned} \quad (5)$$

where $0.33 \leq t \leq 0.72$, and $t = a/w$, $a = w - l$, $w = 9 \times 10^{-3} m$, as shown in Fig. 2.

For the depoled PZT-4 dielectric samples with ligament, l , ranging from 3.2 to 5.2 mm, we had the following energy release rates:

$$G_I^M = \frac{P^2}{b^2 w_1 Y^*} [38.664 - 274.69s + 757.44s^2 - 940.75s^3 + 439.32s^4] \times 10^2 \quad (6)$$

for purely mechanical loading, and

$$G_I^E = \frac{\kappa V^2}{w} [26.231 - 213.07s + 681.45s^2 - 962.53s^3 + 499.49s^4] \quad (7)$$

for purely electrical loading, where $s = l/w$, $Y^* = Y/(1 - \nu^2)$, and κ is the dielectric constant of the material.

4. RESULTS

Figure 3(a) shows the mechanical fracture toughness of the depoled ceramics as a function of the ligament length, where a solid circle represents an experimental datum (hereafter, the same symbol is used in the remaining figures without notation). The mechanical fracture toughness has a mean value of $G_{IC}^M = 30.4 \pm 3.9 N/m$ in terms of the critical energy release rate, which is indicated by the solid line in Fig. 3(a). Clearly, the mechanical fracture toughness is a material property that can serve as a mechanical fracture criterion. To illustrate the mechanical fracture behavior statistically, we plot the failure probability in Fig. 3(b), which follows the Weibull distribution of

$$F(G_{IC}^M) = 1 - \exp \left[- \left(\frac{G_{IC}^M}{32.1} \right)^{8.69} \right] \text{ and } G_{IC}^M \text{ is in units of } N/m, \quad (8)$$

where F is the cumulative failure distribution function. Equation (8) indicates that the depoled PZT-4 ceramics under purely mechanical loading has a Weibull modulus of 8.69, which is more or less the same as the modulus in engineering ceramics. Using the relationship of $G_{IC}^M = (K_{IC}^M)^2 / Y^*$, the mechanical fracture toughness can be expressed in terms of the critical stress intensity factor and it is $K_{IC}^M = 0.947 \pm 0.063 MPa\sqrt{m}$ under purely mechanical loading.

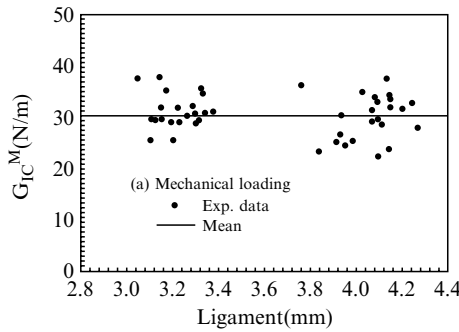


Figure 3(a). The mechanical fracture toughness vs. the ligament.

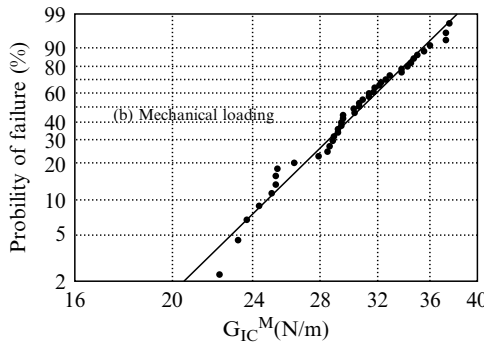


Figure 3(b). Weibull distribution of the mechanical fracture toughness.

Figure 4(a) shows the electrical fracture toughness as a function of the ligament length with the solid line representing the mean value. The mean of the critical energy release rate is $G_C^E = 263 \pm 35 \text{ N/m}$. The experimental results clearly indicate that the depoled ceramics have an electrical fracture toughness, which is also a material property and can serve as a failure criterion for conductive cracks in dielectrics under purely electrical loading. Similarly, we plot the failure probability of the depoled ceramics under purely electrical loading in Fig. 4(b), which follows the Weibull distribution,

$$F(G_C^E) = 1 - \exp \left[- \left(\frac{G_C^E - 150}{125.6} \right)^{3.35} \right] \text{ and } G_C^E \text{ is in units of } \text{N/m}. \quad (9)$$

It is interesting to note that the depoled ceramics has a Weibull modulus of 3.35 under purely electrical loading. The lower the Weibull modulus is, the greater the variability of the fracture toughness. The results indicate that the experimental data for electric fracture toughness are more scattered than those for mechanical fracture toughness. Using the relationship of $G_C^E = \kappa(K_C^E)^2/2$, the electrical fracture toughness

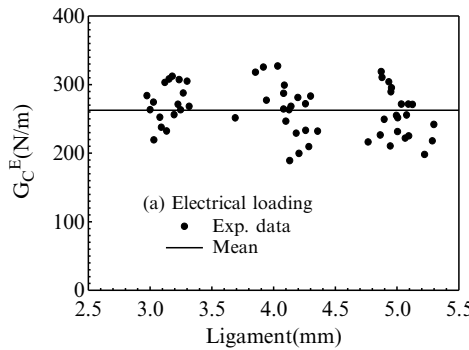


Figure 4(a). The electrical fracture toughness vs. the ligament.

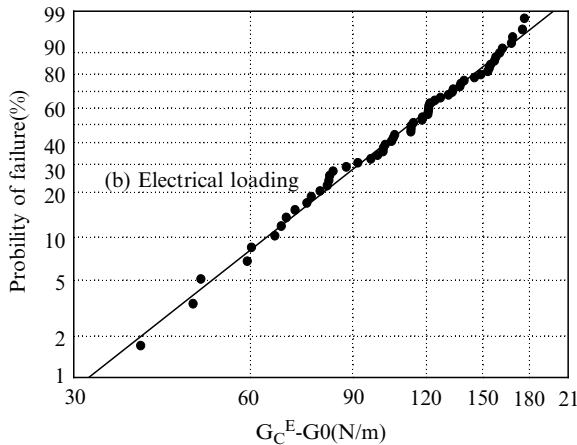


Figure 4(b). Weibull distribution of the electrical fracture toughness.

in terms of the critical electric field intensity factor is given by $K_C^E \equiv K^{E_0} = 0.23 \pm 0.022 MV/\sqrt{m}$ under purely electrical loading.

The electrical fracture toughness is about 9 times higher than the mechanical fracture toughness because *electrical plastic deformation*, including electrical discharge and domain switching, occurs at the tip of the conductive crack, forming an electrical plastic zone. Actually, dielectric breakdown accompanies fracture under purely electrical loading. Figure 5 shows fractographs of the samples fractured under the purely mechanical or purely electrical loading. The fracture surfaces are flat for samples fractured under the mechanical loading, while the electrical loading yields rough fracture surfaces, as shown in Fig. 5. In the electrically fractured samples, any discharge may locally burn the sample, as indicated by the dark area on the right fractograph of Fig. 5. At high magnification, clear grain morphology is revealed on the mechanical fracture surface, whereas some regions of the electrical fracture surface appear to be melted and resolidified. It is the electrical plastic deformation that consumes more energy and thus leads to the high electrical fracture toughness.

Fu *et al.* (2000) and Wang *et al.* (2001) performed fracture tests on conductive cracks in poled PZT-4 piezoelectric ceramics and the poling direction was parallel to the pre-notch. The compact tension samples were prepared in the same way as that used by Wang and Zhang (2001), as described above. The following three types of tests were conducted: 1) purely mechanical loading, 2) purely electric loading, and 3) combined mechanical and electrical loading.

Figure 6(a) shows the critical energy release rate versus the sample ligament under purely mechanical loading. It is clearly seen that the linear regression of the plot is very approximate to the horizontal line, indicating that the critical energy release rate is a material constant independent of the sample ligament. The mechanical fracture toughness can also be expressed in terms of the critical stress intensity factor, which is $K_{IC}^M \equiv K^{\sigma_0} = 0.934 \pm 0.06 MPa\sqrt{m}$ under purely mechanical loading. Figure 6(b) shows that the failure probability of the PZT-4 ceramics under purely mechanical loading follows the Weibull distribution

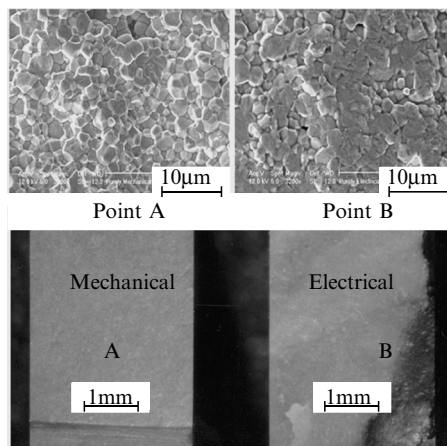


Figure 5. Lower: optical images; Upper: SEM images from the corresponding regions of A and B in the lower optical images.

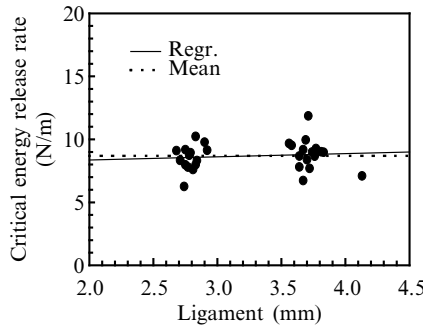


Figure 6(a). The critical energy release rate versus the ligament under purely mechanical loading.

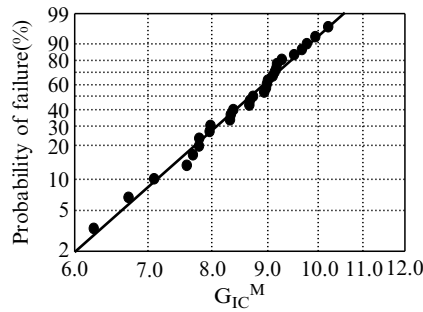


Figure 6(b). Weibull distribution of the critical energy release rate under purely mechanical loading.

$$F(G_{IC}^M) = 1 - \exp \left[- \left(\frac{G_{IC}^M}{9.0103} \right)^{9.6435} \right] \text{ with } G_{IC}^M \text{ in units of } N/m. \quad (10)$$

Under purely mechanical loading, the PZT-4 ceramics has a Weibull modulus of 9.6435, more or less the same as other engineering ceramics.

In the same way, Fig. 7(a) illustrates the critical energy release rate versus the sample ligament under purely electrical loading. Again, the linear regression of the plot is almost a horizontal line. This feature, in analogy with the mechanical case, indicates the existence of the electric fracture toughness under purely electric loading. The electric fracture toughness is a material property and has the value $G_C^E = 223.7 \pm 17.0 N/m$ in terms of the critical energy release rate, which is about 25 times larger than $G_{IC}^M = 8.7 \pm 0.4 N/m$. This is because electrical discharge and domain switching may occur at the tip of the conductive crack, forming an electrically plastic zone. Actually, electric discharge was observed during the tests. This kind of electrical plastic deformation accompanies crack propagation and consumes energy, thus leading to the high electrical fracture toughness. The failure probability of the PZT-4 ceramics under purely electric loading, as shown in Fig. 7(b), follows the Weibull distribution of

$$F(G_C^E) = 1 - \exp \left[- \left(\frac{G_C^E - 130}{110.25} \right)^{2.331} \right] \text{ with } G_C^E \text{ in units of } N/m. \quad (11)$$

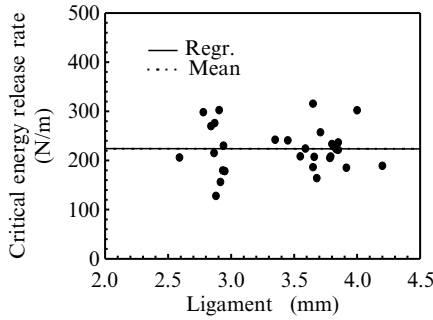


Figure 7(a). The critical energy release rate versus the ligament under purely electrical loading.

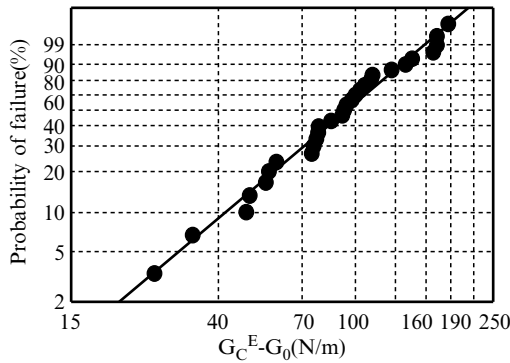


Figure 7(b). Weibull distribution of the critical energy release rate under purely electrical loading.

Comparing Eq. (11) with Eq. (10) indicates that a three parameter Weibull distribution has to be used to describe the failure probability under purely electrical loading, while a two parameter Weibull distribution is sufficient to describe the failure probability under purely mechanical loading. Equation (11) is valid only when G_C^E is larger than 130 N/m. When G_C^E is smaller than 130 N/m, no failure will occur under purely electrical loading. The PZT-4 ceramics under purely electric loading has a Weibull modulus of 2.331, as shown in Eq. (11), which is much smaller than that under purely mechanical loading, indicating again a larger variability of the electric fracture toughness.

Under combined electrical and mechanical loading, we normalize the critical stress intensity factor by the critical stress intensity factor under purely mechanical loading and normalize the critical intensity factor of electric field strength by the critical intensity factor of electric field strength under purely electric loading. Figure 8 shows the relationships of the normalized intensity factor of electric field strength versus the normalized stress intensity factor. The experimental data can be approximately described by the equation

$$(K^E / K_C^E)^2 + (K^\sigma / K_{IC}^M)^2 = 1, \tag{12}$$

where K_C^E denotes the critical intensity factor of electrical field strength under purely electrical loading. Equation (12), shown as the circular curve in Fig. 8, may serve as a

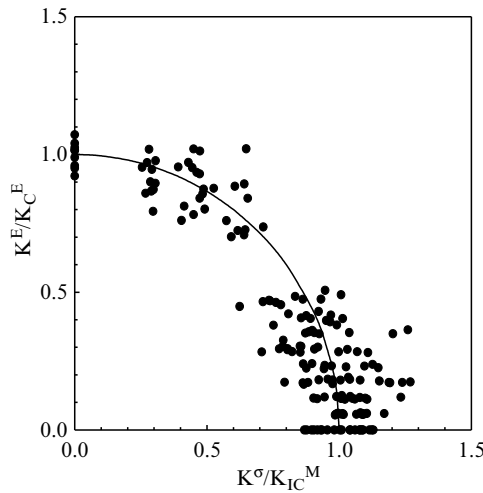


Figure 8. Experimental results for the failure of electrically conductive cracks in the depoled PZT-4 ceramics under combined mechanical and electrical loading.

failure criterion for the depoled PZT ceramics under combined electric and mechanical loading. Based on the experimental results, Zhang *et al.* (2003) developed a Charge-Free Zone (CFZ) model, which successfully explains the experimental observations.

5. THE CHARGE-FREE ZONE MODEL

The charge-free zone (CFZ) model (Zhang *et al.* 2003) was proposed to understand the failure behavior of conductive cracks in dielectric ceramics under electrical and/or mechanical loading. The CFZ model treats dielectric ceramics mechanically brittle and electrically ductile. Charge emission and charge trapping were assumed to occur in the CFZ model, which consume more work and thus lead to a high value of the electric toughness. In the CFZ model, the local electric intensity factor has a non-zero value and consequently there is a non-zero local electric energy release rate, which contributes to the driving force to propagate the conductive crack. The merit of the CFZ model lies in the ability to apply the Griffith criterion directly to link the local energy release rate to the fracture toughness in a completely brittle manner. As a result, an explicit failure criterion results from the CFZ model to predict the failure behavior of conductive cracks in dielectric ceramics under electrical and/or mechanical loading and the theoretical predictions agree perfectly with the experimental observations.

To simplify the analysis, charges were treated as line charges and the trapped charge cloud in front of a conductive crack was modeled as a charge strip in the CFZ model, as shown in Fig. 9, where ob denotes the CFZ size and the region of ba is the charge strip. The trapped charges shield the conductive crack tip from the applied electric field, while the charge-free zone reflects that the shielding is only partial. Therefore, the local value of the intensity factor of electric field intensity, which is

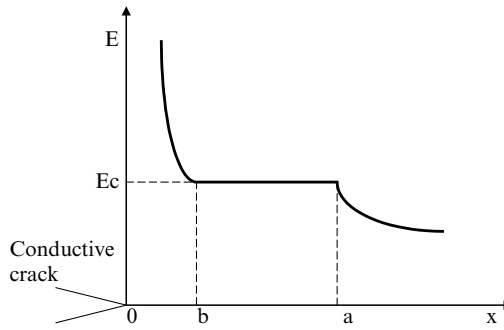


Figure 9. The field distribution in front of a conductive crack, wherein ob is the size of the charge-free zone and ba denotes the charge zone.

called the electric intensity factor for convenience, has a nonzero value. Based on the CFZ model, Zhang *et al.* (2003) derived the local electric intensity factor, $K_E^{(l)}$, which was directly proportional to the applied electric intensity factor, $K_E^{(a)}$, $K_E^{(l)} = \Omega K_E^{(a)}$. For dielectric ceramics there is no interaction between the electrical and mechanical fields. Thus, the local energy release rate for a dielectric ceramic is expressed in terms of the intensity factors as

$$G^l = (K_{\sigma}^a)^2 / Y^* + \frac{\kappa}{2} (K_E^l)^2. \tag{13}$$

Under purely mechanical loading or purely electrical loading, an application of the Griffith criterion to Eq. (13) yields

$$G_C^l = \frac{(K_{IC}^M)^2}{Y^*} = \Gamma, \tag{14}$$

$$G_C^l = \frac{\kappa (K_E^l)^2}{2} = \frac{\kappa (K_C^E)^2 \Omega^2}{2} = \Gamma, \tag{15}$$

where Γ represents the material resistance to failure. Eq. (14) indicates that the value of Γ is identical to the mechanical toughness, G_{IC}^M . Then, the value of Ω was calculated from Eq. (15) with the value of K_C^E . Under combined loading, applying the Griffith criterion to Eq. (13) yields

$$G_C^l = (K_{\sigma,C}^a)^2 / Y^* + \frac{\kappa}{2} (K_{E,C}^l)^2 = \Gamma. \tag{16}$$

The subscript ‘‘C’’ is labeled to indicate the fracture critical condition. Then, using Eqs. (14) and (15) leads to the failure criterion, Eq. (12), which has been observed experimentally.

Very recently, Zhang *et al.*, (2004a) further developed the CFZ model for poled ceramics and verified the model experimentally (Zhang *et al.*, 2004b). Although the coupling between the electrical and mechanical fields makes the mathematic derivation complex, the physical picture remains the same as that described above. Interested readers may refer the original publications (Zhang *et al.*, 2004a and 2004b).

6. CONCLUDING REMARKS

In summary, the experimental results demonstrate that electric fields can fracture the depoled and poled ceramics and that the electric fracture toughness exists under purely electrical loading, which can be expressed in terms of the critical energy release rate or the critical intensity factor of electric field strength. The significance of the existence of electrical fracture toughness is that it enables us to use concepts from fracture mechanics to understand electrically induced failures, and it provides designers of electronic and electromechanical devices with a useful material property. The advantage of applying the concepts of fracture mechanics to dielectric failure lies in the ability to predict the critical electric field at which a dielectric ceramic material containing a conductive crack or an internal electrode fails. The critical electric field is a function of the crack dimension or the length of the electrode, while the electrical fracture toughness is a material constant. Thus, one can predict the critical electric field when information on the sample geometry and the electric fracture toughness is available.

ACKNOWLEDGMENTS

This work is supported by a grant from the Research Grants Council of the Hong Kong Special Administrative Region, China. The author thanks Drs. M.H. Zhao, R. Fu, T.H. Wang, C.F. Qian and Y. Wang and Mr. G.N. Liu for their contributions to the present work.

REFERENCES

- Cherepanov, G.P., 1979, *Mechanics of Brittle Fracture*, McGraw-Hill, New York, p. 317.
- Fu, R., Qian, C.F. and Zhang, T.Y., 2000, Electrical fracture toughness for conductive cracks driven by electric fields in piezoelectric materials, *Appl. Phys. Lett.* **76**:126.
- Garboczi, E.J., 1988, Linear dielectric-breakdown electrostatics, *Phys. Rev. B* **38**:9005.
- Heyer, V., Schneider, G.A., Balker, H., Drescher, J., and Bahr, H.A., 1998, A fracture criterion for conducting cracks in homogeneously poled piezoelectric PZT-PIC 151 ceramics, *Acta mater.* **46**:6615.
- Lynch, C.S., Yang, W., Collier, L., Suo, Z., and McMeeking, R.M., 1995, Electric field induced cracking in ferroelectric ceramics, *Ferroelectrics* **166**:11.
- McMeeking, R.M., 1987, On mechanical stresses at cracks in dielectrics with application to dielectric breakdown, *J. Appl. Phys.* **62**:3116.
- Wang, T.H. and Zhang, T.Y., 2001, Electrical fracture toughness for electrically conductive deep notches driven by electric fields in depoled lead zirconate titanate ceramics, *Appl. Phys. Lett.* **79**:4198.
- Wang, T.H., Fu, R. and Zhang, T.Y., 2001, Fracture behavior of conductive cracks in PZT-4 piezoelectric ceramics, *Proceedings of the 10th International Conference on Fracture*, 2-6 December 2001, Hawaii, USA, CD-ROM Proceedings of ICF10, ICF100475OR.
- Wang, T.H., 2003, Fracture Mechanics Studies of Failures of Lead Zirconate Titanate Ceramics Under Mechanical and/or Electrical Loadings, *PhD Dissertation*, Hong Kong University of Science and Technology.
- Zhang, T.Y., Qian, C.F., and Tong, P., 1998, Linear electro-elastic analysis of a cavity or a crack in a piezoelectric material, *Int. J. Solids Struct.* **35**:2121.
- Zhang, T.Y., Zhao, M.H. and Tong, P., 2002, Fracture of piezoelectric ceramics, *Advances in Applied Mechanics* **38**:147.

- Zhang, T.Y., 2002, Effects of static electric field on the fracture behavior of piezoelectric ceramics, *Acta Mechanica Sinica* **18**:537.
- Zhang, T.Y., Wang, T.H., and Zhao, M.H., 2003, Failure behavior and failure criterion of conductive cracks (deep notches) in thermally depoled PZT-4 ceramics, *Acta Mater.* **51**:4881.
- Zhang, T.Y., Zhao, M.H., and Liu, G.N., 2004a, Failure behavior and failure criterion of conductive cracks (deep notches) in piezoelectric ceramics I – the charge-free zone model, *Acta Mater.* **52**:2013.
- Zhang, T.Y., Liu, G.N., and Wang Y., 2004b, Failure behavior and failure criterion of conductive cracks (deep notches) in piezoelectric ceramics II – experimental verification, *Acta Mater.* **52**:2025.

INCREASING RESISTANCE TO LOW TEMPERATURE AGEING DEGRADATION OF Y-TZP BY SURFACE MODIFICATION

Adrian Feder, Paulina Morcillo, and Marc J. Anglada *

1. INTRODUCTION

The high strength and fracture toughness of yttria doped tetragonal zirconia polycrystals (Y-TZP) make these materials very interesting for some engineering applications. These properties depend on the stability of the different polymorphs of zirconia, which are very sensitive to the quantity and type of stabilizing oxide that is used to decrease the temperature of the tetragonal to monoclinic (t-m) phase transformation. This transformation is martensitic in nature and is accompanied by an increase in volume of nearly 4%. When such transformation becomes active under the high stress field that exists in front of the crack tip, the constrained transformation strain leads to a significant increase in the fracture toughness.¹

The extent of the transformation at the crack flanks is an important parameter, which depends on temperature, the amount and type of stabiliser, and the grain size of tetragonal zirconia. The maximum capability of a material to experience transformation toughening can be expressed as a shielding stress intensity factor, K_s , which is a function of the transformation zone shape, as evaluated by the parameter α , and the zone size, h_0 . It may be expressed as

* Department of Materials Science and Metallurgical Engineering, Universitat Politècnica de Catalunya, ETSEIB, Avda. Diagonal 647, 08028 Barcelona, Spain.

$$K_S = \alpha e^T E f_v \sqrt{h_0} / (1 - \nu) \quad (1)$$

where e^T is the unconstrained dilatational transformation strain, E Young's modulus, ν Poisson's ratio, and f_v the volume fraction of transformed tetragonal phase within the zone.²

Unfortunately, this transformation may also take place spontaneously with the presence of water vapour during ageing at low temperatures (from about 65 to 400 °C) and the phenomenon is referred to as low temperature ageing degradation of Y-TZP. The volume expansion that accompanies the transformation can generate microcracks in the transformed surface, thereby degrading the strength and surface properties of the material [see, for instance, ref. 3].

It is now well established that low temperature ageing degradation is characterised by: a) the transformation proceeds from the surface to the interior; b) when degradation occurs in air, from all constituents of air, only water vapour is responsible; c) both, increasing the amount of oxide stabiliser and decreasing the grains size, can retard the degradation.

Although much research has been performed, the exact mechanism responsible for the spontaneous transformation is not still clear. However, one strategy to increase the resistance of Y-TZP to low temperature ageing degradation is to act upon the microstructure of the material. Along these lines, different methods have been developed such as reduction of grain size, introduction of inert materials, and the increase of either the cation-stabiliser content, or the introduction of an anion-stabiliser such as occurs in nitridation.⁴ The operating mechanism in surface nitridation is the formation of vacancies in the unit-cell of zirconia by high temperature in the presence of nitrogen. This element stabilises the cubic phase of zirconia (c-ZrO₂) by virtue of a partial substitution of oxygen ions (O²⁻) by nitrogen ions (N³⁻) causing in this way the desired vacancies.⁵ This mechanism is identical to the one that allows stabilising the tetragonal and cubic phases of ZrO₂ by the addition of bi- and trivalent cations of, for instance, Mg²⁺ and Y³⁺.

The strength, fracture toughness and stability of nitrided 2.5 mol% of Y-TZP has been recently analysed in air, and also after being in contact with water at 100 °C for long times⁶. The main finding of this work is that a protective surface nitrided layer of non-transformable t'-phase is formed, which is resistant to degradation by water. However, below the t' layer, large tetragonal grains are stabilised by nitrogen and these are easily transformed into the monoclinic structure. The result is that nitrided Y-TZP suffers spontaneous transformation to monoclinic structure by heating to temperatures of about 600 °C in air. This has been associated to the loss of nitrogen, so that the large tetragonal grains become unstable.⁶

In the present paper, it has been studied the feasibility of protecting zirconia from the environment by means of an alumina protective layer produced via a high temperature solid state reaction between zirconia and aluminium nitride in a nitrogen environment. It is shown that the coated Y-TZP that results has an excellent combination of toughness and strength, and also a much higher resistance to environmental slow crack growth. Finally, it is verified that the coated Y-TZP does not suffer from low temperature ageing degradation at 250 °C in air after times of exposure longer than 750 hours.

2. EXPERIMENTAL PROCEDURE

The starting material examined in this work is a zirconia stabilised with 2.5% mole of Y_2O_3 (2.5Y-TZP). Its microstructure consists of tetragonal grains with an average size of $0.3 \mu\text{m}$. The original cylindrical bars of 8 mm in diameter were cut in slices of about 1 mm in thickness. The resulting discs were polished with diamond pastes of 30 and $6 \mu\text{m}$ and then heat treated at 1650°C during 2 hours either in nitrogen with the surface covered with a fine-grain powder of AlN, or just only in air, and the resulting materials are referred to as 2HA and 2H, respectively. The heating and cooling rates applied were both of $20^\circ\text{C}/\text{min}$.

The microstructural evolution resulting from such treatments was assessed through X-ray diffraction, scanning electron microscopy, and Raman microprobe spectroscopy. The fraction of monoclinic phase in the surface of the samples was estimated by the first technique, and the last one was used to calculate the monoclinic fraction present in different places of the fracture surfaces with the help of an equation developed in prior work by calibration with X-ray data.⁷

Microhardness tests were conducted to evaluate the variation in hardness with depth by using an indentation load of 100 g. In addition, Vickers indentations were performed to induce cracks on the surface of the discs by using a load of 294 N and with the objective of estimating the fracture toughness. In prior work, it has been demonstrated that the geometry of cracks introduced by Vickers indentation in 2.5% Y-TZP has a Palmqvist-type shape.⁸ Therefore, the fracture toughness K_{IC} was evaluated by using the following equation,⁹

$$K_{IC} = A(E/H_V)^{2/5}(P/d\sqrt{l}) \quad (2)$$

where E is the Young's modulus, H_V the hardness, P is the applied indentation load, l is the length of the crack, d the semi-diagonal of the indentation imprint, and A is a constant equal to 0.0076.

The mechanical behaviour of the discs has been studied in a miniaturised ball-on-three-balls flexure-testing device. The strength of the discs, σ_{max} , can be obtained by using the equation proposed by Börger et al.¹⁰

$$\sigma_{\text{max}} = (fP_{\text{max}})/t^2 \quad (3)$$

where P_{max} is the fracture load, t the thickness of the discs, and f is a calibration factor given by the following expression:

$$f(t/R, R_a/R, \nu) = c_0 + \{[c_1 + c_2(t/R) + c_3(t/R)^2 + c_4(t/R)^3]/[1 + c_5(t/R)]\}[1 + c_6(R_a/R)] \quad (4)$$

The parameters c_i ($i=1 \dots 6$) depend on the coefficient of Poisson¹⁰, R is the diameter of the discs and R_a is the diameter of the circle defined by the centres of the three balls. In the present case, R and R_a are 4 and 3 mm, respectively, and the diameter of the balls is 2 mm. The tests were carried out in air at two different constant load rates of 200 y 10 N/s with the aim to assess the influence of the laboratory environment on the strength of the heat treated materials. In order to evaluate the resistance to low temperature degradation, the discs were subjected to ageing in air at 250°C for times longer than 750 hours.

3 RESULTS AND DISCUSSION

3.1. Microstructure

The microstructures of the starting material, 2.5Y-TZP, and of 2H are depicted in Fig. 1. The analysis by XRD (Fig. 2) confirms that the original material is formed by only tetragonal grains, while in 2H there is a duplex microstructure of tetragonal and cubic grains with average size much larger than the original tetragonal grains (see Table 1). For 2HA, it appears a surface layer of approximately $3.9\ \mu\text{m}$ in thickness (Fig. 3) as a result of the high temperature reaction of Y-TZP with AlN powder. The analysis by XRD of the surface of 2HA shows the existence of Al_2O_3 , as well as t and c-ZrO₂.

According to Bayern and Mocellin¹¹, a solid state displacement reaction takes place in the ZrO₂-AlN system at the temperature studied:

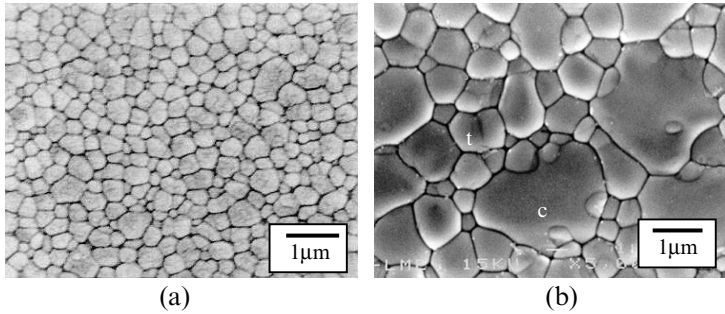


Figure 1. Micrographs showing microstructures of Y-TZP material (a) and Y-TZP heat treated at 1650 °C during 2 hours in air (b); t and c refer to tetragonal and cubic grains respectively.

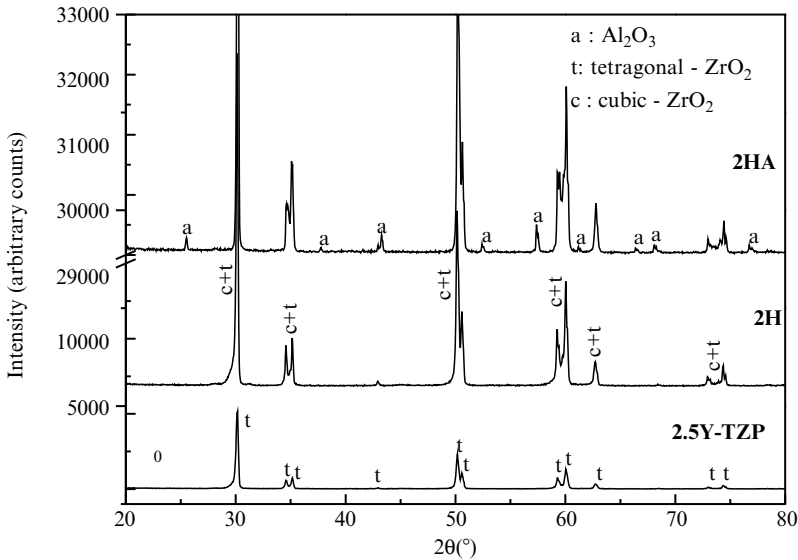
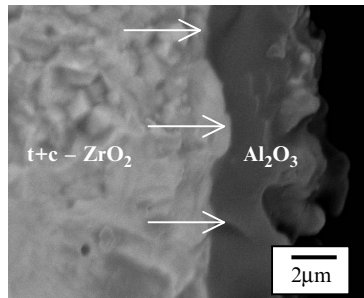
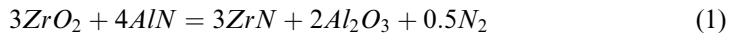


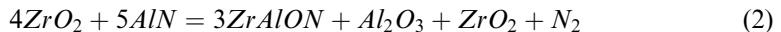
Figure 2. X-ray diffraction patterns of the surface of the materials investigated.

Table 1. Layer thickness and grain size of the materials studied.

| Material | Layer Thickness (μm) | D_g Surface (μm) | D_g Interior (μm) |
|----------|-----------------------------------|--|--|
| 2.5Y-TZP | - | 0.3 ± 0.1 | 0.3 ± 0.1 |
| 2H | - | 1.8 ± 0.1 t-ZrO ₂ 4.4 ± 0.1 c-ZrO ₂ | 1.8 ± 0.1 t-ZrO ₂ 4.4 ± 0.1 c-ZrO ₂ |
| 2HA | 3.9 ± 0.4 | 16 ± 4 | 1.8 ± 0.3 t-ZrO ₂ 4.8 ± 0.1 c-ZrO ₂ |

**Figure 3.** Microstructure of a cut perpendicular to the surface of 2HA.

However, we have not detected ZrN, but only Al₂O₃, and t- and c-ZrO₂. For times of reaction of 1 hour, from X-ray diffraction measurements we have observed the presence of ZrAlON, ZrN, Al₂O₃, and ZrO₂, but for 2 hours, the first compound could not be detected. It should be added that ZrAlON, was also detected by Toy and Savrun¹², which proposed a different reaction between ZrO₂ and AlN:



The reason for these different findings with respect to our results may lie in the fact that in the present experiments there is a large amount of unreacted zirconia that may be a large source of oxygen to oxidise either ZrN or ZrAlON after long times at 1650 °C.

The microstructure of 2HA below the surface layer is practically identical to that originated at the same temperature but only in contact with air (2H). This has been previously described in detail by Casellas et al⁸. It is worthwhile noticing that under these treatments it is possible to retain grains of t-ZrO₂ of average size as large as 3 μm at room temperature.

3.2. Hardness and Fracture Toughness

The microhardness along the depth of the specimens does not change, and it is very similar for all materials. On the surface, the influence of the alumina layer on the

value of the microhardness measured is negligible, because of the relatively high load used and the small thickness of the layer. In the interior of the material, the microhardness for 2H and 2HA are identical, as expected because of similar microstructures.

From Table 2 it can be seen that the length of the indentation cracks nucleated at the surface of 2H and 2HA are much shorter than in Y-TZP, and this corresponds to an increase in K_{IC} of more than 30 % in the former materials. This value of fracture toughness is related to the microstructure developed below the surface layer in 2HA. That is, K_{IC} is not significantly affected by the possible influence of residual stresses in the layer, because similar value of fracture toughness is obtained when the surface thin layer is removed by polishing. Then, the increase in fracture toughness in 2HA with respect to Y-TZP is also due to the more transformable duplex microstructure that develops during the high temperature reaction. This is confirmed by Raman spectroscopy analysis of the fracture surfaces where there are zones largely transformed (up to 50 % of m-ZrO₂), while in 2.5Y-TZP the amount of transformation is very limited.

The nominal expected residual stress in the alumina layer can be estimated by considering that it is very much thinner than the substrate of stabilised zirconia, so that a simplified expression for the biaxial stress (σ_A) developed in the film can be used:

$$\sigma_A = -E_A(\alpha_A - \alpha_Z)\Delta T/(1 - \nu_A) \quad (5)$$

where the average expansion coefficients of alumina and zirconia, α_A and α_Z , are taken as 11.0 and 8.91×10^{-6} K, respectively, and the bulk elastic modulus, E_A , and Poisson's ratio, ν_A , of alumina used here are 400 GPa and 0.23, respectively. By using these bulk values for these properties, the value of σ_A induced by a change in temperature from 1650 °C to room temperature can be estimated, and this gives a value of about 1.6 GPa. Since this residual tensile stress is concentrated in a very thin layer at the surface, its contribution to the residual stress intensity factor of an indentation semicircular crack, which is comparatively much larger, can be estimated as,

$$K_R \approx \beta\sigma_{AS}/\sqrt{l} \quad (6)$$

where β is a factor close to unity, and s is the thickness of the alumina layer. One can see that K_R is appreciably smaller than the fracture toughness, since equation (3) gives values for K_R of about 0.5 MPa m^{1/2}. This explains that not significant differences are found for the fracture toughness of 2HA and 2H.

Table 2. Crack lengths (l) and fracture toughness (K_{IC}) measured by indentation at the surface and in the interior of the discs.

| Material | l (μm) surface | K_{IC} (MPa m ^{1/2}) surface | l (μm) interior | K_{IC} (MPa m ^{1/2}) interior |
|----------|-------------------------------|--|--------------------------------|---|
| 2.5Y-TZP | 174 ± 2 | 4.9 ± 0.1 | – | – |
| 2HA | 98 ± 8 | 6.5 ± 0.2 | 102 ± 4 | 6.4 ± 0.1 |
| 2H | 110 ± 10 | 6.2 ± 0.4 | – | – |

3.3. Biaxial Fracture Strength

The biaxial fracture strength (σ_{\max}), measured by a miniaturised ball-on-three-balls flexure-testing device and by using equation (3) and (4), is presented in Fig. 4 for two different loading rates, of 10 and 200 N/s. It can be noticed that the strength for the highest loading rate is hardly different for the different materials. However, for the lower loading rate there is a very clear decrease in strength for Y-TZP as well as for 2H. On the contrary, 2HA keeps its strength constant for both loading rates and this is an indication of a stronger resistance to environmental slow crack growth, which may be attributed to the alumina surface layer.

Fractographic analysis of the broken specimens shows important differences in the fracture path for the different conditions. Thus, the crack path is completely intergranular in Y-TZP, while in 2H and 2HA there is a mixture of intergranular (tetragonal grains) and transgranular (cubic grains) crack paths.

It should be noticed that the strengths of 2H and 2HA are similar to that of Y-TZP in spite of the much smaller grain size of the latter. A simple explanation for this can be given by looking to the values of strength and fracture toughness of Y-TZP, 2H and 2HA. Using the values for these parameters given in Table 2 and in Fig.4, if R-curve effects are neglected and the plateau toughness is used in the calculations, it is possible to estimate that the critical crack sizes for Y-TZP and 2H are about 15 μm and 25 μm , respectively. This difference in the critical defect sizes may exist since the grain size has increased during exposure at 1650 $^{\circ}\text{C}$ by a factor of near 10. However, at least in Y-TZP, it is clear that the origin of fracture are processing defects, such as porous. Then, if this was still true for 2H, so that no significant increase in defect sizes occurred at 1650 $^{\circ}\text{C}$, there would be only two possibilities to explain the larger critical defect size in 2H. One is that natural critical cracks are too small for developing plateau fracture toughness before fracture, and the other possibility is that transformation takes place locally before fracture at stress concentrations.

Another point worthwhile considering is the influence of residual stresses in the surface layer on the strength of 2HA. Because of the difference in thermal expansion coefficients of alumina and zirconia, tensile stresses should be present in the alumina layer. However, it seems that these do not have an important effect on the strength.

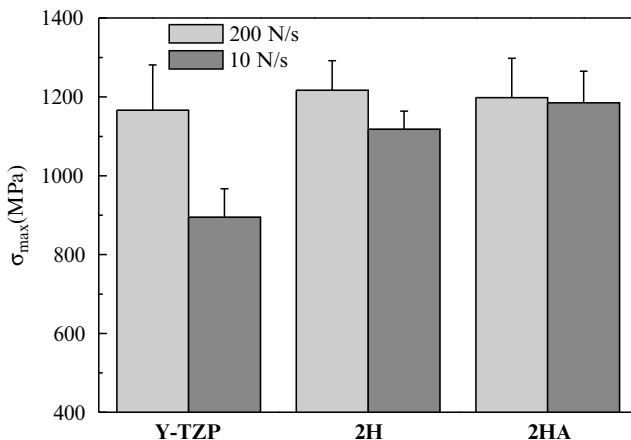


Figure 4. Biaxial fracture strength of different materials investigated.

The reason lies in that possible defects in the alumina layer are necessarily much smaller than the critical defect size for 2H so that the residual stress should be extremely high to have a significant effect on the strength. It is important to emphasise that in 2HA, besides modifying the surface by coating, there is an increase in the fracture toughness whose origin is related to an increase in the fracture toughness of the bulk material.

4. LOW TEMPERATURE AGING DEGRADATION

The change in biaxial strength of discs of 2.5Y-TZP, 2HA and 2H is shown in Fig. 5 in terms of time for ageing at 250 °C in air. It can be observed that for both uncoated materials there is a reduction of σ_{\max} with ageing time, and this is very strong for 2H. On the contrary, the strength of 2HA does not change at all during the range of time studied, in spite that 2HA, in the bulk, has a similar microstructure as 2H. It is then very clear that the alumina surface layer protects the base material to environmental low temperature degradation. The fact that 2H is more susceptible to low temperature ageing degradation can be attributed to the higher transformability of the tetragonal grain because of its larger grain size.

By the above high temperature reaction of AlN with Y-TZP it is possible to produce a layer that protects Y-TZP from the environment, making the material inert to low temperature ageing degradation. In addition, the resulting material, 2HA, does not only have the same biaxial strength as Y-TZP, but also a higher fracture toughness.

In order to correlate the decrease in strength with the appearance of monoclinic phase at the surface, the presence of this phase was checked by X-ray diffraction during ageing. From Fig. 6 it can be noticed that there is an increase in the volume fraction of the monoclinic phase on the surface of Y-TZP and 2H during ageing while this phase is not detected on the surface of 2HA. This is consistent with the variation of the biaxial strength observed in Fig. 5. Finally in Fig 7 (a-c) it can be noticed the

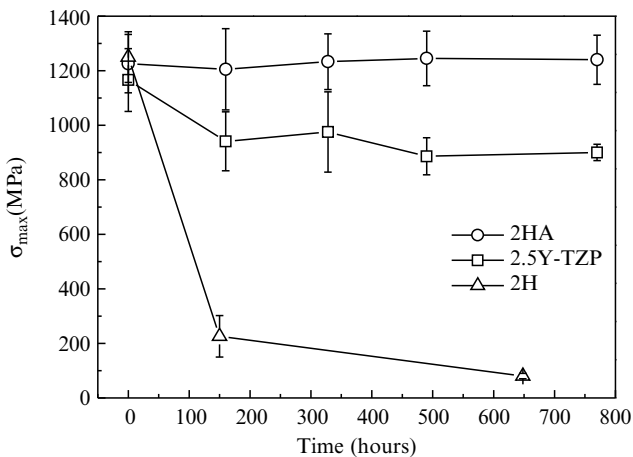


Figure 5. Change in biaxial strength with ageing time at 250°C.

complete cracked surface of a specimen of 2H after ageing for 150 hours at 250 C. The easy activation of the t-m transformation at the surface, because of the high transformability of the large t-ZrO₂ grains, has led to the formation of micro and macro-cracks which have propagated to the interior affecting very strongly the strength. It can be seen that the microcracks propagate through the tetragonal grains, since these are responsible for the expansion that takes place with the transformation (Fig. 7b).

4. SUMMARY AND CONCLUSIONS

It has been investigated the resistance to low temperature aging degradation of 2.5Y-TZP as well as of the materials that result after heat treatment at 1650 °C in air, and after formation of a thin layer of alumina by reaction with AlN powder in a nitrogen atmosphere. In both cases, the strength hardly changes and the fracture toughness increases because it is controlled by the high transformability of the coarser tetragonal grain size that it is induced in the bulk. The larger tetragonal grain size makes the material heat treated in air more sensitive to low temperature ageing degradation

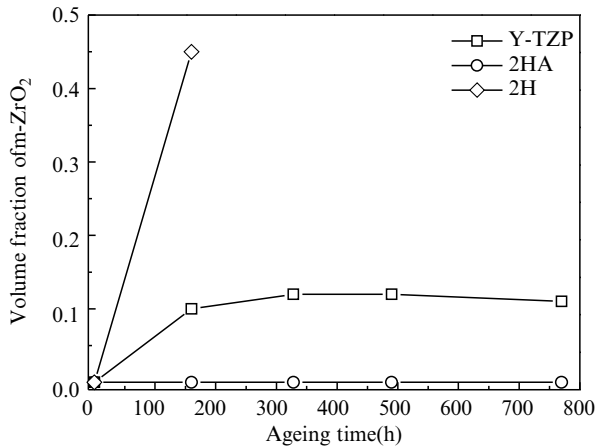


Figure 6. Change in volume fraction of m-ZrO₂ with time at 250 °C.

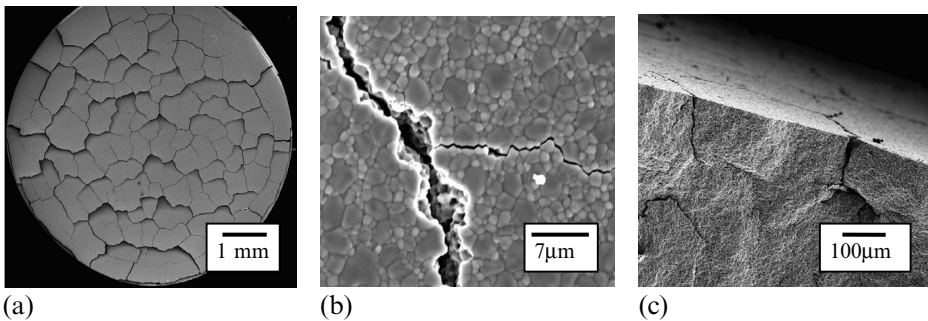


Figure 7. Micrographs of the sample 2H aged at 250 °C: surface of the disc (a); micro- and macro-cracks formed due to t-m phase transformation (b) and fracture surface showing micro- and macro-cracks formed near the surface.

than the starting Y-TZP. By contrast, the surface layer of alumina that is formed after high temperature reaction has a large resistance to t-m transformation during ageing at 250 °C in air, as well as an increased resistance to environmental subcritical crack growth. Then, the final result is a material with high strength, high fracture toughness and inert to low temperature ageing degradation.

ACKNOWLEDGEMENTS

The authors gratefully acknowledge for its financial support to the MCYT under grant No. MAT-99-0781, to DURSI (2001SGR-00229), and also to CIDEM for supporting CIEFMA (XARXA IT).

REFERENCES

1. D.J. Green, R.H.J. Hannink, M.V. Swain, Transformation Toughening of Ceramics. Florida: CRC Press Inc., (1989).
2. R.M. McMeeking and A.G. Evans, Mechanics of transformation toughening in brittle materials, *J. Am. Ceram. Soc.* 65 242–246 (1982)
3. F.F. Lange, G.L. Dunlop and B.I. Davis, Degradation during aging of transformation-toughened ZrO_2 - Y_2O_3 materials at 250 °C, *J. Am. Ceram. Soc.* 69 [3] 237–40 (1986).
4. T.J. Chung, J.S. Lee, D.H. Kim and H. Song, Surface nitridation of yttria-doped tetragonal zirconia polycrystals (Y-TZP): Microstructural evolution and Kinetics, *J. Am. Ceram. Soc.* 82 [11] 3193–99 (1999).
5. N. Claussen, R. Wagner, L. J. Gauckler and G. Petzow, Nitride-stabilized cubic zirconia, *J. Am. Ceram. Soc.* 61 [7–8] 369–70 (1978).
6. A. Feder, J. Alcalá, L. Llanes and M. Anglada, On the stability of nitrided Y-TZP at high temperature, to be published in *J. Eur. Ceram. Soc.* (2003).
7. D. Casellas, F.L. Cumbreira, F. Sánchez-Bajo, W. Forsling, L. Llanes and M. Anglada, On the transformation toughening of Y-ZrO₂ ceramics with mixed Y-TZP/PSZ microstructures, *J. Eur. Ceram. Soc.* 21 765–77 2001.
8. D. Casellas, A. Feder, L. Llanes and M. Anglada, Fracture toughness and mechanical strength of Y-TZP/PSZ ceramics, *Scripta Mater.* 45 213–20 (2001).
9. K. Niihara, R. Morena, D. P. H. Hasselman, Evaluation of K_{IC} of brittle solids by the indentation method with low crack-to-indent ratios, *J. Mat. Sci. Lett.* 1 13–16 (1982).
10. A. Borger, P. Supancic and R. Danzer, The ball on three balls test for strength testing of brittle discs: stress distribution in the disc, *J. Eur. Ceram. Soc.* 22 1425–1436 (2002).
11. G. Bayer and A. Mocellin, Displacement reaction sintering in the system ZrO_2 -AlN, *Rev. Chim. Min.* 23 80–87 (1986).
12. C. Toy and E. Savrun, Novel composites in the aluminum nitride-zirconia and -hafnia systems, *J. Eur. Ceram. Soc.* 18 23–29 (1998).

INDEX

- Acoustic emission, 21
- Alcohols, 104
- Alumina, 29, 65, 69, 78, 123, 177, 185, 199, 227, 298, 356, 366, 399, 401, 540, 574
- ASTM, 499, 515
- Atomic force microscopy, 1

- Biaxial strength, 79
- Bio-active, 388
- Bi-material interface, 376
- Brick and mortar structure, 375
- Brittleness, 246

- Carbon, 31
- Carbon composite, 31
- Ceramic coatings, 28, 437
- Ceramic matrix composites, 203, 221, 233, 287, 297, 307, 375
- Cohesive, 360
- Chevron notch, 513
- Compact tension, 612
- Conductive cracks, 609
- Crack bridging, 310, 399
- Crack growth, 8, 135, 173, 387, 404, 537, 579
- Crack imaging, 6
- Crack path, 375, 139
- Crack velocities, 408
- Creep, 203, 221, 275, 331

- Damage, 211, 280, 357
- Disk-on-rod test, 366
- Double torsion, 390, 401

- Elasto-plastic, 93
- Electric field effects, 297
- Electro ceramic, 1, 411
- Elevated temperature, 121, 451

- Fatigue, 142, 233, 399, 558
- Ferro elastic, 471
- Film, 438
- Finite elements, 317, 377, 414, 613
- Flexible displays, 597
- Flexure test, 61, 81, 339, 453, 488, 501, 532
- Fragmentation, 77, 353

- Glass, 60, 77, 101, 121, 135, 149, 597
- Glassy carbon, 93
- Glass composites, 240, 245, 263
- Granular microstructure, 354
- Graphite, 337

- Hardness, 13, 69, 103, 126, 149, 192, 629
- Hertz crack, 443
- Hydroxyapatite, 387

- Impact, 437, 439
- Indentation, 13, 21, 43, 57, 79, 93, 103, 113, 121, 149, 289, 440
- Indentation fracture, 21, 57, 88, 113, 121, 297, 440
- Indentation size effect (ISE), 13, 149
- Instrumented hardness, 69
- Interface toughness, 31
- Internal fraction, 113
- Ion implanting, 57

- Knoop indentation, 149

- Lateral crack, 447

- Metal particles, 245
- MgO, 287
- Micro-fracture, 365
- Micromechanical simulation, 474
- Mixed mode, 451
- Monte Carlo Simulation, 584, 625

- Nano composites, 191
- Nano impact, 43
- NASA Cares, 555
- Nano indentation, 13, 23, 43, 93
- Nano scratch, 43
- Nanostructure, 43
- Natural shells, 375
- Numerical model, 354

- Piston-on-ring test, 367
- Plasma spray, 437, 451

- Porosity, 427
- Post fracture tensile test, 307
- Proof testing, 555
- PSZT, 485, 492
- PZT, 609

- R-curves, 182, 197, 403
- Reliability, 485, 555
- Residual stress, 192, 543

- Scratch test, 101, 121
- Silica, 44, 153
- Silicon, 29, 43
- Silicon carbide, 29, 177, 211, 221, 275, 413, 444, 531
- Silicon nitride, 327, 413, 444, 499, 536
- Size effect, 13, 149, 337, 412
- Slow crack growth, 175, 558, 579
- Standard reference material, 499, 531
- Strength distribution, 412, 558
- Stress corrosion, 175, 536
- Sub-critical crack growth, 388

- Thermal ageing, 263, 625
- Thermal barrier coating, 451
- Thermal shock, 263, 365, 566
- Thermal stress, 368
- Thin films, 21
- Threshold stress intensity factor, 392
- Titanates, 4, 60, 287, 297, 471, 485, 609, 625
- Trapped crack model, 254
- True hardness, 17

- Ultrasonics, 1

- V-K diagram, 391, 399, 184
- Vickers indentation, 149

- Weibull, 104, 144, 370, 413, 485, 558, 579, 604, 615

- Y-TZP, 625

- Zirconia, 13, 60, 177, 266, 437, 451, 485, 627
- ZnO, 411, 37